STEFANO BOTTACCHI

Multi-gigabit Transmission Over Multimode Optical Fibre

Theory and Design Methods for 10GbE Systems

WILEY

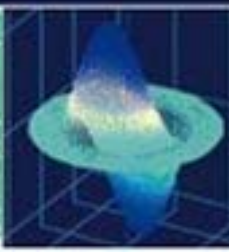

MULTI-GIGABIT TRANSMISSION OVER MULTIMODE OPTICAL FIBRE

Multi-Gigabit Transmission over Multimode Optical Fibre: Theory and Design Methods for 10GbE Systems Stefano Bottacchi
 ISBN: 0-471-89175-4

MULTI-GIGABIT TRANSMISSION OVER MULTIMODE OPTICAL FIBRE

THEORY AND DESIGN METHODS FOR 10GbE SYSTEMS

Stefano Bottacchi

Formerly with Infineon Technology AG,
Fiber Optic, Concept Engineering, Germany

John Wiley & Sons, Ltd

John Wiley & Sons Ltd, The Atrium, Southern Gate, Chichester,
West Sussex PO19 8SQ, England

Telephone (+44) 1243 779777

Email (for orders and customer service enquiries): cs-books@wiley.co.uk
Visit our Home Page on www.wiley.com

Other Wiley Editorial Offices

John Wiley & Sons Inc., 111 River Street, Hoboken, NJ 07030, USA

Jossey-Bass, 989 Market Street, San Francisco, CA 94103-1741, USA

Wiley-VCH Verlag GmbH, Boschstr. 12, D-69469 Weinheim, Germany

John Wiley & Sons Australia Ltd, 42 McDougall Street, Milton, Queensland 4064, Australia

John Wiley & Sons (Asia) Pte Ltd, 2 Clementi Loop #02-01, Jin Xing Distripark, Singapore 129809

John Wiley & Sons Canada Ltd, 6045 Freemont Blvd, Mississauga, ONT, L5R 4J3, Canada

Wiley also publishes its books in a variety of electronic formats. Some content that appears in print may not be available in electronic books.

Library of Congress Cataloging-in-Publication Data:

Bottacchi, Stefano.
Multi-gigabit transmission over multimode optical fibre : theory and design methods for 10GbE systems / Stefano Bottacchi.
p. cm.
Includes bibliographical references and index.
ISBN-13: 978-0-471-89175-8 (cloth : alk. paper)
ISBN-10: 0-471-89175-4 (cloth : alk. paper)
1. Optical communications. 2. Fiber optics. I. Title.
TK5103.59.B68 2006
621.382′7 – dc22

2006014654

British Library Cataloguing in Publication Data

A catalogue record for this book is available from the British Library

ISBN-13: 978-0-471-89175-8
ISBN-10: 0-471-89175-4

Typeset in 9/11pt Times by Laserwords Private Limited, Chennai, India
Printed and bound in Great Britain by Antony Rowe Ltd, Chippenham, Wiltshire
This book is printed on acid-free paper responsibly manufactured from sustainable forestry in which at least two trees are planted for each one used for paper production.

To my wife Laura
and my daughters
Francesca and Alessandra

Contents

Preface

Fast-growing Ethernet demands in the metropolitan area networking have very recently caused the IEEE 802.3 Standardization Committee to develop new transmission system specifications for end-user 10GbE applications over existing multimode optical fiber with a target reach of at least three hundred meters. However, high-speed transmission at multigigabit data rates, combined with the existing multimode optical fiber infrastructure, have led to relevant optical pulse distortion even after only one hundred meters of link length, consequently demanding proper compensation techniques of the time dispersion.

In order to understand better how simultaneous multipath optical pulse dispersion, intersymbol interference (ISI) and several noise sources affect the multigigabit transmission performances over multimode fibers, a detailed analysis of the optical propagation mechanisms has been developed thoroughly in this book. The general theoretical approach favors mathematical modeling, which is better suited to the modular structure of every analytical link simulator. After introducing the physical concepts and the mathematical modeling, each chapter reports extensive working examples based on the developing software Matlab® 7.1 from The MathWorks, Inc. However, despite using an original theoretical approach, this book would not have been complete without the extensive experimental verification reported in the last part of this work, which refers to the pioneering transmission experiments of 10GbE over legacy multimode fibers recently performed at the Fiber Optic Laboratory of Infineon Technologies AG, Berlin.

Multigigabit transmission over multimode optical fiber could never be achieved without implementing proper pulse dispersion equalization techniques. The electronic dispersion compensator (EDC) emerges today as the key factor in achieving the required performance in practical implementations and has accordingly a very relevant role to play in the book. The theoretical approach followed identifies first the ideal inverse linear filtering as the reference compensation method for every pulse dispersion mechanism, in order to qualify and compare more sophisticated equalizing solutions. Although it is well known that inverse linear filtering does not represent a suitable solution, especially under severe signal degradation, its simple and ideal compensation principle makes this filter well suited as the reference dispersion compensator.

The most promising electronic dispersion compensator (EDC) available at the 10GbE data rate and suitable for mass volume access networking is based on the dispersion feedback equalizer (DFE). The theory and the modeling of the dispersion feedback equalizer are presented, based on the minimum mean square error criteria as originally proposed by J. Salz at the beginning of the 1970s. Several numerical calculations of the optical channel metrics follow. It is outside the scope of this book to present equalization techniques based on different approaches like the maximum likelihood sequence equalizer (MLSE). However, the main effort has been spent in identifying ideal system performances, design criteria and limitations inherent to different pulse dispersion mechanisms occurring in multimode optical fibers in order to achieve the required transmission performances.

Stefano Bottacchi
Milan

Book Organization

The book is divided into two parts. The first part deals with the theory and the modeling of the multimode optical fiber propagation, leading to useful closed-form equations well suited for analytical simulation purposes. Particular attention has been devoted to the theoretical modeling of the multimode fiber impulse response, including both the chromatic and the modal responses. A mathematical modeling approach has been preferred in order to arrive at a set of equations suitable for a multimode optical fiber transmission link simulator. The Gaussian response model has been detailed with several numerical examples. The second part deals instead with the optoelectronic subsystems encountered in the implementation of the multigigabit transmission system using the multimode optical fiber. The optical transmitter, the optical receiver and, in particular, the electronic dispersion compensator have been exhaustively analyzed and specified in order to give to the reader the essential directions for proceeding further in the system design optimization. Several experimental results have been added at the end of the book in order to emphasize the open issues and the distance still encompassing the performances required for massive deployment and the state-of-the-art experimental laboratory implementation of 10GbE transmission over multimode optical fibers.

Looking into a more detailed organization of the book, the first chapter serves as the general introduction to the field and overviews almost all aspects developed in subsequent chapters. In particular, Chapter 1 introduces the basic transmission methods and issues encountered when sending multigigabit data over multimode optical fibers. Chapter 2 presents an original analysis of a metallic-based transmission waveguide, leading to different response behaviors used for comparison purposes with the simple Gaussian response model of multimode optical fibers. Chapter 3 to Chapter 7 deal with the propagation theory and modeling of the multimode fibers. Chapter 3 reviews the multimode fiber theory by introducing the principal concepts, parameters and mathematical tools needed for the subsequent development. Chapter 4 presents the theory of the chromatic dispersion in multimode fibers assuming a general multimode source spectrum profile and an arbitrary group delay distribution. The developed theory leads to a closed-form mathematical expression for the chromatic impulse response. Chapter 5 approaches the theory of the modal dispersion assuming a general group delay distribution and modal excitation. The general expression derived for the impulse response includes both embedded effects of chromatic and modal dispersions. Several Matlab® codes written ad hoc provide interesting and original simulation cases for underlying basic physical principles and interaction mechanisms occurring with the total pulse dispersion. Chapter 6 reports the Gaussian model of the multimode fiber response, including benefits and limitations of this easy mathematical approach. Several useful formulas and numerical examples close the chapter. Chapter 7 introduces some important topics encountered in high-speed transmission using multimode fiber. Computer modeling provides interesting examples of impulse response compositions including pulse precursors and postcursors. The modal theory of the step-index fiber is presented as the simpler case for introducing launching condition issues in more complex graded refractive index fibers.

The second part of the book starts with Chapter 8, which introduces the characteristics and gives modeling suggestions for the principal transmission system components. Several optical waveforms are considered and compared as potential light sources for multigigabit transmission. The general architecture of the optical receiver is then analyzed, including the characterization of topic receiving filter models, and a short theoretical approach is given to the intersymbol interference pattern. Chapter 9 presents the theoretical background for the equalization problem in multimode fiber transmission systems. The chapter starts by introducing the noise analysis and the error probability formulation in optical receivers. The ideal inverse filter is then proposed as the reference linear equalizer and the related noise enhancement factor is defined in order to make a quantitative comparison among different solutions. The eye diagram closure and more generally the optical power penalty are among the most relevant engineering tools used for assigning quantitative figures of merit to different equalizer structures. Chapter 10 presents the theory of the decision feedback equalizer as the basic building block of the electronic dispersion compensator solution today, and is proposed as the best solution for achieving 10GbE access networking over the legacy multimode fiber infrastructure. The concept of the channel metric as the measure of the optical power penalty formed by the linear transmission channel is then introduced. Quantitative measures of the linear channel performance, like PIE-L and PIE-D, are defined and compared with the power penalty due to noise enhancement of the ideal inverse linear equalizer. The last Chapter 11 is completely devoted to reporting the transmission experiments performed at the Fiber Optic Laboratory, Infineon Technology AG, Berlin, during 2003–2005. Details of the pulse responses of benchmark multimode fiber and the eye diagram measured at the 10GbE data rate are presented and correlated with system performances. New observations regarding the polarization-induced pulse distortion in multimode fiber links excited with offset launching are then presented. A first theoretical justification of the observed alterations is also approached. The last section reports the first EDC-based multigigabit transmission experiments carried out over multimode fibers. Transmission system performances including sample EDCs are finally evaluated by means of measured bit error rates.

Acknowledgments

The author is personally responsible for all the contents of this book, but feels personally indebted for the beautiful environment and the intellectual creative atmosphere he found at the former Concept Engineering Department of Fiber Optic, Infineon Technologies AG, Berlin, where most of the book content has been conceived. In particular, he is pleased to thank personally former colleagues Mr Jens Fiedler and Dr Joerg Kropp for providing stimulating discussions and leading experiments that guided almost all of the transmission measurements presented in this book.

Finally, yet importantly, the author is grateful to his family and parents who helped during the long development of the book with unlimited trust and patience.

Stefano Bottacchi
Milan

1

Introductory Concepts

Components and Design Issues for a Multigigabit Link over Multimode Fiber

1.1 Introduction

The recent huge demand for Multigigabit Ethernet (10GbE) and Fiber Channel (FC) standard applications in metropolitan areas has very rapidly pushed up the need for broader modulation frequency ranges in deployed multimode optical fibers. Since the beginning of the Gigabit Ethernet (GbE) in 1997, a great effort has been devoted to qualify transmission performances of standard multimode fiber (MMF) deployed in buildings, offices and everywhere around metropolitan areas. Multimode fibers had been developed in the past 20 years and an increase in optical fiber manufacturing and very different manufacturing procedures led to a very different transmission behavior and modal bandwidth optimization. At the beginning of the optical fiber transmission era, about 30 years ago, multimode fibers were deployed for use with light emitting diodes (LED) and low-bit-rate-based optical links, usually operating below 200 Mb/s. Since the advent of the Gigabit Ethernet during the late 1990s, the expected bit rate today has increased demand for multigigabit Internet routing in the metropolitan area, but this may not be possible due to the inherently slow transmission properties of the deployed multimode optical fibers. The transmission speed is no more than 1 Gb/s but 10 Gb/s and beyond are today requested for MMF links from most of the service providers.

Most of the installed multimode fiber base was manufactured during the 1980s and early 1990s, when the multimode optics was conceived essentially for subgigabit transmission applications, using surface emitting LED and large area PIN diodes operating mainly at 850 nm. High-speed optical transmission was concentrated on single-mode fiber technology where high transmission capacity easily allowed 10 Gb/s transmission over several tens of kilometers. High-speed telecommunication was concentrated mainly in the backbone market, where huge transmission capacities were needed to link large and faraway metropolitan areas. As soon as the Internet started to grow more quickly in the local area network, there was a need to increase the transmission capacity of the existing fiber infrastructure. That layout was structured with multimode fiber of use only for previous low-speed applications and the need for new engineering challenges in utilizing deployed multimode fibers at 10 Gb/s appeared as one of the major tasks facing the datacommunication industry. Efficient light sources such as the vertical cavity surface emitting laser (VCSEL) are suitable candidates for high-speed direct modulation, but they require new investigations on the effect of launching conditions

Multi-Gigabit Transmission over Multimode Optical Fibre: Theory and Design Methods for 10GbE Systems Stefano Bottacchi
 ISBN: 0-471-89175-4

on multimode fiber propagation behavior. The conventional multimode fiber coupling technology must be revised to take account of the new laser launching and multigigabit data rate, including fusion splices, connectors and optical couplers. Because of the complexity and the relevance of these applications, the new standard 10BASE-LRM is under development by the IEEE802.3ae committee.

1.2 Multimode Optical Fibers

Optical fibers have been widely deployed to serve extremely high performing transmission channels for both telecommunication and datacommunication applications since their first industrial manufacture in the mid seventies. For almost thirty years, optical fibers have represented the best transmission channel technology available for either long-reach backbone transmission or large local area distribution purposes. In order to serve a multigigabit transmission medium every wired transmission channel should have simultaneously low attenuation and high bandwidth per unit length. Optical fiber meets both of these requirements. Optical attenuation in fact ranges between 0.2 and 2.0 dB/km while the modulation bandwidth is inherently almost infinite in single-mode fibers for most telecommunication applications. In general, it is not possible to specify just one number to characterize either the attenuation or the modulation bandwidth of optical fiber because both parameters are strongly influenced by the operating wavelength and optical waveguide structure. For example, in the limiting case of single-mode optical fiber linearly excited by a highly coherent externally modulated laser source the link bandwidth is limited only by the modulating signal bandwidth and by fiber polarization mode dispersion. Under these conditions, ITU-T STM16 transmission at 2488 and 320 Mb/s can reach more than 1000 km at 1550 nm without being particularly limited by pulse dispersion of the bandwidth limitation. However, even the extremely low attenuation of less then 0.2 dB/km available at 1550 nm would require a link budget of 200 dB in order to be connected. This extremely high attenuation can be overcome by using optical amplifiers with a repetition span of about 25 dB between each of them.

The picture is completely different when using multimode optical fibers. Before entering into more detail, it is useful first to describe the waveguide properties of optical fibers. The optical fiber is a cylindrical dielectric waveguide where the guiding principle is achieved using the refractive index difference between the inner dielectric region, the core and the outside dielectric region, the cladding. Making the refractive index slightly higher in the core than in the cladding ensures optical waveguide operation in a specific wavelength range.

The optical fiber dealt with here is made of a silica glass composition and both the core and the cladding must be carefully doped and processed in order to obtain the exact refractive index profile and high-purity material needed to achieve simultaneously very low dispersion and attenuation. The low attenuation wavelength range is achieved by choosing the correct silica glass to place the dielectric optical waveguide structure within the near-infrared region, $820\,\text{nm} < \lambda < 1620\,\text{nm}$. In this wavelength range, the optical fiber will perform in the single-mode or multimode regimes depending on the radius a of the inner core region. Standard single-mode fibers have the core diameter close to $a = 4\,\mu\text{m}$ or less, while standard multimode fibers have a much larger core radius, either $a = 25\,\mu\text{m}$ or $a = 31.25\,\mu\text{m}$. Other factors affect the modal capability of the fiber, but essentially the core diameter is mainly responsible for the different kinds of waveguide behavior. Figure 1.1 shows a schematic drawing of the multimode fiber geometry.

This book will deal exclusively with multimode fibers, so cylindrical dielectric waveguides made of doped silica glass with a core diameter of either $50\,\mu\text{m}$ or $62.5\,\mu\text{m}$ will be referred to implicitly. These multimode fibers are specified by ISO/IEC 11801 and ITU-T G.651 standards. The multimode regime requires a strong bandwidth limitation compared to single-mode ones. This is essentially because of the multipath propagation and the related group delay per unit length spreading among

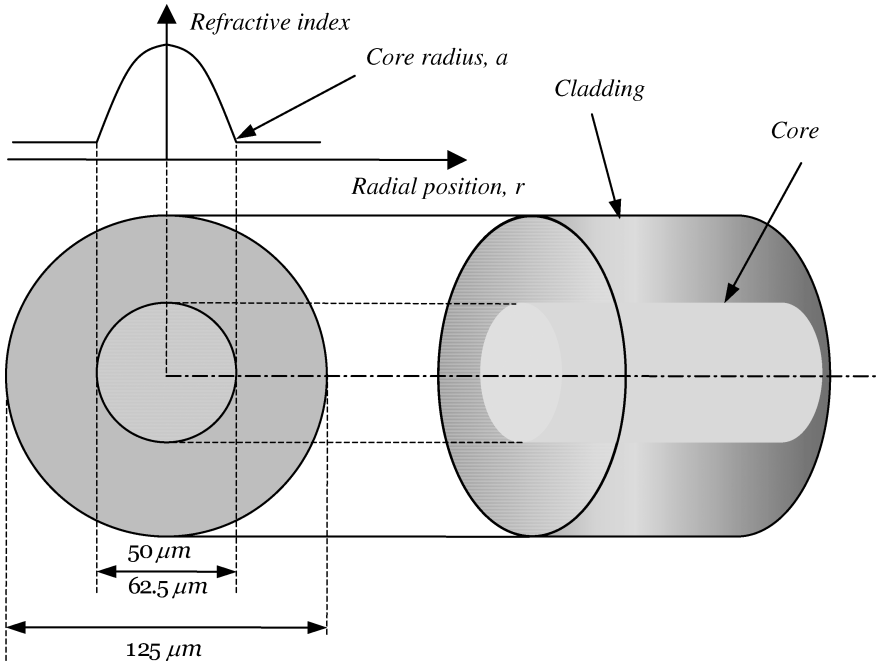

Figure 1.1 Multimode fiber geometry

all allowed and excited modes. The refractive index profile is the only functional parameter that sets the electromagnetic properties of every dielectric waveguide. In order to compensate for different mode delays it is possible to design a graded refractive index profile. Accordingly, the mode delay per unit length is equalized and in principle the modal bandwidth would be infinitely large for perfectly compensated delays. In reality, group delay compensation is an extremely critical function of the refractive index profile and even assuming a highly sophisticate manufacturing process the highest modal bandwidth achieved for commercially available optical fiber usually does not exceed a few gigahertz per kilometer. In addition to modal dispersion, each mode is subjected to intrinsic chromatic dispersion due to the dispersion relationship between the modal propagation constant and the source spectrum width. Chromatic dispersion is otherwise identified as group velocity dispersion (GVD) and is the major drawback in dispersion-limited transmission using single-mode fiber with direct modulated semiconductor laser diode sources.

Every nonlinear behavior and dispersion contribution to pulse propagation experienced by single-mode fiber transmission would in principle be present even for each individual mode of every multimode fiber. Of course, the very different timescales of these phenomena with respect to modal dispersion makes the contribution of almost all of them negligible when considering pulse dispersion in multimode fibers. Accordingly, in the following chapters the theory of the multimode pulse response will be presented, including only modal and chromatic dispersion.

1.3 Semiconductor Laser Sources

There is a need to increase the transmission bit rate for high-speed laser sources, due to well-performing and low-cost direct modulation capabilities of those devices compared with the slow

and much less efficient LED. Recently, VCSEL technology provides a very interesting compromise in terms of speed, cost, yields and power consumption. However, more consolidated light sources for 10GbE, at least in the 1310 nm wavelength range, are still directly modulated Fabry-Perot (FP) lasers and distributed feedback (DFB) lasers. Unfortunately, any kind of laser source is almost a nightmare for every multimode fiber.

There are at least three characteristics of semiconductor lasers that act against the natural behavior of any multimode optical waveguide and of the multimode fiber in particular:

1. The light emitted from the semiconductor laser is spatially localized on to a region that is usually much narrower then the fiber core area. This leads to a partial excitation of a few mode groups allowed by the fiber. If the group delay of the multimode fiber is not compensated enough among excited bound modes (the amount of compensation required depends on the ratio between the bit rate and the differential mode delay), the energy distribution among a few excited modes will result in a consistent pulse broadening at the fiber end facet after just a few hundred meters of propagation length.
2. The laser coherence properties in conjunction with multimode connectors originate in the intensity-dependent Speckle noise term, namely the modal noise.
3. The power distribution among fiber modes is strongly dependent on the combined effect of launch polarization and environmental induced stresses and perturbation, originating in random output pulse fluctuations, which of course make the channel picture even more complicated.

A large number of measurements demonstrates how unpredictable the MMF frequency response would be when the light excitation comes from a laser source. The reason for such unpredictable behavior results from the very spatially localized excitation of a subset of guided modes in the MMF. Depending on which fiber modes are excited by the laser light, either a very high or a very low propagation bandwidth can be experienced on the same MMF link. When the light power is distributed among a few supporting modes, even a small propagation delay difference among excited modes will make a strong output pulse deformation with the creation of relatively large pulse precursors and postcursors that destroy pulse symmetry.

The launching-dependent frequency response of every multimode optical fiber clearly complicates the picture of multigigabit transmission over this dielectric waveguide. The IEEE802.3ae standard for 1GbE specifies the restricted offset launch conditions as the solution to provide suitable fiber mode excitation in order to control differential mode delay and pulse broadening. Even if restricted offset launch conditions provide a more stable multimode fiber bandwidth behavior, their implementation is not so simple as to be widely accepted and leads to increasing cost per module and other practical implications.

1.4 Offset Launch Conditions

A standard solution proposed to improve the multimode fiber bandwidth by limiting multipath propagation relies on specified offset launch conditions and related encircled flux specifications using standard offset launching patchcord. The idea behind offset launching is to excite selectively high-order modes that are localized in the mid-region of the fiber core section. Figure 1.2 shows qualitatively the offset launch case.

Unfortunately, offset launch patchcord is almost impractical today because of its dimensions and the space required to be hosted into small modules or crowded boards, as well as the cost issue. Sometimes, the cost of offset launching patchcord is comparable to the cost of the whole module. In addition, a unique solution for defining offset launch compliant with both 50 μm and 62.5 μm multimode fibers is still under study.

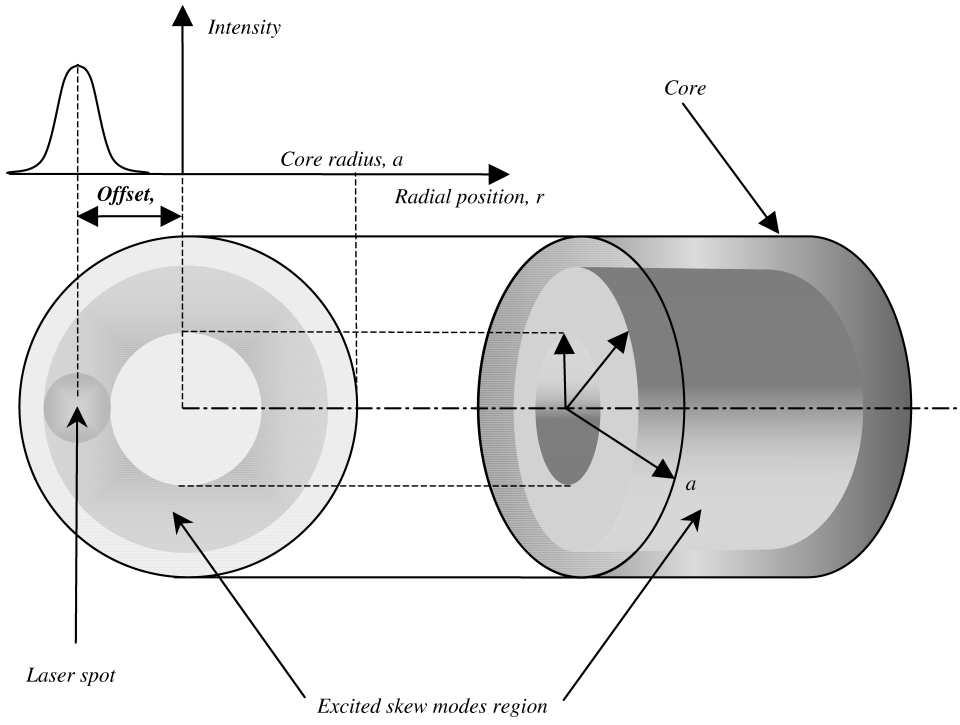

Figure 1.2 Schematic representation of the offset launch in a multimode fiber. The offset coordinate is ρ. Excited skew modes occupy the inner shaded region around the radial position ρ, leaving both the central region and the outer core region almost unoccupied by the electromagnetic energy

1.5 Optical Receivers

The optical receiver converts the optical signal available at the fiber end section into the corresponding electrical signal. This process takes place inside the optical photodetector according to the photoelectric effect. Each incoming photon has a probability of being absorbed, releasing its energy to a conduction band electron. The probability of photodetection depends on several factors involving the detector optical coupling, antireflection coating, depth of the intrinsic absorbing region, leakage currents and so on. All of these factors are usually summarized using a single parameter, namely the photodetector external quantum efficiency, $\eta_p(\lambda)$. Typical values range between $50\,\% < \eta_p(\lambda) < 95\,\%$, depending on the operating wavelength and photodetector structure. Very high-speed photodiodes have among the lowest quantum efficiency values due to width shortening of the absorbing region, thus minimizing the transit time dispersion. Coaxial receptacle photodiodes, designed for 10GbE applications in the second window operations $\lambda = 1310\,\text{nm}$, usually have quantum efficiency in the order of $60\,\% < \eta_p(\lambda) < 80\,\%$.

Each photon brings a fixed energy amount depending on its wavelength. The detected photon rate, namely the number of photons per unit time incident on the photodetector sensible area, is therefore related to the received optical power. The conversion factor is the universal constant R_0:

$$R_0 = \frac{q\lambda}{hc} \quad \text{(A/W)} \tag{1.1}$$

Substituting the speed of light in a vacuum, $c = 2.9979 \times 10^8$ m/s, and the electron charge, $q = 1.6022 \times 10^{-19}$ C, for the Plank constant, $h = 6.626110^{-34}$ J s, the following value for the conversion factor as a function of the wavelength is obtained:

$$R_0 = 0.8066\lambda_{[\mu m]} \Rightarrow \begin{cases} \lambda = 0.850\,\mu m \rightarrow R_0 = 0.686\,A/W \\ \lambda = 1.310\,\mu m \rightarrow R_0 = 1.057\,A/W \\ \lambda = 1.550\,\mu m \rightarrow R_0 = 1.250\,A/W \end{cases} \tag{1.2}$$

The product of the conversion factor $R_0(\lambda)$ with the photodetection external quantum efficiency $\eta_p(\lambda)$ defines the photodetector responsivity $R(\lambda)$:

$$R(\lambda) = R_0(\lambda)\eta_p(\lambda) = \frac{q\lambda}{hc}\eta_p(\lambda) \quad (A/W) \tag{1.3}$$

Assuming that the photodetection external quantum efficiency $\eta_p(\lambda) = 0.7$ is independent of the operating wavelength, from Equation (1.2) the following expected values of photodiode responsivity for 10GbE applications are obtained:

$$\eta_p = 0.7 \Rightarrow \begin{cases} \lambda = 0.850\,\mu m \rightarrow R_0 = 0.480\,A/W \\ \lambda = 1.310\,\mu m \rightarrow R_0 = 0.740\,A/W \\ \lambda = 1.550\,\mu m \rightarrow R_0 = 0.875\,A/W \end{cases} \tag{1.4}$$

It should be noted, however, that the photodetection external quantum efficiency is a decreasing function of the wavelength. This effect compensates partly for the linear reduction of the conversion constant in Equation (1.2) at shorter wavelengths.

The photocurrent is proportional to the envelope of the received optical intensity, and for this behavior the photodiode is defined as a square-law device. The optical power is then converted into electrical current intensity, as clearly reported by the unit of measure of the responsivity function in Equation (1.3). At a limited input optical power level, the photodiode behaves linearly with respect to the incident optical intensity and can be conveniently characterized by the impulse response and the transfer function in the frequency domain. The photodetector therefore performs the first filtering process on the incoming optical signal. The photocurrent pulses are then amplified and converted into more suitable voltage pulses before being processed through conventional clock and data recovery (CDR) circuits. If the multimode fiber bandwidth together with additional electrical low-pass filtering in the optical receiver front end set severe limitations on the signal available at the receiver decision section, a large error rate would be expected and a transmission failure status would therefore be detected. This failure mechanism is referred to as the 'dispersion limited system fault'. The only possible remedies known to overcome this fault condition is either to provide a received pulse reshaping process or to use error correcting code transmission or even reduce the signal bandwidth requirement in the given transmission channel using a proper modulation format. The first approach leads to the electronic dispersion compensation (EDC) technique, while two other solutions, optical mode filtering (OMF) and the multilevel modulation format (PAM-4), tend to either increase the multimode fiber transmission capacity or reduce the signal bandwidth occupation.

1.6 Signal Compensation Techniques

Due to the relatively large differential mode delay (DMD) encountered in multimode fibers when excited by semiconductor laser sources, a strong pulse dispersion and interferometric noise (Speckle pattern) are simultaneously expected as major limitations to multigigabit data transmission over a few hundred meters of link length. These effects lead to different dispersion compensation approaches, namely electronic dispersion compensation (EDC), optical mode filtering (OMF) and

quaternary pulse amplitude modulation (PAM-4). The IEEE 802.3aq 10BASE-LRM Committee is at present carefully investigating these three alternative compensating procedures.

The impulse response of a multimode fiber link distributed over several connected sections is very sensitive to perturbing environmental conditions like temperature mechanical vibration and even the state of polarization. Due to its inherent adaptive architecture, EDC seems to have better control against those environmental effects, making the multimode fiber link more robust under cabled operating conditions. However, it is widely accepted by the IEEE 802.3aq Committee that the complete picture of 10GbE over long-reach multimode fibers remains quite troublesome unless a proper dispersion compensation mechanism is taken into account. Although EDC seems to be the most promising solution for multipath pulse dispersion compensation, the remaining two approaches are still under investigation and merit some attention as alternative methods for potential future approaches. In the following, the operating principles of the above-mentioned three methods will be considered. All of the considered solutions have several issues to be solved in order to become widely deployed on the 10GbE large-volume market expected in 2006 and 2007. The basic principles of these signal compensation techniques for multigigabit transmission over multimode optical fibers will also be reviewed.

1.6.1 Electronic Dispersion Compensation (EDC)

The electronic dispersion compensation (EDC) technique proposes to mitigate optical pulse broadening at the multimode fiber output by means of electronic signal processing directly operating at the signal rate. The optical signal must be first detected and linearly amplified by a proper low-noise receiver before being processed by EDC. This approach requires relatively complex digital signal processing at 10 Gb/s in the case of the 10BASE-LRM standard. The key element is the adaptive finite impulse response (FIR) filter whose tap coefficients are managed through the minimum mean square error (MMSE) algorithm. Among several different available architectures the most suitable for achieving simultaneously a high bit rate capability and relatively low power requirements is based on a combination of the *feedforward equalizer* (FFE) and the *decision feedback equalizer* (DFE). Both sections are realized by means of FIR filters. Key parameters of both the FFE and DFE are the number of taps and the tap delay (tap spacing) used to synthesize each FIR filter. The more dispersed equalizer is expected to be the input pulse and the longer are would be the filter length in order to compensate for longer precursors and postcursors. This produces a trade-off between technological complexity, power consumption and compensation capability. Essentially, the EDC action can be depicted in two steps:

1. The FFE section controls the input pulse shape providing weighted amounts of frequency response equalization in order to re-establish a proper pulse profile, thus reducing the intersymbol interference pattern.
2. The DFE section adaptively adjusts the decision threshold of the digital quantizer in order to minimize the intersymbol interference power at the decision section output. According to standard solutions, the DFE operation requires the clock recovery feature from the incoming data pattern in order to synchronize the decision timing properly.

In this context, relatively relaxed optical constraints including launch conditions, connector tolerances and optical detection architectures are required for the fiber transmission system. The EDC advantage relies on its integrated circuit (IC) structure: low cost, high reliability, compact and easily integrable in a small form factor and pluggable data communication modules. The EDC drawback is that some unstable convergence is experienced when the required filter length increases and the multimode fiber response demands that the compensation capabilities be limited. A low value of the signal-to-noise ratio (SNR) at the optical receiver input places one more constraint on EDC

operation. The electronic compensator architecture should also include an adaptive electrical filter in order to track the compensation profile variations according to the temporal changes of the MMF response and to restore the proper electrical pulse profile at the decision section.

It will be seen in the next chapters that several fiber modes excited by the laser source will propagate, with relative delay differences giving rise to multipath pulse distortion after some distance from the launch section. Due to the large-area photodetection mechanism, interferometric noise plays a marginal role, leaving the complete interferometric pattern inside the detected light area. Spatial averaging over the whole fiber end section due to the large-area detection mechanism makes the detected light intensity spatially averaged and almost unaffected by interferometric noise fluctuations.

Major problems in the EDC approach are:

1. The efficiency of the FFE filter depends on the number of taps and on the relative spacing needed for impulse reconstruction. Due to the strong multipath dispersion usually encountered in legacy multimode fibers, several integral bit time equivalents are needed, leading to long FFE filter structures with more than 9 to 12 sections.
2. Increasing the number of taps leads to an increase in the equalization filter capability of the long pulse tail distortion, but at same time it increases considerably the power consumption and the design implementation complexity for the given technology state.
3. Internal delay of the EDC architecture must match with 10GbE bit-rate requirements (about 100 ps time step) and this leads to state-of-the-art CMOS (complementary metal oxide semiconductor) technology with less than a 90 nm gate length
4. The input stage must account for a linear automatic gain controlled (AGC) microwave amplifier with a proper dynamic range and a smooth bandwidth in excess of 8 GHz.
5. The optical photodetector and related low noise transimpedance amplifier must have a linear (V/W) transfer characteristic.
6. The DFE corrects only the pulse postcursor. Inherent leaking of the compensation capability of either pulse precursor and the dual peak pulse response reveal a severe limitation of the DFE approach for these pulse distortions.

1.6.2 Optical Mode Filtering (OMF)

The optical mode filtering (OMF) technique proposes a reduction in the number of propagating modes in the multimode fiber by selective excitation and detection of the fundamental fiber mode. Optical mode filtering can be summarized using the following basic operations:

1. A selective laser light launch into the multimode fiber input section in order to couple as much power as possible to the fundamental fiber mode only. This is achieved by means of a proper laser coupling mechanism in order to maximize the overlapping integral with the fundamental fiber mode.
2. Selective light detection at the multimode fiber end section by means of a spatial selective filter interposed between the multimode fiber end section and the photodetector active area.

By reducing drastically the number of excited mode groups, modal delay spreading is implicitly reduced. The principal problem encountered by this method is the large amount of power fluctuation (modal noise) induced by the standard connector offset and perturbing environmental conditions. However, under controlled laboratory conditions, this solution provided excellent results. From an application point of view, this solution requires specialized launch and detection tools that add complexity and cost to high-volume market demands. It is a common opinion of the IEEE 802.3aq

Committee that in order to introduce OMF as a valid signal compensation technique it should work together with EDC. Of course, the performance required in this case by EDC would be much less demanding than in a stand-alone application, but would still add more complexity and cost to the module final solution.

As had been anticipated, the basic principle behind OMF is to force as much multimode fiber as possible to operate as nearly single-mode fiber in the 1310 nm region by selective excitation and selective detection of the fundamental fiber mode. In the OMF approach, only the fundamental fiber mode would be excited in principle, leaving a relatively small contribution in terms of pulse energy carried up to the fiber end to the residually excited higher-order modes. In other words, the basic idea behind OMF is to force a single-mode regime into a multimode fiber. Although in principle the differential mode delay and the modal bandwidth concepts no longer apply to the OMF approach, the interferometric noise between excited higher-order modes and the fundamental mode grown at each fiber discontinuity, like connectors and fusion splices, makes the whole channel design much more critical with respect to optical alignment tolerances when compared to the EDC approach. Every misalignment in the fiber core contributes to unwanted higher-order mode excitation and modal noise. An additional effect is represented by the polarization of the fundamental mode respect to the direction connector misalignment. Due to the random nature of the polarization direction of the fundamental mode and to its sensitivity to any environmental condition, a polarization-dependent noise term must be added to light intensity. A careful central spot size launching condition, receiver mode filtering and optical connector alignment statistics all play a dominant role in the OMF approach. Unfortunately, standard tolerances for MMF technology optical connectors are too loose to compete with the OMF requirements. High modal noise due to an interference pattern between higher order modes and the fundamental mode severely limits system performance.

Major problems in the OMF approach are:

1. The laser source coupled field must match the fundamental fiber mode in order to transfer as much power as possible to that mode. This in particular requires numerical aperture adaptation between the laser light and the fundamental fiber mode.
2. Due to almost unavoidable irregularity of the refractive index profile at the fiber center (dip or pin) laser light should not be focused on such a small area around the fiber axis. Laser light should be applied to a larger axial-symmetric region in order to minimize the relative power coupled in the defective central region, but a region not too large to provide unwanted higher mode excitation.
3. Minimize the power transferred to higher-order modes.
4. Connector offset plays a dominant role in OMF penalty calculation. Any offset leads to power coupling that is not optimized, allowing higher-order mode excitation and consequent pulse dispersion.
5. Polarization and connector offset generate relevant modal noise.
6. The modal filter at the receiver end is needed to cut out higher-order mode contributions to the detected intensity, but it generates strong intensity fluctuations when modal noise, polarization and connector offset are produced simultaneously.

1.6.3 Quaternary Pulse Amplitude Modulation (PAM-4)

The basic idea behind the quaternary pulse amplitude modulation (PAM-4) proposal is to reduce the bandwidth requirement of the multimode fiber link in order to allow full 10GbE datastream transmission over a long-reach legacy multimode fiber link. This is achieved by using four-level modulation amplitude instead of the more conventional two-level NRZ (no return to zero) modulation scheme. Adopting the four-level scheme, each sequence of two information bits is coded

into the four-level digital amplitude instead of being simply time multiplexed, as shown by the following encoding logic:

b_1	b_2	L	$I_2 + I_1$	I_{mod}
0	0	L_0	$0 + 0$	0
0	1	L_1	$0 + I$	I
1	0	L_2	$2I + 0$	2I
1	1	L_3	$2I + I$	3I

This shows the encoding relations between the NRZ dual-bit sequence (b_1, b_2) and the logic PAM-4 levels L_k, $k = 0, 1, 2, 3$. Each PAM-4 logic level is then identified by combining the two current generators I_1 and I_2. The corresponding modulation current I_{mod}, reported in the last column, is injected into the laser.

The result is that for the same symbol rate exactly half a bit rate is required. Referring to the 10GbE signaling speed $B = 10.3125$ Gb/s, this translates into one-half of the symbol rate requirement, corresponding to exactly $B_{\text{PAM-4}} = \frac{1}{2}B = 5.156\,25$ Gb/s. Assuming that the multimode fiber modal bandwidth scales inversely with the link length (no mode group mixing), this leads to double the link length or one-half of the link bandwidth requirement for the fixed link length. Since there is interest in transmitting 10GbE, the latter conclusion looks quite attractive, allowing in principle 10GbE transmission over at least 300 m of legacy multimode fiber with a modal bandwidth $\widehat{BW}$(bandwidth per kilometer) = 500 MHz km in the second window region.

Although the conclusion above could justify design efforts in the PAM-4 solution due to sensible relaxation of multimode fiber bandwidth requirements, major constraints will be added to the optoelectronic modules.

1.6.3.1 NRZ to PAM-4 Encoder

Figure 1.3 shows a solution for the PAM-4 encoder operating in the optical domain. The current encoding logic is represented by the following relationships:

$$\begin{cases} I_{\text{mod}} = I_1 + I_2 \\ I_{\text{L}} = I_{\text{mod}} + I_{\text{bias}} \end{cases}, \qquad \begin{cases} I_1 = \begin{pmatrix} I : \text{high} \\ 0 : \text{low} \end{pmatrix} \\ I_2 = \begin{pmatrix} 2I : \text{high} \\ 0 : \text{low} \end{pmatrix} \end{cases} \tag{1.5}$$

The laser diode driver LDD_1 delivers the modulation current I_1 that assumes two digital levels, namely $I_1 = I$ and $I_1 = 0$ in the high state and in the low state respectively. The laser diode driver LDD_2 delivers the modulation current I_2 that still assumes still two digital levels, but of double intensity, namely $I_2 = 2I$ and $I_2 = 0$ in the high state and in the low state respectively. According to the 1:2 demultiplexed function, each laser driver is fed at half the bit rate and each of them supplies the proper output current corresponding to the input digital level. Depending on the input dual-bit sequence, four input combinations are possible and correspondingly four output current levels are coded. Due to the 1:2 demultiplexed function, each output current level is associated with twice the input time step $T = 1/B$, effectively doubling the duration of each PAM-4 coded symbol.

The most relevant problem concerning the optical transmitter for the PAM-4 coding is the linearity of the laser characteristic and the resulting signal-to-noise ratio uniformity achievable for each level difference. It is well known that the laser pulse response is strongly dependent on the biasing position, at least when the laser is biased close to the lasing threshold. Different overshoot and transient time responses are therefore expected for the level transitions $L_0 \rightarrow L_1$ and $L_2 \rightarrow L_3$, due to the different positions of L_0 and L_2 respectively compared to the lasing threshold.

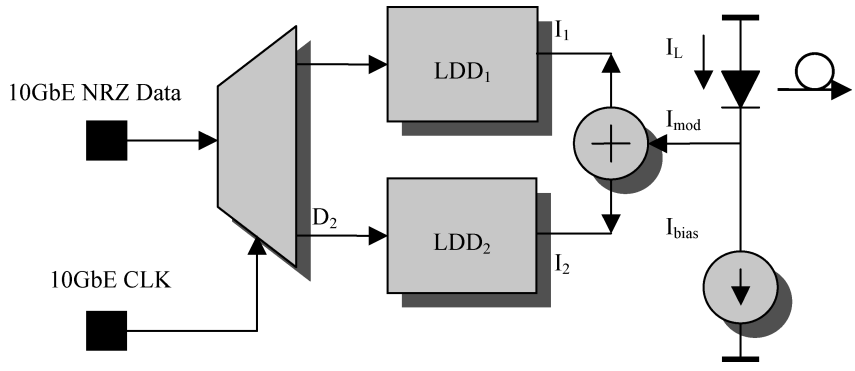

Figure 1.3 Block diagram of the NRZ to PAM-4 optical encoder. The modulation current is given by the sum of the two current components I_1 and I_2

In order to understand the signal differences better, Figure 1.4 illustrates both the NRZ signal and the corresponding PAM-4 converted signal. The first row in Figure 1.4 shows the incoming NRZ pattern. The following two waveforms represent the 1:2 demultiplexed signals with ideal timing. In order to align those waveforms it is necessary to add a time delay equal to one time step T to waveform D_1. The resulting shifted signal is then represented. The current sum shown in the schematic in Figure 1.3 therefore provides the PAM-4 output reported. This is the modulation current pattern that drives the semiconductor laser.

1.6.3.2 PAM-4 to NRZ Decoder

Once the optical PAM-4 signal reaches the photodetector it must be recognized and converted to NRZ using a proper PAM-4 to NRZ decoder. Figure 1.5 gives the block diagram for a plausible solution for the PAM-4 to NRZ decoder.

The basic principle underlying the schematic PAM-4 to NRZ decoder presented in Figure 1.5 considers the three inner level transitions of the PAM-4 signal to be three separate NRZ signals of reduced amplitude. After detection, the logic block recovers the original NRZ pattern. The major constraint in the PAM-4 to NRZ decoder is the reduced signal-to-noise ratio available at each threshold detector in the optical receiving process in comparison to the equivalent NRZ optical receiver. It is important to underline the fact that the comparison between NRZ and PAM-4 optical receivers should be performed using adequate assumptions and available technology.

1.6.3.3 NRZ versus PAM-4: SNR Comparison

In order to calculate the signal-to-noise ratio and proceed to evaluate the different benefits and impairments between NRZ and PAM-4 modulation schemes, consider the following assumptions:

1. NRZ and PAM-4 optical receivers use the same IC technology with the same white thermal noise power spectral density n_{th}. This allows only noise bandwidth differences to be considered as responsible for the different noise powers available in the two receivers.
2. Both optical receivers are thermal noise limited. In other words, thermal noise is the dominant contribution in setting the sensitivity performances.
3. NRZ and PAM-4 optical receivers both have the same frequency response profile, but the NRZ receiver has twice the bandwidth of the PAM-4 receiver.

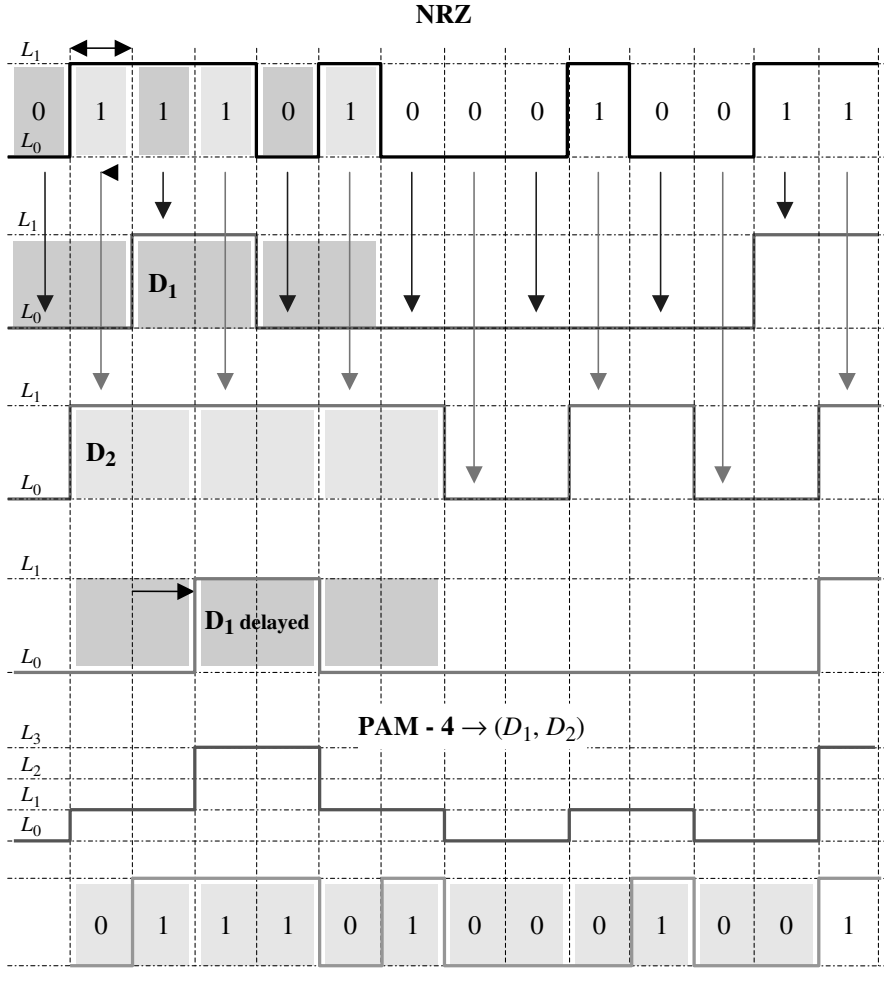

Figure 1.4 NRZ to PAM-4 signal encoding according to the block diagram presented in Figure 1.3. Light waveforms are detected at the 1:2 demultiplexed output including T-delay required in order to align signal wavefronts before the current sum. The waveform shows the total modulation current injected into the laser according to the coded PAM-4 pattern

Figure 1.6 is a schematic representation of the frequency response and related noise bandwidth of both receivers. According to the third assumption, the two receivers have a noise bandwidth ratio equal to their corresponding bandwidths. Therefore:

$$B_{\mathrm{n,NRZ}} = 2B_{\mathrm{n,PAM\text{-}4}} \tag{1.6}$$

From assumptions 1 and 2, it can easily be deduced that the noise power of the NRZ receiver is twice the noise power of the PAM-4 receiver:

$$\sigma^2_{\mathrm{n,NRZ}} = B_{\mathrm{n,NRZ}} n_{\mathrm{th}} = 2B_{\mathrm{n,PAM\text{-}4}} n_{\mathrm{th}} = 2\sigma^2_{\mathrm{n,PAM\text{-}4}} \tag{1.7}$$

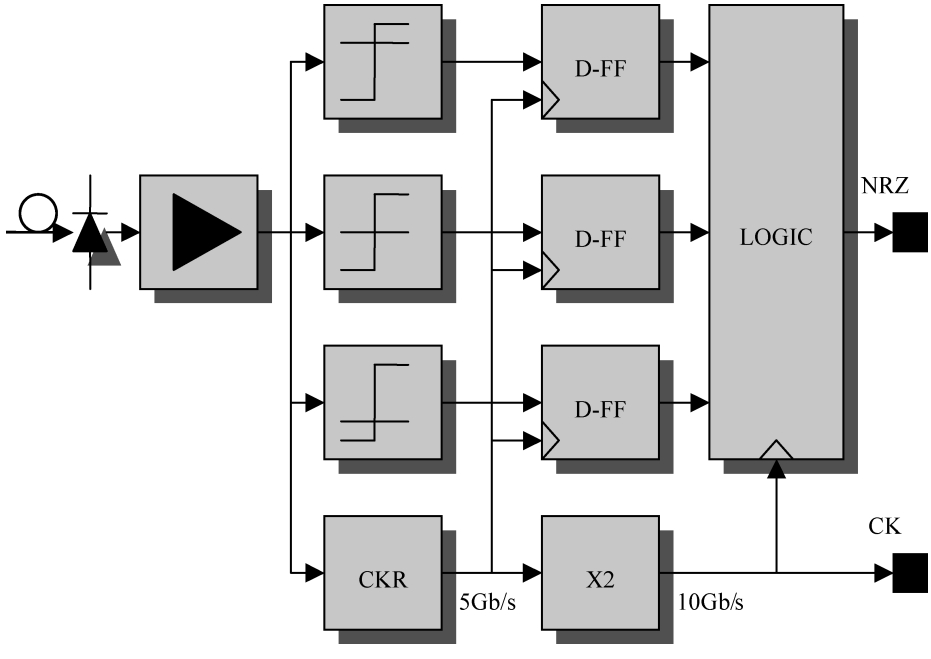

Figure 1.5 Schematic representation of the block diagram of a PAM-4 to NRZ decoder using three threshold detectors and a clock by 2 multiplier. By choosing the correct threshold position of the three threshold detectors, the subsequent logic can reconstruct the original NRZ signal from the PAM-4 detected signal

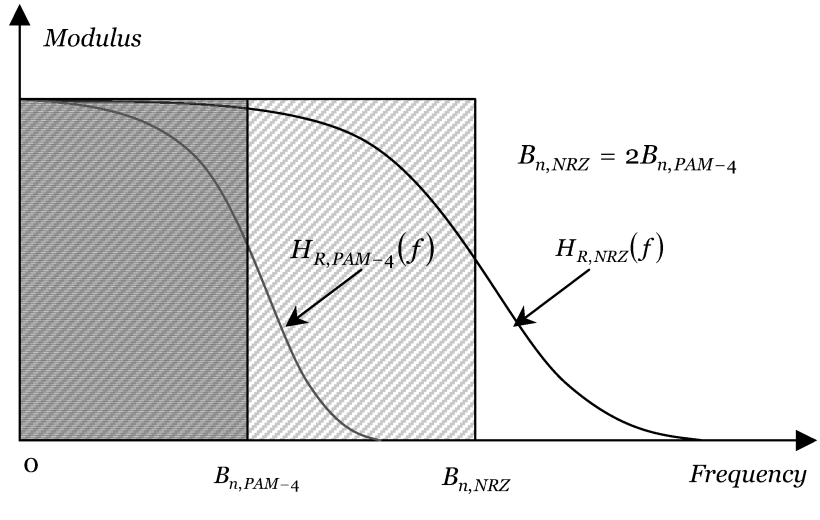

Figure 1.6 Schematic representation of frequency responses and noise bandwidths of NRZ and PAM-4 receivers. According to the third assumption, noise bandwidths have the same ratio of $\frac{1}{2}$ as their respective cut-off frequencies

The RMS (root mean square) noise reduction Δ_n produced using the PAM-4 receiver can be estimated as

$$\Delta_n \equiv 10\log_{10}\left(\frac{\sigma_{n,NRZ}}{\sigma_{n,PAM\text{-}4}}\right) = 10\log_{10}\sqrt{2} \cong 1.5 \text{ dB(optical)} \tag{1.8}$$

The gain factor Δ_n represents the average optical power sensitivity improvement for achieving the same signal-to-noise ratio performances for a given signal amplitude. If the required decision threshold distance had been the same for both NRZ and PAM-4 receivers, it can be concluded that there is a net gain of 1.5 dB (optical) when using the PAM-4 solution versus the NRZ one, but unfortunately this is not the case. In fact, for a given average received optical power P_R, the PAM-4 signal has a one-third decision amplitude with respect to the corresponding NRZ signal. The signal pattern reported in Figure 1.4 gives a qualitative representation of this characteristic behavior. Figure 1.7 shows the computed gain between the PAM-4 and the NRZ line coding versus increasing multimode fiber link length for a specified modal bandwidth of $\widehat{BW} = 500$ MHz km with Gaussian frequency response. Figures 1.8 and 1.9 show instead a more realistic computer simulation of both NRZ and PAM-4 eye diagrams, assuming that they have the same average optical power for the 10GbE case. The pulse has been chosen according to the raised cosine family with unit roll-off.

Since there is no intersymbol interference (ISI) in both cases, the reduction in the decision amplitude experienced for each signal transition in the PAM-4 pattern with respect to the NRZ one

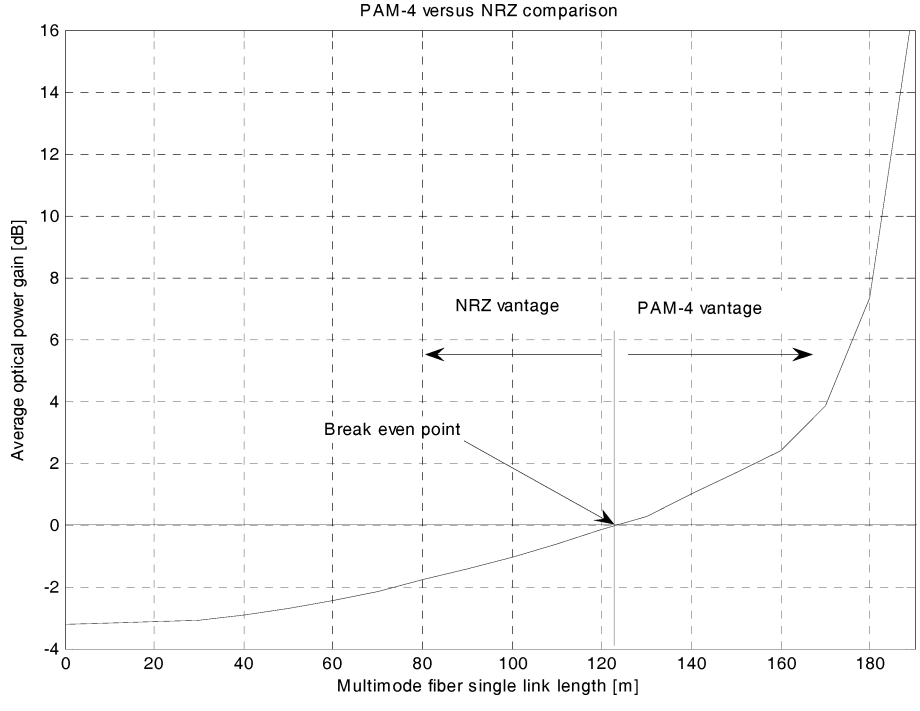

Figure 1.7 Optical sensitivity gain comparison between the PAM-4 and NRZ line codings versus the multimode fiber single link length. The fiber modal bandwidth is $\widehat{BW} = 500$ MHz km. The breakeven distance is about $L_0 = 123$ m

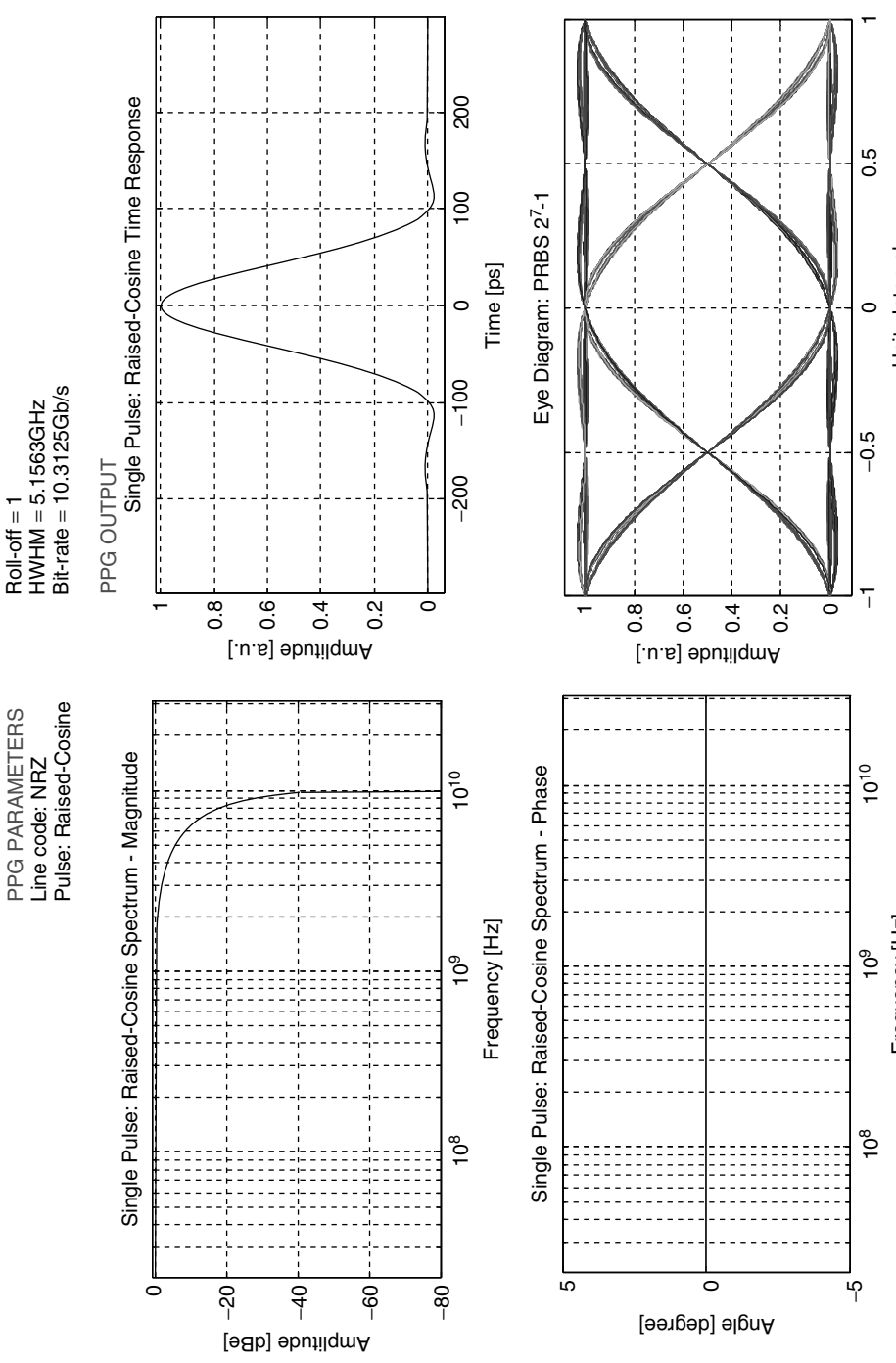

Figure 1.8 Frequency and time domain representations of NRZ PRBS 2^7-1 line code signals at 10GbE data rate. Left top represents the single pulse according to the unity roll-off raised cosine profile, while the left bottom graph shows the corresponding eye diagram in normalized bit time units

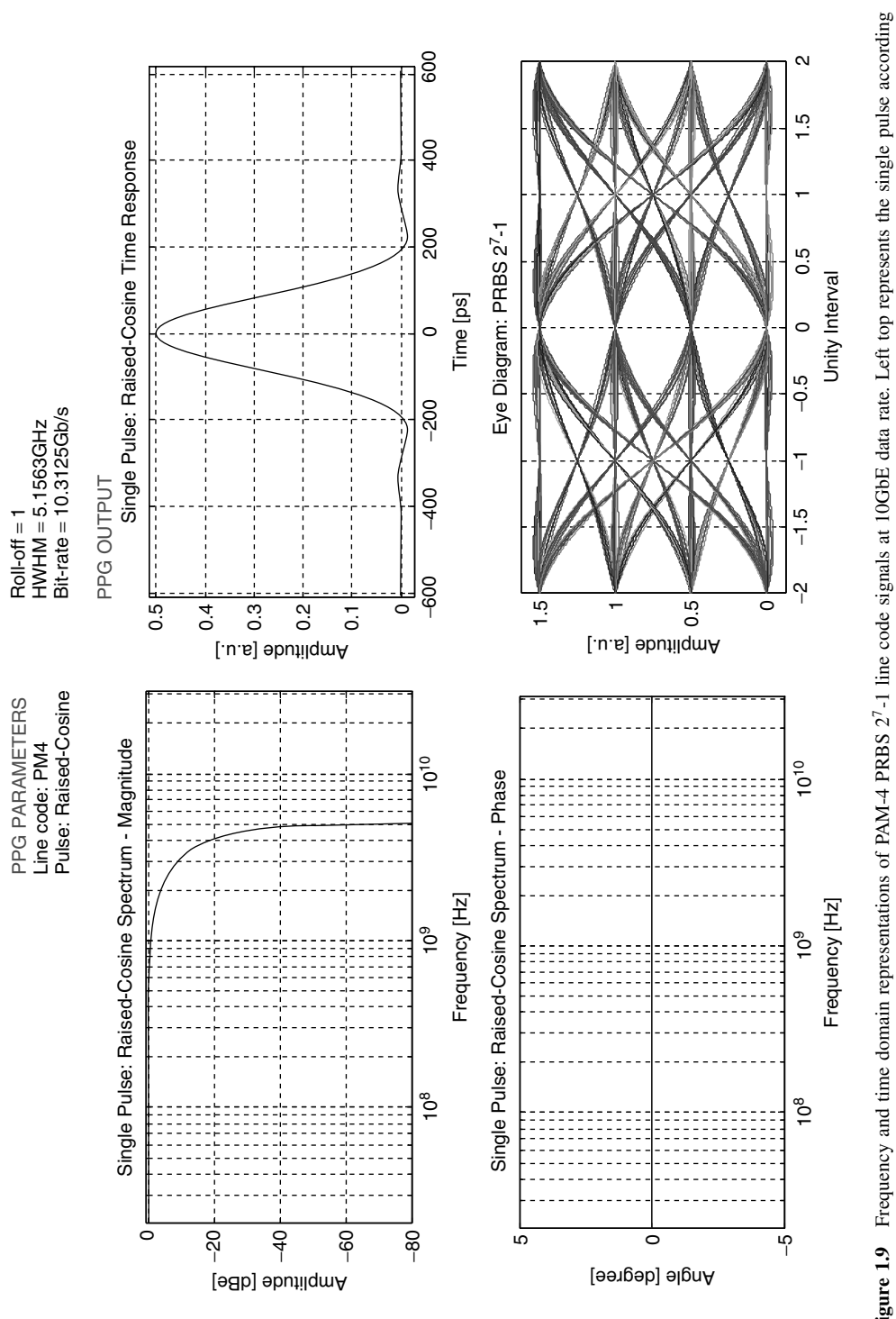

Figure 1.9 Frequency and time domain representations of PAM-4 PRBS 2^7-1 line code signals at 10GbE data rate. Left top represents the single pulse according to the unity roll-off raised cosine profile, while the left bottom graph shows the corresponding eye diagram in normalized bit time units. A scaling factor of 2 has been introduced in the raised cosine pulse profile with respect to the NRZ case shown above

leads to a loss of signal strength of about 4.77 dB (optical):

$$\Delta_s = 10\log_{10}(1/3) \cong -4.77\,\text{dB} \tag{1.9}$$

This value refers to ideal eye diagrams with no added jitter or ISI and the average eye opening coincides with the decision threshold amplitude for each level. The receiver sensitivity for a given bit error rate (BER) is determined by the Q-factor defined below, where d is the decision threshold distance and σ is the total RMS noise amplitude. Assuming thermal noise limited detection and Gaussian noise approximation, then

$$Q \equiv \frac{d}{\sigma}, \qquad \text{BER} = \frac{1}{2}\text{erfc}\left(\frac{Q}{\sqrt{2}}\right) \tag{1.10}$$

Taking into account the reduced noise bandwidth in Equation (1.8) for PAM-4 and the corresponding detection amplitude reduction in Equation (1.9), it can be concluded that the net average optical power gain using the PAM-4 receiver instead of the corresponding NRZ receiver is about 3.27 dB (optical):

$$\Delta_Q = \Delta_s + \Delta_n \cong -4.77 + 1.50 = -3.27\,\text{dB} \tag{1.11}$$

This is essentially the reason for the success of the NRZ solution adopted in almost all optical telecommunication systems. Of course, at least technically the development of the PAM-4 signaling must be justified.

1.6.3.4 NRZ versus PAM-4: Eye Opening Comparison

The general signal-to-noise reduction experienced by the PAM-4 signal must in fact be balanced by the reduced channel bandwidth requirement, as clearly shown by comparing the left top graphs of Figures 1.8 and 1.9. Assuming the same unity roll-off raised cosine signal pulse profile in both modulation codes, it is evident that the PAM-4 pulse requires exactly a bandwidth that is one-half of the corresponding NRZ case. This leads to a considerable pulse spreading reduction after a given link length propagation, which corresponds to a relative increased optical eye opening. Following this reasoning, it is possible to arrive at the obvious conclusion justifying the PAM-4 coding when reduced transmission channel capabilities must be accounted for in the transmission system design.

Figures 1.10 and 1.11 report respectively the PAM-4 and NRZ data stream detected after a single link length of 100 m of a Gaussian bandwidth multimode fiber. Most of the original eye opening reduction due to multilevel coding has been recovered after just 100 m of link length. In fact, the PAM-4 eye opening diagram results from about 27 % of the highest PAM-4 signal amplitude, while the same qualitative calculation performed on the NRZ eye diagram shows that the eye opening results from about 50 %. Referring to the ideal −4.77 dB penalty reported in Equation (1.9), the ratio now gives about −2.67 dB, with a recovery of about 2.1 dB. Assuming the same noise spectral power density for both line codes, the net gain in using PAM-4 versus NRZ is still negative, −1.17 dB, but is much more reduced compared to the back-to-back case in Equation (1.11).

The relative performance of PAM-4 line coding improves at longer link lengths, as shown in Figures 1.12 and 1.13 for the case of a single link length of 150 m of the same Gaussian bandwidth multimode fiber. A qualitative eye opening measurement for both cases gives about the same value of 18 %, leading to a positive net gain of 1.5 dB, which coincides with the noise bandwidth enhancement factor. The breakeven point in using PAM-4 instead of NRZ for this Gaussian bandwidth multimode fiber is therefore somewhere between 100 m and 150 m, where the net gain is zero. For every longer link length, PAM-4 gives theoretically better performances than NRZ.

The last simulated case shown in Figures 1.14 and 1.15 refers to a single link length of 200 m of the same Gaussian bandwidth multimode fiber. The PAM-4 eye diagram looks almost closed, even

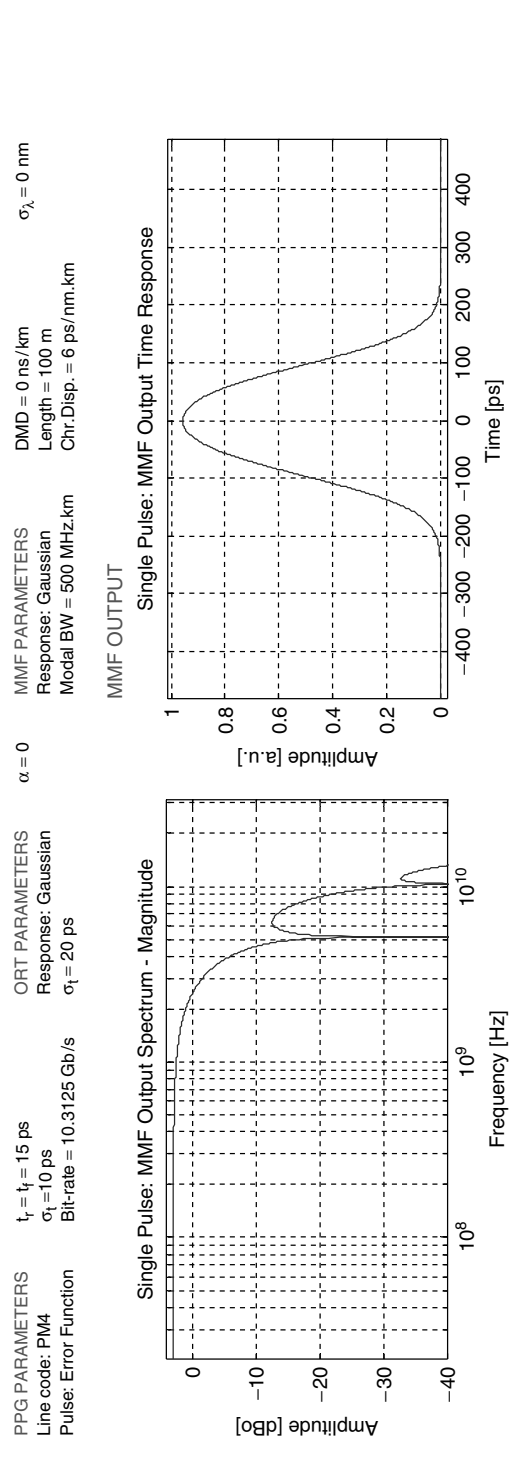

Figure 1.10 Frequency and time domain representations of PAM-4 PRBS 2^7-1 line code signals at 10GbE data rate after a 100 m single link length of Gaussian bandwidth multimode fiber. Left top represents the single pulse fiber output, while the left bottom graph shows the corresponding eye diagram in normalized bit time units. The legend at the top reports the simulated conditions for the pulse pattern generator and the light source impulse response

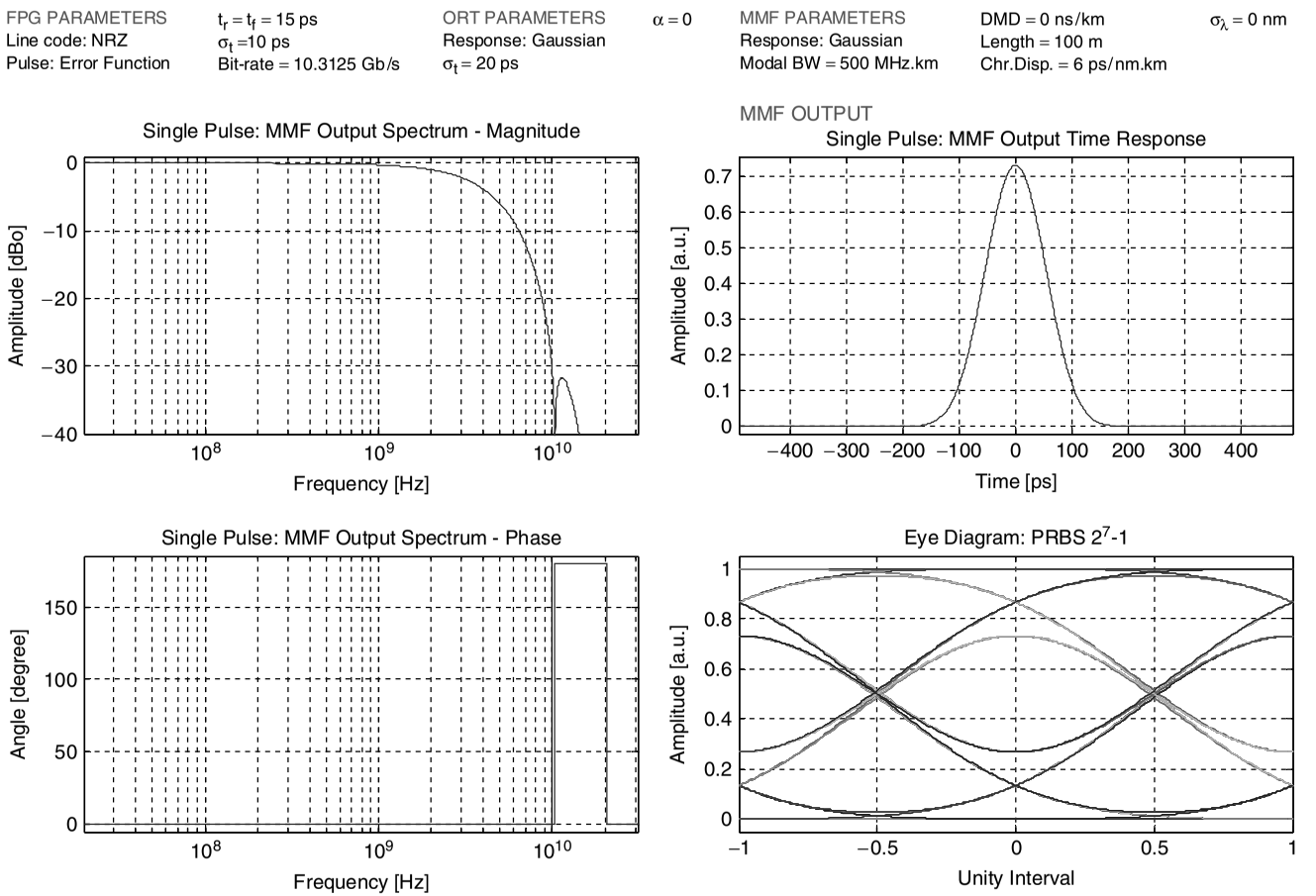

Figure 1.11 Frequency and time domain representations of NRZ PRBS 2^7-1 line code signals at 10GbE data rate after a 100 m single link length of Gaussian bandwidth multimode fiber. Left top represents the single pulse fiber output, while the left bottom graph shows the corresponding eye diagram in normalized bit time units. The legend at the top reports the simulated conditions for the pulse pattern generator and the light source impulse response

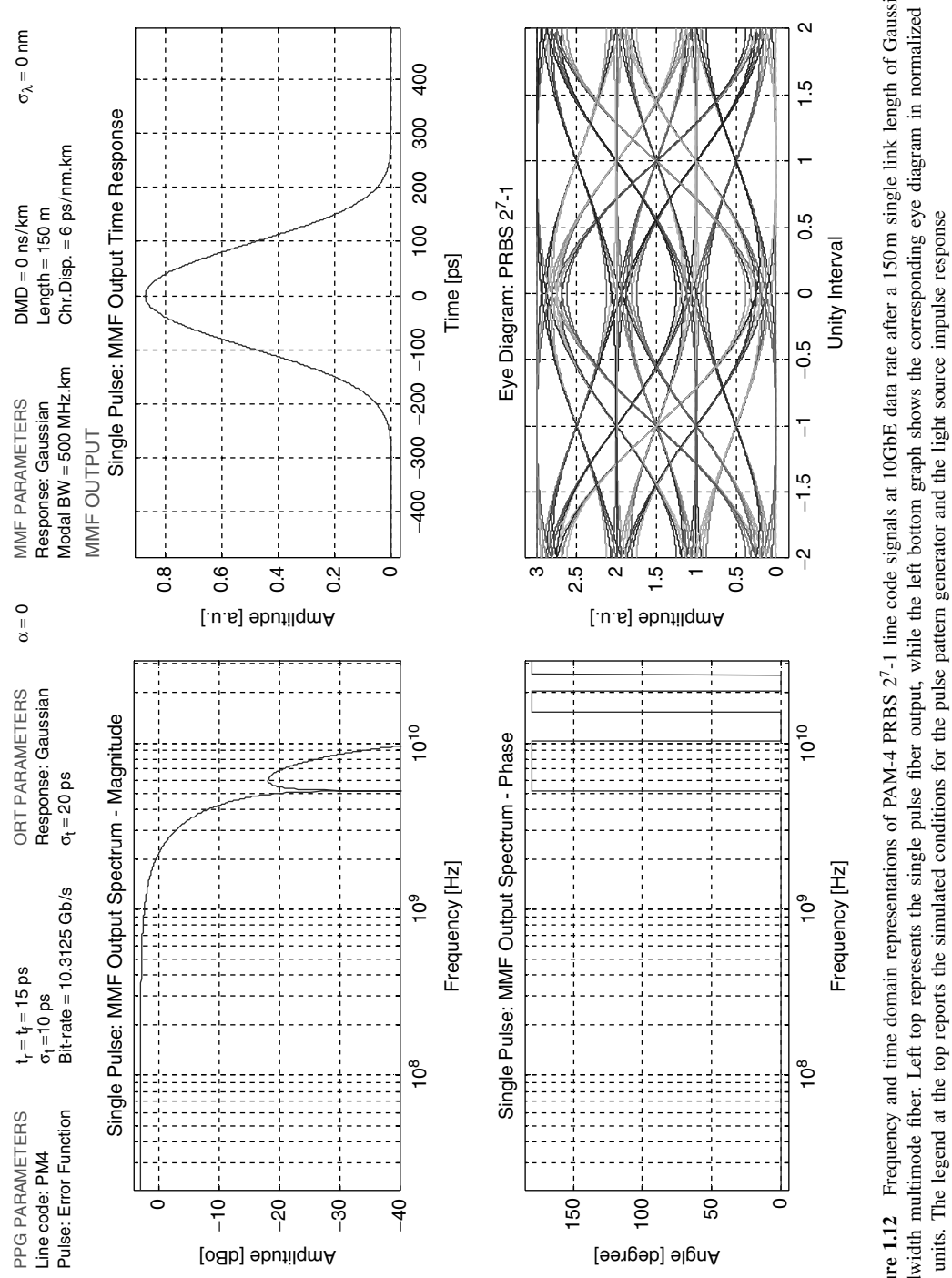

Figure 1.12 Frequency and time domain representations of PAM-4 PRBS 2^7-1 line code signals at 10GbE data rate after a 150 m single link length of Gaussian bandwidth multimode fiber. Left top represents the single pulse fiber output, while the left bottom graph shows the corresponding eye diagram in normalized bit time units. The legend at the top reports the simulated conditions for the pulse pattern generator and the light source impulse response

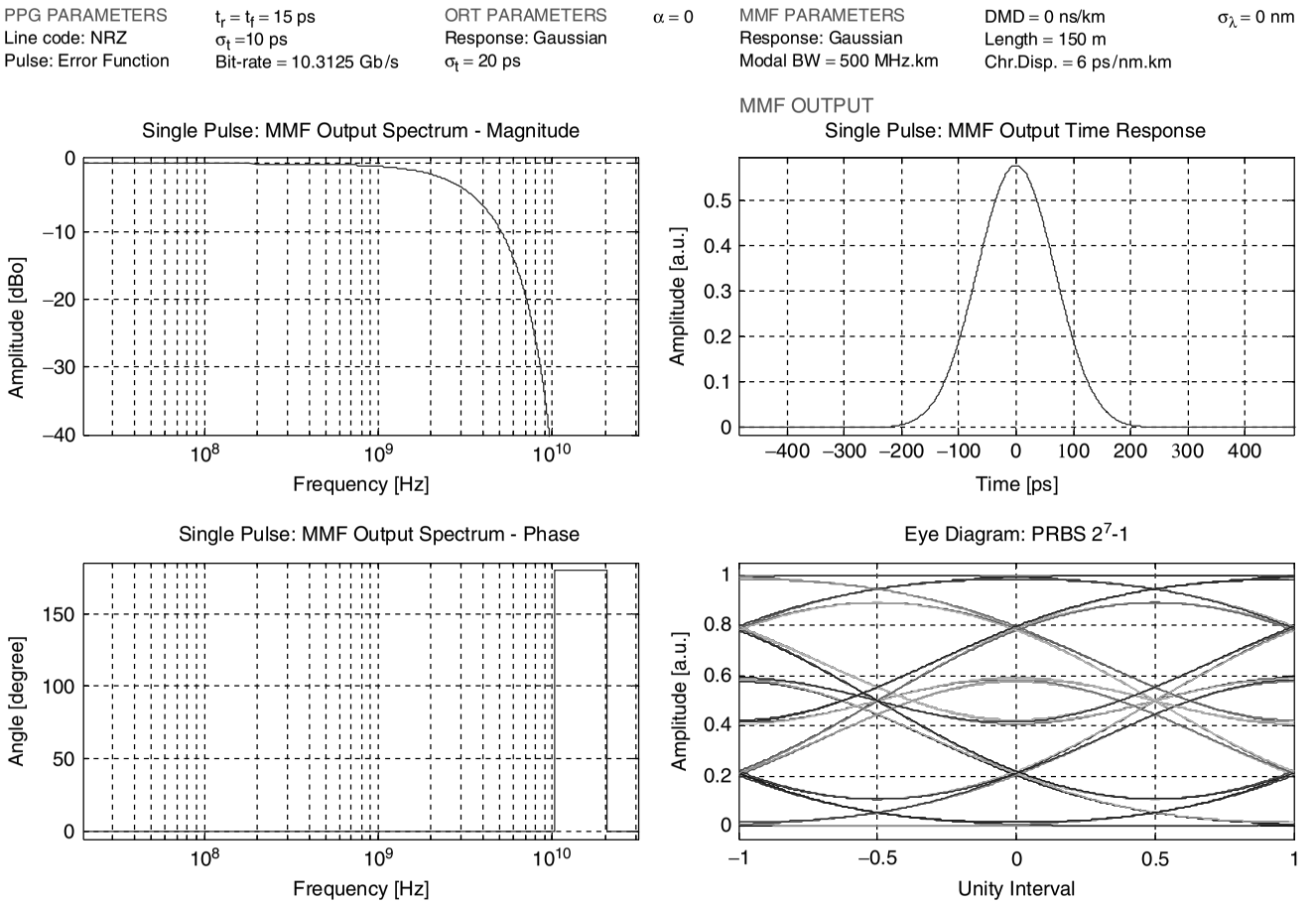

Figure 1.13 Frequency and time domain representations of NRZ PRBS 2^7-1 line code signals at 10GbE data rate after a 150 m single link length of Gaussian bandwidth multimode fiber. Left top represents the single pulse fiber output, while the left bottom graph shows the corresponding eye diagram in normalized bit time units. The legend at the top reports the simulated conditions for the pulse pattern generator and the light source impulse response

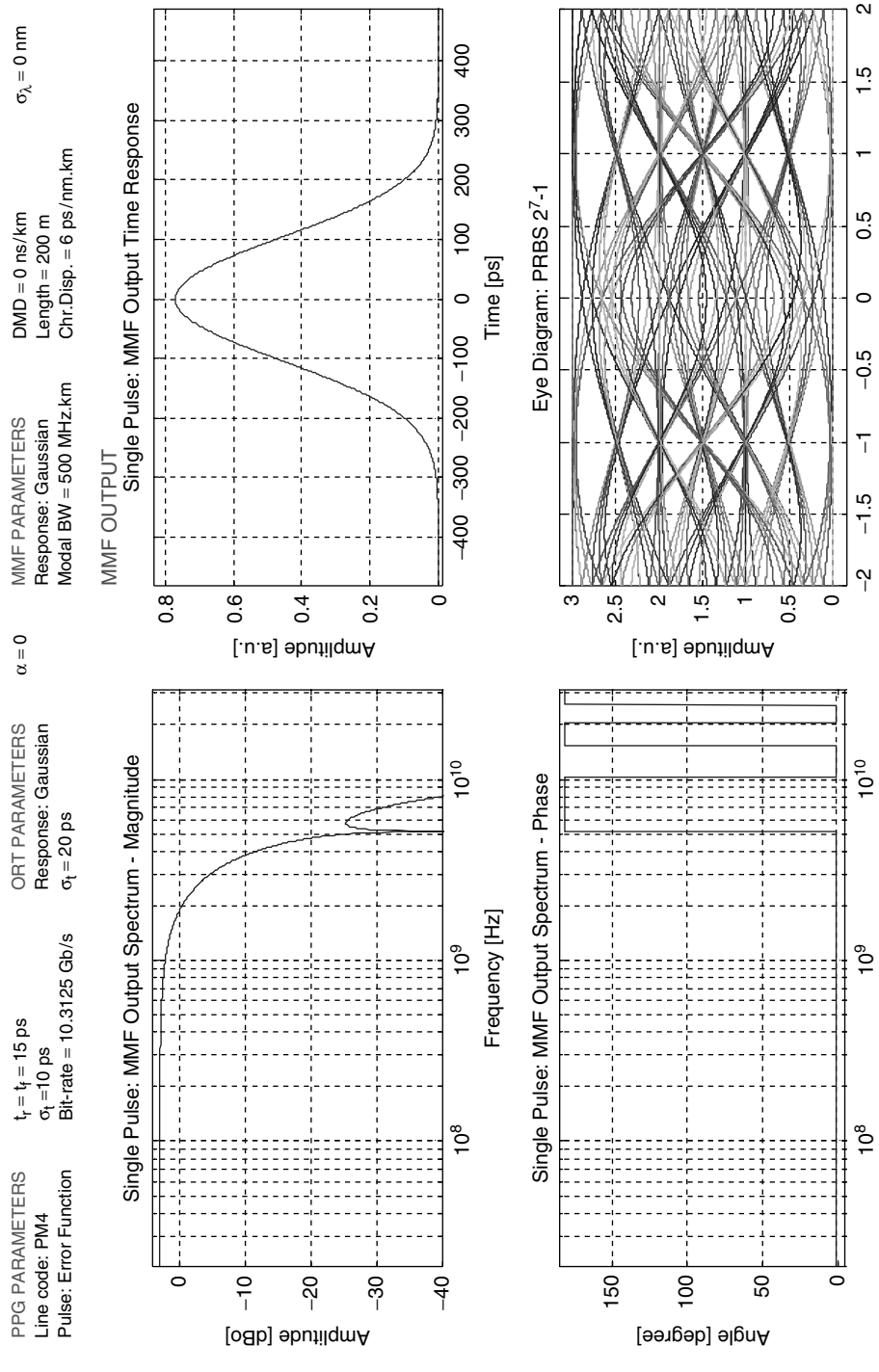

Figure 1.14 Frequency and time domain representations of PAM-4 PRBS 2^7-1 line code signals at 10GbE data rate after a 200 m single link length of Gaussian bandwidth multimode fiber. Left top represents the single pulse fiber output, while the left bottom graph shows the corresponding eye diagram in normalized bit time units. The legend at the top reports the simulated conditions for the pulse pattern generator and the light source impulse response

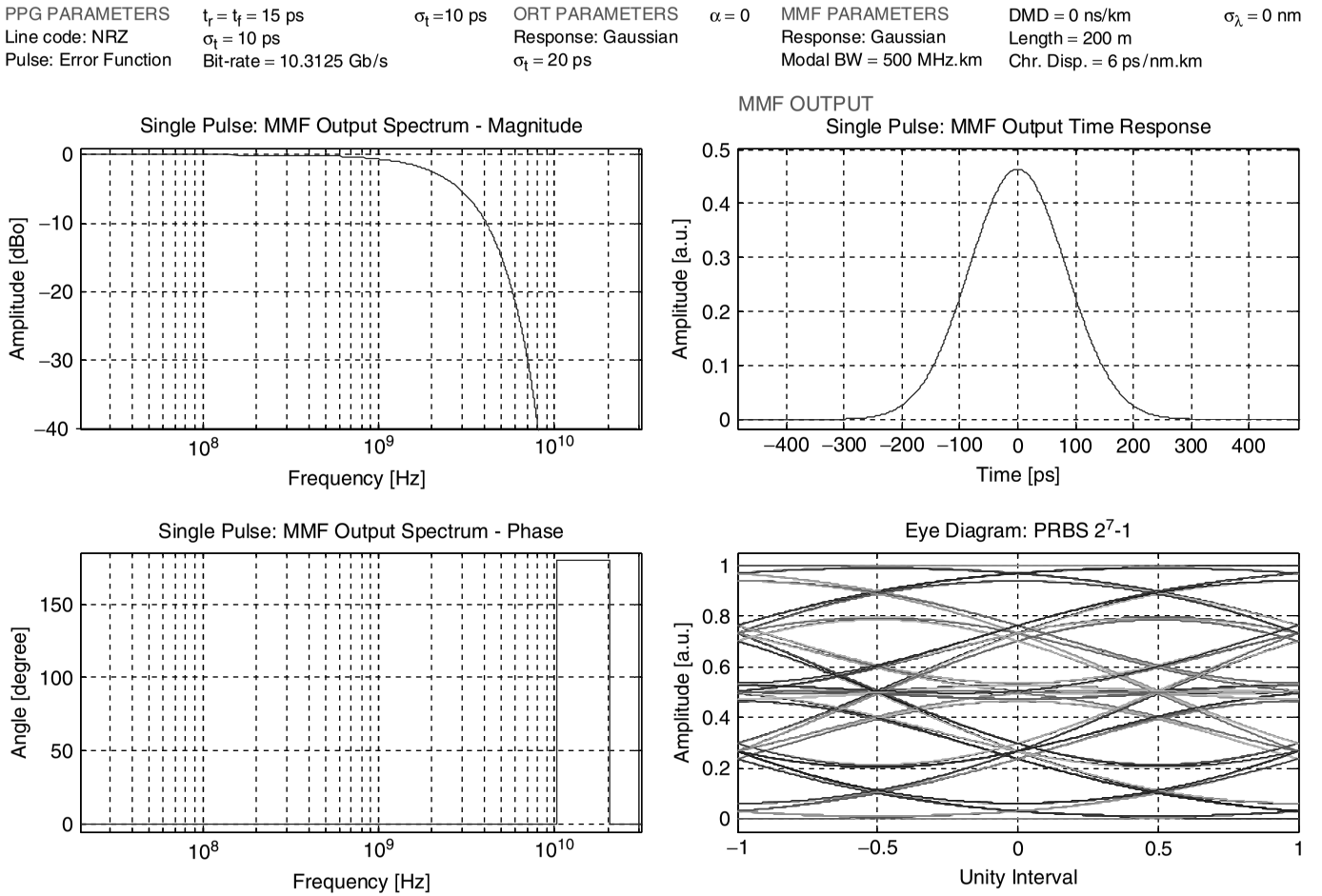

Figure 1.15 Frequency and time domain representations of NRZ PRBS 2^7-1 line code signals at 10GbE data rate after a 200 m single link length of Gaussian bandwidth multimode fiber. Left top represents the single pulse fiber output, while the left bottom graph shows the corresponding eye diagram in normalized bit time units. The legend at the top reports the simulated conditions for the pulse pattern generator and the light source impulse response

if small signal detection still seems possible. There is twice the channel bandwidth requirement in the case of NRZ coding, which leads instead to a completely closed eye diagram.

1.6.3.5 PAM-4 Coding Impairments in Optical Modulation

Previous analysis showed the comparison between NRZ and PAM-4 line code formats. The inherent reduced bandwidth occupancy of the PAM-4 line coding for the same information capacity supported by the NRZ format makes the former solution quite attractive as a valuable coding technique for overcoming the band-limited restrictions of legacy multimode fibers when operated at 10GbE standard. This is clearly summarized by the plot presented in Figure 1.7 between the coding net gain and the link distance for a given single multimode fiber. In that case, when the link length exceeds about 120 m, the PAM-4 coding results in superior performances with an increased signal-to-noise ratio. This is achieved by balancing the initially reduced eye opening due to multilevel modulation with the reduced signal pulse broadening during its propagation along the multimode fiber. The higher frequency content of the NRZ pulse undergoes a stronger interaction with the band-limited operation of the transmission channel, resulting in a relatively larger pulse dispersion.

These considerations are correct but they do not include any design issues or light source specifications. In order to obtain PAM-4 coding there is a need to discriminate among four different signal levels which correspond to three signal intervals. Figure 1.16 shows the PAM-4 signal and noise specifications.

The simple theory presented in the previous section assumes implicitly that the four signal levels are equally spaced and the noise power is uniform among them. This is reasonably true for

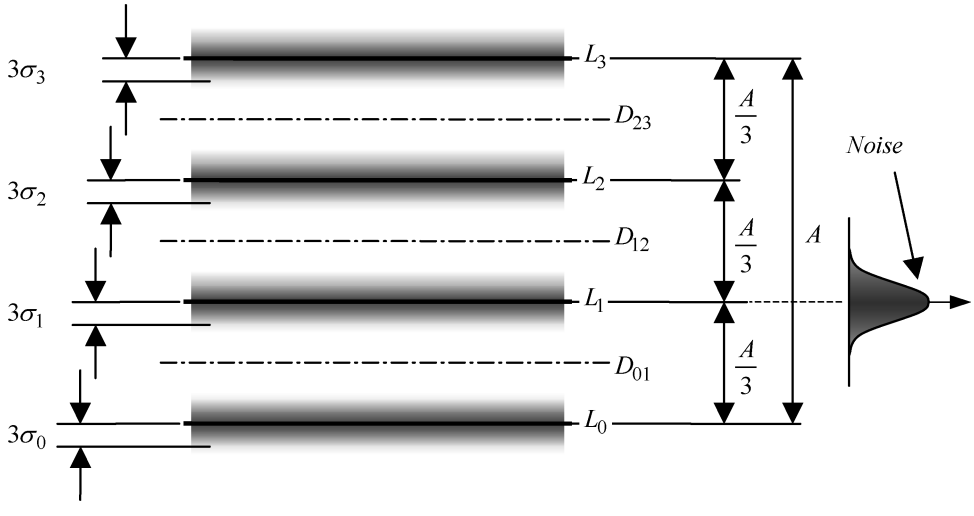

Figure 1.16 The PAM-4 code is represented through four digital levels, L_0, L_1, L_2, L_3, uniformly spaced by $A/3$, where $A = L_3 - L_0$ is the maximum signal amplitude. The noise level is qualitatively represented by $3\sigma_k$ and added over the signal level. Index $k = 0, 1, 2, 3$ indicates the corresponding signal level. Mid-range decision thresholds are respectively D_{01}, D_{12}, D_{23}

electrical PAM-4 modulation but it is not the general case for optical PAM-4 modulation. Different noise contributions on each signal level must be divided according to the source and the detector contribution. Depending on the detection system used, there may be either a negligible or a relevant shot noise contribution, and even a signal-spontaneous beat noise term if optical amplification is used at the receiver end section.

It is well known in optical communication that the shot noise power is proportional to the signal average optical power leading to an increasing signal-to-noise ratio as the square root of the average received optical power. In the case of optically amplified transmission systems, the signal-spontaneous beat noise usually becomes the dominant noise term and the signal-to-noise ratio remains constant versus the received average optical power, which leads to the well-known optical signal-to-noise ratio (OSNR) limited operations. Since both shot noise and signal-spontaneous beat noise are dependent on the optical signal level, it might be expected that optical PAM-4 exhibits a decreasing signal-to-noise ratio moving from the lower signal level towards the higher signal level. This could be compensated by properly adjusting the decision threshold for every signal interval. It this case, moving from the lowest interval towards a higher one, the decision threshold must be positioned correspondingly below the mid-range position, at relatively decreasing distances from the lower signal level. This threshold adjustment will compensate for higher noise fluctuations on the higher signal level.

There is at least one more reason for having different decision conditions corresponding to different intervals in the PAM-4 signal structure shown in Figure 1.16, namely the nonlinearity of the laser source transfer characteristic and the quite different source noise added to different levels due to strong differences in the lasing conditions. Laser nonlinearities in the L-I (eight power–current intensity) characteristic are responsible for different interval amplitudes between consecutive signal levels. Compared to the NRZ line coding, the reduced interval amplitude together with the laser nonlinearities makes the PAM-4 line coding implementation at 10GbE a very challenging design. In addition, the different noise spectral power densities exhibited by every direct modulated laser source at different lasing intensities require a careful decision threshold design. It will be seen later in this book that the optimum decision threshold between any two digital signal levels is determined by the minimum error probability achievable for the given signal amplitude and noise distributions on both levels. If noise distribution is not the same or if it changes during the lasing life, the corresponding optimum decision would require an adaptive threshold capability.

1.6.3.6 EDC-Based PAM-4 to NRZ Decoder

Figure 1.17 shows qualitatively the block diagram for an EDC-based PAM-4 decoder to be used in 10GbE transmission over legacy multimode fiber. The optical line code is assumed to be PAM-4 running at 10.3125 Gb/s. The optical detector followed by the low-noise transimpedance amplifier provides linear conversion to PAM-4 in the electrical domain. This signal simultaneously feeds the three binary signal discriminators operating at the equivalent half-rate NRZ line code. The embedded EDC feature improves the signal recognition after fiber bandwidth limitation added significant distortion. It is important to remark that the electrical signal speed in each discriminator is just half a bit rate, then 5.15625 Gb/s. This makes EDC implementation easier using the same high-speed IC technology as that used for the low-noise front end. Once the signal has been first discriminated among the three possible intervals defined by the PAM-4 coding, the LOGIC block provides the NRZ data coding.

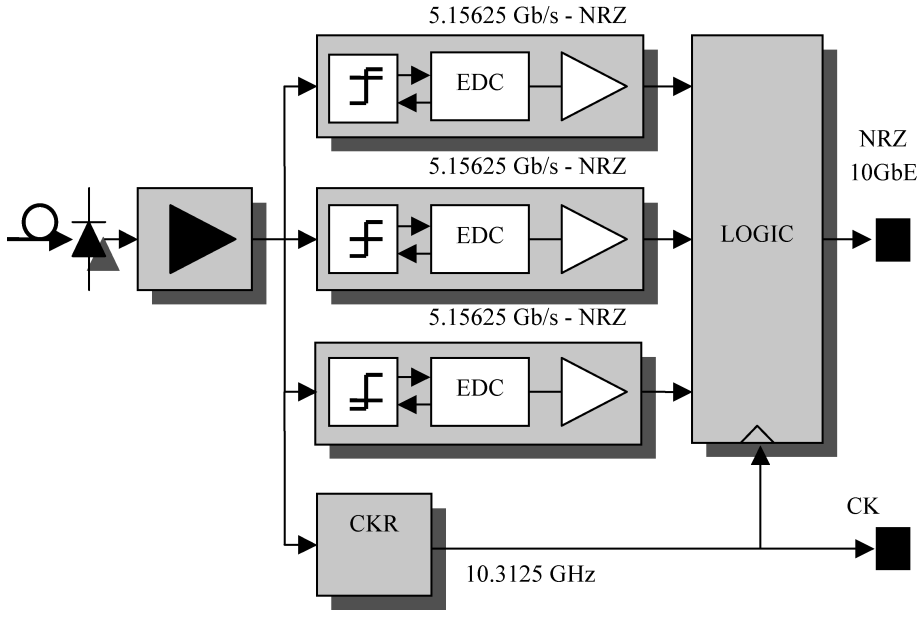

Figure 1.17 Block diagram of the EDC-based PAM-4 receiver. The optical signal is first detected assuming a linear PAM-4 transimpedance amplifier. Then each of the three signal discriminators operates according to the selected threshold with the EDC feature. The LOGIC block provides the NRZ coding output. The required signal speed of each signal discriminator is just one-half of the equivalent NRZ line code

1.7 Conclusions and Recommendations

The three solutions presented so far, namely EDC, OMF and PAM-4, serve as mitigating countermeasures for multimode fiber bandwidth limitation. In principle all these three solutions should allow 10GbE transmission over long-reach multimode fiber, although EDC gains an advantageous position due to the intense development pursued by several IC companies involved in these projects. Electronic dispersion compensation now looks much more promising than the other two alternatives, mainly due to relatively more relaxed optical tolerances required by the fiber channel and the laser source. Although at the present time a solid EDC design capable of successfully linking 300 m of legacy multimode fiber under operating field conditions has not yet been demonstrated, many laboratory experiments have demonstrated its compensation capability, including dynamic multipath adaptations.

In the following some general recommendations are summarized for achieving a successful 10GbE transmission over a multimode fiber link:

1. The 10GbE system must work with legacy MMF. No old fiber replacement should be planned.
2. No special patchcord should be used for restricted launching conditions. Those items will add cost and bulky passive components to the system layout. An integrated offset launching tool should be recommended for high-volume and low-cost production.
3. Low-cost and directly modulated receptacle laser sources must be used, instead of better performing but much more expensive solutions. More sophisticated transmitter solutions using externally modulated laser sources, such as the EAM-DFB laser, do not match both cost requirement and reduced power consumption for high-density pluggable modules. VCSEL, Fabry-Perot (FP) or

Table 1.1 Optical fiber telecommunication standards operating at the bit rate range of 155 Mb/s

Standards	Nominal Rate (Mb/s)	Recommendation	Application	Module MSA	Code	Bit rate (Mb/s)	Fiber	Distance (km)	Nominal WL (nm)	WL range (nm)	Attenuation range (dB)	CD max (ps/nm)	Penalty (dB)	Source	Linewidth RMS (nm)	PSD max (mW/MHz)	PWR range (dBm)	ER (dB)	SMSR (dB)	Detector	ESNR (dB10)	Sensitivity (dBm)	OVL (dBm)	BER
OC-1	51M	Telcordia GR-253-CORE	Telecom	–	SR-1	51 840	SM-G.652	12	1310	1260–1360	0–7	NA	1	MLM-FP-VCSEL LED	80	NA	−23/−14	8.2	NA	PIN	ffs	−31	−14	1.0×10^{-10} 1.0×10^{-10}
					IR-1	51 840	SM-G.652	21	1310	1260–1360	0–12	96	1	MLM-FP-VCSEL	23	NA	−15/−8	8.2	NA	PIN	ffs	−28	−8	1.0×10^{-10}
					IR-2	51 840	SM-G.652	42	1550	1430–1580	0–12	317 NA	1	MLM-FP-VCSEL SLM-DFB/DM	4 1 at −20 dB	NA ffs	−15/−8	8.2	NA 30	PIN	ffs	−28	−8	1.0×10^{-10} 1.0×10^{-10}
					LR-1	51 840	SM-G.652	50	1310	1280–1335	10–28	171 NA	1	MLM-FP-VCSEL SLM-DFB/DM	13 1 at −20 dB	NA ffs	−5/0	10	NA 30	PIN	ffs	−34	−10	1.0×10^{-10} 1.0×10^{-10}
					LR-2	51 840	SM-G.652	100	1550	1480–1580	10–28	20	1	SLM-DFB/DM	1 at −20 dB	ffs	−5/0	10	30	PIN	ffs	−34	−10	1.0×10^{-10}
					LR-3	51 840	SM-G.653	100	1550	1480–1580	10–28	444 NA	1	MLM-FP-VCSEL SLM-DFB/DM	5 1 at −20 dB	NA ffs	−5/0	10	NA 30	PIN	ffs	−34	−10	1.0×10^{-10} 1.0×10^{-10}
STM-1	155M	ITU-TG.957	Telecom	–	I-1	155 520	SM-G.652	2	1310	1260–1360	0–7	18 25	1	MLM-FP-VCSEL LED	40 80	NA	−15/−8	8.2	NA	PIN	ffs	−23	−8	1.0×10^{-10} 1.0×10^{-10}
					S-1.1	155 520	SM-G.652	15	1310	1260–1360	0–12	96	1	MLM-FP-VCSEL	7.7	NA	−15/−8	8.2	NA	PIN	ffs	−28	−8	1.0×10^{-10}
					S-1.2	155 520	SM-G.652	15	1550	1430–1576 1430–1580	0–12	296 NA	1	MLM-FP-VCSEL SLM-DFB/DM	2.5 1 at −20 dB	NA ffs	−15/−8	8.2	NA 30	PIN	ffs	−28	−8	1.0×10^{-10} 1.0×10^{-10}
					L-1.1	155 520	SM-G.652	40	1310	1263–1360	10–28	246 NA	1	MLM-FP-VCSEL SLM-DFB/DM	3 1 at −20 dB	NA ffs	−5/0	10	NA 30	PIN	ffs	−34	−10	1.0×10^{-10} 1.0×10^{-10}
					L-1.2	155 520	SM-G.652/G.654	80	1550	1480–1580	10–28	NA	1	SLM-DFB/DM	1 at −20 dB	ffs	−5/0	10	30	PIN	ffs	−34	−10	1.0×10^{-10}
					L-1.3	155 520	SM-G.653	80	1550	1534–1566 1523–1577 1480–1580	10–28	246 296 NA	1	MLM-FP SLM-DFB/DM	3 2.5 1 at −20 dB	ffs	−5/0	10	NA NA 30	PIN	ffs	−34	−10	1.0×10^{-10} 1.0×10^{-10} 1.0×10^{-10}

(*continued overleaf*)

Table 1.1 (*continued*)

Standards	Nominal Rate (Mb/s)	Recommendation	Application	Module MSA	Code	Bit rate (Mb/s)	Fiber	Distance (km)	Nominal WL (nm)	WL range (nm)	Attenuation range (dB)	CD max (ps/nm)	Penalty (dB)	Source	Linewidth RMS (nm)	PSD max (mW/MHz)	PWR range (dBm)	ER (dB)	SMSR (dB)	Detector	ESNR (dB10)	Sensitivity (dBm)	OVL (dBm)	BER
OC-3	155M	Telcordia GR-253-CORE	Telecom	–	SR-1	155 520	SM-G.652	12	1310	1260–1360	0–7	18 25	1	MLM-FP-VCSEL LED	40 80	NA	−15/−8	8.2	NA	PIN	ffs	−23	−8	1.0×10^{-10} 1.0×10^{-10}
					IR-1	155 520	SM-G.652	21	1310	1261–1360	0–12	96	1	MLM-FP-VCSEL	7.7	NA	−15/−8	8.2	NA	PIN	ffs	−28	−8	1.0×10^{-10}
					IR-2	155 520	SM-G.652	42	1550	1430–1576 1430–1580	0–12	296 NA	1	MLM-FP-VCSEL SLM-DFB/DM	2.5 1 at −20 dB	NA ffs	−15/−8	8.2	NA 30	PIN	ffs	−28	−8	1.0×10^{-10} 1.0×10^{-10}
					LR-1	155 520	SM-G.652	50	1310	1263–1360	10–28	246 NA	1	MLM-FP-VCSEL SLM-DFB/DM	3 1 at −20 dB	NA ffs	−5/0	10	NA 30	PIN	ffs	−34	−10	1.0×10^{-10} 1.0×10^{-10}
					LR-2	155 520	SM-G.652	100	1550	1480–1580	10–28	20	1	SLM-DFB/DM	1 at −20 dB	ffs	−5/0	10	30	PIN	ffs	−34	−10	1.0×10^{-10}
					LR-3	155 520	SM-G.653	100	1550	1534–1566 1523–1577 1480–1580	10–28	246 296 NA	1	MLM-FP-VCSEL MLM-FP-VCSEL SLM-DFB/DM	3 2.5 1 at −20 dB	NA ffs	−5/0	10	NA NA 30	PIN	ffs	−34	−10	1.0×10^{-10} 1.0×10^{-10} 1.0×10^{-10}

Table 1.2 Optical fiber telecommunication standards operating at the bit rate range of 622 Mb/s and 2.5 Gb/s

FO standards	Nominal rate (Mb/s)	Recommendation	Application		Code	Bit rate (Mb/s)	Fiber	Distance (km)	Nominal WL (nm)	WL range (nm)	Attenuation range (dB)	CD_{max} (ps/nm)	Penalty (dB)	Source	Linewidth RMS (nm)	SPD_{max} (mW/MHz)	PWR range (dBm)	ER (dB)	SMSR (dB)	Detector	ESNR (dB10)	Sensitivity (dBm)	OVL (dBm)	BER
STM-4	622M	ITU-T G.957	Telecom	–	I-4	622 080	SM-G.652	2	1310	1261–1360	0–7	13 14	1	MLM-FP-VCSEL LED	14.5 35	NA	−15/−8	8.2	NA	PIN	ffs	−23	−8	1.0×10^{-10} 1.0×10^{-10}
					S-4.1	622 080	SM-G.652	15	1310	1293–1334 1274–1356	0–12	46 74	1	MLM-FP-VCSEL	4 2.5	NA	−15/−8	8.2	NA	PIN	ffs	−28	−8	1.0×10^{-10} 1.0×10^{-10}
					S-4.2	622080	SM-G.652	15	1550	1430–1580	0–12	NA	1	SLM-DFB/DM	1 at −20 dB	ffs	−15/−8	8.2	30	PIN	ffs	−28	−8	1.0×10^{-10}
					L-4.1	622080	SM-G.652	40	1310	1300–1325 1296–1330 1280–1335	10–24	92 109 NA	1	MLM-FP-VCSEL SLM-DFB/DM	2 1.7 1 at −20 dB	NA ffs	−3/+2	10	NA 30	PIN	ffs	−28	−8	1.0×10^{-10} 1.0×10^{-10} 1.0×10^{-10}
					L-4.2	622080	SM-G.652/ G.654	80	1550	1480–1580	10–24	NA	1	SLM-DFB/DM	1 at −20 dB	ffs	−3/+2	10	30	PIN	ffs	−28	−8	1.0×10^{-10}
					L-4.3	622080	SM-G.653	80	1550	1480–1580	10–24	NA	1	SLM-DFB/DM	1 at −20 dB	ffs	−3/+2	10	30	PIN	ffs	−28	−8	1.0×10^{-10}
	622M	ITU-T G.691	Telecom	–	V-4.1	622080	SM-G.652	60	1310	1290–1330	22–33	200	1	SLM-DFB/DM	ffs	ffs	0/+4	10	ffs	PIN/APD	ffs	−34	−18	1.0×10^{-12}
					V-4.2	622080	SM-G.652	120	1550	1530–1565	22–33	2,400	1	SLM-DFB/DM	ffs	ffs	0/+4	10	ffs	PIN/APD	ffs	−34	−18	1.0×10^{-12}
					V-4.3	622080	SM-G.653	120	1550	1530–1565	22–33	400	1	SLM-DFB/DM	ffs	ffs	0/+4	10	ffs	PIN/APD	ffs	−34	−18	1.0×10^{-12}
					U-4.2	622080	SM-G.652	160	1550	1530–1565	33–44	3,200	2	SLM-DFB/EM	ffs	ffs	+12/+15	10	ffs	PIN/APD	ffs	−34	−18	1.0×10^{-12}
					U-4.3	622080	SM-G.653	160	1550	1530–1565	33–44	530	1	SLM-DFB/EM	ffs	ffs	+12/+15	10	ffs	PIN/APD	ffs	−33	−18	1.0×10^{-12}
OC-12	622M	Telcordia GR-253-CORE	Telecom	–	SR-1	622080	SM-G.652	12	1310	1261–1360	0–7	13 14	1	MLM-FP-VCSEL LED	14.5 35	NA	−15/−8	8.2	NA	PIN	ffs	−23	−8	1.0×10^{-10} 1.0×10^{-10}
					IR-1	622080	SM-G.652	21	1310	1293–1334 1274–1356	0–12	46 74	1	MLM-FP-VCSEL	4 2.5	NA	−15/−8	8.2	NA	PIN	ffs	−28	−8	1.0×10^{-10} 1.0×10^{-10}
					IR-2	622080	SM-G.652	42	1550	1430–1580	0–12	NA	1	SLM-DFB/DM	1 at −20 dB	ffs	−15/−8	8.2	30	PIN	ffs	−28	−8	1.0×10^{-10}
					LR-1	622080	SM-G.652	42	1310	1300–1325 1296–1330 1280–1335	10–24	92 109 NA	1	MLM-FP-VCSEL SLM-DFB/DM	2 1.7 1 at −20 dB	NA ffs	−3/+2	10	NA 30	PIN	ffs	−28	−8	1.0×10^{-10} 1.0×10^{-10} 1.0×10^{-10}
					LR-2	622080	SM-G.652	85	1550	1480–1580	10–24	NA	1	SLM-DFB/DM	1 at −20 dB	ffs	−3/+2	10	30	PIN	ffs	−28	−8	1.0×10^{-10}
					LR-3	622080	SM-G.653	85	1550	1480–1580	10–24	NA	1	SLM-DFB/DM	1 at −20 dB	ffs	−3/+2	10	30	PIN	ffs	−28	−8	1.0×10^{-10}

(*continued overleaf*)

Table 1.2 (*continued*)

FO standards	Nominal rate (Mb/s)	Recommendation	Application		Code	Bit rate (Mb/s)	Fiber	Distance (km)	Nominal WL (nm)	WL range (nm)	Attenuation range (dB)	CD_{max} (ps/nm)	Penalty (dB)	Source	Linewidth RMS (nm)	SPD_{max} (mW/MHz)	PWR range (dBm)	ER (dB)	SMSR (dB)	Detector	ESNR (dB10)	Sensitivity (dBm)	OVL (dBm)	BER
STM-16	2.6G	ITU-T G.957	Telecom	300-pin	I-16	2488 320	SM-G.652	2	1310	1266–1360	0–7	12	1	MLM-FP-VCSEL	4	NA	−10/−3	8.2	NA	PIN	ffs	−18	−3	1.0×10^{-10}
					S-16.1	2488 320	SM-G.652	15	1310	1260–1360	0–12	NA	1	SLM-DFB/DM	1 at −20 dB	ffs	−5/0	8.2	30	PIN	ffs	−18	0	1.0×10^{-10}
					S-16.2	2488 320	SM-G.652	15	1550	1430–1580	0–12	NA	1	SLM-DFB/DM	<1 at −20 dB	ffs	−5/0	8.2	30	PIN	ffs	−18	0	1.0×10^{-10}
					L-16.1	2488 320	SM-G.652	40	1310	1280–1335	10–24	NA	1	SLM-DFB/EM	1 at −20 dB	ffs	−2/+3	8.2	30	PIN	ffs	−27	−9	1.0×10^{-10}
					L-16.2	2488 320	SM-G.652/ G.654	80	1550	1500–1580	10–24	1200–1600	1	SLM-DFB/EM	<1 at −20 dB	ffs	−2/+3	8.2	30	PIN	ffs	−28	−9	1.0×10^{-10}
					L-16.3	2488 320	SM-G.653	80	1550	1500–1580	10–24	NA	1	SLM-DFB/EM	1 at −20 dB	ffs	−2/+3	8.2	30	PIN	ffs	−27	−9	1.0×10^{-10}
	2.6G	ITU-T G.691	Telecom	300-pin	V-16.2	2488 320	SM-G.652	120	1550	1530–1565	22–33	2,400	2	SLM-DFB/EM	ffs	ffs	+10/+13	8.2	ffs	PIN/APD	ffs	−25	−9	1.0×10^{-12}
					V-16.3	2488 320	SM-G.653	120	1550	1530–1565	22–33	400	1	SLM-DFB/EM	ffs	ffs	+10/+13	8.2	ffs	PIN/APD	ffs	−24	−9	1.0×10^{-12}
					U-16.2	2488 320	SM-G.652	160	1550	1530–1565	33–44	3,200	2	SLM-DFB/EM	ffs	ffs	+12/+15	10	ffs	APD	ffs	−34	−18	1.0×10^{-12}
					U-16.3	2488 320	SM-G.653	160	1550	1530–1565	33–44	530	1	SLM-DFB/EM	ffs	ffs	+12/+15	10	ffs	APD	ffs	−33	−18	1.0×10^{-12}
OC-48	2.6G	Telcordia GR-253-	Telecom	300-pin	SR-1	2488 320	SM-G.652	12	1310	1266–1360	0–7	12	1	MLM-FP-VCSEL	4	NA	−10/−3	8.2	NA	PIN	ffs	−18	−3	1.0×10^{-10}
					IR-1	2488 320	SM-G.652	21	1310	1260–1360	0–12	NA	1	SLM-DFB/DM	1 at −20 dB	ffs	−5/0	8.2	30	PIN	ffs	−18	0	1.0×10^{-10}
					IR-2	2488 320	SM-G.652	42	1550	1430–1580	0–12	ffs	1	SLM-DFB/DM	<1 at −20 dB	ffs	−5/0	8.2	30	PIN	ffs	−18	0	1.0×10^{-10}
					LR-1	2488 320	SM-G.652	42	1310	1280–1335	10–24	NA	1	SLM-DFB/DM	1 at −20 dB	ffs	−2/+3	8.2	30	PIN	ffs	−27	−9	1.0×10^{-10}
					LR-2	2488 320	SM-G.652	85	1550	1500–1580	10–24	1200–1600	2	SLM-DFB/EM	<1 at −20 dB	ffs	−2/+3	8.2	30	PIN	ffs	−28	−9	1.0×10^{-10}
					LR-3	2488 320	SM-G.653	85	1550	1500–1580	10–24	NA	1	SLM-DFB/DM	1 at −20 dB	ffs	−2/+3	8.2	30	PIN	ffs	−27	−9	1.0×10^{-10}

Table 1.3 Optical fiber telecommunication standards operating at the bit rate range of 10 Gb/s

FO standards	Nominal rate (Mb/s)	Recommendation	Application	Code	Bit rate (Mb/s)	Fiber	Distance (km)	Nominal WL (nm)	WL range (nm)	Attenuation range (dB)	CD_{max} (ps/nm)	Penalty (dB)	Source	Linewidth RMS (nm)	SPD_{max} (mW/MHz)	PWR range (dBm)	ER (dB)	SMSR (dB)	Detector	ESNR (dB10)	Sensitivity (dBm)	OVL (dBm)	BER
10G	10G	ITU-T G.	Telecom	300-pin	VSR600-2M1	9 953 280	SM-G.652	0.6	1310	1260–1360	3–12	4	1	MLM-FP-VCSEL	3	NA	+2/+5	6	NA	PIN	ffs	−11	−1	1.0×10^{-12}
					VSR600-2M2	9 953 280	SM-G.652	0.6	1550	1530–1565	3–12	12	1	MLM-FP-VCSEL	NA	NA	−1/+2	8.2	30	PIN	ffs	−14	−1	1.0×10^{-12}
					VSR600-2M5	9 953 280	SM-G.655	0.6	1550	1530–1565	3–12	10	1	MLM-FP-VCSEL	NA	NA	−1/+2	8.2	30	PIN	ffs	ffs	ffs	1.0×10^{-12}
STM-64	10G	ITU-T G.691	Telecom	300-pin	I-64.1r	9 953 280	SM-G.652	0.6	1310	1260–1360	0–4	4	1	MLM-FP-VCSEL	3	NA	−6/−1	6	NA	PIN	ffs	−11	−1	1.0×10^{-12}
					I-64.1	9 953 280	SM-G.652	2	1310	1290–1330	0–4	7	1	SLM-DFB	<1 at −20 dB	ffs	−6/−1	6	30	PIN	ffs	−11	−1	1.0×10^{-12}
					I-64.2r	9 953 280	SM-G.652	2	1550	1530–1565	0–7	40	2	SLM-DFB	ffs	ffs	−5/−1	8.2	30	PIN	ffs	−14	−1	1.0×10^{-12}
					I-64.2	9 953 280	SM-G.652	25	1550	1530–1565	0–7	500	2	SLM-DFB/EM	ffs	ffs	−5/−1	8.2	30	PIN	ffs	−14	−1	1.0×10^{-12}
					I-64.3	9 953 280	SM-G.653	25	1550	1530–1565	0–7	80	1	SLM-DFB/EM	ffs	ffs	−5/−1	8.2	30	PIN	ffs	−13	−1	1.0×10^{-12}
					I-64.5	9 953 280	SM-G.655	25	1550	1530–1565	0–7	ffs	1	SLM-DFB/EM	ffs	ffs	−5/−1	8.2	30	PIN	ffs	−13	−1	1.0×10^{-12}
					S-64.1	9 953 280	SM-G.652	20	1310	1290–1330	6–11	70	1	SLM-DFB/EM	ffs	ffs	+1/+5	6	30	PIN	ffs	−11	−1	1.0×10^{-12}
					S-64.2a	9 953 280	SM-G.652	40	1550	1530–1565	7–11	800	2	SLM-DFB/EM	ffs	ffs	−5/−1	8.2	30	PIN/APD	ffs	−18	−8	1.0×10^{-12}
					S-64.2b	9 953 280	SM-G.652	40	1550	1530–1565	3–11	800	2	SLM-DFB/EM	ffs	ffs	−1/+2	8.2	30	PIN	ffs	−14	−1	1.0×10^{-12}
					S-64.3a	9 953 280	SM-G.653	40	1550	1530–1565	7–11	130	1	SLM-DFB/EM	ffs	ffs	−5/+1	8.2	30	PIN/APD	ffs	−17	−8	1.0×10^{-12}
					S-64.3b	9 953 280	SM-G.653	40	1550	1530–1565	3–11	130	1	SLM-DFB/EM	ffs	ffs	−1/+2	8.2	30	PIN	ffs	−13	−1	1.0×10^{-12}
					S-64.5a	9 953 280	SM-G.655	40	1550	1530–1565	7–11	130	1	SLM-DFB/EM	ffs	ffs	−5/−1	8.2	30	PIN/APD	ffs	−17	−8	1.0×10^{-12}
					S-64.5b	9 953 280	SM-G.655	40	1550	1530–1565	3–11	130	1	SLM-DFB/EM	ffs	ffs	−1/+2	8.2	30	PIN	ffs	−13	−1	1.0×10^{-12}
					L-64.1	9 953 280	SM-G.652	40	1310	1290–1320	17–22	130	1	SLM-DFB/EM	ffs	ffs	+4/+7	6	30	APD	ffs	−19	−10	1.0×10^{-12}
					L-64.2a	9 953 280	SM-G.652	80	1550	1530–1565	11–22	1,600	2	SLM-DFB	ffs	ffs	−2/+2	10	ffs	PIN/OA	ffs	−26	−9	1.0×10^{-12}
					L-64.2b	9 953 280	SM-G.652	80	1550	1530–1565	16–22	1,600	2	SLM-DFB/EM	ffs	ffs	+10/+13	8.2	ffs	PIN	ffs	−14	−3	1.0×10^{-12}
					L-64.2c	9 953 280	SM-G.652	80	1550	1530–1565	11–22	1,600	2	SLM-DFB	ffs	ffs	−2/+2	10	ffs	PIN/OA	ffs	−26	−9	1.0×10^{-12}
					L-64.3	9 953 280	SM-G.653	80	1550	1530–1565	16–22	260	1	SLM-DFB/EM	ffs	ffs	+10/+13	8.2	ffs	PIN	ffs	−13	−3	1.0×10^{-12}
					V-64.2a	9 953 280	SM-G.652	120	1550	1530–1565	22–33	2,400	2	SLM-DFB/EM	ffs	ffs	+10/+13	10	ffs	PIN/OA	ffs	−25	−9	1.0×10^{-12}
					V-64.2b	9 953 280	SM-G.652	120	1550	1530–1565	22–33	2,400	2	SLM-DFB/EM	ffs	ffs	+12/+15	8.2	ffs	PIN/OA	ffs	−23	−7	1.0×10^{-12}
					V-64.3	9 953 280	SM-G.653	120	1550	1530–1565	22–33	400	1	SLM-DFB/EM	ffs	ffs	+10/+13	8.2	ffs	PIN/OA	ffs	−24	−9	1.0×10^{-12}
OC-192	10G	Telcordia GR-253-CORE	Telecom	300-pin	SR-1	9 953 280	SM-G.652	7	1310	1290–1330	0–4	6.6	1	SLM-DFB/DM	ffs	0.1	−6/−1	6	ffs	PIN	26	−11	−1	1.0×10^{-12}
					SR-2	9 953 280	SM-G.652	25	1550	1530–1565	0–7	500	2	SLM-DFB/EM	ffs	0.1	−5/−1	8.2	ffs	PIN	26	−14	−1	1.0×10^{-12}
					IR-1	9 953 280	SM-G.652	20	1310	1290–1330	6–11	70	1	SLM-DFB/DM	ffs	0.1	+1/+5	6	ffs	PIN	26	−11	−1	1.0×10^{-12}
					IR-2	9 953 280	SM-G.652	40	1550	1530–1565	3–11	800	2	SLM-DFB/EM	ffs	0.1	−1/+2	8.2	ffs	PIN	26	−14	−1	1.0×10^{-12}
					IR-3	9 953 280	SM-G.653	40	1550	1530–1565	3–11	130	1	SLM-DFB/DM	ffs	0.1	−1/+2	8.2	ffs	PIN	26	−13	−1	1.0×10^{-12}
					LR-1	9 953 280	SM-G.652	40	1310	1290–1330	17–22	130	1	SLM-DFB/DM	ffs	0.1	+4/+7	6	ffs	PIN/OA	OSNR 28	−19	−10	1.0×10^{-12}
					LR-2a	9 953 280	SM-G.652	80	1550	1530–1565	11–22	1600	2	SLM-DFB/EM	ffs	0.1	−2/+2	10	ffs	PIN/OA	OSNR 30	−26	−9	1.0×10^{-12}
					LR-2b	9 953 280	SM-G.652	80	1550	1530–1565	16–22	1600	2	SLM-DFB/EM	ffs	0.1	+10/+13	8.2	ffs	PIN	OSNR 30	−14	−3	1.0×10^{-12}
					LR-2c	9 953 280	SM-G.652	80	1550	1530–1565	11–22	1600	2	SLM-DFB/EM	ffs	0.1	−2/+2	10	ffs	PIN/OA	OSNR 30	−26	−9	1.0×10^{-12}
					LR-3	9 953 280	SM-G.653	80	1550	1530–1565	16–22	260	1	SLM-DFB/EM	ffs	0.1	+10/+13	8.2	ffs	PIN	OSNR 28	−13	−3	1.0×10^{-12}
					VR-1	9 953 280	SM-G.652	60	1310	1290–1330	22–33	240	1	SLM-DFB/EM	ffs	0.1	+10/+13	6	ffs	PIN/OA	OSNR ffs	−24	−9	1.0×10^{-12}
					VR-2a	9 953 280	SM-G.652	120	1550	1530–1565	22–33	2400	2	SLM-DFB/EM	ffs	0.1	+10/+13	10	ffs	PIN/OA	OSNR ffs	−25	−9	1.0×10^{-12}
					VR-3	9 953 280	SM-G.653	120	1550	1530–1565	22–33	400	1	SLM-DFB/EM	ffs	0.1	+10/+13	8.2	ffs	PIN/OA	OSNR ffs	−24	−9	1.0×10^{-12}

Table 1.4 Optical fiber telecommunication standards operating at the bit rate range of 40 Gb/s and fiber channel standards

FO standards	Nominal rate (Mb/s)	Recommendation	Application	Code	Bit rate (Mb/s)	Fiber	Distance (km)	Nominal WL (nm)	WL range (nm)	Attenuation range (dB)	CD_{max} (ps/nm)	Penalty (dB)	Source	Linewidth RMS (nm)	SPD_{max} (mW/MHz)	PWR range (dBm)	ER (dB)	SMSR (dB)	Detector	ESNR (dB10)	Sensitivity (dBm)	OVL (dBm)	BER
STM-266	40G	ITU-T G.vst	Telecom	40G MSA 300-pin VSR2000-3L1	39813.120	SM-G.652	2	1310	1290–1330	3–6	6.6	1	SLM-DFB/EM	ffs	ffs	+2/+5	10	35	PIN	ffs	−5	+2	1.0×10^{-12}
				VSR2000-3L2	39813.120	SM-G.652	2	1550	1530–1565	0–6	40	1	SLM-DFB/EM	ffs	ffs	+1/+3	8.2	35	PIN	ffs	−6	+3	1.0×10^{-12}
				VSR2000-3L5	39813.120	SM-G.655					20												1.0×10^{-12}
				VSR2000-3M1	39813.120	SM-G.652	2	1310	1290–1330	3–12	6.6	1	SLM-DFB/EM	ffs	ffs	+8/+10	10	35	PIN	ffs	−5	+2	1.0×10^{-12}
				VSR2000-3M2	39813.120	SM-G.652	2	1550	1530–1565	3–12	40	1	SLM-DFB/EM	ffs	ffs	0/+3	7	35	PIN	ffs	−13	0	1.0×10^{-12}
				VSR2000-3M5	39813.120	SM-G.655					20												1.0×10^{-12}
				VSR2000-3H2	39813.120	SM-G.652	2	1550	1530–1565	3–16	40	1	SLM-DFB/EM	ffs	ffs	0/+3	7	35	PIN	ffs	−17	0	1.0×10^{-12}
				VSR2000-3H5	39813.120	SM-G.655					20												1.0×10^{-12}
		ITU-T G.691	Telecom	40G MSA 300 I-256.2	39813.120	SM-G.652	25	1550	ffs	ffs	ffs	ffs	SLM-DFB/EM	ffs	ffs	ffs	ffs	ffs	ffs	ffs	ffs	ffs	1.0×10^{-12}
				S-256.2	39813.120	SM-G.652	40	1550	ffs	ffs	ffs	ffs	SLM-DFB/EM	ffs	ffs	ffs	ffs	ffs	ffs	ffs	ffs	ffs	1.0×10^{-12}
				S-256.3	39813.120	SM-G.653	40	1550	ffs	ffs	ffs	ffs	SLM-DFB/EM	ffs	ffs	ffs	ffs	ffs	ffs	ffs	ffs	ffs	1.0×10^{-12}
				L-256.2	39813.120	SM-G.652	80	1550	ffs	ffs	ffs	ffs	SLM-DFB/EM	ffs	ffs	ffs	ffs	ffs	ffs	ffs	ffs	ffs	1.0×10^{-12}
				L-256.3	39813.120	SM-G.653	80	1550	ffs	ffs	ffs	ffs	SLM-DFB/EM	ffs	ffs	ffs	ffs	ffs	ffs	ffs	ffs	ffs	1.0×10^{-12}

FO standards	Nominal rate (Mb/s)	Recommendation	Application	Code	Bit rate (Mb/s)	Fiber	Distance (m)	Nominal WL (nm)	WL range (nm)	Attenuation range (dB)	Modal BW (MHz km)	Penalty (dB)	Source	Linewidth RMS (nm)	Tx OMA min (μW)	Tx AVR range (dBm)	ER (dB)	SMSR (dB)	Detector	Rx OMA sen (μW)	Rx AVR sen (dBm)	Rx AVR ovl (dBm)	BER
1GFC	1G	FC-PI	Datacol	SFP-IS 100-SM-LC-L	1062.5	SM-G.652	10000	1310	1285–1345	0–8	NA	2	MLM-FP-VCSEL	3	174	−9.5/−3	9	NA	PIN	15	−20.2	−3	1.0×10^{-12}
				100-M5-SN-I	1062.5	MM-G.651	500.0	850	770–860	0–4	500	3	MLM-FP-VCSEL	1	156	−10/0	9	NA	PIN	31	−17	0	1.0×10^{-12}
		R		100-M6-SN-I	1062.5	MM-62.5μ	300.0	850	770–860	0–3	200	4	MLM-FP-VCSEL	1	156	−10/0	9	NA	PIN	31	−17	0	1.0×10^{-12}
2GFC	2G	FC-PI	Datacol	SFP-IS 200-SM-LC-L	2125	SM-G.652	10000	1310	1290–1340	0–8	NA	2	MLM-FP-VCSEL	2	150	−10.4/−3	10	NA	PIN	15	−20.4	−3	1.0×10^{-12}
				200-M5-SN-I	2125	MM-G.651	300.0	850	830–860	0–3	500	3	MLM-FP-VCSEL	0.85	196	−9.2/0	10	NA	PIN	49	−15.2	0	1.0×10^{-12}
		R		200-M6-SN-I	2125	MM-62.5μ	150.00	850	830–860	0–2	200	4	MLM-FP-VCSEL	−0.85	196	−9.2/0	10	NA	PIN	49	−15.2	0	1.0×10^{-12}
4GFC	4G	FC-PI	Datacol	SFP-IS 400-SM-LC-L	4250	SM-G.652	10000	1310	1265–1365	0–8	NA	2	SLM-DFB	<1 at −20 dB	290	−7.5/−3	10	NA	PIN	29	−17.5	−1	1.0×10^{-12}
				400-M5-SN-I	4250	MM-G.651	150.00	850	830–860	0–2	500	4	MLM-FP-VCSEL	0.85	247	−8.2/0	10	NA	PIN	61	−14.2	0	1.0×10^{-12}
		R		400-M6-SN-I	4250	MM-62.5μ	70.00	850	830–860	0–2	200	4	MLM-FP-VCSEL	0.85	247	−8.2/0	10	NA	PIN	61	−14.2	0	1.0×10^{-12}

Table 1.5 Optical fiber datacommunication standards operating at the bit rate range of 10 Gb/s

FO standards	Nominal rate (Mb/s)	Recommendation	Application	Code	Bit rate (Mb/s)	Fiber	Distance (m)	Nominal WL (nm)	WL range (nm)	Power budget (dB)	Modal BW (MHz km)	Penalty (dB)	Source	Linewidth RMS (nm)	Tx OMA min (μW)	Tx AVR range (dBm)	ER (dB)	SMSR (dB)	Detector	Rx OMA sens (μW)	Rx AVR sens (dBm)	Rx AVR ovl (dBm)	BER
1GbE	1G	IEEE P802.3z/D5.0	Datacom	SFP-ISFP 1000BASE-SX	1250	MM-62.5μ	220	850	770–860	7.5	160	5.1	MLM-FP-VCSEL	0.85	174	−9.5/0	9	NA	PIN	31	−17	0	1.0×10^{-12}
							275				200	4.9											1.0×10^{-12}
						MM-G.651	500	850	770–860	7.5	400	4.1	MLM-FP-VCSEL	0.85	174	−9.5/0	9	NA	PIN	31	−17	0	1.0×10^{-12}
							550				500	3.9											1.0×10^{-12}
				SFP-ISFP 1000BASE-LX	1250	MM-62.5μ	550	1310	1270–1355	7.5	500	5.1	MLM-FP-VCSEL	4	110	−11.5/−3	9	NA	PIN	20	−19	−3	1.0×10^{-12}
						MM-G.651	550	1310	1270–1355	7.5	400	5.1	MLM-FP-VCSEL	4	110	−11.5/−3	9	NA	PIN	20	−19	−3	1.0×10^{-12}
							550				500												1.0×10^{-12}
						SM-G.652	5000	1310	1270–1355	8.0	NA	3.4	MLM-FP-VCSEL	4	124	−11/−3	9	NA	PIN	20	−19	−3	1.0×10^{-12}
10GbE	10G	IEEE P802.3ae	Datacom	XFP-X2-XPAK-XENPAK 10BASE-SW	9953 280	MM-62.5μ	26	850	840–860	7.3	160	5.7	MLM-FP-VCSEL	0.45	124	−7.3/−1	3	NA	PIN	68	−9.9	−1	1.0×10^{-12}
							33				200	5.1											1.0×10^{-12}
						MM-G.651	66				400	5.6											1.0×10^{-12}
							82				500	5.5											1.0×10^{-12}
							300				2000	4.7											1.0×10^{-12}
				10BASE-SR	10312 50	MM-62.5μ	26	850	840–860	7.3	160	5.7	MLM-FP-VCSEL	0.45	124	−7.3/−1	3	NA	PIN	68	−9.9	−1	1.0×10^{-12}
							33				200	5.6											1.0×10^{-12}
						MM-G.651	66				400	5.6											1.0×10^{-12}
							82				500	5.5											1.0×10^{-12}
							300				2000	4.7											1.0×10^{-12}
				10BASE-LW	9953 280	SM-G.652	10000	1310	1260–1355	9.4	NA	3.2	SLM-DFB	NA	116	−8.2/+0.5	3.5	30	PIN	28	−14.4	0.5	1.0×10^{-12}
																							1.0×10^{-12}
				10BASE-LR	10312 50	SM-G.652	10000	1310	1260–1355	9.4	NA	3.2	SLM-DFB	NA	116	−8.2/+0.5	3.5	30	PIN	28	−14.4	0.5	1.0×10^{-12}
																							1.0×10^{-12}
																							1.0×10^{-12}
				10BASE-EW	9953 280	SM-G.652	30000	1550	1530–1565	15.0	NA	4.1	SLM-DFB	NA	226	−4.7/+4.0	3	30	PIN	17.5	−15.8	−1	1.0×10^{-12}
																							1.0×10^{-12}
				10BASE-ER	10312 50	SM-G.652	10000	1550	1530–1565	15.0	NA	4.1	SLM-DFB	NA	100	−8.2/+0.5	3	30	PIN	17.5	−15.8	−1	1.0×10^{-12}
																							1.0×10^{-12}

(*continued overleaf*)

Table 1.5 (*continued*)

FO standards	Nominal rate (Mb/s)	Recommendation	Application	Code	Bit rate (Mb/s)	Fiber	Distance (m)	Nominal WL (nm)	WL range (nm)	Power budget (dB)	Modal BW (MHz km)	Penalty (dB)	Source	Linewidth RMS (nm)	Tx OMA min (μW)	Tx AVR range (dBm)	ER (dB)	SMSR (dB)	Detector	Rx OMA sens (μW)	Rx AVR sens (dBm)	Rx AVR ovl (dBm)	BER
						MM-62.5μ	300	1310-L0	1269.0–1282.4	7.5	500	5.5	MLM-FP-VCSEL	0.62	682	−0.5/+5.5	3.5	NA	PIN	28.5	−14.25	−0.5	1.0×10^{-12}
								1310-L1	1293.5–1306.9														1.0×10^{-12}
								1310-L2	1318.0–1331.4														1.0×10^{-12}
								1310-L3	1342.5–1355.9														1.0×10^{-12}
						MM-G.651	240	1310-L0	1269.0–1282.4	7.5	400	5.6	MLM-FP-VCSEL	0.62	682	−0.5/+5.5	3.5	NA	PIN	28.5	−14.25	−0.5	1.0×10^{-12}
								1310-L1	1293.5–1306.9														1.0×10^{-12}
								1310-L2	1318.0–1331.4														1.0×10^{-12}
								1310-L3	1342.5–1355.9														1.0×10^{-12}
				10GBA SE-LX4	3 125		300	1310-L0	1269.0–1282.4	7.5	500	5.5	MLM-FP-VCSEL	0.62	682	−0.5/+5.5	3.5	NA	PIN	28.5	−14.25	−0.5	1.0×10^{-12}
								1310-L1	1293.5–1306.9														1.0×10^{-12}
								1310-L2	1318.0–1331.4														1.0×10^{-12}
								1310-L3	1342.5–1355.9														1.0×10^{-12}
						SM-G.652	10 000	1310-L0	1269.0–1282.4	8.2	NA	2.0	SLM-DFB	0.62	682	−0.5/+5.5	3.5	NA	PIN	28.5	−14.45	−0.5	1.0×10^{-12}
								1310-L1	1293.5–1306.9														1.0×10^{-12}
								1310-L2	1318.0–1331.4														1.0×10^{-12}
								1310-L3	1342.5–1355.9														1.0×10^{-12}
						MM-62.5μ	300				500	6.5											1.0×10^{-12}
							300				500	6.5											1.0×10^{-12}
				10BA SE-LRM	10 312 50		300	1310	1260–1385	8.5	500	6.5	MLM-FP-VCSEL-DFB	4	355	−6.5/+0.5	3.5	NA	PIN	50	−17	−1	1.0×10^{-12}
						MM-G.651	240				400	6.5											1.0×10^{-12}
							300				500	6.5											1.0×10^{-12}

distributed feedback (DFB) lasers are all recommended due to compact packaging, yield and low cost. On the receiver side, receptacle PIN detectors are highly recommended.
4. Use standard MMF optical connector technology, avoiding any special alignment tolerance requirements.
5. Reduce module power consumption as much as possible in order to be compliant with next-generation higher-density low-profile optical interconnect modules.

State-of-the-art EDC designed using low-cost, high-speed, low-power and high-density CMOS IC technology can accommodate moderate optical pulse distortion, due to insufficient MMF bandwidth. However, OMF, even though it has not even if it been demonstrated to be fully capable of behaving as the outstanding solution due to many layout-dependent problems, could mitigate multimode fiber bandwidth limitation, thus reducing at least the EDC design complexity.

At the present time, EDC design based on high-speed CMOS technology is targeted at a compensation distance of 300 m over a legacy multimode fiber link. Longer distances result in a compensation effect that is not predictable, excessive design complexity and high power consumption. In conjunction with EDC, OMF or PAM-4 could even be the proper 'link extender', used to reach longer distances with stable results.

1.8 Optical Fiber Transmission Standards

Optical fiber transmission protocols and specifications are carefully controlled by several Standards Committees. Depending on the target application, optical fiber transmission systems are addressed for telecommunication and datacommunication areas. Different specifications characterize these two fields: privileged performance and reliability in the first case while stressing engineering solutions for a high-volume and low-cost market in the second case. The same data transmission speed demands quite different laser sources and detection technologies. Long-reach requirements in telecommunications very often need several hundred kilometers of single-mode fiber link, with large use of optical amplifier and dense wavelength division multiplexing (DWDM) technologies. For the large distribution of multigigabit data transmission implementation of legacy multimode fiber deployed in the 1980s and 1990s is required with very sensible bandwidth limitations. This situation sets a great engineering challenge in the local area distribution market. According to these specific business areas, several standards have been proposed. Tables 1.1 to 1.5 report the most relevant optical fiber standards, including the principal parameters for the fiber medium, the optical receiver and the optical transmitter. Major standard committees included are the following:

1. International Telecommunication Union, ITU-T G.XXX
2. Bellcore–Telcordia, GR-253-CORE
3. Fiber Channel, FC-PI
4. IEEE802.3ae, Gigabit Ethernet

2

Conductive Transmission Lines

A Simplified Attenuation Model

2.1 Introduction

This chapter deals with the electromagnetic skin effect as the main agent responsible for the characteristic square root frequency behavior experienced by every metallic conductor or waveguide. All transmission lines exhibit this behavior, but different transmission line topologies have peculiar contributions from the dielectric absorption and the related dispersion characteristic due to their own geometry. In the following simplified analysis all these contributions will be neglected, with the focus just on the skin effect as the major agent responsible for the characteristic attenuation frequency response. This model behaves quite well, allowing very interesting conclusions to be made when it is used to make a comparison between the frequency behavior of metallic transmission lines and multimode optical fibers.

This frequency dependence of the transmission line loss is today at the center of extensive design activity in many semiconductor IC companies devoted to provide electric compensation of the degraded signal through long metallic transmission lines, which can be found in every backplane interconnection operating at the multigigabit signaling rate. The XFP (X small-form factor pluggable) standard is an example of a serial 10GbE optical fiber module where both copper transmission lines and optical fiber compensation schemes are needed. Many debates are now taking place on the merits of the different compensation techniques for copper transmission lines and optical fiber.

This chapter is therefore devoted to a clarification of these different topics, making more evidence available of the different frequency behaviors. The expected frequency response of the transmission line attenuation calculated according to this simplified method is usually a slightly better estimation than the results obtained from a full electromagnetic calculation. This conclusion comes from the missing contributions to the total loss due to the dielectric material absorption and waveguide effect.

2.2 The Attenuation Model

The electrical surface impedance Z_s of the metallic plane shown in Figure 2.1 will now be considered. The plane is assumed to be indefinitely extended in width and length, according to the two Cartesian coordinates y and z respectively. The finite thickness is measured along the x axes.

Multi-Gigabit Transmission over Multimode Optical Fibre: Theory and Design Methods for 10GbE Systems Stefano Bottacchi
 ISBN: 0-471-89175-4

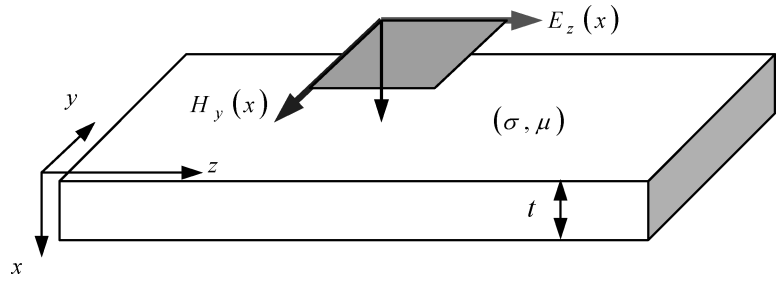

Figure 2.1 Infinite conductive plane for the definition of the surface impedance. The electromagnetic field is described by a plane wave incident normal to the plane surface with the electric field oriented along the z axes

2.2.1 The Surface Impedance

The surface impedance at a given angular frequency ω presented by the indefinite conductive plane in Figure 2.1 is given by the sum of a resistive contribution, R_s, and an inductive term, L_s. Application of electromagnetic theory easily leads to the following result:

$$Z_s = R_s + j\omega L_s \tag{2.1}$$

where the resistive and inductive components have the following expressions:

$$R_s = \sqrt{\frac{\pi \mu f}{\sigma}}, \qquad \omega L_s = R_s \tag{2.2}$$

and μ is the magnetic permeability, σ is the conductivity and $f = \omega/2\pi$ is the frequency of the incident monochromatic electromagnetic field. From Equations (2.1) and (2.2), the surface impedance takes the following form:

$$Z_s = R_s(1 + j) = \sqrt{\frac{\pi \mu f}{\sigma}}(1 + j) \quad (\Omega/\text{square}) \tag{2.3}$$

2.2.2 The Transmission Line Loss Approximation

In order to arrive at a simplified formulation for the frequency response of the skin effect attenuation, the first approximation will be made, namely that:

> The previous results of Equations (2.1), (2.2) and (2.3) are still valid for every finite planar surface, such as a generic transmission line.

This is just an approximation, of course, since the confinement and the guiding properties of the transmission line are easily simplified, assuming no fringe effects and a plane wave field distribution. Nevertheless, a reasonably simple model for the frequency response of the skin effect will be achieved, which will clarify the frequency behavior differences between multimode optical fibers and any generic conductive transmission line.

The surface impedance (2.3) is defined per unit width and per unit length. It is usually referred to as the surface impedance per square. This terminology is quite common in semiconductor integrated circuit technology, where the sheet resistance is defined in terms of ohm per square. In order to

calculate the surface impedance Z_{TL} of a transmission line of width w and length l, it is sufficient to divide expression (2.3) by the line width w and multiply the same expression by the line length l:

$$R_{TL} = R_s \frac{l}{w} \quad (\Omega) \tag{2.4}$$

$$Z_{TL} = R_{TL} + j\omega L_{TL} = R_{TL}(1 + j) \quad (\Omega) \tag{2.5}$$

The transmission line resistance R_{TL}, inductance L_{TL} and impedance Z_{TL} have been introduced in order to keep the same relationship between the plane conductor and the transmission line.

In order to obtain a quantitative idea of the formulation, the following case will be considered.

Example 2.1

Conductivity (copper):	$\sigma = 5.80 \times 10^7$ S/m
Length:	$l = 20$ cm
Width:	$w = 200\,\mu$m
Magnetic permeability:	$\mu_0 = 4\pi \times 10^7$ H/m
Frequency:	$f = 1 \times 10^9$ Hz

In this example the role of the thickness of the transmission line is neglected and it is assumed that it is just thick enough to satisfy the complete skin effect penetration. This argument will be the topic of the next section. From Equations (2.2) and (2.4) the transmission line resistance R_{TL} is calculated at the given frequency f and from Equation (2.3) the corresponding magnitude of the line impedance Z_{TL} is computed:

$$R_{TL} = \sqrt{\frac{\pi\mu f}{\sigma}} \frac{l}{w} = 8.25\,\Omega \tag{2.6}$$

$$|Z_{TL}| = R_{TL} \times \sqrt{2} = 11.67\,\Omega \tag{2.7}$$

2.2.3 Thickness Frequency

The penetration depth of the electric field in any conductor is inversely proportional to the square root of the frequency of the incident electric field. This is the major result of the well-known skin effect. The skin effect penetration depth is given by the following expression:

$$\delta(f) = \sqrt{\frac{1}{\pi\mu\sigma f}} \quad (\text{m}) \tag{2.8}$$

As a consequence, the lower the frequency, the deeper will be the electric field penetration in the conductor thickness. At the limit of a time constant electric field, as it is generated by a constant DC electric current, the penetration depth becomes infinite and the whole thickness of the conductor is therefore occupied by the electromagnetic field. In the constant current case, the electric charges flow within every inner region of the conductor. This is the reason why all conductors exhibit a lower resistance at the DC condition. Figure 2.2 shows the computed skin effect penetration depth versus frequency for copper, gold, silver and aluminum, according to Equation (2.8). Copper has the highest conductivity, so at a fixed frequency the penetration depth of the field in copper is the smallest one. Among the four metals mentioned above, aluminum shows the longest penetration depth.

From a physical point of view, the penetration depth δ is regulated by the shielding effect of the available free electron density. The higher the electron density, the higher the conductivity and the lower the penetration depth will be due to stronger shielding by the free electron gas.

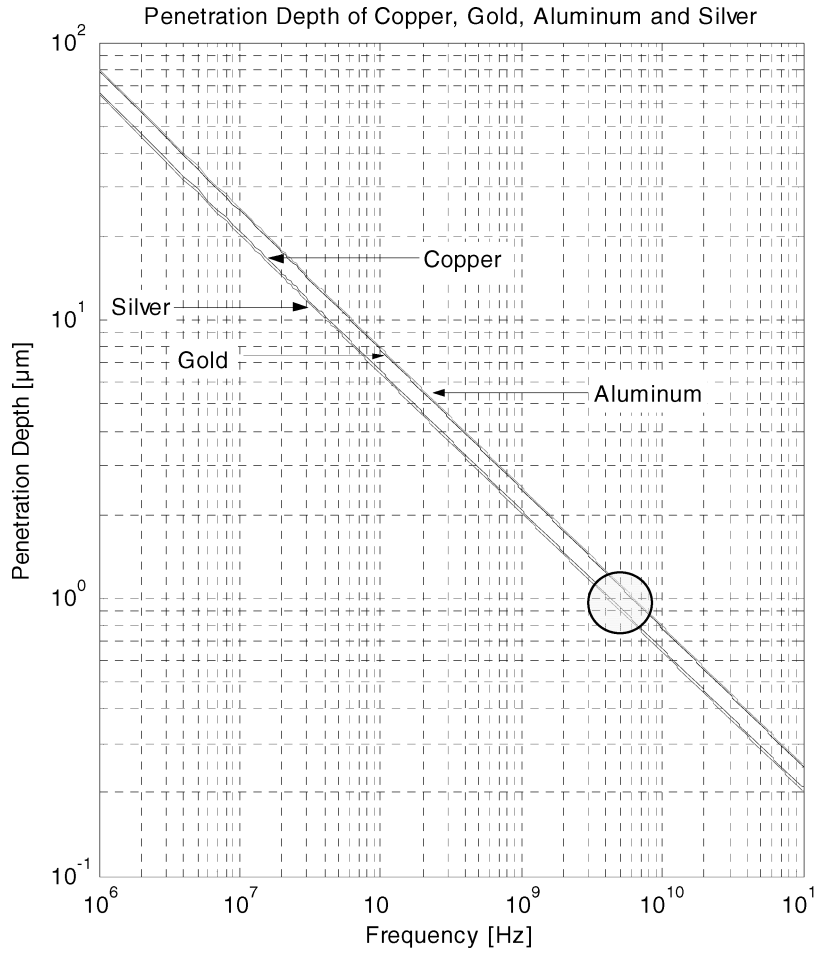

Figure 2.2 Penetration depth for metal planes according to the skin effect expression (2.8). At $f = 5\,\text{GHz}$ all four conductors exhibit a penetration depth very close to 1 μm

The purpose of this section is to compute the frequency at which a conductor stripe of given thickness t becomes completely filled by the electromagnetic field oscillating at a fixed frequency f. This frequency is called the thickness frequency, f_t.

Consider an infinite conductive plane of thickness t, as shown in Figure 2.1, and compute the frequency f_t at which the penetration depth $\delta(f)$ coincides with the thickness t of the conductive plane. Then from Equation (2.8),

$$\delta(f_t) = t \Rightarrow \sqrt{\frac{1}{\pi\mu\sigma f_t}} = t \tag{2.9}$$

and

$$f_t = \frac{1}{\pi\mu\sigma t^2} \tag{2.10}$$

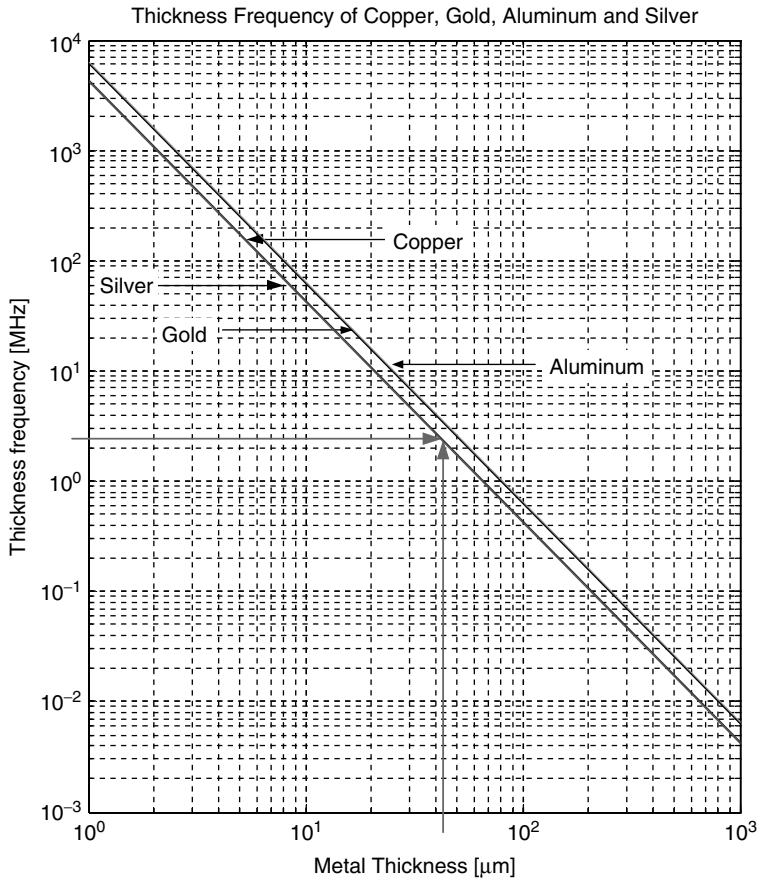

Figure 2.3 Thickness frequency for different metals. For a given metal thickness, a frequency exists at which the metal is filled by the electric field and its surface impedance does not change for lower frequency values

Figure 2.3 shows the computed thickness frequency for copper, silver, gold and aluminum. According to Equation (2.10), the higher the metal conductivity, the lower the thickness frequency will be for a given metal plane thickness t.

The important meaning of the thickness frequency can be summarized as follows:

1. Above the thickness frequency f_t, the skin effect dominates the transmission line impedance.
2. Below the thickness frequency f_t, the line impedance is almost constant as opposed to the frequency and is equal to its DC value (field-filled conductor).

Using the typical thickness value of $t = 42\,\mu\text{m}$ for a copper printed circuit board (PCB), from Equation (2.10) a thickness frequency $f_t = 2.476\,\text{MHz}$ is computed (shown by arrows in Figure 2.3).

2.2.4 DC Resistance

When the transmission line thickness is much smaller than the thickness frequency, the metal sheet is completely filled by the electromagnetic field. In the present approximation, it is therefore

assumed that the transmission line behaves in a DC mode and the surface resistance is given by its DC value. According to this simplified model, the surface resistance takes the following form:

$$R_{\mathrm{DC}} = \frac{l}{t\sigma w} \quad (\Omega) \tag{2.11}$$

Using the case of Example 1, the DC resistance takes the value given in Example 2.

Example 2.2

Conductivity (copper):	$\sigma = 5.80 \times 10^7$ S/m
Length:	$l = 20$ cm
Width:	$w = 200\,\mu$m
Thickness:	$t = 42\,\mu$m

$$R_{\mathrm{DC}} = \frac{1}{t\sigma}\frac{l}{w} = 410\,\mathrm{m}\Omega$$

2.2.5 The Resistance Model

The simple theory developed in previous sections leads to a model for the resistance of a transmission line versus frequency. As already stated, this model is based on the approximation that the electromagnetic field is incident on the transmission line as a plane wave and that the guiding properties of the transmission line does not contribute much to the behavior of the waveguide losses. All those assumptions must be referred to the attenuation analysis that is presented, and not to other transmission line characteristics.

Within the above assumptions, it is easy to arrive at the formulation of the following model for the transmission line resistance versus frequency. From Equations (2.4) and (2.11),

$$f \le f_{\mathrm{t}}, \qquad R_{\mathrm{TL}} = R_{\mathrm{DC}} = \frac{1}{t\sigma}\frac{l}{w} \tag{2.12}$$

$$f \ge f_{\mathrm{t}}, \qquad R_{\mathrm{TL}} = \sqrt{\frac{\pi\mu f}{\sigma}}\frac{l}{w} \tag{2.13}$$

It is easy to arrive at a compact expression using the definition for the thickness frequency. Using Equation (2.10) gives the following identity:

$$\sqrt{\frac{\pi\mu}{\sigma}} = \frac{1}{t\sigma}\frac{1}{\sqrt{f_{\mathrm{t}}}} \tag{2.14}$$

The frequency-dependent transmission line resistance takes the following form:

$$f \ge f_{\mathrm{t}}, \qquad R_{\mathrm{TL}} = \sqrt{\frac{f}{f_{\mathrm{t}}}}\frac{1}{t\sigma}\frac{l}{w} \tag{2.15}$$

By comparison with (2.12), it can immediately be concluded that the transmission line resistance has the following compact form:

$$\begin{aligned} f \le f_{\mathrm{t}}, &\qquad R_{\mathrm{TL}} = R_{\mathrm{DC}} \\ f \ge f_{\mathrm{t}}, &\qquad R_{\mathrm{TL}} = R_{\mathrm{DC}}\sqrt{\frac{f}{f_{\mathrm{t}}}} \end{aligned} \tag{2.16}$$

It is easy to verify the resistance continuity at the thickness frequency f_t. This value satisfies the continuity condition for the resistance across the two frequency ranges. If the decibel definition is used, then

$$f \leq f_t, \qquad R_{TL}^{dB} \equiv 20\log_{10}(R_{DC}) = R_{DC}^{dB} \tag{2.17}$$

$$f \geq f_t, \qquad R_{TL}^{dB}(f) \equiv 20\log_{10}(R_{TL}) = R_{DC}^{dB} + 10\log_{10}\left(\frac{f}{f_t}\right) \tag{2.18}$$

It is evident that the transmission line resistance R_{TL}^{dB} increases with a constant slope of +10 dB/dec (decade) from the thickness frequency f_t. Figure 2.4 shows the computed resistance for the transmission line given in Example 2, assuming different metals.

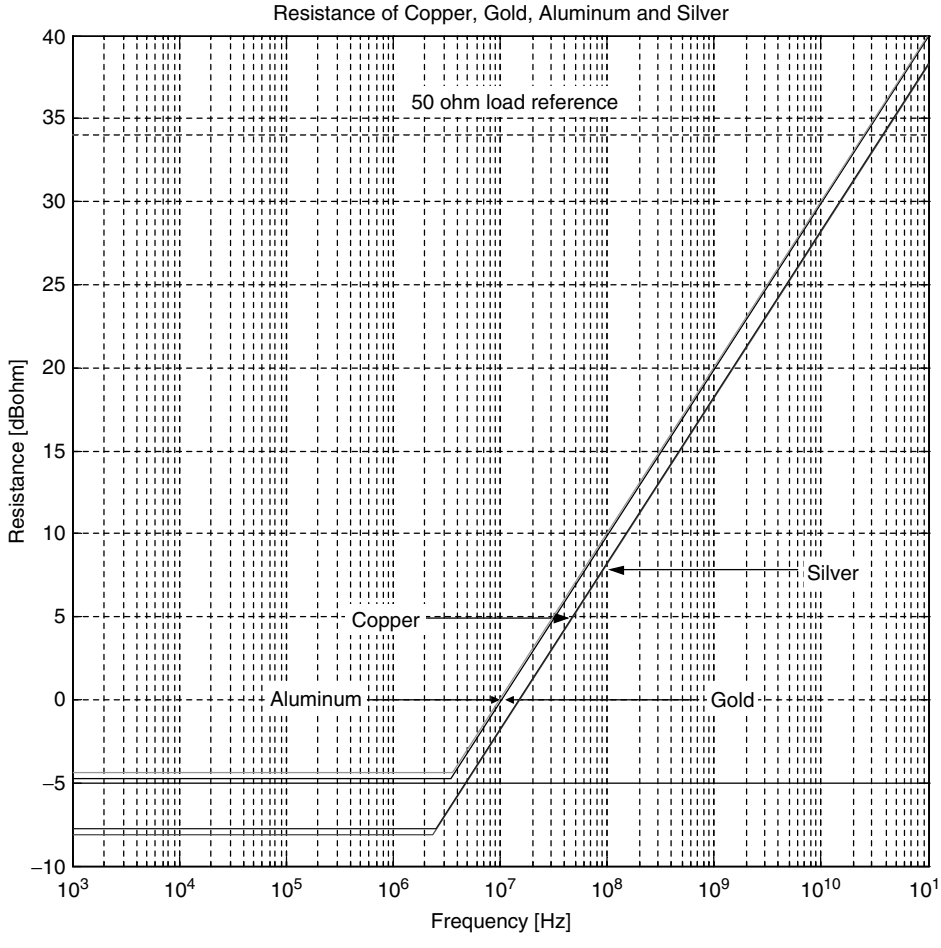

Figure 2.4 Transmission line resistance versus frequency for different conductors. The frequency-independent behavior is characteristic of the low-frequency range, well defined by the thickness frequency corner. Above the thickness frequency, the resistance dependence versus frequency is clearly determined by the skin effect, leading to the constant +10 dB/dec slope. The transmission line parameters are the following: $l = 20\,\text{cm}$, $w = 200\,\mu\text{m}$, $t = 42\,\mu\text{m}$

The top line is the 50 Ω reference load expressed in dB-ohm. Different metal conductivities originate different thickness frequencies, as represented by the corner frequencies positions. According to Equation (2.18), the slope is not a function of metal conductivity, nor of metal thickness. Equations (2.11), (2.12) and (2.16) constitute the transmission line inductance model.

2.2.6 The Inductance Model

In previous sections a simplified model was derived for the resistance R_{TL} of a generic transmission line according to the skin effect and local plane wave approximation. Besides the approximation involved for the resistive model, the model for the inductance of a transmission line due to the skin effect now has to be included. As already introduced in Figure 2.1, if a horizontally polarized plane wave is incident perpendicular to an infinite conductive plane, the surface impedance Z_s exhibits a resistive component R_s and an inductive component L_s, given by Equations (2.1) and (2.2) respectively. Using the same reasoning as for the resistive component, the same concepts can now easily be extended to the inductive term L_s.

Assuming that the frequency of the incident field is still high enough to have the skin effect penetration depth lower than the transmission line thickness, or equivalently $f > f_t$, the transmission line surface inductance L_{TL} is defined according to Equations (2.2) and (2.5) as follows:

$$f \geq f_t, \qquad L_s = \frac{R_s}{2\pi f} \Rightarrow L_{TL} \equiv \frac{R_{TL}}{2\pi f} \tag{2.19}$$

This definition satisfies the general transmission line impedance expression (2.5). Substituting expression (2.16) for the transmission line resistance above the thickness frequency f_t in Equation (2.19), the relationship for the transmission line inductance is

$$f \geq f_t, \qquad L_{TL} = \frac{R_{DC}}{2\pi}\sqrt{\frac{1}{f f_t}} \tag{2.20}$$

In conclusion, above the thickness frequency, the transmission line inductance L_{TL} is proportional to the DC resistance of the transmission line and decreases as the square root of the frequency. It is important to point out that even if the transmission line inductance decreases as the square root of the frequency, from Equation (2.19) it can easily be concluded that the inductive reactance of the transmission line still increases, as expected from Equation (2.5), according to the square root of the frequency:

$$f \geq f_t, \qquad X_{TL} = \omega L_{TL} = R_{DC}\sqrt{\frac{f}{f_t}} \tag{2.21}$$

In particular, if the frequency f coincides with the thickness frequency f_t, the inductance expression (2.20) is still valid and gives

$$f = f_t, \qquad L_{TL}(f = f_t) = \frac{R_{DC}}{2\pi f_t} \tag{2.22}$$

This value represents the lower limit for the applicability of the skin effect model to the inductive components of the surface impedance. As already known, when the applied field frequency is below the thickness frequency f_t, the field completely fills all the metal thickness and the skin effect characteristics are no longer valid. In order to guarantee at least first-order continuity of the transmission line inductance, the DC transmission line inductance is defined according to Equation (2.22) as L_{DC}:

$$L_{DC} = \frac{R_{DC}}{2\pi f_t} \tag{2.23}$$

Equations (2.20), (2.21) and (2.23) give the model for the transmission line inductance:

$$f \leq f_t, \qquad L_{TL} = L_{DC} \tag{2.24}$$

$$f \geq f_t, \qquad L_{TL} = L_{DC}\sqrt{\frac{f_t}{f}} \tag{2.25}$$

Figure 2.5 shows the frequency-dependent behavior of the transmission line inductance for several metals. The transmission line parameters are the same as those used in Example 2. The results clearly show how the skin effect reduces the surface inductance versus frequency. Above the thickness frequency f_t and according to the inverse proportionality of the square root of the frequency,

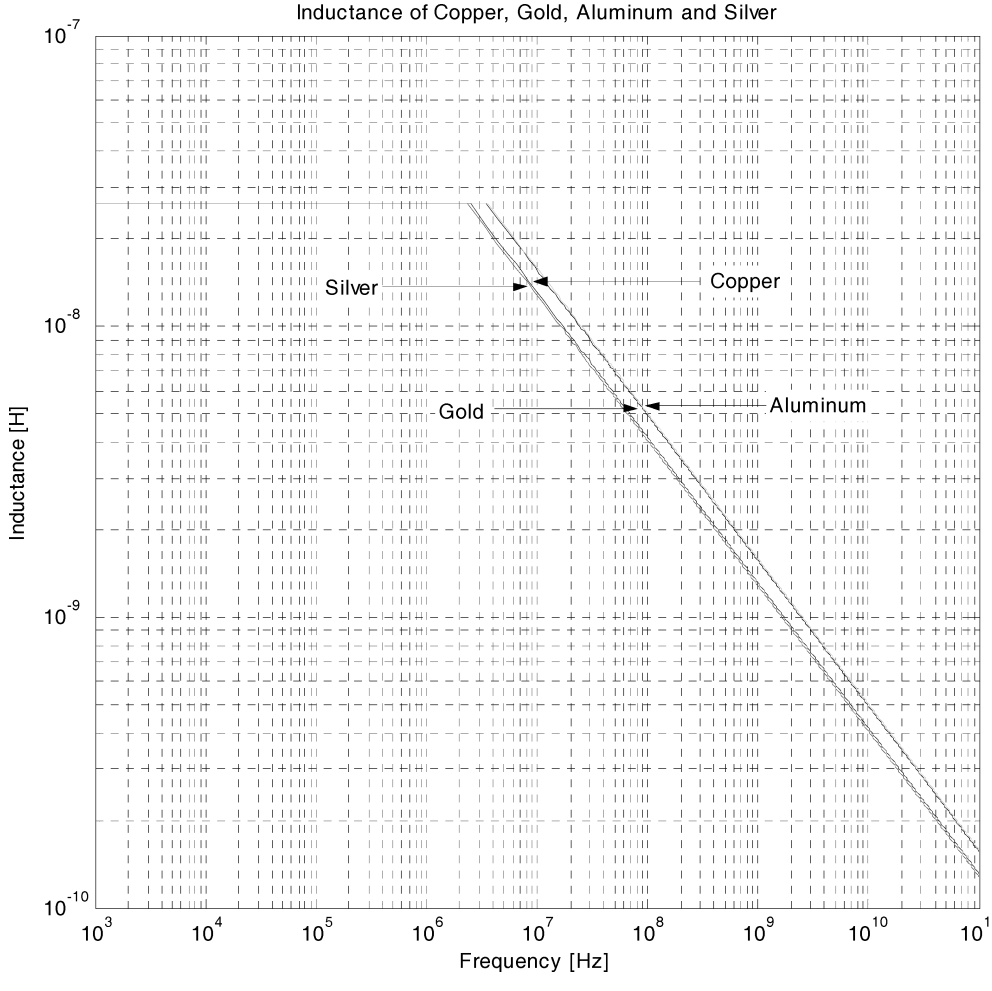

Figure 2.5 Transmission line inductance versus frequency for different metals. The frequency-independent behavior is characteristic of the low-frequency range, well defined by the thickness frequency corner. Above the thickness frequency, the inductance dependence versus frequency is clearly determined by the skin effect, leading to the constant -10 dB/dec slope. The transmission line parameters are the following: $l = 20$ cm, $w = 200\,\mu$m, $t = 42\,\mu$m

the log–log plot used in Figure 2.5 shows a constant negative slope of one inductance decade every two decades of frequency. This decay is characteristic of the inverse square root dependence and is of course independent of the metal used.

In the next section it can be seen how the negative constant slope versus frequency of the transmission line inductance in the log–log scale representation shown in Figure 2.5 will be compensated by the linear frequency dependence of the inductive reactance term, making the whole impedance function still dependent on frequency with a positive constant slope of +10 dB/dec, as expected from the second equation in (2.2).

2.2.7 The Impedance Model

To obtain the transmission line impedance $Z_{TL}(f)$ it is sufficient to take into account the resistive component $R_{TL}(f)$ and the inductance component $L_{TL}(f)$. Therefore, according to Equation (2.5),

$$Z_{TL} = R_{TL} + j\omega L_{TL} \tag{2.26}$$

Substituting expressions (2.12) and (2.16) for the resistive contribution and expressions (2.24) and (2.25) for the inductive term, the expression for the transmission line inductance is finally obtained:

$$f \le f_t, \qquad \left\{ \begin{array}{l} R_{TL} = R_{DC} \\ L_{TL} = L_{DC} \end{array} \right\} \Rightarrow Z_{TL} = R_{DC} + j\omega L_{DC} \tag{2.27}$$

$$f \ge f_t, \qquad \left\{ \begin{array}{l} R_{TL} = R_{DC}\sqrt{\dfrac{f}{f_t}} \\ \\ L_{TL} = L_{DC}\sqrt{\dfrac{f_t}{f}} \end{array} \right\} \Rightarrow Z_{TL} = R_{DC}\sqrt{\frac{f}{f_t}} + j\omega L_{DC}\sqrt{\frac{f_t}{f}} \tag{2.28}$$

Substituting the expression of the DC value for the transmission line inductance (2.23), the following compact and meaningful expression of the transmission line impedance is obtained:

$$f \le f_t, \qquad Z_{TL} = R_{DC}\left(1 + j\frac{f}{f_t}\right) \tag{2.29}$$

$$f \ge f_t, \qquad Z_{TL} = R_{DC}\left(1 + j\sqrt{\frac{f}{f_t}}\right) \tag{2.30}$$

From the above expressions it is easy to conclude that the transmission line impedance is completely characterized by the DC resistance $R_{DC} = l/t\sigma w$, reported in Equation (2.11).

Figure 2.6 shows the modulus and phase of the impedance for the transmission line reported in Example 2. The transmission line impedance represented in Figure 2.6 needs some comments:

1. Even if the resistance contribution R_{TL} is constant and below the thickness frequency, the inductance L_{TL} makes the impedance function not constant in the same frequency range.
2. According to these simplified model assumptions, the magnitude and the phase of the impedance are continuous functions of frequency, but they still have first-order and high-order discontinuities at $f = f_t$.
3. The very low-frequency value of f_t ensures that the higher-order discontinuity point usually falls outside the frequency range of interest; in addition the contribution of the low-frequency range to integral properties or to high-frequency behavior is usually negligible.

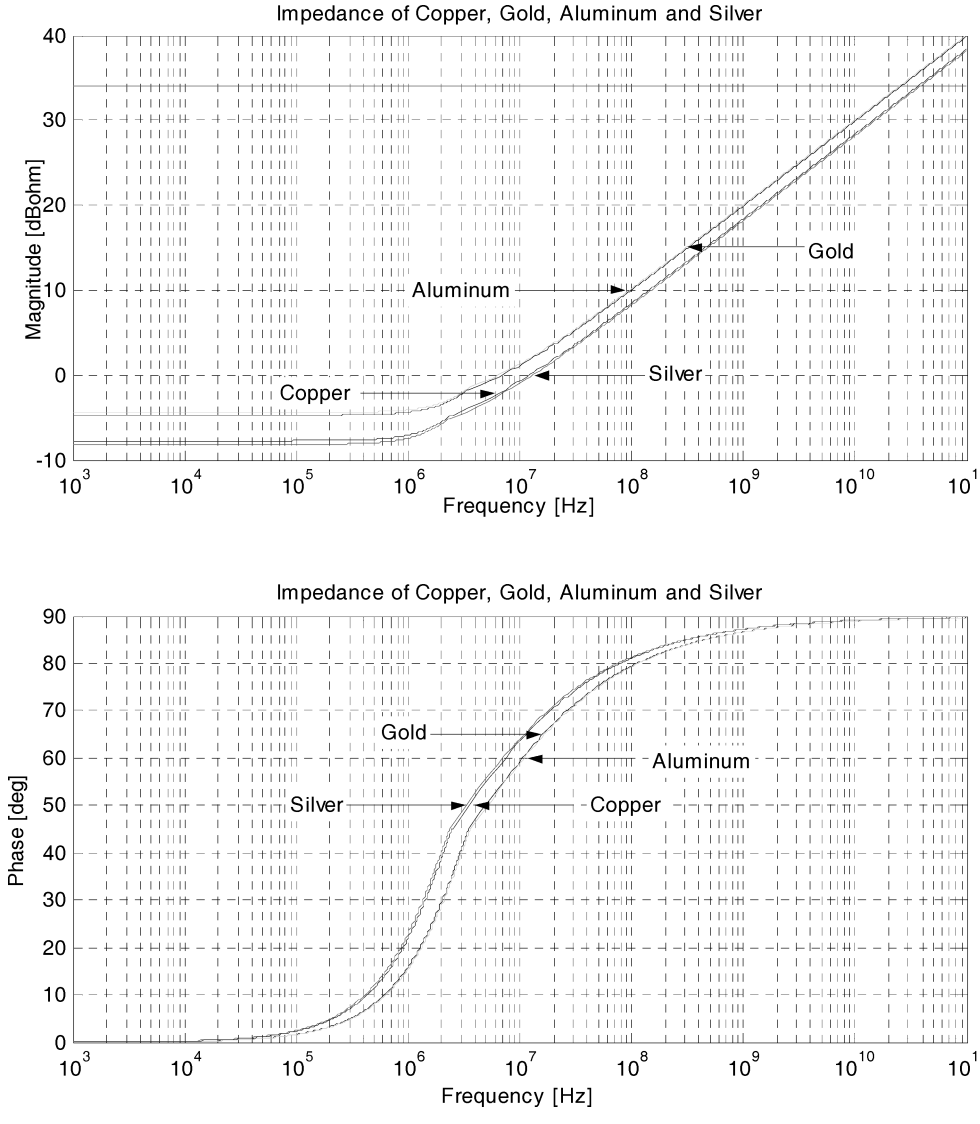

Figure 2.6 Transmission line impedance versus frequency for different metals. The frequency-independent behavior is characteristic of the low-frequency range, well defined by the thickness frequency corner. Above the thickness frequency f_t, the impedance dependence versus frequency is clearly determined by the skin effect. The magnitude (upper graph) presents an asymptotic behavior above the thickness frequency, with a slope of +10 dB/dec. The transmission line parameters are the following: $l = 20$ cm, $w = 200\,\mu$m, $t = 42\,\mu$m. The phase (lower graph) above the thickness frequency is given by the term $\arctan(\sqrt{f/f_t})$

The skin effect approximation of the transmission line impedance formulation led to a transfer function with a single zero behavior located at the thickness frequency f_t. If the impedance magnitude is expressed in decibels, an asymptotic +10 dB/dec slope above the thickness frequency is produced.

2.2.8 Frequency Response

To conclude the approximated theoretical model of a generic transmission line based on the skin effect, the attenuation function versus frequency needs to be derived. Consider the general expressions (2.29) and (2.30) for the transmission line impedance and define the complex function $u(f)$:

$$f \leq f_t, \qquad u(f) = 1 + j\frac{f}{f_t} \tag{2.31}$$

$$f \geq f_t, \qquad u(f) = 1 + j\sqrt{\frac{f}{f_t}} \tag{2.32}$$

The function $u(f)$ takes into account the different frequency dependences within the two frequency intervals defined by the thickness frequency f_t. Using the definition of the function $u(f)$, from Equations (2.29) and (2.30) the general expression for the transmission line impedance takes the following unified form:

$$Z_{TL}(f) = R_{DC}\, u(f) \tag{2.33}$$

The voltage attenuation $A(f)$ of the transmission line is easily derived using the standard phasor partition between the transmission line input section and the resistive load R_L:

$$A(f) \equiv \frac{R_L}{R_L + Z_{TL}(f)} \tag{2.34}$$

Substituting Equation (2.33) gives

$$A(f) = \frac{1}{1 + \rho u(f)} \tag{2.35}$$

The factor ρ

$$\rho \equiv \frac{R_{DC}}{R_L} \tag{2.36}$$

characterizes the DC transmission line attenuation

$$A_0 \equiv A(0) = \frac{1}{1 + \rho} \tag{2.37}$$

In order to proceed further with the derivation of the transfer function of the transmission line attenuation, two intervals below and above the thickness frequency need to be considered separately.

2.2.8.1 Attenuation in the Lower Frequency Range: $f \leq f_t$

Introducing the variable

$$y \equiv \frac{f}{f_t}, \qquad 0 \leq y \leq 1 \tag{2.38}$$

and using the proper definition (2.31) for the function $u(f)$, from Equations (2.35) and (2.37) the following expression for the transmission line attenuation in the lower frequency range is obtained:

$$A_L(f) = \frac{A_0}{1 + j[\rho/(1+\rho)]y} \tag{2.39}$$

where the suffix L stands for the lower frequency range. According to Equations (2.38) and (2.39), the attenuation would have a pole at the frequency

$$\frac{\rho}{1+\rho} y_p = 1 \Rightarrow y_p = 1 + \frac{1}{\rho} = 1 + \frac{R_L}{R_{DC}} \gg 1$$

which is clearly outside the assumed frequency range and therefore is without any physical meaning. After a few algebraic manipulations, from Equation (2.39) the following expression for the attenuation in the lower frequency range is obtained:

$$0 \le f \le f_t \Rightarrow A_L(f) = A_0 \frac{1 - j[\rho/(1+\rho)]y}{1 + \{[\rho/(1+\rho)]y\}^2} \tag{2.40}$$

The modulus and the phase have respectively the following forms:

$$|A_L(f)| = A_0 \frac{1}{\sqrt{1 + \{[\rho/(1+\rho)]y\}^2}} \tag{2.41}$$

$$\Theta_{A_L}(f) = -\arctan\left(\frac{\rho}{1+\rho} y\right) \tag{2.42}$$

From Equation (2.40), at the thickness frequency $f = f_t$, $y = 1$, the attenuation takes the value

$$A_L(f_t) = A_0 \frac{1 - j\rho/(1+\rho)}{1 + [\rho/(1+\rho)]^2} \tag{2.43}$$

2.2.8.2 Attenuation in the Upper Frequency Range: $f \ge f_t$

In the upper frequency range, the variable is defined as

$$x \equiv \sqrt{\frac{f}{f_t}}, \qquad x \ge 1 \tag{2.44}$$

Substituting in the general expression (2.35) of the transmission line attenuation the proper definition (2.32) of the function $u(f)$ and using Equation (2.37), the following expression for the attenuation in the upper frequency range is obtained:

$$A_U(f) = \frac{1}{1 + \rho x + j\rho x} \tag{2.45}$$

where the suffix U stands for the upper frequency range. After simple algebraic manipulations, at the following form is found:

$$f \ge f_t \Rightarrow A_U(f) = \frac{1}{1+\rho x} \frac{1 - j[\rho x/(1+\rho x)]}{1 + [\rho x/(1+\rho x)]^2} \tag{2.46}$$

The modulus and the phase are

$$|A_U(f)| = \frac{1}{1+\rho x} \frac{1}{\sqrt{1 + [\rho x/(1+\rho x)]^2}} \tag{2.47}$$

$$\Theta_{A_L}(f) = -\arctan\left(\frac{\rho x}{1+\rho x}\right) \tag{2.48}$$

At the thickness frequency $f = f_t$, $x = 1$, and from Equation (2.46) the attenuation becomes

$$A_U(f_t) = A_0 \frac{1 - j[\rho/(1+\rho)]}{1 + [\rho/(1+\rho)]^2} \tag{2.49}$$

A comparison with Equation (2.43) reveals the continuity condition for the complex attenuation function:

$$A_U(f_t) = A_L(f_t) \tag{2.50}$$

2.2.8.3 Asymptotic Frequency Behavior: $f \gg f_t$

When the frequency is several orders of magnitude higher than the thickness frequency, the asymptotic frequency behavior of the attenuation function $A_U(f)$ is easy to derive. From Equation (2.47), at the high-frequency limit,

$$\lim_{x\to\infty} |A_U(f)| \to \frac{1}{\sqrt{2}\rho x} = \frac{1}{\rho}\sqrt{\frac{f_t}{2}}\frac{1}{\sqrt{f}} \tag{2.51}$$

$$\lim_{x\to\infty} \Theta_{A_L}(f) = -\frac{\pi}{4} \tag{2.52}$$

High-frequency behavior of the modulus $|A_U(f)|$ of the attenuation function is therefore decaying according to the reciprocal of the square root of the frequency. In addition, it is interesting to note that the asymptotic value of the phase is $\pi/4$ and not $\pi/2$, as would be expected from the single-pole behavior. This is a peculiarity of the skin effect square root frequency dependence. If the magnitude of the attenuation is found, it is easy to find the asymptotic slope of -10 dB/dec:

$$\lim_{f\to\infty} 20\log_{10}|A_U(f)| \to -20\log_{10}\left(\frac{1}{\rho}\sqrt{\frac{f_t}{2}}\right) - 10\log_{10} f \tag{2.53}$$

Figure 2.7 shows the magnitude and phase of the transmission line attenuation function $A(f)$, which had been derived according to Equations (2.40) and (2.46) for the lower and upper frequency ranges respectively. The line parameters used are reported in Example 2 and in the figure caption.

For any given transmission line geometry and operating frequency, higher metal conductivity results in a lower attenuation value. From the frequency behavior simulated above, it is clear that copper and silver at $f = 10$ GHz show an attenuation about 0.8 dB lower than, the same transmission line built using gold or aluminum.

2.2.9 Commenting Model Approximations

Before concluding the chapter on the theory developed for the transmission line attenuation model, it is important to point out the approximations assumed behind its development. First of all, the attenuation model presented should fit for every transmission line structure, once metal conductivity and geometrical parameters have been specified. This means that the model completely neglects the dielectric properties into which the transmission line is embedded. In addition, the line structure is also neglected. No matter what type of transmission lines are used, coplanar, micro-strip or strip-line, once they have the same electrical length, width and thickness, and are built with the same conductor, they show the same attenuation function. It is evident that this will not be the case in reality, due to different dielectric contributions according to a specific transmission line topology. Of course, the more the dielectric affects the electromagnetic field propagation, the more accentuated will be the dielectric contribution to the transmission line attenuation function. This is especially the case for the strip-line structure, where the dielectric completely surrounds the metallic part of the transmission line.

Nevertheless, the attenuation function found in Equations (2.40) and (2.46) represents the true consequence of the skin effect, which takes account of the characteristic square root frequency decay behavior. A more accurate analysis of transmission line attenuation will usually show higher attenuation versus frequency due to the dielectric absorption contribution and peculiar electromagnetic field structures, but the major attenuating term would still remain a consequence of the characteristic skin effect.

The major approximation assumptions are summarized below:

1. The conductor region is a homogeneous infinite plane of finite thickness.

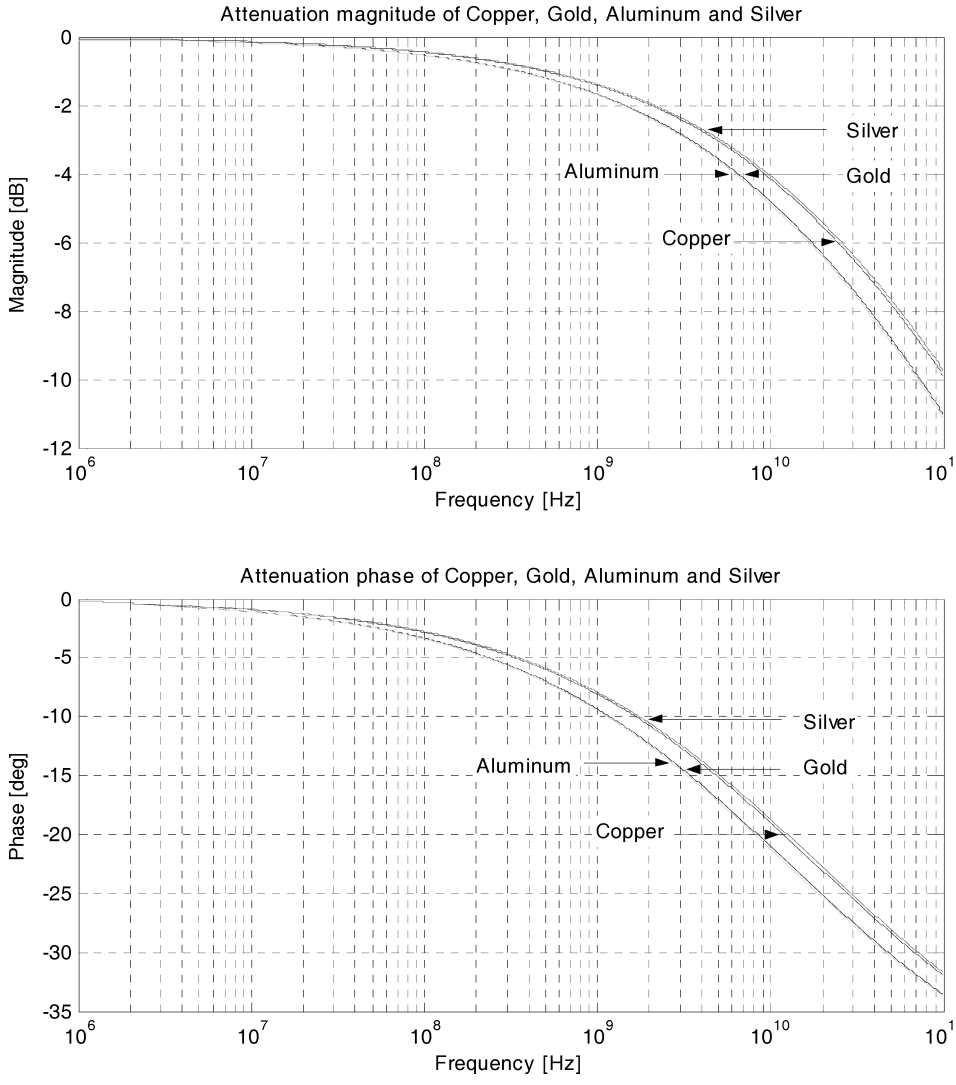

Figure 2.7 Transmission line attenuation versus frequency for different metals. Above the thickness frequency f_t, the impedance dependence versus frequency is clearly determined by the skin effect. The magnitude (upper graph) presents an asymptotic behavior above the thickness frequency, with a slope of -10 dB/dec. The transmission line parameters are the following: $l = 20$ cm, $w = 200\,\mu$m, $t = 42\,\mu$m. The phase (lower graph) above the thickness frequency is given by the term arctan $(\sqrt{f/f_t})$

2. The electromagnetic field is assumed to be incident normal to the metal surface as a plane wave (TEM, or transverse electromagnetic, wave) with the electric field polarized along the plane surface (horizontal polarization).
3. According to the previous two points, the guided electromagnetic field would be approximated as a local plane wave, neglecting the side effect. In order to validate this assumption, the wavelength would be much smaller than the waveguide geometry (geometrical optic conditions).
4. Dielectric contributions are neglected.

2.3 Design Applications

In this section some applications of the attenuation model that have been developed so far will be considered. As already pointed out, this model gives results independently from the transmission line topology and dielectric material. Accordingly, to find the attenuation function $A(f)$ the following four design parameters will need to be specified:

1. Electrical conductivity: $\sigma(\frac{\mathrm{S}}{\mathrm{m}})$
2. Transmission line length: $l(\mathrm{m})$
3. Transmission line width: $w(\mathrm{m})$
4. Transmission line thickness: $t(\mathrm{m})$
5. Load resistor: $R_{\mathrm{L}}(\Omega)$

To make comparison easier, it is assumed that the waveguide metal is copper, $\sigma_{\mathrm{Cu}} = 5.80 \times 10^7$ S/m, and the load resistance is fixed to $R_{\mathrm{L}} = 50\,\Omega$ for all the following cases.

2.3.1 Fixed Length and Width, Variable Thickness

First consider a transmission line of fixed length and width, and assume the metal thickness as the parameter: $l = 20\,\mathrm{cm}$, $w = 200\,\mu\mathrm{m}$, $t = 5, 10, 20, 50, 200\,\mu\mathrm{m}$. From Equations (2.10), (2.11) and (2.36), for each thickness value respectively the thickness frequency f_{t}, the DC resistance R_{DC} and the factor ρ are computed (see Table 2.1).

Figure 2.8 shows the computed transmission line attenuation versus frequency for each of the above thicknesses. Figure 2.9 shows the magnitude of the attenuation function for the same transmission line parameters as above with thickness $t = 42\,\mu\mathrm{m}$. The attenuation at 10 GHz reaches the value $A(f = 10\,\mathrm{GHz}) \cong -4.13\,\mathrm{dB}$.

2.3.2 Fixed Width and Thickness, Variable Length

The transmission lines considered in this section all have the same width and metal thickness, but it is assumed that they can have different lengths. According to Equation (2.10), the frequency thickness is the same for all cases, while DC resistance, Equation (2.11), is clearly linearly increasing with the line length. This affects the ratio ρ, and hence the frequency response versus length. Figure 2.10 presents the frequency response of the attenuation function of five different line lengths. All transmission lines have the same width and thickness.

Figure 2.11 presents the magnitude of the transmission line attenuation for the three lengths of 10 cm, 20 cm and 100 cm.

Table 2.1 Computed parameters for a transmission line of different metal thicknesses

Thickness (μm)	f_{t} (MHz)	$R_{\mathrm{DC}}(\Omega)$	ρ
5	174.69	3.4483	0.0690
10	43.673	1.7241	0.0345
20	10.918	0.8621	0.0172
50	1.7469	0.3448	0.0069
200	0.1092	0.0862	0.0017

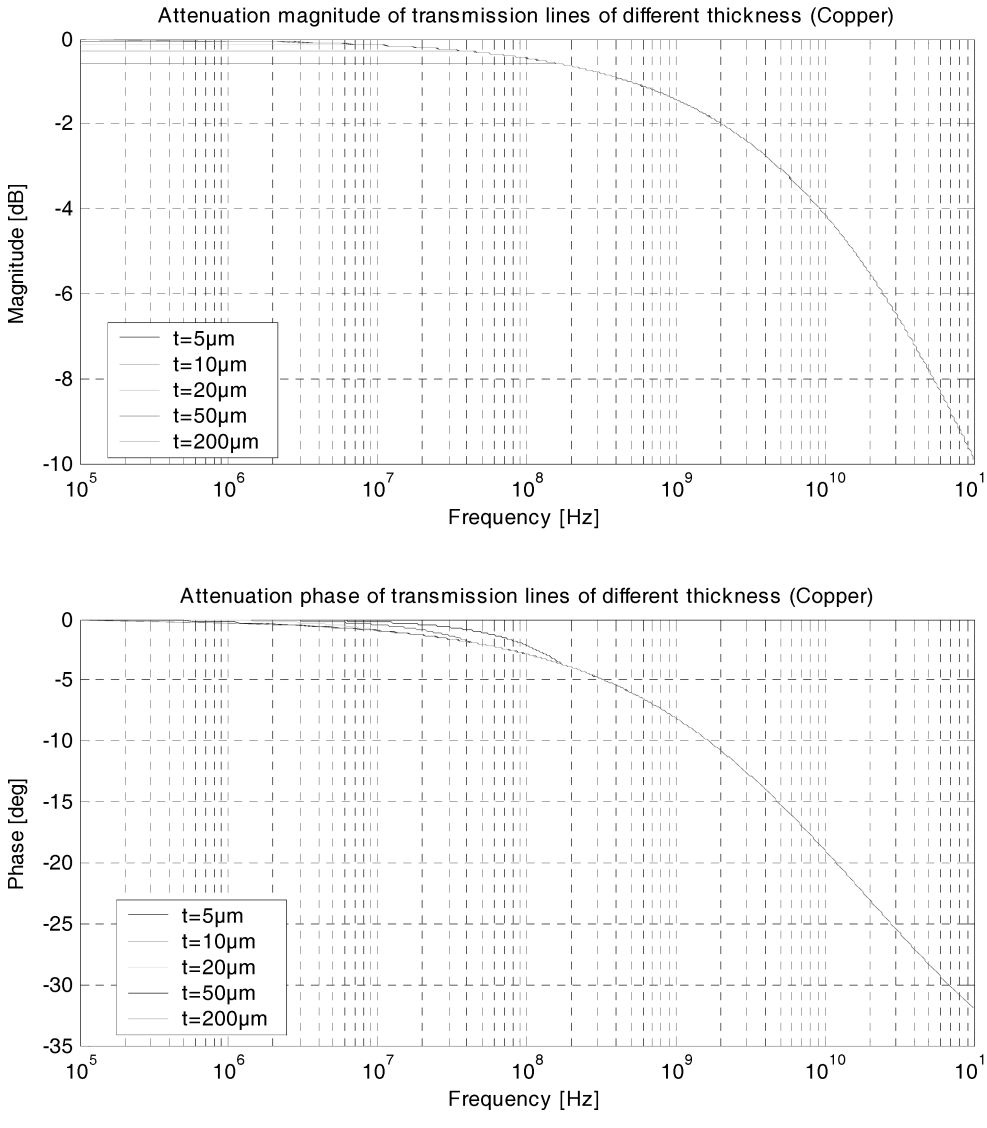

Figure 2.8 Transmission line attenuation versus frequency for different metal thicknesses of copper. Above thickness frequency f_t, the impedance dependence versus frequency is clearly determined by the skin effect and has the same frequency behavior independently from the line thickness. The magnitude (upper graph) presents an asymptotic behavior above the thickness frequency, with a slope of -10 dB/dec. The transmission line parameters are: $l = 20$ cm, $w = 200\,\mu$m, $\sigma = 5.80 \times 10^7$ S/m, $R_L = 50\,\Omega$. The phase (lower graph) above the thickness frequency is given by the term $\arctan\left(\sqrt{f/f_t}\right)$

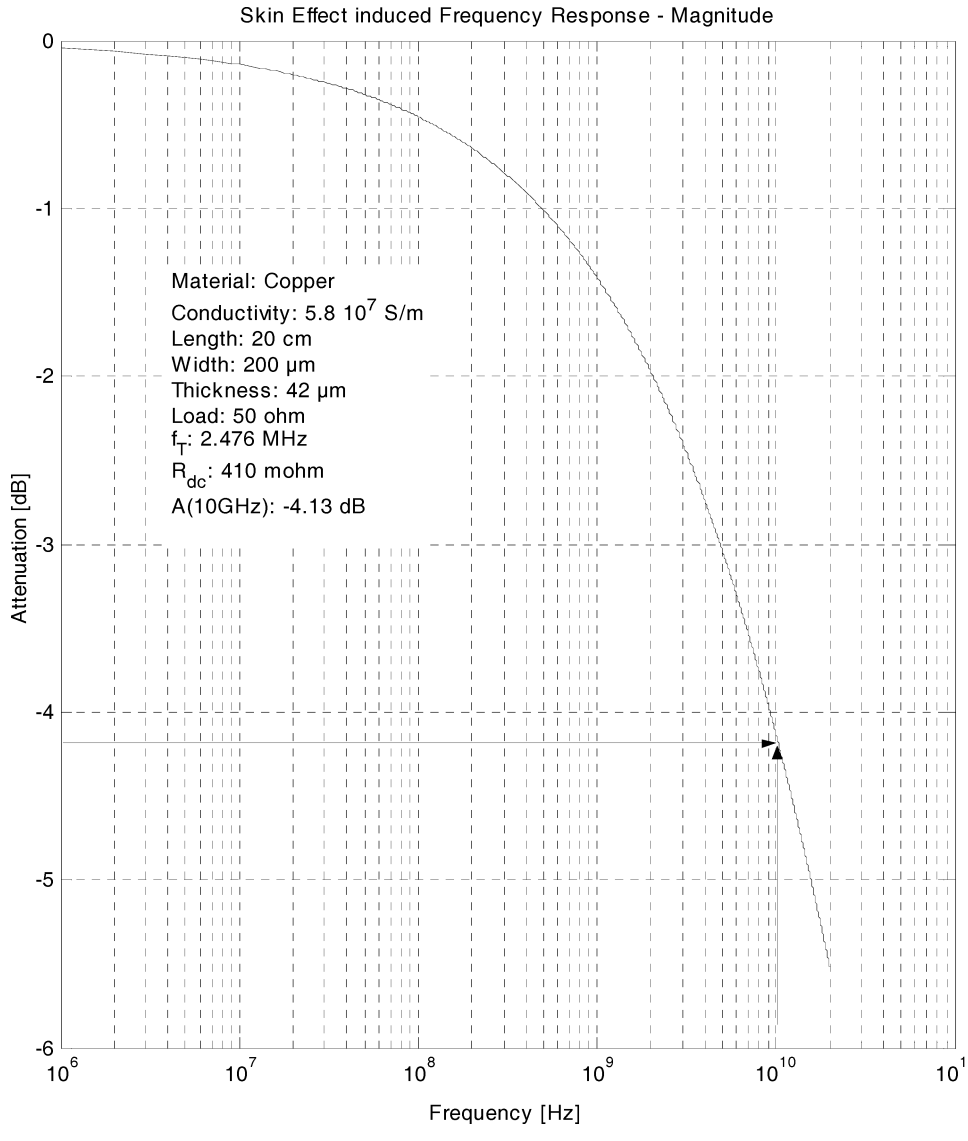

Figure 2.9 Transmission line attenuation magnitude versus frequency for line thickness $t = 42\,\mu\text{m}$. The transmission line parameters are: $l = 20\,\text{cm}$, $w = 200\,\mu\text{m}$, $\sigma = 5.80 \times 10^7\,\text{S/m}$, $R_\text{L} = 50\,\Omega$

Table 2.2 reports the magnitude and the phase of the attenuation function evaluated at $f = 10\,\text{GHz}$ according to different line lengths.

In the next section the impulse response using the fast Fourier transform (FFT) technique will be evaluated.

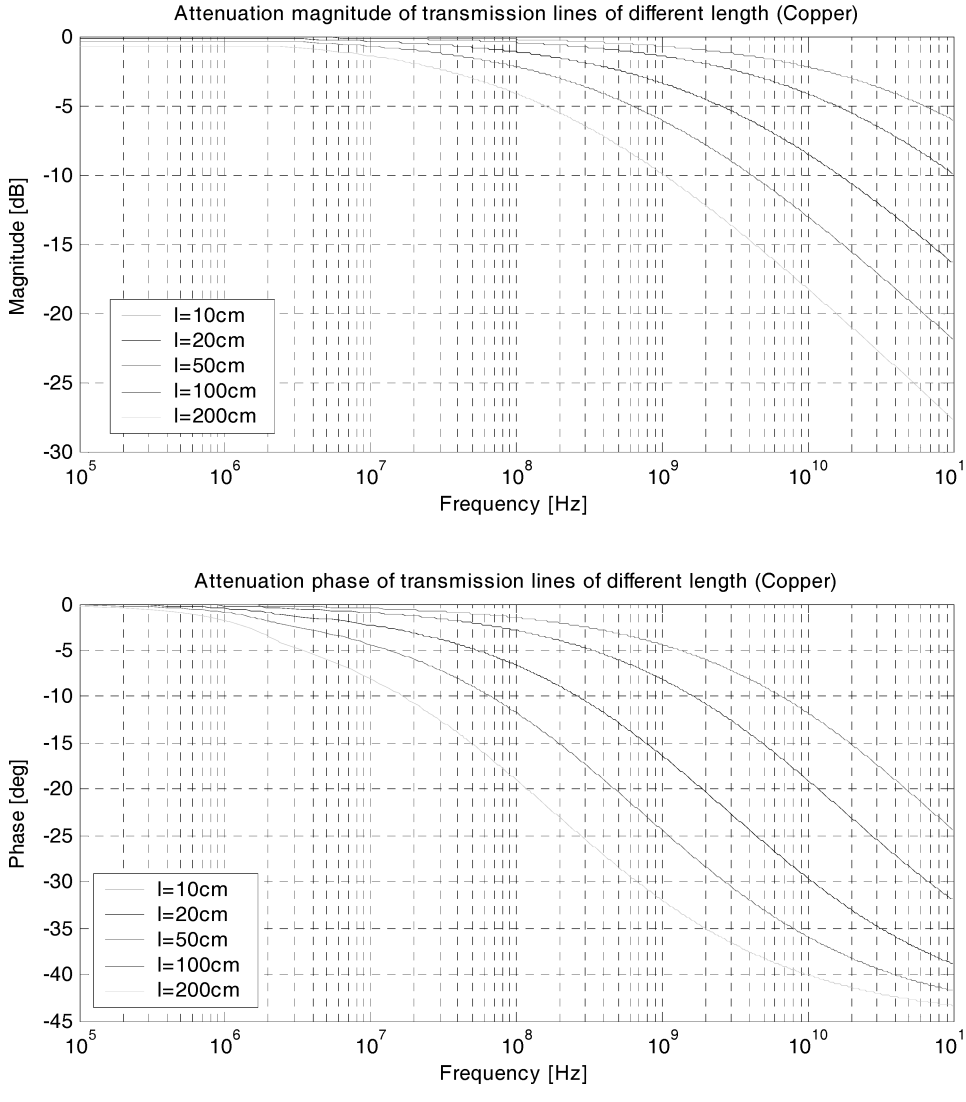

Figure 2.10 Transmission line attenuation versus frequency for different line lengths of copper. The magnitude (upper graph) presents an asymptotic behavior above the thickness frequency, with a slope of -10 dB/dec. The transmission line parameters are: $l = 42\,\mu\text{m}$, $w = 200\,\mu\text{m}$, $\sigma = 5.80 \times 10^7$ S/m, $R_\text{L} = 50\,\Omega$. The phase (lower graph) above the thickness frequency is given by the term arctan $(\sqrt{f/f_\text{t}})$

2.4 Impulse Response

The characteristic square root frequency roll-off of the dominant skin effect based transmission line attenuation gives the peculiar asymptotic slope of -10 dB/decade. This slow-decay behavior is correct within the dominant skin effect approximation that was made earlier, where

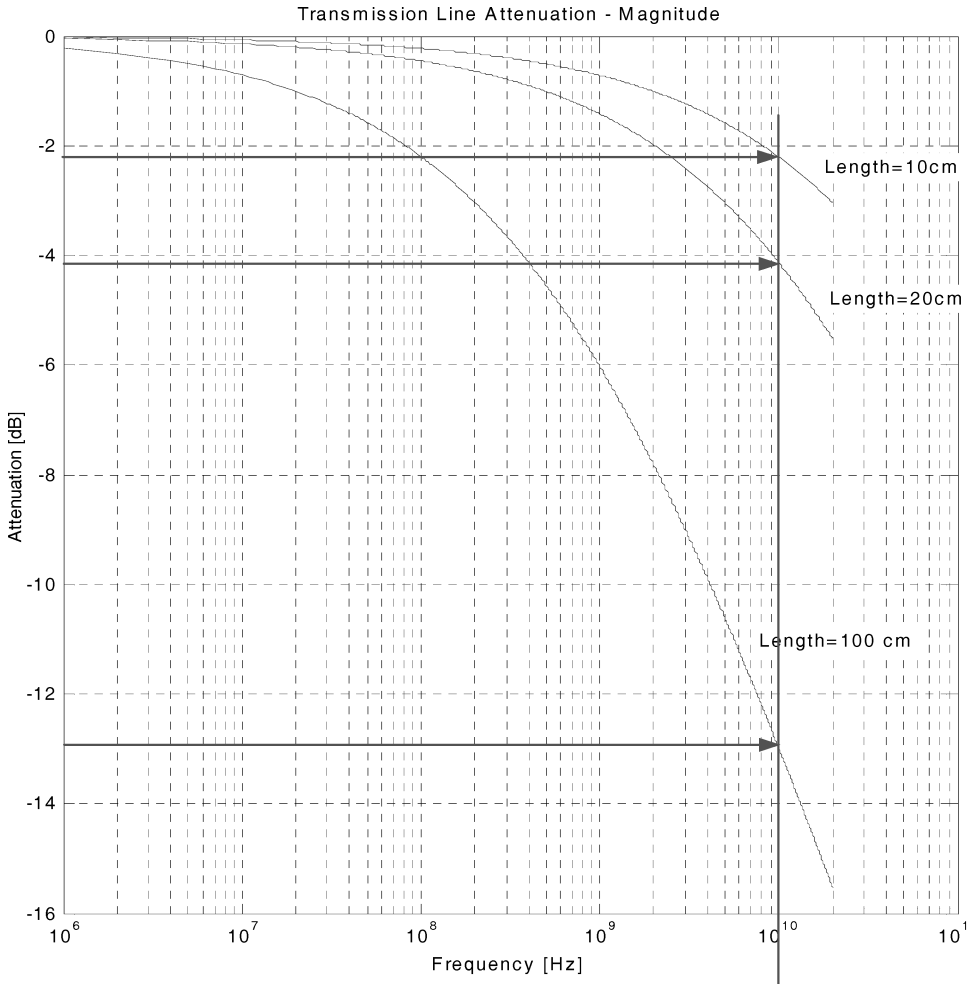

Figure 2.11 Transmission line attenuation versus frequency for three different line lengths of copper. The transmission line parameters are: $l = 42\,\mu\text{m}$, $w = 200\,\mu\text{m}$, $\sigma = 5.80 \times 10^7$ S/m, $R_\text{L} = 50\,\Omega$

Table 2.2 Magnitude and phase of the transmission line transfer function (attenuation) evaluated at 10 GHz versus different line lengths according to the skin effect dominant modeling

Length (cm)	Magnitude (dB) at 10 GHz	Phase (deg) at 10 GHz
10	−2.20	−11.69
20	−4.13	−18.93
50	−8.46	−29.51
100	−12.97	−35.86
200	−18.19	−40.00

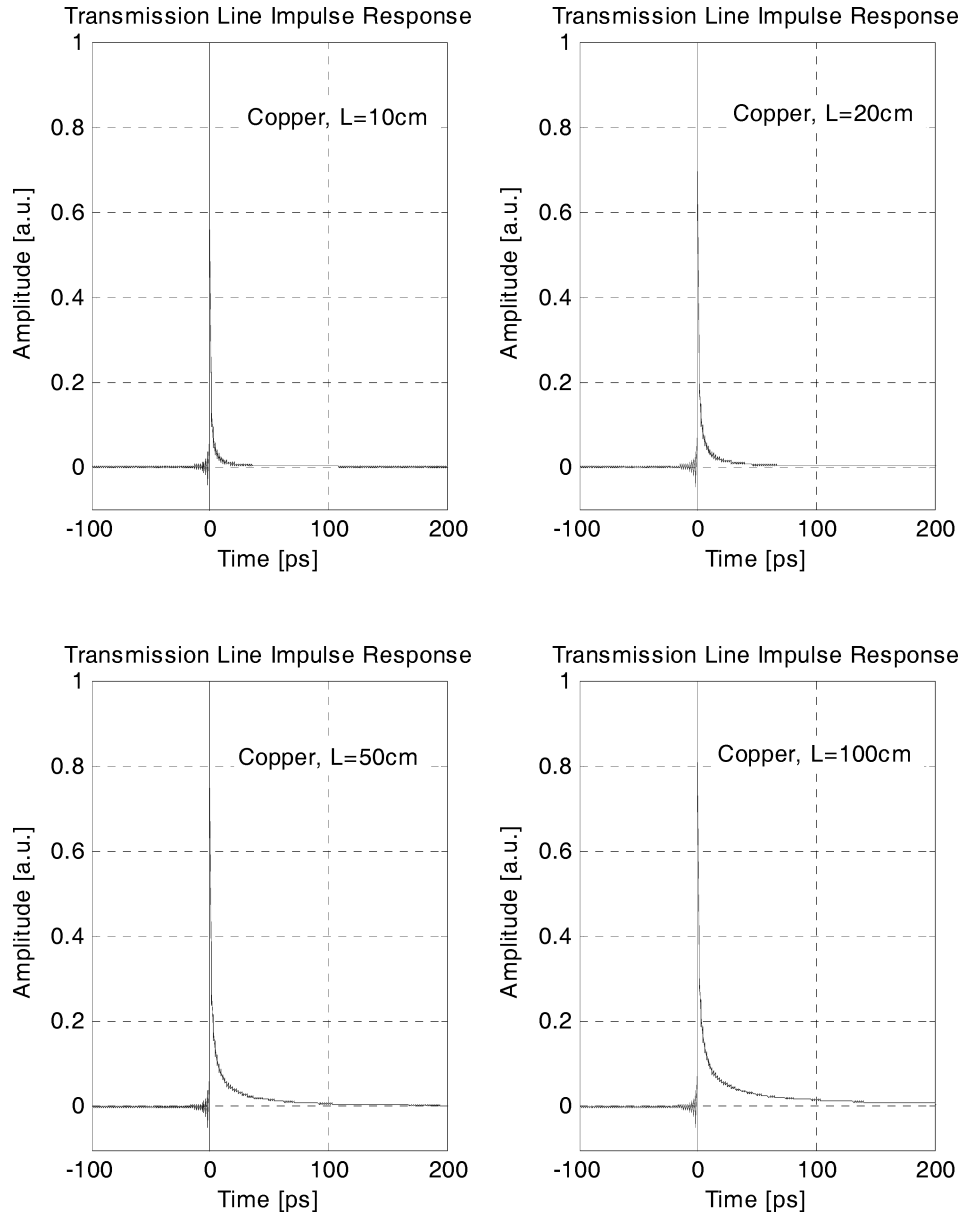

Figure 2.12 Transmission line impulse responses according to the skin effect dominant approximation. Each graph reports the impulse response for the given line length, assuming the same geometrical line parameters as before: $l = 42\,\mu\text{m}$, $w = 200\,\mu\text{m}$, $\sigma = 5.80 \times 10^7$ S/m, $R_\text{L} = 50\,\Omega$. The ripple effect due to high-frequency numerical truncation of the transfer response function according to Equation (2.46) is more evident in shorter line lengths

the dielectric material attenuation has been completely neglected. Real transmission lines show much faster high-frequency decay of the attenuation function, including, of course, frequency-dependent absorption and the dispersion effect due to dielectric material properties. Neglecting those dielectric-related high-frequency effects, the present approximated analysis therefore leads to relevant high-frequency performances.

Time domain analysis is performed by means of a numerical inverse fast Fourier transform (FFT) of the previously derived high-frequency attenuation response (2.46). Due to the smoother frequency response decay resulting from the more common frequency response shapes, the parameter setup for the inverse FFT needs a higher temporal resolution. This leads to a corresponding increase in the frequency sampling interval in order to include almost all the relevant spectrum contributions. Nevertheless, from the mathematical point of view, in order to include a frequency response contribution at least −20 dB below the low-frequency value, it would be necessary to push the frequency analysis range above 1000 GHz, assuming a corner frequency of around 10 GHz. This requirement asks for a sampling interval below 1 ps.

Figure 2.12 shows the numerically computed transmission line impulse response according to the skin effect dominant frequency response reported in Equation (2.46). The same transmission line lengths considered in the previous analysis have been included, providing an inverse FFT response for each of them. All four impulses corresponding respectively to the lengths of 10 cm, 20 cm, 50 cm and 100 cm show the characteristic time ripple as a consequence of the frequency spectrum truncation due to the finite FFT length. The broader the frequency spectrum range, the more enhanced are the results of the time domain ripple amplitude. It is simply a numerical resolution effect and must not be attributed to mathematical modeling.

All impulse responses show the characteristic exponential-like behavior. It should be noted that each impulse response is a real and causal function of the time. The impulse postcursors are more pronounced for a longer transmission line, but they have the same monotonic decaying behavior.

2.5 Conclusions

In this chapter a simple and general model for a transmission line attenuation function has been proposed. Although this model has some restrictions, the frequency profile that has been have achieved clearly represents the major frequency roll-off contribution in every metallic transmission line. The skin effect is usually the dominating term among attenuation contributions and it was the purpose of this work to highlight its characteristic frequency square root behavior.

The principal conclusion about this model relies for its general and simple description on the frequency attenuation profile. The introduction of the thickness frequency allows a definition of the skin effect threshold and the continuity condition for each physical quantity to be described. The whole set of equations (2.10), (2.11), (2.36), (2.40) and (2.43) completely describe the transmission line attenuation model. According to this model, each transmission line, independently from the line structure and dielectric substrate, can be easily introduced into any transmission system simulator, allowing first-order electronic dispersion compensation techniques. A more accurate electromagnetic analysis would be needed for a more suitable dispersion equalization profile.

However, it is important to point out that electronic equalization is inherently approximated due to real filter requirements and design constraints. Very often, even an approximated transmission line frequency response is accurate enough to be only partially equalized by real systems.

3

Principles of Multimode Optical Fiber

Theory and Modeling Issues for Multigigabit Transmission Links

3.1 Introduction

An alternative solution to the consistent bandwidth limitation inherent in the installed multimode fibers infrastructure seems to be the deployment of high-bandwidth multimode fibers made using a new precise manufacturing process and having an optimized refractive index profile, expressly designed to satisfy large-bandwidth requirements in 10 GbE applications. These fibers have only recently been produced in new manufacturing plant and are capable of guaranteeing a modal bandwidth in excess of 2000 MHz km in the 850 nm range, with a very low differential mode delay (DMD) contribution. The fibers make the optical channel well suited for 10 GbE transmission in excess of a 300 m link length. Although they will probably replace almost all the existing old MMF plant, they will effectively increase the final cost per subscriber, making their deployment still more questionable in the present data communication market scenario. It had been thought that the present multimode fiber infrastructure would continue to be used, limiting the high-bandwidth MMF deployment to new link installation. Therefore the old installed multimode fibers would be used as the general channel platform when designing the 10 GbE transmission system in a metropolitan area. High-speed semiconductor lasers provide spatial selective excitation of guided mode groups. The injected pulse energy is therefore distributed among a restricted number of mode groups, a situation complementary to the conventional multimode fiber excitation using LED and any other large numerical aperture source. Refractive index profile optimization for the modal bandwidth is based on overfilled launch (OFL) conditions, a situation where all guided mode groups receive the same amount of source energy.

Proper refractive index profiling ensures a sufficient delay equalization among all mode groups, making the output pulse broadening per unit length suitable for subgigabit transmission requirements. As a consequence of the laser source excitation, usually only a few guided modes bring the launched energy along the fiber extent. Relative power differences among a limited number of modes, together with relevant group delay differences in comparison to the bit duration, make laser excitation quite a difficult matter to cope with multigigabit bandwidth over conventional

Multi-Gigabit Transmission over Multimode Optical Fibre: Theory and Design Methods for 10GbE Systems Stefano Bottacchi
 ISBN: 0-471-89175-4

MMF long-distance links. It is important to point out that 'long distances' in 10 GbE over MMF refers to a few hundred meters, well below a kilometer. Today the IEEE802.3aq Committee for the new standard development 10BASE-LRM has the difficult task of defining the specification for achieving at least 300 meters of legacy multimode fiber with a link length transmission of 10 Gb/s Ethernet. A similar link span could easily be achieved using single-mode fiber technology, even at much higher bit rates.

3.2 The Graded Refractive Index

It is well known from the basic principles of multimode fiber propagation that group delay equalization requires a graded refractive index profile that decreases monotonically from the fiber axis towards the outer cladding region. According to the very basic laws of electromagnetic propagation, the phase velocity v_p of a plane wave of wavelength λ propagating in an homogeneous medium characterized by the refractive index $n(\lambda)$ is given by $v_p(\lambda) = c/n(\lambda)$.

This elementary description holds only for the homogeneous medium with constant refractive index n. As soon as a spatial dependence of the refractive index is introduced, the wave phase fronts will no longer be planar and the propagating wave will follow the refractive index spatial dependence. This is the basic principle behind each wave guiding medium. The plane wave assumption is generalized by introducing the local plane wave concept. Essentially, the local plane wave can be imaged to behave almost like a plane wave if the wave phase fronts are almost constant on the scale length of the refractive index variation. The local plane wave concept leads to the light ray theory as an approximation of the electromagnetic theory in the limiting case of negligible wavelength. By virtue of the local plane wave concept, it is easy to generalize the phase velocity definition given above by introducing the spatial dependence in the refractive index and letting

$$v_p(r, \lambda) = \frac{c}{n(r, \lambda)} \tag{3.1}$$

where $c \cong 2.998 \times 10^8$ m/s is the speed of light in vacuum. The basic principle of mode delay equalization relies on this formula. Making the refractive index higher where the light ray path is shorter leads to a slower phase velocity for low-order mode groups. Conversely, by lowering the refractive index in the outer core region where higher-order helical modes travel longer paths makes their phase velocity higher, thus providing delay equalization.

Figure 3.1 shows a schematic representation of the delay compensation principle of the graded index fiber. Imagine that the axis symmetric graded refractive index of the multimode fiber is sliced into several planar sections along the fiber axis. In addition, within each section with a uniform refractive index, the light ray is assumed to propagate along a straight line path. This of course is just an approximation since the wavelength is usually about the same order of magnitude as the step of the staircase refractive index and geometrical optics loses its validity, but nevertheless the physical picture looks quite clear.

3.2.1 Group Velocity

Phase velocity refers to the velocity of a sine wave propagating in a homogeneous medium, so it cannot represent any physical situation. The infinite sine wave, otherwise stated as the true monochromatic wave, is a mathematical model. When dealing with time-confined events, like pulses, the phase velocity must be replaced by the group velocity v_g. The group velocity represents the velocity of propagation of the center of gravity of the pulse. By definition, in a nondispersive medium the group velocity does not depend on the frequency (wavelength) and the pulse propagation is undistorted (it goes through a temporal translation along the propagation axis). As soon as the group velocity depends on the frequency (wavelength) $v_g(\omega)$, the spectral content of the pulse

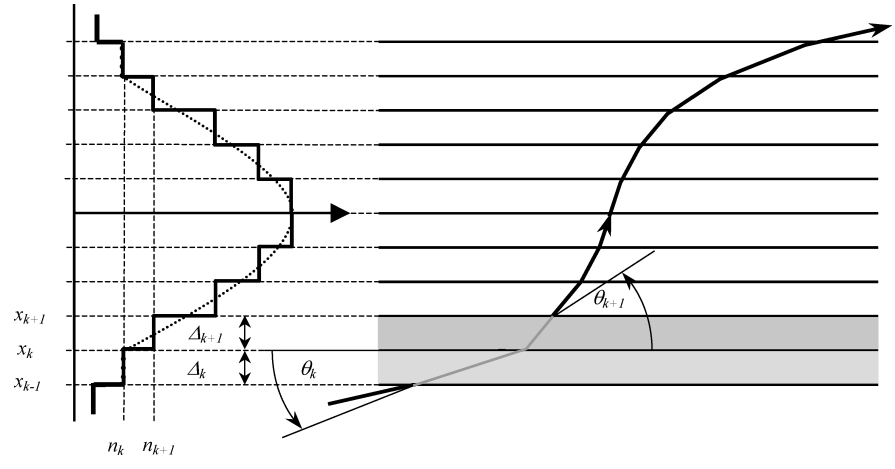

Figure 3.1 Curved ray trajectory in an optical layered medium. To construct the ray trajectory all that is needed is to apply the classical Snell laws between each layer pair. The resulting ray path is a piecewise linear approximation of the gradually varying refractive index profile

induces energy dispersion along with pulse propagation and the dispersion relationship must be accounted for properly.

3.3 Modal Theory of Graded Index Fiber

Like all electromagnetic phenomena, the propagation of optical fields in multimode fiber is governed by the Maxwell equations. Boundary conditions lead to the eigenmode solutions (modes) with related eigenvalues (propagation constants). The cylindrical symmetry of the optical fiber suggests the adoption of the cylindrical coordinate system (r, φ, z) to represent the spatial position. However, the mathematical description of differential operators becomes simpler if Cartesian field components are used instead of cylindrical ones. Accordingly, the generic electric and magnetic fields take the following form:

$$\begin{aligned}\mathbf{E}(\mathbf{r}, t) &= E_x(r, \varphi, z, t)\mathbf{x} + E_y(r, \varphi, z, t)\mathbf{y} + E_z(r, \varphi, z, t)\mathbf{z} \\ \mathbf{H}(\mathbf{r}, t) &= H_x(r, \varphi, z, t)\mathbf{x} + H_y(r, \varphi, z, t)\mathbf{y} + H_z(r, \varphi, z, t)\mathbf{z}\end{aligned} \tag{3.2}$$

The triplet (**x,y,z**) defines the unit reference vector along the Cartesian coordinate axis. Maxwell's vector equations for the electric and the magnetic fields are

$$\nabla^2\mathbf{E}(\mathbf{r}, t) = \frac{n^2(\mathbf{r})}{c^2}\frac{\partial^2\mathbf{E}(\mathbf{r}, t)}{\partial t^2} + \nabla\{\mathbf{E}(\mathbf{r}, t) \cdot \nabla \ln[n^2(\mathbf{r})]\} \tag{3.3}$$

$$\nabla^2\mathbf{H}(\mathbf{r}, t) = \frac{n^2(\mathbf{r})}{c^2}\frac{\partial^2\mathbf{H}(\mathbf{r}, t)}{\partial t^2} + [\nabla \times \mathbf{H}(\mathbf{r}, t)] \times \nabla \ln[n^2(\mathbf{r})] \tag{3.4}$$

A little more detailed analysis shows that the last term in the brace on the right member of the vector wave Equation (3.3) is the divergence of the electric field:

$$\nabla \cdot \hat{\mathbf{E}}(\mathbf{r}, t) \equiv \mathbf{E}(\mathbf{r}, t) \cdot \nabla \ln[n^2(\mathbf{r})] \tag{3.5}$$

where

$$\frac{\nabla n^2(\mathbf{r})}{n^2(\mathbf{r})} = \nabla \ln[n^2(\mathbf{r})] \tag{3.6}$$

In addition, the following identity holds for the last term on the right side of (3.4):

$$\frac{\partial \mathbf{E}(\mathbf{r}, t)}{\partial t} \times \varepsilon_0 \nabla \chi(\mathbf{r}) = [\nabla \times \mathbf{H}(\mathbf{r}, t)] \times \nabla \ln[n^2(\mathbf{r})] \tag{3.7}$$

3.3.1 Physical Medium Assumptions

Vector wave equations derived above for the electromagnetic field are quite general and do not assume implicitly any symmetry of the fiber medium and in particular of the refractive index function $n(\mathbf{r}) = n(r, \varphi, z)$, which is assumed to be a generic spatial dependence. However, it is important to comment about the physical meaning and the consequent mathematical implications of the assumptions underlying Equations (3.3) and (3.4). To be specific, in deriving those vector field equations from Maxwell's equations, it is assumed that the fiber medium is isotropic, instantaneous and linear. The mathematical implications of those physical medium assumptions and how they transfer into each equation term are reviewed.

3.3.1.1 Isotropy

The dielectric susceptibility can be considered as a scalar quantity instead of a tensor. This is a consequence of the amorphous nature of the glass composition of silica based optical fibers:

$$\chi_{ijk}(\mathbf{r}, t) = \chi(\mathbf{r}, t) \tag{3.8}$$

3.3.1.2 Instantaneity

The time response of the dielectric susceptibility is instantaneous with respect to the time evolution of the inducing electric field envelope:

$$\chi(\mathbf{r}, t) = \chi(\mathbf{r})\delta(t) \tag{3.9}$$

3.3.1.3 Linearity

The dielectric induced polarization field $\mathbf{P}(\mathbf{r},t)$ is linearly dependent on the inducing electric field. The quantity that relates the dielectric polarization field to the applied electric field is the first-order dielectric susceptibility $\chi^{(1)}(\mathbf{r}, t)$:

$$\mathbf{P}(\mathbf{r}, t) = \varepsilon_0 \chi^{(1)}(\mathbf{r}, t) * \mathbf{E}(\mathbf{r}, t) = \varepsilon_0 \int_{-\infty}^{+\infty} \chi^{(1)}(\mathbf{r}, \tau) * \mathbf{E}(\mathbf{r}, t - \tau)\, \mathrm{d}\tau \tag{3.10}$$

The first-order (linear) dielectric-induced polarization is given by the time convolution between the first order (linear) susceptibility $\chi^{(1)}(\mathbf{r},t)$ and the inducing electric field. Third-order dielectric susceptibility $\chi^{(3)}(\mathbf{r},t)$ accounts for nonlinear refraction and related effects such as self-phase modulation (SPM), cross-phase modulation (XPM) and four-wave mixing. (FWM).

Including all of the above three assumptions about the fiber optic material allows the dielectric polarization vector to be written in the following simple form:

$$\mathbf{P}(\mathbf{r}, t) = \mathbf{P}^{(1)}(\mathbf{r}, t) = \varepsilon_0 \chi(\mathbf{r}) \int_{-\infty}^{+\infty} \mathbf{E}(\mathbf{r}, \tau)\delta(t - \tau)\, \mathrm{d}\tau = \varepsilon_0 \chi(\mathbf{r})\mathbf{E}(\mathbf{r}, t) \tag{3.11}$$

In addition, the linear dielectric permittivity and the linear refractive index are related to the first-order dielectric susceptibility as follows:

$$\varepsilon(\mathbf{r}, t) = \varepsilon_0[1 + \chi^{(1)}(\mathbf{r})]\delta(t) = n^2(\mathbf{r})\delta(t) \tag{3.12}$$

3.3.2 Wave Equations for Longitudinal Invariance

The vector field Equations (3.3) and (3.4) are valid according to the above assumptions reported in Sections 3.3.1.1 to 3.3.1.3. The only remaining general assumption is the spatial dependence of the refractive index. In both vector Equations (3.3) and (3.4) the refractive index is a function of the spatial position, without any symmetry requirement. This is not the case for optical fibers. In the following it will be assumed that the refractive index is longitudinal invariant. This means that

$$n(\mathbf{r}) = n(r, \varphi) \tag{3.13}$$

Later on, it will be assumed further that the refractive index satisfies additional axial symmetry. For the moment it is sufficient to assume that the refractive index is only longitudinal invariant. In this case, each Cartesian component $F(r, \varphi, z, t)$ of the electromagnetic mode field can be written as the product of the function $\Psi(r, \varphi)$ with the propagation phasor term $e^{j(\omega t - \beta z)}$:

$$F(r, \varphi, z, t) = \Psi(r, \varphi) e^{j(\omega t - \beta z)} \tag{3.14}$$

The electric and magnetic fields can therefore be written as

$$\mathbf{E}(\mathbf{r}, t) = [\mathbf{E}_t(r, \varphi) + E_z(r, \varphi)\mathbf{z}] e^{j(\omega t - \beta z)} \tag{3.15}$$

$$\mathbf{H}(\mathbf{r}, t) = [\mathbf{H}_t(r, \varphi) + H_z(r, \varphi)\mathbf{z}] e^{j(\omega t - \beta z)} \tag{3.16}$$

Substituting field expressions (3.15) and (3.16) into wave Equations (3.3) and (3.4), the vector wave equations are obtained for the electric and the magnetic fields respectively in the case of the translational invariant optical fiber.

3.3.2.1 Vector Wave Equation for the Electric Field

The electric field Equation (3.3) is considered first. The left member of Equation (3.3) is the Laplacian of the electric field and can be written as follows:

$$\begin{aligned} \nabla^2 \mathbf{E}(\mathbf{r}, t) &= \left(\nabla_t^2 + \frac{\partial^2}{\partial z^2} \right) \left\{ [\mathbf{E}_t(r, \varphi) + \mathbf{z} E_z(r, \varphi)] e^{j(\omega t - \beta z)} \right\} \\ &= e^{j(\omega t - \beta z)} (\nabla_t^2 - \beta^2) [\mathbf{E}_t(r, \varphi) + \mathbf{z} E_z(r, \varphi)] \end{aligned} \tag{3.17}$$

In the above derivation decomposition of the Laplacian in the cylindrical coordinate system has been used in terms of the transversal Laplacian and the longitudinal second-order derivative:

$$\nabla^2 = \nabla_t^2 + \frac{\partial^2}{\partial z^2}, \qquad \nabla_t^2 = \frac{\partial^2}{\partial r^2} + \frac{1}{r} \frac{\partial}{\partial r} + \frac{1}{r^2} \frac{\partial^2}{\partial \varphi^2} \tag{3.18}$$

The first term of the right member of Equation (3.3) is the second-order derivative of the electric field. Using the field decomposition (3.15) gives

$$\begin{aligned} \frac{\partial^2 \mathbf{E}(\mathbf{r}, t)}{\partial t^2} &= [\mathbf{E}_t(r, \varphi) + \mathbf{z} E_z(r, \varphi)] \frac{\partial^2}{\partial t^2} e^{j(\omega t - \beta z)} \\ &= -\omega^2 e^{j(\omega t - \beta z)} [\mathbf{E}_t(r, \varphi) + \mathbf{z} E_z(r, \varphi)] \end{aligned} \tag{3.19}$$

The second term of the right member of Equation (3.3) includes the gradient of the logarithmic function of the refractive index:

$$\begin{aligned} \nabla\{\mathbf{E}(\mathbf{r}, t) \cdot \nabla \ln[n^2(r, \varphi)]\} &= \nabla\{e^{j(\omega t - \beta z)} [\mathbf{E}_t(r, \varphi) + \mathbf{z} E_z(r, \varphi)] \cdot \nabla_t \ln[n^2(r, \varphi)]\} \\ &= \nabla\{e^{j(\omega t - \beta z)} \mathbf{E}_t \cdot \nabla_t \ln[n^2]\} + \nabla \left\{ e^{j(\omega t - \beta z)} \underbrace{\mathbf{z} E_z \cdot \nabla_t \ln[n^2]}_{\text{null due to orthogonality}} \right\} \end{aligned}$$

$$= e^{j(\omega t-\beta z)}\nabla_t\{\mathbf{E}_t\cdot\nabla_t\ln[n^2]\} - j\beta\mathbf{z}e^{j(\omega t-\beta z)}\{\mathbf{E}_t\cdot\nabla_t\ln[n^2]\}$$
$$= e^{j(\omega t-\beta z)}(\nabla_t - j\beta\mathbf{z})\{\mathbf{E}_t(r,\varphi)\cdot\nabla_t\ln[n^2(r,\varphi)]\} \quad (3.20)$$

In the above calculation, the decomposition of the gradient operator in cylindrical coordinates into the transversal gradient and the longitudinal derivative has been used accordingly:

$$\nabla = \nabla_t + \mathbf{z}\frac{\partial}{\partial z}, \qquad \nabla_t = \mathbf{r}\frac{\partial}{\partial r} + \boldsymbol{\varphi}\frac{1}{r}\frac{\partial}{\partial\varphi} \quad (3.21)$$

Finally, substituting Equations (3.17), (3.19) and (3.20) into Equation (3.3) and using the definition of the wavenumber $k = \omega/c$ gives the following vector wave equation for the electric field in a longitudinally invariant optical fiber:

$$[\nabla_t^2 + k^2n^2(r,\varphi) - \beta^2][\mathbf{E}_t(r,\phi) + \mathbf{z}E_z(r,\varphi)] = (\nabla_t - j\beta\hat{\mathbf{z}})\{\mathbf{E}_t(r,\varphi)\cdot\nabla_t\ln[n^2(r,\varphi)]\} \quad (3.22)$$

Material properties of the optical fiber are included in the refractive index function $n(r,\varphi)$. From Equations (3.21), the transversal gradient is acting on both the radial and azimuthal components. In standard optical fibers the refractive index changes slightly between the core and the cladding and the weakly guiding approximation usually holds. Furthermore, the logarithmic function smoothes the slight index variation, making the scalar product with the electric field almost negligible when compared to the left side term.

3.3.2.2 Vector Wave Equation for the Magnetic Field

The magnetic field Equation (3.4) is now considered. The first terms on the left and right members of Equation (3.4) are exactly the same as those already solved for the electric field Equation (3.3). Therefore, following the same procedure, after substituting the electric field with the magnetic field, from Equations (3.17) and (3.19),

$$\nabla^2\mathbf{H}(\mathbf{r},t) = \left(\nabla_t^2 + \frac{\partial^2}{\partial z^2}\right)\left\{[\mathbf{H}_t(r,\varphi) + \mathbf{z}H_z(r,\varphi)]e^{j(\omega t-\beta z)}\right\}$$
$$= e^{j(\omega t-\beta z)}\left(\nabla_t^2 - \beta^2\right)[\mathbf{H}_t(r,\varphi) + \mathbf{z}H_z(r,\varphi)] \quad (3.23)$$
$$\frac{\partial^2\mathbf{H}(\mathbf{r},t)}{\partial t^2} = [\mathbf{H}_t(r,\varphi) + \mathbf{z}H_z(r,\varphi)]\frac{\partial^2}{\partial t^2}e^{j(\omega t-\beta z)}$$
$$= -\omega^2e^{j(\omega t-\beta z)}[\mathbf{H}_t(r,\varphi) + \mathbf{z}H_z(r,\varphi)] \quad (3.24)$$

The second term of the right member in Equation (3.4), $[\nabla\times\mathbf{H}(\mathbf{r},t)]\times\nabla\ln[n^2(\mathbf{r})]$, needs more comment. It is the vector product between the curl of the magnetic field intensity $\mathbf{H}(\mathbf{r},t)$ and the gradient of the logarithmic function of the squared refractive index $n(r,\varphi)$. Since the refractive index is assumed to be longitudinal invariant (it does not depend on the longitudinal coordinate z), the gradient is effective only in the (r,φ) transversal plane and the curl expression can be simplified by replacing ∇ with ∇_t. The same conclusion holds for the previous derivation of the electric field equation:

$$\nabla\ln[n^2(r,\varphi)] = \nabla_t\ln[n^2(r,\varphi)] = \left(\mathbf{r}\frac{\partial}{\partial r} + \boldsymbol{\varphi}\frac{1}{r}\frac{\partial}{\partial\varphi}\right)\ln[n^2(r,\varphi)] \quad (3.25)$$

In order to derive the expression for the curl of the magnetic field, the expression (3.16) of $\mathbf{H}(\mathbf{r},t)$ is substituted in terms of the transversal and longitudinal field components:

$$\nabla\times\mathbf{H}(\mathbf{r},t) = \left(\nabla_t + \mathbf{z}\frac{\partial}{\partial z}\right)\times\left\{[\mathbf{H}_t(r,\varphi) + \mathbf{z}H_z(r,\varphi)]e^{j(\omega t-\beta z)}\right\}$$

$$= e^{j(\omega t-\beta z)}[\nabla_t \times \mathbf{H}_t + \nabla_t \times \mathbf{z}H_z - j\beta\mathbf{z} \times \mathbf{H}_t - j\beta\mathbf{z} \times \mathbf{z}H_z]$$
$$= e^{j(\omega t-\beta z)}(\nabla_t - j\beta\mathbf{z}) \times (\mathbf{H}_t + \mathbf{z}H_z) \quad (3.26)$$

Finally, from Equations (3.25) and (3.26) the following expression for the second term on the right-hand side of the magnetic field Equation (3.4) is given:

$$\nabla \times \mathbf{H}(\mathbf{r}, t) \times \nabla \ln[n^2(r, \varphi)] = e^{j(\omega t-\beta z)} \left\{(\nabla_t - j\beta\mathbf{z}) \times \left[\mathbf{H}_t(r, \varphi) + \mathbf{z}H_z(r, \varphi)\right]\right\} \times \nabla_t \ln[n^2(r, \varphi)] \quad (3.27)$$

Substituting Equations (3.23), (3.24) and (3.27) into Equation (3.4) leads to the following vector wave equation for the magnetic field in a longitudinally invariant optical fiber:

$$[\nabla_t^2 + k^2n^2(r, \varphi) - \beta^2][\mathbf{H}_t(r, \varphi) + \mathbf{z}H_z(r, \varphi)] = \left\{(\nabla_t - j\beta\hat{\mathbf{z}}) \times [\mathbf{H}_t(r, \varphi) + \mathbf{z}H_z(r, \varphi)]\right\} \times \nabla_t \ln[n^2(r, \varphi)] \quad (3.28)$$

The two vector Equations (3.22) and (3.28) completely define the electromagnetic field in a cylindrical dielectric waveguide under the assumptions of material isotropy, instantaneity, linearity and longitudinal invariance. In the above derivation the refractive index is allowed to vary arbitrarily in the transversal plane. In general, the transverse plane coordinate set (r, φ) allows the refractive index to have any azimuthal dependence. Of course, the axial symmetric case is just one particular condition. It is relevant that under the above assumptions the equations of the electromagnetic field are separable into two second-order partial differential equations for the electric and the magnetic fields. This is the major consequence of the Cartesian representation for the electromagnetic field components. The case of the axial symmetric refractive index $n(r)$ described in the following section simplifies the mathematical description further.

3.3.3 Wave Equations for Axial Symmetric Fibers

In this section, in addition to the same assumptions reported above, the case of the axial symmetric refractive index $n(r)$ is considered. To be explicit, the conditions satisfied by the dielectric optical waveguide are as follows:

1. Cylindrical symmetry (optical fiber)
2. Isotropy
3. Instantaneity
4. Linearity
5. Longitudinal invariance
6. Axial symmetry

Assumption 6 mathematically translates by setting $n(r, \varphi) = n(r)$ into both vector wave equations (3.22) and (3.28). Due to the radial symmetry, the transversal gradient (3.21) of the logarithmic function of the squared refractive index includes only the first-order radial derivative:

$$\nabla_t \ln[n^2(r)] = \mathbf{r}\frac{d}{dr} \ln[n^2(r)] = \mathbf{r}\frac{2}{n(r)} \frac{dn(r)}{dr} \quad (3.29)$$

Substituting Equation (3.29) into Equations (3.22) and (3.28) gives the following vector equations for the electric and the magnetic fields in longitudinal invariant and axial symmetric optical fibers respectively:

$$[\nabla_t^2 + k^2n^2(r) - \beta^2][\mathbf{E}_t(r, \varphi) + \mathbf{z}E_z(r, \varphi)] = (\nabla_t - j\beta\hat{\mathbf{z}}) \left\{\mathbf{E}_t(r, \varphi) \cdot \mathbf{r}\frac{d}{dr} \ln[n^2(r)]\right\} \quad (3.30)$$

$$[\nabla_t^2 + k^2n^2(r) - \beta^2][\mathbf{H}_t(r, \varphi) + \mathbf{z}H_z(r, \varphi)] = \left\{(\nabla_t - j\beta\hat{\mathbf{z}}) \times [\mathbf{H}_t(r, \varphi) + \mathbf{z}H_z(r, \varphi)]\right\} \times \mathbf{r}\frac{d}{dr} \ln[n^2(r)] \quad (3.31)$$

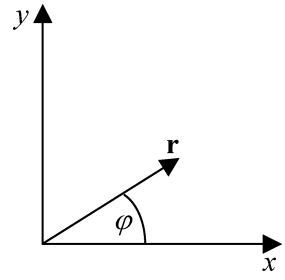

Figure 3.2 Coordinate system representation in the fiber cross-section. The field has Cartesian components while position is represented by cylindrical coordinates

These equations need some comment. First of all, the left member in both equations is the same for either the electric or the magnetic field. The right member includes instead the logarithmic dependence on the squared refractive index profile and it is different for the electric and magnetic field equations. The electric field Equation (3.30) is first considered.

The transversal component of the electric field $\mathbf{E}_t(r, \varphi)$ can be decomposed into two Cartesian components, according to Equations (3.2), and consequently the scalar product with the radial unit vector $\mathbf{r}$ in the cylindrical coordinate system (see Figure 3.2) reduces to the following term:

$$\begin{aligned}\mathbf{E}_t(r, \varphi) \cdot \mathbf{r} &= E_x(r, \varphi)\mathbf{x} \cdot \mathbf{r} + E_y(r, \varphi)\mathbf{y} \cdot \mathbf{r} \\ &= E_x(r, \varphi)\cos\varphi + E_y(r, \varphi)\sin\varphi\end{aligned} \tag{3.32}$$

From Equations (3.30) and (3.32) the right member has the following transversal and longitudinal components:

$$\begin{aligned}&\nabla_t\{[E_x(r, \varphi)\cos\varphi + E_y(r, \varphi)\sin\varphi]\frac{\mathrm{d}}{\mathrm{d}r}\ln[n^2(r)]\} \\ &\quad - \mathrm{j}\beta[E_x(r, \varphi)\cos\varphi + E_y(r, \varphi)\sin\varphi]\frac{\mathrm{d}}{\mathrm{d}r}\ln[n^2(r)]\mathbf{z}\end{aligned} \tag{3.33}$$

However, the logarithmic factor $(\mathrm{d}/\mathrm{d}r)\ln[n^2(r)]$ in Equation (3.30) is usually very weak and its contribution is negligible compared to the left-hand term.

The right member in Equation (3.31) for the magnetic field is more complicated because it includes vector products. However, apart from some what longer calculations, the conclusion is the same as for the electric field equation, namely the logarithmic factor in the right member contributes very little and so is usually neglected. In the following the separate contributions of the individual terms are reported:

$$\begin{aligned}&\left\{(\nabla_t - \mathrm{j}\beta\hat{\mathbf{z}}) \times [\mathbf{H}_t(r, \varphi) + \mathbf{z}H_z(r, \varphi)]\right\} \times \mathbf{r}\frac{\mathrm{d}}{\mathrm{d}r}\ln[n^2(r)] \\ &\quad = \left\{[\nabla_t \times \mathbf{H}_t(r, \varphi)] + [\nabla_t \times \mathbf{z}H_z(r, \varphi)] - [\mathrm{j}\beta\hat{\mathbf{z}} \times \mathbf{H}_t(r, \varphi)] - [\mathrm{j}\beta\hat{\mathbf{z}} \times \mathbf{z}H_z(r, \varphi)]\right\} \\ &\qquad \times \mathbf{r}\frac{\mathrm{d}}{\mathrm{d}r}\ln[n^2(r)]\end{aligned} \tag{3.34}$$

The transversal and longitudinal contributions are considered separately. The curl of the transversal component of the magnetic field in the first term is oriented along the longitudinal axis:

$$\nabla_t \times \mathbf{H}_t(r, \varphi) = \left[\frac{\partial H_y(r, \varphi)}{\partial x} - \frac{\partial H_x(r, \varphi)}{\partial y}\right]\mathbf{z} \tag{3.35}$$

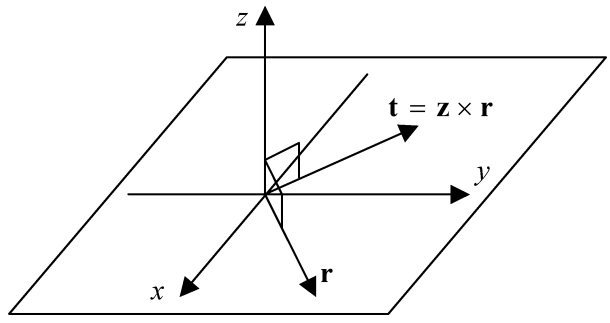

Figure 3.3 Coordinate system representation showing the vector product between the longitudinal unit vector **z** and the radial unit vector **r**. The resulting unit vector lies in the transversal plane

After the vector product with the radial unit vector **r** a transversal contribution to the vector wave Equation (3.31) is produced, as follows (see Figure 3.3):

$$[\nabla_t \times \mathbf{H}_t(r,\varphi)] \times \mathbf{r}\frac{\mathrm{d}}{\mathrm{d}r}\ln[n^2(r)] = (\mathbf{z}\times\mathbf{r})\{|\nabla_t \times \mathbf{H}_t(r,\varphi)|\frac{\mathrm{d}}{\mathrm{d}r}\ln[n^2(r)]\} \tag{3.36}$$

The second term in the left member of Equation (3.34) can be easily transformed as follows:

$$\nabla_t \times \mathbf{z}H_z(r,\varphi) = \nabla_t H_z(r,\varphi) \times \mathbf{z} \tag{3.37}$$

It is oriented in the transversal plane as the third term in the left member of Equation (3.34). After the vector product with the radial unit vector both of those terms give a longitudinal contribution to the vector Equation (3.31). Finally, the fourth term in the left member of Equation (3.34) gives a null contribution.

As already mentioned, the logarithmic term in the right member of both vector equations makes almost no contribution under the weakly guiding condition and so both can be neglected. With this approximation, the vector wave equations for the electromagnetic field of Equations (3.30) and (3.31) reduce to the following more familiar form:

$$[\nabla_t^2 + k^2n^2(r) - \beta^2][\mathbf{E}_t(r,\varphi) + \mathbf{z}E_z(r,\varphi)] = 0 \tag{3.38}$$

$$[\nabla_t^2 + k^2n^2(r) - \beta^2][\mathbf{H}_t(r,\varphi) + \mathbf{z}H_z(r,\varphi)] = 0 \tag{3.39}$$

The great advantages of these equations are that they are separable in the electric and magnetic field components, they are identical and finally, using Cartesian field components, they reduce to the same well-known scalar wave equation for each arbitrary Cartesian field component for the graded index optical fiber. From Equations (3.14), (3.15) and (3.16),

$$[\nabla_t^2 + k^2n^2(r) - \beta^2]\Psi(r,\varphi) = 0 \tag{3.40}$$

The scalar function $\Psi(r,\varphi)$ represents any of the electric or magnetic field Cartesian components. Using the explicit form of the transversal Laplacian operator in the cylindrical coordinates of Equation (3.18) gives the following second-order partial differential equation:

$$\frac{\partial^2\Psi(r,\varphi)}{\partial r^2} + \frac{1}{r}\frac{\partial\Psi(r,\varphi)}{\partial r} + \frac{1}{r^2}\frac{\partial^2\Psi(r,\varphi)}{\partial\varphi^2} + [k^2n^2(r) - \beta^2]\Psi(r,\varphi) = 0 \tag{3.41}$$

The axial symmetry of the refractive index allows for the generic field component $\Psi(r,\varphi)$ to be separated into the product or the radial-dependent function $R(r)$ with the azimuthal-dependent function

$\Phi(\varphi)$. This property only holds due to the axial symmetry of the refractive index $n(r, \varphi) = n(r)$. Setting $\Psi(r, \varphi) = R(r)\Phi(\varphi)$ in the scalar wave Equation (3.41) finally gives the separated form:

$$\frac{\mathrm{d}^2 R_\nu(r)}{\mathrm{d}r^2} + \frac{1}{r}\frac{\mathrm{d}R_\nu(r)}{\mathrm{d}r} + \left[k^2 n^2(r) - \beta^2 - \frac{\nu^2}{r^2}\right] R_\nu(r) = 0 \tag{3.42}$$

$$\frac{\mathrm{d}^2 \Phi_\nu(\varphi)}{\mathrm{d}\varphi^2} + \nu^2 \Phi_\nu(\varphi) = 0 \tag{3.43}$$

In order to satisfy the boundary conditions of the circular fiber, the separation constant ν must be a positive or negative integer, including zero:

$$\nu = 0, \pm 1, \pm 2, \ldots \tag{3.44}$$

The general solution of the harmonic Equation (3.43) is the linear combination of harmonic functions of the azimuthal coordinate φ:

$$\Phi_\nu(\varphi) = \begin{bmatrix} \mathrm{e}^{\mathrm{j}\nu\varphi} \\ \cos(\nu\varphi) \\ \sin(\nu\varphi) \end{bmatrix} \tag{3.45}$$

Any of the above harmonic functions constitutes a possible choice for the angular mode field dependence. In the particular case of $\nu = 0$ the angular contribution reduces to the constant value of 0 or 1 according to the base function chosen.

3.3.4 Modal Field Structure and Properties

In the following reference will be made to the axial symmetric optical fiber, in addition to the six assumptions reported at the beginning of Section 2.2.3. The radial term in Equation (3.42) includes the radial dependence of the axial symmetric refractive index and accordingly characterizes the modal field distribution. For the particular case of the uniform refractive index, otherwise known as the step-index case, the radial Equation (3.42) reduces to the Bessel equation and the general solution is a linear combination of Bessel functions of the first kind and the second kind. Up to now, the modal fields depend on one index, namely the azimuthal mode number ν. Upon satisfaction of the circular boundary condition at the core–cladding interface, a second modal number is needed for matching of the conditions of the radial differential Equation (3.42). This is the radial mode number $\mu = 1, 2, \ldots$.

Each mode field solution is characterized by a pair of mode numbers (ν, μ). In general, for each fixed azimuthal mode number ν many radial mode numbers $\mu_1, \mu_2, \ldots, \mu_{M_\nu}$ are allowable, leading to corresponding modal solutions of the radial Equation (3.42). Radial mode numbers associated with the same azimuthal mode number ν belong to a finite set of dimensions M_ν. Even if the azimuthal mode number ν, as related to the azimuthal field component (3.43), could assume in principle infinite values according to the set in Equation (3.44), the simultaneous satisfaction of the boundary conditions for the radial field component limits the upper value of the allowable range for the azimuthal number ν to the integer N_ν:

$$\nu = 0, \pm 1, \pm 2, \ldots, \pm N_\nu$$

As a consequence of the finite set of both azimuthal and radial mode numbers, it is easy to conclude that all optical fibers must support a finite number $N_\mathrm{G} = N_\nu M_\nu$ of guided (bounded) modes. The corresponding product $\Psi_{\nu\mu}(r, \varphi) = R_{\nu\mu}(r)\Phi_\nu(\varphi)$ for each allowed mode number pairs defines the particular modal field supported by the optical fiber. In addition to the discrete set of guided modes, each optical fiber even allows a continuum set of radiation modes $\psi(r, \varphi, \alpha)$. The

modal decomposition constitutes the basis set for the representation of the general electromagnetic field component $F(r, \varphi)$ supported by the optical fiber in terms of both guided (discrete) modes and radiation (continuum) modes:

$$F(r, \varphi) = \sum_{\nu=1}^{N_\nu} \Phi_\nu(\varphi) \sum_{\mu=1}^{M_\nu} c_{\nu\mu} R_{\nu\mu}(r) + \int_\Omega c(\alpha)\psi(r, \varphi, \alpha)\, \mathrm{d}\alpha \tag{3.46}$$

3.3.5 Comments on Pulse Propagation

The following considerations are quite important for understanding the fundamental pulse propagation physics in optical fibers. The modal field theory that has been presented implicitly assumes a true monochromatic field with uniform field amplitude along the whole fiber length. This is implicitly assumed in the phasor term expression in Equation (3.14), $\mathrm{e}^{\mathrm{j}(\omega t - \beta z)}$. The phase wavefronts have therefore been assumed to be planes without any longitudinal dependence. This is evident when the phase term in Equation (3.14) is considered. Each surface of constant phase $\phi(z, t) = \omega t - \beta z = \phi_0$ moves with the constant phase velocity $v_\mathrm{p} = \omega/\beta$. At the fixed time instant $t = t_0$ the phase surface is the plane defined by $z = (\omega t_0 - \phi_0)/\beta$. This is consistent with the assumption previously made in the modal field theory. Concepts like intermodal dispersion and in particular intramodal (chromatic) dispersion have not been included in the modal field theory presented so far. Even the light source has been implicitly assumed to be ideally monochromatic with the single frequency ω. In order to include pulse distortion and the related propagation concept into optical fiber theory it is necessary to generalize the previous analysis including the field envelope function. In addition, it is necessary to assume that the modal field distribution as deduced from the 'static' field approach presented above still remains valid, even under reasonable envelope distortion. This is the basic approach presented in the literature for pulse propagation theory in optical fibers. Nonlinear effects such as nonlinear refraction can be inserted in the field equation for the pulse propagation based on the approach described above.

Multimode fiber propagation theory relies mainly on the mode group delay concept as the strongly dominant phenomena affecting optical pulse propagation. In this approach, chromatic dispersion does not make a relevant contribution and it can be neglected at a first analysis level. By neglecting chromatic dispersion, each excited mode propagates with its group velocity and contributes to the output section pulse composition with its own energy released at some specific time instant. Since group velocity is in general a function of the mode distribution considered, all energy contributions generally arrive at different time instants at the output fiber section, leading to modal delay pulse broadening. This behavior is common to every multimode waveguide, including of course even metallic waveguides, and is not a peculiarity of either optical fibers or any other dielectric waveguide. Instead, chromatic dispersion acts within each excited mode and refers to the interaction between the source spectrum width and both material and waveguide dispersion relationships.

3.3.6 Weakly Guiding Fibers and Mode Groups

Satisfaction of the boundary conditions for the radial wave Equation (3.42) at the core–cladding interface is demanded for the solution of the eigenvalue equation. The solutions of the eigenvalue equation, namely the eigenvalues, give the phase constants $\beta_{\nu\mu}$ for the corresponding allowed guided modes. The phase constant completely characterizes the propagation behavior of the corresponding mode. Accordingly, the phase constant $\beta_{\nu\mu}$ is also defined as the propagation constant. For a given fiber geometry, the propagation constant $\beta_{\nu\mu}$ is a function of the optical frequency (wavelength). The dependence of $\beta_{\nu\mu}(\omega)$ on the optical frequency ω can be quite cumbersome, since it includes both waveguide dispersion and material dispersion relationships. Even assuming no material dispersion

contribution, the propagation constant will depend on the optical frequency due to the waveguide dispersion relationship. The waveguide dispersion term is of course defined through the refractive index profile. It should be remembered that in this context a given fiber mode is dealt with. The dispersion relationship $\beta_{\nu\mu}(\omega)$ refers to the dependence of the propagation constant on the optical frequency and therefore it generates the chromatic dispersion term previously introduced, otherwise known as the intramodal dispersion component. As already stated in Equation (3.46), the eigenvalue equation admits solutions only for a limited value of the azimuthal mode number ν, precisely for every integer value $|\nu| \leq N_\nu$. These are called proper azimuthal mode numbers.

For any proper azimuthal mode number ν, several radial mode numbers can be associated with it:

$$\forall \nu : |\nu| \leq N_\nu \Rightarrow \exists \mu \in \{1, 2, \ldots, M_\nu\} \Rightarrow (\nu, \mu) \tag{3.47}$$

Each pair (ν, μ) therefore identifies a propagation constant $\beta_{\nu\mu}(\omega)$ and the corresponding guided mode $\Psi_{\nu\mu}(r, \varphi) = R_{\nu\mu}(r)\Phi_\nu(\varphi)$. This correspondence is bidirectional, meaning that each mode solution is uniquely identified by one and only one pair of mode numbers and vice versa. As a consequence, each mode field $\Psi_{\nu\mu}(r, \varphi)$ has its own propagation constant $\beta_{\nu\mu}(\omega)$. Different modes have therefore different propagation constants. This uniquely ordered set will be referred to as a nondegenerate mode set. The following mathematical representation schematizes this concept:

$$(\nu, \mu) \Leftrightarrow \begin{cases} \beta_{\nu\mu}(\omega) \\ \Psi_{\nu\mu}(r, \varphi) \end{cases} \tag{3.48}$$

In optical fibers used for a telecommunication purpose the difference between the maximum value of the refractive index on the fiber axis, $n(0) = n_1$, and the minimum value reached in the cladding region, n_2, is usually much smaller than the average value of the refractive index itself. The proper function used to specify the relative refractive index variation along the radial coordinate is called the refractive index profile height parameter:

$$\Delta \equiv \frac{1}{2}\left[1 - \left(\frac{n_2}{n_1}\right)^2\right] \tag{3.49}$$

Standard telecommunication optical fibers usually have a profile height parameter in the range $0.001 \leq \Delta \leq 0.01$ and are referred to as weakly guiding fibers.

Under weakly guiding fiber approximation the modal solution becomes degenerate and several mode solutions share a common propagation constant. This condition will be referred to as a degenerate mode set. Fiber modes are then grouped together in order to have the same propagation constant. The degeneration order of a mode group is identified by the number of individual modes belonging to it. More precisely, the order of degeneration refers to the eigenvalue associated with the mode group. Mode groups can be identified by a single group index instead of a pair of mode numbers. Of course, even propagation constants will be identified by the same group index. Several mode field distributions therefore belong to the same group and, more importantly, they propagate at the same speed, with the same propagation constant. Individual modes belonging to the same mode group have the same dispersion characteristic and are indistinguishable in terms of their propagation characteristics. Under the degenerate eigenvalue condition, the unique relationship (3.48) no longer holds and must be substituted with the more general relation reported below:

$$\left\{ \begin{array}{c} (\nu_1, \mu_1) \Leftrightarrow \Psi_{\nu_1\mu_1}(r, \varphi) \\ \vdots \\ (\nu_j, \mu_k) \Leftrightarrow \Psi_{\nu_j\mu_k}(r, \varphi) \\ \vdots \end{array} \right\} \Leftrightarrow \begin{cases} \beta_h(\omega) \\ M_h = \{\Psi_{\nu_j\mu_k}\}_{(\nu_j,\mu_k)\in S_h} \end{cases} \tag{3.50}$$

The index $h = 1, 2, \ldots, M$ is the group index and the set S_h includes all the pairs of mode numbers (ν, μ) that identify individual modes $\Psi_{\nu\mu}(r, \varphi)$ belonging to the mode group h. Here it is assumed that all individual modes labeled with radial and azimuthal mode indices ν_j and μ_k with $(\nu_j, \mu_k) \in S_h$ have the same propagation constant $\beta_h(\omega)$ and can consequently be grouped together in the same mode group M_h.

3.4 Theory of the Modal Impulse Response

Before writing the mathematical definition of the group delay, it is important to discuss this concept briefly in order to avoid some common misunderstandings. Mode group and group delay refer to different things. Group delay is not specifically the delay of the mode group. The terminology used, group delay, refers instead to the bundle of pulse energy concentrated around the center of gravity of the pulse. Group delay is quite a fundamental concept and is not only related to optical fiber theory. It is just a mere coincidence that the definition of group delay also applies to the propagation delay of the optical fiber mode group, since individual modes belonging to a given mode group experience the same group delays.

The group delay per unit length $\tau_g(\omega)$ is defined as the reciprocal of the group velocity $v_g(\omega)$. It is given by the first-order derivative of the propagation constant $\beta(\omega)$ with respect to the angular frequency ω:

$$\tau_g(\omega) \equiv \frac{1}{v_g(\omega)} = \frac{d\beta(\omega)}{d\omega} \quad \text{(ns/m)} \tag{3.51}$$

Each mode group supported by the multimode fiber propagates with its own group delay:

$$\tau_{g,h}(\lambda) = \frac{d\beta_h(\omega)}{d\omega}, \quad h = 1, 2, \ldots, M \tag{3.52}$$

The group delay $\tau_{g,h}(\omega)$ of each mode group depends on the dispersion relationship for the selected eigenvalue $\beta_h(\omega)$. The integer M is the total number of guided mode groups supported by the fiber. The task to be solved now is to find the optimum refractive index profile $n(r, \lambda)$ in order to equalize group delays $\tau_{g,h}(\omega)$ among all M guided mode groups supported by the multimode fiber. The refractive index profile optimization depends on the fiber geometry, material properties and wavelength.

According to the group delay compensation principle achieved through proper refractive index profiling for a given light source spectrum, each mode group propagates along the fiber length, reaching the fiber end section at some time instant $t_h, h = 1, 2, \ldots, M$. This time instant, referred to the time origin at the input impulse and measured after the unit length, coincides with the mode group delay defined in Equation (3.52): $\tau_h = \tau_{g,h}, h = 1, 2, \ldots, M$. One question now arises spontaneously. What would be the shape of the impulse response $\upsilon_h(z, t, \lambda)$ of the hth mode group measured at the output fiber section z and excited at the wavelength λ?

If the approximation of neglecting both the effects of the modulated light source spectral width and of the input pulse spectral content is accepted, the answer is the following. Each supported fiber mode will contribute to the total output pulse with the impulse response $\upsilon_h(z, t, \lambda)$ exhibiting the same impulsive temporal profile as the input impulse but delayed by the corresponding mode group delay $\tau_{g,h}(\omega)$ evaluated at the source spectrum wavelength λ:

$$\upsilon_h(z, t, \lambda) = \delta[t - z\tau_{g,h}(\lambda)] \tag{3.53}$$

In this case we have used the wavelength variable λ instead of the optical frequency ω in order to avoid confusion over the spectral content of the pulse envelope. Of course, both the vacuum

wavelength λ and frequency ω refer to the source optical carrier frequency evaluated in vacuum. They are related by the following simple relation, where c is the speed of the light in vacuum:

$$\omega = \frac{2\pi c}{\lambda} \longrightarrow \mathrm{d}\omega = -\frac{2\pi c}{\lambda^2}\mathrm{d}\lambda \tag{3.54}$$

Once the impulse response of the individual hth fiber mode has been found to be the same input impulsive stimulus delayed by the corresponding fiber mode group delay $\tau_{g,h}(\lambda)$, it is easy to agree with the following fundamental statement, which leads directly to the modal impulse response of the multimode fiber. Assuming linear propagation conditions and no mode interaction, the modal impulse response measured at the multimode fiber output section z is obtained by superposing all supported modal contributions reported in Equation (3.53):

$$\upsilon(z, t, \lambda) = \sum_{h=1}^{M} |a_h(\lambda)|^2 \delta[t - z\tau_{g,h}(\lambda)] \tag{3.55}$$

Each single coefficient $|a_h(\lambda)|^2$ is given by the sum of the squared value of the normalized overlap integral between the input exciting field distribution and the corresponding individual mode distribution evaluated at the same input fiber section belonging to the hth mode group:

$$|a_h(\lambda)|^2 = \sum_{\substack{\nu,\mu \\ (\nu,\mu)\in S_h}} |a_{\nu\mu}(\lambda)|^2 \leq 1 \tag{3.56}$$

The coefficient $|a_h(\lambda)|^2$ therefore represents the fraction of input field intensity that has been coupled to the corresponding hth mode group through the individual contribution of each mode belonging to the corresponding mode group. The conservation of launched energy reflects the unit normalization of all mode group coupling coefficients:

$$\sum_{h=1}^{M} |a_h(\lambda)|^2 = 1 \tag{3.57}$$

Figure 3.4 gives a schematic representation of the situation described above. All excited mode groups are launched simultaneously at the input fiber section with the impulsive stimulus. The launched intensity varies for each mode group according to the overlap integral calculation. Assuming there is no additional intramodal (chromatic) pulse dispersion, each mode group brings the corresponding light energy as the same impulse available at the input section. After propagating for some distance, the mode group reaches the output fiber section at different time instants, according to their own group delay. The output intensity is therefore no longer available as a single impulse but instead is spread among all mode group contributions showing different group delays. The picture presented in Figure 3.4 is an approximation of the effective optical excitation, at least for the following two reasons:

1. The modulated source spectrum width cannot be zero as it must have some extent. According to the light modulation technique the source spectrum width can be either very narrow or very large. In the case of external modulation, for instance, the source spectrum width could even coincide with the source CW (continuous wave) condition in the limiting case of very high optical isolation. In the case of direct modulation the situation would be the opposite and the frequency chirping induced by fast input pulse transients would affect the spectrum extent.
2. The input impulse stimulus has an inherently infinite signal bandwidth extent. Even assuming external laser modulation with an infinite modulation bandwidth, the optical spectrum at the fiber input section would be indefinitely wide.

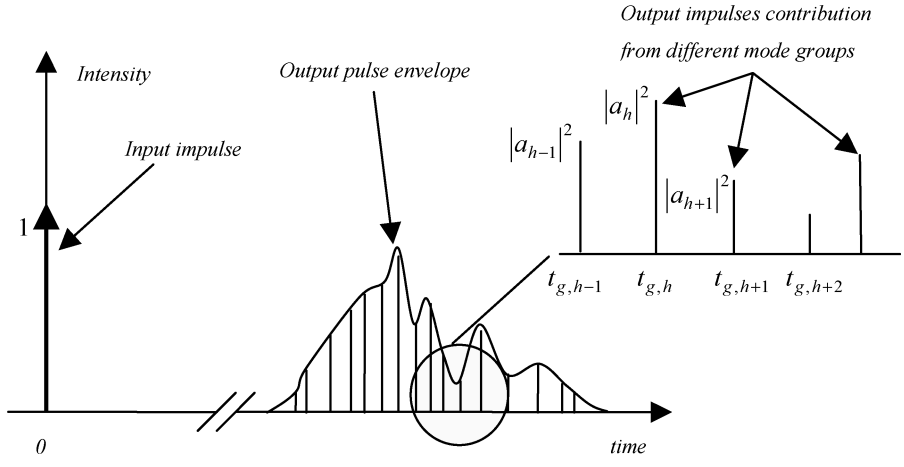

Figure 3.4 Schematic representation of the multimode fiber modal impulse response. Assuming ideal conditions, the impulse response is given by the superposition of each delayed mode group impulse contribution. In the lossless case, the weight $|a_h(\lambda)|^2$ of the output pulse of the jth mode group is given by the square value of the coupling coefficient evaluated at the input section

The above two cases represent an interesting discussion about how to interpret an ideal modeling situation. Both of them should be considered in any real application, and not only as limiting cases, but instead they should serve at least as interesting operating conditions.

3.4.1 The Differential Mode Delay

A fundamental parameter used to determine the degree of mode delay equalization of the graded index multimode fiber is the differential mode delay (DMD). In order to understand the physical concept behind the standard definition of DMD, it is assumed that a unit energy light impulse $\delta(t)$ is launched at the fiber input section according to the over-filled launch (OFL) conditions. This means that all guided modes are excited by the input light source with the same amount of incident light intensity. The amount of light intensity captured by each mode depends instead on the spatial mode distribution, according to the overlap integral. In addition, without losing generality, it can be assumed that the unit light intensity incident on the fiber input section is completely captured by all the guided modes, so that no radiated power appears in the energy conservation balance. All the launched power is therefore transferred to the supported bound modes.

The output pulse detected after a unit length by means of the ideal simplified experiment shown in Figure 3.4 suggests a meaningful interpretation. Since the input impulse has normalized unit energy the following statistical interpretation of the output pulse distribution is made:

1. The output pulse takes the meaning of the statistical distribution of the energy arrival time instants among the set of all excited guided modes. Since the energy arrives at the output section as packets brought by corresponding mode groups at the time instant defined by the group delay, the following statements are also deduced:
2. The output pulse assumes the meaning of the statistical distribution of the group delay variable evaluated at the source wavelength.
3. Each weighted energy contribution therefore assumes the meaning of the probability of finding the corresponding group delay among the detected population.

4. The group delay per unit length can be mathematically described as the discrete random variable $\underline{\tau}_g(\lambda)$ defined over the set $\{\tau_{g,h}(\lambda)\}$ of the group delays allowed by the excited mode groups, where the underscore notation identifies a random variable.
5. The probability of detecting one particular event $\tau_{g,h}(\lambda)$ at the output section after one unit length of pulse propagation is given by the intensity coefficient $|a_h(\lambda)|^2$ of the corresponding mode group.
6. Due to normalization of the total launched energy in Equation (3.57), the intensity distribution of the output pulse takes the meaning of the probability density function of the discrete random variable associated with the group delay:

$$a_h(\lambda) = P\{\underline{\tau}_g(\lambda) = \tau_{g,h}(\lambda)\} = f_{\underline{\tau}_g}[\underline{\tau}_g(\lambda)]$$

Each value $\tau_{g,h}(\lambda)$ of the mode group delay therefore represents a particular event allowed by the random variable $\underline{\tau}_g(\lambda)$. These concepts are shown in Figure 3.5.

Once the energy distribution versus time at the output section is known, it is important to compute the ensemble average group delay $\langle\underline{\tau}_g(\lambda)\rangle$ over the modal distribution:

$$\langle\underline{\tau}_g(\lambda)\rangle = \sum_{h=1}^{M} |a_h(\lambda)|^2 \tau_{g,h}(\lambda) \tag{3.58}$$

The average group delay $\langle\underline{\tau}_g(\lambda)\rangle$ represents the center of gravity of the detected output pulse due to modal distribution, and is shown as the dot–dash vertical line in Figure 3.5.

It is convenient to define the centered group delay distribution by subtracting the average value $\langle\underline{\tau}_g(\lambda)\rangle$ from the original group delay $\underline{\tau}_g(\lambda)$. This leads to the centered process $\hat{\underline{\tau}}_g(\lambda)$, which is identified by adding the hat symbol over the corresponding variables:

$$\hat{\underline{\tau}}_g(\lambda) \equiv \underline{\tau}_g(\lambda) - \langle\underline{\tau}_g(\lambda)\rangle \tag{3.59}$$

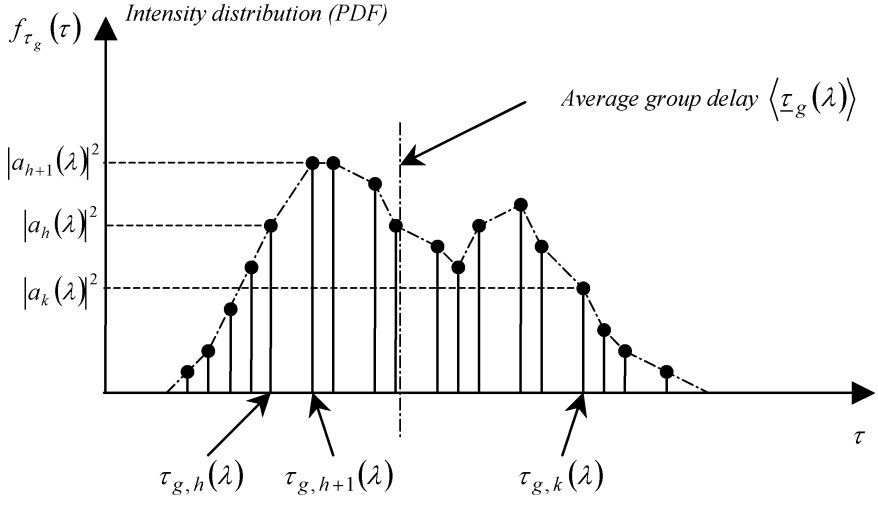

Figure 3.5 Statistical interpretation of the intensity distribution at the optical fiber output section due to the mode group delay as the probability density function $f_{\tau_g}(\tau)$ of the group delay process. The intensity of each group contribution is given by the corresponding excitation coefficient $|a_h(\lambda)|^2$ at the launching section after normalization. The envelope of the distribution gives the intensity profile of the output pulse

From Equations (3.58) and (3.59),

$$\langle \hat{\underline{\tau}}_g(\lambda) \rangle = \sum_{h=1}^{M} |a_h(\lambda)|^2 [\tau_{g,h}(\lambda) - \langle \underline{\tau}_g(\lambda) \rangle] = 0 \tag{3.60}$$

The variance of the group delay distribution of both the centered process and the original one is of course the same. From Equation (3.59) it can be found immediately that

$$\sigma^2_{\hat{\tau}_g}(\lambda) = \sigma^2_{\tau_g}(\lambda) = \sum_{h=1}^{M} |a_h(\lambda)|^2 [\tau_{g,h}(\lambda) - \langle \underline{\tau}_g(\lambda) \rangle]^2 \tag{3.61}$$

According to the statistical interpretation of the modal group delay $\underline{\tau}_g(\lambda)$, the differential mode delay (DMD) can be defined as the average value of the group delay deviation around the expected group delay. Equivalently, it can be said that the parameter DMD coincides with the standard deviation $\sigma_m(\lambda)$ of the modal group delay distribution measured in the normalized temporal variable τ. According to the unit of measure of the group delay $\underline{\tau}_g(\lambda)$, the DMD takes the same meaning as the normalized delay per unit time. From Equation (3.61), therefore,

$$\mathrm{DMD}(\lambda) = \sigma_m(\lambda) = \sqrt{\sum_{h=1}^{M} |a_h(\lambda)|^2 [\tau_{g,h}(\lambda) - \langle \underline{\tau}_g(\lambda) \rangle]^2} \quad \text{(ns/km)} \tag{3.62}$$

The statistical definition of the DMD allows a clear interpretation of this important concept. In practice, the correct way to set up the DMD measurement would be by using an external modulated laser source with a narrow linewidth, modulated by a relatively fast pulse driver whose launched optical pulse duration would be much narrower than the expected resolution needed for collecting separate output mode group contributions, but still wide enough to make a negligible contribution to chromatic dispersion in each mode group. From Equation (3.62) it is concluded that the differential mode delay increases linearly with distance. This suggests that the DMD measurements should be set up using the minimum multimode fiber length in order to have good temporal accuracy for the given source pulse width.

The multimode fiber modal for a generic finite width pulse is considered again. According to the above discussion and neglecting for the moment the chromatic dispersion contribution, the normalized response of each mode group to the input pulse excitation $p(t)$ coincides with the convolution between the impulse response (3.53) with the launched pulse $p(t)$. Due to the impulse response (3.53), the time convolution simply reduced to the input pulse translation of the amount corresponding to the modal group delay:

$$h_h(z, t, \lambda) = p[t - z\tau_{g,h}(\lambda)] \tag{3.63}$$

Under the linear propagating regime, the total response at the fiber output is given by the superposition of each mode group intensity pulse response:

$$h(z, t, \lambda) = \sum_{h=1}^{M} |a_h(\lambda)|^2 h_h(z, t, \lambda) = \sum_{h=1}^{M} |a_h(\lambda)|^2 p[t - z\tau_{g,h}(\lambda)] \tag{3.64}$$

Figure 3.6 shows the situation. Each excited mode propagates the input pulse up to the output section almost unchanged by neglecting any further broadening or distortion due to intramodal (chromatic) dispersion. If the chromatic dispersion effect can be accounted for, each modal contribution will be affected by proper pulse distortion.

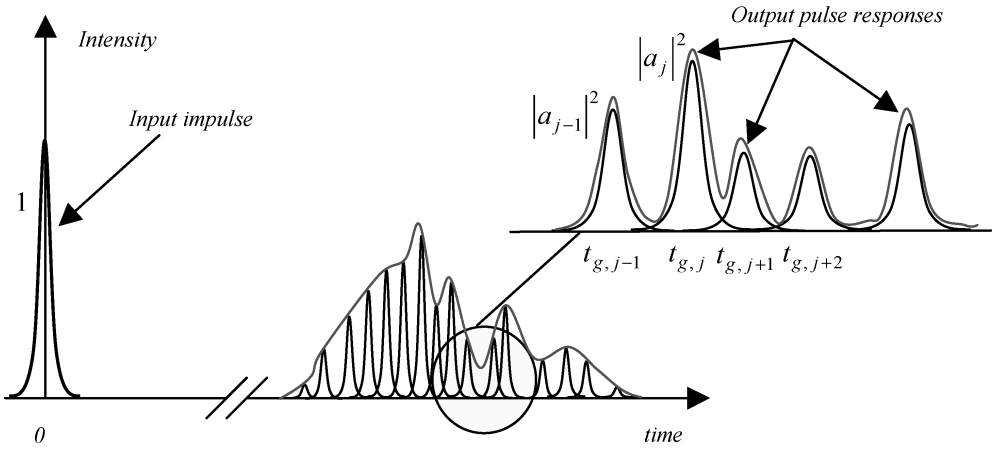

Figure 3.6 Multimode fiber impulse response under the assumption of a not ideal impulse excitation. The impulse response is given by the superposition of each delayed mode group pulse contribution. In the lossless case, the relative weight of the output pulse of the h mode group is given by the square value of the coupling coefficient evaluated at the input section, $|a_h|^2$

The modal impulse expressions derived either in Equation (3.55) for the impulsive stimulus or in Equation (3.64), assuming the finite input pulse (3.63), are general and their validity is not limited by any approximation except for the linear regime assumption among all supported fiber modes. In the next section the linear regime implications will be discussed in more detail. A brief analysis of either expressions (3.55) or (3.63) shows that the impulse response of the multimode fiber is made up of several discrete contributions and the relative weight of those adding terms is governed by the coupling coefficients $|a_h(\lambda)|^2$. The index h identifies the corresponding hth mode group. Moreover, it would be clear that every condition that modifies the energy distribution among the launched modes will generate accordingly different modal impulse responses. This characteristic is the most important property of the modal impulse response. Every modification of the environmental conditions, such as the temperature, the pressure and the polarization, that could determine a variation in the coupling coefficient distribution will be responsible for the corresponding variation in the modal impulse response.

3.5 Linear Propagation Regime

In this section the validity will be discussed of the superposition principle in computing the output pulse intensity as the sum of the individual intensities carried by each mode group. This is a completely different situation from the basic model theory of nonlinear behavior of the single-mode optical fiber, where the nonlinear regime refers to the electric field amplitude and to the consequent nonlinear refraction induced through the third-order susceptibility. In the following context, it will be assumed that the electric field intensity is low enough to validate the linear refraction assumption. High-field nonlinear refraction analysis is outside the scope of this book. Two different conditions will be considered, single-pulse and multiple-pulse excitation of multimode group propagation.

3.5.1 Single-Pulse Excitation

In deriving the total output pulse intensity in Equations (3.55) and (3.64) the assumption of a linear regime has been used. It is important now to spend some time looking at this assumption.

Input pulse energy is distributed among all excited bound modes and each mode group propagates along the fiber, delivering the proper fraction of pulse energy to the fiber end section after some delay from the instant of excitation. This picture, although quite simple and clear, hides instead a subtle argument. The input field from the light source is coupled to the bound mode field by means of overlap integrals. Accordingly, each excited mode field brings the proper amplitude as a consequence of the source electric field and propagates along the fiber. The following two assertions are considered:

1. The linear regime assumption ensures that the total electric field evaluated at the end section of the multimode fiber is given by the sum of the electric field of each individual mode.
2. Assuming weakly guiding conditions, the magnetic field results are almost proportional to the electric field (quasi-transverse electromagnetic (TEM) waves) and the intensity at the output fiber section is therefore proportional to the square modulus of the total electric field.

In general the second assertion does not imply that the total output intensity is equal to the sum of the individual mode group intensities. In order to verify this condition it is necessary that all cross-products between different modes give a null contribution to the total intensity. Since the guided mode set constitutes an orthogonal basis for the guided electromagnetic field, this satisfies the orthogonality condition for the scalar product between any two basis elements. The definition of the scalar product implies the integration of the product of any two basis elements over the infinite cross-section. This means that in order to have a null contribution from any two cross-terms, the collected intensity would be measured over the infinite cross-section. With this observation in mind, it is therefore concluded that:

3. The total intensity collected at the output cross-section is given by the sum of the intensities carried by each individual mode, computed through integration over the infinite cross-section.

3.5.2 Multiple-Pulse Excitation

The second question regarding the plausible nonlinear multimode regime refers to the validity of the intensity superposition when multiple-input pulse excitations are applied. The subject to be investigated here is the intensity response of the multimode fiber to multiple subsequent input pulses measured after a relatively long propagation length at the output section in order to allow several responses to overlap. The propagation length and the input pulse repetition rate should be adjusted in order to cause output pulse overlap according to at least two subsequent input excitation pulses. Stated differently, the total duration τ of the group delay distribution (peak-to-peak extent) measured after the link length should be wider than the time interval ΔT between any two consecutive exciting input pulses. Figure 3.7 shows a schematic representation of this condition.

As already noted, the question dealt with here regards the validity of the linear superposition principle applied to the intensities of each mode group at the output fiber section. In the following it will be shown that the individual intensity contribution from each mode group is linearly superposed at the output fiber section.

To see how the superposition principle of individual mode intensities holds its validity, first the case presented in Figure 3.7 is considered, where two input pulses, completely separated from each other, generate instead overlapping output pulse contributions. In order to cause the output pulses to overlap, it is necessary for the temporal distance between the two input exciting pulses to be less than the pulse broadening response at the output section. Accordingly, it becomes evident that the electric field associated with the same individual mode excited by the first and the second input pulses will overlap.

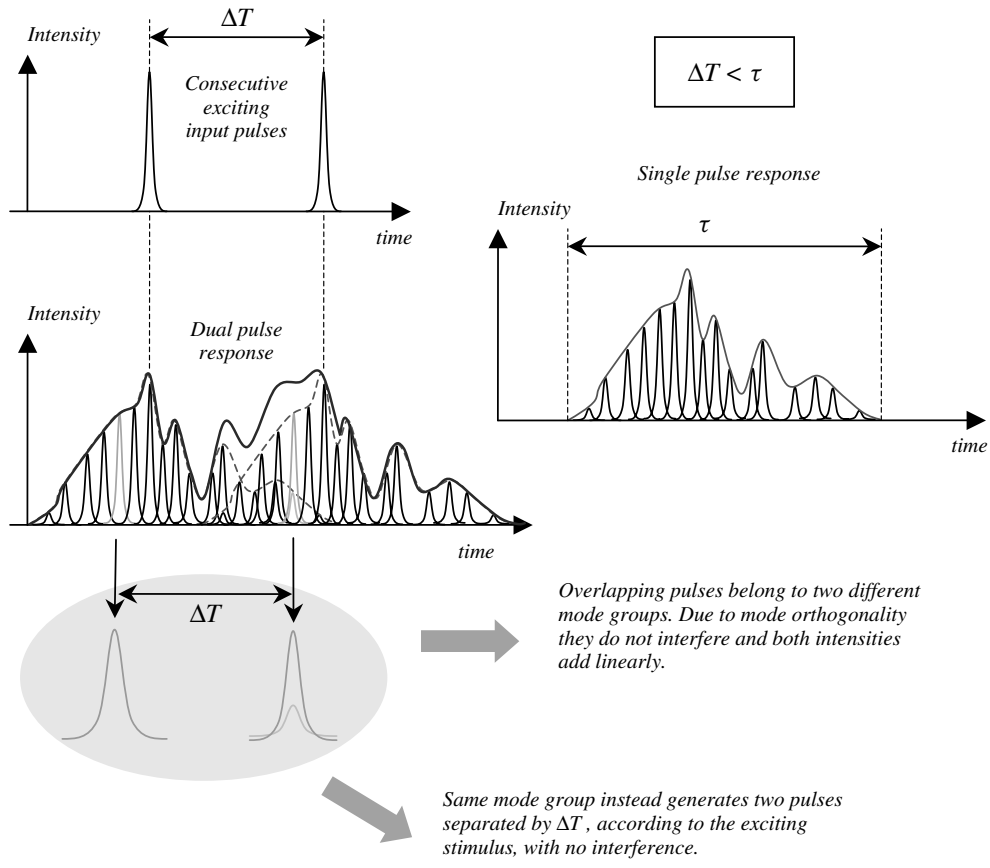

Figure 3.7 The drawing to the right end shows the pulse response of the multimode fiber to the single-input pulse excitation (top left). If the repetition rate of input pulses is fast enough, the envelope of two consecutive output pulses will overlap by some amount (bottom left)

It should be remembered that the total electric field is given by the sum of all excited modes available at every point in the fiber cross-section. If any two individual modes, excited by two different input pulses and propagating at different speeds, overlap during some time interval at the fiber output cross-section, they would contribute to the total intensity with their characteristic interfering terms, thus invalidating the superposition principle of the intensities. However, due to mode orthogonality, after integration over the infinite fiber cross-section, the interfering contribution between any two electric fields belonging to different individual modes will vanish and the total intensity will satisfy the superposition principle.

The second case considered is given by the input stream with a very fast pulse repetition rate, much faster than the duration of each individual stimulating pulse. This case leads to input pulse superposition but, nevertheless, the same orthogonality properties among different individual modes allows for output intensity superposition. In this case, of course, due to input pulse overlap the exciting pulse shape is different from the previous case, but this must not be misunderstood as a non-linear overlap pulse contribution. In multimode fibers, neglecting high-intensity-induced nonlinear refraction, mode orthogonality allows for intensity superposition independently from any launching conditions, pulse repetition rate and spectral coherence. If mode coupling occurs, individual power

contributions are exchanged among coupled modes, but still the intensity superposition at the output cross-section holds its validity. It is, however, relevant to remember that mode orthogonality is an integral property of the modal field. It is not a local property of the spatial field. This means that interfering terms will vanish just after integration of the field distribution over the infinite fiber cross-section.

3.6 The Optimum Refractive Index

The mode field theory of graded index optical fiber allows the optimum refractive index profile to be determined. Index profile optimization refers to the capability of gaining group delay equalization among all excited modes. Assuming the optimum refractive index profile, every mode group propagates with the same component of the group velocity along the longitudinal direction. Accordingly, all mode groups reach in principle every fiber cross-section at the same time instant. This ideal equalized condition leads to a null differential mode delay distribution. Stated differently, the differential mode delay distribution collapses upon a Dirac delta distribution with zero variance.

In any manufactured multimode optical fibers, things are not as easy as they could appear from the above idealized conditions. The optimum profile is found to be strongly dependent on the fiber geometry, material properties and source wavelength. Any defect found during the multimode fiber fabrication process affects the refractive index profile and consequently has a strong impact on the differential mode delay distribution. Manufacturing defects are statistically localized close to the fiber axis and at the core–cladding transition region. Additional profiling changes can also happen in the radial mid-region, with an even stronger impact on the group delay equalization properties. Each defective region contributes consistently in destroying the designed group delay compensation, and a certain amount of the launched pulse energy therefore travels at a slightly different speed, contributing to the output pulse dispersion. Of course, if the differential group delay $\tau_j(\lambda)$ is comparable with the transmitting time step T, a relevant pulse distortion will be produced. Otherwise, for a relatively lower bit rate the group delay dispersion could even be negligible. Just to have an order of magnitude of the dispersion in deployed multimode fibers would produce DMD ranges between 0.5 ns/km and 1.0 ns/km. Assuming a 10 GbE bit rate, the time step T is close to $T \cong 100$ ps and the allowed pulse dispersion would therefore be less than 30 ps for a limited eye optical power penalty. Assuming a quadratic dispersion composition after pulse convolution, this leads to an acceptable DMD of about DMD $\cong$ 83 ps, which corresponds to the worst-case link reach of less then 83 m.

Figure 3.8 gives a qualitative representation of the principal defect regions in the refractive index profile for a graded index multimode fiber. The central region (I) shows typical axial defects recognized as refractive index dip or pin. This defect indicates respectively a refractive index depletion or enhancement on the fiber axis region with respect to the optimum designed refractive index profile. As already mentioned, the mid-radial core region (II) reports some refractive index profile distortions usually due to the manufacturing process and recognized as the multiple-α profile region. Since the delay compensation strongly depends on the grading profile of the refractive index, any perturbation from the ideal situation contributes to pulse broadening. Finally, the outer core region (III) reports typical core–cladding irregular boundary conditions.

It has been mentioned that the optimum refractive index profile depends on the wavelength through the doped glass material dispersion characteristic. Accordingly, a graded index profile can in principle be optimized only for a single wavelength operation. This is in fact what is encountered in all practical situations, where the manufacturing process of the multimode fiber has been designed to achieve the minimum group delay dispersion for a given operating wavelength range. Today, bandwidth-optimized multimode fibers for GbE and 10 GbE standards are available with a bandwidth in excess of 2 GHz km when operated in the 850 nm wavelength region, but most of their performance is lost when operating in the 1310 nm region, degrading the bandwidth down to 500 MHz km. This rapidly degrading behavior is a consequence of the very tight optimization

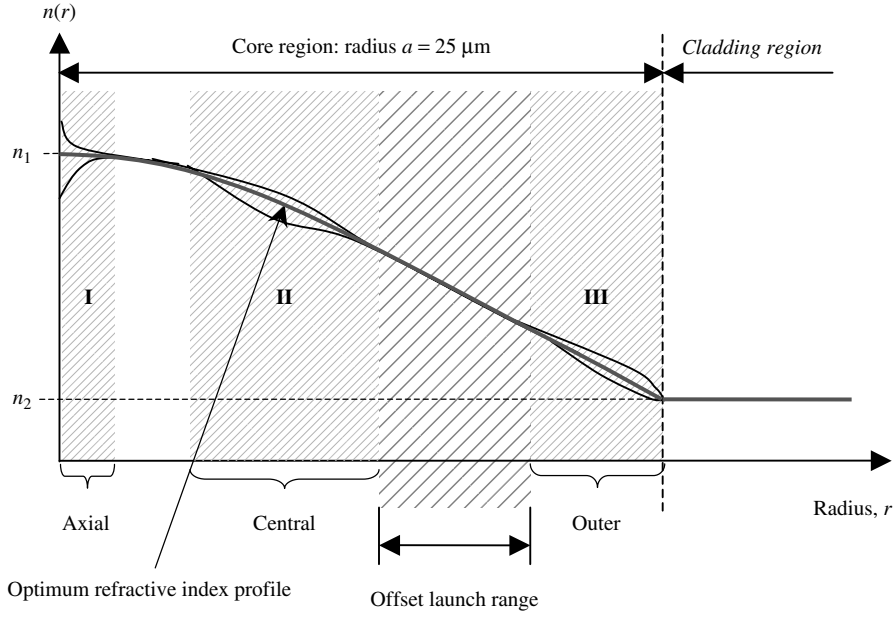

Figure 3.8 Representation of the refractive index for a graded multimode fiber showing defective regions. The optimum refractive index profile is shown. Shadowed regions I, II and III indicate areas where the profiling is perturbed by manufacturing distortion. In the example shown, the dashed region represents the better approximation available to the optimum profile and should be used for the off-set launch (OSL) technique, in order to minimize optical pulse broadening

requirement for the optimum profiling and the dependence of the involved parameters on the operating wavelength. The same high sensitivity to the profiling parameters makes the optimum grading a very challenging task, even for multimode fiber manufacturing today. The large spreading in multimode dispersion performances of deployed multimode fiber is a consequence of the same critical optimum profile function.

3.6.1 Clad Power Law Grading

In order to take a step further in understanding graded index optical fibers, in the following the mathematical model of the profiling function is considered. First of all the graded profile must be assumed to be axial symmetric due to demanding simplicity in the manufacturing process. A very common axial symmetric refractive index function used for minimizing group delay dispersion is known as the 'clad power law profile'. The clad power law refractive index profile is a piecewise function of the radial coordinate only, thus exhibiting the required axial symmetry. The profiling function is defined through the single parameter α, which defines the grading variation between the fiber axis and the core–cladding interface. The clad power law profile assumes the maximum value n_1 on the fiber axis and decreases monotonically towards the cladding boundary at $r = a$ in order to match the uniform cladding refractive index value n_2:

$$n(r,\lambda) = \begin{cases} n_1(\lambda)\sqrt{1 - 2\Delta(\lambda)\left(\dfrac{r}{a}\right)^{\alpha}}, & 0 \le r \le a \\ n_1(\lambda)\sqrt{1 - 2\Delta(\lambda)} = n_2(\lambda), & r \ge a \end{cases} \tag{3.65}$$

The clad power law refractive index just reported refers to the assumption of the linear dispersion regime. In fact, it is assumed that both the maximum $n_1(\lambda)$ and the minimum $n_2(\lambda)$ values of the refractive index on the fiber axis and in the cladding region respectively are dependent on the wavelength of the monochromatic light source. This is due to the material dispersion properties. Of course, the profile height parameter $\Delta(\lambda)$, defined in Equation (3.49), turns out to be a function of the wavelength through the dependence of both $n_1(\lambda)$ and $n_2(\lambda)$. In the formula (3.65) it has implicitly been assumed that the profiling coefficient α is not a function of the wavelength. This assumption is known as the linear dispersion regime approximation for the grading profile of the multimode fibers. Figure 3.9 shows computed profiles according to Equation (3.65) for α varying between 1 and 32, as reported in the legend. The refractive indices $n_1(\lambda) = 1.470$ and $n_2(\lambda) = 1.465$, leading to $\Delta(\lambda) = 3.46 \times 10^{-3}$.

In the limiting case of an infinite value of the α index, the clad power law profile tends to the step index profile. In the case of doped silica fibers the optimum refractive index profile is generated by using the a exponent very close to 2. For this reason it is customary to refer to the optimum

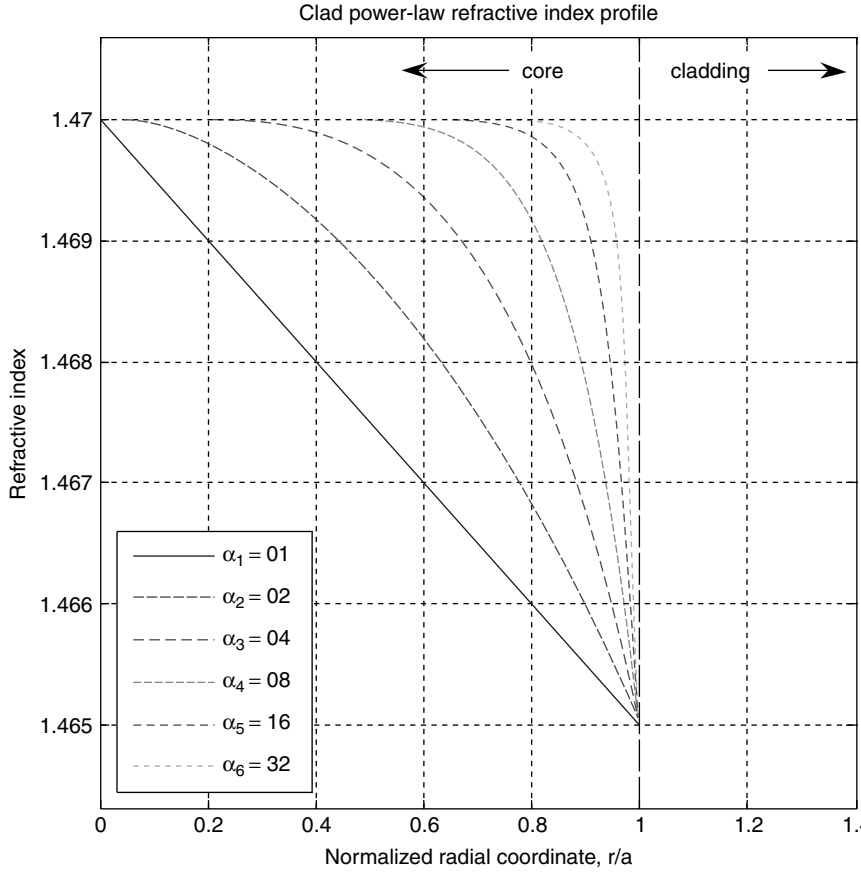

Figure 3.9 Computed clad power law profile for different profile indices α. All profiles have the same values of axis refractive index and profile height. The unit value of the profile index generates the linear shaping (triangular index profile). Higher index values correspond to higher profile concavities. For $\alpha = 2$ the refractive index assumes a true parabolic shape

refractive index profile as the parabolic grading function. Unfortunately, very small variations of the optimum α index are responsible for even one order of magnitude of multimode bandwidth loss. To gain a quantitative idea of the loss, a variation of about 1–2 % of the optimum α can lead to one decade or even more of multimode bandwidth collapse. The situation is critical because the optimum α is quite sensitive to the amount of doping used to provide the profile variation itself. Figure 3.9 gives a qualitative representation of the differential mode delay of Equation (3.62) versus the α index for the clad power law profile.

3.7 Physics of the Chromatic Dispersion

In order to understand the impact of the material dispersion in the spectral dependence of the refractive index $n(\lambda)$ and its role in the optimum grading profile in terms of the operating wavelength, in this section the interaction of the electromagnetic field with the glass-based optical fiber is considered in more detail. When an electromagnetic wave of proper spectral content is incident on a dielectric material, some of the energy of the radiation field is transferred to bound electrons of the medium. The bound electron reaction to that excitation characterizes the dielectric behavior of the medium through the dielectric susceptibility function $\chi(\mathbf{r}, t)$. The dielectric susceptibility $\chi(\mathbf{r}, t)$ directly relates the induced polarization field $\mathbf{P}(\mathbf{r}, t)$ with the exciting electric field $\mathbf{E}(\mathbf{r}, t)$. The general relationship between the exciting field $\mathbf{E}(\mathbf{r}, t)$ and the induced polarization $\mathbf{P}(\mathbf{r}, t)$ can be very complex in the case of nonanisotropic and nonlinear materials. In general, the dielectric susceptibility $\chi(\mathbf{r}, t)$ is a nonlinear tensor quantity. However, the amorphous glass composition of the optical fibers used in conventional telecommunication applications behaves quite linearly if the exciting electric field intensity remains below a critical threshold for the nonlinear refraction. In the case of single-mode optical fibers with a mode field diameter of the order of 10 μm, the threshold intensity for nonlinear refraction effects is around 10 mW. In multimode optical fiber, due to a larger core diameter and therefore reduced field intensity, the threshold value for the nonlinear refraction is much higher and the power level is out of the range of interest for every telecommunication application. The refractive index is related to the dielectric susceptibility by the following simple relation:

$$n^2(\omega) = 1 + \chi(\omega) \tag{3.66}$$

The interaction of an electromagnetic wave with the bound electrons of a dielectric medium depends on the frequency spectrum of the applied field. This behavior can be simply understood by means of the electric dipole approximation and the damped harmonic oscillator model. Even if this analysis is out side the scope of this book, it is nevertheless important to consider some relevant concepts and conclusions. The dependence of the linear susceptibility transfer function $\chi(\mathbf{r}, t)$ on the spectral content of the exciting electromagnetic field leads to the phenomenon of chromatic dispersion and manifests itself through the frequency dependence of the refractive index.

3.7.1 The Sellmeier Equation for the Refractive Index

Bound electrons in dielectric materials are distributed over different binding energies and an accurate model of the interaction between the applied electromagnetic field and the dielectric medium should take care of several electron binding energies, leading to a discrete set of resonant frequencies. The Sellmeier equation represents the linear (first-order) dielectric susceptibility in the frequency domain $\chi(\omega)$ in glass materials as the weighted series expansion of the resonant frequency contributions. Each resonant frequency generates a singularity in the frequency response whose intensity is determined by corresponding weighting coefficients according to the following formula:

$$\chi(\omega) = \sum_{j=1}^{M} \frac{B_j}{1 - (\omega/\omega_j)^2} \tag{3.67}$$

Each different dielectric material is therefore characterized by a proper set of resonant frequencies $\omega_1, \omega_2, \ldots, \omega_M$ and corresponding weighting coefficients $B_1, B_2, \ldots, B_M$. From Equation (3.66) it is deduced that the square value $n^2(\lambda)$ of the refractive index is given by the following simple relation:

$$n^2(\omega) = 1 + \chi(\omega) = 1 + \sum_{j=1}^{M} \frac{B_j}{1 - (\omega/\omega_j)^2} \tag{3.68}$$

known as the Sellmeier equation for the refractive index in a dielectric medium.

Each resonant frequency ω_j determines a resonant peak in the frequency response of the linear refractive index. Model parameters for fused silica glass (undoped) have been obtained experimentally by I. H. Malitson[1] by fitting measured dispersion curves to the three-term Sellmeier equation:

$$n^2(\omega) = 1 + \chi(\omega) \cong 1 + \frac{B_1}{1 - (\omega/\omega_1)^2} + \frac{B_2}{1 - (\omega/\omega_2)^2} + \frac{B_3}{1 - (\omega/\omega_3)^2} \tag{3.69}$$

The value of the refractive index can therefore be computed once the three resonant frequencies $(\omega_1, \omega_2, \omega_3)$ and the corresponding coefficients (B_1, B_2, B_3) are known. In the case of pure fused silica, according to Malitson,

$$\begin{cases} B_1 = 0.696\,166\,3 \\ B_2 = 0.407\,942\,6 \\ B_3 = 0.897\,479\,4 \end{cases} \Leftrightarrow \begin{cases} \lambda_1 = 0.068\,404\,3\,\mu\text{m} \\ \lambda_2 = 0.116\,241\,4\,\mu\text{m} \\ \lambda_3 = 9.896\,161\,\mu\text{m} \end{cases} \Leftrightarrow \begin{cases} \omega_1 = 27.538 \times 10^{15}\,\text{rad/s} \\ \omega_2 = 16.205 \times 10^{15}\,\text{rad/s} \\ \omega_3 = 0.1903 \times 10^{15}\,\text{rad/s} \end{cases} \tag{3.70}$$

The first resonant peak with the shortest wavelength is located in the far-ultraviolet region at $\lambda_1 = 0.0684043\,\mu\text{m}$. The second resonant peak is located in the near-ultraviolet frequency range at $\lambda_2 = 0.116\,241\,4\,\mu\text{m}$, while the third resonant frequency is located instead in the very-far-infrared region at $\lambda_3 = 9.896161\,\mu\text{m}$. It is interesting to observe that all three coefficients have almost the same value, giving similar contributions.

Figure 3.10 gives a logarithmic frequency plot of the linear refractive index according to the three-term Sellmeier Equation (3.70). The frequency profile of the refractive index is strongly affected by the resonance frequencies. Far away from frequency peaks, in particular within the range of interest for optical communication wavelengths, $800\,\text{nm} \leq \lambda \leq 1650\,\text{nm}$ and the corresponding frequency interval $1.14 \times 10^{15}\,\text{rad/s} \leq \omega \leq 2.35 \times 10^{15}\,\text{rad/s}$, the profile is relatively uniform. By comparing the frequency interval used for optical communications with the resonant frequencies of pure silica glass it can be seen that there is about one decade on each side before reaching the corresponding resonant peak respectively at $\omega_2 = 16.205 \times 10^{15}\,\text{rad/s}$ and $\omega_3 = 0.1903 \times 10^{15}\,\text{rad/s}$.

The following relationship between frequency and vacuum wavelength is recalled:

$$\omega = \frac{2\pi c}{\lambda} \Rightarrow \frac{\mathrm{d}}{\mathrm{d}\omega} = -\frac{\lambda^2}{2\pi c}\frac{\mathrm{d}}{\mathrm{d}\lambda} \tag{3.71}$$

After applying these relations to Equation (3.69), the three-term Sellmeier equation for the refractive index $n(\lambda)$ and the dielectric susceptibility $\chi(\lambda)$ takes the following form:

$$n^2(\lambda) = 1 + \chi(\lambda) \cong 1 + \frac{B_1}{1 - (\lambda_1/\lambda)^2} + \frac{B_2}{1 - (\lambda_2/\lambda)^2} + \frac{B_3}{1 - (\lambda_3/\lambda)^2} \tag{3.72}$$

[1] I. H. Malitson, 'Interspecimen Comparison of the Refractive Index of Fused Silica', *J. Optical Society of America*, **55**, 1965, 1205–1209.

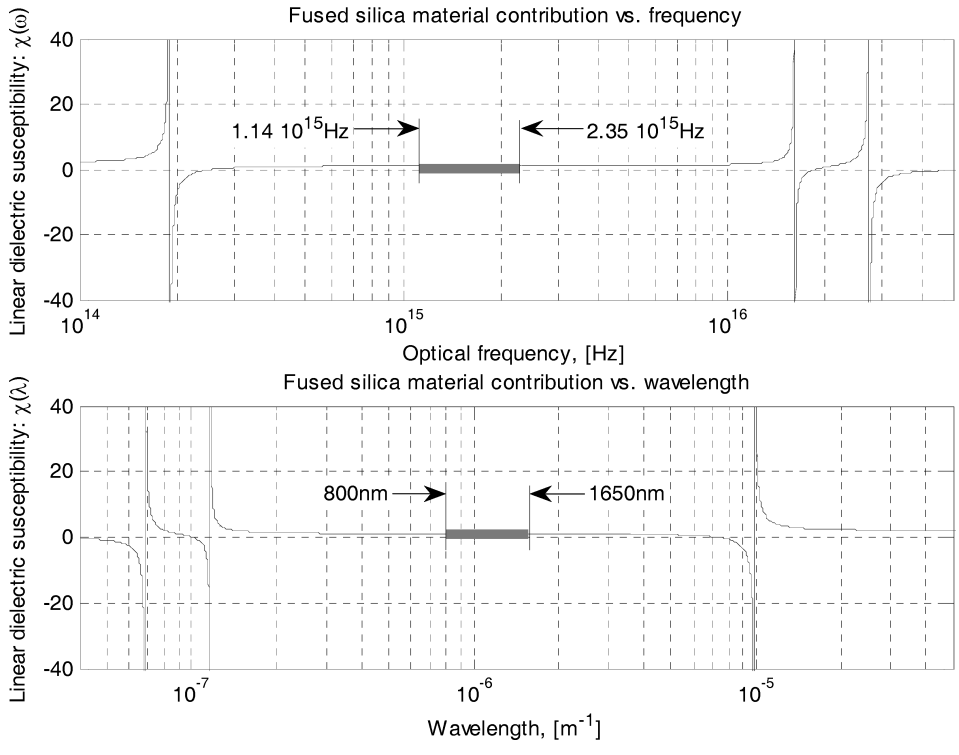

Figure 3.10 Linear dielectric susceptibility of fused silica according to the three-term Sellmeier Equation (3.69). The top graph shows the frequency function $\chi(\omega)$, while the bottom graph reports the dielectric susceptibility as a function of the wavelength, $\chi(\lambda)$. Coefficients and peak locations are defined according to parameters given in Equation (3.70). The interval used for optical communication is located about one decade away from closer resonant peaks, leading to an almost uniform susceptibility profile

3.7.2 Frequency Domain

Restricting the wavelength interval (frequency interval) closer to the optical communication range $800\,\text{nm} \leq \lambda \leq 1800\,\text{nm}$, the three-term Sellmeier equation leads to a very simple and useful representation of the refractive index for undoped fused silica. Knowledge of the refractive index allows all the material-related physical properties to be determined as functions of both wavelength and frequency. In the following the frequency relations of major physical parameters are given.

3.7.2.1 Propagation Constant

$$\beta(\omega) = kn(\omega) = \frac{\omega}{c}n(\omega), \qquad \beta^{(q)}(\omega) = \frac{\mathrm{d}^q \beta(\omega)}{\mathrm{d}\omega^q}, \qquad k = \frac{\omega}{c} \tag{3.73}$$

3.7.2.2 Group Index of Refraction

$$n_\mathrm{g}(\omega) = n(\omega) + \omega\frac{\mathrm{d}n(\omega)}{\mathrm{d}\omega} \tag{3.74}$$

3.7.2.3 Group Velocity

$$v_\mathrm{p}(\omega) = \frac{\omega}{\beta(\omega)} = \frac{c}{n(\omega)}, \qquad v_\mathrm{g}(\omega) = \frac{1}{\beta^{(1)}(\omega)} = \frac{c}{n_\mathrm{g}(\omega)} \tag{3.75}$$

3.7.2.4 Group Delay

$$\tau_g(\omega) = \frac{1}{v_g(\omega)} = \frac{d\beta(\omega)}{d\omega} = \beta^{(1)}(\omega) = \frac{1}{c} n_g(\omega) \tag{3.76}$$

3.7.2.5 Group Dispersion

$$d_g(\omega) = \frac{dt_g(\omega)}{d\omega} = \beta^{(2)}(\omega) = -\frac{1}{v_g^2(\omega)} \frac{dv_g(\omega)}{d\omega} = \frac{1}{c} \frac{dn_g(\omega)}{d\omega} = \frac{1}{c} \left[2\frac{dn(\omega)}{d\omega} + \omega \frac{d^2 n(\omega)}{d\omega^2} \right] \tag{3.77}$$

3.7.2.6 Conclusions

Figure 3.11 shows the computed refractive index and refractive group index according to Equation (3.74) using the three-term Sellmeier Equation (3.69) for the silica glass parameter set given in Equation (3.70). The refractive indices reported below refer to the undoped silica glass. Due

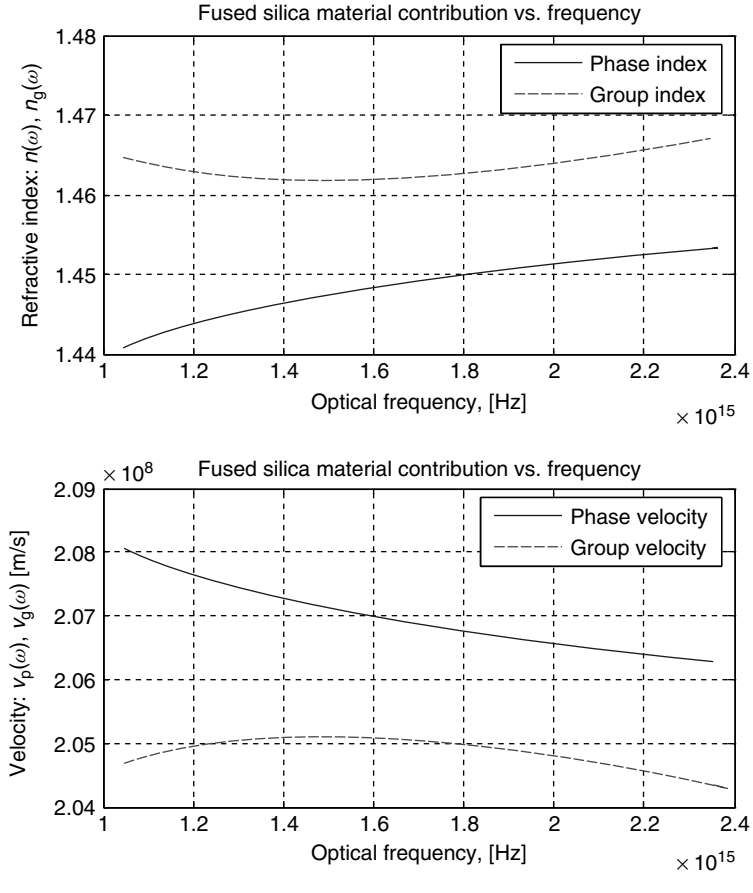

Figure 3.11 Computed frequency dependencies of the refractive index, group index, phase velocity and group velocity using the three-term Sellmeier Equation (3.69) for the undoped fused silica. The frequency variation is responsible for pulse dispersion due to the pulse spectral content

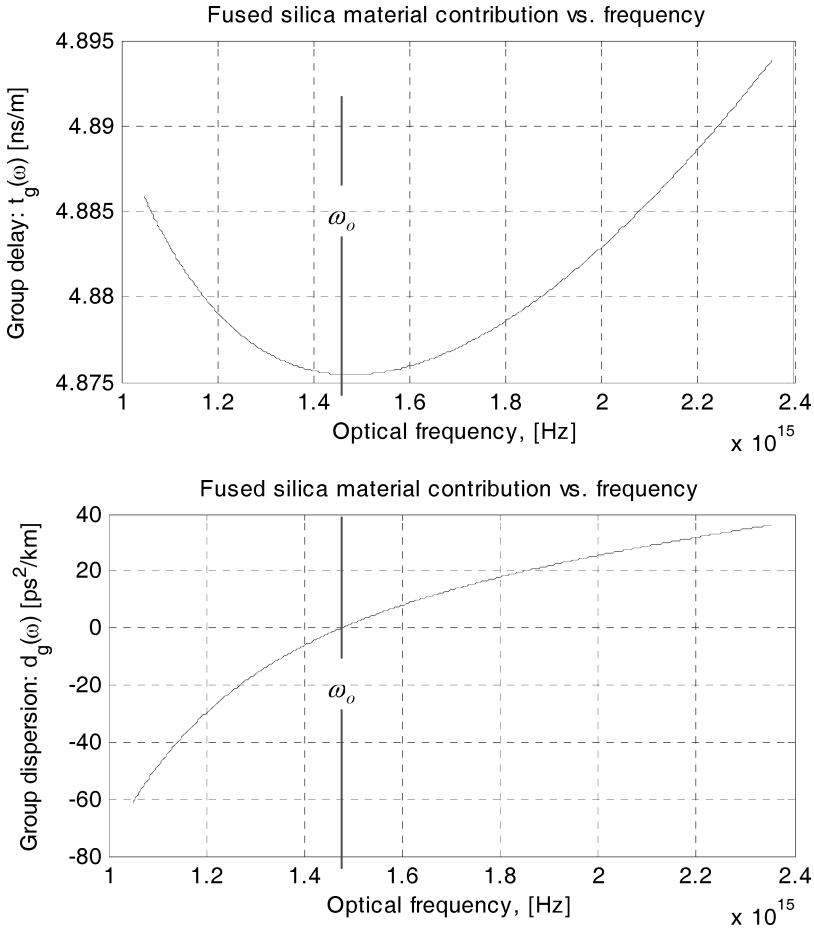

Figure 3.12 Computed frequency dependence of group delay and group dispersion using the three-term Sellmeier Equation (3.69) for the undoped fused silica. In the frequency interval around 1.48×10^{15} Hz corresponding to the wavelength range close to 1300 nm, the group delay for the undoped fused silica reaches the absolute minimum value. Accordingly, the group dispersion reaches the zero value. This frequency is known as the zero-dispersion frequency ω_0 for the undoped fused silica

to material doping the refractive index increases accordingly. The frequency dependencies of the phase and group velocities according to the relationships (3.75) are also shown in Figure 3.11.

Figure 3.12 shows the group delay $\tau_g(\omega)$ and the group dispersion computed for the same undoped silica fiber as above. According to Equation (3.77), group dispersion $d_g(\omega)$ is related to both first-order and second-order frequency derivatives of the refractive index $n(\omega)$.

A few more comments are now considered about results obtained using the three-term Sellmeier approximation for the undoped fused silica refractive index. The group delay showed in the upper graph is within the range $4.875\,\mu s/km < t_g(\omega) < 4.895\,\mu s/km$ in the whole optical communication frequency interval. The group delay variation is therefore less then 20 ns/km in the whole optical frequency interval. This behavior is more precisely expressed by the group delay dispersion (bottom graph), which ranges between $-60\,ps^2/km < d_g(\omega) < 40\,ps^2/km$.

3.7.3 Wavelength Domain

Using the frequency-to-wavelength relationship (3.71), it is possible to represent the same physical quantities as above with respect to the optical wavelength instead of the frequency. However, it is important to point out that the physical definition of the parameters has been set according to the frequency representation. This can be rigorously demonstrated by solving the linear propagation equation for the electric field pulse using the slowly varying envelope approximation (SVEA). The only difference to be taken into account is the mathematical relationship between the frequency and wavelength. This is highlighted below, where the definitions are given for each physical quantity. Some mathematical manipulations give the following relationships.

3.7.3.1 Propagation Constant

$$\beta(\lambda) \equiv kn(\lambda) = \frac{2\pi}{\lambda} n(\lambda), \qquad \beta^{(q)}(\lambda) \equiv \frac{\mathrm{d}^q \beta(\lambda)}{\mathrm{d}\lambda^q}, \qquad k = \frac{2\pi}{\lambda} \tag{3.78}$$

3.7.3.2 Group Index of Refraction

$$n_{\mathrm{g}}(\lambda) \equiv n(\lambda) - \lambda \frac{\mathrm{d}n(\lambda)}{\mathrm{d}\lambda} \tag{3.79}$$

3.7.3.3 Group Velocity

$$v_{\mathrm{p}}(\lambda) \equiv \frac{c}{n(\lambda)} = \frac{2\pi c}{\lambda \beta(\lambda)}, \qquad v_{\mathrm{g}}(\lambda) \equiv \frac{1}{\mathrm{d}\beta[\lambda(\omega)]/\mathrm{d}\omega} - \frac{2\pi c}{\lambda^2} \frac{1}{\mathrm{d}\beta(\lambda)/\mathrm{d}\lambda} = \frac{c}{n_{\mathrm{g}}(\lambda)} \tag{3.80}$$

3.7.3.4 Group Delay

$$\tau_{\mathrm{g}}(\lambda) = \frac{1}{v_{\mathrm{g}}(\lambda)} \equiv \frac{\mathrm{d}\beta[\lambda(\omega)]}{\mathrm{d}\omega} = -\frac{\lambda^2}{2\pi c} \beta^{(1)}(\lambda) = -\frac{\lambda^2}{2\pi c} \frac{\mathrm{d}\beta(\lambda)}{\mathrm{d}\lambda} = \frac{1}{c} n_{\mathrm{g}}(\lambda) \tag{3.81}$$

3.7.3.5 Group Dispersion

$$d_{\mathrm{g}}(\lambda) \equiv \frac{\mathrm{d}t_{\mathrm{g}}[\lambda(\omega)]}{\mathrm{d}\omega} = -\frac{\lambda^2}{2\pi c} \frac{\mathrm{d}t_{\mathrm{g}}(\lambda)}{\mathrm{d}\lambda} = -\frac{\lambda^2}{2\pi c^2} \frac{\mathrm{d}n_{\mathrm{g}}(\lambda)}{\mathrm{d}\lambda} = \frac{\lambda^3}{2\pi c^2} \frac{\mathrm{d}^2 n(\lambda)}{\mathrm{d}\lambda^2} \tag{3.82}$$

3.7.3.6 Conclusions

The expression (3.79) for the group refractive index $n_{\mathrm{g}}(\lambda)$ follows directly from the expressions of the group delay $\tau_{\mathrm{g}}(\lambda)$ and the propagation constant $\beta(\lambda)$. Substituting for the propagation constant expression (3.78) into the group delay (3.81) and taking the first-order derivative with respect to the wavelength gives

$$\tau_{\mathrm{g}}(\lambda) = -\frac{\lambda^2}{2\pi c} \frac{\mathrm{d}\beta(\lambda)}{\mathrm{d}\lambda} = -\frac{\lambda^2}{2\pi c} \frac{\mathrm{d}}{\mathrm{d}\lambda} \left[\frac{2\pi n(\lambda)}{\lambda} \right] = \frac{1}{c} \left[n(\lambda) - \lambda \frac{\mathrm{d}n(\lambda)}{\mathrm{d}\lambda} \right] \tag{3.83}$$

Using the definition of the group index $n_{\mathrm{g}}(\lambda) : \tau_{\mathrm{g}}(\lambda) = n_{\mathrm{g}}(\lambda)/c$ then gives Equation (3.79).

3.7.4 Polynomial Approximation

For a limited wavelength range, sufficiently far away from the resonant peaks, the Sellmeier equation can be approximated by a polynomial series in λ^2 and $1/\lambda^2$. In the particular case

of the fused silica glass, excited in the optical communication range $800\,\text{nm} \leq \lambda \leq 1800\,\text{nm}$, Equation (3.72) can be approximated by the following superposition of second-order polynomials in λ^2 and $1/\lambda^2$:

$$n^2(\lambda) = 1 + \sum_j \frac{B_j}{1 - \lambda_j^2/\lambda^2} \cong 1 + \underbrace{B_1 + B_2}_{M_0} + \underbrace{(B_1\lambda_1^2 + B_2\lambda_2^2)}_{M_2} \frac{1}{\lambda^2} \underbrace{- \frac{B_3}{\lambda_3^2}}_{N_2} \lambda^2 \tag{3.84}$$

$$\left.\begin{aligned} &\underbrace{M_k \equiv \sum_i B_i \lambda_i^k}_{\lambda_i \ll \lambda} \\ &\underbrace{N_k \equiv -\sum_i \frac{B_i}{\lambda_i^k}}_{\lambda_i \gg \lambda} \end{aligned}\right\} \Rightarrow n^2(\lambda) = 1 + M_0 + \frac{M_2}{\lambda^2} + N_2\lambda^2$$

$$\text{for } \lambda_1 < \lambda_2 \ll 800\,\text{nm} \leq \lambda \leq 1800\,\text{nm} \ll \lambda_3 \tag{3.85}$$

Substituting the above approximation of the refractive index into Equation (3.79), it is easy to derive the polynomial approximation for the group index:

$$n_g(\lambda) \cong \frac{1 + M_0 + 2M_2/\lambda^2}{\sqrt{1 + M_0 + M_2/\lambda^2 + N_2\lambda^2}} \tag{3.86}$$

Figure 3.13 gives the computed profiles of the refractive index $n(\lambda)$, the group index $n_g(\lambda)$, the phase velocity $v_p(\lambda)$ and the group velocity $v_g(\lambda)$ as a function of the optical wavelength according to the three-term Sellmeier approximation. In addition to the above four parameters, the top graph in the figure shows the second-order polynomial approximation of the group refractive index.

Differences between the computed phase velocity and group velocity show the dispersive nature of the medium being considered. It is a very fundamental result of physics that in any dielectric medium except the vacuum, the phase velocity of the electromagnetic field is even higher than the corresponding group velocity. In vacuum, both quantities are equal since the refractive index assumes the unit constant value and the energy is transferred at the speed of the light c.

Figure 3.14 shows the computed wavelength profile of the group delay and group dispersion. It is noteworthy that every physical parameter regarding the intramodal pulse propagation can be directly computed by knowing the refractive index as a function of the wavelength.

3.7.5 The Chromatic Dispersion Coefficient

The chromatic dispersion coefficient $D_c(\lambda)$ is defined in the wavelength domain but cannot be deduced directly from the frequency domain as is the case for other parameters. The chromatic dispersion coefficient is defined as the first-order derivative of the group delay $t_g(\lambda)$ with respect to the wavelength:

$$D_c(\lambda) \equiv \frac{dt_g(\lambda)}{d\lambda} \quad (\text{ps/nm km}) \tag{3.87}$$

Equation (3.83) gives the following relation between the chromatic dispersion coefficient and the second-order derivative of the refractive index:

$$D_c(\lambda) \equiv \frac{dt_g(\lambda)}{d\lambda} = \frac{1}{c}\frac{dn_g(\lambda)}{d\lambda} = -\frac{\lambda}{c}\frac{d^2n(\lambda)}{d\lambda^2} \tag{3.88}$$

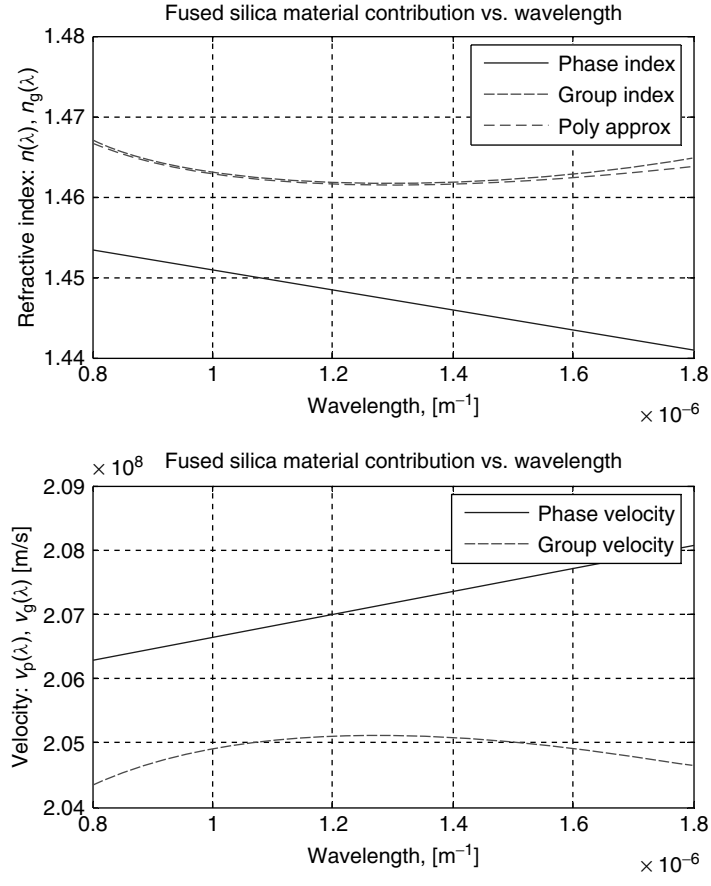

Figure 3.13 Computed wavelength profiles of the refractive index and velocities for the fused silica glass using the three-term Sellmeier formula (3.72) with coefficients given in Equation (3.70). The top graph shows the refractive index, the group index and the polynomial approximation of the group index according to Equations (3.72), (3.79) and (3.86) respectively. The bottom graph shows the phase velocity and group velocity profiles according to Equation (3.80)

From the expression in the wavelength domain of the group dispersion (3.82), it is possible to deduce immediately that the following relation holds:

$$D_c(\lambda) = -\frac{2\pi c}{\lambda^2} d_g(\lambda) \tag{3.89}$$

The chromatic dispersion coefficient is mainly used in pulse broadening calculations under direct modulation of the light source. Once the light source spectrum width σ_λ (nm) is known, the chromatic dispersion of the fiber link is easily computed by multiplying $D_c(\lambda)$ by the source spectrum width. The result has the dimension of ps/km and specifies the fiber link dispersion parameter $\Delta_c(\lambda)$:

$$\Delta_c(\lambda) \equiv D_c(\lambda)\sigma_\lambda \quad \text{(ps/km)} \tag{3.90}$$

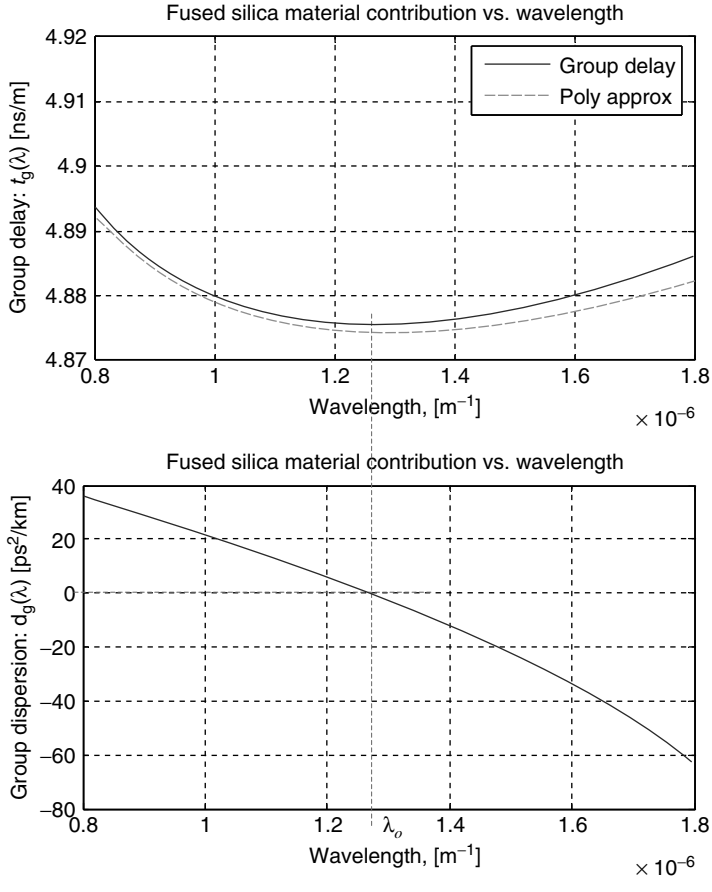

Figure 3.14 Computed group delay (top) for the fused silica glass using Equation (3.81) with the three-term Sellmeier model of the refractive index. The group delay calculation using the group index polynomial approximation has been added on the same graph. Both plots show the characteristic group delay minimum close to 1270 nm, revealing the zero-dispersion wavelength position. The bottom graph reports the computed group dispersion according to Equation (3.82). Dispersion reaches the zero value at the delay minimum wavelength

3.7.5.1 The Chromatic Dispersion Slope

A useful parameter for characterizing the chromatic dispersion wavelength profile is the chromatic dispersion slope $S_c(\lambda)$, defined as the first-order wavelength derivative of the chromatic dispersion coefficient:

$$S_c(\lambda) \equiv \frac{dD_c(\lambda)}{d\lambda} \quad (\text{ps/nm}^2\ \text{km}) \tag{3.91}$$

Equation (3.88) gives the slope expression in terms of the higher-order wavelength derivative of the refractive index:

$$S_c(\lambda) = -\frac{1}{c}\frac{d}{d\lambda}\left[\lambda\frac{d^2n(\lambda)}{d\lambda^2}\right] = -\frac{1}{c}\left[\frac{d^2n(\lambda)}{d\lambda^2} + \lambda\frac{d^3n(\lambda)}{d\lambda^3}\right] \tag{3.92}$$

By comparing Equation (3.92) with the chromatic dispersion coefficient (3.88), the following equivalent expression is derived for the chromatic dispersion slope:

$$S_c(\lambda) = \frac{D_c(\lambda)}{c} - \lambda \frac{d^3 n(\lambda)}{d\lambda^3} \tag{3.93}$$

Once the slope $S_c(\lambda)$ is known it is possible to write down the first-order approximation of the chromatic dispersion coefficient $D_c(\lambda)$ around the generic reference wavelength λ_c:

$$D_c(\lambda) = D_c(\lambda_c) + (\lambda - \lambda_c) S_c(\lambda) + \cdots \tag{3.94}$$

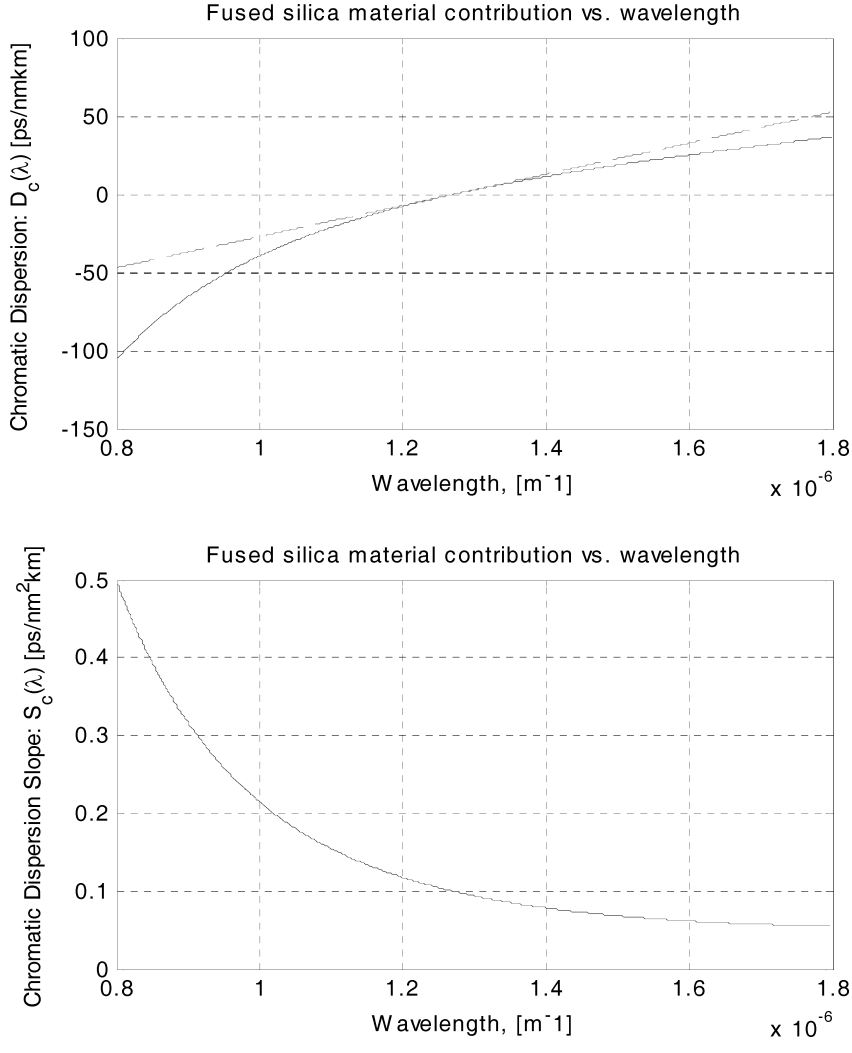

Figure 3.15 Top: computed chromatic dispersion coefficient using the three-term Sellmeier approximation of the refractive index in the case of fused silica glass. The dashed line represents the chromatic dispersion slope evaluated at the zero-dispersion wavelength. Bottom: chromatic dispersion slope computed according to Equation (3.93). The slope evaluated between 800 nm and 1800 nm results in a monotonic decreasing function of the wavelength

Figure 3.15 shows the chromatic dispersion coefficient and the slope function computed using Equations (3.88) and (3.92) or (3.93) respectively, with the refractive index modeled according to the three-term Sellmeier approximation reported in Equation (3.72).

3.8 Waveguide Dispersion

The concept of chromatic dispersion as introduced so far is a property of the pure material constituting the dielectric waveguide. Accordingly, it is more convenient to specify the dispersion coefficient $D_c(\lambda)$ that has been considered up to now as the material chromatic dispersion. In addition, each individual mode supported by the multimode optical fiber exhibits one more chromatic dispersion term, namely the waveguide chromatic dispersion. This term accounts for the peculiar dispersion relationship relating the propagation constant $\beta_{\nu\mu}(\lambda)$ of each individual mode with the wavelength λ of the exciting light source. The waveguide dispersion is indicated by $D_w(\lambda)$ and has the same unit of measure (ps/nm km) as the chromatic dispersion coefficient $D_c(\lambda)$. Assuming that material and waveguide chromatic dispersions are not correlated with each other, the total chromatic dispersion is given by the algebraic sum of both contributions:

$$D(\lambda) = D_c(\lambda) + D_w(\lambda) \tag{3.95}$$

The waveguide chromatic dispersion can be conveniently used to modify the total chromatic dispersion properly in order to have some specific dispersion behavior. Two major examples are the dispersion shifted and dispersion flattened single-mode optical fibers, both of which are extensively used in long-haul and single-wavelength multigigabit transmission links. It is known explicitly that any waveguide dispersion correction is suitable only for single-mode fibers. It is not possible, and would not be justifiable, to design graded index-based multimode fibers with a controlled waveguide dispersion contribution. Without entering into a waveguide dispersion analysis, which would be outside the scope of this book, Figure 3.16 gives a qualitative plot demonstrating the operating principle of the dispersion shifted single-mode optical fiber. In order to achieve a higher waveguide dispersion contribution, the profile of the refractive index must be carefully designed and the manufacturing process requires higher parameter controls. The refractive index profile of

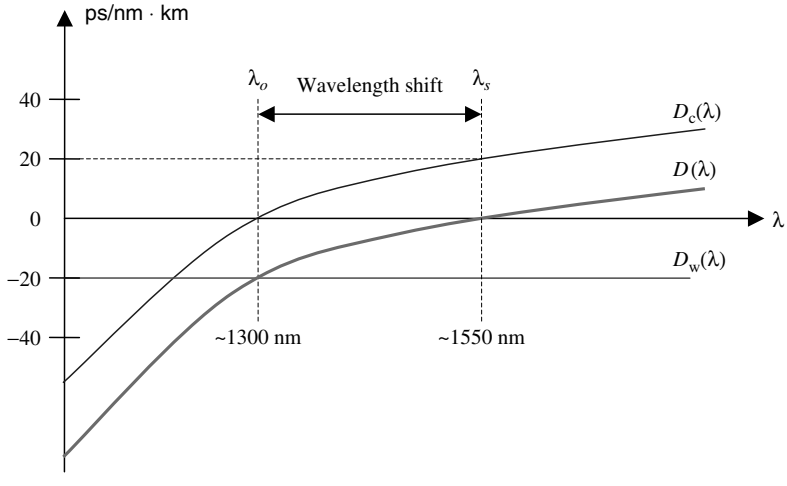

Figure 3.16 Qualitative representation of the waveguide chromatic dispersion correction used in order to achieve dispersion shifted total chromatic dispersion behavior for third-window operation. The total chromatic dispersion is given by the algebraic combination of material and waveguide dispersions

both dispersion shifted and dispersion flattened fibers is usually quite a complex function of the radial coordinate. Some common profiles adopted for single-mode telecommunication optical fiber show triangular or W-shaped profiles in the core and exhibit depressed cladding design in the core–cladding interface region.

3.9 Frequency Chirping

The group delay and the group dispersion defined in Section 3.7.3 refer to the undoped silica glass and therefore their behavior can be used to discuss some general properties of light pulse propagation in glass-based optical fibers. What does a negative dispersion mean? Looking at the frequency interval to the left of the zero-dispersion frequency ω_0 in Figure 3.12, which corresponds to the longer wavelengths, the pulse experiences a negative value of the group dispersion:

$$d_g(\omega)\,\big|_{\omega<\omega_0} < 0$$

On the contrary, in the frequency range to the right of ω_0, which corresponds to the shorter wavelengths, the pulse experiences a positive value of the group dispersion:

$$d_g(\omega)\,\big|_{\omega>\omega_0} > 0$$

In order to find a physical answer to this apparently strange behavior, the group delay curve in the upper graph in Figure 3.17 is considered. In the frequency interval to the left of the zero-dispersion frequency ω_0, the group delay is a monotonically decreasing function of the optical frequency, leading therefore to the negative value of the group dispersion.

The physical interpretation is that the higher frequency components present in the optical pulse spectrum will experience a lower group delay when traveling at a faster group velocity than the lower frequency components, which will, on the contrary, experience a higher group delay when traveling at a slower group velocity. In order to have a clearer understanding of this fundamental concept, the following terminology is introduced. An optical pulse is said to be color biased or frequency chirped when the time-resolved spectrum has different colors according to different pulse transients in the time domain.

If pulse edge precursors and postcursors are color biased or frequency chirped, this would led to quite different pulse distortions after traveling along the dispersive optical fiber. Since the pulse distortion depends on the colored pulse composition, the dispersion considered so far is defined accordingly as chromatic dispersion. These concepts are quite important and are the basis for understanding frequency chirping of the optical pulse when it is traveling in a dispersive medium such as optical fibers.

In the following two sections the two cases of long- and short-wavelength excitations will be considered separately, referring to launched source spectra localized to the left of ω_0 and to the right of ω_0 respectively. The important result is the very different distortion the pulse experiences after a certain propagation length, leading to the opposite behavior, namely pulse broadening or pulse compression depending upon the chirped launched pulse.

3.9.1 Long-Wavelength Region (Anomalous Region)

It is assumed first that the launched optical pulse spectrum is centered to the left of the zero-dispersion frequency ω_0, as depicted in the top graph of Figure 3.17. This condition will be referred to as the long-wavelength region because the lowest frequency range to the left of ω_0 corresponds, through Equation (3.71), to the longer-wavelength interval. Due to the negative slope of the group delay function, components of the source spectrum will experience longer propagation delays, while spectral components will propagate with shorter delay times. What happens after a fixed

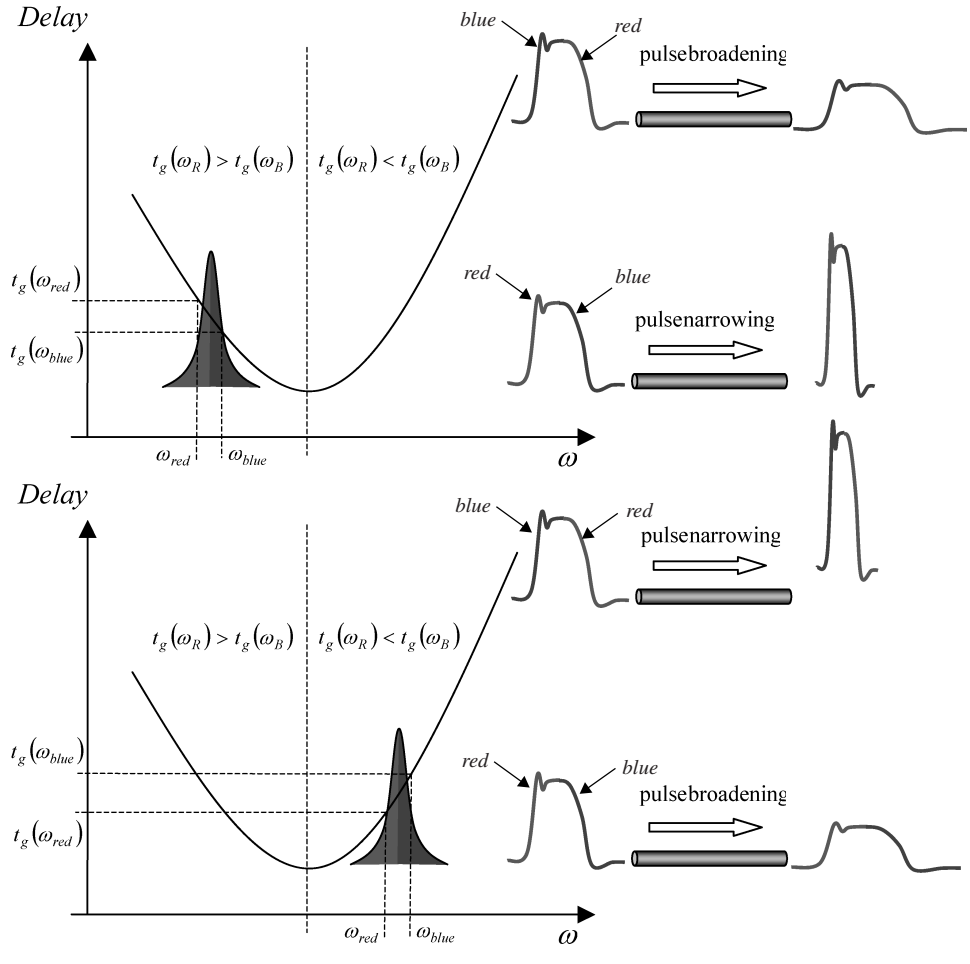

Figure 3.17 Chromatic dispersion effect upon the chirped source optical pulse. The top graph shows the situation when the source spectrum is centered to the left of the zero-dispersion frequency, operating in the long-wavelength range (lower-frequency range). In that case, blue-shifted leading edges and red-shifted trailing edges will generate pulse broadening, while red leading edges and blue trailing edges will generate pulse compression. The opposite situation holds in the right side of the zero-dispersion frequency (bottom graph), operating in the shorter-wavelength range

propagation distance? The answer depends on the time-resolved spectral distribution of the launched optical pulse.

Two complementary cases are possible:

1. The leading edge is blue-shifted and the trailing edge is red-shifted. 

(a) This means that the pulse generation mechanism (inside the laser cavity for example) slightly changes the emission frequency during the optical pulse profile: the optical frequency increases during the pulse rising edge (leading edge), providing the blue-shift behavior, and slightly decreases during the pulse falling edge (trailing edge), providing the spectrum red-shift behavior.
(b) Since in the long-wavelength region spectral blue components travel faster than the red ones, the leading edge of the optical pulse reaches the fiber end section earlier than the trailing edge and the pulse becomes broader as long as it propagates.

2. The leading edge is red-shifted and the trailing edge is blue-shifted.
   (a) This means that the pulse generation mechanism (inside the laser cavity for example) slightly changes the emission frequency during the optical pulse profile: the optical frequency decreases during the pulse rising edge (leading edge), providing the red-shift behavior, and slightly increases during the pulse falling edge (trailing edge), providing the spectrum blue-shift behavior.
   (b) Since in the long-wavelength region spectral blue components travel faster than the red ones, the trailing edge reaches the fiber end section earlier than the leading edge and the pulse becomes narrower as long as it propagates.

In the longer-wavelength region, depending on the frequency chirping of the time-resolved source spectrum, the optical pulse can go through either broadening or narrowing mechanisms due to the fiber group delay characteristic.

3.9.2 Short-Wavelength Region (Normal Region)

It is now assumed that the launched optical pulse spectrum is centered to the right of the zero-dispersion frequency ω_0, as depicted in the bottom graph of Figure 3.17. This condition will be referred to as the short-wavelength region because the highest frequency range to the right of ω_0 corresponds, through Equation (3.71), to the shorter-wavelength interval. Due to the positive slope of the group delay function, red components of the source spectrum will experience shorter propagation delays, while blue spectral components will propagate with longer delay times. After a fixed propagation distance the optical pulse will experience either compression or broadening mechanisms, as depicted in the section above, according to the following two complementary launching cases.

1. The leading edge is blue-shifted and the trailing edge is red-shifted.
   (a) The optical frequency increases during the pulse rising edge (leading edge), providing the blue-shift behavior, and slightly decreases during the pulse falling edge (trailing edge), providing the spectrum red-shift behavior.
   (b) Since in the short-wavelength region spectral blue components travel slower than the red ones, the leading edge of the optical pulse reaches the fiber end section later than the trailing edge and the pulse becomes narrower as long as it propagates.

2. The leading edge is red-shifted and the trailing edge is blue-shifted.
   (a) The optical frequency decreases during the pulse rising edge (leading edge), providing the red-shift behavior, and slightly increases during the pulse falling edge (trailing edge), providing the spectrum blue-shift behavior.
   (b) Since in the short-wavelength region red components travel faster than the blue ones, the red-shifted trailing edge reaches the fiber end section earlier than the blue-shifted leading edge and the pulse becomes broader as long as it propagates.

In conclusion, even in the shorter-wavelength region, depending on the frequency chirping of the time-resolved source spectrum, the optical pulse can go through either broadening or narrowing mechanisms due to the fiber group delay characteristic.

In order to summarize the discussion so far, the following conclusions can be made:

1. Moving to the left of the zero-dispersion frequency, in the case of the red-shifted time-resolved source spectrum the corresponding pulse spectrum enters into the anomalous dispersion regime, which corresponds equivalently to using the right extent of the zero-dispersion wavelength.
2. Standard telecommunication optical fibers exhibit a zero-dispersion wavelength around 1310 nm.
3. System applications centered in the wavelength range of 1550 nm will run under the anomalous propagation regime.
4. System applications centered in the wavelength range of 1310 nm have both anomalous and normal regimes available, depending on the side occupied by the time-resolved source spectrum.
5. The anomalous dispersion regime is of considerable interest because in this regime optical fibers can support optical Solitons balancing between the group velocity dispersion and nonlinear refraction effects.

The discussion so far has referred exclusively to the chromatic dispersion contribution experienced by any optical pulse propagating within a fused silica glass fiber. As already mentioned, these dispersion characteristics are referred to as intramodal dispersion, due to their presence within each individual mode group supported by the multimode optical fiber. In conventional multimode optical fiber operating in the 1310 nm region, even for the latest generation of laser-launch optimized fibers for 10 GbE applications, chromatic dispersion is usually responsible for a small correction of the whole dispersion encountered by the optical pulse during the propagation over a multimode fiber. In the first wavelength region the contribution of the chromatic dispersion is usually not negligible at 10 GbE, due to a higher dispersion contribution, as can be seen in Figure 3.15 in the lower-wavelength range. At an increasing bit rate all pulse dispersion contributions become even more relevant, and system dispersion penalties are not only related to multimode bandwidth limitations. Due to a shorter bit time, chromatic dispersion starts to play a relevant role in defining multimode fiber system limitations and adds more restrictive light source spectrum requirements.

3.10 Higher-Order Linear Dispersion

The dispersion relationship between the propagation constant $\beta_{\nu\mu}(\omega)$ and the optical frequency ω determines the linear propagation characteristics of the optical pulse supported by each individual fiber mode. As seen in Section 3.7.2, Equations (3.76) and (3.77) are directly related to the group

delay and the group dispersion respectively. The first derivative with respect to the frequency of the propagation constant of the mode, identified by the indices (ν, μ), $\beta_{\nu\mu}^{(1)}(\omega) \equiv \mathrm{d}\beta_{\nu\mu}(\omega)/\mathrm{d}\omega$, assumes the meaning of the group delay $t_{\mathrm{g},\nu\mu}(\omega)$. The second derivative, $\beta_{\nu\mu}^{(2)}(\omega) \equiv \mathrm{d}^2\beta_{\nu\mu}(\omega)/\mathrm{d}\omega^2$, coincides with the group dispersion $d_{\mathrm{g},\nu\mu}(\omega)$. A more detailed analysis of the electromagnetic field propagation in optical fibers shows that under the validity of the slowly varying envelope approximation (SVEA) the propagation of the amplitude envelope $A_{\nu\mu}(z, t)$ of the electric field pulse carried by the individual fiber mode (ν, μ) depends on the frequency derivatives of the propagation constant $\beta_{\nu\mu}(\omega)$, evaluated at the optical carrier frequency ω_0.

3.10.1 The Effective Refractive Index

In the linear isotropic medium, the propagation constant of the unguided field $\beta(\omega)$ is simply proportional to the refractive index $n(\omega)$ through the wavenumber $k = \omega/c = 2\pi/\lambda$:

$$\beta(\omega) = \frac{\omega}{c} n(\omega) \tag{3.96}$$

In a guiding medium, the relationship must be generalized in order to include the waveguide mode field structure. The effective refractive index for the guided mode (ν, μ) is defined through the same dispersion relationship as that above, but replacing the unguided medium propagation constant $\beta(\omega)$ with the mode propagation constant $\beta_{\nu\mu}(\omega)$ and the refractive index $n(\omega)$ with the effective refractive index $n_{\mathrm{e},\nu\mu}(\omega)$ for the considered guided mode:

$$\beta_{\nu\mu}(\omega) = \frac{\omega}{c} n_{\mathrm{e},\nu\mu}(\omega) \tag{3.97}$$

Due to the weakly guiding assumption valid for all telecommunication optical fibers, the effective refractive index is only slightly different from the material refractive index, but even such small differences characterize the mode propagation behavior and the mode filed structure. This concept is nearly equivalent to the waveguide group dispersion introduced previously to characterize the waveguide effect from the material unguided dispersion contribution. Of course, each individual mode of any multimode optical fiber is fully characterized by its own propagation constant and under the mystifying use of the same material propagation constant for all guided modes any mode differentiation will be lost. In the following, in order to highlight the physical concepts involved in the mode propagation constant and the related mathematics, the unguided linear isotropic case is considered by replacing the effective refractive index with the material refractive index. Nevertheless, it must be very clear that peculiar results cannot be applied directly to waveguide analysis, but instead to the mathematical methodology. All the analytical results derived below are easily generalized to guided fields by replacing the refractive index with the effective refractive index. Numerical results presented in Figures 3.18 and 3.19 refer exclusively to the Sellmeier approximation of the material refractive index.

3.10.2 General Expression for Higher-Order Dispersion

Starting with the simple relation (3.97) between the modal propagation constant $\beta_{\nu\mu}(\omega)$ and the effective refractive index $n_{\mathrm{e}}(\omega)$ the analytical expression is obtained for every frequency derivative of the mode propagation constant $\beta_{\nu\mu}(\omega)$:

$$\beta_{\nu\mu}^{(q)}(\omega) \equiv \frac{\mathrm{d}^q}{\mathrm{d}\omega^q}\left[\frac{\omega}{c} n_{\mathrm{e},\nu\mu}(\omega)\right] \tag{3.98}$$

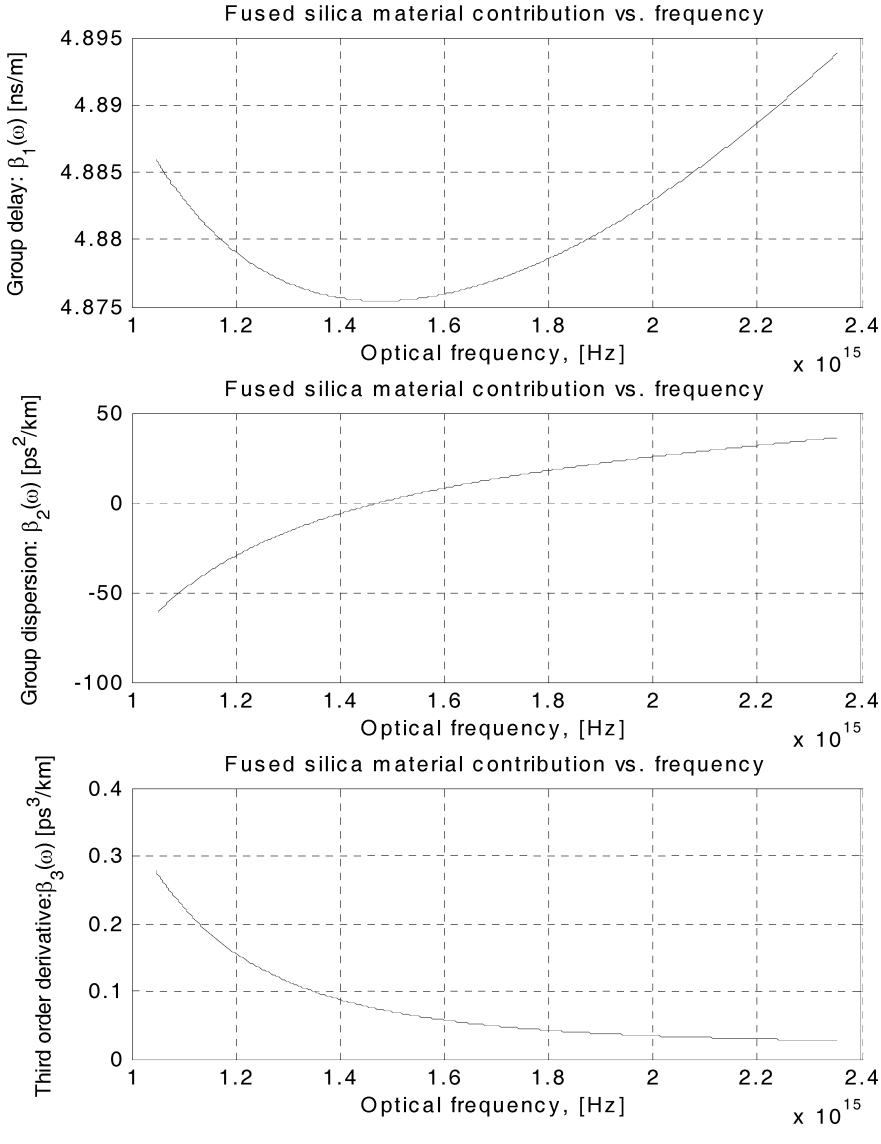

Figure 3.18 First three derivatives of the material propagation constant for the fused silica glass

Generalization of the concept of the group index introduced in Equations (3.73) and (3.74) is found for the effective group index for the guided mode (ν, μ):

$$\beta_{\nu\mu}(\omega) \equiv \frac{\mathrm{d}}{\mathrm{d}\omega}\left[\frac{\omega}{c} n_{\mathrm{e},\nu\mu}(\omega)\right] = \frac{1}{c}\left[n_{\mathrm{e},\nu\mu}(\omega) + \omega \frac{\mathrm{d}n_{\mathrm{e},\nu\mu}(\omega)}{\mathrm{d}\omega}\right] = \frac{1}{c} n_{\mathrm{g},\nu\mu}(\omega) \tag{3.99}$$

$$n_{\mathrm{g},\nu\mu}(\omega) \equiv n_{\mathrm{e},\nu\mu}(\omega) + \omega \frac{\mathrm{d}n_{\mathrm{e},\nu\mu}(\omega)}{\mathrm{d}\omega} \tag{3.100}$$

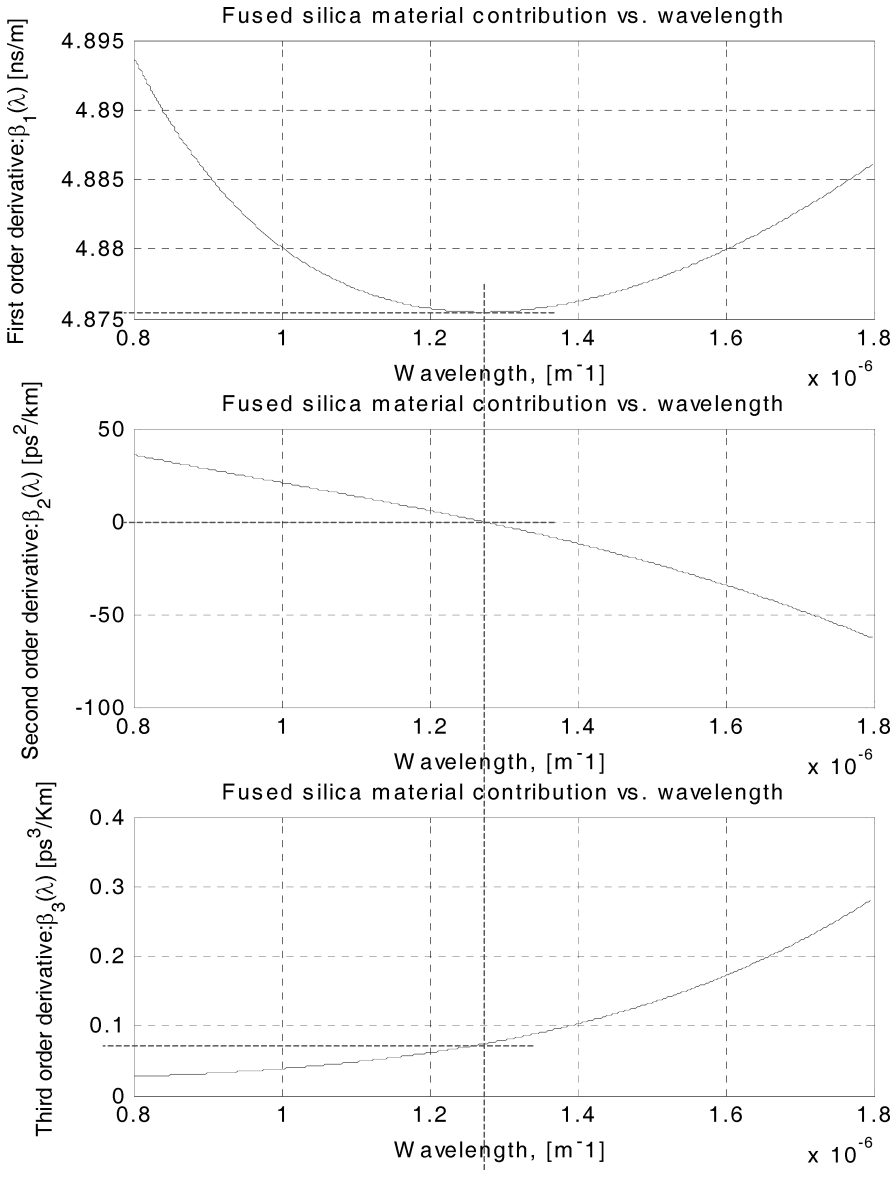

Figure 3.19 Wavelength representation of the first three derivatives of the material propagation constant for the fused silica glass. Dashed lines refer to the zero-dispersion wavelength

By repetitive frequency derivation of Equation (3.98), the following analytical expression of higher-order derivatives of the (ν, μ) guided mode propagation constant $\beta_{\nu\mu}(\omega)$ is found:

$$\beta_{\nu\mu}^{(1)}(\omega) = \frac{1}{c}\left[n_{\mathrm{e},\nu\mu}(\omega) + \omega\frac{\mathrm{d}n_{\mathrm{e},\nu\mu}(\omega)}{\mathrm{d}\omega}\right]$$

$$\beta_{\nu\mu}^{(2)}(\omega) = \frac{1}{c}\left[2\frac{\mathrm{d}n_{\mathrm{e},\nu\mu}(\omega)}{\mathrm{d}\omega} + \omega\frac{\mathrm{d}^2 n_{\mathrm{e},\nu\mu}(\omega)}{\mathrm{d}\omega^2}\right]$$

$$\beta_{\nu\mu}^{(3)}(\omega) = \frac{1}{c}\left[3\frac{\mathrm{d}^2 n_{\mathrm{e},\nu\mu}(\omega)}{\mathrm{d}\omega^2} + \omega\frac{\mathrm{d}^3 n_{\mathrm{e},\nu\mu}(\omega)}{\mathrm{d}\omega^3}\right]$$

$$\vdots$$

$$\beta_{\nu\mu}^{(q)}(\omega) = \frac{1}{c}\left[q\frac{\mathrm{d}^{q-1} n_{\mathrm{e},\nu\mu}(\omega)}{\mathrm{d}\omega^{q-1}} + \omega\frac{\mathrm{d}^q n_{\mathrm{e},\nu\mu}(\omega)}{\mathrm{d}\omega^q}\right], \qquad q = 1, 2, \ldots \tag{3.101}$$

The expression (3.101) for the general qth derivative of the propagation constant can be easily demonstrated by induction. To proceed further, the qth derivative of the propagation constant in Equation (3.98) in terms of the lower-order derivatives is written as

$$\begin{aligned}
\beta_{\nu\mu}^{(q)}(\omega) &\equiv \frac{1}{c}\frac{\mathrm{d}^q}{\mathrm{d}\omega^q}[\omega\, n_{\mathrm{e},\nu\mu}(\omega)] = \frac{1}{c}\frac{\mathrm{d}^{q-1}}{\mathrm{d}\omega^{q-1}}\frac{\mathrm{d}}{\mathrm{d}\omega}[\omega\, n_{\mathrm{e},\nu\mu}(\omega)] \\
&= \frac{1}{c}\frac{\mathrm{d}^{q-1}}{\mathrm{d}\omega^{q-1}}\left[n_{\mathrm{e},\nu\mu}(\omega) + \omega\frac{\mathrm{d}n_{\mathrm{e},\nu\mu}(\omega)}{\mathrm{d}\omega}\right] = \frac{1}{c}\frac{\mathrm{d}^{q-2}}{\mathrm{d}\omega^{q-2}}\frac{\mathrm{d}}{\mathrm{d}\omega}\left[n_{\mathrm{e},\nu\mu}(\omega) + \omega\frac{\mathrm{d}n_{\mathrm{e},\nu\mu}(\omega)}{\mathrm{d}\omega}\right] \\
&= \frac{1}{c}\frac{\mathrm{d}^{q-2}}{\mathrm{d}\omega^{q-2}}\left[2\frac{\mathrm{d}n_{\mathrm{e},\nu\mu}(\omega)}{\mathrm{d}\omega} + \omega\frac{\mathrm{d}^2 n_{\mathrm{e},\nu\mu}(\omega)}{\mathrm{d}\omega^2}\right] = \frac{1}{c}\frac{\mathrm{d}^{q-3}}{\mathrm{d}\omega^{q-3}}\frac{\mathrm{d}}{\mathrm{d}\omega}\left[2\frac{\mathrm{d}n_{\mathrm{e},\nu\mu}(\omega)}{\mathrm{d}\omega} + \omega\frac{\mathrm{d}^2 n_{\mathrm{e},\nu\mu}(\omega)}{\mathrm{d}\omega^2}\right] \\
&= \frac{1}{c}\frac{\mathrm{d}^{q-3}}{\mathrm{d}\omega^{q-3}}\left[3\frac{\mathrm{d}^2 n_{\mathrm{e},\nu\mu}(\omega)}{\mathrm{d}\omega^2} + \omega\frac{\mathrm{d}^3 n_{\mathrm{e},\nu\mu}(\omega)}{\mathrm{d}\omega^3}\right] = \cdots
\end{aligned} \tag{3.102}$$

After p iterations, with $0 \leq p \leq q$, it can be concluded that

$$\beta_{\nu\mu}^{(q)}(\omega) = \frac{1}{c}\frac{\mathrm{d}^{q-p}}{\mathrm{d}\omega^{q-p}}\left[p\frac{\mathrm{d}^{p-1} n_{\mathrm{e},\nu\mu}(\omega)}{\mathrm{d}\omega^{p-1}} + \omega\frac{\mathrm{d}^p n_{\mathrm{e},\nu\mu}(\omega)}{\mathrm{d}\omega^p}\right] \tag{3.103}$$

Setting $p = q$ and using the notation $\mathrm{d}^0 f(\omega)/\,\mathrm{d}\omega^0 = f(\omega)$ gives expression (3.101).

Figure 3.18 shows the first three numerical derivatives of the material propagation constant versus optical frequency using the three-term Sellmeier approximation of the refractive index. Figure 3.19 shows the computed first three order derivatives of the propagation constant in the wavelength domain, where the conversion relationship between frequency and wavelength has been used.

Some comments need to be made about these graphs. As already mentioned, the first-order derivative of the propagation constant $\beta^{(1)}(\omega)$ represents the group delay. The second-order derivative $\beta^{(2)}(\omega)$ accounts instead for the linear dispersion and represents the group velocity dispersion relationship. The third-order derivative $\beta^{(3)}(\omega)$ represents the additional quadratic contribution to the pulse dispersion. It is interesting to observe that the third-order derivative acquires much of its meaning from the zero-dispersion frequency ω_0, where the second-order derivative of the propagation constant is extremely small. In order to compare the relative importance of the second-order derivative $\beta^{(2)}(\omega)$ and the third-order derivative $\beta^{(3)}(\omega)$ it is necessary to solve the linear propagation equation for each guided mode contribution to the optical pulse in a multimode fiber.

3.11 The Gaussian Model

This section deals with the multimode fiber response from the perspective of a transmission system modeling tool. In order to understand the fiber Gaussian model better, the basic assumptions stated in first part of this chapter are reviewed.

3.11.1 Physical Model Review

In this section a list of major conclusions that have been reached about multimode fiber modeling are presented in a summary. This helps to cover most of principal topics related to multimode fiber pulse propagation.

1. The multimode fiber is modeled as a time-independent, isotropic and linear system in the electric field amplitude.

This assumption leads to the important conclusion that two subsequent electric field pulses belonging to the same electromagnetic field mode will overlap each other if their temporal separation is less then their tail extent (pre−postcursors). The fiber propagation characteristics are linear. This assumption means that each fiber coefficient, including the refractive index, is not a function of the electric field amplitude. Fiber propagation characteristics are assumed to be constant over time.

2. The frequency response $H_F(f)$ of the multimode fiber is defined as the Fourier transform of the intensity envelope response to the launched optical intensity impulse, detected after propagating the unit distance from the launching section.
3. The dimension of the frequency response $H_F(f)$ is W/W.
4. The fiber frequency response $H_F(f)$ relates the complex input phasor of the optical power envelope to the output complex phasor of the optical power envelope.
5. No mode coupling is considered in this system model.
6. Fiber bound modes constitute an orthogonal basis for the decomposition of the guided optical power.
7. The radiated field is orthogonal to any bound mode.
8. Mode orthogonality leads to the following fundamental statement: the Poynting vector (power density flux) due to electromagnetic field components belonging to different guided or radiation modes does not contribute to the overall guided power after integration over the infinite fiber cross-section.
9. The total guided power is given by the sum of the power contributions carried by each individual guided mode. Indicating by P_j the time average power of the guided mode j, $j = 1, 2, \ldots, N$, where N is the number of guided modes, the total guided power P is given by the following sum: $P = \sum_{j=1}^{N} P_j$.
10. Optical dispersion induces a distortion of the envelope of the launched pulse around its center of gravity.
11. Optical dispersion in multimode fiber comes mainly from two contributions:
    (a) Intermodal dispersion. In multimode fibers the major term is due to modal group delay (MGD). Each mode supports a fraction of the total launched optical power that travels along the fiber with a peculiar group velocity v_j. Due to differences in group velocities among bound modes the launched pulse energy arrives at the output section with a considerable relative delay, leading to optical pulse broadening. Differential mode delay (DMD) accounts for group delay differences among propagating modes.
    (b) Intramodal dispersion. The amount of optical energy carried by any given mode will experience a temporal dispersion according to several phenomena encountered by the optical pulse propagation.
12. Group velocity dispersion (GVD). The dependence of the group velocity of each allowed mode from the optical frequency, $v_j(\omega)$, induces a temporal broadening of the energy amount carried by that mode. Material dispersion and waveguide dispersion contribute to the group velocity dispersion.

13. Polarization mode dispersion (PMD). Assuming a nonideal optical fiber composition that does not satisfy true axial symmetry, two slightly different refractive indices can be identified along the principal dielectric axes. The fiber in this case behaves in a slightly birefringent way and each mode is allowed to propagate with two orthogonal polarizations. The difference between the fast axis and the slow axis is responsible for a PMD broadening mechanism inside each allowed propagation mode. As a general rule, the electric field travels faster in a region where the refractive index is lower, according to the general relationship $v = c/n$, where c is the speed of light in vacuum.
14. The multimode fiber Gaussian model simply assumes that the frequency response of the multimode fiber has a Gaussian magnitude and a linear phase with a unity concatenation factor, $\gamma = 1$. The unity concatenation factor translates the assumption that the fiber link, even if constituted by several fiber segments, is not experiencing any mode coupling. All excited modes behave independently from each other and propagate along the whole fiber length without any mutual interaction, unless optical connectors and other discontinuities are present along the line.
15. The phase linearity assumption implies a constant group delay. The constant group delay assumption implies a translation of the center of gravity of the Gaussian impulse response as long as it propagates along the fiber, without inducing any pulse dispersion. If not otherwise specified, the group delay will be assumed equal to zero, leading to placement of the center of gravity of the multimode fiber output pulse at the time origin.
16. The over-filled launch (OFL) condition provides uniform excitation of all fiber bound modes by uniform amplitude of the exciting field. Each excited bound mode carries on the characteristic fraction of source optical power resulting from the overlap integral calculation.
17. Assuming the OFL condition, the multimode frequency response is well represented by a Gaussian profile. In order to fulfill the OFL condition the exciting power source must present plane wavefronts with a uniform radial intensity distribution. Large numerical aperture far-field sources, like the surface emitting LED, closely resemble this condition. The launching condition for a laser-based light source is of coarse very different, usually providing only selective mode excitation. In this case, the Gaussian frequency response assumption usually lacks its validity and the frequency response depends on the composition of the exited modes.
18. According to ITU-T G.651, the modal bandwidth (BW) of the multimode fiber is defined as the half-width at half-maximum (HWHM) of the magnitude of its frequency response according to OFL conditions.
19. A multimode fiber bandwidth is defined per unit length of the fiber. Assuming a unity length of one kilometer, the MMF bandwidth is therefore specified in MHz km units. This is a direct consequence of the definition of the group delay per unit length $\tau_{g,j}$ (ns/km).
20. Laser sources required for 10 GbE signaling do not satisfy the OFL condition due to a laser light peculiarity. Consequently, the modal bandwidth is no longer uniquely defined and therefore is not a valid representation of the multimode fiber propagation characteristics. Similar arguments apply to the impulse response.
21. Laser source multimode excitations are grouped under the general acronym of RL (restricted launch) conditions, where only a small fraction of the input fiber cross section is illuminated. Very careful studies are still ongoing toward the best definition of restricted launch in order to guarantee a maximum fiber bandwidth.
22. Both central launch (CL) and offset launch (OSL) are special cases of the restricted launch (RL) condition. Each of them results in better bandwidth performance according to the peculiar multimode fiber profile perturbations.
23. The encircled flux launch (EFL) method proposes a standard procedure in defining the proper RL conditions for both GbE and 10 GbE applications of multimode fibers.

24. Launching conditions are currently under study in order to improve multimode fiber link reliability. The question is complicated by the existence of both 50 μm core and 62.5 μm core multimode fibers as referenced by the standards OM-1, OM-2 and OM-3 fibers.
25. The multimode fiber bandwidth definition involves the frequency cut-off of the optical intensity evaluated at one-half of its maximum. After intensity-to-current conversion in the receiving photodetector, the multimode fiber bandwidth corresponds to the −6 dB electrical bandwidth.
26. The effects of source linewidth and group velocity dispersion are included assuming first-order intramodal pulse broadening by means of the chromatic dispersion coefficient. Intramodal dispersion and modal dispersion add quadratically to set the RMS width of the equivalent Gaussian frequency response profile.
27. The relative angle between the linear polarization of the light source and the radial offset of the launching connector induces selective modal amplitude coupling and consequently induces impulse response distortion when individual modes are considered.
28. This effect has been demonstrated experimentally and leads to sensible link performance degradation. The random polarization fluctuation along the multimode fiber in the presence of several offset connectors generates a new noise term in the output pulse intensity profile.
29. The polarization-induced pulse distortion in the multimode fiber is currently under both theoretical and experimental investigation in multigigabit links.
30. Fiber attenuation and the modal-dependent attenuation are not included in the following MMF model. In the current model no power attenuation is included for each fiber mode. Each guided mode therefore exhibits the same zero power attenuation coefficient $\alpha_j = \alpha = 0$ dB/km.

3.11.2 The Gaussian Frequency Response

This section deals with the mathematical formulation and properties of the Gaussian approximation of the multimode fiber transfer function. The Gaussian function has a very symmetric correspondence between the time and frequency domains, allowing for easy but significant modeling of the MMF impulse response under the assumption of the over-filled launch condition. The implication and the validity of the physical assumptions behind this relevant concept have already been briefly discussed, so in the following sections the mathematical properties and modeling approaches used for the multimode fiber Gaussian response will be presented.

3.11.2.1 The Gaussian Transform Pair

In this subsection the principal properties and relationships of the Gaussian transform pairs in both the time and frequency domains will be summarized. The Fourier transform pair for the Gaussian function are

$$h_{\mathrm{G}}(t) = \sqrt{\frac{\alpha}{\pi}}\, \mathrm{e}^{-\alpha t^2} \overset{\Im}{\longleftrightarrow} \mathrm{e}^{-\pi^2 f^2/\alpha} = H_{\mathrm{G}}(f) \tag{3.104}$$

where α is a real constant and the suffix G stands for Gaussian. Setting $\alpha = 1/(2\sigma_t^2)$ in Equation (3.104) immediately gives the following transform pair, which relates the area normalized Gaussian time pulse with the amplitude normalized Gaussian frequency pulse:

$$h_{\mathrm{G}}(t) = \frac{1}{\sigma_t\sqrt{2\pi}} \mathrm{e}^{-t^2/(2\sigma_t^2)} \overset{\Im}{\longleftrightarrow} \mathrm{e}^{-2\pi^2\sigma_t^2 f^2} = H_{\mathrm{G}}(f) \tag{3.105}$$

The area normalization in the time domain implies that

$$\int_{-\infty}^{+\infty} h_{\mathrm{G}}(t)\,\mathrm{d}t = H_{\mathrm{G}}(0) = \frac{1}{\sigma_t\sqrt{2\pi}} \int_{-\infty}^{+\infty} \mathrm{e}^{-t^2/(2\sigma_t^2)}\,\mathrm{d}t = 1 \tag{3.106}$$

$$h_{\mathrm{G}}(0) = \frac{1}{\sigma_t\sqrt{2\pi}} \tag{3.107}$$

In the frequency domain the corresponding amplitude normalization reads

$$H_{\mathrm{G}}(0) = 1 \tag{3.108}$$

$$\int_{-\infty}^{+\infty} H_{\mathrm{G}}(f)\,\mathrm{d}f = h_{\mathrm{G}}(0) = \frac{1}{\sigma_t\sqrt{2\pi}} \tag{3.109}$$

In order to obtain the standard deviation or RMS width σ_f in the frequency domain it is sufficient to set

$$2\pi^2\sigma_t^2 \equiv \frac{1}{2\sigma_f^2} \tag{3.110}$$

in the exponent of the right member transform (3.105). Consequently, the following fundamental relationship exists between the two dual domains for the Fourier transform pairs of the Gaussian pulse:

$$\left.\begin{aligned}\sigma_f &\equiv \frac{1}{2\pi\sigma_t}\\ \sigma_\omega &\equiv 2\pi\sigma_f\end{aligned}\right\} \Leftrightarrow \sigma_\omega = \frac{1}{\sigma_t} \tag{3.111}$$

The above relationship expresses mathematically the indetermination principle for the Gaussian pulse in the dual domains. This property is general and holds for every Fourier transform pair. The more the pulse is confined in time the more its frequency spectrum is spread out in the dual frequency domain. Equations (3.105) and (3.111) after proper normalization give the following Gaussian transform pair:

$$h_{\mathrm{G}}(t) = \frac{1}{\sigma_t\sqrt{2\pi}}\mathrm{e}^{-t^2/(2\sigma_t^2)} \overset{\Im}{\longleftrightarrow} H_{\mathrm{G}}(f) = \mathrm{e}^{-f^2/(2\sigma_f^2)}, \qquad \sigma_f = \frac{1}{2\pi\sigma_t} \tag{3.112}$$

Figure 3.20 gives the qualitative description of the Gaussian transform pair in both the time and frequency domains.

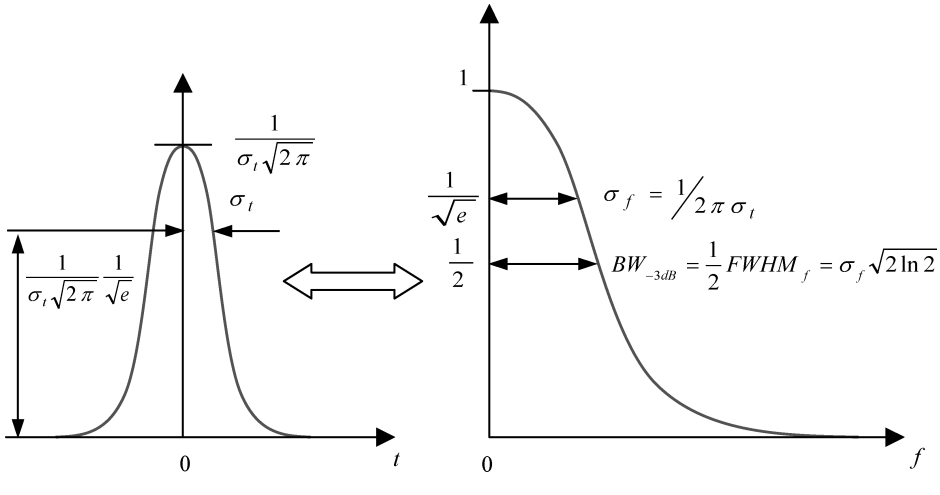

Figure 3.20 Left: time domain representation of the intensity Gaussian impulse response of the MMF. Pulse energy is normalized to unity and the RMS width is σ_t. Right: frequency domain representation of the same Gaussian pulse shown on the left side. The unilateral intensity frequency spectrum is still Gaussian with the RMS width given by $\sigma_f = \frac{1}{2}\pi\sigma_t$

3.11.3 Gaussian Relationships

In addition to the RMS width, another useful parameter is the full-width at half-maximum (FWHM). FWHM_t and FWHM_f are the full-width at half-maximum in the time and frequency domains respectively. From Equations (3.112),

$$\mathrm{e}^{-t^2/(2\sigma_t^2)} = \tfrac{1}{2} \Rightarrow \mathrm{FWHM}_t = 2\sigma_t\sqrt{2\ln 2} \cong 2.355\sigma_t \tag{3.113}$$

$$\mathrm{e}^{-f^2/(2\sigma_f^2)} = \tfrac{1}{2} \Rightarrow \mathrm{FWHM}_f = 2\sigma_f\sqrt{2\ln 2} \cong 2.355\sigma_f \tag{3.114}$$

Remember that FWHM_f is the full-width at half-maximum in the frequency representation of the Gaussian pulse. The unilateral bandwidth (BW) is defined instead as the half-width at half-maximum and it is therefore measured at half the optical intensity of the unilateral frequency spectrum, as reported in Figure 3.20. From Equation (3.114),

$$\mathrm{BW} \equiv \tfrac{1}{2}\,\mathrm{FWHM}_f = \sigma_f\sqrt{2\ln 2} \cong 1.177\sigma_f \tag{3.115}$$

The same relationship also holds in the time domain. By comparing Equations (3.113) and (3.114), the relationship between the time and frequency domain FWHM is obtained for the Gaussian transform pair:

$$\mathrm{FWHM}_f\ \sigma_t = \mathrm{FWHM}_t\ \sigma_f \tag{3.116}$$

Substituting the expression (3.111) of σ_f in Equation (3.114) and using the optical bandwidth definition (3.115), the following useful additional relationships between the optical bandwidth (BW), FWHM_t and the RMS width σ_t in the time domain can be obtained:

$$\begin{aligned}\mathrm{BW} &= \frac{\mathrm{FWHM}_f}{2} = \frac{2\ln 2}{\pi}\frac{1}{\mathrm{FWHM}_t} \cong 0.44\frac{1}{\mathrm{FWHM}_t} \\ &= \frac{\sqrt{2\ln 2}}{2\pi}\frac{1}{\sigma_t} \cong 0.187\frac{1}{\sigma_t}\end{aligned} \tag{3.117}$$

Other useful relationships can be easily demonstrated. In the following additional properties of the Gaussian transform pair are reported:

1. Decaying time versus sigma:

$$h(t_\alpha) \equiv \alpha\ h(0), \quad 0 < \alpha \leq 1 \tag{3.118}$$

$$t_\alpha = \sigma_t\sqrt{2\ln\left(\frac{1}{\alpha}\right)} \tag{3.119}$$

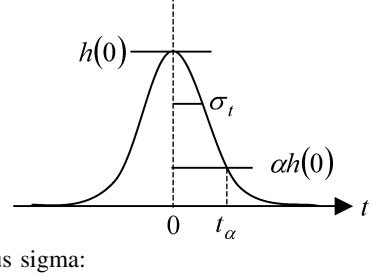

2. Rise time 20 %−80% versus sigma:

$$\Delta t_{20-80} = \left(\sqrt{2\ln\frac{1}{0.2}} - \sqrt{2\ln\frac{1}{0.8}}\right)\sigma_t = 1.1261\ \sigma_t \tag{3.120}$$

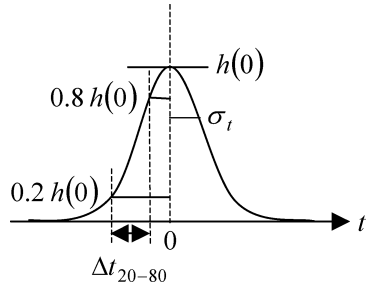

3. Rise time 20 %–80 % versus FWHM_t:

$$\Delta t_{20-80} = \left(\frac{\sqrt{\ln 1/0.2} - \sqrt{\ln 1/0.8}}{2\sqrt{\ln 2}}\right) \mathrm{FWHM}_t \cong 0.4782\ \mathrm{FWHM}_t \tag{3.121}$$

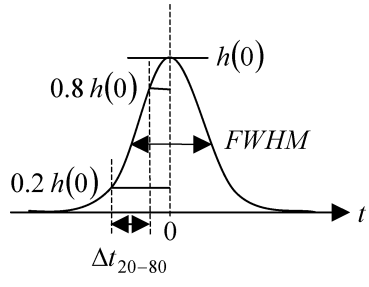

4. Rise time 20 %–80% versus bandwidth:

$$\Delta t_{20-80} = \frac{\sqrt{\ln 2}}{\pi}\left(\sqrt{\ln\frac{1}{0.2}} - \sqrt{\ln\frac{1}{0.8}}\right)\frac{1}{\mathrm{BW}} \cong \frac{0.2110}{\mathrm{BW}} \tag{3.122}$$

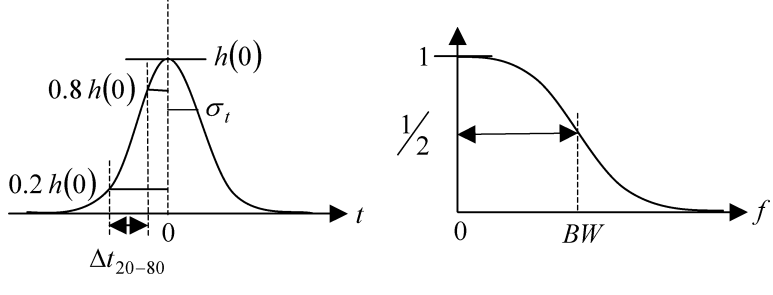

5. Integrals:

$$I_1 = \int_t^{+\infty} h(u)\,\mathrm{d}u = \frac{1}{\sigma_t\sqrt{2\pi}}\int_t^{+\infty} \mathrm{e}^{-u^2/(2\sigma_t^2)}\,\mathrm{d}u = \frac{1}{2}\mathrm{erfc}\left(\frac{t}{\sigma_t\sqrt{2}}\right) \tag{3.123}$$

$$I_2 = \int_0^{t} h(u)\,\mathrm{d}u = \frac{1}{\sigma_t\sqrt{2\pi}}\int_0^{t} \mathrm{e}^{-u^2/(2\sigma_t^2)}\,\mathrm{d}u = \frac{1}{2}\mathrm{erf}\left(\frac{t}{\sigma_t\sqrt{2}}\right) \tag{3.124}$$

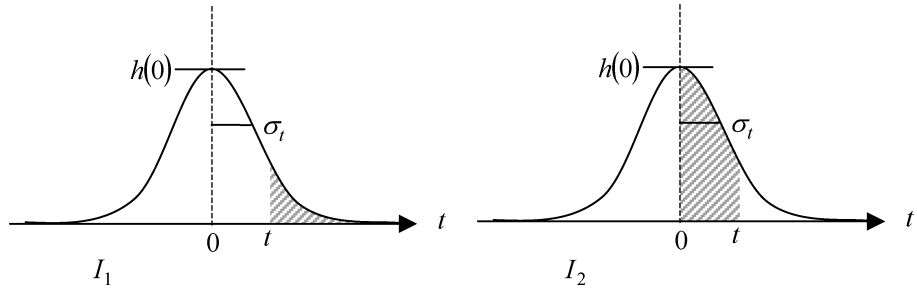

6. Noise bandwidth:

$$B_{\mathrm{n}} = \int_0^{+\infty} |H(f)|^2 \, \mathrm{d}f = \int_0^{+\infty} \mathrm{e}^{-4\pi^2\sigma_t^2 f^2} \, \mathrm{d}f = \frac{1}{4\sigma_t\sqrt{\pi}} \cong \frac{1.4105}{\sigma_t} \tag{3.125}$$

$$B_{\mathrm{n}} = \int_0^{+\infty} |H(f)|^2 \, \mathrm{d}f = \frac{1}{4}\sqrt{\frac{2\pi}{\ln 2}}\mathrm{BW} \cong 0.7527 \ \mathrm{BW} \tag{3.126}$$

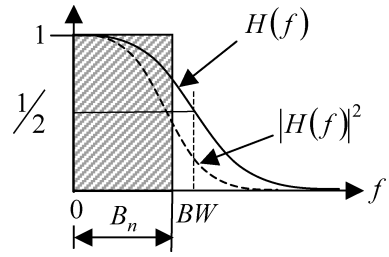

Figure 3.21 reports the computed plots of the standard deviation σ_t (RMS width), FWHM_t, HWHM bandwidth (-3 dB optical) (BW) and the noise bandwidth B_{n}. All four plots are computed for the 20 %–80 % rise time t_{r} varying between 1 ps and 100 ps. By comparing the last two plots regarding the HWHM BW and the noise bandwidth B_{n}, it is interesting to conclude that the noise bandwidth results are lower than the HWHM BW for every Gaussian considered. This property is clearly indicated by Equation (3.126) where the noise bandwidth results are about 75 % of the corresponding HWHM BW.

In order to gain a quantitative idea of the corresponding Gaussian widths in the time and frequency domains, the following examples are considered.

Example 3.1

In Figure 3.22 it is assumed that the multimode fiber has a Gaussian frequency response with half the intensity bandwidth $\mathrm{BW}_{-3\,\mathrm{dB}} = 500$ MHz km. Then the FWHM and rise–fall times of the impulse response are calculated. From Equations (3.117) and (3.122),

$$\mathrm{BW} = 500 \ \mathrm{MHz\,km} \Rightarrow \begin{cases} \mathrm{FWHM}_t \cong 883 \ \mathrm{ps/km} \\ t_{\mathrm{r}} = t_{\mathrm{f}} = 430.20 \ \mathrm{ps/km} \end{cases} \tag{3.127}$$

Example 3.2

In Figure 3.23 it is assumed that the multimode fiber has a Gaussian impulse response (intensity) with RMS width $\sigma_t = 10$ ps. Then the FWHM_t and the half-intensity bandwidth $\mathrm{BW}_{-3\,\mathrm{dB}}$ are

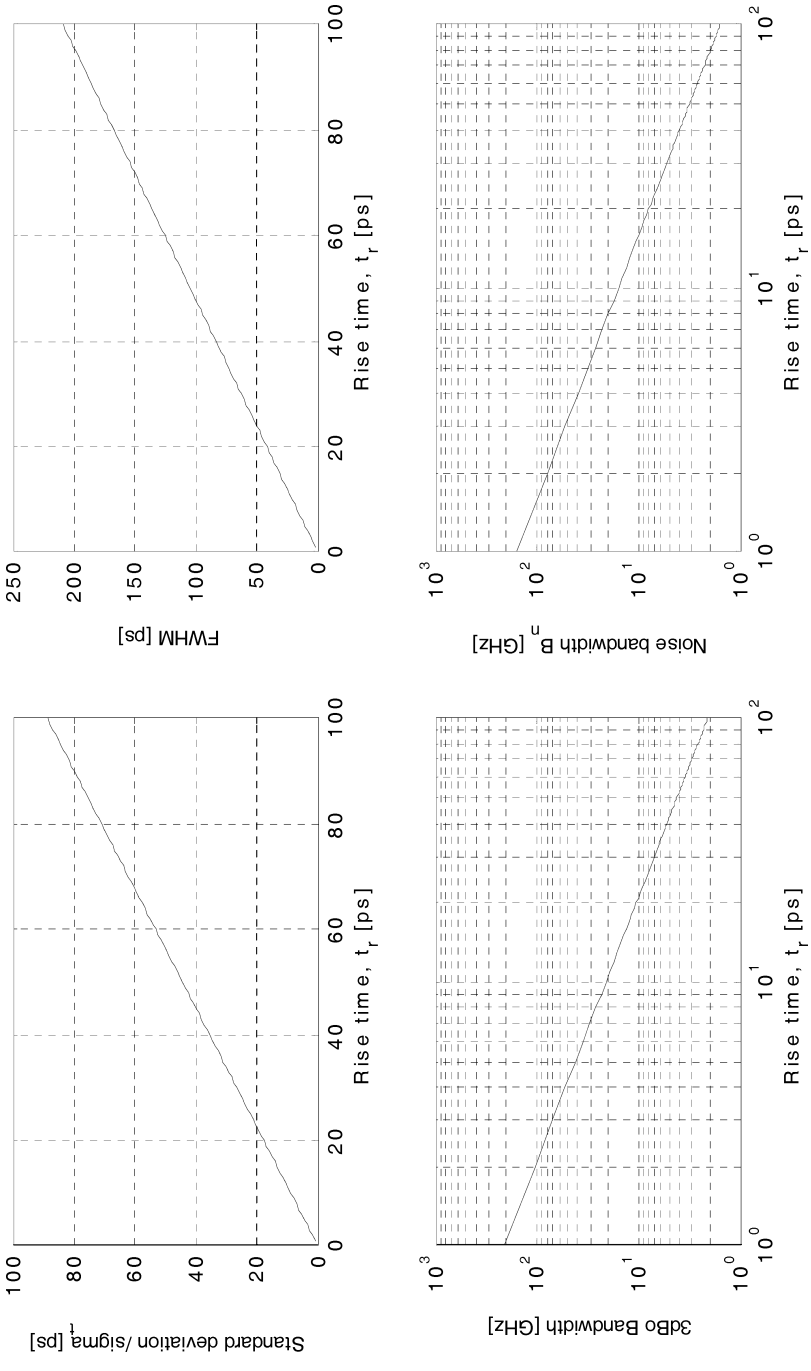

Figure 3.21 Computed Gaussian pulse parameters versus rise–fall times

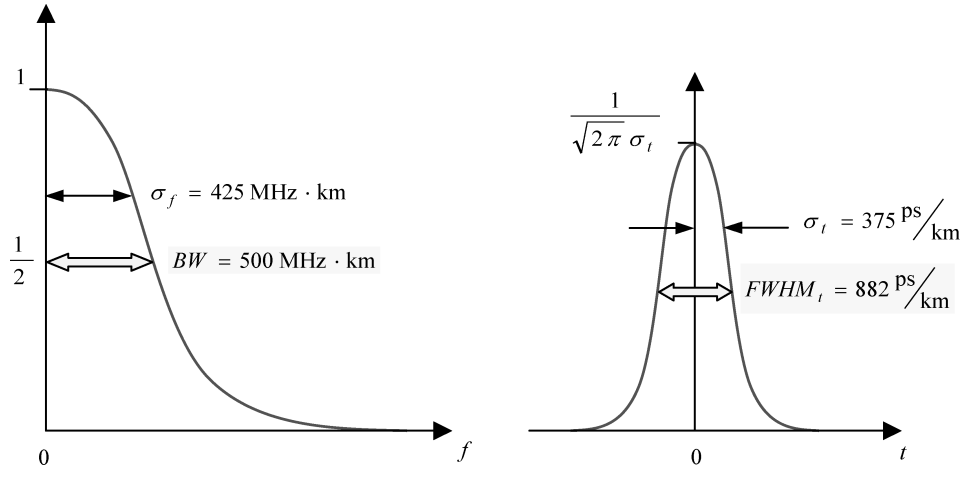

Figure 3.22 Left: Gaussian frequency response of the multimode fiber with a bandwidth $f_m = 500\,\text{MHz km}$. Right: corresponding Gaussian impulse response with $\text{FWHM}_t = 882\,\text{ps/km}$

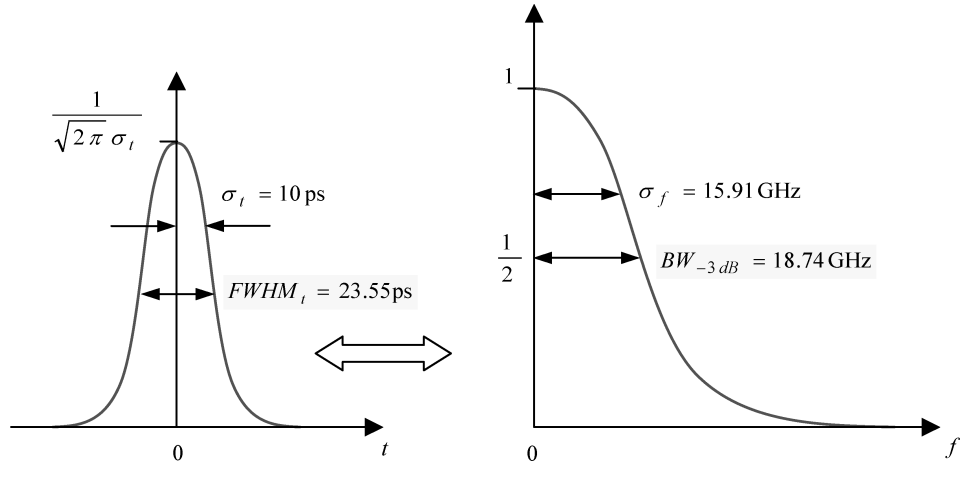

Figure 3.23 Left: time domain representation of the intensity Gaussian impulse response of the MMF with $\text{FWHM} = \Delta_t = 23.55\,\text{ps}$. Pulse energy is normalized to unity. Right: frequency domain representation of the same Gaussian pulse shown on the left side. The unilateral intensity frequency bandwidth is given by $\text{BW}_{-3\,\text{dB}} = 18.74\,\text{GHz}$

calculated. From Equations (3.113), (3.114), (3.115) and (3.121),

$$\sigma_t = 10\,\text{ps} \Rightarrow \begin{cases} \text{FWHM}_t = 23.55\,\text{ps} \\ \sigma_f = 15.91\,\text{GHz} \\ \text{FWHM}_f = 37.48\,\text{GHz} \\ \text{BW}_{-3\,\text{dB}} = 18.74\,\text{GHz} \\ t_\text{r} = t_\text{f} = 11.47\,\text{ps} \end{cases}$$

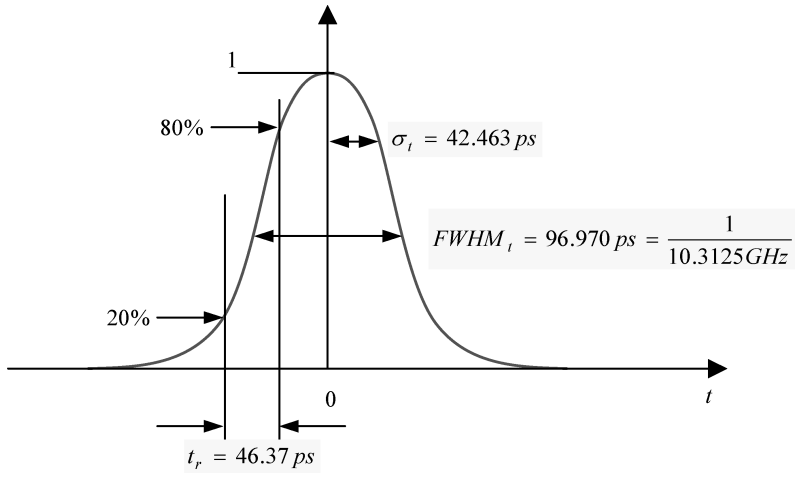

Figure 3.24 Schematic representation of the Gaussian pulse with FWHM_t equal to the time step of the 10 GbE data rate. The corresponding 20 %–80 % rise time equals 46.37 ps

Example 3.3

As the last example, the case of a Gaussian laser pulse of $\text{FWHM}_t = 96.970\,\text{ps} = 1/10.3125\,\text{GHz}$ is considered (see Figure 3.24), which corresponds to the bit period of the 10 GbE standard. Using Equation (3.121), the corresponding rise and fall times are computed immediately:

$$\Delta t_{20-80} \cong 0.4782\ \text{FWHM}_t = 46.37\,\text{ps}$$

3.11.4 Gaussian Responses

The Gaussian model of the multimode fiber intensity impulse response $h_\text{F}\,(z,t)$ is defined using the following Gaussian impulse response $h_\text{G}\,(z,t)$:

$$h_\text{F}(z,t) = h_\text{G}(z,t) = \frac{1}{\sigma_t(z)\sqrt{2\pi}} \text{e}^{-t^2/[2\sigma_t^2(z)]} \tag{3.128}$$

The variable z represents the distance measured along the fiber path from the origin situated at the launching section. The RMS width $\sigma_t(z)$ of the multimode fiber impulse response accounts for all contributions to pulse broadening, including the differential mode delay, group velocity dispersion and eventually other higher-order dispersion effects. The corresponding frequency response of the intensity field of the multimode fiber is given by the Fourier transform of Equation (3.128):

$$H_\text{F}(z,\,f) = H_\text{G}(z,\,f) = \text{e}^{-2[\pi\sigma_t(z)f]^2} \tag{3.129}$$

In the above expression, the frequency f refers to the spectral content of the envelope of the optical intensity field. The modulated optical signal brings the information content in the envelope of the optical field. In the above expression, the multimode fiber frequency response is evaluated at a distance z from the launching section located at $z = 0$ and it is completely characterized by the RMS pulse width $\sigma_t(z)$. In the following model it will be assumed that the various contributions to the pulse dispersion add quadratically. This assumption is correct if all frequency response contributions are Gaussian, or alternatively if all processes involved are not correlated and each

has a zero average. Assuming at least one of these two conditions to be fulfilled, the total RMS pulse width $\sigma_t(z)$ can be written according to the following relation:

$$\sigma_t^2(z,\lambda) = \sigma_m^2(z,\lambda) + \sigma_c^2(z,\lambda) \tag{3.130}$$

where $\sigma_m(z,\lambda)$ (ps) is the RMS width of the modal impulse response due to differential mode delay evaluated at distance z and $\sigma_c(z,\lambda)$ (ps) is the RMS width of the chromatic impulse response due to chromatic dispersion evaluated at distance z.

The analysis of the differential mode delay $\mathrm{DMD}(z,\lambda) \equiv \sigma_m(z,\lambda)$ presented in Section 3.4.1 should be recalled. The RMS width $\sigma_m(z,\lambda)$ of the impulse response due to the modal delay distribution measured at distance z from the launching section coincides with the DMD expression given Equation (3.62). Consequently, expression (3.62) must be inserted in (3.130) for the calculation of the total pulse dispersion. In Chapter 4 the physical principles, the theory and modeling of the chromatic dispersion in optical fibers is considered. Modal dispersion analysis will follow in Chapter 5.

4

Theory of Chromatic Response

Modeling Light Source Effect in Multigigabit Transmission Links

4.1 Introduction and Outline

In this chapter the theory of chromatic dispersion in multimode optical fiber is presented. Some of the theoretical concepts have already been introduced and discussed in Chapter 3. It is the aim of this chapter to present the physical concepts behind the chromatic impulse response in multimode optical fiber and to give a mathematical closed-form description of the propagation phenomena. The mathematical model has been developed in order to find a suitable solution for computer simulation and transmission system design purposes. It is important to remember that all the presented analysis is based on the linear intensity regime assumption: the optical fiber is a linear system capable of transferring the intensity impulse launched at the input section to the intensity impulse response available at the output section.

The next section deals with the theoretical formulation of the optical impulse response from the source spectral characteristics, assuming the propagation to be supported by a fixed allowed mode. Important concepts such as the optical source spectrum and the modulation signal spectrum limiting conditions are introduced in order to define the corresponding different optical propagation regimes. In this book essentially only the spectrum limited propagation condition and the corresponding chromatic impulse response equation have been derived and discussed.

The third section uses the mathematical result achieved when developing the Matlab® 7.0.2 based simulation software which allows several chromatic impulse responses to be computed using both generalized source and group delay distributions. The presented results are quite interesting, showing a large variety of different temporal responses. The cases considered have been grouped according to the wavelength range, source spectrum composition and group delay distribution in the operating wavelength range.

The fourth section defines the principal signal moments of the chromatic impulse response. In particular, the well-known expression for the chromatic impulse response RMS pulse width is derived, which is very often used for a first-order estimation of chromatic response limited transmission system performance. The intent of this section is to clearly define the metrics for the chromatic impulse response evaluation in order to proceed with a quantitative comparison among different source conditions.

Multi-Gigabit Transmission over Multimode Optical Fibre: Theory and Design Methods for 10GbE Systems Stefano Bottacchi
 ISBN: 0-471-89175-4

4.2 Theory of Chromatic Impulse Response

As already introduced in the previous chapter, each individual fiber mode, labeled by the single index $h \equiv (\nu, \mu)$ to simplify the notation, is characterized by the propagation constant or phase constant $\beta_h(\omega)$. All individual modes belonging to the same mode group have the same propagation constant. The number of individual modes coincides with the degree of degeneration of the eigenvalue $\beta_h(\omega)$. The propagation constant $\beta_h(\omega)$ determines the way the mode wavefronts propagate along the optical fiber. Since $\beta_h(\omega)$ depends on the optical frequency ω, the modulated light source spectrum must play a dominant role in the mode propagation characteristics. The dependence of the propagation constant $\beta_h(\omega)$ from the optical frequency defines the dispersion relations for the considered individual mode. The first-order derivative of $\beta_h(\omega)$ with respect to the optical frequency has the meaning of the group delay per unit length $\tau_{g,h}(\omega)$ of the hth mode. It is important to recognize the conceptual difference between the definition reported in Chapter 3 [Equation (3.83)] and the more general definition discussed in this section. Equation (3.83) referred to the material contribution only, disregarding any waveguide effect. In Chapter 3, Section 3.7, the material contribution was conceptually separated from the waveguide contribution. Now it seems physically more appropriate to include both of those effects in the whole propagation constant expression for the selected hth mode leading to the modal chromatic dispersion.

4.2.1 Modal Delay

Once those important concepts are clear, the frequency derivative of the modal propagation constant $\beta_h(\omega)$ includes all frequency-dependent terms, in particular the material contribution and the waveguide contribution. Since both terms depend on the optical frequency both of them will be taken together as the chromatic contribution. In this context it is meaningful to write the generalized expression (3.76) for the total propagation delay of the hth guided mode by just adding the modal index h:

$$\tau_{g,h}(\omega) = \frac{1}{v_{g,h}(\omega)} = \frac{d\beta_h(\omega)}{d\omega} = \beta_h^{(1)}(\omega) = \frac{1}{c} n_{g,h}(\omega) \tag{4.1}$$

All terms involved refer to the selected guided mode identified by the index h.

4.2.2 Modal Chromatic Dispersion

In order to arrive at the concept of chromatic dispersion of the generic jth guided mode, the way in which the group delay per unit length $\tau_{g,h}(\omega)$ depends on the optical frequency of the light source must be considered. In general, the propagation constant can be conveniently expanded in a power series around the central optical frequency emitted by the light source. Limiting the power series expansion of $\beta_h(\omega)$ to the second-order term leads to the first-order group chromatic dispersion term $d_{g,h}(\omega)$. By differentiating Equation (4.1) with respect to ω,

$$d_{g,h}(\omega) = \frac{d\tau_{g,h}(\omega)}{d\omega} = \beta_h^{(2)}(\omega) = -\frac{1}{v_{g,h}^2(\omega)} \frac{dv_{g,h}(\omega)}{d\omega} = \frac{1}{c} \frac{dn_{g,h}(\omega)}{d\omega} \tag{4.2}$$

Each supported mode therefore experiences a characteristic chromatic dispersion for the selected frequency (wavelength). This value is the result of the interaction between the contributions of the waveguide field and the material properties filling the mode volume.

The chromatic dispersion coefficient $D_{c,h}(\lambda)$ for the hth guided mode is defined as the first-order derivative of the group delay $\tau_{g,h}[\omega(\lambda)]$ (Equation (4.1)) with respect to the wavelength. Since $d/d\lambda(\cdot) = d/d\omega(\cdot)d\omega/d\lambda$ and $\omega = 2\pi c/\lambda$, the chromatic dispersion coefficient of the hth guided mode assumes the following expression:

$$D_{c,h}(\lambda) = -\frac{2\pi c}{\lambda^2} \left[\frac{d^2\beta_h(\omega)}{d\omega^2} \right]_{\omega=2\pi c/\lambda} = -\frac{2\pi c}{\lambda^2} d_{g,h}(\omega)\Big|_{\omega=2\pi c/\lambda} \tag{4.3}$$

From Equation (4.3), it can be concluded that the chromatic dispersion is proportional to the second-order derivative of the propagation constant $\beta_h(\omega)$ evaluated at the corresponding wavelength. Due to the close relationship with the chromatic dispersion $d_{g,h}(\lambda)$, the same conclusions as above also hold for the function $D_{c,h}(\lambda)$.

4.2.3 Source Spectrum Conditions

Chromatic dispersion affects pulse propagation in different ways depending on the origin of the source spectrum broadening. To simplify the discussion it is better to refer to the following two extreme cases.

4.2.3.1 Modulation Spectrum Limited Condition

The continuous wave (CW) source linewidth is much narrower than the modulating signal spectrum. In this case the spectrum of the modulated light source is dominated by the signal spectrum and the achievable link distance L decreases as the inverse of the square value of the bit rate B:

$$L \propto \frac{1}{B^2}$$

This case will not be analyzed further. It is very important and finds proper application in almost all externally modulated highly coherent light sources in the multigigabit range. It leads to the solution of the linear or nonlinear wave propagation equation for the optical field envelope and will be the topic for a later book. Since in this case the pulse propagation characteristics are due to the signal spectrum content, the theory refers to mainly single-mode fiber applications with externally modulated highly coherent laser sources. It includes wavelength division multiplexing and generally optically amplified lines operated with light modulators based on the Mach–Zendher interferometer principle.

In order to have a qualitative behavior as a consequence of this spectral condition, the propagation distance achievable for a fixed pulse degradation is inversely proportional to the square value of the transmitting bit rate. As a first case, the SONET hierarchy OC-48 is considered, with a bit rate $B = 2488.320$ Mb/s. The pulse propagation theory under the assumption of modulation spectrum limiting conditions predicts a linear link reach of about $L_{OC48} = 1000$ km, assuming standard step-index single-mode fiber and operating in the third window range, $\lambda = 1550$ nm.

Moving up to the next SONET hierarchy, at an OC-196 signaling rate with $B = 9953.280$ Mb/s, the square-law dependence of the link length over the bit rate implies a link about 16 times shorter, reaching about $L_{OC196} = 62.5$ km. The same criteria lead to a link length of only $L_{OC768} = 3.9$ km link for the latest SONET OC-768 case, with $B = 39\,813.120$ Mb/s.

4.2.3.2 Source Spectrum Limited Condition

The unmodulated source linewidth (CW conditions) is assumed to be much broader than the modulating signal spectrum. In this case the modulated light source spectrum is dominated by the unmodulated source linewidth and the achievable link distance L decreases as the inverse of the bit rate B:

$$L \propto \frac{1}{B}$$

This case refers to directly modulated laser diodes or LED sources, or even to an externally modulated laser source but with consistent chirping behavior. In this case the modulated optical linewidth is some order of magnitude broader than the modulating signal spectral content and the modulated spectrum does not resemble the intensity modulating signal spectrum. Multimode fiber applications at 10GbE standards belong to this case.

In order to become a little more acquainted with a typical situation, a laser linewidth $\Delta\lambda = 1\,\text{nm}$ centered around $\lambda = 1550\,\text{nm}$ is considered and is found to correspond through the frequency wavelength differentiation expression (3.54) to about $\Delta f = 125\,\text{GHz}$. This means that a direct modulated laser running at 10GbE speed occupies no more than 20 % of the assumed laser linewidth and after proper mathematical convolution of both spectra the result is quite unchanged and is represented essentially by the laser linewidth.

The analysis of the pulse propagation condition under broadband optical spectral conditions will be presented in Section 4.3. The important result anticipated here is that under linear group delay approximation, the RMS width broadening $\sigma_{c,h}(z, \lambda)$ of the impulse response of each fiber mode j, due to the combined effects of the first-order chromatic dispersion $D_{c,h}(\lambda)$ and the source spectrum RMS linewidth σ_s, has the following simple and fundamental expression:

$$\sigma_{c,h}(z, \overline{\lambda}) = |D_{c,h}(\overline{\lambda})|\sigma_s z \tag{4.4}$$

The chromatic dispersion contribution in Equation (4.4) is evaluated up to the second-order derivative of the propagation constant of the fiber mode. This condition is referred to as linear dispersion and allows for a very reasonable description of the pulse broadening away from the zero-dispersion wavelength, $\overline{\lambda} \neq \lambda_0$. Close to the zero-dispersion wavelength third-order and higher effects become relevant and the pulse broadening description must be restated.

The parameters involved in Equation (4.4) have the following meanings: σ_s is the standard deviation of the light source spectrum under signal modulated conditions and coincides with the wavelength RMS width of the light source and $\sigma_{c,h}(z, \overline{\lambda})$ is the standard deviation of the induced impulse response broadening by the combined effects of the source spectrum linewidth and the chromatic dispersion coefficient evaluated at the source average wavelength $\overline{\lambda}$.

Since under the linear regime the light spectrum is assumed constant in every fiber section, the standard deviation $\sigma_{c,h}(z, \overline{\lambda})$ of the pulse broadening due to chromatic dispersion interaction results in a linear function of the propagation distance z. This means that the launched pulse broadens uniformly as long as it propagates along the fiber link. In order to understand better the consequences of Equation (4.4) and how the chromatic dispersion interacts with the initial pulse width, the following example is considered in which the Gaussian pulse reported in Figure 3.24 has been assumed as the initial launched pulse.

Example 4.1

1. Source average wavelength $\overline{\lambda} = 1550\,\text{nm}$
2. Source linewidth $\sigma_s = 0.5\,\text{nm}, 1.0\,\text{nm}, 2.0\,\text{nm}$
3. Chromatic dispersion coefficient $D_{c,h}(\overline{\lambda}) = 20\,\text{ps/nm km}$
4. Launched Gaussian pulse of RMS width $\sigma_0 = 42.5\,\text{ps}$
5. Fiber Gaussian impulse response due to chromatic dispersion only

The pulse broadening at a given distance z from the launching section $z = 0$ is computed by convolving the initial Gaussian pulse with the assumed Gaussian impulse response of the fiber mode due to chromatic dispersion only. That would be the case for either a single-mode fiber or any selected individual mode in a multimode fiber where mode coupling has been neglected. Due to well-known Gaussian convolution properties, the convolution output is still a Gaussian pulse, with the variance given by the sum of the variances of the two Gaussian components. From Equation (4.4), the following variance of the output pulse is obtained:

$$\sigma^2(z, \overline{\lambda}) = \sigma_0^2 + \sigma_{c,h}^2(z, \overline{\lambda}) = \sigma_0^2 + \sigma_s^2|D_{c,h}(\overline{\lambda})|^2 z^2 \tag{4.5}$$

Figure 4.1a shows the computed RMS width of the pulse evaluated versus the distance z. Due to the quadratic relation (3.125), the pulse RMS width starts to increase almost linearly with distance after the chromatic dispersion term $\sigma_{c,h}(z, \overline{\lambda})$ starts to dominate the initial pulse width σ_0.

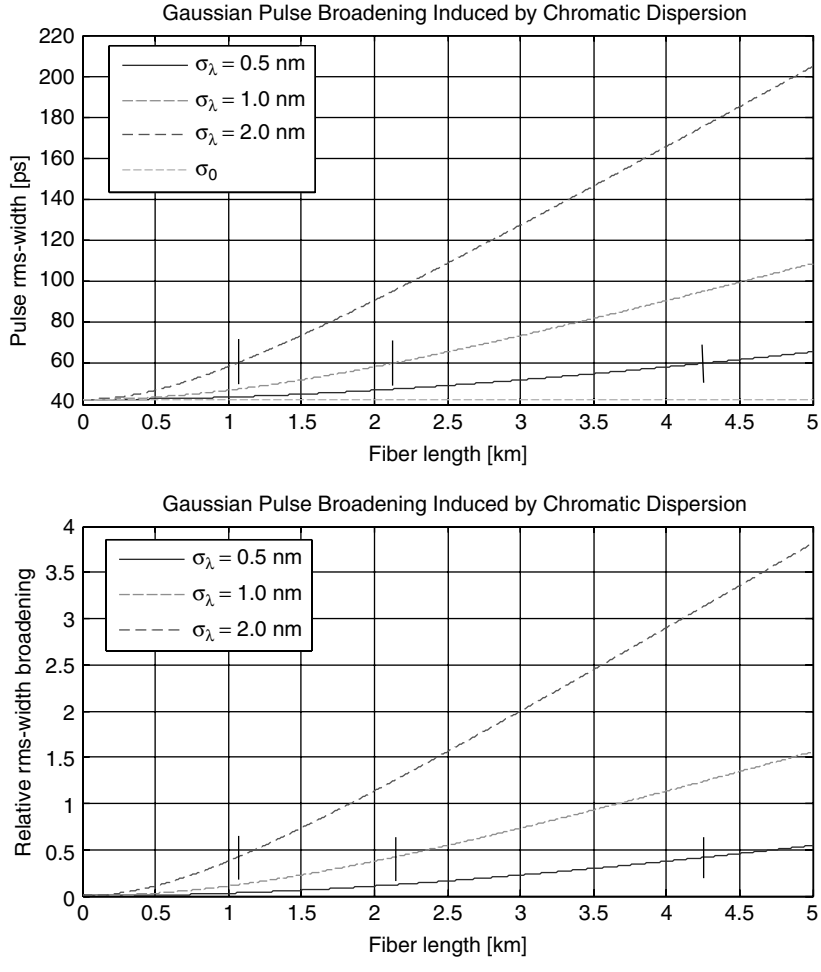

Figure 4.1a Computed Gaussian pulse broadening versus fiber length due to chromatic dispersion for each individual mode. The assumed input pulse corresponds to Figure 3.24, with an RMS width $\sigma_0 = 42.5$ ps according to 10GbE FWHM. The plotted curves refer to three different source spectrum linewidths but to the same chromatic dispersion coefficient. Vertical bars represent the position of the threshold z_0 for the three different wavelengths, according to Equations (4.8). The top graph reports the absolute pulse broadening while the bottom graph refers to the relative broadening

Figure 4.1b shows the relative pulse broadening factor $\eta_{c,h}(z, \overline{\lambda})$ defined as the width increment over the initial width:

$$\eta_{c,h}(z, \overline{\lambda}) \equiv \frac{\sigma(z, \overline{\lambda})}{\sigma_0} - 1 = \sqrt{1 + \frac{\sigma_s^2 |D_{c,h}(\overline{\lambda})|^2 z^2}{\sigma_0^2}} - 1 \cong \left|_{z \gg z_0} \frac{\sigma_s |D_{c,h}(\lambda)| z}{\sigma_0} \right. \tag{4.6}$$

The length z_0 represents the threshold distance where the chromatic dispersion effect starts to dominate the whole pulse width. It can be defined as follows:

$$\frac{\sigma_s |D_{c,h}(\overline{\lambda})| z_0}{\sigma_0} = 1 \Rightarrow z_0(\overline{\lambda}) = \frac{\sigma_0}{\sigma_s |D_{c,h}(\overline{\lambda})|} \tag{4.7}$$

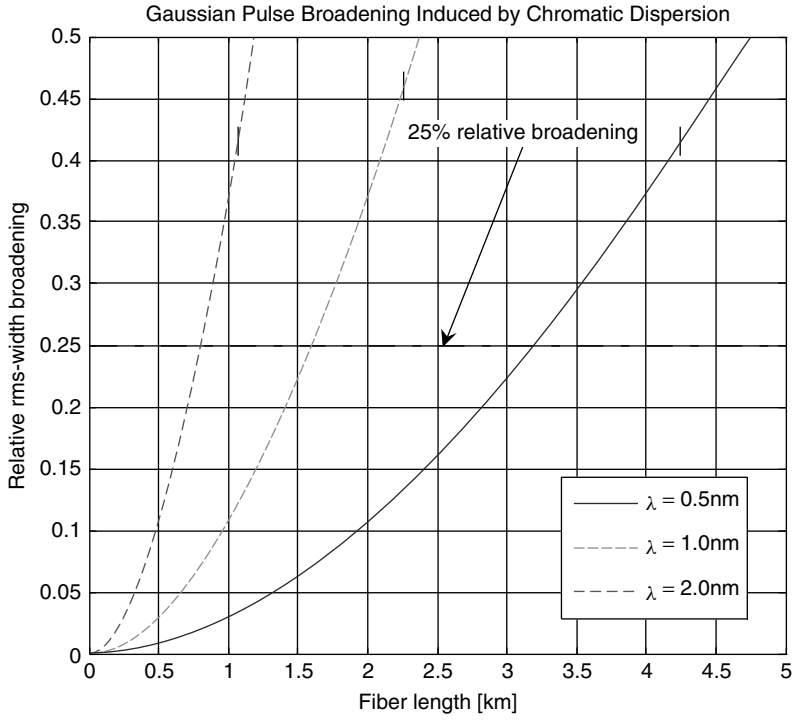

Figure 4.1b Magnification of the plot shown in the bottom graph of Figure 4.1a for a relative pulse broadening factor less than 50 %. The link length must be limited respectively to about 0.8 km, 1.6 km and 3.2 km in order to achieve the relative pulse broadening equal to 25 % for the three laser linewidths considered. Vertical bars represent the position of the threshold z_0 for the three different wavelengths, according to Equations (4.8)

The distance z_0 is inversely proportional to the source linewidth, as indicated by the small vertical segment in the above figure. In the considered case, Equation (4.7) gives the following values:

$$\begin{aligned} z_0|_{\sigma_s=0.5\,\mathrm{nm}}(\overline{\lambda} = 1550\,\mathrm{nm}) &= 4.250\,\mathrm{km} \\ z_0|_{\sigma_s=1.0\,\mathrm{nm}}(\overline{\lambda} = 1550\,\mathrm{nm}) &= 2.125\,\mathrm{km} \\ z_0|_{\sigma_s=2.0\,\mathrm{nm}}(\overline{\lambda} = 1550\,\mathrm{nm}) &= 1.062\,\mathrm{km} \end{aligned} \tag{4.8}$$

For distances z greater then z_0 the chromatic broadening effect dominates over the initial pulse width and the pulse broadens almost linearly as long as it propagates.

This behavior is quite simple but it has interesting consequences when combined with modal pulse dispersion. In fact, due to linear spreading of all modal contributions, the combined effect of both chromatic and modal broadening gives a time-scalable pulse with an invariant shape for distances greater then z_0. This interesting effect will be shown in several numerical applications in the next section.

The values listed in Equations (4.8) give quantitative indications about the maximum allowed source linewidth in order to achieve a minimum link length close to a bit late of 10-Gb/s. Since

σ_0 is proportional to the bit rate, it is evident how a decreasing transmission speed leads to a proportional increase in the achievable distance for a relative pulse broadening factor. Before closing this subsection it is important to remember the following remark: in the example above it was assumed that a single value for the chromatic dispersion coefficient was independent of the individual mode property. This is in general an approximation and should be at least justified. The remaining parameters that were introduced, the RMS width relative broadening and the distance z_0 should therefore have the proper modal index in order to specify their modal dependence.

4.2.4 Broadband Optical Sources

In this section the theory of pulse propagation relative to each multimode fiber mode will be introduced under the assumption that the unmodulated light source spectrum is much broader than the modulating signal spectrum. In Section 4.2.3.2 the chromatic dispersion broadening factor $\sigma_{c,h}(\lambda)$ in Equation (4.4) has been presented almost as a heuristic result, without any formal mathematical demonstration. It is the aim of this section instead to present the physical assumptions behind the mathematical treatment and to provide a closed-form expression of the chromatic dispersion impulse response with a first-order broadening factor given by Equation (4.4). In order to satisfy the broadband optical source condition the unmodulated light source spectrum must be sufficiently broader than the modulating signal spectrum. Before starting the mathematical development, a few practical cases are given to illustrate some typical applications:

1. A direct modulated laser diode operating at 10 Gb/s, 2.5 Gb/s or a lower bit rate with a modulated linewidth of the order of 1 nm. In this case the optical spectral width is in the range of 100 GHz, resulting in at least one order of magnitude larger than the signal spectrum.
2. Externally modulated laser diodes with added phase dithering to increase the linewidth. This technique is used in linear fiber optic systems such as CATV in order to reduce the nonlinear Brillouin scattering effect. By properly choosing a dithered linewidth in the range of 10 GHz, or equivalently about 0.08 nm in the 1550 nm optical wavelength range, a modulating signal with a spectrum below 1 GHz satisfies the broadband optical source condition.
3. LED light sources exhibit a broad spectral width, usually in the range of 20–80 nm, and they fully satisfy the broadband optical source condition for every applicable modulating signal.

Under the broadband optical source condition it can be assumed that the intensity modulated light spectrum remains almost unchanged by the modulation process. This conclusion appears quite a paradox at first thought, but it can easily be justified using basic conclusions from the amplitude modulation process and in particular the frequency convolution theorem. The assumption of the optical source spectrum being much broader than the modulating signal spectrum leads to a frequency convolution spectrum mainly dominated by the broader spectral component, namely the unmodulated optical spectrum. Under these circumstances, the impulse response of the individual fiber mode is dominated by the interaction between the spectrum of the unmodulated light source and the chromatic dispersion relationship of the propagation constant of the considered fiber mode. In the following, a generic fiber mode labeled by the mode index h will be considered.

The power spectral density (PSD) of the unmodulated optical source is given by $S_s(\lambda)$. The unit of measure of $S_s(\lambda)$ is W/nm. The power of the light source included within the wavelength interval between λ_1 and λ_2 is given by the integral of the light source PSD:

$$P_s(\lambda_1, \lambda_2) = \int_{\lambda_1}^{\lambda_2} S_s(\lambda)\, d\lambda \quad \text{(W)} \tag{4.9}$$

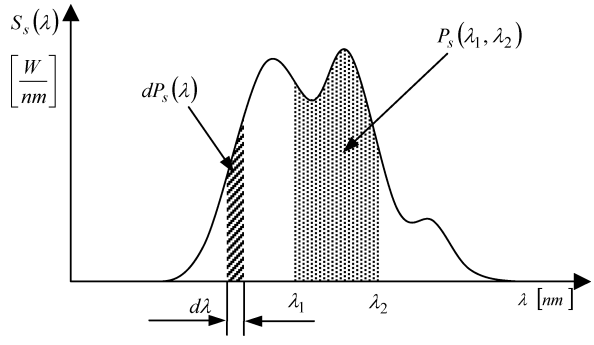

Figure 4.2 Representation of the power spectral density (PSD) of the light source. Dashed areas represent power contributions calculated after integration, as reported in Equation (4.9)

By differentiating the integral relation (4.9) the source power included within the infinitesimal wavelength interval between λ and $\lambda + \mathrm{d}\lambda$ is obtained:

$$\mathrm{d}P_{\mathrm{s}}(\lambda) = S_{\mathrm{s}}(\lambda)\,\mathrm{d}\lambda \tag{4.10}$$

Figure 4.2 shows the graphical interpretation of the concepts just presented.

4.2.4.1 Single-Line Optical Source Spectrum

According to the dispersion relationship, each infinitesimal power contribution $\mathrm{d}P_{\mathrm{s}}(\lambda)$ of the source spectrum localized at the wavelength λ propagates with the group delay $\tau_{\mathrm{g},h}(\lambda)$ per unit length of the launched individual fiber mode. Neglecting the power attenuation, the optical fiber of length z behaves like a delay line supporting the hth mode characterized by the group delay $t_{\mathrm{g},h}(z, \lambda) = z\tau_{\mathrm{g},h}(\lambda)$. The frequency response $G_{\mathrm{c},h}(z, \lambda, f)$ of the signal intensity due to chromatic dispersion (in the electric frequency domain) of the selected hth mode corresponding to the infinitesimal source spectrum contribution $\mathrm{d}P_{\mathrm{s}}(\lambda)$ localized within the interval λ and $\lambda + \mathrm{d}\lambda$ is therefore represented by the well-known frequency response of the delay line:

$$G_{\mathrm{c},h}(z, \lambda, f) = \mathrm{e}^{-\mathrm{j}2\pi f z \tau_{\mathrm{g},h}(\lambda)} \tag{4.11}$$

The corresponding impulse response is given by the Fourier transform of the delay line frequency response (4.11):

$$\Im^{-1}[G_{\mathrm{c},h}(z, \lambda, f)] = g_{\mathrm{c},h}(z, \lambda, t) = \delta[t - z\tau_{\mathrm{g},h}(\lambda)] \tag{4.12}$$

The result obtained so far is consistent with the concept and the definition of the modal group delay given previously. It is important to note, however, the different notation that was used for frequency and impulse responses respectively in Equations (4.11) and (4.12). They refer to the case of a monochromatic light source, localized at the wavelength λ. At first sight this is a contradiction, because the frequency spectrum of the impulse function $\delta(t)$ is indefinitely extended and it cannot therefore be assimilated to a single wavelength. However, optical signals are supposed to be intensity modulated by electrical pulses whose spectral content is usually negligible with respect to the optical carrier. The optical carrier has a frequency that is usually four to five orders of magnitude higher than the spectral content of the modulating signal for relatively fast pulses. In order to satisfy the broadband optical source condition the unmodulated light source spectrum must be sufficiently broader than the modulating signal spectrum. This concept is behind the widely used narrowband

signal modulation approximation. Even relatively fast optical pulses have a wavelength range below one nanometer.

In the following example the case of a modulated light source satisfying both the broadband optical source condition and the Narrowband signal modulation approximation is considered.

Example 4.2

Using the Gaussian relationship reported in Chapter 3, Section 3.11.3, the following parameters of the electrical Gaussian pulse characterized by $\text{FWHM}_t = 100\,\text{ps}$ are computed (see Figure 4.3):

$$\text{FWHM}_t = 100\,\text{ps} \Rightarrow \begin{cases} \sigma_t = 42.46\,\text{ps} \\ \sigma_f = 3.749\,\text{GHz} \\ \text{FWHM}_f = 8.825\,\text{GHz} \\ \text{BW}_{-3\,\text{dB}} = 4.413\,\text{GHz} \\ t_r = t_f = 47.81\,\text{ps} \end{cases}$$

In particular, the Gaussian spectrum width evaluated at half-maximum ($-3\,\text{dB}$ optical) has the following value, according to Equation (3.117):

$$\text{FWHM}_f = 2\text{BW} = \frac{4\ln 2}{\pi}\frac{1}{\text{FWHM}_t} \cong \frac{0.8825}{\text{FWHM}_t} = 8.825\,\text{GHz} \tag{4.13}$$

Due to the intensity modulation process, the Gaussian spectrum of the modulating electrical pulse must be convolved with the carrier light source spectrum in order to give the Gaussian pulse modulated optical spectrum. Since the width of the electrical Gaussian pulse results in $\text{FWHM}_f = 8.825\,\text{GHz}$, this corresponds in the wavelength domain to about $\text{FWHM}_\lambda \cong 50\,\text{pm} = 0.05\,\text{nm}$, evaluated at the central wavelength $\lambda = 1310\,\text{nm}$. Assuming that the unmodulated light source has the spectrum centered at $\lambda = 1310\,\text{nm}$ with a linewidth of the order of 0.5 nm or even less, both the broadband optical source condition and the narrowband signal modulation approximation are simultaneously verified. In the following sections, in order to have some reference cases in mind, it can be assumed that both optical spectral lines and the modulating pulse closely resemble the Gaussian

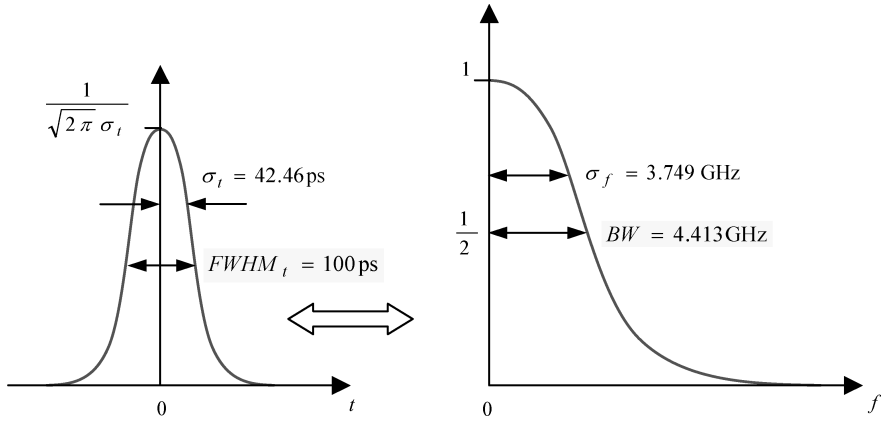

Figure 4.3 Electrical Gaussian pulse used to modulate the intensity of the optical source. Assuming $\text{FWHM}_t = 100\,\text{ps}$, the corresponding frequency spectrum width has $\text{FWHM}_f = 8.825\,\text{GHz}$, which corresponds to $\text{FWHM}_\lambda \cong 50\,\text{pm} = 0.05\,\text{nm}$ evaluated at the central wavelength $\lambda = 1310\,\text{nm}$

case just presented. In addition, it is remarkable that the normalized Gaussian pulse in the limit of infinitely small variance converges toward the Dirac delta:

$$\lim_{\sigma\to 0}\frac{1}{\sigma\sqrt{2\pi}}\mathrm{e}^{-t^2/(2\sigma^2)}=\delta(t) \tag{4.14}$$

The limit is referred to the integral property that defines the Delta distribution:

$$\lim_{\sigma\to 0}\int_{-\infty}^{+\infty}\frac{\phi(t)}{\sigma\sqrt{2\pi}}\mathrm{e}^{-(t-t_0)^2/(2\sigma^2)}\,\mathrm{d}t=\int_{-\infty}^{+\infty}\phi(t)\delta(t-t_0)\,\mathrm{d}t=\phi(t_0) \tag{4.15}$$

where the test function $\phi(t)$ is continuous at the time instant t_0.

In the following mathematical development, both modulating pulses and optical spectra are modeled assuming Dirac delta impulses. Although the mathematical treatment of the Dirac impulse requires the theory of distribution, it can be easily handled using the integral definition as above and a few related properties. Finite pulses like Gaussian or rectangular windows can conveniently represent the Dirac impulse approximation when dealing with numerical and experimental environments.

4.2.4.2 Double-Line Optical Source Spectrum

As a step forward, it is assumed that the optical source PSD is distributed over two spectral lines at λ_1 and λ_2 with intensities $|a_1|^2$ and $|a_2|^2$ respectively satisfying the normalization condition of unity power:

$$|a_1|^2+|a_2|^2=1 \tag{4.16}$$

If each single line spectrum is modeled as a Dirac delta, the source power spectral density is therefore represented by two frequency impulses localized at λ_1 and λ_2 with respective area $|a_1|^2$ and $|a_2|^2$:

$$S_\mathrm{s}(\lambda)=|a_1|^2\delta(\lambda-\lambda_1)+|a_2|^2\delta(\lambda-\lambda_2) \tag{4.17}$$

Assuming a linear transmission regime in the optical fiber, the corresponding chromatic frequency response $H_{\mathrm{c},h}(z,f)$ of the considered hth mode measured after a distance z from the launching section can be written as the sum of the two frequency responses (4.11) corresponding to the PSD in Equation (4.17):

$$\begin{aligned}H_{\mathrm{c},h}(z,f)&=|a_1|^2G_{c,h}(z,\lambda_1,f)+|a_2|^2G_{\mathrm{c},h}(z,\lambda_2,f)\\&=|a_1|^2\mathrm{e}^{-\mathrm{j}2\pi f z\tau_{\mathrm{g},h}(\lambda_1)}+|a_2|^2\mathrm{e}^{-\mathrm{j}2\pi f z\tau_{\mathrm{g},h}(\lambda_2)}\end{aligned} \tag{4.18}$$

The different notation used for identifying the frequency response (4.18) is noted for the case of a multiple-line source spectrum with respect to the single-line source spectrum considered in Equation (4.11). The corresponding impulse response $h_{\mathrm{c},h}(z,f)$ is obtained directly from Equations (4.18) and (4.12) by virtue of the superposition principle:

$$h_{\mathrm{c},h}(z,t)=|a_1|^2\delta[t-z\tau_{\mathrm{g},h}(\lambda_1)]+|a_2|^2\delta[t-z\tau_{\mathrm{g},h}(\lambda_2)] \tag{4.19}$$

It is relevant to observe the optical fiber behavior in this case: the double-delta spectrum (4.17) has been converted into the double-delta impulse response (4.19).

This is a peculiarity of the chromatic impulse response under the assumption of satisfying simultaneously both the broadband optical source condition and the frequency impulsive line shape. Again, the simultaneous satisfaction of both these conditions leads to a conceptual contradiction: a broadband optical spectrum cannot be assigned to an impulsive frequency shaping. This is true,

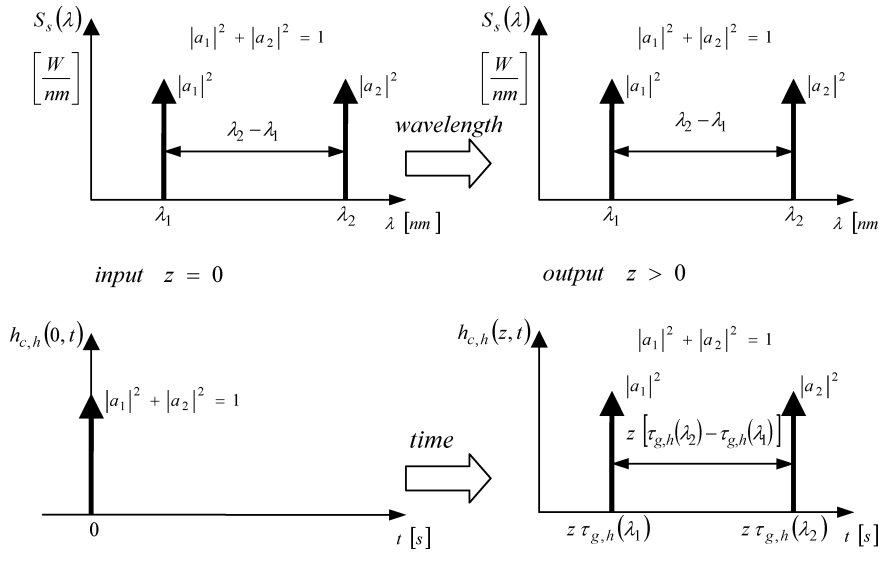

Figure 4.4 The figure shows in the first row the input and output light spectra respectively, while the second row shows corresponding impulse responses. Alternatively, the first column presents (top) the light source spectrum and (bottom) the light source impulse stimulus. The second column shows corresponding by (top) the output spectrum and (bottom) the output impulse response. In this case the impulse response is a time-scaled version of the input source spectrum. The slope of the group delay versus wavelength is assumed to be positive: $\lambda_2 > \lambda_1 \Rightarrow \tau_{g,h}(\lambda_2) > \tau_{g,h}(\lambda_1)$

of course, but once more the narrowband signal modulation approximation allows a relatively broadband spectrum to be considered with respect to the electrical modulating signal extension, with a relatively narrow linewidth in the wavelength domain allowing the impulsive approximation. The behavior just encountered is characteristic of the chromatic impulse response under the broadband optical source condition. The impulse response in the time domain in general resembles the source spectrum in the optical domain.

Figure 4.4 gives a schematic representation of the discrete source spectrum considered in the text.

4.2.4.3 Multiple-Line Optical Source Spectrum

The above procedure can be extended to as many spectral lines as needed: the only physical assumption behind it is the validity of the superposition principle. In the case where the optical source PSD is constituted by a series of wavelength impulses, Equations (4.16) to (4.19) are generalized as follows:

$$S_{\mathrm{s}}(\lambda) = \sum_i |a_i|^2 \delta(\lambda - \lambda_i) \tag{4.20}$$

$$\int_{-\infty}^{+\infty} S_{\mathrm{s}}(\lambda)\,\mathrm{d}\lambda = \sum_i |a_i|^2 \int_{-\infty}^{+\infty} \delta(\lambda - \lambda_i)\,\mathrm{d}\lambda = \sum_i |a_i|^2 = 1 \tag{4.21}$$

$$H_{\mathrm{c},h}(z, f) = \int_{-\infty}^{+\infty} S_{\mathrm{s}}(\lambda) \mathrm{e}^{-\mathrm{j}2\pi f z \tau_{\mathrm{g},h}(\lambda)}\,\mathrm{d}\lambda = \sum_i |a_1|^2 \mathrm{e}^{-\mathrm{j}2\pi f z \tau_{\mathrm{g},h}(\lambda_1)} \tag{4.22}$$

$$h_{\mathrm{c},h}(z, t) = \sum_i |a_i|^2 \delta[t - z\tau_{\mathrm{g},h}(\lambda_i)] \tag{4.23}$$

By comparing Equation (4.19) with Equation (4.23) the same property of the chromatic impulse response introduced above is found for the double-line spectrum. Under the broadband optical source condition, the chromatic impulse response to a succession of light source impulses in the wavelength domain is the equivalent succession of time domain impulses localized at the corresponding group delays and with the same intensity ratios as the line spectra.

The important conclusion deduced from Equation (4.23) is that, assuming the validity of the broadband optical source condition, even for the multiple narrow line spectrum, the impulse response of the chromatic dispersion associated with the individual fiber mode leads to a multiple impulse output, localized on the time axis according to the group delay value experienced at the source line spectrum. As a consequence, if the group delay function is monotonic, the same behavior will be experienced by the chromatic impulse response at the output section, leading to the same sequence of impulse contributions as the input line spectrum. If the slope of the group delay versus wavelength for the individual fiber mode is monotonic positive, this leads in fact to increasing delays at increasing wavelengths. The contrary of course holds in the case of a negative group delay slope. Figure 4.5 presents the situation described above assuming a positive slope group delay.

The validity of the chromatic transfer function (4.22) is subordinated to the broadband optical source condition fulfilled for each spectral line contribution. Each of the spectrum lines in Equation (4.20) must be broad enough to hide the modulating signal spectrum content. This condition can be satisfied, for instance, by using the 100 ps FWHM modulating Gaussian pulse presented in Example 4.2 and but assuming that each spectral line is about 0.5 nm wide. Since the validity for Equation (4.22) is subordinated to the relative width between each spectral line of the light source and the modulating signal spectrum, both quantities can easily be scaled to different values if needed. For example, assuming a Fabry–Perot multilongitudinal mode semiconductor laser emitting at $\lambda = 1310\,\text{nm}$ with an individual linewidth of $\Delta\lambda = 0.1\,\text{nm} = 100\,\text{pm}$, this would require increasing the modulating Gaussian pulse width to about $\text{FWHM}_t = 500\,\text{ps}$, which corresponds to about $\text{FWHM}_\lambda = 10\,\text{pm}$ in the wavelength domain in order to have a ratio of 10 as above.

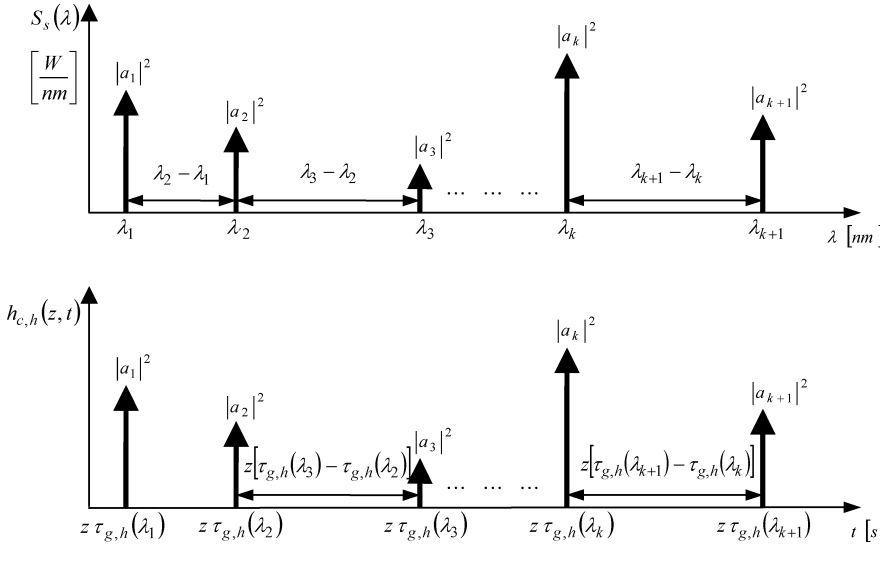

Figure 4.5 The top graph shows the multiple-line input spectrum. The bottom graph shows the corresponding chromatic impulse response assuming the broadband optical source condition as explained in the text. Assuming a positive slope group delay, $\lambda_{k+1} > \lambda_k \Rightarrow \tau_{g,h}(\lambda_{k+1}) > \tau_{g,h}(\lambda_k)$, at an increasing source wavelength impulse responses correspond with increased group delay

4.2.5 Continuous Optical Source Spectrum

If the optical power spectral density (PSD) of the light source $S_s(\lambda)$ is a continuous function of the optical wavelength λ, all previous concepts are easily extended by substituting the discrete summations (4.20) and (4.21) with the corresponding integrals over the wavelength range of definition for the function $S_s(\lambda)$. It is assumed that the optical source spectrum belongs to the space $L^1(\Re)$ of positive definite functions which are integrable over the real axis. This means physically that $S_s(\lambda)$ represents obviously a finite power optical source, where

$$S_s(\lambda) \in L^1(\Re) \tag{4.24}$$

$$\int_{-\infty}^{+\infty} S_s(\lambda)\,\mathrm{d}\lambda = 1 \tag{4.25}$$

$$H_{c,h}(z, f) = \int_{-\infty}^{+\infty} S_s(\lambda)\mathrm{e}^{-\mathrm{j}2\pi f z\tau_{g,h}(\lambda)}\,\mathrm{d}\lambda \tag{4.26}$$

$$h_{c,h}(z, t) = \Im^{-1}[H_{c,h}(z, f)] = \int_{-\infty}^{+\infty} H_{c,h}(z, f)\mathrm{e}^{\mathrm{j}2\pi f t}\,\mathrm{d}f \tag{4.27}$$

Substituting the chromatic frequency response representation (4.26) into Equation (4.27) gives the general expression for the chromatic impulse response subjected to a continuous light source spectrum:

$$h_{c,h}(z, t) = \int_{-\infty}^{+\infty}\int_{-\infty}^{+\infty} S_s(\lambda)\mathrm{e}^{\mathrm{j}2\pi f[t-z\tau_{g,h}(\lambda)]}\,\mathrm{d}\lambda\,\mathrm{d}f \tag{4.28}$$

The expression (4.28) allows an analytical calculation of the general impulse response of each individual hth fiber mode to be made for a given light source spectrum $S_s(\lambda)$.

The integral representation of the chromatic impulse response $h_{c,h}(z, t)$ that has just been derived in Equation (4.28) gives a very remarkable physical interpretation once use is made of the Fourier transform of the Dirac delta impulse. To this end, the following Fourier transform pair is obtained:

$$\delta(t - t_0) \overset{\Im}{\longleftrightarrow} \mathrm{e}^{\mathrm{j}2\pi f t_0} \tag{4.29}$$

or, more explicitly,

$$\delta(t - t_0) = \int_{-\infty}^{+\infty} \mathrm{e}^{\mathrm{j}2\pi f(t-t_0)}\,\mathrm{d}f \tag{4.30}$$

Using Equation (4.30), it is easy to solve the integration in the frequency variable f in the chromatic impulse response (4.28) by means of the Dirac delta function. Since

$$\int_{-\infty}^{+\infty} \mathrm{e}^{\mathrm{j}2\pi f[t-z\tau_{g,h}(\lambda)]}\,\mathrm{d}f = \delta[t - z\tau_{g,h}(\lambda)] \tag{4.31}$$

substituting this in the inner integration over the frequency variable in Equation (4.28) gives the following meaningful expression of the chromatic impulse response for the individual h fiber mode:

$$h_{c,h}(z, t) = \int_{-\infty}^{+\infty} S_s(\lambda)\delta[t - z\tau_{g,h}(\lambda)]\,\mathrm{d}\lambda \tag{4.32}$$

In order to solve the integration in the wavelength variable λ, the inverse function $\lambda = \zeta_{g,h}(\tau)$ of the group delay $\tau = \tau_{g,h}(\lambda)$ for the selected hth fiber mode now needs to be introduced, namely

$$\lambda = \zeta_{g,h}(\tau) \Leftrightarrow \tau = \tau_{g,h}[\zeta_{g,h}(\tau)] \tag{4.33}$$

The group delay versus wavelength usually has a parabolic-like shaping for the parabolic-clad refractive index profile. This leads in general to a double-valued inverse function $\zeta_{g,h}(\tau)$. Even

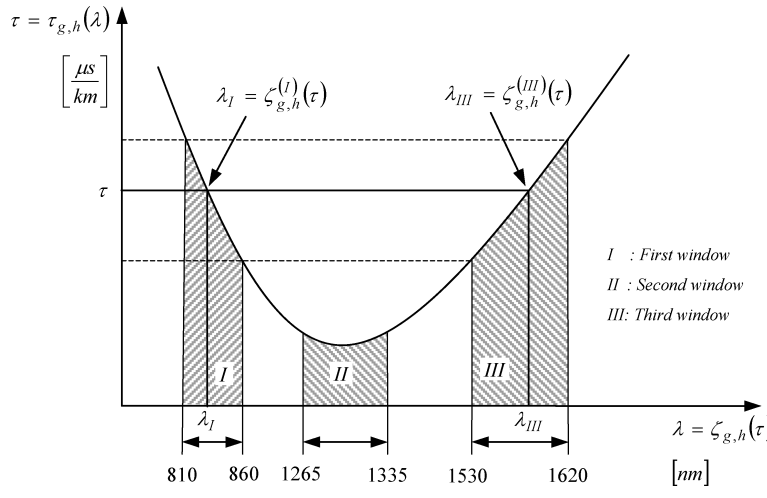

Figure 4.6 Qualitative representation of the group delay function versus the wavelength $\tau = \tau_{g,h}(\lambda)$ for the individual hth fiber mode. In general, the inverse function $\lambda = \zeta_{g,h}(\tau)$ is not single-valued if the inverse function co-dominium included the whole wavelength range. However, if the wavelength co-dominium is restricted to a specified window range, the inverse function $\lambda = \zeta_{g,h}(\tau)$ becomes single-valued

using different refractive index profiles, the inverse function $\zeta_{g,h}(\tau)$ will not be in general be single-valued. Figure 4.6 shows these concepts.

In the following it will be assumed that the wavelength range for the inverse function of the group delay belongs to a specified optical window, as depicted in Figure 4.6. In this case, the group delay inverse function $\lambda = \zeta_{g,h}(\tau)$ becomes single-valued and to each group delay value belonging to the selected window range a well-defined wavelength can be assigned through the inverse function $\lambda = \zeta_{g,h}(\tau)$. According to Equation (4.15), the Dirac delta function is defined by the integral

$$\int_{-\infty}^{+\infty} \phi(t)\delta(t - t_0)\,\mathrm{d}t = \phi(t_0) \tag{4.34}$$

The chromatic impulse response derived in Equation (4.32) has the same mathematical form as Equation (4.34) in which the time constant t_0 is replaced by $z\tau_{g,h}(\lambda)$ and the time integration variable t by the wavelength λ. The latter assertion is important because the test function $\phi(t)$ in Equation (4.32) coincides with the power spectral density $S_s(\lambda)$ of the light source and is defined over the wavelength domain. This is the reason for introducing the inverse function $\lambda = \zeta_{g,h}(\tau)$ of the group delay $\tau = \tau_{g,h}(\lambda)$.

From a conceptual point of view, in order to solve the integral in Equation (4.32) for each pair of distance variable z and time variable t the wavelengths that are the roots of the argument of the Dirac delta need to be found and those wavelength values need to be assigned to the power spectral density of the light source $S_s(\lambda)$. In order to proceed formally to the solution of the problem the integral in Equation (4.32) is considered and the following change of the variable is performed:

$$\begin{aligned} u &= z\tau_{g,h}(\lambda) \\ \mathrm{d}u &= z\frac{\mathrm{d}\tau_{g,h}(\lambda)}{\mathrm{d}\lambda}\mathrm{d}\lambda \\ \mathrm{d}\lambda &= \frac{1}{z}\,\frac{\mathrm{d}\lambda}{\mathrm{d}\tau}\mathrm{d}u = \frac{1}{z}\,\frac{\mathrm{d}\zeta_{g,h}(\tau)}{\mathrm{d}\tau}\mathrm{d}u \end{aligned} \tag{4.35}$$

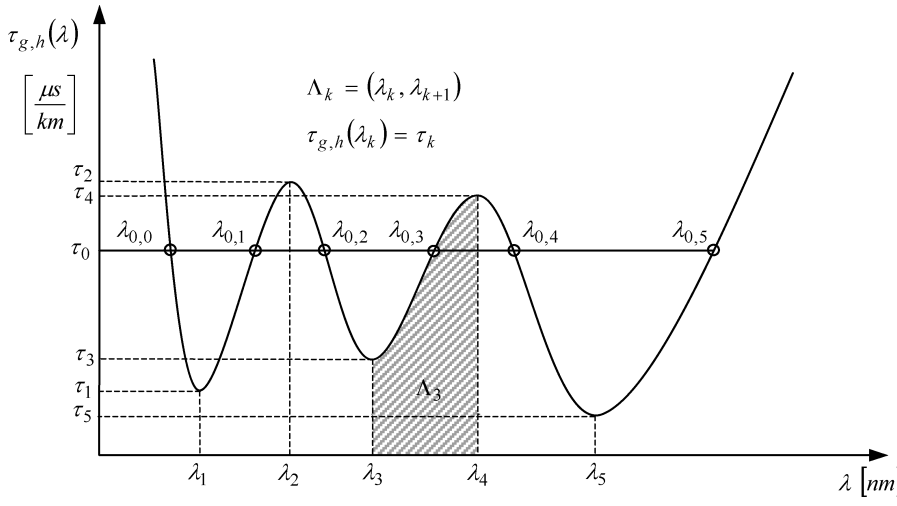

Figure 4.7 Generalized group delay function $\tau = \tau_{g,h}(\lambda)$ showing the multiple-valued inverse function $\{\lambda_{0,k}\} = \zeta_{g,h}(\tau_0)$. Each stationary point λ_k defines the interval $\Delta_k = (\lambda_k, \lambda_{k+1})$ where the inverse group delay function $\lambda = \zeta_{g,h}(\tau)$ is single-valued

In the above expressions the inverse group delay definition (4.33) and the consequent first-order derivative are used:

$$\lambda = \zeta_{g,h}(\tau) \Rightarrow \frac{d\lambda}{d\tau} = \frac{d\zeta_{g,h}(\tau)}{d\tau} \tag{4.36}$$

In order to maintain simultaneously full generality in the mathematical development, but avoiding any ambiguity in inverting the group delay function due to multiple-valued behavior of $\lambda = \zeta_{g,h}(\tau)$, the indefinite integration interval in Equation (4.32) can conveniently be decomposed into a joint finite interval partitioning where each wavelength interval $\Lambda_k = (\lambda_k, \lambda_{k+1})$ is characterized by a single-valued inverse group delay function. Figure 4.7 shows the required integration interval decomposition for a complex case of group delay function exhibiting multiple stationary points (local minima and maxima).

The complexity of the group delay function serves to illustrate the decomposition procedure. Each local minima or maxima is identified sequentially starting from the shortest wavelength as λ_1. The next stationary point will be labeled λ_2 and so on, up to the last stationary point labeled λ_N. There is therefore a total of N stationary points and $N + 1$ decomposing intervals, including the first interval $(-\infty, \lambda_1)$ and the last one $(\lambda_n, +\infty)$. Of course, the sum of the measures of all the $N + 1$ intervals coincides with the real axis $(-\infty, +\infty)$.

Once such decomposition is provided, the chromatic impulse response (4.32) can be rewritten as the overlap of the partial integrals into each of the intervals $\Lambda_k = (\lambda_k, \lambda_{k+1})$:

$$\begin{aligned} h_{c,h}(z,t) = &\int_{-\infty}^{\lambda_1} S_s(\lambda)\delta[t - z\tau_{g,h}(\lambda)]\,d\lambda \\ &+ \sum_{k=1}^{N-1} \int_{\lambda_k}^{\lambda_{k+1}} S_s(\lambda)\delta[t - z\tau_{g,h}(\lambda)]\,d\lambda \\ &+ \int_{\lambda_N}^{+\infty} S_s(\lambda)\delta[t - z\tau_{g,h}(\lambda)]\,d\lambda \end{aligned} \tag{4.37}$$

Substituting the integration variable according to Equation (4.35) and defining the group delay values at each stationary point with

$$\tau_{g,h}(\lambda_k) = \tau_k \tag{4.38}$$

gives

$$\begin{aligned} h_{c,h}(z,t) = {} & \frac{1}{z}\left[\frac{d\zeta_{g,h}(\tau)}{d\tau}\right]_{\Lambda_0}\int_{+\infty}^{z\tau_1} S_s\left[\zeta_{g,h}\left(\frac{u}{z}\right)\right]\delta[t-u]\,du \\ & + \sum_{k=1}^{N-1}\frac{1}{z}\left[\frac{d\zeta_{g,h}(\tau)}{d\tau}\right]_{\Lambda_k}\int_{z\tau_k}^{z\tau_{k+1}} S_s\left[\zeta_{g,h}\left(\frac{u}{z}\right)\right]\delta[t-u]\,du \\ & + \frac{1}{z}\left[\frac{d\zeta_{g,h}(\tau)}{d\tau}\right]_{\Lambda_N}\int_{z\tau_N}^{+\infty} S_s\left[\zeta_{g,h}\left(\frac{u}{z}\right)\right]\delta[t-u]\,du \end{aligned} \tag{4.39}$$

The derivative $[d\zeta_{g,h}(\tau)/d\tau]_{\Lambda_k}$ of the inverse group delay function must be included within the corresponding interval Λ_k in order to have a single-valued function. As a consequence of the definition of the interval Λ_k, the derivative is definite positive or definite negative within each interval. Therefore the derivative sign is constant on the selected interval Λ_k. These latter observations lead to a significant simplification of the above integral representation of the chromatic impulse response. Figure 4.8 shows qualitatively the behavior of the group delay function within each interval Λ_k.

Referring to Figure 4.8, the two possible intervals are considered separately, namely Λ_p with a negative slope and Λ_q characterized instead by a positive group delay slope. In terms of optical fiber transmissions, to Λ_p will be referred to as a normal transmission region and Λ_q as an anomalous transmission region:

1. Λ_p, a normal transmission region:

$$\left[\frac{d\zeta_{g,h}(\tau)}{d\tau}\right]_{\Delta_p} < 0 \Rightarrow \left[\frac{d\zeta_{g,h}(\tau)}{d\tau}\right]_{\Lambda_p} = -\left|\frac{d\zeta_{g,h}(\tau)}{d\tau}\right|_{\Lambda_p} \tag{4.40}$$

$$\tau_p > \tau_{p+1} \Rightarrow \int_{z\tau_p}^{z\tau_{p+1}} S_s\left[\zeta_{g,h}\left(\frac{u}{z}\right)\right]\delta[t-u]\,du = -\int_{z\tau_{p+1}}^{z\tau_p} S_s\left[\zeta_{g,h}\left(\frac{u}{z}\right)\right]\delta[t-u]\,du \tag{4.41}$$

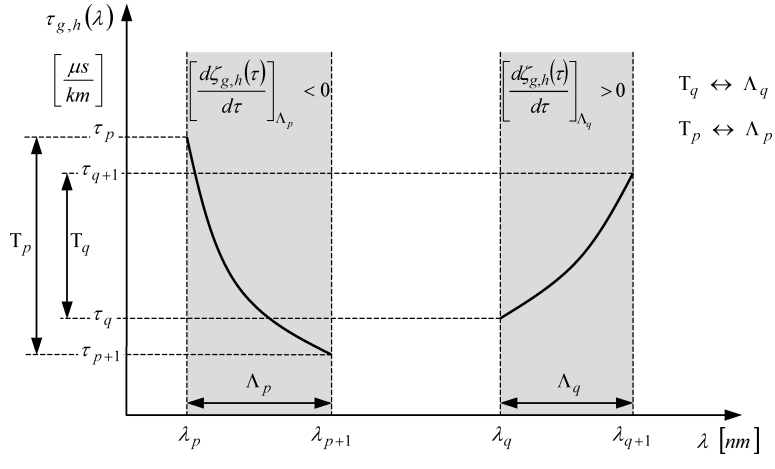

Figure 4.8 Group delay slope and integration extremes

Therefore the corresponding integral contribution becomes

$$\frac{1}{z}\left[\frac{\mathrm{d}\zeta_{\mathrm{g},h}(\tau)}{\mathrm{d}\tau}\right]_{\Lambda_p}\int_{z\tau_p}^{z\tau_{p+1}} S_{\mathrm{s}}\left[\zeta_{\mathrm{g},h}\left(\frac{u}{z}\right)\right]\delta[t-u]\,\mathrm{d}u$$
$$= +\frac{1}{z}\left|\frac{\mathrm{d}\zeta_{\mathrm{g},h}(\tau)}{\mathrm{d}\tau}\right|_{\Lambda_p}\int_{z\tau_{p+1}}^{z\tau_p} S_{\mathrm{s}}\left[\zeta_{\mathrm{g},h}\left(\frac{u}{z}\right)\right]\delta[t-u]\,\mathrm{d}u \tag{4.42}$$

2. Λ_q, an anomalous transmission region:

$$\left[\frac{\mathrm{d}\zeta_{\mathrm{g},h}(\tau)}{\mathrm{d}\tau}\right]_{\Delta_q} > 0 \Rightarrow \left[\frac{\mathrm{d}\zeta_{\mathrm{g},h}(\tau)}{\mathrm{d}\tau}\right]_{\Lambda_q} = +\left|\frac{\mathrm{d}\zeta_{\mathrm{g},h}(\tau)}{\mathrm{d}\tau}\right|_{\Lambda_q} \tag{4.43}$$

$$\tau_q < \tau_{q+1} \Rightarrow \int_{z\tau_q}^{z\tau_{q+1}} S_{\mathrm{s}}\left[\zeta_{\mathrm{g},h}\left(\frac{u}{z}\right)\right]\delta[t-u]\,\mathrm{d}u > 0 \tag{4.44}$$

Therefore the corresponding integral contribution becomes:

$$\frac{1}{z}\left[\frac{\mathrm{d}\zeta_{\mathrm{g},h}(\tau)}{\mathrm{d}\tau}\right]_{\Lambda_q}\int_{z\tau_q}^{z\tau_{q+1}} S_{\mathrm{s}}\left[\zeta_{\mathrm{g},h}\left(\frac{u}{z}\right)\right]\delta[t-u]\,\mathrm{d}u$$
$$= +\frac{1}{z}\left|\frac{\mathrm{d}\zeta_{\mathrm{g},h}(\tau)}{\mathrm{d}\tau}\right|_{\Lambda_q}\int_{z\tau_q}^{z\tau_{q+1}} S_{\mathrm{s}}\left[\zeta_{\mathrm{g},h}\left(\frac{u}{z}\right)\right]\delta[t-u]\,\mathrm{d}u \tag{4.45}$$

In conclusion, independently from the normal or anomalous regions considered, the integral contribution to the chromatic impulse response in Equation (4.39) has a positive value. The derivative of the inverse group delay must be taken as the absolute value and the lower integration extreme must be the lowest value between the group delays corresponding to that interval. From Equation (4.39), the following expression for the chromatic impulse response of the selected hth fiber mode is obtained:

$$h_{\mathrm{c},h}(z,t) = \frac{1}{z}\left|\frac{\mathrm{d}\zeta_{\mathrm{g},h}(\tau)}{\mathrm{d}\tau}\right|_{\Lambda_0}\int_{z\tau_1}^{+\infty} S_{\mathrm{s}}\left[\zeta_{\mathrm{g},h}\left(\frac{u}{z}\right)\right]\delta[t-u]\,\mathrm{d}u$$
$$+\sum_{k=1}^{N-1}\frac{1}{z}\left|\frac{\mathrm{d}\zeta_{\mathrm{g},h}(\tau)}{\mathrm{d}\tau}\right|_{\Lambda_k}\int_{z\min(\tau_k,\tau_{k+1})}^{z\max(\tau_k,\tau_{k+1})} S_{\mathrm{s}}\left[\zeta_{\mathrm{g},h}\left(\frac{u}{z}\right)\right]\delta[t-u]\,\mathrm{d}u$$
$$+\frac{1}{z}\left|\frac{\mathrm{d}\zeta_{\mathrm{g},h}(\tau)}{\mathrm{d}\tau}\right|_{\Lambda_N}\int_{z\tau_N}^{+\infty} S_{\mathrm{s}}\left[\zeta_{\mathrm{g},h}\left(\frac{u}{z}\right)\right]\delta[t-u]\,\mathrm{d}u \tag{4.46}$$

The last step toward the final form of the chromatic impulse response requires the application of the definition of the Dirac delta function, as reported in Equation (4.34). However, according to the definition of the Dirac delta function, the integration interval must coincide with the whole real axis $(-\infty, +\infty)$. In the expression (4.46) of the chromatic impulse response each partial integral refers instead to a finite time interval. The conditions, if any, for the Dirac delta function first need to be found in order to be included in that integration interval, otherwise the result of the integration would be null.

In order to simplify the notation of the generic partial integral in Equation (4.46) the integration extremes with $t_{k,\min} = z\min(\tau_k, \tau_{k+1})$ and $t_{k,\max} = z\max(\tau_k, \tau_{k+1})$ are identified:

$$\int_{t_{k,\min}}^{t_{k,\max}} S_{\mathrm{s}}\left[\zeta_{\mathrm{g},h}\left(\frac{u}{z}\right)\right]\delta[t-u]\,\mathrm{d}u = \begin{cases} S_{\mathrm{s}}\left[\zeta_{\mathrm{g},h}(t/z)\right], & t_{k,\min} < t < t_{k,\max} \\ 0, & t_{k,\min} < t_{k,\max} < t \text{ or} \\ & t < t_{k,\min} < t_{k,\max} \end{cases} \tag{4.47}$$

The notation is further simplified by introducing the Boolean variable B_k associated with the normalized time interval T_k shown in Figure 4.8:

$$\left.\begin{aligned} &B_k = t \cap z\mathrm{T}_k \\ &T_k \leftrightarrow \Lambda_k = (\lambda_k, \lambda_{k+1}) \\ &T_k = (\tau_{k,\min}, \tau_{k,\max}) \\ &\tau_{k,\max} = \max(\tau_k, \tau_{k+1}) \\ &\tau_{k,\min} = \min(\tau_k, \tau_{k+1}) \end{aligned}\right\} \Rightarrow \begin{cases} B_k = 1,\ t \in z\mathrm{T}_k \\ B_k = 0,\ t \notin z\mathrm{T}_k \end{cases} \tag{4.48}$$

With the introduction of the Boolean variable B_k relative to the time interval per unit length T_k, each partial integral of Equation (4.47) can be written in the following simpler way:

$$\int_{t_{k,\min}}^{t_{k,\max}} S_\mathrm{s}\left[\zeta_{\mathrm{g},h}\left(\frac{u}{z}\right)\right]\delta[t-u]\,\mathrm{d}u = B_k\ S_\mathrm{s}\left[\zeta_{\mathrm{g},h}\left(\frac{t}{z}\right)\right] \tag{4.49}$$

Substituting expression (4.49) into Equation (4.46), the following closed form of the chromatic impulse response is found, where all integrals have been solved by means of the Dirac delta definition:

$$\begin{aligned} h_{\mathrm{c},h}(z,t) = {} & \frac{1}{z}\left|\frac{\mathrm{d}\zeta_{\mathrm{g},h}(\tau)}{\mathrm{d}\tau}\right|_{\Lambda_0} B_0\ S_\mathrm{s}\left[\zeta_{\mathrm{g},h}\left(\frac{t}{z}\right)\right] + \frac{1}{z}\left|\frac{\mathrm{d}\zeta_{\mathrm{g},h}(\tau)}{\mathrm{d}\tau}\right|_{\Lambda_N} B_N\ S_\mathrm{s}\left[\zeta_{\mathrm{g},h}\left(\frac{t}{z}\right)\right] \\ & + \frac{1}{z}\sum_{k=1}^{N-1}\left|\frac{\mathrm{d}\zeta_{\mathrm{g},h}(\tau)}{\mathrm{d}\tau}\right|_{\Lambda_k} B_k\ S_\mathrm{s}\left[\zeta_{\mathrm{g},h}\left(\frac{t}{z}\right)\right] \end{aligned} \tag{4.50}$$

It is noteworthy that no integrals appear in the closed form (4.50). The unit of measure of the chromatic impulse response is derived directly from the general expression (4.50). Since all addends have the same dimension, any one of them can be considered:

$$h_{\mathrm{c},h}(z,t)(\mathrm{W/ps}) = \frac{1}{z}(1/\mathrm{km})\left|\frac{\mathrm{d}\zeta_{\mathrm{g},h}(\tau)}{\mathrm{d}\tau}\right|_{\Lambda}(\mathrm{nm\ km/ps})\ S_\mathrm{s}\left[\zeta_{\mathrm{g},h}\left(\frac{t}{z}\right)\right](\mathrm{W/nm}) \tag{4.51}$$

The dimensions of the chromatic impulse response are W/ps and they are therefore consistent with the physical meaning attributed to the light intensity.

Before closing this section it is important to understand the physical meaning of the derivative of the inverse group delay function, given as $\mathrm{d}\zeta_{\mathrm{g},h}(\tau)/\mathrm{d}\tau$. According to the definition (4.47) of the inverse group delay function $\lambda = \zeta_{\mathrm{g},h}(\tau)$, the following relationship holds between the derivatives:

$$\frac{1}{\mathrm{d}\tau/\mathrm{d}\lambda} = \frac{1}{\mathrm{d}\tau_{\mathrm{g},h}(\lambda)/\mathrm{d}\lambda} = \frac{\mathrm{d}\lambda}{\mathrm{d}\tau} = \frac{\mathrm{d}\zeta_{\mathrm{g},h}(\tau)}{\mathrm{d}\tau} \tag{4.52}$$

Therefore, the definition of the chromatic dispersion coefficient $D(\lambda)$ as the wavelength derivative of the group delay gives the following important identification of the first-order derivative of the inverse group delay:

$$\frac{\mathrm{d}\zeta_{\mathrm{g},h}(\tau)}{\mathrm{d}\tau} = \frac{1}{\mathrm{d}\tau_{\mathrm{g},h}(\lambda)/\mathrm{d}\lambda} = \frac{1}{D[\zeta_{\mathrm{g},h}(\tau)]} \tag{4.53}$$

Substituting into Equation (4.50), the general expression of the chromatic impulse response is found using the familiar chromatic dispersion coefficients $D_k(\lambda)$ relative to each partition

interval Λ_k:

$$h_{c,h}(z,t) = \frac{1}{z}\underbrace{\left\{\frac{B_0\ S_s\left[\zeta_{g,h}(t/z)\right]}{\left|D_0\left[\zeta_{g,h}(t/z)\right]\right|}\right\}}_{\substack{\lambda=\zeta_{g,h}(t/z)\in\Lambda_0\\ \Lambda_0=(0,\lambda_1)}} + \frac{1}{z}\underbrace{\left\{\frac{B_N\ S_s\left[\zeta_{g,h}(t/z)\right]}{\left|D_N\left[\zeta_{g,h}(t/z)\right]\right|}\right\}}_{\substack{\lambda=\zeta_{g,h}(t/z)\in\Lambda_N\\ \Lambda_N=(\lambda_N,\infty)}}$$
$$+ \frac{1}{z}\sum_{k=1}^{N-1}\underbrace{\left\{\frac{B_k\ S_s\left[\zeta_{g,h}(t/z)\right]}{\left|D_k\left[\zeta_{g,h}(t/z)\right]\right|}\right\}}_{\substack{\lambda=\zeta_{g,h}(t/z)\in\Lambda_k\\ \Lambda_k=(\lambda_k,\lambda_{k+1})}} \tag{4.54}$$

The above expression represents the most general closed form of the chromatic impulse response once the light source power spectral density $S_s(\lambda)$ and the selected fiber mode group delay function versus wavelength, $\tau = \tau_{g,h}(\lambda)$ are known. According to the partitioning of the wavelength axis due to the eventual multiple stationary point group delay function, each partial wavelength interval contributes a proper portion of the light spectrum weighted by the corresponding chromatic dispersion coefficient.

In the next section the way to proceed toward the computer model of the chromatic impulse response is considered in more detail, starting with the group delay function and the light source power spectral density. In order to use the general expression (4.50) of the chromatic impulse response, the role of the Boolean variables B_k and of the wavelength intervals Λ_k must be clearly understood. In the following section, the role of the various terms composing the chromatic impulse response formula (4.50) will be clarified.

4.2.6 Solution Methods for Impulse Responses

In this section reference will be made first to the situation presented in Figure 4.9, which has been derived from Figure 4.7 by adding a Gaussian-like light source spectrum. The exotic group delay function $\tau = \tau_{g,h}(\lambda)$ presented in Figure 4.9, showing five stationary points in the central wavelength range, is quite interesting and is useful to understand the physical implication of group delay stationary points. In most real cases, assuming the usual parabolic-clad refractive index profile and circular cross-section silica-based optical fibers, the group delay function $\tau = \tau_{g,h}(\lambda)$ usually exhibits one minimum only, which corresponds to the zero-dispersion wavelength. The second case considered in this section will refer to the conventional parabolic-like group delay with only one zero-dispersion wavelength.

4.2.6.1 Multiple-Valued Group Delay Function

As discussed previously, the first derivative of the group delay gives the chromatic dispersion for the selected fiber mode. Assuming several stationary points in the group delay function is equivalent to assuming corresponding zero-dispersion wavelengths. This situation is encountered in several applications of dispersion flattened optical fibers like ITU-T G.655 standards for single-mode fibers. In fact, in order to achieve the chromatic dispersion flattening behavior within a specified wavelength range the group delay function $\tau = \tau_{g,h}(\lambda)$ must exhibit a wavelength ripple behavior in the flattening interval, a situation closely modeled by the group delay function reported in Figure 4.7.

Referring to the light source spectrum shown in Figure 4.9, λ_L and λ_R define the shortest (left) and longest (right) wavelength extremes respectively, which identify the source power spectral

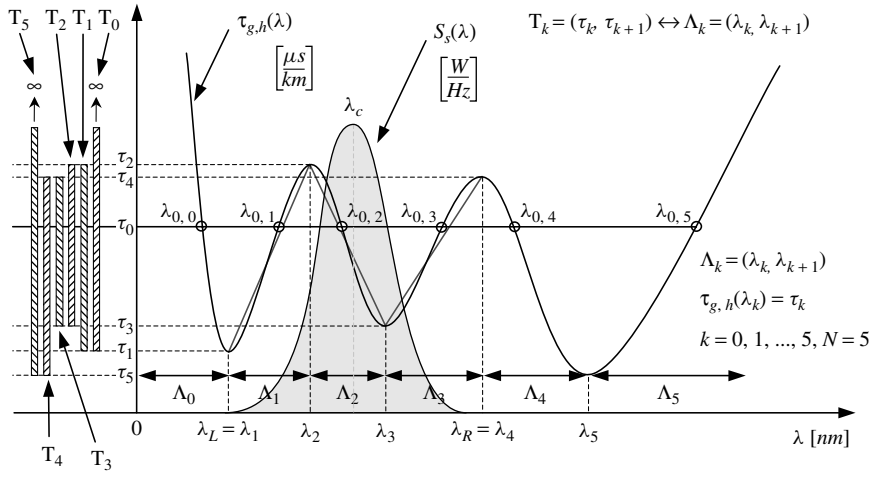

Figure 4.9 Representation of the group delay function $\tau = \tau_{g,h}(\lambda)$ with ripple behavior showing as multivalued inverse function $\lambda = \zeta_{g,h}(\tau)$. The wavelength axis is partitioned into finite wavelength intervals corresponding to the group delay function stationary points λ_k. On the same graph is shown the Gaussian-shaped optical power spectral density function of the optical source. On the left side are reported the temporal intervals T_k. The contributing temporal intervals have been highlighted. The piecewise linear approximation of the group delay in the light spectrum overlapped intervals (λ_1, λ_4) have been highlighted

density contributions. In practical cases it will be assumed that beyond those extremes the power contribution can be neglected without altering the chromatic impulse response. The situation presented in Figure 4.9 simplifies further if it is assumed that the source spectrum wavelength range (λ_L, λ_R) is identified by the wavelength extremes (λ_1, λ_4) defined by the wavelengths corresponding to the stationary points of the group delay function. Accordingly, the integrating interval must be extended from $\lambda_L = \lambda_1$ to $\lambda_R = \lambda_4$. In fact, outside that interval there would be no power spectral density available and consequently there would be no energy contribution for the chromatic impulse response.

Based on Figure 4.9, the contributions of the wavelength intervals labeled Λ_0, Λ_4 and $\Lambda_5 = \Lambda_N$ can be discarded from the chromatic impulse response (4.50), therefore leaving only the remaining three intervals, Λ_1, Λ_2 and Λ_3:

$$h_{c,h}(z,t) = \frac{1}{z}\left\{\left|\frac{d\zeta_{g,h}(\tau)}{d\tau}\right|_{\Lambda_1} B_1\ S_s\left[\zeta_{g,h}\left(\frac{t}{z}\right)\right] + \left|\frac{d\zeta_{g,h}(\tau)}{d\tau}\right|_{\Lambda_2} B_2\ S_s\left[\zeta_{g,h}\left(\frac{t}{z}\right)\right] + \left|\frac{d\zeta_{g,h}(\tau)}{d\tau}\right|_{\Lambda_3} B_3\ S_s\left[\zeta_{g,h}\left(\frac{t}{z}\right)\right]\right\} \tag{4.55}$$

In order to simplify the description the group delay in the three wavelength intervals are approximated by proper linear functions, as illustrated in Figure 4.9 by straight lines. Accordingly, the derivative $|d\zeta_{g,h}(\tau)/d\tau|$ of the linearized group delay characteristic evaluated for each of the intervals Λ_1, Λ_2 and Λ_3 assumes a constant positive value:

$$C_k = \left|\frac{d\zeta_{g,h}(\tau)}{d\tau}\right|_{\Lambda_k} = \frac{1}{|d\tau_{g,h}(\lambda)/d\lambda|_{\Lambda_k}} \equiv \frac{1}{|\hat{D}_k|}, \quad \text{(nm km/ps)} \tag{4.56}$$

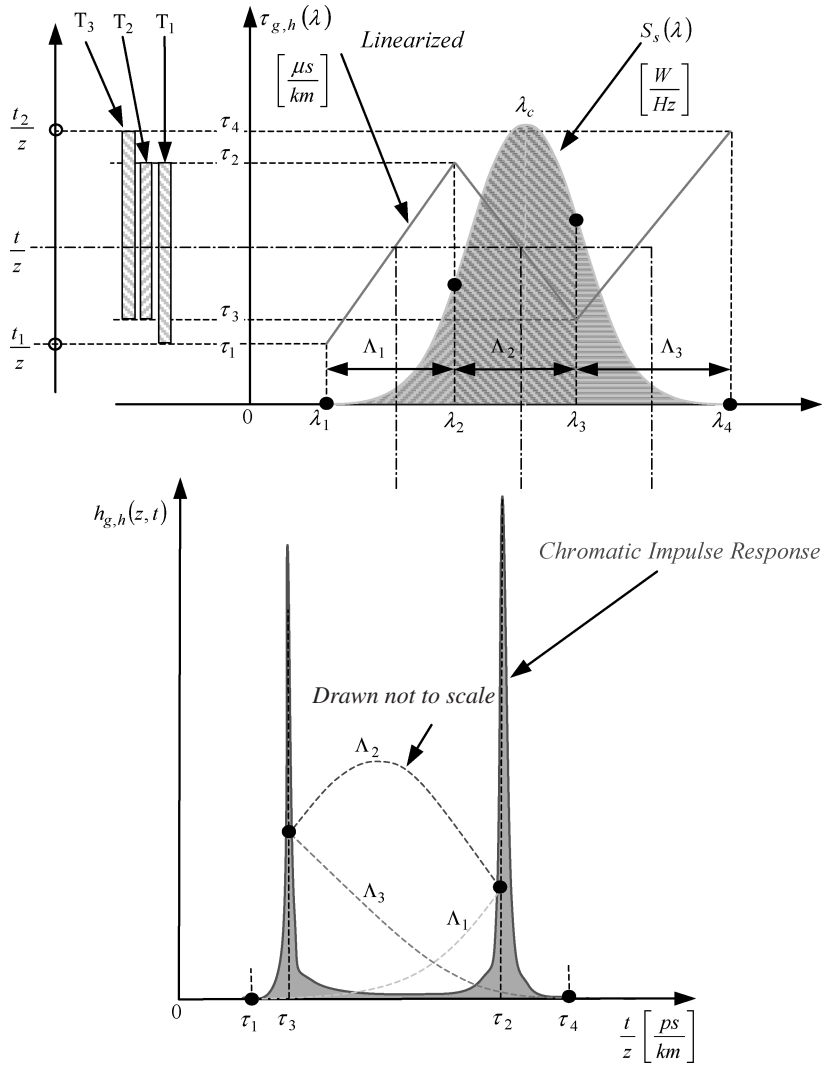

Figure 4.10 Top: graphical representation used for the impulse response computation in the text. The group delay function shows linearized ripple behavior, exhibiting one minimum and one maximum in the source wavelength range. The source power spectral density has a Gaussian-like shape. Bottom: chromatic impulse response achieved using the procedure described in the text. Due to the multiple-valued inverse group delay function, different spectral contributions are superposed on the impulse response build-up. The two zero-dispersion wavelengths λ_2 and λ_3 originate from the corresponding dual-peak chromatic impulse response in τ_2 and τ_3

The general expression of the chromatic impulse response in Equation (4.54) is made up of as many adding terms as there are different wavelength intervals interested by the light source spectrum. Referring to Figure 4.10, where only the interested wavelength intervals are given, for any fixed distance z the time instant t_1 is considered such that the ratio $t_1/z = \tau_1$ coincides with the first point of the interval T_1. For all time instants $t \geq t_1$ such that $t/z \in T_1$, the Boolean variable $B_1 = 1$ and the first term in Equation (4.54) contribute to the chromatic impulse response with the

quantity $(1/z)C_1 S_s[\zeta_{g,h}(t/z)]$. For every time instant $t \geq t_2$ such that $t/z \in T_2$, the Boolean variable $B_2 = 1$ and the second term in Equation (4.54) contribute to the chromatic impulse response with the quantity $(1/z)C_2 S_s[\zeta_{g,h}(t/z)]$. The same reasoning applies to the third term in Equation (4.54) for every time instant $t \geq t_3$ such that $t/z \in T_3$. There is only one more remark to make about the power spectral density $S_s[\zeta_{g,h}(t/z)]$: for the given time instant t the inverse function $\zeta_{g,h}(t/z)$ is associated with a unique wavelength $\lambda \in \Lambda$ in the selected wavelength interval Λ. The contribution to the chromatic impulse response therefore coincides with the light source spectrum evaluated at the wavelength $\lambda = \zeta_{g,h}(t/z)$ with $\lambda \in \Lambda$.

In order to build up the chromatic impulse response for the case considered in Figure 4.10 the three contributions in Equation (4.54) that correspond to proper time intervals for the fixed distance z need to be considered. It is noted that each coefficient $\hat{D}_k$ is defined in Equation (4.56), where $\hat{D}_k$ equals the value of the first-order derivative of the linearized group delay in the wavelength interval Λ_k.

Without losing generality, the treatment can be simplified by assuming that the absolute value of the three slope coefficients are equal: $|\hat{D}_1| = |\hat{D}_2| = |\hat{D}_3| = D$.

1. $\tau_1 < t/z < \tau_3$:

$$h_{c,h}(z,t) = \frac{1}{zD} S_s \left[\zeta_{g,h}\left(\frac{t}{z}\right) \right]_{\lambda = \zeta_{g,h}(t/z) \in \Lambda_1} \tag{4.57}$$

2. $\tau_3 < t/z < \tau_4$:

$$h_{c,h}(z,t) = \frac{1}{zD} \left\{ S_s \left[\zeta_{g,h}\left(\frac{t}{z}\right) \right]_{\lambda = \zeta_{g,h}(t/z) \in \Lambda_1} + S_s \left[\zeta_{g,h}\left(\frac{t}{z}\right) \right]_{\lambda = \zeta_{g,h}(t/z) \in \Lambda_2} + S_s \left[\zeta_{g,h}\left(\frac{t}{z}\right) \right]_{\lambda = \zeta_{g,h}(t/z) \in \Lambda_3} \right\} \tag{4.58}$$

3. $\tau_4 < t/z < \tau_2$:

$$h_{c,h}(z,t) = \frac{1}{zD} \left\{ S_s \left[\zeta_{g,h}\left(\frac{t}{z}\right) \right]_{\lambda = \zeta_{g,h}(t/z) \in \Lambda_1} + S_s \left[\zeta_{g,h}\left(\frac{t}{z}\right) \right]_{\lambda = \zeta_{g,h}(t/z) \in \Lambda_2} \right\} \tag{4.59}$$

Looking at the three contributions to the chromatic impulse response in the corresponding three time intervals reported above, it can be concluded that, apart from the linearization approximation, which is mainly devoted to simplifying the results and highlighting the conclusions, the chromatic impulse response reproduces the source power spectrum density through the inverse group delay function $\lambda = \zeta_{g,h}(t/z)$. The assumption of a linear group delay function within each partition interval Λ_k allows a constant chromatic dispersion coefficient $\hat{D}_k$ to be used within each partition interval Λ_k. This leads analogously to a linear relationship within each partial interval Λ_k between the power spectral density shape and the consequent impulse response. This conclusion is quite important as it helps in understanding the background to the chromatic impulse response behavior. This has been clearly reported in the graphical construction used in Figure 4.10 to draw the qualitative chromatic impulse response. According to the partition of the wavelength interval, the corresponding group delay components lead to the chromatic impulse response made up of several contributions, as expressed in Equations (4.57), (4.58) and (4.59). Computed-generated chromatic impulse responses in different multivalued group delay functions will follow in the next section.

One fundamental remark needs to be understood clearly now. To this end, the following knowledge steps are considered:

1. The linearity assumption of each group delay segment determines the corresponding contribution to the impulse response and coincides with the shape of the portion of the light source spectrum excited by that wavelength interval.
2. Due to the multiple-valued group delay function, the same time interval can generally be interested by multiple wavelength intervals, therefore leading to the superposition of different source spectral components.
3. Each stationary wavelength in the multivalued (ripple) group delay function behaves like a singularity in the chromatic impulse response. According to the general expression (4.54), when the first-order derivative of the group delay has a stationary point, the corresponding null value of the chromatic dispersion coefficient makes its singular contribution to the overall response., when the first order derivative of the group delay has a stationary point, the corresponding null value of the chromatic dispersion coefficient makes its singular contribution to the overall response.
4. Including multiple zero-dispersion wavelengths in the light source spectrum range determines a corresponding multipeak chromatic impulse response. Accordingly, contributions of the linearized parts to the overall impulse response become almost negligible.

In conclusion, in the case presented in Figure 4.9, even if each segmented (linearized) group delay Λ_k leads to a mirroring of the corresponding source spectral shape into a partial contribution to the chromatic impulse response, the two stationary wavelengths λ_2 and λ_3 lead to the characteristic dual-peak chromatic impulse response shown in the Figure 4.10. The spectral superposition due to the multiple-valued group delay function with at least one stationary point in the spectral power range of the optical source has given a false impulse response identification for the source power spectral density.

The intensity of each peak is given by the value of the power spectral density at the corresponding zero-dispersion wavelength. This is a direct consequence of the property of the Dirac delta function. This property is general: corresponding to every zero-dispersion wavelength λ_k in the group delay function, the chromatic impulse response exhibits a sharp peak at the normalized time instant τ_k given by $\tau_k = \tau_{g,h}(\lambda_k)$. The intensity of the peak response is proportional to the value of the source power spectral density measured at the same zero-dispersion wavelength $S_s(\lambda_k)$.

In the following section the more traditional parabolic-like group delay function, as expected in every multimode optical fiber with an optimized profile grading, is considered and the straightforward identification of the assumed power spectral density of the light source with the chromatic impulse response is found.

4.2.6.2 Parabolic-Like Group Delay Functions

In the case of a parabolic-like group delay function exhibiting only one minimum value, the general expression for the chromatic impulse response in Equation (4.54) is considerably simplified. Since the group delay function exhibits only one stationary point, for the zero-dispersion wavelength where the group delay reaches the minimum value, $N = 1$ and Equation (4.54) reduces to the following expression:

$$h_{c,h}(z,t) = \frac{1}{z}\left\{\frac{B_0 S_s[\zeta_{g,h}(t/z)]}{|D_0[\zeta_{g,h}(t/z)]|} + \frac{B_N S_s[\zeta_{g,h}(t/z)]}{|D_N[\zeta_{g,h}(t/z)]|}\right\} \tag{4.60}$$

It was found from Equation (4.53) that the chromatic dispersion coefficient $D_k(\lambda)$ is related to the inverse group delay function $\lambda = \zeta_{g,h}(\tau)$ in the selected single-valued wavelength interval Λ_k by the following equation:

$$\left[\frac{d\zeta_{g,h}(\tau)}{d\tau}\right]_{\tau\in T_k} = \frac{1}{[d\tau_{g,h}(\lambda)/d\lambda]_{\lambda\in\Lambda_k}} = \frac{1}{D_k[\zeta_{g,h}(\tau)]} \tag{4.61}$$

In order to avoid misunderstanding, the chromatic dispersion coefficient $D_0(\lambda)$ coincides with the first-order wavelength derivative of the group delay function evaluated in the wavelength range to the left of the zero-dispersion wavelength, $\Lambda_0 = (\lambda \leq \lambda_0)$, while $D_1(\lambda)$ coincides with the first-order wavelength derivative of the group delay function evaluated in the wavelength range to the right of the zero-dispersion wavelength $\Lambda_1 = (\lambda \geq \lambda_0)$. Similarly, the two Boolean variables B_0 and B_1 refer respectively to the overlapping condition of the normalized time variable $\tau = t/z$ with intervals T_0 and T_1.

In order to understand clearly the interaction between the source power spectral density and the group delay of the selected fiber mode, in the following, three different cases will be considered corresponding to the position of the central wavelength of the source spectrum. Precisely, first the case where the spectrum $S_s(\lambda)$ is completely confined within the normal spectral region will be considered, with energy released to the wavelength portion to the left of the zero-dispersion wavelength λ_0. The second case will deal with a source spectrum centered on the zero-dispersion wavelength, with $\lambda_c = \lambda_0$. Finally, the third case reports the condition of anomalous spectral excitation, assuming that the whole source energy is released to the wavelength portion to the right of the zero-dispersion wavelength.

4.2.6.2.1 Spectral Excitation in the Normal 850 nm Range

The source power spectral density has a Gaussian-like profile but it is limited to the finite wavelength range between λ_L and λ_R, with $\lambda_L < \lambda_R < \lambda_0$:

$$S_s(\lambda) = 0, \qquad (\lambda \leq \lambda_L) \cup (\lambda \geq \lambda_R) \tag{4.62}$$

Figure 4.11 gives the complete graphical description for the normal excitation condition.

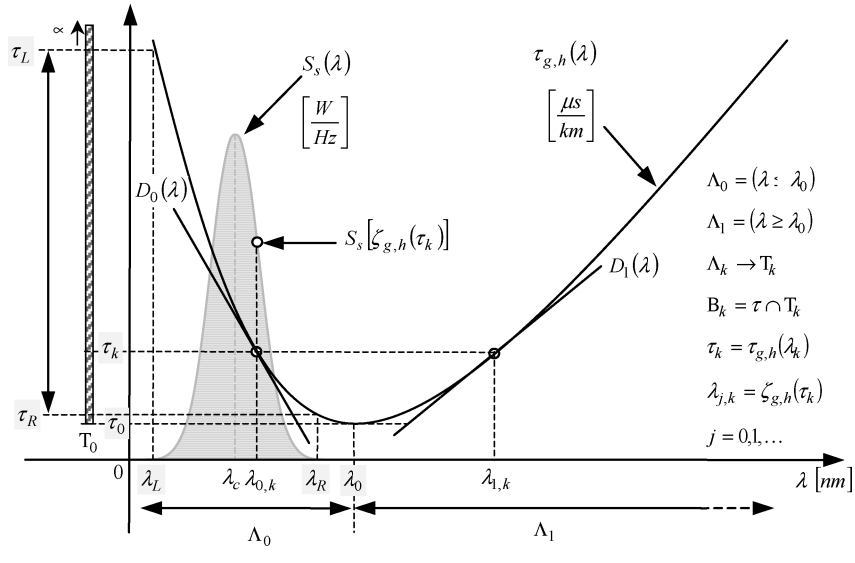

Figure 4.11 Graphical representation of the parabolic-like group delay function for the selected fiber mode and of the source PSD providing mode excitation in the normal region. The optical spectrum is fully confined in the normal region to the left of the zero-dispersion wavelength and consequently the inverse group delay function $\lambda = \zeta_{g,h}(\tau)$ is strictly single-valued for every time $\tau \geq \tau_0$. The source spectral interval is defined by the two limiting wavelengths, $\lambda_L < \lambda_R$. The condition for normal excitation translates into $\lambda_L < \lambda_R < \lambda_0$

Since there is no spectral content to the right side of λ_0, the chromatic impulse response reported in Equation (4.60) reduces to one term only:

$$h_{c,h}(z,t) = \frac{1}{z}\frac{B_0 S_s[\zeta_{g,h}(t/z)]}{|D_0[\zeta_{g,h}(t/z)]|} \tag{4.63}$$

This expression, although quite simple, is the most common chromatic impulse response formula. The only limitation is that the source power spectrum belongs to a single-valued wavelength interval of the group delay function for the selected fiber mode. The Boolean variable $B_0 = \tau \cap T_0$. Referring to Figure 4.11, it is clear that the useful time interval for not having a zero spectral contribution must coincide with the time interval $T_s = (\tau_R, \tau_L)$ defined between normalized instants $\tau_R = \tau_{g,h}(\lambda_R)$ and $\tau_L = \tau_{g,h}(\lambda_L)$. Since $T_s \subset T_0$, it can be concluded that for every normalized time instant $\tau \in T_s \Rightarrow B_0 = \tau \cap T_s = \tau \cap T_0 = 1$. Assuming that $\tau \in T_s = (\tau_R, \tau_L)$, the Boolean variable is always true and the chromatic impulse response (4.63) becomes

$$h_{c,h}(z,t) = \frac{1}{z}\frac{S_s[\zeta_{g,h}(t/z)]}{|D_0[\zeta_{g,h}(t/z)]|}, \quad z\tau_R \le t \le z\tau_L \tag{4.64}$$

The expression above has the following important physical meaning. For any fixed distance z the chromatic impulse response in the normal region is defined in the time interval $z\tau_R \le t \le z\tau_L$ and is given by the source power spectral density weighted by the reciprocal of the chromatic dispersion coefficient.

It is very important to note the linear scaling behavior of the chromatic impulse response with the distance. In fact, by increasing the distance z in Equation (4.64) the corresponding definition interval increases proportionally and the whole chromatic impulse response becomes broader. This is a consequence of the fact that the group delay function is defined as normalized time delay, namely delay per unit distance. Another remarkable corollary of this behavior is that the chromatic impulse response, even if it broadens linearly with the increasing distance, does not change the shape. In other words, the pulse shape is fixed for every distance z regardless of how short or how long it can be, and the time axis t is scaled according to the distance.

Figure 4.12 shows a qualitative drawing of the chromatic impulse response as derived in Equation (4.64) and assumes the same spectral characteristics presented in Figure 4.11. The effect of the nonlinear group delay function in the wavelength region of the source PSD is evident from the qualitative drawing of the chromatic impulse response presented in Figure 4.12. The variation of the slope of the group delay versus the wavelength in the denominator of Equation (4.64) modifies the chromatic impulse response compared to the source PSD. Referring to Figure 4.11, the slope at the initial time instant $t_{start} = z\tau_R$ has a much lower value than the slope at the final time instant $t_{stop} = z\tau_L$. This variation determines a different weighting action on the spectral profile of the source PSD, leading to the impulse response qualitatively presented in Figure 4.12. It is evident from Equation (4.64) that if the group delay can be assumed to be a linear function in the source spectrum wavelength interval, the corresponding chromatic impulse response would have been identical to the source spectrum profile converted in the time domain through the inverse group delay function $\tau = \zeta_{g,h}(\lambda)$.

4.2.6.2.2 Spectral Excitation in the Anomalous 1550 nm Range

In this section the chromatic impulse response is considered when the source power spectral density is localized in the anomalous wavelength region on the right side of the zero-dispersion wavelength. In standard optical fibers based on doped silica glass, the anomalous region corresponds to the third optical window in the 1550 nm wavelength range.

It is assumed again that the source power spectral density has a Gaussian-like profile but it is limited to the finite wavelength range between λ_L and λ_R, with $\lambda_0 < \lambda_L < \lambda_R$:

$$S_s(\lambda) = 0, \qquad (\lambda \le \lambda_L) \cup (\lambda \ge \lambda_R) \tag{4.65}$$

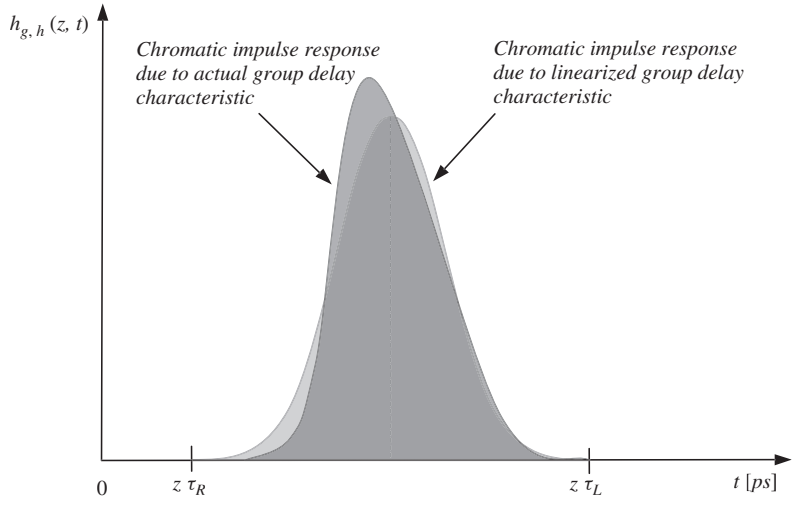

Figure 4.12 Qualitative drawing of the chromatic impulse response for the spectral characteristic presented in Figure 4.11. The initial time instant is $t_{start} = z\tau_R$ and the final time instant is $t_{stop} = z\tau_L$. The normalized instants τ_R and τ_L have been defined in the text. The impulse response corresponding to the source PSD in the case of a linear group delay with a constant chromatic dispersion coefficient is shown in a light shade. The distortion of the real pulse with respect to the source PSD depends on the nonlinear group delay in the source wavelength interval

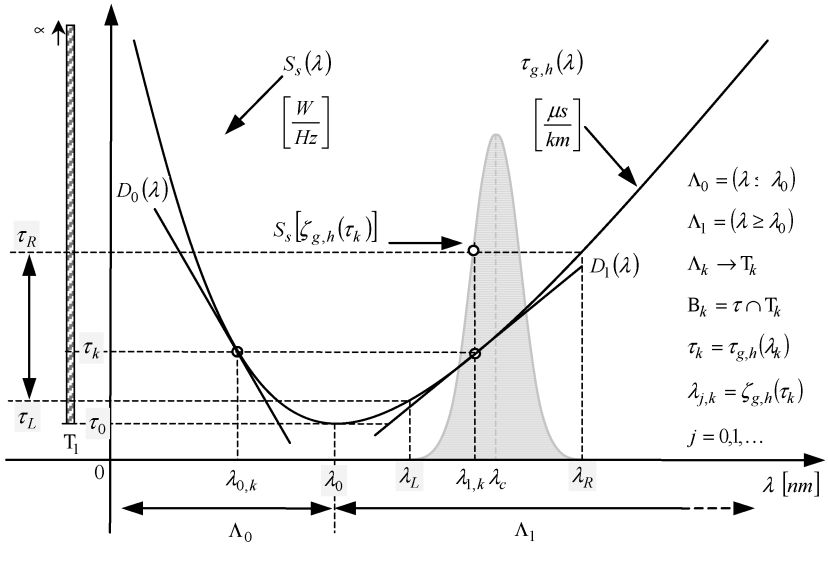

Figure 4.13 Graphical representation of the parabolic-like group delay function for the selected fiber mode and of the source power spectral density which provides mode excitation in the anomalous region. The optical spectrum is fully confined in the region to the right of the zero-dispersion wavelength and consequently the inverse group delay function $\lambda = \zeta_{g,h}(\tau)$ is strictly single-valued for every time $\tau \geq \tau_0$. The source spectral interval is defined by the two limiting wavelengths, $\lambda_L < \lambda_R$. The condition for anomalous excitation requires $\lambda_0 < \lambda_L < \lambda_R$

Figure 4.13 gives a graphical description of the anomalous excitation condition that is being considered. For any fixed distance z, the chromatic impulse response $h_{c,h}(z, t)$ is defined over the time interval $z\tau_L \leq t \leq z\tau_R$, as reported on the left side of Figure 4.13. Due to the inverted sign of the slope between the normal and the anomalous wavelength intervals, the time interval extremes are inverted with respect to the previous case. The slope of the group delay is positive in the anomalous region and the longest wavelength λ_R in the source spectrum corresponds to the longest time τ_R, while at the shortest spectrum wavelength λ_L the group delay is associated with the shortest time τ_L. As already mentioned in the previous section, in the anomalous wavelength region the shortest wavelength spectral components travel faster than the longer wavelength components. Moreover, due to the reduced slope with respect to the previous case of normal excitation, the total impulse response duration is reduced considerably for the same source spectrum. In other words, this means that for a given light source spectrum, the anomalous region produces a faster chromatic impulse response than the normal region. This is understandable because for a given wavelength interval the corresponding variation of the group delay is greater at increasing slope, like in the normal region.

Since there is no spectral content to the left side of λ_0, the general expression (4.60) of the chromatic impulse response for a parabolic-like group delay reduces to only one term again:

$$h_{c,h}(z, t) = \frac{1}{z} \frac{B_1 S_s \left[\zeta_{g,h}(t/z)\right]}{|D_1[\zeta_{g,h}(t/z)]|} \tag{4.66}$$

Following the same reasoning as in the previous section, it can be concluded that the Boolean variable $B_1 = \tau \cap T_1$ is always true for all the temporal subsets $T_s = (\tau_L, \tau_R) \subset T_1$ and so can be removed from the previous expression. In conclusion, Equation (4.66) simplifies further to

$$h_{c,h}(z, t) = \frac{1}{z} \frac{S_s[\zeta_{g,h}(t/z)]}{|D_1[\zeta_{g,h}(t/z)]|}, \qquad z\tau_L \leq t \leq z\tau_R \tag{4.67}$$

Proceeding as in the case of normal excitation, it can be conclude that for any fixed distance z the chromatic impulse response in the anomalous region is defined in the time interval $z\tau_L \leq t \leq z\tau_R$ and is given by the source power spectral density weighted by the reciprocal of the chromatic dispersion coefficient.

Figure 4.14 shows qualitatively the profile of the chromatic impulse response according to Equation (4.67) and the spectral characteristics shown in Figure 4.13. The shortest wavelength components experience a lower value of the chromatic dispersion coefficient with respect to the longer spectral components. This causes a slight distortion of the chromatic impulse response profile when compared with the source power spectral density. According to the chromatic impulse formula (4.67) and Figure 4.13, it is clear that faster spectral components (associated with shorter wavelengths) give corresponding lower values of the chromatic dispersion coefficient and consequently a smoother rise time transient of the impulse response. The opposite effect holds for longer spectral components, which induce instead a steeper falling transient in the pulse falling edge.

The next section will report computed chromatic impulse response examples in order to clarify this behavior.

4.2.6.2.3 Spectral Excitation in the Low-Dispersion 1310 nm Range

In this section the case where the spectral excitation is localized around the minimum group delay wavelength is considered. Since the slope reaches its minimum value, the corresponding impulse response will exhibit the fastest behavior, reaching the minimum pulse width available for the given source power spectral density. This is the reason for having the minimum pulse dispersion in the second window operation of optical transmission systems based on single-mode fiber. As usual, the source power spectral density is assumed to have a Gaussian-like profile, limited to the finite

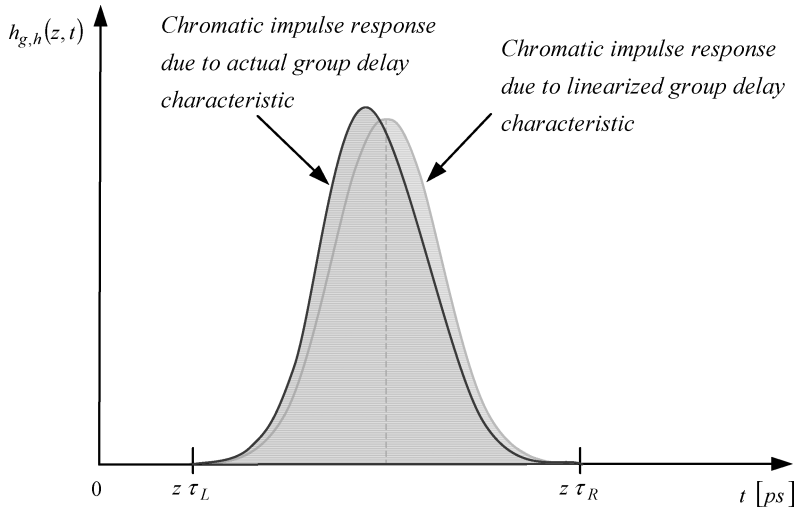

Figure 4.14 Chromatic impulse response for the spectral characteristic presented in Figure 4.13. The initial time instant is $t_{\text{start}} = z\tau_{\text{L}}$ and the final time instant is $t_{\text{stop}} = z\tau_{\text{R}}$. In the anomalous wavelength range, spectral components are associated with the pulse precursors while spectral components generate pulse postcursors. The impulse response corresponding to the source PSD in the case of a linear group delay with a constant chromatic dispersion coefficient is shown in a light shade. The slight distortion of the pulse with respect to the Gaussian source PSD depends on the nonlinear group delay in the source wavelength interval

wavelength range between λ_{L} and λ_{R}, with $\lambda_{\text{L}} < \lambda_0 < \lambda_{\text{R}}$:

$$S_{\text{s}}(\lambda) = 0, \qquad (\lambda \leq \lambda_{\text{L}}) \cup (\lambda \geq \lambda_{\text{R}}) \tag{4.68}$$

Figure 4.15 reports the parabolic-like group delay function with the Gaussian PSD excitation centered in the zero-dispersion wavelength region. In this case the inverse group delay $\lambda = \zeta_{\text{g},h}(\tau)$ is a two-valued function for every normalized time instant $\tau_0 < \tau < \max(\tau_{\text{L}}, \tau_{\text{R}})$, as depicted in Figure 4.15. Then separate contributions are considered from the two partial wavelength intervals, $\lambda_{\text{L}} < \lambda < \lambda_0$ and $\lambda_0 < \lambda < \lambda_{\text{R}}$, as described in the general solution methodology in Section 4.2.6.1.

The chromatic impulse response is given by Equation (4.60). Referring to the situation presented in Figure 4.15, the initial instant for computing $h_{\text{c},h}(z,t)$ is τ_0 and the last instant is τ_{R}. However, the whole interval $T_1 = (\tau_0, \tau_{\text{R}})$, which corresponds to the longest wavelength interval $\Lambda_1 = (\lambda_0, \lambda_R)$, also includes the second contributing interval $T_0 = (\tau_0, \tau_{\text{L}})$, which is associated with the shortest wavelength interval $\Lambda_0 = (\lambda_{\text{L}}, \lambda_0)$. The chromatic impulse response is therefore given by the following expression, where the two separate contributions have been highlighted:

$$h_{\text{c},h}(z,t) = \underbrace{\frac{1}{z}\left\{\frac{S_{\text{s}}[\zeta_{\text{g},h}(t/z)]}{|D_0[\zeta_{\text{g},h}(t/z)]|}\right\}}_{\substack{\lambda=\zeta_{\text{g},h}(t/z)\in\Lambda_0 \\ \Lambda_0=(\lambda_{\text{L}},\lambda_0)}} + \underbrace{\frac{1}{z}\left\{\frac{S_{\text{s}}[\zeta_{\text{g},h}(t/z)]}{|D_1[\zeta_{\text{g},h}(t/z)]|}\right\}}_{\substack{\lambda=\zeta_{\text{g},h}(t/z)\in\Lambda_1 \\ \Lambda_1=(\lambda_0,\lambda_{\text{R}})}} \tag{4.69}$$

Figure 4.16 shows the qualitative profile of the chromatic impulse response according to Equation (4.69) and the spectral characteristics shown in Figure 4.15. In this case since both wavelength

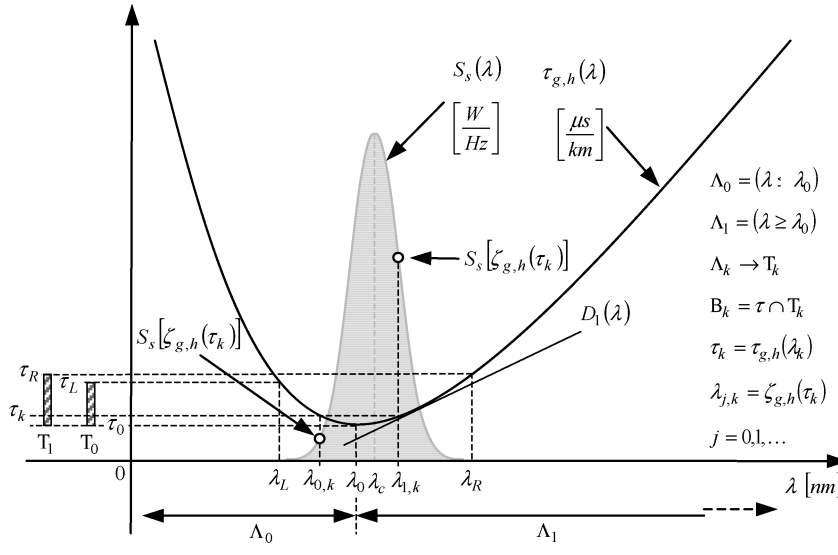

Figure 4.15 Spectral excitation in the zero-dispersion wavelength region corresponding to approximately 1310 nm for silica-based optical fibers. The source PSD is located across the minimum group delay wavelength and the chromatic impulse response requires the excitation interval to be split into two partial intervals for a single-valued inverse group delay function $\lambda = \zeta_{g,h}(\tau)$. The source spectral interval is defined by $\lambda_L < \lambda_0 < \lambda_R$

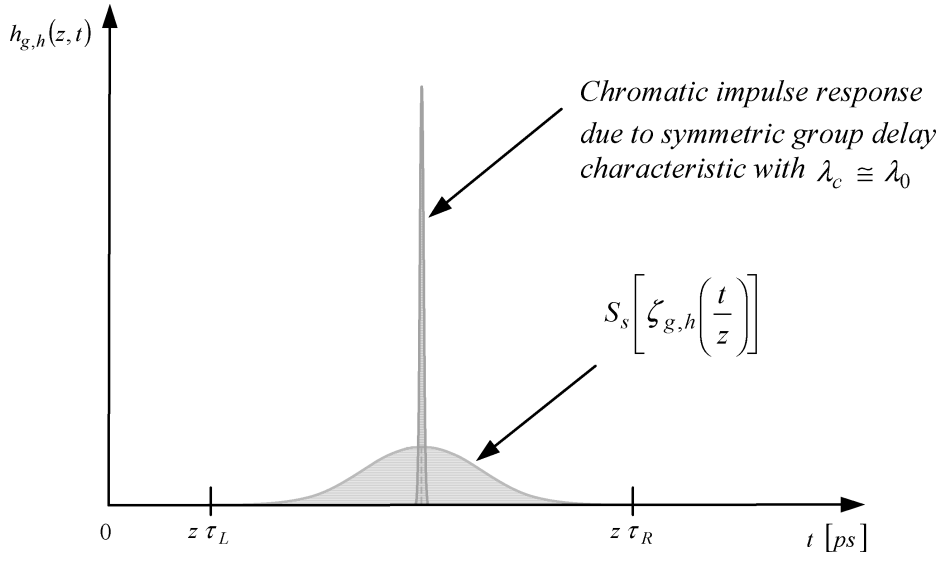

Figure 4.16 Chromatic impulse response for the spectral characteristic shown in Figure 4.15. Due to the almost symmetric group delay in the wavelength range of the source spectrum, the impulse response closely resembles the spectrum shape. However, the negligible value of the first-order derivative of the group delay around the zero-dispersion wavelength λ_0 makes the impulse response quite sharp compared to the source spectrum

intervals have almost symmetric chromatic dispersion coefficients, the impulse response resembles the shape of the source PSD. Even if the group delays change the shape according to the behavior versus wavelength slope, this effect is nearly symmetric as the central wavelength is closer to the zero-dispersion wavelength $\lambda_c \cong \lambda_0$ and the output pulse mainly resembles the shape of the light source spectrum. However, it is very remarkable that when the wavelength is approaching the minimum delay condition, $\lambda \cong \lambda_0$, the slope becomes negligible and the corresponding contribution to the impulse response becomes indefinitely high. This effect reflects of course a very fast impulse response as predicted by the lowest dispersion wavelength region.

The following section presents the numeric solution algorithm together with some interesting examples of the chromatic impulse response for different source spectrum profiles and group delay ripple functions. The algorithm has been developed using Matlab® 7.0.2 software by MathWorks Inc.

4.3 The Chromatic Impulse Response Model

In this section the solution algorithm is presented for the chromatic impulse response calculation according to the general expression in Equation (4.54). The algorithm has been implemented using Matlab® 7.0.2 by MathWorks Inc. The program accepts both source power spectral density and fiber group delay, eventually exhibiting multiple peaks according to individual peak Gaussian modeling. In Section 4.3.2 the whole Matlab® code is reported.

4.3.1 Model Equations

The chromatic impulse response theory was developed in the previous section, 4.2. Here the time domain representation according to Equation (4.54) is given, where a general multiple-valued group delay function is assumed. In the following description, in order to simplify the notation, the individual fiber mode index h has been removed from any modal function, including the group delay, the chromatic dispersion coefficient and the chromatic impulse response. Of course, dealing with multimode fibers it must be remembered that each individual fiber mode has its own group delay function, identified by the index notation $\tau = \tau_{g,h}(\lambda)$.

It is known that if the group delay function $\tau = \tau_g(\lambda)$ exhibits N stationary points, the whole wavelength axis must then be partitioned into $N + 1$ intervals $\Lambda_k = (\lambda_k, \lambda_{k+1})$. Accordingly, in each wavelength interval Λ_k the group delay $\tau = \tau_g(\lambda)$ is single-valued and assumes temporal values belonging to the corresponding interval $T_k = (\tau_k, \tau_{k+1})$. For every time instant $\tau \in T_k$ the inverse function $\lambda = \zeta_g(\tau)$ exists and is unique. Once the inverse group delay is known at every time instant of the interval $T_k = (\tau_k, \tau_{k+1})$, both the source power spectrum and the chromatic dispersion coefficient can be computed and the contribution to the chromatic impulse response can therefore be evaluated. This procedure must be repeated for every time instant belonging to the whole defined interval. The interval of definition T_c of the chromatic impulse response $h_c(z, \tau)$ is given by the continuous interval defined by the minimum and the maximum time instants among the set of partial time intervals $T_k = (\tau_k, \tau_{k+1})$:

$$T_c = (\tau_{\min}, \tau_{\max}) \Rightarrow \begin{cases} \tau_{\min} = \min\{T_k\}_{k=0,1,2,\ldots,N} \\ \tau_{\max} = \max\{T_k\}_{k=0,1,2,\ldots,N} \end{cases} \tag{4.70}$$

The integer N that appears in Equation (4.70) is the number of stationary points of the group delay function. If the group delay has the classical parabolic profile with only one minimum point, $N = 1$, then the generic wavelength interval is divided into two subintervals, like the case

considered in Figure 4.16. The general expression for the impulse response (4.54) where the total response $h_c(z, \tau)$ is equal to the sum of all partial contributions $h_{c,k}(\tau)$, $k = 0, 1, \ldots, N$ divided by the distance z is given below, where the temporal variable has been changed to $\tau = t/z$:

$$\left.\begin{aligned}
&\underbrace{h_{c,0}(\tau) \equiv \frac{S_s\lfloor\zeta_g(\tau)\rfloor}{|D_c[\zeta_g(\tau)]|}}_{\substack{\lambda=\zeta_g(\tau)\in\Lambda_0\\ \Lambda_0=(0,\lambda_1)}}\\
&\underbrace{h_{c,k}(\tau) \equiv \frac{S_s[\zeta_g(\tau)]}{|D_c[\zeta_g(\tau)]|}}_{\substack{\lambda=\zeta_g(\tau)\in\Lambda_k\\ \Lambda_k=(\lambda_k,\lambda_{k+1}),k=1,2,\ldots,N-1}}\\
&\underbrace{h_{c,N}(\tau) \equiv \frac{S_s[\zeta_g(\tau)]}{|D_c[\zeta_g(\tau)]|}}_{\substack{\lambda=\zeta_g(\tau)\in\Lambda_N\\ \Lambda_N=(\lambda_N,\infty)}}
\end{aligned}\right\} \Rightarrow h_c(z,\tau) = \frac{1}{z}\sum_{k=0}^{N} h_{c,k}(\tau) \tag{4.71}$$

Figure 4.17 shows the procedure applied to every partial single- valued wavelength interval $\Lambda_k = (\lambda_k, \lambda_{k+1})$ in order to compute the corresponding contribution $h_{c,k}(\tau)$ to the chromatic impulse response according to Equation (4.71). Referring to Figure 4.17, it is assumed that the normalized

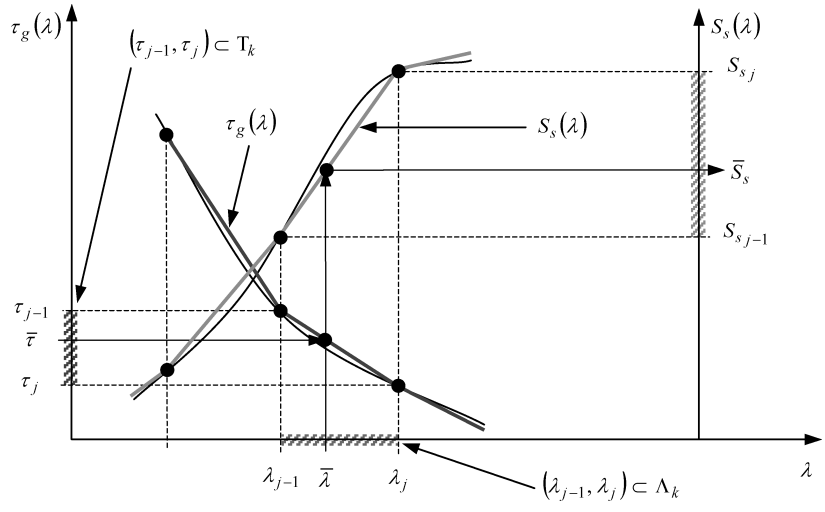

Figure 4.17 Representation of the numerical approximation of the group delay function and of the source power spectral density for numeric analysis of the chromatic impulse response. Discrete wavelengths $\{\lambda_j\}$ belong to the same single-valued interval Λ_k and the corresponding discrete time instants $\{\tau_j\}$ belong to the time interval T_k. For any given time instant $\overline{\tau} \in (\tau_{j-1}, \tau_j)$ the linear approximation leads to the corresponding wavelength $\overline{\lambda}$ and finally to the value $\overline{S}_s$ of the source power spectrum. An analogous procedure holds for calculation of the chromatic dispersion coefficient $\overline{D}_c$

time instant $\overline{\tau}$ belongs to the single-valued interval T_k and the corresponding wavelength $\overline{\lambda}$ is within the interval Λ_k. In the following, the generic contribution $h_{c,k}(\tau)$ to the chromatic impulse response reported in the general expression (4.71) is computed:

$$h_{c,k}(\overline{\tau}) = \frac{S_s[\zeta_g(\overline{\tau})]}{|D_c[\zeta_g(\overline{\tau})]|} = \frac{S_s(\overline{\lambda})}{|D_c(\overline{\lambda})|} = \frac{\overline{S}_s}{|\overline{D}_c|} \tag{4.72}$$

where

$$\overline{\tau} = \frac{\overline{l}}{\overline{z}}, \quad \overline{\tau} \in T_k \longleftrightarrow \Lambda_k, \quad \overline{\lambda} = \zeta_g(\overline{\tau}) \in \Lambda_k, \quad (\lambda_{j-1}, \lambda_j) \subset \Lambda_k$$

The wavelength $\overline{\lambda}$ is easily computed by inverting the linear relationship between the group delay and the wavelength in the considered interval:

$$\overline{\tau} = \tau_{j-1} + \frac{\tau_j - \tau_{j-1}}{\lambda_j - \lambda_{j-1}}(\overline{\lambda} - \lambda_{j-1}) \tag{4.73}$$

and the linear approximation of the inverse group delay function is

$$\overline{\lambda} = \zeta_g(\overline{\tau}) = \lambda_{j-1} + \frac{\overline{\tau} - \tau_{j-1}}{\tau_j - \tau_{j-1}}(\lambda_j - \lambda_{j-1}) \tag{4.74}$$

Either the linear approximation of the source power spectral density $S_s(\overline{\lambda})$ or the chromatic dispersion coefficient $D_c(\overline{\lambda})$ are evaluated at the same wavelength $\overline{\lambda}$ and have a similar expression to Equation (4.73). From Figure 4.17,

$$\overline{S}_s = S_{s_{j-1}} + \frac{S_{s_j} - S_{s_{j-1}}}{\lambda_j - \lambda_{j-1}}(\overline{\lambda} - \lambda_{j-1}) \tag{4.75}$$

$$\overline{D}_c = D_{c_{j-1}} + \frac{D_{c_j} - D_{c_{j-1}}}{\lambda_j - \lambda_{j-1}}(\overline{\lambda} - \lambda_{j-1}) \tag{4.76}$$

Substituting Equation (4.74) into Equations (4.75) and (4.76), from Equation (4.72) the following numerical solution for the general chromatic impulse response contribution at the time instant $\overline{\tau}$ is obtained:

$$h_{c,k}(\overline{\tau}) = \frac{\tau_j S_{s_{j-1}} - \tau_{j-1} S_{s_j} + (S_{s_j} - S_{s_{j-1}})\,\overline{\tau}}{\tau_j D_{c_{j-1}} - \tau_{j-1} D_{c_j} + (D_{c_j} - D_{c_{j-1}})\,\overline{\tau}} \tag{4.77}$$

This expression is used in the developed program reported below to compute the chromatic impulse response of every group delay profile and source power spectral density. Those functions are the only two required inputs for extracting the impulse response. The next section gives a short overview of how the Matlab® program operates.

4.3.2 Computing Algorithm

The main program CIR (chromatic impulse response) requires first the definition of the whole wavelength range and the resolution of each step. Then routine *GROUPDELAY* is called to compute both the group delay function and the chromatic dispersion coefficient by means of numerical differentiation of the group delay. The routine *GROUPDELAY* calls the routine *MGP* (multi-Gaussian profile) in order to allow for superposed multi-Gaussian peak ripples over the uniform Sellmeier group delay profile. The routine *MGP* is used to generate the source spectrum and returns the normalized source power spectral density over the same wavelength axis used for the group delay. The routine *MGP* provides either a single Gaussian peak or a multi-Gaussian peak spectrum for handling different source conditions. According to the solution methods described in the text,

the program searches for every group delay stationary wavelength in order to have the wavelength axis partition for a single-valued group delay function. The corresponding time intervals are then scanned simultaneously from the minimum time instant up to the maximum time instant, assuming that the same number of elementary points are used as for the wavelength axis.

For each time instant, the program computes the chromatic impulse response according to expression (4.77). The plots of the generated group delay and source power spectrum profiles are then represented on the same graph in order to visualize clearly the spectrum interaction used to produce the total impulse response. On a separate graph all the computed time intervals are then shown in order to obtain a clear representation of the way the several chromatic impulse response contributions add together to produce the final response. The last graph finally reports the computed chromatic impulse response without any further processing. The corresponding timescale therefore includes the average group delay of the pulse center of gravity, according to the group delay function and the source spectrum wavelength distribution. The program then computes the average group delay of the resulting impulse response and provides the time-shifted axis by centering the chromatic impulse response on the time origin of the translated axis. Operating in this way, the visible timescale resolution is usually greatly increased and all details of the pulse shape appear with the proper timescale.

The chromatic impulse response is normalized with unit energy, as demonstrated in Section 4.2. The time-centered chromatic impulse response is then plotted on a separate graph together with the RMS width. Depending on the pulse width, the proper timescale can be selected using units of either ps/m or ps/km. The following are reported Matlab® codes for both main program CIR and all the related routines.

4.3.2.1 Program CIR

```
% The program CIR computes the chromatic impulse response for the given
% mode group delay Tg and source power spectral density Ss. The chromatic
% impulse response hc(z,t) is function of the distance z and the normalized
% time t/z.
%
clear;
N0=2000;            % Number of steps in the wavelength axis
Lmin=1530e-9;       % Minimum wavelength in the computing interval
Lmax=1570e-9;       % Maximum wavelength in the computing interval
dL=(Lmax-Lmin)/N0;  % Wavelength step
L=(Lmin:dL:Lmax);   % Wavelength axis for the Sellmeier refractive index
L1=L(1:N0);         % Wavelength axis for the first order derivative Tg
L2=L(1:N0-1);       % Wavelength axis for the second order derivative Dc
%
%------------ Group Delay and Chromatic Dispersion Coefficient ------------
%
Tg=1e9*GROUPDELAY(L);   % [ns/m]
Dc=1e-3*diff(Tg)/dL;    % [ps/nmkm]
%
%------------------- Multi-Gaussian-Profile Source PSD --------------------
%
A=[0.15 0.20 0.30 0.20 0.15]; % Coefficients for the individual Gaussian
   peaks
FWHM=[0.1 0.1 0.1 0.1 0.1]*1e-9; % FHHM [m]
Lambda=[1548.4 1549.2 1550 1550.8 1551.6]*1e-9; % Central Wavelengths [m]
Ss=MGP(A,FWHM,Lambda,L2); % Multi-Gaussian-Profile
%
%----------------------- Chromatic Impulse Response ----------------------
```

```
%
% Finding stationary wavelengths for inverting the group delay function
%
j=1;
k=0;
while j<N0-1,
    Sc=sign(Dc(j));
    j=j+1;
    while j<N0-1 & Sc*sign(Dc(j))==+1,
        j=j+1;
    end;
    if j<N0-1,
        k=k+1;
        Index(k)=j; % Index exceeding the current stationary wavelength
        Lo(k)=L(j-1)-Dc(j-1)*dL/(Dc(j)-Dc(j-1)); % Stationary wavelengths
    end;
end;
if k>0, % At least one stationary wavelength exists in the interval
    N=length(Index); % Number of stationary wavelengths found
    %
    % Finding time intervals corresponding to single-valued wavelength
       intervals
    %
    disp('        Interval     T(min)       T(max)   Lambda(min)  Lambda(max)
Lambda(zero)');
    disp('                      ns/m         ns/m        nm           nm
nm');
    disp(");
    TauL_0=Tg (1);
    TauR_0=Tg(Index (1) -1);
    disp([0 TauL_0 TauR_0 L (1) L(Index (1) -1)]);
    for k=1:N-1,
        TauL(k)=Tg(Index(k));
        TauR(k)=Tg(Index(k+1)-1);
        disp([k TauL(k) TauR(k) L(Index(k))*1e9 L(Index(k+1)-1)*1e9
           Lo(k)*1e9]);
    end;
    TauL(N)=Tg(Index(N));
    TauR(N)=Tg(N0);
    disp([N TauL(N) TauR(N) L(Index(N))*1e9 L(N0+1)*1e9 Lo(N)*1e9]);
    Taumax=max([TauL_0 TauR_0 TauL TauR]); % Maximum normalized time instant
    Taumin=min([TauL_0 TauR_0 TauL TauR]); % Minimum normalized time instant
else
    N=0;
    Taumin=Tg (1);
    Taumax=Tg(N0);
end;
dT=(Taumax-Taumin)/(N0-1); % Normalized time step
T=(Taumin:dT:Taumax); % Normalized time axis
%
% Computing chromatic impulse response contributions of each time interval
%
hc(1:N0)=0;
if N>0,
    for j=1:N0,
        if min([TauL_0 TauR_0])<=T(j) & T(j)<=max([TauL_0 TauR_0]),
```

```
            hc(j)=hc(j)+CIRCON(T(j),Tg,Ss,abs(Dc),1,Index (1) -1);
        end;
        for k=1:N-1,
            if min([TauL(k) TauR(k)])<=T(j) & T(j)<=max([TauL(k) TauR(k)]),
                hc(j)=hc(j)+CIRCON(T(j),Tg,Ss,abs(Dc),Index(k),Index(k+1)-1);
            end;
        end;
        if min([TauL(N) TauR(N)])<=T(j) & T(j)<=max([TauL(N) TauR(N)]),
            hc(j)=hc(j)+CIRCON(T(j),Tg,Ss,abs(Dc),Index(N),N0-1);
        end;
    end;
else,
    for j=1:N0,
        hc(j)=hc(j)+CIRCON(T(j),Tg,Ss,abs(Dc),1,N0-1);
    end;
end;
%
% Chromatic Impulse Response Moments
%
disp('       S_WL_AVE    S_WL_RMS      To_lin         To         Dc_lin
hc_RMS_lin     hc_RMS');
disp('         [nm]        [nm]        [μs/km]      [μs/km]     [ps/nmkm]
[ps/km]      [ps/km]');
disp(");
To=sum(T.*hc)/sum(hc); % Average response delay in normalized time unit
Ts=(T-To)*1e6; % Temporal axis with origin in To [ps/km]
Sigma_hc=sqrt(sum(Ts. ^2.*hc)/sum(hc)); % RMS pulse width [ps/km]
%
% Source PSD Moments
%
Lo_Ss=sum(L2.*Ss)/sum(Ss); % Average wavelength [m]
Sigma_Ss=sqrt(sum((L2-Lo_Ss). ^2.*Ss)/sum(Ss)); % RMS spectral width [m]
%
% Linear Group Delay Approximation
%
k=1;
while L(k)<Lo_Ss & k<N0, k=k+1; end;
if k<N0,
    Dc_lin=(Tg(k)-Tg(k-1))/dL;
    Tau_lin=Tg(k-1)+Dc_lin*(Lo_Ss-L(k-1));
    Sigma_lin=Sigma_Ss*abs(Dc_lin);
    disp([Lo_Ss*1e9 Sigma_Ss*1e9 Tau_lin To Dc_lin*1e-3 Sigma_lin*1e6
       Sigma_hc]);
end;
%
%-------------------------------- Plotting ------------------------------
%
figure (1);
subplot (221); % Fiber Group Delay - Chromatic Dispersion - Light Source PSD
plot(L1*1e6,Tg,L2*1e6,min(Tg)+Ss/max(Ss)*(max(Tg)-min(Tg))); grid on;
title('Fiber Group Delay and Light Source PSD');
xlabel('Wavelength, \lambda [μm]');
ylabel('t_g(\lambda) [ns/m]');
legend('Group Delay','Source PSD');
subplot (222);
plot(L2*1e6,Dc), grid on;
```

```
line([Lmin Lmax]*1e6,[0 0],'LineStyle','-.','Color','r');
title('Chromatic Dispersion');
xlabelW'(avelength, λ [μm]');
ylabel('D_c(λ) [ps/nmkm]');
subplot(223); % Normalized Time Intervals
if N>0,
    plot([0:N],[TauL_0 TauL],'o',[0:N],[TauR_0 TauR],'ro'); grid on;
    line([0 0],[TauL_0 TauR_0],'LineWidth',2,'Color','k');
    for k=1:N,line([k k],[TauL(k) TauR(k)],'LineWidth',2,'Color','k');end;
else
    plot(0,Taumin,'o',0,Taumax,'ro'); grid on;
    line([0 0],[Taumin Taumax],'LineWidth',2,'Color','k');
end;
title('Normalized Time Intervals');
xlabel('Wavelength interval \Lambda_k');
ylabel('Time interval [ns/m]');
legend('\tau_L=ζ(λ_L)','τ_R=ζ(λ_R)');
subplot (224); % Chromatic Impulse Response
plot(T,hc); grid on;
line([To To],[0 1.1*max(hc)],'LineStyle','-.','Color','r');
title('Chromatic Impulse response');
xlabel('Normalized time τ [ns/m]');
ylabel('a.u.');
figure (2); % Time-shifted chromatic impulse response
plot(Ts,hc); grid on;
line([-Sigma_hc -Sigma_hc],[0 1.1*max(hc)],'LineStyle','-.','Color','r');
line([Sigma_hc Sigma_hc],[0 1.1*max(hc)],'LineStyle','-.','Color','r');
text(0.6*Ts(N0),1.05*max(hc),['RMS width σ_τ=' num2str(Sigma_hc)
'[ps/km]'],'BackgroundColor','w');
title('Centered Chromatic Impulse response');
xlabel('Normalized time τ [ps/km]');
ylabel('Unity energy response [a.u.]');
```

4.3.2.2 Function *GROUPDELAY*

```
function tg=GROUPDELAY(L);
N0=length(L)-1;
Lmin=min(L); % Minimum wavelength
Lmax=max(L); % Maximum wavelength
dL=(Lmax-Lmin)/N0; % Wavelength step
c=2.9979e8; % Speed of light in vacuum
%
% Sellmeier equation: coefficients for the fused silica
%
B1=0.6961663;   % Coefficient B1 for Three-term Sellmeier equation
B2=0.4079426;   % Coefficient B2 for Three-term Sellmeier equation
B3=0.8974794;   % Coefficient B3 for Three-term Sellmeier equation
Lambda1=0.0684043e-6;% Peak wavelength L1
Lambda2=0.1162414e-6;% Peak wavelength L2
Lambda3=9.896161e-6; % Peak wavelength L3
%
% Sellmeier component
%
n_S=sqrt(1+B1./(1-(Lambda1./L).^2)+B2./(1-(Lambda2./L).^2)+B3./(1-
    (Lambda3./L).^2));
```

```
% Index of refraction
n1_S=diff(n_S)/dL;      % First order derivative of the refractive index
n2_S=diff(n1_S)/dL;     % Second order derivative of the refractive index
L1=L(1:N0);         % Wavelength axis for the first order derivative
L2=L(1:N0-1);       % Wavelength axis for the second order derivative
ng_S=n_S(1:N0)-L1.*n1_S;  % Group index
tg_S=ng_S/c;        % Sellmeier Group delay [s/m]
%
% Multi-Gaussian-Profile component
%
C_tg=0e-12; % Unit amplitude for the group delay ripple [s]
A_tg=[0.20 0.20 0.125 0.125 0.125 0.10 0.10 0.05]*C_tg; % Coefficients for
   the group delay ripple
FWHM_tg=[75 75 75 75 75 75 75 75]*1e-9; % FHHM of the group delay ripple
Lambda_tg=[850 950 1050 1150 1250 1350 1450 1550]*1e-9; % Central wavelengths
   of the group delay ripple
A_tg=A_tg./(2*sqrt(log (2)/pi)./FWHM_tg); % Amplitude normalization
tg_MGP=MGP(A_tg,FWHM_tg,Lambda_tg,L1); % MGP group delay component [s/m]
%
% Linear combination of Sellmeier and MGP group delays
%
tg=tg_S+tg_MGP; % Total group delay [s/m]
```

4.3.2.3 Function *MGP*

```
% The function MGP provides the Multi-Gaussian-Profile power spectral
% density of the light source based on the linear superposition of the
% input-defined Gaussian functions. Inputs A, FWHM and Lambda represent
% respectively linear vectors containing the weight coefficients, the
% Full-Width-Half-Maximum and the central wavelengths of the Gaussian
% components. There is no limitation to the number of Gaussian components
% used in the linear superposition. The length of each input vector
% specifies the required number of Gaussian components.
%
function S=MGP(A,FWHM,Lambda,L);
N=length(A);
S=0;
for k=1:N,
    Sk=2*sqrt(log(2)/pi)/FWHM(k)*exp(-4*log(2)*(L-Lambda(k)).^2/FWHM(k)^2);
    S=S+A(k)*Sk;
end;
```

4.3.2.4 Function *CIRCON*

```
% The function CIRCON provides the inversion of the group delay function Tg
% limited by the selected wavelength interval defined by two indices j1 and
% j2 and returns the Chromatic Impulse Response CONtribution Ss/Dc. The
% returned value is computed assuming linear interpolation between the two
% subsequent wavelength points available from the two input indices
%
function hc=CIRCON(Tj,Tg,Ss,Dc,j1,j2);
j=j1;
Sgn=sign(Tg(j)-Tj);
j=j+1;
while j<j2 & Sgn*sign(Tg(j)-Tj)==+1,
```

```
    j=j+1;
end;
hc=1e-3*(Tg(j)*Ss(j-1)-Tg(j-1)*Ss(j)+(Ss(j)-Ss(j-1))*Tj)/...
   (Tg(j)*Dc(j-1)-Tg(j-1)*Dc(j)+(Dc(j)-Dc(j-1))*Tj);
```

4.3.3 Numerical Solution Examples

In this section some selected chromatic impulse responses are computed using the solution algorithm presented above. The cases reported have been chosen in order to give clear evidence of the different relevant chromatic impulse response profiles that can be achieved using different source excitation conditions and the group delay functions. The same group delay together with the same source spectrum profile generate very different chromatic impulse responses by simply sliding the source central wavelength. This relevant characteristic of the chromatic impulse response has already been shown in the cases considered in the theoretical part of Section 4.2 above. It would be instructive to have numerical computed solutions for the same cases already considered previously in a qualitative way in order to understand the impulse response mechanism clearly.

The results presented below should help to clarify the physical principles behind the chromatic impulse response. The cases considered below are the following:

1. Sellmeier group delay profile for the fused silica:
   (a) single-Gaussian peak source PSD operating in the first window range at 850 nm;
   (b) single-Gaussian peak source PSD operating in the third window range at 1550 nm;
   (c) single-Gaussian peak source PSD operating in the second window range at 1310 nm.
2. Sellmeier group delay profile for the fused silica with added multi-Gaussian peak ripples:
   (a) single-Gaussian peak source PSD operating in the first window range at 850 nm;
   (b) single-Gaussian peak source PSD operating in the third window range at 1550 nm;
   (c) single-Gaussian peak source PSD operating in the second window range at 1310 nm.
3. Sellmeier group delay profile for the fused silica:
   (a) multi-Gaussian peak source PSD (modeling multilongitudinal Fabry–Perot laser) operating in the first window range at 850 nm;
   (b) multi-Gaussian peak source PSD (modeling multilongitudinal Fabry–Perot laser) operating in the third window range at 1550 nm;
   (c) multi-Gaussian peak source PSD (modeling multilongitudinal Fabry–Perot laser) operating in the second window range at 1310 nm.
4. Sellmeier group delay for the fused silica profile with added multi-Gaussian peak ripples:
   (a) multi-Gaussian peak source PSD (modeling multilongitudinal Fabry–Perot laser) operating in the first window range at 850 nm;
   (b) multi-Gaussian peak source PSD (modeling multilongitudinal Fabry–Perot laser) operating in the third window range at 1550 nm;
   (c) multi-Gaussian peak source PSD (modeling multilongitudinal Fabry–Perot laser) operating in the second window range at 1310 nm.

The selected 12 cases above can be conveniently set up into a 6×2 simulation matrix, as given in Table 4.1.

Before reporting computed chromatic impulse responses versus different source spectrum and group delay conditions according to the Table 4.1, it is instructive to show both group delay functions used in the simulation: the Sellmeier uniform (SU) profile and the Sellmeier ripple (SR) profile. For both representations the same wavelength interval 600 nm–1900 nm has been used.

Table 4.1 Simulation matrix for computing the chromatic impulse response according to different combinations of the group delay function and the source power spectral density. The Sellmeier uniform profile refers to the undoped fused silica (SU, Sellmeier uniform; SR, Sellmeier ripple; SG, single-Gaussian; MG, multi-Gaussian)

Source PSD	Group delay	
	Sellmeier uniform	Sellmeier + multi-Gaussian ripple
Single-Gaussian peak 850 nm	1.a: SUSG850	2.a: SRSG850
Single-Gaussian peak 1550 nm	1.b: SUSG1550	2.b: SRSG1550
Single-Gaussian peak 1310 nm	1.c: SUSG1310	2.c: SRSG1310
Multi-Gaussian peak 850 nm	3.a: SUMG850-A/B	4.a: SRMG850
Multi-Gaussian peak 1550 nm	3.b: SUMG1550-A/B	4.b: SRMG1550
Multi-Gaussian peak 1310 nm	3.c: SUMG1310-A/B	4.c: SRMG1310

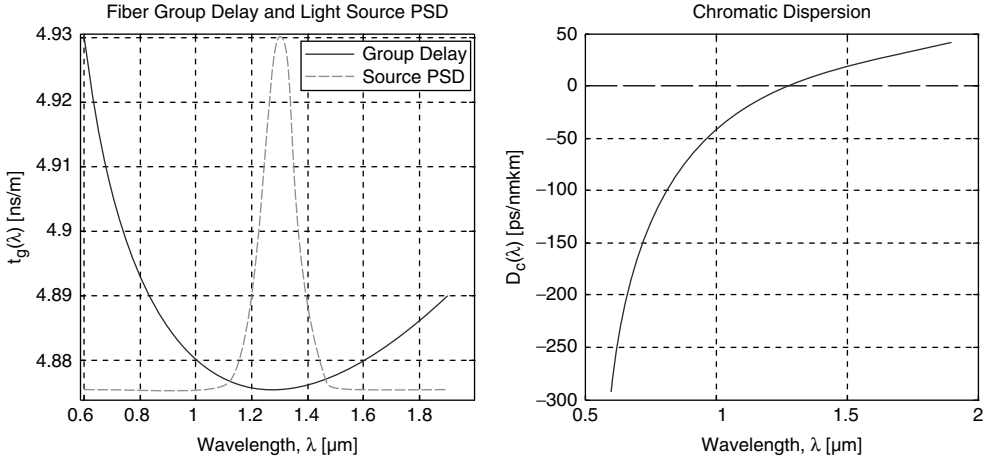

Figure 4.18 Left: uniform group delay of the fused silica according to the Sellmeier approximation with a superposed source single-Gaussian PSD with FWHM = 150 nm, $\lambda_c = 1300$ nm. Right: chromatic dispersion. The zero-dispersion wavelength for fused silica is at $\lambda_0 = 1272.6$ nm

The multi-Gaussian source spectrum has been centered at 1300 nm as a matter of convenience. The remaining two wavelength excitations merely require a spectrum translation over the selected wavelength.

In Figure 4.18 the width of the single-Gaussian PSD has been chosen abnormally wide in order to highlight the consequences on the chromatic impulse response better. The usual values for the LED source spectral width are in the range between 20 nm and 100 nm. Single-line laser sources are much narrower, usually below 1 nm under direct modulated conditions. A multilongitudinal mode laser spectrum, like those of Fabry–Perot lasers, has a larger spectrum envelope, exhibiting several emitted modes spaced about 0.8–1 nm apart. In the following reported cases of numerically computed

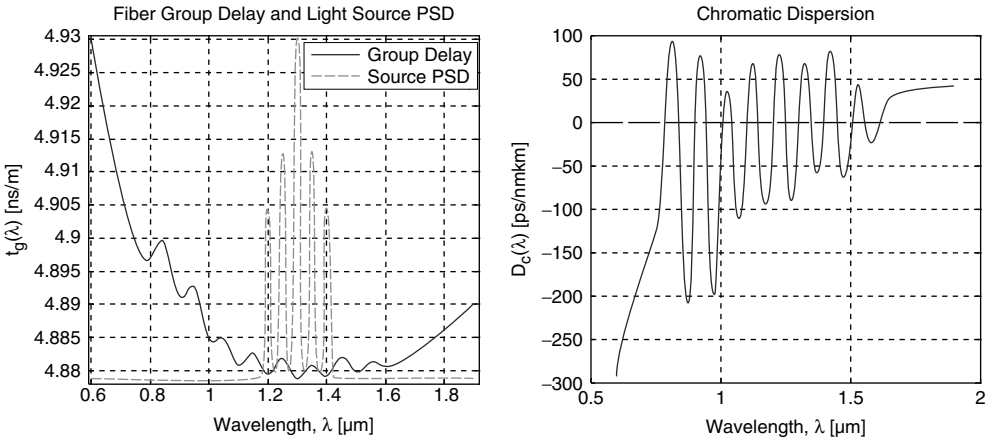

Figure 4.19 Left: ripple group delay of the fused silica according to the Sellmeier approximation with a superposed source multi-Gaussian PSD with FWHM = 20 nm, $\lambda_c = 1300$ nm, $N = 5$, $\Delta\lambda = 1$ nm. Right: chromatic dispersion of the ripple group delay corresponding to the left graph. The number of zero-dispersion wavelengths coincides with the number of group delay stationary wavelengths. In this example 17 zero-dispersion wavelengths are shown

chromatic impulse responses two different source spectral profiles are used, namely the single-Gaussian broad spectrum with FWHM = 150 nm and the multi-Gaussian spectrum. Two different multi-Gaussian spectrum profiles have been used. The first one refers to five lasing modes spaced at 50 nm with FWHM = 20 nm, while the second model of the multi-Gaussian spectrum refers to five lasing modes spaced at 1 nm with FWHM = 0.20 nm, representing a typical Fabry–Perot laser diode. The first model of the multi-Gaussian spectrum does not represent a realistic light source; however, it is believed to be useful in understanding some characteristic mechanisms leading to the chromatic impulse response. Figure 4.19 reports the ripple group delay together with the multi-Gaussian source PSD.

The ripple group delay is obtained by superposition of the uniform Sellmeier term with the multi-Gaussian weighted profile. The corresponding chromatic dispersion is shown on the right side and is obtained by numerical derivation of the group delay. The characteristic ripple of the chromatic dispersion characteristic reflects the multi-Gaussian profile of the group delay. The number of zero-dispersion wavelengths coincides with the number of stationary points of the group delay. Table 4.2 gives the 17 stationary wavelengths and the corresponding 18 partial wavelength intervals used to compute the multivalued inverse group delay function, according to the general chromatic impulse response expression (4.71).

Each wavelength interval Λ_k is identified by the two wavelengths λ_k and λ_{k+1}. Accordingly, the minimum wavelength of interval Λ_{k+1} coincides with the maximum wavelength of the previous interval Λ_k, augmented by the elementary wavelength step $\Delta\lambda$. The zero-dispersion wavelength is computed as the linear interpolation between those two extremes and belongs to the elementary interval, as has been highlighted in the case of $1249.2\,\text{nm} < \lambda_0 = 1249.3\,\text{nm} < 1249.4\,\text{nm}$ in Table 4.2. Figure 4.20 gives a graphical representation of the linear interpolation procedure used to calculate each zero-dispersion wavelength.

Table 4.2 Computed zero-dispersion wavelengths and partial intervals for the numerical calculation of the chromatic impulse response, as reported in the text. The intervals are ordered according to subsequent wavelengths, starting at $\lambda_{min} = 600\,nm$ and ending at $\lambda_{max} = 1900\,nm$

Interval	T_{min} (ns/m)	T_{max} (ns/m)	λ_{min} (nm)	λ_{max} (nm)	λ_0 (nm)
0	4.9302	4.8967	600.00	792.14	–
1	4.8967	4.8996	792.27	840.89	792.26
2	4.8996	4.8910	841.02	907.71	841.02
3	4.8910	4.8928	907.84	943.33	907.80
4	4.8928	4.8843	943.46	1014.6	943.35
5	4.8843	4.8850	1014.7	1042.9	1014.6
6	4.8850	4.8808	1043.0	1103.9	1043.0
7	4.8808	4.8827	1104.0	1147.2	1103.9
8	4.8827	4.8794	1147.3	1201.4	1147.2
9	4.8794	4.8818	1201.5	1249.2	1201.4
10	4.8818	4.8788	1249.4	1303.0	1249.3
11	4.8788	4.8808	1303.2	1351.4	1303.1
12	4.8808	4.8791	1351.5	1397.3	1351.5
13	4.8791	4.8820	1397.4	1452.9	1397.3
14	4.8820	4.8799	1453.1	1505.3	1453.0
15	4.8799	4.8814	1505.4	1558.8	1505.3
16	4.8814	4.8806	1558.9	1609.3	1558.8
17	4.8806	4.8900	1609.4	1900.0	1609.4

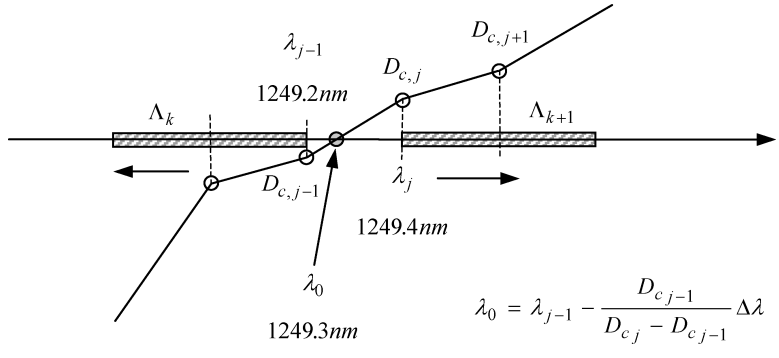

Figure 4.20 Graphical representation of the linear interpolation for the determination of the zero-dispersion wavelengths using the first-order derivative of the group delay function. The algorithm search for the zero-crossing condition of the chromatic dispersion then proceeds with the linear interpolation

4.3.3.1 Example 1.a: SUSG850 (Figures 4.21 and 4.22)

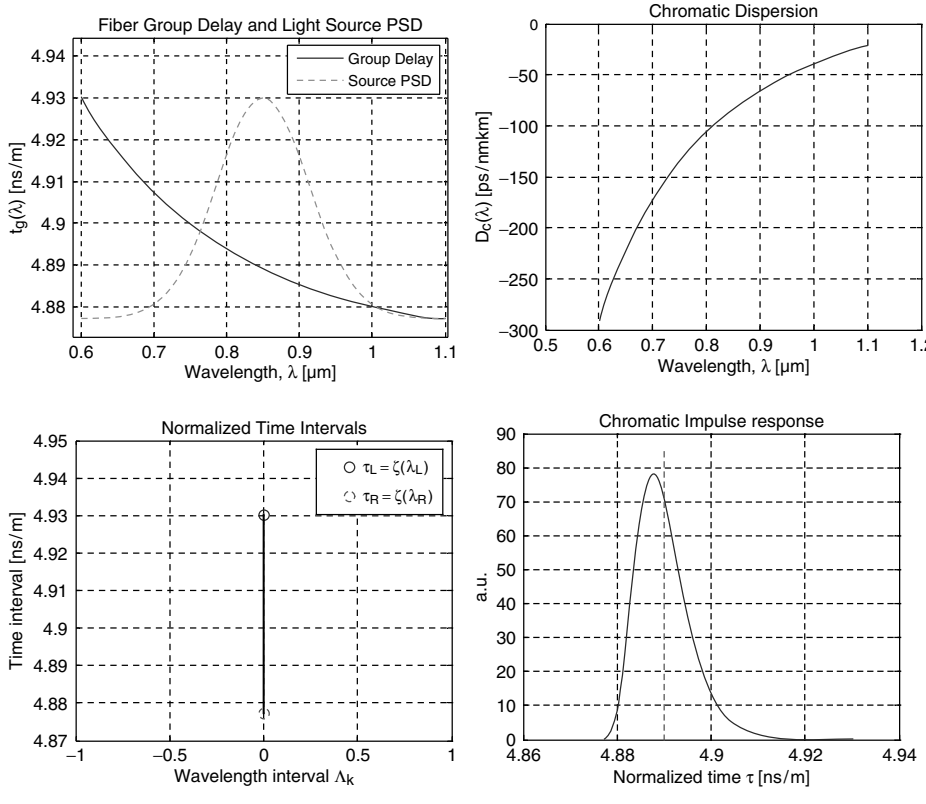

Figure 4.21 Sellmeier group delay. Wavelength interval 600 nm $\leq \lambda \leq$ 1100 nm, single-Gaussian peak source FWHM = 150 nm, λ_c = 850 nm

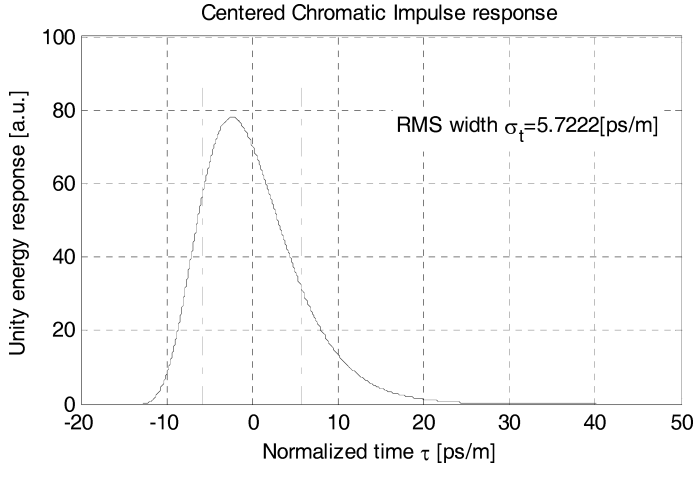

Figure 4.22 Chromatic impulse response to the spectral condition shown above

4.3.3.2 Example 1.b: SUSG1550 (Figures 4.23 and 4.24)

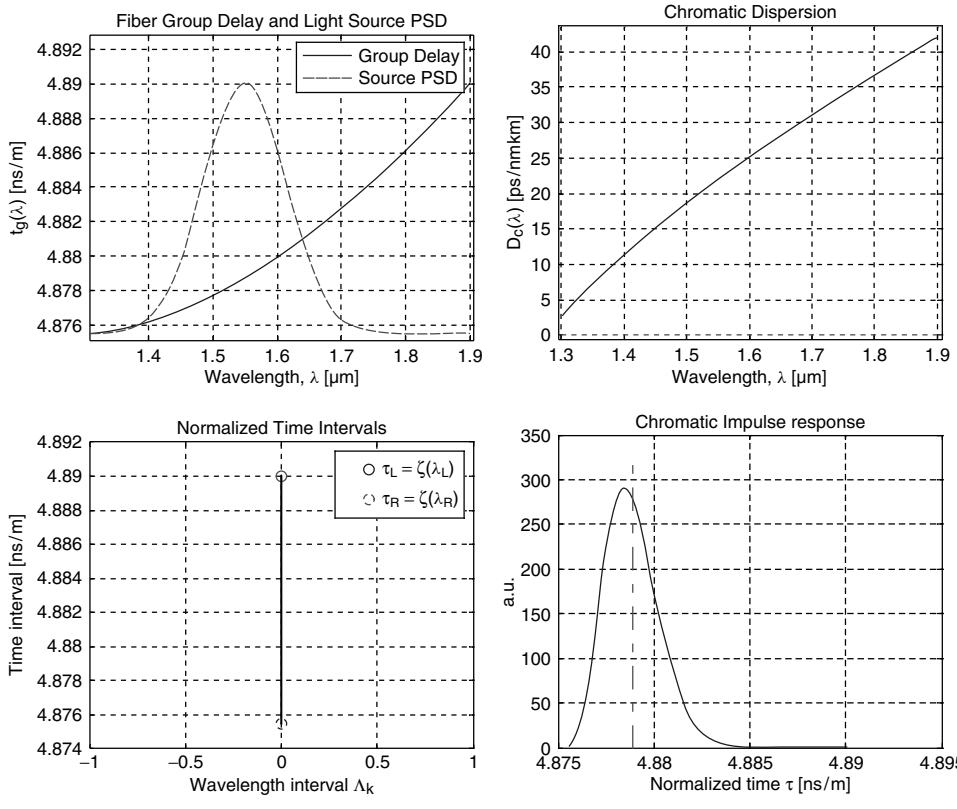

Figure 4.23 Sellmeier group delay. Wavelength interval $1300\,\text{nm} \leq \lambda \leq 1900\,\text{nm}$, single-Gaussian peak source FWHM $= 150\,\text{nm}$, $\lambda_c = 1550\,\text{nm}$

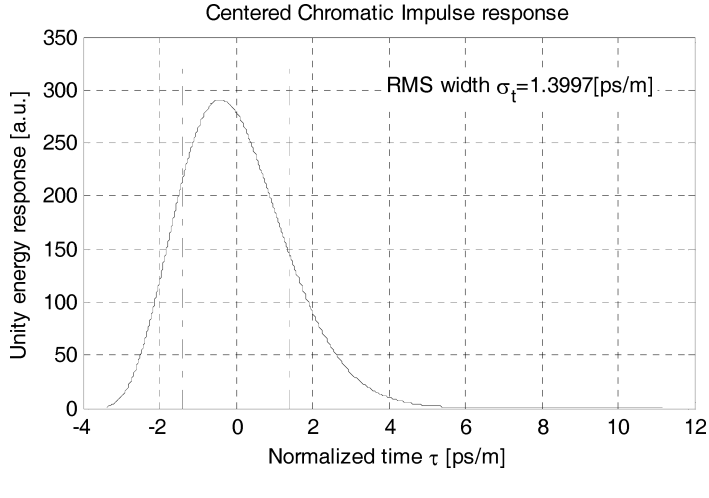

Figure 4.24 Chromatic impulse response to the spectral condition shown above

4.3.3.3 Example 1.c: SUSG1300 (Figures 4.25 and 4.26)

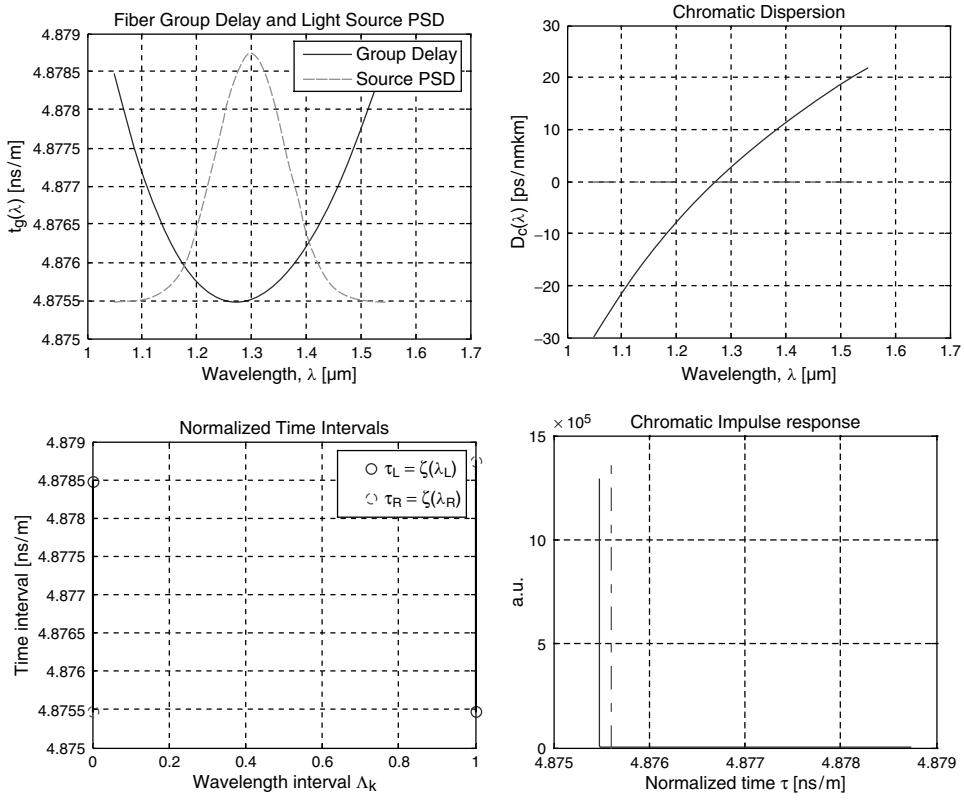

Figure 4.25 Sellmeier group delay. Wavelength interval $1050\,\text{nm} \leq \lambda \leq 1550\,\text{nm}$, single-Gaussian peak source FWHM = 150 nm, $\lambda_c = 1300\,\text{nm}$

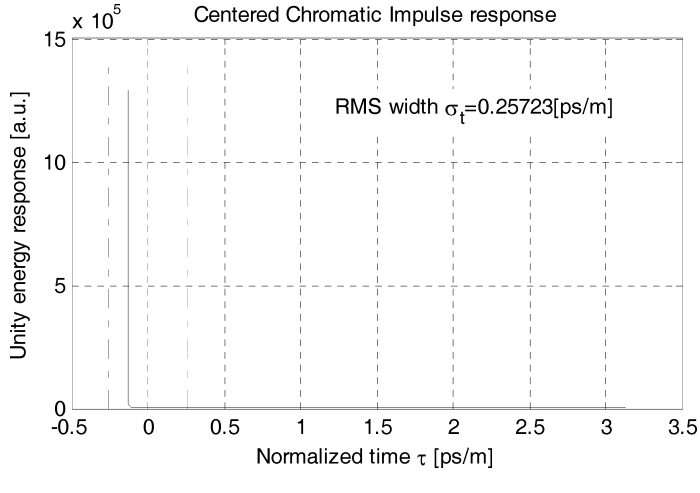

Figure 4.26 Chromatic impulse response to the spectral condition shown above

4.3.3.4 Example 2.a: SRSG850 (Figures 4.27 and 4.28)

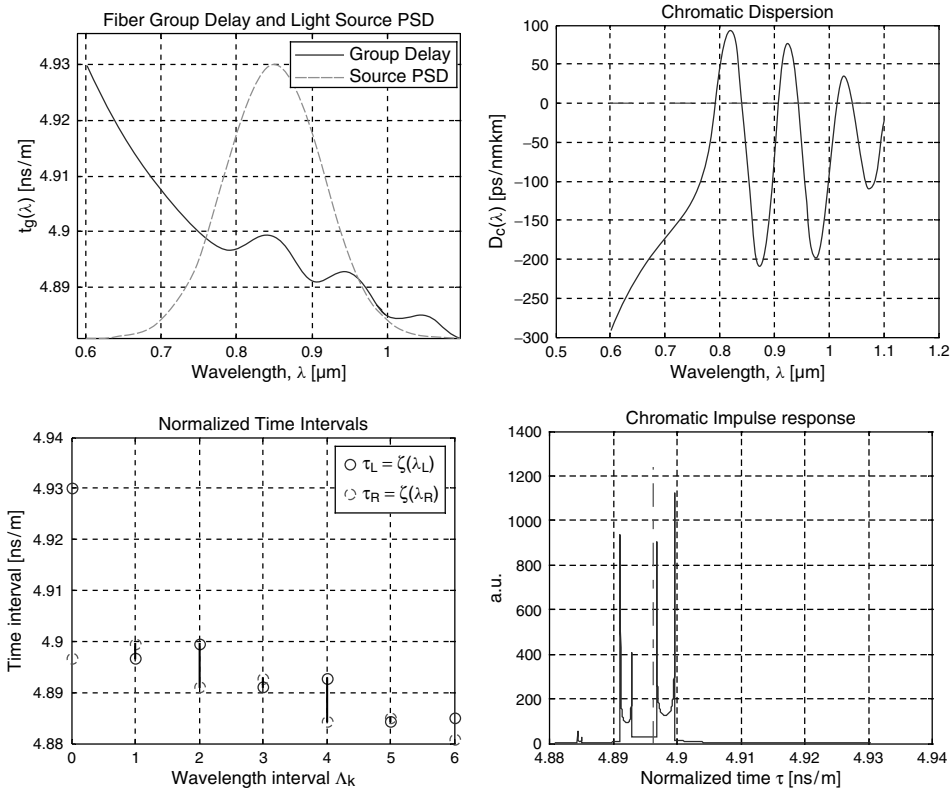

Figure 4.27 Sellmeier group delay with added multi-Gaussian ripple. Wavelength interval 600 nm $\leq \lambda \leq$ 1100 nm, single-Gaussian peak source FWHM = 150 nm, λ_c = 850 nm

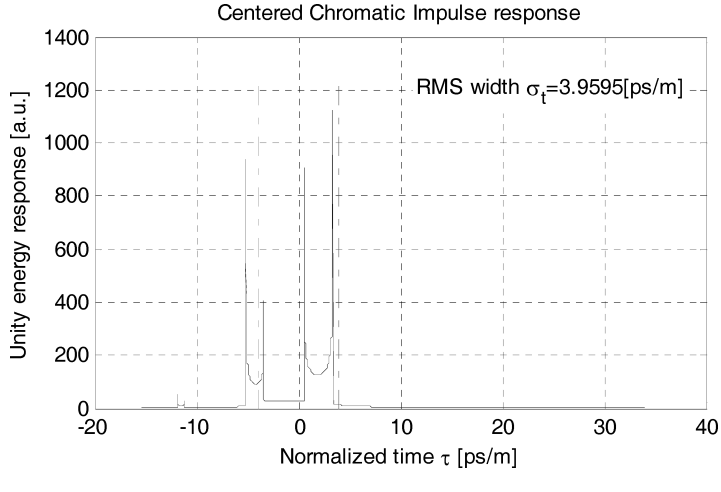

Figure 4.28 Chromatic impulse response to the spectral condition shown above

4.3.3.5 Example 2.b: SRSG1550 (Figures 4.29 and 4.30)

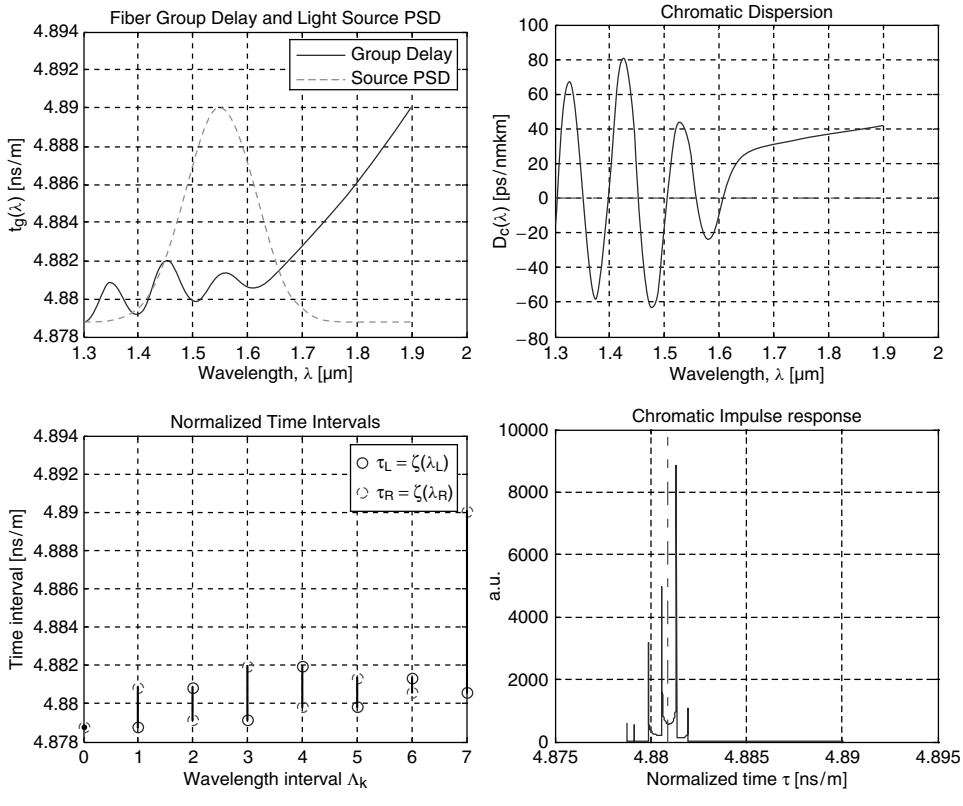

Figure 4.29 Sellmeier group delay with added multi-Gaussian ripple. Wavelength interval 1300 nm $\leq \lambda \leq$ 1900 nm, single-Gaussian peak source FWHM = 150 nm, $\lambda_c = 1550$ nm

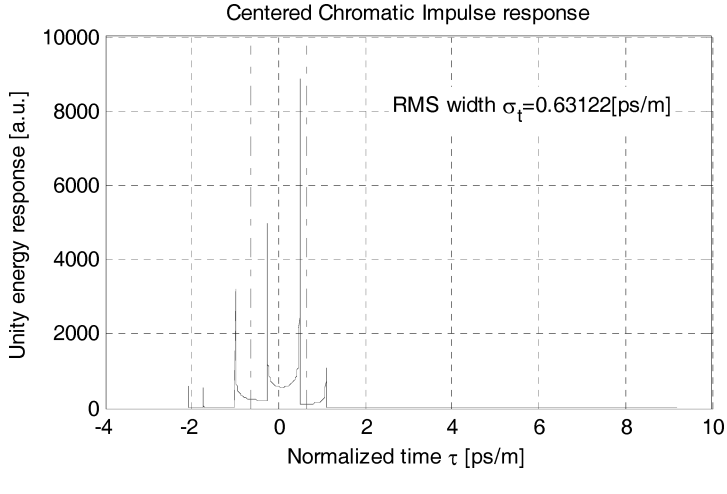

Figure 4.30 Chromatic impulse response to the spectral condition shown above

4.3.3.6 Example 2.c: SRSG1300 (Figure 4.31 and 4.32)

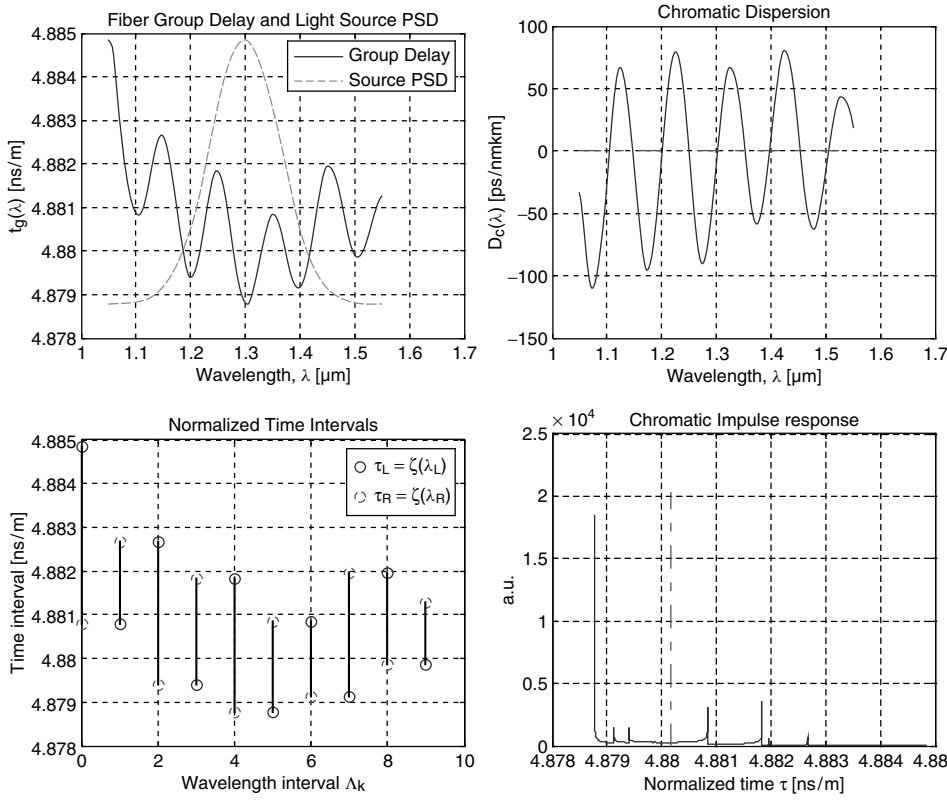

Figure 4.31 Sellmeier group delay with added multi-Gaussian ripple. Wavelength interval 1050 nm $\leq \lambda \leq$ 1550 nm, single-Gaussian peak source FWHM = 150 nm, λ_c = 1300 nm

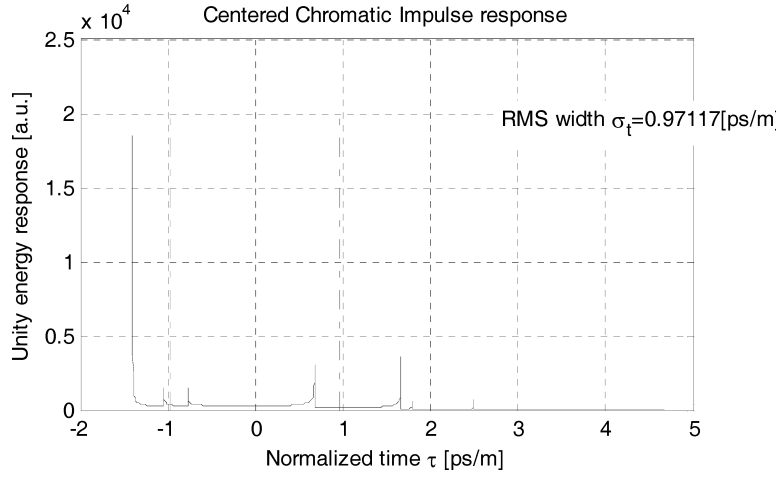

Figure 4.32 Chromatic impulse response to the spectral condition shown above

4.3.3.7 Example 3.a: SUMG850-A (Figures 4.33 and 4.34)

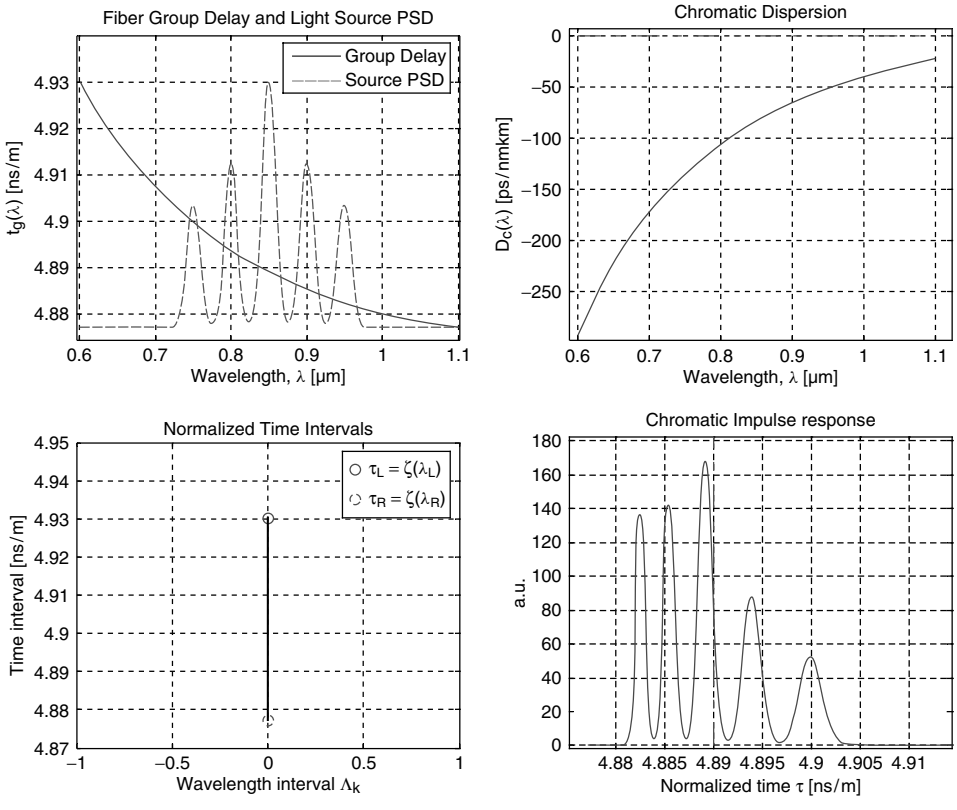

Figure 4.33 Sellmeier group delay. Wavelength interval $600\,\text{nm} \leq \lambda \leq 1100\,\text{nm}$, multi-Gaussian peaks $N_p = 5$, FWHM $= 20\,\text{nm}$, $\Delta\lambda_p = 50\,\text{nm}$, $A = [0.15, 0.20, 0.30, 0.20, 0.15]$, $\lambda_c = 850\,\text{nm}$

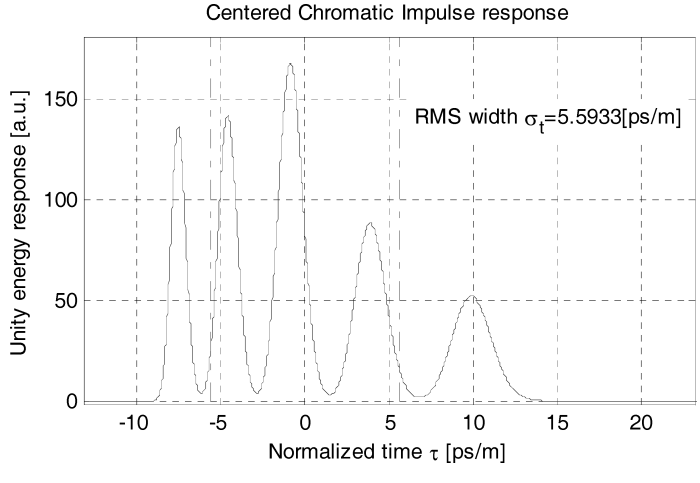

Figure 4.34 Chromatic impulse response to the spectral condition shown above

4.3.3.8 Example 3.a: SUMG850-B (Figures 4.35 and 4.36)

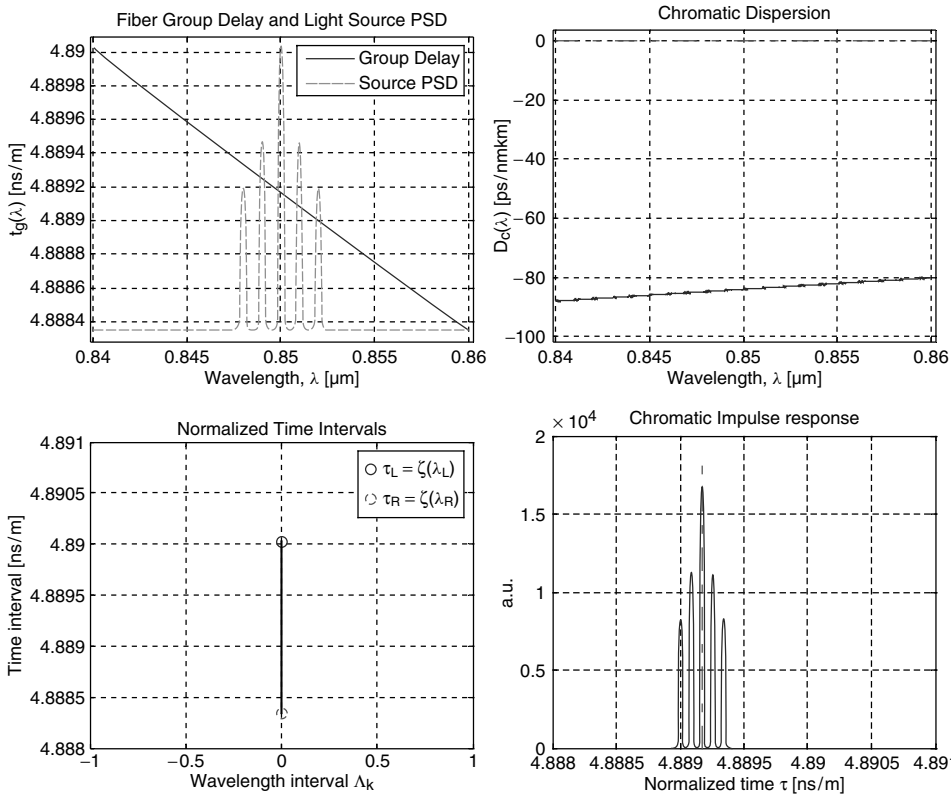

Figure 4.35 Sellmeier group delay. Wavelength interval 840 nm $\leq \lambda \leq$ 860 nm, multi-Gaussian peaks $N_p = 5$, FWHM = 0.20 nm, $\Delta\lambda_p = 1$ nm, $A = [0.15, 0.20, 0.30, 0.20, 0.15]$, $\lambda_c = 850$ nm

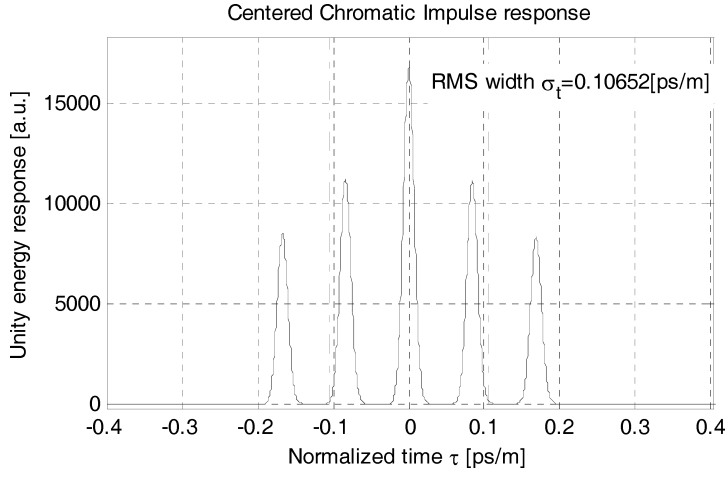

Figure 4.36 Chromatic impulse response to the spectral condition shown above

4.3.3.9 Example 3.b: SUMG1550-A (Figures 4.37 and 4.38)

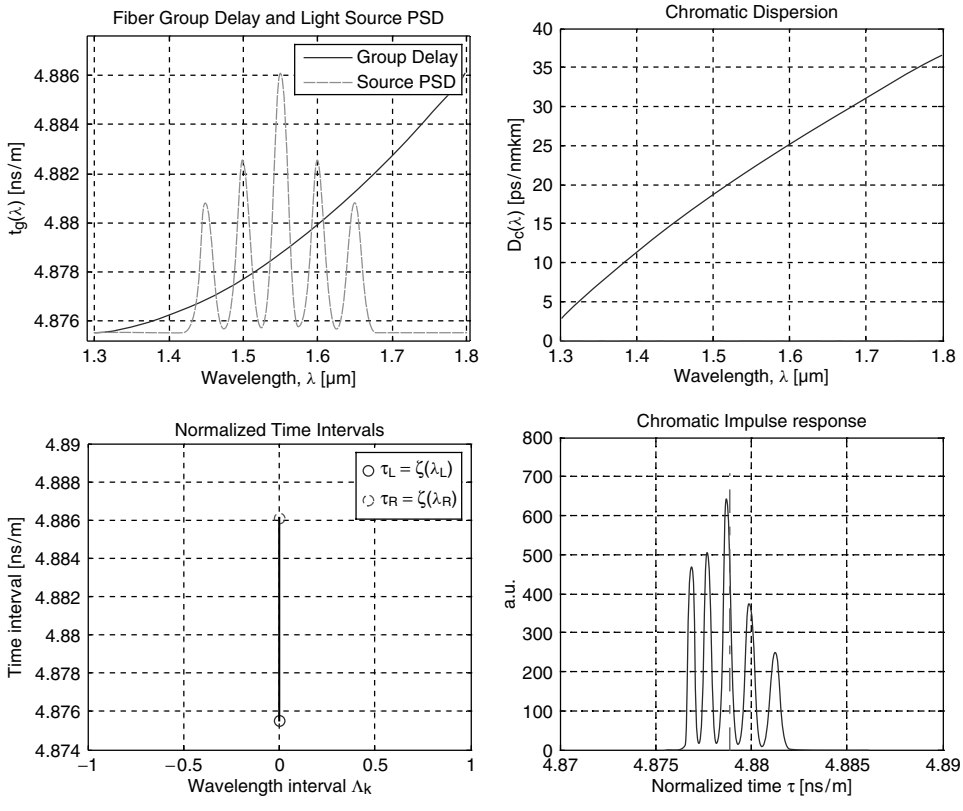

Figure 4.37 Sellmeier group delay. Wavelength interval $1300\,\text{nm} \leq \lambda \leq 1800\,\text{nm}$, multi-Gaussian peaks $N_p = 5$, FWHM $= 20\,\text{nm}$, $\Delta\lambda_p = 50\,\text{nm}$, $A = [0.15, 0.20, 0.30, 0.20, 0.15]$, $\lambda_c = 1550\,\text{nm}$

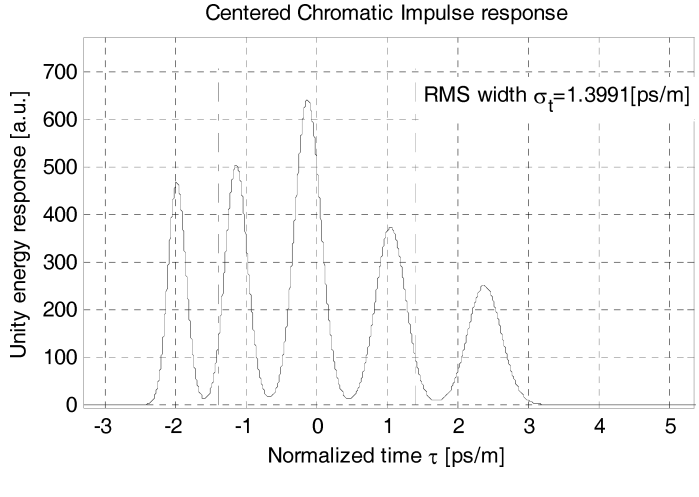

Figure 4.38 Chromatic impulse response to the spectral condition shown above

4.3.3.10 Example 3.b: SUMG1550-B (Figures 4.39 and 4.40)

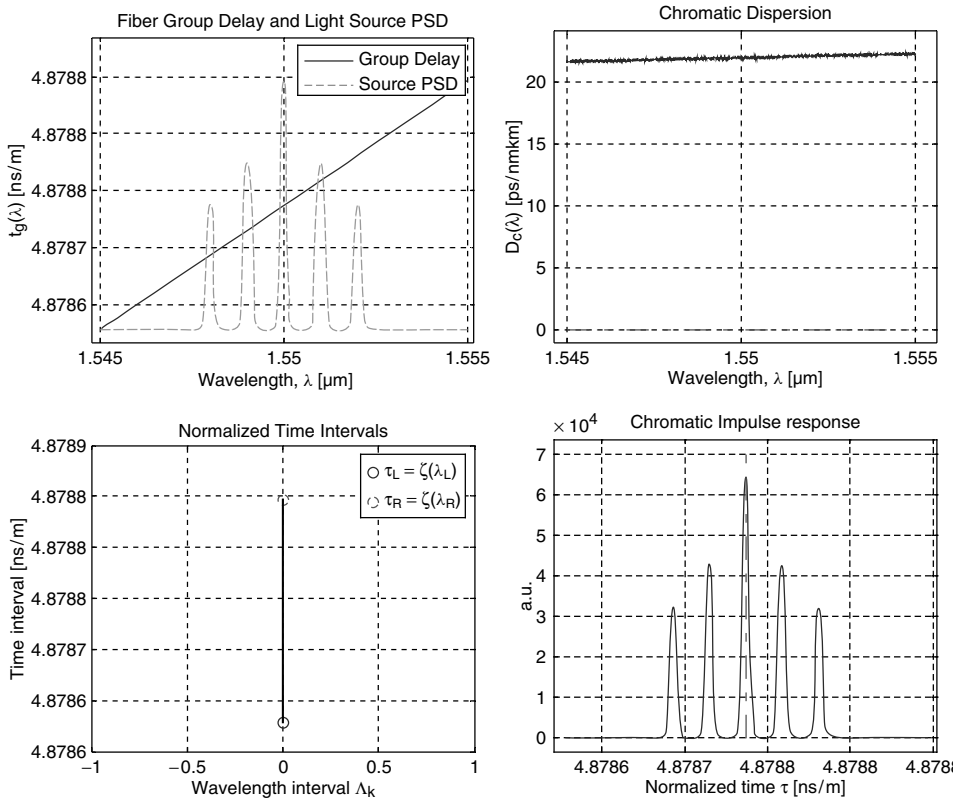

Figure 4.39 Sellmeier group delay. Wavelength interval $1545\,\text{nm} \leq \lambda \leq 1565\,\text{nm}$, multi-Gaussian peaks $N_p = 5$, FWHM $= 0.20\,\text{nm}$, $\Delta\lambda_p = 1\,\text{nm}$, $A = [0.15, 0.20, 0.30, 0.20, 0.15]$, $\lambda_c = 1550\,\text{nm}$

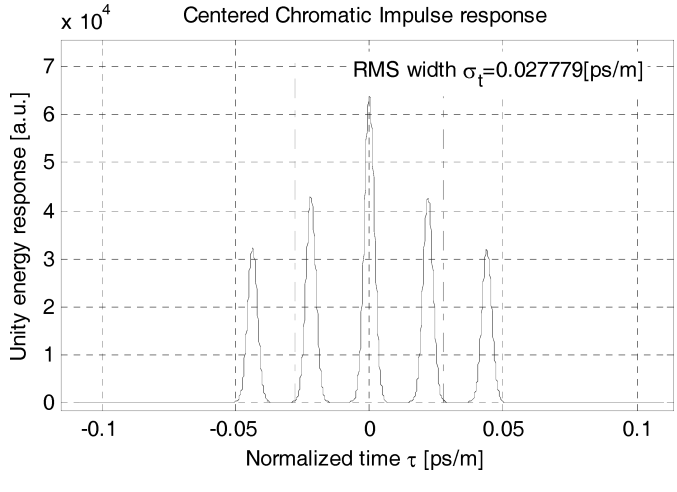

Figure 4.40 Chromatic impulse response to the spectral condition shown above

4.3.3.11 Example 3.c: SUMG1300-A (Figures 4.41 and 4.42)

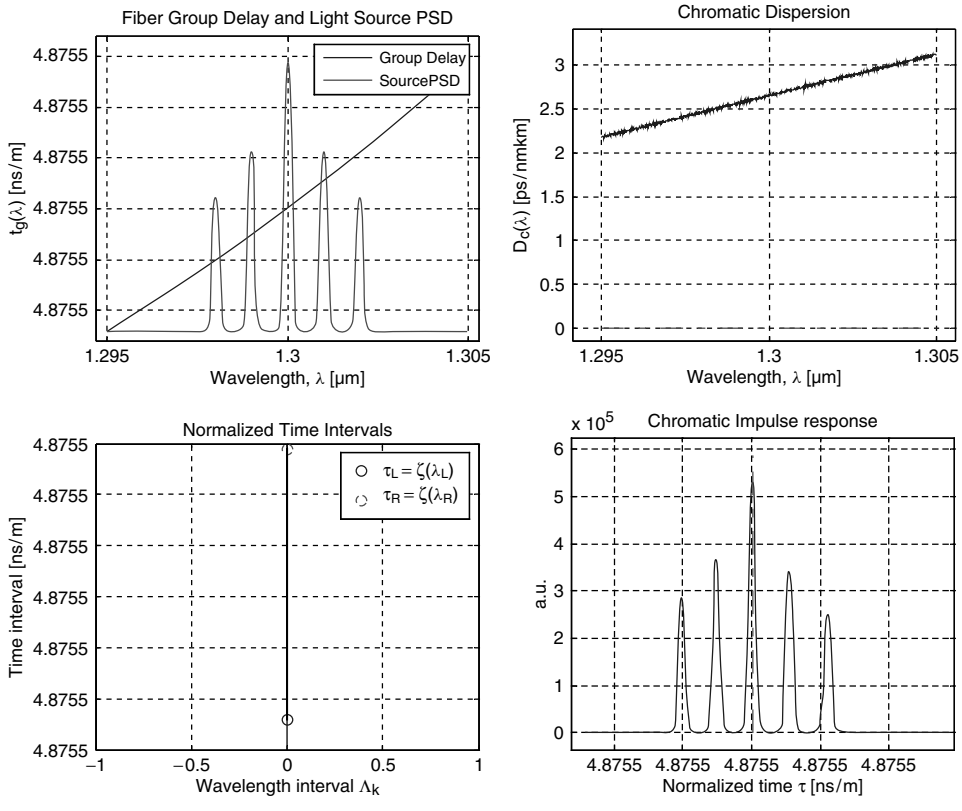

Figure 4.41 Sellmeier group delay. Wavelength interval $1295\,\text{nm} \leq \lambda \leq 1305\,\text{nm}$, multi-Gaussian peaks $N_p = 5$, FWHM $= 0.2\,\text{nm}$, $\Delta\lambda_p = 1\,\text{nm}$, $A = [0.15, 0.20, 0.30, 0.20, 0.15]$, $\lambda_c = 1300\,\text{nm}$

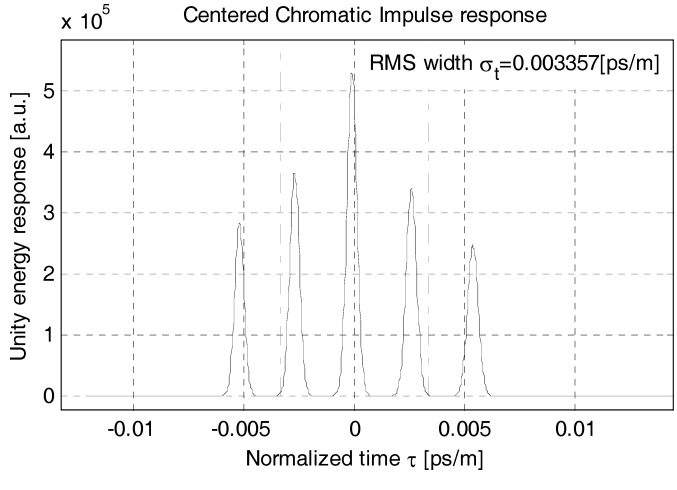

Figure 4.42 Chromatic impulse response to the spectral condition shown above

4.3.3.12 Example 3.c: SUMG1300-B (Figures 4.43 and 4.44)

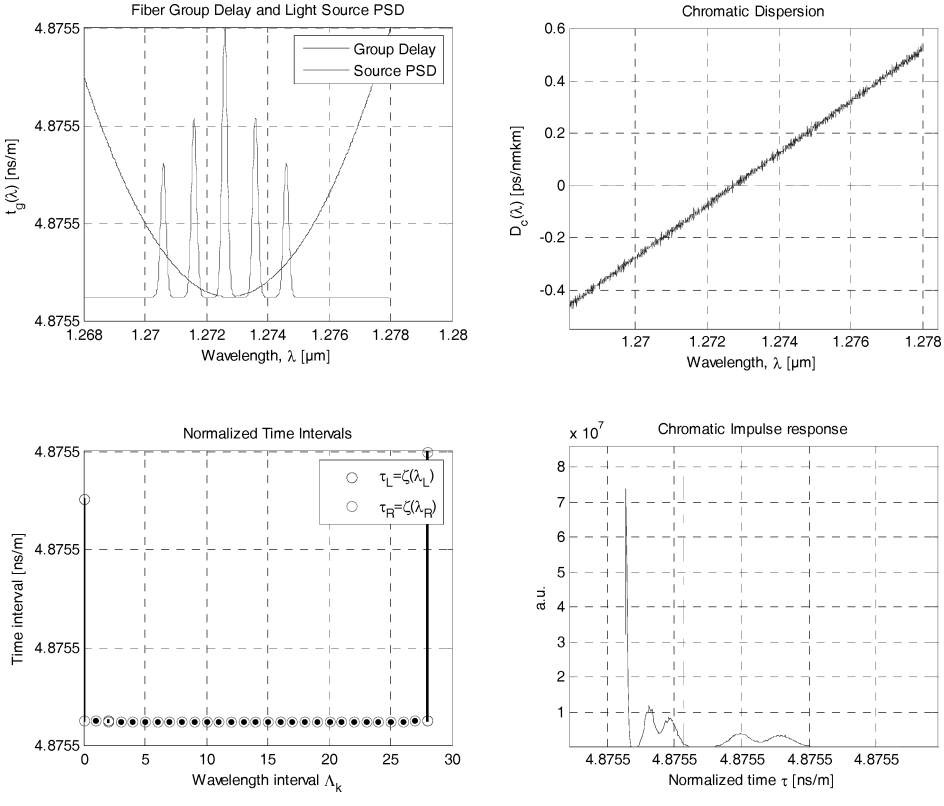

Figure 4.43 Sellmeier group delay. Wavelength interval $1268\,\text{nm} \leq \lambda \leq 1278\,\text{nm}$, multi-Gaussian peaks $N_p = 5$, FWHM $= 0.2\,\text{nm}$, $\Delta\lambda_p = 1\,\text{nm}$, $A = [0.15, 0.20, 0.30, 0.20, 0.15]$, $\lambda_c = 1272.6\,\text{nm}$

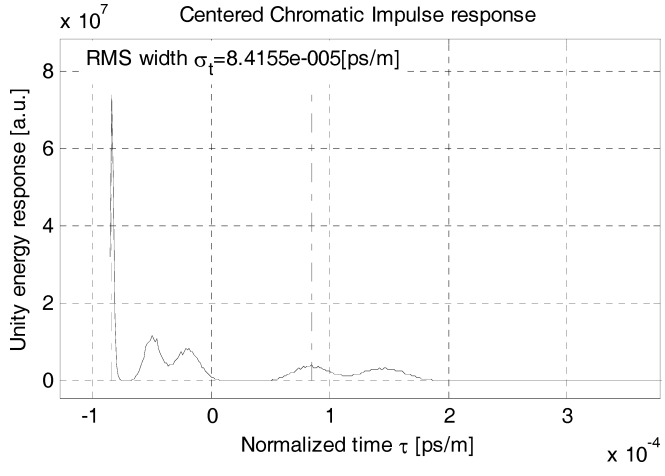

Figure 4.44 Chromatic impulse response to the spectral condition shown above

4.3.3.13 Example 3.c: SUMG1300-C (Figures 4.45 and 4.46)

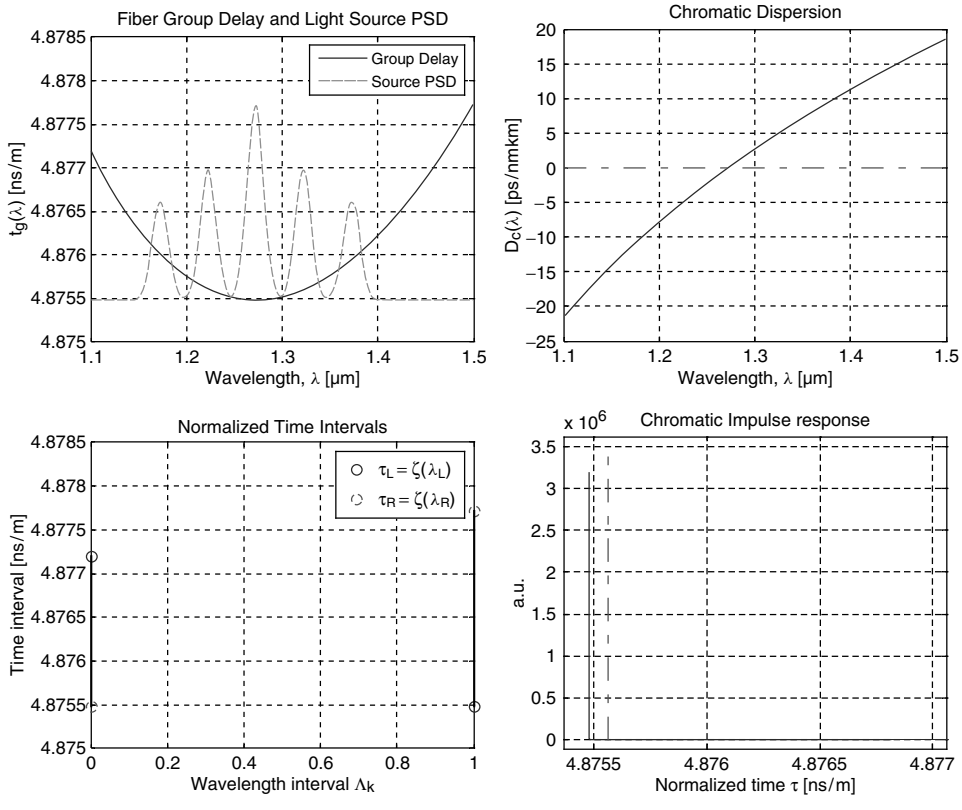

Figure 4.45 Sellmeier group delay. Wavelength interval $1100\,\text{nm} \leq \lambda \leq 1500\,\text{nm}$, multi-Gaussian peaks $N_p = 5$, FWHM $= 20\,\text{nm}$, $\Delta\lambda_p = 50\,\text{nm}$, $A = [0.15, 0.20, 0.30, 0.20, 0.15]$, $\lambda_c = 1272.6\,\text{nm}$

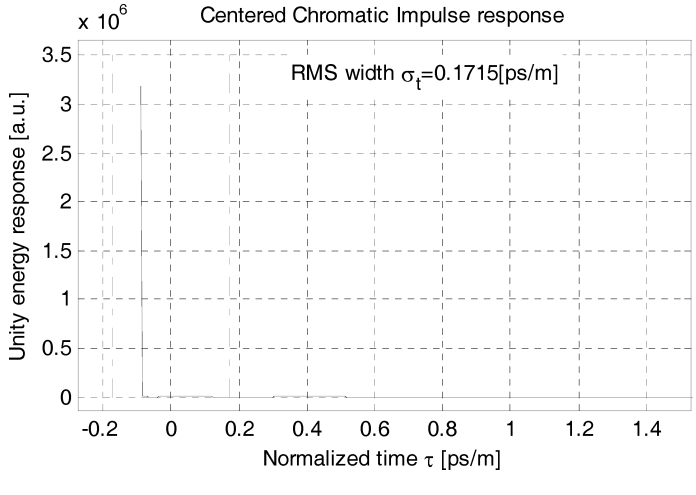

Figure 4.46 Chromatic impulse response to the spectral condition shown above

4.3.3.14 Example 4.a: SRMG850 (Figures 4.47 and 4.48)

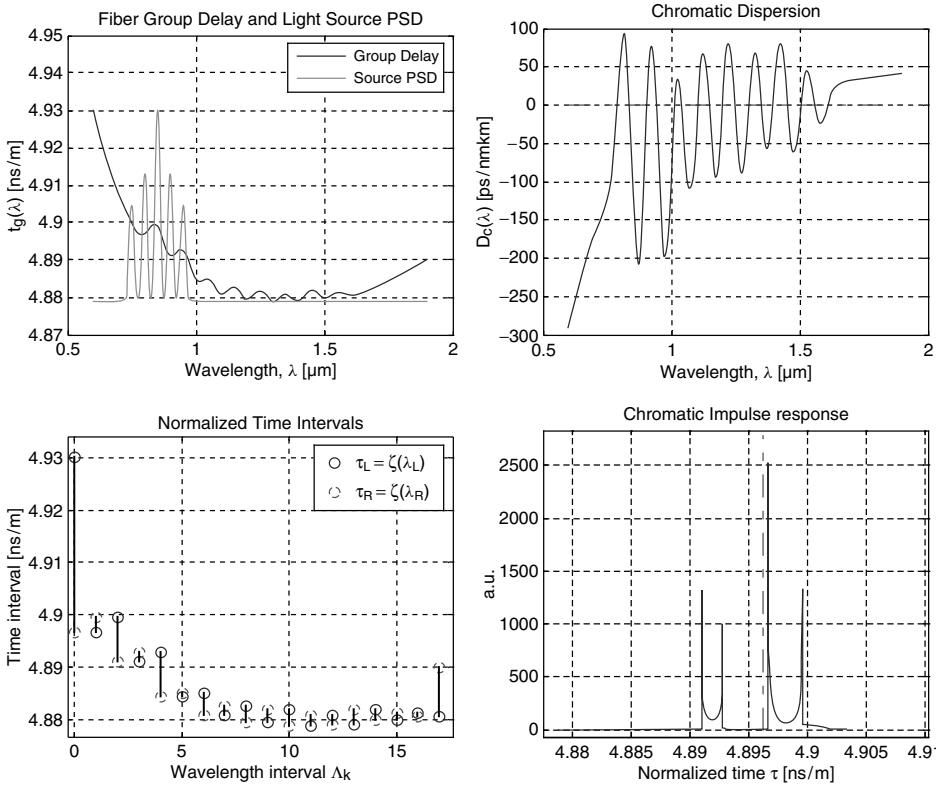

Figure 4.47 Wavelength interval $600\,\text{nm} \le \lambda \le 1900\,\text{nm}$, multi-Gaussian peaks $N_p = 5$, FWHM $= 20\,\text{nm}$, $\Delta\lambda_p = 50\,\text{nm}$, $A = [0.15, 0.20, 0.30, 0.20, 0.15]$, $\lambda_c = 850\,\text{nm}$. Sellmeier group delay with added multi-Gaussian ripple

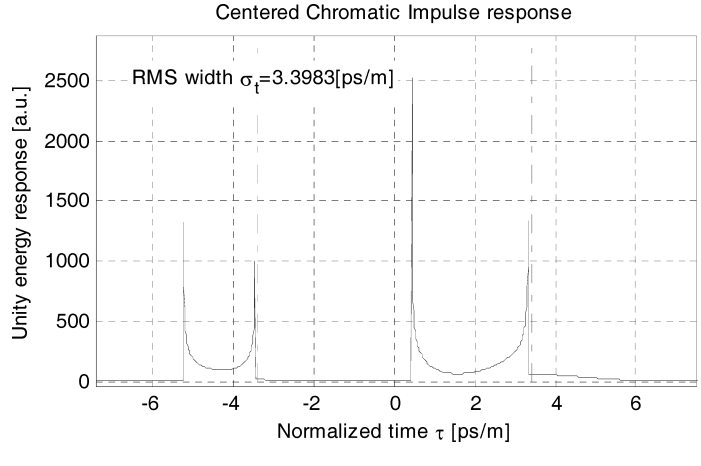

Figure 4.48 Chromatic impulse response to the spectral condition shown above

4.3.3.15 Example 4.b: SRMG1550 (Figures 4.49 and 4.50)

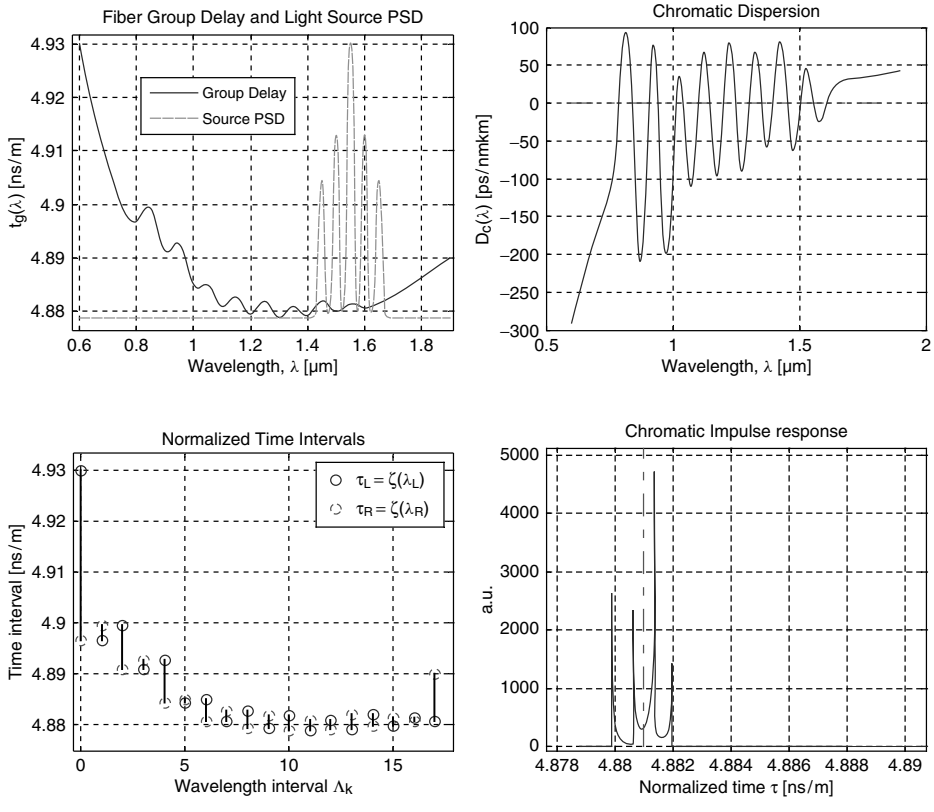

Figure 4.49 Wavelength interval $600\,\text{nm} \leq \lambda \leq 1900\,\text{nm}$, multi-Gaussian peaks $N_p = 5$, FWHM $= 20\,\text{nm}$, $\Delta\lambda_p = 50\,\text{nm}$, $A = [0.15, 0.20, 0.30, 0.20, 0.15]$, $\lambda_c = 1550\,\text{nm}$. Sellmeier group delay with added multi-Gaussian ripple

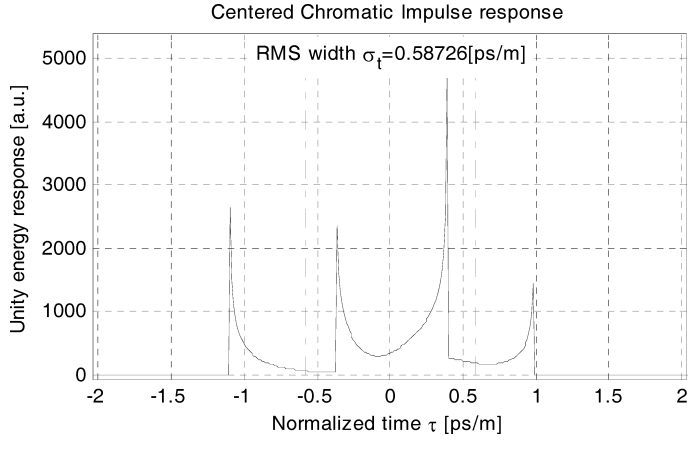

Figure 4.50 Chromatic impulse response to the spectral condition shown above

4.3.3.16 Example 4.c: SRMG1310 (Figures 4.51 and 4.52)

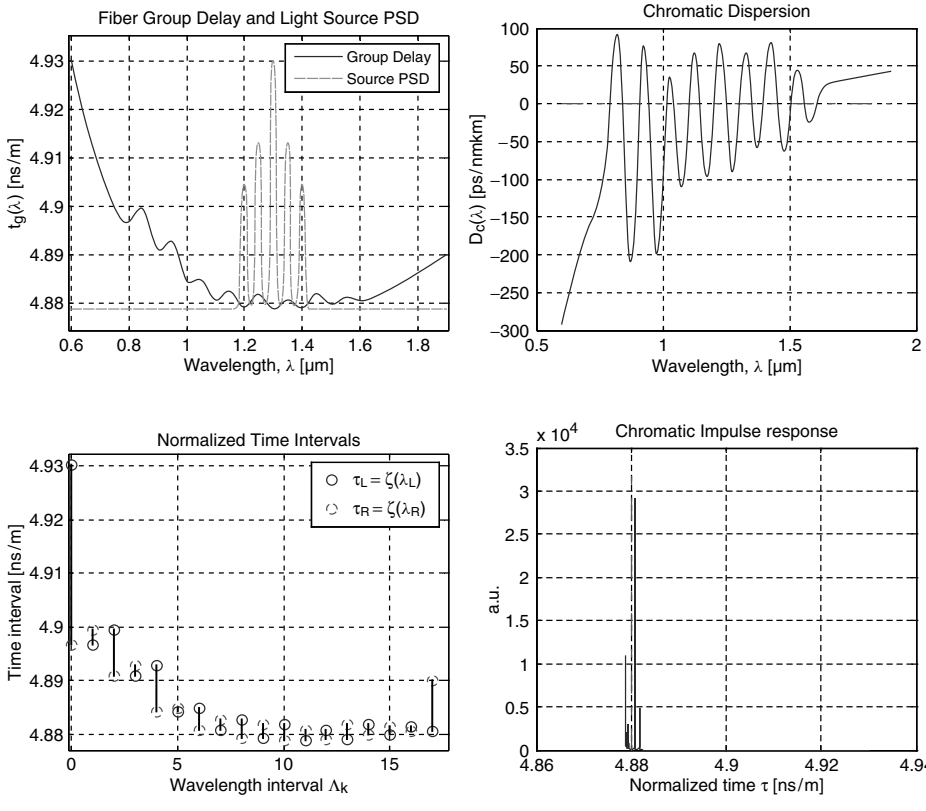

Figure 4.51 Wavelength interval $600\,\text{nm} \le \lambda \le 1900\,\text{nm}$, multi-Gaussian peaks $N_p = 5$, FWHM $= 20\,\text{nm}$, $\Delta\lambda_p = 50\,\text{nm}$, $A = [0.15, 0.20, 0.30, 0.20, 0.15]$, $\lambda_c = 1300\,\text{nm}$. Sellmeier group delay with added multi-Gaussian ripple

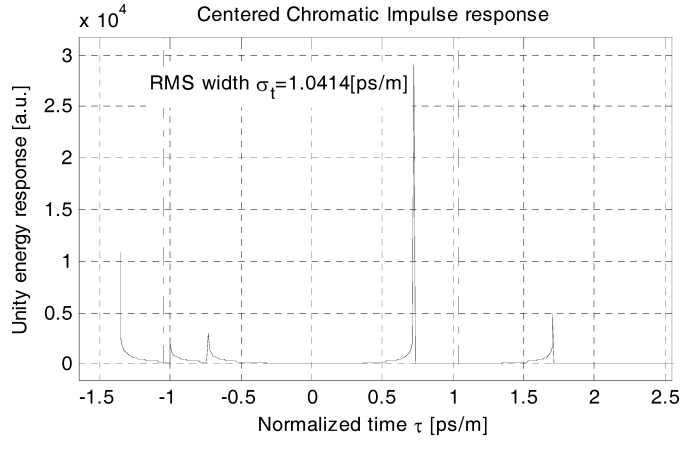

Figure 4.52 Chromatic impulse response to the spectral condition shown above

4.3.4 Comments and Remarks

The results achieved in the previous section are quite remarkable and some comments are needed to point out major conclusions. Assuming two group delay modelings and two source spectrum PSDs, four different propagation conditions have been established for the chromatic impulse response. Those conditions have been grouped in Table 4.1 according to the following four identification codes:

$$SUSG \longrightarrow Sellmeier\ uniform\ single\text{-}Gaussian$$

$$SRSG \longrightarrow Sellmeier\ ripple\ single\text{-}Gaussian$$

$$SRSG \longrightarrow Sellmeier\ uniform\ Multi\text{-}Gaussian$$

$$SRSG \longrightarrow Sellmeier\ ripple\ multi\text{-}Gaussian$$

Each coded condition has been solved for the three wavelength ranges of interest, namely $\lambda_c = 850\,\text{nm}$, $\lambda_c = 1300\,\text{nm}$ and $\lambda_c = 1550\,\text{nm}$, producing 12 basic chromatic impulse responses. In addition to those conditions, four more cases have been added in order to highlight major peculiarities when multi-Gaussian source profiles are considered. Major conclusions are:

1. If the source PSD does not overlap any zero-dispersion wavelength, typically in both $\lambda_c = 850\,\text{nm}$ and $\lambda_c = 1550\,\text{nm}$ wavelength ranges, the chromatic impulse response closely resembles the source power spectral density. This natural behavior of the chromatic impulse response can be clearly seen from the seven computed cases in the following subsections:
   (a) Section 4.3.3.1: SUSG850 (Figure 4.21)
   (b) Section 4.3.3.2: SUSG1550 (Figure 4.23)
   (c) Section 4.3.3.7: SUMG850-A (Figure 4.33)
   (d) Section 4.3.3.8: SUMG850-B (Figure 4.35)
   (e) Section 4.3.3.9: SUMG1550-A (Figure 4.37)
   (f) Section 4.3.3.10: SUMG1550-B (Figure 4.39)
   (g) Section 4.3.3.11: SUMG1300-A (Figure 4.41)
2. If the source PSD spans over one or more zero-dispersion wavelengths of the group delay function the resulting chromatic impulse response is fully unpredictable, as is clearly shown by the computed cases. Essentially, if the source PSD has not a negligible value at the zero-dispersion wavelength, that power contribution strongly dominates the whole response over the remaining source power terms and the chromatic impulse response closely resembles a Dirac delta profile. This situation, which would be quite predictable in the presence of a single zero-dispersion wavelength leading to an almost ideal response, becomes quite unpredictable if more zero-dispersion wavelengths are simultaneously present in the group delay function. This situation is well represented for the modeling of the group delay by adding a weighted Gaussian ripple. Depending on the ripple amplitude, this will reflect a corresponding time shifting of the various impulsive components, leading to a strong echoes-affected impulse response. Such interesting cases have very often been exaggerated in the previous examples by adding a well-defined and consistent ripple to the uniform Sellmeier group delay function. This led to the following six simulation results:
   (a) Section 4.3.3.4: SRSG850 (Figure 4.27)
   (b) Section 4.3.3.5: SRSG1550 (Figure 4.51)
   (c) Section 4.3.3.6: SRSG1300 (Figure 4.29)
   (d) Section 4.3.3.14: SRMG850 (Figure 4.31)
   (e) Section 4.3.3.15: SRMG1550 (Figure 4.47)
   (f) Section 4.3.3.16: SRMG1300 (Figure 4.49)
3. The remaining three cases all refer to the uniform Sellmeier group delay function excited in the $\lambda_c = 1300\,\text{nm}$ range by either a single-Gaussian or a multi-Gaussian source PSD. The interesting

result is that the chromatic impulse response behaves almost independently from the spectrum profile, resulting in a very sharp single-peak impulsive response. This means that the amount of source spectrum energy allocated close to the zero-dispersion wavelength strongly dominates the whole energy distribution of the fiber chromatic response. These cases are reported in the previous subsections:

(a) Section 4.3.3.3: SUSG1300 (Figure 4.25)
(b) Section 4.3.3.12: SUMG1300-B (Figure 4.43)
(c) Section 4.3.3.13: SUMG1300-C (Figure 4.45)

4.4 Moments of Chromatic Impulse Response

In this section the first- and second-order moments of the chromatic impulse response will be discussed. The first-order moment gives the average time value of the response, whereas the second-order moment gives the response temporal dispersion. Those two moments are quite useful in characterizing the chromatic impulse response behavior and are used extensively in first-order estimations of the optical fiber transmission system performance.

4.4.1 Energy Normalization

In order to proceed as easily as possible, it is convenient to consider the chromatic impulse response derived in Equation (4.32). Here, in order to simplify the notation the reference to some specific hth individual mode in the multimode fiber has been removed. This dependence must of course be implicitly intended in the following:

$$h_c(z,t) = \int_{-\infty}^{+\infty} S_s(\lambda)\delta[t - z\tau_g(\lambda)]\,d\lambda \tag{4.78}$$

where the temporal variable is the time t and not the normalized time $\tau = t/z$. This is quite important since the response normalization is defined with respect to the absolute time variable t. The integral of the impulse response in the time variable gives the energy W_c of the pulse $h_c(z,t)$. In the present theory any losses are excluded so energy conservation is expected at every section of the fiber, independently of the distance z:

$$W_c = \int_{-\infty}^{+\infty} h_c(z,t)\,dt = \int_{-\infty}^{+\infty}\int_{-\infty}^{+\infty} S_s(\lambda)\delta[t - z\tau_g(\lambda)]\,d\lambda\,dt \tag{4.79}$$

Performing the integral over time first and using the integral property of the Dirac delta function it is easily concluded that

$$W_c = \int_{-\infty}^{+\infty} h_c(z,t)\,dt = \int_{-\infty}^{+\infty} S_s(\lambda)\,d\lambda \int_{-\infty}^{+\infty} \delta[t - z\tau_g(\lambda)]\,dt = \int_{-\infty}^{+\infty} S_s(\lambda)\,d\lambda \tag{4.80}$$

Finally, due to the assumed source PSD normalization in Equation (4.25), it is concluded that the chromatic impulse response has constant unit energy:

$$W_c = \int_{-\infty}^{+\infty} h_c(z,t)\,dt = 1 \tag{4.81}$$

It is instructive to compute the chromatic response energy in the normalized time domain, using the variable τ. To this end, it is easy to solve the following integral by the variable substitution $\tau = t/z$ and using the result just derived in Equation (4.81):

$$\int_{-\infty}^{+\infty} h_c(z,t)\,d\tau = \frac{1}{z}\int_{-\infty}^{+\infty} h_c(z,t)\,dt = \frac{W_c}{z} = \frac{1}{z} \tag{4.82}$$

In conclusion, the chromatic impulse response energy is conserved and is normalized to the unit. The same normalization integral in the variable τ gives accordingly a decreasing value with the distance z. This result will be used later in the first- and second-order moment calculations.

In the following derivations the explicit expression for the chromatic impulse response given in Equation (4.71) will be needed several times. As mentioned above, any index reference to modal properties will be discarded and the index k will be used instead to refer to the chromatic impulse response contribution of the partial wavelength interval due to the multivalued inverse group delay function. From Equation (4.71),

$$\underbrace{h_{c,k}(\tau) \equiv \frac{S_s[\zeta_g(\tau)]}{|D_c[\zeta_g(\tau)]|}}_{\lambda=\zeta_g(\tau)\in\Lambda_k,k=1,2,\ldots,N-1,\begin{cases}\Lambda_0=(0,\lambda_1)\\ \Lambda_k=(\lambda_k,\lambda_{k+1})\\ \Lambda_N=(\lambda_N,+\infty)\end{cases}} \qquad \Rightarrow h_c(z,\tau)=\frac{1}{z}\sum_{k=0}^{N} h_{c,k}(\tau) \tag{4.83}$$

In the expression above the notation referring to the three different partition intervals Λ_0, Λ_k, Λ_N has been simplified.

4.4.2 Average Value

The average value $\overline{t}(z)$ of the time variable t according to the chromatic impulse response $h_c(z,t)$ is defined by the following integration, where the response normalization (4.81) is used:

$$\overline{t}(z) \equiv \frac{\displaystyle\int_{-\infty}^{+\infty} t\, h_c(z,t)\,\mathrm{d}t}{\displaystyle\int_{-\infty}^{+\infty} h_c(z,t)\,\mathrm{d}t} = \int_{-\infty}^{+\infty} t\, h_c(z,t)\,\mathrm{d}t \tag{4.84}$$

Note that the average time $\overline{t}(z)$ is a function of the distance because the integration operates only over the time variable of the impulse response $h_c(z,t)$. Substituting Equation (4.83) gives

$$\overline{t}(z) = \frac{1}{z}\sum_{k=0}^{N}\int_{zT_k} t\, h_{c,k}(\tau)\,\mathrm{d}t \tag{4.85}$$

Each integral in the sum must be performed over the partial time interval $(t_k, t_{k+1}) = z(\tau_k, \tau_{k+1}) = zT_k$. Substituting the normalized variable $\tau = t/z$ gives

$$\overline{t}(z) = z\sum_{k=0}^{N}\int_{T_k} \tau h_{c,k}(\tau)\,\mathrm{d}\tau \tag{4.86}$$

This expression has a relevant physical meaning. In order to show this, the average value of the normalized temporal variable $\tau = t/z$ is considered. Following the same definition as Equation (4.84) and using the result in Equation (4.82) gives

$$\overline{\tau} \equiv \frac{\displaystyle\int_{-\infty}^{+\infty} \tau h_c(z,t)\,\mathrm{d}\tau}{\displaystyle\int_{-\infty}^{+\infty} h_c(z,t)\,\mathrm{d}\tau} = z\int_{-\infty}^{+\infty} \tau h_c(z,t)\,\mathrm{d}\tau \tag{4.87}$$

Substituting the expression (4.83) of the chromatic impulse response, the following important result of the average value of the normalized time is found:

$$\overline{\tau} = \sum_{k=0}^{N} \int_{T_k} \tau h_{c,k}(\tau)\, d\tau \tag{4.88}$$

note that the average delay $\overline{\tau}$ does not depend upon the distance z. Comparing with Equation (4.86) it is concluded as expected that

$$\overline{t}(z) = z\overline{\tau} \tag{4.89}$$

The average time delay of the chromatic impulse response depends linearly upon the distance z. This statement holds in general without any further assumption.

Expression (4.89) allows a calculation to be made of the average time operating just over the normalized time response, and then multiplying the result by the required distance z. The normalized average delay $\overline{\tau}$ of the chromatic impulse response can be computed explicitly in terms of the source PSD and chromatic dispersion coefficient. Substituting Equation (4.83) into Equation (4.88) and using Equation (4.89), it can be concluded that

$$\overline{\tau} = \underbrace{\sum_{k=0}^{N} \int_{T_k} \tau \frac{S_s[\zeta_g(\tau)]}{|D_c[\zeta_g(\tau)]|}\, d\tau}_{\lambda=\zeta_g(\tau)\in\Lambda_k,k=1,2,\ldots,N-1,\ \begin{cases}\Lambda_0=(0,\lambda_1)\\ \Lambda_k=(\lambda_k,\lambda_{k+1})\\ \Lambda_N=(\lambda_N,+\infty)\end{cases}} \Rightarrow \overline{t} = z\overline{\tau} \tag{4.90}$$

This expression represents the general analytical form of the average delay of the chromatic impulse response. The pulse centering procedure used in the chromatic impulse response solution algorithm presented in Section 4.3 was based on expression (4.90). In the simple case where any stationary wavelength was included in the spectral range Λ_s of the source PSD, the above expression greatly simplifies:

$$\overline{\tau} = \underbrace{\int_{T_s} \tau \frac{S_s[\zeta_g(\tau)]}{|D_c[\zeta_g(\tau)]|}\, d\tau}_{\tau\in T_s \leftrightarrow \lambda=\zeta_g(\tau)\in\Lambda_s} \Rightarrow \overline{t} = z\overline{\tau} \tag{4.91}$$

4.4.3 Linear Approximation of the Group Delay

The average delay $\overline{\tau}$ depends on the whole contribution of the chromatic dispersion function over the wavelength interval defined by the source PSD. In the following the linear approximation of the chromatic dispersion coefficient around the average wavelength of the source spectrum will be introduced. This will allow a significant simplification of the expression (4.90), which will lead to an interesting physical interpretation.

The average wavelength $\overline{\lambda}$ emitted by the source power spectral density is given by the following averaging integral:

$$\overline{\lambda} \equiv \frac{\int_{-\infty}^{+\infty} \lambda S_s(\lambda)\, d\lambda}{\int_{-\infty}^{+\infty} S_s(\lambda)\, d\lambda} = \int_{-\infty}^{+\infty} \lambda S_s(\lambda)\, d\lambda \tag{4.92}$$

Here the normalization property (4.25) of the source PSD was used. Assuming that the group delay function $\tau_g(\lambda)$ can be written as a power series around the average source wavelength $\overline{\lambda}$,

$$\tau_g(\lambda) = \tau_g(\overline{\lambda}) + \sum_{k=1} \left[\frac{d^k \tau_g(\lambda)}{d\lambda^k} \right]_{\overline{\lambda}} \frac{(\lambda - \overline{\lambda})^k}{k!} \tag{4.93}$$

It is important to note that in general the value of the group delay $\tau_g(\overline{\lambda})$ assumed at the average spectrum wavelength $\overline{\lambda}$ is different from the average delay $\overline{\tau}$ of the chromatic impulse response given by Equation (4.90); therefore, in general $\tau_g(\overline{\lambda}) \neq \overline{\tau}$. This is a consequence of the response pulse distortion with respect to the source PSD profile.

Since the chromatic dispersion coefficient is defined as the first-order wavelength derivative of the group delay function, it can be concluded from Equation (4.93) that

$$\begin{aligned} D_c(\lambda) &= \sum_{k=0} \left[\frac{d^{k+1} \tau_g(\lambda)}{d\lambda^{k+1}} \right]_{\overline{\lambda}} \frac{(\lambda - \overline{\lambda})^k}{k!} \\ &= D_c(\overline{\lambda}) + \sum_{k=1} \left[\frac{d^k D_c(\lambda)}{d\lambda^k} \right]_{\overline{\lambda}} \frac{(\lambda - \overline{\lambda})^k}{k!} \end{aligned} \tag{4.94}$$

It is already known that the first derivative of the chromatic dispersion coefficient is usually identified by the symbol $S_c(\lambda)$ in order to remember that it is the slope of the chromatic dispersion coefficient $D_c(\lambda)$, but it must not be confused with the source PSD notation $S_s(\lambda)$ used so far in this chapter. Equations (4.93) and (4.94) give the following linear approximation of the group delay function around the average spectrum wavelength:

$$\tau_g(\lambda) \cong \tau_g(\overline{\lambda}) + (\lambda - \overline{\lambda}) \overline{D}_c \tag{4.95}$$

where

$$\overline{D}_c \equiv D_c(\overline{\lambda}) \tag{4.96}$$

Using the linear approximation (4.95) of the group delay function around the average wavelength $\overline{\lambda}$ of the source spectrum, the average delay $\overline{\tau}$ of the chromatic impulse response in Equation (4.91) takes the simplified form:

$$\overline{\tau} \cong \frac{1}{|\overline{D}_c|} \underbrace{\int_{T_s} \tau S_s[\zeta_g(\tau)] \, d\tau}_{\tau \in T_s \longleftrightarrow \lambda = \zeta_g(\tau) \in \Lambda_s} \tag{4.97}$$

If linear group delay is assumed, implicitly a single-valued inverse group delay function $\lambda = \zeta_g(\tau)$ is then assumed and the wavelength partition is no longer required. Consequently, from Equation (4.90) it is possible to remove the sum symbol, replacing the sum over multiple integrals with the single integral over the wavelength range defined by the source PSD as reported in Equation (4.91). This means that for every instant τ belonging to the integration interval T_s, one and only one wavelength $\lambda = \zeta_g(\tau)$ exists that belongs to the wavelength interval Λ_s defined by the source power spectral density $S_s(\lambda)$.

The approximate expression (4.97) of the average delay of the chromatic impulse response has a meaningful interpretation. In fact, by changing the integration variable to $\lambda = \zeta_g(\tau)$,

$$\lambda = \zeta_g(\tau) \underset{\tau \in T_s}{\longleftrightarrow} \tau = \tau_g(\lambda) \underset{\lambda \in \Lambda_s = (\lambda_{min}, \lambda_{max})}{}, \qquad T_s \longleftrightarrow \Lambda_s, \qquad d\tau = \frac{d\lambda}{d\zeta_g(\tau)/d\tau} = \frac{d\tau_g(\lambda)}{d\lambda} d\lambda \tag{4.98}$$

and

$$\overline{\tau} \cong \frac{1}{|\overline{D}_c|} \int_{\Lambda_s} \left| \frac{d\tau_g(\lambda)}{d\lambda} \right| \tau_g(\lambda) S_s(\lambda)\, d\lambda = \int_{\Lambda_s} \tau_g(\lambda) S_s(\lambda)\, d\lambda \tag{4.99}$$

where the linear approximation $\overline{D}_c \cong [d\tau_g(\lambda)/d\lambda]_{\lambda \in \Lambda_s}$ was used. The modulus of the wavelength derivative of the group delay introduced in the previous expression takes into account the sign of the wavelength increment $d\lambda$ and the positive sign of the integration interval $\Lambda_s = (\lambda_{min}, \lambda_{max})$. Substituting the linear group delay (4.95) into Equation (4.99) gives

$$\begin{aligned} \overline{\tau} &\cong \int_{\Lambda} [\tau_g(\overline{\lambda}) + (\lambda - \overline{\lambda})\overline{D}_c] S_s(\lambda)\, d\lambda \\ &= \tau_g(\overline{\lambda}) \int_{\Lambda} S_s(\lambda)\, d\lambda + \overline{D}_c \int_{\Lambda} (\lambda - \overline{\lambda}) S_s(\lambda)\, d\lambda = \tau_g(\overline{\lambda}) \end{aligned} \tag{4.100}$$

As expected, this gives the following theorem. Under the linear group delay assumption the group delay evaluated at the average wavelength $\overline{\lambda}$ of the source spectrum coincides with the average delay of the corresponding chromatic impulse response $\overline{\tau} = \tau_g(\overline{\lambda})$. This interesting consideration leads to the following fundamental theorem. Assuming the linear group delay approximation, the chromatic impulse response has exactly the same profile as the source PSD.

To prove this fundamental theorem, the general expression for the chromatic impulse response reported in Equation (4.91) is considered one more time. The linear approximation of the group delay allows the single wavelength interval Λ_s defined by the source power spectrum to be used:

$$h_c(z, \tau) = \frac{1}{z} \frac{S_s[\zeta_g(\tau)]}{|D_c[\zeta_g(\tau)]|} \cong \frac{1}{z|\overline{D}_c|} S_s[\zeta_g(\tau)] \tag{4.101}$$

where $\tau \in T_s \leftrightarrow \zeta_g(\tau) = \lambda \in \Lambda_s$. Due to the assumed linear relationship between time and wavelength, the source spectrum profile $S_s(\lambda)$ is converted into the time-scaled profile of the chromatic impulse response. The scale factor is represented by the chromatic dispersion coefficient $\overline{D}_c$. Equation (4.95) gives the following linear inverse group delay:

$$\lambda = \zeta_g(\tau) \cong \overline{\lambda} + \frac{\tau - \overline{\tau}}{\overline{D}_c}, \qquad \overline{\tau} = \tau_g(\overline{\lambda}) \tag{4.102}$$

Substituting the linear inverse group delay function into Equation (4.101) gives the chromatic impulse response under the linear group delay approximation:

$$h_c(z, \tau) \cong \frac{1}{z|\overline{D}_c|} S_s\left(\overline{\lambda} + \frac{\tau - \overline{\tau}}{\overline{D}_c}\right) \tag{4.103}$$

where $\tau \in T_s \leftrightarrow \zeta_g(\tau) = \overline{\lambda} + (\tau - \overline{\tau})/\overline{D}_c = \lambda \in \Lambda_s$.

Figure 4.53 shows the wavelength–time scaling principle. The gray shaded source power spectral density is assumed to be centered in the third optical window, where the group delay has a positive slope. Assuming that the linear approximation holds, the group delay is completely characterized by the average delay at the average spectrum wavelength and the chromatic dispersion coefficient, which represents the group delay slope.

In the figure two different cases have been characterized by two average delay and two chromatic dispersion coefficients. Those two different excitations can be easily achieved by sliding the source average wavelength along the third window range. In order to simplify the graphics, two different group delay slopes at the same average source wavelength have been given.

Expression (4.103) gives the chromatic impulse response under the assumption of a linear group delay approximation. This condition is largely encountered in most practical situations. The source

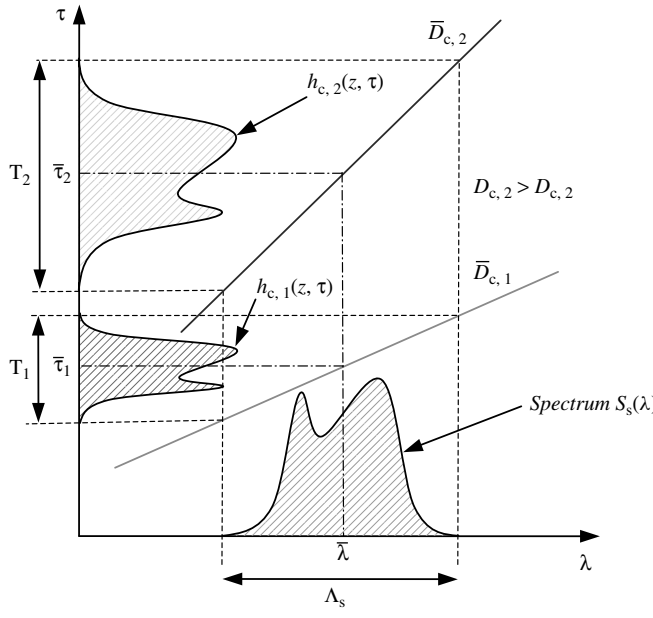

Figure 4.53 Chromatic impulse response with a linear group delay approximation. The linear group delay has a constant chromatic dispersion coefficient which leads to the chromatic impulse response being the time-scaled image of the source power spectral density. The slope of the group delay determines the scaling factor, as reported above for the increasing dispersion coefficient. The linear approximation is of course quite reasonable for a relatively narrow spectrum width located away from the zero dispersion wavelength

spectral width is usually less the 4 nm for any laser light excitation (multilongitudinal mode FP laser) and in this range the group delay is well approximated by a straight line, both in the first (820 nm $\leq \lambda \leq$ 870 nm) and third (1530 nm $\leq \lambda \leq$ 1610 nm) windows. The situation in the second window (1265 nm $\leq \lambda \leq$ 1335 nm) is different and usually requires careful consideration of the zero-dispersion wavelength, as shown in the computer simulation presented in Section 4.3.

4.4.4 Pulse Dispersion: Variance and RMS Width

In order to compute the pulse dispersion needed for the second-order moment of the chromatic impulse response function, the variance $\sigma_c^2(z)$ of the time variable t according to the chromatic impulse response $h_c(z,t)$ is defined by the following integration, where the response energy normalization (4.81) is again used:

$$\sigma_c^2(z) \equiv \frac{\displaystyle\int_{-\infty}^{+\infty} [t-\overline{t}(z)]^2 h_c(z,t)\,\mathrm{d}t}{\displaystyle\int_{-\infty}^{+\infty} h_c(z,t)\,\mathrm{d}t} = \int_{-\infty}^{+\infty} [t-\overline{t}(z)]^2 h_c(z,t)\,\mathrm{d}t \tag{4.104}$$

It is noted that the variance $\sigma_c^2(z)$ is a function of the distance z because the integration operates only over the time variable of the impulse response $h_c(z,t)$. Substituting expression (4.83) of the

chromatic impulse response gives

$$\sigma_c^2(z) = \frac{1}{z}\sum_{k=0}^{N}\int_{zT_k}[t-\overline{t}(z)]^2 h_{c,k}(\tau)\,\mathrm{d}t \tag{4.105}$$

The integration variable is the absolute time t while each response contribution depends on the normalized time τ. In addition, each partial integral must be performed over the time interval $(t_k, t_{k+1}) = z(\tau_k, \tau_{k+1}) = zT_k$ in exactly the same way as encountered for the average delay calculation. Substituting the normalized variable $\tau = t/z$, $\mathrm{d}t = z\,\mathrm{d}\tau$, $t \in zT_k \Rightarrow \tau \in T_k$, and using the result (4.89), expression (4.103) becomes

$$\sigma_c^2(z) = z^2\sum_{k=0}^{N}\int_{T_k}(\tau-\overline{\tau})^2 h_{c,k}(\tau)\,\mathrm{d}\tau \tag{4.106}$$

The expression just derived for the variance of the chromatic impulse response looks quite similar to the expression (4.86) of the average delay $\overline{t}$. This suggests proceeding with the definition of the corresponding chromatic variance σ_τ^2 of the normalized time variable τ:

$$\sigma_\tau^2(z) \equiv \frac{\displaystyle\int_{-\infty}^{+\infty}(\tau-\overline{\tau})^2 h_c(z,t)\,\mathrm{d}\tau}{\displaystyle\int_{-\infty}^{+\infty}h_c(z,t)\,\mathrm{d}\tau} \tag{4.107}$$

From Equation (4.81),

$$\int_{-\infty}^{+\infty}h_c(z,t)\,\mathrm{d}\tau = \frac{1}{z}\int_{-\infty}^{+\infty}h_c(z,t)\,\mathrm{d}\tau = \frac{1}{z} \tag{4.108}$$

and the variance of the normalized time variable τ assumes the following form:

$$\sigma_\tau^2(z) = z\int_{-\infty}^{+\infty}(\tau-\overline{\tau})^2 h_c(z,t)\,\mathrm{d}\tau \tag{4.109}$$

Substituting the chromatic impulse response expression (4.83) gives the following relevant theorem:

$$\sigma_\tau^2 = \sum_{k=0}^{N}\int_{T_k}(\tau-\overline{\tau})^2 h_{c,k}(\tau)\,\mathrm{d}\tau \tag{4.110}$$

The variance of the normalized time variable evaluated by means of the chromatic impulse response no longer depends on the distance z.

Comparing with the expression of the variance given in Equation (4.106), it can be concluded that

$$\sigma_c^2(z) = z^2\sigma_\tau^2 \tag{4.111}$$

The variance of the chromatic impulse response depends quadratically upon the distance z. This statement holds in general, without any further assumption.

The RMS pulse width is defined as the square root of the variance. From Equation (4.110) and (4.111) the following general expression is obtained for the RMS width of the chromatic impulse response:

$$\sigma_\tau = \sqrt{\sum_{k=0}^{N}\int_{T_k}(\tau-\overline{\tau})^2 h_{c,k}(\tau)\,\mathrm{d}\tau} \Rightarrow \sigma_c(z) = z\sigma_\tau \tag{4.112}$$

This general expression allows for the calculation of the RMS pulse width in the absolute time variable just by using the normalized time chromatic impulse response and then multiplying the result by the required distance z. The normalized time RMS pulse width σ_τ of the chromatic impulse response can be computed explicitly in terms of both the source PSD $S_s(\lambda)$ and the chromatic dispersion coefficient $D_c(\lambda)$. Substituting Equation (4.83) into Equation (4.112) gives the general analytical expression for the RMS width of the chromatic impulse response in terms of the source PSD and chromatic dispersion coefficient of the optical fiber:

$$\sigma_\tau = \underbrace{\sqrt{\sum_{k=0}^{N} \int_{T_k} (\tau - \overline{\tau})^2 \frac{S_s[\zeta_g(\tau)]}{|D_c[\zeta_g(\tau)]|} d\tau}}_{\lambda=\zeta_g(\tau)\in\Lambda_k, k=1,2,\ldots,N-1, \begin{cases} \Lambda_0=(0,\lambda_1) \\ \Lambda_k=(\lambda_k,\lambda_{k+1}) \\ \Lambda_N=(\lambda_N,+\infty) \end{cases}} \Rightarrow \sigma_c(z) = z\sigma_\tau \tag{4.113}$$

In the simple case of any stationary wavelength included in the spectral range Λ_s of the source PSD, the above expression reduces to a single integration interval:

$$\sigma_\tau = \underbrace{\sqrt{\int_{T_s} (\tau - \overline{\tau})^2 \frac{S_s[\zeta_g(\tau)]}{|D_c[\zeta_g(\tau)]|} d\tau}}_{\tau\in T_s \leftrightarrow \lambda=\zeta_g(\tau)\in\Lambda_s} \Rightarrow \sigma_c(z) = z\sigma_\tau \tag{4.114}$$

4.4.5 Linear Approximation of the Group Delay

Using the linear approximation (4.95) of the group delay function around the average wavelength $\overline{\lambda}$ of the source spectrum, the chromatic dispersion coefficient $D_c(\lambda) = D_c(\overline{\lambda}) = \overline{D}_c$ can be brought outside the integral in the expression (4.114) of the RMS pulse width σ_τ of the chromatic impulse response:

$$\sigma_\tau = \underbrace{\sqrt{\frac{1}{|\overline{D}_c|} \int_{T_s} (\tau - \overline{\tau})^2 S_s[\zeta_g(\tau)]\, d\tau}}_{\tau\in T_s \leftrightarrow \lambda=\zeta_g(\tau)\in\Lambda_s} \Rightarrow \sigma_c(z) = z\sigma_\tau \tag{4.115}$$

If it is assumed that the linear group delay approximation lies in the source wavelength range, the inverse group delay function $\lambda = \zeta_g(\tau)$ is a single-valued function and the wavelength partition due to stationary points is no longer required. Consequently, the RMS pulse width is given by expression (4.114) and for every instant τ belonging to the integration interval T_s one and only one wavelength defined by the linear inverse function $\lambda = \zeta_g(\tau)$ exists that belongs to the wavelength interval Λ_s defined by the source power spectral density $S_s(\lambda)$.

At this point the same mathematical problem arises that was already encountered in the derivation of the average delay theorem stated in expression (4.100). To proceed analogously, the integration variable τ is changed to $\lambda = \zeta_g(\tau)$ in Equation (4.115) by using the single-valued (linear) inverse group delay function:

$$\underset{\tau\in T_s}{\lambda = \zeta_g(\tau)} \longleftrightarrow \underset{\lambda\in\Lambda_s=(\lambda_{min},\lambda_{max})}{\tau = \tau_g(\lambda)}, \qquad T_s \longleftrightarrow \Lambda_s, \qquad d\tau = \frac{d\lambda}{d\zeta_g(\tau)/d\tau} = \frac{d\tau_g(\lambda)}{d\lambda} d\lambda \tag{4.116}$$

and

$$\sigma_\tau = \sqrt{\int_{\Lambda_s} [\tau_g(\lambda) - \overline{\tau}]^2 S_s(\lambda)\, d\lambda} \tag{4.117}$$

By virtue of the linear approximation of the group delay (4.95), the constant value of the chromatic dispersion coefficient in the wavelength interval Λ_s coincides with the first-order wavelength derivative $\overline{D}_c \cong [d\tau_g(\lambda)/d\lambda]_{\lambda\in\Lambda_s}$. Using expression (4.95) and the property (4.100), the pulse RMS width (4.117) is written as follows:

$$\sigma_\tau = |\overline{D}_c| \sqrt{\int_{\Lambda_s} (\lambda - \overline{\lambda})^2 S_s(\lambda)\, d\lambda} \tag{4.118}$$

The integral under the square root coincides with the variance of the source power spectral density σ_s^2:

$$\sigma_s^2 = \int_{\Lambda_s} (\lambda - \overline{\lambda})^2 S_s(\lambda)\, d\lambda \tag{4.119}$$

Finally, substituting the variance of the source PSD into Equation (4.119) and using the result (4.100) gives the well-known theorem of the RMS pulse width of the chromatic impulse response under a linear group delay approximation:

$$\sigma_c(z, \overline{\lambda}) = |D_c(\overline{\lambda})| \sigma_s z \tag{4.120}$$

The RMS width of the chromatic impulse response, under the assumption of the linear group delay, is given by the product of the chromatic dispersion coefficient with the RMS spectral width of the source power spectral density by the distance z.

In the following, Equation (4.120) will be referred to as the linear chromatic pulse dispersion condition. In Section 4.4.6 the numerical computed RMS pulse dispersion will be compared quantitatively with the linear chromatic pulse dispersion condition (4.120) in order to check the validity of that useful approximation.

4.4.6 Comments on the Linear Approximation

In this section the RMS pulse dispersion computed numerically using expression (4.113) will be compared with the corresponding approximation given in Equation (4.120) which is valid for the linear group delay evaluated at the average wavelength of the source power spectral density for all the cases 1(a) to (g) presented in Section 4.3.4. The comparison results are shown in Table 4.3, where the first column reports the code of the case considered according to the coding detailed in Section 4.3.4 and the last column shows the percentage error. Columns 7 and 8 report respectively the RMS linear chromatic pulse dispersion (4.120) and the RMS numerically computed pulse dispersion according to Equation (4.113).

The results shown in the table are quite interesting and give a clear indication of the validity of the useful linear dispersion approximation. The rows are arranged according to the excited wavelength range, from the first window to the third one. In the following the different results will be briefly analyzed.

The 850 nm wavelength range excitation is presented in the first three rows of the table. It is clear that due to high dispersion coefficient values, a larger spectral width gives a higher error than narrow spectral width sources. This leads to a relative error about 4 % to 6 % depending on the source characteristic. A narrow spectral width leads to a very nice matching between the numerically computed RMS pulse width and the corresponding linear approximation. This is clearly understood if the very narrow spectral interval used by the source and the consequent validity of the linear group delay approximation are considered.

The 1300 nm wavelength range excitation is presented in the subsequent four rows of the table. As expected, the zero-dispersion wavelength leads to very different conclusions depending on whether the source spectrum includes that wavelength or not. This is evident by the first, the

Table 4.3 The table reports the comparison between the linear approximation and the numerically computed parameters for nine cases considered in Section 4.3.4. All the considered cases refer to the Sellmeier uniform group delay, without any ripple added. The second and third columns report respectively the average wavelength and the RMS spectral width of the source power spectral density considered. Those two parameters are used for evaluation of the linear approximation. The last three columns report respectively the RMS linear chromatic pulse dispersion from Equation (4.120), the RMS numerically computed pulse dispersion according to Equation (4.113) and the relative percentage error. It is evident that the different behaviors between the three wavelength windows are characterized by the different values of the chromatic dispersion coefficient. Lower values, but away from the zero-dispersion wavelength, give lower errors

Code	$\overline{\lambda}$ (nm)	σ_s (nm)	$\tau_g(\overline{\lambda})$ (ns/m)	$\overline{\tau}$ (ns/m)	$\overline{D}_c$ (ps/nm km)	$\overline{\sigma}_\tau$ (ps/m)	σ_τ (ps/m)	$\overline{\sigma}_\tau/\sigma_\tau - 1(\%)$
SUSG850	850	63.699	4.8892	4.8900	−84.015	5.3516	5.7222	−6.476
SUMG850-A	850	63.813	4.8892	4.8900	−84.004	5.3606	5.5940	−4.1723
SUMG850-B	850	1.2678	4.8892	4.8892	−84.008	0.1065	0.1065	0
SUSG1300	1300	63.654	4.8755	4.8756	2.6468	0.1685	0.2572	−34.487
SUMG1300-A	1300	1.2678	4.8755	4.8755	2.6479	0.00336	0.00336	0
SUMG1300-B	1272.6	1.2678	4.8755	4.8755	−0.0188	2.389e-5	8.415e-5	−71.61
SUMG1300-C	1272.6	63.813	4.8755	4.8756	−0.0115	73.31e-5	0.1715	−99.573
SUSG1550	1550	63.699	4.8787	4.8789	21.912	1.3958	1.3997	−0.279
SUMG1550-A	1550	63.813	4.8787	4.8789	21.918	1.3987	1.3991	−0.0286
SUMG1550-B	1550	1.2678	4.8787	4.8787	21.916	0.0278	0.0278	0

third and the fourth case where, almost independently of the single-line or multiple-line spectrum profiles, the linear approximation clearly fails. It is remarkable that in the second case presented the narrow spectrum does not include the zero-dispersion wavelength and the correspondence between the RMS pulse widths is extremely precise. This confirms that the linear approximation holds, even very close to any zero-dispersion wavelengths, but that must not be included in the spectral excitation. Otherwise, its contribution will dominate the whole impulse response and the linear approximation will fail.

The 1550 nm wavelength range excitation is presented in the last three rows of the table. The lower value of the slope of the chromatic dispersion coefficient makes this parameter much less dependent on the exciting wavelength and therefore the linear group delay approximation behaves quite well. This is clearly shown in the three cases considered, where almost independently from the source composition the percentage error is well below 0.5 %. This conclusion allows the linear chromatic pulse dispersion to be used with high confidence over the whole third window applications.

Before closing this section, one important remark should be made. The RMS pulse width expressions that have been derived, both the general formula (4.113) and the linear approximate one (4.120), refer to the RMS value only. Both the chromatic impulse response width and the source spectrum width must therefore be considered as RMS values. However, they are not related to any specific profile. This sometimes raises misunderstanding when evaluating system performances.

4.4.7 Summary

In this section the general expressions for first- and second-order moments of the chromatic impulse response have been derived. The theory presented includes general profiles for both the group delay and the source power spectral density, allowing for the ripple profile and the multipeak spectrum

Table 4.4 A summary of the principal equations derived in the text regarding first- and second-order moments of the chromatic impulse response. The third column gives the applicability of the corresponding equation. The last column gives the equation number in the text. The suffix c identifies the chromatic quantity

Parameter	Expression	Validity	Reference equation
Unit energy normalization	$W_{\mathrm{c}} = \int_{-\infty}^{+\infty} h_{\mathrm{c}}(z,t)\,\mathrm{d}t = 1$	General	(4.81)
Chromatic impulse response	$\underbrace{h_{\mathrm{c},k}(\tau) \equiv \dfrac{S_{\mathrm{s}}[\zeta_{\mathrm{g}}(\tau)]}{\lvert D_{\mathrm{c}}[\zeta_{\mathrm{g}}(\tau)]\rvert}}_{\lambda=\zeta_{\mathrm{g}}(\tau)\in\Lambda_k,k=1,2,\ldots,N-1,\ \begin{cases}\Lambda_0=(0,\lambda_1)\\ \Lambda_k=(\lambda_k,\lambda_{k+1})\\ \Lambda_N=(\lambda_N,+\infty)\end{cases}}$	General	(4.83)
	$h_{\mathrm{c}}(z,\tau) = \dfrac{1}{z}\sum_{k=0}^{N} h_{\mathrm{c},k}(\tau)$		
Average delay	$\underbrace{\overline{\tau}_{\mathrm{c}} = \sum_{k=0}^{N}\int_{T_k} \tau\,\dfrac{S_{\mathrm{s}}[\zeta_{\mathrm{g}}(\tau)]}{\lvert D_{\mathrm{c}}[\zeta_{\mathrm{g}}(\tau)]\rvert}\,\mathrm{d}\tau}_{\lambda=\zeta_{\mathrm{g}}(\tau)\in\Lambda_k,k=1,2,\ldots,N-1,\ \begin{cases}\Lambda_0=(0,\lambda_1)\\ \Lambda_k=(\lambda_k,\lambda_{k+1})\\ \Lambda_N=(\lambda_N,+\infty)\end{cases}}$	General	(4.90)
	$\overline{t}_{\mathrm{c}}(z) = z\overline{\tau}_{\mathrm{c}}$		
Linear group delay approximation	$\tau_{\mathrm{g}}(\lambda) \cong \tau_{\mathrm{g}}(\overline{\lambda}) + (\lambda-\overline{\lambda})\overline{D}_{\mathrm{c}}$	Linear	(4.95)
	$\overline{D}_{\mathrm{c}} \equiv D_{\mathrm{c}}(\overline{\lambda})$		
Linear average delay	$\overline{\tau}_{\mathrm{c}} = \tau_{\mathrm{g}}(\overline{\lambda})$	Linear	(4.100)
Chromatic impulse response for the linear group delay approximation	$h_{\mathrm{c}}(z,\tau) \cong \dfrac{1}{z\lvert\overline{D}_{\mathrm{c}}\rvert} S_{\mathrm{s}}\left(\overline{\lambda} + \dfrac{\tau-\overline{\tau}_{\mathrm{c}}}{\overline{D}_{\mathrm{c}}}\right)$	Linear	(4.103)
	$\tau \in T_{\mathrm{s}} \longleftrightarrow \zeta_{\mathrm{g}}(\tau) = \overline{\lambda} + \dfrac{\tau-\overline{\tau}_{\mathrm{c}}}{\overline{D}_{\mathrm{c}}} = \lambda \in \Lambda_{\mathrm{s}}$		
Variance	$\sigma_\tau^2 = \sum_{k=0}^{N}\int_{T_k} (\tau-\overline{\tau}_c)^2 h_{\mathrm{c},k}(\tau)\,\mathrm{d}\tau$	General	(4.111)
	$\sigma_{\mathrm{c}}^2(z) = z^2\sigma_\tau^2$		
RMS pulse width	$\sigma_\tau = \underbrace{\sqrt{\sum_{k=0}^{N}\int_{T_k} (\tau-\overline{\tau}_{\mathrm{c}})^2 \dfrac{S_{\mathrm{s}}[\zeta_{\mathrm{g}}(\tau)]}{\lvert D_{\mathrm{c}}[\zeta_{\mathrm{g}}(\tau)]\rvert}\,\mathrm{d}\tau}}_{\lambda=\zeta_{\mathrm{g}}(\tau)\in\Lambda_k,k=1,2,\ldots,N-1,\ \begin{cases}\Lambda_0=(0,\lambda_1)\\ \Lambda_k=(\lambda_k,\lambda_{k+1})\\ \Lambda_N=(\lambda_N,+\infty)\end{cases}}$	General	(4.113)
	$\sigma_{\mathrm{c}}(z) = z\sigma_\tau$		
Linear RMS pulse width	$\sigma_{\mathrm{c}}(z,\overline{\lambda}) = \lvert D_{\mathrm{c}}(\overline{\lambda})\rvert\sigma_{\mathrm{s}} z$	Linear	(4.120)

respectively. The general expression for the chromatic impulse response $h_c(z, t)$ has been written in Equation (4.83), neglecting any eventual modal dependence.

Section 4.4.1 dealt with normalization integrals and in Equation (4.81) it was demonstrated that if the source PSD $S_s(\lambda)$ has unit energy, even the chromatic impulse response $h_c(z, t)$ has unit energy.

Section 4.4.2 dealt with the average delay $\overline{t}$ of the chromatic impulse response, leading to the general expression reported in Equation (4.90).

Section 4.4.3 presented the linear group delay approximation (4.95). In this case, the response delay $\overline{\tau}$ coincides with the group delay evaluated at the average spectrum wavelength $\tau_g(\overline{\lambda})$ and $\overline{t} = \overline{\tau}\ z = \tau_g(\overline{\lambda})z$, as stated in Equation (4.100). The linear group delay assumption leads to the fundamental result that the chromatic impulse response coincides with the scaled source power spectral density, as given by Equation (4.103).

Section 4.4.4 dealt with the variance of the chromatic impulse response, leading to the general expression reported in Equation (4.111). That expression holds in general without either approximation or group delay and source spectrum restrictions. Similar to the average delay, the RMS pulse width increases linearly with the distance, as given in Equation (4.113).

Section 4.4.5 presented the variance theory for the linear group delay approximation. Under this condition, the RMS pulse width of the chromatic impulse response assumes the familiar expression given in Equation (4.120).

Table 4.4 summarizes all of the above results in order to take a close-up view of the moments of the chromatic impulse response.

4.5 Conclusions and Remarks

In this chapter the theory has been developed of the chromatic impulse response in multimode optical fiber realized using silica-based doped material. The chromatic response depends directly on the dispersion relationship that characterizes each supported fiber mode when the group delay is considered versus the optical source wavelength. The term 'chromatic' indicates the dependence of the propagation characteristics on the light wavelength, which more generally sets the color. For every given fiber mode the source power density and the modal group delay function versus the wavelength determine the way the different spectral contributions of the mode power travel relative to each other in order to reach the output fiber section where they are collected by the optical detector. The dependence of the modal group delay on the wavelength gives the chromatic dispersion property of the considered mode supported by the optical fiber, but the spectral contribution to the composition of the chromatic impulse response depends equally on the spectral distribution of the source power.

In conclusion, the chromatic impulse response is not a property of the optical waveguide as a stand-alone component, but also depends strongly on the spectral characteristics of the light source. This is the reason why the optical source has the well-known dominant role of performing in every optical fiber communication system. In particular, the more the chromatic dispersion makes a high dispersion contribution to the total parameter value, the more effective will be the choice of optical source. This is the physical concept behind the choice between an externally modulated semiconductor laser or an externally modulated light source. The former are used in lower performing transmission systems where the chromatic dispersion is not the dominant limiting factor.

A summary of the most relevant expressions derived in this chapter have been presented in Table 4.4.

5

Theory of Multimode Response

Application to Multigigabit Transmission Links

5.1 Introduction and Outline

In this chapter the theory of modal propagation in a multimode optical fiber is presented. The analysis starts with some basic assumptions and expressions derived previously in Chapter 3, Section 3.4. The modal impulse response is described as the superposition of the impulse response on each excited mode. How does the impulse response of each individual fiber mode form? To answer this question only needs to invoke the modal orthogonality and use the chromatic impulse response of the selected fiber mode. The impulse response of each individual mode is given by the chromatic impulse response of that mode. By virtue of the mode orthogonality, all modes propagate independently from each other, delivering their energy content at the detection section according to the specific group delay constant. The result gives quite a clear picture: the multimode impulse response is given by the intensity superposition of all individual modes reaching the output section and each bringing the assigned amount of optical power.

The chromatic impulse response theory was developed in Chapter 4. In this chapter the theory of modal response will be presented, assuming that no chromatic dispersion accounted for each mode. This is equivalent to assuming that the chromatic impulse response of each mode is the ideal impulse distribution (Dirac delta function), properly delayed by the corresponding modal group delay evaluated at the source wavelength. This approach allows the modal behavior to be conceptually separated from the chromatic behavior, leading to a clear physical picture of the multimode fiber impulse response. The second section starts with calculation of the most used averages of the modal impulse response, namely the mode normalization, the average group delay and the modal dispersion. The third section derives the mathematical closed-form expression of the modal impulse response with the related pulse moments. The fourth section develops the algorithm and computer model of the multimode fiber impulse response, including both the chromatic and the modal contributions. Numerous examples provide a clear understanding of the underlying physical picture and mathematical modeling. The fifth section deals with the fundamental concept of the frequency response, simply derived using the Fourier transform definition. In this section the new

Multi-Gigabit Transmission over Multimode Optical Fibre: Theory and Design Methods for 10GbE Systems Stefano Bottacchi
 ISBN: 0-471-89175-4

concept of the modal function is introduced as a useful tool for understanding the linear modeling behavior of the multimode fiber under some light restrictions. Several mathematical models of group delay distributions are presented in order to predict and manage the modal impulse response profile. This approach leads to defining some functional characteristics of the group delay function and launch condition in order to expect a symmetric Gaussian fit response.

5.2 Moments of Modal Impulse Response

In this section the first- and the second-order moments of the modal impulse response derived in Chapter 3, Section 3.5, will be considered. A similar analysis has already been performed for the chromatic impulse response, in Chapter 4, Section 4.4. As usual, attention will be focused on the ensemble average and on the variance of the modal impulse response, according to expression (3.55). Before computing the related moments, it is convenient to consider first the normalization condition for the modal impulse response.

5.2.1 Energy Normalization

If a multimode fiber with M excited modes at the fixed source wavelength λ is considered, the modal impulse response $\upsilon(z, t, \lambda)$ is given by the set of M impulses properly weighted and delayed. Each impulse is weighted by the square modulus of the coupling coefficient $|a_h(\lambda)|^2$ between the light source distribution and the corresponding modal field distribution, and is translated according to the group delay of the supporting hth fiber mode $\tau_{g,h}(\lambda)$. The Greek letter υ, 'upsilon', is used to indicate the modal impulse response $\upsilon(z, t, \lambda)$ and to distinguish from the chromatic contribution $h_{c,h}(z, t, \lambda)$ derived in previous chapters. In this chapter each mode group is labeled with the index h. The energy of the modal impulse response is given by the following integral, where use is made of the general expression (3.55):

$$W_m = \int_{-\infty}^{+\infty} \upsilon(z, t, \lambda)\, dt = \sum_{h=1}^{M} |a_h(\lambda)|^2 \int_{-\infty}^{+\infty} \delta[t - z\tau_{g,h}(\lambda)]\, dt \tag{5.1}$$

By virtue of the Dirac delta definition and of the normalization property (3.57), it can be concluded immediately that independently from any wavelength and distance z, the modal impulse response is correctly normalized with unit energy:

$$W_m = \int_{-\infty}^{+\infty} \upsilon(z, t, \lambda)\, dt = 1 \tag{5.2}$$

In deriving the normalization property of the modal impulse response the characteristic condition is represented by Equation (3.57). Analogously, the characteristic condition for achieving the normalization of chromatic impulse response was the unit energy requirement of the optical source spectrum (4.25). It is interesting to note that moving from the chromatic to the modal response, the normalizing requirement moves from the spectral integration (4.25) towards the spatial integration (3.57).

Using the temporal variable per unit length $\tau = t/z$ instead of the absolute time t, the normalization condition for the modal impulse response takes the following form:

$$\begin{aligned} \int_{-\infty}^{+\infty} \upsilon(z, t, \lambda)\, d\tau &= \sum_{h=1}^{M} |a_h(\lambda)|^2 \int_{-\infty}^{+\infty} \delta[t - z\tau_{g,h}(\lambda)]\, d\tau \\ &= \frac{1}{z} \sum_{h=1}^{M} |a_h(\lambda)|^2 \int_{-\infty}^{+\infty} \delta[t - z\tau_{g,h}(\lambda)]\, dt = \frac{W_m}{z} = \frac{1}{z} \end{aligned} \tag{5.3}$$

This result has already been obtained in conjunction with the normalization (4.82) of the chromatic impulse response and it can be justified accordingly. In fact, using the variable $\tau = t/z$ to perform the integration, the energy per unit length of the modal impulse response must decrease linearly with the distance due to the corresponding pulse broadening due to the differential mode delay (DMD). This result will be used in the derivation of the first- and second-order moment expressions.

5.2.2 Average Value

The average temporal value of the modal impulse response is given by the integral (4.84), where the chromatic impulse response is substituted by the modal impulse response:

$$\overline{t}_{\mathrm{m}}(z,\lambda) \equiv \frac{\displaystyle\int_{-\infty}^{+\infty} t\upsilon(z,t,\lambda)\,\mathrm{d}t}{\displaystyle\int_{-\infty}^{+\infty} \upsilon(z,t,\lambda)\,\mathrm{d}t} = \int_{-\infty}^{+\infty} t\upsilon(z,t,\lambda)\,\mathrm{d}t \tag{5.4}$$

The index m is added to identify the modal parameter, and the energy normalization (5.2) has been used. Replacing the expression of the modal impulse response (3.55) gives

$$\overline{t}_{\mathrm{m}}(z,\lambda) = \sum_{h=1}^{M} |a_{\mathrm{h}}(\lambda)|^2 \int_{-\infty}^{+\infty} t\ \delta\left[t - z\ \tau_{\mathrm{g},h}(\lambda)\right]\,\mathrm{d}t \tag{5.5}$$

Using the Dirac delta definition gives the following expression of the ensemble average delay $\overline{t}_{\mathrm{m}}(z,\lambda)$:

$$\overline{t}_{\mathrm{m}}(z,\lambda) = z\sum_{h=1}^{M} |a_{\mathrm{h}}(\lambda)|^2 \tau_{\mathrm{g},h}(\lambda) \tag{5.6}$$

This expression has a straightforward physical interpretation: as will be demonstrated below, it corresponds to the ensemble average of the modal group delay weighted by the coupling coefficient distribution. The linear dependence from the distance z makes, as expected, the ensemble average of the absolute time of the modal impulse response proportional to the propagation distance z.

To see this in a formal way, first the ensemble average of the normalized time τ is computed. From Equations (5.3) and (5.4), by definition,

$$\overline{\tau}_{\mathrm{m}}(z,\lambda) \equiv \frac{\displaystyle\int_{-\infty}^{+\infty} \tau\upsilon(z,t,\lambda)\,\mathrm{d}\tau}{\displaystyle\int_{-\infty}^{+\infty} \upsilon(z,t,\lambda)\,\mathrm{d}\tau} = z\int_{-\infty}^{+\infty} \tau\upsilon(z,t,\lambda)\,\mathrm{d}\tau \tag{5.7}$$

Up to this point the ensemble average time $\overline{\tau}_{\mathrm{m}}$ could still depend of the position z and the general notation $\overline{\tau}_{\mathrm{m}}(z,\lambda)$ can be used. However, this dependence can suddenly be removed as expected by the linear regime assumption and as illustrated below. By substituting the modal impulse response (3.55) and changing the integration variable to $\tau = t/z$,

$$\begin{aligned}\overline{\tau}_{\mathrm{m}}(z,\lambda) &= z\sum_{h=1}^{M} |a_{\mathrm{h}}(\lambda)|^2 \int_{-\infty}^{+\infty} \tau\delta[t - z\tau_{\mathrm{g},h}(\lambda)]\,\mathrm{d}\tau \\ &= \frac{1}{z}\sum_{h=1}^{M} |a_{\mathrm{h}}(\lambda)|^2 \int_{-\infty}^{+\infty} t\delta[t - z\tau_{\mathrm{g},h}(\lambda)]\,\mathrm{d}t\end{aligned} \tag{5.8}$$

By virtue of the Dirac delta definition the ensemble average of the normalized time variable τ can be obtained:

$$\overline{\tau}_{\mathrm{m}}(\lambda) = \sum_{h=1}^{M} |a_{\mathrm{h}}(\lambda)|^2 \tau_{\mathrm{g},h}(\lambda) \tag{5.9}$$

As expected, the ensemble average no longer depends on the distance z and this has the physical justification in terms of the linear regime assumption. Since excited modes neither interfere nor couple with each other, the normalized ensemble average time must remain constant versus the propagation length. Finally, by comparing with Equation (5.6), it can be concluded that

$$\overline{t}_{\mathrm{m}}(z, \lambda) = z\ \overline{\tau}_{\mathrm{m}}(\lambda) \tag{5.10}$$

5.2.3 Pulse Dispersion: Variance and RMS Width

The variance $\sigma_{\mathrm{m}}^2(z, \lambda)$ of the time variable t computed using the modal impulse response $\upsilon(z, t, \lambda)$ is defined by the following integration, where the energy normalization (5.2) has been used:

$$\sigma_{\mathrm{m}}^2(z, \lambda) \equiv \frac{\displaystyle\int_{-\infty}^{+\infty} [t - \overline{t}_{\mathrm{m}}(z, \lambda)]^2 \zeta(z, t, \lambda)\, \mathrm{d}t}{\displaystyle\int_{-\infty}^{+\infty} \upsilon(z, t, \lambda)\, \mathrm{d}t} = \int_{-\infty}^{+\infty} [t - \overline{t}_{\mathrm{m}}(z, \lambda)]^2 \upsilon(z, t, \lambda)\, \mathrm{d}t \tag{5.11}$$

The variance $\sigma_{\mathrm{m}}^2(z, \lambda)$ results in a function of the distance z because the ensemble integration (5.11) operates over the absolute time variable and the impulse response $\upsilon(z, t, \lambda)$ broadens with the propagation distance. Substituting expression (3.55) of the modal impulse response and using the Dirac delta definition gives

$$\begin{aligned} \sigma_m^2(z, \lambda) &= \sum_{h=1}^{M} |a_{\mathrm{h}}(\lambda)|^2 \int_{-\infty}^{+\infty} [t - \overline{t}_{\mathrm{m}}(z, \lambda)]^2 \delta[t - z\tau_{\mathrm{g},h}(\lambda)]\, \mathrm{d}t \\ &= \sum_{h=1}^{M} |a_{\mathrm{h}}(\lambda)|^2 [z\tau_{\mathrm{g},h}(\lambda) - \overline{t}_{\mathrm{m}}(z, \lambda)]^2 \end{aligned} \tag{5.12}$$

Using the result (5.10) for the average time $\overline{t}_{\mathrm{m}}(z, \lambda)$ gives the following expression for the variance of the modal impulse response:

$$\sigma_{\mathrm{m}}^2(z, \lambda) = z^2 \sum_{h=1}^{M} |a_{\mathrm{h}}(\lambda)|^2 [\tau_{\mathrm{g},h}(\lambda) - \overline{\tau}_{\mathrm{m}}(\lambda)]^2 \tag{5.13}$$

The expression just derived has the same straightforward physical interpretation as Equation (5.6): the term under the summation sign corresponds to the variance of the modal group delay weighted by the coupling coefficient distribution. The quadratic dependence from the distance z makes, as expected, the RMS pulse width proportional to the propagation distance z when referred to the absolute time units. In other words, as will be seen below, the RMS pulse width of the modal impulse response increases linearly with the distance. To show this it is sufficient to proceed as in Section 5.2.2 for the ensemble average $\overline{\tau}_{\mathrm{m}}(\lambda)$ of the time variable τ.

The variance $\hat{\sigma}_{\mathrm{m}}^2(\lambda)$ of the normalized time variable τ is given by the following integral, where the normalization energy (5.3) is used to compute the integral at the denominator:

$$\hat{\sigma}_{\mathrm{m}}^2(z,\lambda) \equiv \frac{\displaystyle\int_{-\infty}^{+\infty} [\tau - \overline{\tau}_{\mathrm{m}}(\lambda)]^2 \upsilon(z,t,\lambda)\,\mathrm{d}\tau}{\displaystyle\int_{-\infty}^{+\infty} \upsilon(z,t,\lambda)\,\mathrm{d}\tau} = z\int_{-\infty}^{+\infty} [\tau - \overline{\tau}_{\mathrm{m}}(\lambda)]^2 \upsilon(z,t,\lambda)\,\mathrm{d}\tau \tag{5.14}$$

Again, in general a dependence from the distance z is assumed, since it is implicit in the impulse response $\upsilon(z,t,\lambda)$. After substituting the modal impulse response (3.55), changing the integration variable to $\tau = t/z$ and using the Dirac delta definition, the expression of the variance of the impulse response evaluated with respect to the normalized time variable is obtained:

$$\hat{\sigma}_{\mathrm{m}}^2(\lambda) = \sum_{h=1}^{M} |a_h(\lambda)|^2 [\tau_{\mathrm{g},h}(\lambda) - \overline{\tau}_{\mathrm{m}}(\lambda)]^2 \tag{5.15}$$

As expected, the spatial dependence has disappeared. Comparing with (5.13), it can be conclude that

$$\sigma_{\mathrm{m}}^2(z,\lambda) = z^2 \hat{\sigma}_{\mathrm{m}}^2(\lambda) \tag{5.16}$$

The RMS pulse width is defined as the square root of the variance. Equations (5.15) and (5.16) immediately give

$$\hat{\sigma}_{\mathrm{m}}(\lambda) = \sqrt{\sum_{h=1}^{M} |a_h(\lambda)|^2 [\tau_{\mathrm{g},h}(\lambda) - \overline{\tau}_{\mathrm{m}}(\lambda)]^2} \Rightarrow \sigma_{\mathrm{m}}(z,\lambda) = z\hat{\sigma}_{\mathrm{m}}(\lambda) \tag{5.17}$$

As anticipated, the RMS pulse width of the modal impulse response increases linearly with the propagation distance. This is a consequence of the linear regime assumption, without any mode interference or coupling.

Before closing this section, it is important to point out that the characteristic behavior of the modal response of the multimode fiber is completely determined by the coupling coefficient distribution $\{a_h(\lambda)\}$. Once the modal group delay function is given at the operating wavelength, the only characterizing function for the modal impulse response is the coupling coefficient distribution. This reasoning leads to the fundamental role of the optical launching condition in the modal impulse response determination. Figure 5.1 shows the graphical interpretation of the first- and second-order moments that have been derived.

5.2.4 Conclusions and Remarks

In this section the general expressions of the average delay time and the RMS width of the modal impulse response of a multimode optical fiber have been deducted. The theory presented allows for any general profile of the group delay, and it assumes a linear propagation regime. This condition is required so that each excited mode can propagate independently from any other supported mode. The major conclusion is that for each given group delay profile, an infinite number of different modal impulse responses are allowed according to the infinite possibilities of different coupling coefficient distributions. This is a peculiarity of the multimode impulse response.

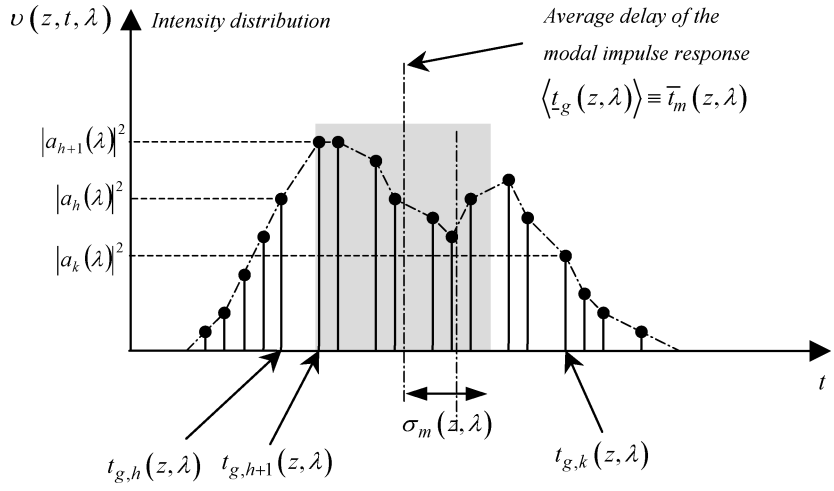

Figure 5.1 Qualitative representation of the modal impulse response of a multimode fiber. Each excited mode contributes to the energy amount defined by the corresponding coupling coefficient and is located at the time instant given by the group delay at the operating wavelength. The dot–dash line indicates the ensemble average time value according to Equation (5.10) and the shadowed area identifies the RMS pulse width according to Equation (5.17). Both the time average and RMS pulse width are linear functions of the distance

For a given group delay profile and coupling coefficient distribution, the general expression for the modal impulse response $\upsilon(z, t, \lambda)$ has been derived in Equation (3.55). Section 5.2.1 defines the normalization integrals and in Equation (5.2) it was demonstrated that if the coupling coefficient distribution is properly normalized, even the modal impulse response $\upsilon(z, t, \lambda)$ has unit energy. The average delay $\overline{t}_{\mathrm{m}}(z, \lambda)$ of the modal impulse response has been derived in Section 5.2.2 and the general expression of $\overline{t}_{\mathrm{m}}(z, \lambda)$ is given in Equation (5.10). The average delay of the response results in a linear function of the distance z. The normalized average delay is given in Equation (5.9) and does not depend upon length, as expected by the linear regime assumption.

Section 5.2.3 deals with the variance $\sigma^2_{\mathrm{m}}(z, \lambda)$ of the modal impulse response, leading to the general expression reported in Equation (5.16), where the normalized time variance $\hat{\sigma}^2_{\mathrm{m}}(\lambda)$ was introduced in Equation (5.15). As expected, it does not depend upon the distance z once the linear regime condition is assumed among the excited modes. The RMS pulse width expression (5.17) holds in general, without any further assumption except the linear regime. Similar to the average delay, the RMS pulse width $\sigma_{\mathrm{m}}(z, \lambda)$ increases linearly with the distance.

Table 5.1 summarizes the expressions derived for the moments of the modal impulse response.

5.3 Theory of Multimode Impulse Response

In Chapter 4 the expressions for the chromatic impulse response under general conditions were derived. Both first- and second-order moments have been derived and extensively analyzed, resulting in general and linearly approximated expressions. All those formulas have been summarized in Table 4.4 in Chapter 4 and Table 5.1 for the chromatic impulse response and the modal impulse response respectively.

5.3.1 Problem Statement and Discussion

It is known that chromatic dispersion affects every propagating mode, because of the source spectrum interacting with the supporting fiber mode dispersion characteristic. This relation includes

Table 5.1 Principal expressions regarding first- and second-order moments of the modal impulse response. Except for the linear regime assumption, all equations have general validity. The last column gives the equation number in the text

Parameter	Expression	Validity	Reference
Unit energy normalization	$W_{\mathrm{m}} = \int_{-\infty}^{+\infty} \upsilon(z,t,\lambda)\,\mathrm{d}t = 1 \Leftrightarrow \sum_{h=1}^{N} \lvert a_h(\lambda)\rvert^2 = 1$	General	(5.2)
Modal impulse response	$\upsilon(z,t,\lambda) = \sum_{h=1}^{M} \lvert a_h(\lambda)\rvert^2 \delta[t - z\tau_{\mathrm{g},h}(\lambda)]$	General	(3.55)
Average modal delay	$\overline{\tau}_{\mathrm{m}}(\lambda) = \sum_{h=1}^{M} \lvert a_h(\lambda)\rvert^2 \tau_{\mathrm{g},h}(\lambda)$ $\overline{t}_{\mathrm{m}}(z,\lambda) = z\overline{\tau}_{\mathrm{m}}(\lambda)$	General	(5.10)
Variance	$\hat{\sigma}_{\mathrm{m}}^2(\lambda) = \sum_{h=1}^{M} \lvert a_h(\lambda)\rvert^2 [\tau_{\mathrm{g},h}(\lambda) - \overline{\tau}_{\mathrm{m}}(\lambda)]^2$ $\sigma_{\mathrm{m}}^2(z,\lambda) = z^2\hat{\sigma}_{\mathrm{m}}^2(\lambda)$	General	(5.16)
RMS pulse width	$\hat{\sigma}_{\mathrm{m}}(\lambda) = \sqrt{\sum_{h=1}^{M} \lvert a_h(\lambda)\rvert^2 [\tau_{\mathrm{g},h}(\lambda) - \overline{\tau}_{\mathrm{m}}(\lambda)]^2}$ $\sigma_{\mathrm{m}}(z,\lambda) = z\hat{\sigma}_{\mathrm{m}}(\lambda)$	General	(5.17)

both material and waveguide contributions to the dispersion relationship. The impulse response of each mode will therefore be affected by some amount of temporal broadening due to the chromatic dispersion mechanism. The question to answer now is the following: what would be the interaction of chromatic dispersion with the modal dispersion in order to have a closed-form expression of the impulse response of the multimode optical fiber?

In order to proceed toward the general solution of this problem, from the discussion in Chapter 4 the following three fundamental input parameters that characterize the output impulse response of every multimode optical fiber need to be known:

1. The source power spectral distribution $S_{\mathrm{s}}(\lambda)$
2. The group delay distribution $\{\tau_{\mathrm{g},h}(\lambda)\}$
3. The source coupling coefficient distribution $\{a_h(\lambda)\}$

The second and the third parameter sets depend on the modal index h. This means that they refer to every specific fiber mode that has been excited by the light source. Even if the variation of the group delay profile among different modes are usually limited to the group delay value at the average source wavelength $\tau_{\mathrm{g},h}(\overline{\lambda}) = \overline{\tau}_{\mathrm{g},h}$, it is convenient for clarity to include the complete modal group delay dependence in the following general multimode fiber impulse response expression.

In order to answer to the question above, the following assumptions are formulated:

1. Chromatic dispersion affects the impulse response of each excited mode independently from any other propagating mode.
2. Modal dispersion affects the relative group delay of each excited mode, without altering the pulse shape, independently from any other propagating mode.

The second assumption is equivalent to the well-known linear multimode regime, where any kind of mode interaction is postulated. According to the above two modeling assumptions, the general expression of the impulse response of the multimode fiber can be written as the linear superposition of the chromatic impulse response of each excited mode, properly weighted by the power coupling coefficients and translated by the corresponding group delay.

Before writing the impulse response expression, one more remark is necessary. Both the coupling coefficient distribution $\{a_h(\lambda)\}$ and the modal group delay $\{\tau_{g,h}(\lambda)\}$ are functions of the source spectrum through the wavelength. This is important because in the general model the source PSD is not necessarily concentrated around a single wavelength as the case of a narrow linewidth laser source. This leads unavoidably to an approximation in the impulse response modeling. It is assumed that each mode propagates with a specific delay, but one question arises spontaneously: which wavelength would it be? In general, there is no one single wavelength emitted by the light source but instead there is a continuous wavelength spectrum. The approximation here essentially assumes that the multimode behavior of the optical fiber is determined according to the average wavelength of the spectrum, leaving the chromatic impulse response to take care of the effects of the source spectral distribution around the average wavelength.

This is, on the other hand, the very fundamental postulate of the modal analysis of every multimode waveguide, either metallic or dielectric. Maxwell equations are written for a monochromatic electromagnetic source. The modal analysis of every waveguide structure postulates that the exciting field is true monochromatic, closely defined by a single wavelength, and that the whole modal field solution which derives from that excitation is referring to that single wavelength. The more general approach assuming a polychromatic light source can be solved by linear superposition of the monochromatic field solution, and essentially that approach has been used to define the chromatic modal dispersion.

However, the fundamental difference between the general theory of the impulse response using a polychromatic light source and the present approximated approach is that the same modal field solution is postulated for all the spectral wavelengths included in the polychromatic light source, and of course it should be clear that this is not the exact solution since the modal fields are dependent on the exciting wavelength.

5.3.2 The Mathematical Model

With the above discussion in mind, from Equations (3.55) and (4.83), it is therefore possible to approach the general (approximated) expression of the multimode optical fiber impulse response $h_F(z, t, \overline{\lambda})$. However, before writing down the expression by simply superposing each chromatic impulse response with the corresponding modal delay, one more issue needs to be discussed. The chromatic impulse response of the hth excited mode $h_{c,h}(z, t)$ in Equation (4.83) includes the pulse translation according to the average time delay $\overline{t}_{c,h} = z\overline{\tau}_{c,h}$ reported either in Equation (4.90) or in Table 4.4. This time delay is in general different from the modal group delay $\overline{t}_{g,h} = z\tau_{g,h}(\overline{\lambda})$ evaluated at the average wavelength spectrum $\overline{\lambda}$. This is because the group delay $\tau_{g,h}(\lambda)$ is not a linear function of the wavelength in the source spectrum wavelength range and in general the chromatic impulse response $h_{c,h}(z, t)$ differs from the time equivalent replica of the source spectrum profile and some pulse distortion usually occurs. In conclusion, for the general group delay function and source PSD,

$$\left.\begin{aligned} \overline{t}_{g,h} &= z\tau_{g,h}(\overline{\lambda}) \\ \overline{t}_{c,h} &= z\overline{\tau}_{c,h} \end{aligned}\right\} \Rightarrow \overline{t}_{g,h} \neq \overline{t}_{c,h} \tag{5.18}$$

The equality sign holds only in the case of the linear group delay, independently from the source spectrum profile, as can be clearly seen from the delay time expression (4.98) in Chapter 4,

Section 4.3, of the chromatic impulse response. Of course, for a narrow source spectrum centered away from any zero-dispersion wavelength, the equality is almost satisfied, even assuming a nonlinear group delay, as extensively discussed in the examples reported in Chapter 4, Section 4.3.

In order to proceed toward the mathematical expression of the multimode fiber impulse response, first the centered chromatic impulse response $\hat{h}_{c,h}(z, t)$ of each excited mode is written by temporal translation of the corresponding average time $\overline{t}_{c,h} = z\overline{\tau}_{c,h}$:

$$\hat{h}_{c,h}(z, t) \equiv h_{c,h}(z, t + z\overline{\tau}_{c,h}) \Rightarrow t = 0, \hat{h}_{c,h}(z, 0) \equiv h_{c,h}(z, \overline{t}_{c,h}) \tag{5.19}$$

The 'hat' symbol was used to refer to the time-centered response. Figure 5.2 shows the pulse centering procedure.

Once the chromatic impulse response of each excited mode has been centered at the time origin, all of the modes are superposed after translating each of them by the corresponding modal group delay evaluated at the average source spectrum wavelength, $\overline{t}_{g,h} = z\tau_{g,h}(\overline{\lambda})$ and multiplying by the coupling power coefficient. From Equation (3.55),

$$h_F(z, t, \overline{\lambda}) = \sum_{h=1}^{M} |a_h(\overline{\lambda})|^2 \hat{h}_{c,h}[z, t - z\tau_{g,h}(\overline{\lambda})]$$

Using Equation (5.19) gives

$$h_F(z, t, \overline{\lambda}) = \sum_{h=1}^{M} |a_h(\overline{\lambda})|^2 h_{c,h}[z, t - z(\overline{\tau}_{g,h} - \overline{\tau}_{c,h})] \tag{5.20}$$

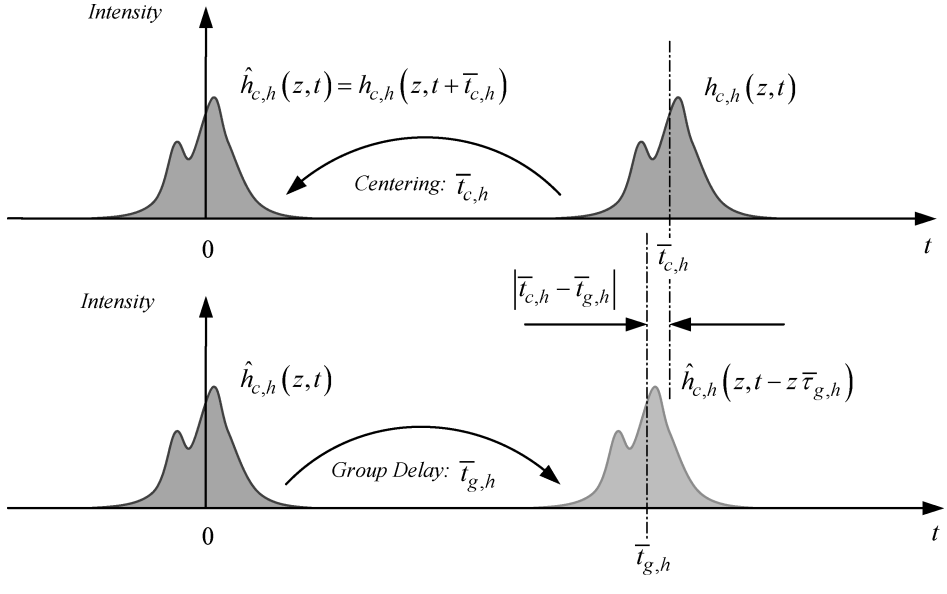

Figure 5.2 Centering procedure of the chromatic impulse response of the excited mode hth. The pulse $\hat{h}_{c,h}(z, t)$ has the average time delay centered on the time origin. The pulse $\hat{h}_{c,h}(z, t - \overline{t}_{g,h})$ has shifted with the average value centered on the time instant $\overline{t}_{g,h} = z\tau_{g,h}(\overline{\lambda})$

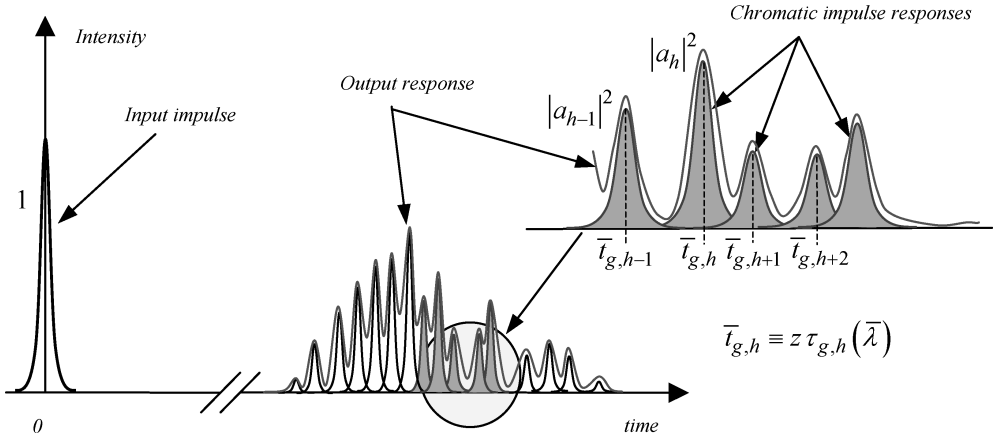

Figure 5.3 Qualitative representation of the multimode fiber impulse response showing the contribution of the chromatic response to the broadening factor of each excited mode. The total impulse response assumes the linear superposition form referred to in the text, where the fiber modal solution is defined as the average source power spectral density wavelength $\overline{\lambda}$

where

$$\overline{\lambda} \equiv \frac{\int_0^{+\infty} \lambda S_s(\lambda)\,\mathrm{d}\lambda}{\int_0^{+\infty} S_s(\lambda)\,\mathrm{d}\lambda}$$

is the average wavelength of the source power spectral density. Figure 5.3 shows a qualitative representation of the multimode fiber impulse response according to the superposition (5.20).

Each fiber mode hth is affected by the chromatic broadening due to the impulse response $h_{c,h}(z, t)$ derived in Equation (4.83). The same chromatic impulse response expression is given below, where for completeness the modal index dependence, h, has been added. Here the index k refers to each wavelength segment $\Lambda_h^{(k)}$ identified in the ripple group delay profile $\tau_{g,h}(\lambda)$ of the hth mode, as discussed in Chapter 4, Section 4.2:

$$h_{c,h}(z,t) = \frac{1}{z}\sum_{k=0}^{N} h_{c,h}^{(k)}\left(\frac{t}{z}\right) \tag{5.21}$$

and

$$\underbrace{h_{c,h}^{(k)}\left(\frac{t}{z}\right) \equiv \frac{S_s[\zeta_{g,h}(t/z)]}{|D_{c,h}[\zeta_{g,h}(t/z)]|}}_{\lambda=\zeta_{g,h}\left(\frac{t}{z}\right)\in\Lambda_h^{(k)},k=1,2,\ldots,N-1,\ \begin{cases}\Lambda_h^{(0)}=(0,\lambda_1)\\ \Lambda_h^{(k)}=(\lambda_k,\lambda_{k+1})\\ \Lambda_h^{(N)}=(\lambda_N,+\infty)\end{cases}} \tag{5.22}$$

$h=1,2,\ldots,M$ fiber modes

The multimode fiber impulse response is completely determined by the set of equations derived above. Table 5.2 summarizes the major conclusions.

Table 5.2 Expressions for the mathematical model of the multimode fiber impulse response, including all the required components, are given. The last column indicates the equation reference in the text. The first row of the table shows the impulse response as a superposition of all the excited mode contributions, including intramodal pulse broadening due to chromatic dispersion

Parameter	Expression	Validity	Reference
General impulse response	$h_{\mathrm{F}}(z,t,\overline{\lambda}) = \sum_{h=1}^{M} \lvert\overline{a}_h\rvert^2 h_{\mathrm{c},h}[z, t - z(\overline{\tau}_{\mathrm{g},h} - \overline{\tau}_{\mathrm{c},h})]$	Linear regime	(5.20)
Chromatic impulse response of the hth mode	$h_{\mathrm{c},h}(z,t) = \frac{1}{z}\sum_{k=0}^{N} h_{\mathrm{c},h}^{(k)}\left(\frac{t}{z}\right)$	General	(5.21)
Chromatic impulse response contribution of segment $\Lambda_h^{(k)}$ of the hth mode	$\underbrace{h_{\mathrm{c},h}^{(k)}\left(\frac{t}{z}\right) \equiv \frac{S_{\mathrm{s}}[\zeta_{\mathrm{g},h}(t/z)]}{\lvert D_{\mathrm{c},h}[\zeta_{\mathrm{g},h}(t/z)]\rvert}}_{\lambda=\zeta_{\mathrm{g},h}\left(\frac{t}{z}\right)\in\Lambda_h^{(k)},k=1,2,\ldots,N-1,\ \begin{cases}\Lambda_h^{(0)}=(0,\lambda_1)\\ \Lambda_h^{(k)}=(\lambda_k,\lambda_{k+1})\\ \Lambda_h^{(N)}=(\lambda_N,+\infty)\end{cases}}$ $h=1,2,\ldots,M$ fiber modes	General	(5.22)
Average source wavelength	$\overline{\lambda} \equiv \frac{\int_0^{+\infty} \lambda S_{\mathrm{s}}(\lambda)\,\mathrm{d}\lambda}{\int_0^{+\infty} S_{\mathrm{s}}(\lambda)\,\mathrm{d}\lambda}$	General	(4.92)
Coupling coefficients of the hth mode	$\lvert\overline{a}_h\rvert^2 = \lvert a_h(\overline{\lambda})\rvert^2, \qquad \sum_{h=1}^{M} \lvert\overline{a}_h\rvert^2 = 1$	General	(3.57)
Group delay of the hth mode at the average source wavelength	$\overline{\tau}_{\mathrm{g},h} = \tau_{\mathrm{g},h}(\overline{\lambda})$	General	(4.100)
Average delay of the chromatic impulse response of the hth mode	$\overline{\tau}_{\mathrm{c},h} = \underbrace{\sum_{k=0}^{N}\int_{T_k} \tau \frac{S_{\mathrm{s}}[\zeta_{\mathrm{g},h}(t/z)]}{\lvert D_{\mathrm{c},h}[\zeta_{\mathrm{g},h}(t/z)]\rvert}\,\mathrm{d}\tau}_{\lambda=\zeta_{\mathrm{g},h}\left(\frac{t}{z}\right)\in\Lambda_h^{(k)},k=1,2,\ldots,N-1,\ \begin{cases}\Lambda_h^{(0)}=(0,\lambda_1)\\ \Lambda_h^{(k)}=(\lambda_k,\lambda_{k+1})\\ \Lambda_h^{(N)}=(\lambda_N,+\infty)\end{cases}}$ $h = 1, 2, \ldots, M$ fiber modes	General	(4.90)

5.3.3 Impulse Response Moments

In this section the general expression for the normalization condition, the average time and the RMS pulse width of the multimode fiber impulse response will be derived, as depicted in Table 5.2. The procedure follows the same approach already used in the analysis of either the chromatic impulse response or the modal impulse response. In order to have a consistent theory both of those two partial responses must as particular cases of the general impulse response must be found. The consistency of the mathematical model will be verified at the end of this section.

5.3.3.1 Energy Normalization

It has been affirmed several times that the general impulse response of the multimode fiber requires the knowledge of the source power spectral density, the group delay function for every excited mode

and the source power coupling coefficient distribution. Any mode group is effectively excited by the light source if the corresponding power coupled coefficient has not a negligible value. Of course the set of power coupling coefficients satisfies the energy conservation condition reported in Equation (3.57) in Chapter 3 for every source wavelength. In particular, for the average source wavelength $\overline{\lambda}$ defined in Equation (4.92),

$$|\overline{a}_h|^2 = |a_h(\overline{\lambda})|^2, \qquad \sum_{h=1}^{M} |\overline{a}_h|^2 = 1 \tag{5.23}$$

This condition has already been included in Table 5.2. The energy W_F of the general impulse response $h_F(z, t, \overline{\lambda})$ of the multimode fiber, reported in Equation (5.22), is given by the following integral:

$$W_F = \int_{-\infty}^{+\infty} h_F(z, t, \overline{\lambda})\, dt = \sum_{h=1}^{M} |\overline{a}_h|^2 \int_{-\infty}^{+\infty} h_{c,h}[z, t - z(\overline{\tau}_{g,h} - \overline{\tau}_{c,h})]\, dt \tag{5.24}$$

From Chapter 4, Section 4.4.1, the integral of the chromatic impulse response was found to give the energy of the pulse and this value is normalized, as shown in Equation (4.81). The pulse translation in Equation (5.24) does not alter this conclusion because the integration interval is infinite. From the energy normalization of the chromatic impulse response and the normalization condition for the coupling coefficients, (3.57), it can be concluded that the energy of the multimode fiber general impulse response $h_F(z, t, \overline{\lambda})$ is normalized:

$$W_F = \int_{-\infty}^{+\infty} h_F(z, t, \overline{\lambda})\, dt = 1 \tag{5.25}$$

As a consequence of the constant value of the energy in the lossless assumption, the impulse response subtends the same area along the propagation. It is interesting to observe that the unit energy conservation of the general impulse response was found using both properties needed for the energy conservation of the chromatic impulse response (4.81) and the modal impulse response (3.57) respectively.

5.3.3.2 Average Value

The average value of the temporal variable for the general impulse response of the multimode fiber is given by the following integral, where the energy normalization in Equation (5.25) is used:

$$\overline{t}_F(z, \overline{\lambda}) \equiv \frac{\int_{-\infty}^{+\infty} t h_F(z, t, \overline{\lambda})\, dt}{\int_{-\infty}^{+\infty} h_F(z, t, \overline{\lambda})\, dt} = \int_{-\infty}^{+\infty} t h_F(z, t, \overline{\lambda})\, dt \tag{5.26}$$

Substituting the impulse response expression (5.20) gives

$$\overline{t}_F(z, \overline{\lambda}) = \sum_{h=1}^{M} |\overline{a}_h|^2 \int_{-\infty}^{+\infty} t h_{c,h}[z, t - z(\overline{\tau}_{g,h} - \overline{\tau}_{c,h})]\, dt \tag{5.27}$$

As demonstrated below, the average value of the translated chromatic impulse response $h_{c,h}[z, t - z(\overline{\tau}_{g,h} - \overline{\tau}_{c,h})]$ of the hth mode coincides with the temporal group delay evaluated at the

source average wavelength $\overline{t}_{g,h}(z) = z\tau_{g,h}(\overline{\lambda}) = z\overline{\tau}_{g,h}$. Substituting the integration variable $\xi = t - z(\overline{\tau}_{g,h} - \overline{\tau}_{c,h})$ and using the energy normalization (4.81), from Equation (4.84)

$$\begin{aligned}\int_{-\infty}^{+\infty} t h_{c,h}[z, t - z(\overline{\tau}_{g,h} - \overline{\tau}_{c,h})]\,\mathrm{d}t &= \int_{-\infty}^{+\infty} [\xi + z(\overline{\tau}_{g,h} - \overline{\tau}_{c,h})] h_{c,h}(z, \xi)\,\mathrm{d}\xi \\ &= z\overline{\tau}_{c,h} + z(\overline{\tau}_{g,h} - \overline{\tau}_{c,h}) \int_{-\infty}^{+\infty} h_{c,h}(z, \xi)\,\mathrm{d}\xi \qquad (5.28) \\ &= z\overline{\tau}_{g,h} = \overline{t}_{g,h}(z)\end{aligned}$$

In conclusion, the temporal average value of the translated chromatic impulse response $h_{c,h}[z, t - z(\overline{\tau}_{g,h} - \overline{\tau}_{c,h})]$ of the hth mode coincides with the group delay $\overline{t}_{g,h}(z)$ of the hth mode of Equation (5.18) evaluated at the average source spectrum wavelength $\overline{\lambda}$. This result is consistent with the theory developed for the two partial impulse responses. Substituting Equation (5.28) into Equation (5.27), the average value $\overline{t}_F(z, \overline{\lambda})$ of the multimode fiber impulse response delay coincides with the average value (5.10) of the modal delay evaluated at the average source spectrum wavelength $\overline{\lambda}$:

$$\overline{t}_F(z, \overline{\lambda}) = z \sum_{h=1}^{M} |\overline{a}_h|^2 \tau_{g,h}(\overline{\lambda}) = z\overline{\tau}_m(\overline{\lambda}) = \overline{t}_m(\overline{\lambda}) \qquad (5.29)$$

This result is relevant for three reasons:

1. It has the expected form and from Equation (5.10) it coincides with the average modal delay $\overline{t}_m(\overline{\lambda})$ evaluated at the average source spectrum wavelength $\overline{\lambda}$. Therefore the following clear physical meaning is obtained: the average delay of the multimode fiber impulse response is the weighted average among individual mode delays through the power coupling coefficients.
2. It depends on the modal parameters only. This is a consequence of the previous assumption of centering each chromatic impulse response over the corresponding modal group delay evaluated at the average source spectrum wavelength, and weighting with the corresponding power coupling coefficient, as shown in Equation (5.20). It confirms the consistency of the mathematical modeling.
3. It depends linearly on the distance z. Again, this result is expected within the assumption of the linear propagation regime, when no mode interactions are allowed in the optical fiber.

5.3.3.3 Pulse Dispersion: The Variance Theorem

The variance $\sigma_F^2(z, \overline{\lambda})$ of the temporal variable of the multimode fiber impulse response $h_F(z, t, \overline{\lambda})$ is defined as the square value of the expected deviation of the pulse profile from the average delay $\overline{t}_F(z, \overline{\lambda})$:

$$\sigma_F^2(z, \overline{\lambda}) \equiv \frac{\displaystyle\int_{-\infty}^{+\infty} [t - \overline{t}_F(z, \overline{\lambda})]^2 h_F(z, t, \overline{\lambda})\,\mathrm{d}t}{\displaystyle\int_{-\infty}^{+\infty} h_F(z, t, \overline{\lambda})\,\mathrm{d}t} = \int_{-\infty}^{+\infty} [t - \overline{t}_F(z, \overline{\lambda})]^2 h_F(z, t, \overline{\lambda})\,\mathrm{d}t \qquad (5.30)$$

where the energy normalization property in Equation (5.25) is used. Replacing the impulse response (5.20) by the following expression gives

$$\sigma_F^2(z, \overline{\lambda}) = \sum_{h=1}^{M} |\overline{a}_h|^2 \int_{-\infty}^{+\infty} [t - \overline{t}_F(z, \overline{\lambda})]^2 h_{c,h}[z, t - z(\overline{\tau}_{g,h} - \overline{\tau}_{c,h})]\,\mathrm{d}t \qquad (5.31)$$

In the following the very useful theorem of the variance will be demonstrated.

Theorem of the Variance

The variance $\sigma_F^2(z, \overline{\lambda})$ of the multimode fiber impulse response $h_F(z, t, \overline{\lambda})$ is given by the sum of the modal variance $\sigma_m^2(z, \overline{\lambda})$ and the average chromatic variance $\overline{\sigma}_c^2(z)$.

Before proceeding with the demonstration, it is important to note that this result is related neither to any approximation nor to Gaussian pulse modeling. Instead, it is verified for every general chromatic impulse response, including the multiple line source spectrum and the ripple group delay function, with every modal distribution. Besides that, this relevant and expected result confirms the validity and the internal consistency of the multimode fiber modeling presented here.

By changing the integration variable in Equation (5.31) to $\xi = t - z(\overline{\tau}_{g,h} - \overline{\tau}_{c,h})$,

$$\sigma_F^2(z, \overline{\lambda}) = \sum_{h=1}^{M} |\overline{a}_h|^2 \int_{-\infty}^{+\infty} \left\{(\xi - z\overline{\tau}_{c,h}) + [z\overline{\tau}_{g,h} - \overline{t}_F(z, \overline{\lambda})]\right\}^2 h_{c,h}(z, \xi)\, d\xi \tag{5.32}$$

The squared term has been grouped in order to provide decomposition into the following three relevant integrals, where the time variable t has again been indicated:

$$\begin{aligned}\sigma_F^2(z, \overline{\lambda}) = &\sum_{h=1}^{M} |\overline{a}_h|^2 \int_{-\infty}^{+\infty} (t - z\overline{\tau}_{c,h})^2 h_{c,h}(z, t)\, dt \\ &+ \sum_{h=1}^{M} |\overline{a}_h|^2 \int_{-\infty}^{+\infty} [z\overline{\tau}_{g,h} - \overline{t}_F(z, \overline{\lambda})]^2 h_{c,h}(z, t)\, dt \\ &+ 2\sum_{h=1}^{M} |\overline{a}_h|^2 \int_{-\infty}^{+\infty} (t - z\overline{\tau}_{c,h})[z\overline{\tau}_{g,h} - \overline{t}_F(z, \overline{\lambda})] h_{c,h}(z, t)\, dt\end{aligned} \tag{5.33}$$

In the following the three integral terms separately. The temporal average value $\overline{t}_{c,h}(z)$ of the chromatic impulse response $h_{c,h}(z, t)$ of the hth excited mode is given by Equation (4.89): $\overline{t}_{c,h}(z) = z\overline{\tau}_{c,h}$. The integral in the first addend of Equation (5.33) therefore coincides with expression (4.104) of the variance of the chromatic impulse response of the hth excited mode:

$$\sigma_{c,h}^2(z) = \int_{-\infty}^{+\infty} (t - z\overline{\tau}_{c,h})^2 h_{c,h}(z, t)\, dt \tag{5.34}$$

It should be remembered that each propagating mode supports its own chromatic dispersion. Accordingly, with M propagating modes account must be taken of M different chromatic impulse response variances $\sigma_{c,h}^2(z)$. This is exactly the role of the weighting sum in the first addend of Equation (5.33) over the power coupling coefficients. The result is the ensemble average value of the variance among all the supported fiber modes, according to their own coupling coefficients. Equations (5.33) and (5.34) define $\overline{\sigma}_c^2(z)$ as the ensemble average of the chromatic variance:

$$\overline{\sigma}_c^2(z) \equiv \sum_{h=1}^{M} |\overline{a}_h|^2 \sigma_{c,h}^2(z) = z^2 \sum_{h=1}^{M} |\overline{a}_h|^2 \hat{\sigma}_{c,h}^2 = z^2 \hat{\overline{\sigma}}_c^2 \tag{5.35}$$

Using this definition, the first addend of Equation (5.33) becomes

$$\sum_{h=1}^{M} |\overline{a}_h|^2 \int_{-\infty}^{+\infty} (t - z\overline{\tau}_{c,h})^2 h_{c,h}(z, t)\, dt = \overline{\sigma}_c^2(z) \tag{5.36}$$

The second term in Equation (5.33) has a straightforward meaning. In Section 5.3.3.2 it was recognized that the average value of the delay of the multimode fiber impulse response $\overline{t}_F(z, \overline{\lambda})$

coincides with the average value of the modal delay $\overline{t}_{\mathrm{m}}(z, \overline{\lambda})$, both evaluated at the average source spectrum wavelength $\overline{\lambda}$, as reported in Equation (5.29). The term in parentheses does not depend on the time and can therefore be taken out of the integration. Using the energy normalization (4.81) for the chromatic impulse response, it is easy to recognize that the second term coincides with the variance $\sigma_{\mathrm{m}}^2(z, \overline{\lambda})$ of the modal impulse response, as derived previously in Equation (5.16):

$$\sum_{h=1}^{M} |\overline{a}_h|^2 \int_{-\infty}^{+\infty} [z\overline{\tau}_{\mathrm{g},h} - \overline{t}_{\mathrm{F}}(z, \overline{\lambda})]^2 h_{\mathrm{c},h}(z, t)\, \mathrm{d}t = \sigma_{\mathrm{m}}^2(z, \overline{\lambda}) = z\hat{\sigma}_{\mathrm{m}}^2(z, \overline{\lambda}) \tag{5.37}$$

The third term in Equation (5.33) gives a null contribution, as demonstrated below. The term in square brackets does not depend on the time variable and it can be taken out of the integral. Each term of the sum is therefore multiplied by the corresponding integral in the chromatic impulse response of the hth modal component, as shown below:

$$\sum_{h=1}^{M} |\overline{a}_h|^2 [z\overline{\tau}_{\mathrm{g},h} - \overline{t}_{\mathrm{F}}(z, \overline{\lambda})] \int_{-\infty}^{+\infty} (t - z\overline{\tau}_{\mathrm{c},h}) h_{\mathrm{c},h}(z, t)\, \mathrm{d}t$$

It is a simple matter to conclude from Equations (4.89) and (4.81) that each of those integrals gives a null contribution, leading to a null value of the whole third term in Equation (5.33). In fact,

$$\begin{aligned} &\int_{-\infty}^{+\infty} (t - z\overline{\tau}_{\mathrm{c},h}) h_{\mathrm{c},h}(z, t)\, \mathrm{d}t \\ &\quad = \int_{-\infty}^{+\infty} t h_{\mathrm{c},h}(z, t)\, \mathrm{d}t - z\overline{\tau}_{\mathrm{c},h} \int_{-\infty}^{+\infty} h_{\mathrm{c},h}(z, t)\, \mathrm{d}t = z\overline{\tau}_{\mathrm{c},h} - z\overline{\tau}_{\mathrm{c},h} = 0 \end{aligned}$$

Therefore

$$\sum_{h=1}^{M} |\overline{a}_h|^2 [z\overline{\tau}_{\mathrm{g},h} - \overline{t}_{\mathrm{F}}(z, \overline{\lambda})] \int_{-\infty}^{+\infty} (t - z\overline{\tau}_{\mathrm{c},h}) h_{\mathrm{c},h}(z, t)\, \mathrm{d}t = 0 \tag{5.38}$$

In conclusion, from Equations (5.33), (5.35), (5.36), (5.37) and (5.38), the following relevant result is obtained. The variance of the multimode fiber impulse response is given by the sum of the ensemble average of the chromatic variance with the modal variance evaluated at the source average wavelength:

$$\sigma_{\mathrm{F}}^2(z, \overline{\lambda}) = \overline{\sigma}_{\mathrm{c}}^2(z) + \sigma_{\mathrm{m}}^2(z, \overline{\lambda}) \tag{5.39}$$

From Equations (4.111), (5.35) and (5.17) it is concluded that the variance of the multimode fiber impulse response scales quadratically with the propagated distance z:

$$\sigma_{\mathrm{F}}^2(z, \overline{\lambda}) = z^2[\hat{\overline{\sigma}}_{\mathrm{c}}^2 + \hat{\sigma}_{\mathrm{m}}^2(\overline{\lambda})] \tag{5.40}$$

It should be remembered that the overbar sign indicates the ensemble average of the corresponding entity. In addition, when requested, the wavelength-dependent functions are assumed to be evaluated at the average wavelength of the source spectrum.

The result just obtained is very relevant because it summarizes into a single and simple formula both the chromatic and modal dispersion effects encountered by the propagating pulse in a multimode optical fiber. Table 5.3 summarizes the major expressions that have been derived in this section for the general impulse response of the multimode optical fiber.

If all excited modes experience the same first-order derivative of the group delay function, otherwise stated as the chromatic dispersion coefficient, the ensemble average of the chromatic variance defined in Equation (5.35) reduces to the same value, $\sigma_{\mathrm{c},h}^2(z) = \sigma_{\mathrm{c}}^2(z)$, for every modal

Table 5.3 Expressions of the first- and second-order moments of the multimode fiber impulse response. The last column indicates the equation reference in the text. The last row gives the variance theorem

Parameter	Expression	Validity	Reference
Energy normalization	$W_{\mathrm{F}} = \int_{-\infty}^{+\infty} h_{\mathrm{F}}(z, t, \overline{\lambda})\,\mathrm{d}t = 1$	General	(5.25)
Average delay	$\overline{t}_{\mathrm{F}}(z, \overline{\lambda}) = z\sum_{h=1}^{M} \lvert\overline{a}_h\rvert^2 \tau_{\mathrm{g},h}(\overline{\lambda}) = z\overline{\tau}_{\mathrm{m}}(\overline{\lambda}) = \overline{t}_{\mathrm{m}}(\overline{\lambda})$	General	(5.29)
Ensemble average of the chromatic variance	$\overline{\sigma}_{\mathrm{c}}^2(z) \equiv \sum_{h=1}^{M} \lvert\overline{a}_h\rvert^2 \sigma_{\mathrm{c},h}^2(z)$	General	(5.35)
Variance	$\sigma_{\mathrm{F}}^2(z, \overline{\lambda}) = \overline{\sigma}_{\mathrm{c}}^2(z) + \sigma_{\mathrm{m}}^2(z, \overline{\lambda})$	General	(5.40)

chromatic contribution. According to the normalization (3.57) of the power coupling coefficients, it is therefore concluded that $\overline{\sigma}_{\mathrm{c}}^2(z) = \sigma_{\mathrm{c}}^2(z)$.

In the following section basic concepts and conclusions analyzed so far will be reviewed in order to avoid misunderstanding and to underline system design considerations clearly. Basic concepts such as broadband and narrowband source spectrum conditions, the multimode fiber impulse response and the -3 dB bandwidth will shortly be reviewed.

5.3.4 System Design Considerations

When involved in a multimode optical fiber transmission system design that is mainly concerned with feasibility criteria and a maximum allowed signal distortion penalty, the RMS pulse width of the general impulse response of the multimode fiber assumes the principal role in setting a maximum allowable link length for a given transmission rate. According to the analysis in the previous section, the RMS pulse width of the general impulse response is given by the square root of the total variance in Equation (5.40):

$$\sigma_{\mathrm{F}}(z, \overline{\lambda}) = z\sqrt{\hat{\overline{\sigma}}_{\mathrm{c}}^2(z) + \hat{\sigma}_{\mathrm{m}}^2(z, \overline{\lambda})} \tag{5.41}$$

The physical principles behind the total RMS dispersion contributions are quite different.

5.3.4.1 Chromatic Dispersion or Intramodal Dispersion

Chromatic dispersion or intramodal dispersion act inside each guided mode, providing the distortion of the envelope of the optical pulse depending on the operating wavelength region and the source spectral characteristics. So far the situation where the source spectrum dominates over the modulation spectrum has been extensively studied. This situation was identified as the broadband optical source condition. A detailed analysis of chromatic dispersion of the complementary situation, when the source spectrum collapses into a very narrowband linewidth with respect to the modulation spectrum, will not be included in this book. The analysis of the narrowband optical source condition can be found in many references and reveals that the pulse distortion can have a broadening or a compressive behavior depending on the sign of the product between the source frequency chirping coefficient and the second-order derivative of the propagation constant. The relevant consequences of the sign of the source spectrum chirping coefficient find major applications in either very high speed or very long haul digital transmission systems operating over single-mode fibers using the external optical modulation technique. Typical transmission speed–length products for including

significant limitations due to group velocity dispersion start at 2.5 Gb/s, reaching about 900 km of unregenerated link length, reducing to about 60 km when operating at 10 Gb/s and limited to below 3 km for 40 Gb/s transmission speed. It is the characteristic quadratic link length limitation versus the signaling speed that marks the group velocity dispersion as the dominant transmission behavior.

In applications of standard single-mode or multimode fibers operating in either the 850 nm or 1300 nm region (the normal regime, the second-order derivative of the propagation constant, has a positive sign) and fed with direct modulated semiconductor laser sources exhibiting a typical positive chirping coefficient, the propagating pulse versus distance goes into initial compression. This is the effect of the source chirped pulse spectrum. With a further increase of the distance, the pulse dispersion starts to be dominated by the fiber-induced chirping and the pulse begins to broaden. This is the usual well-known pulse broadening effect when no source chirping is included. On the other hand, if the source is negatively chirped, the pulse would start to broaden immediately after the launching section. The opposite situation happens in the 1550 nm region, where the standard fiber falls into the anomalous regime with negative sign of the second-order derivative of the propagation constant. In this case a direct modulated laser diode with a positive chirping coefficient will generate optical pulses that will start to broaden as soon as they leave the launching section. In order to have pulse compression in the third window a negatively chirped source spectrum is needed.

Independently from the operating region and fiber characteristics, if the source is assumed to operate without frequency chirping, the propagating pulse starts to broaden monotonically as soon as it leaves the launching section. In order to avoid too sophisticated a dependence on fiber specifications, the operating wavelength region and source spectral characteristics have been widely assumed to consider the fact that the chromatic dispersion induces a general pulse broadening. This essentially resembles the chirp-free source condition. Finally, considering multimode propagation, chromatic dispersion pulse broadening induces fiber mode contributions to overlap along the propagation.

5.3.4.2 Modal Dispersion or Intermodal Dispersion

Modal dispersion acts among guided modes, providing the mode energy partition to be detected at different time instants after some propagation length. It is important to note that modal dispersion is not related to the signal frequency content. Instead, modal dispersion is a direct consequence of the differential mode delay (DMD) among all excited modes. The differentiation concept regards the modal index in this sense. Once the fiber characteristics have been fixed by means of a specified group delay for each supported mode, the modal impulse response becomes a function of the source power distribution among allowable modes. This is a very peculiar behavior of the multimode fiber modal response and makes usual meaningful concepts like impulse response and bandwidth lose their role in the design methodology of multimode fiber transmission systems. The modal impulse response changes according to the source power coupling at the launching section and therefore acquires a strong dependence on any kind of environmental perturbation that can interfere with the source power coupling coefficient distribution. Mechanical vibration and temperature stresses can strongly change the multimode fiber impulse response. Even multimode fiber optical connectors are quite involved in the impulse response stability.

One more remark is needed concerning the meaning of the modal bandwidth, which are usually considered in design procedures. Once the modal impulse response has been determined using the techniques presented in previous sections, the Fourier transform is of course uniquely defined and the multimode fiber frequency response is uniquely related to the corresponding impulse response. The question arises when the frequency response is reduced to a single convenient number showing the -3 dB bandwidth. The multimode fiber propagation characteristic is not uniquely identified in terms of the simple -3 dB bandwidth definition. In fact, according to the large variability of the multimode fiber impulse response versus launching conditions and environmental perturbations, a

very large number of different frequency responses can exhibit instead the same −3 dB bandwidth. As will be seen in the next section, even slight changes in the launching conditions can generate different multiple peak impulse responses due to various mode excitations. Correspondingly, the multiple peak impulse response generates high-frequency ripple behavior in the frequency response and very often the −3 dB bandwidth interests only the lower range of the frequency response, where the ripple is still not present. It is evident that in this case the −3 dB bandwidth concept would lose most of its meaning in characterizing the multimode fiber frequency behavior.

This multimode fiber bandwidth characterization generates a lot of discussion in many standard committees about how to achieve at the same time an effective bandwidth definition without losing too much in terms of practical engineering design procedures. This issue belongs to the more general channel metric problem: which metric would be suitable for the multimode fiber transmission channel in order to have as many correct predictions as possible in terms of transmission system performances? To answer this question, finding the most suitable channel metric requires a deep knowledge of the whole transmission system, including both the optical transmitter and the optical receiver architectures. Modulation formats and detected signal processing are intimately involved in the channel metric definition for the multimode fiber transmission system. It will be seen later in this book that 10 Gb/s transmission over multimode fiber suggests the application of the electronic dispersion compensator (EDC) in order to correct some of the band-limited pulse distortion. The EDC is based on the combined architecture of a feedforward equalizer and a decision feedback equalizer and in this case the proposed channel metrics is known as the penalty of ideal equalizer-digital (PIE-D).

5.4 The Multimode Impulse Response Model

In this section a computer modeling will be presented of a multimode fiber transmission behavior computing the whole impulse response (including both chromatic and modal responses) using Matlab® 7.0. The corresponding frequency response will follow in Section 5.5. Assuming a fixed multimode fiber with a known group delay function for each allowed mode, the program will change the launched power distribution, clearly showing the large expected variability of the impulse response and of the corresponding frequency response. The meaning of the −3 dB bandwidth will be commented on accordingly. The modeling presented does not reflect either any real multimode fiber or any light source device, but instead serves as a useful tool for studying the behavior of different impulse responses when changing the source power distribution at the launching section.

5.4.1 Model Assumptions

The multimode fiber transmission system modeling is based on the following assumptions:

1. *Linear regime.* The multimode fiber supports a linear propagation regime. Mode groups do not interfere with each other and the modal power distribution remains constant during the pulse propagation.
2. *Uniform chromatic dispersion.* The chromatic dispersion coefficient in the wavelength range occupied by the source spectrum is assumed to have the same value for all excited modes, leading therefore to the same contribution at the average wavelength $\overline{\lambda}$ of the source spectrum:

$$D_{c,h}(\overline{\lambda}) = \overline{D}_c, \qquad h \in N\ (1, M) \tag{5.42}$$

The notation $h \in N\ (1, M)$ is used to indicate the positive integer numbers included between 1 and the mode group number M. Since the chromatic dispersion coefficient is defined as the first-order wavelength derivative of the modal group delay, the uniform chromatic dispersion assumption is equivalent to assuming that the modal group delays $\tau_{g,h}(\lambda)$ have all the same

wavelength dependence, at least in the wavelength interval occupied by the source spectrum. The modal group delays therefore differentiate only for the value $\tau_{g,h}(\overline{\lambda}) = \overline{\tau}_{g,h}$ that they assume at the average wavelength $\overline{\lambda}$ of the source spectrum. Using the power series expansion of the group delay function, this leads to the following representation:

$$\tau_{g,h}(\lambda) = \tau_{g,h}(\overline{\lambda}) + (\lambda - \overline{\lambda}) D_c(\overline{\lambda}) + \cdots + \text{ higher order terms}, \qquad h \in N\ (1, M) \tag{5.43}$$

This hypothesis is equivalent to assuming that the group delay of the generic supported fiber mode can be expressed as the sum of the delay value $\overline{\tau}_{g,h}$ at the average wavelength $\overline{\lambda}$ plus the same wavelength function for each allowed fiber mode. According to Equation (5.42), the first derivative of that wavelength function therefore gives the same chromatic dispersion coefficient $D_{c,h}(\overline{\lambda}) = \overline{D}_c$ for all supported modes.

3. *Group delay distribution versus modal index.* In order to complete the description of the group delay of each allowed fiber mode there is a need to specify further how those values $\overline{\tau}_{g,h}$ are distributed according to the modal group index $h \in N(1, M)$. It is assumed that the values $\overline{\tau}_{g,h}$ of the modal group delays evaluated at the average source spectrum wavelength $\overline{\lambda}$ are distributed versus the modal index h according to a specified discrete function $f_\tau(h)$.

   The profile of the function $f_\tau(h)$ reflects the amount of delay equalization achieved using the proper grading of the refractive index, as discussed briefly in Chapter 3, Section 3.7. In the case of perfect delay equalization, the delay distribution $f_\tau(h)$ versus the modal index h would be a constant. In that case, every excited fiber mode will experience the same group delay, delivering the fraction of launched power simultaneously with all the remaining excited modes. According to the present multimode propagation modeling, under perfect delay equalization the only source of pulse distortion would be the chromatic dispersion. Any deviation from the constant profile of the delay distribution $f_\tau(h)$ indicates a mismatch in the group delay equalization. In the following three simple but relevant discrete functions $f_\tau(h)$ will be presented for modeling the group delay distributions among allowed fiber modes.

   (a) *Constant.* In this case, the modal group delay $\tau_{g,h}(\overline{\lambda}) = \overline{\tau}_{g,h}$, evaluated at the average source spectrum wavelength $\overline{\lambda}$, assumes the constant value $\overline{\tau}_g$ for every excited fiber mode. This case corresponds to the perfect modal delay equalization:

$$\overline{\tau}_{g,h} = f_\tau(h) = \overline{\tau}_g, \qquad h \in N\ (1, M) \tag{5.44}$$

   (b) *Linear.* The modal group delay $\tau_{g,h}(\overline{\lambda}) = \overline{\tau}_{g,h}$, evaluated at the average source spectrum wavelength $\overline{\lambda}$, shows a linear dependence from the from the modal index $h \in N(1, M)$. The straight-line profile passing through two given points $P_1 = (x_1, y_1)$ and $P_2 = (x_2, y_2)$ has the following general equation:

$$\frac{y - y_1}{y_2 - y_1} = \frac{x - x_1}{x_2 - x_1}, \quad \begin{cases} x_1 \neq x_0 \\ y_1 \neq y_0 \end{cases} \tag{5.45}$$

   Using physical variables, this equation translates into the following discrete straight-line group delay profile:

$$\overline{\tau}_{g,h} = f_\tau(h) = \tau_1 + (\tau_2 - \tau_1)\frac{h - h_1}{h_2 - h_1}, \quad \begin{cases} (h, h_0, h_1) \in N\ (1, M) \\ \tau_1 = \overline{\tau}_{g,h_1} \\ \tau_2 = \overline{\tau}_{g,h_2} \end{cases} \tag{5.46}$$

   (c) *Quadratic.* The modal group delay $\tau_{g,h}(\overline{\lambda}) = \overline{\tau}_{g,h}$, evaluated at the average source spectrum wavelength $\overline{\lambda}$, shows a quadratic dependence from the modal index $h \in N(1, M)$. Since the parabolic profile requires the definition of three independent conditions to be uniquely

determined, the parabolic group delay distribution will be defined starting from the following general equation $y = f(x)$ of the parabola which satisfies the following conditions:

1. The vertex has position $V = (x_0, y_0)$.
2. It passes through point $P = (x_1, y_1)$:

$$\frac{y - y_0}{y_1 - y_0} = \left(\frac{x - x_0}{x_1 - x_0}\right)^2, \quad \begin{cases} x_1 \neq x_0 \\ y_1 \neq y_0 \end{cases} \tag{5.47}$$

Using the physical delay variables and the related discrete modal indices, the parabolic profile $f_\tau(h)$ having the vertex at the point (h_0, τ_0) and passing through the point (h_1, τ_1), with indices $h_0, h_1 \in N\ (1, M)$, satisfies the following expression:

$$\overline{\tau}_{g,h} = f_\tau(h) = \tau_0 + (\tau_1 - \tau_0)\left(\frac{h - h_0}{h_1 - h_0}\right)^2, \begin{cases} (h, h_0, h_1) \in N(1, M) \\ \tau_0 = \overline{\tau}_{g,h_0} \\ \tau_1 = \overline{\tau}_{g,h_1} \end{cases} \tag{5.48}$$

with $V = (h_0, \tau_0)$, the vertex and $P = (h_1, \tau_1)$. The parabolic profile has some interesting features: it can represent either a monotonically decreasing or increasing profile versus the modal index h. The distance $\tau_1 - \tau_0$ is related to the profile curvature and for the limiting value $\tau_1 - \tau_0 \to 0$, the profile tends to be constant. The position of the vertex h_0 defines the center of a region of maximally flat group delay dependence, approximating good local delay compensation. Figure 5.4 shows the quadratic group delay distribution highlighting principal features.

Figure 5.5 shows qualitatively the three distributions $f_\tau(h)$ considered so far for modeling the group delay profiles. The solid lines refer to the quadratic profiles. In the case shown these

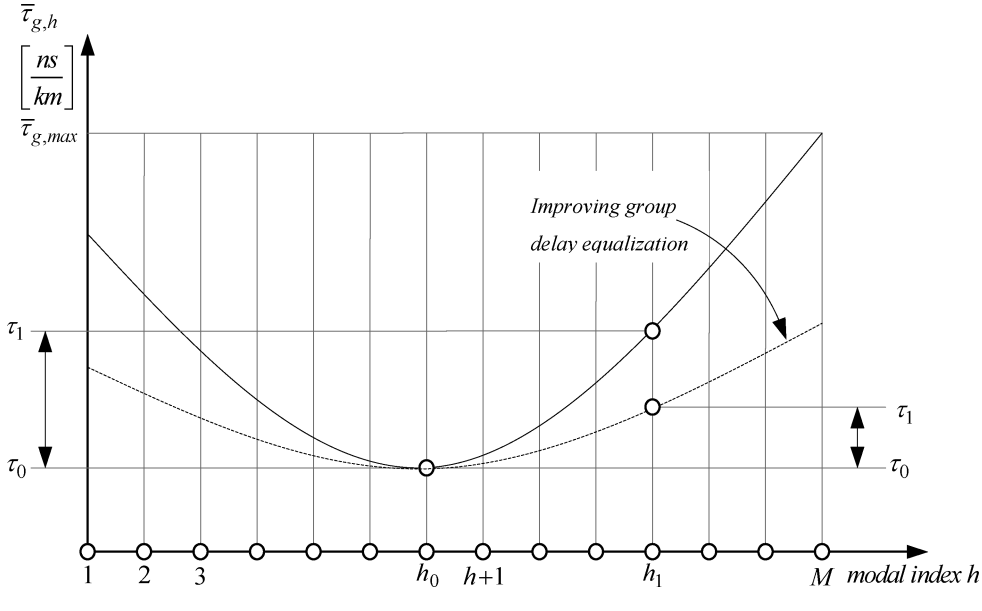

Figure 5.4 Qualitative representation of the quadratic relationship between the modal group delay values at the average wavelength of the source spectrum and the modal index. According to the definition given in the text, the parabolic profile is defined by setting the vertex (h_0, τ_0) and one other arbitrary point (h_1, τ_1)

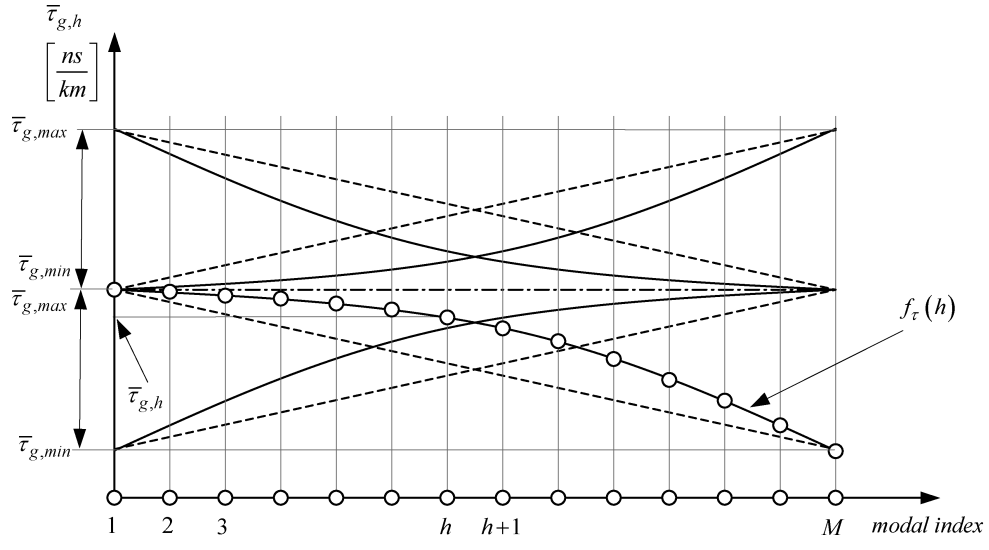

Figure 5.5 Modal group delay distribution according to the constant, linear and quadratic models presented in the text. The white circles correspond to discrete modal index values. Due to a profile equalization that is not perfect, the modal group delay $\tau_{g,h}(\overline{\lambda}) = \overline{\tau}_{g,h}$ belongs to the interval $\overline{\tau}_{g,\min} \leq \overline{\tau}_{g,h} \leq \overline{\tau}_{g,\max}$, $h \in N(1, M)$

profiles have the vertex respectively either at $h = 1$ or $h = M$, exhibiting both positive and negative curvatures.

4. *Modal average delay and RMS pulse width.* For every specific launching condition, the corresponding coupled source power coefficient distribution $\{|a_h(\overline{\lambda})|^2\} = \{|\overline{a}_h|^2\}$ can be achieved. According to each coupled power coefficient and group delay function $f_\tau(h)$ distributions, the resulting modal impulse response $h_m(z, t, \overline{\lambda})$ will be characterized by the average modal delay $\overline{t}_m = z\overline{\tau}_m$ and by the RMS pulse width $\sigma_m(z, \overline{\lambda}) = \overline{\sigma}_m(z)$ reported respectively in Equations (5.10) and (5.17).
   The DMD (λ), defined in Equation (3.62), therefore coincides with the RMS pulse width $\overline{\sigma}_m(z) = \mathrm{DMD}(z, \overline{\lambda})$ of the modal impulse response.
5. *Source power spectrum.* The source power spectral density $S_s(\lambda)$ is assumed to be shaped as a single-peak Gaussian function with full width at half maximum $\mathrm{FWHM}_s = 5\,\mathrm{nm}$. Using the Gaussian relationship (3.113) in Section 3.11.3, Chapter 3, the corresponding RMS spectral width becomes

$$\sigma_s = \frac{\mathrm{FWHM}_s}{2\sqrt{2\ln 2}} \cong 0.425\ \mathrm{FWHM}_s = 2.123\,\mathrm{nm}|_{\mathrm{FWHM}_s=5\,\mathrm{nm}} \tag{5.49}$$

The five assumptions discussed so far define the modeling set that is needed for the numerical computation of the multimode fiber impulse response. Once the group delay profile, the coupled source power coefficient distribution and the source power spectral distribution have been specified, the multimode fiber impulse response can be computed using the set of equations in Table 4.4 of Chapter 4 and Tables 5.1 and 5.2.

5.4.2 Computer Simulation Procedure

In this section the model assumptions introduced in the previous section will be used to create the simulation environment and to compute the multimode fiber impulse response, including both

chromatic and modal dispersion with arbitrary group delay and source power coupling coefficient distributions.

5.4.2.1 Chromatic Impulse Response

According to assumption 2, each excited fiber mode will experience the same chromatic dispersion, leading to a consistent simplification of the general impulse response Equation (5.20). By setting

$$h_{c,h}[z, t - z(\overline{\tau}_{g,h} - \overline{\tau}_{c,h})] = h_c[z, t - z(\overline{\tau}_{g,h} - \overline{\tau}_c)] \tag{5.50}$$

only one chromatic impulse response profile is obtained for all the excited modes used for generating the impulse response of the multimode fiber. In addition, it should be noted that even the chromatic average delay $\overline{\tau}_{c,h}$ of the hth mode in Equation (5.50) is the same for all the excited modes, $\overline{\tau}_{c,h} = \overline{\tau}_c$.

5.4.2.2 Linear Regime

The linear regime assumption (assumption 1) allows the time-centered chromatic impulse response to be superposed when properly translated with the corresponding group delay value $\overline{\tau}_{g,h}$ and weighted by the source power coupled coefficient $\overline{a}_h$ as many times as the number of allowed fiber modes. Each chromatic impulse response contribution $h_c(z, t)$ must first be centered according to the chromatic average delay $h_c(z, t + z\overline{\tau}_c)$ and then it must be translated by the group delay value of the corresponding mode $h_c(z, t + z\overline{\tau}_c - z\overline{\tau}_{g,h})$.

5.4.2.3 Source Spectrum

Assumption 5 specifies the source power spectral density and is strictly related to the chromatic impulse response, at least away from the zero-dispersion wavelength. Accounting for the above three assumptions, Equation (5.50) of the general multimode impulse response can therefore be simplified to the following expression:

$$h_F(z, t, \overline{\lambda}) = \sum_{h=1}^{M} |\overline{a}_h|^2 h_c[z, t - z(\overline{\tau}_{g,h} - \overline{\tau}_c)] \tag{5.51}$$

In order to proceed toward computing the multimode fiber impulse response using the simplified expression (5.51) the distributions of both the group delay values $\overline{\tau}_{g,h}$ and the source power coupled coefficients $\overline{a}_h$ need to be specified, in agreement with the remaining third and fourth assumptions.

5.4.2.4 Group Delay Distribution

In order to model the group delay $\overline{\tau}_{g,h}$ evaluated at the average wavelength of the source spectrum, the quadratic distribution according to Equation (5.48) is chosen by assigning specific values to the parabolic profile parameters. Precisely, some criteria must be specified when assigning the required coordinate pairs (h_0, τ_0) and (h_1, τ_1). These criteria define the group delay gauge. The vertex of the parabola is set at the first modal index value $h_0 = 1$ with the corresponding minimum delay value $\tau_0 = \overline{\tau}_{g,\min}$ while assigning at h_1 the last modal index value, $h_1 = M$, associated with the maximum delay value, $\tau_1 = \overline{\tau}_{g,\max}$. This is just one arbitrary choice leading to the upward group delay distribution shown in Figure 5.6. The minimum delay $\tau_0 = \overline{\tau}_{g,\min}$ is associated with the lowest-order mode with $h_0 = 1$ and the maximum delay value $\tau_1 = \overline{\tau}_{g,\max}$ is associated instead with the highest-order mode. This choice of the group delay gauge has the maximum flatness in correspondence with the lowest-order mode as a consequence of coincidence with the parabola vertex location. In order to have a physical picture in mind, it is imagined that all the allowed

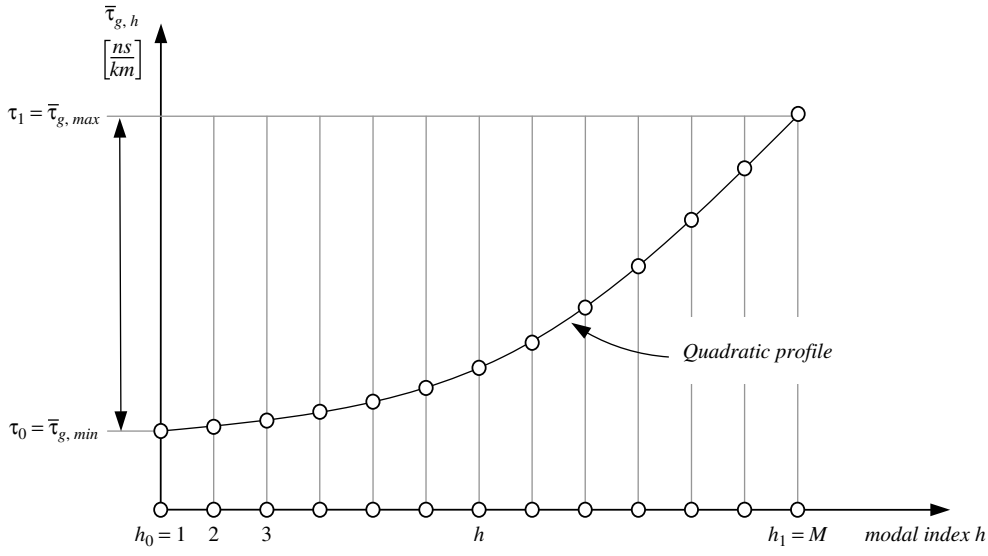

Figure 5.6 Graphical representation of the quadratic group delay gauge. The abscissa reports the discrete modal index value h as indicated by the white circles. The ordinate scale shows the corresponding modal group delay evaluated at the same average wavelength of the source spectrum. The difference $\overline{\tau}_{g,max} - \overline{\tau}_{g,min}$ gives a quantitative indication of the unmatched delay equalization

modes are ordered with the lowest index value $h = 1$ associated with the fundamental fiber mode, and the highest-order mode associated with the highest index value $h = M$.

The distribution of the group delay at the fixed average wavelength of the source spectrum has a major impact on shaping the modal impulse response. The case considered above produces a monotonic increasing relationship between the modal index and the corresponding group delay. This means that the lowest-order mode will travel the fastest, determining the pulse leading edge profile. Accordingly, the highest-order mode will travel the slowest, leading to the trailing edge shape. However, it will be the amount of fractional power delivered to those modes that will definitely set the output modal impulse response. From Equation (5.48), the following parabolic upward group delay distribution is obtained:

$$\left.\begin{array}{l} h_0 = 1 \\ h_1 = M \\ \tau_0 = \overline{\tau}_{g,1} = \overline{\tau}_{g,min} \\ \tau_1 = \overline{\tau}_{g,M} = \overline{\tau}_{g,max} \end{array}\right\} \Rightarrow \overline{\tau}_{g,h} = \overline{\tau}_{g,min} + (\overline{\tau}_{g,max} - \overline{\tau}_{g,min}) \left(\frac{h-1}{M-1}\right)^2, \quad h \in N(1, M) \quad (5.52)$$

It should be remembered that this is just an arbitrary choice for the group delay distribution used in order to forward the simulation procedure. Of course, using a multimode fiber mode solver based on the numerical solution of the scalar wave equation with a given refractive index profile, a more correct group delay distribution will be achieved, at least consequent to the assumed refractive index profile and fiber geometry. However, the simulation procedure will remain exactly the same, even when the assumed delay profile is released from an accurate mode solver or from the simple quadratic model. Figure 5.7 shows the computed parabolic profile using Equation (5.52) with $\overline{\tau}_{g,max} - \overline{\tau}_{g,min} = \Delta_\tau = \pm 2$ ns/km and $\overline{\tau}_{g,min} = \tau_{g,1}$.

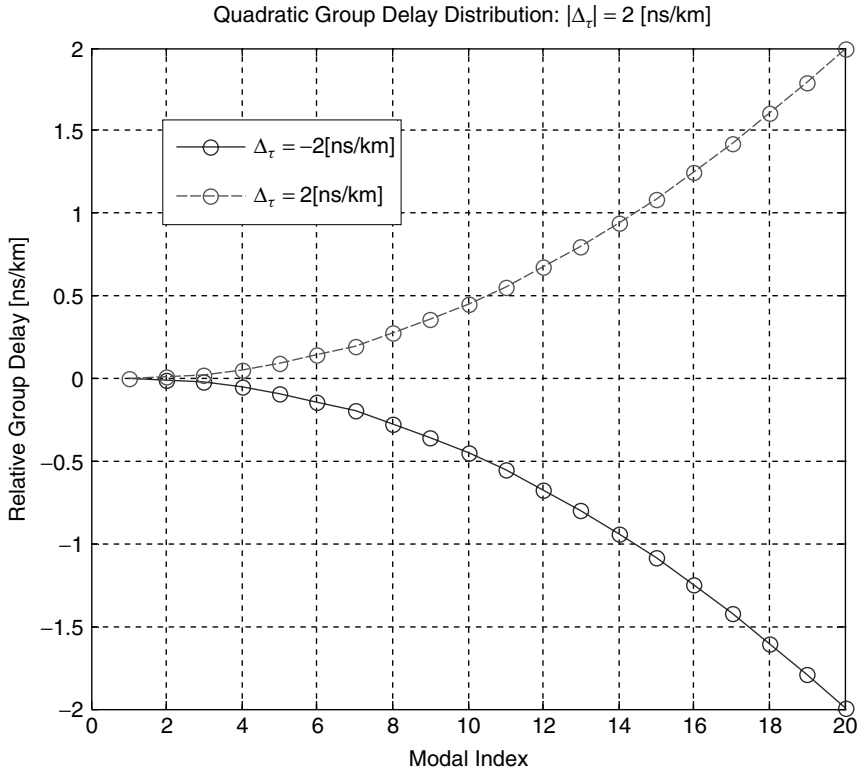

Figure 5.7 Quadratic group delay distribution computed according to Equation (5.52) assuming relative delay from the minimum value corresponding to the modal index $h_0 = 1$. The group delay variation has been set positive and equal to $\overline{\tau}_{g,max} - \overline{\tau}_{g,min} = \Delta_\tau = 2\,\text{ns/km}$

5.4.2.5 Source Power Coupling Coefficients

In order to find the complete set of parameters used to solve the simplified expression of the multimode fiber impulse response (5.51), the source power coupling coefficient distribution $\overline{a}_h$ needs to be specified. Chapter 7 will introduce in Section 7.3 the source power coupling theory and show the influence of the launching conditions over the multimode impulse response. For the moment it is sufficient to use any finite sequence satisfying the unit normalization condition (3.57). To this end, a start is made using the well-known geometric progression:

$$1 + \sum_{h=1}^{M-1} q^h = \frac{1 - q^M}{1 - q} \tag{5.53}$$

The square value of the source power coupling coefficient $|\overline{a}_h|^2$ is defined as the element of the following normalized geometric progression of the variable q with M elements:

$$|a_h|^2 \equiv \frac{1 - q}{1 - q^M} q^{h-1}, \quad |q| < 1 \tag{5.54}$$

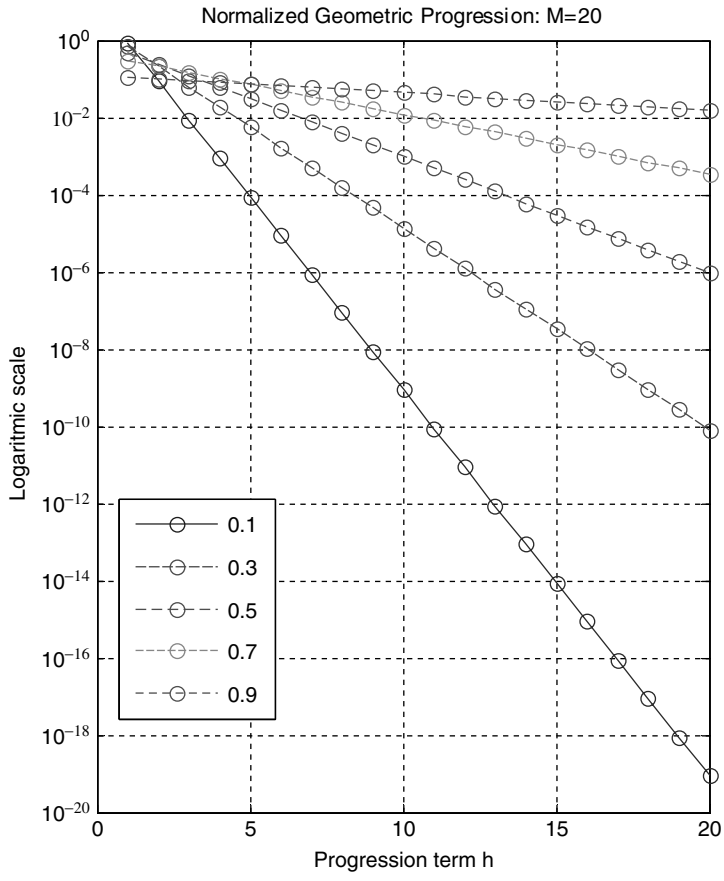

Figure 5.8 Computed elements of the normalized geometric progression in Equation (5.54) for the cases $M = 20$, $q = 0.1, 0.3, 0.5, 0.7, 0.9$. All cases satisfy the unit normalization condition (3.57)

Using the result in Equation (5.53), the finite set of M elements satisfies the normalization condition (3.57) is

$$\sum_{h=1}^{M} |a_h|^2 = \frac{1-q}{1-q^M} \sum_{h=1}^{M} q^{h-1} = 1 \tag{5.55}$$

Figure 5.8 shows the computed elements of the normalized geometric progression in Equation (5.54), represented in the logarithmic scale, for $M = 20$ and $q = 0.1, 0.3, 0.5, 0.7, 0.9$. The five sequences satisfy the unit normalization condition (5.55). For a fixed number M of elements, the sequence profile depends strongly on the value of the variable q. A smaller q value corresponds to a steepest sequence, where only the first few terms take relevant contributions. However, a larger q value corresponds instead to a smoother sequence where many more terms assume the relevant contribution.

This behavior is very visible in the logarithmic scale representation of Figure 5.8 where smaller q values are associated with flatter curves. In terms of the multimode fiber impulse response this means that smaller q value power distributions spread out over a larger number of allowed fiber modes, showing a multiple pulse profile response. Of course, due to the normalization constraint,

decreasing the q value also corresponds to a lower intensity contribution from the first few terms, leading to a more homogeneous power distribution among allowed modes. At higher q values the relative weight of the first or second term contribution is much more relevant, bringing a higher fraction of the total launched optical power.

In the following, the simulation output assuming all five normalized geometric progressions shown in the figure will be considered. All the cases will exhibit the same group delay distribution in order to highlight the consequences of the different excitations on the multimode impulse response.

5.4.2.6 Algorithms and Matlab® Codes

The multimode fiber impulse response (MMFIR) simulator is based on the main routine *MMFIR* and the following six subroutines used for computing specific multimode fiber and source spectrum profiles. Slightly different versions of some of these routines have already been used previously.

1. *MGP (multi-Gaussian profile).* It provides a multi-Gaussian peak spectrum profile or group delay profile, depending on the calling routine.
2. *GROUPDELAY.* It computes the group delay function of the wavelength according to the linear superposition of the Sellmeier three-term equation and the multi-Gaussian peak ripple contribution.
3. *CIRCON (chromatic impulse response contribution).* It provides the individual segment chromatic impulse response contribution when the ripple group delay function or zero-dispersion wavelengths have been included in the source spectral range.
4. *CIR (chromatic impulse response).* It provides the chromatic impulse response according to the given group delay function and source spectrum.
5. *SPCC (source power coupling coefficient).* It provides the power coefficient distribution at the launching section.
6. *QGDD (quadratic group delay distribution).* It provides the quadratic group delay distribution at the average wavelength of the source spectrum.

5.4.2.6.1 MMFIR

```
% MMFIPR: Multi-Mode-Fiber-Impulse-Response
% The function MMFIR computes the impulse response of the multimode fiber
% including both chromatic and modal responses. Input parameters are:

%
function hf=MMFIR;
global  T NTS NSYM time tplot tindex...
    N0 Lmin Lmax A_s FWHM_s L_s A_tg FWHM_tg L_tg M
%
% Source Power Spectral Density
%
A_s=[0 0 1 0 0]; % Coefficients for the individual Gaussian peaks
FWHM_s=[0.1 0.1 1 0.1 0.1]*1e-9; % FHHM [m]
L_s=[1548.4 1549.2 1550 1550.8 1551.6]*1e-9; % Central Wavelengths [m]
%
% Group Delay Wavelength Function
%
N0=1000;            % Number of steps in the wavelength axis
Lmin=1535e-9;       % Minimum wavelength in the computing interval
Lmax=1565e-9;       % Maximum wavelength in the computing interval
C_tg=0e-12;         % Unit amplitude for the group delay ripple [s]
A_tg=[0.20 0.20 0.125 0.125 0.125 0.10 0.10 0.05]*C_tg; % Coefficients for
   the group delay ripple
```

```
FWHM_tg=[75 75 75 75 75 75 75 75]*1e-9; % FHHM of the group delay ripple
L_tg=[850 950 1050 1150 1250 1350 1450 1550]*1e-9; % Central wavelengths of
   the group delay ripple
A_tg=A_tg./(2*sqrt(log(2)/pi)*FWHM_tg); % Amplitude normalization
%
% Source Power Coupling Coefficient
%
M=20; % Number of mode groups
q=0.999; % Geometric progression coefficient
A_D=SPCC(M,q); % Source Power Coupling Coefficients
%
% Quadratic Group Delay Distribution
%
ho=1; % Index of the parabola vertex
h1=M; % Index of the maximum delay absolute value
Delta_Tau=2e-3; % [ns/m]
Tau_D=QGDD(ho,h1,Delta_Tau); % Quadratic Group Delay Distribution [ns/m]
Tm=sum(A_D.*Tau_D); % Ensemble average group delay [ns/m]
Tau_D=(Tau_D-Tm)*1e6; % Centered group delay distribution [ps/km]
%
% Chromatic Impulse Response
[Ts,hc]=CIR;
%
% Multimode Fiber Impulse Response
%
% The chromatic impulse response is centered over each value of the group
% delay distribution and weighted by the coupling coefficients A_D. The
% time axis Tf of the multimode impulse response has the same resolution of
% the chromatic dispersion time axis Ts, but its extremes extend in order
% to include the whole superposition.
%
Ts_min=min(Ts);
Ts_max=max(Ts);
dT=(Ts_max-Ts_min)/(N0-1); % Time step
Tf_min=floor((min(Tau_D)-abs(Ts_min))/dT)*dT; % Minimum time instant
Tf_max=ceil((max(Tau_D)+abs(Ts_max))/dT)*dT; % Maximum time instant
Tf=(Tf_min:dT:Tf_max); % Temporal axis of the multimode impulse response
Nf=length(Tf);
hf(1:Nf)=0;
%
% Finding the index ko of the origin of the centered time axis
%
ko=1;
while Ts(ko)<=0 & ko<N0,
    ko=ko+1;
end;
ko=ko-1;
%
% Finding the index vector Index of the group delay distribution
%
for k=1:M,
    j=1;
    S=sign(Tf(j)-Tau_D(k));
    while sign(Tf(j)-Tau_D(k))==S & j<Nf,
        j=j+1;
    end;
```

```
    Index(k)=j-1;
end;
figure(4);
for k=1:M,
    hfk(1:Nf)=0;
    hfk(Index(k)-ko+1:Index(k)-ko+N0)=hc;
    plot(Tf,A_D(k)*hfk);
    hold on;
hf=hf+A_D(k)*hfk;
end;
grid on;
plot(Tf,hf,'r');
title('Multimode Fiber Impulse Response');
ylabel('Arbitrary Unit');
xlabel('Time [ps/km]');
hold off;
```

5.4.2.6.2 MGP

```
% The function MGP provides the Multi-Gaussian-Profile power spectral
% density of the light source based on the linear superposition of the
% input-defined Gaussian functions. Inputs A, FWHM and Lambda represent
% respectively linear vectors containing the weight coefficients, the
% Full-Width-Half-Maximum and the central wavelengths of the Gaussian
% components. There is no limitation to the number of Gaussian components
% used in the linear superposition. The length of each input vector
% specifies the required number of Gaussian components.
%
function S=MGP(A,FWHM,Lambda,L);
N=length(A);
S=0;
for k=1:N,
    Sk=2*sqrt(log(2)/pi)/FWHM(k)*exp(-4*log(2)*(L-Lambda(k)).^2/FWHM(k)^2);
    S=S+A(k)*Sk;
end;
```

5.4.2.6.3 GROUPDELAY

```
function tg=GROUPDELAY(L);
global A_tg FWHM_tg L_tg;
N0=length(L)-1;
Lmin=min(L); % Minimum wavelength
Lmax=max(L); % Maximum wavelength
dL=(Lmax-Lmin)/N0; % Wavelength step
c=2.9979e8; % Speed of light in vacuum
%
% Sellmeier equation: coefficients for the fused silica
%
B1=0.6961663;   % Coefficient B1 for Three-term Sellmeier equation
B2=0.4079426;   % Coefficient B2 for Three-term Sellmeier equation
B3=0.8974794;   % Coefficient B3 for Three-term Sellmeier equation
Lambda1=0.0684043e-6;% Peak wavelength L1
Lambda2=0.1162414e-6;% Peak wavelength L2
Lambda3=9.896161e-6; % Peak wavelength L3
%
% Sellmeier component
%
n_S=sqrt(1+B1./(1-(Lambda1./L).^2)+B2./(1-(Lambda2./L).^2)+B3./(1-
    (Lambda3./L).^2));
```

```
% Index of refraction
n1_S=diff(n_S)/dL;      % First order derivative of the refractive index
L1=L(1:N0);         % Wavelength axis for the first order derivative
L2=L(1:N0-1);       % Wavelength axis for the second order derivative
ng_S=n_S(1:N0)-L1.*n1_S;  % Group index
tg_S=ng_S/c;        % Sellmeier Group delay [s/m]
%
% Multi-Gaussian-Profile component
%
tg_MGP=MGP(A_tg,FWHM_tg,L_tg,L1); % MGP group delay component [s/m]
%
% Linear combination of Sellmeier and MGP group delays
%
tg=tg_S+tg_MGP; % Total group delay [s/m]
```

5.4.2.6.4 CIRCON

```
% The function CIRCON provides the inversion of the group delay function Tg
% limited by the selected wavelength interval defined by two indices j1 and
% j2 and returns the Chromatic Impulse Response CONtribution Ss/Dc. The
% returned value is computed assuming linear interpolation between the two
% subsequent wavelength points available from the two input indices
%
function hc=CIRCON(Tj,Tg,Ss,Dc,j1,j2);
j=j1;
Sgn=sign(Tg(j)-Tj);
j=j+1;
while j<j2 & Sgn*sign(Tg(j)-Tj)==+1,
    j=j+1;
end;
hc=1e-3*(Tg(j)*Ss(j-1)-Tg(j-1)*Ss(j)+(Ss(j)-Ss(j-1))*Tj)/...
   (Tg(j)*Dc(j-1)-Tg(j-1)*Dc(j)+(Dc(j)-Dc(j-1))*Tj);
```

5.4.2.6.5 CIR

```
% The function CIR computes the chromatic impulse response for the given
% mode group delay Tg and source power spectral density Ss. The chromatic
% impulse response hc(z,t) is function of the distance z and the normalized
% time t/z.
%
function [Ts,hc]=CIR;
global N0 Lmin Lmax A_s FWHM_s L_s;
dL=(Lmax-Lmin)/N0;  % Wavelength step
L=(Lmin:dL:Lmax);   % Wavelength axis for the Sellmeier refractive index
L1=L(1:N0);         % Wavelength axis for the first order derivative Tg
L2=L(1:N0-1);       % Wavelength axis for the second order derivative Dc
%
%------------ Group Delay and Chromatic Dispersion Coefficient ------------
%
Tg=1e9*GROUPDELAY(L);   % [ns/m]
Dc=1e-3*diff(Tg)/dL;    % [ps/nmkm]
%
%------------------- Multi-Gaussian-Profile Source PSD --------------------
%
Ss=MGP(A_s,FWHM_s,L_s,L2); % Multi-Gaussian-Profile
%
%----------------------- Chromatic Impulse Response -----------------------
%
```

```
% Finding stationary wavelengths for inverting the group delay function
%
j=1;
k=0;
while j<N0-1,
    Sc=sign(Dc(j));
    j=j+1;
    while j<N0-1 & Sc*sign(Dc(j))==+1,
        j=j+1;
    end;
    if j<N0-1,
        k=k+1;
        Index(k)=j; % Index exceeding the current stationary wavelength
        Lo(k)=L(j-1)-Dc(j-1)*dL/(Dc(j)-Dc(j-1)); % Stationary wavelengths
    end;
end;
if k>0, % At least one stationary wavelength exists in the interval
    N=length(Index); % Number of stationary wavelengths found
    %
    % Finding time intervals corresponding to single-valued wavelength
       intervals
    %
    disp('        Single-valued Intervals Decomposition for Ripple Group
       Delay');
    disp(");
    disp('        Interval     T(min)       T(max)   Lambda(min)  Lambda(max)
       Lambda(zero)');
    disp('                       ns/m         ns/m        nm           nm
       nm');
    disp(");
    TauL_0=Tg(1);
    TauR_0=Tg(Index(1)-1);
    disp([0 TauL_0 TauR_0 L(1) L(Index(1)-1)]);
    for k=1:N-1,
        TauL(k)=Tg(Index(k));
        TauR(k)=Tg(Index(k+1)-1);
        disp([k TauL(k) TauR(k) L(Index(k))*1e9 L(Index(k+1)-1)*1e9
           Lo(k)*1e9]);
    end;
    TauL(N)=Tg(Index(N));
    TauR(N)=Tg(N0);
    disp([N TauL(N) TauR(N) L(Index(N))*1e9 L(N0+1)*1e9 Lo(N)*1e9]);
    Taumax=max([TauL_0 TauR_0 TauL TauR]); % Maximum normalized time instant
    Taumin=min([TauL_0 TauR_0 TauL TauR]); % Minimum normalized time instant
else
    N=0;
    Taumin=Tg(1);
    Taumax=Tg(N0);
end;
dT=(Taumax-Taumin)/(N0-1); % Normalized time step
T=(Taumin:dT:Taumax); % Normalized time axis
%
% Computing chromatic impulse response contributions of each time interval
%
hc(1:N0)=0;
if N>0,
```

```
    for j=1:N0,
        if min([TauL_0 TauR_0])<=T(j) & T(j)<=max([TauL_0 TauR_0]),
            hc(j)=hc(j)+CIRCON(T(j),Tg,Ss,abs(Dc),1,Index(1)-1);
        end;
        for k=1:N-1,
            if min([TauL(k) TauR(k)])<=T(j) & T(j)<=max([TauL(k) TauR(k)]),
                hc(j)=hc(j)+CIRCON(T(j),Tg,Ss,abs(Dc),Index(k),Index(k+1)-1);
            end;
        end;
        if min([TauL(N) TauR(N)])<=T(j) & T(j)<=max([TauL(N) TauR(N)]),
            hc(j)=hc(j)+CIRCON(T(j),Tg,Ss,abs(Dc),Index(N),N0-1);
        end;
    end;
else,
    for j=1:N0,
        hc(j)=hc(j)+CIRCON(T(j),Tg,Ss,abs(Dc),1,N0-1);
    end;
end;
%
% Chromatic Impulse Response Moments
%
disp('       Chromatic Impulse Response Parameters');
disp(");
disp('       S_WL_AVE    S_WL_RMS      To_lin         To         Dc_lin
   hc_RMS_lin     hc_RMS');
disp('          [nm]         [nm]         [μs/km]       [μs/km]      [ps/nmkm]
    [ps/km]       [ps/km]');
disp(");
To=sum(T.*hc)/sum(hc); % Average response delay in normalized time unit
Ts=(T-To)*1e6; % Temporal axis with origin in To [ps/km]
Sigma_hc=sqrt(sum(Ts.^2.*hc)/sum(hc)); % RMS pulse width [ps/km]
%
% Source PSD Moments
%
Lo_Ss=sum(L2.*Ss)/sum(Ss); % Average wavelength [m]
Sigma_Ss=sqrt(sum((L2-Lo_Ss).^2.*Ss)/sum(Ss)); % RMS spectral width [m]
%
% Linear Group Delay Approximation
%
k=1;
while L(k)<Lo_Ss & k<N0, k=k+1; end;
if k<N0,
    Dc_lin=(Tg(k)-Tg(k-1))/dL;
    Tau_lin=Tg(k-1)+Dc_lin*(Lo_Ss-L(k-1));
    Sigma_lin=Sigma_Ss*abs(Dc_lin);
    disp([Lo_Ss*1e9 Sigma_Ss*1e9 Tau_lin To Dc_lin*1e-3 Sigma_lin*1e6
       Sigma_hc]);
end;
%
%--------------------------------- Plotting ------------------------------
%
figure(1);
subplot(221); % Fiber Group Delay - Chromatic Dispersion - Light Source PSD
plot(L1*1e6,Tg,L2*1e6,min(Tg)+Ss/max(Ss)*(max(Tg)-min(Tg))); grid on;
title('Fiber Group Delay and Light Source PSD');
xlabel('Wavelength, \lambda [μm]');
```

```
ylabel('t_g(\lambda) [ns/m]');
legend('Group Delay','Source PSD');
subplot(222);
plot(L2*1e6,Dc), grid on;
line([Lmin Lmax]*1e6,[0 0],'LineStyle','-.','Color','r');
title('Chromatic Dispersion');
xlabel('Wavelength, \lambda [μm]');
ylabel('D_c(\lambda) [ps/nmkm]');
subplot(223); % Normalized Time Intervals
if N>0,
    plot([0:N],[TauL_0 TauL],'o',[0:N],[TauR_0 TauR],'ro'); grid on;
    line([0 0],[TauL_0 TauR_0],'LineWidth',2,'Color','k');
    for k=1:N,line([k k],[TauL(k) TauR(k)],'LineWidth',2,'Color','k');end;
else
    plot(0,Taumin,'o',0,Taumax,'ro'); grid on;
    line([0 0],[Taumin Taumax],'LineWidth',2,'Color','k');
end;
title('Normalized Time Intervals');
xlabel('Wavelength interval \Lambda_k');
ylabel('Time interval [ns/m]');
legend('\tau_L=\zeta(\lambda_L)','\tau_R=\zeta(\lambda_R)');
subplot(224); % Chromatic Impulse Response
plot(T,hc); grid on;
line([To To],[0 1.1*max(hc)],'LineStyle','-.','Color','r');
title('Chromatic Impulse response');
xlabel('Normalized time \tau [ns/m]');
ylabel('a.u.');
figure(2); % Time-shifted chromatic impulse response
plot(Ts,hc); grid on;
line([-Sigma_hc -Sigma_hc],[0 1.1*max(hc)],'LineStyle','-.','Color','r');
line([Sigma_hc Sigma_hc],[0 1.1*max(hc)],'LineStyle','-.','Color','r');
text(0,1.05*max(hc),['RMS width \sigma_\tau=' num2str(Sigma_hc)
   '[ps/km]'],'BackgroundColor','w');
title('Centered Chromatic Impulse response');
xlabel('Normalized time \tau [ps/km]');
ylabel('Unity energy response [a.u.]');
```

5.4.2.6.6 SPCC

```
% Normalized Geometric progression with M elements of characteristic q
%
function A=SPCC(M,q);
H=(1:M);
A=(1-q)/(1-q M)*q.^(H-1);
figure(3);
subplot(122);
semilogy(H,A,'-o');
grid on;
title(['Source Power Coupling Coefficients: q=' num2str(q)]);
ylabel('Coupling - Log scale');
xlabel('Mode group number');
```

5.4.2.6.7 QGDD

```
% The function QGDD computes the Group Delay distribution at the source
% spectrum average wavelength of the M supported fiber modes. The
% distribution is computed according to the quadratic model with the
% following parameters:
```

```
% h0   : mode index corresponding to the vertex of the parabola
% Tau_0: group delay value at the vertex of the parabola
% h1   : mode index corresponding to the group delay Tau_1
% Tau_1: group delay value at the mode index h1
%
function Tau_D=QGDD(ho,h1,Delta_Tau);
global N0 Lmin Lmax A_s FWHM_s L_s M;
dL=(Lmax-Lmin)/N0;  % Wavelength step
L=(Lmin:dL:Lmax);   % Wavelength axis for the Sellmeier refractive index
L1=L(1:N0);         % Wavelength axis for the first order derivative Tg
Tg=1e9*GROUPDELAY(L);   % [ns/m]
Ss=MGP(A_s,FWHM_s,L_s,L1); % Multi-Gaussian-Profile
Lo=sum(L1.*Ss)/sum(Ss); % Average wavelength [m]
k=1;
while L1(k)<Lo & k<N0
    k=k+1;
end;
if k<N0,
    Tgo=Tg(k-1)+(Tg(k)-Tg(k-1))/dL*(Lo-L1(k-1));
else
    Tgo=Tg(N0);
end;
Tau_0=Tgo;
H=(1:M);
Tau_D=Tau_0+Delta_Tau*((H-1)/(M-1)).^2;
figure(3);
subplot(121);
plot(H,(Tau_D-Tgo)*1e3,'-o');
grid on;
title(['Quadratic Group Delay Distribution: \Delta_\tau='
   num2str(Delta_Tau*1e3) '[ns/km]']);
xlabel('Modal Index');
ylabel('Relative Group Delay [ns/km]');
```

5.4.3 Simulation Results

In this section the computed multimode fiber impulse response according to the set of parameters reported in Table 5.4 will be presented and discussed. The simulation outputs refer to the Matlab® code reported in the previous section 5.4.2.

It is assumed that the light source emits a single Gaussian spectrum profile centered at $\lambda_c = 1550\,\text{nm}$ with $\text{FWHM} = 5\,\text{nm}$. The group delay function is modeled according to the three-term Sellmeier approximation without any ripple contribution. According to these assumptions the chromatic impulse response profile is uniquely determined. Figure 5.9 shows the computed chromatic impulse response determined using this simulation environment. The chromatic impulse response in the bottom right picture is not centered and is represented with the absolute delay time per unit length.

The time-centered chromatic impulse response is represented in Figure 5.10. The pulse has been time translated around the ensemble average group delay per unit length. The time-centered pulse presented in Figure 5.10 is the same for all excited modes, according to the assumption of having the same chromatic dispersion among the mode groups. The multimode fiber impulse response therefore differentiates for the modal group delay, which characterized the position of the pulse on the normalized time axis and for the source power coupling coefficient. Table 5.5 shows the computed output parameters of the chromatic impulse response.

Table 5.4 Parameters used for the computation of the multimode fiber impulse response

Parameter	Value	Unit	Comments
N0	1000	–	Computing steps for the chromatic impulse response (wavelength and time)
$L_{\min}$	1535×10^{-9}	m	Start wavelength
$L_{\max}$	1565×10^{-9}	m	Stop wavelength
A_s	1	–	Normalized source coefficient vector
$\mathrm{FWHM_s}$	5×10^{-9}	m	Source full-width at half-maximum
L_s	1550×10^{-9}	m	Source peak wavelengths
C_{tg}	0	s	Unit amplitude for the group delay ripple
A_{tg}	0	–	Coefficients for the group delay ripple
$\mathrm{FWHM_{tg}}$	0	m	FHHM of the group delay ripple
L_{tg}	0	m	Central wavelengths of the group delay ripple
M	20	–	Number of allowed mode groups
q	$0 < q < 1$	–	Geometric progression coefficient
h_0	1	–	Index of the group delay parabola vertex
h_1	M	–	Index of the maximum group delay variation
Δ_τ	2	ns/km	Variation of the group delay distribution

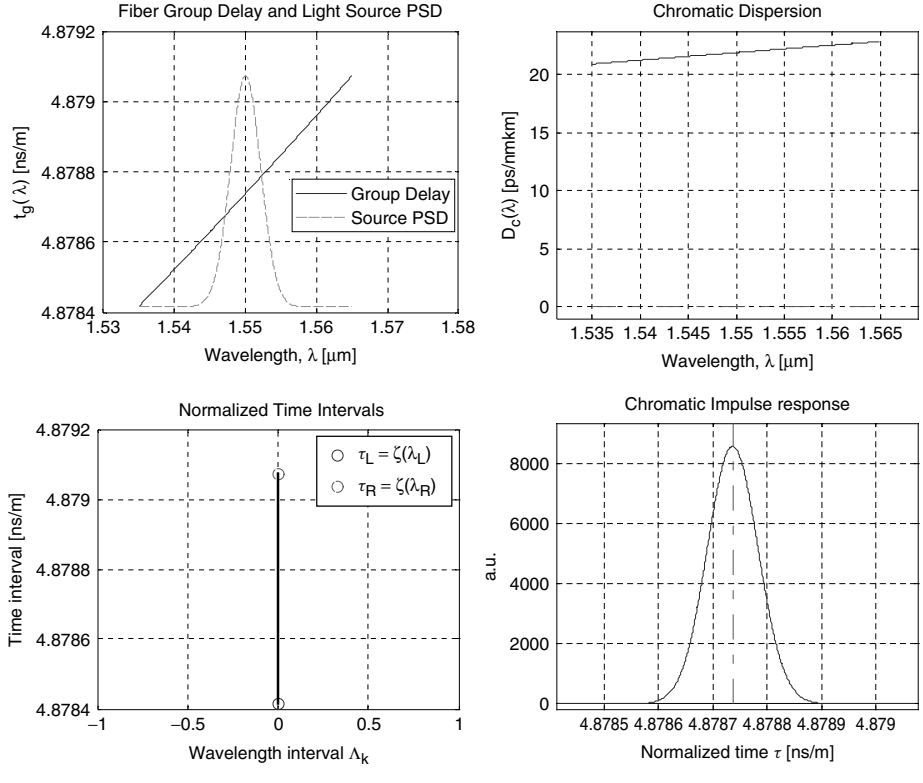

Figure 5.9 Chromatic impulse response of each mode computed for the parameter set specified in Table 5.4. As reported in the text, the simulation assumes the same chromatic dispersion coefficient for all mode groups. The group delay value for each mode group is instead distributed according to the quadratic model

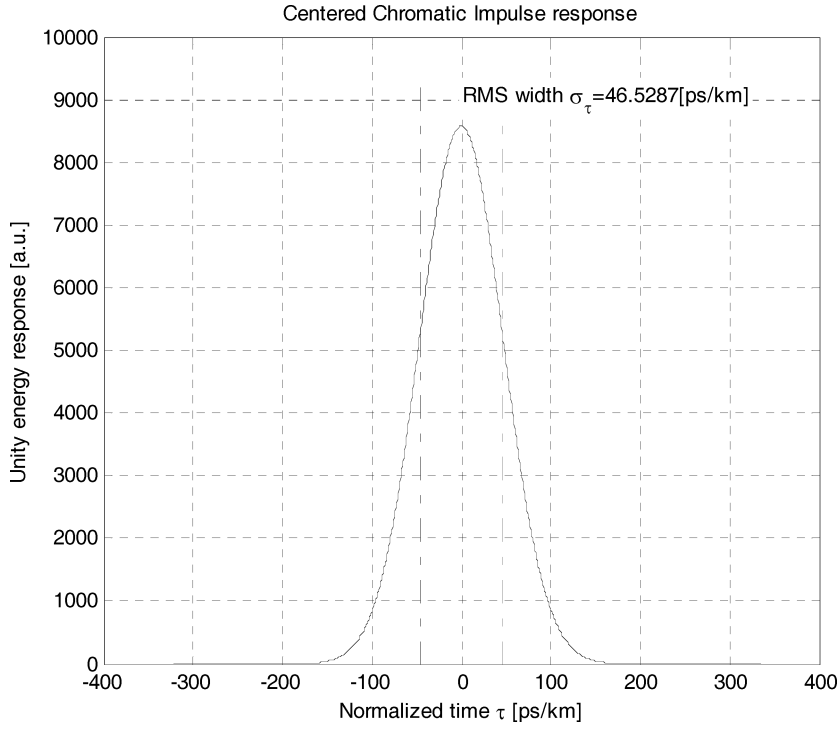

Figure 5.10 Time-centered computed chromatic impulse response for the parameter set specified in Table 5.4. The full-width at half-maximum is $\text{FWHM}_\tau = 109.567\,\text{ps/km}$

Table 5.5 Computed parameters of the chromatic impulse response. The average exciting wavelength coincides with the central wavelength of the single-peak Gaussian spectrum. The assumed $\text{FWHM}_s = 5\,\text{nm}$ coincides with the RMS source spectrum width $\sigma_s = 2.1233\,\text{nm}$, in agreement with the Gaussian relationship (3.114). The RMS width of the chromatic impulse response results $\sigma_\tau = 46.529\,\text{ps/km}$ correspond to $\text{FWHM}_\tau = 109.567\,\text{ps/km}$

Code	$\overline{\lambda}$ (nm)	σ_s (nm)	$\tau_g(\overline{\lambda})$ (μs/km)	$\overline{\tau}_c$ (μs/km)	$\overline{D}_c = D_c(\overline{\lambda})$ (ps/nm km)	$\overline{\sigma}_c$ (ps/km)	σ_c (ps/km)	$\frac{\overline{\sigma}_c}{\sigma_c} - 1(\%)$
SUSG1550-5	1550	2.1233	4.8787	4.8787	21.912	46.526	46.529	0.00645

As already explained, in this simulation example the group delay distribution due to nonperfect delay equalization is represented by a quadratic profile. Each modal group delay value is calculated at the average wavelength $\overline{\lambda} = \lambda_c = 1550\,\text{nm}$ of the source spectrum. In the following eight simulation results are reported, corresponding to different choices of the mode group number M, the group delay distribution and the geometric progressions used to model the source power coupling coefficient profile. Precisely, the selected cases are grouped according to the mode number M, the group delay variation Δ_τ and the geometric progression coefficient q. These parameters will assume specific values corresponding to small, medium and large numbers of their respective ranges, resulting in a partial set of eight multimode impulse response simulations, as reported in Table 5.6.

Table 5.6 Selected eight configurations for the simulation of the multimode impulse response. The simulation identifier XMXDXQ refers to the following codification: X stands for one of the values L, large; M, medium; S, small; M, D and Q stand respectively for the corresponding parameters M, mode number; D, group delay variation; Q, geometric progression coefficient

Number	Code	M	Δ_τ (ns/km)	q
1	LMLDLQ	200	±2	0.999
2	LMLDSQ	200	±2	0.500
3	LMMDLQ	200	±1	0.999
4	MMLDLQ	20	±2	0.999
5	MMLDSQ	20	±2	0.500
6	MMMDLQ	20	±1	0.999
7	SMLDLQ	5	±2	0.999
8	SMMDSQ	5	±1	0.500

The intention of the following simulations is to show the relevance of the three above-mentioned parameters in leading to very different multimode impulse response profiles. In general, when the mode number is large the effect is an averaging of the individual mode contribution over the whole population. This leads to a smoothed impulse response, characterized usually by either a long precursor tail or a long postcursor tail. The energy carried by each mode is usually a small fraction of the launched amount and unless the group delay distribution exhibits abrupt fluctuations, the energy would be smoothly distributed along the normalized timescale. On the contrary, when the excited mode number is small, the energy content of each mode is relatively more consistent, and impulse responses characterized by sparse impulsive contributions are quite usual.

5.4.3.1 Configuration 1: LMLDLQ

Following the simulation scheme listed in Table 5.6, the first case considered counts a large mode number, $M = 200$, with a peak-to-peak quadratic group delay distribution of $\Delta_\tau = \pm 2$ ns/km and an almost uniform geometric progression power coupling coefficient. All these three ingredients lead to almost the same individual contribution from all excited modes, even if their density is not uniform. The time position of the contributing pulses is determined by the group delay distribution, and therefore they are denser toward either the minimum or the maximum delay time, according respectively to the positive or negative group delay variation $\Delta_\tau = \pm 2$ ns/km.

This situation is clearly shown in the simulation results given in Figure 5.11, where the positive group delay variation $\Delta_\tau = +2$ ns/km leads to the left side multimode impulse response plotted and shown in Figure 5.12. Instead, the negative group delay variation $\Delta_\tau = -2$ ns/km plotted leads to the right side multimode impulse response shown in Figure 5.12. It is important to remark that the two multimode impulse responses shown in Figure 5.12 are antisymmetric: they are the mirrored representation of each other. This behavior is general for symmetric group delay variations as shown in Figure 5.11.

In order to explain the computed multimode impulse response, first the upward group delay distribution in Figure 5.11 is considered, which corresponds to a positive variation $\Delta_\tau = +2$ ns/km. The quadratic distribution concentrates the lower group delay values in the vertex region, close to lower mode group numbers. This determines the higher concentration of mode contributions per unit time in the neighborhood of the minimum delay value, leading to a corresponding huge pulse body in the initial region of the pulse distribution. As long as the group delay spread out over higher mode numbers, the corresponding energy is delivered along the time axis in a spared way, determining the long postcursor tail.

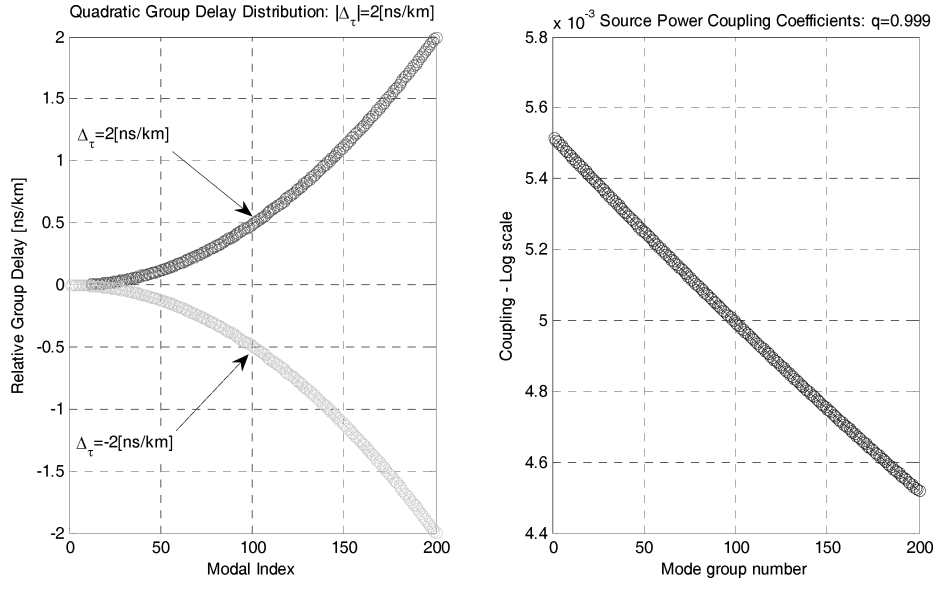

Figure 5.11 Quadratic group delay (left) and geometric progression (right) distributions computed using the data reported in Table 5.6. The sign of the parameter $\Delta_\tau = \pm 2\,\text{ns/km}$ leads to either increasing or decreasing group delay distribution

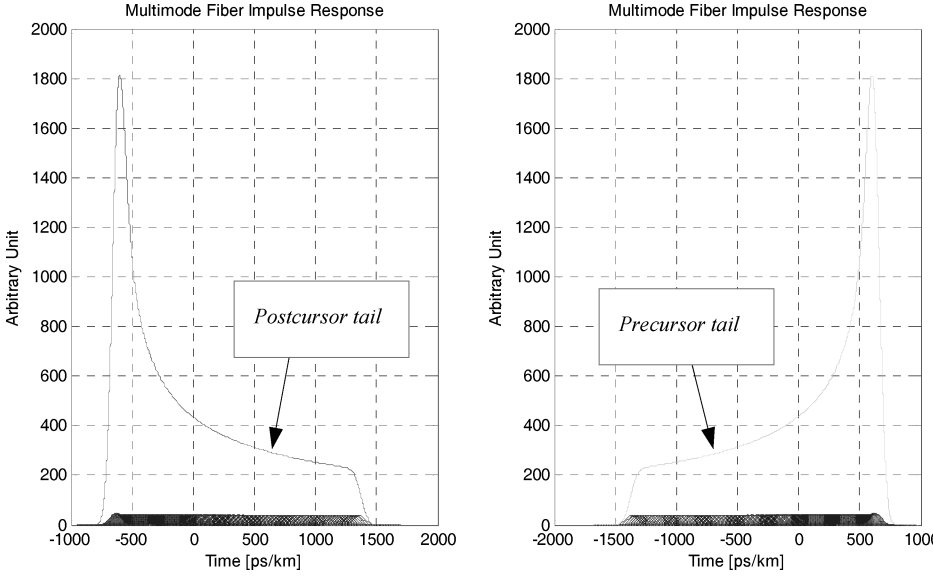

Figure 5.12 Computed multimode fiber impulse response for the case $M = 200$, $\Delta_\tau = \pm 2\,\text{ns/km}$, $q = 0.999$. The plot on the left side refers to the increasing group delay distribution, while the right side plot corresponds to the decreasing ones. The relevant peak behavior of both responses depends on the parabolic distribution of group delay values that increases the low-order mode density

The downward group delay distribution in Figure 5.11 corresponds to a negative variation $\Delta_\tau = -2\,\text{ns/km}$. In this case, the quadratic distribution concentrates the higher group delay values in the vertex region of the parabola, determining the higher concentration of mode contributions per unit time in the neighborhood of the maximum delay value and leading to the corresponding huge pulse body. However, the downward quadratic group delay makes the fastest modes sparsely distributed on to the time axis, leading to exactly the symmetrical behavior encountered before. The multimode impulse response exhibits in this case a long precursor tail with the huge pulse body and the ending region of the pulse distribution. Figure 5.13 illustrates the magnification of the bottom view of both impulse responses shown in Figure 5.12, in order to highlight the mode superposition. This is performed by the computational method.

The modal chromatic impulse responses are quite visible with the Gaussian-like profile. This is a consequence of the Gaussian source PSD and the almost linear group delay function of the wavelength in the source spectrum range. Each modal chromatic impulse response is properly delayed according to the quadratic group delay distribution. The left graph in Figure 5.13 shows very high-density mode contributions due to the upward group delay parabolic profile. Since modes superpose linearly, a higher mode density corresponds to a higher intensity, and the result is the huge pulse body shown in the left inset of Figure 5.12. The right inset of Figure 5.13 shows the complementary tail behavior of the impulse response in the case of the downward group delay distribution. The relatively sparse mode arrivals lead to the formation of the long low intensity tail of Figure 5.12.

Besides the discussion about the consequences of the group delay distribution, it is fundamental to take into account the contribution of the source power coupling coefficients. In the present case, the coupling coefficient profile is almost uniform, and this has been achieved using the q coefficient of the geometric progression very close to unity, $q = 0.999$. The source energy is

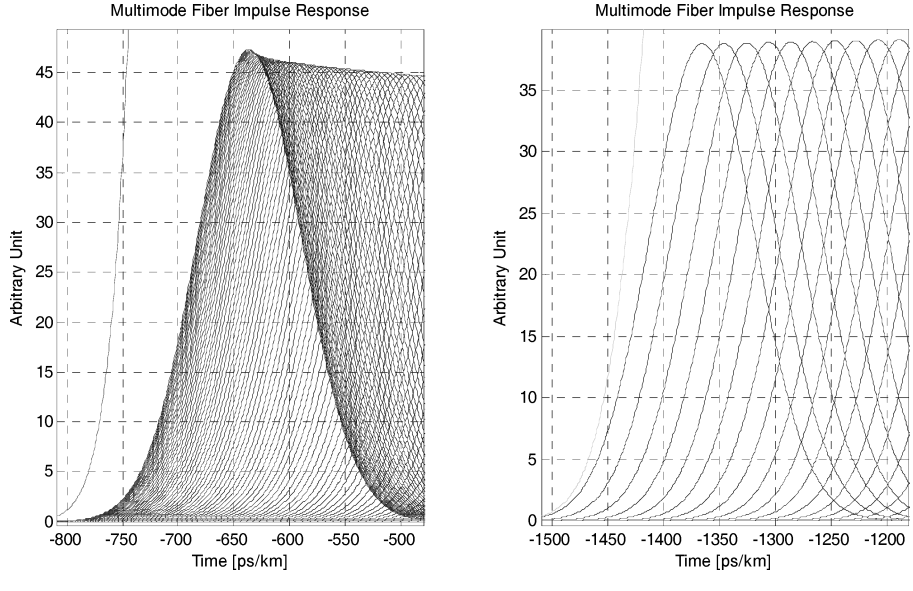

Figure 5.13 Mode superposition leading to the different pulse postcursor and precursor of Figure 5.12. Each Gaussian-like pulse coincides with the modal chromatic impulse response. The left graph shows high-density mode overlap, leading to the huge pulse body corresponding to the positive group delay variation. The right graph shows the complementary situation, where the negative group delay variation determines low-density mode energy contributions with the formation of the almost uniform long precursor tail

almost uniformly distributed among all allowed modes, which highlighted the consequences of the delay distribution. The next example shows the effect of a lower-order selective excitation assuming a lower q coefficient, namely $q = 0.50$, with the same large mode number, $M = 200$, and the same peak-to-peak quadratic group delay distribution with $\Delta_\tau = \pm 2\,\text{ns/km}$.

5.4.3.2 Configuration 2: LMLDSQ

This case is interesting for highlighting the consequences of a more selective mode excitation characterized by a small $q = 0.50$, but still assuming a very large mode number and group delay per unit length. Figure 5.14 shows on the left graph the two mirrored group delay distributions assuming $\Delta_\tau = \pm 2\,\text{ns/km}$, while the right plot shows the power coupling coefficient profile. In comparison with Figure 5.11, the stronger concentration of the launched power into lower-order modes is evident.

The restricted central launching conditions are quite well synthesized in Figure 5.15, where both plots have been magnified in the lower mode number range. The coupled power reduces to less than 1 % after the first seven excited mode groups and the resulting delay variation among them is quite negligible, below $\Delta_\tau(h = 1, \ldots, 7) = \pm 5\,\text{ps/km}$. This leads to the sharp impulse response reproduced in Figure 5.16.

5.4.3.3 Configuration 3: LMMDLQ

In this case it is assumed that the fiber supports still have a high number of guided modes, but with a better group delay equalization $\Delta_\tau = \pm 1\,\text{ns/km}$, which is only one-half of the value used in the previous case in Section 5.4.3.1. The quadratic excitation distribution is almost uniform, with $q = 0.999$ providing the same energy contribution from each guided mode. Figure 5.17 shows in the left graph the computed group delay distributions for both positive and negative delay variations. The right plot shows the source power coupling coefficient distribution.

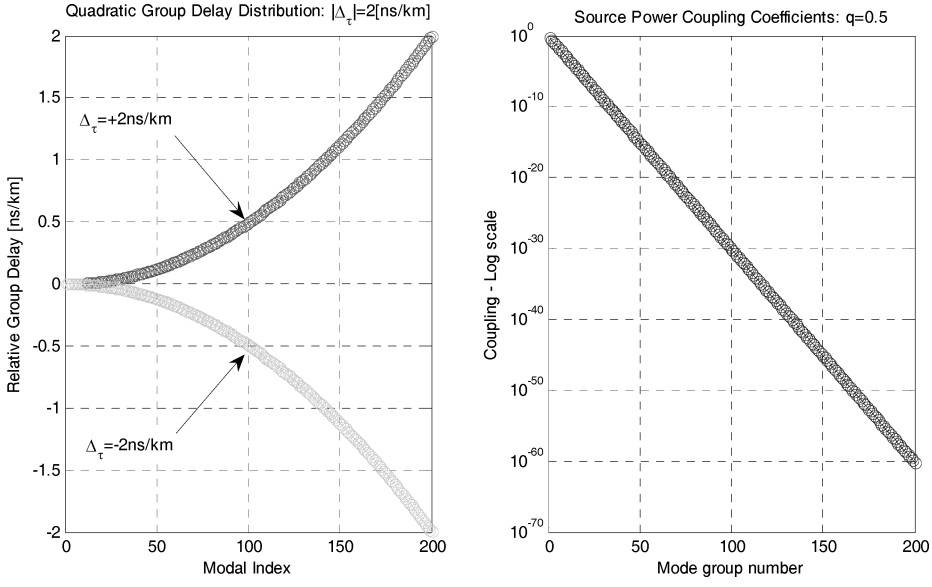

Figure 5.14 Quadratic group delay (left) and geometric progression (right) distributions reproducing restricted central launch conditions, with $q = 0.50$

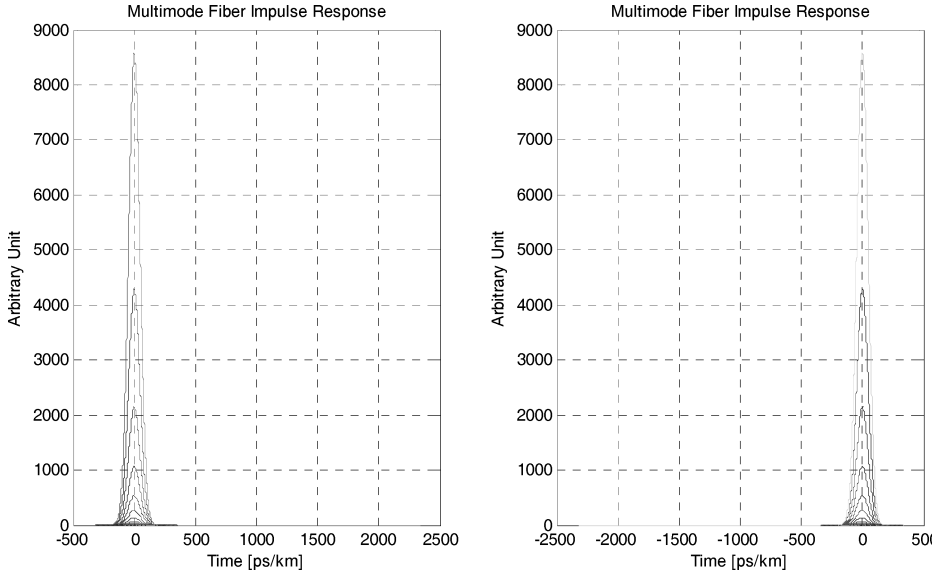

Figure 5.15 Multimode fiber impulse response according to the selected conditions reported in Table 5.6: $M = 200$, $\Delta_\tau = \pm 2$ ns/km, $q = 0.50$. The reduced number of excited modes with nonnegligible source coupled power leads to a very sharp impulse response. In fact, due to the quadratic delay distribution, the few selected low-order modes exhibit very small group delay differences. Those conditions are usually identified as restricted central launch conditions

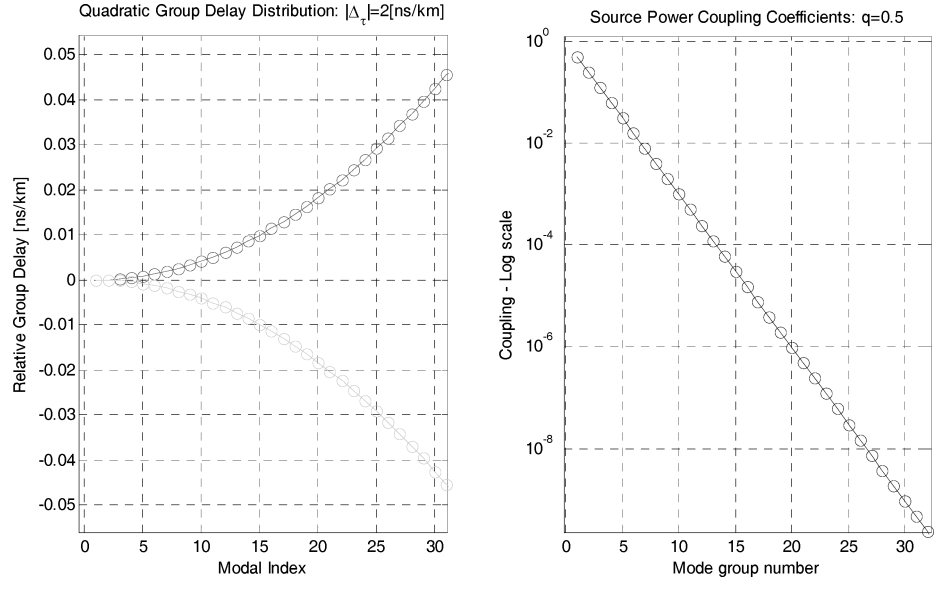

Figure 5.16 Magnified view of the lower order range of the quadratic group delay (left) and geometric progression (right) distributions reproducing restricted central launch conditions, with $M = 200$, $\Delta_\tau = \pm 2$ ns/km, $q = 0.50$

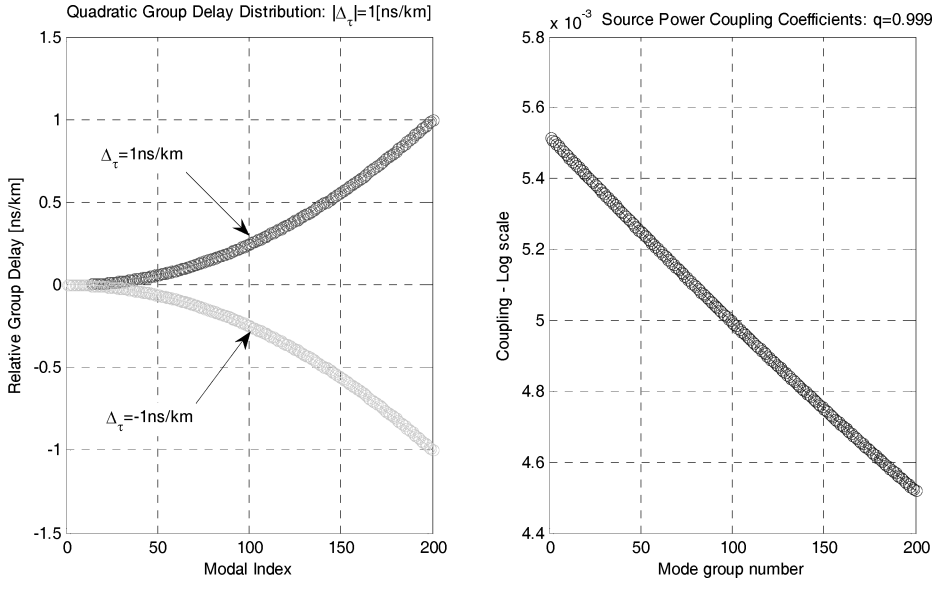

Figure 5.17 Quadratic group delay (left) and geometric progression (right) distributions reproducing almost uniform excitation conditions, with $q = 0.999$

The flat energy distribution makes almost all participating modes have the same output pulse with the same intensity. However, the quadratic group delay determines a higher intensity accumulation at shorter group delay values, leading to the unsymmetrical output pulse reported in Figure 5.18. The width of both pulses, measured at a very low intensity as expected, tends to be the assumed group delay variation $\Delta_\tau = \pm 1$ ns/km.

In comparison with the impulse response shown in Figure 5.12, it can be concluded that pulses are quite similar to each other, showing just a time scaling difference due to the different group delay variation. The multimode fiber impulse response in both cases is therefore mainly characterized by the large mode number and by the uniform modal excitation. In this case the group delay does not affect the response profile very much.

5.4.3.4 Configuration 4: MMLDLQ

In the previous sections, 5.4.3.1 and 5.4.3.3, the averaging effect of the uniform excitation of a large number of excited modes have been seen. Conceptually, each mode carries a very small amount of energy with a correspondingly very small relative delay with respect to adjacent modes, leading to an almost smoothed pulse profile when linear superposition is taken into account. In the following case a smaller number of excited modes is assumed, while still retaining a, large delay variation and uniform excitation. Figure 5.19 refers to these conditions. By comparing Figures 5.11, 5.14 and 5.17 the effect of a lower mode number can clearly be seen. The mode density per unit group delay is correspondingly lower and each mode is much better separated by adjacent ones. The interesting result shown in Figure 5.20 is a more granular profile of the impulse response, where the chromatic impulse response of higher-order modes is quite visible after superposition.

5.4.3.5 Configuration 5: MMLDSQ

What happens to the multimode impulse response of the previous configuration in Section 5.4.3.4 if restricted central launching conditions are assumed by setting $q = 0.50$? The group delay profile

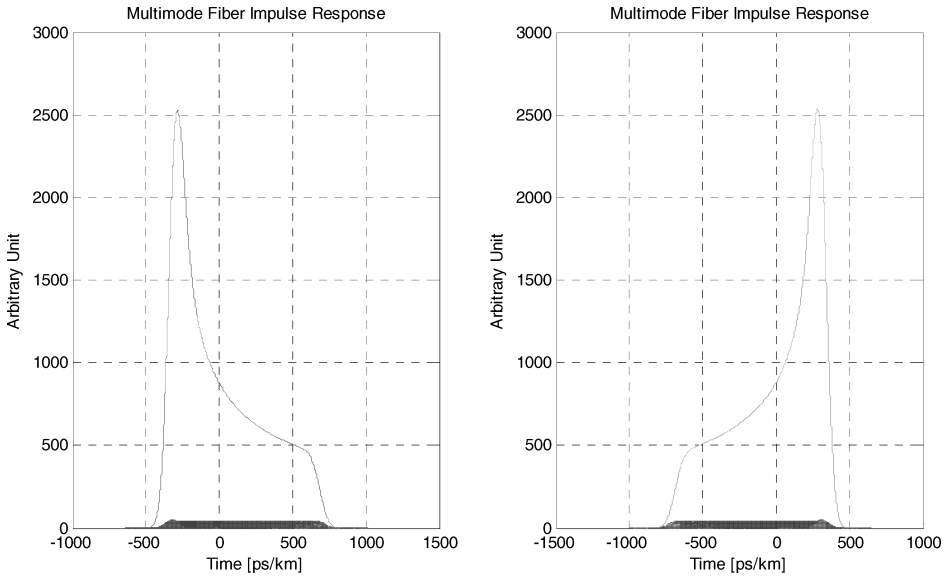

Figure 5.18 Computed multimode fiber impulse response for positive and negative group delay distributions respectively, with $M = 200$, $\Delta_\tau = \pm 1$ ns/km, $q = 0.999$. The peaking behavior of both responses depends on the parabolic distribution of group delay values located in the low-order mode region

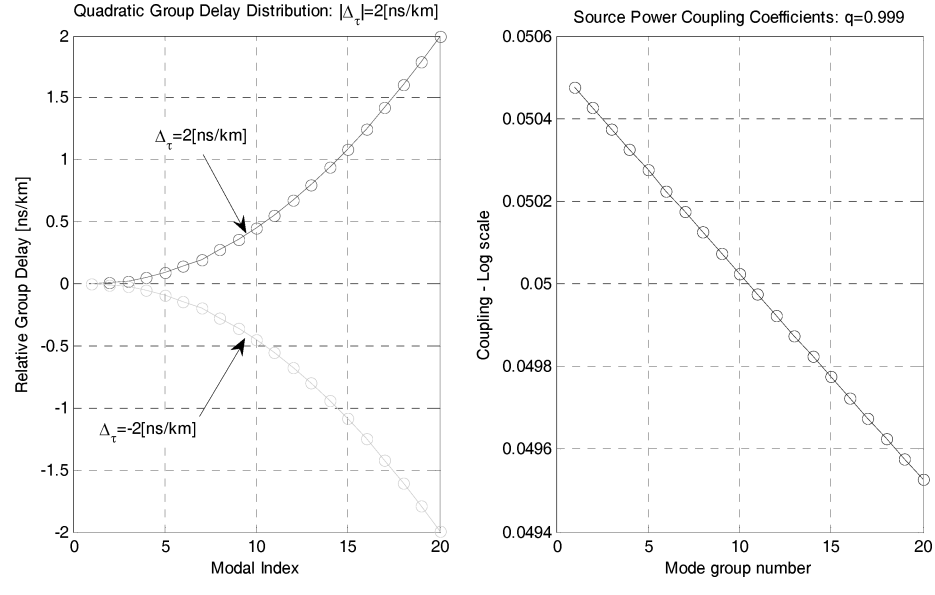

Figure 5.19 Quadratic group delay (left) and geometric progression (right) distributions reproducing almost uniform excitation conditions for a lower number of modes. Reducing the number of fiber supported modes, but still assuming the same group delay variation of $\Delta_\tau = \pm 2$ ns/km, makes each modal chromatic impulse response more isolated from neighborhood contributions

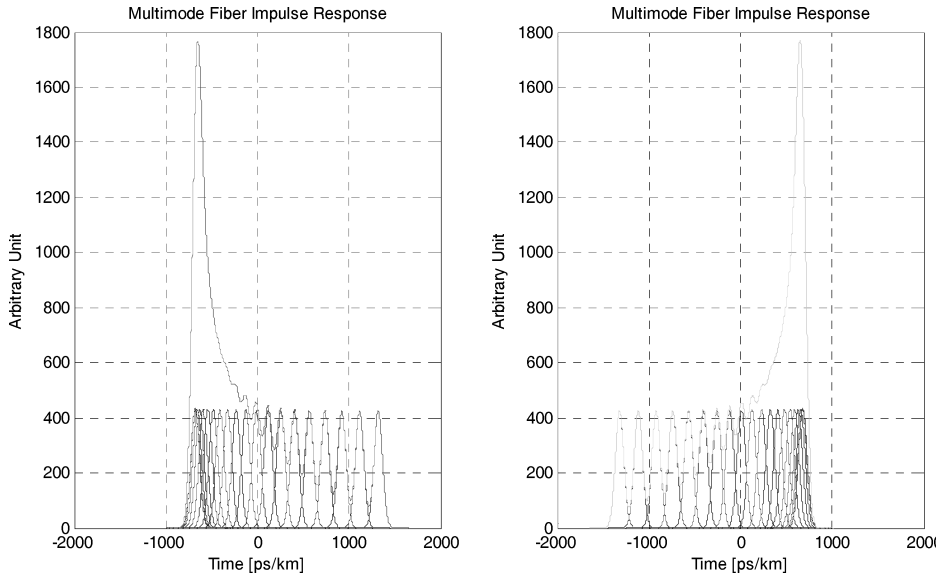

Figure 5.20 Computed multimode impulse response for the case $M = 20$, $\Delta_\tau = \pm 2$ ns/km, $q = 0.999$. Higher differential delay among higher-order modes leads to the granular resolution in the multimode response. Even after superposition, the chromatic impulse response contribution of each individual higher-order mode group is still clearly recognizable

and the exciting distributions are shown in Figure 5.21. The reduced value of the coefficient q selects only low-order modes, leading to a modal intensity contribution of less then 1 % for mode numbers exceeding seven. This means that only about the first seven low-order modes will contribute significantly to the intensity composition of the output pulse with the relevant reduction of the modal dispersion.

Elimination of higher-order modal contributions makes the resulting impulse response shown in Figure 5.22 much narrower than the case presented in Figure 5.20. Long tail behavior, either with a precursor or postcursor, is no longer present and the resulting impulse response shows strongly reduced intersymbol interference when used in digital NRZ transmission systems. The impulse response structure shown in Figure 5.22 reveals that the differential delay among the first seven modal chromatic impulse responses is significantly smaller than the chromatic RMS pulse width and the resulting output pulse is no longer very different from the single chromatic impulse response. The slight asymmetry in the trailing edge of the left side pulse (leading edge of the right side pulse) is due to the group delay contribution among the selected modes.

5.4.3.6 Configuration 6: MMMDLQ

This configuration differs from the one considered in Section 5.4.3.4 for the reduced group delay variation. Figure 5.23 shows both the group delay and the power coupling excitation distributions.

Due to the uniform excitation all 20 allowed modes contribute to the multimode impulse response with the same intensity, overlapping each other according to the assumed quadratic group delay distribution. Figure 5.24 shows as usual the individual modal chromatic impulse responses and their superposition. The reduced group delay variation in conjunction with the chromatic impulse response width makes the resulting pulse almost smooth. The granularity shown in Section 5.4.3.4

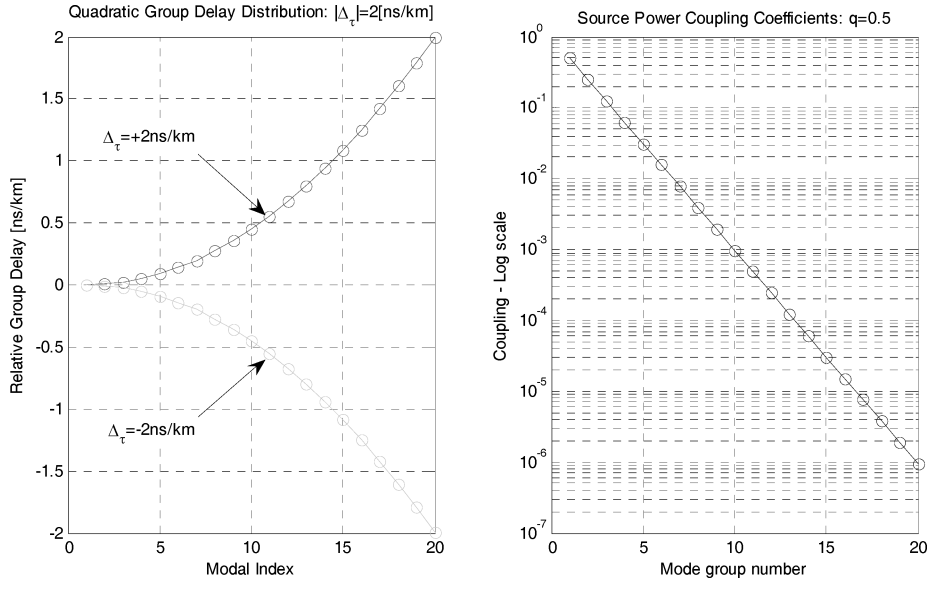

Figure 5.21 Quadratic group delay distribution (left) for $M = 20$ allowed fiber modes. The selective excitation (right) provides a source energy transfer only to low-order modes. Relative coupled power reduces to less than 1 % for a mode group number exceeding seven

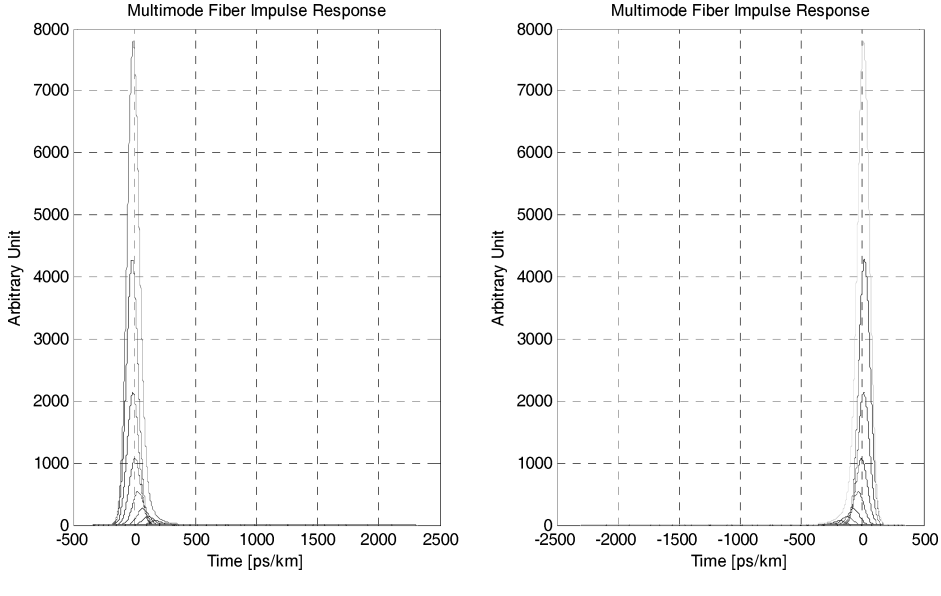

Figure 5.22 Computed multimode impulse response for the case $M = 20$, $\Delta_\tau = \pm 2$ ns/km, $q = 0.50$. Higher differential delay among higher-order modes has almost been eliminated by means of the selective low-order mode excitation

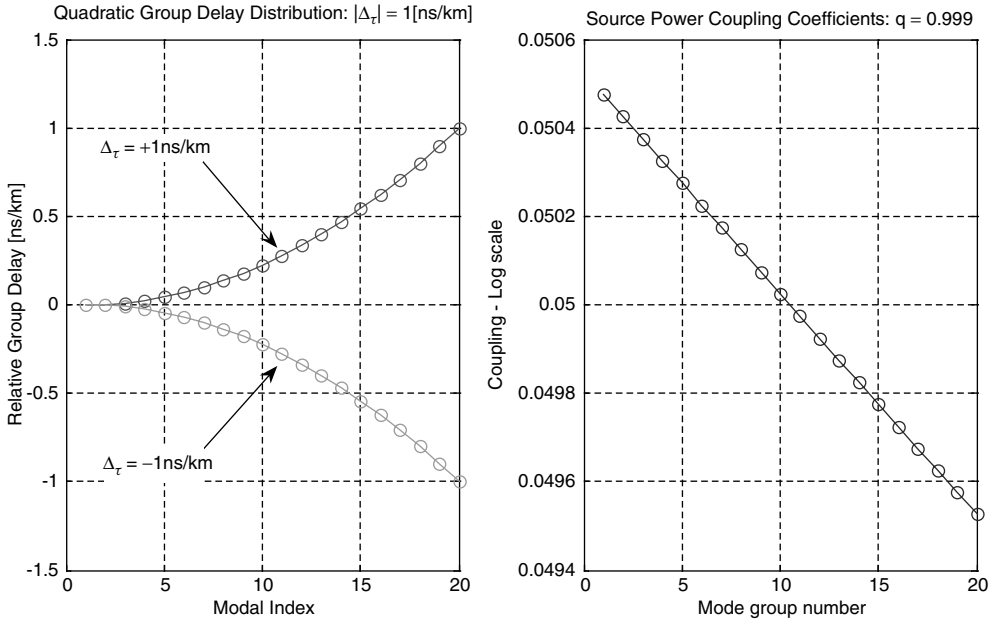

Figure 5.23 Group delay and power coupling coefficients distributions

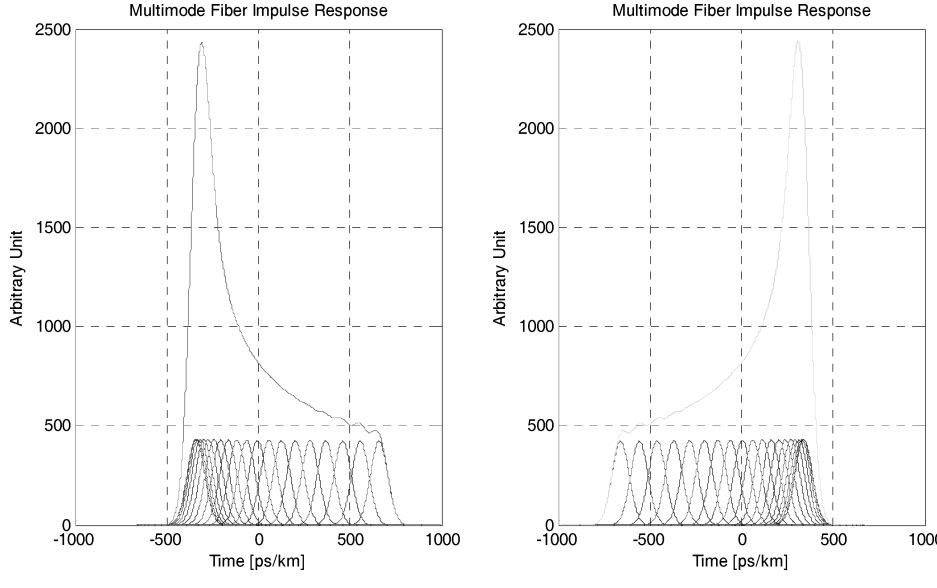

Figure 5.24 Computed multimode impulse responses for the case $M = 20$, $\Delta_\tau = \pm 1$ ns/km, $q = 0ext.999$. The modal chromatic impulse responses are easily visible, each properly translated according to the group delay value. Their weighted superposition produces the multimode impulse response shown left and right for positive and negative group delay variations respectively

is no longer visible in this case and the multimode impulse response closely resembles the case presented in Section 5.4.3.3, where a larger number of modes was assumed, with $M = 200$.

5.4.3.7 Configuration 7: SMLDLQ

These last three cases deal with very low allowed fiber modes. Only $M = 5$ fiber modes are assumed and the group delay variation and the coupling distribution will be changed in order to have corresponding different multimode impulse responses. Among those three mentioned, the most severe condition refers to the case of equally excited modes with a relatively high group delay variation, namely $q = 0.999$ and $\Delta_\tau = \pm 2\,\text{ns/km}$, as reported in Figure 5.25.

The resulting multimode fiber impulse response is shown in Figure 5.26. The multipeak profile makes this pulse response not suitable for any digital NRZ transmission system due to the strong intersymbol interference produced. According to the sign of the group delay variation, either three postcursors or three precursors are produced. Precisely, the positive group delay variation $\Delta_\tau = +2\,\text{ns/km}$ leads to the postcursor formation, while the negative group delay $\Delta_\tau = -2\,\text{ns/km}$ determines the pulse precursor. It is important to note that the total pulse width nearly coincides with the sum of the respective modal and chromatic pulse widths. This is due to the granular profile of the response, with individual modal responses almost completely separated from each other. In this case the geometric sum coincides with the linear sum of the pulse components.

5.4.3.8 Configuration 8: SMSDSQ

This simulation example shows the effect of selective low-order excitation, even for very few allowed fiber modes. The source power is no longer distributed equally among allowed modes and higher-order modes carry less power than lower-order ones. The resulting impulse response is shown in Figure 5.27. It has a smoother granular profile in comparison with the one shown in

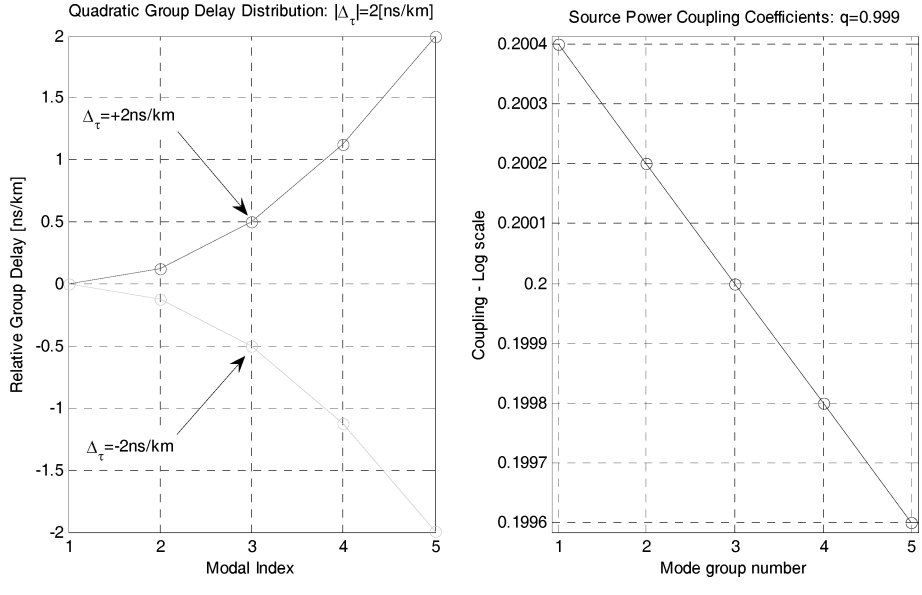

Figure 5.25 Group delay distribution for the case of only five allowed fiber modes. The almost uniform source power coupling coefficients distribution delivers about 20 % of the total launched power to each fiber mode

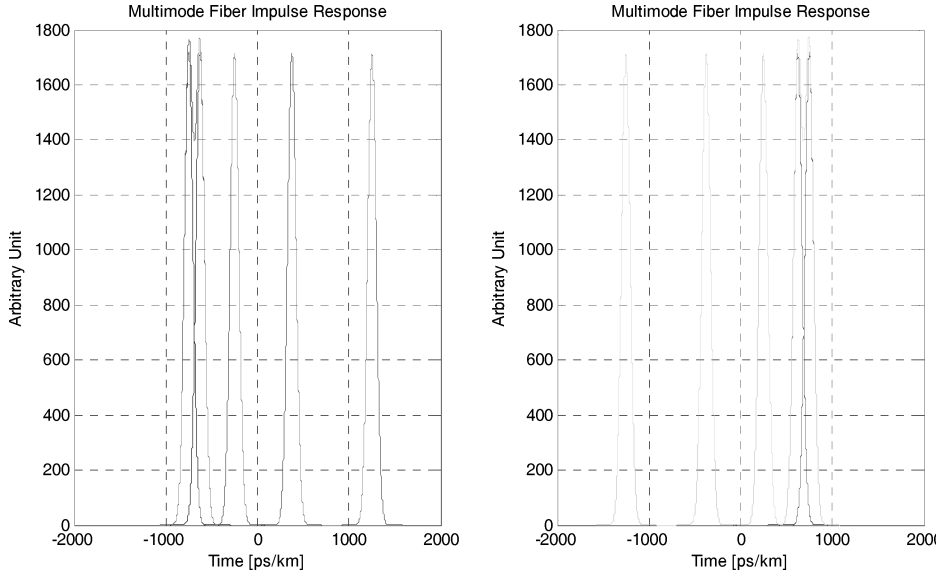

Figure 5.26 Computed multimode impulse responses for the case $M = 5$, $\Delta_\tau = \pm 2\,\text{ns/km}$, $q = 0.999$. The very low number of allowed modes together with the high group delay variation leads to a strong granularity of the multimode impulse response. Strong postcursors or precursors are therefore generated corresponding to positive and negative group delay variations respectively

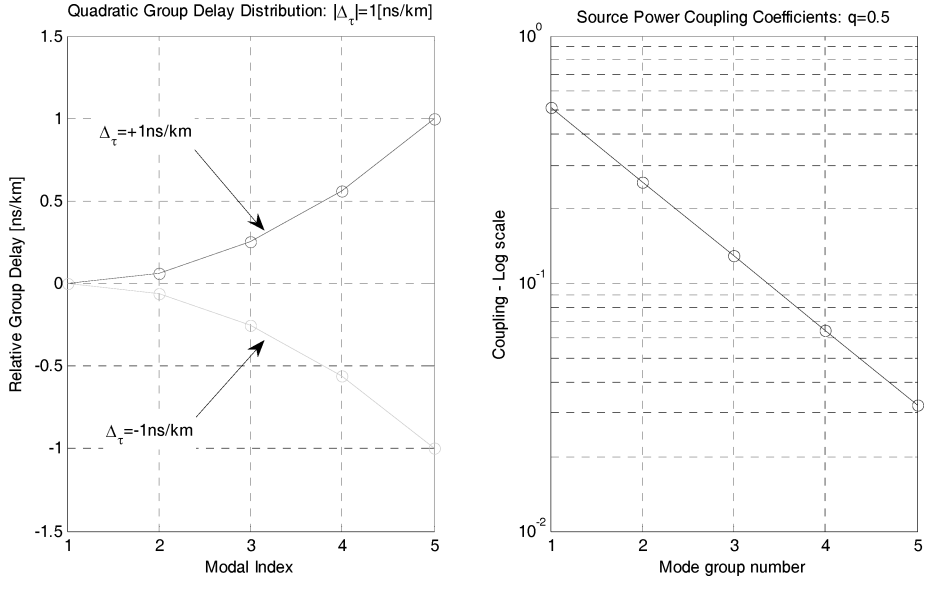

Figure 5.27 Quadratic group delay distribution on the left side for the case of only five allowed fiber modes. The group delay variation has been set equal to $\Delta_\tau = \pm 1\,\text{ns/km}$. The right side plot shows the geometric progression distribution of the coupling coefficient with $q = 0.50$

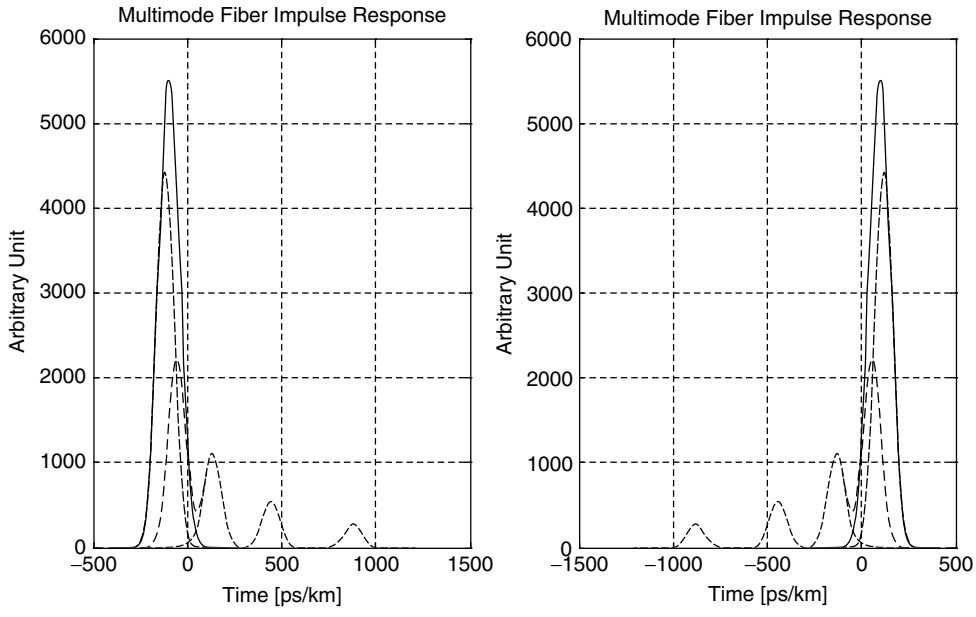

Figure 5.28 Computed multimode impulse response using the configuration $M = 5$, $\Delta_\tau = \pm 1\,\text{ns/km}$, $q = 0.50$. The granularity of the group delay of the allowed fiber mode is partially compensated by the selective low-order mode excitation achieved using a low q geometric progression coefficient distribution

Figure 5.26. From the multimode impulse response presented in Figure 5.28, the same granularity of the previous case but with a smoothed profile due to selective low-order mode excitation is evident.

5.4.3.9 Conclusions

The eight configurations presented in this section represent typical impulse response profiles achievable by multimode fibers. Simplified mathematical modeling has been used to evaluate the different configurations, but as mentioned at the beginning of this section, the simulator can be easily adapted to handle more realistic multimode fiber configuration conditions. Both group delay distribution and source power coupling coefficients can be computed accurately using either a deterministic model or a statistical approach. Even experimental data can be uploaded into the simulation program in order to emulate experimental multimode fiber impulse responses. The mathematical modeling used in this section was mainly conceived for handling an easy simulation environment, so that it could be focused instead on the interesting response profiles. It should be clear that the multimode fiber impulse response is governed by the combination of the group delay distribution at the operating wavelength and the excited mode distribution. The fiber can support a large number of modes, but the modes effectively concurring to the impulse response are of course only those excited by the input launching conditions.

The same fiber has as many impulse responses as there are launching conditions defined. This discussion leads directly to the concept of multimode fiber behavior when it is excited by laser light, as required by multigigabit transmission systems. LED light sources characterized by a high numerical aperture produce a more uniform excitation, but they are not suitable for multigigabit direct modulation. On the other hand, laser light has an inherently lower numerical aperture with a much greater limit on spot size. Typical spot size values for a semiconductor laser diode are

of the order of a few micrometers, usually much less than the standard multimode fiber core diameter ranging between 50 μm and 62.5 μm. As a consequence, laser excitation belongs to the restricted launching conditions, providing the selective excitation of a small fraction of the allowed fiber modes. The impulse response will therefore depend on the group delay distribution among the excited mode fractions. Due to the strong influence of the refractive index grading profile on the group delay equalization, very small differences in the grading profile during either the manufacturing process or the environmental conditions can lead to a sensible uncompensated group delay profile with a strong dependence of the multimode fiber impulse response on the launching conditions.

The next section analyzes in more detail the effect of the group delay distribution on the impulse response profile.

5.4.4 Influence of the Group Delay Distribution

In this section we will discuss in more detail the consequences of the group delay distribution on the modal impulse response while assuming uniform mode excitation. In fact, as learned from the simulation configuration in the previous section, once the mode excitation is uniform, the multimode impulse response is mainly governed by the group delay distribution evaluated at the average source wavelength. The next sections will introduce the group delay analysis in order to forecast principal impulse response characteristics.

5.4.4.1 General Concepts

Figure 5.29 qualitatively reports symmetric group delay profiles. It is evident that in the cases represented the outer range values of the group index will be responsible for either the fastest or

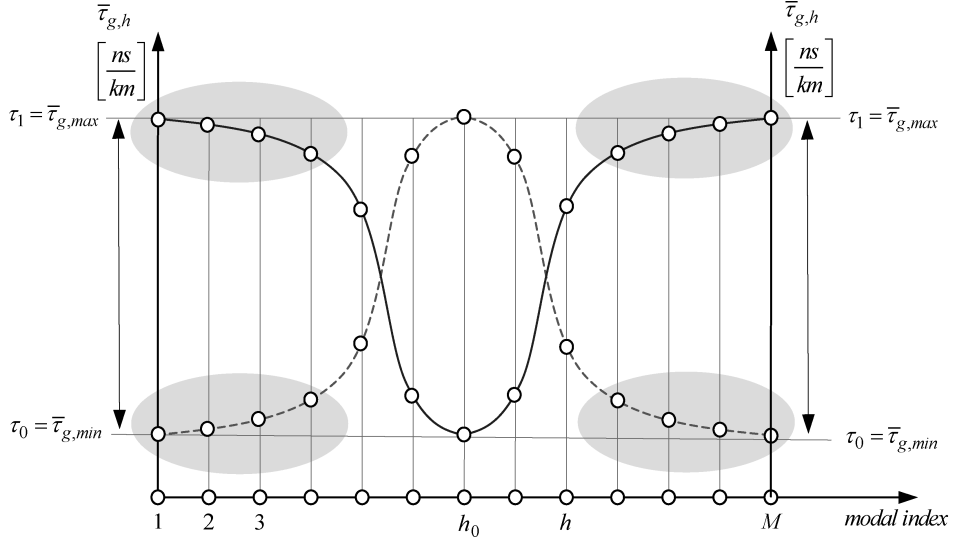

Figure 5.29 Bell-shaped group delay distributions leading to mirrored behaviors of the modal impulse response. The profile leads to weak precursors followed by a high-intensity pulse. The profile leads to a high-intensity pulse followed by weak postcursors. This interesting complementary behavior of the modal impulse response is consequent to the complementary density distributions of the allowed group delay values between the profiles. Shadowed regions highlight higher densities of allowable group delays

the slowest modal contributions. It is the density of allowable delay values that determines the largest intensity contribution to the output pulse. Again, the coupled power distribution will be responsible for the weighting of those allowable delay contributions.

The profiles represented in Figure 5.29 are an interesting example of a complementary group delay distribution, which give mirrored modal impulse responses, once it is assumed that both of them are excited by the same coupled source power distribution. To have a clear representation of this effect, it is convenient to assume uniform mode excitation, with the same amount of optical source energy distributed to each allowed fiber mode. Moreover, each impulse response can be shaped with the simple square pulse, as represented in Figure 5.30. Then the impulse response can be built up by adding together the square pulses according to the corresponding group delay experienced.

Figure 5.29 shows the individual modal impulse responses corresponding to each group delay profile distribution, assuming uniform coupled power distribution. Each mode will therefore bring the same intensity to the output fiber section and consequently the output impulse response shape

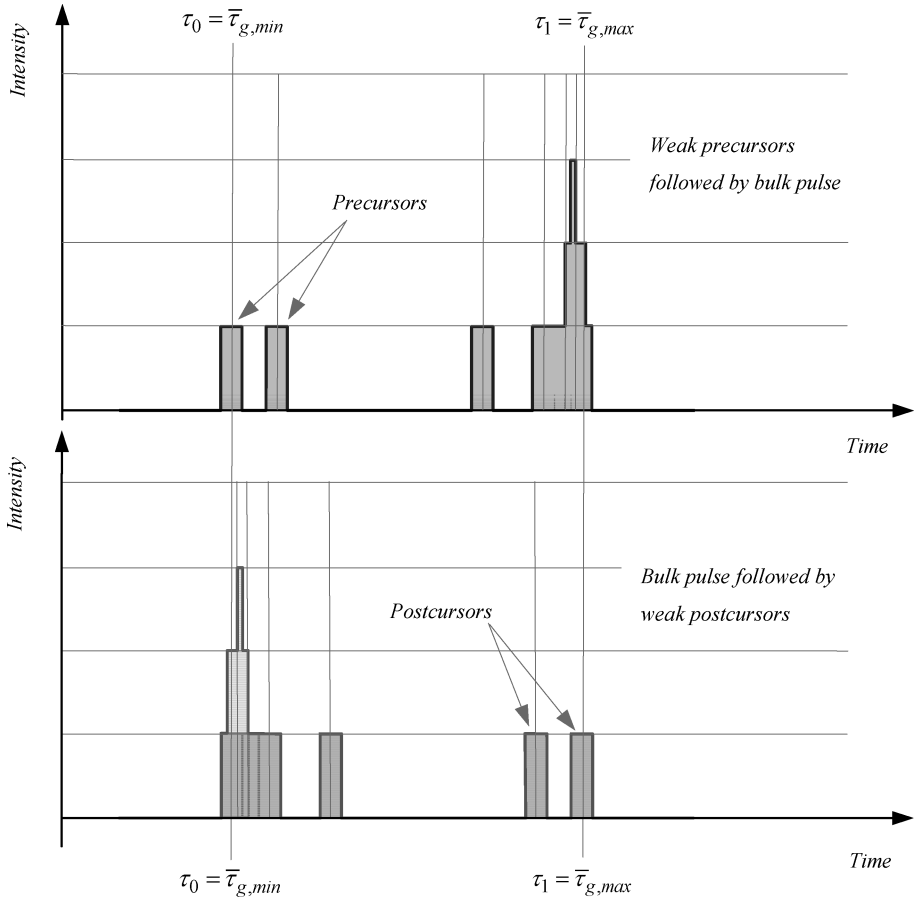

Figure 5.30 Modal impulse responses corresponding to the group delay distributions shown in Figure 5.29, assuming a uniform intensity distribution among all allowed modes. The top impulse response shows a weak precursor followed by a bulk response and refers to the group delay distribution shown at the top of Figure 5.29. The complementary situation holds for the impulse response shown in the bottom graph

will be determined by the modal delay distribution. Quantitative demonstrations of these interesting effects will be seen using computer modeling results in the following section. Referring to the group delay distribution in Figure 5.29, it is concluded immediately that the fastest square pulses will be sparsely distributed in the leading tail (precursor), due to the low concentration of group delay values available in this region. Instead, slower pulses will tend to concentrate as long as they spread out over a longer timescale in the trailing tail. The result is shown in the top graph of Figure 5.30. The impulse response is composed of a weak precursor in the leading edge, followed by the principal pulse. The reversed group delay distribution, drawn in Figure 5.29, leads to the mirrored multimode impulse response with a characteristic weak postcursor in the trailing edge, as depicted by the bottom graph in Figure 5.30.

5.4.4.2 Linear Distribution

The general introduction presented in the previous section suggested that a more systematic way should be followed in order to understand better and manage the influence of group delay distribution on the multimode impulse response. In this section, as well as in the following ones, uniform mode excitation by setting will be assumed, unless otherwise stated:

$$|\overline{a}_h|^2 = \frac{1}{M} \Rightarrow \sum_{h=1}^{M} |\overline{a}_h|^2 = 1 \tag{5.56}$$

A start is made using the simplest modal delay distribution available, namely the linear relationship. The value $\tau_0 \equiv \overline{\tau}_{g,h_0}$, $h_0 \in N(1, M)$ and the slope $\Delta_\tau/(M-1)$ of the linear distribution are assigned, where h_0 is any modal index between $h = 1$ and $h = M$, assuming M excited modal groups, and Δ_τ is the total variation of the modal group delay evaluated at the source spectrum average wavelength $\overline{\lambda}$. Once those parameters are known, the linear group delay distribution from Equation (5.46) has the following expression:

$$\tau_h = \tau_0 + \frac{\Delta_\tau}{M-1}(h - h_0) \tag{5.57}$$

Figure 5.31 shows the definition of the linear distribution. Multimode impulse responses computed assuming uniform excitation and linear group delay distributions are presented below. The remaining parameters are the same as in Table 5.4. The simulation output of the spectral condition and of the chromatic impulse response are also the same as shown in Figures 5.8 and 5.9 and will not be reproduced here.

In Figure 5.32 the multimode impulse response assuming a large mode number $M = 200$ and $\Delta_\tau = \pm 2$ ns/km is shown. The uniform superposition of individual chromatic impulse responses gives, as apparently expected, an almost uniformly flat-shaped multimode impulse response characterized by a half-width at half-maximum value approximately equal to the assumed group delay variation, $|\Delta_\tau| = 2$ ns/km. The exact computation of the FWHM value of the impulse response must include the chromatic impulse FWHM value. Of course, due to symmetric linear delay distributions in Figure 5.33, both mirrored impulse responses in Figure 5.32 are identical. It is important to remark that although the flat-shaped response obtained in this case could be expected as a general consequence of the linear delay and uniform excitation assumptions, the generalization of this conclusion is absolutely not correct. It is just a matter of coincidence that the superposition of the delay-shifted Gaussian-like chromatic impulse responses gives the almost flat output pulse computed in Figure 5.32.

For a given chromatic impulse response, the almost flat profile depends on the particular choices of both the mode number M and the total delay Δ_τ, as shown in the second case reported in Figures 5.34 and 5.35, just after limiting the mode number to $M = 20$. Reducing the mode number

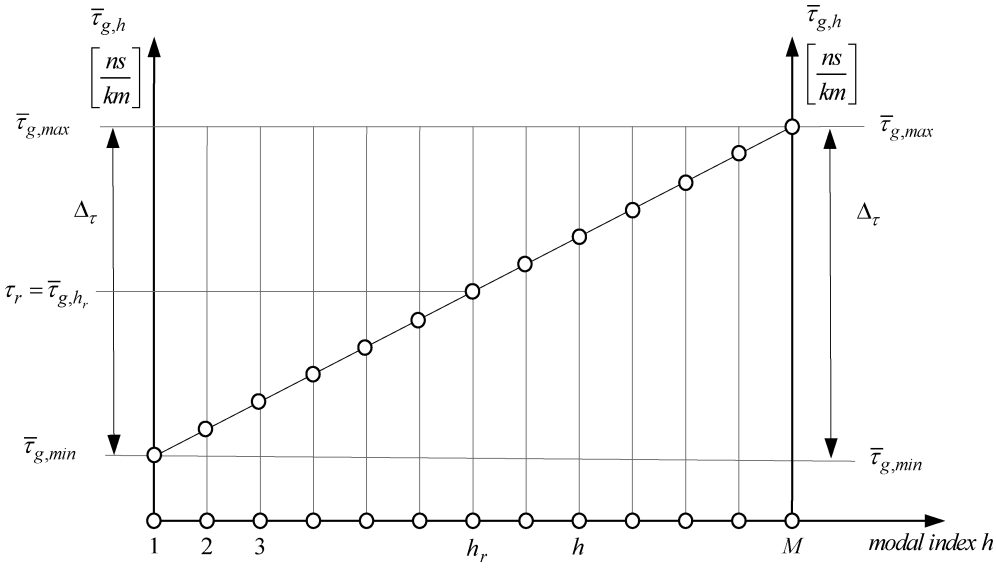

Figure 5.31 Linear group delay distribution. The modes are uniformly ordered according to their delay value. The total delay variation is $\Delta_\tau = \overline{\tau}_{g,max} - \overline{\tau}_{g,min}$ and the reference delay $\tau_{g,h_r}(\overline{\lambda}) = \overline{\tau}_{g,h_r} = \tau_r$ is evaluated at the source spectrum average wavelength

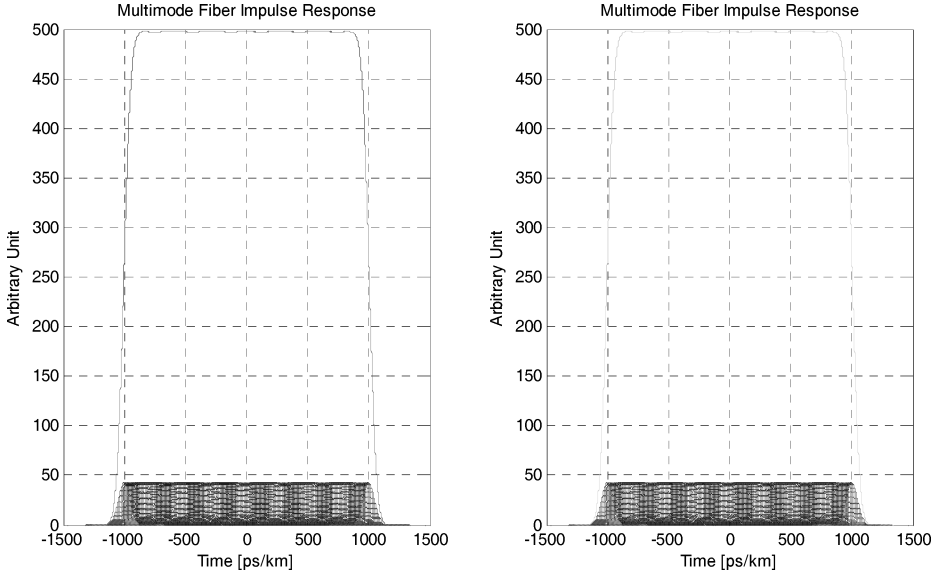

Figure 5.32 Computed multimode impulse response in the case the of linear delay distribution with $M = 200$, $\Delta_\tau = \pm 2$ ns/km, $q = 1.00$. The individual superposition of the chromatic impulse response leads to almost a square pulse profile. The symmetry of the linear delay distributions shown in Figure 5.33 gives identical mirrored multimode impulse responses

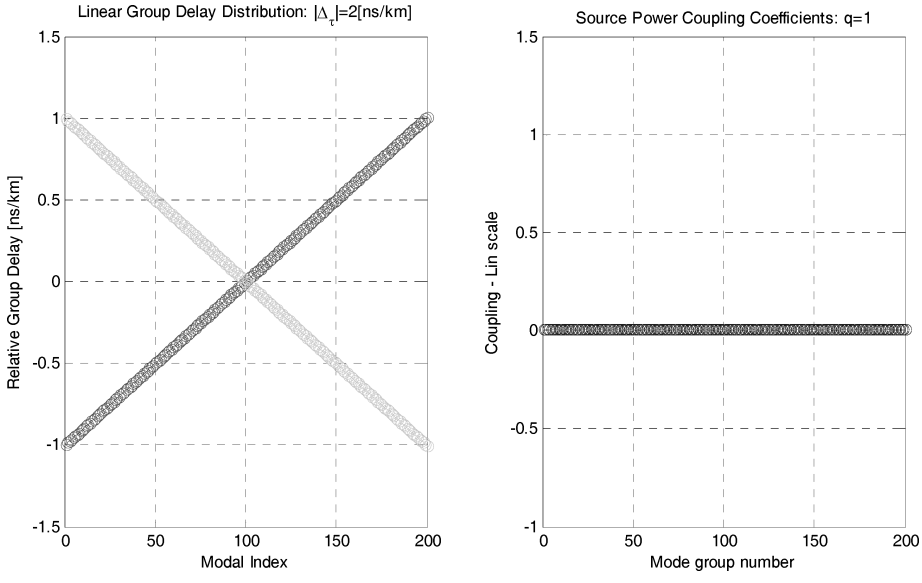

Figure 5.33 Computed linear group delay distribution (left) and uniform excitation (right) for the following parameters: $M = 200$, $\Delta_\tau = \pm 2$ ns/km, $q = 1.00$. The delay distribution is referenced to the value assumed at the source average wavelength $\tau_{g,h_r}(\overline{\lambda}) = \overline{\tau}_{g,h_r} = \tau_r$

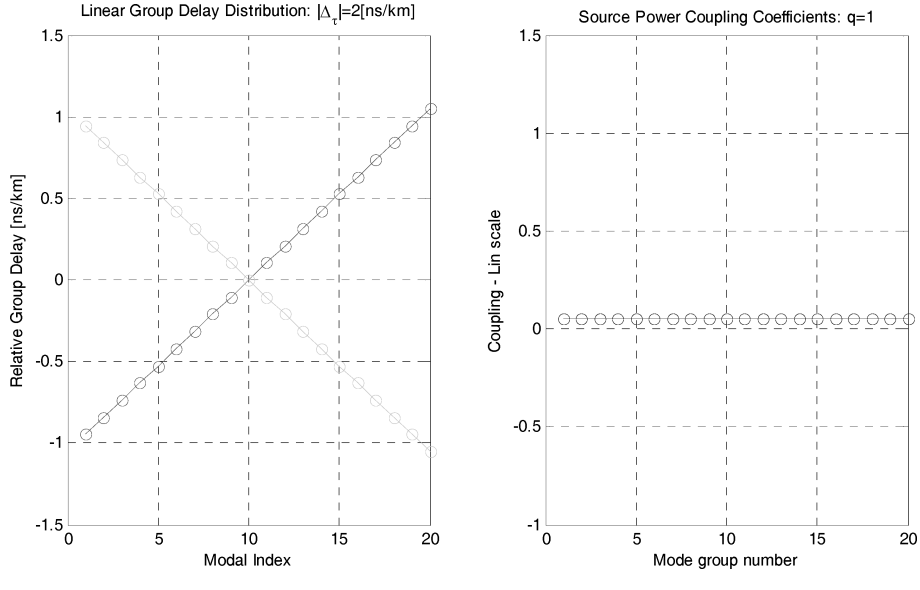

Figure 5.34 The linear group delay distribution has the same total delay value $\Delta_\tau = \pm 2$ ns/km of the preceding case but the number of modes has been reduced to $M = 20$. This leads to a larger delay difference between any adjacent mode pairs. The right plot shows the uniform excitation. The delay distribution is referenced to the value assumed at the source average wavelength $\tau_{g,h_r}(\overline{\lambda}) = \overline{\tau}_{g,h_r} = \tau_r$

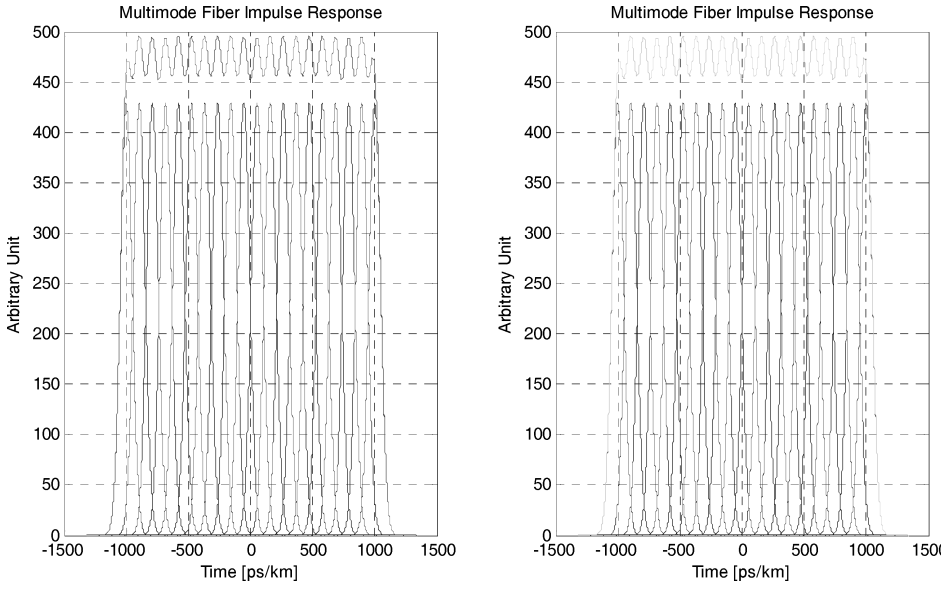

Figure 5.35 Computed multimode impulse response in the case of the linear delay distribution with $M = 20$, $\Delta_\tau = \pm 2$ ns/km, $q = 1.00$. The superposition of the individual chromatic impulse response leads to the ripple pulse profile. The symmetry of the linear delay distributions shown in Figure 5.30 is responsible for identical mirrored responses

but leaving the same total delay variation Δ_τ corresponds to an equivalent increment of the delay difference between adjacent modes, leading to a different chromatic impulse response overlap. In this case the Gaussian-like chromatic impulse responses in Figure 5.9 superpose by a different amount with respect to the preceding condition, giving a multimode response with a characteristic ripple profile.

Figure 5.35 presents the computed multimode impulse response according to considered linear delay distribution and uniform excitation. As mentioned, the same chromatic impulse response gives a different multimode response due to the different overlapping conditions. It is evident that either increasing the total delay or reducing the excited mode number will result in a more granular response, where individual chromatic responses will be more isolated from each other. If the third condition is assumed (see Figure 5.36) to excite the same large mode number used in the first case, $M = 200$, but reduces the total delay variation to only $|\Delta_\tau| = 0.25$ ns/km, therefore allowing a closer chromatic response superposition, the multimode impulse response assumes a smoothed bell-shaped profile, as reported in Figure 5.37, which closely resembles a Gaussian-like pulse.

5.4.4.3 Piecewise Linear Distribution

The mathematical modeling presented in the preceding section easily generalizes to a multisegmented or piecewise linear group delay profile. This technique is quite interesting because it allows the general delay distribution to be approximated by means of a sequence of linear group delays. It is easy to generalize the linear delay modeling into a multisegment linear profile. Figure 5.38 shows the piecewise linear specifications. Each segment T_k is defined by specifying the modal indices and

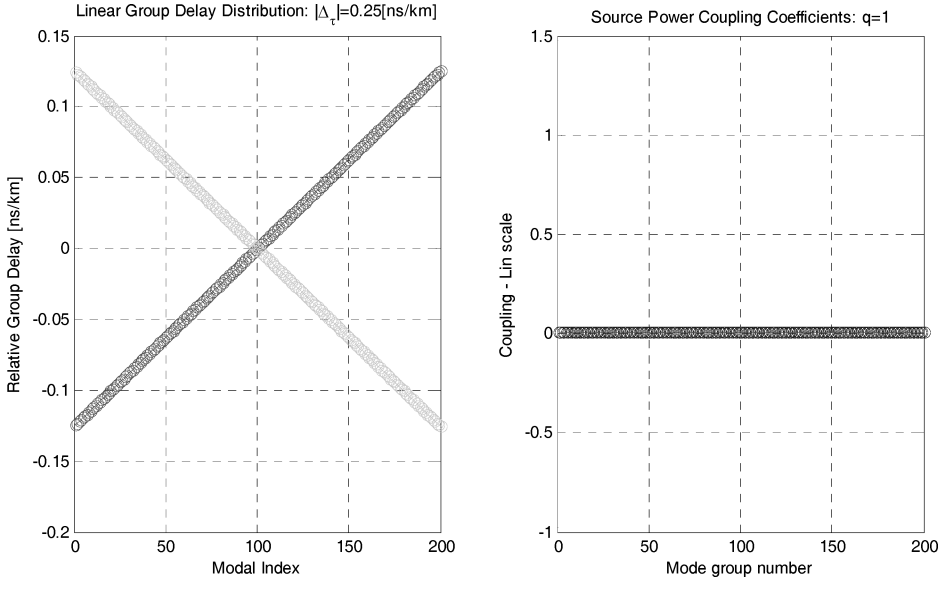

Figure 5.36 Computed linear group delay distribution (left) and uniform excitation (right) for the following parameters: $M = 200$, $\Delta_\tau = \pm 0.25$ ns/km, $q = 1.00$. The delay distribution is referenced to the value assumed at the source average wavelength $\tau_{g,h_r}(\overline{\lambda}) = \overline{\tau}_{g,h_r} = \tau_r$

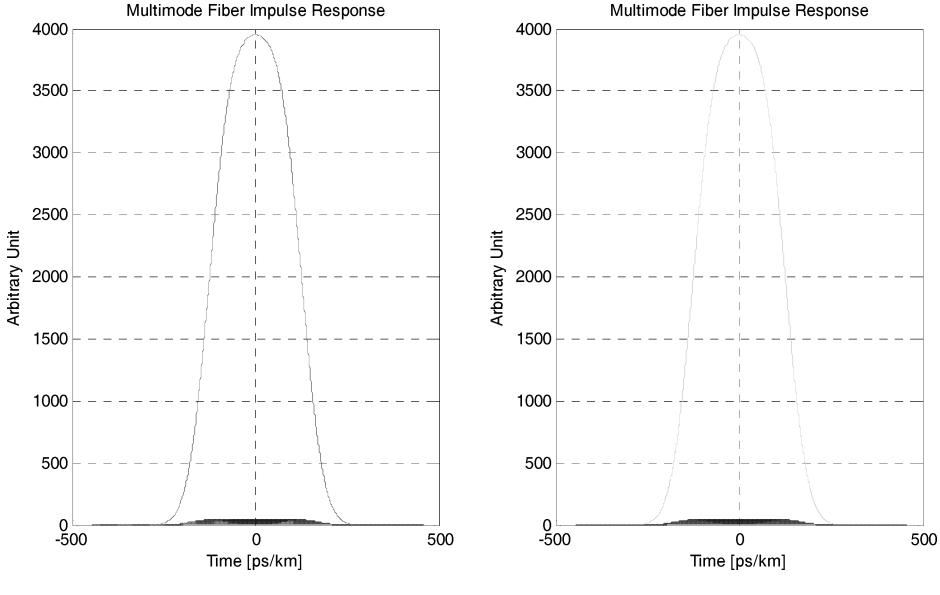

Figure 5.37 The multimode impulse response shown here refers to the linear group delay reported in Figure 5.36 with $M = 200$ and uniform excitation. The low value of the total delay together with the large mode number leads to a small delay difference between adjacent chromatic mode responses. After the superposing process, the resulting multimode impulse response assumes a more smoothed Gaussian-like profile

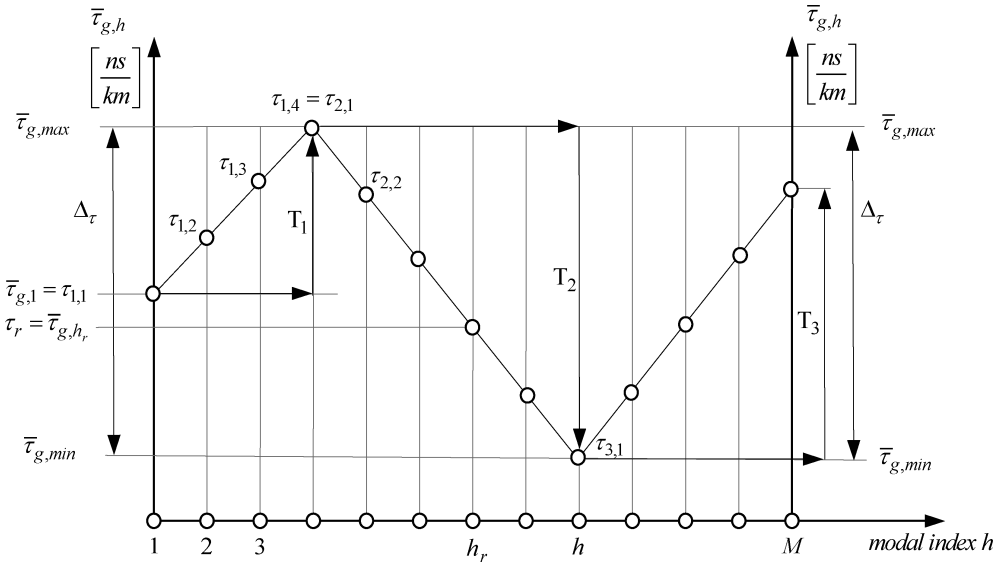

Figure 5.38 Piecewise linear group delay distribution. The first index $h = 1$ refers to the group delay value $\tau_{1,1} = \overline{\tau}_{g,1}$. In this representation three segments are included. The reference group delay can be assigned to each one of the M mode groups. By definition, the reference delay is assigned to the value τ_r of the group delay function $\tau_{g,h_r}(\overline{\lambda})$ of the selected reference mode h_r, evaluated at the source average wavelength $\overline{\lambda} : \tau_{g,h_r}(\overline{\lambda}) = \overline{\tau}_{g,h_r} = \tau_r$

the corresponding delay values of the two extremes, $(h_{k,1}, \tau_{k,1})$ and $(h_{k,p}, \tau_{k,p})$, $h \in N$ $(h_{k,1}, h_{k,p})$, $\tau \in T_k = (\tau_{k,1}, \tau_{k,p})$:

$$\tau_{k,h} = \tau_{k,1} + \frac{\Delta_k}{M_k}(h - h_{k,1}), \quad \begin{cases} \Delta_k \equiv \tau_{k,p} - \tau_{k,1} \\ M_k \equiv h_{k,p} - h_{k,1} \end{cases} \tag{5.58}$$

In order to have the delay distribution continuous at each segment, the following condition needs to be satisfied:

$$\tau_{k+1,1} = \tau_{k,p} \tag{5.59}$$

Substituting into (5.58) satisfies the following equation by the piecewise linear group delay distribution:

$$\left.\begin{array}{l} \tau_{2,1} = \tau_{1,1} + \Delta_1 \\ \tau_{3,1} = \tau_{2,1} + \Delta_2 \\ \vdots \\ \tau_{k+1,1} = \tau_{k,1} + \Delta_k \\ \vdots \end{array}\right\} \Rightarrow \underset{(\tau_{1,1} \equiv \overline{\tau}_{g,1})}{\tau_{k+1,1} = \overline{\tau}_{g,1} + \sum_{j=1}^{k} \Delta_j} \tag{5.60}$$

The definition of the group delay variation in each segment implies the sign of the variable Δ_k, which must be accounted for in the algebraic sum in Equation (5.60). Figure 5.38 gives an example of this issue where the delay value $\overline{\tau}_{g,min}$ is obtained according to Equation (5.60) as $\overline{\tau}_{g,min} = \tau_{3,1} = \tau_{1,1} + \Delta_1 - |\Delta_2|$.

5.4.4.4 Inverse Hyperbolic Tangent Distribution

The multimode impulse response of the optical fiber depends on two fundamental factors: the group delay distribution at the source average wavelength and the source power coupling coefficient distribution. In the following uniform mode excitation will continue to be assumed, launching the same amount of optical energy into each mode group. Under uniform mode excitation, the impulse response will no longer depend on the launch conditions but instead, for a given chromatic impulse response, it will be governed by the group delay distribution. In previous sections it was observed how different the multimode impulse response could be by selecting the mode number, the delay distribution and the mode excitation parameter set.

The scope of this section is to introduce some general criteria for the group delay profile in order to have a regular, axial-symmetric, single-body and bell-shaped multimode impulse response. Which general criteria should satisfy the group delay distribution for having such a multimode impulse response while assuming uniform excitation? To answer this question a start could be made using some conclusions obtained after the previous computed multimode impulse responses.

1. Assuming a single-peak Gaussian-shaped source spectrum, the chromatic impulse response of each supporting mode closely resembles a Gaussian pulse. This is due to the relatively narrow linewidth of the light source with respect to the scale of variation of the group delay function that allows a linear delay approximation.
2. High density of allowable mode group delays induces a smoothed peak formation in the multimode impulse response. This effect is due to the relevant overlapping of adjacent Gaussian-shaped chromatic impulse responses.
3. Symmetric group delay distribution corresponds to a balanced precursor and postcursor distribution, leading to a symmetric multimode impulse response around the ensemble average group delay.
4. In order to model infinite time length tails of the multimode impulse response, the group delay distribution must have vertical asymptotes corresponding to extreme values of the modal index. The infinite time extent response does not have any direct physical justification, but this is a useful mathematical feature that can be adjusted to fit both experimental data and required test pulse performances. Gaussian modeling of physical events is an example of this conceptual approach.

One possible candidate for the group delay distribution that satisfies both the last three requirements is the inverse hyperbolic tangent. This function has odd symmetry; it has an inflection point with a minimum derivative value at the origin and it exhibits two vertical asymptotes. In order to generalize the modeling capabilities of the function, the inverse hyperbolic tangent function is defined by introducing three parameters as follows:

$$
\begin{aligned}
&y(x) = a + \frac{c}{2}\log\left(\frac{1+bx}{1-bx}\right), \quad |x| < \frac{1}{|b|} \\
&y(0) = a, \quad \lim_{x\to\pm 1/b} y(x) = \pm\infty \\
&\frac{\mathrm{d}y}{\mathrm{d}x} = \frac{bc}{1-b^2x^2} \Rightarrow \begin{cases} \left(\dfrac{\mathrm{d}y}{\mathrm{d}x}\right)\Big|_{x=0} = bc \\ \left(\dfrac{\mathrm{d}y}{\mathrm{d}x}\right)\Big|_{x=1} = \dfrac{bc}{1-b^2} \end{cases}
\end{aligned}
\tag{5.61}
$$

The physical meaning of the three parameters a, b and c is evident: they are related to the reference group delay at the source average wavelength, to the slope at the $|x| = 1$ and to the slope of the inflection point at the origin respectively. Assuming uniform excitation, the product bc is

directly related to the multimode impulse response full-width at half-maximum. In fact, the lower the *bc* product, the lower is the slope at the inflection point according to Equation (5.61), and the modal chromatic impulse responses will concentrate closer to the reference delay. The resulting multimode superposition will therefore be strongly peaked at the reference group delay with a narrow full-width at half-maximum value.

Using physical variables, the discrete version of expression (5.61) becomes

$$\tau(h) = \tau_r + \frac{\gamma}{2}\log\left[\frac{1+\frac{2\kappa}{M}\left(h-\frac{M+1}{2}\right)}{1-\frac{2\kappa}{M}\left(h-\frac{M+1}{2}\right)}\right], \quad h \in N(1, M) \tag{5.62}$$

where $\tau(h)$ is used to indicate the group delay value for the hth excited mode, evaluated at the source average wavelength. Dependence of the discrete variable h has been explicitly reported in parentheses. The parameter κ controls the curvature of the discrete inverse hyperbolic tangent closer to the extremes $h = 1$ and $h = M$, while the parameter γ sets the slope of the inflection point at the reference group delay. The parameter γ has the dimension of normalized delay and sets the timescale of group delay variation. The physical meaning and limitation of these shaping parameters will be discussed below.

When the total mode number is odd, the reference group delay τ_r is associated with the mode index $h_r = (M + 1)/2$, which has been set equal to the average value of the modal index interval. This value can either belong or not to the discrete indices. However, this choice ensures a symmetric variation around the central symmetry of the inverse hyperbolic tangent. Below are reported significant values of the discrete inverse hyperbolic tangent distributions for even mode numbers M:

$$\begin{aligned}
&h = 1 \Rightarrow \tau(1) = \tau_r + \frac{\gamma}{2}\log\left[\frac{1-\kappa(M-1)/M}{1+\kappa(M-1)M}\right] \\
&h = M \Rightarrow \tau(M) = \tau_r + \frac{\gamma}{2}\log\left[\frac{1+\kappa(M-1)/M}{1-\kappa(M-1)/M}\right] \\
&h = \frac{M}{2} \Rightarrow \tau\left(\frac{M}{2}\right) = \tau_r + \frac{\gamma}{2}\log\left(\frac{1-\kappa/M}{1+\kappa/M}\right) \\
&h = \frac{M}{2}+1 \Rightarrow \tau\left(\frac{M}{2}+1\right) = \tau_r + \frac{\gamma}{2}\log\left(\frac{1+\kappa/M}{1-\kappa/M}\right)
\end{aligned} \tag{5.63}$$

From Equations (5.63), using the property of the logarithmic function, it follows that

$$\tau(1) - \tau_r = \tau_r - \tau(M), \qquad \tau\left(\frac{M}{2}\right) - \tau_r = \tau_r - \tau\left(\frac{M}{2}+1\right) \tag{5.64}$$

Figure 5.39 reports a qualitative drawing of the inverse hyperbolic tangent distribution of the group delay, according to Equations (5.63). The most important parameter values have been indicated for illustration.

One more remark is useful about the choice of the total mode number M:

- M is even. If the mode number M is even, both indices $h = M/2$ and $h = M/2 + 1$ referred to in Equations (5.63) are integers and are valid numbers for identifying mode groups. The reference group delay τ_r instead cannot be associated with a particular mode group because $h_r = (M + 1)/2$ would not be a valid mode index. In this case τ_r is just assumed to be the reference value around which the total delay variation can be added symmetrically according to Equation (5.62). This is the reason for specifying the relationships (5.63) only for the even mode number M.

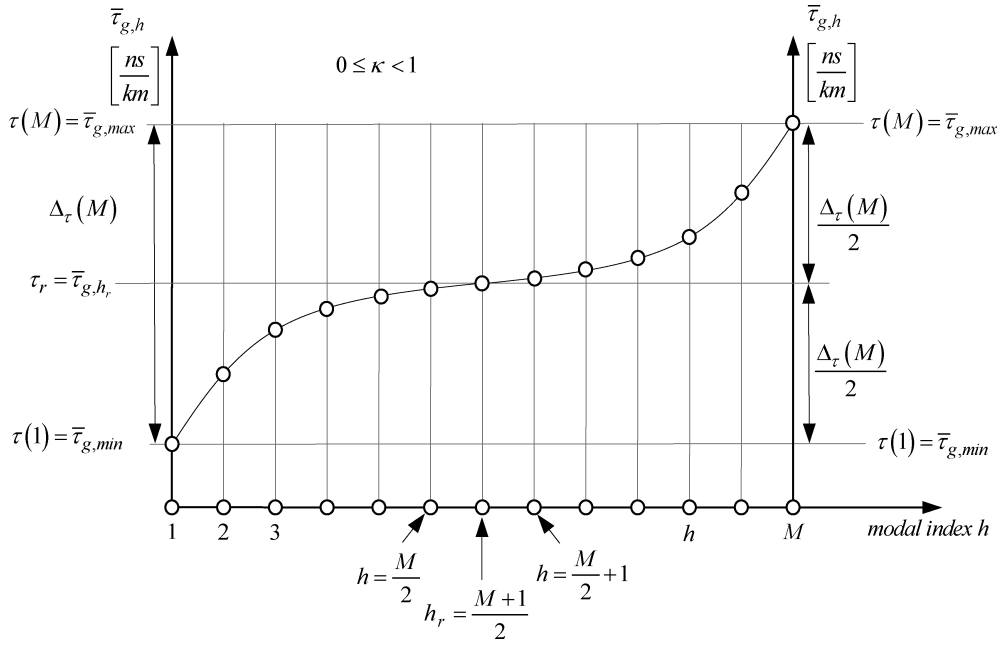

Figure 5.39 Qualitative representation of the inverse hyperbolic tangent group delay distribution according to Equations (5.63). This particular function allows symmetric mode concentration around the reference group delay τ_r, which therefore assumes the meaning of the average delay. Low-order and high-order modes give a symmetric tail contribution generating a symmetric bell-shaped profile which often closely resembles a Gaussian pulse

- M is odd. When the mode number is odd, the reference delay τ_r is associated with the index $h_r = (M+1)/2$ and the two adjacent modes become $h = (M+1)/2 - 1$ and $h = (M+1)/2 + 1$, as reported in Figure 5.39 for the case $M = 13$.

5.4.4.4.1 Shaping parameters κ and γ

The discrete inverse hyperbolic tangent distribution (5.62), evaluated at the two extreme indices $h = 1$ and $h = M$, assumes the corresponding values $\tau(1)$ and $\tau(M)$ reported in Equations (5.63). In order to have both values finite and positive, the logarithmic argument in Equations (5.63) must be greater than one. If

$$|\kappa| < 1 \tag{5.65}$$

the argument of the logarithmic function is positive for every large mode number M, leading to physical consistent results. The difference between $\tau(M)$ and $\tau(1)$ represents the total group delay variation $\Delta_\tau(M)$ evaluated among all M excited modes. From Equations (5.63) and (5.64) the following expression for the total group delay variation is obtained:

$$\Delta_\tau(M) \equiv \tau(M) - \tau(1) = \gamma \log\left[\frac{1 + \kappa(M-1)/M}{1 - \kappa(M-1)/M}\right] \tag{5.66}$$

The dependence of the group delay variation over the finite number of modes M has been explicitly indicated in order to distinguish it from the asymptotic value for $M \to \infty$.

To find the relationship between the parameters κ and γ, it is convenient to consider the case of an indefinitely large mode number, with $M \to \infty$. To this purpose, the limit of the two distributions

$\tau(1)$ and $\tau(M)$ in Equations (5.63) is evaluated for $M \to \infty$:

$$\begin{aligned} \lim_{M\to\infty} \tau(1) &= \tau_\tau + \frac{\gamma}{2}\log\left(\frac{1-\kappa}{1+\kappa}\right) \\ \lim_{M\to\infty} \tau(M) &= \tau_\tau + \frac{\gamma}{2}\log\left(\frac{1+\kappa}{1-\kappa}\right) \end{aligned} \tag{5.67}$$

Here the consistency of the requirement (5.65) for the parameter κ can clearly be seen. No limitation exists instead for the second shaping parameter γ, and so $|\gamma| < +\infty$. The limits in Equations (5.67) constitute a relationship between the two parameters κ and γ. From Equations (5.66) and (5.67) it can be concluded that the group delay variation $\Delta_\tau(M)$ tends to the following limiting value Δ_τ for indefinitely large mode number $M \to +\infty$:

$$\Delta_\tau \equiv \lim_{M\to\infty} \Delta_\tau(M) = \gamma \log\left(\frac{1+\kappa}{1-\kappa}\right) \tag{5.68}$$

and

$$\gamma = \frac{\Delta_\tau}{\log[(1+\kappa)/(1-\kappa)]} = \frac{\Delta_\tau}{2\tanh^{-1}(\kappa)} \tag{5.69}$$

Inverting Equation (5.68), the expression for κ can be found in terms of Δ_τ and γ:

$$e^{\Delta_\tau/\gamma} = \frac{1+\kappa}{1-\kappa} \Rightarrow \kappa = \frac{e^{\Delta_\tau/\gamma}-1}{e^{\Delta_\tau/\gamma}+1} = \frac{e^{+\Delta_\tau/(2\gamma)} - e^{-\Delta_\tau/(2\gamma)}}{e^{+\Delta_\tau/(2\gamma)} + e^{-\Delta_\tau/(2\gamma)}} \tag{5.70}$$

or

$$\kappa = \tanh\left(\frac{\Delta_\tau}{2\gamma}\right)$$

In conclusion:

1. The shaping parameter κ is related to the curvature of the distribution in regions close to both low-order and high-order mode delays and is given by Equations (5.70). Values closer to one correspond to a smaller curvature radius (steeper curvature).
2. The shaping parameter γ is related to the slope at the inflection point of the reference group delay and is given by Equation (5.69).
3. For a large but still finite mode number M, the group delay variation will be upward bounded by Δ_τ when the parameters γ and κ satisfy either Equation (5.69) or Equations (5.70).
4. Only two parameters among γ, κ and Δ_τ are independent, the third one being related through Equation (5.69) or Equations (5.70).

5.4.4.5 Simulation Results

In the followings pages some computed multimode impulse responses are presented, where an inverse hyperbolic tangent group delay distribution according to Equation (5.62) is assumed. The total delay variation Δ_τ and the shaping factor κ are chosen as an independent set of parameter, and the shaping parameter γ is determined by the relationship (5.69). For every finite mode number M the total group delay variation $\Delta_\tau(M)$ supported by the inverse hyperbolic tangent distribution is given by Equation (5.66). Two different shaping factors κ with assumed very low and very large mode number cases respectively are considered. Both the total group delay variation and the excitation are assumed to be the same among all the computed cases. As a consequence, the four computed multimode impulse responses differentiate with respect to the shaping factor and the mode numbers.

5.4.4.5.1 Configuration 1: $\kappa = 0.999$, $M = 20$, $q = 1$, $\Delta_\tau = \pm 2\,ns/km$

Due to the low number of modes, the energy distributed to each excited mode is relatively higher, but the modes are quite sparsely distributed. This leads to the multimode impulse response presented in Figure 5.40. As usual, individual weighted mode contributions are shown together with their superposition.

As expected, higher concentrations of modes around the average delay makes the central part of the superposed impulse response highly peaked, resembling a Gaussian pulse. The two symmetrical side peaks correspond to the lowest- and highest-order modes, which experience corresponding extreme delays. The symmetry of the inverse hyperbolic tangent together with the uniform excitation makes the mirrored multimode impulse responses corresponding to both positive and negative total group delays quite symmetrical, as clearly shown in Figure 5.41. In particular in the left plot, corresponding to the positive group delay variation, the lowest-order mode is associated with the lowest group delay. The right plot refers to the negative group delay and the lowest-order mode exhibits a higher group delay, as reported in Figure 5.40.

5.4.4.5.2 Configuration 2: $\kappa = 0.999$, $M = 2000$, $q = 1$, $\Delta_\tau = \pm 2\,ns/km$

The following simulation has the same configuration as the first case, except for the much larger number of excited modes, $M = 2000$. Owing to the uniform excitation, a corresponding two orders of magnitude lower energy is distributed to each mode, with two orders of magnitude higher density over the same total group delay variation. This leads to the superposition of a very tight chromatic impulse response, which gives a more smoothed multimode impulse response. Figure 5.42 shows the group delay distribution and the corresponding uniform excitation. Figure 5.43 presents the impulse response.

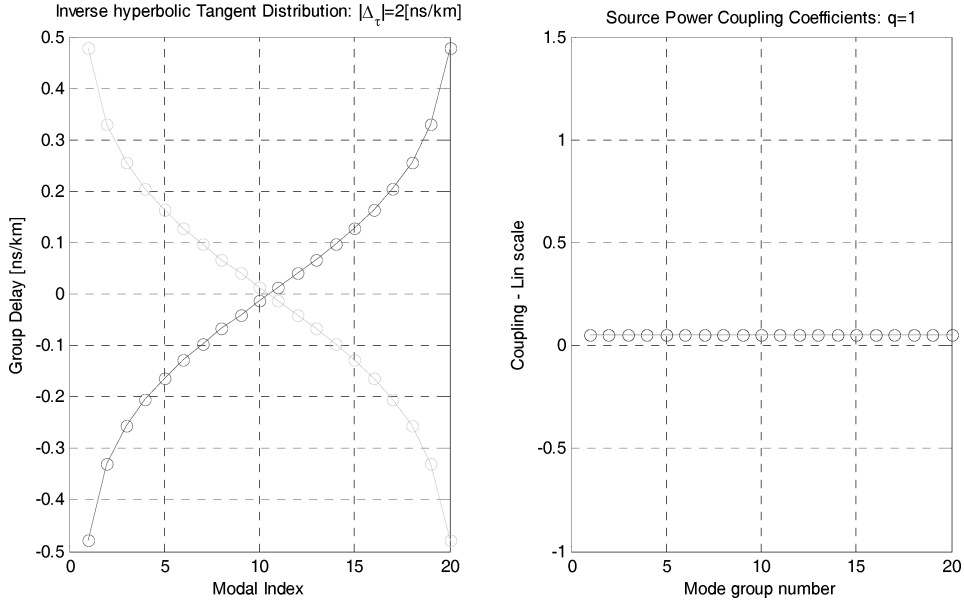

Figure 5.40 Computed group delay distribution (left) with uniform excitation $q = 1$, according to the inverse hyperbolic tangent with $M = 20$, $\kappa = 0.999$, $\Delta_\tau = \pm 2$ ns/km. The group delay variation is $\Delta_\tau(M) = 0.959$ ns/km. Both positive and negative delay variations are reported

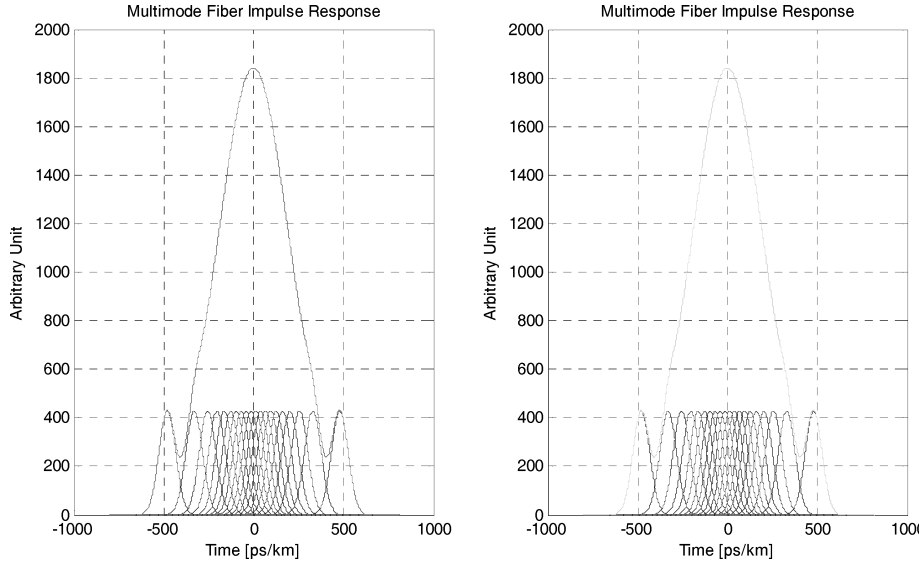

Figure 5.41 Computed multimode impulse response for the case shown in Figure 5.40. The left graph refers to the positive group delay variation while the right graph reports the case of the negative group delay. Due to the symmetry of the inverse hyperbolic tangent and the uniform excitation both impulse responses are almost identical. Negligible differences are due to the slight asymmetry of the chromatic impulse response with respect to the average value

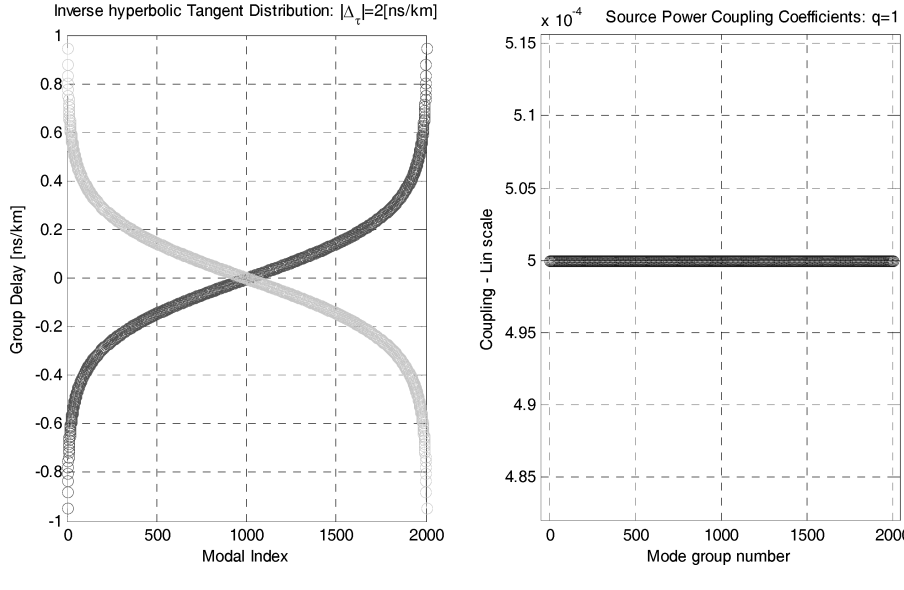

Figure 5.42 Computed group delay distribution (left) with uniform excitation $q = 1$, according to the inverse hyperbolic tangent with $M = 2000$, $\kappa = 0.999$, $\Delta_\tau = \pm 2\,\text{ns/km}$. The group delay variation is $\Delta_\tau(M) = 1.895\,\text{ns/km}$, closer to the asymptotic value $\Delta_\tau = 2\,\text{ns/km}$. Both positive and negative delay variations are reported. The uniform source power coupling coefficient is $|a_h|^2 = 1/M = 5 \times 10^{-4}$

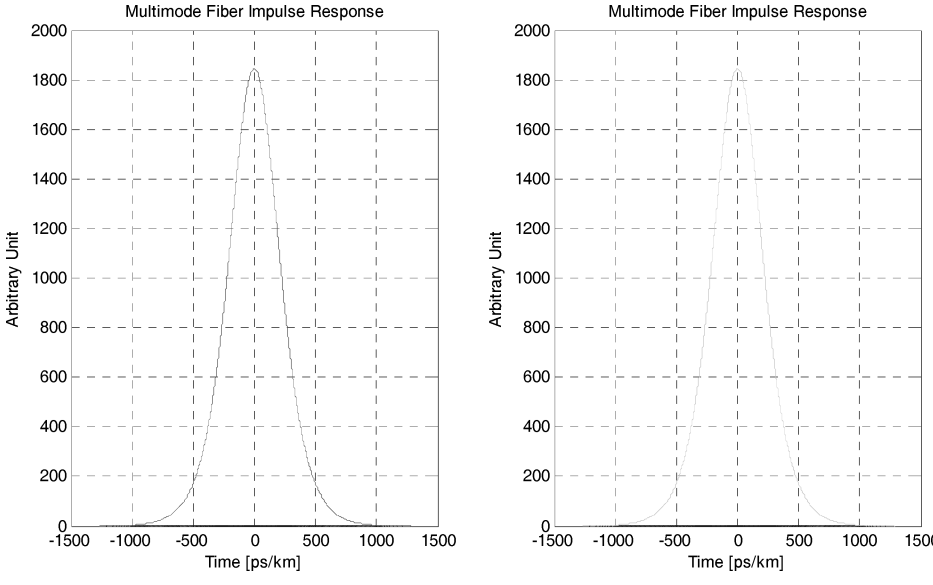

Figure 5.43 Computed multimode impulse responses for the case shown in Figure 5.42. Both positive and negative group delay impulse responses are reported. A higher density of allowed modes together with the inverse hyperbolic tangent distribution and uniform excitation makes the impulse response symmetrical and Gaussian shaped

This computational example reveals some already known conclusions. The multimode impulse response under the following three operating conditions:

(a) a large mode number ($M \to \infty$),
(b) a symmetrical group delay variation ($\kappa \to 1$, inverse hyperbolic tangent) and
(c) a uniform excitation ($q \to 1$),

has a symmetric, Gaussian-shaped profile. This result, even if referred to specific operating conditions, is quite important because in most practical design issues the multimode fiber is assumed to be almost Gaussian. In this sense, it is important to remember which mathematical modeling condition must be respected in order to have at least a Gaussian approximation of the multimode impulse response. In Chapter 6 the Gaussian approximation modeling will be discussed.

5.4.4.5.3 Configuration 3: $\kappa = 0.900$, $M = 20$, $q = 1$, $\Delta_\tau = \pm 2$ ns/km

In this case less pronounced curvature of the inverse hyperbolic tangent distribution is assumed by setting the shaping factor $\kappa = 0.900$ instead of $\kappa = 0.999$ as in configuration 1. The consequence is a slightly more uniform distribution of the group delays around the average value compared to configuration 1. Figure 5.44 shows the group delay distribution together with the uniform excitation for the low mode number case, $M = 20$. The lower shaping factor κ not only affects the curvature of the distribution but also changes the total excursion of the group delay. Comparing Figure 5.40 with Figure 5.44, it can be seen, for example, that the mode identified by the index $h = 15$ in the first case experiences a relative group delay of about $\tau_{15} \cong 13$ ps/km, while the same mode, again identified by the index $h = 15$, experiences more than twice the delay in the second case, with $\tau_{15} \cong 30$ ps/km. This difference is common for all modes between the two considered configurations. Those two effects, namely the reduced distribution curvature and the extended group delay variation, lead to

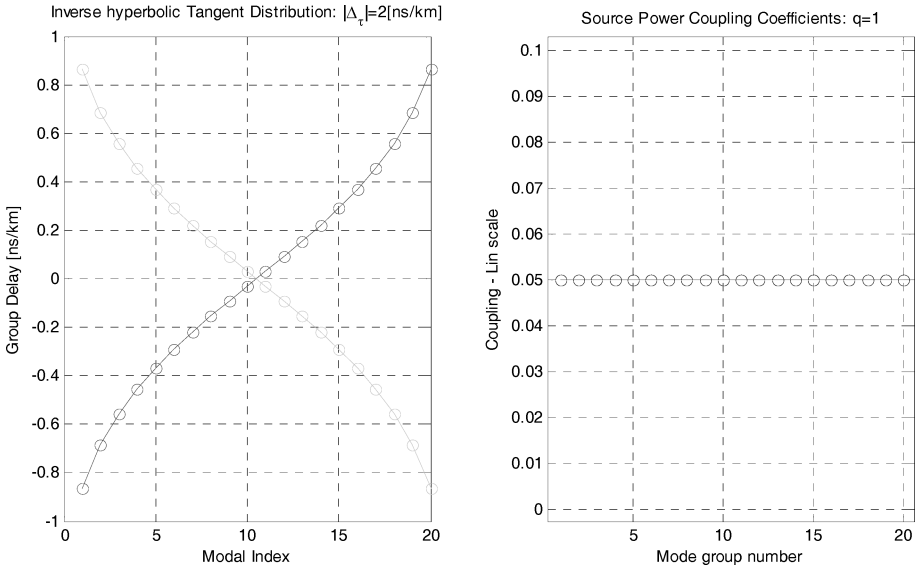

Figure 5.44 Computed group delay distribution (left) with uniform excitation $q = 1$, according to the inverse hyperbolic tangent with $M = 20$, $\kappa = 0.900$, $\Delta_\tau = \pm 2$ ns/km. The group delay variation is $\Delta_\tau(M) = 1.731$ ns/km and is much closer to the asymptotic value $\Delta_\tau = 2$ ns/km with respect to the case in Figure 5.40. Both positive and negative delay variations are reported. The uniform source power coupling coefficient is $|a_h|^2 = 1/M = 5 \times 10^{-2}$

a more pronounced granular aspect of the resulting multimode impulse response. This is clearly visible in the computed plots given in Figure 5.45, where the looser superposition of each chromatic impulse response gives the characteristic symmetrical ripple in the leading and trailing edges of the multimode impulse response.

5.4.4.5.4 Configuration 4: $\kappa = 0.900$, $M = 2000$, $q = 1$, $\Delta_\tau = \pm 2$ ns/km

In this last configuration, the same operating conditions are assumed as in the previous case, except for a much larger number of modes. Again, increasing the mode number while maintaining the same total group delay variation leads to a corresponding higher density of excited modes per unit delay. This mostly eliminates the granular profile of the resulting multimode impulse response, as clearly shown in Figures 5.46 and 5.47.

The multimode impulse response shown in Figure 5.47 is identical in the central body section to the result presented in Figure 5.45. The main difference is in the leading and trailing edges, which are completely smoothed with respect to the granular aspect they both have in the response shown in Figure 5.45. The superposed pulse is symmetrical but in this case the Gaussian interpolation does not fit as well as that in configuration 2. This is essentially due to the lack of smoothed tails in this impulse response due to the lower value of the κ parameter, which leads to a delay distribution much less dense in both extreme regions of low and high index numbers.

5.4.4.6 Conclusions

These simulation results close the section on computer modeling of the multimode impulse response. Several configurations have been considered and the effects have been seen of all the modeling parameters in shaping the impulse response output. Again, the relevant role of both the group delay and source power coupling coefficient distributions have been confirmed in defining the multimode

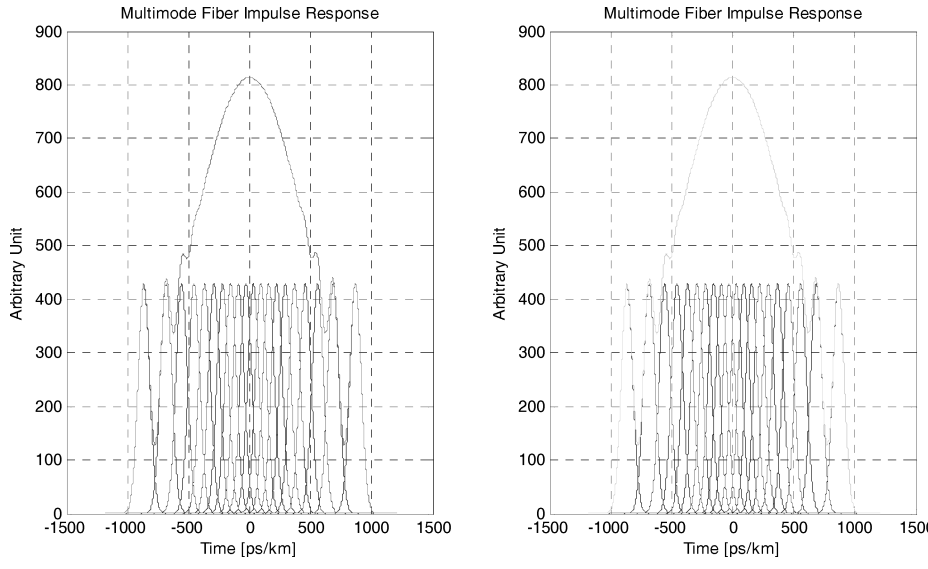

Figure 5.45 Computed multimode impulse response for the case shown in Figure 5.44. Both positive and negative group delay impulse responses are reported. A lower density of excited modes makes the superposition looser than in configuration 1, leading to a more granular multimode impulse response with a pronounced ripple at both the leading and trailing edges. The central body is still smoothed

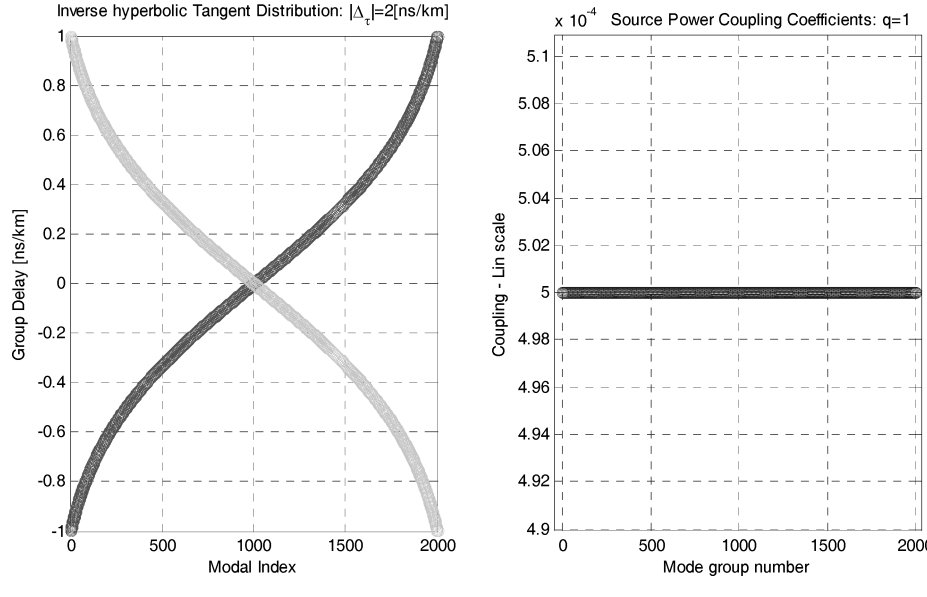

Figure 5.46 Computed group delay distribution (left) with uniform excitation $q = 1$, according to the inverse hyperbolic tangent with $M = 2000$, $\kappa = 0.900$, $\Delta_\tau = \pm 2$ ns/km. The group delay variation is $\Delta_\tau(M) = 1.997$ ns/km, almost approximating the asymptotic value $\Delta_\tau = 2$ ns/km. Both positive and negative delay variations are reported. The uniform source power coupling coefficient is $|a_h|^2 = 1/M = 5 \times 10^{-4}$

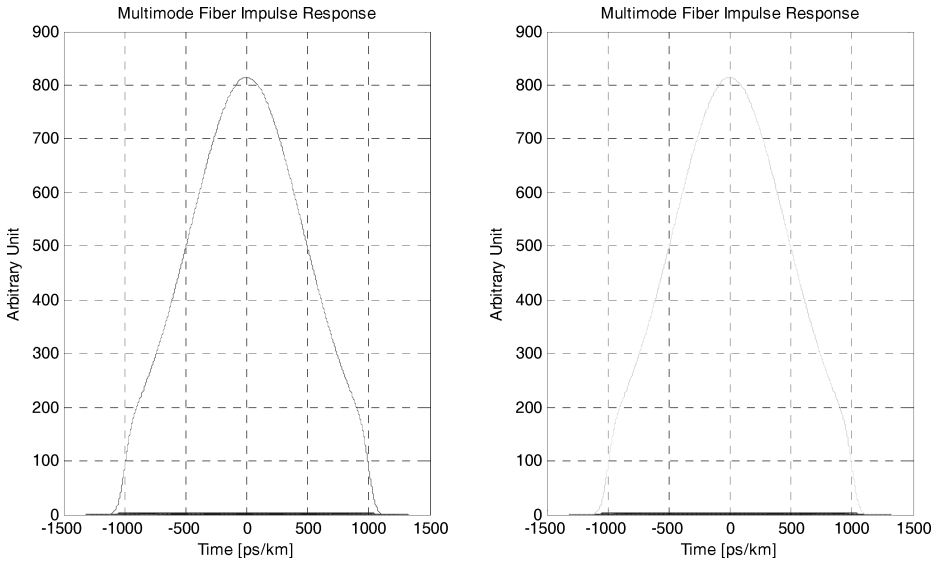

Figure 5.47 Computed multimode impulse response for the case shown in Figure 5.46. A higher density of excited modes makes the superposition tighter than in configuration 3, leading to a more smoothed multimode impulse response with sharp tails at both the leading and trailing edges

impulse response. The first distribution depends directly on the level of delay equalization achieved during the multimode fiber design and manufacturing, while the second distribution depends exclusively on the adopted launching conditions. The source spectrum and the consequent chromatic impulse response usually play a minor role in defining the multimode impulse response, especially for large numbers of modes where the output pulse granularity due to the single-mode contribution is almost negligible. Gaussian modeling is an interesting candidate for system design when the required conditions for a symmetric bell-shaped impulse response can be fulfilled. As stated above, the Gaussian modeling condition can be summarized as having both a symmetric, center denser, group delay distribution and an almost uniform mode excitation. While the excitation requirement can be approximated by means of the over-filled launch technique, the first condition remains in almost every case just a useful assumption that is almost never verified or controllable. This last issue makes the Gaussian modeling a simple but still quite questionable tool.

5.5 Theory of Multimode Frequency Response

The theory of the impulse response of the multimode fiber developed in Section 5.3 was written directly in the time domain, assuming only the superposition principle as the basic physical requirement for composing all the modal contributions. This is an important prerequisite, which is usually common to several signal or circuit simulators. The modeling architecture is first developed in the time domain by means of both linear assumptions among the physical quantities involved and the related set of linear equations. The solution is directly obtained in the time domain whereas the frequency domain is derived through the Fourier integral.

The linearity of the optical field together with the orthogonal property of the modal decomposition of the electromagnetic field led to the superposition principle with respect to the transmitted optical power. This allows summing of the intensity contribution of each excited fiber mode. Mode orthogonality in fact guarantees that the intensity contribution of each field cross-term vanishes

when the power is calculated by integrating the Poynting vector of each mode pair over the infinite fiber cross-section. In other words, if the fiber supports M guided modes, the multimode impulse response in terms of the intensity of the optical field is given by the weighted sum of the intensities of all M impulse responses.

The theory of the multimode fiber frequency response will be derived from the impulse response by means of the well-known Fourier integral theory. The linearity of the impulse response in fact guarantees the applicability of the Fourier transform properties, reducing the theory of the multimode fiber impulse response mainly to an application of the Fourier transform technique. Nevertheless, many interesting features of the frequency response will be introduced and analyzed in terms of the multimode fiber bandwidth and frequency profile.

5.5.1 Basic Concepts and Definitions

If the signal $f(t)$ of the temporal real variable t belongs to the space $L^1(\Re)$, and therefore it is absolutely integrable on the whole real axis $\Re$:

$$f(t) \in L^1(\Re) \Rightarrow \int_{-\infty}^{+\infty} |f(t)|\,\mathrm{d}t < +\infty \tag{5.71}$$

then the function $f(t)$ admits the Fourier integral representation $F(\omega)$:

$$f(t) \in L^1(\Re) \Rightarrow F(\omega) = \int_{-\infty}^{+\infty} f(t)\ \mathrm{e}^{-\mathrm{j}\omega t}\,\mathrm{d}t \tag{5.72}$$

The following basic equation, known as the inversion formula, permits the representation of the function $f(t)$ in terms of its Fourier integral $F(\omega)$:

$$f(t) = \frac{1}{2\pi}\int_{-\infty}^{+\infty} F(\omega)\ \mathrm{e}^{+\mathrm{j}\omega t}\,\mathrm{d}\omega \tag{5.73}$$

The temporal real variable t and the frequency real variable ω constitute the conjugate domains of the Fourier integral representation of the function $f(t)$. The Fourier transform pair is indicated as $f(t) \overset{\Im}{\leftrightarrow} F(\omega)$ and establishes a biunivocal relationship between the two functional representations. The properties and the relationships between the two space representations of the Fourier integral theory will not be discussed further, but instead the reader is referred to the book by A. Papoulis, which is a valuable reference on this subject.[1]

The time domain representation of the multimode fiber impulse response has been derived in Equation (5.20). For the sake of clarity, the same expression is given again:

$$h_{\mathrm{F}}(z, t, \overline{\lambda}) = \sum_{h=1}^{M} |a_h(\overline{\lambda})|^2 h_{\mathrm{c},h}[z, t - z(\overline{\tau}_{\mathrm{g},h} - \overline{\tau}_{\mathrm{c},h})]$$

According to the definition of the frequency response of a single-port, time-invariant linear system, the Fourier transform of the multimode impulse response (5.20) is taken. Using the linear property and the time-shifting theorem of the Fourier transform, it is easy to derive the frequency response of the multimode fiber:

$$H_{\mathrm{F}}(z, \omega, \overline{\lambda}) = \Im[h_{\mathrm{F}}(z, t, \overline{\lambda})] = \sum_{h=1}^{M} |a_h(\overline{\lambda})|^2 \Im\left\{h_{\mathrm{c},h}[z, t - z(\overline{\tau}_{\mathrm{g},h} - \overline{\tau}_{\mathrm{c},h})]\right\} \tag{5.74}$$

[1] A. Papoulis, *The Fourier Integral and Its applications*, McGraw-Hill, 1987.

Using the time-shifting theorem:

$$\Im[f(t-t_0)] = \mathrm{e}^{-\mathrm{j}\omega t_0}\Im[f(t)] = \mathrm{e}^{-\mathrm{j}\omega t_0}F(\omega) \tag{5.75}$$

it is concluded from Equation (5.74) that the frequency response of the multimode fiber has the following general expression:

$$H_{\mathrm{F}}(z,\omega,\overline{\lambda}) = \sum_{h=1}^{M} |a_h(\overline{\lambda})|^2 H_{\mathrm{c},h}(z,\omega)\ \mathrm{e}^{-\mathrm{j}\omega z(\overline{\tau}_{\mathrm{g},h}-\overline{\tau}_{\mathrm{c},h})} \tag{5.76}$$

The function

$$H_{\mathrm{c},h}(z,\omega) = \Im[h_{\mathrm{c},h}(z,t)] \tag{5.77}$$

is the Fourier transform of the chromatic impulse response of the hth fiber mode.

5.5.2 Spectral Characteristics and Physical Properties

The multimode fiber frequency response (5.76) needs some discussion. First of all, the time-shifting theorem converts the modal delay translation into an equivalent shifting of the phase term. The weighting terms $|a_h(\overline{\lambda})|^2$ are the same as those defined in the time domain, but now they act over the phase components generated by the group delay distribution. These phase terms are represented by complex exponential factors $\Phi_h(z,\omega) = \mathrm{e}^{-\mathrm{j}\omega z(\overline{\tau}_{\mathrm{g},h}-\overline{\tau}_{\mathrm{c},h})}$.

5.5.2.1 Two Cascaded Linear Systems

In general, each mode has its own chromatic impulse response, which is represented by the h index of the chromatic impulse response $h_{\mathrm{c},h}(z,t)$ and average delay $\overline{\tau}_{\mathrm{c},h}$ indicated in formula (5.76) above. If it is assumed that all modes have almost the same chromatic impulse response, neglecting small differences due to second-order modal dispersion relationships, both the chromatic response and the relative phase term can be taken out of the summation in Equation [5.76], leading to the following approximated expression for the multimode fiber frequency response:

$$H_{\mathrm{F}}(z,\omega,\overline{\lambda}) \cong H_{\mathrm{c}}(z,\omega)\ \mathrm{e}^{+\mathrm{j}\omega z\overline{\tau}_{\mathrm{c}}} \sum_{h=1}^{M} |a_h(\overline{\lambda})|^2\ \mathrm{e}^{-\mathrm{j}\omega z\overline{\tau}_{\mathrm{g},h}} \tag{5.78}$$

The term in front of the summation symbol coincides with the frequency response of the time-centered chromatic impulse response:

$$\hat{H}_{\mathrm{c}}(z,\omega,\overline{\lambda}) \equiv \Im[\hat{h}_{\mathrm{c}}(z,t,\overline{\lambda})] = \Im[h_{\mathrm{c}}(z,t-z\overline{\tau}_{\mathrm{c}},\overline{\lambda})] \tag{5.79}$$

The average chromatic impulse response delay of $\hat{h}_{\mathrm{c}}(z,t,\overline{\lambda})$ is of course zero, $\overline{\tau}_{\mathrm{c}} = 0$, and the approximated frequency response (5.78) reduces to the simpler form:

$$H_{\mathrm{F}}(z,\omega,\overline{\lambda}) \cong \hat{H}_{\mathrm{c}}(z,\omega)\left[\sum_{h=1}^{M} |a_h(\overline{\lambda})|^2\ \mathrm{e}^{-\mathrm{j}\omega z\overline{\tau}_{\mathrm{g},h}}\right] \tag{5.80}$$

Note that there is no additional approximation between Equation (5.78) and the above expression. This is simply a definition of the centered chromatic impulse response. Of course, behind the modal delay affecting the average value of each chromatic impulse response there is an assumption that all the centered chromatic impulse responses are equal to each other, which reduces to having the same profile for each chromatic impulse response, regardless of the average delay. This hypothesis

coincides with assuming the same value of the second order propagation constant for each fiber mode.

The meaningful concept behind the approximated expression (5.80) is the separation of the multimode fiber system into two cascaded linear systems equivalent to the time-centered chromatic impulse response and the modal impulse response respectively. This comes directly from the mathematical expression (5.80) as a product of the two frequency responses.

5.5.2.2 The Modal Function

The expression (5.80), although approximated in the sense discussed above, is quite useful for understanding the physical interaction between modal propagation and chromatic dispersion. To this purpose, the modal function $\Upsilon(z, \omega, \overline{\lambda})$ is introduced:

$$\Upsilon(z, \omega, \overline{\lambda}) \equiv \sum_{h=1}^{M} |a_h(\overline{\lambda})|^2 \, \mathrm{e}^{-\mathrm{j}\omega z \tau_{\mathrm{g},h}(\overline{\lambda})} \tag{5.81}$$

This gives the frequency representation of the excited modal structure of the multimode fiber, without referring to any chromatic effect. It links the source power coupling coefficients with the corresponding modal delay, both evaluated at the source average wavelength $\overline{\lambda}$. Using the definition (5.81), the multimode frequency response (5.80) assumes the following form of product of two frequency-dependent functions:

$$H_{\mathrm{F}}(z, \omega, \overline{\lambda}) \cong \hat{H}_{\mathrm{c}}(z, \omega) \Upsilon(z, \omega, \overline{\lambda}) \tag{5.82}$$

According to this expression, the modal function $\Upsilon(z, \omega, \overline{\lambda})$ therefore assumes the meaning of the frequency shaping profile.

This conclusion is very relevant and needs a few more comments. First of all, in the frequency domain there is now the clear meaning of the usual negligible contribution of the chromatic dispersion in a multimode propagation regime. In fact, the short chromatic impulse response translates in the frequency domain into a broad, smoothed frequency response when compared to the narrow frequency occupancy of the modal function $\Upsilon(z, \omega, \overline{\lambda})$, leaving to the shaping profile $\Upsilon(z, \omega, \overline{\lambda})$ essentially the leading role in defining the multimode frequency response. In order to investigate further the nature of the modal function $\Upsilon(z, \omega, \overline{\lambda})$, the following particular case of uniform modal excitation will be considered.

5.5.2.3 Uniform Modal Excitation

Assuming uniform modal excitation, all coupling coefficients in Equation (5.80) must have the same value. Therefore, according to the energy normalization with M excited modes,

$$|a_h(\overline{\lambda})|^2 = \frac{1}{M} \tag{5.83}$$

Substituting in Equation (5.81), the following expression of the modal function is obtained:

$$\Upsilon(z, \omega, \overline{\lambda}) = \frac{1}{M} \sum_{h=1}^{M} \mathrm{e}^{-\mathrm{j}\omega z \overline{\tau}_{\mathrm{g},h}} \tag{5.84}$$

This approximated expression of the multimode fiber frequency response holds by virtue of the following two assumptions:

1. Each fiber mode has the same time-centered chromatic impulse response.
2. There is uniform excitation of M fiber modes.

Following the same approach used in the previous section, the value Δ_τ is assigned to the total modal delay per unit length. This means that every excited mode will present the group delay value within the interval Δ_τ:

$$\forall h \in N(1, M) \Rightarrow \overline{\tau}_{g,h} \in \Delta_\tau \tag{5.85}$$

At this point the third assumption is formulated:

3. The M group delay values $\overline{\tau}_{g,h}$ are uniformly distributed in the interval Δ_τ:

$$\forall h \in N(1, M) \Rightarrow \overline{\tau}_{g,h} = \frac{\Delta_\tau}{M-1} h \in \Delta_\tau \tag{5.86}$$

In order to simplify the mathematical description, an irrelevant phase term assuming that the total modal delay Δ_τ is centered on the time origin can be removed, and the modal indices can be reordered with corresponding positive and negative values for a total of $M+1$ symmetrically located modal delays. Accordingly, using the uniform spacing with $M+1$ modes, the modal function (5.84) assumes the following form:

$$\Upsilon(z, \omega, \overline{\lambda}) = \frac{1}{M+1} \sum_{h=-M/2}^{M/2} \mathrm{e}^{-\mathrm{j}\omega(z\Delta_\tau/M)h} \tag{5.87}$$

This expression is the discrete representation of the Fourier integral of the uniform time window pulse. Its Fourier transform is the well-known sinc function. In order to see this, each time instant $t_h = (z\Delta_\tau/M)h$ is defined. The time step is given by $\delta t = z\Delta_\tau/M = T/M$ and at the two extreme index values $h = \pm M/2$ the corresponding time instants are $t_{\pm M/2} = \pm z\Delta_\tau/2 = \pm T/2$. Substituting in Equation (5.87) gives

$$\Upsilon(z, \omega, \overline{\lambda}) = \frac{M}{M+1} \frac{1}{T} \sum_{h=-M/2}^{M/2} \mathrm{e}^{-\mathrm{j}\omega t_h} \delta t \tag{5.88}$$

At the limiting condition of infinite mode numbers $M \to \infty$, the sum merges into the continuous integration, leading to the well-known Fourier integral:

$$\Upsilon(z, \omega, \overline{\lambda}) = \frac{1}{T} \int_{-T/2}^{T/2} \mathrm{e}^{-\mathrm{j}\omega t}\, \mathrm{d}t = \mathrm{sinc}(\pi f T) = \frac{\sin(\pi f T)}{\pi f T} \tag{5.89}$$

Expressions (5.87) and (5.89) are equivalent: the first one is simply the discrete approximate representation of the Fourier integral for a finite mode number. Of course, the numeric solution of the sinc function must refer to the discrete sum in Equation (5.87). The result obtained here is a clear example of the effect of the shaping behavior of the modal function in Equation (5.82). The interaction between the chromatic frequency response and the modal frequency response, in this case, depends on the ratio between the resonance modal frequency $f_0 = 1/T$ and the corresponding bandwidth f_c of the chromatic frequency response.

As long as $f_c >> f_0$, the multimode frequency response will be essentially determined by the modal frequency response $\Upsilon(z, \omega, \overline{\lambda})$. In the top graph of Figure 5.48 a sketch is presented of the uniform distribution of the group delay assumed in the derivation of Equations (5.87) and (5.89), including the major parameters. It was assumed that there were $M+1$ modes, equally spaced with a uniform intensity distribution. Each mode has therefore a power coupling coefficient $|\overline{a}_h|^2 = 1/(M+1)$, while the spacing δt between adjacent mode delays is given by the total group delay $T = z\Delta_\tau$ divided by the number M of modal delay steps.

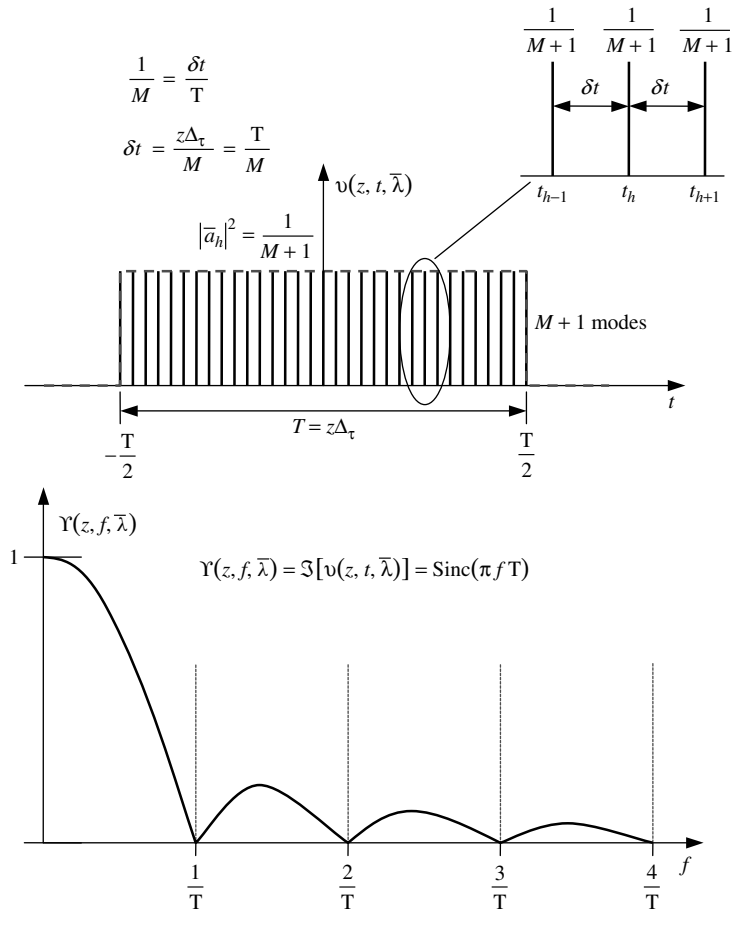

Figure 5.48 Top: uniform modal excitation distribution with uniformly spaced group delay samples. The height of each line represents the intensity coupled to the corresponding mode. The total width of all $M+1$ group delays coincides with the total delay per unit length Δ_τ. Bottom: modal function $\Upsilon(z, f, \overline{\lambda}) = \mathrm{sinc}(\pi f T)$ in the limit of the infinite mode number corresponding to the uniform excitation and uniformly spaced group delay samples. The total delay value is fixed at $T = z\Delta_\tau$

The computed results of expression (5.87) for increasing mode numbers compared with the numerical solution of the integral in Equation (5.89) are presented instead in Figure 5.49. The case reported here refers to $\Delta_\tau = 2\,\mathrm{ns/km}$ for the unit length $z = 1\,\mathrm{km}$, leading to the resonant frequency $f_0 = 1/T = 1/(z\Delta_\tau) = 500\,\mathrm{MHz}$. The vertical scale is reported in both linear and dB units to provide better evidence of the zero locations. The frequency scale is linear.

The expression (5.82) is of great conceptual importance since it allows the multimode fiber to be considered as being composed of a cascade of two linear systems, namely one system providing the chromatic impulse response and the other characterized by the modal impulse response. This conclusion has already been encountered in a previous time domain analysis, but the frequency domain picture highlights this significant representation. It should be remembered that factorization of the multimode fiber linear system into two independent and cascaded linear systems is allowed under the approximation of a unique time-centered chromatic impulse response common to every

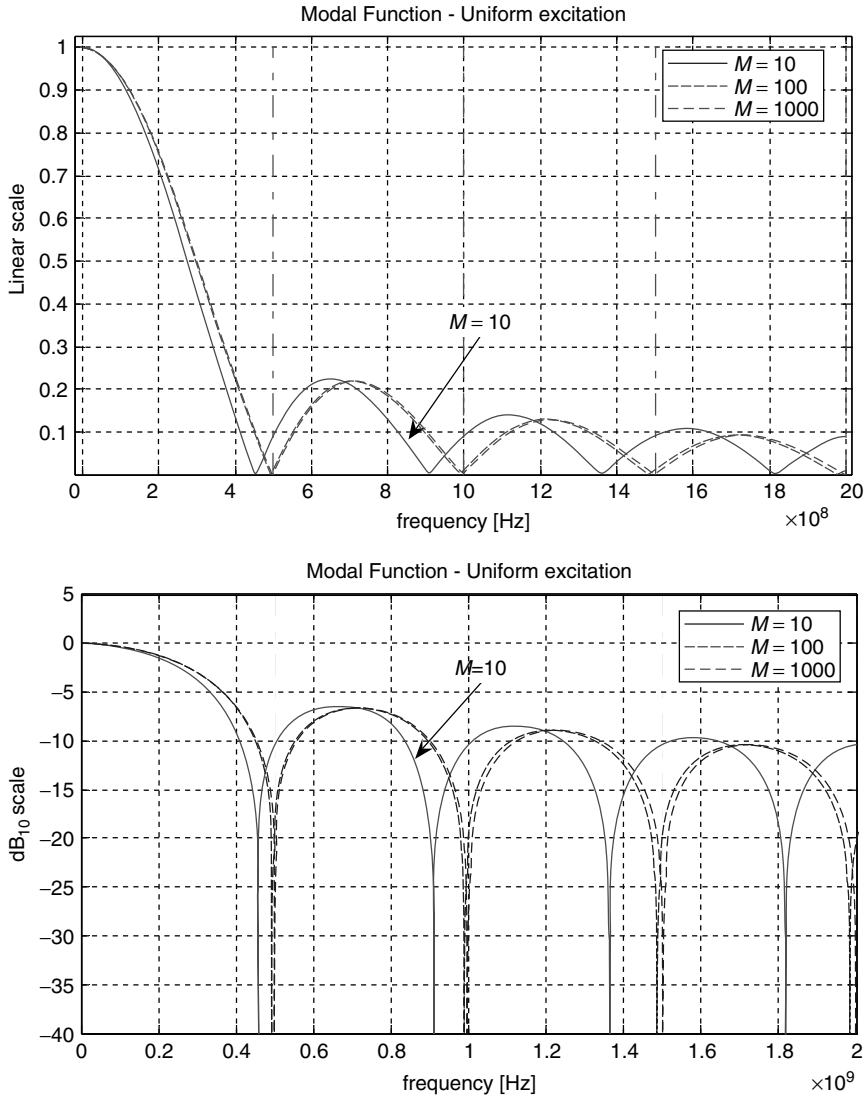

Figure 5.49 Computed modal function $\Upsilon(z, f, \overline{\lambda})$ for the case of uniform excitation with uniform group delay spacing for different mode numbers in linear (top) and logarithmic scales. By increasing the mode number the frequency profile of the modal function tends to the $\Upsilon(z, f, \overline{\lambda}) = \mathrm{sinc}(\pi f T)$ function reported in Equation (5.89). The case given here refers to a total group delay $\Delta_\tau = 2$ ns/km for the unit length $z = 1$ km, leading to the asymptotic resonant frequency $f_0 = 1/T = 1/(z\Delta_\tau) = 500$ MHz, indicated by dot–dash lines in both graphs

excited fiber mode. This assumption is widely verified since the physical parameters involved are related to the second-order derivative of the propagation constant, which is slightly affected by the waveguide contribution to the total dispersion relationship. However, the material dispersion is a common factor affecting all fiber modes in the same way. These results can be summarized by the following statement. If the time-centered chromatic response $\hat{H}_c(z, f, \overline{\lambda})$ is the same for

all excited fiber modes, then the frequency response $H_F(z, f, \overline{\lambda})$ of the multimode fiber is given by the product of the modal function $\Upsilon(z, f, \overline{\lambda})$ by the chromatic response $\hat{H}_c(z, f, \overline{\lambda})$. According to the approximate expression (5.82), once the modal function $\Upsilon(z, f, \overline{\lambda})$ is obtained, in order to compute the multimode fiber frequency response $H_F(z, f, \overline{\lambda})$, $\Upsilon(z, f, \overline{\lambda})$ needs to be multiplied by the Fourier transform of the centered chromatic impulse response $\hat{H}_c(z, f, \overline{\lambda})$.

In order to finalize the calculation to the uniform excitation case now being considered, the treatment is simplified for the moment assuming that the time-centered modal chromatic impulse response has a Gaussian shaping:

$$\hat{h}_c(z, t) = \frac{1}{\overline{\sigma}_t(z)\sqrt{2\pi}} \, e^{-t^2/[2\overline{\sigma}_t^2(z)]} \overset{\Im}{\longleftrightarrow} e^{-2\pi^2\overline{\sigma}_t^2(z)f^2} = \hat{H}_c(z, f, \overline{\lambda}) \tag{5.90}$$

The centered Gaussian chromatic frequency response $\hat{H}_c(z, f, \overline{\lambda})$, after multiplication by the modal function $\Upsilon(z, f, \overline{\lambda})$, leads to the total multimode response exhibiting the characteristic resonance frequencies corresponding to the reciprocal of the total group delay, as shown in Figure 5.50. Figures 5.51 to 5.54 present more response configurations.

5.5.2.4 Physical Interpretation of the Modal Function

In this section the case of a generic modal excitation will be considered, with no particular restriction on the source power coupling coefficient distribution. In order to continue using expression (5.82), only a mode independent and time-centered chromatic frequency response $\hat{H}_c(z, \omega)$ needs to be assumed. The expression of the modal function $\Upsilon(z, f, \overline{\lambda})$ is shown in Equation (5.81) and includes both any generic modal excitation $|\overline{a}_h|^2 = |a_h(\overline{\lambda})|^2$ and group delay distribution $\overline{\tau}_{g,h} = \tau_{g,h}(\overline{\lambda})$, where $\overline{\lambda}$ is the average wavelength of the spectral power density of the light source. In the following the fiber supports M modes and the modal index $h \in N\ (1, M)$. The modal function has a straightforward physical interpretation, which will be illustrated below. To this purpose, the expression for the modal impulse response, defined in Equation (3.53), is considered:

$$\upsilon(z, t, \overline{\lambda}) = \sum_{h=1}^{M} |\overline{a}_h|^2 \delta[t - z\overline{\tau}_{g,h}]$$

Both the group delay and the coupling coefficients are evaluated at the source average wavelength. By virtue of the linearity property and using the time-shifting theorem, the Fourier transform of the above modal impulse response has the following expression:

$$\Im[\upsilon(z, t, \overline{\lambda})] = \Im\left\{\sum_{h=1}^{M} |\overline{a}_h|^2 \delta[t - z\overline{\tau}_{g,h}]\right\} = \sum_{h=1}^{M} |\overline{a}_h|^2 \, e^{-j\omega z\overline{\tau}_{g,h}}$$

Comparing this with the definition (5.81) gives the fundamental result, which provides a physical interpretation of the definition given for the modal function. The modal function $\Upsilon(z, f, \overline{\lambda})$ coincides with the Fourier transform of the modal impulse response $\upsilon(z, t, \overline{\lambda})$ given in Equation (3.53), and assumes the meaning of the modal frequency response:

$$\Upsilon(z, f, \overline{\lambda}) = \Im[\upsilon(z, t, \overline{\lambda})] \tag{5.91}$$

This conclusion holds for every modal excitation defined through the coefficient distribution and for every general group delay distribution. The case of uniform excitation with uniformly spaced group delays considered in the previous section is, of course, a very special case, which gives a simple and useful understanding of the concepts behind the conclusion that has been achieved.

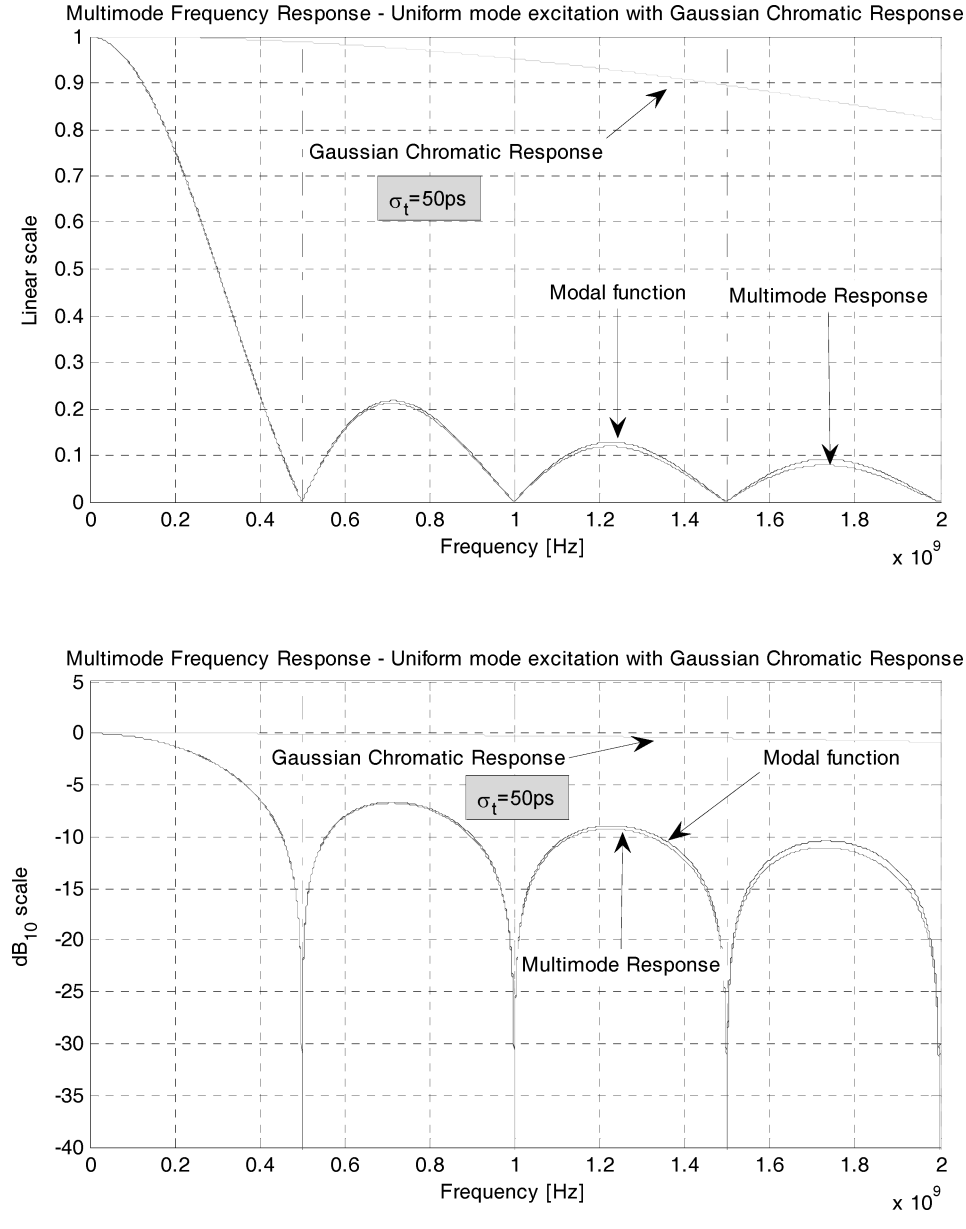

Figure 5.50 Computed multimode fiber frequency response respectively in the linear (top) and logarithmic (bottom) scales for the case of uniform modal excitation with total group delay per unit length $\Delta_\tau = 2\,\text{ns/km}$ over the fiber length $z = 1\,\text{km}$. The centered chromatic frequency response is Gaussian with the RMS width $\sigma_t = 50\,\text{ps}$. According to Equation (5.82), the multimode fiber frequency response is given by the product of the modal function $\Upsilon(z, f, \overline{\lambda}) = \text{sinc}(\pi f T)$ with the centered chromatic response $\hat{H}_c(z, f, \overline{\lambda})$. The relative broadband Gaussian response has a negligible effect on the total multimode response which is determined essentially by the modal function

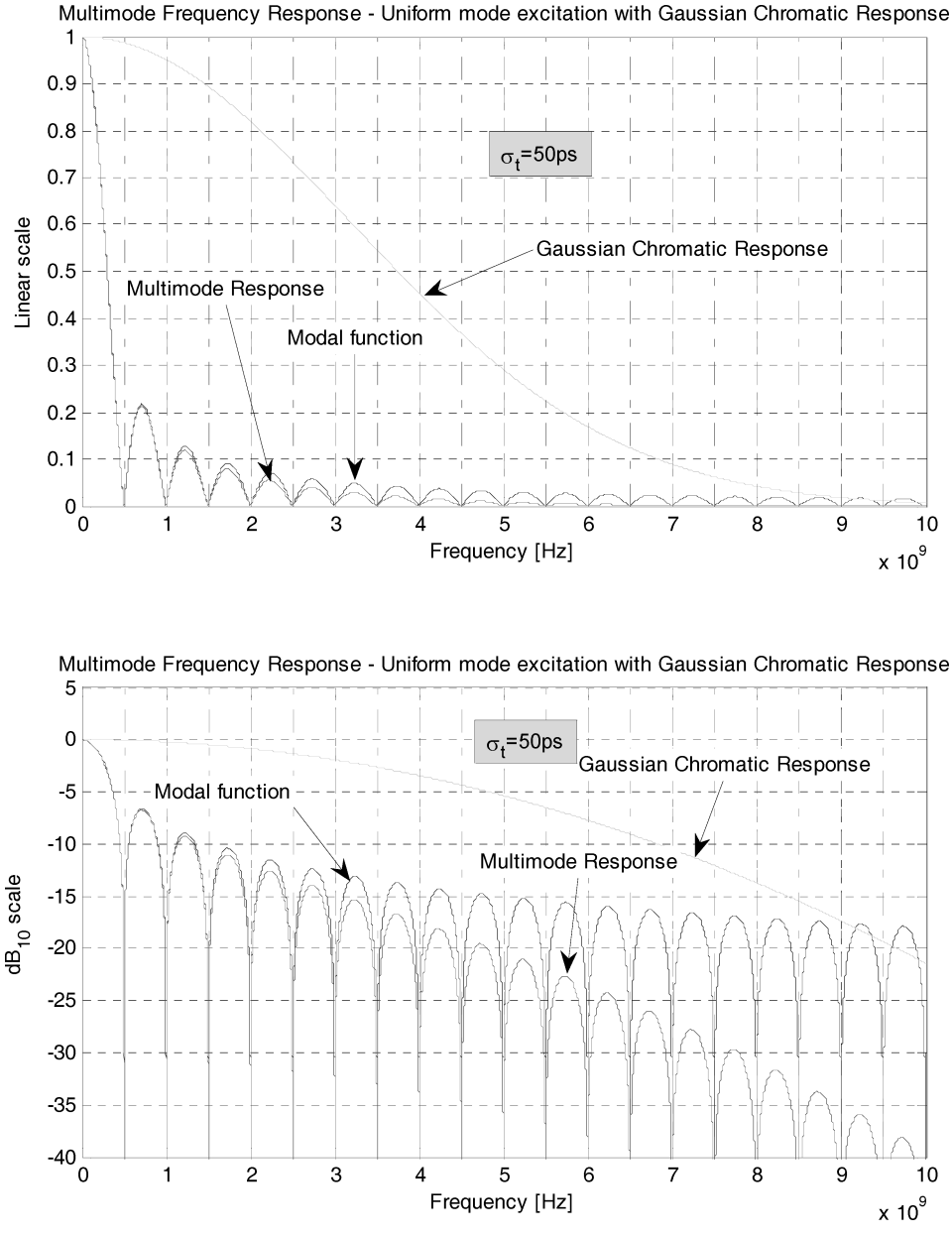

Figure 5.51 Same operating conditions as in Figure 5.50 computed using an extended frequency scale up to 10 GHz. The broadband Gaussian chromatic response starts to affect the multimode fiber response from approximately 4 GHz. At about the same frequency, the modal function is more then 13 dB down with respect to the low-frequency amplitude. The frequency multiples of the reciprocal of the total group delay time $T = z\Delta_\tau = 2\,\text{ns}$ are clearly visible as sharp notches with a period of $f_0 = 1/T = 500\,\text{MHz}$. The top graph shows the linear amplitude scale, while the bottom graph shows the logarithmic representation

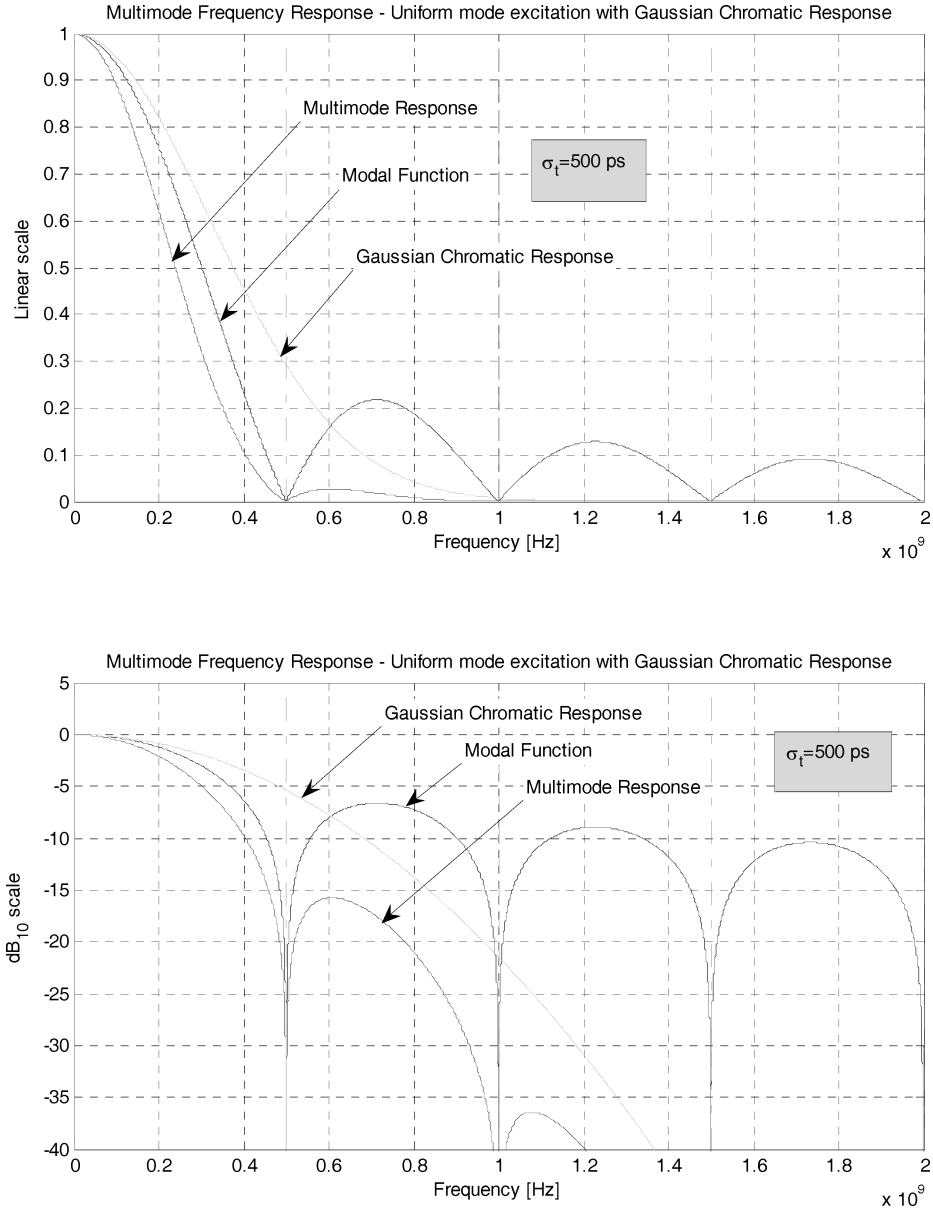

Figure 5.52 Computed multimode fiber frequency response for the case of uniform modal excitation with a total group delay per unit length $\Delta_\tau = 2\,\text{ns/km}$ over the fiber length $z = 1\,\text{km}$. The centered chromatic frequency response is Gaussian with the RMS width $\sigma_t = 500\,\text{ps}$. The relative narrowband Gaussian response has a sensible bandwidth reduction effect on the total multimode response, which still exhibits sharp notches due to the modal function

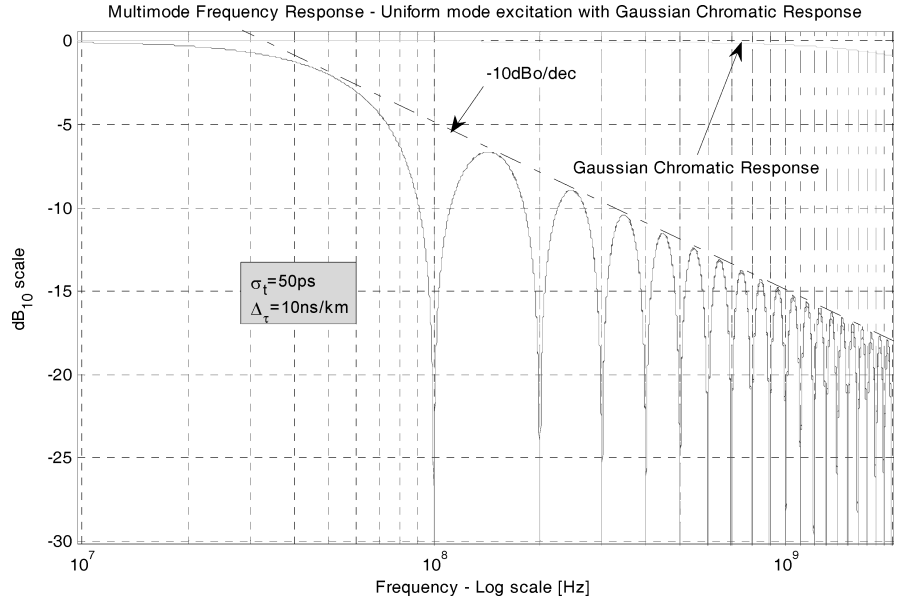

Figure 5.53 Computed multimode frequency response in the case of uniform modal excitation with a total group delay per unit length $\Delta_\tau = 10\,\text{ns/km}$ over the fiber length $z = 1\,\text{km}$, leading to a fundamental resonant frequency $f_0 = 1/T = 100\,\text{MHz}$. The chromatic frequency response is Gaussian with the RMS width $\sigma_t = 50\,\text{ps}$ with a negligible effect on the multimode fiber response

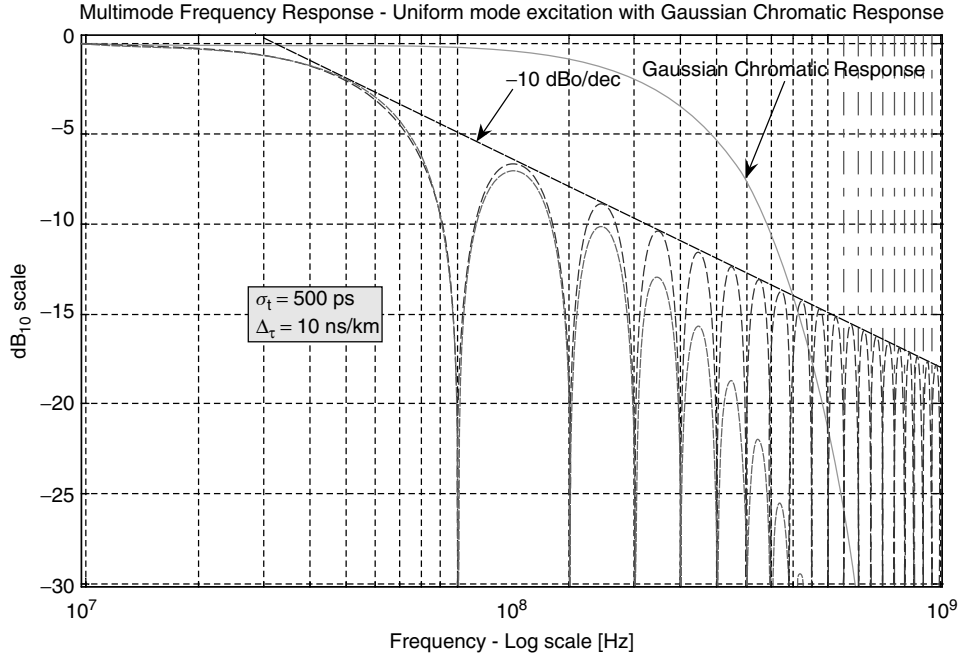

Figure 5.54 Same conditions as Figure 5.53, but with one order of magnitude slower chromatic impulse response, $\sigma_t = 500\,\text{ps}$. As expected, the chromatic response starts to affect the multimode fiber bandwidth

In general, it has been demonstrated that under the assumption that the time-centered chromatic response $\hat{H}_c(z, f)$ is the same for every excited mode, the multimode response is given by multiplying the modal function $\Upsilon(z, f, \overline{\lambda})$ by the time-centered chromatic response. This is the characteristic behavior of the frequency response of two time-invariant and independent cascaded linear systems. In terms of a physical interpretation this means that in the multimode fiber under the linear field regime, the profile of the chromatic response is approximately independent of the distribution of the optical power among all excited modes. Each mode is therefore assumed to respond to the source spectrum stimulus with the same impulse response, except for the characteristic group delay. The factorization of the multimode frequency response demonstrated in Equation (5.82) suggests the following physical picture of the multimode optical fiber response:

1. The spectral characteristics of the light source determine the chromatic impulse response profile of each excited mode.
2. The power of the light source is spatially partitioned into the excited modes by means of the launch conditions. Each mode delivers the amount of power after the characteristic group delay per unit length.
3. The group delay is evaluated at the average source wavelength, leaving the role of specifying the dependence from the source power spectral distribution to the chromatic response profile.
4. The chromatic and the modal responses do not interact, leading to the cascaded linear system model with the frequency response (5.82).
5. Changing the source power coupled distribution, without changing the source spectrum, affects the modal response only.
6. Given the group delay $\overline{\tau}_{g,h}$ and the coupling coefficient distributions $|\overline{a}_h|^2$ of M modes, the modal frequency response is given by the Fourier transform of the finite sequence of M impulses located at the group delay instants, whose area is given by the corresponding source power coupling coefficient.

In the next section some examples will be given of multimode frequency responses based on the approximated expression given in Equation (5.82). In order to find evidence of the profiling characteristic in the modal function $\Upsilon(z, f, \overline{\lambda})$, the same chromatic response used in Section 5.4.2.2 will be assumed.

5.5.3 Simulation of Multimode Frequency Responses

Table 5.7 summarizes major conclusions achieved during multimode frequency response modeling. In the following, both the computed modal functions $\Upsilon(z, f, \overline{\lambda})$ and the multimode impulse responses $h_F(z, t, \overline{\lambda})$ will be given using Equations (5.81) and (5.20) respectively. In the derivation of the multimode frequency response the same simulation environment that has already been used in Section 5.4.4.5 will be assumed.

The time-centered chromatic impulse response $\hat{h}_c(z, f)$ is calculated assuming a Gaussian source spectrum centered in the third window of a silica-based multimode fiber. As usual, the spectral dependence of the group delay is modeled using the three-term Sellmeier equation and it is assumed that there is no contribution to the modal dispersion relations except for the modal delay evaluated at the average wavelength of the source spectral power density. The modal delay distribution $\overline{\tau}_{g,h}$ versus the modal index is modeled assuming either a linear, quadratic or inverse hyperbolic tangent profile and the source power coupling coefficient distribution $|\overline{a}_h|^2 = |a_h(\overline{\lambda})|^2$ is modeled using the well-known geometric progression.

In the following five cases are presented, each of which is characterized by a specific issue. All cases considered present the same chromatic dispersion conditions, characterized by a single-peak Gaussian light source spectrum centered at $\lambda_c = 1550\,\text{nm}$ with $\text{FWHM}_t = 5\,\text{nm}$, which corresponds to an RMS width $\sigma_s = 2.12\,\text{nm}$. The total wavelength range spans for 30 nm between $\lambda_{min} =$

Table 5.7 Major equations derived in the text regarding the frequency response relationships of the multimode fiber. The last two columns give the validity of the equation and its reference in the text respectively

Parameter	Expression	Validity	Reference
Multimode impulse response	$h_{\mathrm{F}}(z,t,\overline{\lambda}) = \sum_{h=1}^{M} \lvert a_h(\overline{\lambda})\rvert^2 h_{\mathrm{c},h}[z, t - z(\overline{\tau}_{\mathrm{g},h} - \overline{\tau}_{\mathrm{c},h})]$	General	(5.20)
Multimode frequency response	$H_{\mathrm{F}}(z,\omega,\overline{\lambda}) = \sum_{h=1}^{M} \lvert a_h(\overline{\lambda})\rvert^2 H_{\mathrm{c},h}(z,\omega)\ \mathrm{e}^{-\mathrm{j}\omega z(\overline{\tau}_{\mathrm{g},h} - \overline{\tau}_{\mathrm{c},h})}$	General	(5.76)
Time-centered chromatic response	$\hat{H}_{\mathrm{c}}(z,f) = H_{\mathrm{c}}(z,f)\ \mathrm{e}^{+\mathrm{j}2\pi f z\overline{\tau}_{\mathrm{c}}}$ $\updownarrow\ \Im$ $\hat{h}_{\mathrm{c}}(z,t) = h_{\mathrm{c}}(z, t - z\overline{\tau}_{\mathrm{c}})$	General	(5.79)
Modal function	$\Upsilon(z,f,\overline{\lambda}) \equiv \sum_{h=1}^{M} \lvert a_h(\overline{\lambda})\rvert^2\ \mathrm{e}^{-\mathrm{j}2\pi f z\tau_{\mathrm{g},h}(\overline{\lambda})}$ $\updownarrow\ \Im$ $\upsilon(z,t,\overline{\lambda}) = \sum_{h=1}^{M} \lvert a_h(\overline{\lambda})\rvert^2 \delta[t - z\overline{\tau}_{\mathrm{g},h}]$	General	(5.81)
Multimode frequency response	$H_{\mathrm{F}}(z,f,\overline{\lambda}) \cong \hat{H}_{\mathrm{c}}(z,f)\Upsilon(z,f,\overline{\lambda})$	Approximate	(5.82)

1535 nm and $\lambda_{\max} = 1565$ nm for a total of $N_0 = 1000$ uniformly spaced wavelength samples. The modal group delay is modeled according to the three-term Sellmeier equation for the fused silica without any ripple contribution. The modal group delay is assumed to have the same wavelength profile for each mode, thus exhibiting the same wavelength derivatives, and in particular the same chromatic dispersion coefficient. The group delay distribution evaluated at the average wavelength of the source PSD is modeled according to the inverse hyperbolic tangent (IHT) or quadratic (QDR) distributions. The fiber mode number is set equal to either $M = 200$ or $M = 500$ and the total delay variation among the modes is represented by the parameter Δ_τ.

The last parameter involved is the coefficient q defining the geometric progression used to model the source power coupling coefficient distribution. This parameter has quite an effect on the multimode impulse response because according to its value the coupled power distribution ranges between uniform excitation for $q = 1$ and an almost restricted center launch condition for a lower q value, such as $q = 0.7 \div 0.9$.

As a general comment about the following simulations, it should be noted that while the multimode impulse response includes both chromatic and modal contributions, the multimode frequency response refers only to the modal function $\Upsilon(z, f, \overline{\lambda})$. It is the purpose of this section to highlight this important concept as introduced and defined above. Moreover, it is important to remark that although the modal impulse response is given by a sequence of impulses (Dirac delta function) the modal function does not have in general a line spectrum. This is due to the following two reasons:

1. The group delay is not indefinitely extended over the time axis, but instead is a time-limited function.
2. The group delay does not have a constant step between adjacent delay samples.

In the only special case of a uniformly spaced and indefinitely extended group delay distribution, the modal function is an indefinite sequence of equally spaced impulses.

This case is of course a pure theoretical concept but, as with most of the content of this chapter, it is of fundamental importance in understanding the physical background and the related mathematical

modeling validity and limitations. Besides using some what fascinating conclusions of mathematical modeling, it is most important to have the validity of the modeling clearly in mind. Without this, it is very often quite dangerous or at least misleading to refer to simulation results. Everybody involved in simulation development and applications should be first of all conscious of the validity of the produced results. This approach is of course well known to all theoretical physicists: theory success is first based on the assumption phase.

One comment is needed with regards to the approach followed through the simulated cases in this book. The principal task has been to define as clearly as possible the simulating environment for understanding the multimode fiber propagation behavior and the way different variables and physical quantities are involved is producing results. In this context, suitable mathematical functions have been used to describe source power coupling coefficients and modal group delay distributions, such as geometric progression and the inverse hyperbolic tangent. These choices may possibly cause concern in the reader with regards to their physical validity, but this should not change the validity of the general modeling approach.

Once more realistic physical modeling of the multimode fiber behavior becomes available, including a two-dimensional electromagnetic mode solver for graded index fibers, more suitable source power coupling coefficients and modal group delay distributions will be available from the field simulator, but the logic process for the derivation of the multimode fiber response will remain exactly the same as that presented here. It is beyond the scope of this book to provide an electromagnetic mode solution for general graded index fibers, but this does not change the general validity of the theoretical modeling presented here. All that is needed afterwards is to change the abstract distribution models used here with more realistic ones taking into account refractive index profile-dependent modal solutions.

5.5.3.1 Restricted Excitation, Small Delay, IHT Distribution

The first case to consider assumes a very restricted low-order mode launch with $q = 0.7$, over a relatively large mode number fiber, $M = 200$. This leads to less then seven modes (about only 3.5 %), contributing significantly to the output impulse response. All remaining modes are of extremely low power coupled to the light source and bring a negligible intensity contribution to the output impulse response. The group delay distribution in the following Figure 5.55 is assumed to follow the inverse hyperbolic tangent function with a total (asymptotic) group delay per unit length of $\Delta_\tau = 2\,\text{ns/km}$.

The modal function presents an almost regular Gaussian-shaped frequency profile up to about one-third of the spectrum amplitude; it then shows a deep notch at about 2.4 GHz, leaving the Gaussian profile. This resonance is represented in the time domain by the dual-peak time centered impulse response shown in Figure 5.56. On the same graph the Gaussian fit using the same RMS width of the impulse response is also shown. The dual-peak impulse response is a consequence of the reduced number of excited modes and the relatively sparse distributed group delay they experience due to the long tail of the inverse hyperbolic tangent distribution.

Figure 5.56 also shows the corresponding modal function $\Upsilon(z, f, \overline{\lambda})$ computed using Equation (5.81) and plotted versus the logarithmic frequency scale. It is evident that there is good Gaussian frequency fitting up to about $-5\,\text{dB}$ with respect to the low-frequency spectrum amplitude. The deep notch at about 2.4 GHz reaches a relative intensity of $-20\,\text{dB}$.

5.5.3.2 Uniform Excitation, Small Delay, IHT Distribution

The second case to be considered has the same parameter set as the previous example, except that it shows a uniform excitation of $q = 1$ and a higher mode number of $M = 500$. Figure 5.57 presents the inverse hyperbolic tangent distribution computed with $M = 500$ modes and the uniform power distribution with $|\overline{a}_h|^2 = 2 \times 10^{-3}$. The resulting multimode impulse response has a more

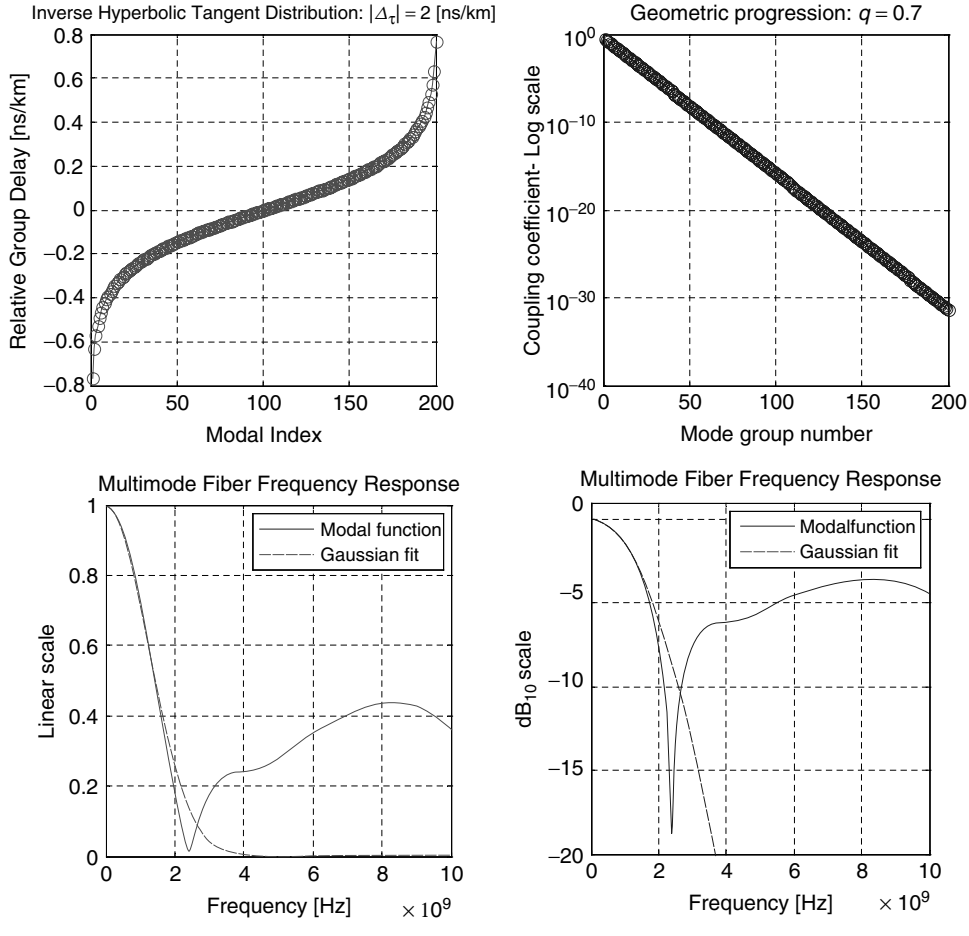

Figure 5.55 Top: inverse hyperbolic tangent (IHT) group delay distribution and geometric progression coupling coefficient sequence for the case $M = 200$, $q = 0.7$, $\Delta_\tau = 2$ ns/km. Bottom: modal function frequency response in linear (left) and dB (right) scales. The Gaussian fit of the whole multimode frequency response has been also plotted

symmetric shape and closely fits with the Gaussian approximation. The uniform excitation over the symmetric group delay distribution results, as expected, in a more symmetric multimode impulse response and a corresponding high-frequency smoothed modal function. Figure 5.58 shows the computed multimode impulse response with the modal function, both fitted with the corresponding Gaussian profiles.

Although the low-frequency part of the modal function looks similar to the previous case, with a different scale factor, the high-frequency portion is completely different. The smoothed and symmetric impulse response corresponds in fact to the much more regular profile in the high-frequency range, leading to a closer Gaussian approximation, even in the high-frequency spectrum portion. Nevertheless, it should be noted that including all supported fiber modes with the same power contribution leads to a broader impulse response than the one obtained in the restricted excitation case. In the next section the Gaussian approximation of the multimode fiber response will

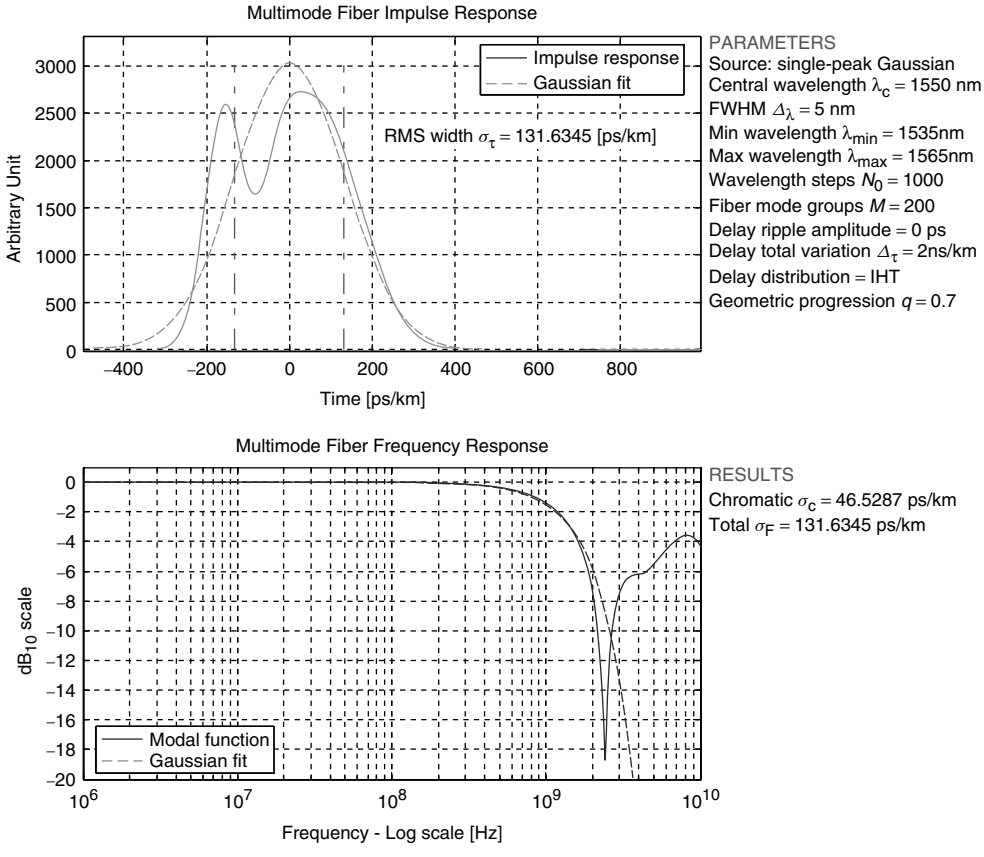

Figure 5.56 Computed multimode impulse response (top) and the corresponding modal function (bottom) for the parameter set $M = 200$, $q = 0.7$, $\Delta_\tau = 2$ ns/km. Both plots show the Gaussian fitting assuming the same total RMS width $\sigma_F = 131.63$ ps/km of the impulse response

be used as a convenient simulation tool for providing a reasonable transmission system performance prediction.

5.5.3.3 Uniform Excitation, Small Delay, QDR Distribution

The multimode impulse response is essentially determined by the group delay and the source power distributions among the supported fiber modes. In this example, the same configuration used in the previous case in Section 5.4.3.2 is used, except for the quadratic modal delay distribution. The effect of a different modal delay distribution among the same number of uniformly excited modes gives quite a clear representation of the relevance of this fiber characteristic.

Figure 5.59 shows the computed modal solution assuming a quadratic group delay (QDR) and uniform geometric progression. In the same graph the modal function $\Upsilon(z, f, \overline{\lambda})$ and the corresponding Gaussian fitting are also shown, using both linear and logarithmic scales. It is evident that although the Gaussian profile fits the modal function quite well up to about -5 dB in the low-frequency reference amplitude, at higher frequencies the Gaussian fit is no longer sustainable and the modal function almost follows the hyperbolic decaying profile. In order to understand this behavior, there is a need to refer to the multimode impulse response shown in Figure 5.60. The

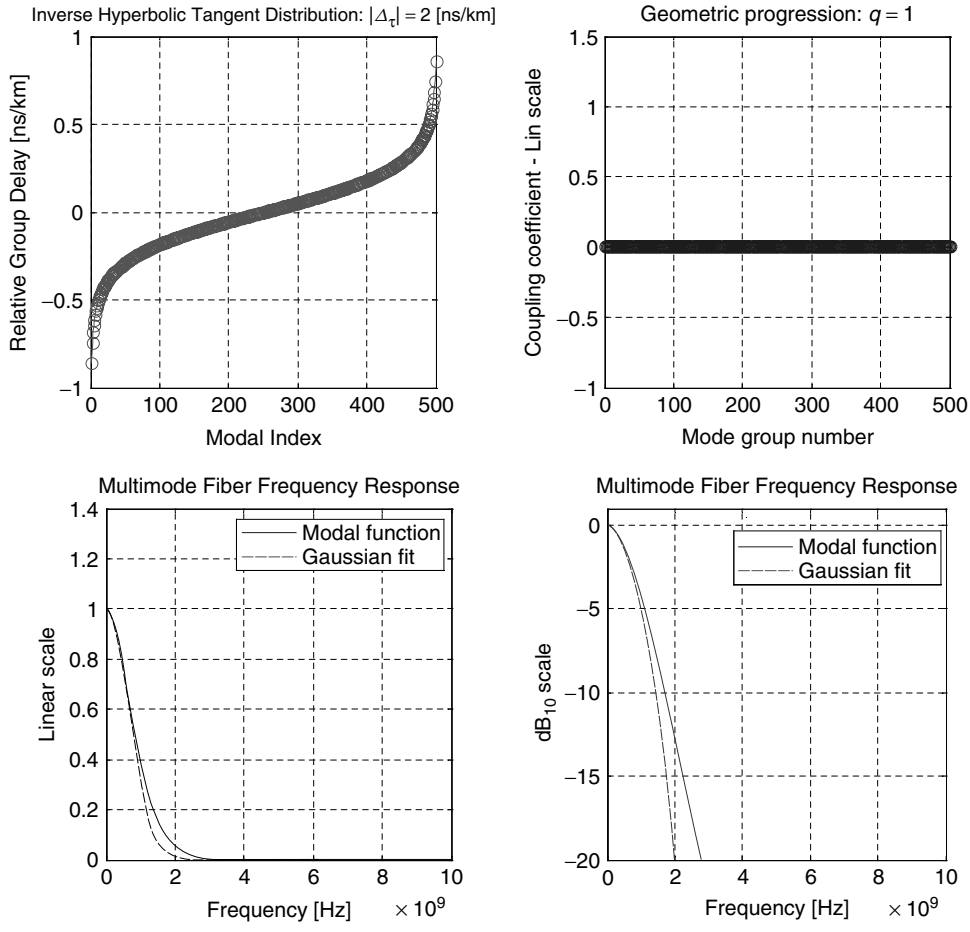

Figure 5.57 Top: inverse hyperbolic tangent (IHT) group delay distribution and the geometric progression coupling coefficient sequence for the case $M = 500$, $q = 1$, $\Delta_\tau = 2$ ns/km. Bottom: modal function frequency response in linear (left) and dB (right) scales. The more regular high-frequency shape of the modal function fits better with the Gaussian profile

impulse response profile looks quite different from that of the inverse hyperbolic tangent modal delay distribution shown in Figure 5.58.

In this case in fact, the strong asymmetry of the quadratic modal delay distribution makes the impulse response strongly asymmetrical, with pronounced peaking in correspondence with the higher density of available low-order modal delays. This causes the impulse response to peak at the leading edge, with a precursor-like profile. The total variation of the modal delay is limited to $\Delta_\tau = 2$ ns/km and the quadratic distribution ends almost abruptly, making the impulse response clearly time limited over the same temporal interval. This leads to the asymptotic ripple-shaped frequency response according to the frequency convolution of the corresponding sinc function. This ripple was not present in the previous case in Section 5.4.3.2 because the inverse hyperbolic tangent distribution exhibits a very gradual decaying profile at both delay interval extremes. The

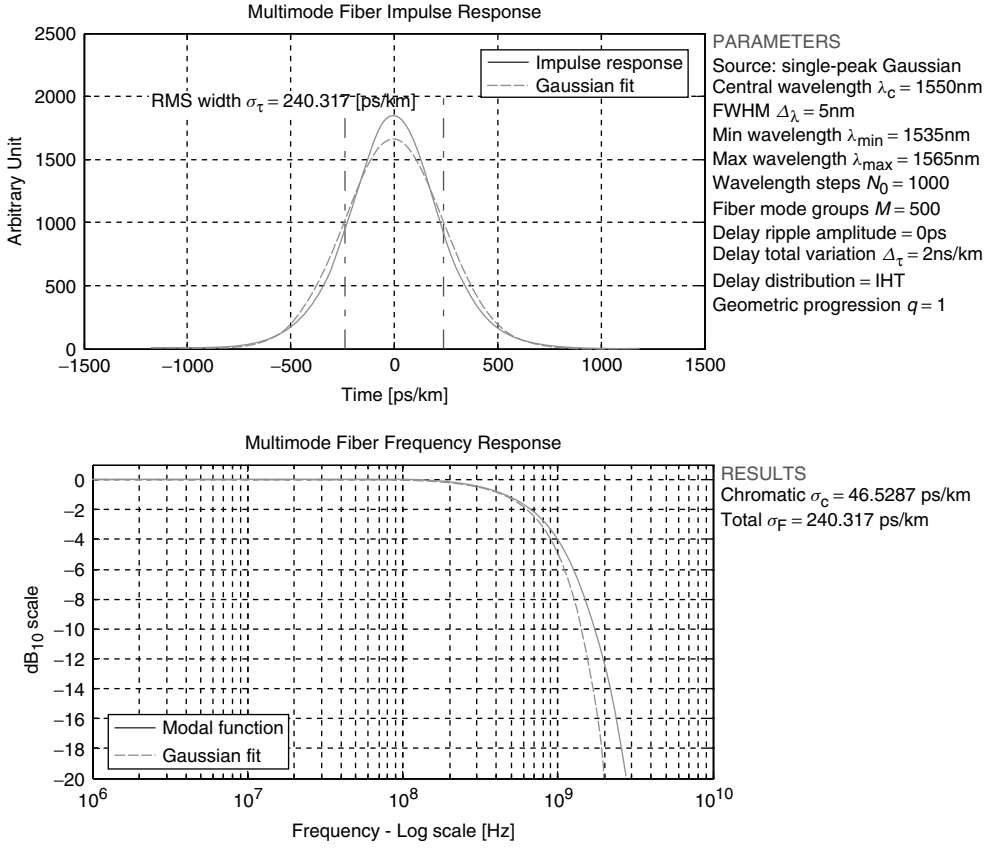

Figure 5.58 Computed multimode impulse response (top) and the corresponding modal function (bottom) for the parameter set $M = 500$, $q = 1$, $\Delta_\tau = 2$ ns/km assuming an inverse hyperbolic tangent distribution. Both plots report the Gaussian fitting of the multimode impulse response assuming the same RMS pulse width $\sigma_F = 240.32$ ps/km

multimode impulse response is reported in Figure 5.60, together with the modal function and the Gaussian approximation.

The impulse response presents the characteristic rising edge peaking followed by the long and almost uniform tail due to the contribution of the higher delay interval of the quadratic delay profile. The peaked response is a result of the relatively dense accumulation of group delay values close to the vertex of the parabolic distribution. Many energy contributions sum up together almost at the same time instant, leading to the huge intensity peak. Higher-order modes are instead sparser along the time axis and their energy is delivered with a decreasing time concentration, therefore leading to the long pulse tail.

The Gaussian fitting in this case is very poor, as clearly shown in the top graph of Figure 5.60. The modal function and the related Gaussian fitting profile are reported in the bottom graph using the logarithmic frequency scale. The high-frequency behavior of the spectrum of the modal function, apart from the decaying ripple, shows an asymptotic decaying constant of about 5 dB/dec, which implies the factor $1/\sqrt{f}$ when plotted in the dB_{10} scale. It is very interesting to compare the frequency response of the last two cases. Exactly the same parameter set has been assumed,

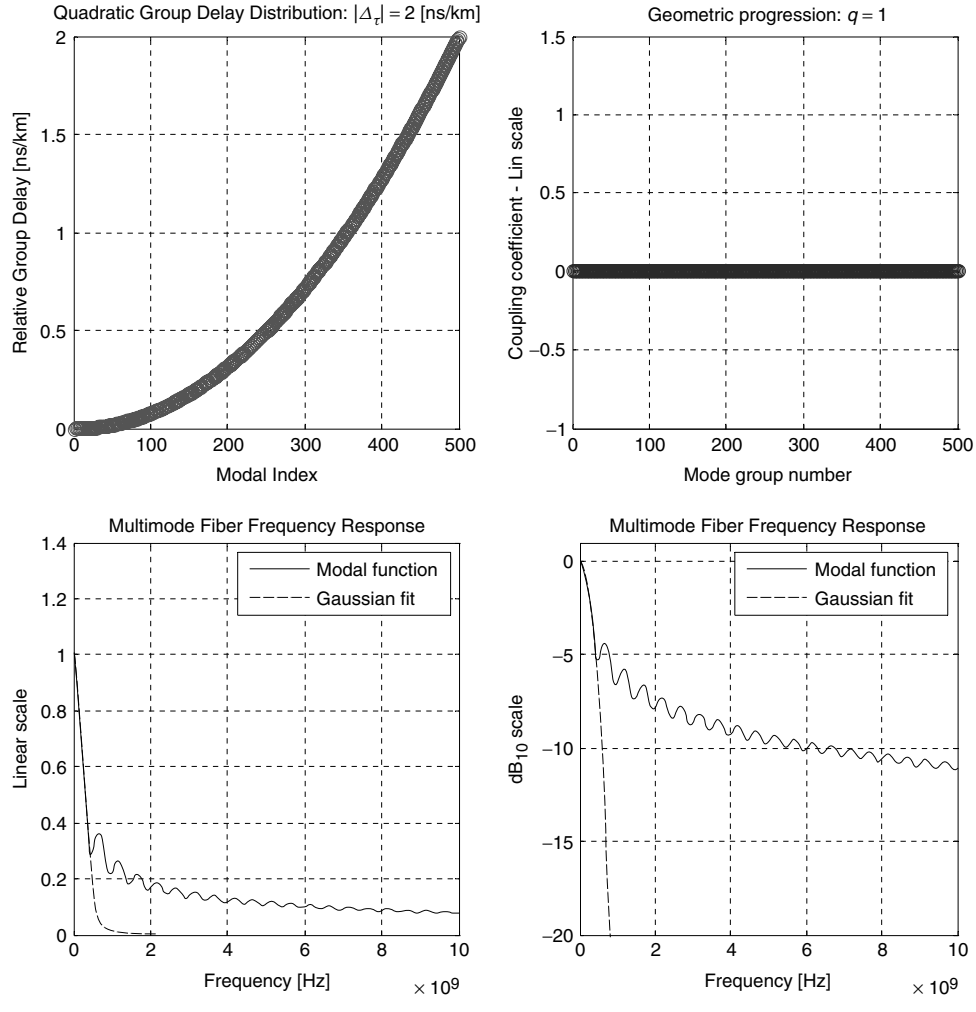

Figure 5.59 Top: quadratic group delay distribution (QDR) and the geometric progression coupling coefficient sequence for the case $M = 500$, $q = 1$, $\Delta_\tau = 2$ ns/km. Bottom: modal function frequency response and Gaussian fitting in the linear (left) and dB (right) scales. The high-frequency ripple is due to the abrupt time-limited impulse response. The more the impulse pulse terminates abruptly, the more persistent will be the high-frequency ripple

including the uniform modal excitation. The difference between the two cases is the group delay distribution, which is responsible for the great difference in the multimode fiber response.

The group delay distribution in standard manufactured optical fiber depends essentially on the manufacturing tolerances, and not on the design specification for the graded refractive index profile. The refractive index is designed in order to compensate the modal delay theoretically, but the high sensitivity of the modal impulse response from the group delay distribution makes the achieved compensation only approximate. The multimode fiber performance evaluated at a transmission rate of 10 Gb/s is extremely demanding and the degree of modal delay compensation required usually allows the transmission only for a few hundred meters of link length. In addition to that, it is

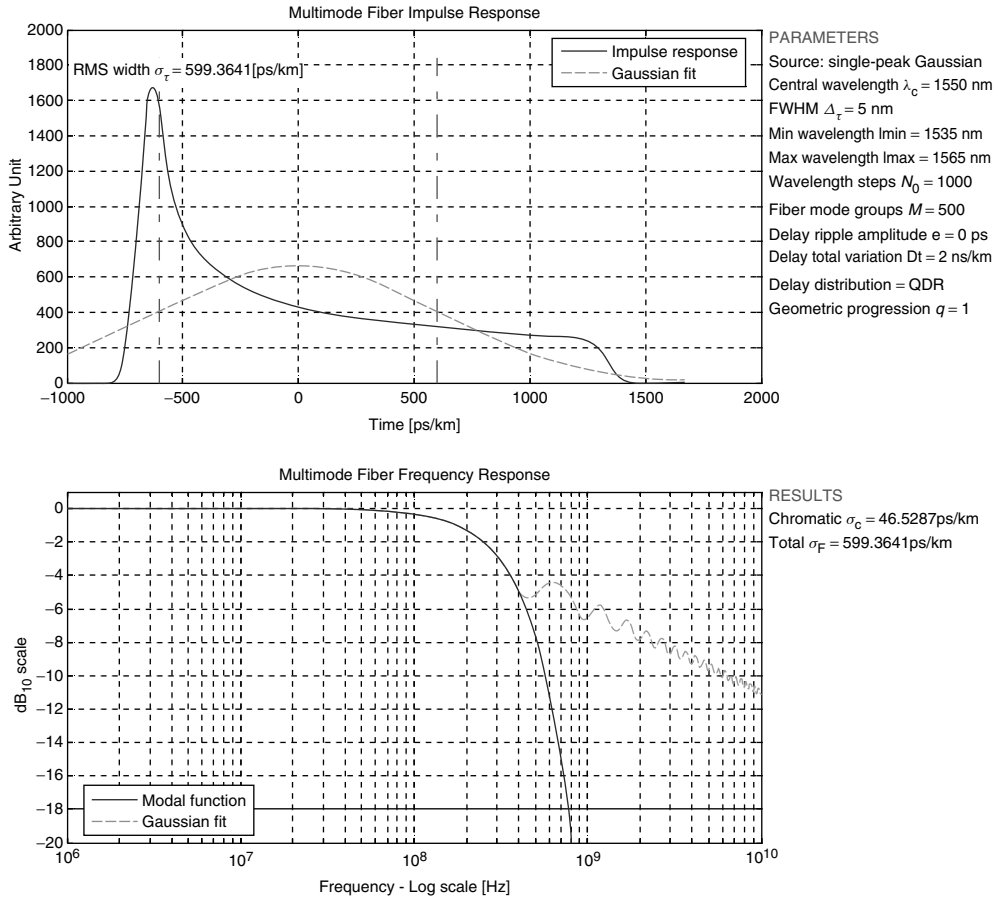

Figure 5.60 Computed multimode impulse response (top) and corresponding modal function (bottom) for the parameter set $M = 500$, $q = 1$, $\Delta_\tau = 2$ ns/km, assuming a quadratic group delay distribution. Both plots report the Gaussian fitting of the multimode impulse response with the same RMS pulse width $\sigma_F = 599.36$ ps/km

the second leading factor affecting the multimode fiber response in the source power coupling distribution.

Even if the launching section can be accurately designed to optimize the coupling distribution, every discontinuity along the fiber link length creates a different power coupling to the fiber modes and the link response becomes less predictable. This is the case for optical connectors or fusion splices, which can be located everywhere along the fiber link. The more optical connectors added between fiber sections, the more perturbed does the optical pulse propagation become, and the impulse response collected at the end section usually shows highly increased sensitivity to environmental conditions such as mechanical vibrations and thermal stresses and light polarization. Since the group delay and definitely the impulse response of the multimode fiber are defined over the unit fiber length, of course all these considerations become amplified when either the link length is extending or the bit rate is increasing. Both of these effects are simultaneously present in LAN (local area network)-based 10 GbE communication systems, which strongly affect multimode fiber performance.

5.5.3.4 Restricted Excitation, Medium Delay, IHT Distribution

These last two cases are an interesting example of split-pulse profiles assuming symmetric inverse hyperbolic tangent group delay distributions. The pulse splitting profile is characteristic of restricted launching conditions because a reduced number of modes needs to be selected with a proper relative group delay. In the case of uniform excitation the very large mode number acts to average the power content over the whole population and individual pulse contributions are much less significant. In both of these examples the geometric progression factor is set to $q = 0.85$, giving a reasonably low number of excited modes. Finally, in order to produce better evidence of the impulse response pulse splitting the absolute value of the total delay variation has been increased up to $\Delta_\tau = 5$ ns/km with respect to the lower value of $\Delta_\tau = 2$ ns/km, which was assumed in all three previous cases. Figure 5.61 shows the first case of the negative total delay variation $\Delta_\tau = -5$ ns/km.

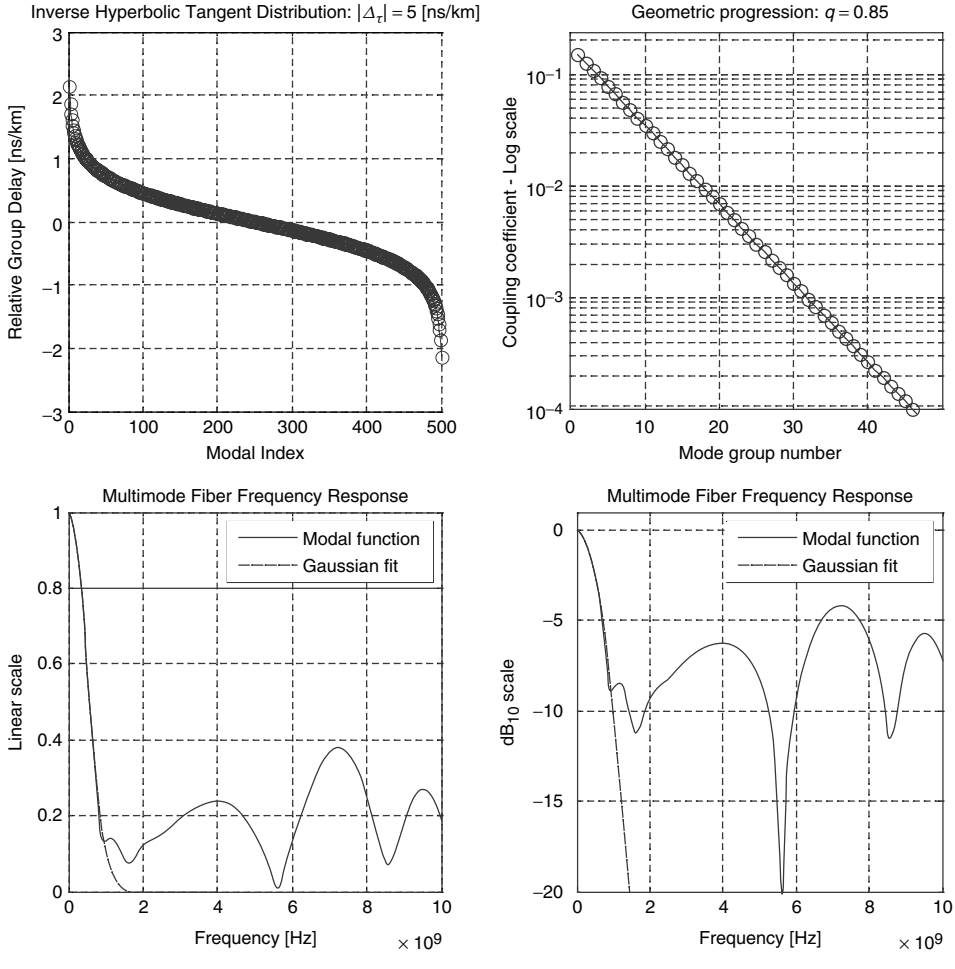

Figure 5.61 Top: inverse hyperbolic tangent (IHT) group delay distribution and the geometric progression coupling coefficient sequence for the case $M = 500$, $q = 0.85$, $\Delta_\tau = -5$ ns/km. Only about the first 30 modes contribute to the impulse response, corresponding to less the 6 % of the total supported fiber modes. Bottom: modal function frequency response in the linear (left) and dB (right) scales. The Gaussian fit of the whole multimode frequency response has been also plotted

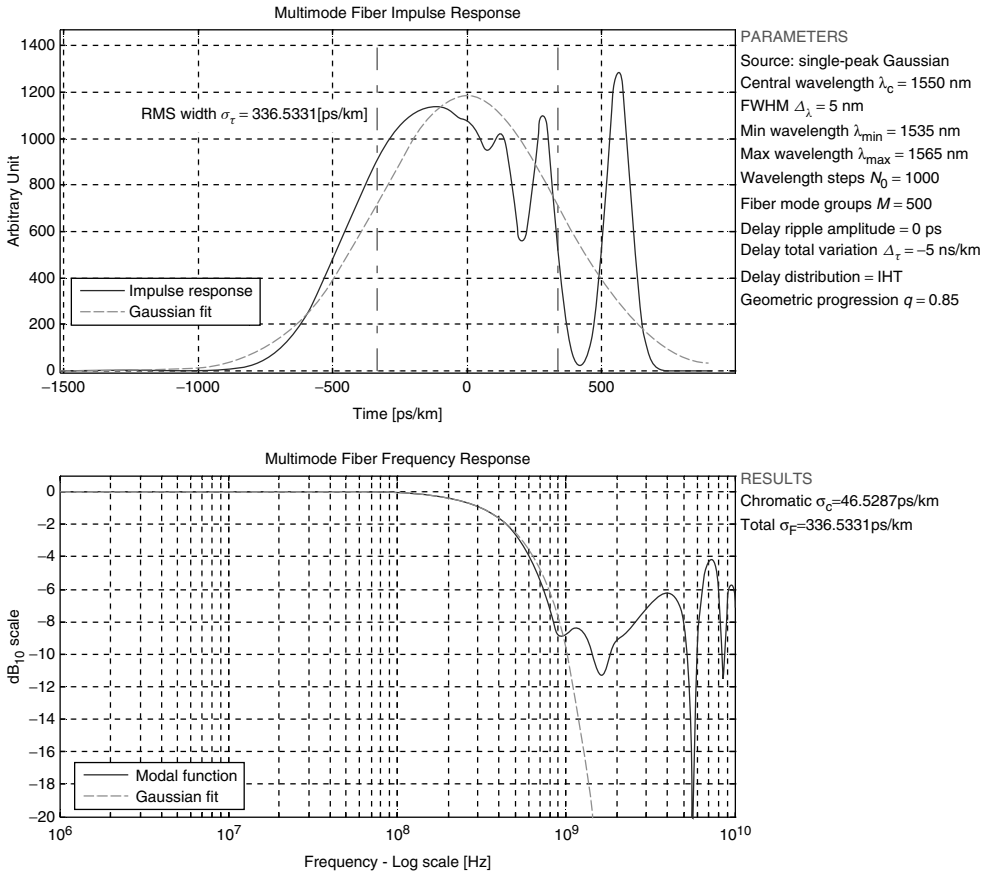

Figure 5.62 Computed multimode impulse response (top) and the corresponding modal function (bottom) for the parameter set $M = 500$, $q = 0.85$, $\Delta_\tau = -5$ ns/km, assuming an inverse hyperbolic tangent group delay distribution. The negative total group delay value sets the condition for a strong pulse postcursor. The split-pulse profile leads to the multiple-notch modal frequency response, as clearly shown in the bottom graph. Both plots report the Gaussian fitting of the multimode impulse response with the same RMS pulse width $\sigma_F = 336.53$ ps/km

The modal function presents strong notches at several frequencies, which is a characteristic of the split profile of the impulse response shown in Figure 5.62. The negative total group delay variation implies that the lower-order mode selected by the coupling coefficients exhibits a higher delay value. These lower-order modes are also less concentrated in time due to the long tail of the inverse hyperbolic tangent distribution, leading to the bulk body of the multimode impulse response. The following intense postcursor peak is determined by the highest group delay value, which is also the one most coupled to the light source since it corresponds to the lowest-order mode. Essentially, due to the long tail distribution of the assumed group delay, the postcursor almost corresponds to the chromatic impulse response of the lowest-order mode, due to the lack of adjacent pulse overlapping.

The modal function shown in Figure 5.62 fits the Gaussian profile quite well up to about 1 GHz, corresponding to −9 dB in the low-frequency amplitude. The relevant amplitude fluctuation encountered at higher frequencies reflects the multiple peak impulse response and this profile cannot be

approximated by any single-peak smoothed function such as the Gaussian pulse. To conclude this section, the computed multimode impulse response is given in the case of the symmetrical group delay distribution with a positive total delay variation of $\Delta_\tau = +5$ ns/km, as shown in Figure 5.63.

The same considerations made for the previous case still hold for this example. The interesting conclusion is that, being reversed, the delay distribution, which is now the multimode impulse response given in Figure 5.63, mirrors the results of the negative delay variation presented in Figure 5.62. In fact, in this case the highest value of the coupled power refers to the slowest mode, exhibiting a relative delay of about -2 ns/km. This mode, being almost isolated, determines

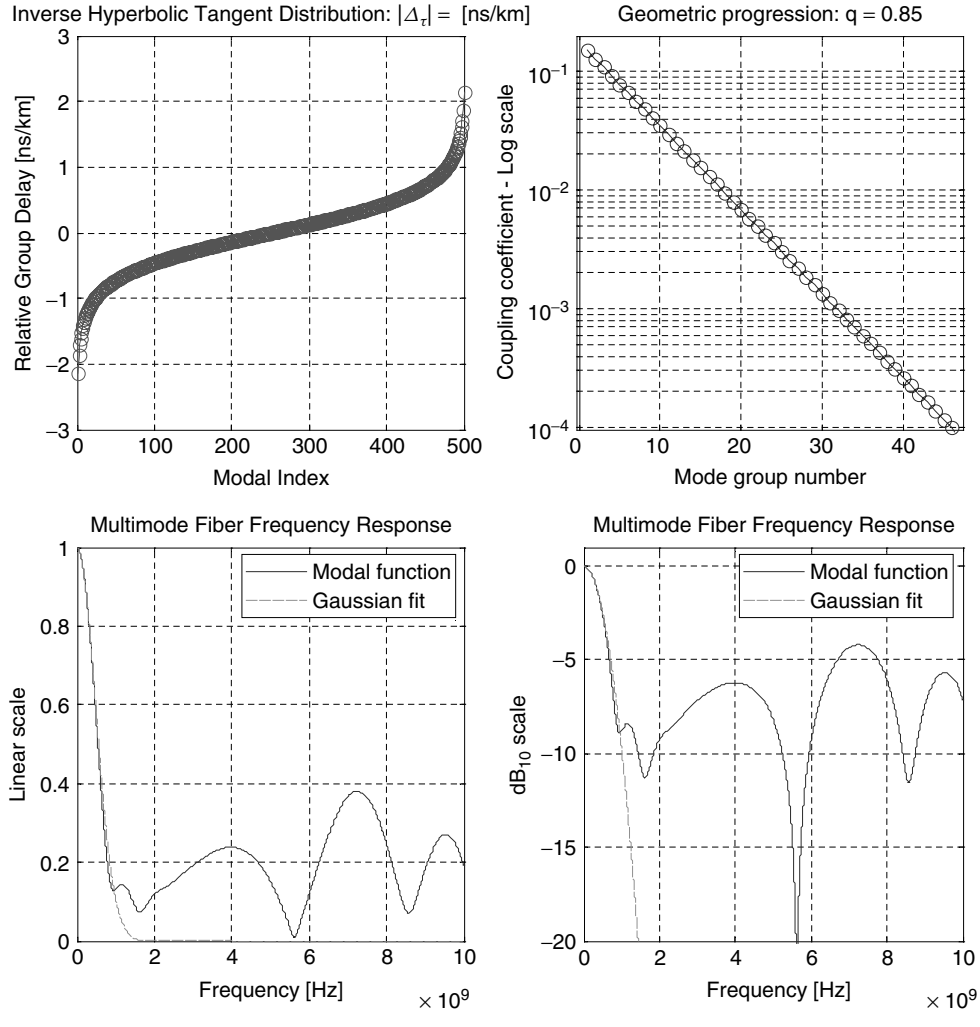

Figure 5.63 Top: inverse hyperbolic tangent (IHT) group delay distribution and the geometric progression coupling coefficient sequence for the case $M = 500$, $q = 0.85$, $\Delta_\tau = +5$ ns/km. Only about the first 30 modes contribute to the impulse response, corresponding to less the 6 % of the total supported fiber modes. Bottom: modal function frequency response in the linear (left) and dB (right) scales. The Gaussian fit of the whole multimode frequency response has been also plotted

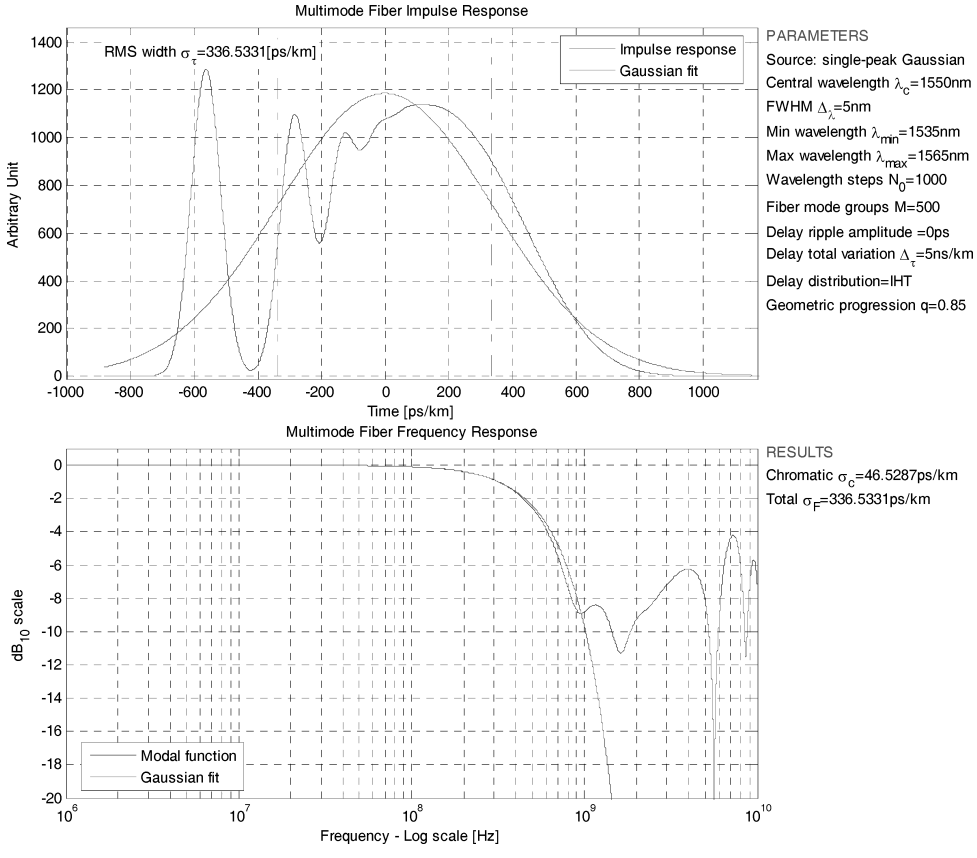

Figure 5.64 Computed multimode impulse response (top) and corresponding modal function (bottom) for the parameter set $M = 500$, $q = 0.85$, $\Delta_\tau = +5$ ns/km, assuming an inverse hyperbolic tangent group delay distribution. The positive total group delay value sets the condition for a strong pulse precursor. The split-pulse profile leads to the multiple-notch modal frequency response, as clearly shown in the bottom graph. Both plots report the Gaussian fitting of the multimode impulse response with the same RMS pulse width $\sigma_F = 336.53$ ps/km

the strong precursor shown in the multimode impulse response in Figure 5.64. The remaining few excited modes (less than 30 modes according to the geometric progression distribution) are responsible for the following main pulse body.

5.5.4 Concluding Remarks

In this section the theory has been presented of the frequency response of the generic multimode fiber based on the simple properties of the Fourier transform of the multimode impulse response. The multimode response depends on the combination of both chromatic and modal dispersions, but in almost all cases the modal response is highly dominant. Under the assumption of no mode coupling or interaction, the modal response is completely characterized by two factors:

(a) the source power coupling coefficient distribution at the input section;
(b) the modal group delay distribution at the output section, evaluated at the average wavelength of the light source spectrum.

Three different mathematical models have been proposed for the group delay distribution. Using these artificial distributions, very interesting results have been computed and presented in graphic form. The source power coupling distribution has been modeled assuming geometric progression with different coefficients, obtaining a very easy way of handling either the uniform excitation condition or the restricted excitation and thus providing a source power transfer only to low-order central modes.

Besides the computation of frequency responses, one important issue of this section has been to define the modal function. Under the simplifying assumption that the modal chromatic impulse response differentiates only for the average delay and not for the time-centered profile, the multimode frequency response simply reduces to the product of the modal function with the Fourier transform of the time-centered chromatic impulse response. This property allows interesting modeling of the multimode fiber to be made as the cascade of two linear systems, either with the chromatic impulse response only or with the modal impulse response only. Conceptually, this also allows the intramodal and intermodal dispersion to be considered as two independent linear phenomena, which can therefore be treated independently from each other.

In the next chapter the Gaussian approximation of the multimode fiber response will be considered in more detail, leading to validity conditions and approximations.

5.6 Summary and Conclusions

In this chapter a general expression has been derived for the multimode fiber impulse response under the assumption of no modal coupling. According to this assumption, all excited modes propagate independently from each other and their optical intensity is collected at the fiber detecting section. The general expression of the multimode impulse response is given in Equation (5.20) while Equation (5.76) reports the corresponding general expression for the multimode frequency response. As expected, the RMS width $\sigma_{\mathrm{m}}(z, \overline{\lambda}) = z\hat{\sigma}_{\mathrm{m}}(z, \overline{\lambda})$ of the modal impulse response in Equation (5.17) scales linearly with the propagated distance z. The same also occurs for the RMS width of the ensemble average of the chromatic impulse response given in Equation (5.35). The cumulative variance of the multimode impulse response adds up quadratically, leading to the RMS pulse width in Equation (5.40), and scales linearly with the distance z.

The multimode impulse response has been presented in Section 5.4, leading to eight different simulation cases characterized by peculiar choices of group delay distribution and source coupled power coefficients. The computed results give evidence of the large variety of impulse responses achievable from the multimode fiber, changing either the group delay or the source coupling distributions. In order to acquire a quantitative feeling of the consequences of group delay profiling, Section 5.4.4 introduces the piecewise linear distribution and the inverse hyperbolic tangent distribution. It is convenient to use the latter distribution to model the symmetric Gaussian- like multimode impulse response, which can be conveniently fitted with the Gaussian interpolation. This will be the subject of Chapter 6. The last part of this chapter dealt with the multimode fiber frequency response by means of the Fourier transform. Using simple definitions and properties of the Fourier integral, the general expression for the multimode frequency response was derived. Under the assumption of the uniform chromatic response profile among the excited mode population, the useful concept of the modal function was introduced. This led to the multimode fiber equivalent model in terms of two cascaded linear systems. The first system is characterized by the chromatic impulse response profile, while the second one shows the modal response according to the source coupled excitation and the selected group delay distribution. The results presented are quite interesting, showing both smoothed, notch-free and frequency ripple spectra, according to the selected case.

The next chapter will deal with the Gaussian approximation of the multimode fiber frequency response, which contains configuration conditions assumed to have a reasonable Gaussian fitting of the output response.

6

Gaussian Approximation and Applications

Link Bandwidth Calculations

6.1 The Gaussian Model Approximation

In Chapter 5 the multimode fiber theory of impulse response and the related frequency response were presented. If there is no mode coupling, the principal physical entities involved in the determination of the multimode fiber response can be stated, namely:

1. The spectral power density of the light source determines the chromatic response.
2. The group delay function versus the wavelength for each supported fiber mode determines both the chromatic and modal responses.
3. The light source power coupling distribution evaluated at the input section among all the supported fiber modes determines the weighting function for the modal response superposition.

As well as these three primary factors and under the approximation that the time-centered modal chromatic response has the same profile for each excited mode, the following requirement can be added:

4. The modal group delay distribution at the output section, evaluated at the average wavelength of the light source spectrum, determines the approximate multimode frequency response as the product of the time-centered chromatic frequency response with the modal function.

Multigigabit transmission requires a laser light source due to high-speed direct modulation capabilities. Under laser modulation the chromatic response contribution per unit length is relatively negligible compared to the modal contribution, resulting in a relatively broadband frequency response. In order to have a quantitative idea of the laser light modulation condition, it is sufficient to consider the case of a multilongitudinal mode semiconductor laser source emitting in the high dispersive first window at $\lambda_c = 850\,\text{nm}$ with an envelope linewidth $\sigma_\lambda = 2\,\text{nm}$. From Equation (4.120), the linear approximation of the RMS pulse width per unit length due to chromatic dispersion is given by $\sigma_c = |\overline{D}_c|\sigma_\lambda$. Assuming $|D_c(850\,\text{nm})| \cong 100\,\text{ps/nm km}$, it is concluded that $\sigma_c \cong 200\,\text{ps/km}$. The contribution of the modal dispersion depends on the launch condition and on

Multi-Gigabit Transmission over Multimode Optical Fibre: Theory and Design Methods for 10GbE Systems Stefano Bottacchi
 ISBN: 0-471-89175-4

the group delay distribution. Without specifying too much detail, it can reasonably be assumed that $\sigma_m \cong 1000$ ps/km. Using the quadratic composition of chromatic and modal dispersions reported in Equation (5.40), it is concluded that the total RMS width of the multimode impulse response has the value of $\hat{\sigma}_F = \sqrt{\hat{\overline{\sigma}}_c^2 + \hat{\sigma}_m^2} \cong 1020$ ps/km, hence resulting in a value only 2 % higher than the modal dispersion alone. This example gives a quantitative feeling of the relative contributions between chromatic and modal dispersions in a laser-based transmission system and it is clearly concluded that the multimode fiber frequency response is essentially determined by the modal function.

The characteristic profiles of this relevant function has been extensively discussed with numerous examples. It mainly depends upon both the modal delay distribution and the source coupling distribution. According to the distribution chosen, the impulse response can be assumed to be almost an infinite variety of profiles, ranging from the symmetric single-pulse shape, to the multiple-peak pulse waveform, to the wide and almost uniform narrowband pulse. It is evident at this point that any move to force the Gaussian profile to model the multimode fiber impulse response seems to be more an artificial exercise rather than a physical supported argument.

Next the formulation of the Gaussian model of the multimode fiber response will be carried out, keeping these limitations cleared in mind. As already stated, before using any model there must be an awareness of the assumptions and limitations of the model that is to be used. This is of course also valid for the Gaussian modeling. The first important issue is to find the parameter conditions needed to support a multimode impulse response that can be reasonably fitted by the Gaussian profile. This will be the argument of the next section. Once a single-pulse response with an almost symmetric profile can reasonably be expected to satisfy the Gaussian fitting, the multimode fiber Gaussian response modeling will be developed.

6.1.1 Prescriptions for Gaussian Modeling

In Chapter 5 numerous examples were presented to show different group delay and source coupling coefficient distributions and the corresponding different impulse responses were found. The purpose now is to find and select some qualitative prescriptions for expecting a Gaussian-shaped response. For a given multimode fiber the group delay distribution is fixed by the refractive index profile and more generally by the material composition and environmental conditions. Changing the environmental conditions like temperature and mechanical stresses induces mode coupling and optical power redistribution at every optical link discontinuity. This reflects on the frequency response and the related Gaussian fitting validity. Even if the modal group delay distribution at a given wavelength is specified for every multimode fiber, the variability of the launch condition at every fiber section corresponding to the location of an optical connector makes the multimode response highly dependent on environmental conditions.

In Chapter 4 it was seen that the chromatic impulse response profile resembles quite closely the light source spectral distribution, in particular for relatively narrow linewidth sources like semiconductor lasers. This allows the chromatic impulse response shaped like a Gaussian with a linearly approximated RMS width given by Equation (4.120) to be considered. As a consequence, to obtain a smoothed single-pulse multimode response the proximity condition should be set: adjacent modal contributions must be closer together than the chromatic RMS width. This leads to a smoothed superposition of each Gaussian chromatic response. Of course, the wider the chromatic impulse response, the easier it is to satisfy the proximity condition and the closer the multimode response will be to the Gaussian profile. That is true, for example, for LED broad linewidth optical sources. Semiconductor laser excitation is characterized by a narrower linewidth and consequently requires a more uniform and closer spacing of the group delay distribution in order to release a Gaussian-like multimode response. In order to fix the proximity condition in mind, reference needs to be made to the hyperbolic tangent distribution with uniform excitation presented

in Section 5.5.3.2, Figures 5.57 and 5.58 of Chapter 5. The multimode impulse response was in that case quite well fitted by a Gaussian pulse, leading to a smoothed and notch-free frequency response.

The Gaussian response prescription can therefore be summarized as follows:

1. The modal group delay distribution evaluated at the source average wavelength must satisfy the proximity condition, at least for the more excited modes. The delay variation between any two relatively intense and adjacent modes must be shorter than the chromatic response RMS pulse width.
2. The mode excitation must be almost uniform relative to the more intense modes.

In the following, when the Gaussian approximation is referred to, it will be assumed, unless otherwise stated, that the Gaussian response prescription above is almost satisfied.

6.1.2 The Gaussian Response Model

According to the ITU-T G.651 standard, the fiber modal bandwidth BW is defined as follows. The fiber modal bandwidth BW is given by the half-width at half-maximum of the unilateral intensity transfer function, at a given distance z from the launching section set at the origin.

The modal bandwidth refers to the intensity transfer function $H_F(z, f, \overline{\lambda})$ obtained under the assumption that the chromatic frequency response has a negligible contribution. In the limiting case where the time-centered chromatic impulse response coincides with the Dirac delta impulse, the chromatic response has a constant frequency spectrum and the multimode fiber intensity transfer function coincides with the modal function defined in Equation (5.81). Conceptually the modal bandwidth per unit length $\widetilde{BW}$ therefore coincides with the half-width at half-maximum bandwidth of the spectrum of the modal function $\Upsilon(z, f, \overline{\lambda})$ defined in Equation (5.81).

6.1.2.1 Impulsive Spectral Excitation

To demonstrate this important statement, the limiting case is considered of the light source spectrum coinciding with the delta distribution centered at the wavelength λ_c:

$$S_s(\lambda) = \delta(\lambda - \lambda_c) \tag{6.1}$$

Before proceeding with the mathematical demonstration, it is important to comment on the physical implications and the consistency of this assumption. The chromatic dispersion modeling of the multimode fiber is based on the assumption of the broadband light source. In particular, the modulation bandwidth is embedded into the light source spectrum width. Of course these assumptions are now violated because the impulsive spectrum is by definition indefinitely narrowband and every modulation signal will be broadening that ideal optical carrier.

Nevertheless, with this warning in mind the derivation will continue of the modal chromatic impulse response assuming impulsive spectral excitation. The more general analysis of the impulse response to a very small narrowband (impulsive spectrum) is outside the scope of this book.

The light intensity in Equation (6.1) satisfies the normalization condition $\int_{-\infty}^{+\infty} S_s(\lambda)\, d\lambda = 1$ and the general chromatic impulse response of the hth mode is given by the Fourier integral (4.32) in Chapter 4, Section 4.2.5:

$$h_{c,h}(z, t) = \int_{-\infty}^{+\infty} S_s(\lambda)\, \delta[t - z\tau_{g,h}(\lambda)]\, d\lambda \tag{6.2}$$

This expression is valid without any restriction and in particular, for the Dirac delta light source spectrum (6.1), it gives the following impulse response:

$$h_{c,h}(z,t) = \int_{-\infty}^{+\infty} \delta(\lambda - \lambda_c)\delta[t - z\tau_{g,h}(\lambda)]\,d\lambda = \delta[t - z\tau_{g,h}(\lambda_c)] \tag{6.3}$$

This result should have been expected, because the impulsive source linewidth cannot induce any chromatic dispersion and the chromatic impulse response of each excited mode must therefore coincide with the Dirac delta function located at the group delay value corresponding to the single exciting wavelength λ_c.

Once the chromatic impulse response has been calculated for each excited mode, substituting expression (6.3) into Equation (5.20) gives the corresponding multimode impulse response:

$$h_F(z,t,\overline{\lambda}) = \sum_{h=1}^{M} |a_h(\overline{\lambda})|^2 \delta\{t - z[2\tau_{g,h}(\lambda_c) - \overline{\tau}_{c,h}]\} \tag{6.4}$$

In this case the source average wavelength $\overline{\lambda}$ defined in Equation (4.92) coincides with the wavelength location of the Dirac delta spectrum in Equation (6.1), $\overline{\lambda} = \lambda_c$. The normalized time $\overline{\tau}_{c,h}$ in Equation (6.4) is the average delay of the chromatic impulse response of the mode hth and is given in Equation (4.90). Although the formal mathematical demonstration is a very interesting application of the mathematical properties of the impulse distribution, it is clear from the physical picture involved in Equation (6.3) that the time $\overline{\tau}_{c,h}$ coincides with the modal group delay evaluated at the wavelength λ_c of the impulsive spectrum. Therefore,

$$\tau_{g,h}(\lambda_c) = \overline{\tau}_{c,h} \tag{6.5}$$

Substituting in Equation (6.4), the multimode impulse response assumes the form

$$h_F(z,t,\lambda_c) = \sum_{h=1}^{M} |a_h(\lambda_c)|^2 \delta[t - z\tau_{g,h}(\lambda_c)] \tag{6.6}$$

If the above chromatic impulse response is compared with the modal impulse response (3.53), it can easily be concluded that they are completely identical and the multimode fiber impulse response under the assumption of spectral impulsive excitation coincides with the modal impulse response given in Equation (3.53):

$$\upsilon(z,t,\lambda_c) = \sum_{h=1}^{M} |a_h(\lambda_c)|^2 \delta[t - z\tau_{g,h}(\lambda_c)]$$

Hence, it is concluded that

$$h_F(z,t,\lambda_c) = \upsilon(z,t,\lambda_c) \tag{6.7}$$

From the above identity and the uniqueness of Fourier transform pairs $\upsilon(z,t,\lambda) \overset{\Im}{\longleftrightarrow} \Upsilon(z,f,\lambda)$ and $h_F(z,t,\lambda) \overset{\Im}{\longleftrightarrow} H_F(z,f,\lambda)$, it follows that the multimode fiber frequency response $H_F(z,f,\lambda)$ under impulsive spectral excitation coincides with the modal function $\Upsilon(z,f,\lambda)$ given in Equation (5.81):

$$H_F(z,f,\lambda_c) = \Upsilon(z,f,\lambda_c) = \sum_{h=1}^{M} |a_h(\lambda_c)|^2 e^{-j2\pi f z\tau_{g,h}(\lambda_c)} \tag{6.8}$$

It a valid broadband spectrum condition is assumed, the modal function coincides with the multimode fiber frequency response under impulsive spectral excitation.

Once the modal intensity transfer function is identified as the modal function, it is easy to introduce the definition of the modal bandwidth $\widehat{\mathrm{BW}}$ (MHz km) per unit length: the modal bandwidth per unit length $\widehat{\mathrm{BW}}$ (MHz km) of the modal intensity transfer function is defined as the unilateral cut-off frequency corresponding to a decrease in the intensity response spectrum of a half, or equivalently -3 dB (optical).

From the general expression (6.8), the following equation must be satisfied by the modal bandwidth:

$$|\Upsilon(z, \widehat{\mathrm{BW}}, \lambda_c)| = \left| \sum_{h=1}^{M} |a_h(\lambda_c)|^2 e^{-j2\pi \widehat{\mathrm{BW}} z \tau_{g,h}(\lambda_c)} \right| = \frac{1}{2} \tag{6.9}$$

The modal bandwidth defined in Equation (6.9) is not related to any Gaussian approximation. It is simply defined through the modal function assuming impulsive spectral excitation. In order to make a step forward, the intensity frequency response must now be assumed to be approximated by the Gaussian profile. Without caring about the conditions for having a reasonably Gaussian fitting, as already discussed before, it will now be assumed that the modal frequency response $\Upsilon(z, f, \lambda)$ is reasonably interpolated by the Gaussian transfer function. To define the Gaussian frequency interpolation the only parameter needed is the spectrum bandwidth. This parameter will be represented by means either of the RMS width or the half-width at half-maximum of the intensity transfer function in the frequency domain.

6.1.2.2 Modal Bandwidth

Assuming Gaussian modeling and using the Gaussian relationships between the half-width at half-maximum bandwidth and the corresponding standard deviation in the time domain derived in Chapter 3, Section 3.11.3, Equation (3.117), the modal RMS pulse width $\sigma_m(z, \lambda_c)$ in Equation (5.17) can be expressed in terms of the modal fiber bandwidth per unit length $\widehat{\mathrm{BW}}$ (MHz km):

$$\sigma_m(z, \lambda_c) = \frac{z}{\pi} \sqrt{\frac{\ln 2}{2}} \frac{1}{\widehat{\mathrm{BW}}(\lambda_c)} \cong 0.187 \frac{z}{\widehat{\mathrm{BW}}(\lambda_c)} \quad \text{(ps)} \tag{6.10}$$

Both the modal RMS pulse width $\hat{\sigma}_m(\lambda_c)$ and the modal bandwidth $\widehat{\mathrm{BW}}$ are defined over a specific unit length of optical fiber link. The time scaling assumption states that without any mode coupling each individual modal group delay $t_{g,h}(z, \lambda_c)$ measured after the distance z from the launching section is directly proportional to the propagated distance z. This means that under the time scaling assumption the group delay of each individual mode measured after a propagation length z can be expressed as the product of the group delay per unit length $\tau_{g,h}(\lambda_c)$ expressed in ns/km and the distance z (km) propagated along the multimode fiber:

$$t_{g,h}(z, \lambda_c) = \tau_{g,h}(\lambda_c) z \tag{6.11}$$

The ensemble averaged modal delay time $\overline{t}_m(\lambda_c)$ and the corresponding RMS pulse width $\sigma_m(z, \lambda_c)$ are expressed by Equations (5.6) and (5.17) respectively, which are reproduced here and evaluated more conveniently using the impulsive spectral excitation λ_c:

$$\overline{t}_m(z, \lambda) = z \overline{\tau}_m(\lambda_c) = z \sum_{h=1}^{M} |a_h(\lambda)|^2 \tau_{g,h}(\lambda) \tag{6.12}$$

$$\sigma_m(z, \lambda_c) = z \sqrt{\sum_{h=1}^{M} |a_h(\lambda_c)|^2 [\tau_{g,h}(\lambda_c) - \overline{\tau}_m(\lambda_c)]^2} \tag{6.13}$$

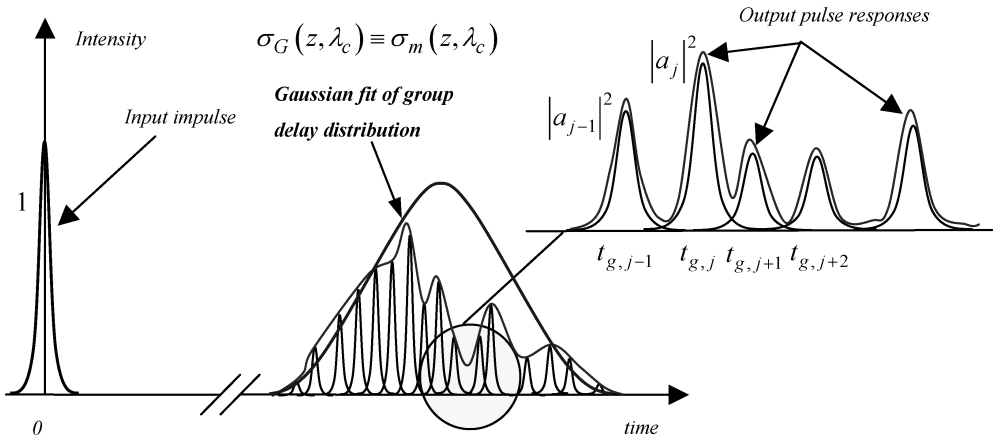

Figure 6.1 Description of the Gaussian fit procedure of the group delay distribution measured at distance z from the launching section. The group delay distribution is assumed to be a centered process with a zero average value. The RMS width of the group delay distribution is used to generate the Gaussian model

Figure 6.1 shows qualitatively the concepts that have just been introduced. At this point, in order to have a Gaussian model of the modal impulse response, the following condition is set:

$$\sigma_{\mathrm{G}}(z, \lambda_{\mathrm{c}}) \equiv \sigma_{\mathrm{m}}(z, \lambda_{\mathrm{c}}) \tag{6.14}$$

This is the meaning of the Gaussian modeling: it assumes that the modal impulse response after a distance z from the launching section can be fitted by the Gaussian function having the standard deviation $\sigma_{\mathrm{G}}(z, \lambda_{\mathrm{c}})$ equal to $\sigma_{\mathrm{m}}(z, \lambda_{\mathrm{c}})$. Substituting Equation (6.10) into Equation (6.14) gives the relationship between the Gaussian fitting of the modal impulse response RMS width and the modal bandwidth.

To conclude this section, the expression (3.117) of the full-width at half-maximum $\mathrm{FWHM_t}(\lambda_{\mathrm{c}})$ of the modal impulse response is given for the modal bandwidth in the Gaussian approximation:

$$\mathrm{FWHM_t}(\lambda_{\mathrm{c}}) = \frac{2\ln 2}{\pi} \frac{z}{\mathrm{BW}(\lambda_{\mathrm{c}})} \cong 0.44 \frac{z}{\mathrm{BW}(\lambda_{\mathrm{c}})} \tag{6.15}$$

In order to have a quantitative idea of the above relationship, a multimode fiber with a modal bandwidth $\mathrm{BW} = 500\,\mathrm{MHz\,km}$ produces a Gaussian modal impulse response with $\mathrm{FWHM_t} \cong 883\,\mathrm{ps/km}$.

6.1.2.3 Total Pulse Dispersion

In the previous section the modal bandwidth was related to the modal impulse response RMS width in the time domain. In order to include the chromatic dispersion in the Gaussian modeling there is a need to generalize the relationship (6.14) adding the chromatic dispersion. Using the result in Chapter 5, the variances of the modal impulse response and the chromatic impulse response are added together, as reported in Equation (5.40). To simplify the modeling it will be assumed, unless otherwise stated, that the linear chromatic dispersion approximation is as derived in Equation (4.120):

$$\sigma_{\mathrm{c}}(z, \overline{\lambda}) = |D_{\mathrm{c}}(\overline{\lambda})| \sigma_{\mathrm{s}} z \tag{6.16}$$

Here the average wavelength $\overline{\lambda}$ source spectrum was used instead of λ_{c} to identify the reference wavelength for evaluating the spectral properties of the group delay function. Substituting

Equations (6.10) and (6.16) into Equation (5.40) gives the expression of the total pulse RMS width for the Gaussian approximation:

$$\sigma_{\mathrm{G}}(z,\overline{\lambda}) = \sqrt{\sigma_{\mathrm{m}}^2(z,\overline{\lambda}) + \sigma_{\mathrm{c}}^2(z,\overline{\lambda})} = z\sqrt{\frac{\ln 2}{2\pi^2}\frac{1}{\widehat{\mathrm{BW}}^2(\overline{\lambda})} + |D_{\mathrm{c}}(\overline{\lambda})|^2\sigma_{\mathrm{s}}^2} \quad \text{(ps)} \tag{6.17}$$

The normalized Gaussian pulse approximation of the time-centered multimode fiber impulse response is therefore given by the following expression:

$$h_{\mathrm{F}}(z,t,\overline{\lambda}) \cong h_{\mathrm{G}}(z,t,\overline{\lambda}) = \frac{\exp -\left\{\dfrac{(t/z)^2}{(\ln 2/\pi^2)[1/\widehat{\mathrm{BW}}^2(\overline{\lambda})] + 2|D_{\mathrm{c}}(\overline{\lambda})|^2\sigma_{\mathrm{s}}^2}\right\}}{z\sqrt{\dfrac{\ln 2}{\pi}\dfrac{1}{\widehat{\mathrm{BW}}^2(\overline{\lambda})} + 2\pi|D_{\mathrm{c}}(\overline{\lambda})|^2\sigma_{\mathrm{s}}^2}} \tag{6.18}$$

6.1.2.4 Frequency Response

The Fourier transform pair of the Gaussian pulse is given by Equation (3.105):

$$h_{\mathrm{G}}(t) = \frac{1}{\sigma_{\mathrm{t}}\sqrt{2\pi}}\mathrm{e}^{-t^2/(2\sigma_{\mathrm{t}}^2)} \overset{\Im}{\longleftrightarrow} \mathrm{e}^{-2\pi^2\sigma_{\mathrm{t}}^2 f^2} = H_{\mathrm{G}}(f)$$

Using the total dispersion in Equation (6.17), the following frequency response is found:

$$H_{\mathrm{G}}(z,f,\overline{\lambda}) = \exp -2\pi^2\left[\frac{\ln 2}{2\pi^2}\frac{1}{\widehat{\mathrm{BW}}^2(\overline{\lambda})} + |D_{\mathrm{c}}(\overline{\lambda})|^2\sigma_{\mathrm{s}}^2\right] z^2 f^2 \tag{6.19}$$

Due to the time domain normalization, $H_{\mathrm{G}}(z,0,\overline{\lambda}) = 1$. The expression of the multimode fiber frequency response just derived needs some relevant comments:

1. The exponent of Equation (6.19) shows that both the frequency f and the distance z play the same role from a mathematical point of view:
   (a) For any fixed distance $z = z_0$, the transfer function is a Gaussian function in the frequency domain.
   (b) For any fixed frequency value $f = f_0$ the frequency response evaluated at f_0 shows a Gaussian shape with the distance.
2. Due to the spatial Gaussian decay, increasing the distance from the launching section corresponds to narrowing the frequency response. This is of course expected and is the effect of pulse broadening in the time domain at longer propagation distances.
3. The factor in brackets in the following equation of the Gaussian link dispersion $C_{\mathrm{G}}(\lambda)$ has the dimension of a time over unit length and includes both contributions from chromatic and modal dispersions:

$$C_{\mathrm{G}}^2(\overline{\lambda}) \equiv 4\pi^2\left[\frac{\ln 2}{2\pi^2}\frac{1}{\widehat{\mathrm{BW}}^2(\overline{\lambda})} + |D_{\mathrm{c}}(\overline{\lambda})|^2\sigma_{\mathrm{s}}^2\right] \tag{6.20}$$

Comparing this with the expression for the total pulse RMS width of the Gaussian approximation given in Equation (6.17), it is concluded that

$$\begin{aligned} C_{\mathrm{G}}(\overline{\lambda}) &= 2\pi\hat{\sigma}_{\mathrm{G}}(\overline{\lambda}) \\ \sigma_{\mathrm{G}}(z,\overline{\lambda}) &= z\hat{\sigma}_{\mathrm{G}}(\overline{\lambda}) \end{aligned} \tag{6.21}$$

In order to highlight the symmetry of the Gaussian frequency response, the variable x equal to the distance–frequency product is introduced:

$$x \equiv z \cdot f \tag{6.22}$$

Using the definitions of Equations (6.20) and (6.22), the Gaussian approximation of the multimode fiber frequency response in Equation (6.19) takes the following canonical form:

$$H_{\mathrm{G}}(x, \overline{\lambda}) = \mathrm{e}^{-\frac{1}{2}C_{\mathrm{G}}^2(\overline{\lambda})x^2} \tag{6.23}$$

6.2 Comparing Engineering Solutions

High-speed datacommunication relies today mostly on directly modulated semiconductor lasers. As already introduced, semiconductor lasers are the only light source available today that simultaneously satisfies such basic requirements as high-speed direct modulation, low cost, low power and easy optical coupling to multimode fibers. Nevertheless, in the following examples multigigabit semiconductor lasers will be compared with light emitting diodes (LED), essentially characterized by a lower modulation speed, a broader emitted spectrum but still a lower cost compared to laser diodes. To this purpose, it is interesting to compare the chromatic and modal dispersion contributions to the total pulse RMS width for the Gaussian approximation given in Equation (6.17). It is known that the light source spectrum directly influences the chromatic response and by approximating the modal response using the Gaussian profile, the single-parameter modal bandwidth completely specifies the frequency transfer function. The first term in the second member of the total dispersion in Equation (6.17) comes from the modal response while the second one represents the contribution of chromatic dispersion.

In the following two applications of the multimode fiber operating at 1310 nm and 850 nm respectively are considered. In both cases, the light source is assumed to be either a single-mode VCSEL (vertical cavity semiconductor emitting laser) or a standard surface emitting LED, resulting in a total of four transmission applications. In order to simplify the approach without losing the generality of the conclusions, it is assumed that both light source spectra are characterized by a single peak of different widths. The very different spectrum widths and contributions of the chromatic dispersion between the two light sources and wavelength windows cause the total dispersion composition to range from almost a modal contribution only up to a dominant chromatic dispersion term. The total dispersion in Equation (6.17) has been referred to the unit fiber length, $z = 1$ km. Table 6.1 summarizes the four cases considered.

Table 6.1 The four cases considered giving the corresponding source and fiber parameters used to determine the dispersion performances. The values presented are indicative and usually correspond to worst-case conditions

Source	Wavelength	
	MMF 850 nm	MMF 1310 nm
VCSEL	$\sigma_{\mathrm{s}} = 0.6$ nm $\widehat{\mathrm{BW}} = 160$ MHz km $\lvert D_{\mathrm{c}} \rvert = 116$ ps/nm km	$\sigma_{\mathrm{s}} = 1$ nm $\widehat{\mathrm{BW}} = 500$ MHz km $\lvert D_{\mathrm{c}} \rvert = 6$ ps/nm km
LED	$\sigma_{\mathrm{s}} = 30$ nm $\widehat{\mathrm{BW}} = 160$ MHz km $\lvert D_{\mathrm{c}} \rvert = 116$ ps/nm km	$\sigma_{\mathrm{s}} = 40$ nm $\widehat{\mathrm{BW}} = 500$ MHz km $\lvert D_{\mathrm{c}} \rvert = 6$ ps/nm km

Example 6.1

Source: VCSEL
Fiber: MMF $\longrightarrow$ Modal dispersion is limited
Wavelength: 850 nm

$$\left.\begin{array}{l}\sigma_s = 0.6\,\text{nm} \\ |D_c| = 116\,\text{ps/nm km} \\ \widehat{\text{BW}} = 160\,\text{MHz km}\end{array}\right\} \Rightarrow \left\{\begin{array}{l}\sigma_c = 69.6\,\text{ps} \\ \sigma_m = 1170\,\text{ps}\end{array}\right\} \Rightarrow \sigma_G = 1172\,\text{ps}$$

In this case the contribution from chromatic dispersion to total dispersion is almost negligible. The multimode fiber impulse response per unit length is then dominated by modal dispersion.

Example 6.2

Source: LED
Fiber: MMF $\longrightarrow$ Chromatic dispersion is limited
Wavelength: 850 nm

$$\left.\begin{array}{l}\sigma_s = 30\,\text{nm} \\ |D_c| = 116\,\text{ps/nm km} \\ \widehat{\text{BW}} = 160\,\text{MHz km}\end{array}\right\} \Rightarrow \left\{\begin{array}{l}\sigma_c = 3480\,\text{ps} \\ \sigma_m = 1170\,\text{ps}\end{array}\right\} \Rightarrow \sigma_G = 3671\,\text{ps}$$

In this case the contribution from modal dispersion is much less relevant than that from chromatic dispersion. The multimode fiber impulse response per unit length is therefore dominated by chromatic dispersion.

Example 6.3

Source: VCSEL
Fiber: MMF $\longrightarrow$ Modal dispersion is limited
Wavelength: 1310 nm

$$\left.\begin{array}{l}\sigma_s = 1\,\text{nm} \\ |D_c| = 6\,\text{ps/nm km} \\ \widehat{\text{BW}} = 500\,\text{MHz km}\end{array}\right\} \Rightarrow \left\{\begin{array}{l}\sigma_c = 6\,\text{ps} \\ \sigma_m = 375\,\text{ps}\end{array}\right\} \Rightarrow \sigma_G = 375.05\,\text{ps}$$

In this case the contribution from chromatic dispersion is even less significant than in Example 6.1. The reduced chromatic dispersion coefficient in the 1310 nm wavelength region makes the role of the modal dispersion over the chromatic term much more evident. The multimode fiber impulse response per unit length is dominated by modal dispersion.

Example 6.4

Source: LED
Fiber: MMF $\longrightarrow$ Modal dispersion and chromatic dispersion are comparable
Wavelength: 1310 nm

$$\left.\begin{array}{l}\sigma_s = 40\,\text{nm} \\ |D_c| = 6\,\text{ps/nm km} \\ \widehat{\text{BW}} = 500\,\text{MHz km}\end{array}\right\} \Rightarrow \left\{\begin{array}{l}\sigma_c = 240\,\text{ps} \\ \sigma_m = 375\,\text{ps}\end{array}\right\} \Rightarrow \sigma_G = 445\,\text{ps}$$

In this case the contributions from chromatic dispersion and modal dispersion are within the same order of magnitude and no dominating term exists. Depending on the LED spectral width and fiber modal bandwidth, the major broadening role can depend on either of these two factors.

Table 6.2 The results of the dispersion calculations given in the text. Using semiconductor lasers like VCSEL the link bandwidth limitation comes from the multimode fiber modal dispersion, both in the first and second windows. Using an LED light source, chromatic dispersion is dominant in the first window due to a higher dispersion coefficient, and both chromatic and modal dispersions give comparable contributions to the total dispersion in the second window

Source	Wavelength	
	MMF 850 nm	MMF 1310 nm
VCSEL	Modal dispersion	Modal dispersion
LED	Chromatic dispersion	Modal and chromatic dispersion are comparable

Table 6.2 summarizes the calculation results. The examples lead to the following conclusions:

1. Using semiconductor lasers like VCSEL, the modal bandwidth has the dominant role in defining the total dispersion of the impulse response in both operating windows.
2. Using an LED, the comparison depends on the operating windows. At 850 nm, the large chromatic dispersion coefficient of the multimode fiber together with the large spectrum width of the LED makes the chromatic dispersion highly dominant over the modal bandwidth. Operating at 1310 nm instead, the lower value of chromatic dispersion raises the relevance of the modal bandwidth and both dispersion contributions become comparable to each other.
3. The comparison of the last two cases in Examples 6.3 and 6.4 reveals the interesting conclusion that when operating at 1310 nm the fiber link bandwidth gains less than 20 % using the VCSEL instead of the LED. The modal bandwidth in fact almost dominates both transmission conditions.

The last point does not seem to justify the effort required to achieve a market-oriented VCSEL operating at 1310 nm, since 1310 nm LEDs have been available in the market since the mid 1980s. However, it is important to note two more points:

1. In the examples it was assumed that a legacy MMF bandwidth of 500 MHz/km was used when operated in the 1310 nm region. This assumption corresponds to choosing the worst-case commercial fiber available to date. Improving the fiber bandwidth at 1310 nm makes sense only if VCSEL sources are going to be used or unless LED chromatic dispersion limitations saturate overall link performances.
2. The modulation bandwidth of the LED is not comparable to the VCSEL capability and multigigabit transmission can be achieved only using semiconductor laser light sources.

In addition to these considerations, it must be made clear that all multigigabit transmission standards today require semiconductor lasers as the proper light source. This means that every standard multigigabit module will be assembled with a direct modulated semiconductor laser like the VCSEL, Fabry-Perot (FP) or distributed feedback (DFB) laser. As often happens in every engineering field, if one parameter is chosen to improve a particular performance some other related characteristics are going in another direction, inducing different but still performance-related

impairments. This is also the case for semiconductor lasers operating in multigigabit transmission over multimode fiber links, which creates high variability in the modal impulse response profile due to restricted launch conditions.

6.2.1 The Gaussian Link Dispersion Factor

The expression derived for the Gaussian approximation of the multimode fiber transfer function (6.23) allows an easy interpretation of the Gaussian link dispersion $C_G(\overline{\lambda})$. Setting $\overline{x}_C = 1/C_G(\overline{\lambda})$ in Equation (6.23), the transfer function takes the value

$$H_G\left(\frac{1}{C_G(\overline{\lambda})}, \overline{\lambda}\right) = \frac{1}{\sqrt{e}} \cong 0.607 \cong -2.17\,\text{dB}$$

Hence:

1. The reciprocal of the Gaussian link dispersion $C_G(\overline{\lambda})$ coincides with the contour $\overline{x}_G = z \cdot f = 1/C_G(\overline{\lambda})$ in the $(z,\ f)$ plane at which the transfer function $H_G(\overline{x}_C, \overline{\lambda})$ decays at $1/\sqrt{e}$ of the value it reaches at the origin, $x = 0$, or equivalently decays at -2.17 dB.

The transfer function has been defined for the intensity of the optical field and all logarithmic ratios are calculated according to the $10\log_{10}$ definition. The smaller the Gaussian link dispersion $C_G(\overline{\lambda})$, the larger the value x_c becomes and the more the MMF link performs. The present analysis also has a very simple geometrical interpretation, presented below:

2. Given a multimode fiber link specified by the Gaussian link dispersion $C_G(\overline{\lambda})$, the $1/\sqrt{e}$ roll-off of the transfer frequency function gives the hyperbola $z \cdot f = \overline{x}_C$ between the link distance z and the frequency f with constant $\overline{x}_C = 1/C_G(\overline{\lambda})$.

Figure 6.2 presents the qualitative behavior of the hyperbolic contour at constant Gaussian link dispersion $C_G(\overline{\lambda})$ corresponding to the intensity transfer function decaying of $1/\sqrt{e} \cong -2.17$ dB.

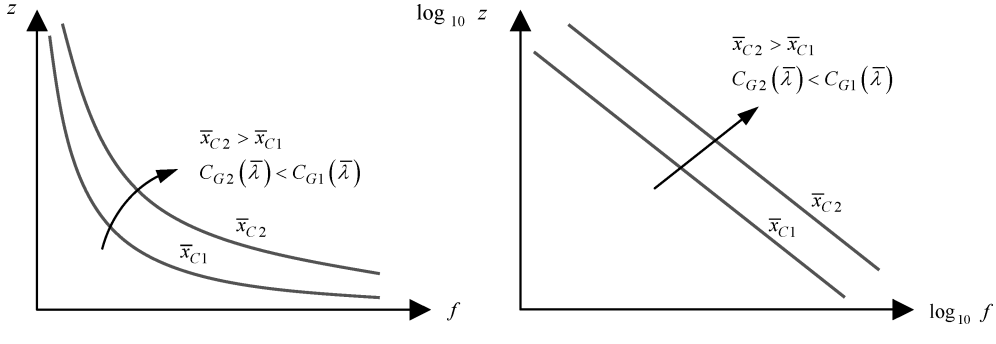

Figure 6.2 Qualitative drawing of the hyperbolic relationship between the distance and frequency in the Gaussian transfer function (6.23) of the multimode fiber. Left: linear scale representation of the hyperbola between the distance and frequency for two different values of the Gaussian link dispersion. Right: logarithmic scale representation of the same case reported in the linear scale. In this case the hyperbolic relationship is of course plotted as a straight line

Assuming similar conditions to those reported in Examples 6.1 to 6.4, the Gaussian link dispersion $C_G(\overline{\lambda})$ takes the following values respectively:

Case A

Source: VCSEL
Fiber: MMF
Wavelength: 850 nm

$$\left.\begin{array}{l}\sigma_s = 0.6\,\text{nm} \\ |D_c| = 116\,\text{ps/nm km} \\ \widehat{\text{BW}} = 160\,\text{MHz km}\end{array}\right\} \Rightarrow C_G(\overline{\lambda}) = 7.37\,\text{ns/km}$$

Case B

Source: LED
Fiber: MMF
Wavelength: 850 nm

$$\left.\begin{array}{l}\sigma_s = 30\,\text{nm} \\ |D_c| = 116\text{ps/nm km} \\ \widehat{\text{BW}} = 160\,\text{MHz km}\end{array}\right\} \Rightarrow C_G(\overline{\lambda}) = 23.07\,\text{ns/km}$$

Case C

Source: VCSEL
Fiber: MMF
Wavelength: 1310 nm

$$\left.\begin{array}{l}\sigma_s = 1\,\text{nm} \\ |D_c| = 6\,\text{ps/nm km} \\ \widehat{\text{BW}} = 500\,\text{MHz km}\end{array}\right\} \Rightarrow C_G(\overline{\lambda}) = 2.36\,\text{ns/km}$$

Case D

Source: LED
Fiber: MMF
Wavelength: 1310 nm

$$\left.\begin{array}{l}\sigma_s = 40\,\text{nm} \\ |D_c| = 6\,\text{ps/nm km} \\ \widehat{\text{BW}} = 500\,\text{MHz km}\end{array}\right\} \Rightarrow C_G(\overline{\lambda}) = 2.80\,\text{ns/km}$$

Figures 6.3 to 6.6 give the three-dimensional plots of the Gaussian approximations of the multimode fiber transfer function (6.23) assuming the Gaussian link dispersion $C_G(\overline{\lambda})$ values corresponding to the four cases A to D listed above.

The three-dimensional functional plots have been computed using Matlab® 7.0.2 code. In order to show the functional symmetry between the distance and frequency clearly, the graph of the multimode fiber transfer Gaussian function (6.23) has been plotted on to a four quadrants representation. Negative values of both variables have no physical meaning in this case. The characteristic cross-like shape of $H_G(z, f, \overline{\lambda})$ derives from the symmetry of the function with respect to the two variables, as stated above. As long as the optical pulse propagates along the fiber length z, the functional dependence from the frequency becomes narrower, following a Gaussian shape. The same conclusions are valid when assuming a fixed frequency f and analyzing pulse intensity versus the position coordinate. For any fixed frequency the pulse intensity decreases with increasing distance z according to the Gaussian profile. Figures 6.4, 6.5 and 6.6 show the same calculations for the other

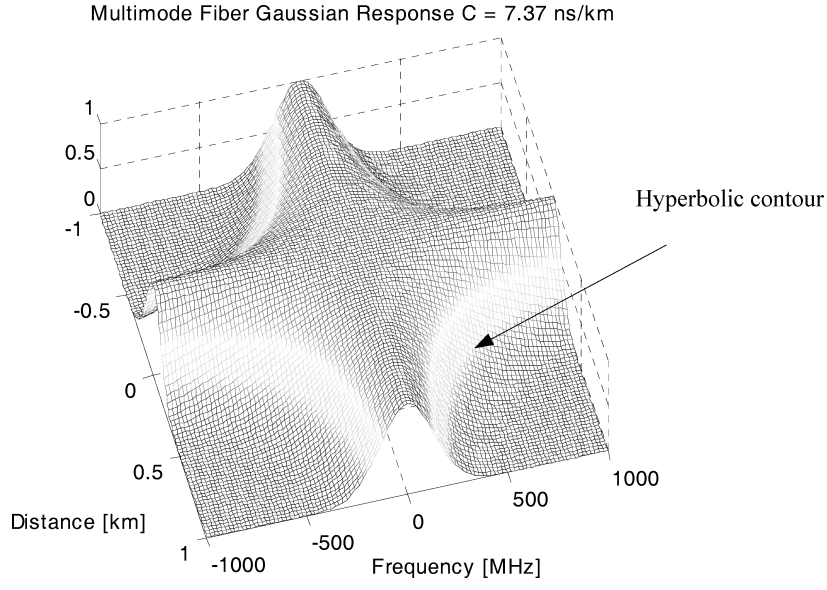

Figure 6.3 Numerical evaluation of the Gaussian approximation of the multimode fiber transfer function $H_G(z, f, \overline{\lambda})$ given in Equation (6.23). The value of the Gaussian link dispersion $C_G(\overline{\lambda}) = 7.37$ ns/km corresponds to case A

three cases B, C and D presented above. In each figure the physical first quadrant representation has been added.

6.2.2 Hyperbolic Contour at Fixed Intensity

The orthogonal projection of the multimode fiber Gaussian transfer function (6.23) on to the (z, f) plane clearly reveals the hyperbolic constant contour property. The constant contour curves are all hyperbolas whose characteristic constant $\kappa(\lambda)$ is proportional to the reciprocal of the Gaussian link dispersion $C_G(\overline{\lambda})$. Equation (6.23) gives the following equation for the generic hyperbolic projection:

$$H_G(z, f, \overline{\lambda})|_{z\ f=\kappa} = e^{-\frac{1}{2}C_G^2(\overline{\lambda})\kappa^2} = \frac{1}{\alpha}, \qquad z\ f = \kappa, \quad 1 < \alpha < +\infty \tag{6.24}$$

Then

$$z = \left[\frac{\sqrt{2\log\alpha}}{|C_G(\overline{\lambda})|}\right]\frac{1}{f} \tag{6.25}$$

The parameter α defines the reciprocal of the relative intensity level of the hyperbolic contour. For the special hyperbola characterized by the constant value $\alpha = \sqrt{e}$, the above equation gives the following hyperbolic contour:

$$z = \frac{1}{|C_G\ (\overline{\lambda})|}\frac{1}{f} \tag{6.26}$$

Figure 6.7 gives the three-dimensional plot of the transfer function for case A. The contour line at $1/\sqrt{e}$ has been added. The comparison between the multimode fiber Gaussian transfer functions for the two cases A and C is presented in Figure 6.8. Both plots show the projections of the Gaussian

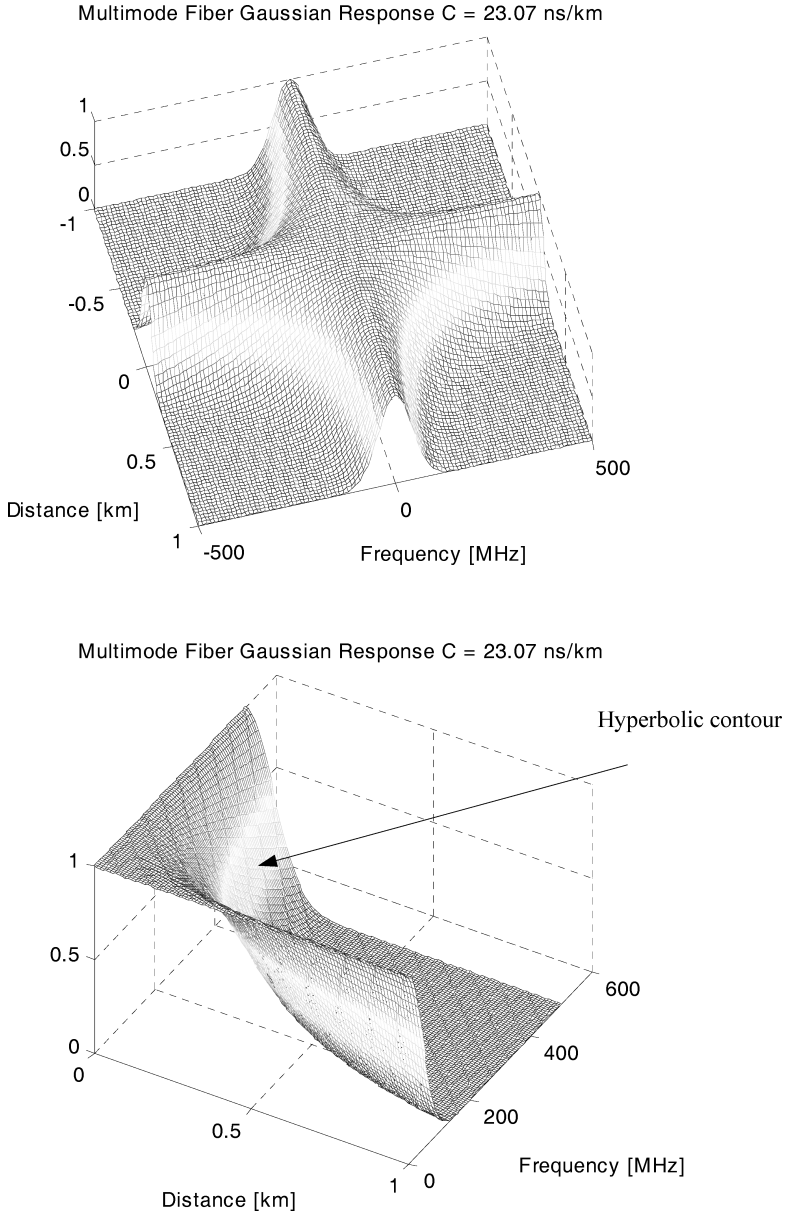

Figure 6.4 Top: numerical evaluation of the multimode fiber transfer function $H_{\mathrm{G}}\ (z, f, \overline{\lambda})$ given in Equation (6.23). The value of the Gaussian link dispersion $C_{\mathrm{G}}(\overline{\lambda}) = 23.07$ ns/km corresponds to case B. Bottom: first quadrant representation ($z > 0$, $f > 0$)

transfer function on to the (z, f) plane, where the two corresponding hyperbolic contours at $1/\sqrt{\mathrm{e}}$ have been added. It is evident that case C refers to a multimode fiber link with a higher transmission bandwidth per unit length than that of case A. The lower Gaussian link dispersion $C_{\mathrm{G}}(\overline{\lambda})$ shown for case C causes the hyperbolic line to be located further away from the origin than that for case A.

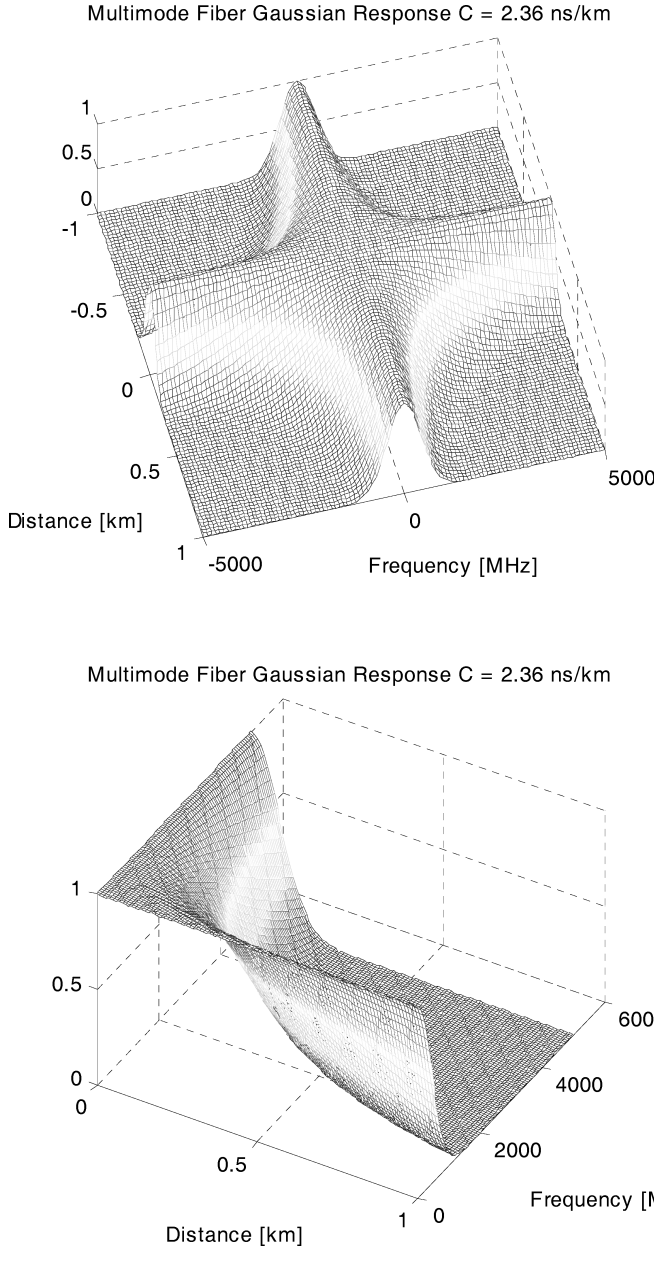

Figure 6.5 Top: numerical evaluation of the multimode fiber transfer function $H_{\mathrm{G}}\ (z,\ f, \overline{\lambda})$ given in Equation (6.23). The value of the Gaussian link dispersion $C_{\mathrm{G}}(\overline{\lambda}) = 2.36$ ns/km corresponds to case C. Bottom: first quadrant representation ($z > 0$, $f > 0$)

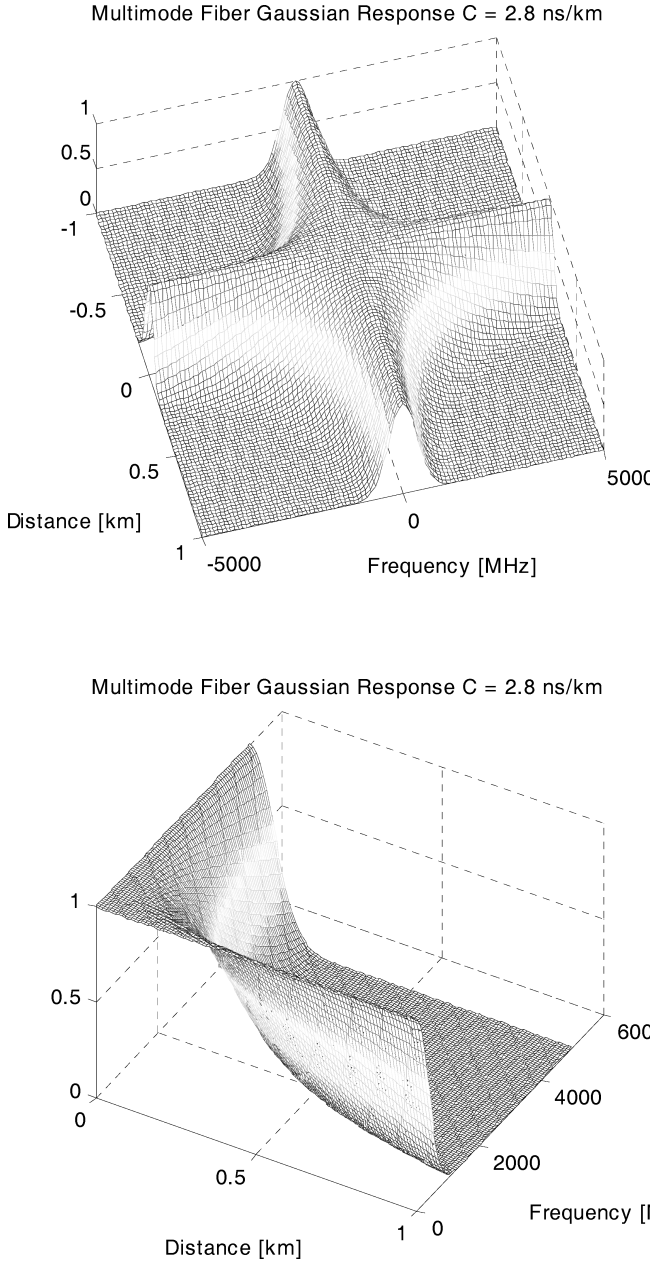

Figure 6.6 Top: numerical evaluation of the multimode fiber transfer function $H_{\mathrm{G}}\ (z, f, \overline{\lambda})$ given in Figure (6.23). The value of the Gaussian link dispersion $C_{\mathrm{G}}(\overline{\lambda}) = 2.8\,\mathrm{ns/km}$ corresponds to case D. Bottom: first quadrant representation ($z > 0$, $f > 0$)

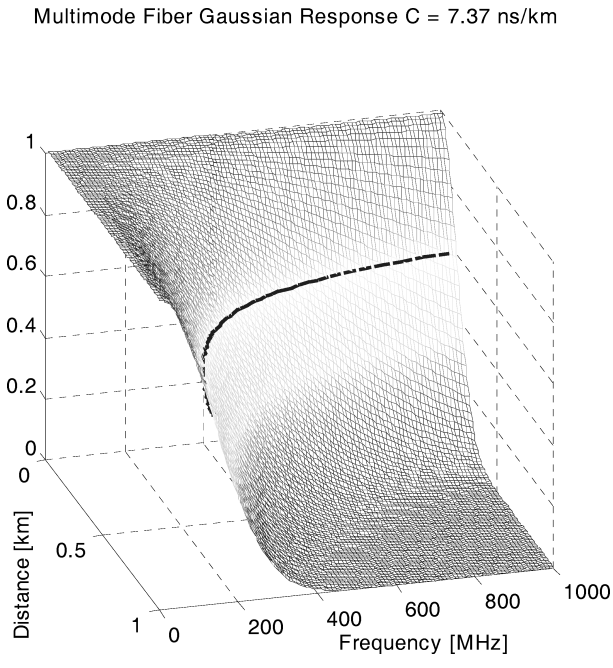

Figure 6.7 Projection of the transfer function for case A on to the (z, f) plane. The hyperbola corresponding to the intensity decaying at $1/\sqrt{e}$ is also shown

6.2.3 Gaussian Equivalent Link Bandwidth

In the following the Gaussian equivalent link bandwidth $B_G\ (z, \overline{\lambda})$ is defined as the half-width at half-maximum of the equivalent Gaussian frequency response of the optical intensity characterized by the total dispersion $\sigma_G\ (z, \overline{\lambda})$ given in Equation (6.17). Inverting the Gaussian relationship (6.10) and substituting $\sigma_G\ (z, \overline{\lambda})$ for $\sigma_m\ (z, \overline{\lambda})$ and $B_G\ (z, \overline{\lambda})$ z instead of $\widetilde{\mathrm{BW}}(\overline{\lambda})$, the Gaussian equivalent link bandwidth, including chromatic dispersion effects, is given by

$$B_G(z, \overline{\lambda}) = \frac{1}{\pi}\sqrt{\frac{\ln 2}{2}}\,\frac{1}{\sigma_G(z, \overline{\lambda})} \quad \text{(MHz)} \tag{6.27}$$

The link bandwidth is measured at the Half-Width at Half-Maximum of the whole Gaussian frequency response of the optical intensity, including both the effect of modal broadening and chromatic dispersion. The link bandwidth defined in Equation (6.27) has the dimension of frequency. The dependence upon the distance is included in the total dispersion $\sigma_G(z, \overline{\lambda})$.

The Gaussian equivalent link bandwidth $B_G(z, \overline{\lambda})$ is related to the Gaussian link dispersion $C_G(\overline{\lambda})$. Solving Equation (6.21) for $\sigma_G(z, \overline{\lambda})$ and substituting into Equation (6.27) gives

$$B_G(z, \overline{\lambda}) = \frac{\sqrt{2 \log 2}}{z C_G(\overline{\lambda})} \quad \text{(MHz)} \tag{6.28}$$

The Gaussian equivalent link bandwidth $B_G(z, \overline{\lambda})$ results are therefore inversely proportional to the Gaussian link dispersion $C_G(\overline{\lambda})$. Note that all of the above relations are valid in the Gaussian approximation and cannot be applied to any other transfer function profile other than the Gaussian interpolation.

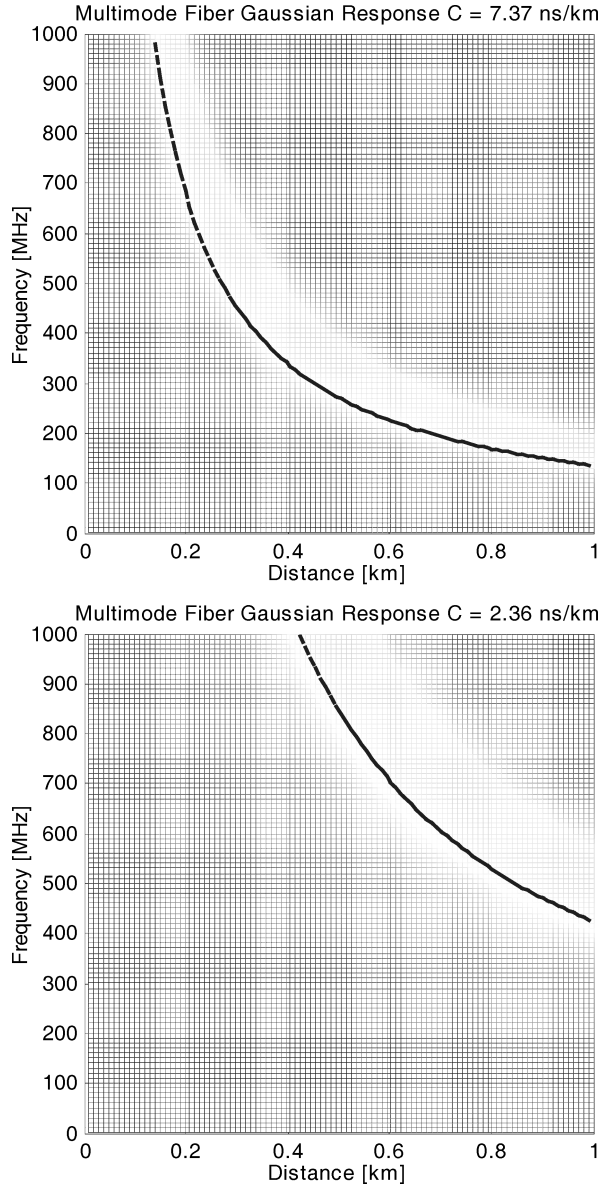

Figure 6.8 Projections of the multimode fiber Gaussian transfer function for case A (top) and for case C (bottom) on to the (z, f) plane. Hyperbolic contour lines corresponding to the intensity decaying at $1/\sqrt{e}$ are also shown. Case C with a Gaussian link dispersion of $C_G(\overline{\lambda}) = 2.36$ ns/km is characterized by a hyperbola located further away from the origin than that for case A, whose Gaussian link dispersion is $C_G(\overline{\lambda}) = 7.37$ ns/km

6.2.4 Application to Legacy MMF

In this section the standardization of the multimode fibers according to their worst-case bandwidth capability will be considered. The fiber bandwidth is defined by the ITU.T G.651 standard (September 2000) and refers to the Gaussian best fit of the measured intensity profile versus modulating

Table 6.3 Standard multimode fiber specifications according to ISO/IEC and related operating wavelength ranges. The gray-shaded specifications refer to the three cases considered in the text

Wavelength	MMF type		
	OM1 (ISO/IEC 11801)	OM2 (ISO/IEC 11801)	OM3 (ISO/IEC 11801)
850 nm	$2a = 62.5\,\mu\text{m}$ $\widehat{\text{BW}} = 160\,\text{MHz km}$ $\lvert D_\text{c}\rvert = 120\,\text{ps/nm km}$	$2a = 50\,\mu\text{m}$ $\widehat{\text{BW}} = 500\,\text{MHz km}$ $\lvert D_\text{c}\rvert = 120\,\text{ps/nm km}$	$2a = 50\,\mu\text{m}$ $\widehat{\text{BW}} = 1500\,\text{MHz km}$ $\lvert D_\text{c}\rvert = 120\,\text{ps/nm km}$
1310 nm	$2a = 62.5\,\mu\text{m}$ $\widehat{\text{BW}} = 500\,\text{MHz km}$ $\lvert D_\text{c}\rvert = 6\,\text{ps/nm km}$	$2a = 50\,\mu\text{m}$ $\widehat{\text{BW}} = 500\,\text{MHz km}$ $\lvert D_\text{c}\rvert = 6\,\text{ps/nm km}$	$2a = 50\,\mu\text{m}$ $\widehat{\text{BW}} = 500\,\text{MHz km}$ $\lvert D_\text{c}\rvert = 6\,\text{ps/nm km}$

frequency, assuming over-filled launching (OFL) conditions. Implications of the launch condition and the effectiveness of the Gaussian approximation have already been discussed. In Table 6.3 three legacy multimode fibers are considered that satisfy *a priori* the Gaussian frequency response under the assumption of over-filled launch conditions. Each fiber is excited both at 850 nm and 1310 nm wavelength regions.

According to ISO/IEC 11801: 2002 standards, all three fiber types OM1, OM2 and OM3 have the same over-filled launch modal bandwidth of 500 MHz when excited in the 1310 nm wavelength region. This is important because it leads to the same link bandwidth for a given link length when operating at 1310 nm independently from the installed fiber type. The situation is, however, much more critical in the first optical window, where the modal bandwidth strongly depends on the selected fiber standard. From Table 6.3 it is evident that changing the fiber type from OM1 to OM2 and to OM3 the modal bandwidth greatly increases from 160 MHz km to 500 MHz km and to 1500 MHz km respectively.

In the following three application cases will be considered of OM1 fiber at 850 nm, OM2 fiber at 1310 nm and exceeding OM3 fiber specification operating at 850 nm.

6.2.4.1 OM1 Fiber at 850 nm

Multimode optical fiber type OM1, with a core diameter of $2a = 62.5\,\mu\text{m}$ and operating in the 850 nm wavelength region.

$$\text{Link parameters:} \begin{cases} \text{Modal bandwidth} : \widehat{\text{BW}}(850\,\text{nm}) = 160\,\text{MHz km} \\ \text{Chromatic dispersion} : \lvert D_\text{c}\rvert = 120\,\text{ps/nm km} \\ \text{Source spectral width} : \sigma_\text{s} = 0.6\,\text{nm} \end{cases}$$

Gaussian link dispersion (6.20): $C_\text{G}(850\,\text{nm}) = 7.373\,\text{ns/km}$

Link bandwidth (6.28):

$$B_\text{G}(z, 850\,\text{nm}) = \begin{pmatrix} 1\,\text{km} & 300\,\text{m} & 100\,\text{m} & 26\,\text{m} \\ \downarrow & \downarrow & \downarrow & \downarrow \\ 159.7\,\text{MHz} & 532.3\,\text{MHz} & 1597.0\,\text{MHz} & 6142.3\,\text{MHz} \end{pmatrix}$$

Figure 6.9 shows the computed Gaussian frequency response assuming four different link lengths for the OM1 multimode fiber. Due to the requested applications in the 10BASE-SR standards, the link length of 26 m has been highlighted. As expected, the modal bandwidth increases inversely

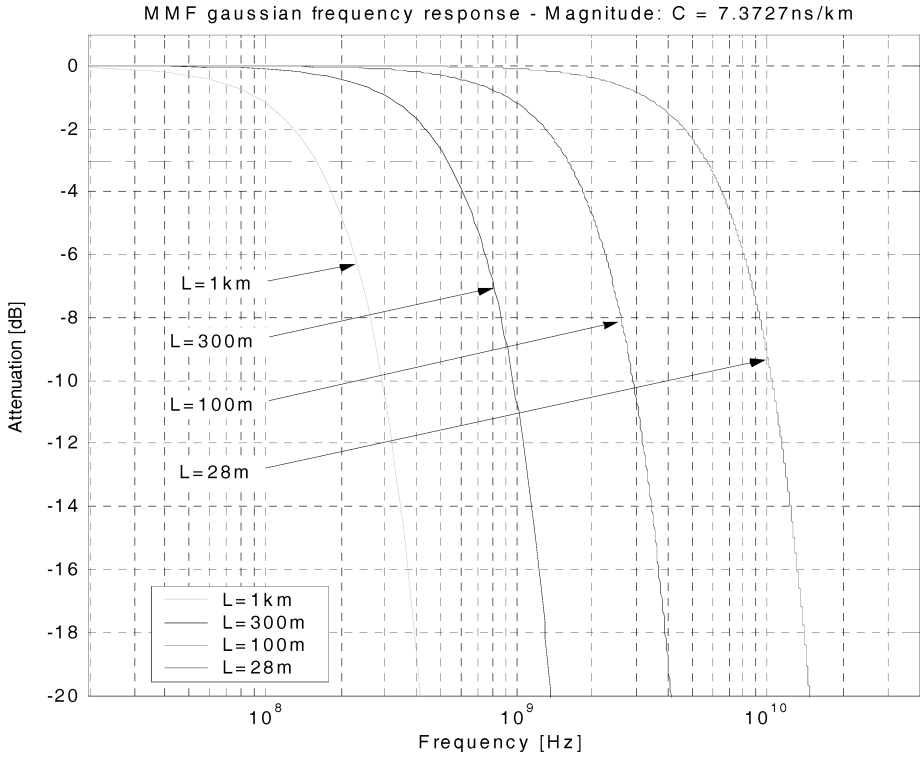

Figure 6.9 OM1 multimode fiber Gaussian frequency response versus link length. The fiber parameters refer to the legacy fiber with a core diameter of 62.5 μm operating at 850 nm, with a chromatic dispersion coefficient $|D_c| = 120$ ps/nm km. The source linewidth (VCSEL) has been assumed to be $\sigma_s = 0.6$ nm. The Gaussian link dispersion of the MMF link is $C_G(850\,\text{nm}) = 7.373$ ns/km. The link bandwidth is in excess of 6.5 GHz after the length of 24 m

in proportion to the link length, reaching the required channel bandwidth for the 10 GbE signal at about the link length of 26 m.

The Gaussian modeling greatly facilitates the link design but it should be noted that in field deployments of multimode fiber links the effective frequency response rarely matches the Gaussian shape. In particular, for multigigabit transmission the over-filled launch condition cannot be satisfied by laser sources due to the restricted far-field angle and small intensity spot size. As described in Chapter 5, the uniform modal excitation is one of the primary conditions to be verified in order to expect a Gaussian-like impulse response. Accordingly, it should be concluded that in multigigabit transmissions requiring a high-speed directly modulated laser source, the Gaussian impulse response would only rarely be expected. However, in multigigabit transmissions the standardization suggests the offset launch technique in order to excite a relatively large number of higher-order modes in the multimode fiber, enabling a relatively tight group delay matching and consequently an almost Gaussian fitted impulse response.

To gain an idea of the relationship between the link length and data rate transmitted over the multimode fiber, the one-half bit rate bandwidth criteria can be considered as a 'rule-of-the-thumb'. Basically, the required channel bandwidth, in order to allow reasonable data transmission without caring about any data pulse shaping optimization, would be about one-half of the bit rate. It is noted that Nyquist signaling with sinc pulses requires exactly one-half of a bandwidth. Referring

to the computed Gaussian responses in Figure 6.9, it can be concluded that OM1 fiber allows NRZ data transmission at 1250 Mb/s (1 GbE) over about 250 m of fiber link length, reaching about 70 m of link length at 4250 Mb/s, which corresponds to the 4GFC standard.

6.2.4.2 OM2 Fiber at 1310 nm

Multimode optical fiber type OM2, with a core diameter of $2a = 50\,\mu\text{m}$ and operating in the 1310 nm wavelength region.

$$\text{Link parameters:} \begin{cases} \text{Modal bandwidth} : \widehat{\text{BW}}(1310\,\text{nm}) = 500\,\text{MHz km} \\ \text{Chromatic dispersion} : |D_c| = 6\,\text{ps/nm km} \\ \text{Source spectral width} : \sigma_s = 1\,\text{nm} \end{cases}$$

Gaussian link dispersion (6.20): $C_G(1310\,\text{nm}) = 2.355\,\text{ns/km}$

Link bandwidth (6.28):

$$B_G(z, 1310\,\text{nm}) = \begin{pmatrix} 3\,\text{km} & 1\,\text{km} & 300\,\text{m} & 82\,\text{m} \\ \downarrow & \downarrow & \downarrow & \downarrow \\ 166.7\,\text{MHz} & 499.7\,\text{MHz} & 1666.6\,\text{MHz} & 6097.3\,\text{MHz} \end{pmatrix}$$

Figure 6.10 shows the computed Gaussian frequency response assuming four different link lengths for the OM2 multimode fiber. Multigigabit applications in the 10BASE-LRM and 10BASE-SR standards require link lengths of 300 m and 82 m respectively. Due to a higher modal bandwidth of OM2 fiber than the OM1 case, the link bandwidth available after 300 m is still reasonable for digital signal restoration by means of the electronic dispersion compensation technique. As expected, the modal bandwidth increases inversely in proportion to the link length, reaching the required channel bandwidth for the 10 GbE signal at about the link length of 82 m.

The multimode fiber designated as OM2 refers to the ISO/IEC standard and has many common parameters with the telecommunication multimode optical fiber specified in the ITU-T G.651 (1998) standards. This graded index multimode optical fiber is specified in operation of both the first and second windows. At 1310 nm it has the numerical aperture (NA) $0.20 \leq \text{NA} \leq 0.23$ and the attenuation $\alpha \leq 2\,\text{dB/km}$.

6.2.4.3 OM3 Fiber at 850 nm

Multimode optical fiber exceeding OM3 specifications, with a core diameter of $2a = 50\,\mu\text{m}$ and operating in the 850 nm wavelength region.

$$\text{Link parameters:} \begin{cases} \text{Modal bandwidth} : \widehat{\text{BW}}(850\,\text{nm}) = 2000\,\text{MHz km} \\ \text{Chromatic dispersion} : |D_c| = 120\,\text{ps/nm km} \\ \text{Source spectral width} : \sigma_s = 0.6\,\text{nm} \end{cases}$$

Gaussian link dispersion (6.20): $C_G(850\,\text{nm}) = 0.590\,\text{ns/km}$

Link bandwidth (6.28):

$$B_G(z, 1310\,\text{nm}) = \begin{pmatrix} 12\,\text{km} & 3\,\text{km} & 1\,\text{km} & 300\,\text{m} \\ \downarrow & \downarrow & \downarrow & \downarrow \\ 166.3\,\text{MHz} & 665.2\,\text{MHz} & 1995.6\,\text{MHz} & 6652.0\,\text{MHz} \end{pmatrix}$$

Figure 6.11 shows the computed Gaussian frequency response assuming four different link lengths for the OM3 multimode fiber. Multigigabit applications in the 10BASE-LRM and 10BASE-SR standards require link lengths of 300 m. Due to the higher modal bandwidth with respect to the OM2 case, the link bandwidth available after 300 m is sufficient for direct detection and decision

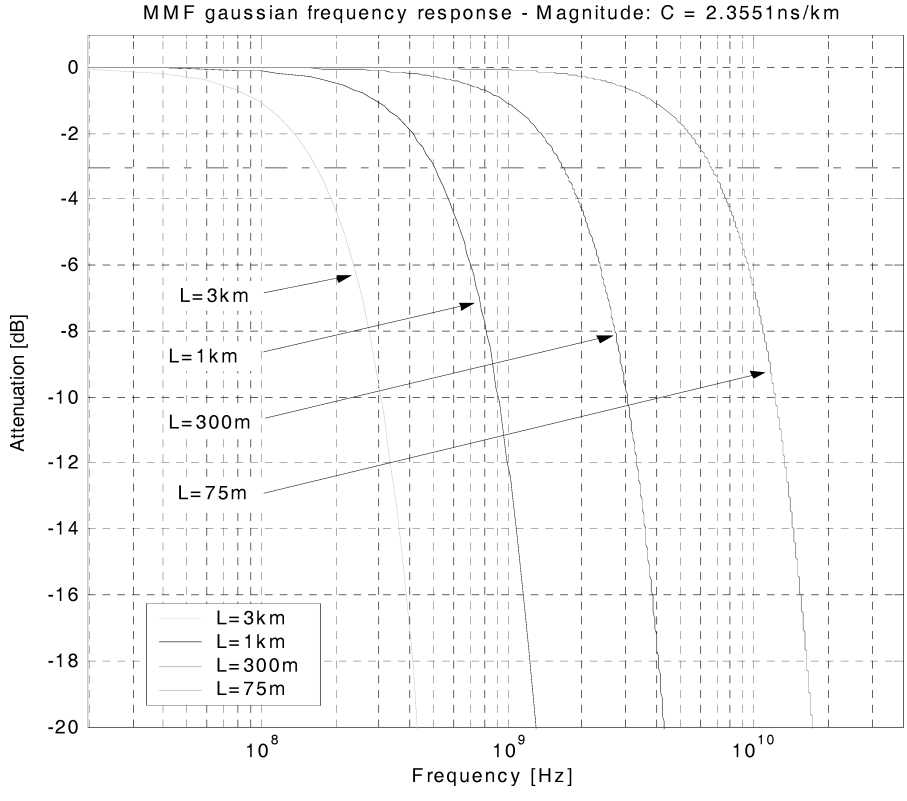

Figure 6.10 OM2 multimode fiber Gaussian frequency response versus link length. The fiber parameters refer to the legacy fiber with a core diameter of 50 μm operating at 1310 nm, with a chromatic dispersion coefficient $|D_c| = 6$ ps/nm km. The source linewidth (VCSEL) has been assumed to be $\sigma_s = 0.6$ nm. The Gaussian link dispersion of the MMF link is $C_G(1310\,\text{nm}) = 2.355$ ns/km. The link bandwidth is in excess of 6.5 GHz after the length of 75 m

without any digital signal restoration. As expected, the modal bandwidth decreases inversely in proportion to the link length, reaching about 2 GHz after 1 km. This channel bandwidth is sufficient for 10 GbE operation supported by electronic dispersion compensator architecture.

The fiber designated in OM3 ISO/IEC standards represents the high-speed proposal for using multimode optical fibers in multigigabit transmission systems. These fibers are relatively new ones as they have been installed after 1998. All remaining installed bases refer to older and lower-performance multimode optical fibers. The ISO/IEC multimode fiber standards have been written in order to designate multimode fiber into these three large categories depending on their bandwidth performances.

The population of multimode fibers actually deployed spans these three categories and multigigabit transmissions must account for very different transmission and bandwidth performances. This is the reason for the great effort in specifying the new 10 GbE IEEE.802.aq standard 10BASE-LRM in order to get the multigigabit optical link working independently from whichever fiber, ISO/IEC OM1, OM2 or OM3, has been assumed. In order to guarantee 10 GbE transmission over a minimum link length of 300 m operating in the 1310 nm wavelength region, both the transmitter and receiver must be properly specified and designed, and in particular new dispersion compensation techniques must be installed in the optical receiving unit.

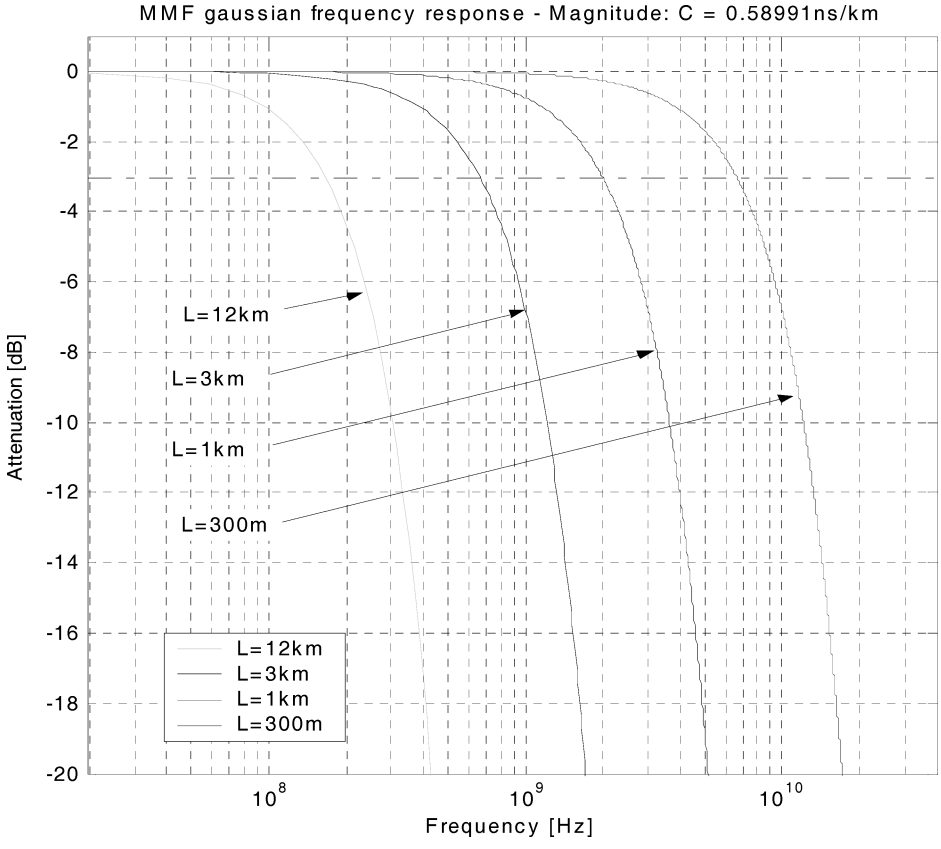

Figure 6.11 OM3 multimode fiber Gaussian frequency response versus link length. The fiber parameters refer to the legacy fiber with a core diameter of 50 μm operating at 1310 nm, with a chromatic dispersion coefficient $|D_c| = 6$ ps/nm km. The source linewidth (VCSEL) has been assumed to be $\sigma_s = 1$ nm. The Gaussian link dispersion of the MMF link is $C_G(1310\,\text{nm}) = 0.590$ ns/km. The link bandwidth is still in excess of 6.5 GHz after the length of 300 m

6.2.4.4 Comments

The computed frequency response of the three multimode fiber links considered above reveal an almost linear behavior between the fiber modal bandwidth $\widehat{\text{BW}}(\overline{\lambda})$ and the link bandwidth $B_G(z, \overline{\lambda})$ achieved for a given distance z. The mainly linear relationship that has been found means that the chromatic dispersion contribution is negligible in all the cases considered, which is easily proved below. Substituting the Gaussian link dispersion $C_G(\overline{\lambda})$ (6.20) into the expression of the link bandwidth $B_G(z, \overline{\lambda})$ (6.28) gives the following general relationship between the link bandwidth and the modal bandwidth:

$$B_G(z, \overline{\lambda}) = \frac{1}{2\pi z} \sqrt{\frac{2\log 2}{[\ln 2/(2\pi^2)][1/\widehat{\text{BW}}^2(\overline{\lambda})] + |D_c(\overline{\lambda})|^2\ \sigma_s^2}} \quad \text{(MHz)} \tag{6.29}$$

Independently from the relative contribution between the modal dispersion and the chromatic dispersion, the link bandwidth decreases inversely to the link distance z.

Assuming that the chromatic dispersion contribution is negligible with respect to the modal one, the above expression greatly simplifies, giving the following expected result:

$$B_{\mathrm{G}}(z, \overline{\lambda}) = \frac{1}{z}\widehat{\mathrm{BW}}(\overline{\lambda}) \quad (\mathrm{MHz}) \tag{6.30}$$

1. As long as modal bandwidth $\widehat{\mathrm{BW}}(\overline{\lambda})$ is the dominant effect, the link bandwidth $B_{\mathrm{G}}(z, \overline{\lambda})$ scales with the distance z.

This behavior is quite evident from the computed frequency response:

2. The link bandwidth $B_{\mathrm{G}}(z, \overline{\lambda})$ is almost constant if modal bandwidth $\widehat{\mathrm{BW}}(\overline{\lambda})$ compensates linearly for the increased link length.

According to Figures 6.9, 6.10 and 6.11, approximate link bandwidths of 530 MHz, 500 MHz and 660 MHz respectively have been achieved after 300 m, 1 km and 3 km of fiber length with corresponding modal bandwidths of 160 MHz km, 500 MHz km and 2000 MHz km. These relationships clearly confirm Equation (6.30), revealing the expected linearity between the link bandwidth and the modal bandwidth in the presence of negligible chromatic dispersion.

It is interesting to verify that the IEEE 802.3ae standards for 10 GbE applications recommend using a design with maximum link lengths of 26 m (850 nm), 82 m (1310 nm) and 300 m (850 nm) respectively using multimode fibers with modal bandwidths of 160 MHz km, 500 MHz km and 2000 MHz km respectively. In all these cases the link bandwidth $B_{\mathrm{G}}(z, \overline{\lambda})$ is almost independent of the chromatic dispersion and reaches approximately the value of 6.5 GHz.

6.3 Comparison with Transmission Lines

In this section the Gaussian modeling of the multimode fiber frequency response will be compared with the frequency response of the metallic transmission line presented in Chapter 2 with reference to the 10 GbE application case. This comparison clearly reveals the major difficulties encountered when achieving good frequency response compensation of the multimode fiber with respect to the case of the metallic transmission line. The principal difference is the characteristic square-root frequency roll-off of the transmission due to the skin effect. The square root frequency response in fact demands a smoother high-frequency compensation than the equivalent bandwidth of the multimode fiber Gaussian response would require.

Figure 6.12 shows on the same graph a comparison of the frequency response of four different multimode fibers with four different lengths of the same transmission lines. Each multimode fiber is assumed to have a Gaussian frequency response according to Equation (6.19) with a defined modal bandwidth $\widehat{\mathrm{BW}}(\overline{\lambda})$ and length z. The light source is a single-line semiconductor laser with $\sigma_{\mathrm{s}} = 1$ nm emitting either at 850 nm or 1310 nm according to the selected multimode fiber specification. The transmission line frequency response is given by Equations (2.40) and (2.46) respectively in the lower and higher frequency ranges. As discussed in Chapter 2, the transmission line model that was developed is approximated and takes into account only the skin effect in order to achieve the characteristic square root frequency response. A more accurate model of the metallic transmission line would include, however, the effects of the dispersion of the surrounding dielectric material and of the waveguide structure. Nevertheless, at least for comparison purposes, the characteristic frequency behavior is well interpreted by the present simplified model.

The fiber length has been assumed to be $z = 300$ m for all cases, while the modal bandwidth changes for each fiber type. All transmission lines have the same transversal geometry, which leads to the common value $f_{\mathrm{t}} = 2.476$ MHz for the thickness frequency. Without entering the details for the calculation of the required channel bandwidth for a 10 GbE transmission system, it can be assumed that a transmission channel bandwidth of approximately 5 GHz evaluated at -3 dBe

(decibel-electrical) would guarantee a reasonable eye diagram opening with acceptable intersymbol interference (ISI) at the receiving section. This is consistent with the one-half bit rate bandwidth rule introduced previously. These qualitative criteria will be used in this section to compare the multimode optical fiber with a transmission line frequency roll-off. In Chapter 8 the theoretical model and the design prescriptions for the 10 GbE multimode optical fiber based transmission system will be analyzed.

It is evident from Figure 6.12 that just one fiber configuration would allow for the required transmission length $z = 300\,\text{m}$ and bandwidth conditions, namely the multimode fiber with a

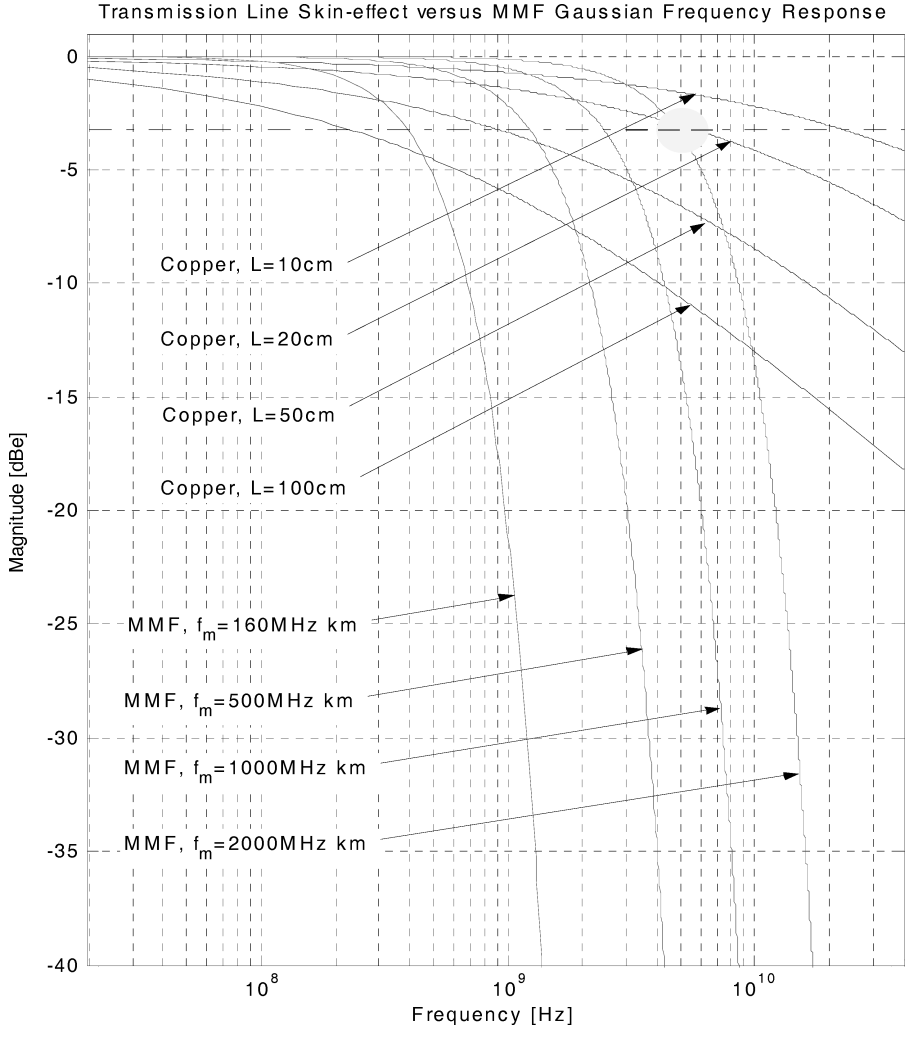

Figure 6.12 Frequency response comparison between the multimode fiber Gaussian response of a fixed link length and a copper transmission line of several lengths. The fiber bandwidth varies according to MMF specifications. The highlighted dot indicates the $-3\,\text{dB}$ link bandwidth requirement needed to achieve a reasonable 10 GbE eye diagram with an acceptable amount of ISI. This diagram reveals that the multimode fiber bandwidth requirement would not be below 2000 MHz km. The same conclusion leads to a copper transmission line length of about 20 cm

bandwidth coefficient $\widehat{\mathrm{BW}}(\overline{\lambda}) = 2000\,\mathrm{MHz\,km}$. The same bandwidth on the copper transmission line would be achieved approximately after a line length of only $L_\mathrm{T} = 20\,\mathrm{cm}$. All other cases reported in Figure 6.12 would not allow error-free transmission without being involved in signal compensation algorithms and techniques.

The computed frequency response clearly reveals the expected differences between the multimode fiber Gaussian response and the skin effect based response of the transmission line. Both models rely upon approximations, as already mentioned, but their very different frequency profiles need some more comments. In order to compare quantitatively multimode fibers and copper transmission lines, a reference level needs to be defined. To compare them the same $-3\,\mathrm{dBe}$ cut-off frequency criteria is chosen. This is just one possible choice among many others, but it relies on a very common understanding. The $-3\,\mathrm{dBe}$ cut-off frequency using the dB-electrical definition was chosen, using the $20\log_{10}$ operator. This is consistent with the electrical pulse signal achieved after the optoelectrical conversion takes place in the optical receiver. It is assumed that the multimode fiber parameter set used before is characterized by the same length, $L_\mathrm{F} = 300\,\mathrm{m}$, each with an individual modal bandwidth, namely:

1. OM1: $\widehat{\mathrm{BW}}(850\,\mathrm{nm}) = 160\,\mathrm{MHz\,km}$
2. OM2: $\widehat{\mathrm{BW}}(1310\,\mathrm{nm}) = 500\,\mathrm{MHz\,km}$
3. OM2: $\widehat{\mathrm{BW}}(1310\,\mathrm{nm}) = 1000\,\mathrm{MHz\,km}$
4. OM3: $\widehat{\mathrm{BW}}(850\,\mathrm{nm}) = 2000\,\mathrm{MHz\,km}$

Transmission line lengths L_T are chosen in order to match exactly the same $-3\,\mathrm{dBe}$ cut-off frequency of the multimode fiber links after $L_\mathrm{F} = 300\,\mathrm{m}$. Table 6.4 summarizes the operating conditions for each case considered. The last column refers to the corresponding figures given below. The computed copper line length giving the same cut-off frequency of the corresponding multimode fiber link is also added.

The comparison between the frequency domain and the corresponding impulse response becomes more evident. The fiber link bandwidth is derived using both modal dispersion and chromatic dispersion contributions, and the latter one depends on the source wavelength and linewidth.

It is interesting to observe that in all the cases the optical link bandwidth is slightly lower than the fiber modal cut-off frequency due to the contribution of the chromatic dispersion. Higher bandwidth fibers are more sensitive to the chromatic dispersion effect due to the relatively higher contribution of GVD with respect to the differential mode delay.

Figure 6.17 shows the computed impulse responses for the four cases examined above. The time domain comparison reveals the dramatic differences in pulse shaping and duration between any two pairs examined. It should be mentioned one more time that the transmission line results are valid under the assumption of a dominant skin effect. A more accurate transmission line modeling including material dispersion and waveguide effects will have a broader impulse response, but is nevertheless still more regular and narrower than the equivalent bandwidth multimode optical fiber can exhibit.

Table 6.4 Fiber link parameters used for comparison with an equivalent transmission line

Wavelength range	Modal bandwidth	Chromatic dispersion	Source linewidth	Link bandwidth	Transmission line length	Figure reference
850 nm	160 MHz km	120 ps/nm km	0.6 nm	376.0 MHz	72.14 cm	6.13
1310 nm	500 MHz km	6 ps/nm km	1 nm	1176.3 MHz	40.77 cm	6.14
1310 nm	1000 MHz km	6 ps/nm km	1 nm	2351.7 MHz	28.81 cm	6.15
850 nm	2000 MHz km	120 ps/nm km	0.6 nm	4696.3 MHz	20.39 cm	6.16

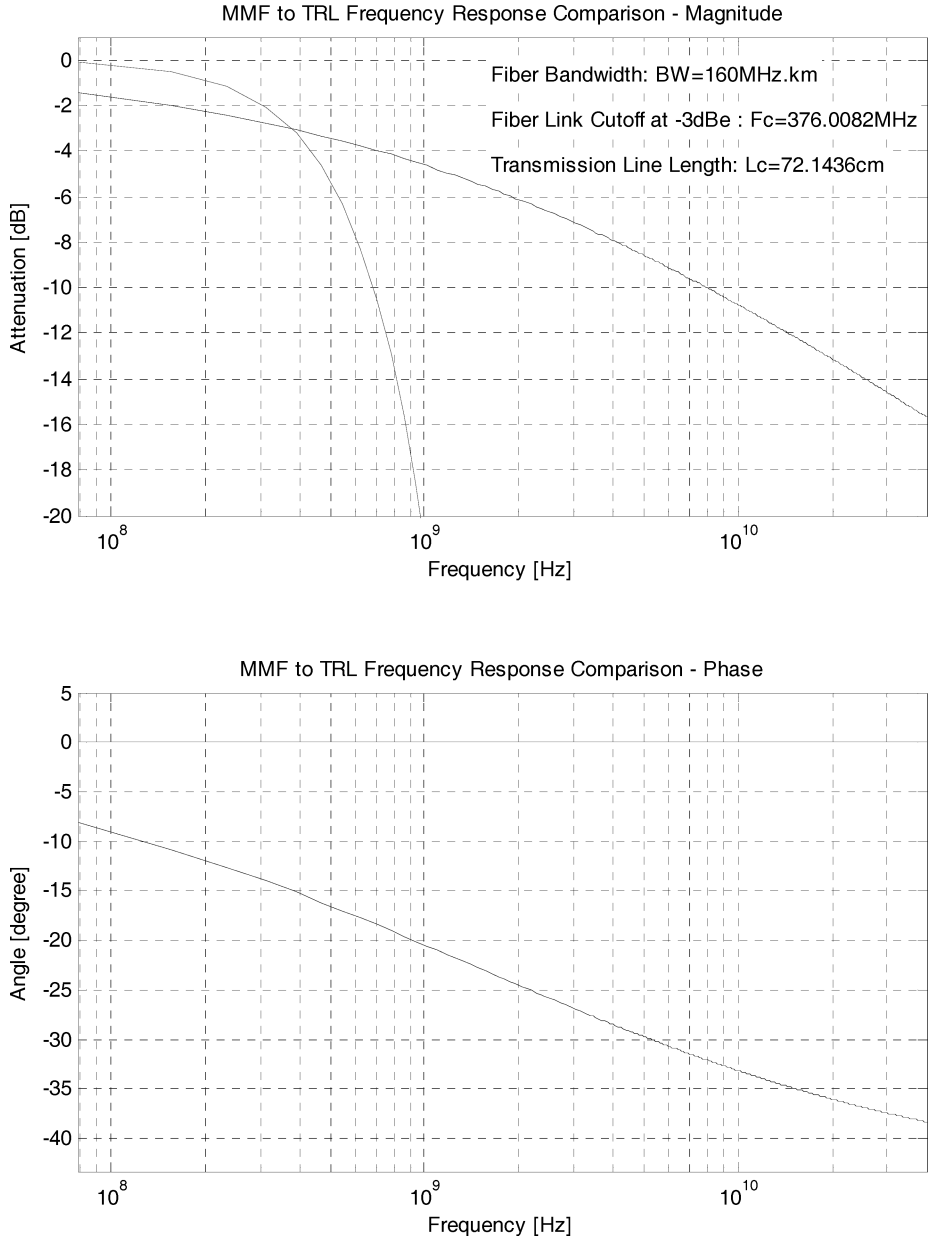

Figure 6.13 Frequency response comparison between the Gaussian approximation of the multimode fiber frequency response of a fixed link length $L_F = 300\,\text{m}$ and the copper transmission line whose length $L_T = 72.14\,\text{cm}$ gives the same $-3\,\text{dBe}$ link cut-off frequency $f_c = 376\,\text{MHz}$ as the fiber link. The fiber bandwidth is $\widehat{\text{BW}}(850\,\text{nm}) = 160\,\text{MHz km}$, the chromatic dispersion coefficient is $|D_c| = 120\,\text{ps/nm km}$ and the source linewidth is $\sigma_s = 0.6\,\text{nm}$. The smoother square root frequency response decay of the transmission line is evident

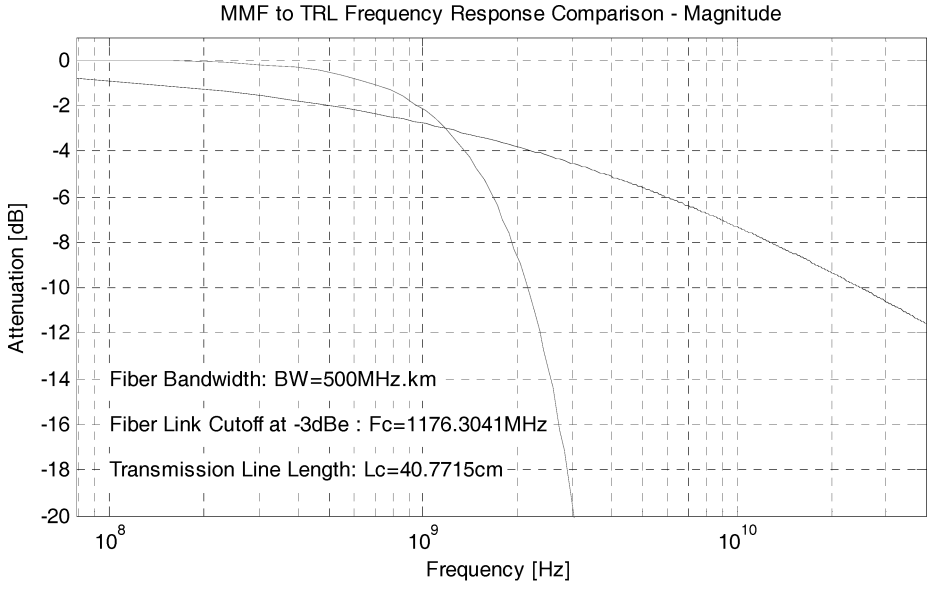

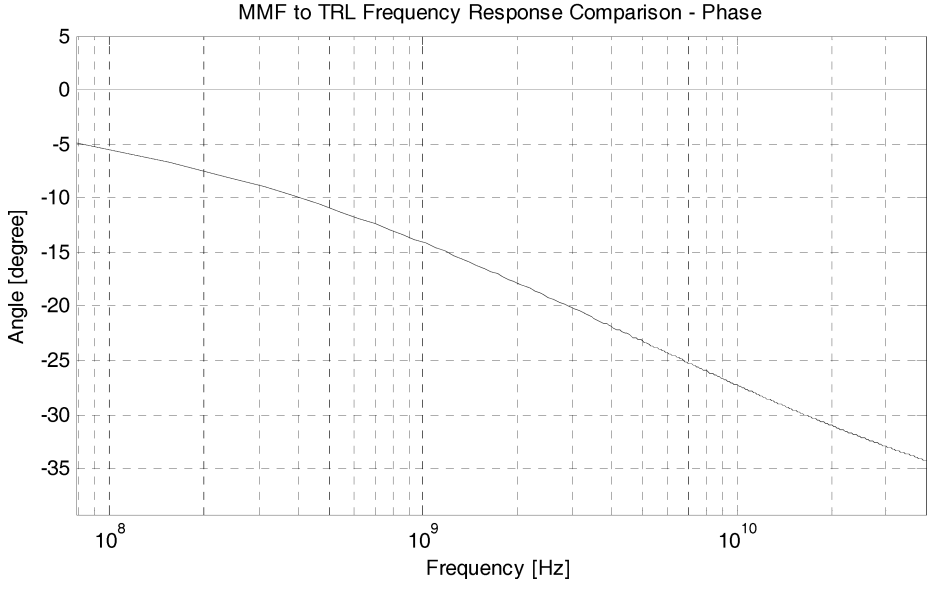

Figure 6.14 Frequency response comparison between the Gaussian approximation of the multimode fiber frequency response of a fixed link length $L_F = 300\,\text{m}$ and the copper transmission line whose length $L_T = 40.77\,\text{cm}$ gives the same $-3\,\text{dBe}$ link cut-off frequency $f_c = 1176.3\,\text{MHz}$ as the fiber link. The fiber bandwidth is $\widetilde{\text{BW}}(1310\,\text{nm}) = 500\,\text{MHz km}$, the chromatic dispersion coefficient is $|D_c| = 6\,\text{ps/nm km}$ and the source linewidth is $\sigma_s = 1\,\text{nm}$. The smoother square root frequency response decay of the transmission line is evident

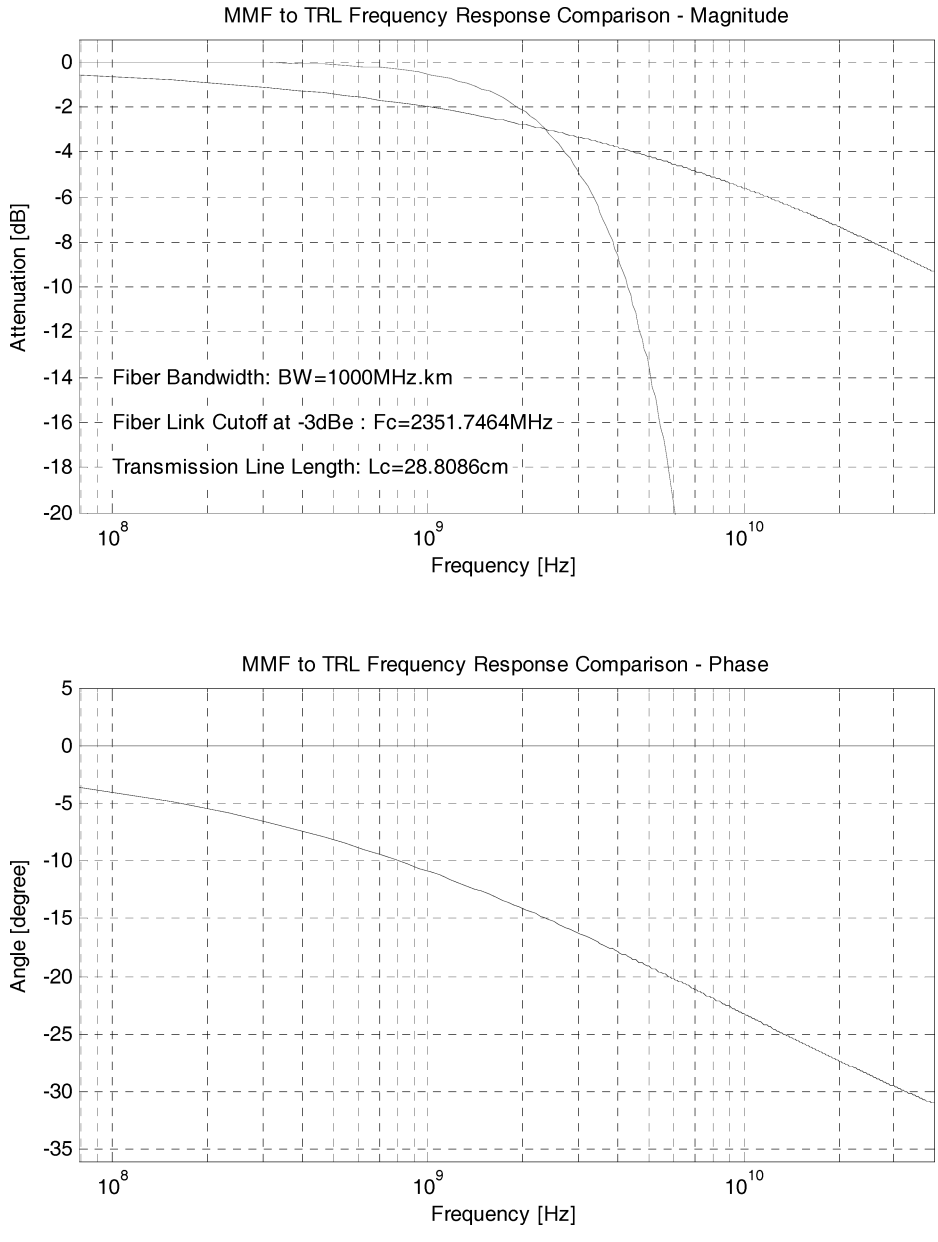

Figure 6.15 Frequency response comparison between the Gaussian approximation of the multimode fiber frequency response of a fixed link length $L_F = 300\,\text{m}$ and the copper transmission line whose length $L_T = 28.8\,\text{cm}$ gives the same $-3\,\text{dBe}$ link cut-off frequency $f_c = 2531.7\,\text{MHz}$ as the fiber link. The fiber bandwidth is $\widetilde{\text{BW}}(1310\,\text{nm}) = 1000\,\text{MHz km}$, the chromatic dispersion coefficient is $|D_c| = 6\,\text{ps/nm km}$ and the source linewidth is $\sigma_s = 1\,\text{nm}$. The smoother square root frequency response decay of the transmission line is evident

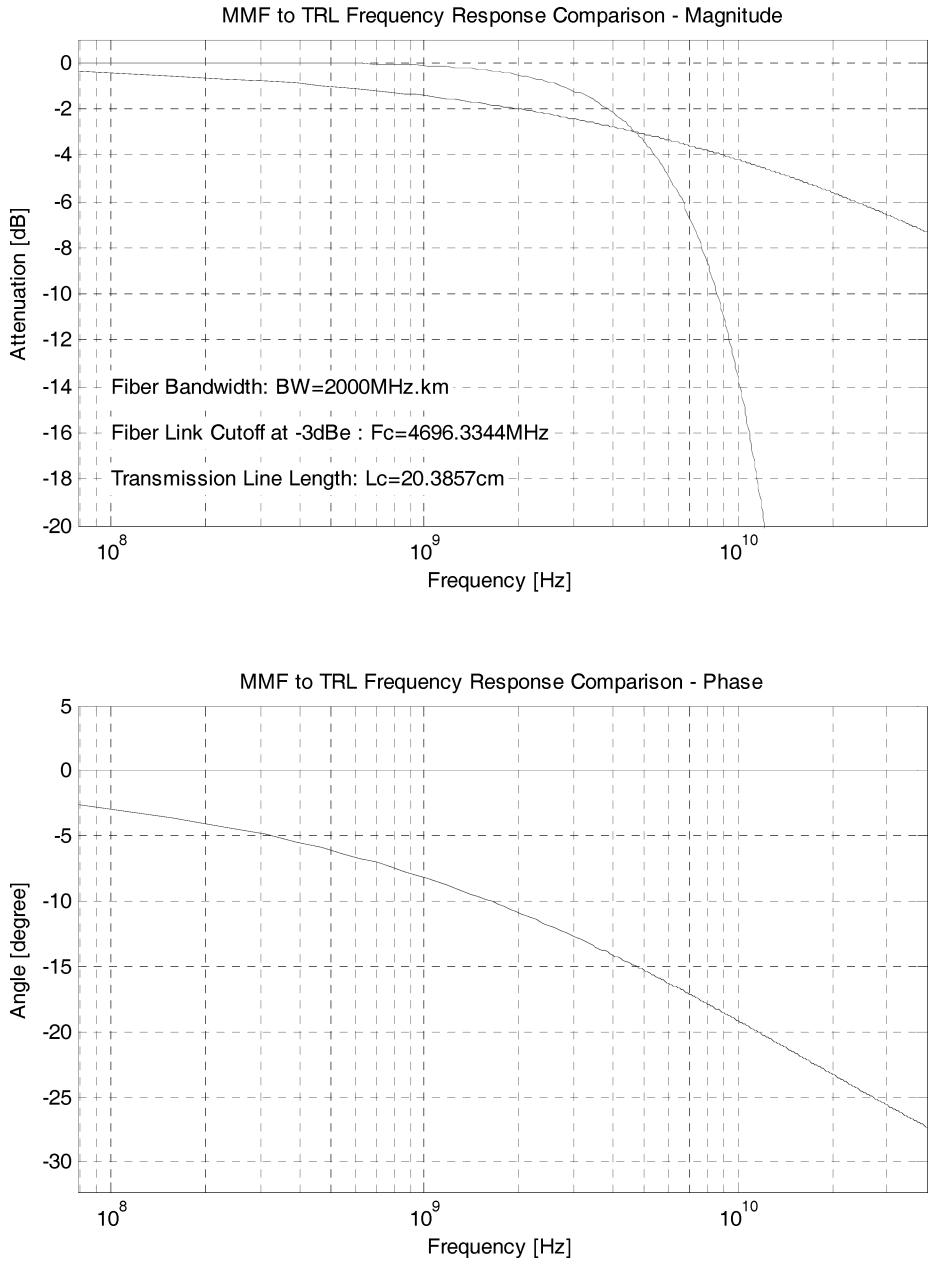

Figure 6.16 Frequency response comparison between the Gaussian approximation of the multimode fiber frequency response of a fixed link length $L_F = 300\,\text{m}$ and the copper transmission line whose length $L_T = 20.39\,\text{cm}$ gives the same $-3\,\text{dBe}$ link cut-off frequency $f_c = 4696.3\,\text{MHz}$ as the fiber link. The fiber bandwidth is $\widehat{\text{BW}}(850\,\text{nm}) = 2000\,\text{MHz km}$, the chromatic dispersion coefficient is $|D_c| = 120\,\text{ps/nm km}$ and the source linewidth is $\sigma_s = 0.6\,\text{nm}$. The smoother square root frequency response decay of the transmission line is evident

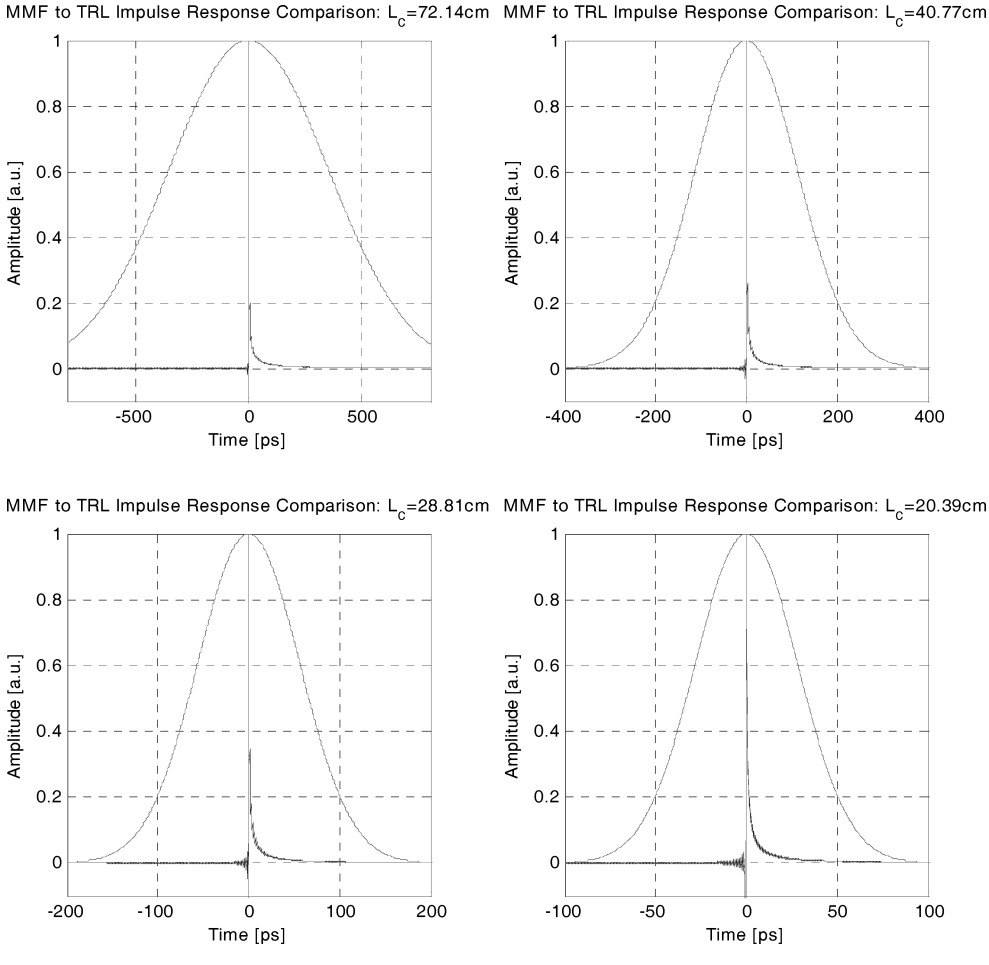

Figure 6.17 Comparison between the multimode fiber Gaussian impulse responses and the transmission line impulse responses of the same −3 dBe cut-off frequency. The transmission line length has been computed in order to have the same cut-off frequency as the corresponding multimode fiber

6.4 Conclusions and Remarks

The Gaussian transfer function used for modeling the multimode fiber response represents a useful solution to the transmission system simulation based on multimode fibers. There is no satisfactory physical explanation to justify the Gaussian pulse response, but it is widely used and referred to by both Standardization Committees ITU-T and IEEE 802.3ae. Depending on both the launching conditions and the fiber delay distribution, the Gaussian model could more or less fit the real measurements. Starting with the Gaussian assumption as a modeling approach, the theory relating the frequency and time domain was developed, including a quantitative comparison using copper transmission lines.

The accuracy of multimode fiber response modeling has attracted much interest in recent years since new high-speed transmission applications like 10 GbE and 4GFC have been proposed by the standardization community. Data transmission infrastructure must therefore use existing multimode

fiber plants for those newly increased transmission speeds, using single longitudinal mode semiconductor laser sources such as VCSEL instead of the slower LED. Selective fiber mode excitation leads directly to the strongly launching condition which is dependent on the multimode fiber impulse response. A unified form of multimode fiber impulse response modeling is not available, except for Gaussian interpolation as an average impulse response. More realistic modeling must therefore rely on the physical model of the multimode fiber, solving the waveguide modal equation according to the applied launching condition and to the measured refractive index profile. A statistical approach would be more adequate due to the variability of the measured refractive index profile among deployed multimode fibers. All those complexities make the Gaussian approach a reasonable and useful compromise between transmission system design criteria and real measurement expectations. Gaussian modeling is a simple design tool and must be properly used in order to have realistic design criteria.

7

Multimode Fiber Selected Topics

Impairments and Methods for Multigigabit Transmission Links

7.1 Impulse Response and Modal Bandwidth

The theory of multimode fibers presented so far allows direct representation of the multimode fiber impulse response as the linear combination of individual mode contributions in the time domain, including both modal group delays and chromatic dispersion. The list below summarizes the fundamental steps that were achieved in understanding the physical description and the mathematical modeling of the impulse response behavior of the multimode fiber:

1. As derived in Chapter 3, each excited mode group presents the fraction reported in Equation (3.56) of the total launched optical power and is represented by the intensity weighting coefficient $|a_j(\lambda)|^2$. The energy conservation (3.57) of the launched input optical pulse among the whole set of guided modes implies that $\sum_{j=1}^{M} |a_j(\lambda)|^2 = 1$, M being the number of mode groups.
2. The impulse response of each hth mode group is indicated by the function $\upsilon_h(z, t, \lambda)$, $h = 1, 2, \ldots, M$. According to Equation (3.53), the modal impulse response coincides with the impulse distribution at the input section translated by the corresponding group delay $t_{g,j}(z, \lambda) = z\tau_{g,j}(\lambda)$:
$$\upsilon_h(z, t, \lambda) = \delta[t - z\tau_{g,h}(\lambda)] \tag{7.1}$$
3. The chromatic dispersion $\sigma_{c,h}(z)$ adds the characteristic RMS width broadening to the modal impulse response $\upsilon_h(z, t, \lambda)$, $h = 1, 2, \ldots, M$, of each mode group. Assuming source spectrum limited conditions and a linear approximation of the modal group delay, the chromatic dispersion of each hth mode group is given by the product of the chromatic dispersion coefficient $|D_{c,h}(\overline{\lambda})|$ evaluated at the source average wavelength $\overline{\lambda}$ with the source linewidth σ_s, as reported in (4.120):
$$\sigma_{c,h}(z, \overline{\lambda}) = |D_{c,h}(\overline{\lambda})|\sigma_s z \tag{7.2}$$
4. In general, without any linear approximation of the group delay function, the chromatic impulse response experienced by the hth mode group is indicated by the function $h_{c,h}(z, t)$ and does not depend explicitly on any particular wavelength. Instead, the chromatic impulse response is an

Multi-Gigabit Transmission over Multimode Optical Fibre: Theory and Design Methods for 10GbE Systems Stefano Bottacchi
 ISBN: 0-471-89175-4

integral functional of the source power spectral density and results in a function of the distance z from the launch section and the temporal variable t. The function $\sigma_{c,h}(z)$ characterizes the RMS width of the chromatic impulse response $h_{c,h}(z,t)$, and does not necessarily need to be a Gaussian pulse in the time domain. For the moment, the general assumption is made that the chromatic impulse response belongs to the space of modulus integrable functions over the time axis, for every distance z and wavelength λ:

$$\begin{aligned} &h_{c,h}(z,t) \in L^1(\Re),\ t \in \Re \\ &\int_{-\infty}^{+\infty} |h_{c,h}(z,t)|\,\mathrm{d}t < +\infty \end{aligned} \tag{7.3}$$

Since the impulse response $h_{c,h}(z,t)$ represents the optical power it must be definite positive over the whole time axis and therefore Equation (7.3) coincides with the finite energy requirement.

5. The effect of chromatic dispersion over each mode group response is given by the time convolution of the modal impulse response $\upsilon_h(z,t,\overline{\lambda})$, $h = 1, 2, \ldots, M$, with the corresponding time-centered chromatic impulse response $\hat{h}_{c,h}(z,t) \equiv h_{c,h}(z, t - z\overline{\tau}_{c,h})$:

$$h_{F,h}(z,t,\overline{\lambda}) \equiv \upsilon_h(z,t,\overline{\lambda}) * \hat{h}_{c,h}(z,t) \tag{7.4}$$

6. Under the assumption of the linear mode power superposition, the multimode fiber impulse response $h_F(z,t,\overline{\lambda})$, subjected to the chromatic dispersion effect, can be defined as the weighted sum of all excited mode group contributions $h_{F,h}(z,t,\overline{\lambda})$:

$$h_F(z,t,\overline{\lambda}) \equiv \sum_{h=1}^{M} |a_h(\overline{\lambda})|^2 h_{F,h}(z,t,\overline{\lambda}) \tag{7.5}$$

7. Substituting Equation (7.1) into Equation (7.4) and using the summation (7.5) gives the explicit form of the multimode fiber impulse response:

$$h_F(z,t,\overline{\lambda}) = \sum_{h=1}^{M} |a_h(\lambda)|^2 \hat{h}_{c,h}[z, t - z\tau_{g,h}(\overline{\lambda})] \tag{7.6}$$

Substituting for the centered chromatic impulse response in terms of the original one gives the following expression, which coincides with expression (5.20) derived in Chapter 5, obtaining the general multimode fiber impulse response under the linear intensity superposition assumption, including both modal and chromatic dispersions:

$$h_F(z,t,\overline{\lambda}) = \sum_{h=1}^{M} |a_h(\overline{\lambda})|^2 h_{c,h}\{z, t - z[\tau_{g,h}(\overline{\lambda}) - \overline{\tau}_{c,h}]\} \tag{7.7}$$

Note that the quantity $\overline{\tau}_{c,h}$ is the value of the average delay of the chromatic impulse response of the hth excited fiber mode and in general is different from the value of the group delay of the same hth mode evaluated at the source average wavelength. This is due to the chromatic distortion of the nonlinear group delay profile in the spectral range of the light source spectrum. If the group delay is linearly approximated, of course both terms coincide. No other dispersion effects have been considered in Equation (7.7). Each mode is affected by chromatic dispersion through the impulse response $h_{c,h}(z,t)$, without specifying the general function used to model the chromatic impulse response.

The next section analyses the interesting case of the Gaussian chromatic impulse response. This case represents a valid assumption for laser-based transmission systems where the almost Gaussian

shaped and narrow light spectrum allows for consistent linear approximation of the multimode fiber group delay profile. In the following, it will be assumed that the Gaussian chromatic impulse response will have the same variance for every fixed distance. In other words, the chromatic impulse response will be represented by the same Gaussian profile with the proper group delay characteristic of the corresponding mode group delay.

7.1.1 Gaussian Chromatic Response

In this section, modeling of the chromatic impulse response $h_{c,h}(z, t, \overline{\lambda})$ will be considered by means of a suitable Gaussian function. Both the source spectrum limited condition and the linear chromatic dispersion given by Equation (4.120) will be assumed. The time-centered Gaussian chromatic impulse response is defined as follows:

$$\hat{h}_c(z, t, \overline{\lambda}) \equiv \frac{1}{z\sigma_s|D_c(\overline{\lambda})|\sqrt{2\pi}} e^{-t^2/[2z^2\sigma_s^2|D_c(\overline{\lambda})|^2]} \tag{7.8}$$

At any fixed section z and source average wavelength $\overline{\lambda}$, the time-centered chromatic impulse response $\hat{h}_c(z, t, \overline{\lambda})$ in Equation (7.8) results in a normalized Gaussian pulse with zero mean, $\overline{\tau}_{c,h} = 0$, $h \in N$ (1,M), and variance given by the following term:

$$\begin{aligned} \overline{\tau}_c &= 0 \\ \sigma_c^2(z, \overline{\lambda}) &= z^2\sigma_s^2|D_c(\overline{\lambda})|^2 \end{aligned} \tag{7.9}$$

Increasing the distance z from the origin, the RMS width $\sigma_c(z, \overline{\lambda})$ increases linearly. It is important to remark that the Gaussian chromatic impulse response in Equation (7.8) is the same for every mode group. Is it time-centered and, due to the assumed linearity of the group delay in the interval interested by the light source spectrum, the chromatic dispersion coefficient is the same for all modes.

Substituting Equation (7.8) into Equation (7.7) gives the multimode fiber impulse response with the approximation of the Gaussian chromatic impulse response:

$$h_F(z, t, \overline{\lambda}) = \frac{1}{z\sigma_s|D_c(\overline{\lambda})|\sqrt{2\pi}} \sum_{h=1}^{M} |a_h(\overline{\lambda})|^2 \exp - \frac{[t - z\tau_{g,h}(\overline{\lambda})]^2}{2z^2\sigma_s^2|D_c(\overline{\lambda})|^2} \tag{7.10}$$

This expression gives interesting multimode fiber impulse response simulations by assuming the Gaussian chromatic impulse response. However, depending on the modal delay distribution $\tau_{g,h}(\overline{\lambda})$ and the coefficients $|a_h(\overline{\lambda})|$, very different impulse responses can be achieved. This is the most distinctive peculiarity of the multimode fiber response. It will be seen in the next section that launching conditions strongly affect the energy distribution among guided modes and group delays, and consequently the impulse response detected at the output section.

The above expression (7.10) should not be confused with the much more severe approximation presented in Chapter 6, where the whole impulse response of the multimode fiber was considered, including modal delay contributions, as a Gaussian pulse. In the following sections it will be shown how this is a special case of the more general multimode fiber impulse response presented in Equation (7.9). In order to achieve a completely Gaussian response, in fact both the modal excitation and group delay distribution must satisfy the general prescriptions indicated in Chapter 6. In that case the multimode fiber impulse response could be approximated using Gaussian functions.

Once the multimode fiber impulse response has been derived as a superposition of weighted Gaussians pulses, by virtue of the linearity and of the time-shifting theorem of the Fourier transform

pair it is easy to derive the corresponding frequency response of the multimode fiber with the approximation of the Gaussian chromatic impulse response:

$$H_{\mathrm{F}}(z, f, \overline{\lambda}) = \mathrm{e}^{-2\pi^2 z^2 \sigma_{\mathrm{s}}^2 |D_{\mathrm{c}}(\overline{\lambda})|^2 f^2} \sum_{h=1}^{M} |a_h(\overline{\lambda})|^2 e^{-\mathrm{j}2\pi f z \tau_{\mathrm{g},h}(\overline{\lambda})} \tag{7.11}$$

By comparing this equation with Equation (5.81) it can be concluded that the summation term coincides with the modal function $\Upsilon(z, f, \overline{\lambda})$. Hence, this gives the following relevant result. The frequency response $H_{\mathrm{F}}(z, f, \overline{\lambda})$ of the multimode fiber with the approximation of the Gaussian chromatic impulse response is given by the product of the Gaussian transfer function corresponding to the chromatic impulse response with the modal function $\Upsilon(z, f, \overline{\lambda})$:

$$H_{\mathrm{F}}(z, f, \overline{\lambda}) = \mathrm{e}^{-2\pi^2 z^2 \sigma_{\mathrm{s}}^2 |D_{\mathrm{c}}(\overline{\lambda})|^2 f^2} \Upsilon(z, f, \overline{\lambda}) \tag{7.12}$$

The result just derived is consistent with the general theory of the multimode fiber frequency response developed in Chapter 5. In particular, expression (7.12) derives directly from Equation (5.81).

7.1.2 Modeling Impulse Responses

In order to expand the view of multimode fiber impulse responses, some interesting applications of the previous modeling will be considered in the following. The chromatic impulse response is assumed to be Gaussian and the multimode fiber response is computed according to Equations (7.10) and (7.12). Once the chromatic dispersion parameters σ_{s} and $|D_{\mathrm{c}}(\overline{\lambda})|$ have been fixed, the impulse response at any given section z becomes a function of the two distributions $\{a_h(\overline{\lambda})\}$, $\{\tau_{\mathrm{g},h}(\overline{\lambda})\}$. It will be seen later that for a given multimode fiber both the power coefficients and the delay distribution are not independent of each other, but are instead related to the same launching conditions. For a given multimode fiber, the light source parameters $(\overline{\lambda}, \sigma_{\mathrm{s}})$ and the spectrum profile together with the launching conditions uniquely specify the impulse response at every distance z from the input section. For the moment, without entering into this mathematical analysis, some relevant delay distributions $\{\tau_{\mathrm{g},h}(\overline{\lambda})\}$ and power coefficient distributions $\{a_h(\overline{\lambda})\}$ will be defined *a priori* in order to obtain some specified response shape at the output section z. For each multimode impulse response computed using Equation (7.10) the corresponding frequency response according to Equation (7.12) has also been added. The application considered below can be grouped into four different cases, according to the shape of the impulse response. In order to simplify the mathematical description and to highlight the physical meaning behind it, in all four cases presented a uniform modal excitation will be assumed, namely:

$$\begin{aligned} |a_h(\overline{\lambda})|^2 &= \frac{1}{M} \\ \sum_{h=1}^{M} |a_h(\overline{\lambda})|^2 &= \sum_{h=1}^{M} \frac{1}{M} = 1 \end{aligned} \tag{7.13}$$

Consequently, different impulse responses are due exclusively to different group delay distributions. Proceeding in this way, the physical role of this fundamental multimode fiber parameter is highlighted. Substituting the condition (7.13) into both expressions (7.10) and (7.11) gives

$$h_{\mathrm{F}}(z, t, \overline{\lambda}) = \frac{1}{Mz\sigma_{\mathrm{s}}|D_{\mathrm{c}}(\overline{\lambda})|\sqrt{2\pi}} \sum_{h=1}^{M} \exp -\frac{[t - z\tau_{\mathrm{g},h}(\overline{\lambda})]^2}{2z^2\sigma_{\mathrm{s}}^2 |D_{\mathrm{c}}(\overline{\lambda})|^2} \tag{7.14}$$

$$H_{\mathrm{F}}(z, f, \overline{\lambda}) = \mathrm{e}^{-2\pi^2 z^2 \sigma_{\mathrm{s}}^2 |D_{\mathrm{c}}(\overline{\lambda})|^2 f^2} \frac{1}{M} \sum_{h=1}^{M} \mathrm{e}^{-\mathrm{j}2\pi f z \tau_{\mathrm{g},h}(\overline{\lambda})} \tag{7.15}$$

In the following cases the same parameters values will be assumed:

$$\begin{aligned} \overline{\lambda} &= 1300\,\text{nm} \\ z &= 1\,\text{km} \\ \sigma_s &= 4\,\text{nm} \\ |D_c(\overline{\lambda})| &= 6\,\text{ps/nm km} \\ M &= 500 \end{aligned} \tag{7.16}$$

The only condition responsible for different impulse responses is therefore the group delay distribution $\{\tau_{g,h}(\overline{\lambda})\}$. Before using simulation results it is, however, important to discuss briefly the characteristic profile of the group delay distributions in order to satisfy the required multimode impulse response. To this purpose the conditions discussed in Chapter 6 concerning the Gaussian-shaped impulse response are recalled. Since the power coupling coefficient distribution can be assumed to be uniform for all the considered cases, the modal contribution to the impulse response depends exclusively on the group delay distribution $\{\tau_{g,h}(\overline{\lambda})\}$. In the following, without losing any generality, it will be assumed that the fiber modes are ordered according to the required group delay profile. The group delay distribution is sketched versus the mode group index, $h = 1, 2, \ldots, M$. In the following examples, every stationary interval of the delay distribution leads to the accumulation of the corresponding chromatic impulse responses, almost all on the same delay value. This condition will be referred to as a synchronous superposition.

Similarly, every abrupt change of the delay distribution corresponds to a low-energy contribution to the optical impulse response, due to the limited mode group that satisfies the very restricted delay values. These low-energy intervals extend for the corresponding value of the abrupt group delay variation.

7.1.2.1 Symmetric Single-Peak Response

Following the discussion and the prescriptions reported in Chapter 6, it can be concluded that in order to have a symmetric single-peak impulse response, the group delay distribution $\{\tau_{g,h}(\overline{\lambda})\}$ must have an odd symmetry around the average value, as sketched in Figure 7.1. The lower slope central region is responsible for the main body of the impulse response because most of the modal

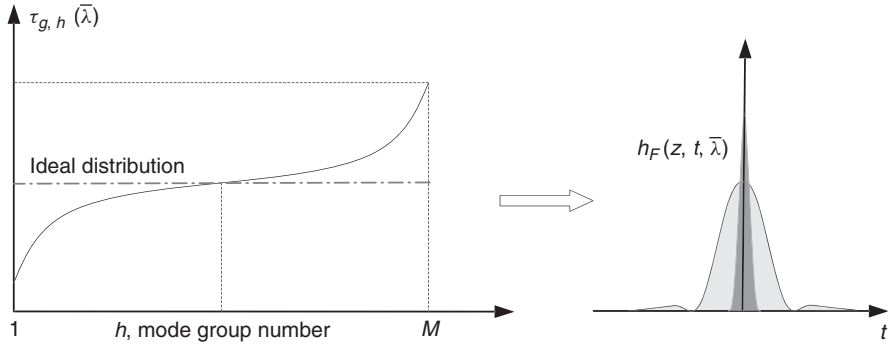

Figure 7.1 Qualitative representation of the odd-symmetric group delay distribution and of the corresponding symmetric single-peak multimode impulse response, assuming uniform mode group excitation. The ideal group delay distribution with perfect delay compensation is shown as the dot–dash line and the corresponding multimode impulse response on the right side exhibits only a chromatic dispersion contribution

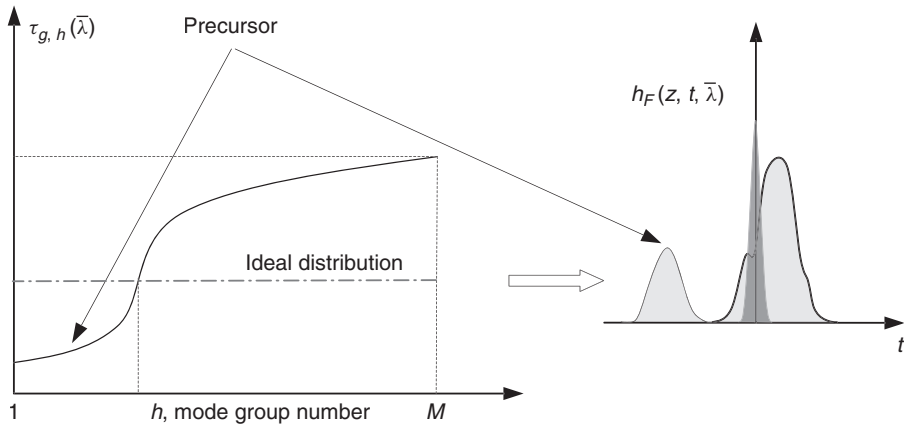

Figure 7.2 Qualitative representation of the group delay distribution and of the corresponding precursor single-peak multimode impulse response, assuming uniform mode group excitation. The ideal group delay distribution with perfect delay compensation is shown as the dot–dash line and the corresponding multimode impulse response on the right side exhibits only a chromatic dispersion contribution

contributions arrive almost at the same time. Pulse tails are determined instead by the outer regions of the group delay distribution.

The dot–dash line represents the uniform group delay distribution, as expected after perfect delay compensation. The corresponding multimode impulse response coincides with the synchronous superposition of the chromatic impulse responses, resulting in the sharpest pulse profile available for the given operating conditions.

7.1.2.2 Precursor Single-Peak Response

Figure 7.2 shows the qualitative behavior of the group delay distribution in order to have a precursor single-peak impulse response. Generally, every mode group bundle that exhibits almost the same group delay value originates of course a peak in the impulse response. This is due essentially to the almost synchronous superposition of the chromatic impulse responses. The relative position and the intensity of the precursor depend on the location and on the fraction of the mode bundle delay distribution.

Because of these concepts, it could be argued that a staircase group delay distribution will generate a multiple peak impulse response. In the next section some computer simulations will be presented of the multimode impulse response, assuming mathematical modeling of the group delay distribution.

It is important to remark that under uniform excitation, if an almost flat group delay distribution results in a Gaussian-like impulse response, a very steep group delay profile variation results in almost a lack of energy content along the corresponding time interval. This gives a hint that almost separated multipeak impulse responses can be achieved. The same conclusions do not hold in general for nonuniform excitation. This is due to the relative weight given to the source coupled power coefficients among different mode groups.

7.1.2.3 Postcursor Single-Peak Response

Proceeding in the same way as the precursor single-peak response, the postcursor single-peak response is obtained by simply, providing a mirrored group delay distribution. In the case reported

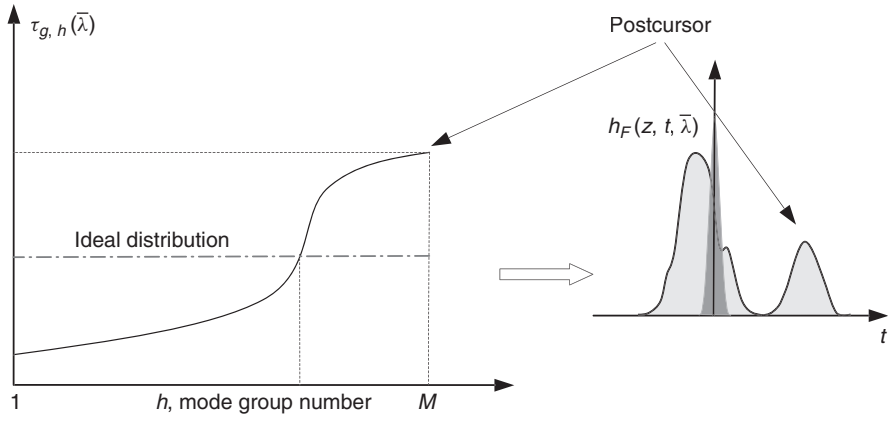

Figure 7.3 Qualitative representation of the group delay distribution and of the corresponding postcursor single-peak multimode impulse response, assuming uniform mode group excitation. The ideal group delay distribution with perfect delay compensation is shown as the dot–dash line and the corresponding multimode impulse response on the right side exhibits only a chromatic dispersion contribution

in Figure 7.3, the higher mode numbers correspond to higher delay values, thus providing the postcursor behavior. The main body depends instead on the lower- to mid-order mode groups.

The ideal group delay distribution, which represents the ideal compensation for every mode delay, is drawn as the horizontal dot–dash straight line. In that case, the impulse response is characterized by the synchronous superposition of all excited modes, leading to a single very sharp chromatic impulse response.

In this representation of the group delay distribution the same upside down mirrored distribution used for the previous case of the precursor single-peak response has been assumed. This transformation of the group delay distribution, together with the assumption of uniform excitation, leads to the postcursor single-peak impulse response coincident with the time-mirrored replica of the precursor single-peak response. These symmetry concepts have already been introduced in several numerical examples presented in Chapter 5.

7.1.2.4 Symmetric Dual-Peak Response

The last case considered refers to the symmetric dual-peak impulse response. According to the concept described above, the group delay distribution must have an odd symmetry of opposite sign with respect to the first case examined of a single-peak response. In this case, in fact, the central part of the distribution should provide relatively less energy contribution, allowing for the central darker region of the impulse response, as shown in Figure 7.4.

The symmetrical impulse response is a direct consequence of the symmetric group delay distribution and of the uniform excitation assumptions. The higher slope interval of the delay distribution $\{\tau_{g,h}(\bar{\lambda})\}$, in correspondence with the central range of mode numbers in Figure 7.4 leads to a reduced energy transfer corresponding to the average delay value. The lower slope outer intervals instead determine higher energy accumulation among corresponding mode numbers, leading to symmetrical pronounced energy peaks in the optical impulse response. In conclusion, the expected impulse response has the typical saddle-like shaping with the characteristic dual peaks separated by a relatively low energy interval in correspondence to the average delay value.

The next section presents numerical solutions of the multimode impulse response according to the Gaussian chromatic impulse response and an analytical group delay distribution satisfying the required symmetry.

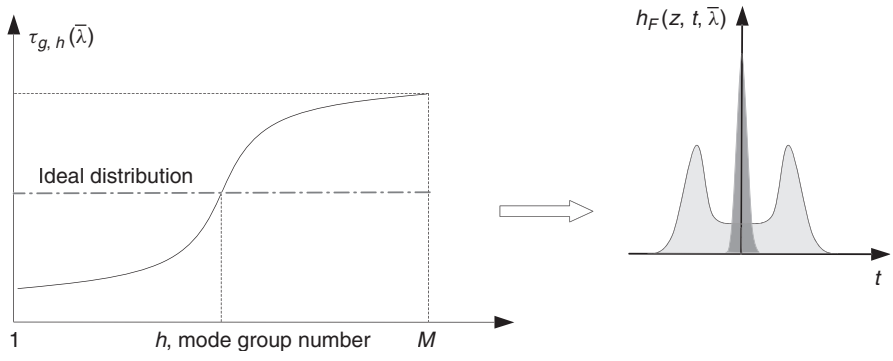

Figure 7.4 Qualitative representation of the group delay distribution and of the corresponding symmetric dual-peak multimode impulse response, assuming uniform mode group excitation. The ideal group delay distribution with perfect delay compensation is shown as the dot–dash line and the corresponding multimode impulse response on the right side exhibits only a chromatic dispersion contribution

7.1.3 Computer Simulation

Dual-peak impulse responses are conveniently modeled assuming a modified inverse hyperbolic sine group delay distribution, as given below:

$$\tau_{g,h}(\bar{\lambda}) = \tau_{\min} + \frac{y(h;a,b) - y_{\min}}{y_{\max} - y_{\min}}(\tau_{\max} - \tau_{\min}), \quad h = 1, 2, \ldots, M \tag{7.17}$$

$$y(h;a,b) = \sinh^{-1}\left(\frac{h-a}{b}\right) = \ln\left[\frac{h-a}{b} + \sqrt{1 + \left(\frac{h-a}{b}\right)^2}\right] \tag{7.18}$$

The parameters a, b set the abscissa and the slope of the inflection point respectively. Figure 7.5 gives the numerically computed group delay distribution according to Equations (7.17) and (7.18), where

$$\begin{aligned} a &= \left[\frac{M}{4}, \frac{M+1}{2}, \frac{3M}{4}\right], \quad 1 \le a \le M \\ b &= 0.2, \quad 0 < b < \infty \\ M &= 100 \end{aligned} \tag{7.19}$$

and

$$\tau_{\min} = 5.000\,\mu\text{s/km}, \quad \tau_{\max} = 5.002\,\mu\text{s/km} \tag{7.20}$$

for a total variation of $\Delta\tau = 2\,\text{ns/km}$. The three distributions correspond respectively to the three cases presented in the previous sections, namely the precursor single-peak, symmetric dual-peak and postcursor single-peak responses, as reported in the plot legend. The mathematical model of Equations (7.17) and (7.18) allows for easy configuration of the required group delay by changing either one or both shaping parameters a, b. The lower the parameter b, the steeper are the results for the inflection point of the given total group delay variation.

In order to compute the multimode fiber response in the Gaussian approximation of the chromatic response, the assumed parameters set in Equations (7.16) together with the inverse hyperbolic sine group delay distribution need to be inserted in the analytical expressions (7.14) and (7.15) respectively to achieve the impulse response and transfer function.

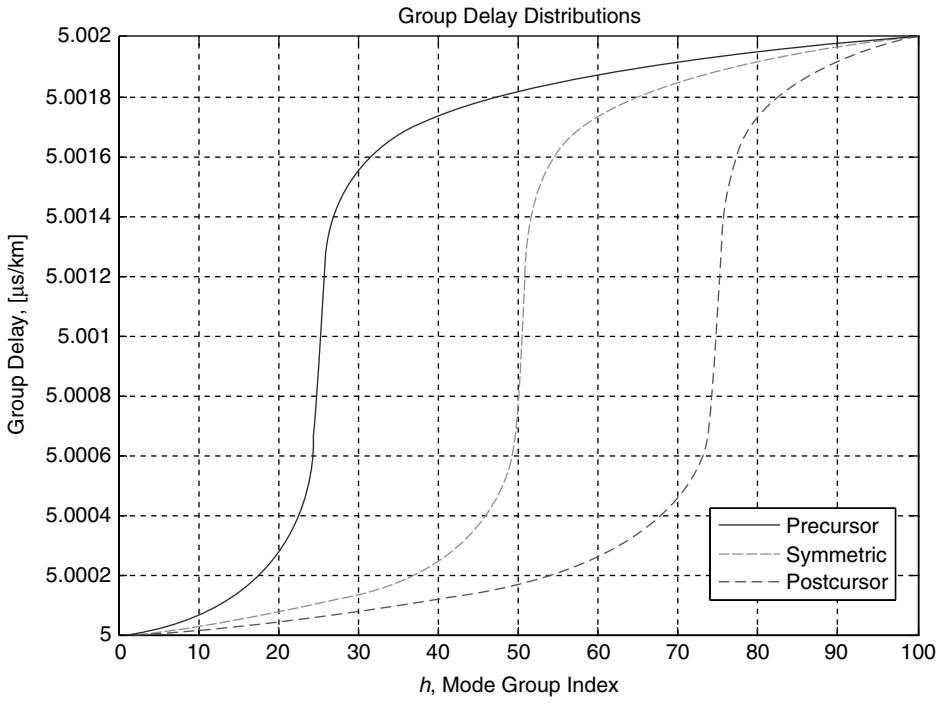

Figure 7.5 Computed group delay distribution according to the inverse hyperbolic sine function reported in Equation (7.18). The shaping parameters a, b have the values given in Equation (7.19). The group delay exhibits the total variation according to Equation (7.20). The three computed distributions should be compared with the qualitative pictures reported in Figures 7.2, 7.4 and 7.3 respectively for the precursor single-peak, symmetric dual-peak and postcursor single-peak impulse responses

Figures 7.6, 7.7 and 7.8 show the impulse responses and the transfer functions for the same cases considered above. In order to achieve more uniform results the number of modes has been increased to $M = 500$ and the shaping coefficient has been set to $b = 1$ for the precursor and postcursor responses and $b = 5$ for the symmetric dual-peak response. The impulse response clearly behaves as expected, exhibiting either a precursor, postcursor or symmetrical dual-peak shape depending on the group delay profile chosen. The distance between the secondary peak (precursor or postcursor) and the main body depends on the step amplitude of the inverse hyperbolic sine distribution.

The frequency response shows the characteristic periodic ripple behavior. This effect is expected every time the impulse response exhibits isolated pulses. The distance of the frequency notches is equal to the reciprocal of the maximum variation of the assumed group delay. Thus, in all the considered cases $\Delta\tau = \tau_{\max} - \tau_{\min} = 2\,\text{ns/km}$ and $\Delta f = 1/(\tau_{\max} - \tau_{\min}) = 500\,\text{MHz km}$. Due to the sharp profile exhibited by the symmetric dual-peak response in Figure 7.8, the corresponding magnitude of the frequency response clearly shows deep notches separated by about 500 MHz km, as expected. Both precursor and postcursor single-peak responses shown in Figures 7.6 and 7.7 reflect the symmetry property of the group delay distribution discussed in Section 7.1.2.

7.1.4 Modal Bandwidth Discussion

According to the standard reference ITU-T G.650 the modal bandwidth is defined as the half-width at half-maximum of the frequency response of the optical field intensity propagated along a unit

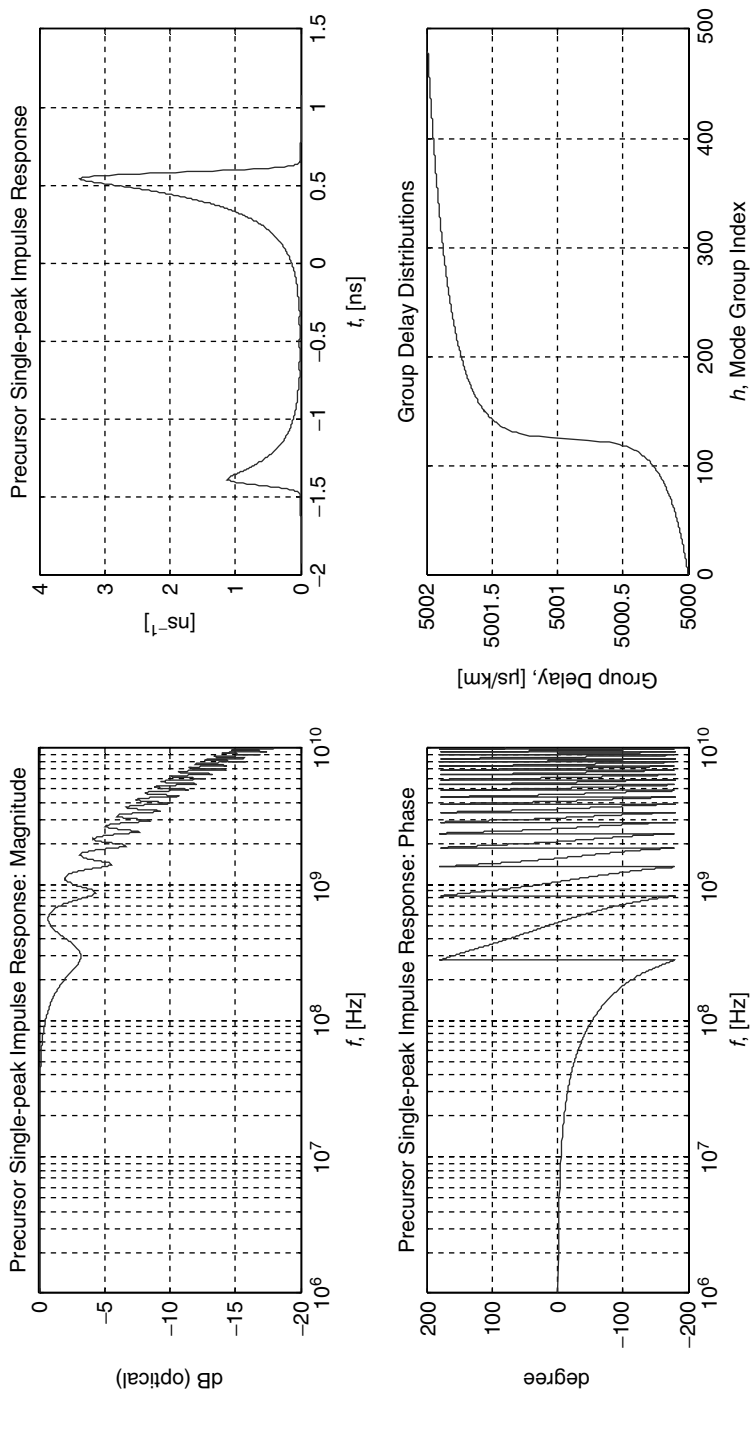

Figure 7.6 Precursor single-peak computed response of the multimode fiber under uniform excitation and Gaussian chromatic impulse response assumptions. The group delay distribution has the inverse hyperbolic sine profile reported in the bottom right graph: $a = M/4$, $b = 1$. The impulse response is shown in the top right plot. The magnitude and the phase of the frequency response are shown in the logarithmic scale in the top left and bottom left plots

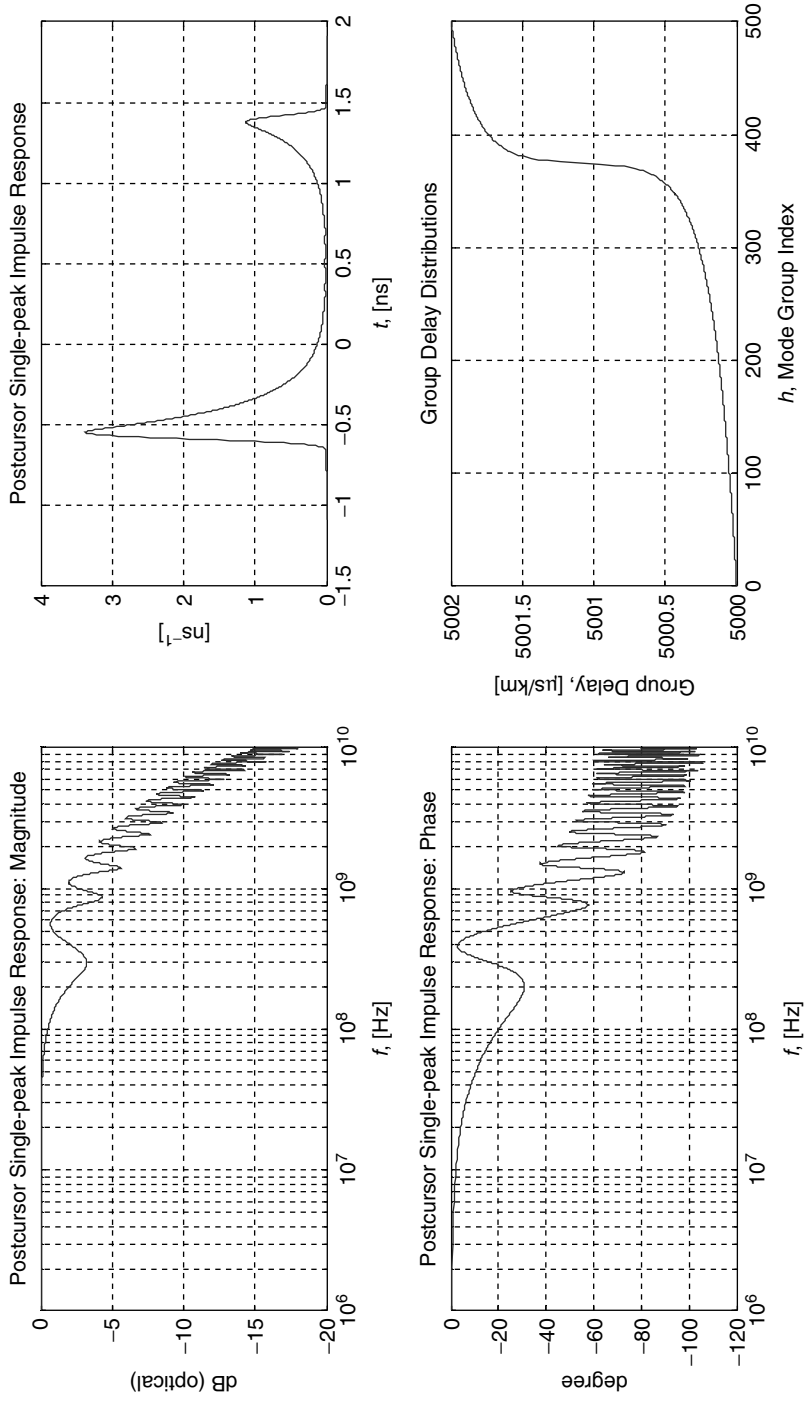

Figure 7.7 Postcursor single-peak computed response of the multimode fiber under uniform excitation and Gaussian chromatic impulse response assumptions. The group delay distribution has the inverse hyperbolic sine profile reported in the bottom right graph: $a = 3M/4$, $b = 1$. The impulse response is shown in the top right plot. The magnitude and the phase of the frequency response are shown in the logarithmic scale in the top left and bottom left plots

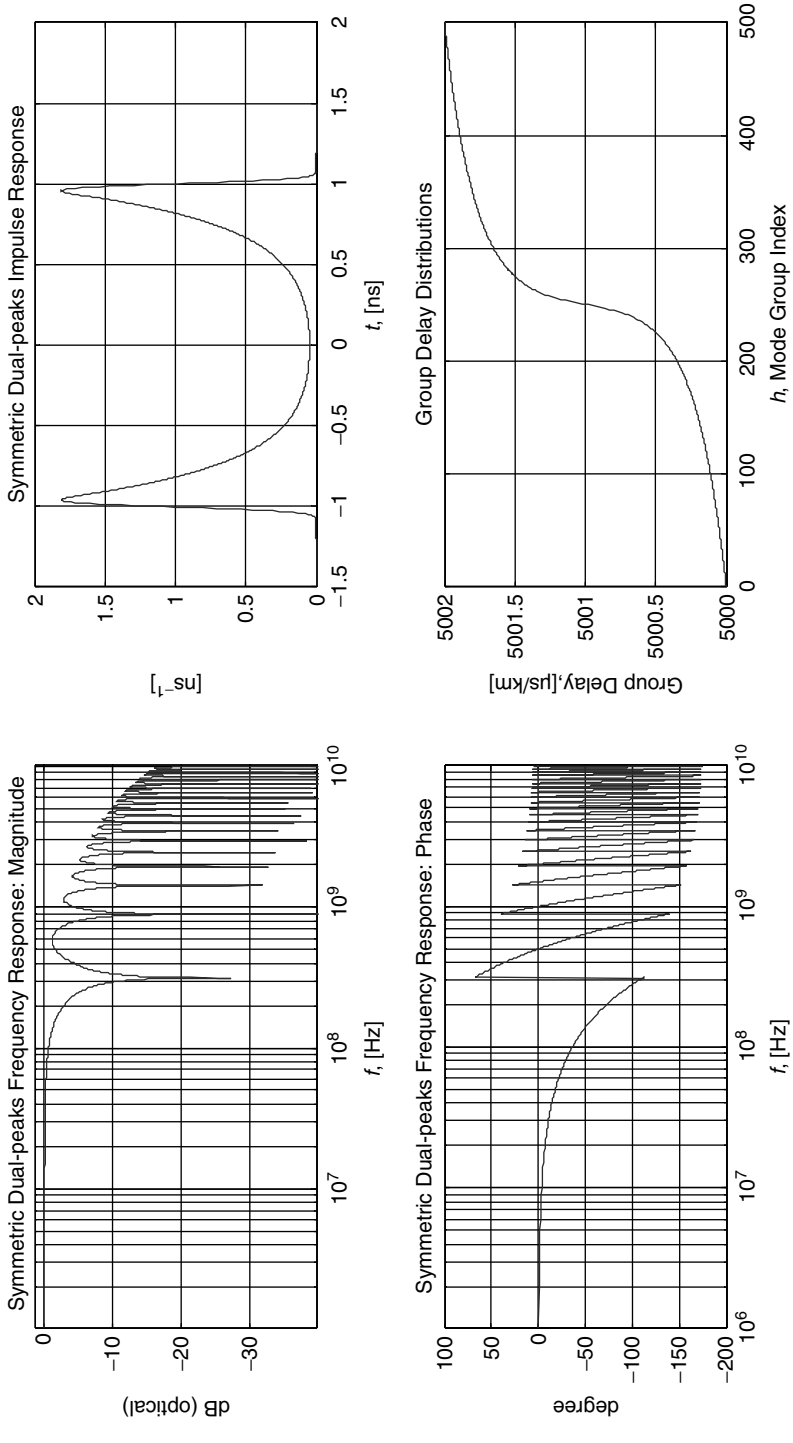

Figure 7.8 Symmetric dual-peak computed response of the multimode fiber under uniform excitation and Gaussian chromatic impulse response assumptions. The group delay distribution has the inverse hyperbolic sine profile reported in the bottom right graph: $a = (M + 1)/2$, $b = 5$. The impulse response is shown in the top right plot. The magnitude and the phase of the frequency response are shown in the logarithmic scale in the top left and bottom left plots

distance of the multimode fiber under over-filled launch (OFL) conditions. There are at least two reasons for considering the modal bandwidth concept of minor concern in multigigabit transmission over multimode fibers:

1. The launching conditions achieved with laser sources are quite a long way from satisfying the over-filled launch. Laser light in fact exposes only a small region of the multimode fiber input section, with usually a low numerical aperture, therefore originating from only selected mode excitations. Due to the restricted number of excited modes, the corresponding frequency response is strongly dependent on the restricted launch (RL) conditions imposed by the laser light source. Laser spot position, distance and tilt angle are all act together to determine the corresponding multimode fiber impulse response and transfer function.
2. Residual group delay equalization has a comparable order of magnitude as high-speed optical pulses used for multigigabit transmission. The average distance between subsequent multipeaks of the impulse response is of the same order of magnitude as the signaling time step, allowing for false signal pulse detection, unless electronic dispersion compensation countermeasures have been installed in the optical receiver. The corresponding frequency response will exhibit a characteristic ripple with even more pronounced frequency notches, which will mystify the modal bandwidth concept.

Everything must be quantitatively related to the modulating signal spectrum. Of course, for low-speed operation, well below 1 Gb/s, the signal pulse width is large enough to smooth out every multimode fiber frequency response ripple consistently, leading to a smooth single-body output pulse, preserving the applicability of the modal bandwidth concept. However, when the signal pulse duration is one order of magnitude shorter, as it is in the case of the 10 GbE transmission speed, the time convolution with a multipeak impulse response of the multimode fiber will form a very distorted output pulse, which is no longer suitable for direct signal detection and decision processes.

In the three numerical examples considered in this section, the -3 dB optical bandwidth is about 300 MHz for the precursor and postcursor cases, and only about 200 MHz for the symmetric dual-peak impulse response. All three bandwidths refer to the same link length of 1 km.

7.1.5 Conclusions and Remarks

In this section the theoretical principles and mathematical modeling of the multimode impulse response are based on the assumption of the Gaussian chromatic impulse response. The time domain and frequency domain general response equations have been derived in Equations (7.10) and (7.12) respectively. As expected after the conclusions of Chapter 5, the multimode transfer function is presented as the product of the Gaussian chromatic frequency response and the modal function. Under the additional assumption of uniform excitation, the simplified expressions (7.14) and (7.15) have been conveniently used for computer simulations of multimode responses using the analytical form of the group delay distribution. The mathematical modeling of the group delay distribution uses the inverse hyperbolic sine function, properly modified in order to handle a useful shaping factor for generating precursor pulses, postcursor pulses or symmetric dual peaks responses. The computed results for precursor and postcursor single-peak and symmetric dual-peak impulse responses have been shown in Figures 7.6, 7.7 and 7.8 respectively. The modal bandwidth concept loses its meaning when both the multi-peak response and high-speed transmission are encountered simultaneously.

Laboratory measurements of the multimode fiber impulse response give similar results, depending on the operating conditions. As will be seen in more detail in the next sections, launching conditions greatly affect the multimode fiber response, making this topic one of the most important to be used in the careful control of achieving multigigabit transmission over long-distance legacy multimode fibers.

7.2 Modal Theory of the Step-Index Fiber

In this section the mathematical theory of the modal fields in a step-index multimode fiber is presented. Some general concepts regarding the modal theory of graded index fiber have already been introduced in Chapter 3. There the fundamental assumption behind the mathematical formulation of the scalar field equations was discussed.

7.2.1 Introduction

As a general premise, the cylindrical symmetry of the optical fiber suggests using the cylindrical polar coordinate system to represent the spatial dependence of each Cartesian field component. This choice is made in order to have a fixed unit vector orientation in space while using the geometrical symmetries of the boundary conditions to implement the mathematical model:

1. The electric and magnetic field components are referred to a fixed Cartesian coordinate reference system, $\mathbf{E} = (E_x, E_y, E_z)$ and $\mathbf{H} = (H_x, H_y, H_z)$. The spatial dependence of each Cartesian field component is represented in the cylindrical polar coordinate system (r, ϕ, z).
2. The longitudinal dependence of each field component is represented by the complex phasor term $e^{j(\omega t - \beta z)}$ characteristic of every time-harmonic field:

$$\begin{aligned} \tilde{\mathbf{E}}(\mathbf{r}, t) &= \tfrac{1}{2}[\mathbf{E}(r, \phi)e^{j(\omega t - \beta z)} + \text{c.c.}] \\ \tilde{\mathbf{H}}(\mathbf{r}, t) &= \tfrac{1}{2}[\mathbf{H}(r, \phi)e^{j(\omega t - \beta z)} + \text{c.c.}] \end{aligned} \tag{7.21}$$

$$\begin{aligned} \mathbf{E}(r, \phi) &= \mathbf{x}E_x(r, \phi) + \mathbf{y}E_y(r, \phi) + \mathbf{z}E_z(r, \phi) \\ \mathbf{H}(r, \phi) &= \mathbf{x}H_x(r, \phi) + \mathbf{y}H_y(r, \phi) + \mathbf{z}H_z(r, \phi) \end{aligned} \tag{7.22}$$

3. The Cartesian reference system and the cylindrical polar reference system are related through the following differential transform operators:

$$\begin{aligned} \frac{\partial}{\partial x} &= \cos(\phi)\frac{\partial}{\partial r} - \sin(\phi)\frac{1}{r}\frac{\partial}{\partial \phi} \\ \frac{\partial}{\partial y} &= \sin(\phi)\frac{\partial}{\partial r} + \cos(\phi)\frac{1}{r}\frac{\partial}{\partial \phi} \end{aligned} \tag{7.23}$$

Using the time-harmonic field representation of Equations (7.21) and (7.22) and the Maxwell equations for the dielectric, time-invariant, homogeneous and isotropic system, the following representation is obtained of the transversal field components E_x, E_y, H_x, E_y in terms of both electrical and magnetic longitudinal field components E_z, H_z:

$$\begin{aligned} E_x &= \frac{1}{j\kappa^2}\left\{\beta\left[\cos(\phi)\left(\frac{\partial E_z}{\partial r}\right) - \frac{\sin(\phi)}{r}\left(\frac{\partial E_z}{\partial \phi}\right)\right] + \omega\mu\left[\sin(\phi)\left(\frac{\partial H_z}{\partial r}\right) + \frac{\cos(\phi)}{r}\left(\frac{\partial H_z}{\partial \phi}\right)\right]\right\} \\ E_y &= \frac{1}{j\kappa^2}\left\{\beta\left[\sin(\phi)\left(\frac{\partial E_z}{\partial r}\right) + \frac{\cos(\phi)}{r}\left(\frac{\partial E_z}{\partial \phi}\right)\right] - \omega\mu\left[\cos(\phi)\left(\frac{\partial H_z}{\partial r}\right) - \frac{\sin(\phi)}{r}\left(\frac{\partial H_z}{\partial \phi}\right)\right]\right\} \\ H_x &= \frac{1}{j\kappa^2}\left\{\beta\left[\cos(\phi)\left(\frac{\partial H_z}{\partial r}\right) - \frac{\sin(\phi)}{r}\left(\frac{\partial H_z}{\partial \phi}\right)\right] - \omega\varepsilon\left[\sin(\phi)\left(\frac{\partial E_z}{\partial r}\right) + \frac{\cos(\phi)}{r}\left(\frac{\partial E_z}{\partial \phi}\right)\right]\right\} \\ H_y &= \frac{1}{j\kappa^2}\left\{\beta\left[\sin(\phi)\left(\frac{\partial H_z}{\partial r}\right) + \frac{\cos(\phi)}{r}\left(\frac{\partial H_z}{\partial \phi}\right)\right] + \omega\varepsilon\left[\cos(\phi)\left(\frac{\partial E_z}{\partial r}\right) - \frac{\sin(\phi)}{r}\left(\frac{\partial E_z}{\partial \phi}\right)\right]\right\} \end{aligned} \tag{7.24}$$

The quantity

$$\kappa^2 \equiv k^2 n^2 - \beta^2 \tag{7.25}$$

is the transverse phase constant.

In the step-index optical fiber the refractive index n assumes different constant values both in the core region and in the cladding region. Figure 7.9 shows the reference system representation of the electromagnetic field in the axial symmetric optical fiber. The generic electric field $\mathbf{E}(r, \phi, z)$ is given by the vector sum of the three Cartesian components along the fixed spatial directions identified by the unit vectors (**x,y,z**), as reported in Equations (7.22). Each of the three field components has its own dependence over the transversal plane coordinate (r, ϕ), while exhibiting the same longitudinal dependence from the variable z through the common phasor term $e^{j(\omega t - \beta z)}$.

The logarithmic term in the right member of both vector equations for the electric and the magnetic fields derived in Chapter 3 disappears under the constant refractive index assumption. Consequently, both vector wave equations (3.30) and (3.31) in the case of the step index optical fiber reduce exactly to the following forms:

$$(\nabla_t^2 + k^2 n^2 - \beta^2)\mathbf{E}(r, \phi) = 0 \tag{7.26}$$

$$(\nabla_t^2 + k^2 n^2 - \beta^2)\mathbf{H}(r, \phi) = 0 \tag{7.27}$$

The electric and magnetic fields are expressed in Cartesian representation according to Equations (7.22). The term is used exactly because the refractive index is constant by definition, both in the core and in the cladding region, and there is no approximation this time.

As discussed extensively in Chapter 3, these equations are separable, leading to the same scalar wave equation for the generic Cartesian field component. The generic scalar function $\Psi(r, \phi)$ is

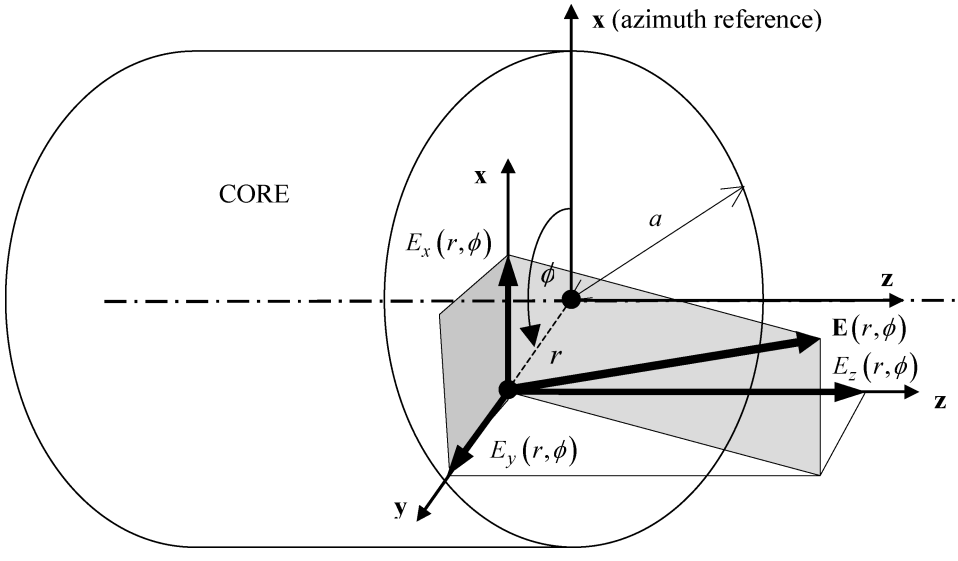

Figure 7.9 Cylindrical polar coordinate system used for the description of the spatial dependence of each Cartesian component of the electric field. A similar description holds for the magnetic field. Even if the modal electric field has in general all three Cartesian components simultaneously, their spatial dependence is limited to the transversal plane only. The longitudinal dependence upon the variable z is the same for all electromagnetic field components and is given by the phasor term $e^{j(\omega t - \beta z)}$

defined over the transversal plane and represents any one of the electric or magnetic field Cartesian components:

$$(\nabla_t^2 + k^2 n^2 - \beta^2)\Psi(r,\phi) = 0 \tag{7.28}$$

Using the explicit form of the transversal Laplacian operator in cylindrical coordinates reported in Chapter 3, Equation (3.18), gives the following second-order partial differential equation to be satisfied by the scalar field component $\Psi(r,\phi)$ for the step-index optical fiber with cylindrical symmetry:

$$\frac{\partial^2\Psi(r,\phi)}{\partial r^2} + \frac{1}{r}\frac{\partial\Psi(r,\phi)}{\partial r} + \frac{1}{r^2}\frac{\partial^2\Psi(r,\phi)}{\partial\phi^2} + (k^2n^2 - \beta^2)\Psi(r,\phi) = 0 \tag{7.29}$$

Setting

$$\Psi(r,\phi) \equiv R(r)\Phi(\phi) \tag{7.30}$$

finally gives the separated form:

$$\frac{\mathrm{d}^2R_\nu(r)}{\mathrm{d}r^2} + \frac{1}{r}\frac{\mathrm{d}R_\nu(r)}{\mathrm{d}r} + \left[k^2n^2 - \beta^2 - \frac{\nu^2}{r^2}\right]R_\nu(r) = 0 \tag{7.31}$$

$$\frac{\mathrm{d}^2\Phi_\nu(\phi)}{\mathrm{d}\varphi^2} + \nu^2\Phi_\nu(\phi) = 0 \tag{7.32}$$

The radial equation (7.31) is identical to Equation (3.42), except for the constant refractive index. This characteristic makes the equation analytically solvable, as will be seen later. The second equation is the well-known harmonic equation. For every real value of the constant ν, the solution is a linear combination of harmonic functions of the azimuth angle ϕ:

$$\Phi_\nu(\phi) = \begin{bmatrix} \mathrm{e}^{\mathrm{j}\nu\phi} \\ \cos(\nu\phi) \\ \sin(\nu\phi) \end{bmatrix} \tag{7.33}$$

Any of the above harmonic functions, including any linear combination, constitutes a possible choice for the angular dependence of the modal field. In the particular case $\nu = 0$ the angular contribution reduces to the constant value 0 or 1 according to the base function chosen. In order to satisfy boundary conditions of the circular fiber, later it will be seen that the separation constant ν must be a positive or negative integer, including zero:

$$\nu = 0, \pm1, \pm2, \ldots \tag{7.34}$$

The next section shows how to solve the above field equations in order to have a physical consistent solution.

7.2.2 Field Solutions in the Core and in the Cladding

The radial equation (7.31) for the step-index optical fiber coincides with the well-known Bessel differential equation. Its general solution is a linear combination of the Bessel functions. For any given integer ν, Bessel's differential equation has a different general solution according to the value of the transverse phase constant $\kappa^2 \equiv k^2n^2 - \beta^2$ defined in Equation (7.25). The general solution depends on the value of the transverse phase constant:

1. If the transverse phase constant is real

$$\kappa^2 > 0 \Rightarrow \beta < kn \tag{7.35}$$

the general solution of the Bessel differential equation (7.31) is a linear combination of the Bessel function of the first kind $J_\nu(\kappa r)$ and of the second kind $Y_\nu(\kappa r)$, both of the same argument κr:

$$R_\nu(r) = A\ J_\nu\ (\kappa r) + A' Y_\nu\ (\kappa r), \quad \kappa^2 > 0 \Rightarrow \beta < kn \tag{7.36}$$

2. If the transverse phase constant is imaginary

$$\kappa^2 < 0 \Rightarrow \beta > kn \tag{7.37}$$

the general solution of the Bessel differential equation (7.31) is a linear combination of the modified Bessel function of the first kind $K_\nu(|\kappa|r)$ and of the second kind $I_\nu(|\kappa|r)$, both of the same argument $|\kappa|r$:

$$R_\nu(r) = C\ K_\nu(|\kappa|r) + C' I_\nu\ (|\kappa|r), \quad \kappa^2 < 0 \Rightarrow \beta > kn \tag{7.38}$$

In the region where the transverse phase constant is imaginary, it is sometimes convenient to introduce the modified transverse phase constant γ:

$$\gamma^2 \equiv |\kappa|^2 \equiv \beta^2 - k^2 n^2, \quad \beta > kn \tag{7.39}$$

In addition, the general solution (7.38) of the Bessel equation takes the following form:

$$R_\nu(r) = C\ K_\nu(\gamma r) + C' I_\nu(\gamma r), \Rightarrow \beta > kn \tag{7.40}$$

Equations (7.36) and (7.40) represent both the general solution of the radial component of the scalar wave equation (7.31), depending on the sign of the transverse phase constant κ^2. However, according to the physical consistency of the field solution in the core and in the cladding regions, some of the mathematical solutions must be discarded. First the general behavior is considered of the four Bessel functions $J_\nu(\kappa r)$, $Y_\nu(\kappa r)$, $I_\nu(\kappa r)$ and $K_\nu(\kappa r)$.

Figure 7.10 shows qualitative drawings of the Bessel functions of the first kind $J_\nu(\kappa r)$ and the second kind $Y_\nu(\kappa r)$ for the first low orders. The characteristic feature of these functions is the oscillatory decaying behavior towards infinity. In particular, the function $J_\nu(\kappa r)$ assumes the following finite values on the axis, depending on the order:

$$\begin{aligned} J_0(0) &= 1, \quad \nu = 0 \\ J_\nu(0) &= 0, \quad |\nu| \geq 1 \end{aligned} \tag{7.41}$$

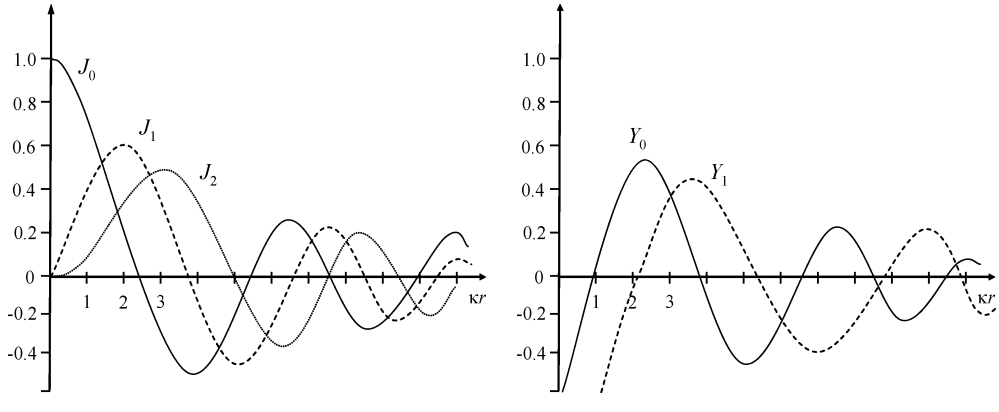

Figure 7.10 Qualitative representation of the Bessel functions of the first and second kinds in the argument κr for real values of the transverse phase constant

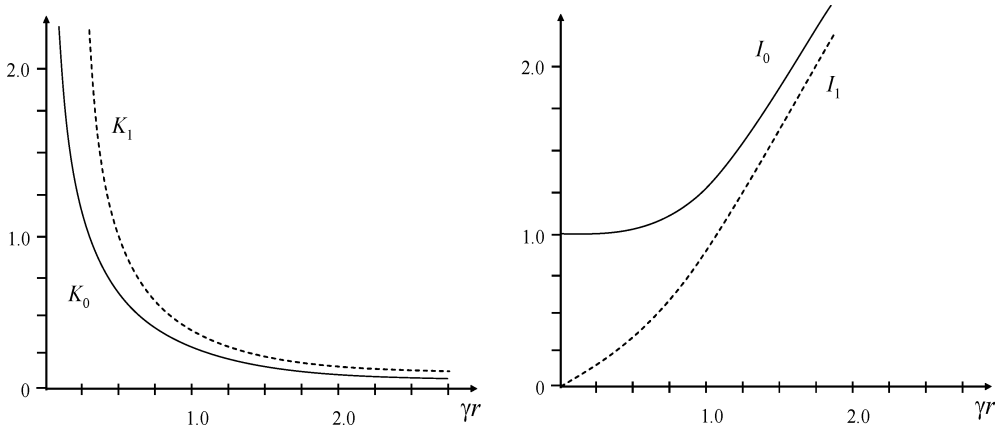

Figure 7.11 Qualitative representation of the modified Bessel functions of the first and second kinds in the argument $|\kappa|r = \gamma r$ for imaginary values of the transverse phase constant

Conversely, the function $Y_\nu(\kappa r)$ tends to minus infinite for every order on the fiber axis, $r \to 0$:

$$\lim_{\kappa r \to 0} Y_\nu(\kappa r) = -\infty, \quad |\nu| \geq 0 \tag{7.42}$$

Figure 7.11 shows qualitative drawings of the modified Bessel functions of the first kind $K_\nu(|\kappa|r)$ and the second kind $I_\nu(|\kappa|r)$. The characteristic feature of the modified Bessel functions is the monotonic behavior towards infinity. In particular, the function $K_\nu(|\kappa|r)$ tends to zero asymptotically for every order, while the function $I_\nu(|\kappa|r)$ diverges towards infinity for every order:

$$\begin{aligned} &\lim_{|\kappa|r \to +\infty} K_\nu(|\kappa|r) = 0, \qquad |\nu| \geq 0 \\ &\lim_{|\kappa|r \to +\infty} I_\nu(|\kappa|r) = +\infty, \quad |\nu| \geq 0 \end{aligned} \tag{7.43}$$

At this point, the first physical requirement can be stated:

1. For the light energy to be guided by the optical fiber it should at least be radial bounded from the fiber axis towards infinity.
   Accordingly,
2. Any linear combination of the Bessel functions must be rejected from the general solution of the Bessel equation that could originate a singularity both at the fiber axis and at an increasing distance from the fiber axis.
3. Looking at the Bessel function behaviors reported in Figures 7.10 and 7.11, it is easy to conclude that both Bessel functions of the second kind $Y_\nu(\kappa r)$ and $I_\nu(|\kappa|r)$ must be discarded due to their divergence behavior on the fiber axis and toward infinity respectively.
4. The physical solution must therefore be accomplished using any linear combination of the Bessel function of the first kind $J_\nu(\kappa r)$ in the core region and of the modified Bessel function of the first kind $K_\nu(|\kappa|r)$ in the cladding region. Introducing two generic complex constants A and C gives

$$R_\nu(r) = \begin{cases} A J_\nu\ (\kappa r), & \beta_\nu < kn_1, \quad A \in N, \quad \text{CORE} \\ C\ K_\nu(|\kappa|r), & \beta_\nu > kn_2, \quad C \in N, \quad \text{CLADDING} \end{cases} \tag{7.44}$$

5. In order to have a consistent physical solution $\kappa^2 > 0$ is chosen in the core region while in the cladding region $\kappa^2 < 0$ is chosen. Consequently, the following fundamental property of the

phase constant β is chosen for every guided fiber mode:

$$kn_2 < \beta < kn_1 \tag{7.45}$$

where n_1 and n_2 are the value of the refractive index in the core and in the cladding regions respectively. As a corollary, it is concluded that in order to have the guided mode the refractive index must satisfy the following inequality:

$$n_2 < n_1 \tag{7.46}$$

Once the proper mathematical structure of the radial solution in Equation (7.44) has been found, in order to find physical consistent solutions, the complete modal field, including the angular dependence, can easily be found from Equations (7.30) and (7.33):

$$\Psi(r,\phi) = \begin{cases} AJ_\nu(\kappa r)\begin{Bmatrix}\sin(\nu\phi)\\ \cos(\nu\phi)\end{Bmatrix} & \Rightarrow \quad \text{CORE}, \qquad 0 \le r \le a \\ CK_\nu(\gamma r)\begin{Bmatrix}\sin(\nu\phi)\\ \cos(\nu\phi)\end{Bmatrix} & \Rightarrow \quad \text{CLADDING}, \quad a \le r < \infty \end{cases} \tag{7.47}$$

The parameters κ and γ are defined in Equations (7.25) and (7.39) respectively. It is customary to introduce normalized and dimensionless arguments for the Bessel functions. The following normalized transversal frequencies are defined in the core and the cladding regions respectively:

$$u \equiv a\kappa = a\sqrt{n_1^2k^2 - \beta^2} \Rightarrow u \in N \tag{7.48}$$

$$w \equiv a\gamma = a\sqrt{\beta^2 - n_2^2k^2} \Rightarrow w \in N \tag{7.49}$$

The most important property of those normalized parameters is that the sum of their squared values is a constant for all fiber modes. Given the fiber core radius, the operating wavelength and the refractive index values in the core and in the cladding, the sum of their squared values defines a constant for the modal solution of the optical fiber. From Equations (7.48) and (7.49),

$$u^2 + w^2 = a^2(\kappa^2 + \gamma^2) = a^2k^2(n_1^2 - n_2^2) \tag{7.50}$$

It is customary to define the parameter V or normalized frequency of the optical fiber by the function

$$V \equiv \sqrt{u^2 + w^2} = 2\pi\frac{a}{\lambda}\sqrt{n_1^2 - n_2^2} \tag{7.51}$$

This parameter has a fundamental importance in the modal theory of the optical fiber. Its value sets the conditions for having a single-mode or a multimode regime in the optical fiber. In particular, the parameter V is directly related to the number of supported guided modes.

Once the normalized frequencies u and w have been defined in the core and the cladding respectively, the modal solution can conveniently be written in terms of the normalized radial coordinate:

$$\rho \equiv \frac{r}{a} \tag{7.52}$$

From Equations (7.49), (7.50) and (7.52), the general modal solution (7.47) assumes the following familiar form:

$$\Psi(\rho,\phi) = \begin{cases} A\ J_\nu(u\rho)\begin{Bmatrix}\sin(\nu\phi)\\ \cos(\nu\phi)\end{Bmatrix} & \Rightarrow \quad \text{CORE}, \qquad 0 \le \rho \le 1 \\ C\ K_\nu(w\rho)\begin{Bmatrix}\sin(\nu\phi)\\ \cos(\nu\phi)\end{Bmatrix} & \Rightarrow \quad \text{CLADDING}, \quad 1 \le \rho < \infty \end{cases} \tag{7.53}$$

In the following, reference will be made to this solution of the scalar wave equation (7.29) representing the guided modal field of the step-index optical fiber. The choices between sine and cosine functions are intended to obtain a complete set of orthogonal functions to represent any electromagnetic guided field in the optical fiber. Since both sine and cosine functions are allowed as solutions of the scalar wave equation (7.29) both functions are needed to represent the general solution in Equation (7.53).

The scalar wave function $\Psi_\nu(r,\phi)$ represents any one of the Cartesian components of the electromagnetic field. However, it is convenient to identify the scalar function $\Psi_\nu(r,\phi)$ with the longitudinal component of the electric field. Therefore,

$$E_z(\rho,\phi) \equiv \Psi_\nu(\rho,\phi) \tag{7.54}$$

For simplicity the dependence of the electric field has been omitted from the modal index ν. Therefore, from Equations (7.53) and (7.54),

$$E_z(\rho,\phi) = \begin{cases} A\ J_\nu(u\rho) \begin{Bmatrix} \sin(\nu\phi) \\ \cos(\nu\phi) \end{Bmatrix} & \Rightarrow \quad \text{CORE}, \qquad 0 \le \rho \le 1 \\ C\ K_\nu(w\rho) \begin{Bmatrix} \sin(\nu\phi) \\ \cos(\nu\phi) \end{Bmatrix} & \Rightarrow \quad \text{CLADDING}, \quad 1 \le \rho < \infty \end{cases} \tag{7.55}$$

Since the scalar wave equation for the magnetic field is the same as for the electric field, the scalar wave function $\Psi_\nu(r,\phi)$ must also be proportional to the longitudinal component of the magnetic field. The only difference between the mathematical solutions of the longitudinal components of the electric and magnetic fields must therefore be identified in a different complex constant. Accordingly,

$$H_z(\rho,\phi) = \begin{cases} B\ J_\nu(u\rho) \begin{Bmatrix} \sin(\nu\phi) \\ \cos(\nu\phi) \end{Bmatrix} & \Rightarrow \quad \text{CORE}, \qquad 0 \le \rho \le 1 \\ D\ K_\nu(w\rho) \begin{Bmatrix} \sin(\nu\phi) \\ \cos(\nu\phi) \end{Bmatrix} & \Rightarrow \quad \text{CLADDING}, \quad 1 \le \rho < \infty \end{cases} \tag{7.56}$$

Once the general solution for the longitudinal components of the electric and the magnetic fields has been found the electromagnetic field representation in the step index optical fiber can be completed by computing the general expressions for the transversal Cartesian field components $E_x(\rho,\phi)$, $E_y(\rho,\phi)$, $H_x(\rho,\phi)$ and $H_y(\rho,\phi)$ using the general relationships reported in Equations (7.24). In the following section, the general solution scheme for the modal fields in the step-index optical fiber is proposed.

7.2.2.1 Modal Field Solution Scheme

1. Choose the expressions for the angular dependence of the longitudinal components $E_z(\rho,\phi)$ and $H_z(\rho,\phi)$ of the electric and magnetic fields according to the general solutions (7.55) and (7.56).
2. Compute the four first-order partial derivatives of the longitudinal components of the electric and magnetic fields:

$$\begin{aligned} \left(\frac{\partial E_z}{\partial \rho}\right) &= a\left(\frac{\partial E_z}{\partial r}\right)\left(\frac{\partial E_z}{\partial \phi}\right) \\ \left(\frac{\partial H_z}{\partial \rho}\right) &= a\left(\frac{\partial H_z}{\partial r}\right)\left(\frac{\partial H_z}{\partial \phi}\right) \end{aligned} \tag{7.57}$$

3. Substitute the corresponding longitudinal field derivatives into the transformation relations (7.24) separately in the core and in the cladding regions using the following recurrence relations of the Bessel functions and the basic trigonometric properties:

$$\begin{aligned}
&\text{(a)} \quad J_{\nu-1}(z) + J_{\nu+1}(z) = \frac{2\nu}{z} J_\nu(z) \\
&\text{(b)} \quad J_{\nu-1}(z) - J_{\nu+1}(z) = 2J'_\nu(z) \\
&\text{(c)} \quad J'_\nu(z) = J_{\nu-1}(z) - \frac{\nu}{z} J_\nu(z) \\
&\text{(d)} \quad J'_\nu(z) = -J_{\nu+1}(z) + \frac{\nu}{z} J_\nu(z) \\
&\text{(e)} \quad K_{\nu+1}(z) - K_{\nu-1}(z) = \frac{2\nu}{z} K_\nu(z) \\
&\text{(f)} \quad K_{\nu+1}(z) + K_{\nu-1}(z) = -2K'_\nu(z) \\
&\text{(g)} \quad K'_\nu(z) = -K_{\nu-1}(z) - \frac{\nu}{z} K_\nu(z) \\
&\text{(h)} \quad K'_\nu(z) = -K_{\nu+1}(z) + \frac{\nu}{z} K_\nu(z)
\end{aligned} \tag{7.58}$$

$$\sin[(\nu \pm 1)\phi] = \sin(\nu\phi)\cos(\phi) \pm \sin(\phi)\cos(\nu\phi) \tag{7.59}$$

$$\cos[(\nu \pm 1)\phi] = \cos(\nu\phi)\cos(\phi) \mp \sin(\nu\phi)\sin(\phi) \tag{7.60}$$

It should be noted that in the core and the cladding regions, the transversal phase constant κ assumes real and imaginary values respectively, leading to different relationships.

7.2.3 Paraxial Approximation

The modal field solution procedure shown in the previous section, together with the general solution for the longitudinal electric and magnetic field components in Equations (7.56) and (7.57), allows determination of the general solution for any guided mode in the step-index optical fiber. Although the general procedure is correct, it is convenient to proceed further with a significant simplification in the modal analysis of the optical fibers used for telecommunication purposes. Again the relationships (7.24) are considered between the transversal and the longitudinal components of the electromagnetic field. In particular the relationships (7.24) highlighting the similarities between the components $E_y(r, \phi)$ and $H_x(r, \phi)$, and between $E_x(r, \phi)$ and $H_y(r, \phi)$ of the transversal field can be rewritten as

$$\begin{aligned}
E_x &= +\frac{\beta}{\mathrm{j}\kappa^2}\left\{\cos(\phi)\left(\frac{\partial E_z}{\partial r}\right) - \frac{\sin(\phi)}{r}\left(\frac{\partial E_z}{\partial \phi}\right) + \frac{\omega\mu}{\beta}\left[\sin(\phi)\left(\frac{\partial H_z}{\partial r}\right) + \frac{\cos(\phi)}{r}\left(\frac{\partial H_z}{\partial \phi}\right)\right]\right\} \\
H_y &= +\frac{\omega\varepsilon}{\mathrm{j}\kappa^2}\left\{\cos(\phi)\left(\frac{\partial E_z}{\partial r}\right) - \frac{\sin(\phi)}{r}\left(\frac{\partial E_z}{\partial \phi}\right) + \frac{\beta}{\omega\varepsilon}\left[\sin(\phi)\left(\frac{\partial H_z}{\partial r}\right) + \frac{\cos(\phi)}{r}\left(\frac{\partial H_z}{\partial \phi}\right)\right]\right\}
\end{aligned} \tag{7.61}$$

$$\begin{aligned}
E_y &= -\frac{\omega\mu}{\mathrm{j}\kappa^2}\left\{\cos(\phi)\left(\frac{\partial H_z}{\partial r}\right) - \frac{\sin(\phi)}{r}\left(\frac{\partial H_z}{\partial \phi}\right) - \frac{\beta}{\omega\mu}\left[\sin(\phi)\left(\frac{\partial E_z}{\partial r}\right) + \frac{\cos(\phi)}{r}\left(\frac{\partial E_z}{\partial \phi}\right)\right]\right\} \\
H_x &= +\frac{\beta}{\mathrm{j}\kappa^2}\left\{\cos(\phi)\left(\frac{\partial H_z}{\partial r}\right) - \frac{\sin(\phi)}{r}\left(\frac{\partial H_z}{\partial \phi}\right) - \frac{\omega\varepsilon}{\beta}\left[\sin(\phi)\left(\frac{\partial E_z}{\partial r}\right) + \frac{\cos(\phi)}{r}\left(\frac{\partial E_z}{\partial \phi}\right)\right]\right\}
\end{aligned} \tag{7.62}$$

These equations are valid in general, without any approximation, but the terms in Equations (7.24) have been reordered. The following question can now be answered. Which approximate conditions are required in order for the magnetic field components to be proportional to the electric field components? After a short examination of Equations (7.61) and (7.62) it is easy to conclude that the required condition is the following:

$$\frac{\omega\mu}{\beta} = \frac{\beta}{\omega\varepsilon} \tag{7.63}$$

In this case, the relations between the transversal components of the magnetic fields H_x, H_y and the corresponding orthogonal transversal components of the electric fields E_y, E_x become

$$\begin{aligned} H_x &= -\frac{\omega\varepsilon}{\beta} E_y \\ H_y &= +\frac{\omega\varepsilon}{\beta} E_x \end{aligned} \tag{7.64}$$

The transversal components of the magnetic field are proportional through the constant $\omega\varepsilon/\beta$ to the cross-orthogonal components of the transversal electric field.

It should be remembered that there are no approximations in these equations. They follow directly from the Maxwell equations for the monochromatic electromagnetic field and are valid in general for every dielectric medium.

7.2.3.1 Transversal Orthogonality

One remarkable consequence of the proportionality between the transversal components of the magnetic and electric fields in Equations (7.64) is their orthogonal relationship. Introducing the transversal vector fields $\mathbf{E}_t(r,\phi)$ and $\mathbf{H}_t(r,\phi)$ gives

$$\begin{aligned} \mathbf{E}(r,\phi) &= \mathbf{E}_t(r,\phi) + \mathbf{z}E_z(r,\phi) \\ \mathbf{H}(r,\phi) &= \mathbf{H}_t(r,\phi) + \mathbf{z}H_z(r,\phi) \\ \mathbf{E}_t(r,\phi) &= \mathbf{x}E_x(r,\phi) + \mathbf{y}E_y(r,\phi) \\ \mathbf{H}_t(r,\phi) &= \mathbf{x}H_x(r,\phi) + \mathbf{y}H_y(r,\phi) \end{aligned} \tag{7.65}$$

From Equations (7.64) it is immediately deduced that

$$\mathbf{E}_t \cdot \mathbf{H}_t = E_x H_x + E_y H_y = -\frac{\omega\varepsilon}{\beta} E_x^2 + -\frac{\omega\varepsilon}{\beta} E_x^2 \equiv 0 \tag{7.66}$$

Then

$$\mathbf{E}_t \perp \mathbf{H}_t \tag{7.67}$$

The condition (7.63) that was used to find the transversal field orthogonality leads to the concept of paraxial approximation. First, it was easily demonstrated that the monochromatic electromagnetic field in every homogeneous dielectric medium satisfies Equation (7.63). In fact, from Equation (7.63),

$$\beta^2 = \omega^2\varepsilon\mu = \omega^2 n^2 \varepsilon_0 \mu \cong \omega^2 n^2 \varepsilon_0 \mu_0 \tag{7.68}$$

Since

$$c = \frac{1}{\sqrt{\varepsilon_0\mu_0}}, \qquad k = \frac{\omega}{c} \tag{7.69}$$

it was concluded that condition (7.63) gives

$$\beta = nk \tag{7.70}$$

This is the phase constant of an unbounded electromagnetic wave propagating in the homogeneous medium with a refractive index n and vacuum wavenumber $k = 2\pi/\lambda$. In the above derivation, the magnetic permeability of the dielectric medium has been approximated, with the magnetic permeability of the vacuum $\mu \cong \mu_0$. Similar concepts can be used to introduce the paraxial approximation in weakly guiding optical fibers. It is known that the guiding principle is dependent on the refractive index difference between the core and the cladding regions. The higher the refractive index step, the stronger will be the guiding effect of the fiber structure. In other words, the limit angle for total internal reflection increases with the refractive index profile height parameter. It is intuitive, however, that in order to achieve low dispersion in pulse propagation, the limit angle should be as low as possible to minimize the multipath delay dispersion.

To this end, the two members of Equation (7.63) are considered separately, where $\mu = \mu_0$ is assumed and $\beta \cong n_1 k$ is set approximately in the core:

$$\begin{aligned} \frac{\omega\mu_0}{\beta} = \frac{k\mu_0}{\beta\sqrt{\varepsilon_0\mu_0}} &\underset{(\beta\cong n_1 k)}{\cong} \frac{\mu_0}{n_1\sqrt{\varepsilon_0\mu_0}} = \frac{Z_0}{n_1} \\ \frac{\beta}{\omega\varepsilon} = \frac{\beta\sqrt{\varepsilon_0\mu_0}}{n_1^2 k\varepsilon_0} &\underset{(\beta\cong n_1 k)}{\cong} \frac{\sqrt{\varepsilon_0\mu_0}}{n_1\varepsilon_0} = \frac{Z_0}{n_1} \end{aligned} \tag{7.71}$$

The parameters ε_0 and μ_0 are the vacuum dielectric permittivity $\varepsilon_0 = 8.85410^{-12}$ F/m and the vacuum magnetic permeability $\mu_0 = 4\pi \times 10^{-7}$ H/m respectively. The parameter $Z_0 = \sqrt{\mu_0/\varepsilon_0} \cong 376.73\,\Omega$ is the vacuum impedance.

The condition

$$\beta \cong n_1 k \cong n_2 k \tag{7.72}$$

used in Equations (7.71) in order to satisfy Equation (7.63) approximately is know as the paraxial approximation. It assumes that the variation of the phase constant β among guided modes is almost negligible with respect to its average value. The propagation direction of the fiber modes is therefore almost parallel to the fiber axis direction, and hence is given the terminology paraxial approximation.

Using the approximated values in Equations (7.71), the relationships (7.64) between the transversal components of the electromagnetic fields in optical fiber under the paraxial approximation become

$$\begin{aligned} H_x &\cong -\frac{n_1}{Z_0} E_y \\ H_y &\cong +\frac{n_1}{Z_0} E_x \end{aligned} \tag{7.73}$$

The paraxial approximation therefore allows a calculation of the magnetic field to be made using the linear relationship (7.73), simplifying the modal problem to determination of the electric field only.

7.2.4 Mode Classification

Electromagnetic modes in every waveguide structure are classified according to their electric and magnetic field components. As will be seen later, depending on the boundary conditions some of the electric and magnetic field components might be missing, leading to particular field structures. Conductive waveguides support electromagnetic field solutions that can be classified into the three following modes:

1. *TE (transverse electric) modes.* The electric field has no longitudinal component and consequently lies on the transversal plane to the waveguide axis.
2. *TM (transverse magnetic) modes.* The magnetic field has no longitudinal component and consequently lies on the transversal plane to the waveguide axis.
3. *TEM (transverse electromagnetic) modes.* Both the electric and the magnetic fields lie on the transversal plane to the waveguide axis. The Poynting vector is therefore aligned with the direction of the waveguide axis.

What would be the mode classification for a dielectric waveguide and in particular for the optical fiber? According to the modal analysis derived in the previous section for the step-index fiber, the following general classification holds in general for every graded index fiber:

1. Optical fibers do not support TEM modes. The longitudinal component of either the electric field or the magnetic field or both must not be null.
2. Optical fibers support both TE modes and TM modes.
3. Optical fibers support HE hybrid modes and EH hybrid modes, where both longitudinal components of the electric and magnetic fields are simultaneously present.
4. Due to the weakly guiding properties of optical fibers designed for telecommunication purposes, the paraxial approximation leads to mode degeneracy. It will be seen in the next sections that, some modes exhibit the same propagation constant, behaving in exactly the same way in terms of propagation properties. Those modes can be grouped in a different way, leading to the well-known linearly polarized (LP) modes of the optical fiber. The LP classification is the same as grouping TE, TM, HE and EH modes according to their common value of the propagation constant.

7.2.4.1 TE Modes

In this section, the transverse electric (TE) mode is considered in more detail. From the general electromagnetic field solutions in Equations (7.55) and (7.56), the sin ($\nu\phi$) dependence of the longitudinal component of the electric field and the cos ($\nu\phi$) dependence of the longitudinal component of the magnetic field are found:

$$E_z(\rho,\phi) = \begin{cases} AJ_\nu(u\rho)\sin(\nu\phi), & 0 \le \rho \le 1 \\ CK_\nu(w\rho)\sin(\nu\phi), & 1 \le \rho < \infty \end{cases} \tag{7.74}$$

$$H_z(\rho,\phi) = \begin{cases} BJ_\nu(u\rho)\cos(\nu\phi), & 0 \le \rho \le 1 \\ DK_\nu(w\rho)\cos(\nu\phi), & 1 \le \rho < \infty \end{cases} \tag{7.75}$$

The integration constant pairs A, C and B, D will be determined by the boundary conditions and the corresponding eigenvalue equation produces the second radial modal number. The solution given in Equations (7.74) and (7.75) has in general both longitudinal components unless the azimuth mode number is set at $\nu = 0$. Setting the azimuth mode number at $\nu = 0$, the previous modal equations become

$$TE_0 \text{ modes} \begin{cases} E_z(\rho,\phi) = 0, \quad 1 \le \rho < \infty & (7.76) \\ H_z(\rho,\phi) = \begin{cases} BJ_0(u\rho), & 0 \le \rho \le 1 \\ DK_0(w\rho), & 1 \le \rho < \infty \end{cases} & (7.77) \end{cases}$$

This corresponds to a family of TE modes. As mentioned above, an individual mode specification depends on the boundary conditions to be satisfied. Once the longitudinal solution has been defined, the transversal field component relationships shown in Equations (7.61) and (7.62) complete the mode description. According to the paraxial approximation, only the transversal components of the

electric field need to be computed; then using Equation (7.73) the transversal components of the magnetic field are found. Substituting Equation (7.76) into Equations (7.61) and (7.62) gives the following equations for the transverse components of the electric field versus the longitudinal magnetic field components, where the equations in the core and the cladding regions are reported separately:

$$E_z \equiv 0 \Rightarrow \begin{cases} \underset{\kappa^2 \equiv k^2 n_1^2 - \beta^2 > 0}{\text{CORE}} \begin{cases} E_x = +\dfrac{\omega\mu}{\mathrm{j}\kappa^2}\left[\sin(\phi)\left(\dfrac{\partial H_z}{\partial r}\right) + \dfrac{\cos(\phi)}{r}\left(\dfrac{\partial H_z}{\partial \phi}\right)\right] \\ E_y = -\dfrac{\omega\mu}{\mathrm{j}\kappa^2}\left[\cos(\phi)\left(\dfrac{\partial H_z}{\partial r}\right) - \dfrac{\sin(\phi)}{r}\left(\dfrac{\partial H_z}{\partial \phi}\right)\right] \end{cases} \\ \underset{\gamma^2 \equiv \beta^2 - k^2 n_2^2 > 0}{\text{CLADDING}} \begin{cases} E_x = -\dfrac{\omega\mu}{\mathrm{j}\gamma^2}\left[\sin(\phi)\left(\dfrac{\partial H_z}{\partial r}\right) + \dfrac{\cos(\phi)}{r}\left(\dfrac{\partial H_z}{\partial \phi}\right)\right] \\ E_y = +\dfrac{\omega\mu}{\mathrm{j}\gamma^2}\left[\cos(\phi)\left(\dfrac{\partial H_z}{\partial r}\right) - \dfrac{\sin(\phi)}{r}\left(\dfrac{\partial H_z}{\partial \phi}\right)\right] \end{cases} \end{cases} \tag{7.78}$$

The only difference in the equation structure between the two regions is the value of the transverse phase constant:

$$\begin{aligned} \text{CORE}: \quad & \kappa^2 \equiv k^2 n_1^2 - \beta^2, \quad \beta < k n_1 \\ \text{CLADDING}: \quad & \gamma^2 \equiv \beta^2 - k^2 n_2^2, \quad \beta > k n_2 \end{aligned} \tag{7.79}$$

Note that the longitudinal component of the magnetic field in Equation (7.77) shows axial symmetry, having no dependence on the azimuth angle ϕ. Deriving the magnetic field (7.77) with respect to both position coordinates and using the Bessel function relationships (7.58d) and (7.58h) gives

$$\begin{aligned} \frac{\partial H_z}{\partial r} &= \begin{cases} -B\kappa J_1(u\rho), & 0 \le \rho \le 1, \quad \text{CORE} \\ -D\gamma K_1(w\rho), & 1 \le \rho < \infty, \quad \text{CLADDING} \end{cases} \\ \frac{\partial H_z}{\partial \phi} &\equiv 0, \quad 0 \le \rho < \infty \end{aligned} \tag{7.80}$$

Substituting the spatial derivatives of the longitudinal component of the magnetic field in Equation (7.78) and using Equations (7.48) and (7.49) gives the following expressions for the transversal components of the electric field in the core and in the cladding regions:

CORE: $0 \le \rho \le 1$	CLADDING: $\rho \ge 1$
$E_x = -B\dfrac{\omega\mu}{\mathrm{j}\kappa} J_1(u\rho)\sin(\phi)$	$E_x = +D\dfrac{\omega\mu}{\mathrm{j}\gamma} K_1(w\rho)\sin(\phi)$
$E_y = +B\dfrac{\omega\mu}{\mathrm{j}\kappa} J_1(u\rho)\cos(\phi)$	$E_y = -D\dfrac{\omega\mu}{\mathrm{j}\gamma} K_1(w\rho)\cos(\phi)$
$E_z \equiv 0$	$E_z \equiv 0$

(7.81)

To derive the transversal components of the magnetic field, the paraxial approximation (7.63) is used, leading to the simplified relationships reported in Equations (7.73):

CORE: $0 \le \rho \le 1$	CLADDING: $\rho \ge 1$
$H_x = -B\dfrac{n_1}{Z_0}\dfrac{\omega\mu}{\mathrm{j}\kappa} J_1(u\rho)\cos(\phi)$	$H_x = +D\dfrac{n_2}{Z_0}\dfrac{\omega\mu}{\mathrm{j}\gamma} K_1(w\rho)\cos(\phi)$
$H_y = -B\dfrac{n_1}{Z_0}\dfrac{\omega\mu}{\mathrm{j}\kappa} J_1(u\rho)\sin(\phi)$	$H_y = +D\dfrac{n_2}{Z_0}\dfrac{\omega\mu}{\mathrm{j}\gamma} K_1(w\rho)\sin(\phi)$
$H_z = +B J_0(u\rho)$	$H_z = +D K_0(w\rho)$

(7.82)

Equations in (7.81) and (7.82) define the generic TE_0 mode for the step-index fiber. However, in order to complete the mode field equations the integration constants B and D need to be specified. Integration constants specify the matching conditions at the core–cladding interface and the mode intensity. The next section shows how boundary conditions for the electromagnetic field at the core–cladding interface lead to the eigenvalues equation and to the introduction of the second modal number, namely the radial mode number μ.

7.2.4.2 TM Modes

In order to arrive at the general expression for the transverse magnetic (TM) modes, a consistent solution with null longitudinal components of the magnetic field is needed. This must be true for every point in the transversal fiber section. Once again, the general electromagnetic field solutions in Equations (7.55) and (7.56) are used, and the $\cos(\nu\phi)$ dependence of the longitudinal component of the electric field and the $\sin(\nu\phi)$ dependence of the longitudinal component of the magnetic field are found:

$$E_z(\rho,\phi) = \begin{cases} AJ_\nu(u\rho)\cos(\nu\phi), & 0 \le \rho \le 1 \\ CK_\nu(w\rho)\cos(\nu\phi), & 1 \le \rho < \infty \end{cases} \tag{7.83}$$

$$H_z(\rho,\phi) = \begin{cases} BJ_\nu(u\rho)\sin(\nu\phi), & 0 \le \rho \le 1 \\ DK_\nu(w\rho)\sin(\nu\phi), & 1 \le \rho < \infty \end{cases} \tag{7.84}$$

According to this choice from the general solutions in Equations (7.55) and (7.56) it can be seen from Equations (7.74) and (7.75) that the complementary azimuth dependence between the TE and TM modes is found. The integration constant pairs A, C and B, D will be determined by the boundary conditions and the corresponding eigenvalues equation produces the second radial modal number. Proceeding as in the previous section for the derivation of the TE modes, the solution chosen in Equations (7.83) and (7.84) has in general both longitudinal components unless the azimuth mode number $\nu = 0$ is set. Setting the azimuth mode number $\nu = 0$, the previous modal equations become

$$\text{TM}_0 \text{ modes} \begin{cases} E_z(\rho,\phi) = \begin{cases} AJ_0(u\rho), & 0 \le \rho \le 1, \quad \text{CORE} \\ CK_0(w\rho), & 1 \le \rho < \infty, \quad \text{CLADDING} \end{cases} & (7.85) \\ H_z(\rho,\phi) \equiv 0 & (7.86) \end{cases}$$

which corresponds to the required transverse magnetic field for the TM modes. The mathematical structure of the longitudinal fields for TM modes is identical to the TE modes except for the exchanging role between the electrical and the magnetic fields. Proceeding as for the case of TE modes, the following equations for the transversal components of the electric field are

$$H_z \equiv 0 \Rightarrow \begin{cases} \underset{\kappa^2 \equiv k^2 n_1^2 - \beta^2 > 0}{\text{CORE}} & \begin{cases} E_x = +\dfrac{\beta}{\mathrm{j}\kappa^2}\left[\cos(\phi)\left(\dfrac{\partial E_z}{\partial r}\right) - \dfrac{\sin(\phi)}{r}\left(\dfrac{\partial E_z}{\partial \phi}\right)\right] \\ E_y = +\dfrac{\beta}{\mathrm{j}\kappa^2}\left[\sin(\phi)\left(\dfrac{\partial E_z}{\partial r}\right) + \dfrac{\cos(\phi)}{r}\left(\dfrac{\partial E_z}{\partial \phi}\right)\right] \end{cases} \\ \underset{\gamma^2 \equiv \beta^2 - k^2 n_2^2 > 0}{\text{CLADDING}} & \begin{cases} E_x = -\dfrac{\beta}{\mathrm{j}\gamma^2}\left[\cos(\phi)\left(\dfrac{\partial E_z}{\partial r}\right) - \dfrac{\sin(\phi)}{r}\left(\dfrac{\partial E_z}{\partial \phi}\right)\right] \\ E_y = -\dfrac{\beta}{\mathrm{j}\gamma^2}\left[\sin(\phi)\left(\dfrac{\partial E_z}{\partial r}\right) + \dfrac{\cos(\phi)}{r}\left(\dfrac{\partial E_z}{\partial \phi}\right)\right] \end{cases} \end{cases} \tag{7.87}$$

In this case, of course, the longitudinal component of the magnetic field is null and both transversal field components depend exclusively on the longitudinal electric field $E_z(\rho, \phi)$.

Deriving the electric field in Equation (7.85) and using the Bessel function relationships (7.58d) and (7.58h) gives

$$\frac{\partial E_z}{\partial r} = \begin{cases} -A\kappa J_1(u\rho), & 0 \le \rho \le 1, \quad \text{CORE} \\ -C\gamma K_1(w\rho), & 1 \le \rho < \infty, \quad \text{CLADDING} \end{cases}$$
$$\frac{\partial E_z}{\partial \phi} \equiv 0, \quad 0 \le \rho < \infty \tag{7.88}$$

Substituting the spatial derivatives of the longitudinal component of the electric field in Equation (7.87) and again using Equations (7.48) and (7.49) gives the following expressions for the transversal components of the electric field in the core and in the cladding regions:

CORE : $0 \le \rho \le 1$	CLADDING : $\rho \ge 1$
$E_x = -A\dfrac{\beta}{\mathrm{j}\kappa} J_1(u\rho)\cos(\phi)$	$E_x = +C\dfrac{\beta}{\mathrm{j}\gamma} K_1(w\rho)\cos(\phi)$
$E_y = -A\dfrac{\beta}{\mathrm{j}\kappa} J_1(u\rho)\sin(\phi)$	$E_y = +C\dfrac{\beta}{\mathrm{j}\gamma} K_1(w\rho)\sin(\phi)$
$E_z \equiv +A J_0(u\rho)$	$E_z \equiv +A K_0(w\rho)$

(7.89)

To compute the transversal components of the magnetic field, the paraxial approximation (7.63) is again used to obtain the simplified relationships reported below:

CORE : $0 \le \rho \le 1$	CLADDING : $\rho \ge 1$
$H_x = +A\dfrac{n_1}{Z_0}\dfrac{\beta}{\mathrm{j}\kappa} J_1(u\rho)\sin(\phi)$	$H_x = -C\dfrac{n_2}{Z_0}\dfrac{\beta}{\mathrm{j}\gamma} K_1(w\rho)\sin(\phi)$
$H_y = -A\dfrac{n_1}{Z_0}\dfrac{\beta}{\mathrm{j}\kappa} J_1(u\rho)\cos(\phi)$	$H_y = +C\dfrac{n_2}{Z_0}\dfrac{\beta}{\mathrm{j}\gamma} K_1(w\rho)\cos(\phi)$
$H_z \equiv 0$	$H_z \equiv 0$

(7.90)

The equations shown in (7.89) and (7.90) define the generic transverse magnetic mode, TM_0, for the step-index fiber. Again, in order to specify the transverse magnetic mode field distribution completely the integration constants B and D need to be determined.

7.2.5 Boundary Conditions and Eigenvalues Problem

The electromagnetic mode derived so far for the step-index fiber is still dependent on two constants, either (B,D) or (A,C) for the transverse electric or transverse magnetic fields respectively. As required in general by every physical problem, the matching conditions of the electromagnetic field at the boundary surface between the core and the cladding leads to a first relationship between each constant pair. The second independent relationship comes from the mode power requirement. In this section, the boundary condition for the optical fiber will be introduced and the corresponding eigenvalue equation to be satisfied will be derived in order to obtain a consistent field solution. The theory of the boundary conditions for the electromagnetic field is well known and is presented in every textbook on electromagnetic field theory.

In this section, several aspects of the boundary conditions theory that are peculiar to optical fiber behavior and will clarify most of the modal properties used later will be introduced. However, as detailed mathematical aspects would be beyond the scope of this book only some of the major milestones and related consequences will be presented. The reader is referred to specialized books on these topics for further reading.

7.2.5.1 General Concepts

In every static medium, in the absence of both surface charge density ρ ($\mathbf{r}$,t) and surface current density $\mathbf{K}(\mathbf{r},t)$, the boundary conditions for the electromagnetic field require:

1. The continuity of the normal component of the electric displacement vector:

$$D_{1,n} = D_{2,n} \tag{7.91}$$

2. The continuity of the tangential component of the electric vector:

$$\mathbf{E}_{1,t} = \mathbf{E}_{2,t} \tag{7.92}$$

3. The continuity of the normal component of the magnetic induction vector:

$$B_{1,n} = B_{2,n} \tag{7.93}$$

4. The continuity of the tangential component of the magnetic intensity vector:

$$\mathbf{H}_{1,t} = \mathbf{H}_{2,t} \tag{7.94}$$

Figure 7.12 gives a mathematical description of the boundary conditions reported above for a generic surface delimiting two media, medium 1 and medium 2. The equations for the boundary

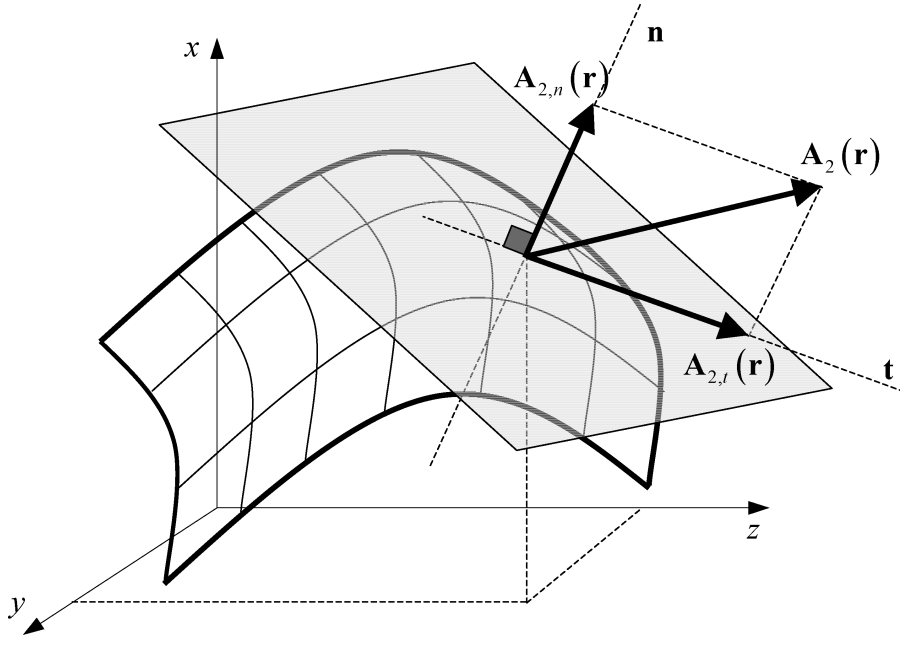

Figure 7.12 Geometrical representation of the boundary conditions for the electromagnetic field across the surface between two different media. Unit vectors **n** and **t** define the normal and the tangential directions respectively at a given point on the surface

conditions of the electromagnetic field components across the boundary surface are

$$\begin{aligned} \mathbf{n} \cdot (\mathbf{D}_2 - \mathbf{D}_1) &= \mathbf{0} \\ \mathbf{n} \times (\mathbf{E}_2 - \mathbf{E}_1) &= \mathbf{0} \\ \mathbf{n} \cdot (\mathbf{B}_2 - \mathbf{B}_1) &= \mathbf{0} \\ \mathbf{n} \times (\mathbf{H}_2 - \mathbf{H}_1) &= \mathbf{0} \end{aligned} \tag{7.95}$$

The electromagnetic boundary conditions for dielectric and nonmagnetic media characterized by a uniform refractive index n_1 and n_2 respectively become simply

$$\begin{aligned} n_1^2 E_{1,n} &= n_2^2 E_{2,n} \\ \mathbf{E}_{1,t} &= \mathbf{E}_{2,t} \\ H_{1,n} &= H_{2,n} \\ \mathbf{H}_{1,t} &= \mathbf{H}_{2,t} \end{aligned} \tag{7.96}$$

7.2.5.2 Boundary Conditions for the Step-Index Fiber

Applying the general theory of the boundary conditions presented in the previous section to the step-index optical fiber, the following fundamental statement can be concluded. Across the core–cladding interface of a step-index fiber, the boundary conditions for the electromagnetic field require the continuity of both the magnetic field vector and of the tangential component of the electric field vector, while the normal component of the electric field must satisfy the first equation in (7.96):

$$\mathbf{H}_1 = \mathbf{H}_2 \qquad \begin{cases} \mathbf{E}_{1,t} = \mathbf{E}_{2,t} \\ n_1^2 E_{1,n} = n_2^2 E_{2,n} \end{cases} \tag{7.97}$$

The solution of the boundary problem must conveniently reflect the symmetry available at the boundary interfaces. In the case of optical fibers, the boundary between the core and the cladding regions is a cylindrical surface.

According to the fiber geometry, the followings statements hold:

1. The most convenient choice for solving the electromagnetic field boundary problem is to represent each electromagnetic field component A at the core–cladding interface in a cylindrical reference system.
2. According to this choice, the normal component of the core–cladding interface coincides with its radial component $A_n \equiv A_r$, while the tangential field component of the core–cladding interface is given by the vector sum of the azimuth component with the longitudinal component $\mathbf{A}_t \equiv \mathbf{A}_\phi + \mathbf{A}_z$.
3. Assuming that $\mathbf{A} \equiv \mathbf{E}$ or $\mathbf{H}$, the following relationships are valid at every point in the space and in particular at the core–cladding interface:

$$\mathbf{A} = \mathbf{A}_t + \mathbf{A}_n \Rightarrow \begin{cases} \mathbf{A}_t = \mathbf{A}_\phi + \mathbf{A}_z \\ \mathbf{A}_n = \mathbf{A}_r \end{cases} \tag{7.98}$$

Figure 7.13 presents the geometry involved in the core–cladding cylindrical interface with the normal and tangent components of the generic vector field $\mathbf{A}(r, \phi, z)$. Using the cylindrical representation (7.98), the boundary condition (7.97) for the electromagnetic field simplifies considerably,

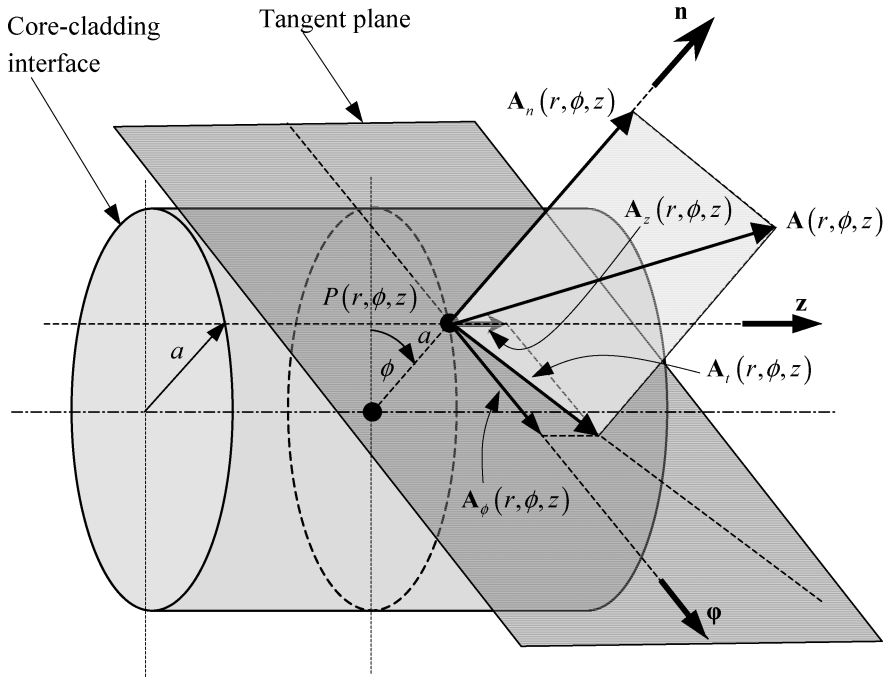

Figure 7.13 Geometrical representation of the cylindrical core–cladding interface for the optical fiber with a circular cross-section. The generic vector field $\mathbf{A} \equiv \mathbf{E}$ or $\mathbf{H}$ decomposes into the normal and the tangent component according to the cylindrical reference system. For every point P(r, ϕ, z) in the fiber cross-section, the cylindrical reference system represents the vector field as $\mathbf{A} = \mathbf{A}_r + \mathbf{A}_\phi + \mathbf{A}_z$

giving

$$\begin{pmatrix} H_{1r} = H_{2r} \\ H_{1\phi} = H_{2\phi} \\ H_{1z} = H_{2z} \end{pmatrix} \quad \begin{pmatrix} n_1^2 E_{1,r} = n_2^2 E_{2,r} \\ E_{1\phi} = E_{2\phi} \\ E_{1\phi} = E_{2\phi} \end{pmatrix} \tag{7.99}$$

The boundary condition for the step-index fiber in condition (7.99) can be conveniently simplified further by applying the paraxial approximation (7.72). Setting $n_1 \cong n_2$, condition (7.99) assumes the following easiest and symmetrical form:

$$\begin{pmatrix} H_{1r} = H_{2r} \\ H_{1\phi} = H_{2\phi} \\ H_{1z} = H_{2z} \end{pmatrix} \quad \begin{pmatrix} E_{1,r} = E_{2,r} \\ E_{1\phi} = E_{2\phi} \\ E_{1\phi} = E_{2\phi} \end{pmatrix} \tag{7.100}$$

Every component of the electric and magnetic fields must be continuous across the core–cladding interface.

In the following steps, the solution procedure is summarized of the boundary condition problem for the step-index fiber, as derived so far:

1. The electromagnetic field is represented using Cartesian components in both the core and the cladding regions.
2. Each field component is expressed in the cylindrical polar coordinate system in both the core and the cladding regions in terms of the corresponding Cartesian components by means of the

following general transformations:

$$\mathbf{A} = \begin{pmatrix} \mathbf{E} \\ \mathbf{H} \end{pmatrix} \Rightarrow \begin{cases} \mathbf{A}_r(r,\phi,z) = +\mathbf{A}_x(r,\phi,z)\cos\phi + \mathbf{A}_y(r,\phi,z)\sin\phi \\ \mathbf{A}_\phi(r,\phi,z) = -\mathbf{A}_x(r,\phi,z)\sin\phi + \mathbf{A}_y(r,\phi,z)\cos\phi \\ \mathbf{A}_z(r,\phi,z) = \mathbf{A}_z(r,\phi,z) \end{cases} \tag{7.101}$$

3. Assuming the weakly guiding approximation, or paraxial approximation, the boundary conditions for the electromagnetic field are given by Equation (7.100).
4. According to the boundary conditions, the twelve electric and magnetic field components (six in the core and six in the cladding) must be equal at the radial coordinate $r = a$, resulting in an homogeneous linear system of six equations into four unknowns, the coefficients A, B, C and D.
5. Paraxial approximation adds two more equations between the transversal component of the magnetic and electric fields, leading in conclusion to the homogeneous linear system of four independent equations in four unknowns, the coefficients A, B, C and D.
6. A homogeneous linear system of four independent equations in four unknowns gives a nontrivial solution if and only if the system determinant is null.

7.2.6 Mode Classification

The condition for having a nontrivial solution at point (6) leads directly to the formulation of the following eigenvalue equation for the step-index optical fiber, under the paraxial approximation:

$$\frac{J_\nu'(u)}{uJ_\nu(u)} + \frac{K_\nu'(w)}{wK_\nu(w)} = \pm\nu\left(\frac{1}{w^2} + \frac{1}{u^2}\right) \tag{7.102}$$

The general form of the eigenvalue equation just derived is the same for all bound modes, according to the general field solutions (7.55) and (7.56). It should be recalled that the normalized frequencies in the core and in the cladding, u and w respectively, have the expressions in (7.48) and (7.49), given again here for convenience:

$$u \equiv a\kappa = a\sqrt{n_1^2k^2 - \beta^2} \Rightarrow u \in N$$

$$w \equiv a\gamma = a\sqrt{\beta^2 - n_2^2k^2} \Rightarrow w \in N$$

Which is the unknown in the eigenvalue equation (7.102)? The fiber core radius a and the refractive indices in the core n_1 and in the cladding n_2 are fixed and, of course, it is assumed to be operating at a single optical wavelength λ. Once the azimuth mode number ν is fixed, due to the smoothed oscillatory behavior of the Bessel function of first kind $J_\nu(u)$, a finite number of solutions (even zero solutions) of the eigenvalue equation (7.102) is expected. The unknown variable in the eigenvalue equation is the propagation constant β. Once the azimuth mode number ν is fixed, the corresponding eigensolutions of the propagation constant will be labeled with a first suffix ν and a second suffix μ in order to identify all the subsequent values: $\beta_{\nu\mu}$. Using this labeling, the normalized frequencies in the core and in the cladding assume the following forms:

$$u_{\nu\mu} \equiv a\kappa_{\nu\mu} = a\sqrt{n_1^2k^2 - \beta_{\nu\mu}^2} \tag{7.103}$$

$$w_{\nu\mu} \equiv a\gamma_{\nu\mu} = a\sqrt{\beta_{\nu\mu}^2 - n_2^2k^2} \tag{7.104}$$

As expected from Equation (7.51), the sum of the square of the normalized frequencies in the core and in the cladding is invariant for all fiber modes, it does not depend on any modal index and it takes the meaning of the fiber invariant V or normalized frequency V:

$$V \equiv \sqrt{u_{\nu\mu}^2 + w_{\nu\mu}^2} = 2\pi\frac{a}{\lambda}\sqrt{n_1^2 - n_2^2} \tag{7.105}$$

The eigenvalue equation (7.102) has several interesting features, but a detailed analysis is beyond the scope of this book. The discussion is therefore limited in the following to only some of the relevant conclusions. A more detailed analysis will be found in a planned book on optical fiber theory.

For every value of the azimuth mode number $\nu = 0, 1, 2, \ldots$, the solutions of the eigenvalue equation are ordered according to the radial mode number $\mu = 1, 2, \ldots, M_\nu$. The value of M_ν gives the maximum number of eigensolutions for the given azimuth mode number ν. For every allowed pair of mode numbers (ν, μ) the solution of the eigenvalue equation relies on the pair of corresponding normalized frequencies $(u_{\nu\mu}, w_{\nu\mu})$. In order to derive the value of the corresponding propagation constant Equations (7.103) and (7.104) need do be solved for the propagation constant $\beta_{\nu\mu}$. To this purpose, Equation (7.103) is divided by Equation (7.104) and then solved for $\beta_{\nu\mu}$:

$$\beta_{\nu\mu} = k\sqrt{\frac{u_{\nu\mu}^2 n_2^2 + w_{\nu\mu}^2 n_1^2}{u_{\nu\mu}^2 + w_{\nu\mu}^2}} \tag{7.106}$$

Using Equation (7.105), the following expressions of the propagation constant are finally obtained in terms of the two normalized eigensolutions in the core and in the cladding:

$$\beta_{\nu\mu} = \frac{k}{V}\sqrt{u_{\nu\mu}^2 n_2^2 + w_{\nu\mu}^2 n_1^2} = \frac{1}{a}\sqrt{\frac{u_{\nu\mu}^2 n_2^2 + w_{\nu\mu}^2 n_1^2}{n_1^2 - n_2^2}} \tag{7.107}$$

Each fiber mode is therefore characterized by a pair of mode numbers (ν, μ) and each pair of mode numbers identifies a value of the propagation constant $\beta_{\nu\mu}$. It is clear from the mathematical structure of the modal solution in Equation (7.55) and (7.56) that the azimuth mode number identifies the order of the Bessel functions in the core and in the cladding.

The radial mode number has a different meaning. The radial mode number acts as a scaling factor for the radial dependence. This concept is important and can be clearly understood by looking at the normalized frequency expressions in both the core and in the cladding. The argument of each Bessel function is simply the product of the corresponding normalized frequency and the geometrical radial coordinate. This assigns the meaning of the scale factor to the radial mode number μ.

All fiber modes characterized by the same azimuth mode number ν have therefore the same order of Bessel functions. The second fundamental implication of the radial mode number is the different value generally assigned to the propagation constant. This means that, in general, every fiber mode has a proper propagation constant. However, the inverse statement is not true in general. The same value of the propagation constant can be common to different mode structures. It will be seen later that, for some different pairs of mode numbers, the eigenvalue equation has the same solution, meaning the same propagation constant. This characteristic leads to the important concept of mode degeneracy. Different mode structures can be grouped in order to have the same propagation constant. This leads to the concept of the mode group: all modes belonging to the same group have the same propagation characteristics.

Last but not least, the eigenvalue equation exhibits wavelength cut-off properties for all modes except in the case of the mode HE_{11}, which assumes the meaning of a fundamental fiber mode. The fundamental fiber mode HE_{11} has no wavelength cut-off and can be sustained by the optical fiber at every wavelength, leading to the single-mode fiber propagation regime.

In the following sections, the conditions on the eigenvalue equation for generating the four kinds of allowed fiber modes, namely TE, TM, HE and EH modes, will be considered separately.

7.2.6.1 $TE_{0\mu}$ and $TM_{0\mu}$ Modes

It is known from previous analyses that setting $\nu = 0$ leads to TE or TM modes, depending on the angular function that was chosen. This is the first indication of the existence of mode degeneracy. In

fact, both TE and TM modes satisfy the same eigenvalue equation, so necessarily must have the same propagation constant for every fixed radial mode number. Substituting $\nu = 0$ in Equation (7.102) gives the eigenvalue equation for TE and TM modes:

$$\frac{J_0'(u)}{uJ_0(u)} + \frac{K_0'(w)}{wK_0(w)} = 0 \tag{7.108}$$

Using the Bessel identities (7.58d) and (7.58h),

$$\left.\begin{array}{ll} \mathrm{TE}_{0\mu} \\ \mathrm{TM}_{0\mu} \end{array} \quad \begin{array}{l} \dfrac{u_{0\mu}J_0(u_{0\mu})}{J_1(u_{0\mu})} + \dfrac{w_{0\mu}K_0(w_{0\mu})}{K_1(w_{0\mu})} = 0 \\ u_{0\mu} = a\kappa_{0\mu} = a\sqrt{n_1^2k^2 - \beta_{0\mu}^2} \\ w_{0\mu} = a\gamma_{0\mu} = a\sqrt{\beta_{0\mu}^2 - n_2^2k^2} \end{array} \right\} \Rightarrow \underset{(\mu=1,2,\ldots,M_0)}{\beta_{0\mu}} \tag{7.109}$$

This equation needs to be solved numerically. The physical parameters involved are the fiber core radius a, the refractive indices n_1, n_2 and the wavelength λ. In general, several solutions are available, which can be ordered according to the increasing value of the propagation constant using the radial mode number $\mu : \beta_{01} < \beta_{02} < \beta_{03} < \cdots < \beta_{0M_0}$. The value M_0 gives the number of eigensolutions available for the selected fiber parameters and azimuth mode number $\nu = 0$.

In the following a numerical solution of the eigenvalue equation (7.109) is considered using Matlab® 7.0.4, SP2. The fiber parameters are

$$a = 25\,\mu\mathrm{m}, \qquad \lambda = 1310\,\mathrm{nm}, \qquad n_1 = 1.480, \qquad n_2 = 1.465$$

Using Equation (7.105) gives $V = 25.2021$. Table 7.1 reports the numerically computed normalized frequencies in the core and in the cladding and the corresponding propagation constants $\beta_{0\mu}$, assuming $\nu = 0$.

Figure 7.14 shows the numerical solution of the eigenvalue equation (7.109) for the considered case, using the graphical intersection method. Both curves are plotted as functions of the propagation constant. Vertically shaped curves represent the first member in Equation (7.109), while the horizontally shaped curves represent the second member of the same eigenvalue equation.

The propagation constant is expressed in $\mu\mathrm{m}^{-1} = 10^6/\mathrm{m}$. In it quite interesting at this point to compute the modal delay per unit length of each TE and TM modes. To this purpose, the modal

Table 7.1 Computed eigenvalues for $\mathrm{TE}_{0\mu}$ and $\mathrm{TM}_{0\mu}$ modes of the step-index fiber with $a = 25\,\mu\mathrm{m}$, $\lambda = 1310\,\mathrm{nm}$, $n_1 = 1.480$, $n_2 = 1.465$. The total number of allowed modes with $\nu = 0$ is $M_0 = 8$

$\mathrm{TE}_{0\mu}$, $\mathrm{TM}_{0\mu}$: μ	$u_{0\mu}$	$w_{0\mu}$	$\beta_{0\mu}\,(\mu\mathrm{m}^{-1})$
1	24.5605	5.6504	7.0302
2	21.7216	12.7797	7.0452
3	18.7756	16.8114	7.0587
4	15.7935	19.6395	7.0704
5	12.7915	21.7146	7.0801
6	9.7752	23.2291	7.0878
7	6.7447	24.2828	7.0934
8	3.6850	24.9312	7.0970

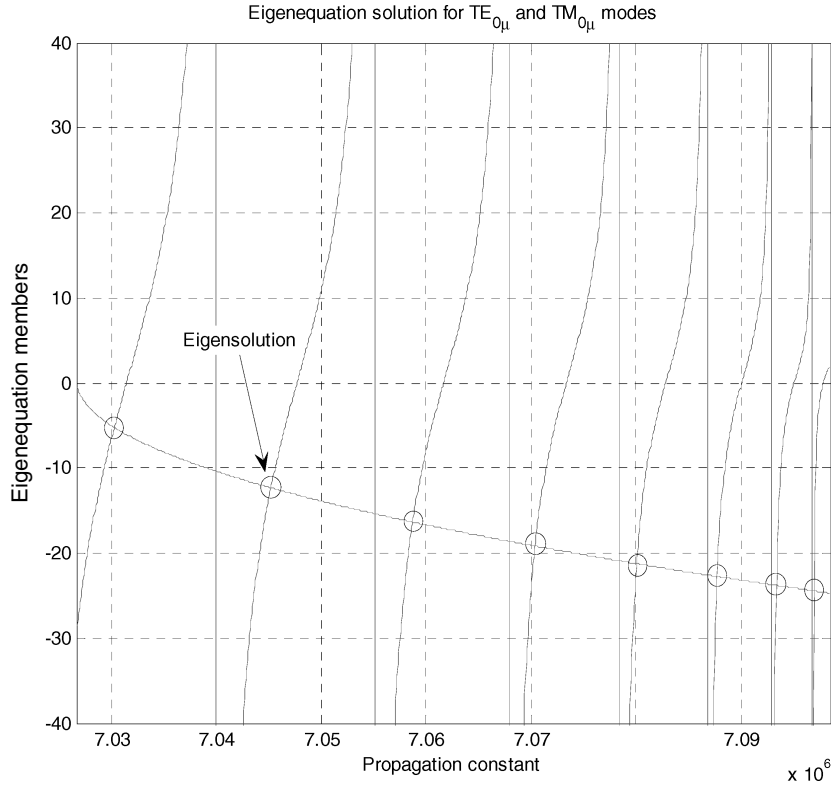

Figure 7.14 Graphical representation of the solutions of the eigenvalue equation for $TE_{0\mu}$ and $TM_{0\mu}$ of the step-index fiber with $a = 25\,\mu\text{m}$, $\lambda = 1310\,\text{nm}$, $n_1 = 1.480$, $n_2 = 1.465$. The total number of modes with $\nu = 0$ is given by the number of intersections, so $M_0 = 8$

delay per unit length $\tau_{\nu\mu}(\lambda)$ of the mode (ν, μ) is given by the ratio of the mode propagation constant $\beta_{\nu\mu}$ with the angular frequency $\omega = 2\pi c/\lambda$:

$$\tau_{\nu\mu}(\lambda) = \frac{\lambda}{2\pi c}\beta_{\nu\mu} \tag{7.110}$$

Substituting the values of the propagation constant reported in Table 7.1 and assuming $\lambda = 1310\,\text{nm}$ gives the modal delays per unit length of the computed eight modes shown in Table 7.2.

As expected from the delay per unit length of the plane wave propagating in the homogeneous medium with a refractive index $n = 1.5$, the modal delay of the selected modes in the step-index optical fiber is of the order of $5\,\mu\text{s/km}$. It is interesting to compare the incremental delay between any two adjacent modes. This parameter is directly related to the differential mode delay introduced in previous chapters. From the data computed in Table 7.2, it can be concluded that the incremental delay decreases at higher-order modes. It is noteworthy to compare, for example, the incremental delay between $\tau_{02} - \tau_{01} = 10.387\,\text{ns/km}$ and $\tau_{08} - \tau_{07} = 2.5023\,\text{ns/km}$.

Table 7.2 Computed mode delay for $TE_{0\mu}$ and $TM_{0\mu}$ modes of the step-index fiber with $a = 25\,\mu m$, $\lambda = 1310\,nm$, $n_1 = 1.480$, $n_2 = 1.465$. The third column gives the incremental variation of the mode delay between two subsequent supported modes. The incremental delay is defined as $\tau_{0\mu} - \tau_{0\mu-1}$ and it is expressed in ns/km

μ	$\tau_{0\mu}$ (μs/km)	$\tau_{0\mu} - \tau_{0\mu-1}$ (ns/km)
1	4.889	
2	4.900	10.387
3	4.909	9.4122
4	4.917	8.1184
5	4.924	6.7479
6	4.929	5.3458
7	4.933	3.9282
8	4.936	2.5023

7.2.6.2 $EH_{\nu\mu}$ Modes

If a nonzero value of the azimuth mode number is assumed, $\nu \geq 1$, in the eigenvalue equation (7.102) account has to be taken of the sign of the second member. According to the sign chosen, this leads to two different eigenvalue equations and consequently to two different sets of modal solution, namely $EH_{\nu\mu}$ and $HE_{\nu\mu}$ modes. If the positive sign is considered in Equation (7.102) the $EH_{\nu\mu}$ modal solution is referred to, while the $HE_{\nu\mu}$ modal solution is associated with the negative sign. In this section, only $EH_{\nu\mu}$ modes will be considered. Using the Bessel function recurrence relations, after some manipulations the following form of the eigenvalue equation for the $EH_{\nu\mu}$ modes is found:

$$\left.\begin{array}{ll} \mathrm{EH}_{\nu\mu} & \dfrac{u_{\nu\mu}J_{\nu}(u_{\nu\mu})}{J_{\nu+1}(u_{\nu\mu})} + \dfrac{w_{\nu\mu}K_{\nu}(w_{\nu\mu})}{K_{\nu+1}(w_{\nu\mu})} = 0 \\ & u_{\nu\mu} = a\kappa_{\nu\mu} = a\sqrt{n_1^2k^2 - \beta_{\nu\mu}^2} \\ & w_{\nu\mu} = a\gamma_{\nu\mu} = a\sqrt{\beta_{\nu\mu}^2 - n_2^2k^2} \end{array}\right\} \Rightarrow \underset{\substack{\nu\geq 1 \\ \mu=1,2,\ldots,M_{\nu}}}{\beta_{\nu\mu}} \tag{7.111}$$

For every fixed value of the azimuth mode number $\nu \geq 1$, several eigensolutions of Equation (7.111) are available and can be ordered according to the increasing value of the propagation constant using the radial mode number $\mu = 1, 2, \ldots, M_{\nu}$, $\beta_{\nu 1} < \beta_{\nu 2} < \beta_{\nu 3} < \cdots < \beta_{\nu M_{\nu}}$. In this case, the value M_{ν} gives the number of eigensolutions available for the selected fiber parameters and azimuth mode number $\nu \geq 1$.

In the following, a numerical solution to the eigenvalue equation (7.111) using Matlab® 7.0.4, SP2 is considered. The fiber parameters are the same as those used for the previous case of TE and TM modes:

$$a = 25\,\mu m, \qquad \lambda = 1310\,nm, \qquad n_1 = 1.480, \qquad n_2 = 1.465$$

The normalized frequency V of the fiber is computed using Equation (7.105), which gives $V = 25.2021$. Table 7.3 reports the numerically computed propagation constants $\beta_{1\mu}, \beta_{2\mu}, \beta_{3\mu}, \beta_{4\mu}, \beta_{5\mu}$, assuming $\nu = 1, 2, 3, 4, 5$ respectively. For every value of the azimuth mode number ν, the number of eigensolutions is not constant but decreases as ν increases. From Table 7.3 it can be seen that

Table 7.3 Computed propagation constants $\beta_{\nu\mu}$ for $EH_{\nu\mu}$ modes of the step-index fiber with $a = 25\,\mu m$, $\lambda = 1310\,nm$, $n_1 = 1.480$, $n_2 = 1.465$. The total number of allowed modes decreases with increasing value of the azimuth mode number

$EH_{\nu\mu}$: μ	$\nu = 1$ $\beta_{1\mu}(\mu m^{-1})$	$\nu = 2$ $\beta_{2\mu}(\mu m^{-1})$	$\nu = 3$ $\beta_{3\mu}(\mu m^{-1})$	$\nu = 4$ $\beta_{4\mu}(\mu m^{-1})$	$\nu = 5$ $\beta_{5\mu}(\mu m^{-1})$
1	7.0381	7.0309	7.0392	7.0324	7.0412
2	7.0525	7.0460	7.0537	7.0476	7.0558
3	7.0651	7.0595	7.0664	7.0612	7.0685
4	7.0758	7.0712	7.0771	7.0729	7.0793
5	7.0845	7.0809	7.0858	7.0827	7.0883
6	7.0912	7.0886	7.0926	7.0905	
7	7.0958	7.0943			

for $\nu = 1$ and $\nu = 2$ the number of eigensolutions is $M_1 = M_2 = 7$, while for $\nu = 3$ and $\nu = 4$ the number of eigensolutions reduces to $M_3 = M_4 = 6$ and for $\nu = 5$ only five modes, $M_5 = 5$, are allowable. Figures 7.15 and 7.16 show the numerical solution of the eigenvalue equation (7.111) for the considered case, using the same graphical intersection method introduced briefly in the previous section. In this case, however, the eigenvalue equation depends on the azimuth mode number ν. Accordingly, for each azimuth mode number, the corresponding graphical solution is shown with all the allowable intersections.

Figure 7.15 and 7.16 show the graphical solution for the optical fiber considered here in the cases of $\nu = 1$ and $\nu = 5$. Similar plots can be easily generated for every other azimuth number.

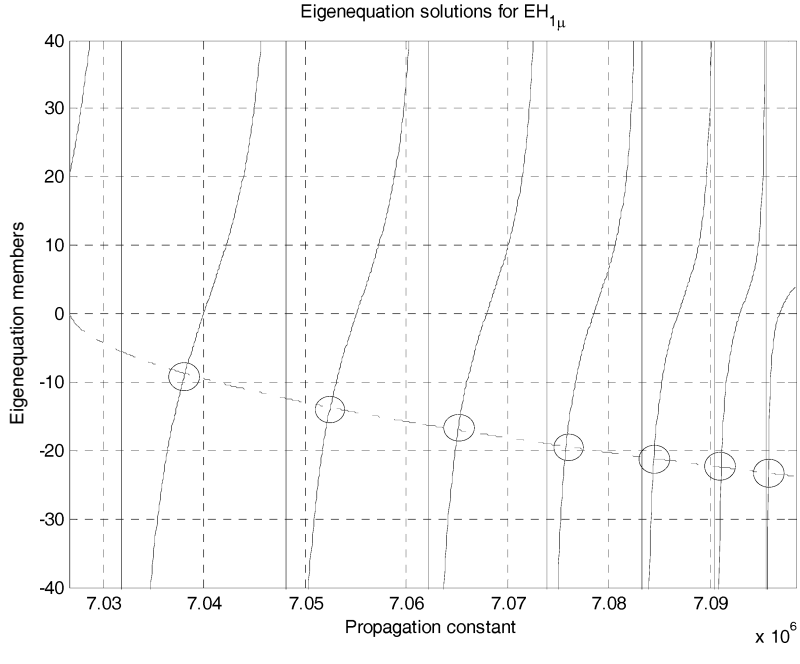

Figure 7.15 Graphical representation of the solutions of the eigenvalue equation (7.111) for $EH_{1\mu}$ of the step-index fiber with $a = 25\,\mu m$, $\lambda = 1310\,nm$, $n_1 = 1.480$, $n_2 = 1.465$. The total number of modes with $\nu = 1$ is given by the number of intersections, so $M_1 = 7$

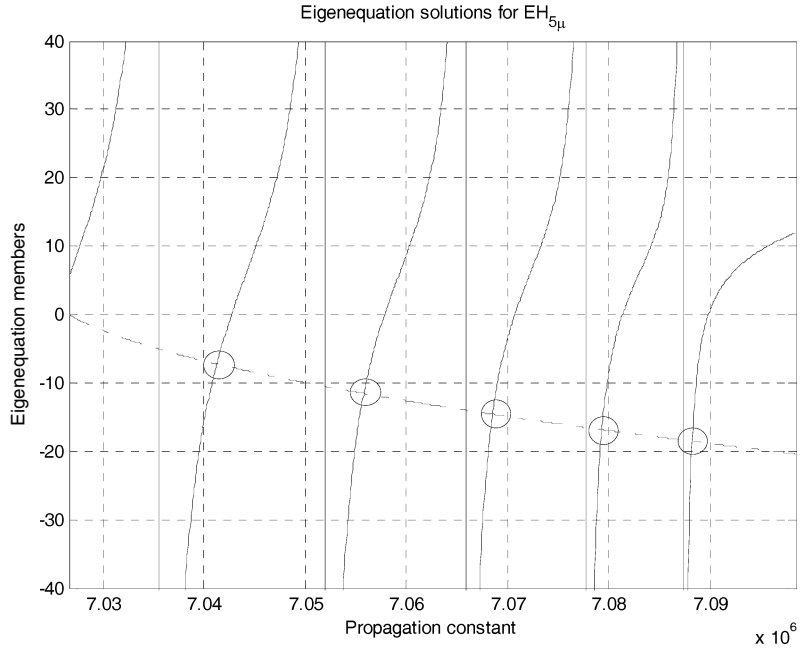

Figure 7.16 Graphical representation of the solutions of the eigenvalue equation (7.111) for $\mathrm{EH}_{5\mu}$ of the step-index fiber with $a = 25\,\mu\mathrm{m}$, $\lambda = 1310\,\mathrm{nm}$, $n_1 = 1.480$, $n_2 = 1.465$. The total number of modes with $\nu = 5$ is given by the number of intersections, so $M_1 = 5$

It is important to remark, however, that if the azimuth mode number exceeds the cut-off value, no more intersections would be allowable, leading to no more mode solutions for that mode family.

Figure 7.17 shows the situation close to the mode cut-off. In particular, for the specific fiber example the mode $\mathrm{EH}_{19,1}$ is still supported but the successive value of the azimuth number leads to no mode solution of the eigenvalue equation and therefore the mode $\mathrm{EH}_{20,1}$ cannot be sustained by the fiber.

Comparing the solution of the eigenvalue equation for the $\mathrm{EH}_{\nu\mu}$ modes with the one used for the $\mathrm{TE}_{0\mu}$ and $\mathrm{TM}_{0\mu}$ modes a close similarity is found. If $\nu = 0$ is taken in the eigenvalue equation (7.111), the eigenvalue equation (7.109) for the $\mathrm{TE}_{0\mu}$ and $\mathrm{TM}_{0\mu}$ modes is exactly the same. This identity is not accidental but instead reflects a more general property of the degenerate mode solutions of the ideal unperturbed optical fiber under a weakly guiding approximation. The next section deals with the third mode family of the optical fiber, namely modes $\mathrm{HE}_{\nu\mu}$.

7.2.6.3 $\mathrm{HE}_{\nu\mu}$ Modes

If the negative sign in the general eigenvalue equation (7.102) is considered, the eigenvalue equation for the $\mathrm{HE}_{\nu\mu}$ modes is obtained. After using recurrence relations for the Bessel function, the following form is found:

$$\left.\begin{aligned} \mathrm{HE}_{\nu\mu} \quad & \frac{u_{\nu\mu} J_\nu(u_{\nu\mu})}{J_{\nu-1}(u_{\nu\mu})} - \frac{w_{\nu\mu} K_\nu(w_{\nu\mu})}{K_{\nu-1}(w_{\nu\mu})} = 0 \\ & u_{\nu\mu} = a\kappa_{\nu\mu} = a\sqrt{n_1^2 k^2 - \beta_{\nu\mu}^2} \\ & w_{\nu\mu} = a\gamma_{\nu\mu} = a\sqrt{\beta_{\nu\mu}^2 - n_2^2 k^2} \end{aligned}\right\} \Rightarrow \underset{\left(\substack{\nu\geq 1 \\ \mu=1,2,\ldots,M_\nu}\right)}{\beta_{\nu\mu}} \tag{7.112}$$

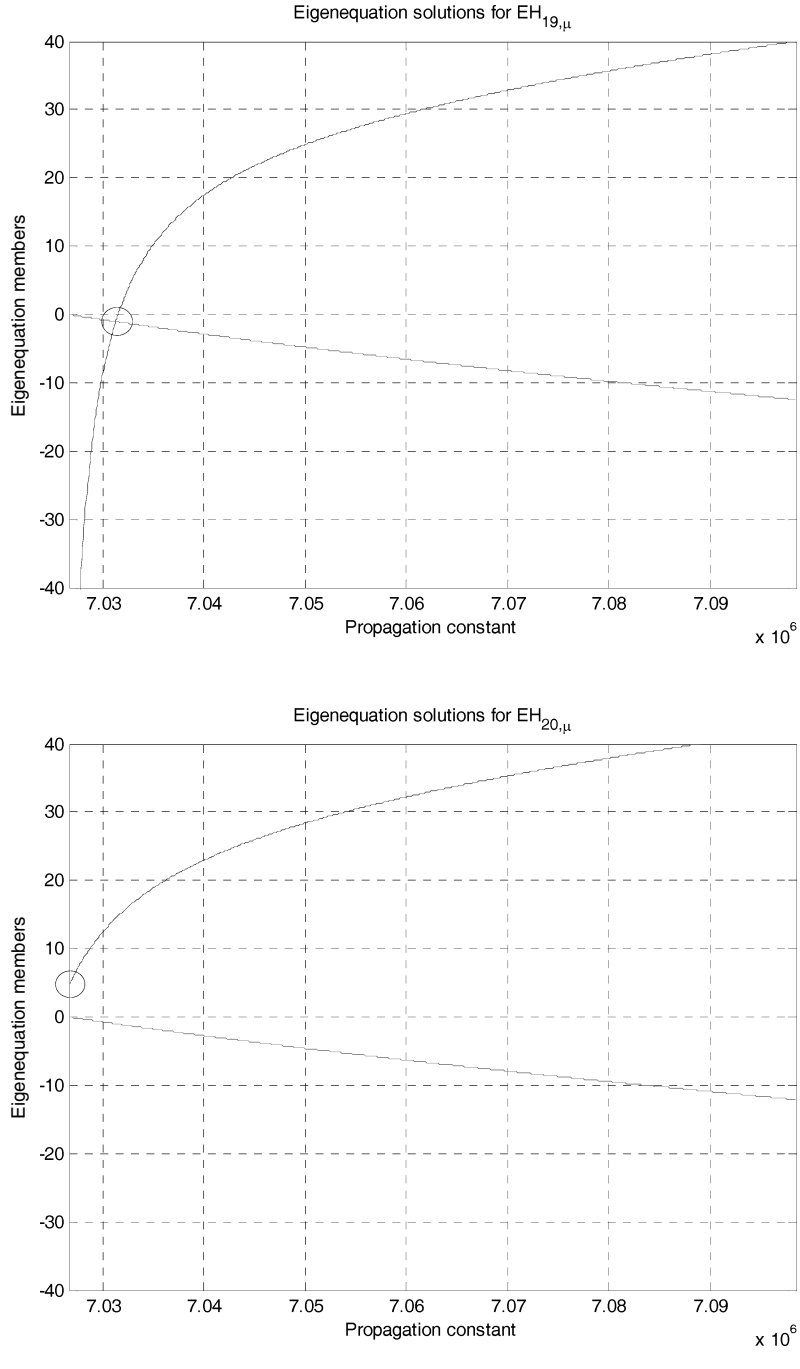

Figure 7.17 Graphical representation of the solutions of the eigenvalue equation (7.111) for $EH_{19\mu}$ (top) and $EH_{20\mu}$ (bottom) of the step-index fiber with $a = 25\,\mu\text{m}$, $\lambda = 1310\,\text{nm}$, $n_1 = 1.480$, $n_2 = 1.465$. Assuming $\nu = 19$ only one mode is supported, the mode $EH_{19\mu}$, while in the case $\nu = 20$ the mode $EH_{20\mu}$ will never be sustained by this fiber

Table 7.4 Computed propagation constants $\beta_{\nu\mu}$ for $HE_{\nu\mu}$ modes of the step-index fiber with $a = 25\,\mu m$, $\lambda = 1310\,nm$, $n_1 = 1.480$, $n_2 = 1.465$. The total number of allowed modes decreases with increasing value of the azimuth mode number

$HE_{\nu\mu}$: μ	$\nu = 1$ $\beta_{1\mu}(\mu m^{-1})$	$\nu = 2$ $\beta_{2\mu}(\mu m^{-1})$	$\nu = 3$ $\beta_{3\mu}(\mu m^{-1})$	$\nu = 4$ $\beta_{4\mu}(\mu m^{-1})$	$\nu = 5$ $\beta_{5\mu}(\mu m^{-1})$
1	7.0377	7.0302	7.0381	7.0309	7.0392
2	7.0521	7.0452	7.0525	7.0460	7.0537
3	7.0647	7.0587	7.0651	7.0595	7.0664
4	7.0754	7.0704	7.0758	7.0712	7.0771
5	7.0841	7.0801	7.0845	7.0809	7.0858
6	7.0908	7.0878	7.0912	7.0886	7.0926
7	7.0954	7.0934	7.0958	7.0943	
8	7.0980	7.0970			

It is remarkable that setting $\nu = 0$ in the eigenvalue equation (7.112) for the $HE_{\nu\mu}$ modes gives the eigenvalue equation for $TE_{0\mu}$ and $TM_{0\mu}$ modes derived previously in Equation (7.109). To show this, it is sufficient to use the recursive relations between the Bessel functions of integer order:

$$J_{-\nu}(z) = (-1)^{\nu} J_{\nu}(z), \qquad K_{-\nu}(z) = K_{\nu}(z) \tag{7.113}$$

For every fixed value of the azimuth mode number $\nu \geq 1$, the eigenvalue equation (7.112) for $HE_{\nu\mu}$ modes behaves like the other two considered cases, giving several values of the propagation constant. This gives the propagation constants using the radial mode number $\mu = 1, 2, \ldots, M_{\nu}, \beta_{\nu 1} < \beta_{\nu 2} < \beta_{\nu 3} < \cdots < \beta_{\nu M_{\nu}}$. The value M_{ν} is the number of eigensolutions available for the selected fiber parameters and azimuth mode number $\nu \geq 1$.

Table 7.4 reports the computed propagation constants $\beta_{1\mu}, \beta_{2\mu}, \beta_{3\mu}, \beta_{4\mu}, \beta_{5\mu}$ for the $HE_{\nu\mu}$ modes, assuming $\nu = 1, 2, 3, 4, 5$ respectively. Each azimuth mode number allows several eigensolutions, as explained above. The fiber parameters are the same as those used for the previous cases, with the normalized frequency $V = 25.2021$:

$$a = 25\,\mu m, \qquad \lambda = 1310\,nm, \qquad n_1 = 1.480, \qquad n_2 = 1.465$$

Figures 7.18 and 7.19 show the numerical solution of the eigenvalue equation (7.112) for the optical fiber being considered, for $\nu = 1$ and $\nu = 5$ respectively. The numerical solution uses the same graphical intersection method as adopted previously. Accordingly, for each azimuth mode number $\nu \geq 1$, the corresponding graphical solutions of Equation (7.112) are given using all the allowable intersections. The opposite sign in the eigenvalue equations for $HE_{\nu\mu}$ modes with respect to $EH_{\nu\mu}$ reflects the opposite curvature of the plot of the second member in Equation (7.112). In this case the number of allowable $HE_{1\mu}$ modes exceeds the number of $EH_{1\mu}$ modes by one unit, $M_1^{HE} = 8$. The suffix HE has been used to distinguish between $M_1^{EH} = 7$. Similar behavior is reported in the Figure 7.19 for the case $\nu = 5$, with only six solutions, $M_5^{HE} = 6$.

7.2.6.4 The Mode Groups

The eigenvalues shown in Table 7.4 for $HE_{\nu\mu}$ modes have very peculiar relationships with the eigenvalues of $EH_{\nu\mu}$ modes presented in Table 7.3. In order to distinguish between $HE_{\nu\mu}$ and $EH_{\nu\mu}$ propagation constants, the suffix with the modal notation TE, TM, EH, HE is appended, for the moment, to the corresponding propagation constant:

$\beta_{\nu\mu}^{EH}$: propagation constant of the $EH_{\nu\mu}$ mode

$\beta_{\nu\mu}^{HE}$: propagation constant of the $HE_{\nu\mu}$ mode

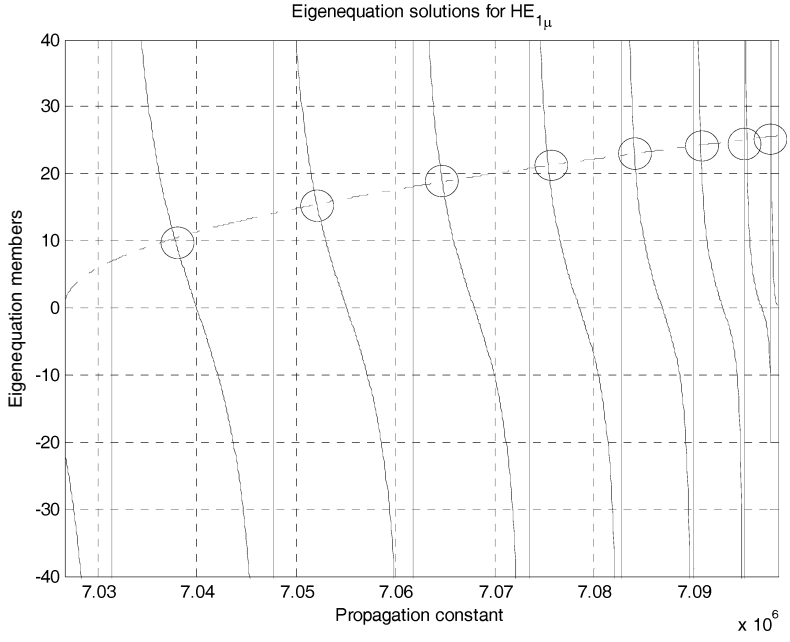

Figure 7.18 Graphical representation of the solutions of the eigenvalue equation (7.112) for $HE_{1\mu}$ of the step-index fiber with $a = 25\,\mu\text{m}$, $\lambda = 1310\,\text{nm}$, $n_1 = 1.480$, $n_2 = 1.465$. The total number of modes with $v = 1$ is given by the number of intersections, so $M_1 = 8$

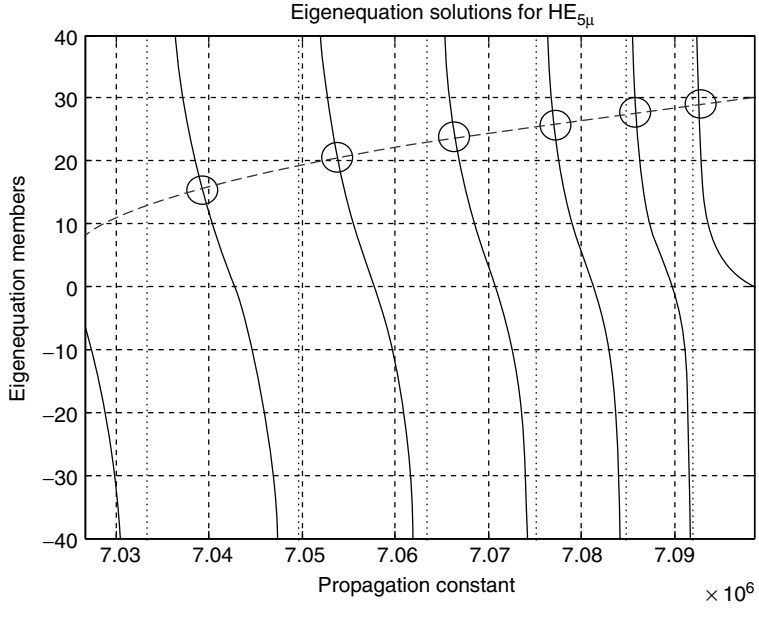

Figure 7.19 Graphical representation of the solutions of the eigenvalue equation (7.112) for $HE_{5\mu}$ of the step-index fiber with $a = 25\,\mu\text{m}$, $\lambda = 1310\,\text{nm}$, $n_1 = 1.480$, $n_2 = 1.465$. The total number of modes with $v = 5$ is given by the number of intersections, so $M_1 = 6$

Comparing Table 7.3 with Table 7.4 it is easily concluded that

$$\begin{aligned}\beta_{1\mu}^{\mathrm{EH}} &\equiv \beta_{3\mu}^{\mathrm{HE}} \\ \beta_{2\mu}^{\mathrm{EH}} &\equiv \beta_{4\mu}^{\mathrm{HE}} \\ \beta_{3\mu}^{\mathrm{EH}} &\equiv \beta_{5\mu}^{\mathrm{HE}}\end{aligned} \tag{7.114}$$

This property of the propagation constants of the step-index optical fiber is not a coincidence. It reflects recursive properties of the Bessel functions under a weakly guiding approximation, leading to the degenerate mode set. From a physical point of view, the coincidence of the propagation constants means that all dispersion relationships of the corresponding modes are the same. This makes all modes with the same propagation constant undistinguishable in terms of their propagation characteristics. To this purpose, it is usual to collect all degenerate modes within the same mode group. The obvious generalization of the property (7.114) leads to the following propagation constant identity:

$$\beta_{\nu\mu}^{\mathrm{EH}} \equiv \beta_{\nu+2,\mu}^{\mathrm{HE}} \tag{7.115}$$

To proceed further with this interesting degeneration property, $\mathrm{TE}_{0\mu}$ and $\mathrm{TM}_{0\mu}$ eigenvalues in Table 7.1 are compared with the eigenvalues of modes $\mathrm{HE}_{\nu\mu}$ reported in Table 7.4. Again, it is found that $\mathrm{TE}_{0\mu}$ and $\mathrm{TM}_{0\mu}$ modes have the same propagation constants as $\mathrm{HE}_{2\mu}$ modes. Therefore,

$$\beta_{0\mu}^{\mathrm{TE,TM}} \equiv \beta_{2\mu}^{\mathrm{HE}}$$

Without entering further into a mathematical description of the optical fiber eigenvalues properties, the following important conclusions can be outlined:

1. Assuming a weakly guiding approximation (otherwise stated as the paraxial approximation), the step-index optical fiber shows mode degeneracy: several modes have the same eigenvalues and hence the same propagation constant.
2. Accordingly, degenerate modes are grouped together into mode groups, each characterized by the unique propagation constant.
3. Mode degeneration occurs between the following two sets of modes:

$$\begin{aligned}&\mathrm{LP}_{1\mu} \equiv (\mathrm{TE}_{0\mu}, \mathrm{TM}_{0\mu}, \mathrm{HE}_{2\mu}) \\ &\mathrm{LP}_{l\mu} \equiv (\mathrm{EH}_{\nu\mu}, \mathrm{HE}_{\nu+2,\mu}), \quad \nu \geq 1, l = \nu + 1 \geq 2\end{aligned} \tag{7.116}$$

4. Mode groups are constituted by the following linearly polarized (LP) mode designation:

$$\begin{aligned}&\mathrm{LP}_{0\mu} \equiv (\mathrm{HE}_{1\mu}) \\ &\mathrm{LP}_{1\mu} \equiv (\mathrm{TE}_{0\mu}, \mathrm{TM}_{0\mu}, \mathrm{HE}_{2\mu}) \\ &\mathrm{LP}_{l\mu} \equiv (\mathrm{EH}_{\nu\mu}, \mathrm{HE}_{\nu+2,\mu}), \quad \nu \geq 1, l = \nu + 1 \geq 2\end{aligned} \tag{7.117}$$

5. The fiber mode $\mathrm{LP}_{01} \equiv \mathrm{HE}_{11}$ is the fundamental fiber mode and has the lowest designation order.

One fundamental result of the modal theory of the optical fiber is the capability of the fiber to support the fundamental mode $\mathrm{LP}_{01} \equiv \mathrm{HE}_{11}$ for every wavelength, refractive index height and core radius. In other words, the optical fiber supports at least the fundamental mode under every exciting condition. The fundamental mode, in fact, has no cut-off property. Once the fiber structure has been fixed, it is possible to show the propagation constant distribution for each mode versus the optical

wavelength. From that distribution, every individual mode shows a specific cut-off wavelength, above which the mode will never be sustained. This is true for all modes except the fundamental one, which has no cut-off wavelength.

Figures 7.20 and7.21 show a particular fiber structure designed to support single-mode operation above the cut-off wavelength $\lambda_{11} \cong 1560\,\text{nm}$ for the first higher-order mode group available, namely the mode group $LP_{11} \equiv (TE_{01}, TM_{01}, HE_{21})$. Figure 7.20 gives the graphical solution of the eigenvalues equation for the first-order modes, reporting the propagation constant at $\lambda = 850\,\text{nm}$, while Figure 7.21 shows the same situation but evaluated at $\lambda = 1550\,\text{nm}$, very close to the single-mode operation condition.

To conclude this section, the linearly polarized mode classification, known as the LP_{lm} classification, is derived from the individual mode classification using (ν, μ) indexing. Using the reported index transformations gives the following relationships between the individual mode and linearly

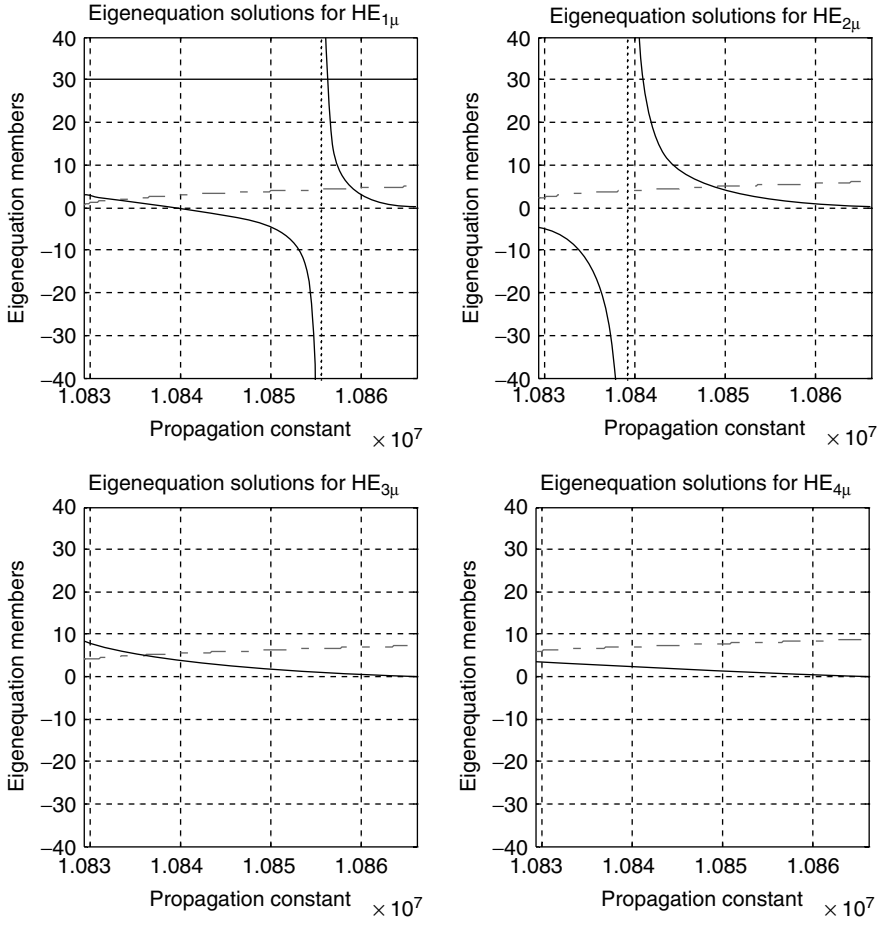

Figure 7.20 Eigenvalue equation solutions for four supported modes in the fiber defined by the following parameters: $a = 5\,\mu\text{m}$, $\lambda = 850\,\text{nm}$, $n_1 = 1.470$, $n_2 = 1.465$. All other higher-order modes are under cut-off conditions. The normalized frequency is $V = 4.4773$. The eigensolutions are represented by the intersection of the continuous lines with the dash–dot ones

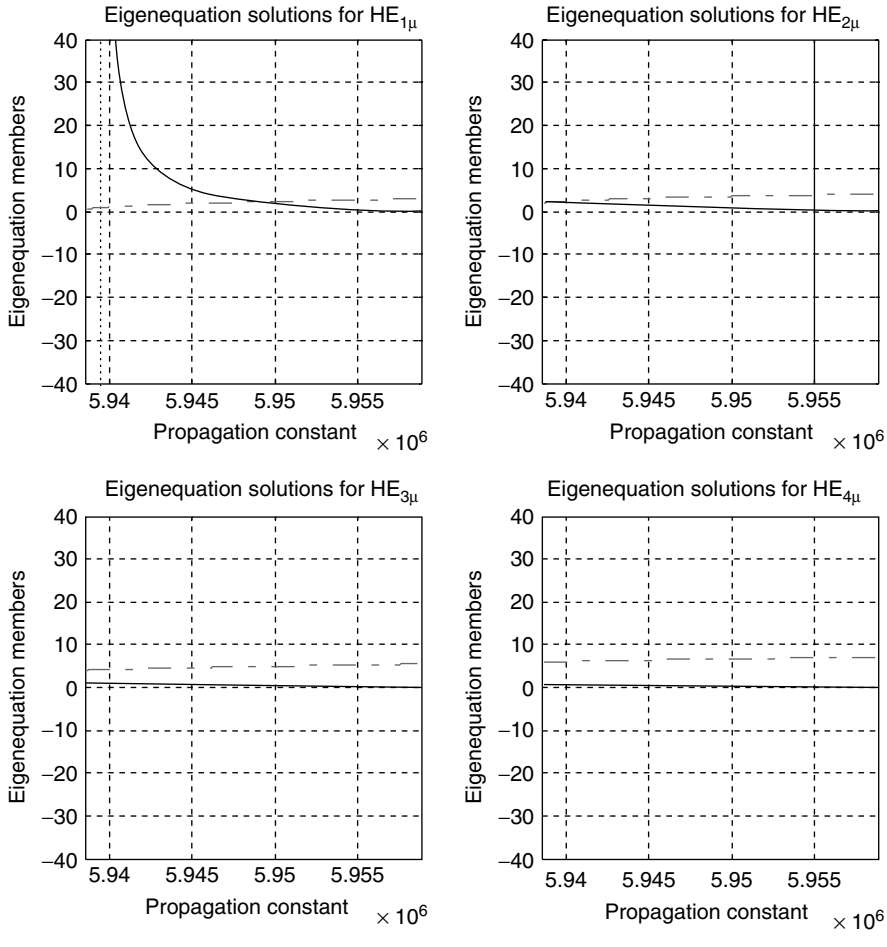

Figure 7.21 Eigenvalue equation solutions for four supported modes in the fiber defined by the following parameters: $a = 5\,\mu\text{m}$, $\lambda = 1550\,\text{nm}$, $n_1 = 1.470$, $n_2 = 1.465$. The existence of the eigenvalue solution is represented by the intersection between the two curves plotted. All other higher-order modes are under cut-off conditions. The normalized frequency is $V = 2.4553$

polarized mode classifications:

$$\begin{pmatrix} \text{TE}_{0\mu} \\ \text{TM}_{0\mu} \end{pmatrix} \longrightarrow \begin{pmatrix} l = \nu + 1 \\ m = \mu \\ \nu = 0 \end{pmatrix} \longrightarrow \begin{pmatrix} l = 1 \\ m \geq 1 \end{pmatrix} \longrightarrow \text{LP}_{1,m}$$

$$\text{EH}_{\nu\mu} \longrightarrow \begin{pmatrix} l = \nu + 1 \\ m = \mu \\ \nu \geq 1 \end{pmatrix} \longrightarrow \begin{pmatrix} l \geq 2 \\ m \geq 1 \end{pmatrix} \longrightarrow \text{LP}_{2,m}, \text{LP}_{3,m}, \text{LP}_{4,m}, \ldots, \text{LP}_{lm} \quad (7.118)$$

$$\text{HE}_{\nu\mu} \longrightarrow \begin{pmatrix} l = \nu - 1 \\ m = \mu \\ \nu \geq 1 \end{pmatrix} \longrightarrow \begin{pmatrix} l \geq 0 \\ m \geq 1 \end{pmatrix} \longrightarrow \text{LP}_{0,m}, \text{LP}_{1,m}, \text{LP}_{2,m}, \ldots, \text{LP}_{lm}$$

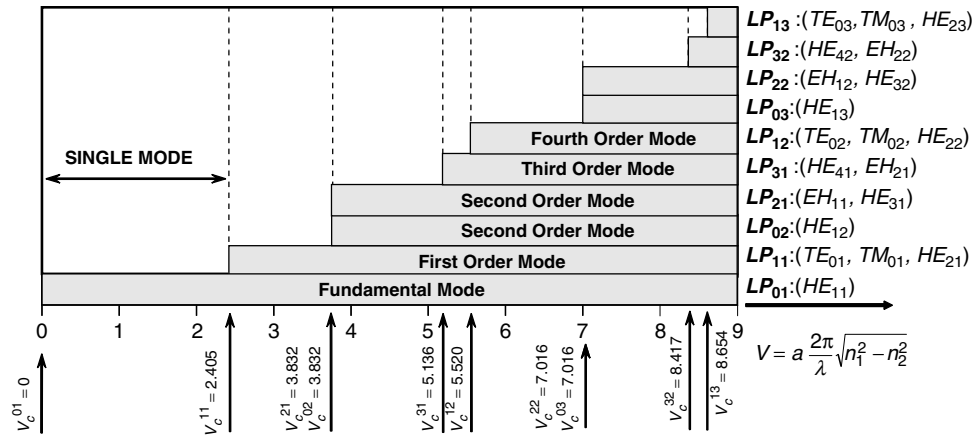

Figure 7.22 Schematic representation of the individual mode distributions according to the LP_{lm} mode classification. The abscissa reports the normalized cut-off frequency for the individual modes. Single-mode operation is achieved when the normalized frequency is below $V_c^{01} \cong 2.405$

Conversely, the mode grouping shown in Equations (7.117) is found according to the LP_{lm} classification. Each individual mode belonging to the LP_{lm} mode group exhibits the same propagation constant. Figure 7.22 shows the LP_{lm} classification as a function of the normalized cut-off frequency V_c^{lm} of individual modes.

In the next section some computed mode structures are given for the step-index optical fiber.

7.2.7 Mode Distributions of the Step-Index Fiber

In this section, the field and intensity distributions of some low-order modes supported by the step-index optical fiber are presented. The following six modes were selected according to the classification presented in the previous section:

$$\mathrm{LP}_{01} = (\mathrm{HE}_{11})$$

$$\mathrm{LP}_{02} = (\mathrm{HE}_{12})$$

$$\mathrm{LP}_{03} = (\mathrm{HE}_{13})$$

$$\mathrm{LP}_{11} = (\mathrm{TE}_{01}, \mathrm{TM}_{01}, \mathrm{HE}_{21})$$

$$\mathrm{LP}_{12} = (\mathrm{TE}_{02}, \mathrm{TM}_{02}, \mathrm{HE}_{22})$$

$$\mathrm{LP}_{21} = (\mathrm{EH}_{11}, \mathrm{HE}_{31})$$

As a general behavior of the intensity of the LP_{lm} mode, the azimuth mode index l gives half the number of maxima in a 2π rotation around the fiber axis or, equivalently, the number of maxima in a π rotation around the fiber axis. The radial mode index m gives the number of maxima along the radial direction, including the on-axis maximum if $l = 0$. Instead, if $l \geq 1$ the radial mode index m gives the total number of maxima along the radial direction, excluding the on-axis minimum intensity.

According to these general properties, it is easy to conclude that the above six mode distributions must exhibit the following characteristic shaping:

$$\mathrm{LP}_{01} : \begin{cases} l = 0 \longrightarrow \text{no azimuth variation, axial symmetry} \\ m = 1 \longrightarrow \text{one radial maximum on-axis} \end{cases}$$

$$\mathrm{LP}_{02}: \begin{cases} l = 0 \longrightarrow \text{no azimuth variation, axial symmetry} \\ m = 2 \longrightarrow \text{two decreasing radial maxima, the first on-axis} \end{cases}$$

$$\mathrm{LP}_{03}: \begin{cases} l = 0 \longrightarrow \text{no azimuth variation, axial symmetry} \\ m = 3 \longrightarrow \text{three decreasing radial maxima, the first on-axis} \end{cases}$$

$$\mathrm{LP}_{11}: \begin{cases} l = 1 \longrightarrow \text{two azimuth maxima, no axial symmetry} \\ m = 1 \longrightarrow \text{one radial maximum off-axis and one minimum on-axis} \end{cases}$$

$$\mathrm{LP}_{12}: \begin{cases} l = 1 \longrightarrow \text{two azimuth maxima, no axial symmetry} \\ m = 2 \longrightarrow \text{two decreasing radial maxima off-axis and one minimum on-axis} \end{cases}$$

$$\mathrm{LP}_{21}: \begin{cases} l = 2 \longrightarrow \text{four azimuth maxima, no axial symmetry} \\ m = 1 \longrightarrow \text{one radial maximum off-axis and one minimum on-axis} \end{cases}$$

7.2.7.1 LP_{01}

The fundamental fiber mode LP_{01} has axial symmetry and a single maximum located on the axis. The computed field distributions refer to the excitation of the E_y component only, as clearly shown in Figures 7.23 and 7.24 for the electric field amplitude and intensity respectively. The absence of any angular dependence of the modal field leads to the expected axial symmetry and a positive amplitude field everywhere in both the core and the cladding regions. Figure 7.23 shows the spatial distribution of the electric field amplitude. Figure 7.24 shows instead the intensity individually associated with each transversal electric field component, namely $|E_x(\rho, \phi)|^2$ and $|E_y(\rho, \phi)|^2$. In the particular case of axial symmetry, the intensity of each individual field component follows almost the same shape as the total intensity distribution (see Figure 7.25), leading to apparently obvious results.

The situation is completely different when the field exhibits azimuth dependence. As will be seen later, in that case the total field intensity $I(\rho, \phi) = |E_x(\rho, \phi)|^2 + |E_y(\rho, \phi)|^2$ under uniform

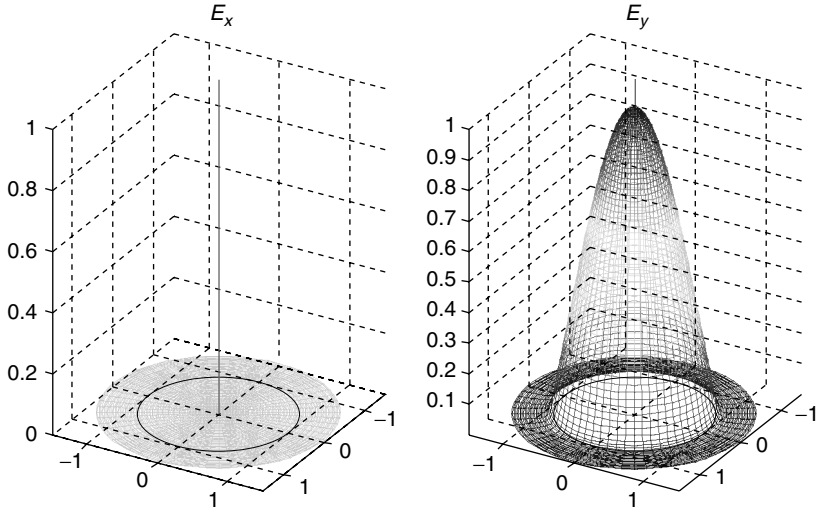

Figure 7.23 Color-graded representation of the amplitude distribution of the electric field components $E_x(\rho, \phi)$ and $E_y(\rho, \phi)$ of the fundamental mode $\mathrm{LP}_{01} = (\mathrm{HE}_{11})$ of the step-index fiber: $a = 25\,\mu\mathrm{m}$, $\lambda = 1310\,\mathrm{nm}$, $n_1 = 1.480$, $n_2 = 1.465$. The circular line defines the core–cladding interface

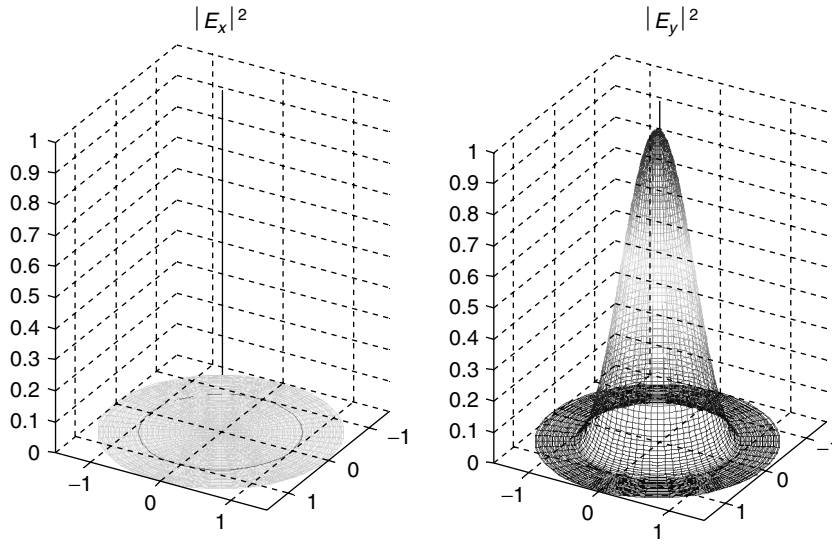

Figure 7.24 Color-graded graphical representation of the intensity distribution of the electric field components $|E_x(\rho, \phi)|^2$ and $|E_y(\rho, \phi)|^2$ of the fundamental mode $\mathrm{LP}_{01} = \mathrm{HE}_{11}$ for the optical fiber defined by $a = 25\,\mu\mathrm{m}$, $\lambda = 1310\,\mathrm{nm}$, $n_1 = 1.480$, $n_2 = 1.465$

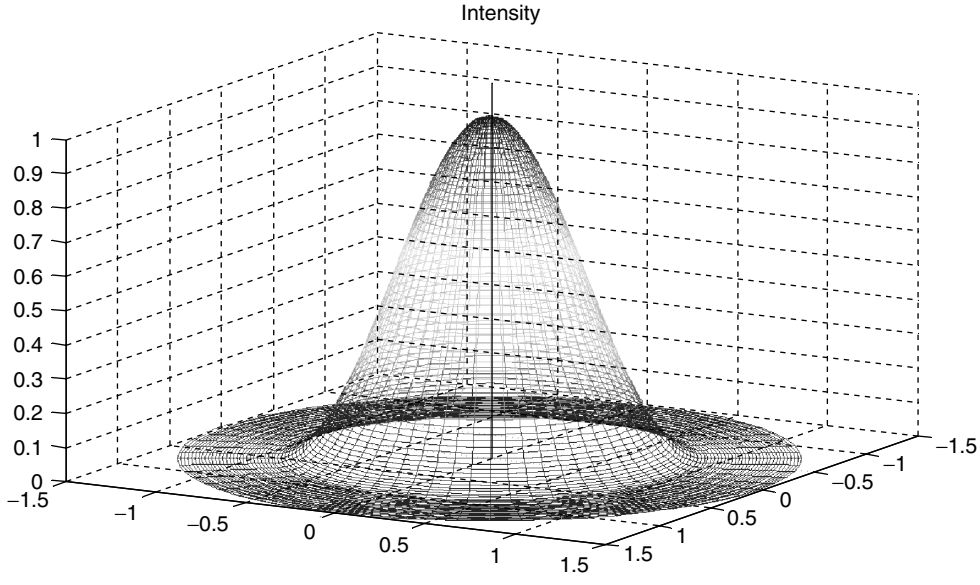

Figure 7.25 Color-graded representation of the total intensity distribution of the electric field $I_{01}(\rho, \phi) = |E_{01}(\rho, \phi)|^2 = |E_x(\rho, \phi)|^2 + |E_y(\rho, \phi)|^2$ of the linearly polarized mode $\mathrm{LP}_{01} = (\mathrm{HE}_{11})$ of the step-index fiber: $a = 25\,\mu\mathrm{m}$, $\lambda = 1310\,\mathrm{nm}$, $n_1 = 1.480$, $n_2 = 1.465$. The circular line at the bottom of the distribution defines the core–cladding interface

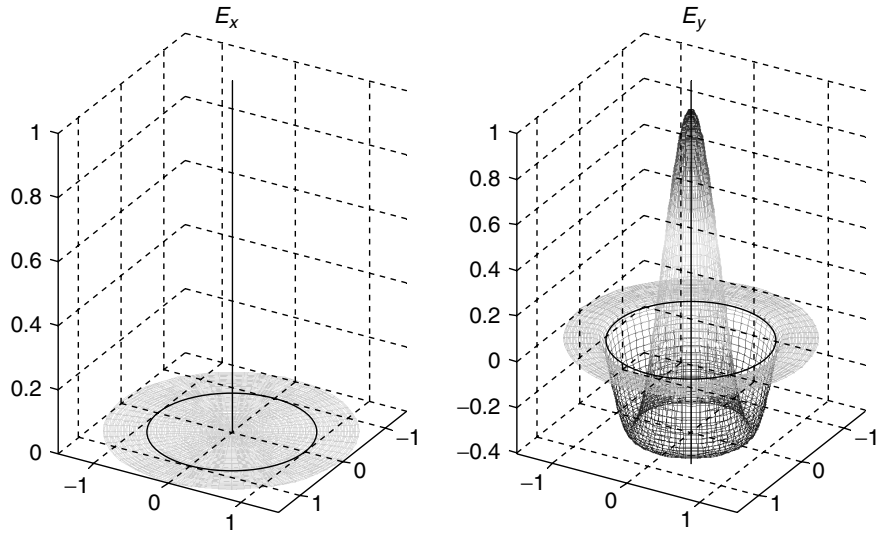

Figure 7.26 Color-graded representation of the amplitude distribution of the electric field components $E_x(\rho, \phi)$ and $E_y(\rho, \phi)$ of the linearly polarized mode $LP_{02} = (HE_{12})$ of the step-index fiber: $a = 25\,\mu m$, $\lambda = 1310\,nm$, $n_1 = 1.480$, $n_2 = 1.465$. The circular line defines the core–cladding interface

modal field component excitations preserves axial symmetry, while its individual components have intensity distributions strongly depending on the angular coordinate.

7.2.7.2 LP_{02}

Increasing the radial mode number by one unit with respect to the fundamental mode LP_{01} adds one more maximum in the radial dependence of the intensity profile of the LP_{02} mode. Figures 7.26 and 7.27 show the amplitude and the intensity respectively of the electric field component $E_y(\rho, \phi)$. Due to null azimuth dependence, the mode field has axial symmetry, showing an intense contribution to the inner core region, close to the fiber axis. By comparison with LP_{01}, it is concluded that by increasing the radial mode number the corresponding on-axis peak of the intensity profile becomes sharper, leading to a smaller inner circle closer to the fiber axis (see Figure 7.28). Moving along the outside radial direction, the remaining core region is divided instead into alternate interference fringes, with characteristic dark and light circles. This behavior becomes much more evident at increasing radial order.

7.2.7.3 LP_{03}

The last case of an axial symmetric field to be considered is the mode LP_{03}. Again, the null value of the azimuth mode number determines the axial symmetric field profile of both the amplitude and the intensity. The reason for adding this mode field representation is to illustrate as clearly as possible the implications of the radial mode number once the azimuth mode number has been fixed to zero. Every unit the radial mode number increases leads to an additional relative maximum in the radial profile of both the amplitude (Figure 7.29) and the intensity representation (Figure 7.30) of the LP_{0m} mode. The total intensity distribution is given in Figure 7.31. It is important to note the following important properties of the whole family of allowed LP_{0m} modes:

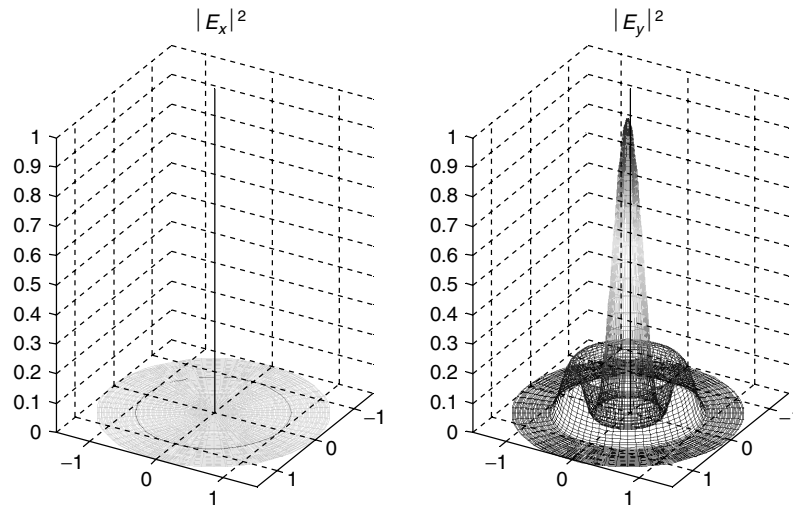

Figure 7.27 Color-graded representation of the intensity distribution of the electric field components $|E_x(\rho, \phi)|^2$ and $|E_y(\rho, \phi)|^2$ of the linearly polarized mode $LP_{02} = (HE_{12})$ of the step-index fiber: $a = 25\,\mu m$, $\lambda = 1310\,nm$, $n_1 = 1.480$, $n_2 = 1.465$. The circular line defines the core–cladding interface

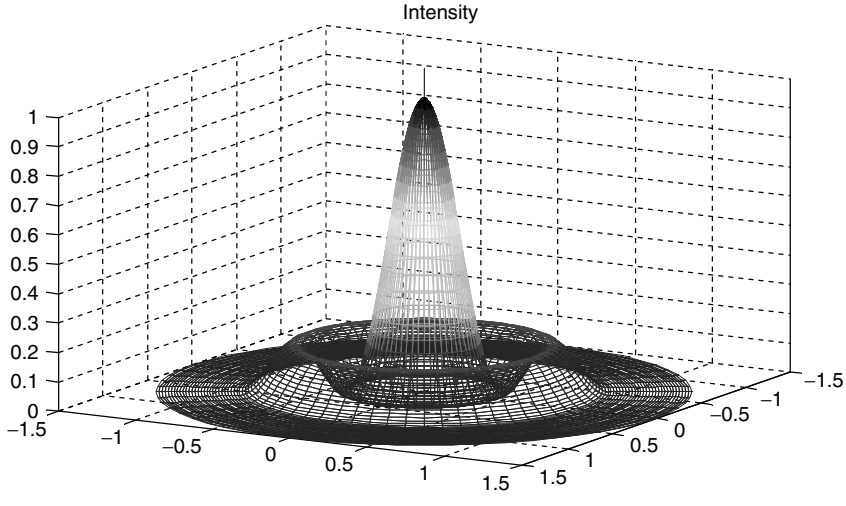

Figure 7.28 Color-graded representation of the total intensity distribution of the electric field $I_{02}(\rho, \phi) = |E_{12}(\rho, \phi)|^2 = |E_x(\rho, \phi)|^2 + |E_y(\rho, \phi)|^2$ of the linearly polarized mode $LP_{02} = (HE_{12})$ of the step-index fiber: $a = 25\,\mu m$, $\lambda = 1310\,nm$, $n_1 = 1.480$, $n_2 = 1.465$. The circular line at the bottom of the distribution defines the core–cladding interface

1. Every LP_{0m} mode, with $1 \leq m \leq M_0$, exhibits the maximum field amplitude located on the fiber axis. The remaining $m - 1$ radial maxima have a decreasing profile with the radial distance from the fiber axis.
2. Conversely, every LP_{lm} mode with $l \geq 1$, independently from each allowed radial mode number m, does not exhibit an on-axis maximum.

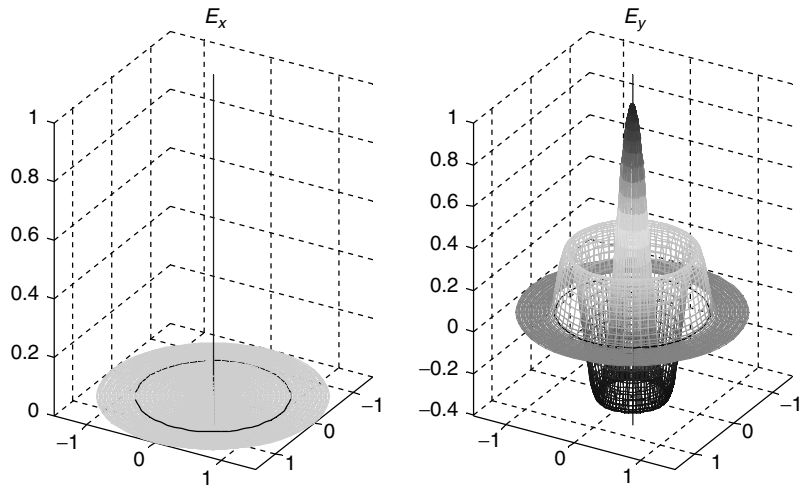

Figure 7.29 Color-graded representation of the amplitude distribution of the electric field components $E_x(\rho, \phi)$ and $E_y(\rho, \phi)$ of the linearly polarized mode $\mathrm{LP}_{11} = (\mathrm{HE}_{21}, \mathrm{TE}_{01}, \mathrm{TM}_{01})$ of the step-index fiber: $a = 25\,\mu\mathrm{m}$, $\lambda = 1310\,\mathrm{nm}$, $n_1 = 1.480$, $n_2 = 1.465$. The circular line defines the core–cladding interface

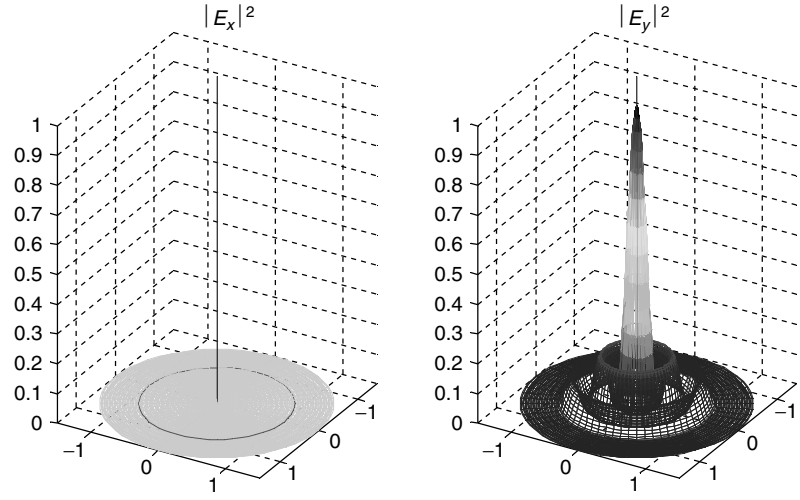

Figure 7.30 Color-graded representation of the intensity distribution of the electric field components $|E_x(\rho, \phi)|^2$ and $|E_y(\rho, \phi)|^2$ of the linearly polarized mode $\mathrm{LP}_{03} = (\mathrm{HE}_{13})$ of the step-index fiber: $a = 25\,\mu\mathrm{m}$, $\lambda = 1310\,\mathrm{nm}$, $n_1 = 1.480$, $n_2 = 1.465$. The circular line defines the core–cladding interface

These two statements set the important condition for having only on-axis mode excitation and are related to the optical mode filtering approach that was briefly discussed in the first chapter of this book.

7.2.7.4 LP_{11}

Once the azimuth mode number assumes any nonzero integer value, the field amplitude and the corresponding intensity of each Cartesian component lose any axial symmetry, thus exhibiting

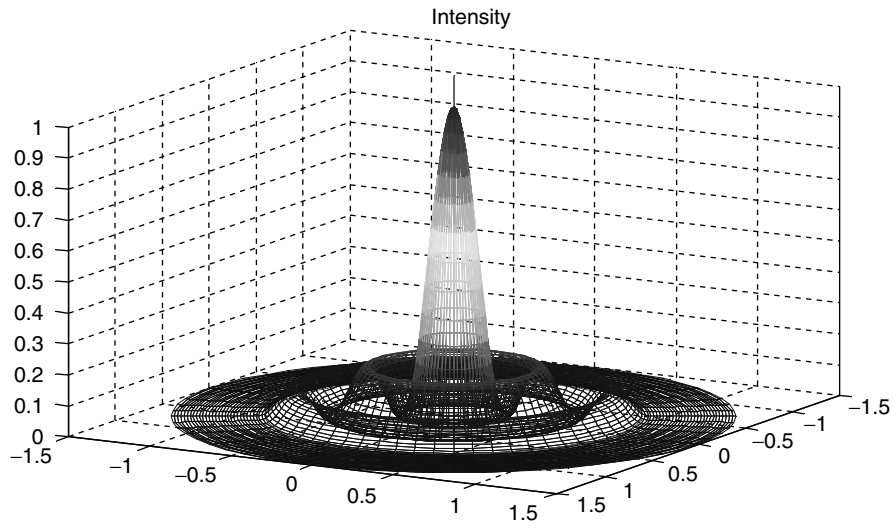

Figure 7.31 Color-graded representation of the total intensity distribution of the electric field $I_{03}(\rho, \phi) = |E_{03}(\rho, \phi)|^2 = |E_x(\rho, \phi)|^2 + |E_y(\rho, \phi)|^2$ of the linearly polarized mode $LP_{03} = (HE_{13})$ of the step-index fiber: $a = 25\,\mu m$, $\lambda = 1310\,nm$, $n_1 = 1.480$, $n_2 = 1.465$. The circular line at the bottom of the distribution defines the core–cladding interface

periodical behavior according to the azimuth position. This is a direct consequence of the harmonic solution for the azimuth dependence of each transversal field component. The first low-order mode with a nonaxial symmetric profile is the LP_{11} mode. As already mentioned, this mode configuration includes three individual modes, namely TE_{01}, TM_{01} and HE_{21}. In this case, the electric field components have a complementary azimuth dependence: assuming that the x-oriented component varies as $\sin \phi$, the y-oriented component shows a $\cos \phi$ dependence, and vice versa. Since the azimuth mode number $\nu = 1$, both components have in angular periodicity of 2π. The two pronounced peaks located symmetrically along the core diameter of each transversal Cartesian components of the electric field, as clearly shown in the computed field profiles in Figures 7.32 and 7.33, represent the major characteristic of the LP_{11} mode. This characteristic behavior is most important when there is an interested in computing the coupled optical power through the launching conditions. Assuming the input field is linearly polarized, just one of the two available electric field components would be excited and only one of the dual-peak intensity profiles would be detected after a short length of fiber. The total intensity profile shown in Figure 7.34 refers to the uniform excitation of both electric field components by means of circularly polarized light.

7.2.7.5 LP_{12}

By increasing the radial mode number of the elementary unit step, the mode LP_{11} transforms into LP_{12}, as shown in Figures 7.35 and 7.36. The nonzero azimuth mode number $l = 1$ determines the same values as discussed in the previous section. In particular, the intensity of each component of the electric field shows the characteristic dual-peak profile, both off-axis and located along the core diameter. The radial mode number $m = 2$ leads to a second smoothed peak along the same radial direction of the two main lobes. Figure 7.36 shows the intensities of each electric field transversal component, according to the complementary azimuth harmonic dependence. Assuming uniform excitation of both transversal electric field components, the total intensity results in the axial symmetric profile reported in Figure 7.37. The axial symmetry under uniform excitation is a direct

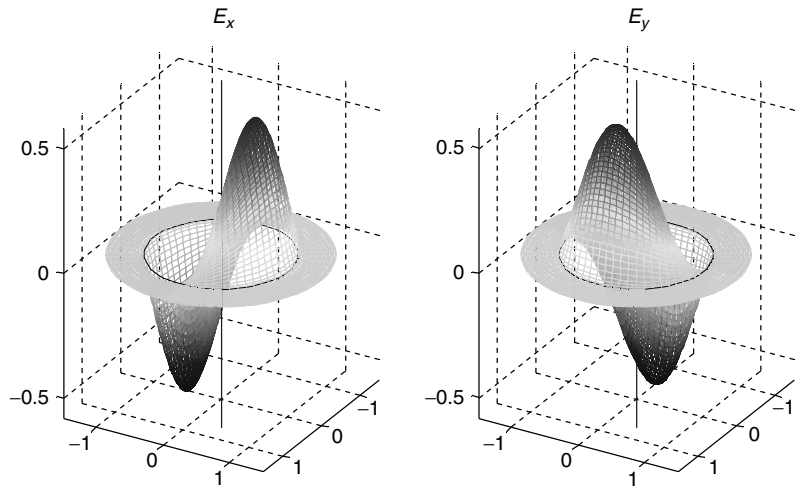

Figure 7.32 Color-graded representation of the amplitude distribution of the electric field components $E_x(\rho, \phi)$ and $E_y(\rho, \phi)$ of the linearly polarized mode $\mathrm{LP}_{11} = (\mathrm{HE}_{21}, \mathrm{TE}_{01}, \mathrm{TM}_{01})$ of the step-index fiber: $a = 25\,\mu\mathrm{m}$, $\lambda = 1310\,\mathrm{nm}$, $n_1 = 1.480$, $n_2 = 1.465$. The circular line defines the core–cladding interface

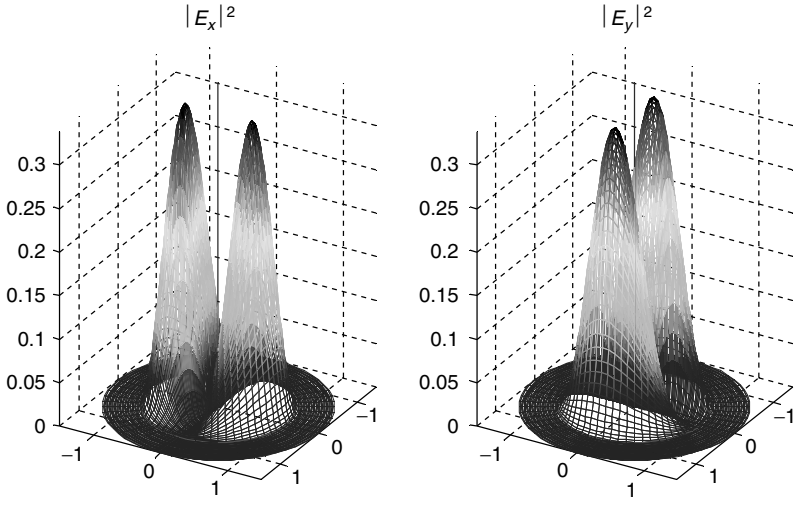

Figure 7.33 Color-graded representation of the intensity distribution of the electric field components $|E_x(\rho, \phi)|^2$ and $|E_y(\rho, \phi)|^2$ of the linearly polarized mode $\mathrm{LP}_{11} = (\mathrm{HE}_{21}, \mathrm{TE}_{01}, \mathrm{TM}_{01})$ of the step-index fiber: $a = 25\,\mu\mathrm{m}$, $\lambda = 1310\,\mathrm{nm}$, $n_1 = 1.480$, $n_2 = 1.465$. The circular line defines the core–cladding interface

consequence of the complementary azimuth harmonic dependence. This property is common to every supported fiber mode under uniform excitation of both electric field transversal components.

7.2.7.6 LP_{21}

The last step-index fiber mode configuration considered here is the LP_{21} mode, as shown in Figures 7.38 and 7.39. In this case, the second-order azimuth dependence leads to the characteristic

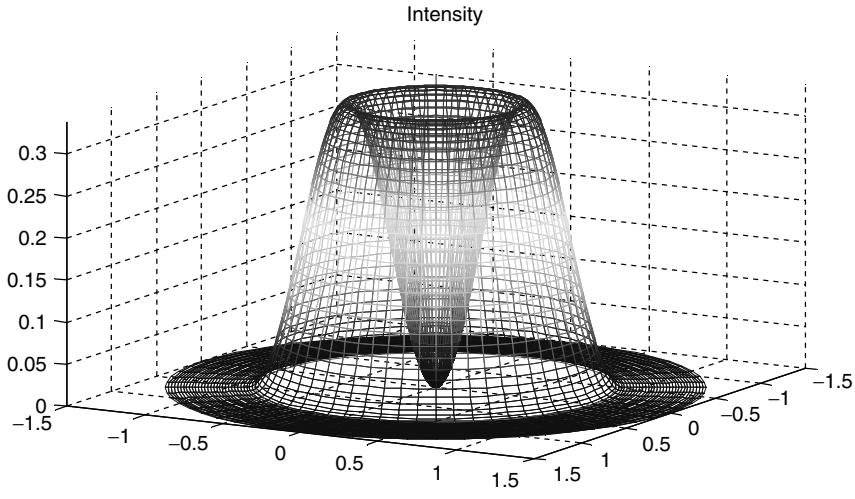

Figure 7.34 Color-graded representation of the total intensity distribution of the electric field $I_{11}(\rho, \phi) = |E_{11}(\rho, \phi)|^2 = |E_x(\rho, \phi)|^2 + |E_y(\rho, \phi)|^2$ of the linearly polarized mode $\mathrm{LP}_{11} = (\mathrm{HE}_{21}, \mathrm{TE}_{01}, \mathrm{TM}_{01})$ of the step-index fiber: $a = 25\,\mu\mathrm{m}$, $\lambda = 1310\,\mathrm{nm}$, $n_1 = 1.480$, $n_2 = 1.465$. The circular line at the bottom of the distribution defines the core–cladding interface

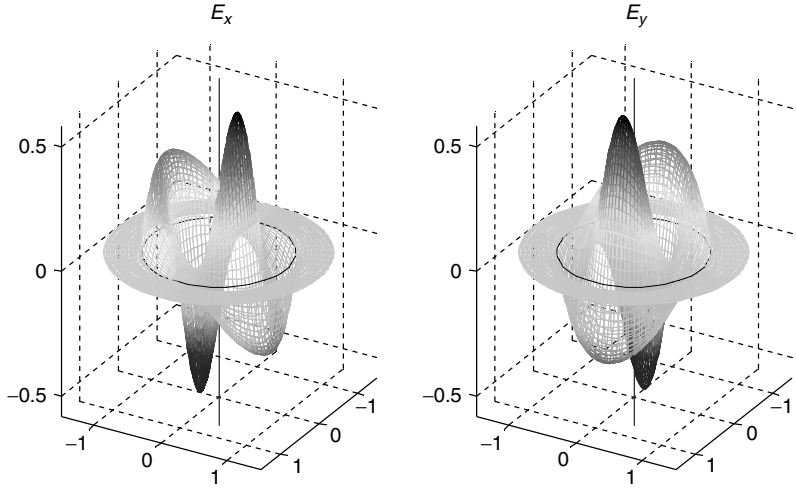

Figure 7.35 Color-graded representation of the amplitude distribution of the electric field components $E_x(\rho, \phi)$ and $E_y(\rho, \phi)$ of the linearly polarized mode $\mathrm{LP}_{12} = (\mathrm{HE}_{22}, \mathrm{TE}_{02}, \mathrm{TM}_{02})$ of the step-index fiber: $a = 25\,\mu\mathrm{m}$, $\lambda = 1310\,\mathrm{nm}$, $n_1 = 1.480$, $n_2 = 1.465$. The circular line defines the core–cladding interface

quadruple peaks of the intensity profile of each transversal electric field component, as shown in Figure 7.39. Again, there is the same complementary behavior of the two electric field transversal component intensities that have already been observed in the previous cases. Assuming uniform excitation of both electric field components determines the axis symmetric total intensity profile shown in Figure 7.40.

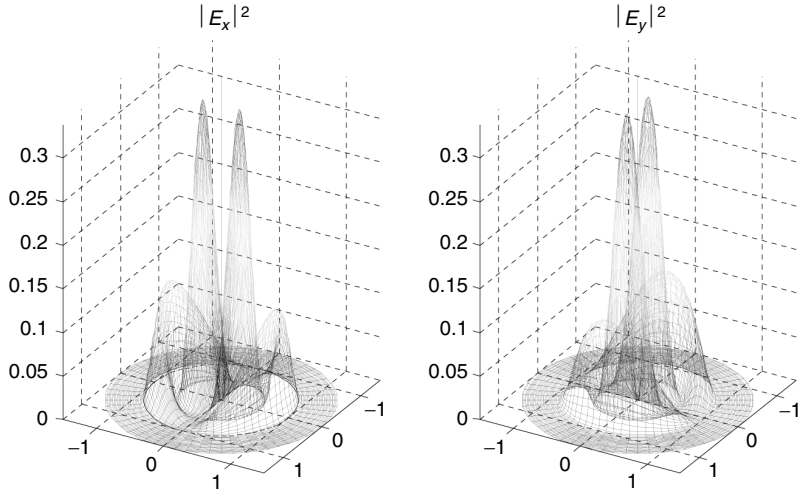

Figure 7.36 Color-graded representation of the intensity distribution of the electric field components $|E_x(\rho,\phi)|^2$ and $|E_y(\rho,\phi)|^2$ of the linearly polarized mode $LP_{12} = (HE_{22}, TE_{02}, TM_{02})$ of the step-index fiber: $a = 25\,\mu m$, $\lambda = 1310\,nm$, $n_1 = 1.480$, $n_2 = 1.465$. The circular line defines the core–cladding interface

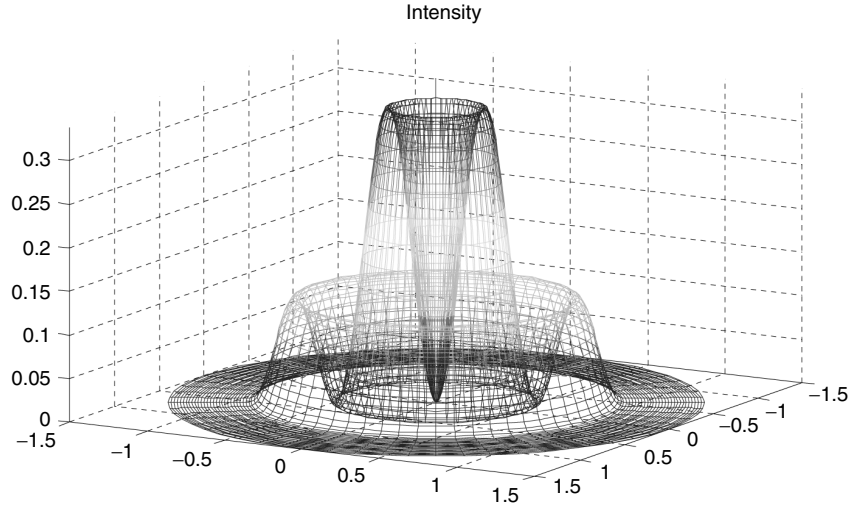

Figure 7.37 Color-graded representation of the total intensity distribution of the electric field $I_{12}(\rho,\phi) = |E_{12}(\rho,\phi)|^2 = |E_x(\rho,\phi)|^2 + |E_y(\rho,\phi)|^2$ of the linearly polarized mode $LP_{12} = (HE_{22}, TE_{02}, TM_{02})$ of the step-index fiber: $a = 25\,\mu m$, $\lambda = 1310\,nm$, $n_1 = 1.480$, $n_2 = 1.465$. The circular line at the bottom of the distribution defines the core–cladding interface

7.2.7.7 On-Axis Peak and Notch Modes

To conclude this section on the step-index fiber mode distributions, it is useful to discuss briefly the fundamental difference found between fiber modes that support on-axis intensity and fiber modes that do not have on-axis intensity. In the following, these will be referred to as on-axis peak modes and on-axis notch modes respectively. Figure 7.41 shows the computed intensity profile of the y component of the electric field of the mode LP_{08}.

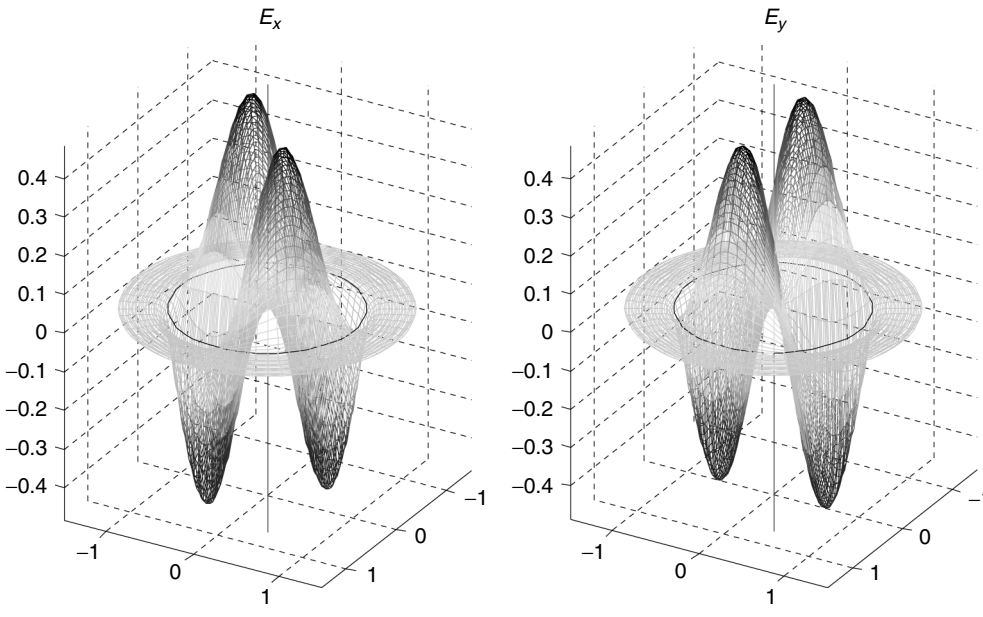

Figure 7.38 Color-graded representation of the amplitude distribution of the electric field components $E_x(\rho, \phi)$ and $E_y(\rho, \phi)$ of the linearly polarized mode $\mathrm{LP}_{21} = (\mathrm{HE}_{31}, \mathrm{EH}_{11})$ of the step-index fiber: $a = 25\,\mu\mathrm{m}$, $\lambda = 1310\,\mathrm{nm}$, $n_1 = 1.480$, $n_2 = 1.465$. The circular line defines the core–cladding interface

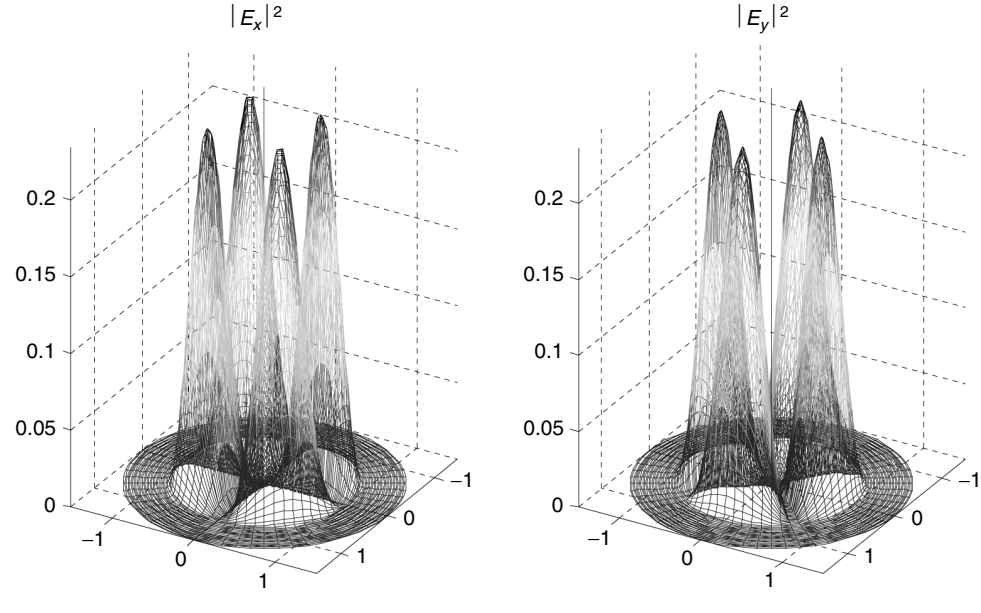

Figure 7.39 Color-graded representation of the intensity distribution of the electric field components $|E_x(\rho, \phi)|^2$ and $|E_y(\rho, \phi)|^2$ of the linearly polarized mode $\mathrm{LP}_{21} = (\mathrm{HE}_{31}, \mathrm{EH}_{11})$ of the step-index fiber: $a = 25\,\mu\mathrm{m}$, $\lambda = 1310\,\mathrm{nm}$, $n_1 = 1.480$, $n_2 = 1.465$. The circular line defines the core–cladding interface

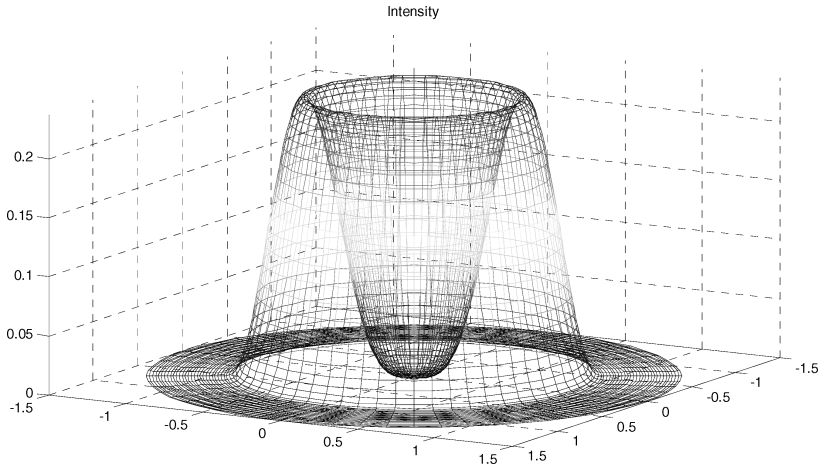

Figure 7.40 Color-graded representation of the total intensity distribution of the electric field $I_{21}(\rho, \phi) = |E_{21}(\rho, \phi)|^2 = |E_x(\rho, \phi)|^2 + |E_y(\rho, \phi)|^2$ of the linearly polarized mode $\mathrm{LP}_{21} = (\mathrm{HE}_{31}, \mathrm{EH}_{11})$ of the step-index fiber: $a = 25\,\mu\mathrm{m}$, $\lambda = 1310\,\mathrm{nm}$, $n_1 = 1.480$, $n_2 = 1.465$. The circular line at the bottom of the distribution defines the core–cladding interface

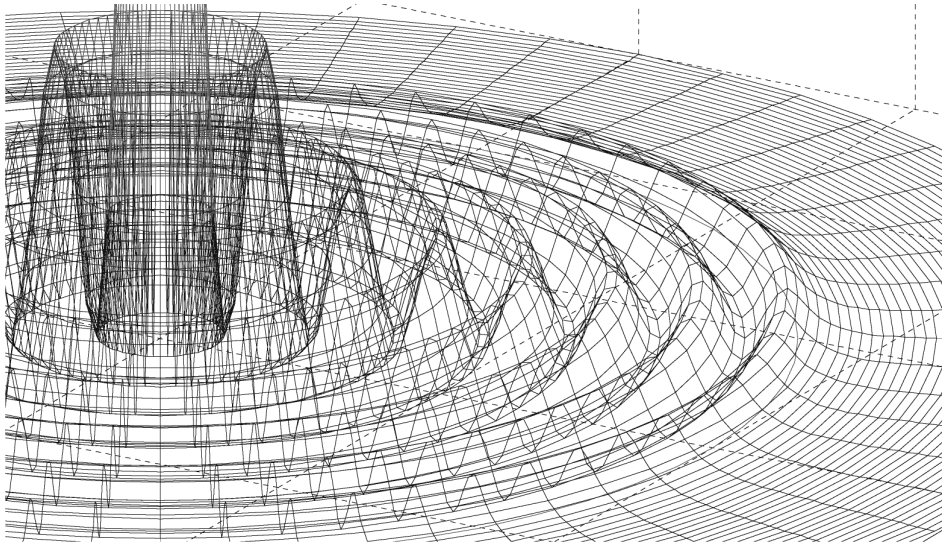

Figure 7.41 Magnification of the intensity distribution of the y component of the electric field $|E_y(\rho, \phi)|^2$ of the linearly polarized mode $\mathrm{LP}_{08} = (\mathrm{HE}_{18})$ of the step-index fiber: $a = 25\,\mu\mathrm{m}$, $\lambda = 1310\,\mathrm{nm}$, $n_1 = 1.480$, $n_2 = 1.465$. The field is represented in the low-intensity region, where the expected eight decreasing smoothed maxima, including the on-axis maximum, are clearly visible. The null azimuth mode number leads to the axial peak intensity

The null value of the azimuth number leads to the expected on-axis peak intensity profile. This statement is true for both the individual electric field components intensity and for the total field under uniform transversal component excitation. In the case shown, the radial mode number $m = 8$ reflects into eight subsequent radial maxima. Figure 7.42 shows the computed intensity profile for

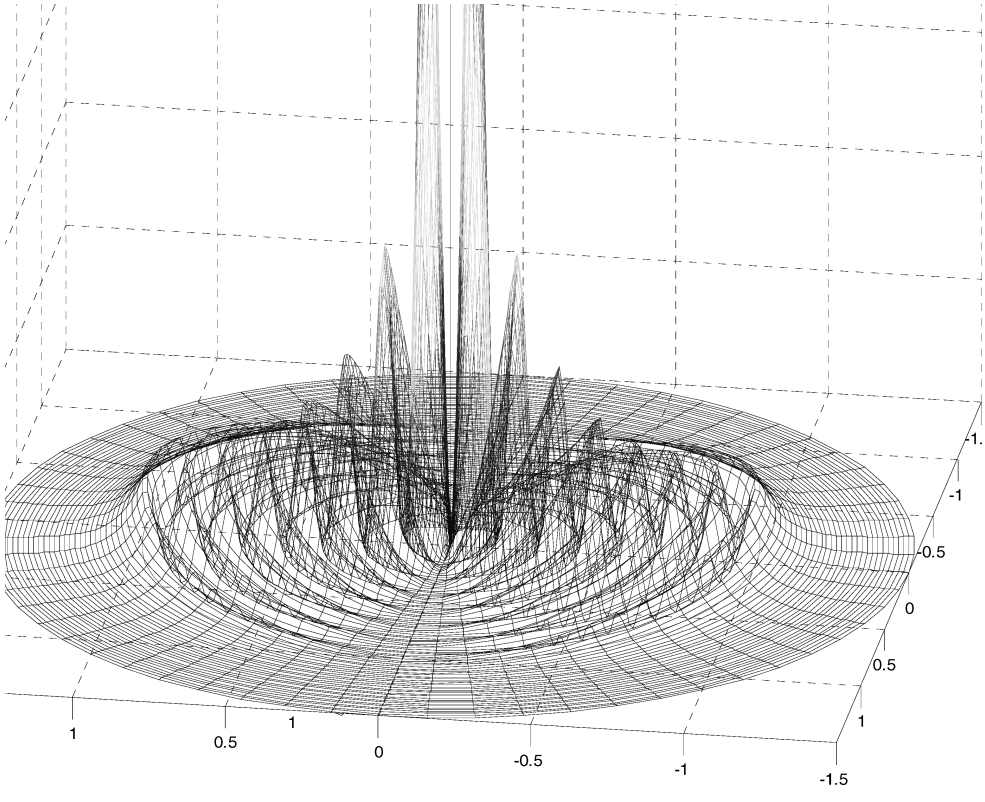

Figure 7.42 Computed intensity profile of the step-index fiber mode LP_{18} showing the on-axis intensity notch consequent to the azimuth mode number $l = 1$. The fiber parameters are $a = 25\,\mu m$, $\lambda = 1310\,nm$, $n_1 = 1.480$, $n_2 = 1.465$. Eight radial maxima are clearly visible in the color-graded plot

the y-oriented component of the electric field for the mode LP_{18}. Choosing $l = 1$ leads to the on-axis intensity peak minimum and to eight radial maxima. Figure 7.43 shows the cross-section view of the step index mode LP_{44}.

7.2.8 Conclusions and Remarks

In this section, the principal aspects of the modal theory of the step-index multimode fiber have been presented. A more complete analysis is beyond the scope of this book and has been planned for a book dedicated to the optical fiber theory. The first important remark concerns the assumption made at the beginning about the monochromatic optical field. Modal theory implicitly assumes only a monochromatic electromagnetic field. This leads to some conceptual discrepancy when the modal theory is considered as the starting point for optical pulse propagation. This argument has already been discussed in the previous chapter with reference to the chromatic impulse response. Once the monochromatic field assumption has been justified and accepted, the mathematical development of the modal theory proceeds directly from Maxwell equations and related boundary conditions for the cylindrical dielectric waveguide.

The step-index assumption greatly simplifies the mathematics involved, leading to the analytical field solutions in term of the Bessel function of the first kind in the core and the modified Bessel function in the cladding. Satisfaction of the boundary conditions determines the eigenvalue structure of the modal solution, leading to consistent interference patterns. Further mathematical

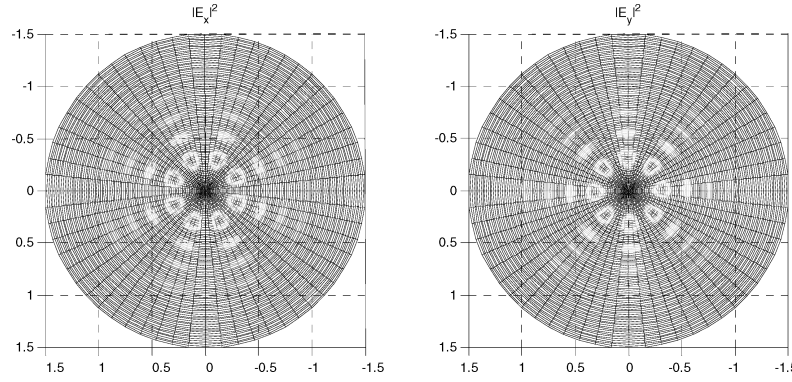

Figure 7.43 Computed intensity profile of the step-index fiber mode LP_{44} showing the on-axis intensity notch consequent to the azimuth mode number $l = 4$. The fiber parameters are $a = 25\,\mu m$, $\lambda = 1310\,nm$, $n_1 = 1.480$, $n_2 = 1.465$. Four radial maxima and eight azimuth maxima are clearly visible in the color-graded plot of the intensity distribution in the fiber cross-section

simplification derives from the assumption of weakly guiding fibers, leading to transverse magnetic field components that are proportional to the cross-related transversal electric field components.

Once the modal fields have been written using mathematical formulas assuming the Cartesian reference system for the electromagnetic field components and polar cylindrical coordinate for the spatial dependence, the amplitude and intensity of each supported mode can be easily computed and represented using powerful graphics aids by Matlab® 7.0.2 software. The results have been presented in graphical form showing interesting properties among supported modes in the LP_{lm} classification. Knowledge of the numeric field distribution is essential for calculating the coupling power coefficients and determining the source energy distribution among the excited fiber modes. As introduced in previous chapters, the power coupling coefficient distribution is chiefly responsible for the multimode fiber impulse response and consequently for quantifying the fiber impact in the link budget dispersion calculation for multigigabit transmission systems.

The next section will present the computational technique for evaluating the power coupling coefficient distribution, starting from the modal fiber solution.

7.3 Mode Power and Launch Conditions

In this section, the mathematical theory will be presented of the mode power coupling coefficients and of the related launching conditions using the step-index fiber mode solution derived in the previous section. However, except for using the mathematical expression of the mode fields for the step-index fiber in the last part of the derivation, the theory to be presented holds in general and is based on fundamental properties of the electromagnetic field in wave guiding structures.

7.3.1 Field Expansion

The general guided fiber mode in the LP_{lm} classification is indicated by

$$\begin{aligned} \mathbf{E}_{lm}(\rho,\phi) &= \mathbf{E}_{t,lm}(\rho,\phi) + E_{z,lm}(\rho,\phi)\mathbf{z} \\ \mathbf{H}_{lm}(\rho,\phi) &= \mathbf{H}_{t,lm}(\rho,\phi) + H_{z,lm}(\rho,\phi)\mathbf{z} \end{aligned} \tag{7.119}$$

which are the electric and the magnetic field components respectively. Both the electric and the magnetic fields have the modal indices l and m and are each represented as the sum of the transversal and longitudinal components. It is assumed that the longitudinal field component depends on the same pair of modal indices, as also does the transversal one.

The modal amplitude a_{lm} is assigned to each supported LP_{lm} mode. For the moment, no further conditions are specified for the modal coefficients. With the whole set of modal amplitudes, the following total bound field expansion is formed in the forward propagating direction, where, for simplicity, the symmetric back propagating contribution is ignored:

$$\begin{aligned} \mathbf{E}_{\mathrm{b}}(\rho,\phi) &= \textstyle\sum_{l,m} a_{lm}\mathbf{E}_{lm}(\rho,\phi), \\ \mathbf{H}_{\mathrm{b}}(\rho,\phi) &= \textstyle\sum_{l,m} a_{lm}\mathbf{H}_{lm}(\rho,\phi), \end{aligned} \quad l = 0,1,2,\ldots, m = 1,2,\ldots, M_l \tag{7.120}$$

The azimuth mode number ranges up to the maximum allowed value while still satisfying at least one solution of the eigenvalue equation. The radial mode number ranges up to the allowed number of eigensolutions M_l for each selected azimuth number. It should be noted that it is implicitly assumed that the modal amplitudes a_{lm} for the electric and magnetic field components of the same LP_{lm} mode are the same. This is consistent with the paraxial approximation, according to which the magnetic field is proportional to the electric field. However, even without returning to any approximation, the equality of the modal amplitudes between the electric and magnetic components reflects the meaning of each mode as the base element of the electromagnetic field in the waveguiding structure and is a direct consequence of the Maxwell equations.

The total electromagnetic field is represented by the sum of the bound field with the radiated field, $\mathbf{E}_{\mathrm{rad}}(\rho,\phi)$ and $\mathbf{H}_{\mathrm{rad}}(\rho,\phi)$ respectively:

$$\begin{aligned} \mathbf{E}(\rho,\phi) &= \mathbf{E}_{\mathrm{b}}(\rho,\phi) + \mathbf{E}_{\mathrm{rad}}(\rho,\phi) = \sum_{l,m} a_{lm}\mathbf{E}_{lm}(\rho,\phi) + \mathbf{E}_{\mathrm{rad}}(\rho,\phi) \\ \mathbf{H}(\rho,\phi) &= \mathbf{H}_{\mathrm{b}}(\rho,\phi) + \mathbf{H}_{\mathrm{rad}}(\rho,\phi) = \sum_{l,m} a_{lm}\mathbf{H}_{lm}(\rho,\phi) + \mathbf{H}_{\mathrm{rad}}(\rho,\phi) \end{aligned} \tag{7.121}$$

The aim is to arrive at a closed-form expression for the calculation of the modal amplitudes a_{lm}, given the exciting source field. This will solve the important problem of the calculation of the source coupled power coefficients.

7.3.2 Modal Power

The power flow of the electromagnetic field is given by the Poynting vector. The Poynting vector represents the electromagnetic power flux density across the unit surface normal to the power flux direction:

$$\mathbf{S} \equiv \tfrac{1}{2}\mathrm{Re}[\mathbf{E} \times \mathbf{H}^*]$$

Referring to the field expressions in (7.119) of the LP_{lm} mode and computing the corresponding longitudinal component $S_{z,lm}$ of the Poynting vector in the direction of the fiber axis gives

$$\begin{aligned} S_{z,lm}(\rho,\phi) &= \tfrac{1}{2}\mathrm{Re}[\mathbf{E}_{t,lm}(\rho,\phi) \times \mathbf{H}^*_{t,lm}(\rho,\phi)] \cdot \mathbf{z} \\ &= \tfrac{1}{2}|\mathrm{Re}[\mathbf{E}_{t,lm}(\rho,\phi) \times \mathbf{H}^*_{t,lm}(\rho,\phi)]| \end{aligned} \tag{7.122}$$

Introducing the modal amplitude a_{lm} and assuming that the transversal component of the generic LP_{lm} mode are real, from Equation (7.122) the following form of the electromagnetic power flux density propagating in the fiber axis direction is obtained:

$$S_{z,lm}(\rho,\phi) = \tfrac{1}{2}|a_{lm}|^2[\mathbf{E}_{t,lm}(\rho,\phi) \times \mathbf{H}^*_{t,lm}(\rho,\phi)] \cdot \mathbf{z} \tag{7.123}$$

The electromagnetic power P_{lm} associated with the LP_{lm} mode is therefore given by the integration of the power flux density across the infinite fiber section A_∞:

$$P_{lm} = \int_{A_\infty} S_{z,lm}(\rho,\phi)\,\mathrm{d}A \tag{7.124}$$

Using Equation (7.123) gives

$$P_{lm} = \tfrac{1}{2}|a_{lm}|^2 \int_{A_\infty} [\mathbf{E}_{t,lm}(\rho,\phi) \times \mathbf{H}^*_{t,lm}(\rho,\phi)] \cdot \mathbf{z}\, \mathrm{d}A \tag{7.125}$$

Of course, the total bound power P_b is given by the sum of all supported mode powers. From Equations (7.120) and (7.125),

$$P_\mathrm{b} = \sum_{l,m} P_{lm} = \tfrac{1}{2} \sum_{l,m} |a_{lm}|^2 \int_{A_\infty} [\mathbf{E}_{t,lm}(\rho,\phi) \times \mathbf{H}^*_{t,lm}(\rho,\phi)] \cdot \mathbf{z}\, \mathrm{d}A \tag{7.126}$$

The integral in the above expression leads to the mode normalization concept.

7.3.3 Mode Normalization

According to the expression of the modal power (7.125), it is convenient to define the mode power normalization constant N_{lm} as

$$N_{lm} \equiv \tfrac{1}{2} \int_{A_\infty} [\mathbf{E}_{t,lm}(\rho,\phi) \times \mathbf{H}^*_{t,lm}(\rho,\phi)] \cdot \mathbf{z}\, \mathrm{d}A \tag{7.127}$$

Using this definition, the mode power of the LP_{lm} mode from Equation (7.125) becomes

$$P_{lm} = |a_{lm}|^2 N_{lm} \tag{7.128}$$

The total bound power in Equation (7.126) then becomes

$$P_\mathrm{b} = \sum_{l,m} |a_{lm}|^2 N_{lm} \tag{7.129}$$

From expression (7.128), it follows that the normalization constant N_{lm} assumes the meaning of mode power with unitary mode amplitude:

$$|a_{lm}| = 1 \Rightarrow P_{lm} = N_{lm} \tag{7.130}$$

The paraxial approximation allows for a simple expression of the mode normalization constant in terms of the square modulus of the electric field only. From Equation (7.127), using Equations (7.67) and (7.73),

$$N_{lm} \equiv \frac{1}{2Z_0} \left[\int_0^1 \int_0^{2\pi} n_1 |\mathbf{E}_{t,lm}(\rho,\phi)|^2 \rho\, \mathrm{d}\rho\, \mathrm{d}\phi + \int_1^{+\infty} \int_0^{2\pi} n_2 |\mathbf{E}_{t,lm}(\rho,\phi)|^2 \rho\, \mathrm{d}\rho\, \mathrm{d}\phi \right] \tag{7.131}$$

In the expression above, the integration variables have been written explicitly, separating the integrals between the core and the cladding regions. In order to assign a direct physical meaning to the modal amplitudes, it is convenient to normalize the electromagnetic field of each mode solution. To this end, the normalized mode fields are defined as follows:

$$\begin{aligned} \hat{\mathbf{E}}_{lm}(\rho,\phi) &\equiv \frac{1}{\sqrt{N_{lm}}} \mathbf{E}_{lm}(\rho,\phi) \\ \hat{\mathbf{H}}_{lm}(\rho,\phi) &\equiv \frac{1}{\sqrt{N_{lm}}} \mathbf{H}_{lm}(\rho,\phi) \end{aligned} \tag{7.132}$$

At last, if these are referred to as power-normalized mode fields (7.132), the following relationships can easily be demonstrated:

$$\begin{aligned} \hat{N}_{lm} &= 1 \\ \hat{P}_{lm} &= |a_{lm}|^2 \\ \hat{P}_{\mathrm{b}} &= \sum_{l,m} |a_{lm}|^2 \end{aligned} \tag{7.133}$$

The 'hat' symbol refers, of course, to normalized quantities. Expressions (7.127), (7.132) and (7.133) specify the mode field normalizations.

7.3.4 Mode Orthogonality

In order to determine the modal amplitudes a_{lm} of each guided mode in the field expansion (7.121), the orthogonal property of the bound mode set needs to be used. This property is derived from the reciprocity theorem of the Maxwell equation applied to the nonabsorbing waveguide. The demonstration is reported by Snyder and Love.[1]

Assuming that the waveguide is nonabsorbing, the modal fields of $\mathrm{LP}_{l_j m_j}$ and $\mathrm{LP}_{l_k m_k}$ modes satisfy to the following orthogonality condition:

$$\begin{aligned} &\int_{A_\infty} \left[\mathbf{E}_{t,l_j m_j}(\rho,\phi) \times \mathbf{H}^*_{t,l_k m_k}(\rho,\phi)\right] \cdot \mathbf{z}\, \mathrm{d}A = 0, \quad j \neq k \\ &\int_{A_\infty} \left[\mathbf{E}^*_{t,l_j m_j}(\rho,\phi) \times \mathbf{H}_{t,l_k m_k}(\rho,\phi)\right] \cdot \mathbf{z}\, \mathrm{d}A = 0, \quad j \neq k \end{aligned} \tag{7.134}$$

note that these orthogonality conditions hold only when the integration extends over the infinite cross-section. Using the definition of the normalization constant in Equation (7.127), the above orthogonality conditions can be specified as follows:

$$\begin{aligned} &\tfrac{1}{2}\int_{A_\infty} \left[\mathbf{E}_{t,l_j m_j}(\rho,\phi) \times \mathbf{H}^*_{t,l_k m_k}(\rho,\phi)\right] \cdot \mathbf{z}\, \mathrm{d}A = N_{lm}\delta_{jk} \\ &\tfrac{1}{2}\int_{A_\infty} \left[\mathbf{E}^*_{t,l_j m_j}(\rho,\phi) \times \mathbf{H}_{t,l_k m_k}(\rho,\phi)\right] \cdot \mathbf{z}\, \mathrm{d}A = N_{lm}\delta_{jk} \end{aligned} \tag{7.135}$$

The function

$$\delta_{jk} = \begin{cases} 0, & j \neq k \\ 1, & j = k \end{cases}$$

is the Krönecker delta. The notation has been simplified by assuming that if the integrand fields refer to the same mode with $l_j = l_k$, $m_j = m_k$, $j = k$, the normalization constant is given by N_{lm}. The modal orthogonality is verified between any forward-propagating bound mode pair. In particular, two modes specified by the same azimuth number $l_1 = l_2$, but with different radial numbers $m_1 \neq m_2$, are orthogonal in the sense of Equation (7.135). Similar orthogonality relations hold between any bound mode and the radiation mode introduced in Equation (7.121):

$$\begin{aligned} &\int_{A_\infty} \left[\mathbf{E}_{t,lm}(\rho,\phi) \times \mathbf{H}^*_{\mathrm{rad}}(\rho,\phi)\right] \cdot \mathbf{z}\, \mathrm{d}A = 0 \\ &\int_{A_\infty} \left[\mathbf{E}^*_{\mathrm{rad}}(\rho,\phi) \times \mathbf{H}_{t,lm}(\rho,\phi)\right] \cdot \mathbf{z}\, \mathrm{d}A = 0 \end{aligned} \tag{7.136}$$

[1] Allan W. Snyder and John Love, *Optical Waveguide Theory*, Chapman and Hall, London, 1983.

In the following, a short comment is made about forward-propagating and backward-propagating modes. According to the Snyder and Love reference, the same convention will be used for mode propagation identification, precisely:

$$\text{Forward-propagating mode}: \begin{cases} \mathbf{E}_{lm} = \mathbf{E}_{\boldsymbol{t},lm} + E_{z,lm}\mathbf{z} \\ \mathbf{H}_{lm} = \mathbf{H}_{\boldsymbol{t},lm} + H_{z,lm}\mathbf{z} \end{cases} \tag{7.137}$$

$$\text{Backward-propagating mode}: \begin{cases} \mathbf{E}_{-l,-m} = \mathbf{E}_{-\boldsymbol{t},lm} + E_{-z,lm}\mathbf{z} \\ \mathbf{H}_{-l,-m} = \mathbf{H}_{-\boldsymbol{t},lm} + H_{-z,lm}\mathbf{z} \end{cases} \tag{7.138}$$

and

$$\left.\begin{aligned} \mathbf{E}_{-l,-m} &= +\mathbf{E}_{\boldsymbol{t},lm} - E_{z,lm}\mathbf{z} \\ \mathbf{H}_{-l,-m} &= -\mathbf{H}_{\boldsymbol{t},lm} + H_{z,lm}\mathbf{z} \end{aligned}\right\} \Rightarrow \begin{cases} \mathbf{E}_{-\boldsymbol{t},lm} = +\mathbf{E}_{\boldsymbol{t},lm} \\ E_{-z,lm} = -E_{z,lm} \\ \mathbf{H}_{-\boldsymbol{t},lm} = -\mathbf{H}_{\boldsymbol{t},lm} \\ H_{-z,lm} = H_{z,lm} \end{cases} \tag{7.139}$$

One important question regards the orthogonality relationships between forward-propagating and backward-propagating modes. According to Equations (7.138) and (7.139), each back-propagating mode can be expressed in terms of the corresponding forward-propagating mode with proper sign changes. Since the sign does not affect the conclusions regarding the mode orthogonality, it is concluded that the orthogonality condition is preserved between either or both forward-propagating and backward-propagating modes. In particular, since only transversal components are involved in the orthogonality relations, the same mode distributions in the forward propagation and in the backward propagation are not orthogonal. However, different bound modes in the forward-propagation direction and in the backward-propagation direction are orthogonal. Finally, the same orthogonality condition (7.136) holds between backward-propagating modes and the radiation field.

Referring to power-normalized mode fields in Equations (7.132), the orthogonality conditions simplify, and the following orthonormal condition can be written:

$$\begin{aligned} &\tfrac{1}{2}\int_{A_\infty}\left[\hat{\mathbf{E}}_{t,l_jm_j}(\rho,\phi)\times\hat{\mathbf{H}}^*_{t,l_km_k}(\rho,\phi)\right]\cdot\mathbf{z}\,\mathrm{d}A = \delta_{jk} \\ &\tfrac{1}{2}\int_{A_\infty}\left[\hat{\mathbf{E}}^*_{t,l_jm_j}(\rho,\phi)\times\hat{\mathbf{H}}_{t,l_km_k}(\rho,\phi)\right]\cdot\mathbf{z}\,\mathrm{d}A = \delta_{jk} \\ &\int_{A_\infty}\left[\mathbf{E}_{t,lm}(\rho,\phi)\times\mathbf{H}^*_{\mathrm{rad}}(\rho,\phi)\right]\cdot\mathbf{z}\,\mathrm{d}A = 0 \\ &\int_{A_\infty}\left[\mathbf{E}^*_{\mathrm{rad}}(\rho,\phi)\times\mathbf{H}_{t,lm}(\rho,\phi)\right]\cdot\mathbf{z}\,\mathrm{d}A = 0 \end{aligned} \tag{7.140}$$

The orthonormal conditions that have been derived are valid for the power-normalized fields in Equations (7.132) and represent very fundamental properties among modal fields, including continuum radiation modes.

7.3.5 Modal Amplitudes

The first application of orthogonal conditions (7.140) is the calculation of the modal amplitudes. To this purpose, the total electromagnetic modal field expansion in Equations (7.121) are again considered, where the power-normalized transversal and longitudinal components of the bound

fields are substituted according to Equations (7.119) and (7.132):

$$\begin{aligned}\mathbf{E}(\rho,\phi) &= \mathbf{E}_{\text{rad}}(\rho,\phi) + \sum_{l,m} a_{lm}\left[\mathbf{E}_{t,lm}(\rho,\phi) + E_{z,lm}(\rho,\phi)\mathbf{z}\right] \\ \mathbf{H}(\rho,\phi) &= \mathbf{H}_{\text{rad}}(\rho,\phi) + \sum_{l,m} a_{lm}\left[\mathbf{H}_{t,lm}(\rho,\phi) + H_{z,lm}(\rho,\phi)\mathbf{z}\right]\end{aligned} \tag{7.141}$$

The field expansion written above does not depend on the longitudinal coordinate z. The characteristic approach of the modal theory has been implicitly used by assuming the steady state conditions in the nonabsorbing waveguide with the modal phase factor $\mathrm{e}^{\mathrm{j}(\omega t-\beta_{lm}z)}$. In order to proceed with the derivation of the modal amplitudes as consequent to a given source field excitation, the total electromagnetic field must be equalized at the launching section at $z = 0$ to the source field. The total field expansion in Equations (7.141), evaluated at the launching section at $z = 0$, must therefore coincide with the source electromagnetic field $\mathbf{E}_{\text{s}}$, $\mathbf{H}_{\text{s}}$. Assuming that the longitudinal dependence of the source field an be factorized using the same phase factor $\mathrm{e}^{\mathrm{j}(\omega t-\beta_{\text{s}}z)}$ shown by the modal expansion, the electromagnetic field expansion at the input section can be written as follows:

$$\begin{aligned}\mathbf{E}_{\text{s}}(\rho,\phi) &= \mathbf{E}_{\text{rad}}(\rho,\phi) + \sum_{l,m} a_{lm}\left[\mathbf{E}_{t,lm}(\rho,\phi) + E_{z,lm}(\rho,\phi)\mathbf{z}\right] \\ \mathbf{H}_{\text{s}}(\rho,\phi) &= \mathbf{H}_{\text{rad}}(\rho,\phi) + \sum_{l,m} a_{lm}\left[\mathbf{H}_{t,lm}(\rho,\phi) + H_{z,lm}(\rho,\phi)\mathbf{z}\right]\end{aligned} \tag{7.142}$$

Given the generic bound mode LP_{l_k,m_k} characterized by the index pair (l_k, m_k), the following vector product is formed between the source electric field $\mathbf{E}_{\text{s}}$ at the launching section at $z = 0$ and the complex conjugate of the power-normalized magnetic field $\mathbf{H}^*_{l_k,m_k} = \mathbf{H}^*_{t,l_k,m_k} + H^*_{z,l_k,m_k}\mathbf{z}$, which is then integrate over the infinite fiber cross-section A_∞:

$$\begin{aligned}\int_{A_\infty}\left[\mathbf{E}_{\text{s}}(\rho,\phi)\times\mathbf{H}^*_{l_k,m_k}(\rho,\phi)\right]\cdot\mathbf{z}\,\mathrm{d}A &= \int_{A_\infty}\left[\mathbf{E}_{\text{rad}}(\rho,\phi)\times\mathbf{H}^*_{l_k,m_k}(\rho,\phi)\right]\cdot\mathbf{z}\,\mathrm{d}A \\ &\quad + \sum_{l,m} a_{lm}\int_{A_\infty}\left\{\left[\mathbf{E}_{t,lm}(\rho,\phi) + \hat{E}_{z,lm}(\rho,\phi)\mathbf{z}\right]\right. \\ &\quad \left.\times\mathbf{H}^*_{l_k,m_k}(\rho,\phi)\right\}\cdot\mathbf{z}\,\mathrm{d}A\end{aligned} \tag{7.143}$$

By virtue of the orthogonality condition (7.140) between the radiation field and each bound mode, the first integral at the second member is identically null:

$$\int_{A_\infty}\left[\mathbf{E}_{\text{rad}}(\rho,\phi)\times\mathbf{H}^*_{l_k,m_k}(\rho,\phi)\right]\cdot\mathbf{z}\,\mathrm{d}A \equiv 0 \tag{7.144}$$

The second integral term includes the summation over all bound modes. Again, by virtue of the orthonormal conditions (7.140) between bound mode pairs, the following straightforward result is obtained:

$$\begin{aligned}&\sum_{l,m} a_{lm}\int_{A_\infty}\left\{\left[\mathbf{E}_{t,lm}(\rho,\phi) + E_{z,lm}(\rho,\phi)\mathbf{z}\right]\times\mathbf{H}^*_{l_k,m_k}(\rho,\phi)\right\}\cdot\mathbf{z}\,\mathrm{d}A \\ &\quad = \sum_{l,m} a_{lm}\int_{A_\infty}\mathbf{E}_{t,lm}(\rho,\phi)\times\mathbf{H}^*_{t,l_k,m_k}(\rho,\phi)\cdot\mathbf{z}\,\mathrm{d}A = 2a_{l_km_k}N_{l_km_k}\end{aligned} \tag{7.145}$$

Substituting Equations (7.144) and (7.145) into Equation (7.143) gives the requested expression for the modal amplitude a_{l_k,m_k}:

$$a_{l_k m_k} = \frac{1}{2N_{l_k m_k}} \int_{A_\infty} \left[\mathbf{E}_s(\rho,\phi) \times \mathbf{H}^*_{t,l_k,m_k}(\rho,\phi)\right] \cdot \mathbf{z}\, dA \tag{7.146}$$

The modal amplitude a_{lm} of the LP_{lm} mode excited by the given electric field $\mathbf{E}_s(\rho,\phi)$ is given by the overlapping integral in Equation (7.146). The mode is assumed to be power-normalized according to Equations (7.132).

7.3.5.1 Weakly Guiding Fibers

In the following, some simplifications are considered of the overlapping integral (7.146) due to weakly guiding fiber approximation. The definition of the power normalization constant N_{lm} is given in Equation (7.127). Using the approximate expressions (7.73) valid for weakly guiding fibers gives the following vector representation of the transversal magnetic field component $\mathbf{H}_{t,lm}$ in terms of the cross-related transversal electric field component $\mathbf{E}_{t,lm}$:

$$\mathbf{H}_{t,lm}(\rho,\phi) \cong \frac{n_{1,2}}{Z_0}\mathbf{z} \times \mathbf{E}_{t,lm}(\rho,\phi) \tag{7.147}$$

Figure 7.44 shows the vector relationships among electric and magnetic transversal field components under the weakly guiding fiber approximation.

Substituting Equation (7.147) into Equation (7.127) gives the normalization constant under the paraxial approximation:

$$N_{lm} \equiv \frac{n_{1,2}}{2Z_0} \int_{A_\infty} \left\{\mathbf{E}_{t,lm}(\rho,\phi) \times \left[\mathbf{z} \times \mathbf{E}^*_{t,lm}(\rho,\phi)\right]\right\} \cdot \mathbf{z}\, dA \tag{7.148}$$

This vector form is easy to solve: first the transversal unit vector **e** for the electric field is introduced. Since **e** lies on the transversal plane by definition, the vector identity $\mathbf{e} \times (\mathbf{z} \times \mathbf{e}) = \mathbf{z}$ is formed and

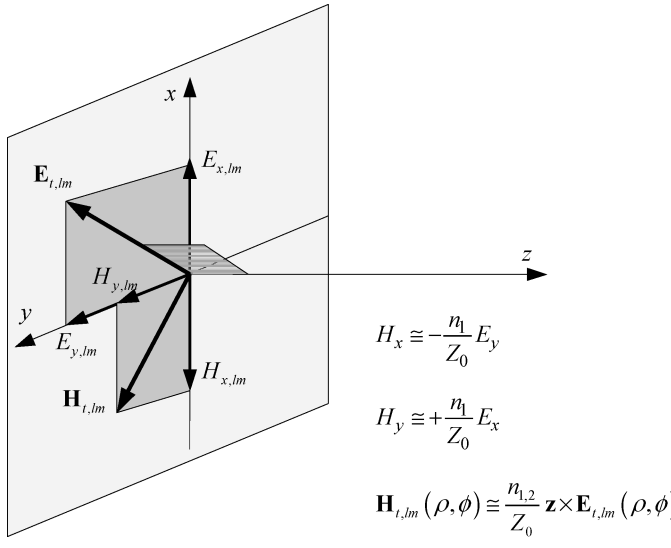

Figure 7.44 Vector relations between transversal magnetic and electric components under the weakly guiding fiber approximation

the integrand reduces to the square modulus of the transversal electric field:

$$\mathbf{E}_{t,lm}(\rho,\phi)\times\left[\mathbf{z}\times\mathbf{E}^{*}_{t,lm}(\rho,\phi)\right]\cdot\mathbf{z}=|\mathbf{E}_{t,lm}(\rho,\phi)|^{2}$$

The normalization constant then assumes the following simpler expression:

$$N_{lm}\equiv\frac{n_{1,2}}{2Z_0}\int_{A_\infty}|\mathbf{E}_{t,lm}(\rho,\phi)|^{2}\,\mathrm{d}A \tag{7.149}$$

Under the paraxial approximation, the modal amplitude in Equation (7.146) can be expressed in terms of the electric field only. To this purpose, the approximated transversal component of the magnetic field in Equation (7.147) is substituted into Equation (7.146), and the approximated expression of the normalization constant is used in Equation (7.149):

$$a_{lm}=\frac{\int_{A_\infty}\left[\mathbf{E}_{\mathrm{s}}(\rho,\phi)\times\mathbf{z}\times\mathbf{E}^{*}_{t,lm}(\rho,\phi)\right]\cdot\mathbf{z}\,\mathrm{d}A}{\int_{A_\infty}|\mathbf{E}_{t,lm}(\rho,\phi)|^{2}\,\mathrm{d}A} \tag{7.150}$$

The expression of the modal amplitudes just derived is meaningful and at the same time has a simple structure. It requires a knowledge of the transverse component of the modal electric field and the exciting electric field. Explicit fiber parameters, such as refractive indices and the core diameter, are not involved. Once the source field $\mathbf{E}_{\mathrm{s}}(\rho,\phi)$ is given, the modal amplitude a_{lm} depends exclusively on the transversal component $\mathbf{E}_{t,lm}(\rho,\phi)$ of the modal electric field. Equation (7.128) gives the expression of the power carried by the LP_{lm} mode as the product of the square modulus of the amplitude coefficient and the power normalization constant. The explicit expression of the modal power has been found from Equations (7.149) and (7.150) as follows:

$$P_{lm}=\frac{n_{1,2}}{2Z_0}\frac{\left|\int_{A_\infty}\left[\mathbf{E}_{\mathrm{s}}(\rho,\phi)\times\mathbf{z}\times\mathbf{E}^{*}_{t,lm}(\rho,\phi)\right]\cdot\mathbf{z}\,\mathrm{d}A\right|^{2}}{\int_{A_\infty}|\mathbf{E}_{t,lm}(\rho,\phi)|^{2}\,\mathrm{d}A} \tag{7.151}$$

According to Equation (7.129), the total power carried by the bound modes is given by summing over all the allowed modes contribution:

$$P_{\mathrm{b}}=\frac{n_{1,2}}{2Z_0}\sum_{l,m}\frac{\left|\int_{A_\infty}\left[\mathbf{E}_{\mathrm{s}}(\rho,\phi)\times\mathbf{z}\times\mathbf{E}^{*}_{t,lm}(\rho,\phi)\right]\cdot\mathbf{z}\,\mathrm{d}A\right|^{2}}{\int_{A_\infty}|\mathbf{E}_{t,lm}(\rho,\phi)|^{2}\,\mathrm{d}A} \tag{7.152}$$

It is noted that if each mode is normalized according to Equations (7.132), the power it brought coincides with the square modulus of the modal amplitude and that the sum over all of them gives the total bound power. In some applications, it is convenient to refer to the unit normalized source power, leading to the condition

$$P_{\mathrm{b}}=\sum_{l,m}|a_{lm}|^{2}=1 \tag{7.153}$$

7.3.6 Source Field

The expression of the modal amplitude derived in the previous section depends on the source electric field vector $\mathbf{E}_{\mathrm{s}}(\rho,\phi)$. In this section, some properties and modeling issues of the source field will be discussed.

The first condition to be satisfied regards the boundary condition for the transversal component of the electric field at the launching section. Boundary conditions for the electromagnetic field require the continuity of the transversal component of the electric field in the absence of any surface charge. This leads to the continuity of the transversal component of the refracted source electric field $\mathbf{E}_{\mathrm{s}}(\rho,\phi)$ with the transversal component $\mathbf{E}_{t}(\rho,\phi)$ of the total modal field, including

both bound modes and radiation modes, as reported in the field expansion (7.121):

$$\begin{aligned}\mathbf{E}_t(\rho,\phi) &= \mathbf{E}_{t,\mathrm{b}}(\rho,\phi) + \mathbf{E}_{t,\mathrm{rad}}(\rho,\phi) = \sum_{l,m} a_{lm}\mathbf{E}_{t,lm}(\rho,\phi) + \mathbf{E}_{t,\mathrm{rad}}(\rho,\phi) \\ \mathbf{H}_t(\rho,\phi) &= \mathbf{H}_{t,\mathrm{b}}(\rho,\phi) + \mathbf{H}_{t,\mathrm{rad}}(\rho,\phi) = \sum_{l,m} a_{lm}\mathbf{H}_{t,lm}(\rho,\phi) + \mathbf{H}_{t,\mathrm{rad}}(\rho,\phi)\end{aligned} \tag{7.154}$$

In order to proceed with the calculation of the refracted (transmitted) component of the source field $\mathbf{E}_\mathrm{s}(\rho,\phi)$ into the fiber regions (core and cladding), it is convenient to assume the following simplifications:

1. The source power flow $\mathbf{S}_\mathrm{s}(\rho,\phi)$ is aligned along the fiber axis, leading to the normal incidence conditions:
$$\mathbf{S}_\mathrm{s} = \tfrac{1}{2}\mathrm{Re}\,(\mathbf{E}_\mathrm{s} \times \mathbf{H}_\mathrm{s}) = |\mathbf{S}_\mathrm{s}|\mathbf{z} \tag{7.155}$$
2. The source field is approximated by means of local plane waves.
3. Indicating the refractive indices by n_0 and n_1 respectively of the launching medium and the fiber core, and neglecting the fraction of the power source coupled into the cladding, the refracted (transmitted) component $\mathbf{E}_\mathrm{s}^\mathrm{tr}(\rho,\phi)$ of the source electric field $\mathbf{E}_\mathrm{s}(\rho,\phi)$ is given by the Fresnel relationships for normal incidence:
$$\begin{aligned}\mathbf{E}_\mathrm{s}^\mathrm{tr}(\rho,\phi) &= \frac{2n_0}{n_0+n_1}\mathbf{E}_\mathrm{s}(\rho,\phi) \\ \mathbf{H}_\mathrm{s}^\mathrm{tr}(\rho,\phi) &= \frac{2n_1}{n_0+n_1}\mathbf{H}_\mathrm{s}(\rho,\phi)\end{aligned} \tag{7.156}$$
4. The contribution of the excited radiation mode is negligible with respect to the contribution of the transversal component of the total bound electric field:
$$\mathbf{E}_\mathrm{rad}(\rho,\phi) \ll \mathbf{E}_{t,\mathrm{b}}(\rho,\phi) \tag{7.157}$$

Due to the normal incidence assumption, the incident electric field and the refracted electric field lie completely on the transversal fiber cross-section. In conclusion, from Equations (7.154), (7.156) and (7.157), the continuity of the transversal component of the electric field at the launching fiber cross-section leads to the following equation:

$$\mathbf{E}_{t,\mathrm{b}}(\rho,\phi) = \sum_{l,m} a_{lm}\mathbf{E}_{t,lm}(\rho,\phi) \cong \frac{2n_0}{n_0+n_1}\mathbf{E}_\mathrm{s}(\rho,\phi) \tag{7.158}$$

Once the source electric field lying in the fiber transverse plane has been approximated, without losing generality, it can be assumed that it is linearly polarized along one of the two coordinate axes. According to the local plane wave assumption, the source magnetic field will be aligned along the complementary axis and the source power flow will be directed along the fiber axis in the z direction.

7.3.6.1 Linear Polarized Source: x Axis

If the source electric field is linearly polarized along the x axis $\mathbf{E}_\mathrm{s}(\rho,\phi) = E_\mathrm{s}(\rho,\phi)\mathbf{x}$, the general expression for the modal amplitudes in Equation (7.150) becomes

$$a_{lm} = \frac{\int_{A_\infty}\left[E_\mathrm{s}(\rho,\phi)\mathbf{x}\times\mathbf{z}\times\mathbf{E}_{t,lm}^*(\rho,\phi)\right]\cdot\mathbf{z}\,\mathrm{d}A}{\int_{A_\infty}|\mathbf{E}_{t,lm}(\rho,\phi)|^2\,\mathrm{d}A} \tag{7.159}$$

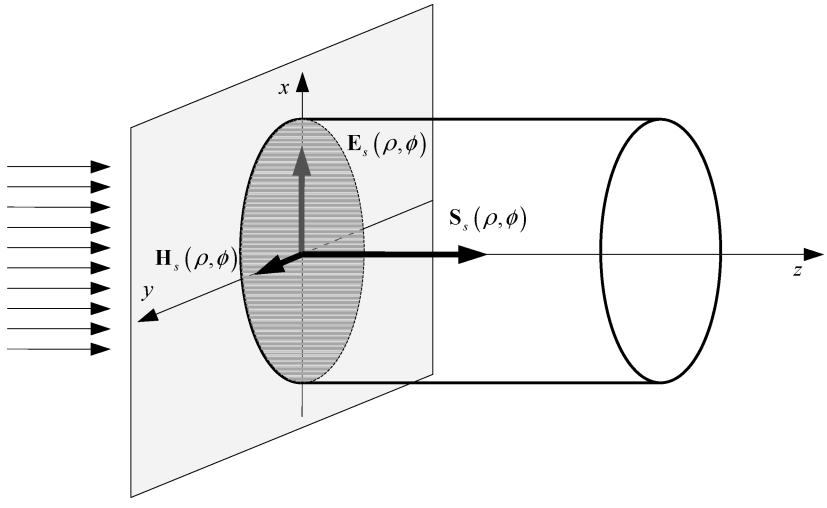

Figure 7.45 Source field at the launching section as assumed in the text. The electric field lies completely in the fiber cross-section and is oriented along the x axis. The source field has been modeled as a local plane wave in the TEM configuration with the magnetic field oriented along the y axis

To solve the vector product in the integrand only the basic unit vector relationships in Cartesian reference system are needed. Since the generic modal electric field $\mathbf{E}^*_{t,lm} = E^*_{x,lm}\mathbf{x} + E^*_{y,lm}\mathbf{y}$ lies in the transverse plane by definition, the vector product in Equation (7.159) becomes

$$\mathbf{x} \times \mathbf{z} \times (E^*_{x,lm}\mathbf{x} + E^*_{y,lm}\mathbf{y}) = \mathbf{x} \times (E^*_{x,lm}\mathbf{y} - E^*_{y,lm}\mathbf{x}) = E^*_{x,lm}\mathbf{z} \tag{7.160}$$

The expression of the modal amplitudes a_{lm} for a linearly polarized and x-oriented source electric field is

$$\mathbf{E}_s(\rho,\phi) = E_s(\rho,\phi)\mathbf{x} \Rightarrow a_{lm} = \frac{\int_{A_\infty} E_s(\rho,\phi)E^*_{x,lm}(\rho,\phi)\,\mathrm{d}A}{\int_{A_\infty} |\mathbf{E}_{t,lm}(\rho,\phi)|^2\,\mathrm{d}A} \tag{7.161}$$

It is relevant to note that the x-polarized source electric field requires only the x component of the modal electric field for the calculation of the corresponding modal amplitude. Figure 7.45 shows the geometry involved at the launching section for the linear polarized electric field along the x axis.

7.3.6.2 Linear Polarized Source: *y* Axis

The complementary case of linear polarization along the y axis can be solved in a very similar way. If the source electric field is linearly polarized along the y axis $\mathbf{E}_s(\rho,\phi) = E_s(\rho,\phi)\mathbf{y}$, the expression for the modal amplitudes in Equation (7.150) becomes

$$a_{lm} = \frac{\int_{A_\infty} \left[E_s(\rho,\phi)\mathbf{y} \times \mathbf{z} \times \mathbf{E}^*_{t,lm}(\rho,\phi)\right] \cdot \mathbf{z}\,\mathrm{d}A}{\int_{A_\infty} |\mathbf{E}_{t,lm}(\rho,\phi)|^2\,\mathrm{d}A} \tag{7.162}$$

The generic modal electric field $\mathbf{E}^*_{t,lm} = E^*_{x,lm}\mathbf{x} + E^*_{y,lm}\mathbf{y}$ lies in the transverse plane by definition and the vector product in Equation (7.162) becomes

$$\mathbf{y} \times \mathbf{z} \times (E^*_{x,lm}\mathbf{x} + E^*_{y,lm}\mathbf{y}) = \mathbf{y} \times (E^*_{x,lm}\mathbf{y} - E^*_{y,lm}\mathbf{x}) = E^*_{y,lm}\mathbf{z} \tag{7.163}$$

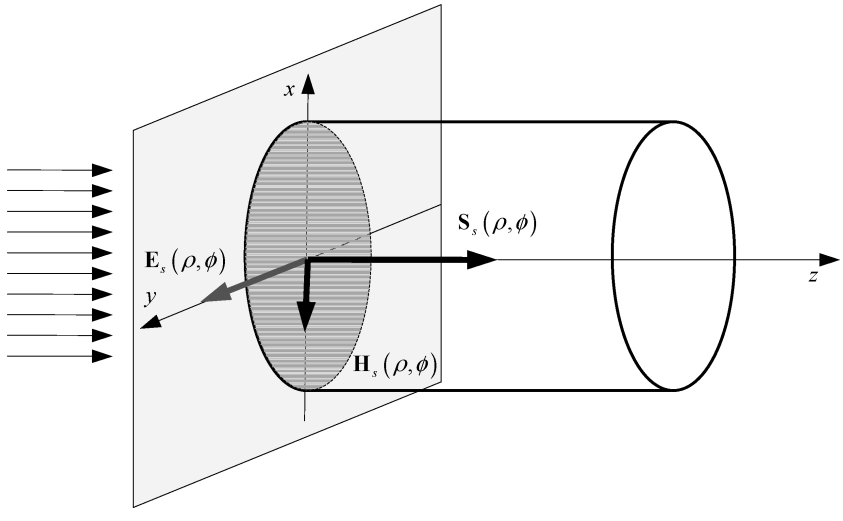

Figure 7.46 Source field at the launching section as assumed in the text. The electric field lies completely in the fiber cross-section and is oriented along the y axis. The source field has been modeled as a local plane wave in the TEM configuration with the magnetic field oriented along the x axis in the negative direction

The modal amplitudes a_{lm} for a linearly polarized and y-oriented source electric field assume the following form:

$$\mathbf{E}_{\mathrm{s}}(\rho,\phi) = E_{\mathrm{s}}(\rho,\phi)\mathbf{y} \Rightarrow a_{lm} = \frac{\int_{A_\infty} E_{\mathrm{s}}(\rho,\phi)E^*_{y,lm}(\rho,\phi)\,\mathrm{d}A}{\int_{A_\infty} |\mathbf{E}_{t,lm}(\rho,\phi)|^2\,\mathrm{d}A} \tag{7.164}$$

In conclusion, the same relationship was found between the orientation of the linearly polarized source and the transversal component of the electric field involved in the integral expression of the modal amplitude. However, the general linear polarization state can always be decomposed into the sum of the contributions of the x-axis and y-axis oriented linear polarizations. This generalizes the two cases considered above. Depending on the linear polarization state of the light source, only one of the two possible modal field solutions will therefore be excited. Stated differently, this means that assuming the source electric field is linearly polarized along the x axis, only the x component of each modal field will be engaged by the source power transfer. In this case, the y components of the modal fields will never take part to the source-to-fiber energy transfer.

Figure 7.46 shows the geometry involved at the launching section for the linear polarized electric field along the y axis. Further discussions on the polarization-dependent launching effects will lead to interesting theoretical results about impulse response dependencies on the input polarization fluctuation. However, a detailed discussion of these aspects is beyond the scope of this book and the reader is referred to literature that is more specialized.

7.4 Conclusions

This chapter dealt with three major topics of the multimode optical fiber theory, namely the impulse response, the modal theory of the step-index fiber and the mode power and launch conditions. All three arguments would require a more complete treatment and it has not been the intention here to give an exhaustive coverage of these fields. The relationship between the modal impulse response and the frequency response is a central issue in multigigabit transmission engineering using

multimode fiber links. Due to the multipath impulse response characteristic, the simple bandwidth cut-off concept is no longer valid to predict system performances. Depending on the group delay distribution and on the source excitation, very different impulse responses are achievable by the same multimode fiber sample. These impulse responses include precursor, postcursor or even dual-peak balanced impulse responses.

In order to have a clear picture of the modal structure and composition of the multimode fiber, the simple step-index profile has been analyzed and the filed structure presented by means of a computed filed calculation based on Matlab® 7.0.2. The results show clearly how the mode structure complexity increases as the mode order increases, showing different radial and azimuth symmetries. A discussion of the boundary conditions and allowable field solution leads to the concepts of the eigenvalue equation and linearly polarized modes.

The third section dealt with some fundamental properties of waveguide modes, and in particular with the orthogonality property. Using mode orthogonality, the closed form of the modal amplitudes was discussed as relevant to a specified source filed excitation. The modal amplitude calculation is the fundamental issue that needs to be managed in order to design proper launching conditions for achieving multimode impulse response optimization. A brief description of the source polarization and of its effect on mode coupling closes the chapter.

8

The Optical Link Model

Modeling the Optical Channel Behavior for Multigigabit Transmission

8.1 Introduction

This chapter introduces the fundamental assumption regarding the mathematical model of a single-wavelength multimode fiber optical transmission system. The single-mode fiber transmission will not be considered here. As already known, the multimode fiber propagation regime is dominated by the intermodal dispersion due to different group delay distributions among different mode groups. Intermodal dispersion theory allows a simplified approach in comparison to the propagation theory for single-mode optical fiber, leading to a heuristic model based on the differential mode delay (DMD) as the physical phenomenon supporting the characteristic frequency response ripple.

The modeling environment has been developed on Matlab® 7.0.2, Release 14 (The MathWorks Inc., January 2005). The optical fiber transmission system model is continuously upgraded, including the analytical description of major phenomena involved in the multimode fiber link operating at 10GbE standards. Great attention has been devoted to the signal propagation characteristic through the entire optical channel, including the optical transmitter, the multimode fiber, the optical receiver and the ideal linear equalizer. Additive noise sources, signal-dependent noise terms, random jitter and pattern-dependent jitter have been planned in the analytical model of the link simulator in order to complete the transmission system modeling and statistical error performances. However, an analysis of the entire simulation environment, including a detailed description of several mathematical solutions used is beyond the scope of this book and is under consideration for a future book and courses. Nevertheless, in this book some features of the link simulator will be used to show characteristic multimode fiber system behavior, providing a useful reference for a future design comparison.

8.2 System Models and Assumptions

The conventional approach followed in designing the multimode optical fiber link simulator is quite usual for almost every optical fiber communication system. The fiber channel is assumed to be the perturbing medium inserted between the optical transmitter and the ideally matched optical receiver. Before discussing modeling assumptions of real subsystems, which would be demanded

Multi-Gigabit Transmission over Multimode Optical Fibre: Theory and Design Methods for 10GbE Systems Stefano Bottacchi
 ISBN: 0-471-89175-4

of the optical transmitter and the optical receiver, it turns out to be very advisable to discuss briefly the concept of a common reference transmission system.

Everybody dealing with mathematical modeling devoted to the prediction of real system behavior should be aware how of different the real design could be from the ideal transmission system. This is the *a priori* approach needed to have a design improving transmission system. In order to assign a quantitative figure of merit to every designed subsystem, at the beginning the ideal reference subsystem and the proper metrics need to be specified in order to measure the performances. According to these concepts, the first step is to define the mathematical models for each ideal reference subsystem encountered in the transmission system chain.

The ideal reference subsystem should specify the limiting conditions that every real design should approximate in order to achieve ideal performances. Only a continuous improvement in component selection and design architectures could approach that ideal limiting case. Although in practice this condition will never be achieved, from the mathematical modeling point of view, ideal subsystems are the easiest functional blocks to be handled. One fundamental question arising from this approach is the sensitivity of the performances of the ideal reference subsystem to accessible design parameter fluctuations. Sometimes, a great effort in achieving a closer fitting to the idealized subsystem does not correspond to the expected improvement in system performances.

The ideal linear filter equalizer represents an example of an ideal reference subsystem. No matter how severely the pulse dispersion can degrade the information content of the optically transmitted signal, an ideal equalizer can, in principle, recover the requested pulse shaping, providing no intersymbol interference at the decision section port but increasing the input equivalent noise power due to high-frequency boosting. Unfortunately, those simple equalizing functions can never be completely synthesized, leaving some amount of unequalized pulse contribution. They can be accurately approximated by high-order polynomials, leading to higher complexity of the filter topology. In conclusion, even if the signal shaping could be almost recovered by the linear equalization filter, some extra noise will affect the receiving system and unavoidably will add a degradation term to the receiver optical sensitivity.

A similar approach can be used for both the optical transmitter and the optical receiver, defining the corresponding mathematical model of the respective ideal reference subsystem. In the following, some remarks about signal quality and dispersion compensation in the multimode optical fiber link are considered.

8.2.1 Optical Equalization Issues

1. Optical link performances depend on all subsystems cascaded in the transmission path, in particular the transmitter, the fiber and the receiver.
2. In the time domain, the bit error rate (BER) is the most relevant measure of system performances while the eye diagram is the proper representation of the transmission system performances.
3. Statistical analysis of the eye diagram available during the decision section only allows an approximate evaluation of the bit error rate, but provides very useful information about the pulse distortion under random pattern generation.
4. Several factors affect the eye diagram and consequently the transmission system performances. Three major factors are:
   (a) Eye opening: average amplitude and dispersion of the eye diagram evaluated at the decision time instant:
      (i) Bandwidth limitation
      (ii) Intersymbol interference
      (iii) Linearity
   (b) Eye width: average width and dispersion of the eye diagram evaluated at the decision threshold:
      (i) Random jitter: amplitude to phase noise

(ii) Jitter transfer function: clock recovery bandwidth
(iii) Pattern-dependent jitter: decision threshold crossing

(c) Amplitude noise: amplitude random fluctuation of each eye transition due to joint noise processes. Noise fluctuations are usually sampled at the decision time instant:
(i) Additive noise: thermal noise
(ii) Linear signal-dependent noise: shot noise
(iii) Quadratic signal-dependent noise: beat noise

5. Pulse dispersion does not generate noise directly. Pulse dispersion is responsible for the generation of Intersymbol interference (ISI) and hence for the pattern-dependent jitter and amplitude fluctuation contributions.
6. Intersymbol interference and pattern-dependent jitter can be completely recovered by an ideal filter equalizer, but extra equalization noise must be taken into account according to the amount of equalization required and to the equalization architecture adopted.
7. The efficiency or the figure of merit of every equalizer must be evaluated at the optical sensitivity condition. Eye diagram equalization at a higher received power level, where high SNR occurs, is misleading when the recovery of the dispersionless sensitivity value is targeted. The receiver sensitivity defines the minimum signal-to-noise ratio for achieving the required bit error rate for the requested signal quality. The input equivalent noise power at the sensitivity condition defines the noise operating conditions for the dispersion equalizer.
8. If system performances are targeted, the optimum equalizer must be designed in order to minimize the overall sensitivity degradation, and not only to cancel out ISI. This is a very important concept and should be the goal for transmission system equalization.
9. The overall sensitivity degradation under dispersion equalizer operations therefore depends on the amount of residual ISI and on the increase of the system noise bandwidth due to high frequency boosting in the equalization filter section.
10. Residual ISI and enhanced noise bandwidth play a trade-off situation in the architecture and design of the electronic dispersion equalizer. Forcing the residual ISI to zero leads to higher noise power enhancement, although limiting noise power to very low values demands a higher residual ISI. In order to optimize the optical receiver sensitivity in a dispersion channel, some residual ISI can be justified after the electrical equalizer as it can be associated with noise optimized design.

8.2.2 Optical Link Modeling

In the following, a summary of the basic assumptions used to model the optical fiber transmission system is given. The modular modeling approach used throughout the Matlab® 7.0.2 simulation environment allows easy inclusion of every improvement, as soon as a new subsystem model or a new feature becomes available. First, the signal propagation aspects are modeled, including the transmitter, the fiber link and the receiver. The multimode fiber optical transmission system can be conveniently partitioned into the following five blocks:

1. *Electrical pulse pattern generator (PPG).* This unit delivers the pseudo-random binary sequence (PRBS) datastream according to the NRZ pulse format at the selected bit rate. The length of the PRBS datastream determines the low-frequency content of the signal power spectral density and affects the output eye diagram due to pulse response distortion. By definition, the PPG is a linear module. This means that once the source impulse response $x_s(t)$ is known, it can be used to generate the PRBS output sequence by linearly superposing the time-shifted impulse response $x_s(t - kT)$ with the proper PRBS weight coefficient.
2. *Optical transmit unit (OTU).* This unit converts electrical pulses $x_s(t - kT)$ generated by the PPG unit into corresponding optical pulses. From the system design point of view, the OTU includes the optical modulator driver and semiconductor laser. By definition, the OTU is a linear system

converting the input electrical signal amplitude (voltages and currents) into the corresponding optical intensity pulses. No differences are therefore expected between small signal and large signal behavior. The system characterization is completely defined by the impulse response and the corresponding transfer function. One important consequence of the linearity assumption consists of the independence of the optical intensity response to the input level and, to some extent, to the PRBS length.

3. *Optical channel unit (OCU).* This unit represents the optical channel used to transmit information between the optical transmitter and the optical receiver. It includes every optical passive component inserted between the OTU output and the ORU input (see the subsection below) and of course includes the main multimode fiber (MMF) link. A typical OCU structure includes optical connectors with multimode fiber jumpers and the main multimode fiber link. In order to be consistent with the system linearity assumption, the optical channel unit has been assumed to be linear with respect to the optical intensity. Due to multimode propagation, optical connectors are not only involved as they contribute to the power transfer attenuation but they also affect the frequency response of the entire optical channel unit due to the different mode power distribution induced by their mutual misalignment (offset value).
4. *Optical receive unit (ORU).* This unit detects the optical power signal coming from the multimode fiber termination and provides proper electrical signal amplification and filtering. Depending on the frequency response shaping of the electrical receiver, and including the photodetector response, the ORU leads to the concepts of the optical reference receiver, the optical matched receiver and the optical standard receiver, whose definitions are of major importance in order to have clear references but quantitatively different receiver approaches.
   (a) The optical reference receiver performs signal filtering in order to compensate for the optical transmitter pulse through a predefined frequency response. The output of the optical reference receiver provides no intersymbol interference (ISI) signal at the decision section. By definition, the output signal of the optical reference receiver is adaptive and is shaped according to the raised cosine family, independently from the transmit pulse. Consequently, it is not a matched receiver. Due to the analytical nature of the system responses involved, the optical reference receiver represents a mathematical model.
   (b) The optical matched receiver represents the second type of reference receiver. In order to have a noise matched filter and simultaneously to satisfy no intersymbol interference (ISI) at the decision section, the optical matched receiver is no longer adaptive but instead requires knowledge of the proper transmitted optical pulse shape. Assuming the transmitted optical pulse is shaped according to the square root of the raised cosine profile, the optical matched receiver must perform the same square root of the raised cosine profile filtering, achieving at the same time a minimum noise bandwidth and ISI-free signal detection. Due to the analytical nature of the system responses involved, the optical matched receiver represents a mathematical model.
   (c) The optical standard receiver represents the third available reference for the optical receiver and represents a solution closer to the real designed system than the other two reported above. The optical standard receiver is neither adaptive nor matched and consequently it does not have a minimum noise bandwidth and is affected by intersymbol interference at the decision section. It represents the receiver solution designed using standard available filters like the IV-order Bessel–Thompson filter.
5. *Dispersion equalizer unit (DEU).* The detected optical signal, after propagating along the dispersive multimode fiber, presents a large amount of optical pulse broadening and consequently a consistent intersymbol interference pattern. The dispersion equalizer unit must then be added to the transmission system configuration in order to provide signal pulse reshaping and a restored eye diagram at the decision section. In order to achieve this feature, the dispersion equalizer unit must therefore be cascaded at the optical receiver unit, before the signal decision section. Available electronic dispersion compensators (EDCs) are based on a feedforward equalizer (FFE)

implemented by means of a finite impulse response (FIR) filter, followed by a decision feedback equalizer (DFE). These blocks are implemented using digital signal processing technology and they must be supported by proper firmware in order to perform the required operation. The operation principle can be easily understood in terms of a linear filtering performed by the FFE section followed by ISI average value removal operated by the DFE section. Stated in a different way, the adaptive decision threshold follows the optimum detection position according to the estimated ISI value in order to preserve the minimum bit error rate.

However, in the system model being presented, the reference dispersion equalizer unit is represented by the simplest ideal compensator available, namely the ideal inverse linear filter, sometimes called the boosting filter. This filter reaches zero residual error under every input signal condition, providing a theoretically ISI-free signal patter output. Unfortunately, this ideal restoring operation is achieved at the expense of very high and very often unacceptable noise bandwidth enhancement. This is the reason for the development of digital-based EDCs, as briefly depicted above. Nevertheless, the ideal inverse linear filter represents the most suitable reference equalization scheme in order to quantify the figure of merit of any other electronic dispersion equalizer.

Figure 8.1 shows a block diagram of the optical fiber transmission system model.

In the following subsections, a summary is given of the operating principles, the features and the specifications of the multimode fiber transmission system sections briefly introduced above. A more detailed discussion, including mathematical modeling solutions and results, will be presented in the next dedicated sections.

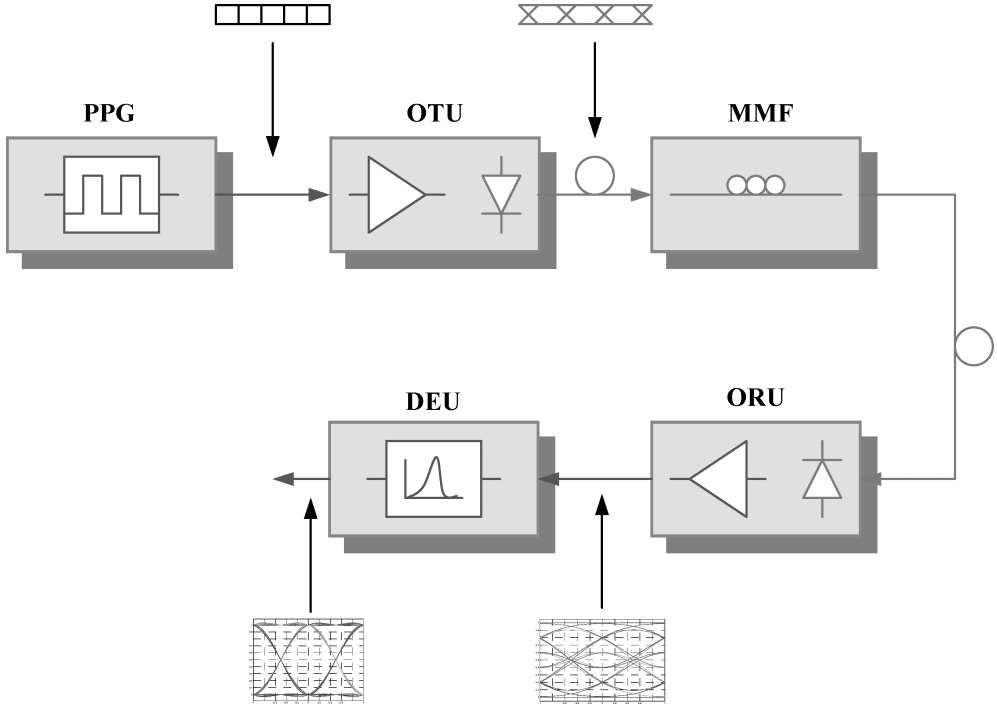

Figure 8.1 Block diagram of the fiber optic transmission system used for the link model. The definition of each subsystem follows in the sections below

8.2.2.1 Pulse Pattern Generator (PPG)

The pulse pattern generator is the signal generation module for the entire transmission system. The signal generation proceeds in two independent blocks, the pulse shaper and the PRBS sequence generator. The PRBS sequence generator provides the Delta sequence feeding the pulse shaper module. The available pulse shapes are listed below:

1. Trapezoid. Trapezoid pulse, with equal rise and fall times. The pulse full-with at half-maximum (FWHM or -3 dB full width) is set equal to the bit time step: $T = 1/B$, where B is the bit rate.
2. Gaussian. The impulse response is normalized with unit energy and the RMS pulse width is defined through the parameter σ_t.
3. Raised cosine. The generated single pulse is shaped using the raised cosine profile with synchronized zero transitions to the given time step. The roll-off coefficient sets the profile shape and the position of zero transitions.
4. Error function. The pulse is given by the analytical time convolution of the trapezoid pulse with a Gaussian pulse. The RMS width of the Gaussian pulse and the transition times of the trapezoid pulse define the error function pulse shape.
5. IV-order Bessel–Thompson. The impulse response is given by the fourth-order Bessel–Thompson filter output when the input stimulus coincides with the delta function. This impulse response is closely related to the measured pulse output from available filters.
6. Delta function. The impulse response is given by the impulsive function (Dirac delta) allowing for the ideal signal source.
7. External downloaded pulse. This feature allows the impulse response to be downloaded directly from PPG measured data as part of the modeling structure.

8.2.2.2 Optical Transmit Unit (OTU)

The optical transmitter is an electrooptic converter (E/O). It converts the electrical input pulse (current or voltages) into the optical output pulse (optical power). The optical transmitter is assumed to be a time-independent and linear E/O system. An electrical input sequence (voltage or current signal) is therefore linearly converted into the same optical power sequence. The optical power output sequence is given by the linear superposition, along the time axis, of the single optical output pulse properly shifted and weighted according to the digital input sequence coefficients. The optical impulse response (W/A or W/V) of the optical transmitter has a unit of optical power-to-electrical amplitude ratio and is modeled according to the following pulse functions:

1. Gaussian. The impulse response is normalized with unit energy and the RMS pulse width defined through the parameter σ_t. The model allows for a complex exponent Gaussian profile by introducing the chirping coefficient α.
2. Nyquist. The impulse response is shaped as the Fourier transform of the square root of the raised cosine frequency response. This model allows for an optical matched receiver, assuming the same filtering in the receiver section.
3. Delta function. The impulse response is given by the impulsive function (Dirac delta), allowing for an ideal response.
4. External downloaded pulse. This feature allows the impulse response to be downloaded directly from the optical transmitter measured data as part of the modeling structure.

According to the pulse pattern generator module, the optical transmitter generates an optical pseudo-random binary sequence (PRBS) according to any of the following lengths available in the PPG module:

$$\text{PRBS:} \quad 2^n - 1, \quad n = 7, 9, 11, 15, 20, 23, 31$$

In the actual model development, the transmitter noise sources and random jitter are neglected. Pattern-dependent jitter is instead automatically included by the PRBS datastream composition.

Relative intensity noise (RIN), mode partition noise (MPN) and reflection noise (RN) are neglected. Phase noise and frequency chirping effects are modeled through the definition of the modulated spectrum linewidth and the chirping coefficient introduction for the Gaussian impulse response. As extensively discussed in the first part of this book, the laser source spectrum slightly limits the propagation performance of MMF, which is much more degraded than by modal delay.

The single optical pulse is normalized with unity energy. Consequently, the optical pulse energy spectrum assumes a unit value at the frequency origin.

8.2.2.3 Optical Channel Unit (OCU)

The optical channel unit includes the entire passive optical network linking the OUT with the ORU. The multimode fiber (MMF) is the principal component of the OCU and is modeled as a time-independent and linear system in the electric field amplitude.

The frequency response of the multimode fiber refers to the transfer function of the optical intensity (W/W). Neglecting any mode coupling, bound fiber modes constitute an orthogonal set for the decomposition of the guided optical power. In addition, the radiated field is orthogonal to any bound mode. Because of the above assumptions, the total guided power is given by the sum of the power carried by each individual mode. Any mode cross-term of the Poynting vector does not contribute to the overall guided power after integration over the infinite fiber cross-section. This is a consequence of the mode orthogonality.

The multimode fiber transfer function is defined according to the intensity of the electromagnetic field. The phase of the transfer function is assumed constant (a linear phase with a null slope leading to an impulse response with a group delay equal to zero). The impulse response of the multimode fiber is modeled by the following pulse functions:

1. Gaussian. The impulse response is normalized with the unit energy and RMS pulse width defined through the parameter σ_t.
2. Delta function. The delta function is an impulse response which is given by the impulsive function (Dirac delta) allowing for ideal fiber response.
3. External downloaded pulse. This feature allows the impulse response to be downloaded directly from the multimode fiber measured data as part of the modeling structure. Of course, pulse de-embedding is needed for a proper impulse response.

Under the phase linearity assumption, the constant group delay therefore coincides with the delay of the center of gravity of the Gaussian impulse response. If not otherwise specified, the group delay time constant will be assumed to be equal to zero. This assumption simply translates the center of the output optical pulse at the time origin.

The bandwidth (BW) of the Gaussian magnitude is defined as the half-width at half-maximum, or equivalently a -3 dB bandwidth of the unilateral frequency response. The fiber attenuation has not been taken into account so far. In this model, there is no specific attenuation for each fiber mode. Each guided mode therefore exhibits the same zero power attenuation $\alpha_{lm} = \alpha = 0$ dB/km.

The effects of source linewidth and of fiber chromatic dispersion are included, assuming first-order pulse broadening using the chromatic dispersion formula (4.120). Chromatic dispersion and the modal bandwidth add quadratically to set the width of the overall Gaussian profile.

8.2.2.4 Optical Receive Unit (ORU)

The optical receive unit terminates the OCU providing optical signal detection and amplification. The ORU is assumed to be linear with the frequency response defined by the following impulse responses:

1. Single pole. This is the simplest receiver impulse response available and assumes a single time constant frequency response. It is important to remember that the phase transfer function follows the inverse tangent of the modulation frequency leading to consistent phase distortion if the cut-off frequency is lower than the required signal frequency content.
2. Gaussian. The impulse response is normalized with the unit energy and RMS pulse width defined through the parameter σ_t.
3. Raised cosine. The impulse is shaped using the Raised cosine profile with synchronized zero transitions to the given time step. The roll-off coefficient sets the profile shape and the position of the zero transitions.
4. IV-order Bessel–Thompson. The optical receiver impulse response is given by the fourth-order Bessel–Thompson filter output when the input stimulus coincides with the delta function. This impulse response is closely related to the measured pulse output from available filters.
5. Nyquist. The impulse response is shaped as the Fourier transform of the square root of the raised cosine frequency response. This model allows the optical matched receiver to assume the same transmitted optical pulse spectrum at the receiving section.
6. Delta function. In the delta function the impulse response is given by the impulsive function (Dirac delta), allowing for an ideal optical receiver response.
7. External Downloaded Pulse. This feature allows the impulse response to be downloaded directly from the optical receiver measured data as part of the modeling structure. Of course, pulse de-embedding is needed for a proper impulse response.

8.2.2.4.1 Optical Reference Receiver (ORR)

Following previous definitions, the optical reference receiver (ORR) performs first the linear conversion of the optical intensity to the electrical current (O/E). The recovered electrical pulse is then filtered according to the receiving filter listed above. By definition, the optical reference receiver operates adaptive signal filtering to provide the ideal raised cosine output pulse, with no intersymbol interference (ISI).

The optical reference receiver is designed according to the back-to-back link configuration, without the optical fiber transmission contribution. According to the transmitted optical pulse, the receiving filter produces the raised cosine pulse output in the back-to-back system configuration. The shaping factor m of the raised cosine pulse is adjustable between 0 and 1, providing increasing output pulse smoothness.

According to the linearity assumptions, any input PRBS sequence of delta impulses will generate, at the output of the optical reference receiver, the corresponding PRBS sequence of raised cosine pulses without any intersymbol interference (ISI = 0). The optical reference receiver (ORR) so far considered has a noise bandwidth which of course depends on the transmitted pulse shape.

8.2.2.4.2 Optical Matched Receiver (OMR)

The optical reference receiver (ORR) presents one characteristic difference from the optical matched receiver (OMR). Precisely, the optical matched receiver provides, at the same time, both no ISI and the minimum noise bandwidth available for the given pulse and transmission rate (maximum SNR). To achieve simultaneously no ISI and optimum SNR, the optical matched receiver needs the transmitted optical pulses to be properly shaped, not just like a simple trapezoid or Gaussian, but instead they must have a profile coincident with the square root of the corresponding raised cosine function.

In this sense, the optical reference receiver (ORR) is suboptimal with respect to the optical matched receiver (OMR), providing no ISI but in general a wider noise bandwidth with suboptimal SNR and related worse BER performances.

8.2.2.5 Dispersion Equalizer Unit (DEU)

Once multimode fiber has been added between the transmitter and the receiver, extra pulse broadening will occur. Depending on the excited fiber frequency response, pulse dispersion can induce

weak or severe eye closure, with relevant consequences for transmission performances. The dispersion equalizer unit (DEU) is targeted to eliminate or at least reduce system impairments due to an insufficient fiber link bandwidth.

According to the definitions of either the optical reference receiver or the optical matched receiver, the reference electronic dispersion Equalizer (REDC) is defined as the ideal linear inverse filter whose frequency response coincides with the reciprocal of the frequency response of the multimode fiber link. This gives the zero forcing equalization (ZFE) condition under the assumption of using either ORR or OMR in the back-to-back mode.

Once REDC has been added to either ORR or OMR, the proper output pulse will be completely recovered, giving an ISI-free output eye diagram. The above conclusions are valid in principle for any amount of pulse broadening and consequent eye closure. The REDC equalizer can recover in principle any amount of fiber dispersion. Throughout this book, REDC will be used as the reference structure for comparing different equalization architectures.

In contrast to the ideal equalization of REDC is the amount of extra noise bandwidth that the equalizer drags into the receiving system. Nevertheless, the reference electronic dispersion compensation represents a suitable reference term to compare the effectiveness of any real implementation of EDC. The phase of the REDC is assumed to be linear, according to the linear phase transfer function of the multimode fiber. Slight deviations from the linearity of the phase transfer function of the REDC makes noticeable distortions of the recovered output eye diagram.

8.3 The Optical Transmitter

The optical fiber transmitter can be specified, using the following three basic characteristics, independently from any system architecture and implemented technology:

1. The signal shaping obtained in the time domain in response to the random data pattern for a predefined transmission format (NRZ (no return to zero), RZ (return to zero), CMI (coded mark inversion), etc.).
2. The modulated optical spectrum, which differs consistently from the CW optical spectrum due to several phenomena involved during the light modulation process. The frequency chirping is the instantaneous frequency deviation during modulation of the light intensity.
3. The noise characteristic of the modulated optical signal. The optical noise contribution can be additive or proportional to the modulating signal. In the case of additive noise, the noise power is independent of the signal power (modulation depth) and this contribution reduces proportionally by increasing the signal power. In the case of signal-dependent noise, the noise source is related (linear, quadratic, etc.) to the signal power, depending on the physical phenomena involved.

The following derivation of the transmitter model will focus on the mathematical description of the signal shaping in both the time and frequency domains. Noise characteristics will be included at the receiver section, avoiding modeling the optical signal directly as a true random process. Noise effects will therefore be included as perturbations of the received optical signal.

The optical transmitter can be represented by two main blocks (see Figure 8.2)

1. The laser diode driver (LDD) feeds the laser diode with the required biasing and modulation currents. The input of the laser driver is connected to the pulse pattern generator output and is fed by the electrical datastream.
2. The laser diode (LD) converts the modulated injection current into the corresponding optical pulse at the selected wavelength.

The optical transmitter presents electrical and optical characteristics that can in principle be specified separately. However, it is important to remark that both electro-optical characteristics

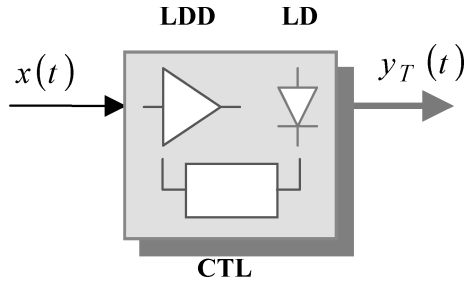

Figure 8.2 Block diagram of the optical transmitter including the laser diode driver (LDD) and the semiconductor laser (LD). The control circuit (CTL) provides optimum biasing and driving conditions for the semiconductor laser diode

affect the transmission performances in optical fibers. The interaction between electrical and optical characteristics of the transmitter increases with the transmission system performances, demanding a more accurate design and parameter specifications.

The following sections will focus on the modeling issues and specifications of the modulated signal of the optical transmitter. In particular, two simple modeling waveforms, namely the Trapezoid and error function light pulses, will be discussed.

8.3.1 Trapezoid Optical Pulse

The transmitter is assumed to generate optical pulses whose intensity envelope is shaped according to a symmetric trapezoid waveform. Each optical pulse is generated by the laser source in response to a single square wave stimulus, as is reported in the Figure 8.3.

The filtering performed by the optical transmitter is easily modeled using the time domain convolution between the input electrical pulse $x(t)$ and the transmitter impulse response $h_T(t)$. In order to validate this procedure the following two assumptions must be fulfilled:

1. The electro-optical conversion performed by the optical transmitter is a linear operation.
2. The optical transmitter is a time-invariant system. Its performances are assumed constant versus time.

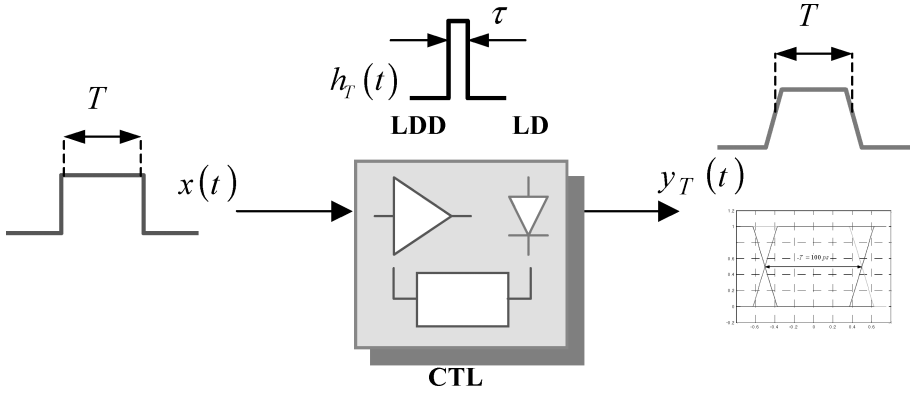

Figure 8.3 Schematic representation of the electro-optic conversion performed by the optical transmitter. The ideal square electrical pulse is converted into the optical intensity pulse. The optical pulse envelope is assumed to fit a symmetric trapezoid shape

It will be seen in the following section that, for simplicity, the electrical pulse pattern generator (PPG) is assumed to provide ideal square pulses of duration T equal to the unity time step, with instantaneous rise and fall times. According to the time convolution theorem for linear and time invariant systems, the output pulse is given by the time convolution of the input pulse with the impulse time response. In order to have a trapezoid pulse at the transmitter output, the impulse response $h_T(t)$ of the electrical to optical (E/O) converter must be modeled as an ideal square pulse of duration τ equal to the required transition time of the trapezoid output pulse. Assuming a smoother time response, such as the Gaussian impulse response, it is possible to model a large variety of optical pulses with rounded wavefronts. In the following, reference will first be made to the simplest trapezoid output pulse as a valid first-order modeling for real optical pulses.

8.3.1.1 Time Representation

The E/O converter impulse response is shown in Figure 8.4, defined by

$$h_T(t) = \begin{cases} \dfrac{1}{\tau}, & |t| \le \dfrac{\tau}{2} \\ 0, & |t| > \dfrac{\tau}{2} \end{cases} \tag{8.1}$$

The ideal square pulse generated by the PPG is shown in Figure 8.5, defined by

$$x(t) = \begin{cases} \dfrac{1}{T}, & |t| \le \dfrac{T}{2} \\ 0, & |t| > \dfrac{T}{2} \end{cases} \tag{8.2}$$

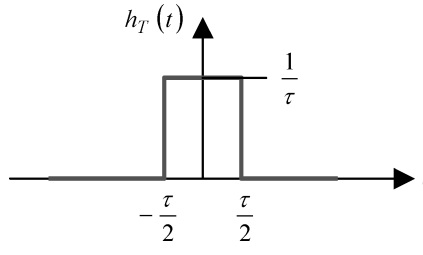

Figure 8.4 Ideal impulse response of the electro-optical converter. The pulse duration τ coincides with the symmetrical rise and fall times of the trapezoid output pulse $t_r = t_f = \tau$ evaluated between 0 and 100 % of the pulse amplitude. The impulse response is normalized with unity energy

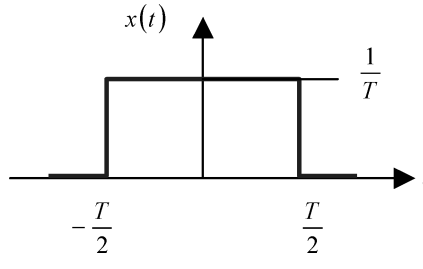

Figure 8.5 Ideal square pulse generated by the PPG. The pulse duration T coincides with the unity time step of the transmitted bit rate $T = 1/B$. The impulse response is normalized with unity energy

Referring to Figures 8.4 and 8.5 and to the analytical pulse definitions of Equations (8.1) and (8.2), the output pulse $y_T(t)$ is given by the following time convolution:

$$y_T(t) = h_T(t) * x(t) = \int_{-\infty}^{+\infty} x(\tau) h_T(t-\tau)\,d\tau = \frac{1}{T}\int_{-T/2}^{+T/2} h_T(t-\tau)\,d\tau \tag{8.3}$$

Due to the time symmetry of both convolved impulses, the output pulse exhibits the same symmetry. Solving the integral for the positive time axis gives the well-known trapezoid pulse:

$$\begin{aligned} &0 \le t \le \frac{T-\tau}{2}, && y_T(t) = \frac{1}{T} \\ &\frac{T-\tau}{2} \le t \le \frac{T+\tau}{2}, && y_T(t) = -\frac{1}{T\tau}\left(t - \frac{T+\tau}{2}\right) \\ &t \ge \frac{T+\tau}{2}, && y_T(t) = 0 \end{aligned} \tag{8.4}$$

Figure 8.6 shows the plot of the trapezoid optical pulse $y_T(t)$ available at the transmitter output assuming the modeling condition reported above. The trapezoid profile refers to the envelope of the optical intensity represented in the time domain and consequently the unit of measure is J/s = W. The energy W_T (J) of the output optical pulse in the time domain is immediately computed by calculating the trapezoid pulse area:

$$W_T = \int_{-\infty}^{+\infty} y_T(t)\,dt = \frac{1}{2}\frac{1}{T}[(T+\tau) + (T-\tau)] = 1 \tag{8.5}$$

8.3.1.2 Frequency Representation

The convolution theorem allows immediate frequency representation of the envelope of the output pulse. Indicating with $Y_T(f)$ the frequency spectrum of the intensity of the transmitted optical pulse, from Equation (8.3)

$$Y_T(f) = X(f)H_T(f) \tag{8.6}$$

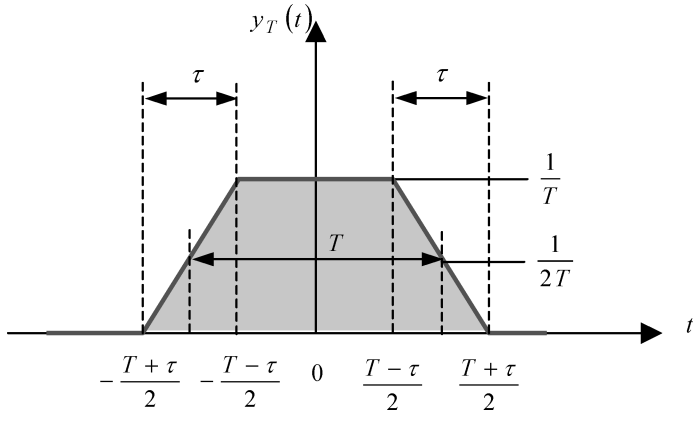

Figure 8.6 Optical pulse generated by the electro-optical converter when stimulated by the ideal square pulse from the PPG. The pulse duration measured as full-width at half-maximum coincides with the unity time step T of the transmitted bit rate $T = 1/B$. The rise and fall times are equal to the duration τ of the ideal square impulse response of the E/O unit: $t_r = t_f = \tau$. The output optical pulse still has unit energy

Equations (8.1) and (8.2) give the transfer function and the frequency representation respectively of the corresponding square pulses:

$$X(f) = \frac{\sin(\pi f T)}{\pi f T} \tag{8.7}$$

$$H_{\mathrm{T}}(f) = \frac{\sin(\pi f \tau)}{\pi f \tau} \tag{8.8}$$

Equation (8.6) gives the well-known frequency representation of the trapezoid optical pulse emitted from the transmitter output:

$$Y_{\mathrm{T}}(f) = \frac{\sin(\pi f T)}{\pi f T} \frac{\sin(\pi f \tau)}{\pi f \tau} \tag{8.9}$$

What is the physical meaning of the function $Y_{\mathrm{T}}(f)$ that has just been derived? The transmitter output pulse $y_{\mathrm{T}}(t)$ has the meaning of the optical intensity envelope versus time and has the dimension of the optical power. The Fourier transform $Y_{\mathrm{T}}(f)$ therefore assumes the meaning of the spectral density of the optical power envelope and has the dimension of W/Hz = J:

$$y_{\mathrm{T}}(t) \longrightarrow \mathrm{W} : \text{power}$$

$$y_{\mathrm{T}}(\mathrm{f}) \longrightarrow \mathrm{W/Hz} = \mathrm{W\ s} = \mathrm{J} : \text{energy}$$

Due to pulse normalization in the time domain, the energy $Y_{\mathrm{T}}(f)$ evaluated at the frequency origin has unity value: $Y_{\mathrm{T}}(0) = 1$. In addition, using the Fourier transform relationship, from Figure 8.6 it can be seen that

$$\int_{-\infty}^{+\infty} Y_{\mathrm{T}}(f)\,\mathrm{d}f = y_{\mathrm{T}}(0) = \frac{1}{T} \longrightarrow \mathrm{W} : \text{power} \tag{8.10}$$

8.3.1.3 Computed Spectrum

In Figure 8.7 the simulated spectra are shown for the trapezoid optical output pulse, according to different rise and fall times. All time parameters are related to the time step T. The logarithmic scale on the ordinate axis refers to the magnitude of the output pulse spectrum. This choice allows representation of the electrical signal spectrum after the photodetection in the optical receiver:

$$|H_{\mathrm{T}}(f)|_{\mathrm{dB}} = 20 \log_{10} |H_{\mathrm{T}}(f)| \tag{8.11}$$

It is evident from the computed spectra that the fastest transition time is associated with the frequency response with the highest peak structure. Smoother transition times have a smoother spectrum, with less high-frequency peak contributions. In order to highlight this behavior, Figure 8.8 shows the magnification of the computed spectra around the first zero at $f_1 = B$. In general, the nth zero is located at $f_n = nB$. It is evident from Figure 8.7 that the major differences in transmitted spectra resulting from different transition times are localized in the higher frequency range, at least beyond the first zero at $f_1 = B$. If it is assumed that the transmission channel bandwidth connected to the transmitter output is limited to about a half bit rate, the detected optical pulse will only be slightly affected by the transition edges of the transmitter output. This consideration should be addressed in choosing carefully high-frequency and expensive laser sources when the band-limited channel effectively drops out of the transmission response.

As expected, the lower spectral content corresponds to the smoother transition in the time domain pulse with $\tau = 50\,\mathrm{ps}$. This means that smoother wavefronts in the optical pulses at the transmitter output will be less distorted by reduced channel bandwidth. At approximately 1.5 times the bit rate frequency, the smoother transition spectrum is almost 10 dB below the steeper transition spectrum.

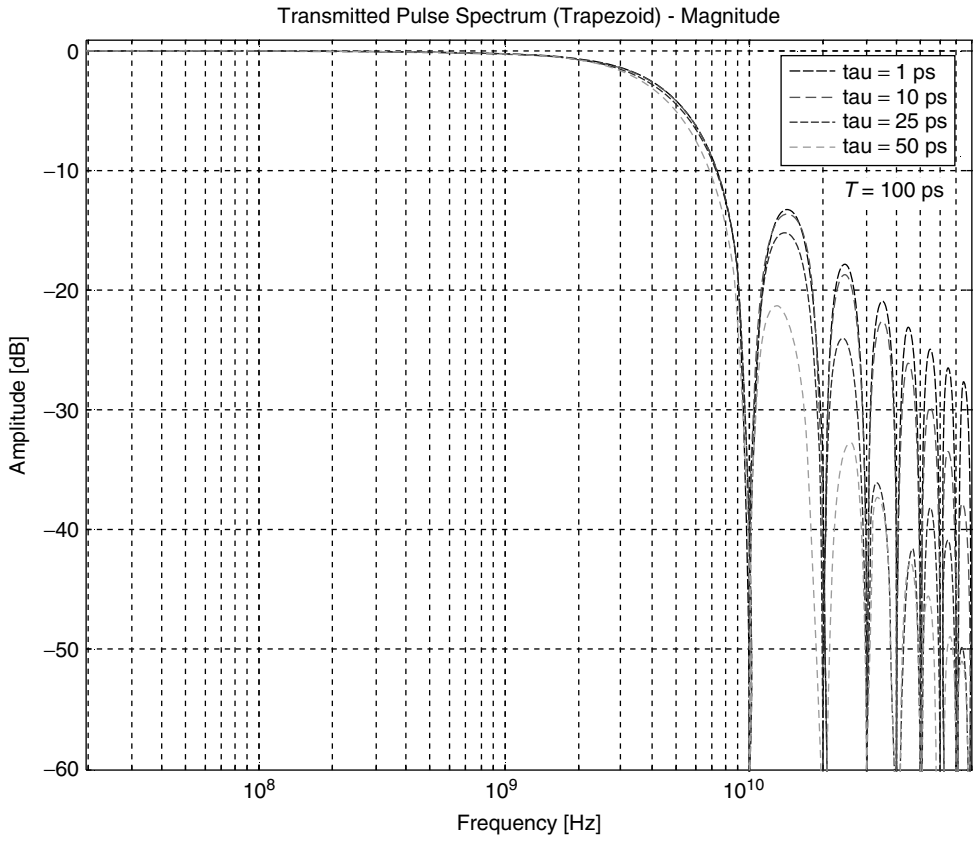

Figure 8.7 Spectrum of the transmitted optical pulse with different but symmetric rise and fall times. The time domain pulse is represented by a symmetric trapezoid of unit energy. The pulses in the time domain have all the same duration measured at half-maximum: FWHM $= T = 100$ ps. As the legend reports, four different rise and fall times have been considered, namely 1 ps, 10 ps, 25 ps and 50 ps

In the example considered, the bit rate is $B = 10$ Gb/s with the NRZ data format. According to the logarithmic scale definition (8.11), the HWHM bandwidth corresponds to -6 dB on the above figure. The half-width at half-maximum (HWHM) bandwidth of the optical trapezoid spectrum ranges between 5.5 GHz and 6.0 GHz, with a slight variation of less than 8 % versus the assumed wavefront transitions.

8.3.1.4 Computed Pulses and Eye Diagrams

In this section, a report is given on the effects of the sampling time resolution on the actual shape of the optical transmitted pulse versus different rise and fall time values. Although this argument deals mainly with the numerical aspects of the optical pulse computer simulation, it gives some interesting overview about frequency domain windowing and related time domain pulse overshooting. In this context, the time sampling resolution is given by the parameter NTS that corresponds to the number of sampling points for every unity time step T. All the following cases refer to the time step $T = 100$ ps. The ripple effect at the transition edge is a clear indication of

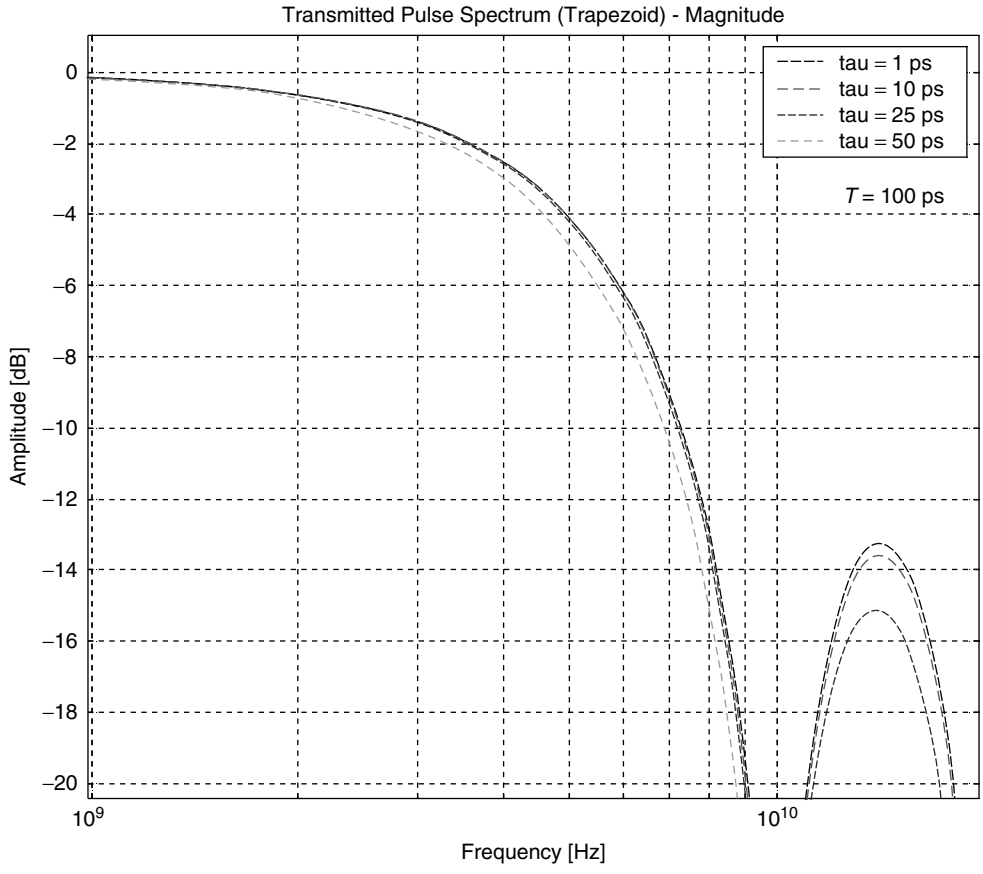

Figure 8.8 Spectrum detail around the first zero for the same cases in Figure 8.7

high-frequency truncation of the pulse spectrum, and is a consequence of the sampling theorem applied to the discrete Fourier transform. For a given sampling resolution, the ripple effect at each transition edge is more evident for faster transition times. This is of course easy to understood due to the extended spectrum occupancy required by the fastest transient time with respect to the same pulse duration but with smoother transitions. In the fastest transition case, the frequency truncation due to the discrete Fourier transform sampling theorem is relatively more effective and determines a stronger pulse ripple.

Figures 8.9 to 8.14 report three different computed trapezoid optical pulses with the same duration measured at FWHM but with increasing transition times. In particular, Figures 8.9 and 8.10 refer to the trapezoidal optical pulse with $T = 100\,\text{ps}$ and $t_r = t_f = 1\,\text{ps}$. Extremely short transition times make the ripple effect clearly visible. Figures 8.11 and 8.12 report the case of longer transition times and a reduction in the intensity ripple is clearly visible. Finally, Figures 8.13 and 8.14 refer to the smoother available transition time, $t_r = t_f = 25\,\text{ps}$. In this case, the intensity ripple is almost negligible and is almost independent from the reported sampling resolution.

To conclude this section, Figures 8.15 and 8.16 show respectively a comparison among several transmitted optical pulses of various relative transition times and the transmitted eye diagram for the particular case $t_r = t_f = 20\,\text{ps}$.

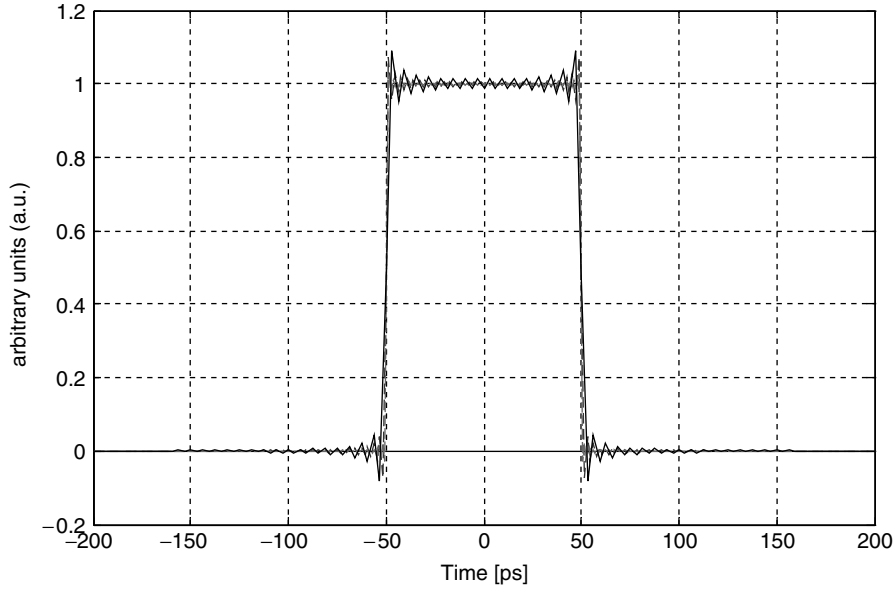

Figure 8.9 Transmitted output pulse of duration FWHM $= T = 100$ ps. The rise and fall times have been set to $t_r = t_f = 1$ ps. Three different sampling resolutions have been adopted to show the effect on the pulse shape. The curves refers to NTS $= 32$ samples per unity time step and NTS $= 64$ and NTS $= 128$ respectively. It is evident that the pulse ripple reduces as the sampling time resolution increases

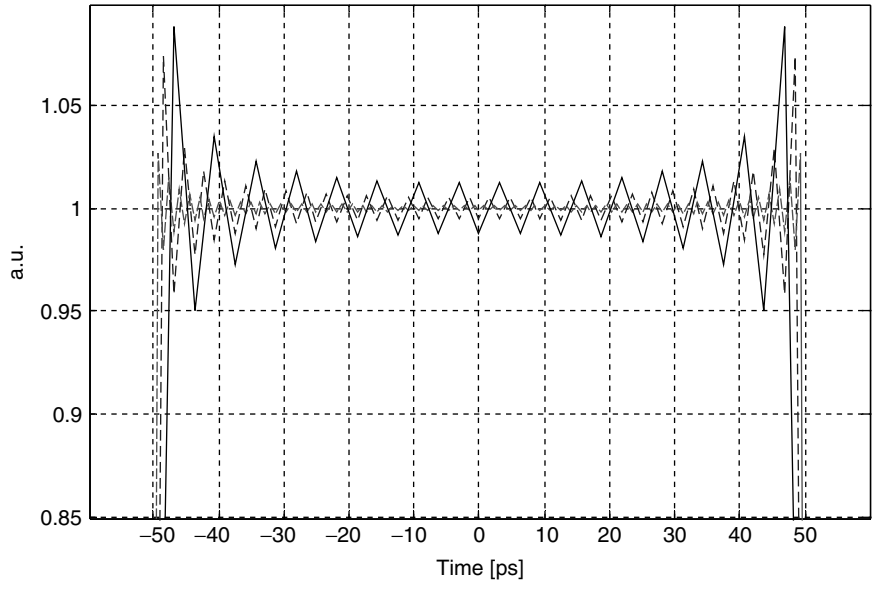

Figure 8.10 A magnified view of the upper power level of the trapezoidal pulse reported in Figure 8.9, using different sampling time resolutions. The curves refer to NTS $= 32$, NTS $= 64$ and NTS $= 128$ respectively

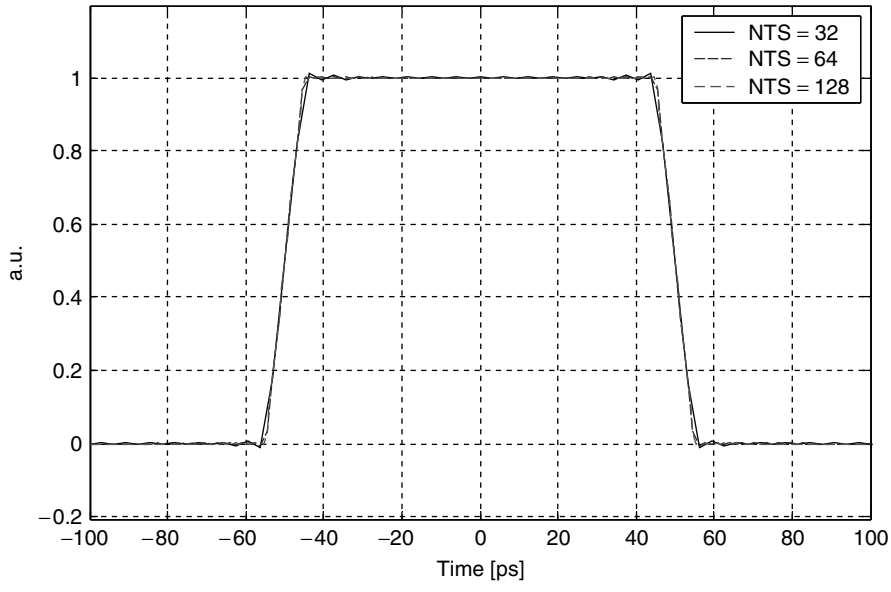

Figure 8.11 Transmitted output pulse with FWHM $= T = 100$ ps. The rise and fall times have been set to $t_r = t_f = 10$ ps. The influence of the sampling time resolution is less relevant to pulse shaping due to a smoother transition time

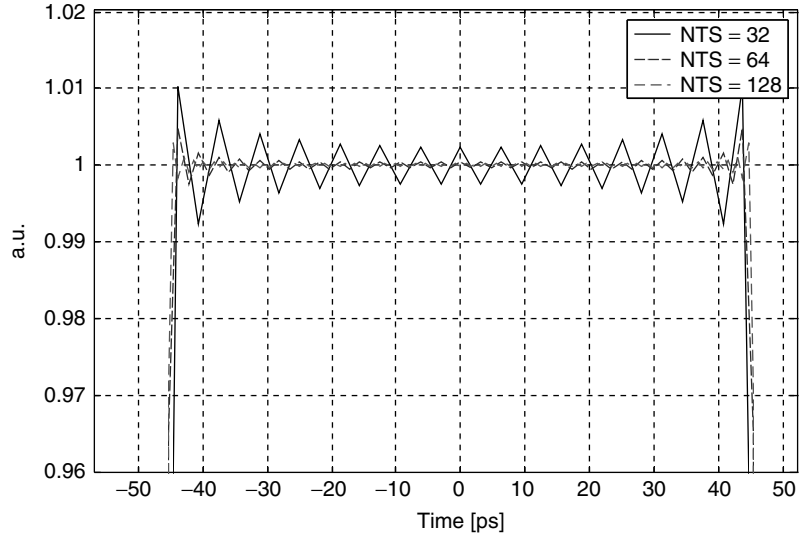

Figure 8.12 Magnification of the high power level of the pulse reported in Figure 8.11. A comparison with Figure 8.9 reveals fewer ripples for any time resolution, due to the smoother transition time

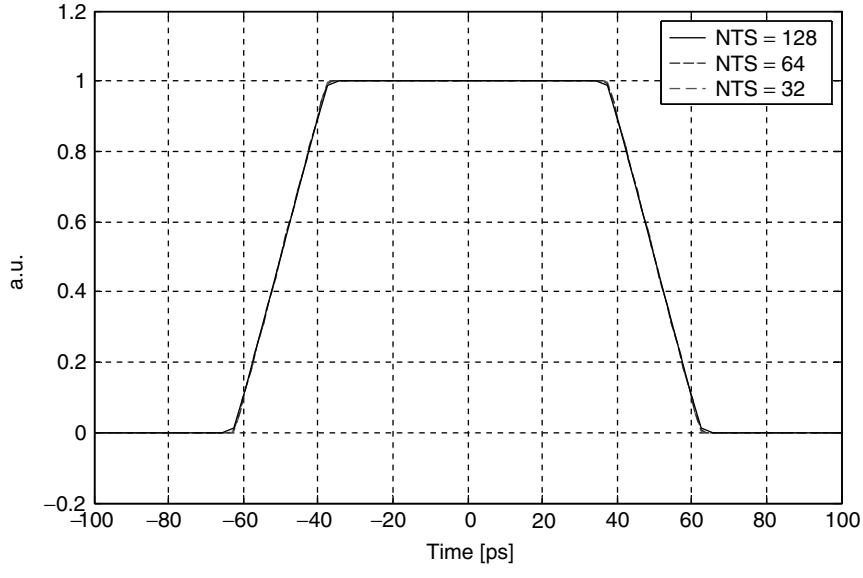

Figure 8.13 Transmitted output pulse of duration FWHM $= T = 100$ ps. The rise and fall times have been set to $t_r = t_f = 25$ ps. Increasing the transition time up to a quarter of the unity time step makes the output pulse shape almost identical for the three sampling time resolutions used

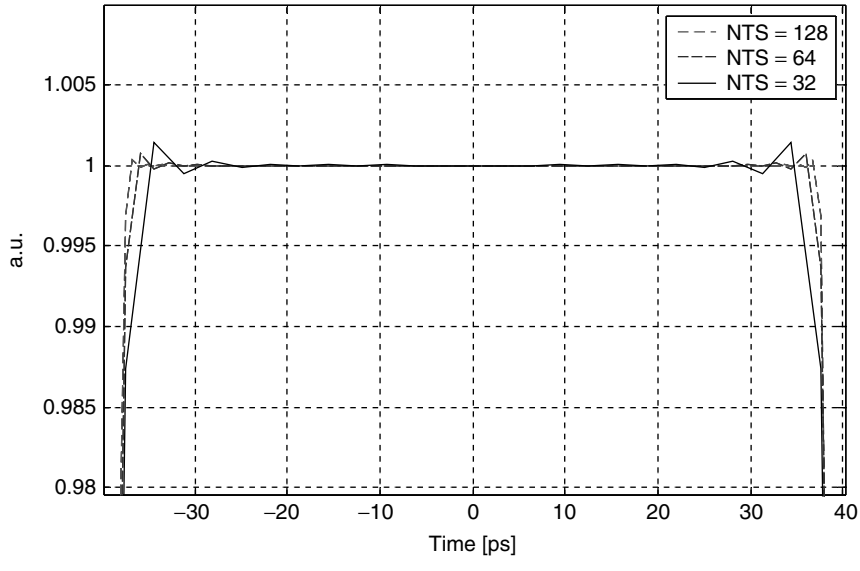

Figure 8.14 Magnification of the high power level of the pulse reported in Figure 8.13. Due to a relatively longer transition time, the output pulse ripple is reduced to be less than 0.5 % of the normalized intensity, almost independently from the sampling time resolution

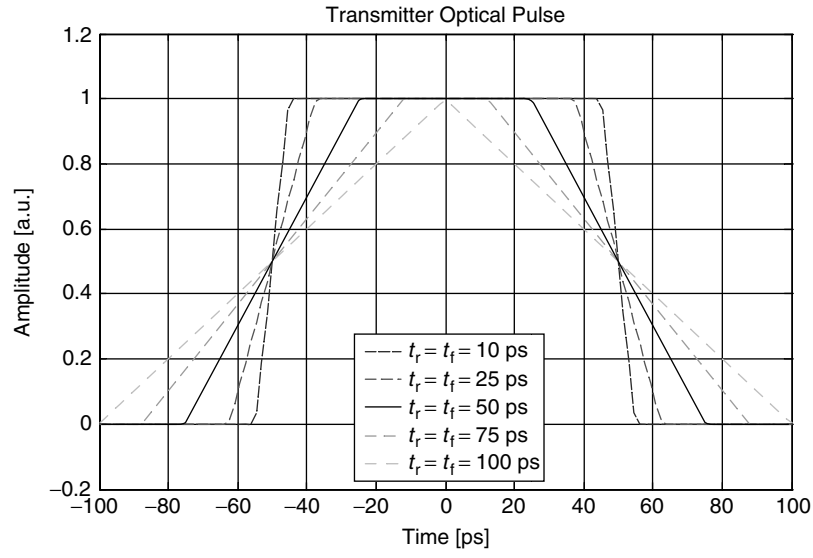

Figure 8.15 Transmitted optical pulses of the same duration FWHM $= T = 100$ ps with different symmetric transition times

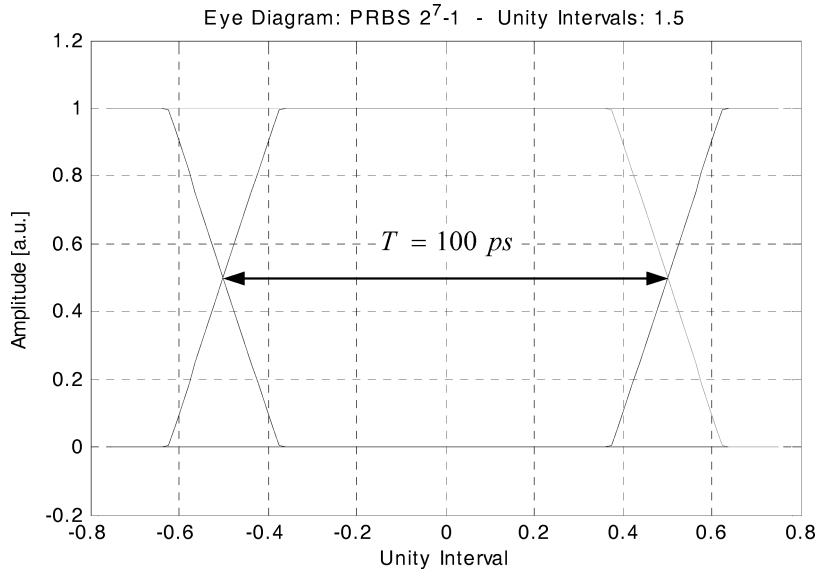

Figure 8.16 Example of the 10 Gb/s NRZ transmitted eye diagram: FWHM $= T = 100$ ps, $t_r = t_f = 25$ ps

These numerical examples conclude the description of the trapezoid pulse as the simplest but most useful modeling tool of a transmitted optical symbol in the NRZ data format. The next section deals with the more sophisticated error function based pulse, with symmetric round smoothed wavefronts.

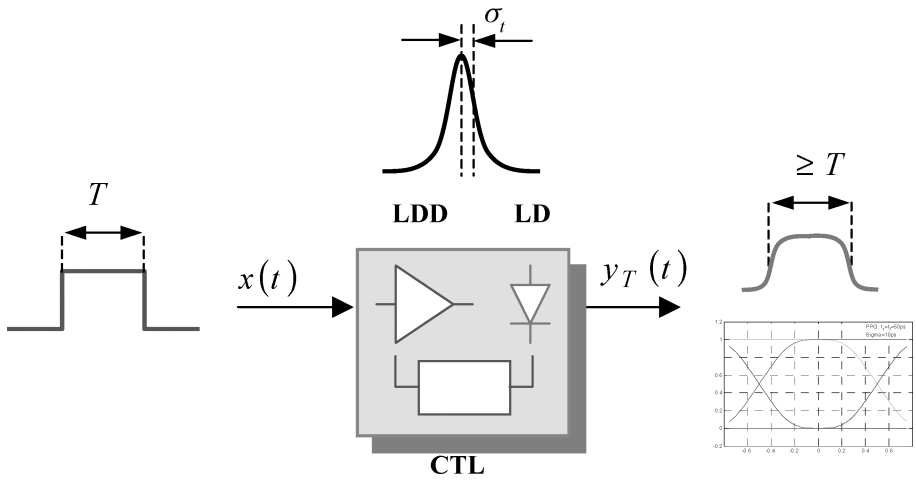

Figure 8.17 Schematic representation of the electro-optical conversion performed by the optical transmitter. The ideal square electrical stimulus from the pulse pattern generator (PPG) is converted into the optical envelope intensity pulse by the optical transmitter. If the optical impulse response to the electrical stimulus of the electro-optical converter is Gaussian, then the optical output pulse will result in the error function shaped pulse

8.3.2 Error Function Shaped Optical Pulse

The second optical pulse source considered for the optical transmitter output is the error function pulse. This terminology arises from the closed-form expression of the pulse function in terms of a linear combination of error functions. Despite its mathematical feeling, this pulse resembles real signals very closely, as laboratory instrumentation and equipment can generate them. The close relationship with real signals can be found by looking behind the pulse modeling assumption. In fact, passing an ideal square pulse through a system with a Gaussian impulse response generates the error function pulse. Figure 8.17 gives a schematic block diagram for the generation of the error function shaped pulse.

The same procedure can be applied to any linear and time invariant electro-optical converter, with a very different impulse response. Accordingly, a more complete library of several optical pulse shapes can be realized. It is important to point out that the pulse pattern generator can be modeled better using both the trapezoidal shaped pulse and the error function shaped pulse, instead of the simple assumption of the ideal square wave with instantaneous transition times.

8.3.2.1 Temporal Representation

It is assumed that the impulse response of the electro-optical converter is given by the following Gaussian pulse:

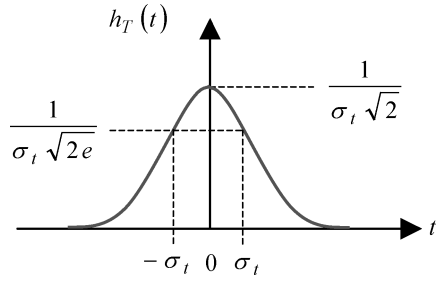

defined by

$$h_T(t) = \frac{1}{\sigma_t\sqrt{2\pi}}\, e^{-t^2/(2\sigma_t^2)}$$
$$\int_{-\infty}^{+\infty} h_T(t)\, dt = 1 \tag{8.12}$$

The pulse pattern generator produces the ideal square pulse $x(t)$ of duration T and instantaneous rise and fall times, as reported in Equation (8.2) and in Figure 8.5, reproduced here for more convenience:

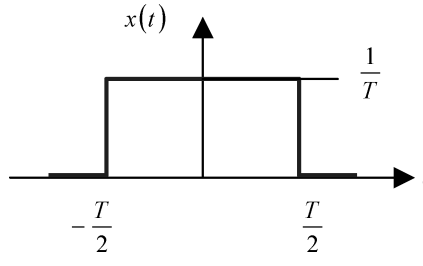

defined by

$$x(t) = \begin{cases} \dfrac{1}{T}, & |t| \le \dfrac{T}{2} \\ 0, & |t| > \dfrac{T}{2} \end{cases}$$

According to the linear system assumption, the output pulse $y_T(t)$ from the optical transmitter is given by the time convolution between the input pulse definition (8.2) and the Gaussian impulse response (8.12):

$$\begin{aligned} y_T(t) &= x(t) * h_T(t) \\ &= \int_{-\infty}^{+\infty} x(\tau) h_T(t-\tau)\, d\tau \\ &= \frac{1}{T}\frac{1}{\sigma_t\sqrt{2\pi}} \int_{t-T/2}^{t+T/2} e^{-u^2/(2\sigma_t^2)}\, du \end{aligned} \tag{8.13}$$

After the substitution $\xi = u/(\sigma_t\sqrt{2})$, from Equations (8.12) and (8.13) the following integral representation of the output optical pulse is obtained:

$$y_T(t) = \frac{1}{T}\frac{1}{\sqrt{\pi}} \int_{(t-T/2)/(\sigma_t\sqrt{2})}^{(t+T/2)/(\sigma_t\sqrt{2})} e^{-\xi^2}\, d\xi \tag{8.14}$$

In order to solve the integral the error function is introduced:

$$\mathrm{erf}(x) \equiv \frac{2}{\sqrt{\pi}} \int_0^x e^{-\xi^2}\, d\xi \tag{8.15}$$

In particular, the error function $\mathrm{erf}(x)$ satisfies the following properties:

$$\begin{gathered} \mathrm{erf}(-x) = -\mathrm{erf}(x) \\ \lim_{x\to+\infty} \mathrm{erf}(x) = 1 \\ \mathrm{erf}(0) = 0 \end{gathered} \tag{8.16}$$

Using the definition (8.15) gives the solution for the definite integral (8.14) of the Gaussian function:

$$\frac{1}{\sqrt{\pi}}\int_a^b \mathrm{e}^{-\xi^2}\,\mathrm{d}\xi = \frac{1}{2}[\mathrm{erf}(b) - \mathrm{erf}(a)] \tag{8.17}$$

Applying these results to the integral (8.14) gives the following closed form of the error function optical pulse:

$$y_{\mathrm{T}}(t) = \frac{1}{2T}\left[\mathrm{erf}\left(\frac{t + T/2}{\sigma_t\sqrt{2}}\right) - \mathrm{erf}\left(\frac{t - T/2}{\sigma_t\sqrt{2}}\right)\right] \tag{8.18}$$

It should be remembered that the above formula is valid, assuming that the time convolution with the ideal square pulse is generated from the PPG, characterized by full-width at half-maximum duration T and instantaneous wavefronts ($t_{\mathrm{r}} = t_{\mathrm{f}} = 0$). The parameter σ_t in the above formula is the RMS width of the Gaussian impulse response of the optical transmitter.

From the analytical expression (8.18) and using the properties (8.16), it is easy to conclude that the error function optical pulse has the following characteristics:

1. Even symmetry:

$$y_{\mathrm{T}}(-t) = y_{\mathrm{T}}(t) \tag{8.19}$$

2. Maximum value at the time origin:

$$\begin{aligned} y_{\mathrm{T}}(0) &= \frac{1}{T}\,\mathrm{erf}\left(\frac{T}{\sigma_t 2\sqrt{2}}\right) \\ T \gg \sigma_t \Rightarrow y_{\mathrm{T}}(0) &\cong \frac{1}{T} \end{aligned} \tag{8.20}$$

3. Null value at infinite time coordinate:

$$\lim_{t\to+\infty} y_{\mathrm{T}}(t) = 0 \tag{8.21}$$

4. Full-width at half-maximum FWHM $= 2t_0$:

$$t_0: \quad y_{\mathrm{T}}(t_0) = \frac{1}{2}y_{\mathrm{T}}(0) \Rightarrow y_{\mathrm{T}}(t_0) = \frac{1}{2T}\,\mathrm{erf}\left(\frac{T/2}{\sigma_t\sqrt{2}}\right) \tag{8.22}$$

and hence

$$\mathrm{erf}\left(\frac{t_0 + T/2}{\sigma_t\sqrt{2}}\right) - \mathrm{erf}\left(\frac{t_0 - T/2}{\sigma_t\sqrt{2}}\right) = \mathrm{erf}\left(\frac{T/2}{\sigma_t\sqrt{2}}\right) \tag{8.23}$$

Calculation of the FWHM requires the implicit solution of Equation (8.23), which can only be accomplished numerically. Besides computing the exact value of the FWHM, it is possible to make the following conclusions:

1. For every $\sigma_t > 0$, $t_0 > T/2$. In fact, assuming $t_0 < T/2$ gives $\mathrm{erf}[(t_0 - T/2)/(\sigma_t\sqrt{2})] < 0$. Due to the monotonic behavior of the error function, equation (8.23) would have no real solution. Therefore, it is concluded that $t_0 > T/2$.
2. At the limit for a relative small RMS pulse width, $\sigma_t \to 0$, or equivalently $\sigma_t \ll T$, then $t_0 \to T/2$ and from Equation (8.23) it is found that FWHM $\to T$. This conclusion is of course quite consistent with the assumption of a very short Gaussian impulse response. After the time convolution with the square pulse, the output profile must resemble very closely the PPG output.

At the limit of the Dirac delta impulse response, the effect of time convolution leads to a simple temporal translation at the Dirac delta impulse center of gravity.

3. Relatively broad Gaussian impulse responses produced by the laser transmitter lead to an output optical pulse whose width is strongly influenced by the laser performance. According to the definition (8.13), each pulse resulting from the convolution with a single time step square pulse has unity area. Therefore, broader single pulses must have a lower peak intensity. Accordingly, time convolution with a multiple NRZ PPG pulse width, like the one generated by several consecutive ones, will produce distorted output waveforms, with a large intersymbol interference pattern and consequent eye diagram closure.
4. An important consequence of the above discussion is the generation of the pattern-dependent jitter (dealt with in more detail in the next section). The amount of jitter due to the PPG pattern is more pronounced for an increasing Gaussian RMS width σ_t relative to the ideal square pulse duration nT. The parameter n gives the integer multiple of the elementary time step T.

Figure 8.18 shows some computed optical pulses according to the error function shaped profile. The PPG produces an ideal square pulse of fixed FWHM equal to $T = 100\,\text{ps}$, while different Gaussian laser responses have been considered. The vertical axis gives a normalized unit. In order to have an optical pulse with unit energy (area) it is sufficient to use a vertical unit scaled by $1/T$.

The next section presents the calculation of the pattern-dependent jitter for the sequence of error function pulses. This is an interesting example showing the analytical procedure used to determine the interval definition of the jitter variable. In order to complete the statistical description, the

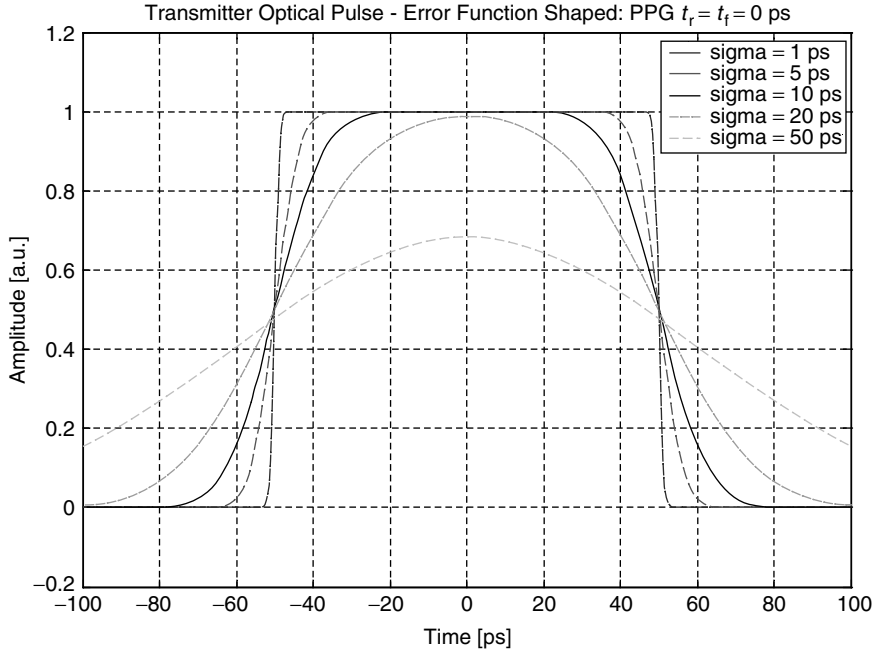

Figure 8.18 Computed error function shaped output optical pulses according to Equation (8.18). The plotted curves refer to an ideal square pulse generated by the PPG and passed through the Gaussian frequency response electro-optical converter with different RMS widths. The ideal square pulse has the same duration $T = 100\,\text{ps}$ for all curves. From these curves, it is easily to conclude that when the ratio $\sigma_t / T > 0.2$ the output pulse is strongly determined by the Gaussian impulse response

probability density function of the expected data sequences needs to be included. A similar approach can be used for every waveform and signal condition.

8.3.2.2 Pattern-Dependent Jitter (PDJ)

In this section, the theory of the pattern-dependent jitter for the case of the error function pulse is introduced. The error function optical pulse is given by the time convolution between the ideal square pulse of duration T and the Gaussian impulse response of the electro-optical converter. As clearly stated by Equation (8.23), the pulse width is dependent on both parameters σ_t and T. If the RMS Gaussian pulse width σ_t is very small compared to T, the FWHM of the error function optical pulse becomes coincident with the square pulse duration T. On the other hand, when σ_t is no longer negligible with respect to T, the FWHM becomes larger than T, thus originating the pattern-dependent jitter. Stated differently, for a fixed RMS width σ_t of the Gaussian pulse, the FWHM of the error function optical pulse resulting from the convolution with the PPG square wave depends on the duration nT of the generated data sequence. Since the discrete variable n is random within the PRBS generation length, the pattern-dependent jitter will result accordingly in the output signal.

8.3.2.2.1 Normalized FWHM Deviation

In order to compute the FWHM of the optical pulse as a function of the ratio σ_t/T, the following definitions in the implicit equation (8.23) are introduced:

$$\text{FWHM} \equiv 2t_0 \equiv \Delta \tag{8.24}$$

$$x \equiv \frac{\Delta}{T} \tag{8.25}$$

$$\delta \equiv 2\sqrt{2}\frac{\sigma_t}{T} \tag{8.26}$$

The new parameter x assumes the meaning of the pulse FWHM relative to the unity time step T. The parameter δ is proportional to the ratio σ_t/T between the RMS width of the Gaussian impulse response and the unit time interval. After substitution into Equation (8.23), the following implicit equation is derived whose solution $x(\delta)$ represents the functional dependence for deriving the pattern-dependent jitter:

$$\text{erf}\left(\frac{x+1}{\delta}\right) - \text{erf}\left(\frac{x-1}{\delta}\right) = \text{erf}\left(\frac{1}{\delta}\right) \tag{8.27}$$

This equation refers to the simplest case of the ideal square pulse duration and is equal to one single time step T. In order to arrive at the final equation valid for any time step duration, there is a need to take into account any integer multiple nT of the unity time step T. In fact, it is well known that the PPG can generate any NRZ sequence of proper length, according to the PRBS generation polynomials. Substituting the parameter T by nT in Equation (8.23) and making use of the above parameters definition, it can be conclude that

$$x_{\substack{n \\ n=1,2,\ldots}}(\delta): \quad \text{erf}\left(\frac{x+n}{\delta}\right) - \text{erf}\left(\frac{x-n}{\delta}\right) = \text{erf}\left(\frac{n}{\delta}\right) \tag{8.28}$$

Equation (8.28) is the generalization of Equation (8.27) for any integer value of the parameter n. Figure 8.19 shows the computed implicit solution of Equation (8.28) using a Matlab® code. The

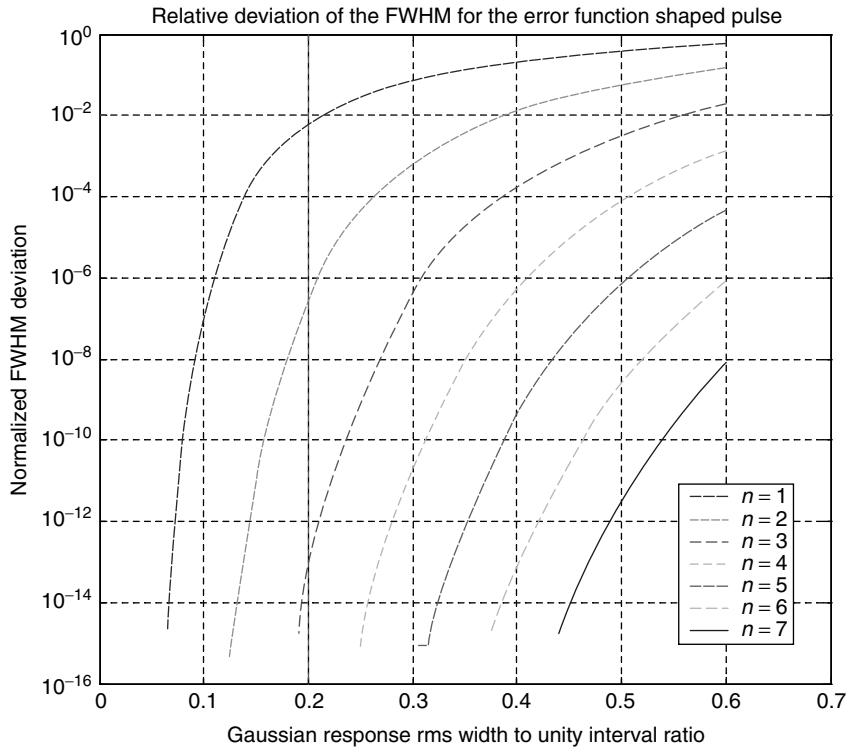

Figure 8.19 Normalized FWHM deviation $\Gamma_n(\delta)$ computed using formula (8.28) versus the ratio σ_t/T. The bit length n sets the curve parameter. The ordinate is defined in Equation (8.29). A longer bit length corresponds to an extremely small value of the normalized FWHM deviation from the ideal bit length nT. In order to limit the FWHM deviation to less than 1 % it is necessary to set $\sigma_t/T < 0.2$

abscissa shows the ratio σ_t/T and the ordinate shows the normalized deviation $\Gamma_n(\delta)$ of the FWHM with respect to the ideal pulse width:

$$\Gamma_n(\delta) \equiv \frac{\Delta_n(\delta) - nT}{T} = \frac{\Delta_n(\delta)}{T} - n = x_n(\delta) - n \tag{8.29}$$

In a PRBS pattern of length $2^n - 1$ all bit lengths up to qT, $q = 1, 2, \ldots, n$, are present, and different FWHM are obtained when they are convolved with the same Gaussian impulse response of RMS width σ_t. The relative deviation $\Gamma_n(\delta)$ of the normalized FWHM generates the pattern-dependent jitter (PDJ).

Figure 8.20 shows a detailed view of Figure 8.17, where the normalized deviation $\Gamma_n(\delta)$ has been computed for bit lengths $n = 1, 2, 3$. It is evident that a broader Gaussian response relative to the unity interval gives a higher value of $\Gamma_1(\delta)$. It is important to note that longer bit sequences are much less affected by relative FWHM variations than shortest ones. In Figure 8.20 it can be seen that even assuming a broader Gaussian response with $\sigma_t/T = 0.55$, the contribution $\Gamma_3(\delta)$ of the bit length $n = 3$ is less than 1 %, but the unity step bit, $n = 1$, gives a much higher $\Gamma_1(\delta)$ contribution of about 50 %, making the eye width highly reduced.

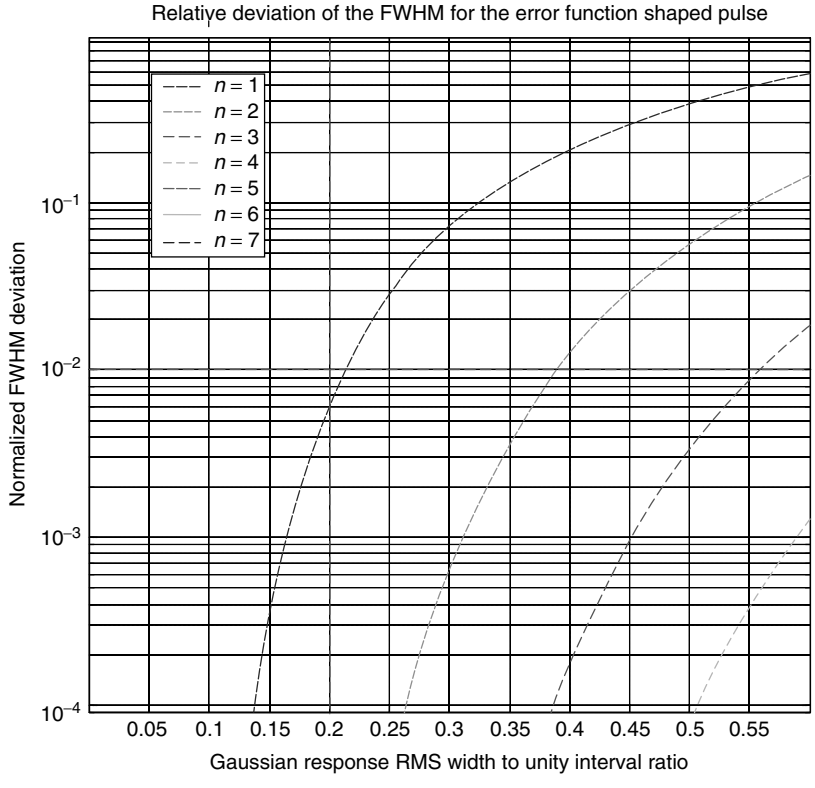

Figure 8.20 Higher value of the ratio σ_t/T leads to higher $\Gamma_n(\delta)$ values. Assuming $\sigma_t/T = 0.4$, the first three normalized PDJ contributions $\Gamma_n(\delta)$ are $\Gamma_1(\delta) = 0.21$, $\Gamma_2(\delta) = 1.3 \times 10^{-2}$, $\Gamma_3(\delta) = 2 \times 10^{-4}$

8.3.2.2.2 Jitter analysis

The normalized relative FWHM $\Gamma_n(\delta)$ derived in the previous section is related to the pattern-dependent jitter (PDJ), but is not suitable for calculation when the eye diagram is represented. In order to have a consistent definition of the pulse width to be used in conjunction with the eye diagram representation and PDJ, a new variable $\Theta_n(\delta)$ needs to be introduced. $\Theta_n(\delta)$ is the Normalized pulse width deviation measured when pulse wavefronts cross the absolute value of one-half, assuming that the indefinitely long pulse is normalized with unit amplitude.

The new pulse width deviation $\Theta_n(\delta)$ leads immediately to the concept of pattern-dependent jitter (PDJ). However, in the actual definition of the function $\Theta_n(\delta)$, it is implicitly assumed that the jitter is evaluated at one-half of the asymptotic amplitude. This choice corresponds to setting the decision threshold at one-half of the asymptotic eye diagram amplitude.

In order to define $\Theta_n(\delta)$, consider the schematic representation of the error function shaped pulse reported in Figure 8.21. The following parameters are introduced:

$$t_w: \quad y_T(t_w) = \frac{1}{2} \lim_{\sigma_t \to 0} y_T(0) = \frac{1}{2T} \tag{8.30}$$

$$w_n(\delta) \equiv \frac{2t_w}{T} \tag{8.31}$$

$$\delta \equiv 2\sqrt{2}\frac{\sigma_t}{T} \tag{8.32}$$

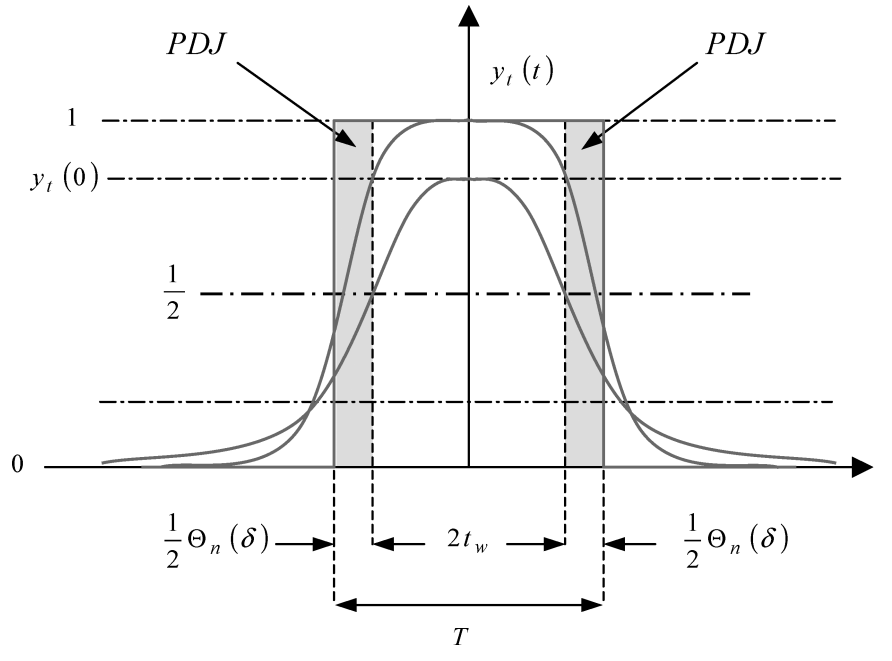

Figure 8.21 Schematic representation of the optical pulse for the definition of the pattern-dependent jitter (PDJ)

The normalized deviation $\Theta_n(\delta)$ is defined as follows:

$$\Theta_n(\delta) \equiv \frac{nT - 2t_w}{T} = n - w_n(\delta) \tag{8.33}$$

Substituting Equations (8.30), (8.31) and (8.33) into Equation (8.28) gives the following equation for the normalized pulse width $w_n(\delta)$:

$$\underset{n=1,2,\ldots}{w_n}(\delta): \quad \operatorname{erf}\left(\frac{w+n}{\delta}\right) - \operatorname{erf}\left(\frac{w-n}{\delta}\right) = 1 \tag{8.34}$$

This equation has the same form as Equation (8.28), except for the variable $w_n(\delta) \equiv 2t_w/T$ used instead of x and for the constant right-end term. Using the same Matlab® code with minor modifications, the normalized pulse width $w_n(\delta)$ is found for any given parameter n. After substituting $w_n(\delta)$ into Equation (8.33), the normalized pulse width deviation $\Theta_n(\delta)$ is obtained.

Figure 8.22 shows the computed width deviation using Matlab® code. It is evident from the plotted results that for pulses longer than three time steps, $n \geq 2$, the amount of PDJ is quite negligible. However, it is important to recognize that even if longer sequences do not exhibit any significant width deviation, a single bit pulse might have a relevant deviation if $\delta > 0.4$. Due to the computation resolution, only the first four-bit length values have been used: $n = 1, 2, 3, 4$, while the ratio parameter ranges between $0.1 \leq \delta \leq 0.7$.

In order to evaluate the PDJ contribution of the shortest bit lengths better, Figure 8.23 shows the solution for $n = 1, 2$. Assuming a relative large Gaussian impulse response $\sigma_t/T = 0.60$, the first two PDJ contributions corresponding to $n = 1$ and $n = 2$ are

$$\mathrm{PDJ}_1 = 2 \times 10^{-1}\,\mathrm{UI}, \qquad \mathrm{PDJ}_2 = 1.4 \times 10^{-3}\,\mathrm{UI\ (unit\ interval)}$$

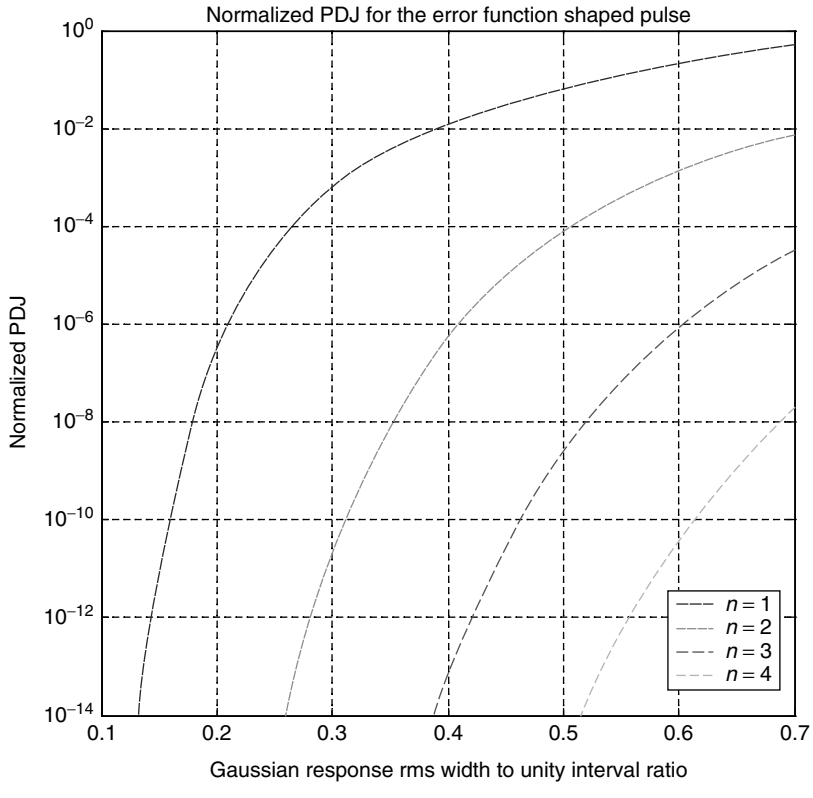

Figure 8.22 Normalized pulse width deviation $\Theta_n(\delta)$ computed using formulas (8.33) and (8.34) versus the increasing bit length n. The abscissa gives the ratio σ_t/T. The ordinate is defined in Equation (8.33). It is evident that a bit length $n \geq 3$ corresponds to an extremely small value of the normalized pulse width deviation $\Theta_n(\delta)$. In order to limit $\Theta_n(\delta)$ to less than 1 % it is necessary to set $\sigma_t/T \leq 0.38$

The random jitter (RJ) variable sums linearly to the pattern dependent jitter variable, and the joint probability density function of the resulting stochastic process is given by the convolution of both PDJ and RJ processes. The variance of the joint process is given by the sum of both process variances. Once the weighted distribution of the PDJ is known, it is easy to conclude that the joint jitter probability density function is given by the RJ distribution shifted and properly weighted around each PDJ contribution. In this sense, the PDJ acts like a weighted phase shifter.

8.3.2.3 Frequency Representation

The frequency representation of the error function pulse is easily derived by virtue of the convolution theorem. Indicating by $X_T(f)$ and $H_T(f)$ the Fourier transform of the ideal pulse $x_T(t)$ in Equation (8.2) produced by the pattern generator and of the Gaussian impulse response $h_T(t)$ of the electro-optical converter respectively gives

$$x_T(t) \overset{\Im}{\longleftrightarrow} X_T(f) = \frac{\sin(\pi f T)}{\pi f T} \tag{8.35}$$

$$h_T(t) \overset{\Im}{\longleftrightarrow} H_T(f) = e^{-2\pi^2\sigma_t^2 f^2} \tag{8.36}$$

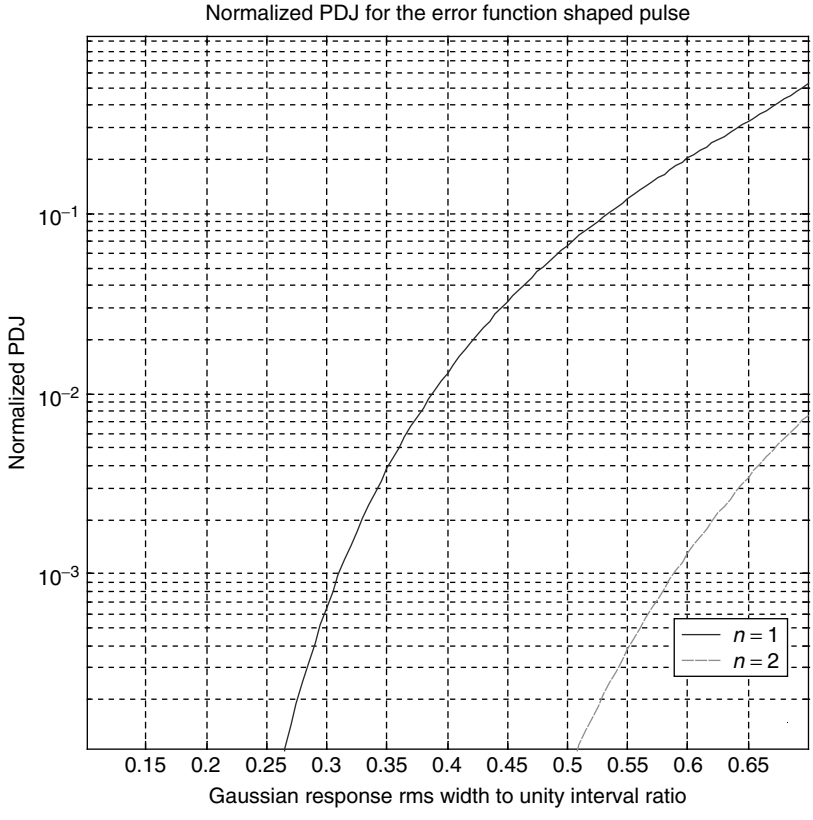

Figure 8.23 Normalized pulse width deviation $\Theta_n(\delta)$ versus the ratio σ_t/T for two bit lengths $n = 1, 2$

Applying the convolution theorem immediately gives the expression for the spectrum of the error function shaped pulse as the product of spectra in Equations (8.35) and (8.36):

$$y_{\mathrm{T}}(t) \overset{\Im}{\longleftrightarrow} Y_{\mathrm{T}}(f) = \frac{\sin(\pi f T)}{\pi f T}\, \mathrm{e}^{-2\pi^2\sigma_t^2 f^2} \tag{8.37}$$

The very simple analytical form of the spectrum of the error function pulse, together with a close-up pulse shape, makes it very attractive for computer modeling and theoretical system analysis. Figure 8.24 shows the computed spectrum of the error function pulse using the dB scale and logarithmic frequency representations.

The computed frequency spectra refer to increasing Gaussian pulse widths, starting from $\sigma_t = 1\,\mathrm{ps}$ up to $\sigma_t = 50\,\mathrm{ps}$. The smoothing effect of the Gaussian contribution is quite evident in the high-frequency behavior of the plotted spectra. In the case of $\sigma_t = 20\,\mathrm{ps}$, the first lobe is about 26 dB down from the normalized low-frequency content.

8.3.2.4 FWHM and 3 dB Cut-Off

In order to compute the frequency cut-off of the error function pulse it is sufficient to refer to the magnitude of the spectrum expression (8.37). The cut-off coefficient α is introduced:

$$|Y_{\mathrm{T}}(f_\alpha)| = \left|\frac{\sin(\pi f_\alpha T)}{\pi f_\alpha T}\right| \mathrm{e}^{-2\pi^2\sigma_t^2 f_\alpha^2} = \alpha, \quad 0 < \alpha \leq 1 \tag{8.38}$$

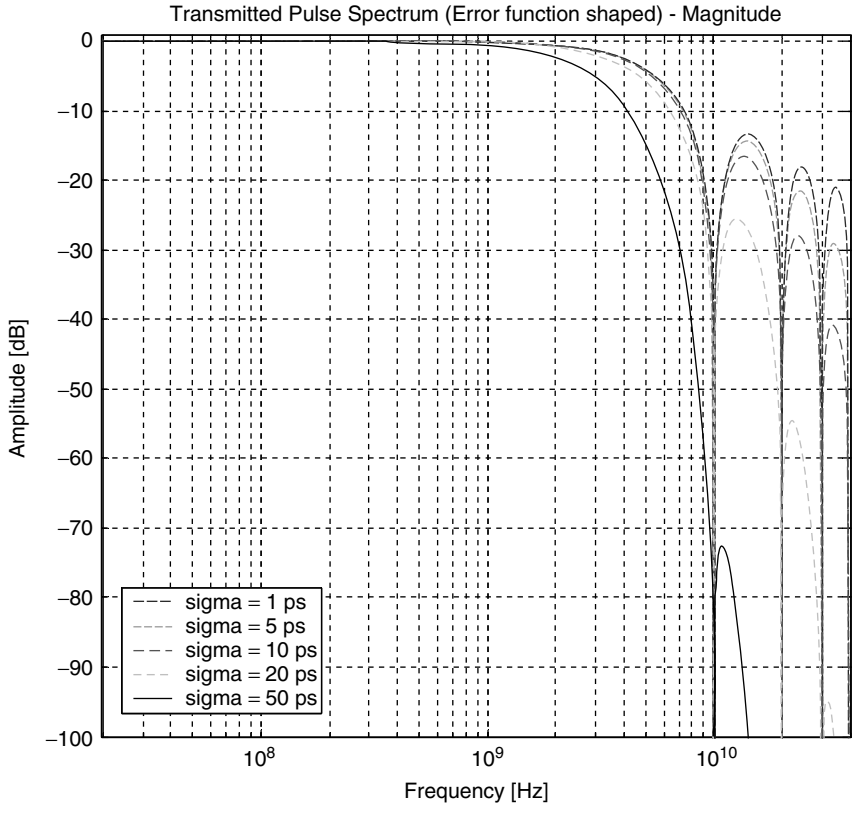

Figure 8.24 Frequency spectra of the error function pulse versus different ratios σ_t/T. The assumed unity time step is $T = 100\,\text{ps}$. The transition times of the electrical PPG pulse are assumed to be instantaneous. Increasing the RMS width of the Gaussian impulse response causes the corresponding spectrum to become smoother with less pronounced lobes

In particular, setting $\alpha = 1/2$ and $\alpha = 1/\sqrt{2}$ gives the unilateral bandwidth at FWHM ($-6\,\text{dB}$) and the $-3\,\text{dB}$ cut-off frequency respectively. Solving Equation (8.38) with respect to the frequency f_α, gives the following transcendental equation:

$$f_\alpha = \frac{1}{\pi\sigma_t\sqrt{2}}\sqrt{\log\left[\frac{1}{\alpha}\left|\frac{\sin(\pi f_\alpha T)}{\pi f_\alpha T}\right|\right]}, \quad 0 < \alpha \leq 1 \tag{8.39}$$

Besides the numerical computation of the cut-off frequency f_α, some properties of the solution can be anticipated. The term $|\sin(\pi f T)/(\pi f T)|$ is a monotonic decreasing function of the frequency f in the interval between the origin and the first zero $f_1 = 1/T$. Since the function $\sqrt{\log(x)}$ has a monotonic increasing dependence versus the argument x, it can easily be concluded that the right member of Equation (8.39) is a monotonic decreasing function of the frequency f_α. Hence, the solution f_α is given by the intersection between the line $G(f) = f$ and the right-hand term

$$H(f) = \frac{1}{\pi\sigma_t\sqrt{2}}\sqrt{\log\left[\frac{1}{\alpha}\left|\frac{\sin(\pi f T)}{\pi f T}\right|\right]}$$

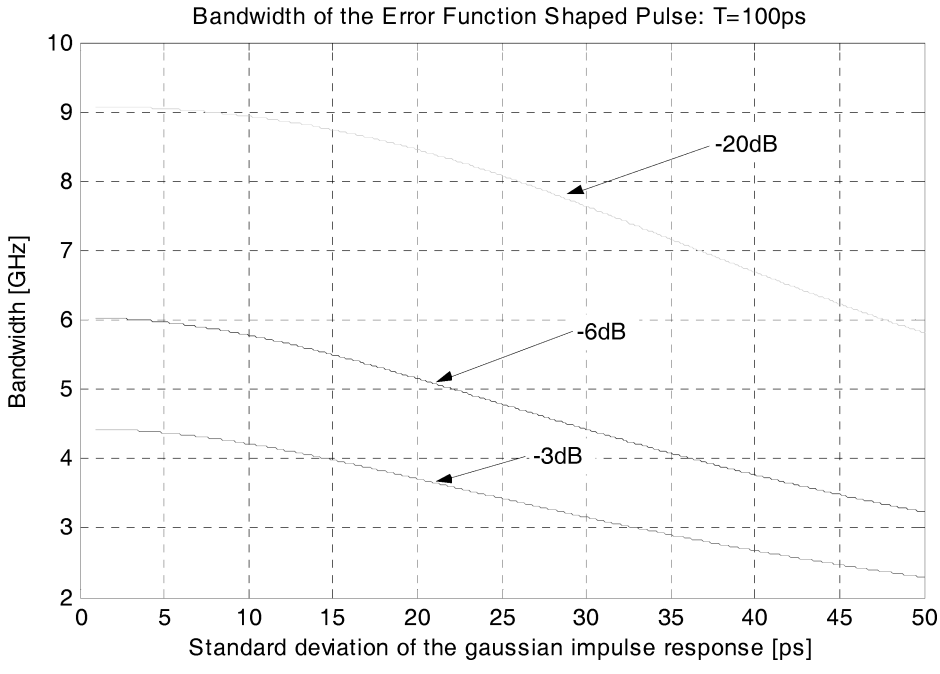

Figure 8.25 Cut-off frequency of the error function shaped pulse versus the standard deviation of the Gaussian impulse response σ_t. The assumed unity time step is $T = 100\,\text{ps}$. For the case $\sigma_t = 20\,\text{ps}$, the bandwidth evaluated at $-3\,\text{dB}$ is $f_{-3\text{dB}} \cong 3.70\,\text{GHz}$, while the $-6\,\text{dB}$ bandwidth gives $f_{-6\text{dB}} \cong 5.15\,\text{GHz}$

For every value of the parameter α, the solution must belong to the frequency interval $0 < f_\alpha \leq 1/T$.

Figure 8.25 gives the solution of Equation (8.39) using a simple Matlab® code. For the fixed unity time step $T = 100\,\text{ps}$, three solutions are plotted versus the Gaussian pulse width σ_t assuming three different cut-off conditions, namely $\alpha = 1/2$, $\alpha = 1/\sqrt{2}$ and $\alpha = 1/10$, corresponding to one-half FWHM (or $-6\,\text{dB}$ electrical bandwidth), $-3\,\text{dB}$ electrical bandwidth and $-20\,\text{dB}$ electrical bandwidth respectively.

The curves in Figure 8.25 clearly show the reduction of the transmitted pulse bandwidth at increasing values of the RMS width of the Gaussian impulse response of the electro-optical converter. At the limit for a negligible impulse response contribution, the plotted curves coincide with the ideal square wave spectrum generated by the pulse pattern generator.

8.3.2.5 Generalized Error Function Pulse

In order to take into account the nonideal square pulse generated by the pulse pattern generator, the following analytical form of the spectrum of the generalized error function pulse is considered by introducing the trapezoid pulse sequence generated by the PPG, instead of the simple ideal square pulses.

Although the analytical form of the output pulse in the time domain can be quite cumbersome, its frequency representation is easier and more elegant. By virtue of the convolution theorem, it is well known that the spectrum of the trapezoid pulse is given by the product of the spectra of the two convolving square pulses. Moreover, due to the associative property of the convolution,

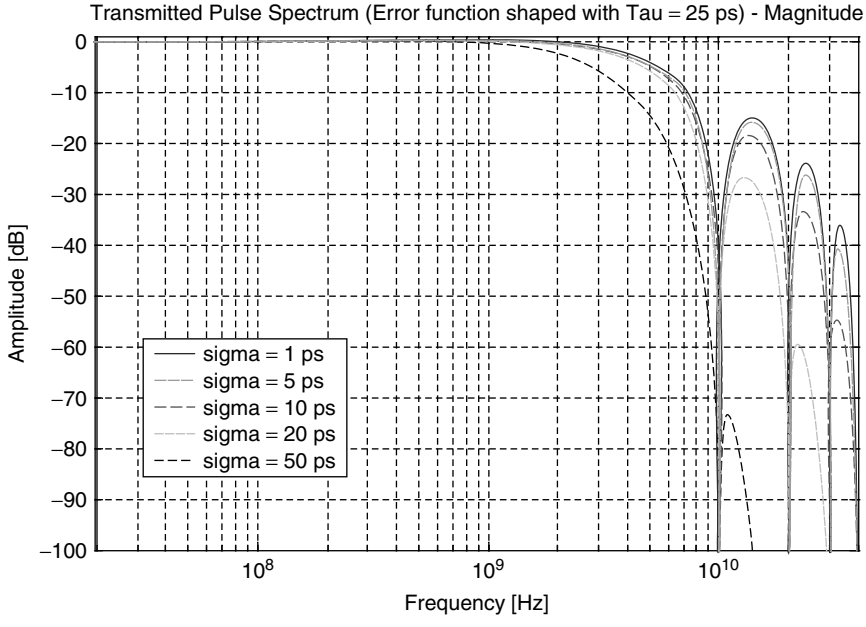

Figure 8.26 Magnitude of the frequency spectra of the error function pulse versus different ratios σ_t / T with a fixed transition time for the PPG trapezoid pulse. The assumed unity time step is $T = 100\,\text{ps}$

the spectrum of the generalized error function pulse is given by the product of the spectrum of the trapezoid pulse produced by the PPG with the Gaussian impulse response spectrum (8.36):

$$y_{\text{T}}(t) \overset{\Im}{\longleftrightarrow} Y_{\text{T}}(f) = \left[\frac{\sin(\pi f T)}{\pi f T}\right]\left[\frac{\sin(\pi f \tau)}{\pi f \tau}\right](\text{e}^{-2\pi^2\sigma_t^2 f^2}) \tag{8.40}$$

The same functional definition $y_{\text{T}}(t) \overset{\Im}{\longleftrightarrow} Y_{\text{T}}(f)$ as the original error function pulse expression (8.37) is used, disregarding the fact that it comes from the ideal square pulse or the trapezoid pulse. By comparing Equation (8.37) with (8.40), the factor $\left[\sin(\pi f \tau)/(\pi f \tau)\right]$ in the latter equation is found to be responsible for the finite transition time of the trapezoid PPG pulse. The PPG pulse has a fixed value of FWHM, equal to the unity time step T, which is independent of the value chosen for the transition time τ. This property of the PPG pulses leads qualitatively to the same conclusion about the pattern-dependent jitter discussed in a previous section.

Figure 8.26 shows several computed spectra according to expression (8.40) for the same cases considered in Figure 8.24, but assuming the finite transition time $\tau = 25\,\text{ps}$ of the trapezoid pulse. Figure 8.27 shows the effect of the finite transition time on the spectrum of the error function pulse.

8.3.2.6 Simulated Pulses and Eye Diagrams

In this section are discussed some computed optical pulses and the corresponding eye diagrams generated according to the general formula of the error function pulse reported in expression (8.40). The aim of this exercise is to show the implications of the optical pulse profile with the eye diagram and the relevant intersymbol interference contribution that arises when the elementary error function

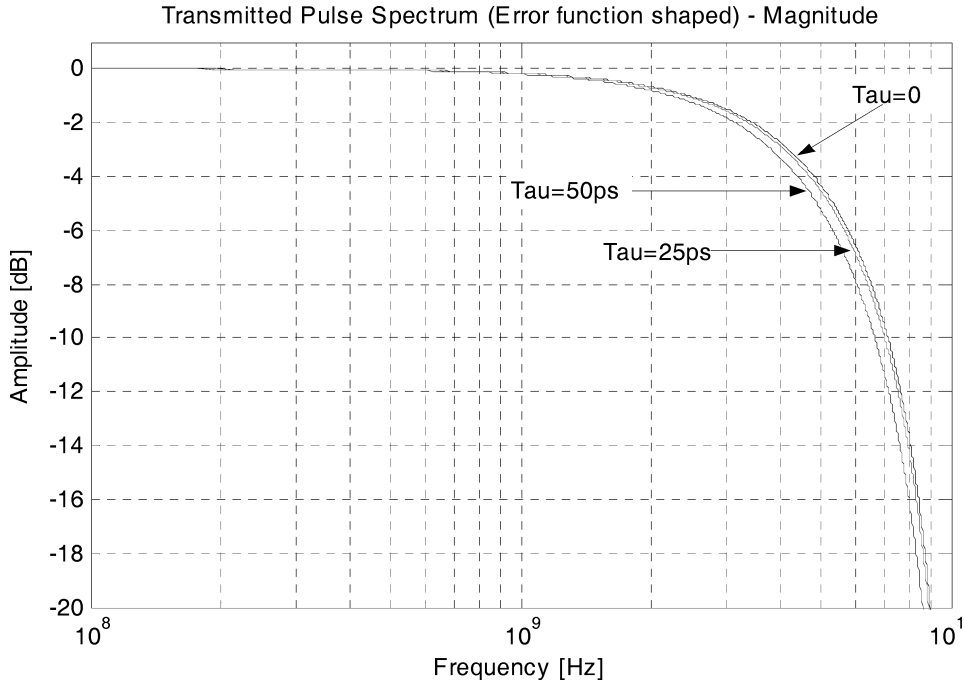

Figure 8.27 A comparison among frequency spectra of the error function pulse versus three transition times for the PPG trapezoid pulse: $\tau = 0$, $\tau = 25\,\text{ps}$, $\tau = 50\,\text{ps}$, with a fixed ratio σ_t / T. The assumed unity time step is $T = 100\,\text{ps}$

pulse becomes too smoothed relative to the required time step. Figure 8.28 presents an example of computed error function pulses with different Gaussian contributions.

Once the pulse response is known, it is relatively easy to build up the eye diagram according to the transmitted PRBS sequence. Figures 8.29 to 8.33 give five different eye diagrams corresponding to different combinations of trapezoid transient times and Gaussian pulse widths. All reported eye diagrams refer to the same time step $T = 100\,\text{ps}$.

8.3.3 Conclusion

In this chapter two analytical models have been presented of the optical pulse suitable for representing a light source intensity profile for optical communication: the trapezoid pulse and the error function pulse. Both time domain and frequency domain responses have been derived, including the corresponding eye diagram outputs. The trapezoid function pulse is easier to handle but does not include ISI or the pattern dependent jitter effect. Conversely, the error function pulse model allows better modeling of real pulses, where both ISI and jitter take place. The optical pulse model presented so far refers to the transmitted signal pattern, neglecting all noise and spectral contributions. Those should be included in a transmission system simulation as a separate analysis tool.

The optical signal represented in this chapter must be intended as the ensemble average of the transmitted optical intensity. Around the time-varying average power level, statistical fluctuations due to amplitude and phase fluctuations act as random perturbation.

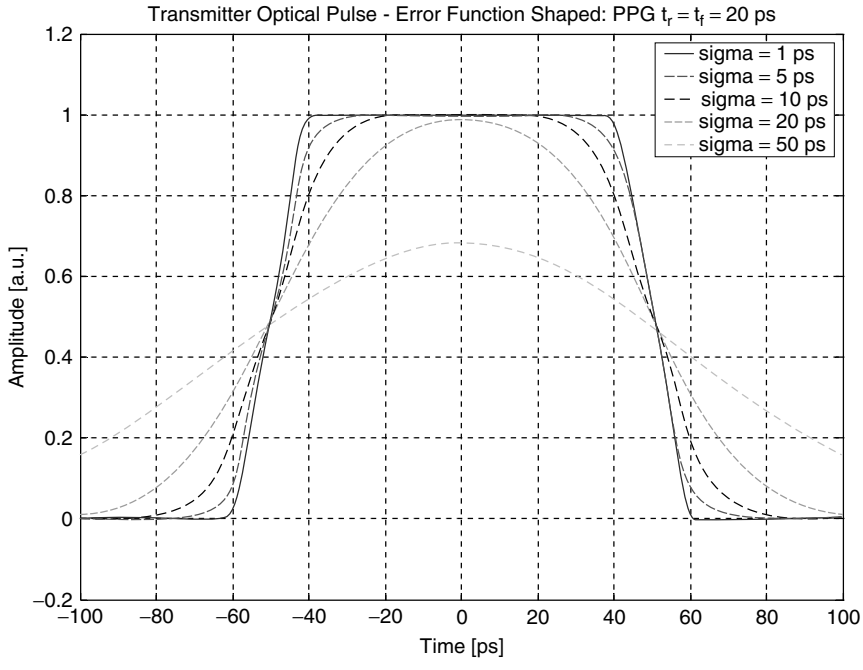

Figure 8.28 Error function pulses corresponding to the frequency representation in expression (8.40). The plotted curves refer to the trapezoid pulse generated by the PPG and passed through the Gaussian frequency response of the electro-optical converter with different RMS durations. The trapezoid pulses have the same FWHM with $T = 100$ ps and transition time $\tau = 20$ ps. From these curves, it is easy to conclude that when the ratio $\sigma_t / T \geq 0.2$ the output pulse is strongly affected by the Gaussian impulse contribution

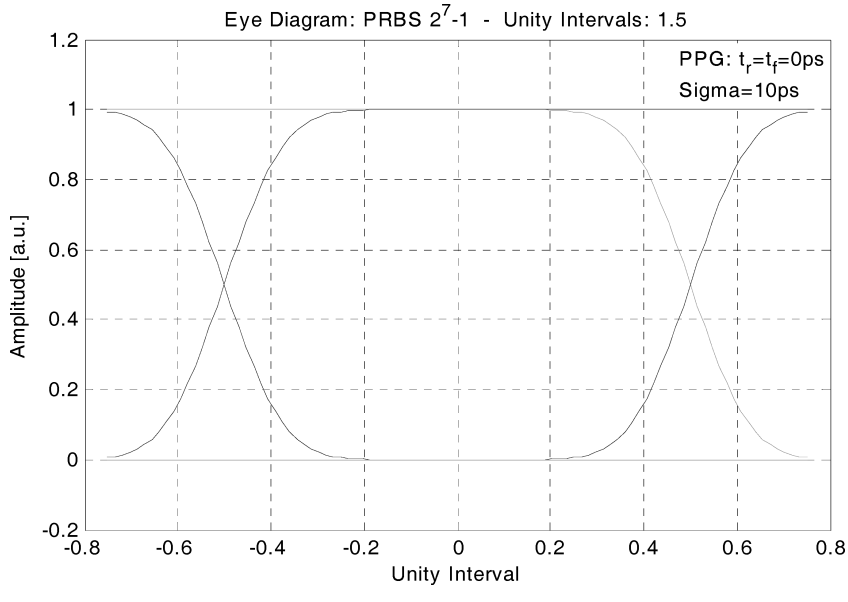

Figure 8.29 Error function shaped eye diagram: $T = 100$ ps, $\sigma_t / T = 0.1$, $t_r = t_f = 0$

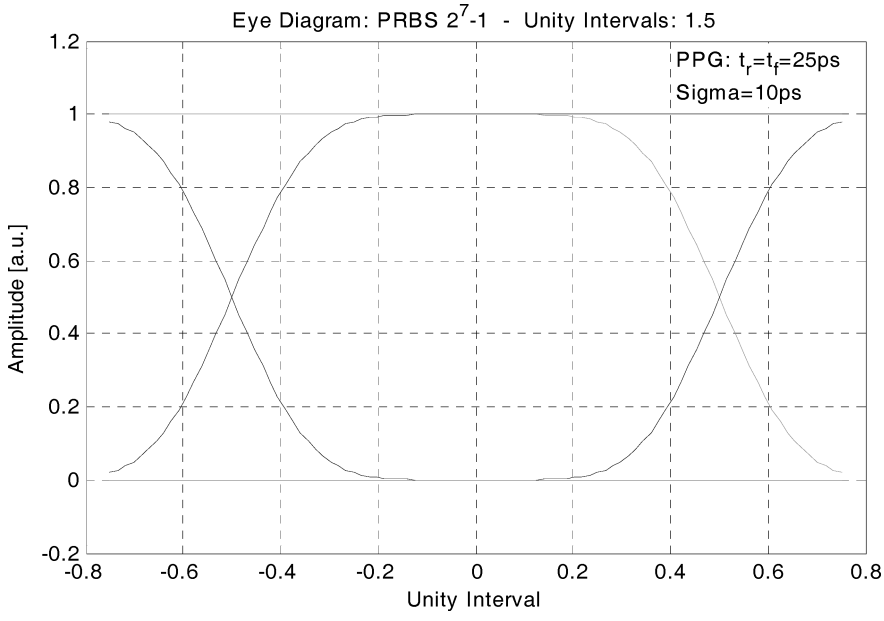

Figure 8.30 Error function shaped eye diagram: $T = 100\,\text{ps}$, $\sigma_t/T = 0.1$, $t_\text{r} = t_\text{f} = 25\,\text{ps}$

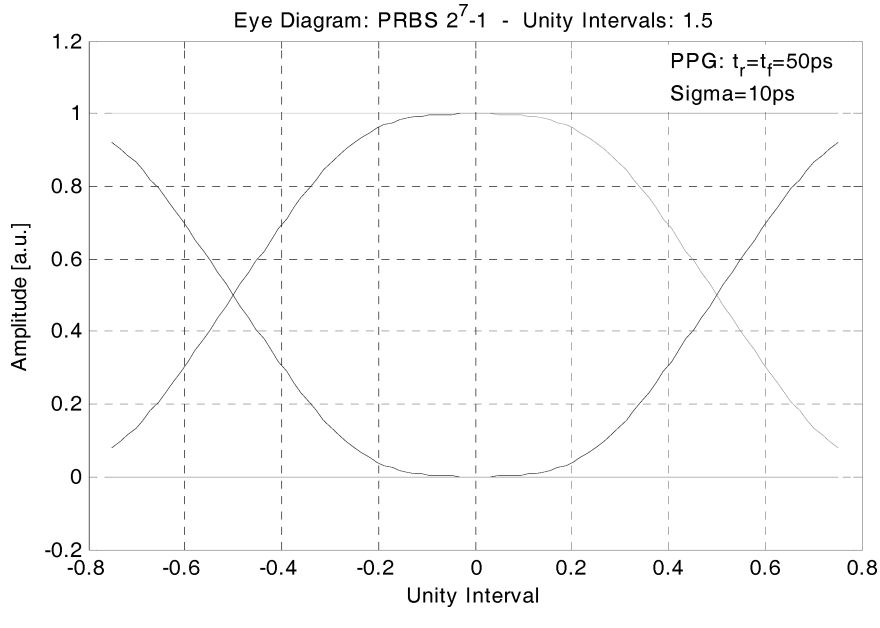

Figure 8.31 Error function shaped eye diagram: $T = 100\,\text{ps}$, $\sigma_t/T = 0.1$, $t_\text{r} = t_\text{f} = 50\,\text{ps}$

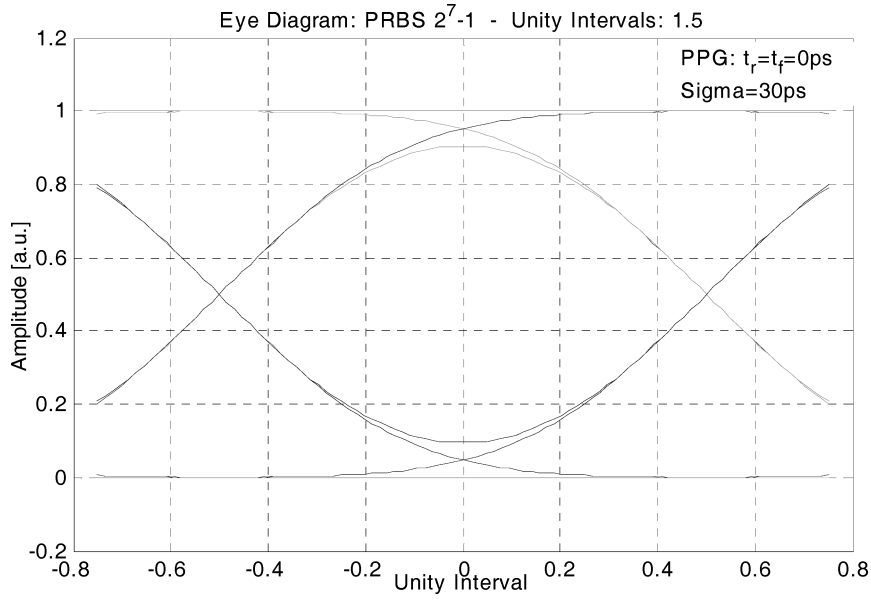

Figure 8.32 Error function shaped eye diagram: $T = 100\,\text{ps}$, $\sigma_t/T = 0.3$, $t_\text{r} = t_\text{f} = 0$. The intersymbol interference (ISI) at the ideal sampling time is clearly visible

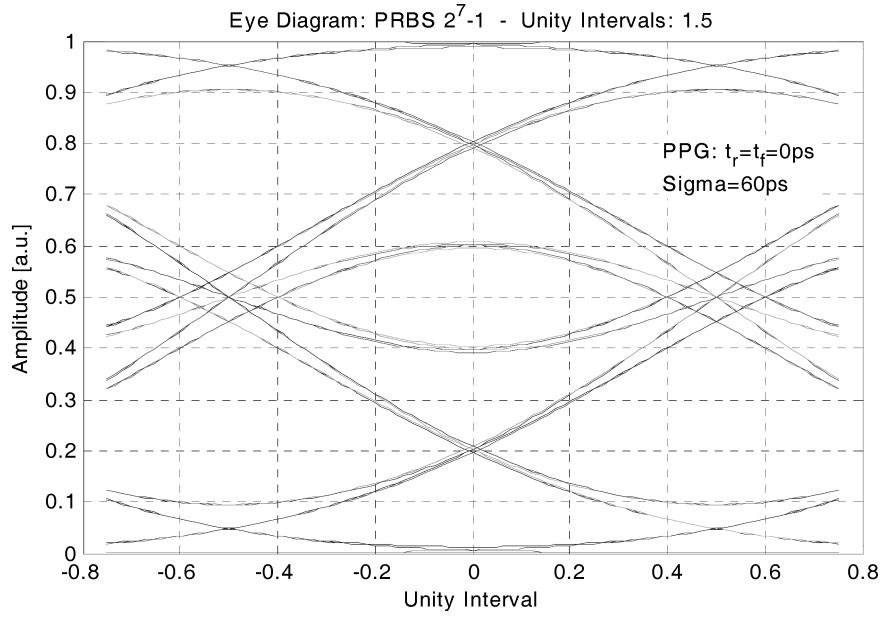

Figure 8.33 Error function shaped eye diagram: $T = 100\,\text{ps}$, $\sigma_t/T = 0.6$, $t_\text{r} = t_\text{f} = 0$. In this case, the intersymbol interference (ISI) strongly affects the eye shaping. The eye diagram closure can be estimated as $\Delta_P \cong 10\log\left(\frac{1}{5}\right) \cong -7\,\text{dB}$

8.4 Intersymbol Interference

The optical receiver performs a signal conversion from the optical domain to the electrical domain. In the electrical domain, it performs the signal amplification and the required electrical filtering for noise reduction. Additional optical filtering could be added in front of the optical receiving section for improved noise performance in optical amplified systems (ASE (amplified spontaneous emission) noise from optical amplifiers, DWDM (dense wavelength division multiplexing) cross-talk from adjacent channels, etc.).

Noise analysis for the optical receiver will not be covered in this chapter, as the optical signal characteristics, including pulse dispersion and the related profile equalization, are analyzed first This must not be intended as an oversimplification of the optical receiver theory, but instead as a restricted modeling, focused mainly on the detected signal processing. Noise is unavoidable for every physical system and, in particular, the detection process of optical signals is intimately related to the noise process. Any theoretical conclusion regarding optical signal detection and receiver sensitivity without including the noise effect would of course be meaningless. In this order, we will include the noise in the out treatment, assuming the simplified additive white Gaussian noise (AWGN) conditions. A detailed analysis of the noise contributions in the optical detection theory is beyond the scope of this book and will be considered for another planned book.

What does the statement 'the required electrical filtering for noise reduction' mean that was mentioned above? The answer to this question leads to the concept of either the optical reference receiver or the optical matched receiver. The optical transmitter signal modeling has been introduced in previous sections, and, according to the optical modulation process, it can be assumed that the time-dependent envelope of the optical intensity launched from the transmitter into the optical fiber would be shaped according to a proper pulse profile. The pulse profile can then be modeled using some analytical functions and the corresponding eye diagram can easily be built up in order to predict the effect of a random pattern generator on the signal decision process.

There is interest in the envelope of the optical intensity because the optical detection process converts the optical intensity envelope into the corresponding electric current intensity. The mathematical theory of the photodetection process is complex and requires a statistical approach in order to have a meaningful model. The shot noise arises consistently with the photodetection theory as the variance of the detected light intensity. The photon counting process follows the well-known Poisson distribution and the variance of the Poisson process is proportional to the ensemble average of the detected light. Accordingly, the intensity fluctuation of the detected light increases proportionally to the intensity itself, resulting in the well-known signal-dependent shot noise contribution. In this simplified treatment, it will be assumed that the photodetection statistics collapses on a Dirac delta probability density function (PDF), located at the required average intensity level. Proceeding in this way, the stochastic characteristic of the photodetection process is effectively removed, relying on the simpler deterministic approach. The shot noise will be added to the remaining noise terms as an independent Gaussian contribution whose variance is proportional to the detected intensity.

8.4.1 Introduction

In order to understand the meaning of 'the required electrical filtering for noise reduction', it is important to introduce some basic concepts regarding intersymbol interference. This concept is of basic importance to every digital transmission system and is not a peculiarity of optical systems only. Assuming a base band digital binary on–off keying (OOK) modulation format as the typical line code for the direct detection optical system, the detected electrical pulse sample $y_s(t_k) \equiv y_k$ is

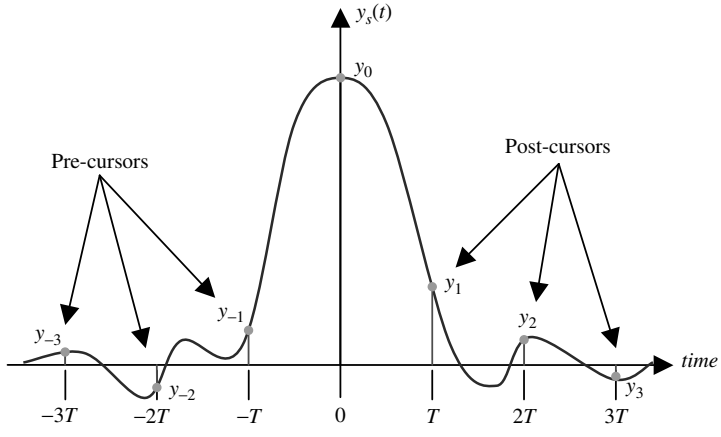

Figure 8.34 Received single electrical pulse. Sampling time instants $t_k = kT$, $k = \pm 1, \pm 2, \ldots$, have been assumed at every integer multiple of the time step T, starting from $t = 0$. The corresponding pulse values $y_s(t_k) \equiv y_k$, constitute the intersymbol interference (ISI) components

evaluated at the time instants $t_k = kT$, $k = 0, \pm 1, \pm 2, \ldots$, according to the transmitted time step T. The detected pulse $y_s(t)$ can exhibit residual nonzero precursor and postcursor contributions, which will disturb the synchronous signal detection. Assuming a linear photodetection process, consecutive detected current pulses are added together, and tail superposition in correspondence with the signal sampling time instants $t_k = kT$ can strongly degrade the digital signal recognition. The noise is present every time, even at the sampling time instant of course, and it is intuitive that maximizing the amplitude of the signal sample with respect to the RMS noise level will improve the signal decision process, at least up to some asymptotic condition.

Due to the arbitrariness of the timescale, it is assumed that the time origin $t = 0$ is located at the optimum sampling time for maximizing the signal-to-noise ratio. First the signal sample $y_s(0) = y_0$ will be defined. This sample represents the information content needed to make a proper deduction. It has been found that if the detected optical pulse shows time symmetry with the maximum amplitude located at the time symmetry instant, the optimum sampling time coincides with that instant. Figure 8.34 gives a qualitative description of the received signal pulse, without referring to any particular pulse symmetry. The amount of pulse energy distributed beyond the central body is usually identified as a pulse postcursor, while the energy located before the pulse body constitutes a pulse precursor.

In order to minimize the probability of making an erroneous electrical pulse decision (binary pulses have two logical levels, namely level 0 and level 1), the signal pulse amplitude $y_s(0) = y_0$ at the sampling time $t = 0$ must be maximized with respect to the average RMS noise value σ_n. The noise at the sampling time can have either a signal-dependent contribution or an additive signal-independent term, or both. In the following treatment, all noise components, either additive or signal-dependent, will be assumed to exhibit a Gaussian probability density function with a white power spectral density. A further simplification arises if the signal-dependent shot noise contribution is calculated using the average signal power, thus losing the true time-dependent behavior.

8.4.2 Definitions

Referring to the pulse sketched in Figure 8.34, the intersymbol interference (ISI) term at the sampling time $t = 0$ is defined as the random variable $\underline{\delta}(T)$ defined by the summation of all off-time

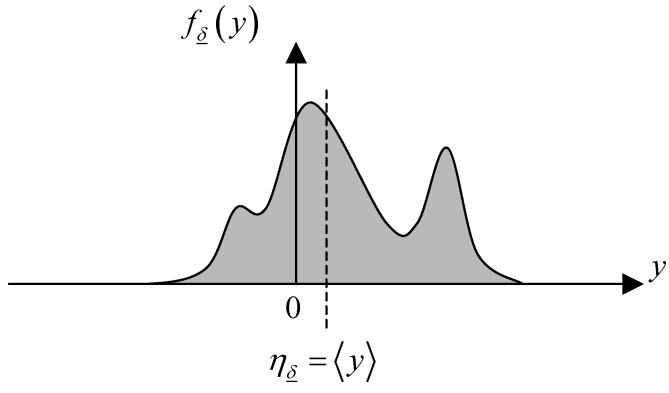

Figure 8.35 Probability density function of the intersymbol interference random variable $\underline{\delta}(T)$. The dashed line gives the average value that in general is not zero

samples, $t \neq 0$, arising from all the available binary weighted combinations of the detected current pulses:

$$\underline{\delta}(T) \equiv \sum_{\substack{k=-\infty \\ k\neq 0}}^{k=+\infty} \underline{a}_k y_k$$
$$y_k = y_s(kT), k = \pm 1, \pm 2, \ldots \tag{8.41}$$

The weighting terms are the realizations $\{a\}_k$ of the random sequence $\underline{a}_k$ of the discrete binary random variable $\underline{a} = (0, 1)$. Figure 8.35 gives a sketch of the ISI probability density function $f_{\underline{\delta}}(y)$.

Neglecting the noise contribution, the random nature of the intersymbol interference variable $\underline{\delta}(T)$ relies exclusively on the randomness of the sequence $\underline{a}_k$ of the binary weights considered, and not on the off-time signal samples y_k. Assuming an infinite pulse extent, each realization $\{a\}_k$ of the random sequence generates the event $\delta_k(T)$. In this case, the ISI value $\delta_k(T)$ corresponding to a fixed sequence $\{a\}_k$ is a deterministic quantity. In order to clarify this concept, the following example should be considered:

$$\{a\}_k = (\ldots 10011101 \uparrow 10111110 \ldots) \tag{8.42}$$

The up-arrow $\uparrow$ identifies the position of the sampling instant at $t = 0$. The eight binary weights reported on the left and the right sides represent the weighted signal pulses considered before and after the sampling time respectively. In this case only eight bits on both pulse sides have been included, but the extent of the significant binary sequence depends of course on the received pulse duration and how it decays over the relative time interval. Associated with sequence (8.42) the corresponding off-time pulse sample sequence should be considered:

$$\{y\}_k = (\ldots y_{-8} y_{-7} y_{-6} y_{-5} y_{-4} y_{-3} y_{-2} y_{-1} \uparrow y_1 y_2 y_3 y_4 y_5 y_6 y_7 y_8 \ldots) \tag{8.43}$$

Only off-time contributions y_k associated with nonzero binary coefficients will be contributing to the corresponding ISI term. In the example considered so far, from Equations (8.42) and (8.43),

$$\delta_k(T) = \cdots + y_{-8} + y_{-5} + y_{-4} + y_{-3} + y_{-1} + y_1 + y_3 + y_4 + y_5 + y_6 + y_7 + \cdots \tag{8.44}$$

Changing the random sequence $\{a\}_j$ gives in general a different value for the intersymbol interference contribution. Assuming, for example, the sequence realization $\{a\}_j$:

$$\{a\}_j = (\ldots 01010101 \uparrow 11110011 \ldots) \tag{8.45}$$

the following ISI contribution is obtained:

$$\delta_j(T) = \cdots + y_{-7} + y_{-5} + y_{-3} + y_{-1} + y_1 + y_2 + y_3 + y_4 + y_7 + y_8 + \cdots \tag{8.46}$$

and, in general, $\delta_k(T) \neq \delta_j(T)$.

8.4.3 Population Dimension

Assuming a fixed number of significant off-time samples contributing on the left side and on the right side of the sampling time (eight time steps in the example above), the statistic of the random variable $\underline{\delta}(T)$ is completely defined by the finite distribution of the corresponding ISI values. This conclusion is very important from a practical point of view, and allows the probability density function of $\underline{\delta}(T)$ to be computed once the finite number of binary sequences are known.

The symbols L and R are used to show the number of significant time steps on the left side and on the right side respectively of the sampling instant. The extent of a significant off-time sample can easily be defined by comparing it with the amplitude y_0 of the normalized signal sample and assuming monotonic decay of the absolute value of the pulse on both sides of the sampling instant. The total number N_L of allowable binary sequences that produce a significant ISI contribution to the left side is given by

$$N_L = 2^L - 1 \tag{8.47}$$

This number coincides with the total number of combinations of $k = L$ elements of class $n = 2$, [0,1](binary code), including repetitions but excluding the trivial case with L elements equal to 0. For example, choosing $L = 3$ gives

[001], [010], [011], [100], [101], [110], [111]

The meaningless sequence corresponding to the all-zero coefficient gives no ISI contribution, of course, and has been removed from the number N_L of significant binary sequences. Using exactly the same arguments gives the number N_R of allowable binary sequences that can produce a significant ISI contribution due to the right side of the pulse:

$$N_R = 2^R - 1 \tag{8.48}$$

The total number of all binary sequences that generate significant ISI contributions is therefore given by multiplying each single-sided sequence by the total number of allowable sequences on the other side of the sampling instant. In conclusion, the total number N_{ISI} of ISI generating sequences is given by

$$N_{\mathrm{ISI}} = N_R N_L + N_L + N_R \tag{8.49}$$

The additive term $N_L + N_R$ takes into account the extra sequences corresponding to the all-zero condition on one side only of the sampling instant. Substituting Equations (8.47) and (8.48) into Equation (8.49) gives the following expression for the total dimension of the ISI population contributions:

$$N_{\mathrm{ISI}} = 2^{(R+L)} - 1 \tag{8.50}$$

Assuming, for example, that $L = 8$ and $R = 8$, the dimension of the ISI population is $N_{\mathrm{ISI}} = 65\,535$. Expression (8.50) easily reveals that if the same number of time step contributions is accounted for on each pulse side $N_L = N_R$, the ISI population grows as the square of the significant time steps:

$$L = R \Rightarrow N_{\mathrm{ISI}} = 2^{2R} - 1 = (2^R)^2 - 1 \tag{8.51}$$

Referring to the previous case and considering now only four steps on each pulse side $L = 4$, $R = 4$, the ISI population reduces considerably to only $N_{ISI} = 255$ elements. To conclude this section, it should be noted that assuming finite binary sequences of $L + R$ elements each, the probability of occurrence of each realization is uniformly distributed and equals the value $1/N_{ISI}$ (neglecting the identically null trivial sequence). Consequently, the ISI distribution would be uniform, unless different coefficient sequences originate the same ISI contribution.

8.4.4 Signal–ISI Joint Statistic

Following the discussion of the previous section, it is important to remark explicitly that the ISI statistic is exactly the same and affects both detected pulse levels $y_0 = a_0$ and $y_0 = a_1$. This statement is self-evident since in the present derivation the value of the pulse at the sampling time $t = 0$ is neglected. Neglecting pattern-dependent jitter, ISI and noise, the ideal sampled signal value y_0 of the received pulse can assume only one of the two binary values, namely a_0 and a_1. Those values are therefore not affected by any signal statistics and the decision process is true deterministic. The probability density function of the sampled signal y_0 is given by two Dirac delta functions, each located at one of the two possible sampled amplitudes, namely $y_0 = a_0$ and $y_0 = a_1$, and weighted by the probabilities p_0 and p_1 of the corresponding event. Figure 8.36 gives a graphical representation of the mathematical model just introduced.

As long as the transmission channel is deterministic and time invariant, the detected pulse shape remains fixed and the off-time samples y_k, $k \neq 0$, are the same for every single-pulse realization. The consequences of the pattern-dependent jitter (PDJ) as one of the most relevant contributions to the random data jitter of the detected signal will not be discussed. Of course, once the PDJ is included in the analysis of the detected signal, the off-time samples of the detected single pulse y_k, $k \neq 0$, will no longer be a fixed deterministic sequence, but instead they must be described as a random sequence whose statistic is a consequence of the random datastream through the system PDJ characteristic. Accordingly, the intersymbol interference distribution will be affected by the joint

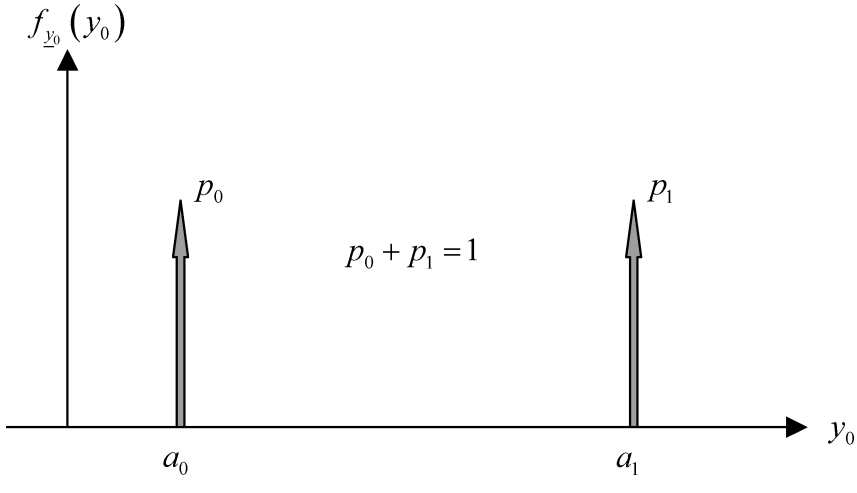

Figure 8.36 Probability density function of the detected isolated pulse amplitude. Neglecting the pattern-dependent jitter, ISI and noise, the binary single-pulse sampled amplitude can have only two values: $y_0 = a_0$ and $y_0 = a_1$. The mathematical model can be conveniently expressed using Dirac delta functions, each located at the corresponding signal sample and weighted by the probability of the corresponding event. For every event distribution, $p_0 + p_1 = 1$. In particular, assuming equiprobable events, $p_0 = p_1 = \frac{1}{2}$

statistic of the random data sequence $\underline{a}_k$ with the system generated PDJ. It is important to point out that even the PDJ has its statistical nature relying on the random data sequence $\underline{a}_k$ and not on the single-pulse system response. The transmission system has a deterministic single-pulse response; when several random weighted pulses are sequenced together the system response depends on the particular sequence realization $\{a\}_k$, leading to the pattern-dependent jitter.

Neglecting both the PDJ and noise contributions and assuming a linear channel and linear photodetection, the sampled signal value y_0 and the intersymbol interference random variable $\underline{\delta}(T)$ will be added together. The total signal $\underline{z}(T)$ at the sampling instant $t = T$ is still a random variable and is given by the sum of the sampled value $\underline{y}_0$ with the ISI random variable $\underline{\delta}(T)$:

$$\underline{z}(T) = \underline{y}_0 + \underline{\delta}(T) \tag{8.52}$$

Note that the total signal amplitude is a random variable and not a random process because the time variable has been fixed in the sampling instant. It is a fundamental result of the theory of random processes[1] that the joint probability density function of the sum of two statistically independent random variables is given by the convolution of their respective probability densities. This useful theorem will be invoked several times in the following derivations. The independency requirement between the sampled signal amplitude and the corresponding ISI value is fully satisfied, since the ISI random variable is not related in any way to the signal value sampled at the time instant $t = 0$. Two definitions are given:

$f_{\underline{y}_0}(y)$: probability density function of the pulse sample $\underline{y}_0$ at the sampling time instant $t = 0$
$f_{\underline{\delta}}(y)$: probability density function of the ISI random variable $\underline{\delta}(T)$

The probability density function of the joint statistics of the sum of noise and ISI becomes

$$f_{\underline{z}}(y) = f_{\underline{y}_0}(y) * f_{\underline{\delta}}(y) \tag{8.53}$$

According to the deterministic distribution assigned to the signal pulse at the sampling time instant $t = 0$, as reported in Figure 8.36, the probability density function $f_{\underline{y}_0}(y)$ of the signal sample $\underline{y}_0$ assumes the following expression:

$$f_{\underline{y}_0}(y) = p_0\ \delta(y - a_0) + p_1\ \delta(y - a_1) \tag{8.54}$$

The probability density function $f_{\underline{\delta}}(y)$ depends strictly on the received pulse shape $y_s(t)$ and on the random data sequence $\underline{a}_k$. It is assumed that the probability density function $f_{\underline{\delta}}(y)$ of the ISI random variable $\underline{\delta}(T)$ is known. From Equations (8.52), (8.53) and (8.54) the probability density function $f_{\underline{z}}(y)$ of the random variable $\underline{z}(T)$ is obtained. Due to the property of the delta function, it can immediately be concluded that the probability density function $f_{\underline{z}}(y)$ is given by translation of $f_{\underline{\delta}}(y)$ with the origin centered at the two detected levels a_0 and a_1:

$$f_{\underline{z}}(y) = f_{\underline{y}_0}(y) * f_{\underline{\delta}}(y) = p_0\ f_{\underline{\delta}}(y - a_0) + p_1\ f_{\underline{\delta}}(y - a_1) \tag{8.55}$$

Even if the ISI distribution is the same around both low and high decision levels, its effect is different in general for the two decision processes. This is evident from Figure 8.37, where an asymmetric PDF has been assumed. It should be noted explicitly that according to Equation (8.55), the origin of the probability density function of the intersymbol interference is translated on to the sampled signal levels, namely a_0 and a_1. Consequently, if the average value $\eta_{\underline{\delta}}$ is nonzero, the PDF will have a different effect on the two signal levels. Referring to the case presented in

[1] A. Papoulis, *Probability, Random Variables and Stochastic Processes*, McGraw-Hill, 1991.

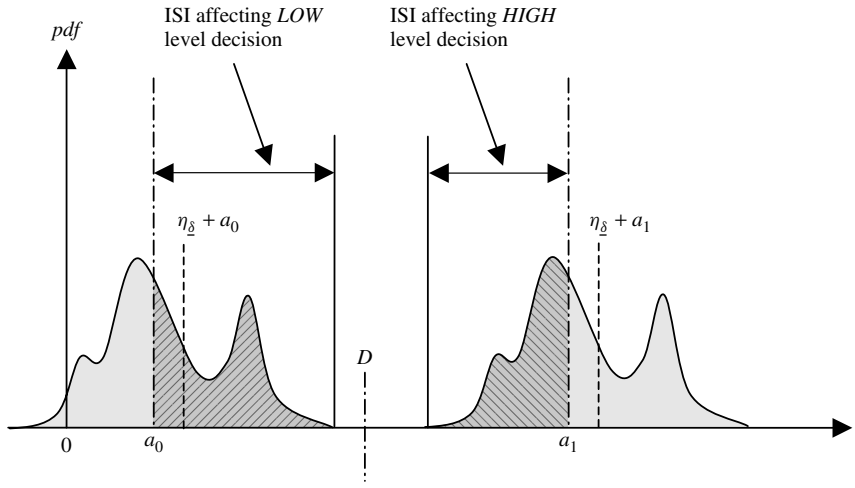

Figure 8.37 The PDF for the signal pulse decision in the presence of ISI, but without noise or pattern-dependent jitter

Figure 8.37, it evident that the ISI contribution on the lower decision level defined by a_0 is stronger than on the higher level. In this case, it would be advisable to move the threshold level D to a higher value with respect to the middle position. This procedure will compensate for different error contributions, balancing the error probability between the two signal levels (binary system). Of course, if ISI has a symmetric probability density function with a zero average value, the optimum decision threshold would be located at the middle of the signal levels.

Before concluding this short introduction on the intersymbol interference effects in binary systems, it is important to note that if the ISI distribution has a peak value lower than the decision distance, no decision error would be produced in the absence of noise. This statement is quite important in understanding the decision process and sometimes it is underestimated. For moderate ISI and additive Gaussian noise, the noise statistic determines the error probability, while ISI mainly affects the optimum threshold position. For a given noise, the optimum threshold position minimizes the error probability, balancing the error contribution from both signal levels. Even assuming an optimum threshold position, the bit error rate is still a steeply increasing function of the relative noise power allocated to each signal level.

The effect of moderate ISI distribution is to translate the error probability curve to higher received power levels, in order to overcome the ISI-induced closure of the eye diagram. Figure 8.38 illustrates this concept. In order to understand how ISI probability density works in conjunction with the noise channel, it is necessary to remember that the total PDF, including ISI and additive noise, is given by the convolution of the two corresponding densities. Assuming for simplicity an additive Gaussian noise, moderate ISI distribution can be quantitatively referred to if the result of the convolution between the two probability densities still closely resembles a Gaussian-like function. From a rigorous mathematical point of view, the output of the convolution will be a Gaussian if and only if both convolving densities are Gaussian.

It is a well-known property of the convolution (see the Papoulis reference, 1991) that if one of the two convolving functions is relatively broader than the other, the shaping of the convolution output will be dominated by the broader function. A limiting case is the convolution of any suitable function with a Delta distribution. In that case, the convolution output is given by the original function translated at the Delta position, without any reshaping effect. As a rule of the thumb, in order to maintain qualitatively the same Gaussian-like PDF it is necessary that the extent of the

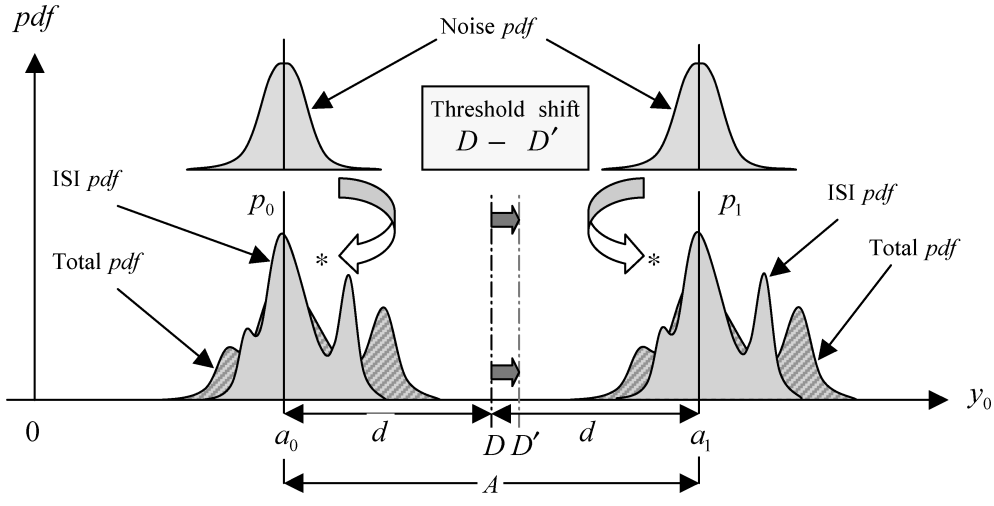

Figure 8.38 Representation of the Gaussian noise density function and digital signal levels with a relatively strong ISI probability density function superposed for the decision process. The ISI probability density function is represented, with the noise PDF shown above. The total (dashed) PDF is given by the convolution of the ISI PDF with the noise PDF. The total PDF is responsible for the bit error rate performance. The decision threshold must be chosen accordingly in order to minimize the bit error rate for the given total probability density function

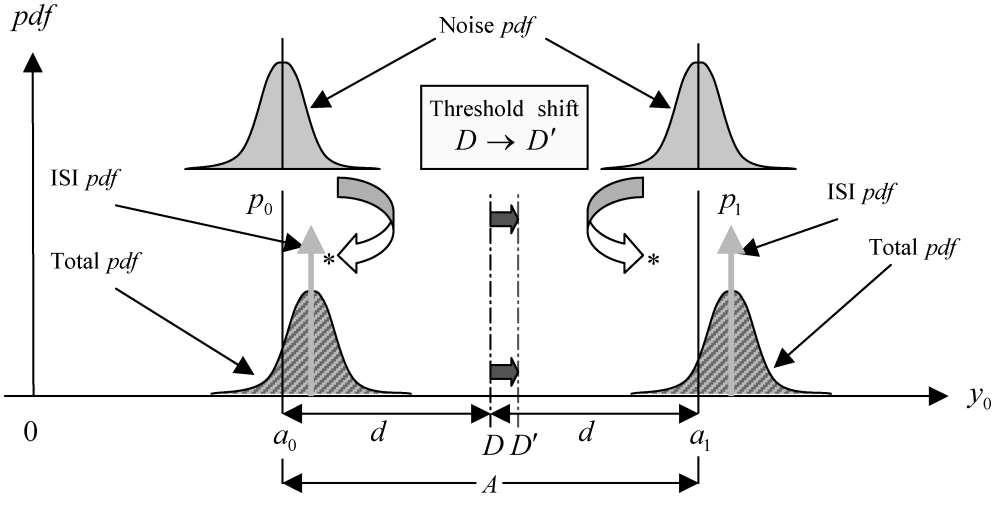

Figure 8.39 Representation of the Gaussian noise density function and digital signal levels with a relatively strong ISI probability density function superposed for the decision process. The ISI probability density function is represented, with the noise PDF shown above. The total (dashed) PDF is given by the convolution of the ISI PDF with the noise PDF. The total PDF is responsible for the bit error rate performance. The decision threshold must be chosen accordingly in order to minimize the bit error rate for the given total probability density function

probability density function of the intersymbol interference is limited to less then one sigma of the additive noise distribution. This condition results in a total output PDF that resembles very closely the Gaussian distribution of the noise density, but with increased width. This increased width of the total PDF reflects a higher error probability corresponding to a given input optical power level, representing the quantitative degradation of the digital signal detection process due to the intersymbol interference.

From Figure 8.38 it is found that in order to maintain fixed bit error rate performances for the received optical power when moderate ISI is added to the signal, it is necessary to increase the received power level to the amount corresponding to the increased width of the total PDF.

Another condition that would be reflected in an overall right shift of the total error probability, with a corresponding loss of receiver sensitivity, is shown in Figure 8.39. The intersymbol interference PDF consists of a very sharp, delta-like function, with a nonzero average value. In this case, the convolution between the Gaussian noise PDF and the ISI PDF consists of a Gaussian-like function, with almost the same width as the original Gaussian, but with the average value shifted to the average value of the intersymbol interference distribution. Translation of the noise probability density reflects the same error probability as that for the ISI-free operation but requiring more received optical power in order to compensate for the translated noise distribution.

The concepts presented in this section would need a complete mathematical treatment in order to acquire a proper knowledge to manage system design and to predict correctly the system performances. Error probability in the presence of noise, intersymbol interference and jitter will not be covered here, but they will be a major topic in a planned book.

8.5 The Optical Receiver

In the previous section, the intersymbol interference was introduced as one of the major impairments of the detected optical pulse profile for a given transmission timing T. It is clear that even neglecting the pattern-dependent jitter, the sampled signal $z_0 = y_0 + \underline{\delta}(T)$ must be considered as a random variable due to the random weighted contributions $\underline{\delta}(T)$ from adjacent precursors and postcursors.

The aim of this section is to present the mathematical modeling of the optical fiber receiver. As seen previously, among major degradations affecting the detected optical pulse and the related eye diagram are noise and intersymbol interference. Other important contributions to eye diagram degradation come from jitter, signal-dependent noise, phase distortion and nonlinear effects. In the present analysis, all these signal distortion contributions will be neglected, concentrating only on additive white Gaussian noise (AWGN) and intersymbol interference (ISI).

Depending on which of these two signal-degrading causes are minimized (noise) or even canceled (ISI), the corresponding optical fiber receiver takes the meaning of optical matched receiver (OMR) or optical reference receiver (ORR) respectively. These concepts are of basic importance in understanding real receiver operation and how far away from the optimum receiver they are or even how to improve their performances in the correct direction. It is self-evident that without knowledge of how much improvement could be obtained on a given design any proper direction would be very often a blind trial.

The optical matched receiver represents the theoretical best solution, but it requires a control of the signal transmitted spectrum in order to achieve simultaneously a minimum additive noise contribution and a full ISI cancellation. The requirement for a well-defined transmitted signal spectrum is often not achievable from optical transmitters or at least it would require too much technology effort to justify the gain in system performances.

The optical reference receiver represents the linear suboptimal optical receiver needed to approximate best optical transmission system performances for any arbitrary transmitted signal spectrum.

No stringent conditions are therefore required on the transmitter side. The definition of the ORR is based on the linear inverse spectrum filter (LISF). Given a transmitted signal spectrum, the ORR must perform proper signal filtering in order to have a signal spectrum at the decision section belonging to the particular class satisfying the condition of zero intersymbol interference. It is customary to define all functions and filters parameterized to the signaling time T. Any real receiver implementation would therefore be compared with either the ORR or the OMR in order to obtain a quantitative figure of merit for its performances.

8.5.1 The Optical Reference Receiver (ORR)

In the following the symbols $\Theta_X(f)$ and $H_S(f)$ will be used to refer to the signal spectrum available at the generic section $X-X'$ of the optical receiver and to the transfer function of the system S respectively. Below is a list summarizing the major assumptions and features of the model adopted for the optical reference receiver. Most of these assumptions serve as guidelines for understanding model limitations and improvements.

1. The photodetection statistics collapse upon a delta-like probability density function (PDF). The average value of the time-dependent optical intensity distribution is therefore represented by the position of the delta-like PDF, with no fluctuations and uncertainty. So far, the detection process has been reduced to a noiseless deterministic process.
2. The noise generated during the photodetection process, including the optical noise embedded in the received pulse, is included in the total average white Gaussian noise (AWGN) term at the receiver electrical reference section.
3. In a first-order low-signal analysis, signal-dependent noise contributions, such as RIN (relative intensity noise), shot noise and signal-spontaneous beat noise, are implicitly assumed negligible compared with signal-independent noise terms.
4. The ensemble average of the time-dependent optical intensity envelope detected at the receiver fiber end is converted by the photodetector into an identical photocurrent pulse profile, with unity conversion efficiency. The photodetector behaves like the ideal photoelectric converter with a delta impulse response (instantaneous response) and unity conversion efficiency.
5. The optical transmitter output is directly connected to the optical receiver input using a very short length of optical fiber so that the launched signal spectrum does not need to be modified. The source signal spectrum available at the fiber launching section $S-S'$ is $\Theta_S(f)$. These transmitting conditions are referred to as back-to-back conditions.
6. The optical reference receiver includes the electrical linear filter with the frequency response $H_R(f)$. The filter $H_R(f)$ takes into account all receiver transfer functions, including the photodetector, the low-noise front end, the linear amplifier and the frequency response of the reference filter.

According to assumptions 4 and 5 and referring to Figure 8.40, the electrical signal spectrum $\Theta_D(f)$ available at the decision section $D-D'$ is given by

$$\Theta_D(f) = \Theta_S(f)H_R(f) \tag{8.56}$$

The optical reference receiver is defined as the optical receiver whose total frequency response $H_R(f)$ applied to the transmitted spectrum $\Theta_S(f)$ gives a signal spectrum $\Theta_D(f)$ at the decision section $D-D'$ belonging to a special class of functions:

$$\begin{aligned} &\Theta_D(f) \equiv \Gamma_T(f) \\ &\gamma_T(t) \overset{\Im}{\longleftrightarrow} \Gamma_T(f) \in L^1(\Re) \end{aligned} \tag{8.57}$$

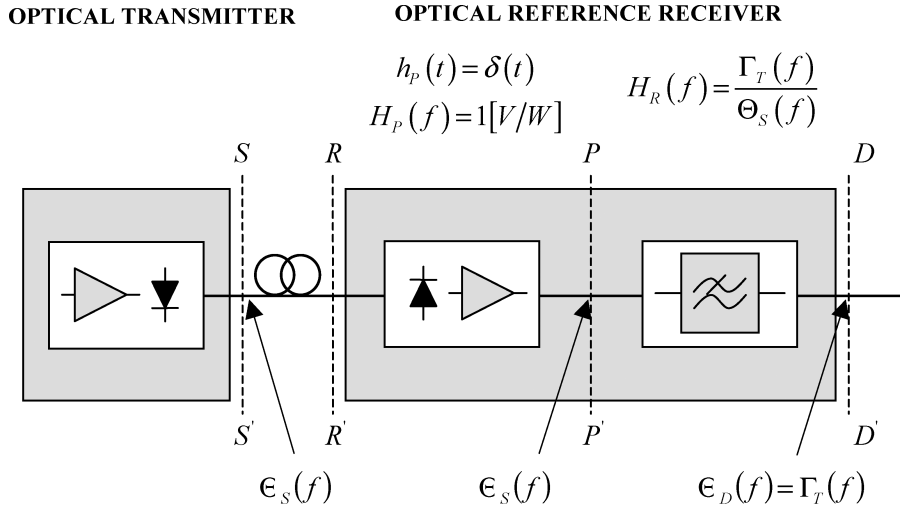

Figure 8.40 Block diagram of the optical reference receiver. The fiber link is assumed to be in the back-to-back configuration and the fiber jumper does not affect the optical transmitted signal spectrum

The time domain representation $\gamma_T(t)$ satisfies the following condition:

$$\gamma_T(kT) = 0, \quad k = \pm 1, \pm 2, \ldots \tag{8.58}$$

The function $\Gamma_T(f)$ is defined as the reference signal spectrum (RSS). According to the functions (8.57), each function $\Gamma_T(f)$ satisfies the condition of zero intersymbol interference over the sampling rate T. From conditions (8.56) and (8.57) the required filter expression $H_R(f)$ for the optical reference receiver is found to be

$$H_R(f) = \frac{\Gamma_T(f)}{\Theta_S(f)} \tag{8.59}$$

Figure 8.40 presents a block diagram of the optical reference receiver with the definition of the electrical section involved. The receiver input section is represented by the photodetector followed by the linear amplification section. The photodetected and amplified signal is therefore available at section $P-P'$ as the electrical amplitude (either current or voltage), assuming a unity conversion gain $H_P(f) = 1\ V/W$.

The receiving section is assumed to have an ideal electro-optical delta impulse response in order for the optical received signal spectrum not to be modified. The frequency response of the received signal at the intermediate section $P-P'$ therefore coincides with the spectrum $\Theta_S(f)$ of the transmitted signal at the source section $S-S'$. The detected signal at $P-P'$ is then filtered according to Equation (8.56) in order to deliver a specified output signal spectrum at the decision section $D-D'$ belonging to the reference family $\Gamma_T(f)$.

In the next section, a general class of functions $\Gamma_T(f)$ will be introduced, characterized by having no intersymbol interference. Those functions will be referred to as the reference receiver spectrum (RRS) at the decision section $D-D'$ and will be specified in a simple mathematical form. Once the received signal spectrum $\Theta_S(f)$ is known, the optical reference receiver filter $H_R(f)$ will be completely specified by Equation (8.56). In the following, both the received signal spectrum $\Theta_S(f)$ and the reference receiver spectrum $\Gamma_T(f)$ will be described in terms of analytical mathematical functions. Real filters must therefore be designed in order to approximate the mathematical function $H_R(f)$ by means of proper polynomial fitting.

8.5.2 The Reference Receiver Spectrum (RRS)

The aim of this section is to define a general class of functions that satisfy the requirements (8.58) for the reference receiver spectrum $\Gamma_T(f)$. In order to arrive at a definition of a general class of those functions, first the well-known raised cosine pulse will be analyzed, which satisfies conditions (8.58). After that, a simple condition will be deduced that is useful for generalizing the required behavior to a more general class of function. The aim of the following generalization is to find a wide class of functions that can fit real system responses using finite impulse response (FIR) filter realization.

8.5.2.1 The Raised Cosine Pulse

The time domain expression of the raised cosine pulse defined over a time step T is as follows:

$$\gamma_T(t) = \frac{1}{T}\frac{\cos(m\pi t/T)}{1-(2mt/T)^2}\frac{\sin(\pi t/T)}{\pi t/T}, \quad 0 \le m \le 1 \tag{8.60}$$

The parameter m defines the shaping of the pulse and the position of a subset of zeros. It is the shaping coefficient. The raised cosine function has two sets of zeros:

1. The first set of zeros belongs to the roots of the first factor in Equation (8.60):

$$\frac{\cos(m\pi t/T)}{1-(2mt/T)^2} = 0 \quad \Rightarrow \quad t_k = \pm\frac{T}{2m}(2k+1), \quad k = 1, 2, \ldots \tag{8.61}$$

The even symmetry of the function in Equation (8.60) allows only the positive time axis to be considered. According to Equation (8.61), the first positive zero corresponds to $k = 1$ and falls at $t_1 = \frac{3}{2}(T/m)$. Subsequent zeros are found at the following time instants:

$$t_2 = 5\left(\frac{T}{2m}\right), \qquad t_3 = 7\left(\frac{T}{2m}\right), \qquad t_4 = 9\left(\frac{T}{2m}\right), \qquad \ldots \tag{8.62}$$

The distance Δt_k between any two consecutive zeros of the first factor in Equation (8.61) is given by

$$\Delta t_k \equiv t_{k+1} - t_k = \frac{T}{2m}[2(k+1) + 1 - 2k - 1] = \frac{T}{m} \tag{8.63}$$

This result gives the meaning to the shaping coefficient m of the raised cosine pulse in Equation (8.60): the reciprocal of the shaping coefficient $1/m$ represents the normalized period of the zeros of the shaping factor.

Since the distance between any two consecutive zeros is constant, it can immediately be concluded that all zeros of the shaping factor of the raised cosine pulse constitute a periodic sequence, the period being $\Delta t_k = T/m$. In the limiting case of $m = 1$ from Equation (8.63), it can be concluded that the zeros t_k will be spaced exactly one time step apart from each other, starting from $t_1 = \frac{3}{2}(T/m) : t_{k+1} - t_k = T$, $k = 1, 2, \ldots$; $m = 1$.

Finally, to solve the indetermination for $k = 0$ in Equation (8.61), use can easily be made of the elementary calculus theorems and find the following continuity condition at $t = \pm T/(2m)$:

$$\lim_{t \to \pm T/(2m)} \frac{\cos(m\pi t/T)}{1-(2mt/T)^2} = +\frac{\pi}{4} \tag{8.64}$$

2. The second set of zeros belongs to the roots of the second factor in Equation (8.60), namely the sinc function:

$$\frac{\sin(\pi t/T)}{\pi t/T} = 0 \quad \Rightarrow \quad t_j = \pm jT, \; j = 1, 2, \ldots \tag{8.65}$$

These zeros fall exactly every time step interval T. This property is most important since it characterizes the sampling rate behavior of raised cosine pulse sequences. This second set of zeros does not depend upon any shaping factor. It is strictly defined by the sampling window T. According to Equation (8.65), the first zero falls at $t_1 = T$, the second at $t_2 = 2T$, and so on.

Both sequences in Equations (8.61) and (8.65) represent the set of all the zeros of the raised cosine function. The expressions below summarize the two sequences:

$$\text{Shaping factor zeros :} \qquad t_k = \pm\frac{T}{2m}(2k+1), \quad k = 1, 2, \ldots$$

$$\text{Windowing factor zeros :} \qquad t_j = \pm jT, \quad j = 1, 2, \ldots$$

To illustrate the zero sequence, let us consider three different values of the shaping coefficient m. The zeros have been identified graphically using two different characters, depending on whether they are related to the shaping factor or to the windowing function in Equation (8.60). The character 'x' refers to a zero related to the shaping factor, while the character 'o' refers to a zero of the windowing function.

1. $m = 1$:

$$\left\{\begin{array}{c} t_k = (2k+1)\dfrac{T}{2} \\ t_j = jT \end{array}\right\} \quad \Rightarrow \quad \left(\begin{array}{c} T, \dfrac{3}{2}T, 2T, \dfrac{5}{2}T, 3T, \ldots \\ \text{o} \quad \text{x} \quad \text{o} \quad \text{x} \quad \text{o} \end{array}\right) \tag{8.66}$$

   In this case, the zeros of the two factors in Equation (8.60) are interleaved and all zeros are of first order. No zeros are therefore coincident.

2. $m = 0.5$:

$$\left\{\begin{array}{c} t_k = (2k+1)T \\ t_j = jT \end{array}\right\} \quad \Rightarrow \quad \left(\begin{array}{c} T, 2T, 3T, 4T, 5T, \ldots \\ \text{o} \quad \text{o} \quad \text{o} \quad \text{o} \quad \text{o} \\ \qquad\quad \text{x} \qquad \text{x} \end{array}\right) \tag{8.67}$$

   In this case all the zeros come from the windowing factor sinc and are located at the integer multiplet j of the time step T. In this particular case, starting from the time instant $3T$ the zeros t_k of the shaping are found, with the periodicity $2T$, as expected from Equation (8.63). The superposition between the two sequences of zeros leads to the second-order zero subsequence located at time instants t_k.

3. $m = \frac{1}{3}$:

$$\left\{\begin{array}{c} t_k = (2k+1)\dfrac{3T}{2} \\ t_j = jT \end{array}\right\} \quad \Rightarrow \quad \left(\begin{array}{c} T, 2T, 3T, 4T, \dfrac{9}{2}T, 5T, 6T, 7T, \dfrac{15}{2}T, \ldots \\ \text{o} \quad \text{o} \quad \text{o} \quad \text{o} \quad \text{x} \quad \text{o} \quad \text{o} \quad \text{o} \quad \text{x} \end{array}\right) \tag{8.68}$$

   In this case, the first four zeros come from the windowing function. The contribution from the shaping factor starts at $\frac{9}{2}T$ with a period $3T$, as expected. All the zeros are interleaved and of first order only.

The analysis presented here suggests that two different names should be introduced for the two functions constituting the raised cosine expression in Equation (8.60). This approach serves as an introduction to the next section where a general class of reference receiver spectrum functions will be defined. Referring to Equation (8.60) gives the following definitions:

$$\text{shaping pulse } s(t) \Rightarrow \quad s(t) \equiv \frac{\cos(m\pi t/T)}{1-(2mt/T)^2}, \quad 0 \le m \le 1 \tag{8.69}$$

$$\text{Windowing function } w(t) \Rightarrow \quad w_T(t) \equiv \frac{1}{T}\,\frac{\sin(\pi t/T)}{\pi t/T} \tag{8.70}$$

From the previous analysis, it is observed that:

1. The windowing function $w_T(t)$ is responsible for setting the zero sequence at each multiple of the time step T. This guarantees no intersymbol interference at signaling T.
2. The shaping function $s(t)$ in Equation (8.69) is responsible for setting different raised cosine pulse shapes, depending on the value of the parameter m.

The important conclusion is that for every value of the parameter $0 \leq m \leq 1$, the raised cosine pulse presents the zero sequence at least corresponding to the multiple of the time step T. This is a clear consequence of using the windowing function $w_T(t)$ as a factor in the product (8.60) of the raised cosine pulse expression. Other eventual zeros will emerge from the shaping function properties through the parameter m. However, those zeros do not influence the intersymbol interference contribution, since they are out of the sampling time instants $t_k = kT$, $k = \pm 1, \pm 2, \ldots$. As will be seen in the next section, the interesting properties of the raised cosine pulse shown above clearly suggest using the same approach to introduce a more general class of functions, such as the reference receiver spectrum.

Before closing this section, three computed raised cosine pulses are reported with reference to the theory presented above. Figure 8.41 shows the raised cosine pulses using three different shaping factors m, but exhibiting the same windowing pulse $w_T(t)$ with $T = 100$ ps. It is interesting to see the two factors $w(t)$ and $s(t)$ interacting together, giving the well-known output pulse shaping.

Figure 8.41 showed the computed raised cosine pulse assuming a fixed windowing of $T = 100$ ps and a shaping coefficient $m = 1$. According to Equation (8.63), the highest value of the shaping coefficient corresponds to the tightest zero sequence, spaced exactly as the unit time step T. This reflects the sharpest shaping function available for the given time step T. The zero sequence follows the structure reported in Equation (8.66). Figure 8.42 presents the case of the reduced

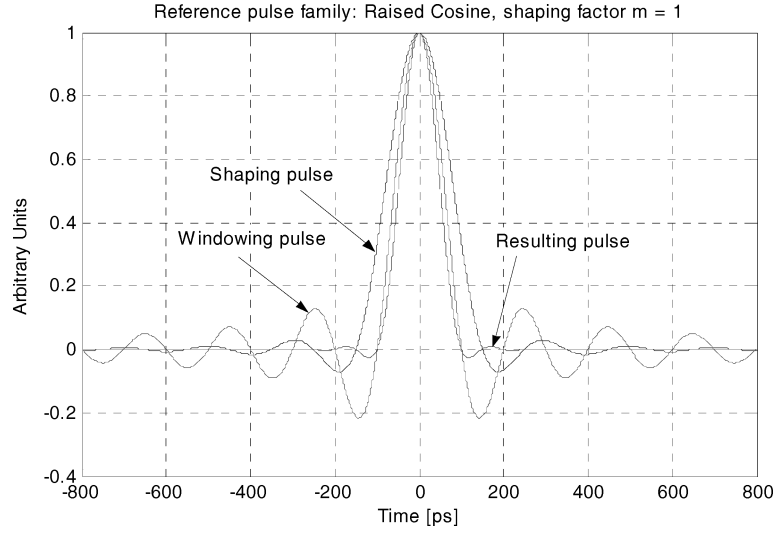

Figure 8.41 Raised cosine pulse computed according to Equation (8.60). Two pulse factors are shown, namely the shaping pulse and the windowing pulse. The combination of these two factors gives the raised cosine pulse. The windowing pulse is designed for a time step $T = 100$ ps while the shaping coefficient is $m = 1$. It is evident that the shaping pulse has zeros corresponding to every $T = 100$ ps, starting with the first zero at $t_1 = 150$ ps, in agreement with Equation (8.66)

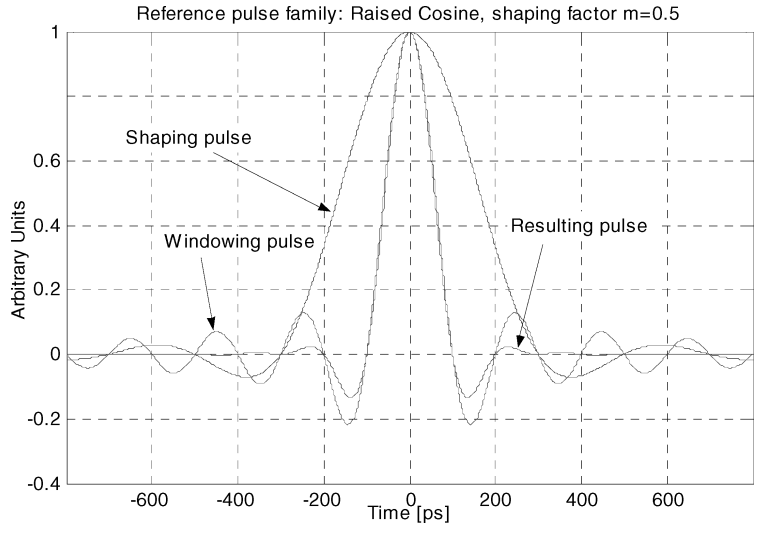

Figure 8.42 Raised cosine pulse computed using Equation (8.60). The windowing pulse is designed for a time step $T = 100\,\text{ps}$ while the shaping coefficient is $m = 0.5$. The shaping pulse has zeros corresponding to every $T = 200\,\text{ps}$, starting from the first zero at $t_1 = 300\,\text{ps}$, in agreement with Equation (8.66)

shaping coefficient $m = \frac{1}{2}$, maintaining the same windowing function as considered above. The resulting shaping function is smoother and the density of the corresponding zeros is one-half of the windowing zeros, as expected from Equation (8.63).

The third case considered is presented in Figure 8.43 where the shaping function exhibits the very low coefficient $m = \frac{1}{10}$. The shaping function is very smooth and the raised cosine pulse closely resembles the windowing function. In the limiting case of a null shaping coefficient, the raised cosine pulse coincides with the windowing function and the result is the well-known sinc function. From Equation (8.61) the first zero of the shaping function is set at $t_1 = 15T$.

In this section, the behavior of the raised cosine pulse has been analyzed and the interesting contribution of the two factors, namely the windowing function and the shaping function, has been found. These results, although not new, suggest using the same modular approach in order to synthesize the proper reference receiver spectrum (RSS) using the ISI-free requirements. In the next section this approach leads to the definition of a generalized class of Reference Receiver Spectrum (RSS), which is quite useful when modeling the optical reference receiver.

8.5.3 A General Class of RRS

The knowledge learnt about the raised cosine pulse in the previous section suggests the introduction of a new family of pulses that can be conveniently used to model a large variety of optical reference receivers. The interesting feature common to all these pulse functions is the complete absence of any intersymbol interference at the decision section. Starting with the definition (8.70) of the windowing function

$$w_T(t) \equiv \frac{1}{T}\,\frac{\sin(\pi t/T)}{\pi t/T}$$

the generalized reference receiver spectrum (RRS) $\Gamma_T(f)$ is defined as the Fourier transform of the product $\gamma_T(t)$ of the windowing function pulse $w_T(t)$ with every kind of shaping function pulse

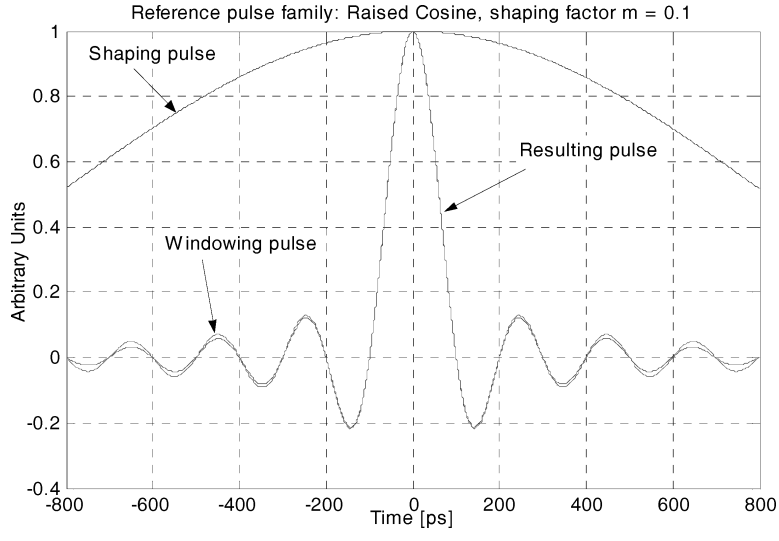

Figure 8.43 Raised cosine pulse computed according to Equation (8.60). The windowing pulse is designed for a time step $T = 100\,\text{ps}$ while the shaping coefficient is $m = 0.1$. It is evident that the effect of the shaping pulse is weaker than in the two previous cases and the resulting pulse closely resembles the windowing pulse (sinc)

$s(t)$ belonging to the space $L^1(\Re)$ of absolutely integrable functions over the real axis $\Re$:

$$\begin{aligned} &\gamma_T(t) \equiv s(t)w_T(t), \qquad \gamma_T(t) \overset{\Im}{\longleftrightarrow} \Gamma_T(f) \\ &s \in L^1(\Re) \wedge \{s(kT) \neq \infty\}, \quad k = \pm 1, \pm 2, \ldots \end{aligned} \tag{8.71}$$

It is simple to verify that the function $\gamma_T(t)$ satisfies the requirement for having no intersymbol interference:

$$\left.\begin{aligned} &t_k = kT, \qquad k = \pm 1, \pm 2, \ldots \\ &w_T(t_k) = 0 \\ &s(t_k) \neq \infty \end{aligned}\right\} \quad \Leftrightarrow \quad \gamma_T(t_k) \equiv s(t_k)w_T(t_k) = 0 \tag{8.72}$$

The function $s(t)$ should not exhibit a singularity at the time instants t_k. This condition is reported in (8.71), together with the existence condition for the absolute integral over the real axis.

It should be noted that the singularity requirement $s(t_k) \neq \infty$ is not a necessary condition for satisfying the definition of the generalized reference receiver spectrum $\Gamma_T(f)$. It is instead a sufficient condition. The condition for having no ISI requires in fact that the product $\gamma_T(t)$ of the two functions $s(t)$ and $w_T(t)$, evaluated at every integer multiple of the time step T, has a zero. This can be achieved even if the shaping function $s(t)$ has a local singularity at $t_k = kT$ of lower order than the zero of the windowing function $w_T(t)$ at the same sampling time instant.

It is important to note that the generalized reference receiver spectrum is not the frequency response of the receiver, but instead is the required output signal spectrum that is needed in order to have ISI cancellation. This is clearly stated by Equation (8.59). In the following subsections several examples are given of shaping functions $s(t)$ used to build up the generalized reference receiver pulses $\gamma_T(t)$ according to the conditions in (8.71).

8.5.3.1 Gaussian Shaped Reference Pulse

The Gaussian shaped reference pulse is defined by setting the following shaping function:

$$s(t) = \mathrm{e}^{-(t/\sigma)^2/2} \tag{8.73}$$

Figure 8.44 shows the Gaussian shaped reference pulse computed for three different increasing values of the ratio between the standard deviation σ and the time step T : $\sigma/T = 1$, $\sigma/T = 2$, $\sigma/T = 5$. Since the Gaussian function has no zero, the shaping function $s(t)$ in Equation (8.73) does not contribute to any additional zeros, and the zeros of the Gaussian shaped reference pulse in Equation (8.71) are coincident with the same set of zeros generated by the windowing function $w_T(t)$.

The smaller the relative standard deviation σ/T, the smoother the Gaussian shaped reference pulse becomes over the time step scale, and the characteristic oscillations of the sinc windowing function becomes more and more damped. For increasing values of the Gaussian standard deviation, the reference pulse becomes closer to the windowing function, showing correspondingly increasing oscillations, as can be seen in the following figures. As a general rule, the lower the slope at the zero transition, the better does the jitter immunity become, making the Gaussian shaped reference pulse better suited for operation under highly jittered timing. From Equations (8.70), (8.71) and (8.73) the complete analytical expression of the Gaussian reference pulse is derived:

$$\gamma_T(t) \equiv \frac{1}{T} \frac{\sin(\pi t/T)}{\pi t/T} \mathrm{e}^{-(t/\sigma)^2/2} \tag{8.74}$$

Figures 8.45 and 8.46 present the resulting Gaussian shaped pulse assuming a larger standard deviation. It is clear that by increasing the width of the Gaussian contribution, the resulting pulse follows more closely the profile defined by the windowing function, exhibiting almost the same oscillation amplitude in the pulse tails. A similar behavior has been verified in the previous raised cosine examples.

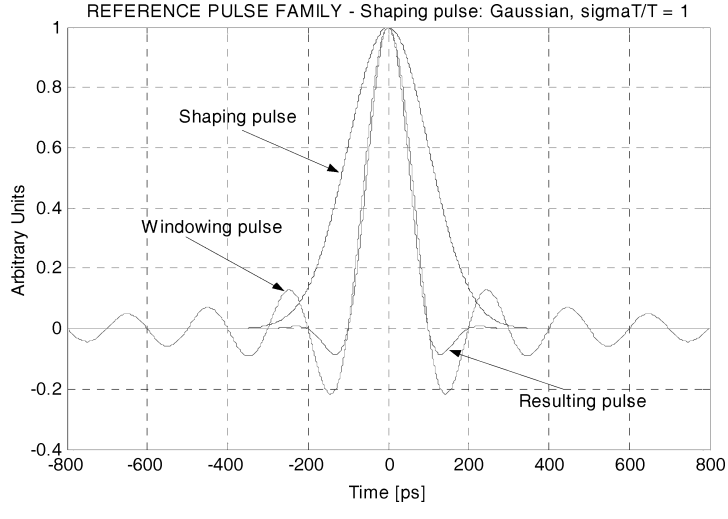

Figure 8.44 Gaussian shaped reference pulse computed according to Equations (8.70) and (8.73). Two pulse factors are shown, namely the Gaussian shaping pulse $s(t)$ and the windowing pulse $w(t)$. The combination of the two factors gives the Gaussian shaped reference pulse $\gamma_T(t)$. The windowing pulse is designed for a time step $T = 100\,\mathrm{ps}$. The relative standard deviation is $\sigma/T = 1$. The Gaussian shaped pulse has the same zeros as the windowing pulse, every $T = 100\,\mathrm{ps}$

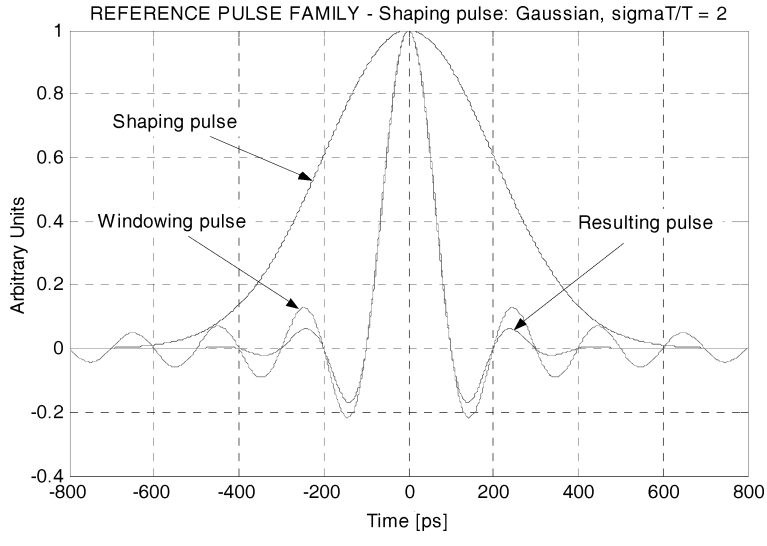

Figure 8.45 Gaussian shaped reference pulse computed according to Equation (8.74). The windowing pulse is designed for a time step $T = 100\,\text{ps}$ and the relative standard deviation is $\sigma/T = 2$. The Gaussian shaped pulse exhibits the same zeros as the windowing pulse

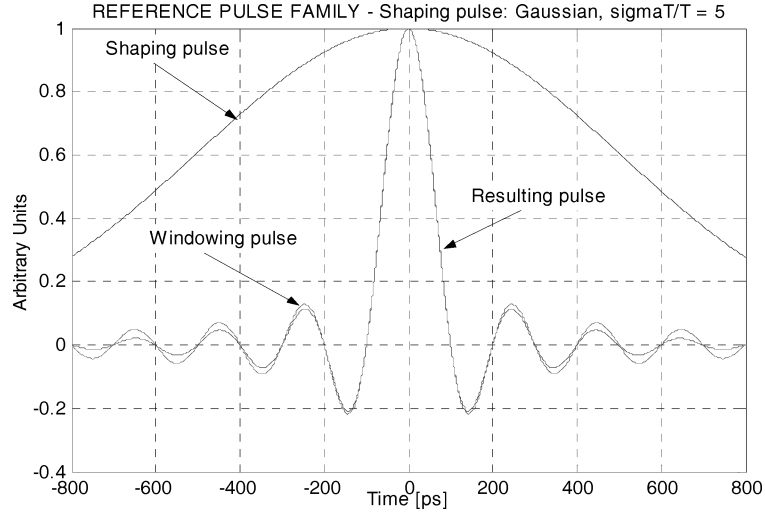

Figure 8.46 Gaussian shaped reference pulse computed according to Equation (8.74). The windowing pulse is designed for a time step $T = 100\,\text{ps}$ and the relative standard deviation is $\sigma/T = 5$. A comparison with the previous two cases reveals the almost negligible effect of the Gaussian shaping pulse due to a relative broader standard deviation

8.5.3.2 Lorenzian Shaped Reference Pulse

The next shaping function $s(t)$ being considered is the Lorenzian pulse. The terminology comes from the Fourier spectral representation that is the Lorenzian function. In the time domain, the

Lorenzian pulse is well known as the symmetric exponential pulse. It can be defined as

$$s(t) = \mathrm{e}^{-|t|/\tau} \tag{8.75}$$

The Lorenzian pulse is a monotonic exponential decreasing function of the time t and the parameter τ characterizes the decay behavior (time constant). It has even symmetry. At the time origin $t = 0$, the Lorenzian pulse (8.75) is normalized to unity. Since $s(t)$ has no zero at all, the same conclusions regarding the Gaussian pulse are also valid for the Lorenzian pulse. The zeros of the Lorenzian shaped reference pulse are therefore coincident with the zeros of the windowing function. From Equations (8.70), (8.71) and (8.75) the complete analytical expression of the Lorenzian shaped reference pulse is derived:

$$\gamma_T(t) \equiv \frac{1}{T} \frac{\sin(\pi t/T)}{\pi t/T} \mathrm{e}^{-|t|/\tau} \tag{8.76}$$

Figure 8.47 shows the computed Lorenzian shaped reference pulse according to three different values of the normalized time constant: $\tau/T = 1$, $\tau/T = 2$, $\tau/T = 5$. The conclusions are quite similar to the Gaussian shaped pulse of the previous subsection. From the computed Lorenzian profile shown in Figure 8.47 it is evident that a time constant τ equal to the time step T makes the pulse tail contribution quite negligible after about three time steps. A similar result was obtained with the Gaussian shaped pulse in Figure 8.44. It is important to remember that the even symmetry of the shaping function reflects of course the even symmetry of the whole pulse. This characteristic is noteworthy, as we will see in the next example of the asymmetric single-pole response pulse.

Figures 8.48 and 8.49 show a less damped pulse profile due to the narrower time constant $\tau < T$.

8.5.3.3 Single-Pole Shaped Reference Pulse

The three different reference pulses considered so for refer to time domain pulses with even symmetry. This is in fact the case for the raised cosine, the Gaussian and the Lorenzian shaped reference

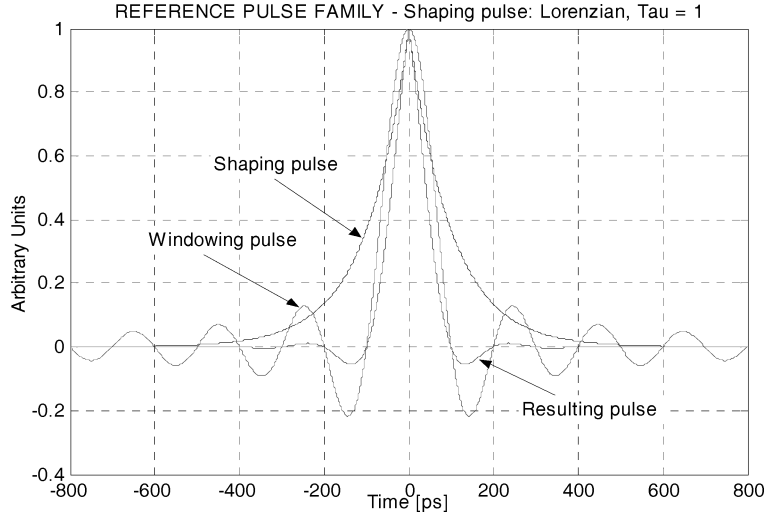

Figure 8.47 Lorenzian shaped reference pulse computed according to Equation (8.76). Two pulse factors are shown, namely the Lorenzian shaping pulse $s(t)$ and the windowing pulse $w(t)$. The combination of these two factors gives the Lorenzian shaped reference pulse. The windowing pulse is designed for a time step $T = 100\,\mathrm{ps}$. The relative time constant is $\tau/T = 1$. The Lorenzian shaped pulse has the same zeros as the windowing pulse, every $T = 100\,\mathrm{ps}$

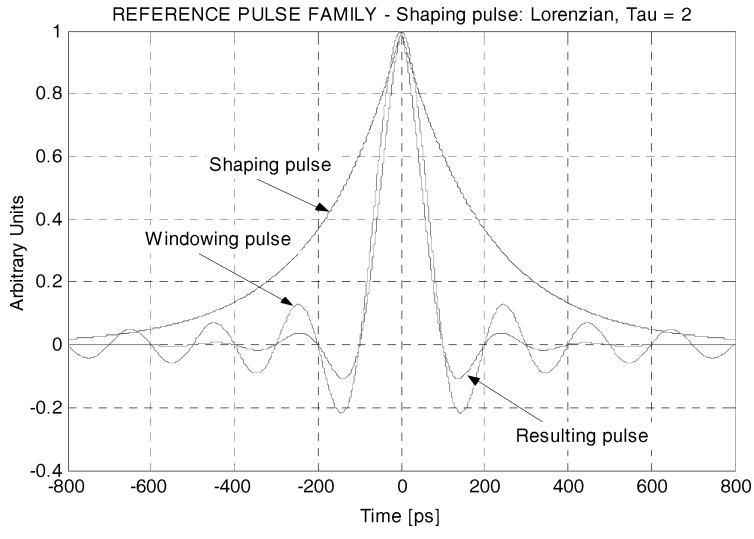

Figure 8.48 Lorenzian shaped reference pulse computed according to Equation (8.76). The windowing pulse is designed for a time step $T = 100\,\text{ps}$. The relative time constant is $\tau/T = 2$. The Lorenzian shaped pulse has the same zeros as the windowing pulse, every $T = 100\,\text{ps}$

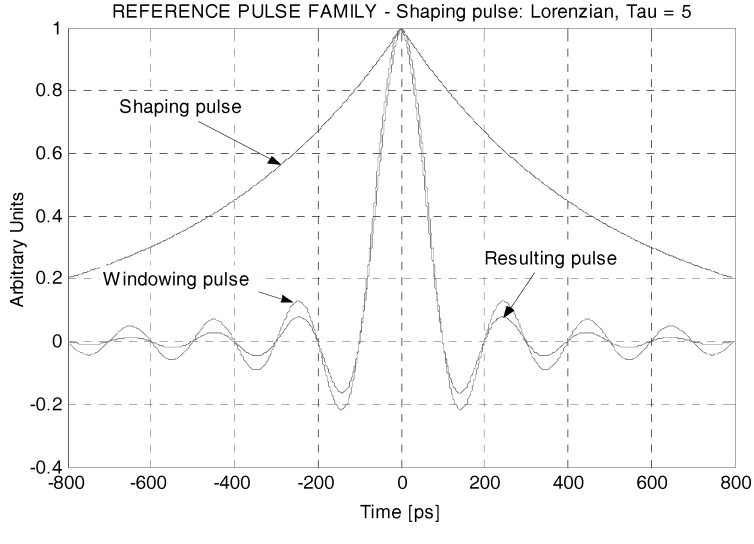

Figure 8.49 Lorenzian shaped reference pulse computed according to Equation (8.76). The windowing pulse is designed for a time step $T = 100\,\text{ps}$. The relative time constant is $\tau/T = 5$. The Lorenzian shaped pulse has the same zeros as the windowing pulse, every $T = 100\,\text{ps}$

pulses. The next two cases to be introduced refer to causal pulses, characterized by having a null value in the negative time axis. The causality arises from the assumption that the pulse response does not exist before the causal stimulus is applied at the time origin $t = 0$. The first case to consider is the very common impulse response of a single-pole time-invariant linear system. The second case uses the well known and most useful IV-order Bessel–Thompson impulse response.

The single-pole shaped reference pulse assumes the same time dependence as the Lorenzian pulse for a positive time axis, but is zero on the negative time axis:

$$s(t) = \begin{cases} e^{-t/\tau}, & t \geq 0 \\ 0, & t < 0 \end{cases} \tag{8.77}$$

The single-pole pulse is a monotonic exponential decreasing function of the time $t > 0$ and the parameter τ characterizes the decay behavior (time constant). At the time origin $t = 0$, the single-pole pulse has a finite discontinuity. From Equation (8.77),

$$\begin{aligned} t &\to 0^-, \quad s(0^-) \to 0 \\ t &\to 0^+, \quad s(0^+) \to 1 \end{aligned} \tag{8.78}$$

Since $s(t)$ has no zero at all, the single-pole shaped reference pulse has the same zeros as the windowing function. From Equations (8.70), (8.71) and (8.78) the complete analytical expression of the single-pole shaped reference pulse is derived:

$$\gamma_T(t) \equiv \begin{cases} \dfrac{1}{T} \dfrac{\sin(\pi t/T)}{\pi t/T} e^{-t/\tau}, & t \geq 0 \\ 0, & t < 0 \end{cases} \tag{8.79}$$

Figure 8.50 reports the computed single-pole shaped reference pulse using three different values of the normalized time constant: $\tau/T = 1$, $\tau/T = 2$, $\tau/T = 5$. Figures 8.51 and 8.52 show the same single-pole shaped reference pulse as above but characterized by longer time constants. The resulting pulse on the positive time axis closely resembles the oscillatory behavior of the windowing function.

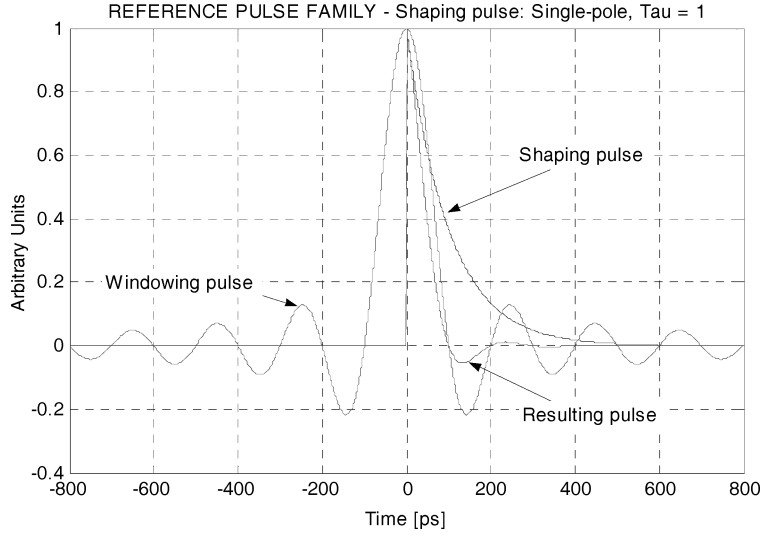

Figure 8.50 Single-pole shaped reference pulse computed according to Equation (8.79). The single-pole shaping pulse $s(t)$ and the windowing pulse $w(t)$ are represented as components of the pulse. The combination of these two factors gives the single-pole shaped reference pulse. The windowing pulse is designed for a time step $T = 100$ ps. The relative time constant is $\tau/T = 1$. As expected, the single-pole shaped pulse has a zero every $T = 100$ ps

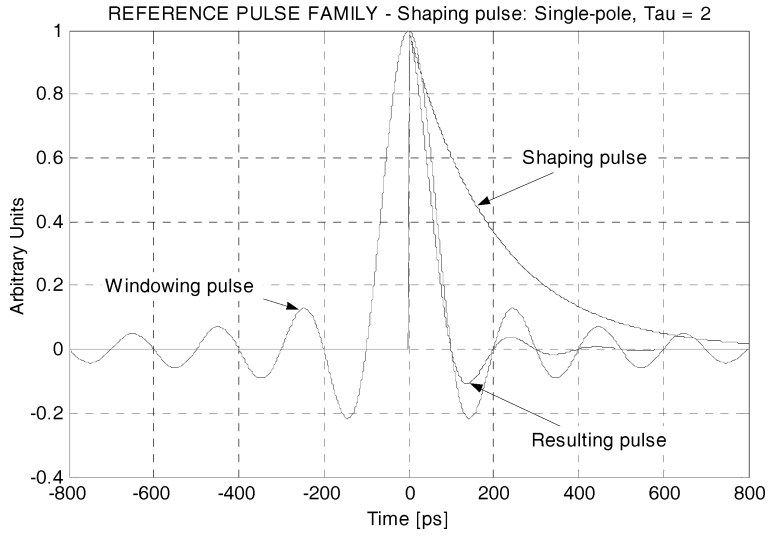

Figure 8.51 Single-pole shaped reference pulse computed according to Equation (8.79). The relative time constant is $\tau/T = 2$. The increased relative time constant makes the tail oscillations more pronounced. The single-pole shaped pulse has a zero every $T = 100$ ps, according to the windowing function

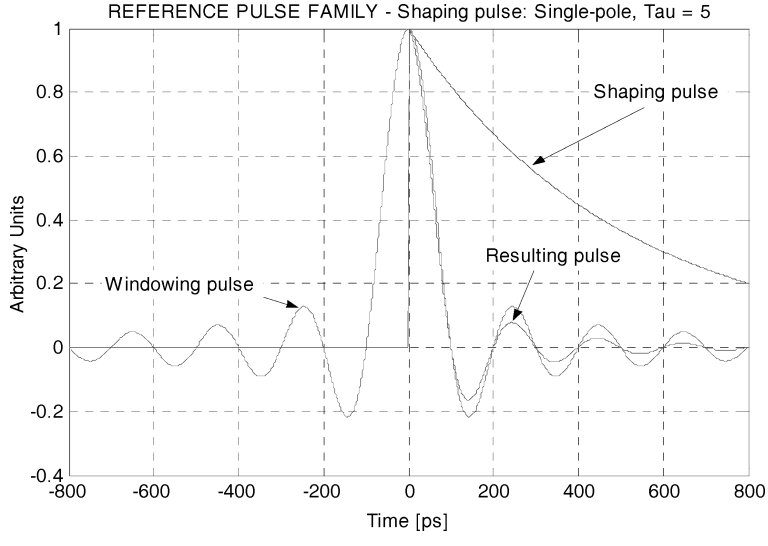

Figure 8.52 Single-pole shaped reference pulse computed according to Equation (8.79). The relative time constant has been increased to $\tau/T = 5$. The tail oscillations are more sustained and closer to the windowing pulse. The single-pole shaped pulse has a zero every $T = 100$ ps, according to the windowing function

It will be seen later that even if the single-pole and the Lorenzian shaped pulses are close to each other, their frequency responses are quite different. In particular, the single-pole shaped reference pulse has a wider spectrum than the Lorenzian one. One important difference between the previous three pulses and the causal single-pole pulse relies on their spectral characteristics. In fact, it is

well known[2] that the real signal $f(t)$ has a conjugated antisymmetric spectrum $F(\omega)$, while real and even signals have a real and even spectrum.

Causal signals have the real and imaginary spectral components linked together by the Hilbert transforms.[2] This has very important physical consequences in a real system. In any dielectric waveguide, the causality of the relationship between the linear dielectric polarization field in response to the applied electric field is the fundamental reason for the frequency chirping of light modulators and sources under modulated conditions. The reason relies on the Hilbert transforms that link together the real and the imaginary parts of the refractive index. Note that in every dielectric waveguide the real part of the refractive index is responsible for the phase constant while the imaginary part of the refractive index accounts for the waveguide absorption. A variation in the imaginary part of the refractive index at the operating optical frequency, needed for the light modulation purpose, will determine a corresponding variation of the real part of the refractive index, inducing a phase modulation of the transmitted field. The same relations in theoretical physics are known as the Kramers–Kronig dispersion relations.[3]

8.5.3.4 IV-Order Bessel–Thompson Shaped Reference Pulse

In this section, a very important shaping pulse will be considered. Fourth-order Bessel–Thompson (IV-BT) filters are extensively used in optical fiber transmission systems as the reference channel due to the important characteristic of exhibiting the maximally flat delay transfer curve. For any given order, the BT filter has the maximally flat group delay available among all other filter topologies of the same order. The uniformity of the group delay in every transmission channel is among the most important characteristics for preserving pulse skew and serious eye diagram degradation.

In this context, there is no interest in designing filters, but in analyzing properly shaped reference pulses that can be used at the decision section of the optical reference receiver for achieving ISI-free operation. In the following, it will be assumed that the pulse available at the decision section of the optical reference receiver is shaped according to the fourth-order Bessel–Thompson profile. This does not mean that a fourth-order Bessel–Thompson filter is used. In order to introduce the fourth-order Bessel–Thompson (IV-BT) shaping pulse, it is convenient to start with the frequency response function $S(f)$.[4] The filter transfer function is needed in order to arrive at the impulse response $s(t)$ by using the numerical fast Fourier transform (FFT) of $S(f)$. Then the impulse response of the IV-BT filter is used to build up the fourth-order Bessel–Thompson shaped reference pulse according to Equations (8.70) and (8.71). It is important to remark that the analytical closed-form expression of the IV-BT filter impulse response is not available, so it must be derived numerically from the well-known frequency response.

The frequency response $S(f)$ of the fourth-order Bessel–Thompson filter is given by the following rational expression:

$$S(f) = \frac{105}{105 + 105y + 45y^2 + 10y^3 + y^4}, \quad y = \mathrm{j}2\pi f\tau \tag{8.80}$$

The constant τ has the meaning of the group delay $t_g(f)$ at the limit of very low frequency (DC condition, $f \to 0$). The imaginary frequency variable y has been normalized using the time constant τ. If the fourth-order Bessel–Thompson transfer function (8.80) is represented in terms of the modulus and phase, the group delay $t_g(f)$ is easily calculated as the frequency derivative of the phase:

$$S(f) = A(f)\mathrm{e}^{\mathrm{j}}\phi(t) \quad \Rightarrow \quad t_g(f) \equiv \frac{1}{2\pi}\frac{\mathrm{d}\phi(f)}{\mathrm{d}f}, \qquad \lim_{f\to 0} t_g(f) = \tau \tag{8.81}$$

[2] A. Papoulis, *The Fourier Integral and Its Applications*, McGraw-Hill, 1987.
[3] H. Römer, *Theoretical Optics, an Introduction*, John Wiley & Sons, Ltd, 2005.
[4] ITU-T G.691, October 2000.

The transfer function (8.80) is normalized at the frequency origin (DC condition):

$$\lim_{f \to 0} S(f) = 1 \tag{8.82}$$

According to the property of the Fourier transform pair (see the Papoulis reference, 1987), this normalization condition reflects the unity area condition for the time domain representation $s(t)$:

$$s(t) \overset{\Im}{\longleftrightarrow} S(f), \qquad \int_{-\infty}^{+\infty} s(t)\,\mathrm{d}t = S(0) = 1 \tag{8.83}$$

It is convenient to introduce the dimensionless constant a in order to express the DC value τ of the group delay $t_g(f)$ in terms of the cut-off frequency f_c:

$$a \equiv \omega_c \tau = 2\pi f_c \tau \tag{8.84}$$

The cut-off frequency f_c is not specified in general. To be explicit, up to this point the value that must be satisfied by the modulus $|S(f)|$ of the transfer function when $f = f_c$ has not been required. According to the value attributed to the modulus $|S(f)|$ at the cut-off condition, the characteristic constant a will assume a determined value. In order to clarify this important point, the definition (8.84) of the parameter a is substituted into the expression of the imaginary frequency variable y in Equation (8.80):

$$y = \mathrm{j}a\frac{f}{f_c} \tag{8.85}$$

The relevant consequence of definition (8.84) is that at the cut-off frequency $f = f_c$,

$$y_c = \mathrm{j}a \tag{8.86}$$

Substituting Equation (8.86) at the cut-off frequency $f = f_c$ into the fourth-order Bessel–Thompson transfer function (8.80), gives the following equation for the parameter a:

$$S(f_c) = \frac{105}{105 + 105(\mathrm{j}a) + 45(\mathrm{j}a)^2 + 10(\mathrm{j}a)^3 + (\mathrm{j}a)^4} \tag{8.87}$$

Once the value of the transfer function $S(f_c)$ at the cut-off frequency has been fixed, the expression (8.87) allows calculation of the characteristic constant a and finally the definition of the filter characteristic. Choosing the cut-off frequency as the frequency at which the modulus $|S(f_c)|$ of the transfer function decays to $1/\sqrt{2} = -3\,\mathrm{dB_e}$ of the value reached at zero frequency, the characteristic constant a of the fourth-order Bessel–Thompson filter is found:

$$|S(f_c)| = \frac{1}{\sqrt{2}} \quad \Rightarrow \quad a = 2.1139 \tag{8.88}$$

The same procedure can be repeated for every other cut-off condition. Once $|S(f_c)| = \alpha$ is set, from Equation (8.87) the following equation needs to be solved in the variable a:

$$\alpha = \frac{105}{|105 + 105(\mathrm{j}a) + 45(\mathrm{j}a)^2 + 10(\mathrm{j}a)^3 + (\mathrm{j}a)^4|} \tag{8.89}$$

To find the physical meaning of the characteristic constant a, it is sufficient to consider the definition (8.84). The characteristic constant a of the fourth-order Bessel–Thompson transfer function has the meaning of the DC limit τ of the group delay expressed in terms of the reciprocal of the cut-off angular frequency $\omega_c = 2\pi f_c$:

$$\lim_{f \to 0} t_g(f) = \tau = \frac{a}{2\pi f_c} \tag{8.90}$$

Once the -3 dB cut-off frequency f_c has been fixed, the DC limit τ of the group delay is determined by Equation (8.90). This is valid for every order of the Bessel–Thompson filter. In particular, for the fourth-order Bessel–Thompson transfer function,

$$\tau = \frac{2.1139}{2\pi} \frac{1}{f_c} \cong \frac{0.3364}{f_c} \tag{8.91}$$

These properties are common to all Bessel–Thompson filters of any order. The DC value of the group delay is exclusively determined by the -3 dB cut-off frequency.

Of course, for any given filter order there corresponds a proper value of the characteristic constant a. As already specified, for the fourth-order Bessel–Thompson transfer function, the characteristic constant is given by Equation (8.91). Thus

$$f_c = 7.5\,\text{GHz} \quad \Rightarrow \quad \tau = 44.853\,\text{ps} \tag{8.92}$$

This value is typical for the ITU-T G.691 specification of the fourth-order Bessel–Thompson filters operating at 10 Gbit/s, where the -3 dB cut-off frequency is fixed at 75 % of the bit rate.

Figure 8.53 reports the modulus and the phase of the transfer functions of four different fourth-order Bessel–Thompson filters computed according to Equations (8.80), (8.85) and (8.91) using Matlab® 7.0.2. The four transfer functions differ for the cut-off frequency values, as reported in the corresponding legend. The top graph shows the magnitude $|S(f)|$ of the transfer function expressed in decibels. The normalization bit rate is $B = 10$ Gbit/s, corresponding to the time step $T = 10$ ps. The bottom graph shows the corresponding group delay versus frequency using unity step normalization. It is evident that for $f_c = 0.75B = 7.5$ GHz the DC value of the group delay is in agreement with Equation (8.92).

Figure 8.54 presents the impulse responses of the same fourth-order Bessel–Thompson transfer functions reported in Figure 8.53. The time domain pulses have been computed using a proper Matlab® 6.5 routine with the fast fourier Transform (FFT) algorithm.

The ITU-T standard requires the implementation of the IV-BT filter with a -3 dB cut-off at 75 % of the signaling bit rate as the reference for validating the transmitted eye diagram. Figure 8.55 gives a detailed representation of the IV-BT impulse response corresponding to the required cut-off frequency at $f_c = 0.75B = 7.5$ GHz. It is evident that with causal pulse behavior no pulse amplitude is available on the negative time axis. In addition, the bottom graph of the same figure shows a magnification of the negative postcursor tail showing very low residual intersymbol interference contributions. The first intersymbol contribution at $t = T$ is less the 2 % of the normalized sample amplitude. Subsequent postcursors give a negligible contribution. This low intersymbol characteristic of the fourth-order Bessel–Thompson impulse response with a cut-off frequency set at 75 % of the bit rate justifies the choice as the standard reference filter for transmitter eye mask testing in ITU-T G.957 and G.691.

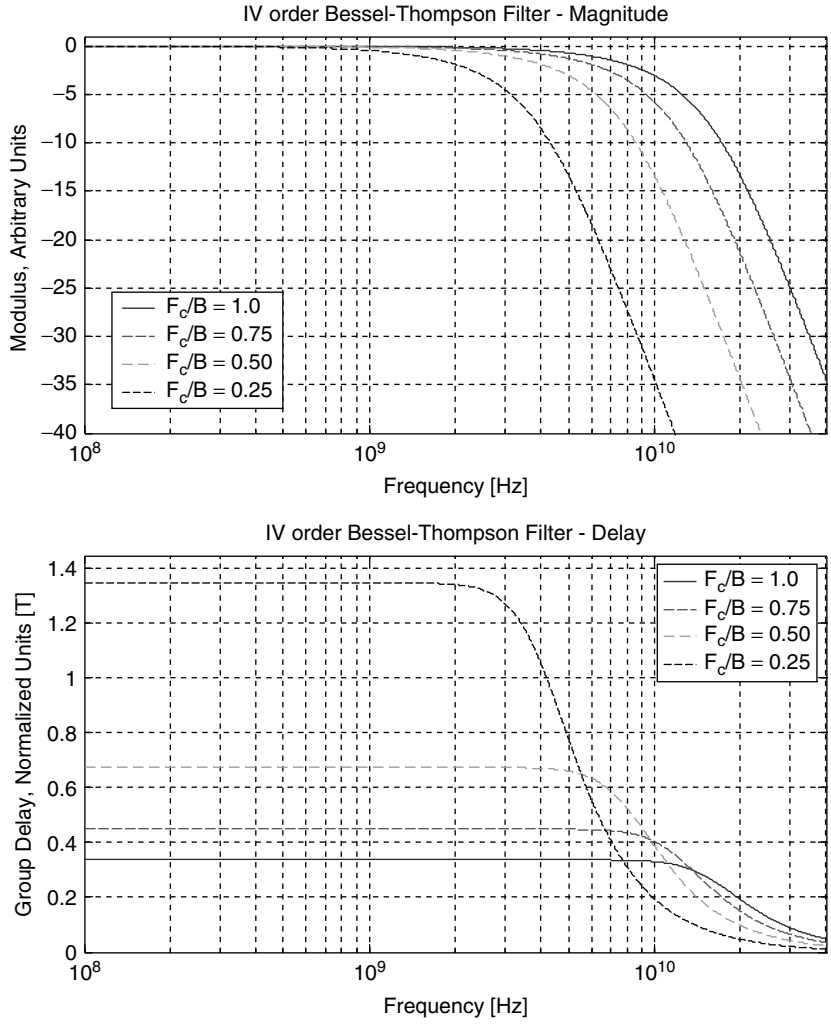

Figure 8.53 Top: magnitude of the IV-BT transfer functions for four different cut-off frequencies. Bottom: group delay of the same IV-BT transfer functions with the corresponding cut-off frequencies

Once the basic properties of the fourth-order Bessel–Thompson impulse response have been derived, construction of the fourth-order Bessel–Thompson reference shaped pulse can proceed. In this case, the analytical form of the shaping pulse is not available, but the numerical evaluation according to the FFT algorithm can be used. Figure 8.56 show the numerically evaluated IV-BT shaped reference pulse according to three different cut-off conditions for the shaping pulse. It is evident that the broader the shaping pulse, the weaker is the damping action over the windowing function and the stronger is the tail ripple sustained on the pulse postcursors. Of course, in the case of causal shaping pulses, no tail precursor would be available at all.

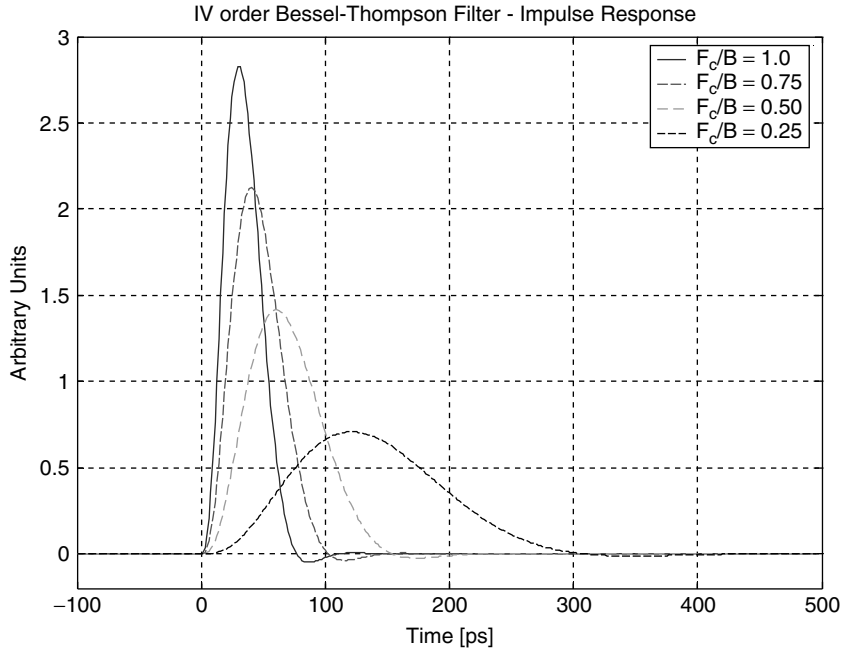

Figure 8.54 Impulse responses of the IV-BT transfer functions reported in Figure 8.53. All four impulse responses have unity area due to proper normalization in Equation (8.83). It is of interest to note that the impulse response corresponding to $f_c = 0.75B$ has approximately FWHM $\cong 100\,\text{ps} = T$ and the zeros are quite equally spaced for every time step T. This property justifies the choice for standard ITU-T G.691 and G.954 optical transmitter reference filter

Figures 8.57 and 8.58 show the case of a lower-frequency cut-off of the IV-BT shaping transfer function. The IV-BT shaping pulse is broader than in the above case and its intersymbol contribution is no longer negligible at the first time step, $t = T$. Figure 8.58 shows the interesting case of an even lower cut-off frequency of the IV-BT pulse. In this case, both the windowing pulse and the IV-BT pulse interfere with each other, creating a new output pulse with a strong tail ripple. Even if the resulting IV-BT shaped reference pulse does not have any ISI contribution due to the windowing pulse synchronization action, this pulse is not suitable for implementing reference eye diagrams.

8.5.4 Integral Representation Theorem of the RRS

In the previous section, the time domain representation of the reference receiver pulse $\gamma_T(t)$ has been defined as the product of the shaping pulse $s(t)$ and the windowing pulse $w_T(t)$, according to conditions (8.71). The product of any two functions in the time domain belonging to $L^1(\Re)$ has a convenient representation in the frequency domain, by virtue of the frequency convolution theorem (see the Papoulis reference, 1987). Moreover, the windowing function $w_T(t)$ has the well-known ideal frequency window representation that allows easy mathematical handling. According to conditions (8.71), the function $s(t)$ belongs to the space $L^1(\Re)$ and therefore has the Fourier

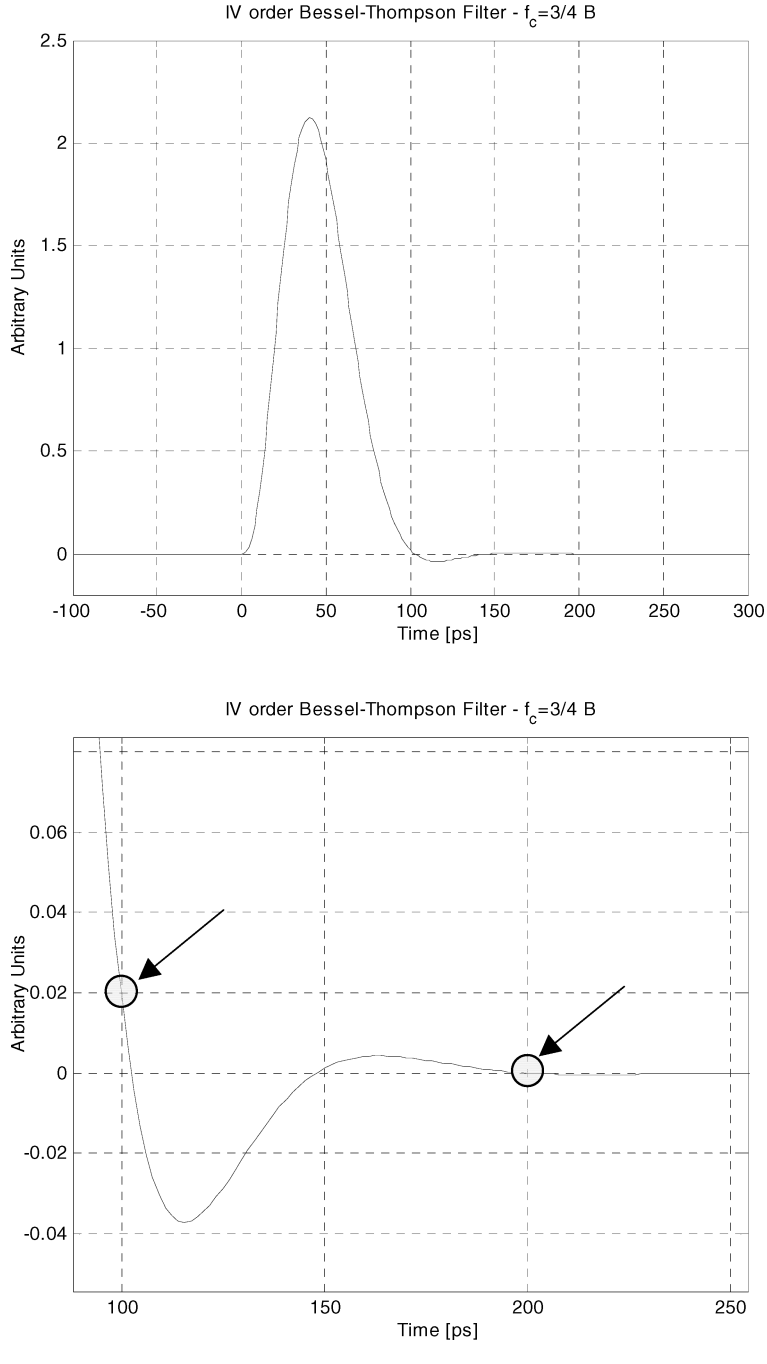

Figure 8.55 Computed IV-BT impulse response with the cut-off frequency $f_c = 0.75B = 7.5\,\text{GHz}$. The top graph shows the complete impulse response while the bottom graph gives the magnification of the zero-crossing region (marked with circles), showing the very low ISI contribution available from this pulse even if it is without the windowing function

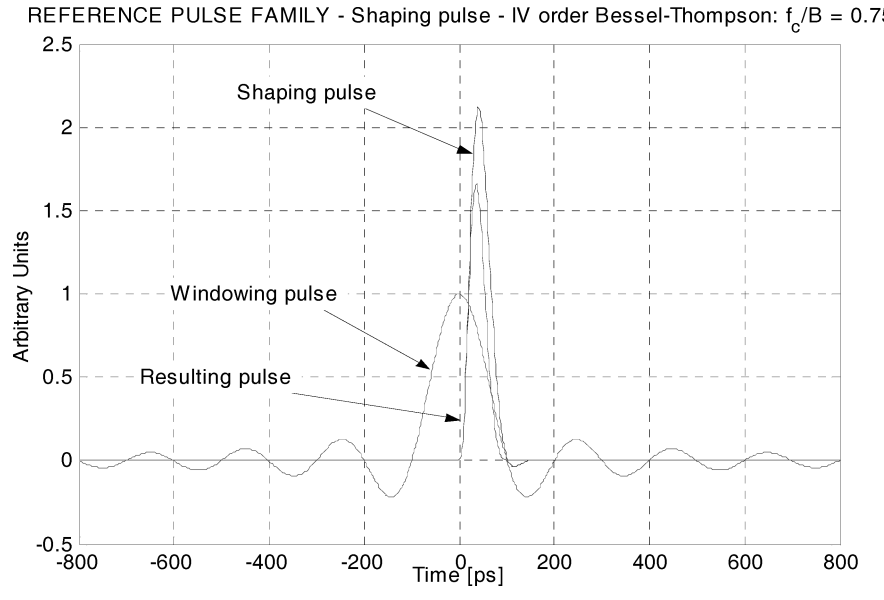

Figure 8.56 Numerical evaluation of the IV-BT shaped reference pulse with the IV-BT pulse cut-off frequency at $f_c = 0.75B$. The IV-BT shaping pulse makes a negligible tail contribution for a time greater than two time steps. Consequently, the output pulse is weakly affected by the windowing pulse

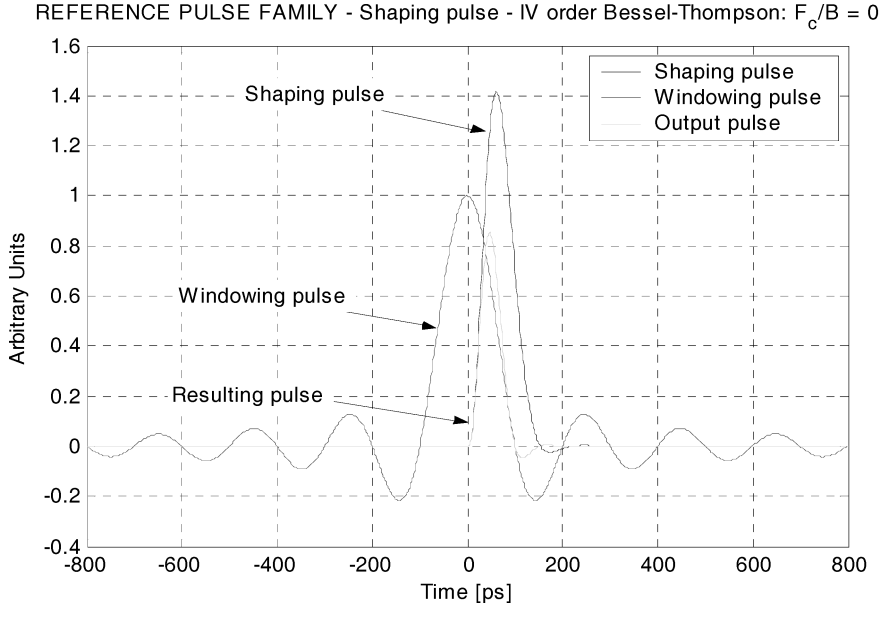

Figure 8.57 Numerical evaluation of the IV-BT shaped reference pulse with the IV-BT pulse cut-off frequency at $f_c = 0.50B$. The IV-BT shaping pulse makes a relevant intersymbol contribution at $t = T$ but the tail postcursors rapidly fall off for a time greater than two time steps. The windowing pulse provides tail synchronization, causing the null ISI output pulse at every multiple of the time step

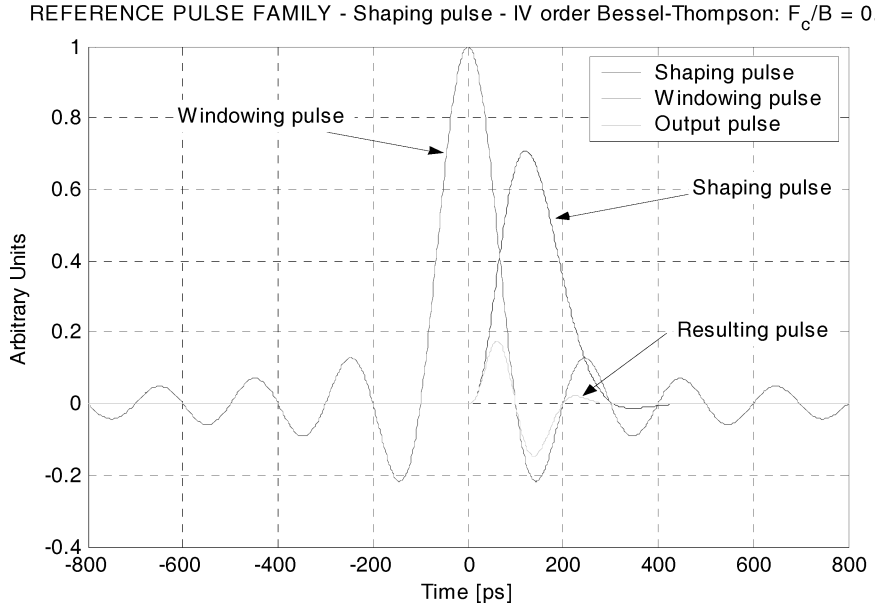

Figure 8.58 Numerical evaluation of the IV-BT shaped reference pulse with the IV-BT pulse cut-off frequency at $f_c = 0.25B$. The IV-BT shaping pulse makes a very strong intersymbol contribution up to $t = 2T$, but the tail postcursors rapidly fall off for a time greater than three time steps. The windowing pulse provides tail synchronization, causing the null ISI output pulse at every multiple of the time step

integral representation. All these facts suggest a very easy and elegant way of finding the integral representation of the reference receiver pulse. To demonstrate the integral representation theorem of RSS, the Fourier Transform pairs are given as follows:

$$s, S \in L^1(\Re) \quad \Rightarrow \quad S(f) = \int_{-\infty}^{+\infty} s(t)\mathrm{e}^{-\mathrm{j}2\pi ft}\,\mathrm{d}t \quad \overset{\Im}{\longleftrightarrow} \quad s(t) = \int_{-\infty}^{+\infty} S(f)\mathrm{e}^{+\mathrm{j}2\pi ft}\,\mathrm{d}f \tag{8.93}$$

The same Fourier representation holds for the windowing function and for the reference receiver pulse $\gamma_T(t)$. The Fourier transform of the Reference receiver pulse $\gamma_T(t)$ gives the reference receiver spectrum (RRS), $\Gamma_T(f)$:

$$\begin{aligned} w_T(t) &\overset{\Im}{\longleftrightarrow} W_T(f) \\ \gamma_T(t) &\overset{\Im}{\longleftrightarrow} \Gamma_T(f) \end{aligned} \tag{8.94}$$

According to the frequency convolution theorem, the frequency representation of the reference receiver spectrum $\Gamma_T(f)$ has the following form:

$$\Gamma_T(f) = S(f) * W_T(f) \equiv \int_{-\infty}^{+\infty} W_T(\alpha)S(f-\alpha)\,\mathrm{d}\alpha \tag{8.95}$$

The asterisk * denotes the convolution integral between the two functions $S(f)$ and $W_T(f)$.

The spectrum of the windowing function $w_T(t)$ is the elementary ideal square frequency window of width T and unity height:

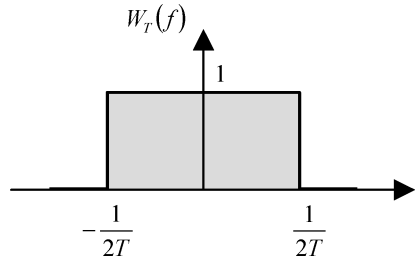

defined by

$$W_T(f) = \begin{cases} 1, & |f| \leq \dfrac{1}{2T} \\ 0, & |f| > \dfrac{1}{2T} \end{cases} \tag{8.96}$$

Substituting the spectrum of the windowing function (8.96) into Equation (8.95) gives the following integral representation of the reference receiver spectrum:

$$\Gamma_T(f) = \int_{f-1/(2T)}^{f+1/(2T)} S(y)\,\mathrm{d}y \tag{8.97}$$

From the above expression, it is interesting to remark that:

1. The integral representation of the reference receiver spectrum coincides with the frequency smoothing over the bit rate window width $B = 1/T$ of the reference shaping spectrum. Accordingly, the windowing pulse $w_T(t)$ acquires the meaning of the smoothing window.
2. The integral representation of the reference receiver spectrum $\Gamma_T(f)$ preserves the same symmetry as the shaping spectrum $S(f)$.

Substituting $u = -x$ in Equation (8.97) gives the following identity:

$$\Gamma_T(-f) = \int_{-f-1/(2T)}^{-f+1/(2T)} S(y)\,\mathrm{d}y = -\int_{f+1/(2T)}^{f-1/(2T)} S(-u)\,\mathrm{d}u = \int_{f-1/(2T)}^{f+1/(2T)} S(-u)\,\mathrm{d}u \tag{8.98}$$

Hence, the symmetry of the shaping spectrum $S(f)$ is preserved by the reference receiver spectrum $\Gamma_T(f)$:

$$S(-f) = \pm S(f) \quad \Rightarrow \quad \Gamma(-f) = \pm\Gamma(f) \tag{8.99}$$

8.5.4.1 Application to the Gaussian Shaped RRS

To illustrate the integral representation theorem (8.97), the case of the Gaussian reference shaping pulse presented in Section 8.5.3.1 is considered. The Fourier transform of the Gaussian pulse (8.73) is given by the following expression (see the Papoulis, reference, 1987), where σ_t is used explicitly instead of σ in order to specify the time domain RMS width:

$$S(f) = \sigma_t\sqrt{2\pi}\,\mathrm{e}^{-2\pi^2\sigma_t^2 f^2} = \frac{1}{\sigma_f\sqrt{2\pi}}\mathrm{e}^{-f^2/(2\sigma_f^2)} \tag{8.100}$$

The corresponding standard deviations σ_t and σ_f satisfy the well-known uncertainty relationship for the Gaussian transform pair:

$$\sigma_f = \frac{1}{2\pi\sigma_t} \tag{8.101}$$

Substituting Equation (8.100) into Equation (8.97), the integral expression for the Gaussian shaped reference spectrum is found. With the substitution $u = \sqrt{2}\pi\sigma x$, the integral (8.97) for the Gaussian profile takes the following form:

$$\Gamma_T(f) = \frac{1}{\sqrt{\pi}} \int_{\sqrt{2}\pi\sigma[f-1/(2T)]}^{\sqrt{2}\pi\sigma[f+1/(2T)]} \mathrm{e}^{-y^2}\,\mathrm{d}y \tag{8.102}$$

Using the definition of the error function (see the Römer reference, 2005), it is easy to derive the following closed-form expression of the Gaussian shaped reference spectrum:

$$\Gamma_T(f) = \frac{1}{2}\left\{\mathrm{erf}\left[\sqrt{2}\pi\sigma\left(f+\frac{1}{2T}\right)\right] - \mathrm{erf}\left[\sqrt{2}\pi\sigma\left(f-\frac{1}{2T}\right)\right]\right\} \tag{8.103}$$

According to the corollary (8.98), the spectrum $\Gamma_T(f)$ generated using Equation (8.100) must have an even symmetry, as it is used for the Gaussian spectrum. This is easily verified from Equation (8.103) using the odd symmetry property of the error function:

$$\mathrm{erf}(x-a) = -\mathrm{erf}(a-x), \quad (x,a) \in R \tag{8.104}$$

Setting the frequency variable to $-f$ and using the odd symmetry of (8.104) gives the required even symmetry of the Gaussian shaped reference receiver spectrum:

$$\begin{aligned}\Gamma_T(-f) &= \frac{1}{2}\left\{\mathrm{erf}\left[\sqrt{2}\pi\sigma\left(-f+\frac{1}{2T}\right)\right] - \mathrm{erf}\left[\sqrt{2}\pi\sigma\left(-f-\frac{1}{2T}\right)\right]\right\} \\ &= \frac{1}{2}\left\{-\mathrm{erf}\left[\sqrt{2}\pi\sigma\left(+f-\frac{1}{2T}\right)\right] + \mathrm{erf}\left[\sqrt{2}\pi\sigma\left(f+\frac{1}{2T}\right)\right]\right\} \\ &= \Gamma_T(f)\end{aligned} \tag{8.105}$$

Figure 8.59 shows the Gaussian shaped reference receiver spectrum $\Gamma_T(f)$ computed using either the expression (8.103) or the fast Fourier transform routine of the corresponding time domain pulse $\gamma_T(t)$ with $\sigma = 1$.

8.5.5 Examples of Reference Receiver Spectra

In this section are given the computed spectra of the reference receiver pulse families analyzed in Section 5.4. In order to present the results as clearly as possible, every figure gives in the upper graph the pulse composition in terms of the windowing pulse and of the shaping pulse, while the lower graph shows the corresponding spectral composition. After computation of the detailed pulse and spectrum compositions of a single sample for each pulse family, several examples of reference pulses belonging to the same family have been presented, together with the corresponding spectra reproduced in the lower graph. The spectrum composition in terms of the convolution of the windowing spectrum with the shaping spectrum is not reported in this latter case in order to

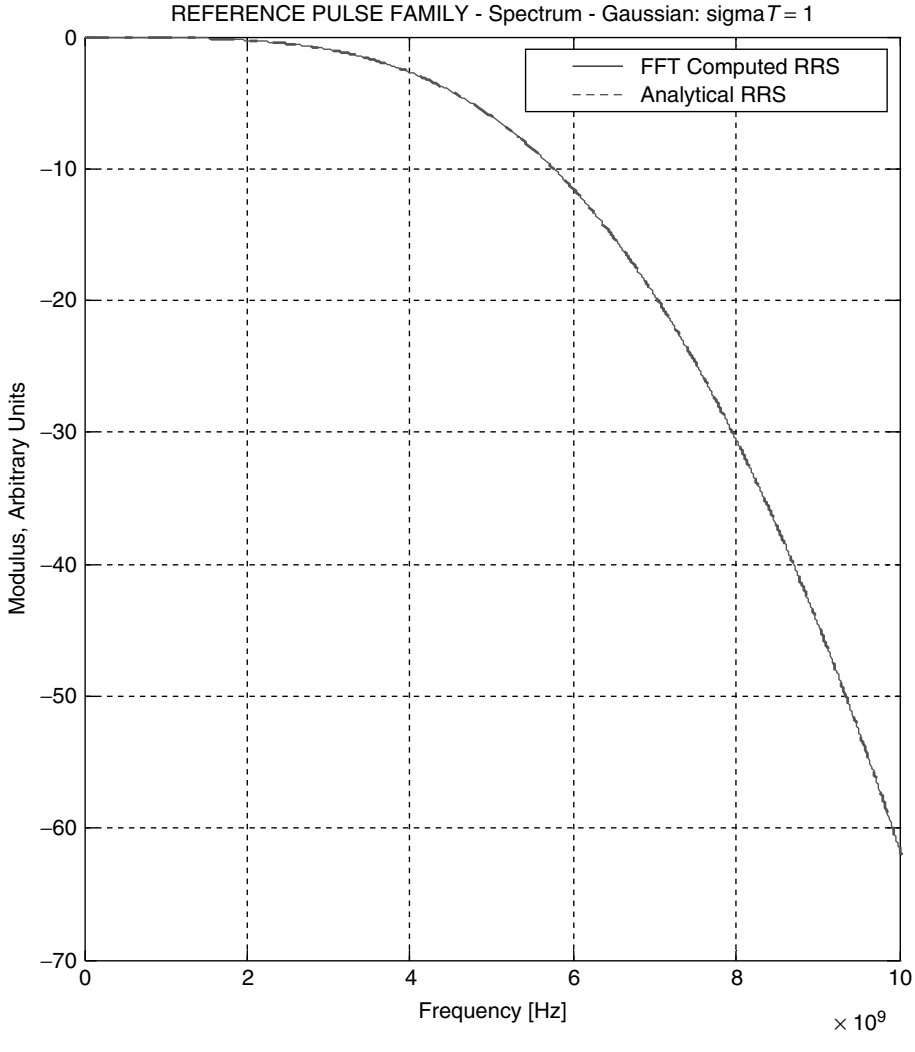

Figure 8.59 Gaussian shaped reference receiver spectrum for $\sigma = 1$. The comparison between the FFT spectrum and the spectrum evaluated according to expression (8.103) clearly confirms numerically the validity of the integral representation theorem (8.97)

simplify the graphical notation. Once the validity of the integral representation (8.97) has been demonstrated, the reported spectra are computed using the Matlab® 7.0.2 code based on the FFT algorithm. The same results would have been obtained of course using the expression (8.97). In order to make the spectrum comparison easier all spectra have been normalized to the DC value.

8.5.5.1 Raised Cosine Shaped Pulse (Figure 8.60)

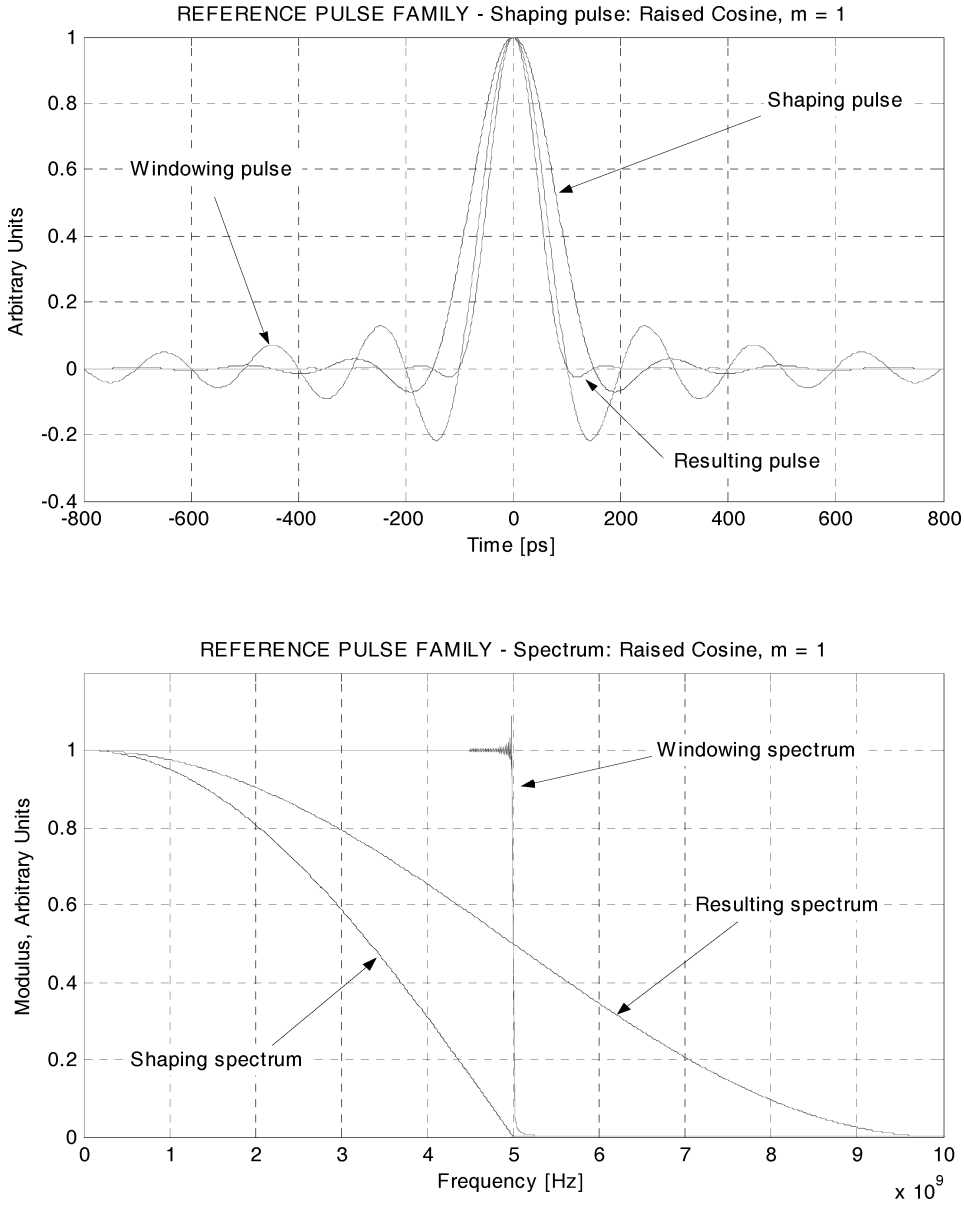

Figure 8.60 Top: raised cosine shaped reference pulse with roll-off coefficient $m = 1$. Bottom: spectral composition. According to Equation (8.95), the resulting pulse spectrum is given by the frequency convolution of the windowing spectrum with the shaping spectrum. The reported pulses are referred to a time step $T = 100\,\text{ps}$ corresponding to the bit rate $B = 10\,\text{Gb/s}$

8.5.5.2 Gaussian Shaped Pulse (Figure 8.61)

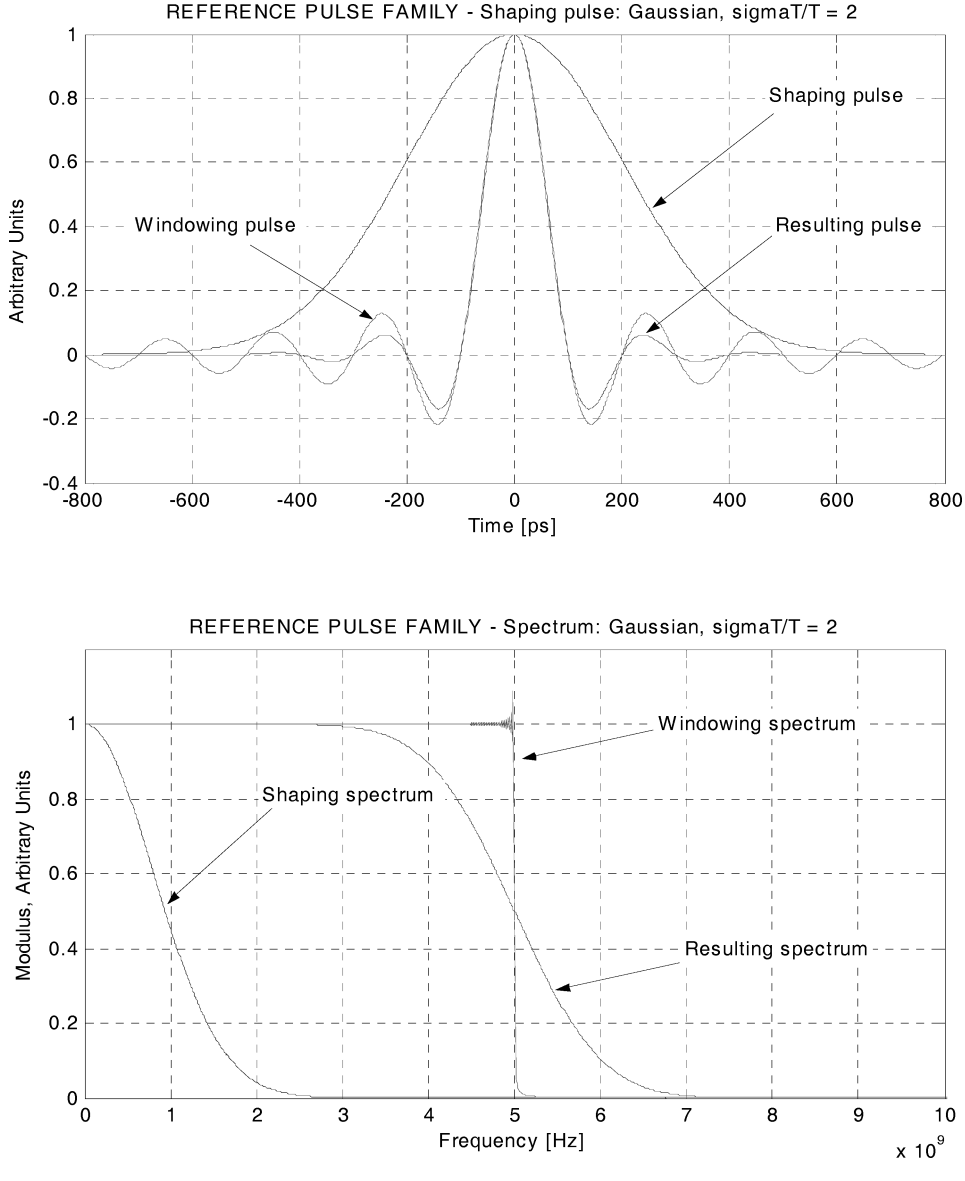

Figure 8.61 Top: Gaussian shaped reference pulse with a normalized standard deviation $\sigma/T = 2$. Bottom: spectral composition. According to Equation (8.95), the resulting pulse spectrum is given by the frequency convolution of the windowing spectrum with the shaping spectrum. The reported pulses are referred to a time step $T = 100\,\text{ps}$ corresponding to the bit rate $B = 10\,\text{Gb/s}$

8.5.5.3 Lorenzian Shaped Pulse (Figure 8.62)

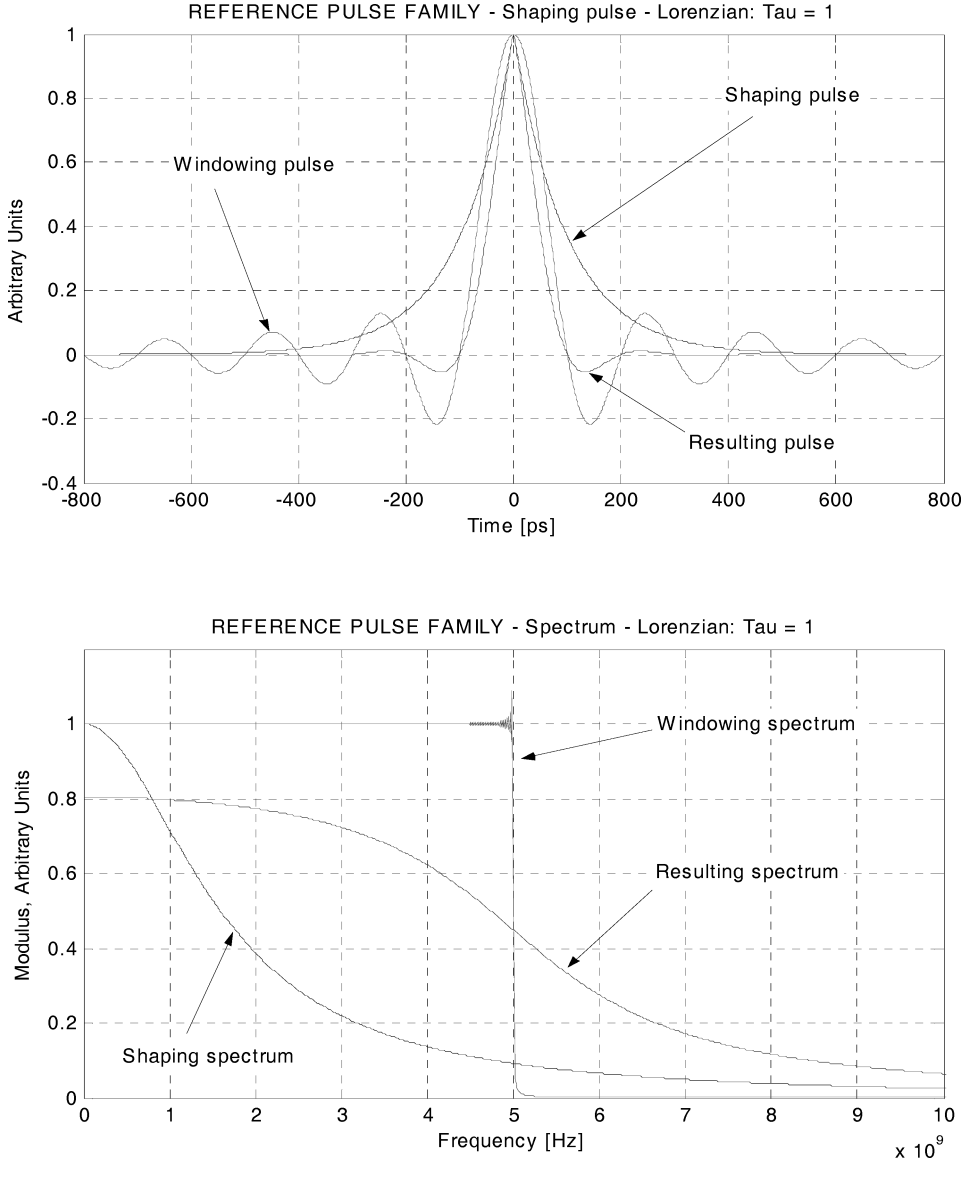

Figure 8.62 Top: Lorenzian shaped reference pulse with a normalized time constant $\tau/T = 1$. Bottom: spectral composition. According to Equation (8.95), the resulting pulse spectrum is given by the frequency convolution of the windowing spectrum with the shaping spectrum. The reported pulses are referred to a time step $T = 100\,\text{ps}$ corresponding to the bit rate $B = 10\,\text{Gb/s}$

8.5.5.4 Single-Pole Shaped Pulse (Figure 8.63)

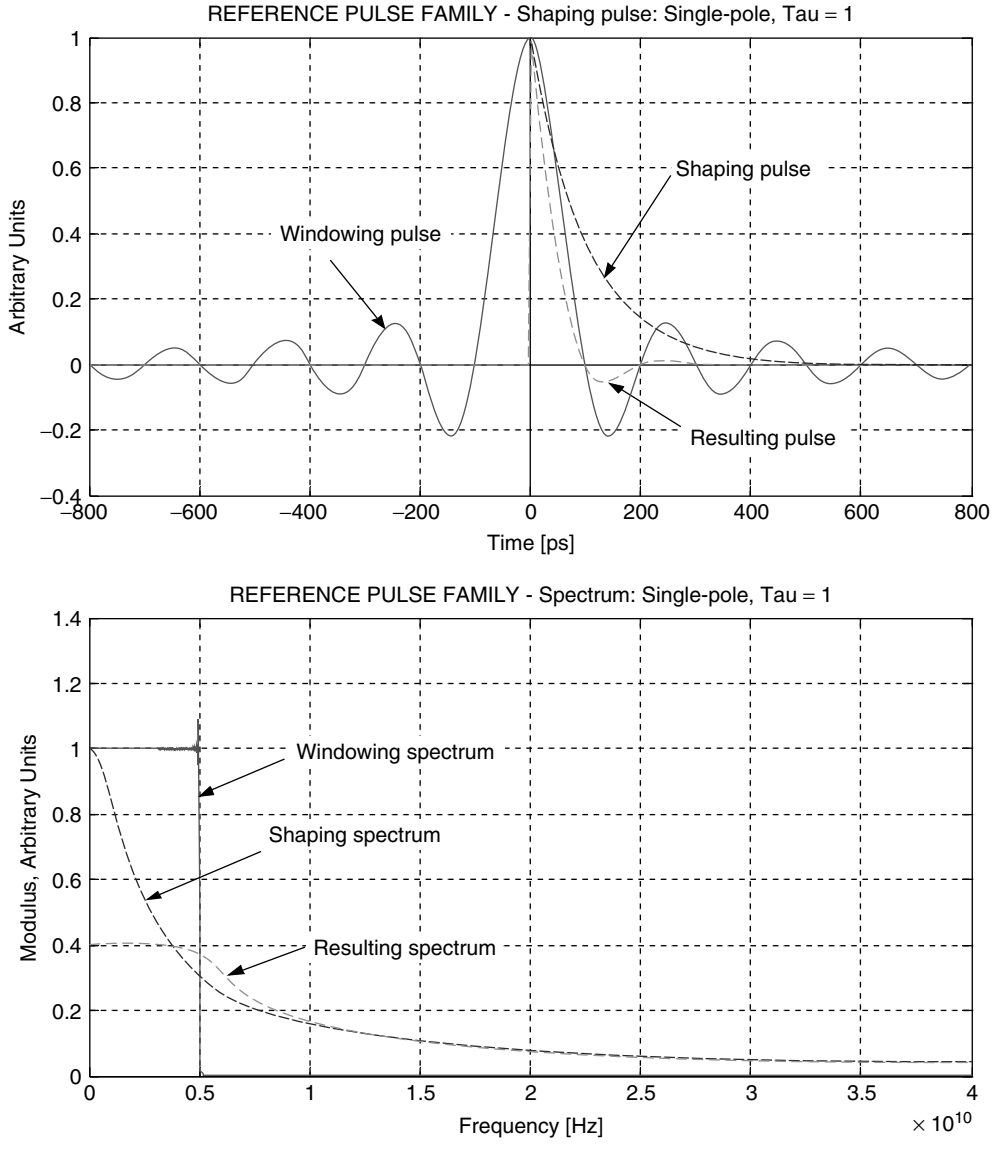

Figure 8.63 Top: single-pole shaped reference pulse with a normalized time constant $\tau/T = 1$. Bottom: spectral composition. According to Equation (8.95), the resulting pulse spectrum is given by the frequency convolution of the windowing spectrum with the shaping spectrum. The reported pulses are referred to a time step $T = 100\,\text{ps}$ corresponding to the bit rate $B = 10\,\text{Gb/s}$

8.5.5.5 IV-order Bessel–Thompson Shaped Pulse (Figure 8.64)

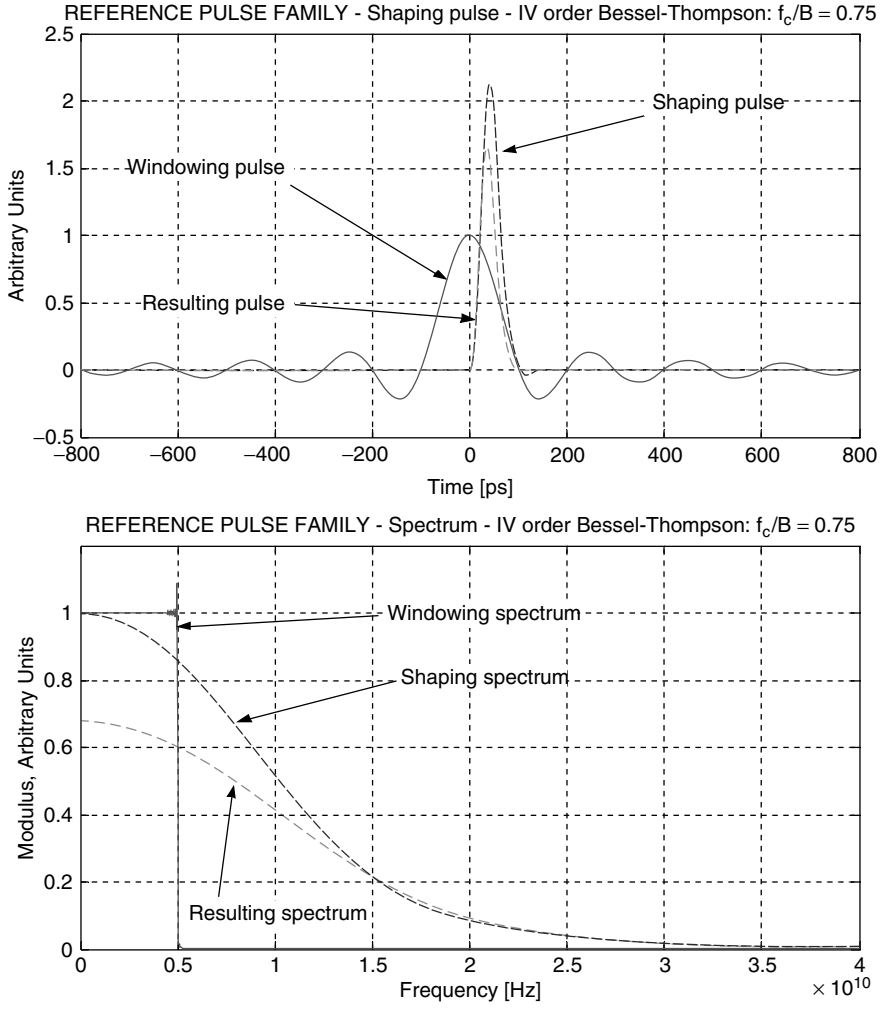

Figure 8.64 Top: IV-order Bessel–Thompson shaped reference pulse with normalized cut-off frequency $f_c/B = 0.75$. Bottom: spectral composition. According to Equation (8.95), the resulting pulse spectrum is given by the frequency convolution of the windowing spectrum with the shaping spectrum. The reported pulses are referred to a time step $T = 100\,\text{ps}$ corresponding to the bit rate $B = 10\,\text{Gb/s}$

8.5.5.6 Raised Cosine Shaped Pulse Family

In Figure 8.65 shows both time domain pulses and frequency domain spectra modulus belonging to the raised cosine shaped reference family, according to the following four values of the roll-off coefficient: $m = 0.1, 0.25, 0.50, 1.0$. All considered cases refer to the time step $T = 100\,\text{ps}$.

8.5.5.7 Gaussian Shaped Pulse Family

Figure 8.66 shows the computed pulses and spectra modulus belonging to the Gaussian shaped reference family. According to the reference pulse definition (8.74), all considered pulses satisfy the

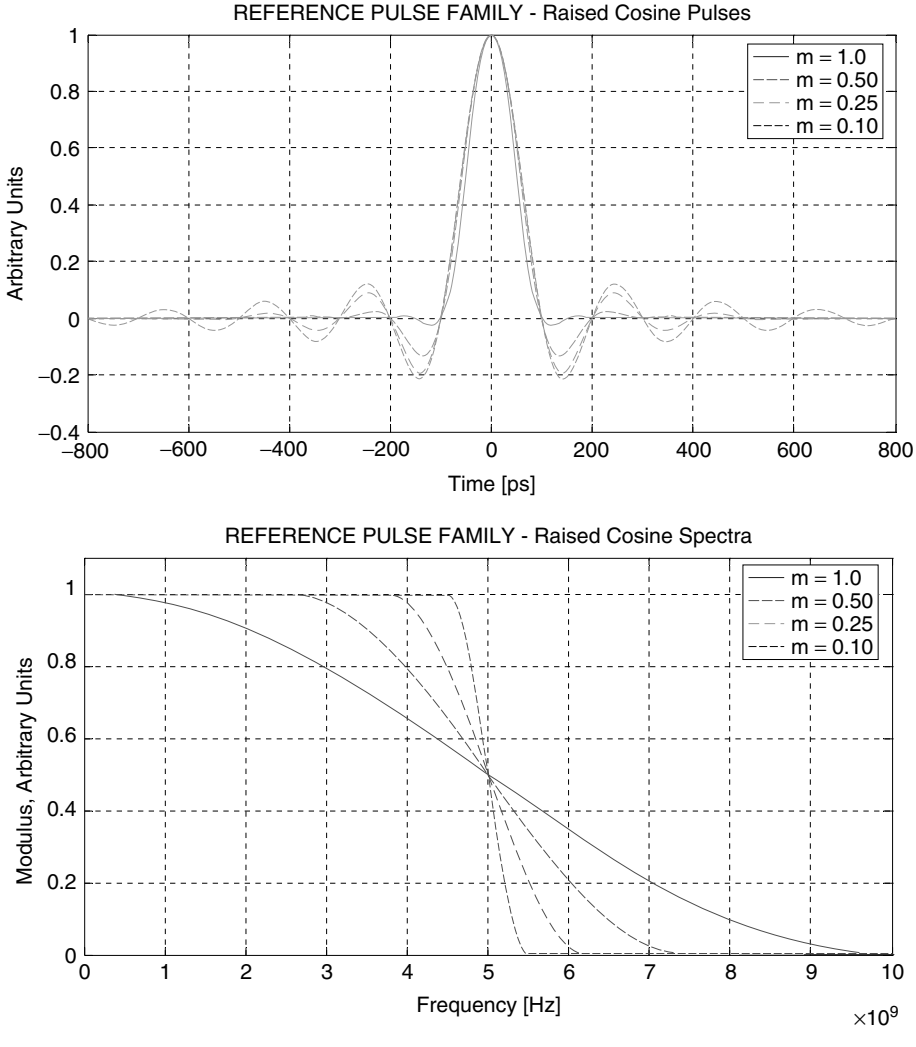

Figure 8.65 Raised cosine reference pulse family. Top: time domain pulses. Bottom: frequency spectra representation. All pulses are referred to the time step $T = 100\,\text{ps}$. It is evident in the top representation that all pulses satisfy the requirement for no ISI contribution at every multiple of the time step

requirement for no ISI contribution to every multiple of the sampling time step T. It is remarkable how pulses characterized by larger values of the normalized shaping sigma exhibit longer oscillating tails due to the dominant contribution of the windowing function.

8.5.5.8 Lorenzian Shaped Pulse Family

Figure 8.67 presents the time domain and frequency domain representation of four pulses of the Lorenzian shaped reference family in Equation (8.76). In order to make a quantitative comparison with a previous Gaussian family, the same values are chosen for the normalized time constant as for the standard deviation of the Gaussian shaped pulses: $\tau/T = 0.5,\ 1,\ 2,\ 5$.

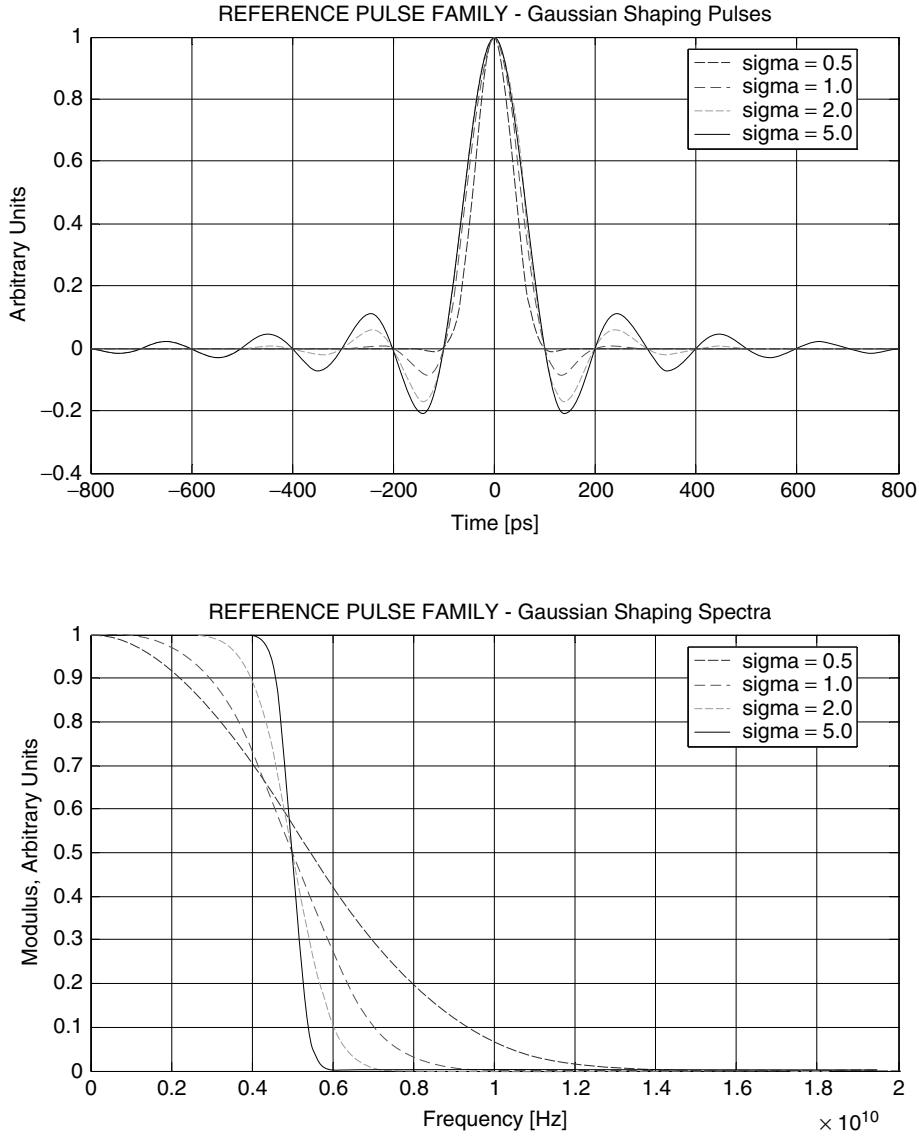

Figure 8.66 Gaussian shaped reference family. Top: time domain pulses. Bottom: frequency spectra representation. All pulses are referred to the time step $T = 100\,\text{ps}$

8.5.5.9 Single-Pole Shaped Pulse Family

Figure 8.68 shows the numerically computed time and frequency domain representations of four elements of the single-pole shaped reference family in Equation (8.79). The normalized time constant has the same values $\tau/T = 0.5,\ 1,\ 2,\ 5$.

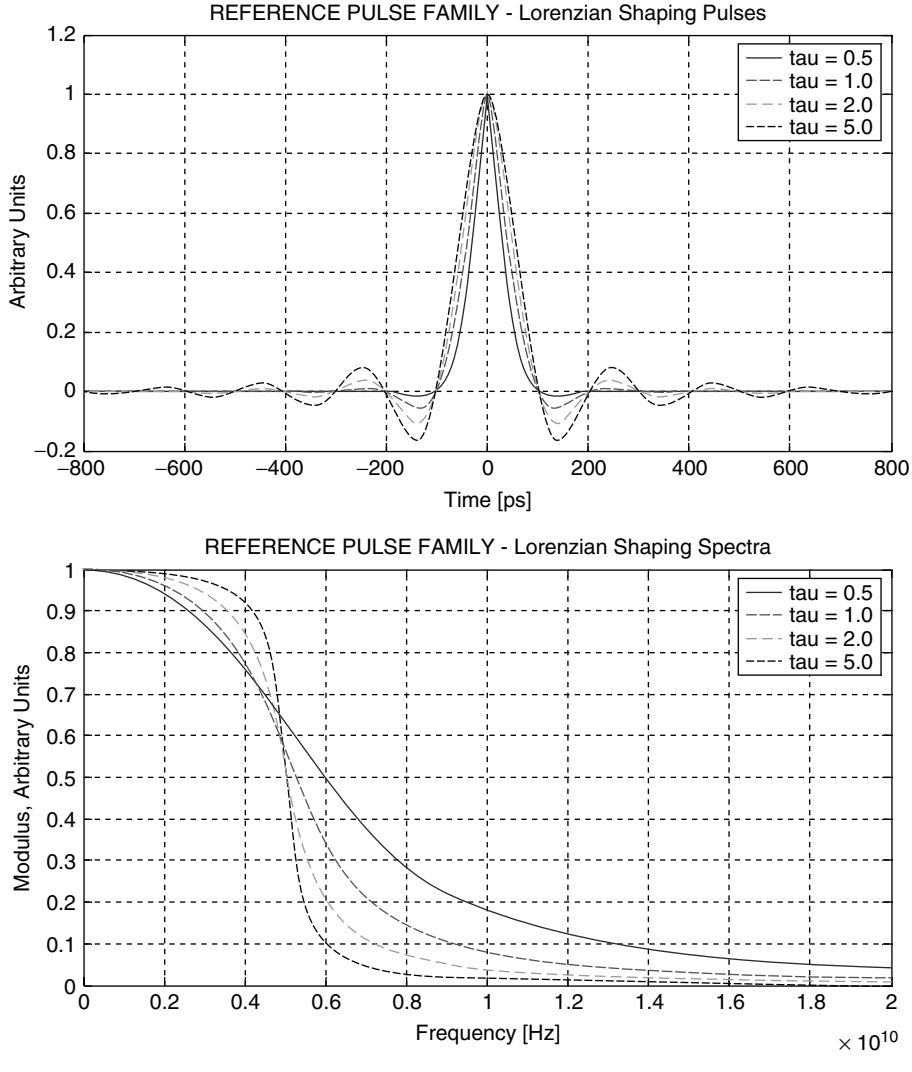

Figure 8.67 Lorenzian shaped reference family. Top: time domain pulses. Bottom: frequency spectra representation. All pulses are referred to the time step $T = 100\,\text{ps}$

8.5.5.10 IV-order Bessel–Thompson Shaped Pulse Family

The last reference receiver output response being investigated is the IV-order Bessel–Thompson pulse family. Figure 8.69 reports the computed time domain and frequency domain representations according to the procedure described in Section 8.5.3.4 for three different normalized cut-off frequencies. In this case, the windowing pulse and the shaping pulse are presented together with the resulting output pulse. The same procedure has also been used for the corresponding frequency spectra:

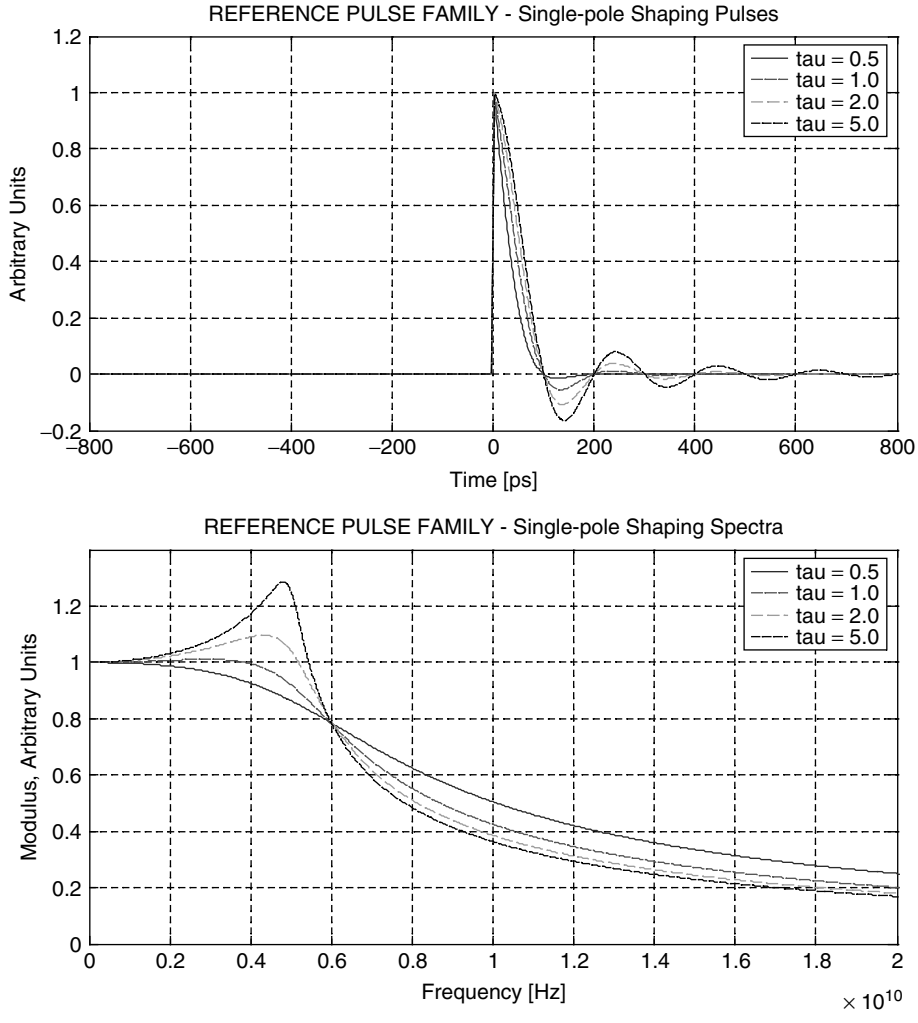

Figure 8.68 Single-pole shaped reference family. Top: time domain pulses. Bottom: frequency spectra representation. All pulses are referred to the time step $T = 100\,\text{ps}$

8.5.6 Summary

In this section, several mathematical functions used for modeling the linear impulse response and related spectra of the optical reference receiver (ORR) are presented. Noise analysis and any time recovery and jitter impairments are neglected, focusing only on the required pulse shape at the decision section in order to avoid any intersymbol interference. This led to the concept of the optical reference receiver as the suboptimal receiver, which is not necessarily matched to the transmitted spectrum but satisfies the ISI-free operation. Once the transmitted spectrum is known, the receiving filter allows the production of a proper output spectrum, leading to pulse detection without an intersymbol contribution from adjacent pulses. In order to manage the mathematical modeling of the output spectrum of the optical reference receiver, the corresponding output pulse has been written as the product of the windowing function with the shaping function, leading to the

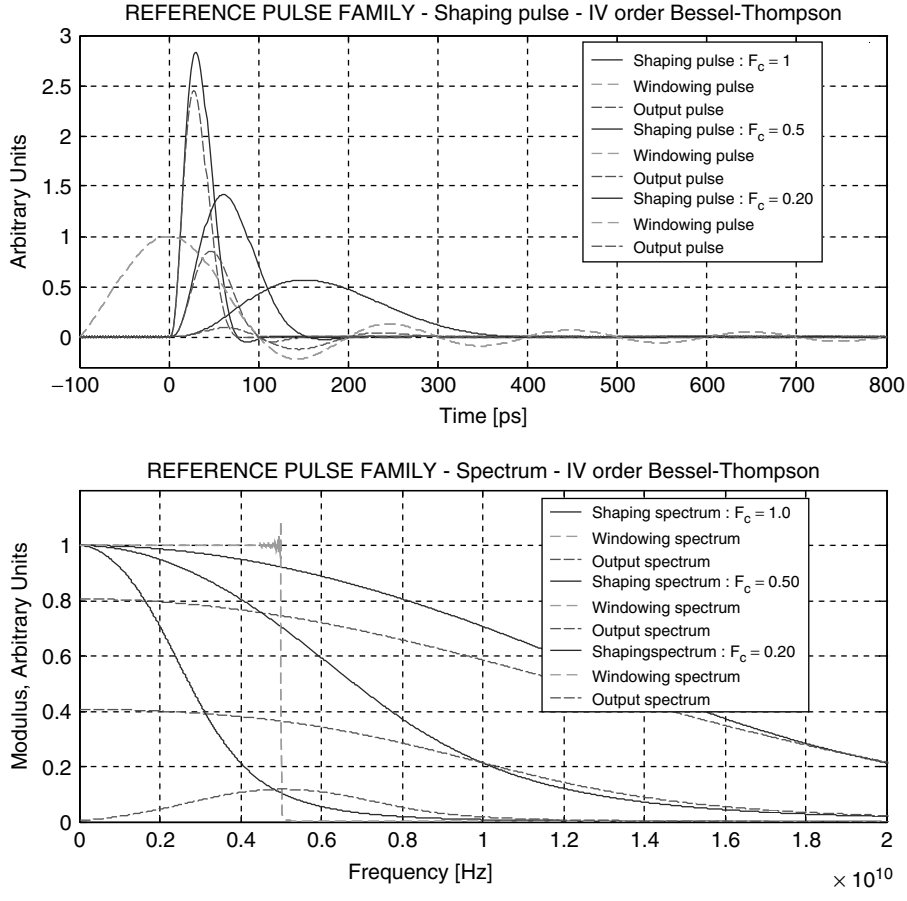

Figure 8.69 Top: representation of the IV-BT reference family with the relative components from the windowing pulse and the shaping pulse. According to shaping pulse causality, all output pulses are causal, but the pulse profile is quite different depending on the normalized cut-off frequency. When the cut-off frequency decreases below $f_c/B = 0.2$, the IV-BT pulse component starts slowly and then interacts with the oscillating behavior of the windowing function, giving rise to the characteristic oscillating output response. Bottom: corresponding frequency spectra

interesting results presented in the text. All the presented pulses satisfy the ISI-free requirements at the decision section. Of course, they are differentiated from each other according to the filtering requirements and the related noise bandwidths.

Table 8.1 presents a summary of the mathematical models used for the optical reference receiver output spectra described in the text.

8.6 Conclusions

This chapter has dealt with the basic concepts for modeling the optical link in a multigigabit transmission using multimode fiber. More attention has been paid to the signal modeling of the transmitter and the receiver, neglecting noise aspects and other biasing-dependent phenomena in the laser transmitter. The intention has been to give a quantitative expression that is useful for

Table 8.1 Output pulse model expressions of the optical reference receiver

Pulse	Expression	Reference
Raised cosine	$\gamma_T(t) = \frac{1}{T}\,\frac{\cos(m\pi t/T)}{1-(2mt/T)^2}\,\frac{\sin(\pi t/T)}{\pi t/T}, \quad 0 \le m \le 1$	(8.60)
Gaussian	$\gamma_T(t) \equiv \frac{1}{T}\,\frac{\sin(\pi t/T)}{\pi t/T}\,\mathrm{e}^{-(t/\sigma)^2/2}$	(8.74)
Lorenzian	$\gamma_T(t) \equiv \frac{1}{T}\,\frac{\sin(\pi t/T)}{\pi t/T}\,\mathrm{e}^{-\lvert t\rvert/\tau}$	(8.76)
Single-pole	$\gamma_T(t) \equiv \begin{cases} \frac{1}{T}\,\frac{\sin(\pi t/T)}{\pi t/T}\mathrm{e}^{-t/\tau}, & t \ge 0 \\ 0, & t < 0 \end{cases}$	(8.79)
Bessel–Thompson (spectrum)	$S(f) = \frac{105}{105 + 105y + 45y^2 + 10y^3 + y^4}$	
	$y = \mathrm{j}2\pi f\tau, \qquad y = \mathrm{j}a\frac{f}{f_\mathrm{c}}$	(8.80)
	$\lvert S(f_\mathrm{c})\rvert = \frac{1}{\sqrt{2}} \quad \Rightarrow \quad a = 2.1139$	

both transmitter and receiver modeling, including new contributions to the intersymbol interference concept. A new approach to output pulse synthesis using the windowing function led to generalized output spectra and the integral representation theorem. Many worked numerical examples complete this chapter.

9

Principles of Electronic Dispersion Compensation

Concepts and Limitations Applied to Multimode Fiber Transmission

9.1 Introduction

The multimode fiber transmission system presented in Chapter 8 is based on the intensity modulation and direct detection (IMDD) scheme. Using lightwaves by means of intensity modulation is the simplest way to transfer information content over optical fibers. Other light modulation schemes are of course available, but in this context reference will be made exclusively to IMDD. The basic requirement for achieving proper IMDD transmission can be summarized in having as much light energy as possible confined within each single time step. The capability of the decision process in the optical receiver to recognize the information content associated to the single bit depends on the ratio between the amount of signal energy E_0 and the noise energy N_0 included in the single bit duration. The higher the ratio the easier it becomes to detect the signal information.

Among several causes that can lead to erroneous signal detection, two assume the highest priority, namely the energy spreading outside the bit time and the noise increasing inside the bit time. If a unit energy amount is assumed to transmit into the defined time step, but if according to dispersive propagation behavior in the optical channel only a fraction, $p < 1$, of that energy arrives at its destination within the time step, correspondingly $1 - p$ information energy will have been lost, leading to sensible degradation in the decision process. Similarly, even assuming ideal channel transmission, with the detected pulse showing unit energy per time step, if the amount of noise dragged inside the same time step hides most of the signal recognition capability, the decision process would be seriously damaged, leading to a high probability of making a wrong binary decision. In this chapter, both of these decision process degradation causes will be discussed.

The purpose of each electronic equalizer is to reconfigure disperse optical pulses into the assigned time step, effectively increasing the amount of useful signal density (energy per time step). Unfortunately, the signal equalization cannot be performed without finding some additional noise degradation. This effect is common to every equalizer, both to the simplest linear equalizer and to the more complicated digital equalizers based on the minimum mean squared error principle. The problem arises because conceptually the equalizer needs to restore the missing response of the

Multi-Gigabit Transmission over Multimode Optical Fibre: Theory and Design Methods for 10GbE Systems Stefano Bottacchi
 ISBN: 0-471-89175-4

transmission channel and this operation increases the noise power at the decision process. In this chapter, the ideal inverse filter equalizer (IFE) will be analyzed, which, although achieve zero-forcing equalization, leads to an unacceptable noise increment for most of the multimode optical fiber responses.

9.2 The Optical Decision Process

The purpose of this section is to introduce the detection theory of the optical signal in the presence of several noise terms simultaneously affecting the optical receiver input in a multimode fiber link operating at 10 GbE. Most of the following concepts are introduced without developing the complete treatment that would be required in a book dedicated to this subject. Noise theory in optical fiber transmission is a fundamental knowledge milestone and will be extensively covered in a planned book on this subject. It is assumed here that the reader is almost familiar with the concepts being presented. Nevertheless, each new concept introduced in this chapter has been presented for a self-consistent understanding.

9.2.1 Noise Models and Approximations

In order to consider the different noise contributions impairing the optical detection and decision processes, the optical fiber transmission systems and the modulation format must first be identified. The system under consideration in this book operates with a single wavelength, at a multigigabit data rate, without any optical amplification stage, using the conventional intensity modulation and direct detection (IMDD) architecture. Noise contributions such as mode partition noise (MPN), reflection noise (RN) and modal noise (MN) will not be included in the following first-order calculations. Accordingly, the noise contributions that will be considered are the following:

1. Receiver thermal noise
2. Dark current shot noise
3. Signal shot noise
4. Laser source relative intensity noise

Mode partition noise arises when a multilongitudinal laser source, like the Fabry–Perot cavity structure, feeds a multimode fiber. In this case, the time-dependent random distribution of the emitted light power among several excited lasing modes at different wavelengths interacts with the chromatic dispersion of the fiber, leading to a random profile output pulse. Amplitude fluctuations of the output pulse are easily recognized as noise. Mode partition noise is not a peculiarity of multimode fiber since it depends on interaction with the chromatic dispersion characteristic of the fiber.

Reflection noise arises from the interaction of the laser source cavity with the light power reflected back from the line. This interaction can generate a random contribution to the lasing process with consequent frequency chirping and mode hopping. Reflection noise is present in every optical fiber link, either multimode or single-mode.

Modal noise is instead a peculiarity of the multimode regime in a multimode fiber. It depends on the interaction of the modal field distribution at every fiber link discontinuity, like the ones produced by optical connectors, splices and any other passive optical component placed along the fiber link. The modal power distribution (MPD) of the incoming light will suffer a variation at the discontinuity, with some power exchange among excited modes, leading to random fluctuation of the output pulse.

One relevant aspect considered in the analysis below is the dependence of noise terms with respect to the average optical power at the receiver input. Depending on that relationship, a very

different receiver behavior is expected at low or high optical power levels. The following general assumptions are assumed to be verified:

1. All noise sources have zero mean and are stationary and ergodic processes.
2. All noise sources are assumed to be statistically independent and are described by a Gaussian probability density function.
3. The average power of each noise source coincides with the variance of the process.
4. All processes are described as white Gaussian noise (WGN), with constant power spectral density.

Assumption 1 holds for CW operation under stationary environmental conditions and is based on the fundamental physics of each process. It is accepted as a basic requisite for all noise analysis.

Assumption 2 requires that all noise sources are independent from each other and that each noise term is described as a normal process with a Gaussian probability density function. The mutual independency imposes a relatively weak condition on the different processes involved and is widely verified under standard operating conditions with relatively low optical power levels.

The Gaussian assumption, however, needs some comments for each specific noise source. Thermal noise has a Gaussian probability density function (PDF) and needs no more justification or comments. Shot noise is described by the Poisson probability density function, since shot noise is a Poisson process. Nevertheless, it is well known that under high rate conditions, the fluctuations of any Poisson process converge toward a Gaussian process and the equivalent centered Poisson process is well depicted as a zero-mean Gaussian process. Under a relatively high rate occurrence of the Poisson event, it is therefore customary to adopt a Gaussian approximation of the shot noise process. According to the previous four noise terms contributions, it is therefore reasonable to use the Gaussian approximation for the second and third noise terms involved, namely the signal-induced shot noise and the dark current-induced shot noise.

The fourth noise term refers to the relative intensity noise (RIN) of the laser source. The relative intensity noise is a peculiarity of the light source and is related to the amount of laser light intensity fluctuations with respect to the average intensity emitted. It is well known that RIN is not a white process, meaning that the power spectral density is not a flat distribution versus the frequency. The RIN power spectrum usually exhibits a frequency peaking depending on the relaxation oscillation frequency of the laser and on the associated package. In order to avoid long settling times and dangerous ringing in the impulse response, laser module manufacturers usually keep RIN peaking as far away as possible from the modulation frequency range of the laser. Under this assumption, the relevant in-band contribution of the RIN behaves in an almost flat way and can be approximated as white noise. The Gaussian assumption for the probability density function of the RIN allows easily handling of the mathematics involved with the error probability calculation. This is not of course a valid justification for adopting a Gaussian probability density function, but since the fundamental physics behind the RIN deals with electron thermal agitation and spontaneous emission, the Gaussian approximation behaves fairly well for including RIN in any optical receiver noise calculation.

Assumption 3 is a consequence of the ergodicity condition. It is a fundamental result of the theory of stochastic processes that every ergodic process has time averages coincident with ensemble averages. This identity holds at least up to second-order averages involving the autocorrelation, the mean and the power of the noise process. In particular, ergodicity leads to the coincidence of the time-averaged power and the variance of each noise process.

The last assumption (4) deals with the spectral properties of the noise process. To simplify the mathematical modeling, it will be assumed that every noise term has a flat power spectral density, at least in the frequency range of the optical receiver. This characteristic will be referred to as in-band white noise. This assumption allows the important concept of noise bandwidth to be used as the

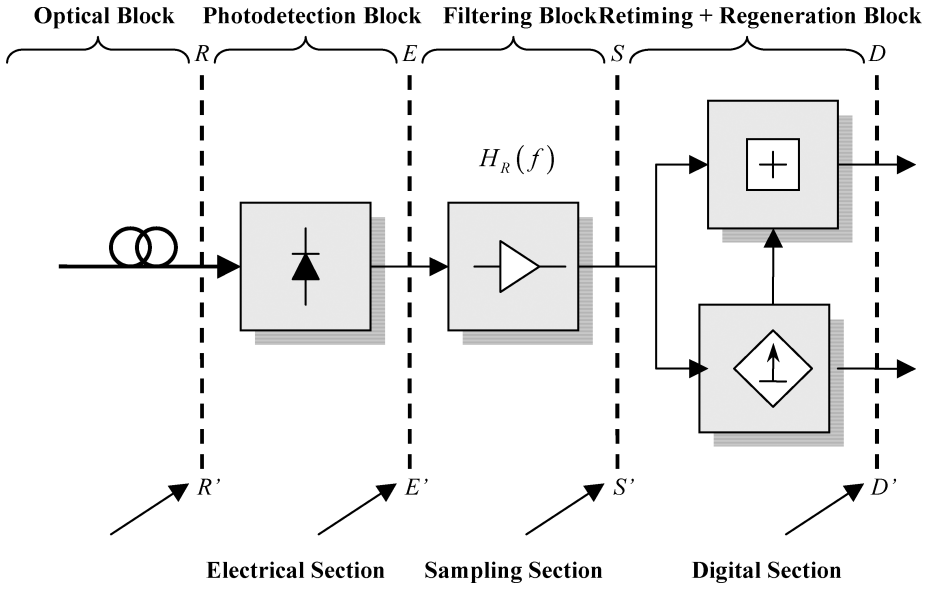

Figure 9.1 Block diagram of the optical receiver. Different signal sections have been reported. Equivalent noise contributions are applied at the electrical input, section $E-E'$

metric for comparing the sensitivity performances among several optical receivers characterized by the same data rate. As well as being used in this way, the first three terms, thermal noise, dark shot noise and signal shot noise, are clearly white noise processes, while RIN needs some restrictions, as introduced above. Figure 9.1 presents a block diagram of the optical receiver including the different noise contributions.

9.2.1.1 The Noise Bandwidth

The noise bandwidth concept is widely used in every telecommunication field. The definition and principal features will be reviewed shortly. It is well known from the noise theory of linear systems that the power spectral density $G_{\text{out}}(f)$ of the noise at the output of a linear system is given by the product of the noise power spectral density $G_{\text{in}}(f)$ at the input by the square modulus $|H(f)|^2$ of the transfer function:

$$G_{\text{out}}(f) = |H(f)|^2 G_{\text{in}}(f) \tag{9.1}$$

The integral of the power spectral density $G_{\text{out}}(f)$ gives the noise power at the output section:

$$N_{\text{out}} = \int_{-\infty}^{+\infty} |H(f)|^2 G_{\text{in}}(f)\,\mathrm{d}f \tag{9.2}$$

If it is assumed that the power spectral density of noise at the input is constant, or at least it is constant in the band-limited frequency range of the system transfer function, $G_{\text{in}}(f)$ can easily be taken out of the integral (9.2) and written as

$$N_{\text{out}} = |H(0)|^2 G_{\text{in}} \int_{-\infty}^{+\infty} \frac{|H(f)|^2}{|H(0)|^2}\,\mathrm{d}f \tag{9.3}$$

The transfer function has been normalized using the DC value. This is one common choice, but it is not of course the only one possible. The integral in Equation (9.3) takes the meaning of the noise bandwidth of the linear system. It coincides with the bandwidth seen by the uniform noise density G_{in} at the input in order to generate the same output noise power N_{out} given in Equation (9.2). Consequently, the noise bandwidth B_{n} can be defined as

$$B_{\text{n}} \equiv \int_{-\infty}^{+\infty} \frac{|H(f)|^2}{|H(0)|^2}\,\mathrm{d}f \tag{9.4}$$

Using the noise bandwidth definition gives

$$\begin{aligned} N_{\text{in}} &= G_{\text{in}} B_{\text{n}} \\ N_{\text{out}} &= |H(0)|^2 N_{\text{in}} \end{aligned} \tag{9.5}$$

which gives physical meaning to the definition (9.4). Figure 9.2 shows the graphical interpretation of the noise bandwidth concept presented above.

The noise bandwidth can be considered as the metric of the linear system with respect to the white noise stimulus. In other words, different linear systems can be compared quantitatively using their noise bandwidth and assuming the same white noise distribution at the input. In particular, for a given bit rate, it can reasonably be assumed that different optical receivers have the same electrical bandwidth but different transfer functions, with different frequency profiles. This discussion leads to the concept of the optimum optical receiver as the receiver that simultaneously maximizes the signal-to-noise ratio (SNR) and minimizes the residual intersymbol interference power. It is clear at this point that the larger noise bandwidth will allow higher noise power and more degraded (suboptimal) sensitivity performances. It is already known that not only does noise power interfere with the sensitivity performance but also the amount of residual intersymbol interference. A narrower system bandwidth will lead to less noise power, of course, but will increase the ISI signal degradation.

9.2.1.2 Thermal Noise

The contribution of thermal noise in the optical receiver is described by the input equivalent noise current density i_{c}, expressed in $\text{pA}/\sqrt{\text{Hz}}$. Thermal noise comes from the electrical circuit of the optical front end, mainly due to the input stage amplifier. In order to give a quantitative indication of

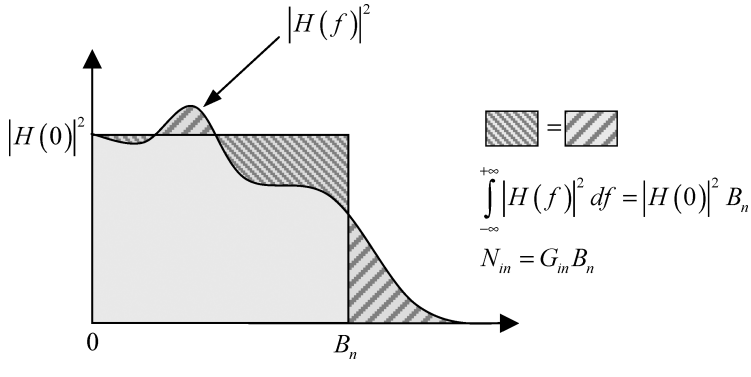

Figure 9.2 Graphical representation of the noise bandwidth. The sum of the areas of the dashed regions outside and inside the rectangle is equal. This makes the gray rectangle subtended by the noise bandwidth equivalent to the area subtended by the square modulus of the transfer function of the linear system

Table 9.1 System specification of the optical receiver used for the computation of the input equivalent noise current density

Wavelength	$\lambda = 1310\,\text{nm}$
Photodetector efficiency	$\eta = 0.6$
Bit rate	$B = 10.3125\,\text{Gb/s}$
Receiver type	IV - order Bessel–Thompson
Cut-off frequency	$f_c = 7.734\,\text{GHz}$
Noise bandwidth	$B_n = 11.14\,\text{GHz}$
Q-factor	7, BER $= 10^{-12}$
Extinction ratio	ER $\rightarrow \infty$
Sensitivity limit	$P_R = -17\,\text{dBm} = 20\,\mu\text{W}$

the input equivalent thermal noise current density i_c available in optical receivers, some parameters of the transmission system must be introduced. Table 9.1 gives some parameters used for noise calculation assuming that the optical receiver sensitivity is determined exclusively by the thermal noise contribution. This approximation will be referred to as the thermal noise limited receiver. In addition, it will be assumed that the optical receiver transfer function is shaped according to the fourth-order Bessel–Thompson frequency response.

The photocurrent equivalent I_R to the input average optical power evaluated at the sensitivity limit P_R is given by

$$I_R = \frac{q\lambda}{hc}\eta P_R = 12.7\,\mu\text{A} \tag{9.6}$$

where $q = 1.602 \times 10^{-19}\text{C}$ is the electron charge, $h = 6.626 \times 10^{-34}$ J s is the Planck constant and $c = 2.998 \times 10^8$ m/s is the speed of light in vacuum.

Figure 9.3 shows the model used for the signal decision process. Since the extinction ratio is infinite, the photocurrent equivalent I_{OMA} corresponding to the optical modulation amplitude (OMA) is just twice the photocurrent equivalent generated by the input average optical power. The thermal noise is completely characterized by the RMS value σ_c of the Gaussian distribution. The suffix c stands for 'circuit', due to the source of thermal noise in every electronic receiver.

In a binary decision process with equiprobable symbols and uniformly distributed noise fluctuations with power σ_c^2 over both logic levels, the decision distance d coincides with the average photocurrent equivalent $d = I_R$. The required standard deviation σ_c of the additive thermal noise is therefore computed from the required Q-factor:

$$\sigma_c = \frac{I_R}{Q} = 1.81\,\mu\text{A}, \qquad \sigma_c^2 = 3.27 \times 10^{-12}\text{A}^2 \tag{9.7}$$

Once the input equivalent noise power σ_c^2 and the noise bandwidth are known, the input equivalent noise current density is computed:

$$i_c = \sqrt{\frac{\sigma_c^2}{B_n}} \cong 17\ \text{pA}/\sqrt{\text{Hz}} \tag{9.8}$$

By definition, the input equivalent noise current density is therefore constant versus the frequency. It generates the required noise power at the receiver output after frequency integration over the receiver total noise bandwidth. This value will be used through this book as the current density of the input equivalent noise for a typical 10 GbE optical receiver.

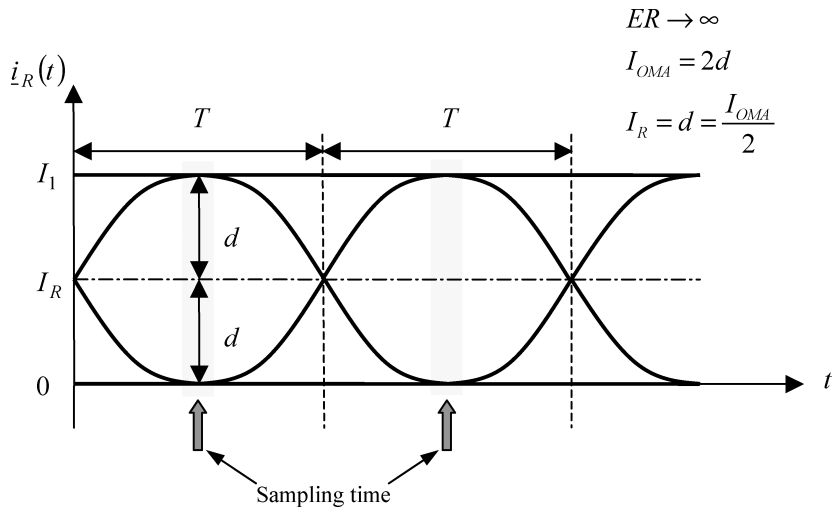

Figure 9.3 Schematic representation of the eye diagram obtained with an equalized signal pulse profile at the decision section. In the considered case, the optical power associated at the low signal level is assumed to be zero, leading to an infinite (ideal) extinction ratio. As described in the text, under this condition the average optical power coincides with the decision amplitude and the optical modulation amplitude is given by twice the average power

9.2.1.3 Dark Shot Noise

The dark current in the photodetector produces the shot noise contribution known as dark shot noise. Assuming the photodiode dark current is $I_D = 5$ nA, the corresponding shot noise power becomes

$$\sigma_d^2 = 2q I_D B_n = 17.8 \times 10^{-18} A^2 \tag{9.9}$$

The value is almost negligible compared to the circuit noise current density calculated in Equation (9.8). It is important to note that both circuit noise current density and dark shot noise are independent of the input optical power level. This means that their relative contribution to the signal-to-noise ratio becomes smaller as long as the input optical power level increases.

9.2.1.4 Signal Shot Noise

The average value of the photocurrent generated by the incoming signal power produces a second contribution of shot noise, known as the *signal shot noise*. The contribution of shot noise power due to the received optical power is given by the following expression:

$$\sigma_s^2 = 2q R P_R B_n \quad (A^2) \tag{9.10}$$

where

$$R = \frac{q\lambda}{hc}\eta \quad (A/W) \tag{9.11}$$

The constant R is the photodetector responsivity and includes the external quantum efficiency η and the optical wavelength λ. Assuming that the operating wavelength $\lambda = 1310$ nm, the photodetector responsivity R is

$$R(\lambda = 1310\,\text{nm}) \cong 1.057\eta \quad (A/W) \tag{9.12}$$

A typical value for the quantum efficiency of 10 Gb/s PIN diode ranges between $0.5 \leq \eta \leq 0.7$.

The important difference between the previous two terms is the linear dependence of the signal shot noise power from the received average optical power. The shot noise power increases proportionally to the received optical power. This is the reason for having a negligible shot noise contribution at a low power level, where it usually dominates receiver thermal noise. At a higher power level, shot noise usually dominates thermal noise. Nevertheless, other second-order noise contributions, like RIN and signal spontaneous beat noise in optically amplified links, usually do not make signal shot noise the dominant term for optical receiver noise performances.

9.2.1.5 Relative Intensity Noise (RIN)

The last noise term being considered is relative intensity noise (RIN). This noise contribution is due to light intensity fluctuations within the laser cavity caused by spontaneous emission amplification. RIN is defined as the ratio between the spectral power density $S_{\underline{I}}(f)$ of the photocurrent equivalent $\underline{I}(t)$ and the square value of its average $\langle \underline{I} \rangle^2$:

$$\text{RIN } (f) \equiv \frac{S_{\underline{I}}(f)}{\langle \underline{I} \rangle^2} \quad \text{(dB/Hz)} \tag{9.13}$$

RIN is expressed as the ratio between the power spectral density (W/Hz) and the average power (W). The dimension is therefore a time and the unit of measure is seconds, or more often dB/Hz. It is important to remark that RIN is measured using the spectral distribution of the detected photocurrent equivalent. Because of the definition, RIN is a function of electrical frequency. Assuming that the spectral power density of the photocurrent equivalent is constant, the RIN coefficient therefore becomes a constant over frequency. It is very easy to write the noise power contribution due to the laser RIN coefficient. From the definition above, the noise power contribution at the receiver input can be written as follows:

$$\sigma^2_{\text{RIN}} = R^2 P_{\text{R}}^2 \text{ RIN } B_{\text{n}} \quad (\text{A}^2) \tag{9.14}$$

The most important characteristic of RIN is the dependence of the noise power on the square of the received average optical power level. This characteristic makes RIN the dominating contribution at the high power level over the remaining constant noise terms (thermal noise and dark shot noise) and the linear noise term (signal shot noise).

9.2.1.6 Total Noise Power

The total noise power at the electrical input of the optical receiver is therefore given by summing all four terms of the noise power, namely the thermal noise, the dark shot noise, the signal shot noise and the relative intensity noise:

$$\sigma^2_{\text{tot}}(P_{\text{R}}) = \sigma^2_{\text{c}} + \sigma^2_{\text{d}} + \sigma^2_{\text{s}}(P_{\text{R}}) + \sigma^2_{\text{RIN}}(P_R) \tag{9.15}$$

After substituting the expressions of the noise components, from Equations (9.7), (9.9), (9.10) and (9.14), the following explicit form is obtained:

$$N_{\text{tot}}(P_{\text{R}}) = (i^2_{\text{c}} + 2q I_{\text{D}} + 2q R P_{\text{R}} + R^2 P_{\text{R}}^2 \text{ RIN }) B_{\text{n}} \tag{9.16}$$

Figure 9.4 gives the results of the computation of the individual noise contributions and the total noise power versus the received average optical power. The parameters used for the calculations are the same as reported in Table 9.1, plus the detector dark current $I_{\text{D}} = 5$ nA. The noise

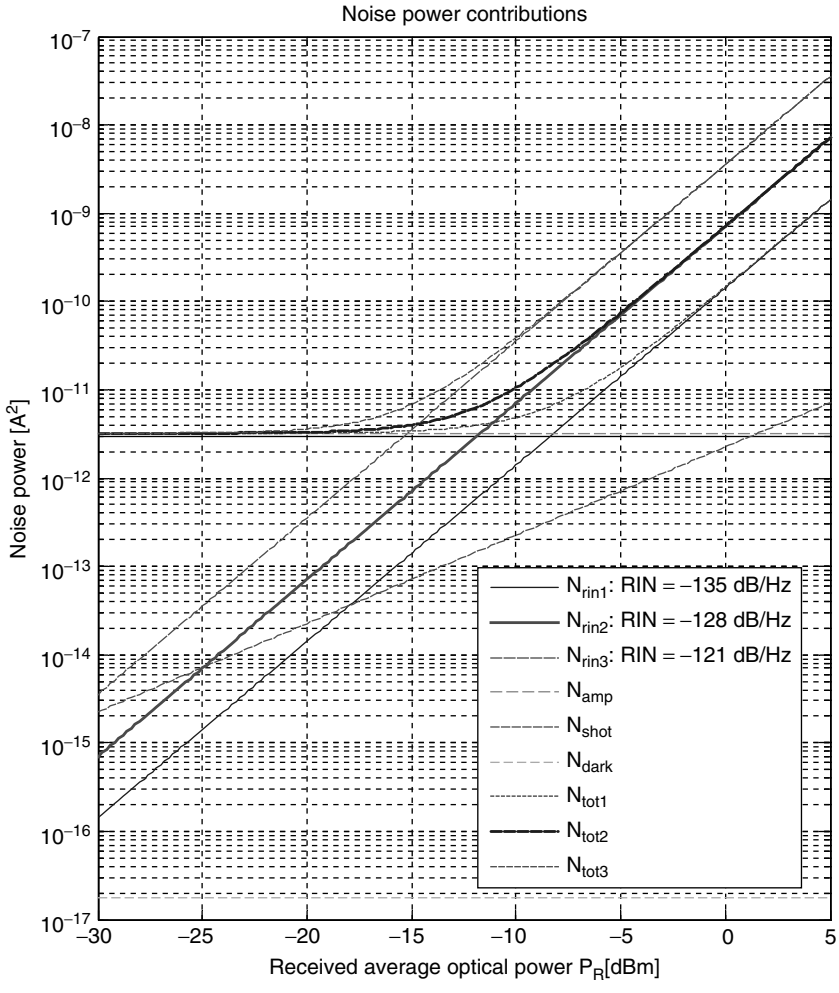

Figure 9.4 Noise power plots of the four noise terms considered above. Thermal noise and dark shot noise appear as constant lines. Signal shot noise has a slope of one decade/10 dB while RIN has a slope of two decades/10 dB, as reported in the relative expressions

bandwidth B_n refers to the fourth-order Bessel–Thompson filter with cut-off at 75 % of the 10 GbE bit rate:

$$\left.\begin{array}{l} i = 17\,\text{pA}/\sqrt{\text{Hz}} \\ \lambda = 1310\,\text{nm} \\ \eta = 60\,\% \\ B_n = 11.14\,\text{GHz} \\ {\scriptstyle (IV\text{-}BT filter,\, f_c = 0.75B)} \\ I_{\text{dark}} = 5\,\text{nA} \end{array}\right\} \Rightarrow \text{Sensitivity} = -17\,\text{dBm at BER} = 10^{-12},\ B = 10.3125\,\text{Gb/s} \qquad (9.17)$$

Different noise terms are clearly identified by their characteristic slope. Thermal noise and dark shot noise are constant contributions versus input average optical power. Signal shot noise has a unit slope showing one decade of noise power contribution every 10 dB of input average optical power. Three different RIN contributions have been included in order to highlight the relative RIN composition of the total noise power. RIN terms are clearly recognized by their double slope, showing two decades of noise power contribution every 10 dB of input average optical power. All three RIN coefficients considered here assume the dominant noise power contribution over the remaining noise terms at some input optical power level in the range $-16\,\text{dBm} \leq P_R \leq -7\,\text{dBm}$. The highlighted line corresponds to the total noise power for the case of RIN $= -128$ dB/Hz. This value is adopted in the IEEE 802.3, 10GBASE-LRM standard requirement. In the example above, the breakeven point between thermal noise and RIN depends on the RIN coefficient considered. In the case of RIN $= -128$ dB/Hz, the RIN takes a dominating role at about $P_R = -12$ dBm. This point can easily be determined as the intersection between the constant thermal noise line and the RIN contribution line. Since at $P_R = -12$ dBm the corresponding RIN contribution is more then one decade lower it is reasonable to conclude that the optical receiver sensitivity is limited by thermal noise of the input circuit. The same conclusion does not hold if the RIN coefficient is higher, RIN $= -121$ dB/Hz. It that case, the breakeven point is close to $P_R = -16$ dBm and even at $P_R = -17$ dBm the RIN contribution is not negligible with respect to the assumed thermal noise term.

9.2.2 Electrical Signal Power

The classical theory of decision for NRZ pulses is based on the additive Gaussian noise assumption evaluated at the decision section. In this case, the ratio between the electrical signal amplitude and the RMS noise value at the sampling instant takes the role of a dominant variable in the bit error rate (BER) calculation. It is known that optical detection is a square low process; hence, the electrical signal amplitude is proportional to the optical signal intensity. This makes the decision theory in optical fiber receivers easier and linearly related to the optical signal intensity. Nevertheless, it is instructive to relate the BER calculation to the electrical signal-to-noise ratio (SNR) computed at the decision section of the optical receiver. However, it should be remarked that the electrical SNR must not be confused with the ratio d/σ between the signal amplitude at the sampling instant and the RMS noise value. Sometimes, this misunderstanding creates an erroneous estimation of the system performances. In fact, the electrical SNR involves the integration of the square of the electrical pulse at the decision section in order to compute the average power.

In order to compute the electrical Signal-to-Noise ratio at the optical receiver input it is necessary to define the signal pulse shape. The error probability of the binary detection process depends directly on the ratio between the distance d of the sampled signal amplitude and the decision level with the RMS noise amplitude σ. In order to relate the electrical average signal power S_e to the decision distance d and to the error probability it is therefore necessary to define the pulse shape of the sampled signal.

In the following derivation, reference will be made to the optical signal schematic reported in Figure 9.5. Assuming the NRZ coding and equiprobable bits, the average optical power P_R, the optical modulation amplitude P_{OMA} and the extinction ratio r are related by the following relationship:

$$P_R = \frac{1}{2} P_{OMA} \frac{r+1}{r-1} \tag{9.18}$$

The two power levels P_0 and P_1 shown in Figure 9.5 must be intended as the ensemble average values of the high logic level and the low logic level respectively, after coding in the optical domain. To derive the previous equation, the following definitions of the extinction ratio r, the

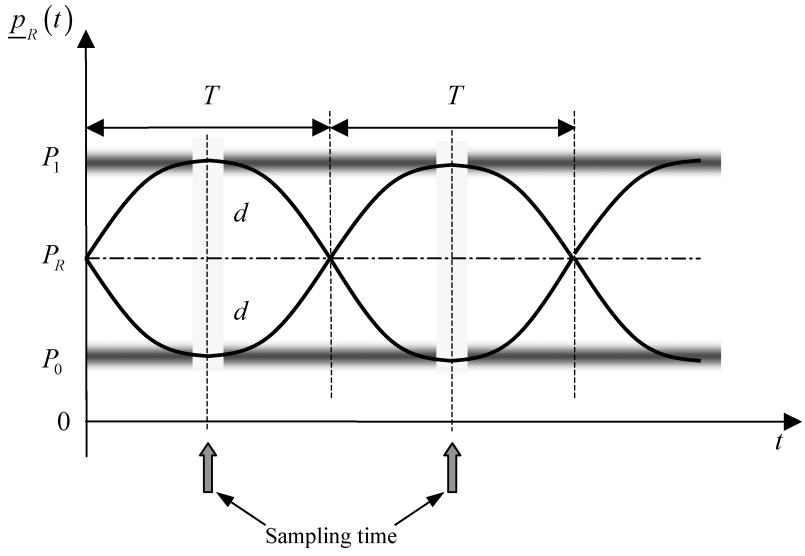

Figure 9.5 Schematic representation of the optical signal at the receiver input. The optical signal consists of the intensity envelope modulating the optical field emitted by the light source. The intensity modulation is affected by noise fluctuation, and the ensemble average of the light intensity corresponding to the high and low logic levels are identified as P_1 and P_0

average received optical power P_R and the optical modulation amplitude P_{OMA} are given:

$$r \equiv \frac{P_1}{P_0} \tag{9.19}$$

$$P_R \equiv \tfrac{1}{2}(P_0 + P_1) \tag{9.20}$$

$$P_{OMA} \equiv P_1 - P_0 \tag{9.21}$$

Substituting Equation (9.19) into definitions (9.20) and (9.21), and equating equal terms, it is easy to obtain Equation (9.18).

Introducing the photocurrents corresponding to the average power level P_R and to the optical modulation amplitude P_{OMA} gives the same relationships as above between the average value I_R of the detected photocurrent and the current swing I_{OMA} corresponding to the optical modulation amplitude:

$$\begin{aligned} I_R &= R P_R \\ I_{OMA} &= R P_{OMA} \end{aligned} \tag{9.22}$$

Defining d as the half-amplitude of I_{OMA}, $d \equiv I_{OMA}/2$, from Equations (9.18) and (9.22), the following expression is obtained:

$$I_R = d\frac{r+1}{r-1} \tag{9.23}$$

From this simple expression it is seen immediately that when the extinction ratio tends to infinite, the distance d coincides with the average current I_R. For every finite value of the extinction ratio, the distance d is even lower than the average detected photocurrent. This is the explanation for the average optical power penalty corresponding to every finite value of the extinction ratio. From

Equations (9.23) and (9.22), the simple relationship between the distance d and the average optical power P_R is derived:

$$d = \frac{r-1}{r+1} R P_R \tag{9.24}$$

Decreasing the extinction ratio, the average optical power must consequently be increased in order to maintain the same value of the signal distance d. This is the concept of the optical power penalty due to the finite value of the extinction ratio.

The total electric signal power S_e is given by the sum of the average electrical power $S_R = I_R^2$ with the power S_{OMA} of the optical modulated signal shifted to the zero mean value:

$$S_e \equiv S_R + S_{OMA} \tag{9.25}$$

Using Equation (9.23) gives

$$S_e = d^2 \left(\frac{r+1}{r-1} \right)^2 + S_{OMA} \tag{9.26}$$

The total electric signal power S_e is composed by two terms: the first term S_R depends on the sampled amplitude d and on the extinction ratio r, but is independent of the pulse shape, and the second term S_{OMA} depends instead on the pulse profile. Referring to Figure 9.5, the average power S_{OMA} is defined by the integration

$$S_{OMA} \equiv \frac{1}{2T} \int_{-T}^{T} |\underline{i}_R(t) - I_R|^2 \, dt \tag{9.27}$$

This signal power contribution S_{OMA} is the useful power, corresponding to the information content included in the total receiving signal. The average power S_R does not add any information to the signal decision process and can be considered as the waist power. In the following, four cases of pulse profiles will be considered: the rectangular pulse, the truncated sine pulse, the triangular pulse and the trapezoid pulse. All four cases have a sampled amplitude equal to $2d$, as reported in the corresponding figures below.

9.2.2.1 Rectangular Pulse

Figure 9.6 shows the signal modeling for the rectangular pulse profile. The pulse has amplitude $I_{OMA} = 2d$ and width equal to the time step T. The pulse has the following equation:

$$\underline{i}_R(t) = \begin{cases} I_R + d, & |t| \le \dfrac{T}{2} \\ I_R - d, & |t| > \dfrac{T}{2} \end{cases} \tag{9.28}$$

In order to have a general case, in Figure 9.6 a finite extinction ratio $r = 3$ has been assumed. From Equations (9.27) and (9.26),

$$S_{OMA,rect} = \frac{d^2}{2T} \int_{-T}^{+T} dt = d^2, \qquad S_{e,rect} = d^2 \left[1 + \left(\frac{r+1}{r-1} \right)^2 \right] \tag{9.29}$$

Figure 9.7 gives a simple hint for calculating the average signal power associated with the rectangular pulse. Assuming an infinite extinction ratio, Equation (9.29) gives $S_{\substack{e,rect \\ r \to \infty}} = 2d^2$.

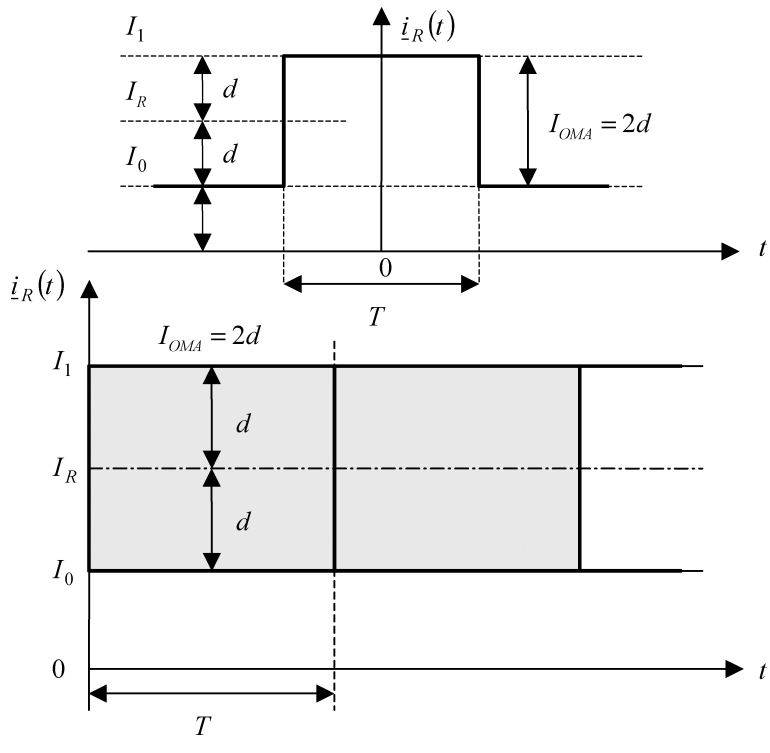

Figure 9.6 Rectangular pulse of amplitude $I_{\mathrm{OMA}} = 2d$ and width T. The extinction ratio is $r = I_1/I_0 = 3$

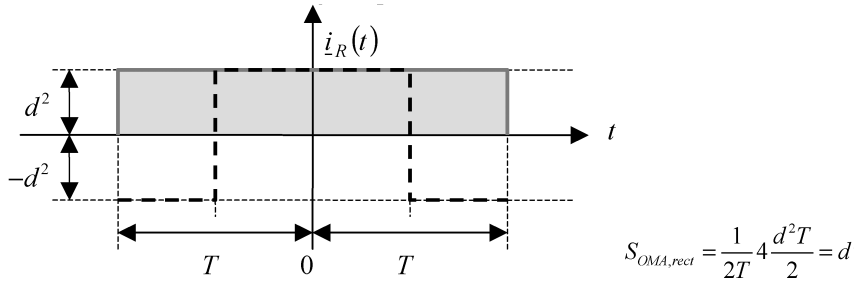

Figure 9.7 Graphical calculation of the average signal power associated with the rectangular pulse

9.2.2.2 Sinusoidal Pulse

The truncated sinusoidal pulse resembles some band-limited pulse shape encountered during transmission measurements and it is useful to include this pulse in the modeling. The truncated sinusoidal pulse has the following equation:

$$\underline{i}_{\mathrm{R}}(t) = \begin{cases} I_{\mathrm{R}} + d\cos\left(\dfrac{\pi t}{T}\right), & |t| \le T \\ I_{\mathrm{R}} - d, & |t| > T \end{cases} \tag{9.30}$$

and is presented in the following Figure 9.8.

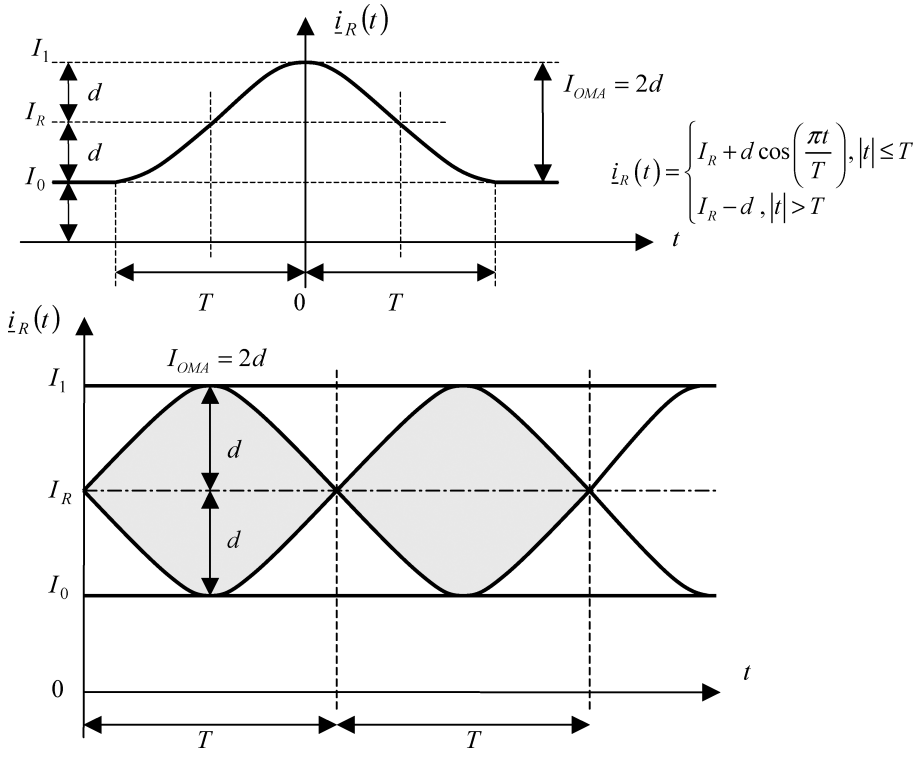

Figure 9.8 Sinusoidal pulse of amplitude $I_{\mathrm{OMA}} = 2d$ and period $2T$. The extinction ratio is $r = I_1/I_0 = 3$. A qualitative drawing of the eye diagram has been added

The period of the truncated sinusoidal pulse has been set equal to $2T$ in order to account for the NRZ line code with an equiprobable bit sequence. From Equations (9.27) and (9.26) the following is obtained immediately:

$$S_{\mathrm{OMA,sine}} = \frac{1}{2T}\int_{-T}^{+T} d^2 \sin^2\left(\frac{\pi t}{T}\right) \mathrm{d}t = \frac{1}{2}d^2, \qquad S_{\mathrm{e,sine}} = d^2\left[\frac{1}{2} + \left(\frac{r+1}{r-1}\right)^2\right] \tag{9.31}$$

As discussed in the previous chapter, one of the most relevant pulse shapings available at the decision section for avoiding any intersymbol interference pattern is the raised cosine function. This particular pulse exhibits the characteristic oscillatory behavior along the symmetric tails. If the raised cosine pulse is passed through a low-pass filter with the cut-off frequency slightly lower than the signaling rate $B = 1/T$, the output pulse will closely resemble the sinusoidal shaping encountered in this section, with almost smooth and flat tails.

9.2.2.3 Triangular Pulse

Figure 9.9 shows the model used for the triangular pulse. The triangular pulse represents a stronger band-limited modeling of the signal at the decision section of the receiver than the truncated sinusoidal pulse. The spectral content of the triangular pulse is in fact less than the truncated sinusoidal pulse presented in the previous section and can be used to model a stronger bandwidth

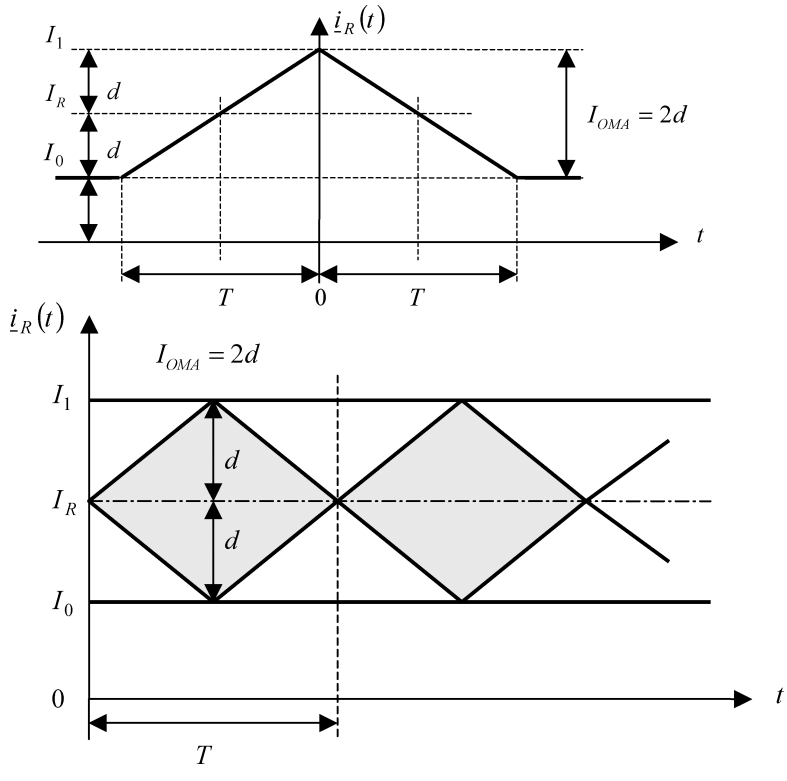

Figure 9.9 Triangular pulse of amplitude $I_{\mathrm{OMA}} = 2d$ and period $2T$. The extinction ratio is $r = I_1/I_0 = 3$

limitation of the transmission channel. The triangular pulse consistent with the data signaling rate $B = 1/T$ is represented by the following equation:

$$\underline{i}_{\mathrm{R}}(t) = \begin{cases} I_{\mathrm{R}} - d, & t \le -T \\ I_{\mathrm{R}} + \dfrac{2d}{T}\left(t + \dfrac{T}{2}\right), & -T \le t \le 0 \\ I_{\mathrm{R}} - \dfrac{2d}{T}\left(t - \dfrac{T}{2}\right), & 0 \le t \le T \\ I_{\mathrm{R}} - d, & t \ge T \end{cases} \tag{9.32}$$

The pulse amplitude, the pulse width and the extinction ratio are assumed to be the same as in the previous two cases. Using Equations (9.27) and (9.26), the following values have been obtained for the average signal power and total electric power associated with the triangular pulse sequence:

$$S_{\mathrm{OMA}} = \frac{1}{3}d^2, \qquad S_{\mathrm{e,trng}} = d^2\left[\frac{1}{3} + \left(\frac{r+1}{r-1}\right)^2\right] \tag{9.33}$$

The calculation of the signal average power S_{OMA} can easily be performed by observing that the shape of the squared pulse $|\underline{i}_{\mathrm{R}}(t) - I_{\mathrm{R}}|^2$ is represented by two symmetric parabolic arms, as depicted

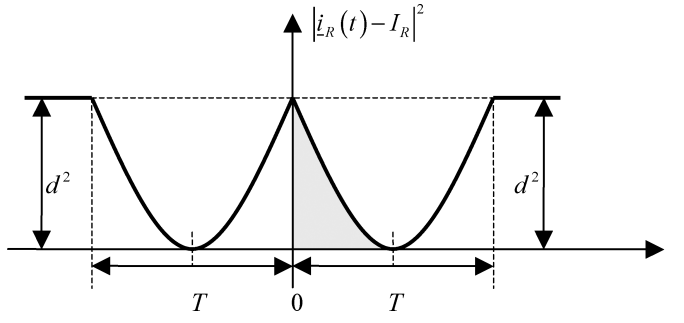

Figure 9.10 Graphical representation of the squared value $|\underline{i}_R(t) - I_R|^2$ of the triangular pulse in Figure 9.10 after offset removal. The integration can be conveniently performed over one-half of the time step

in the Figure 9.10. From Equations (9.27) and (9.32),

$$S_{\mathrm{OMA}} = \frac{1}{2T}\int_{-T}^{T} |\underline{i}_{\mathrm{R}}(t) - I_{\mathrm{R}}|^2 \,\mathrm{d}t = \frac{2}{T}\int_{0}^{T/2} |\underline{i}_{\mathrm{R}}(t) - I_{\mathrm{R}}|^2 \,\mathrm{d}t$$
$$= \frac{2}{T}\int_{0}^{T/2} \frac{4d^2}{T^2}\left(t - \frac{T}{2}\right)^2 \mathrm{d}t = \frac{8d^2}{T^3}\,\frac{1}{3}\,\frac{T^3}{8} = \frac{1}{3}d^2 \tag{9.34}$$

9.2.2.4 Trapezoid Pulse

The last case to be considered is the trapezoidal pulse shown in Figure 9.11. The pulse is consistent with the signaling data rate $B = 1/T$ measured as the full-width at half-maximum, with symmetrical transition times equal to τ. The pulse amplitude is equal to $2d$.

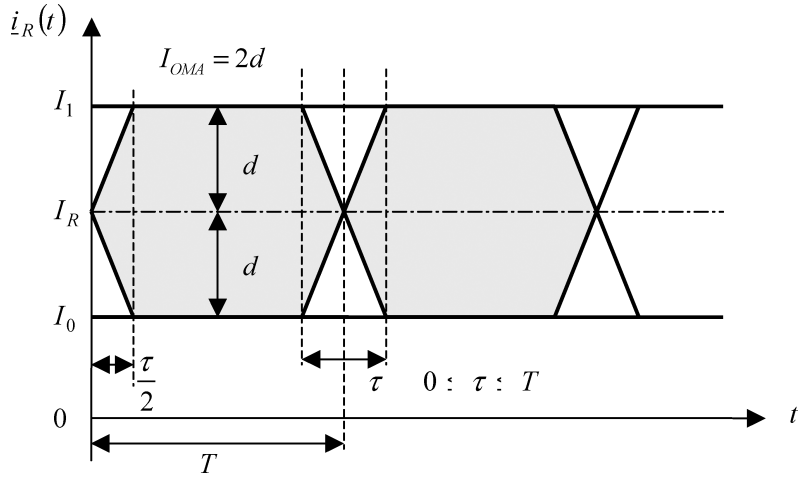

Figure 9.11 Trapezoid pulse of amplitude $I_{\mathrm{OMA}} = 2d$ and period $2T$. The extinction ratio is $r = I_1/I_0 = 3$

Using the pulse symmetry, the average signal power S_{OMA} is easily computed using Equation (9.27):

$$S_{\mathrm{OMA}} = \frac{1}{2T}\int_0^{2T} |\underline{i}_{\mathrm{R}}(t) - I_{\mathrm{R}}|^2 \,\mathrm{d}t = \frac{1}{2T} 4 \left[\int_0^{\tau/2} \left(\frac{2d}{\tau} t\right)^2 \mathrm{d}t + \int_{\tau/2}^{T/2} d^2 \,\mathrm{d}t \right] = d^2 \left(1 - \frac{2}{3}\,\frac{\tau}{T}\right) \tag{9.35}$$

The total signal power is then given by adding the average current power, according to Equation (9.26):

$$S_{\mathrm{e,trpz}} = d^2 \left[1 - \frac{2}{3}\,\frac{\tau}{T} + \left(\frac{r+1}{r-1}\right)^2 \right], \quad 0 \le \tau \le T \tag{9.36}$$

Once the electric signal power S_{OMA} has been related to the sampling amplitude d for different pulse shapes, it is convenient to express the electric average power S_{e} in terms of the optical average power P_{R}. From Equation (9.24) the decision distance d can be expressed as a function of the received average optical power P_{R}. Substituting Equation (9.24) into Equations (9.29), (9.31), (9.33) and (9.36) gives the expressions reported in Table 9.2. It is important to note the quadratic dependence of the average electrical signal power on the average optical power, which is characteristic of the photodetection process.

9.2.3 Electrical Noise-to-Signal Power Ratio: NSR

The total noise-to-signal power ratio is defined as the ratio between the total electric noise power N_{tot} (P_{R}) and the total electric signal power S_{e} (P_{R}), corresponding to the selected pulse profile:

$$\mathrm{NSR}(P_{\mathrm{R}}) \equiv \frac{N_{\mathrm{tot}}(P_{\mathrm{R}})}{S_{\mathrm{e}}(P_{\mathrm{R}})} \tag{9.37}$$

According to the expression (9.15) of the total noise power N_{tot} (P_{R}), it is convenient to define the noise-to-signal power ratio (NSR) for each noise component involved, comparing different NSR contributions corresponding to each noise source involved. From Equations (9.15) and (9.37),

$$\mathrm{NSR}(P_{\mathrm{R}}) = \frac{\sigma_{\mathrm{c}}^2 + \sigma_{\mathrm{d}}^2 + \sigma_{\mathrm{s}}^2(P_{\mathrm{R}}) + \sigma_{\mathrm{RIN}}^2(P_{\mathrm{R}})}{S_{\mathrm{e}}(P_{\mathrm{R}})} \tag{9.38}$$

Table 9.2 Average electrical power associated with the corresponding pulse profiles for the consistent signaling data rate $B = 1/T$, assuming NRZ binary and equiprobable bit sequences. The electrical power is expressed as a function of the received average optical power P_{R}, the detector responsivity R and the extinction ratio r

Pulse	Average electrical power	Reference
Rectangular	$S_{\mathrm{e,rect}} = R^2 P_{\mathrm{R}}^2 \left[1 + \left(\frac{r-1}{r+1}\right)^2 \right]$	(9.24)
Truncated sinusoidal	$S_{\mathrm{e,sine}} = R^2 P_{\mathrm{R}}^2 \left[1 + \frac{1}{2}\left(\frac{r-1}{r+1}\right)^2 \right]$	(9.29)
Triangular	$S_{\mathrm{e,trng}} = R^2 P_{\mathrm{R}}^2 \left[1 + \frac{1}{3}\left(\frac{r-1}{r+1}\right)^2 \right]$	(9.31)
Trapezoid	$S_{\mathrm{e,trpz}} = R^2 P_{\mathrm{R}}^2 \left[1 + \left(1 - \frac{2}{3}\,\frac{\tau}{T}\right)\left(\frac{r-1}{r+1}\right)^2 \right]$	(9.36)

Using the individual expressions of noise contributions in Equations (9.7), (9.9), (9.10) and (9.14), the following components of the noise-to-signal ratio can be obtained:

$$\mathrm{NSR_c} \equiv \frac{i_c^2 B_n}{S_e(P_R)} \tag{9.39}$$

$$\mathrm{NSR_d} \equiv \frac{2q I_D B_n}{S_e(P_R)} \tag{9.40}$$

$$\mathrm{NSR_s} \equiv \frac{2q R P_R B_n}{S_e(P_R)} \tag{9.41}$$

$$\mathrm{NSR_{RIN}} \equiv \frac{R^2 P_R^2 \ \mathrm{RIN} \ B_n}{S_e(P_R)} \tag{9.42}$$

Figure 9.12 gives the plots of each component together with the total noise-to-signal ratio, assuming three different RIN coefficients. The scale is reported in $\mathrm{dB_{10}}$.

The computed noise-to-signal ratios in Figure 9.12 need some comment. Noise terms with constant values versus the optical power, like thermal noise and dark shot noise, appear as a straight line with a negative slope equal to −20 dB/10 dB. The shot noise term, with the linear dependence from the ensemble average of the optical power, is a straight line with a negative slope equal to −10 dB/10 dB. Finally, the NSR due to RIN appears as the constant line as a consequence of the quadratic dependence from the noise term of the optical average power. This behavior clearly shows the performance limitation of the optical receiver affected by the laser RIN when the optical average power reaches the threshold value. Figure 9.12 shows that the power threshold decreases according to the RIN value. Assuming that the threshold is set by the intersection between the thermal noise line and the RIN line, it has been concluded that the threshold decreases by one-half of the RIN value reduction. In Figure 9.12 three different RIN values were considered, −121 dB/Hz, −128 dB/Hz, −135 dB/Hz, with a 7 dB decrease for each step. Correspondingly, the threshold decreases by 3.5 dB for each RIN value. Including the shot noise contribution, that simple relationship would be altered.

9.2.4 Electrical Signal-to-Noise Power Ratio: SNR

In the previous section, the noise-to-signal ratio was considered because it has a simple linear relationship with the different noise contributions. This means that by analyzing the NSR it is possible to identify the dominant noise term by measuring the NSR slope around the required optical power level. A similar motivation leads to the reciprocal function, namely the signal-to-noise power ratio (SNR). This function is directly involved in the error performance of the optical receiver. The electrical signal-to-noise ratio is defined as follows:

$$\mathrm{SNR}(P_R) \equiv \frac{S_e(P_R)}{N_{tot}(P_R)} \tag{9.43}$$

Substituting the expressions of the total noise term in Equation (9.16) gives

$$\mathrm{SNR}(P_R) = \frac{S_e(P_R)}{(i_c^2 + 2q I_D + 2q R P_R + R^2 P_R^2 \ \mathrm{RIN} \ ) B_n} \tag{9.44}$$

The electrical signal power S_e depends on the pulse shape, as derived in Section 9.2.3. In the following, the case of the trapezoid pulse defined in Equation (9.36) is first considered. It is important to remark that the trapezoid pulse leads to either the rectangular pulse or the triangular pulse,

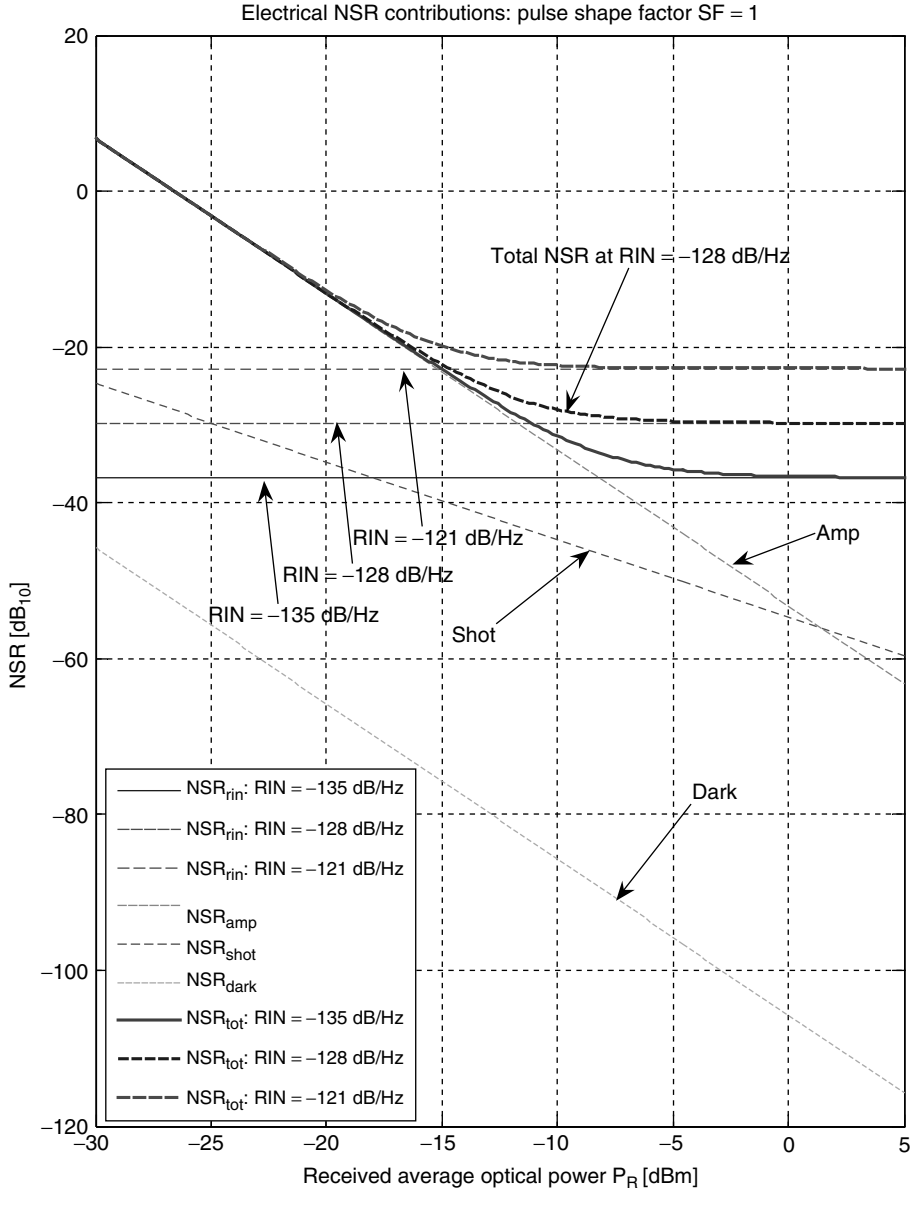

Figure 9.12 Components of the noise-to-signal power ratio for the four noise terms considered above. The extinction ratio has been set to $r = 10$. The NSR due to thermal noise and dark shot noise have the same slope of $-20\,\text{dB}/10\,\text{dB}$. The NSR due to signal shot noise has a slope of $-10\,\text{dB}/10\,\text{dB}$ while the NSR due to RIN has a constant behavior according to the quadratic dependence of the optical power

depending on the value of the transition time τ. Substituting Equation (9.36) into Equation (9.44) leads to the following expression of the electrical SNR for the generalized trapezoid pulse:

$$\mathrm{SNR}(P_\mathrm{R}) = \frac{R^2 P_\mathrm{R}^2 \left[1 + \left(1 - \frac{2}{3}\frac{\tau}{T}\right)\left(\frac{r-1}{r+1}\right)^2\right]}{(i_\mathrm{c}^2 + 2qI_\mathrm{D} + 2qRP_\mathrm{R} + R^2 P_\mathrm{R}^2\ \mathrm{RIN}\ )B_\mathrm{n}}, \quad 0 \le \tau \le T, \quad T = \frac{1}{B} \tag{9.45}$$

In order to proceed with the generalization, it is first noted that the expressions of the total electric power S_e derived so far can be written in a simple common form by introducing the shape coefficient δ_R. To this end, the function $\zeta_\mathrm{R}(t)$ is defined as the normalized photocurrent pulse:

$$\underline{i}_\mathrm{R}(t) \equiv I_\mathrm{R} + d\ \underline{\zeta}_\mathrm{R}(t) \tag{9.46}$$

The signal average power S_OMA in Equation (9.27) then takes the following form:

$$S_\mathrm{OMA} = d^2 \frac{1}{2T} \int_{-T}^{+T} |\zeta_\mathrm{R}(t)|^2\, \mathrm{d}t = d^2 \delta_\mathrm{R} \tag{9.47}$$

where the shape coefficient is defined as

$$\delta_\mathrm{R} \equiv \frac{1}{2T} \int_{-T}^{+T} |\zeta_\mathrm{R}(t)|^2\, \mathrm{d}t \tag{9.48}$$

From Equations (9.25) and (9.47) the following general expression for the total electrical signal power is found:

$$S_\mathrm{e} = I_\mathrm{R}^2 + S_\mathrm{OMA} = d^2 \left[\left(\frac{r+1}{r-1}\right)^2 + \delta_\mathrm{R}\right] \tag{9.49}$$

Expressing the signal amplitude d using Equation (9.24) in terms of the average received optical power and extinction ratio gives

$$S_\mathrm{e} = R^2 P_\mathrm{R}^2 \left[1 + \delta_\mathrm{R}\left(\frac{r-1}{r+1}\right)^2\right] \tag{9.50}$$

According to previous analysis, the shaping factor therefore takes the following values:

$$\begin{aligned}
\delta_\mathrm{R,rect} &= 1 \\
\delta_\mathrm{R,sine} &= \tfrac{1}{2} \\
\delta_\mathrm{R,trng} &= \tfrac{1}{3} \\
\delta_\mathrm{R,trpz} &= \left(1 - \frac{2}{3}\frac{\tau}{T}\right), \quad 0 \le \tau \le T
\end{aligned}$$

Substituting the expression (9.50) of the electric signal power S_e into Equation (9.45), the SNR for the generic pulse profile takes the following form:

$$\mathrm{SNR} = \frac{R^2 P_\mathrm{R}^2 \left\{1 + \delta_\mathrm{R}[(r-1)/(r+1)]^2\right\}}{(i_\mathrm{c}^2 + 2qI_\mathrm{D} + 2qRP_\mathrm{R} + R^2 P_\mathrm{R}^2\ \mathrm{RIN}\ )B_\mathrm{n}} \tag{9.51}$$

This formula generalizes the four cases considered above using an arbitrary pulse profile defined in Equations (9.46) and (9.48). This formula includes four noise terms in the denominator, but it

is possible to extend the validity to any other noise term with the only condition being of mutual independency. In this case, in fact, noise powers will add together, and it will be sufficient to add new terms in the denominator of Equation (9.51). A further assumption is related to the noise bandwidth and to the white noise equivalent concept, discussed in the previous section.

9.2.5 The Q-Factor

A parameter related to the electrical SNR and to the error performance calculation of the optical receiver is the Q-factor. For a binary system with the same noise power distribution on both signal levels, the Q-factor is given by the ratio between the sampled signal amplitude d and the RMS value of the total noise power σ_{tot} affecting both signal levels:

$$Q \equiv \frac{d}{\sigma_{\text{tot}}} \tag{9.52}$$

The Q-factor is therefore a factor-of-merit of the decision process. The higher the Q-factor, the lower is the error probability. It is a measure of the eye diagram opening referred to the RMS noise amplitude at the decision section of the receiver. First the relationship between the Q-factor and the received average optical power P_{R} is considered. Substituting Equation (9.24) into Equation (9.52), immediately gives

$$Q = \frac{r-1}{r+1}\frac{\text{RP}_{\text{R}}}{\sigma_{\text{tot}}} \tag{9.53}$$

The Q-factor can be related to the electrical SNR using the previous analysis. To this purpose, using Equation (9.52) the total RMS noise σ_{tot} can be expressed in terms of the SNR and the relationship can be substituted in Equation (9.53). After simple manipulations, it is found that

$$Q = \sqrt{\frac{\text{SNR}}{[(r+1)/(r-1)]^2 + \delta_{\text{R}}}} \tag{9.54}$$

In general, the Q-factor is a function of both the extinction ratio and the shaping coefficient. Different pulse profiles satisfying the same extinction ratio and the same electrical SNR therefore give different error probabilities. This is a consequence of the pulse profile and, in particular, how the electrical average power is related to the pulse amplitude d. For the simplest case of the infinite extinction ratio and an ideal rectangular pulse shape, the above relationship assumes the following well-known form:

$$\lim_{\substack{r\to\infty \\ \delta_{\text{R}}=1}} Q = \sqrt{\frac{\text{SNR}}{2}} \tag{9.55}$$

It is convenient to write the relationship between the Q-factor and the electrical SNR using the logarithmic transformation of the decibel. This transforms the parameter relationship into a linear one. The following are defined:

$$Q_{\text{dB}} \equiv 20\log_{10} Q, \qquad \text{SNR}_{dB} \equiv 10\log_{10}\text{SNR} \tag{9.56}$$

From Equation (9.54),

$$Q_{\text{dB}} = \text{SNR}_{\text{dB}} - 10\log_{10}\left[\left(\frac{r+1}{r-1}\right)^2 + \delta_{\text{R}}\right] \tag{9.57}$$

This relation is important because it gives clear evidence of the performance degradation induced by every finite value of the extinction ratio and increasing values of the shaping coefficient. In other words, both the higher extinction ratio and lower shaping coefficient give better performances.

Figure 9.13 shows the Q-factor and the electrical SNR versus the average received optical power and the extinction ratio for the same cases considered in Table 9.1 and Figure 9.12. Figure 9.14 shows the relation between the Q-factor and the electrical SNR expressed in decibels for different values of the extinction ratio. Both figures refer to the ideal rectangular pulse with $\delta_R = 1$. In both figures, RIN varies according to the usual three values of -121 dB/Hz, -128 dB/Hz and -135 dB/Hz, in order to show the threshold effect at relatively high power levels. RIN sets hard limitations on the maximum value reached by the Q-factor. It will be seen in the next section that this limits the minimum error rate achievable, leading to the characteristic error floor behavior.

It should be remembered that the total electrical signal power, including the DC average value, are considered. For the ideal rectangular pulse, the DC component and the signal related component are equal to each other.

9.2.6 Error Probability: BER

The bit error rate (BER) of a binary decision system affected by symmetric Gaussian noise on both signal levels is given by the following expression:

$$\mathrm{BER}(P_R) = \frac{1}{2}\mathrm{erfc}\left[\frac{Q(P_R)}{\sqrt{2}}\right] \tag{9.58}$$

The relation between the Q-factor and the average received optical power has been derived in Equation (9.53). The followings assumptions are assumed to be verified:

1. Binary signal with equiprobable logic levels.
2. The noise has the same probability density distribution on both signal levels.
3. The noise has a Gaussian probability density function with zero mean.
4. The sampled signal has no intersymbol interference and the sampled amplitude is constant for every sample.
5. The decision process is ideal without an uncertainty interval.

The complementary error function (erfc) is a direct consequence of the Gaussian noise assumption. Substituting the expression (9.53) of the Q-factor gives the required relationship between the error probability and the optical power P_R:

$$\mathrm{BER}(P_R) = \frac{1}{2}\mathrm{erfc}\left[\frac{RP_R}{\sigma_{tot}\sqrt{2}}\left(\frac{r-1}{r+1}\right)\right] \tag{9.59}$$

This expression relates the bit error rate to the extinction ratio and the total noise RMS value. It is noted that the total noise includes all terms, constant, linear and quadratic contributions. This reflects the very interesting profile of the BER function when it is plotted against the received optical average power. Figure 9.15 reports the computed BER for the case of the optical receiver considered in Table 9.1 and the eye diagram plotted in Figure 9.3. As usual, the extinction ratio has been set at $r = 10$ and the total noise includes all the four contributions from thermal noise, dark shot noise, signal shot noise and laser RIN. Three different RIN coefficients have been assumed, namely RIN $= -121$ dB/Hz, RIN $= -128$ dB/Hz and RIN $= -135$ dB/Hz, and for each of them the corresponding error probability curve has been computed and plotted.

It is interesting that, accordingly to previous noise plot behaviors, RIN values become the dominant factor for the BER floor at high power levels. This is evident in Figure 9.15 as the BER plots

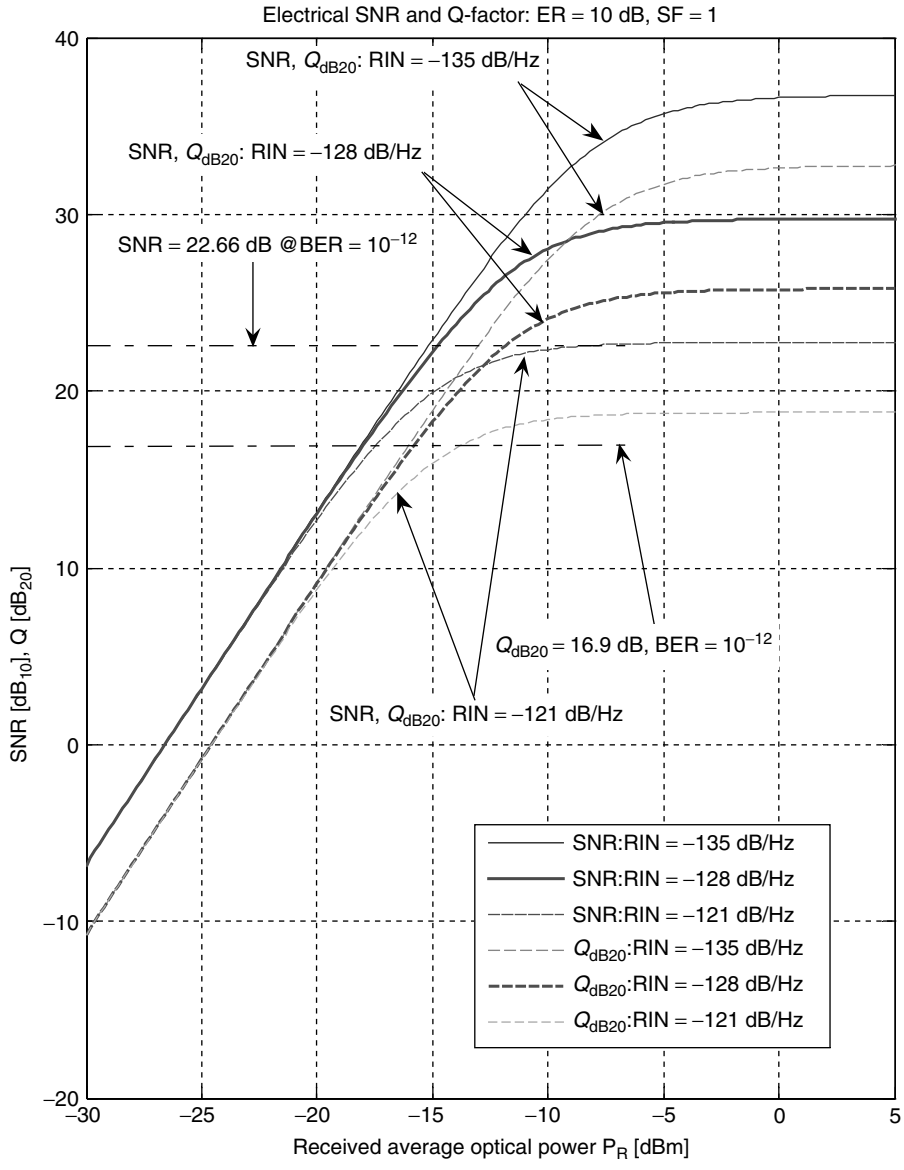

Figure 9.13 Electrical SNR and Q-factor versus three different RIN coefficients for the optical receiver case considered in the text. The extinction ratio has been set to $r = 10$ for all cases. The dash–dot lines represent the required electrical *SNR* and Q-factor values in order to achieve the error probability BER $= 10^{-12}$ for the given extinction ratio $r = 10$

bend just above the threshold power values. Of course, the limiting BER value depends on the noise parameters involved and it does not represent any real problem if it is located some orders of magnitude below the required BER standards. Figure 9.16 shows a detailed view of the same calculation for the higher range of useful BER values.

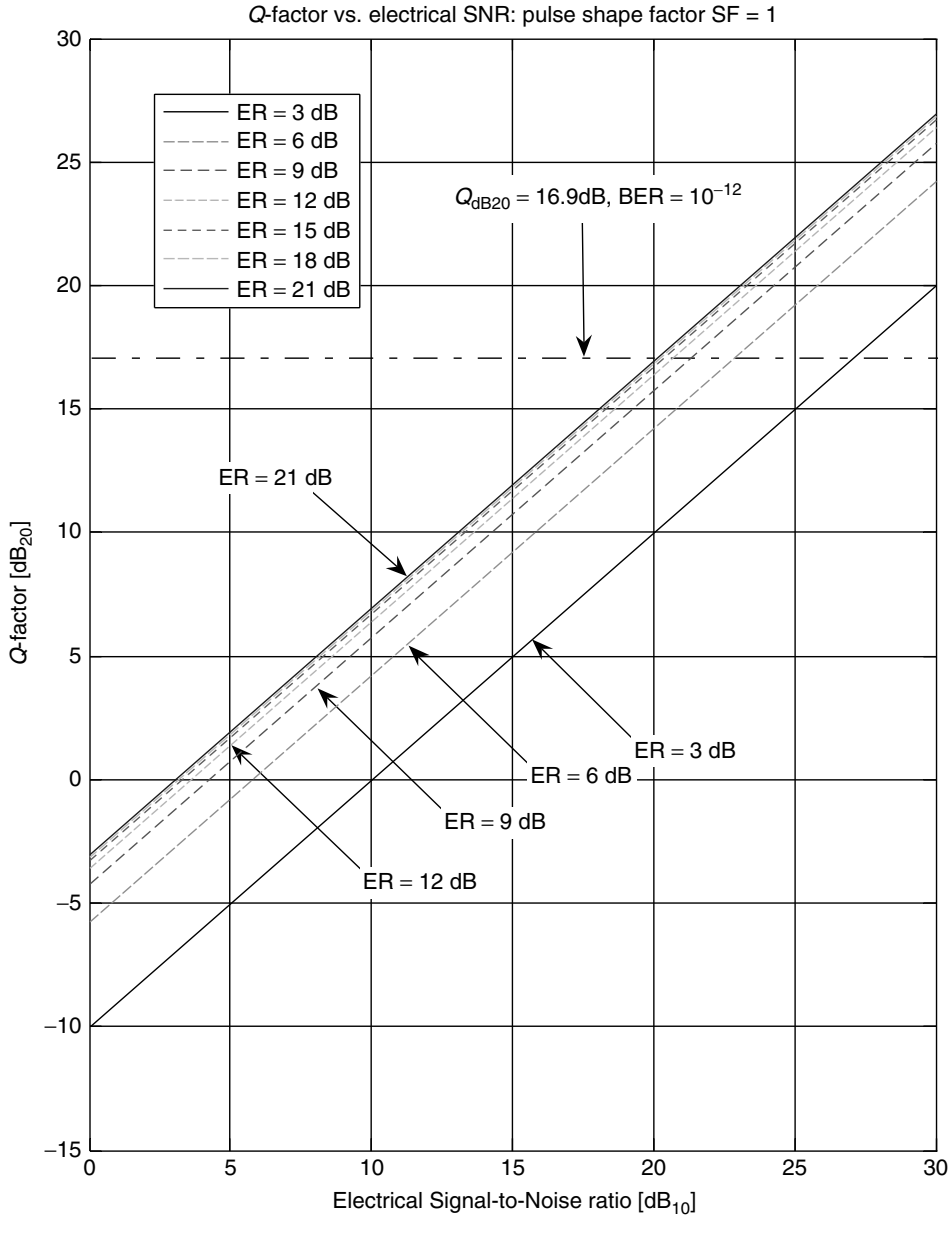

Figure 9.14 The plot reports the relationship between the Q-factor and the electrical SNR versus different values of the extinction ratio assuming an ideal square pulse shape. For the limiting case of the infinite extinction ratio the Q-factor results 3 dB less than the SNR, according to the expression reported in the text. The dash–dot line represents the required Q-factor for achieving BER $= 10^{-12}$. The corresponding electrical SNR depends on the extinction ratio

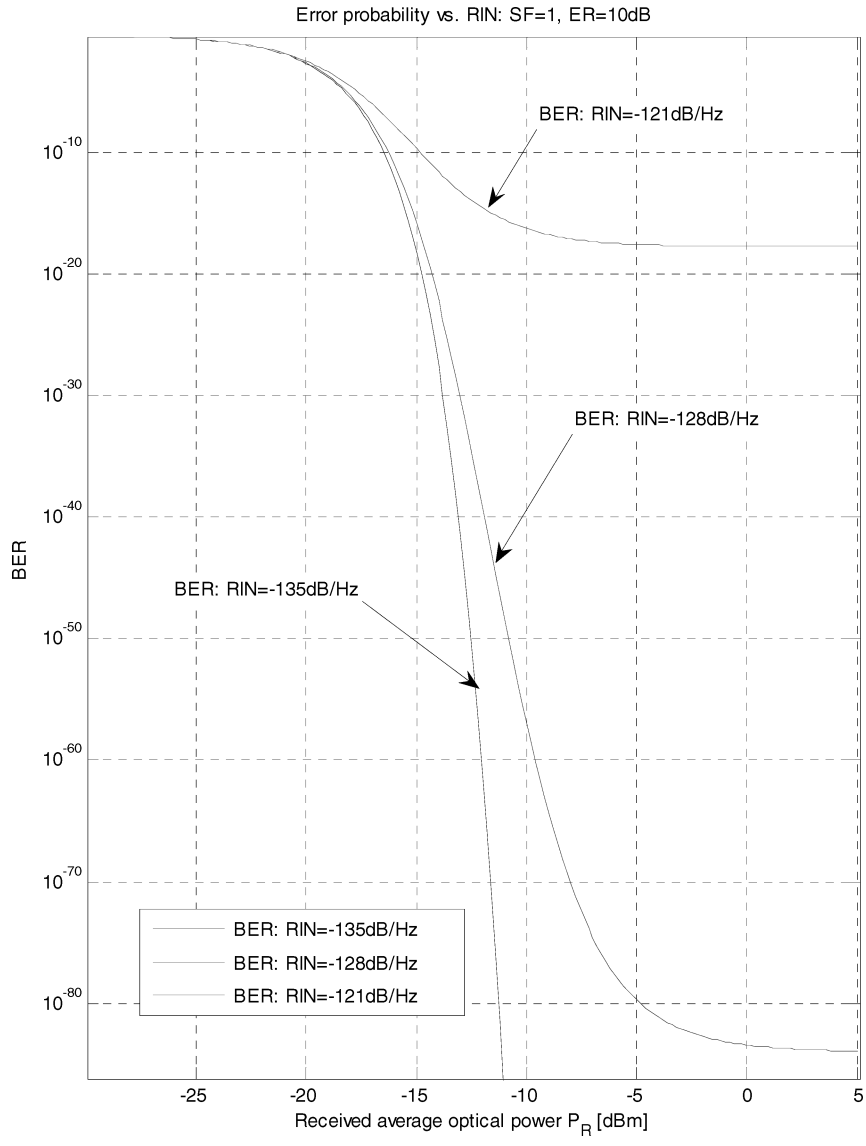

Figure 9.15 Error probability of the optical receiver considered in the text as a function of the received average optical power, for three different RIN coefficients

Assuming a reference error probability of BER $= 10^{12}$, the optical power penalty due to RIN degradation is about $\Delta P_R = 2$ dB when RIN increases between RIN $= -128$ dB/Hz and RIN $= -121$ dB/Hz, but is only $\Delta P_R = 0.3$ dB when RIN increases between RIN $= -135$ dB/Hz and RIN $= -128$ dB/Hz. This effect is due to RIN dominance as the quadratic noise term versus the received optical power and justifies the assumption that RIN $= -128$ dB/Hz, as required by 10 GbE standards.

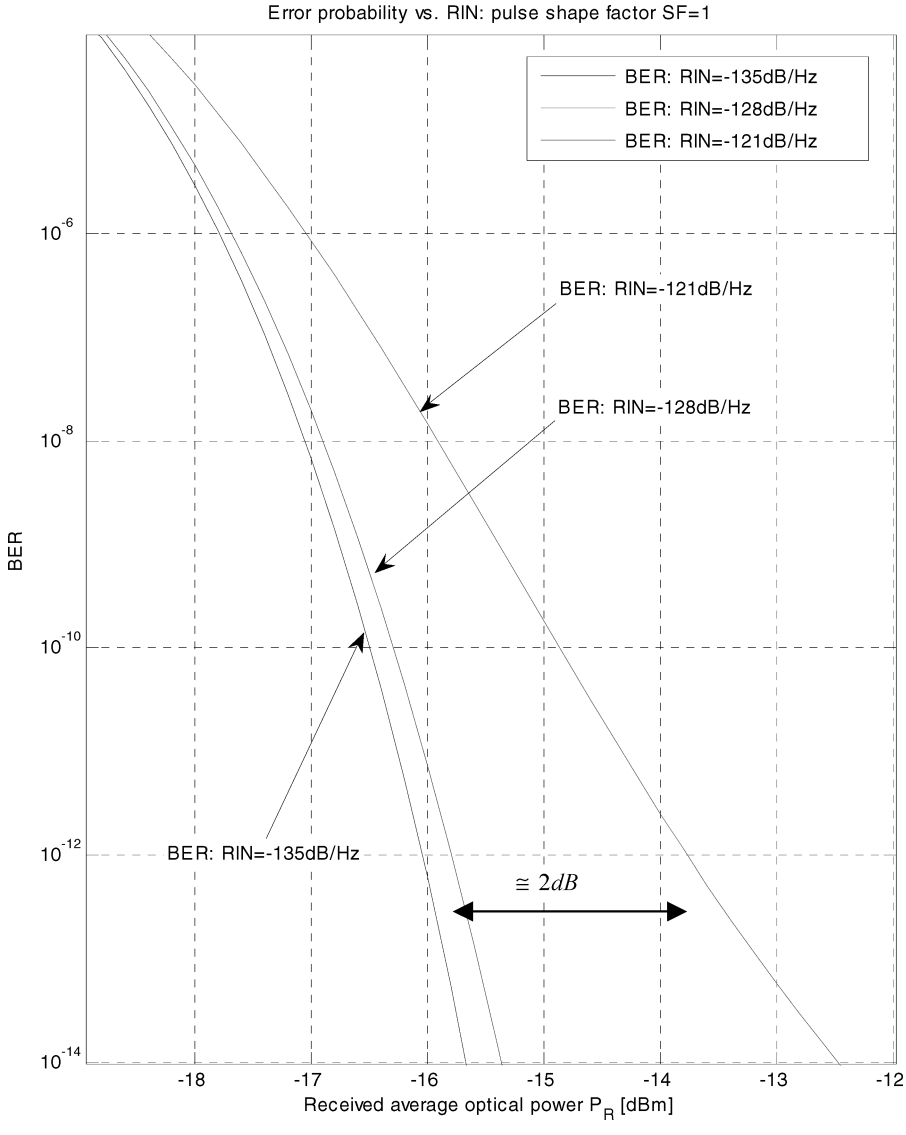

Figure 9.16 Detailed view of the error probability of the optical receiver considered in the text as a function of the received average optical power, for three different RIN coefficients

Figure 9.17 shows the BER as a function of the electrical SNR for different values of the extinction ratio. Of course, in this case there is no longer any dependence on the RIN coefficients because the independent variable is the SNR.

9.2.7 Conclusions

The sensitivity of a fiber optic receiver has been analyzed, including several noise contributions. The total noise power presents a characteristic dependence versus the received average optical

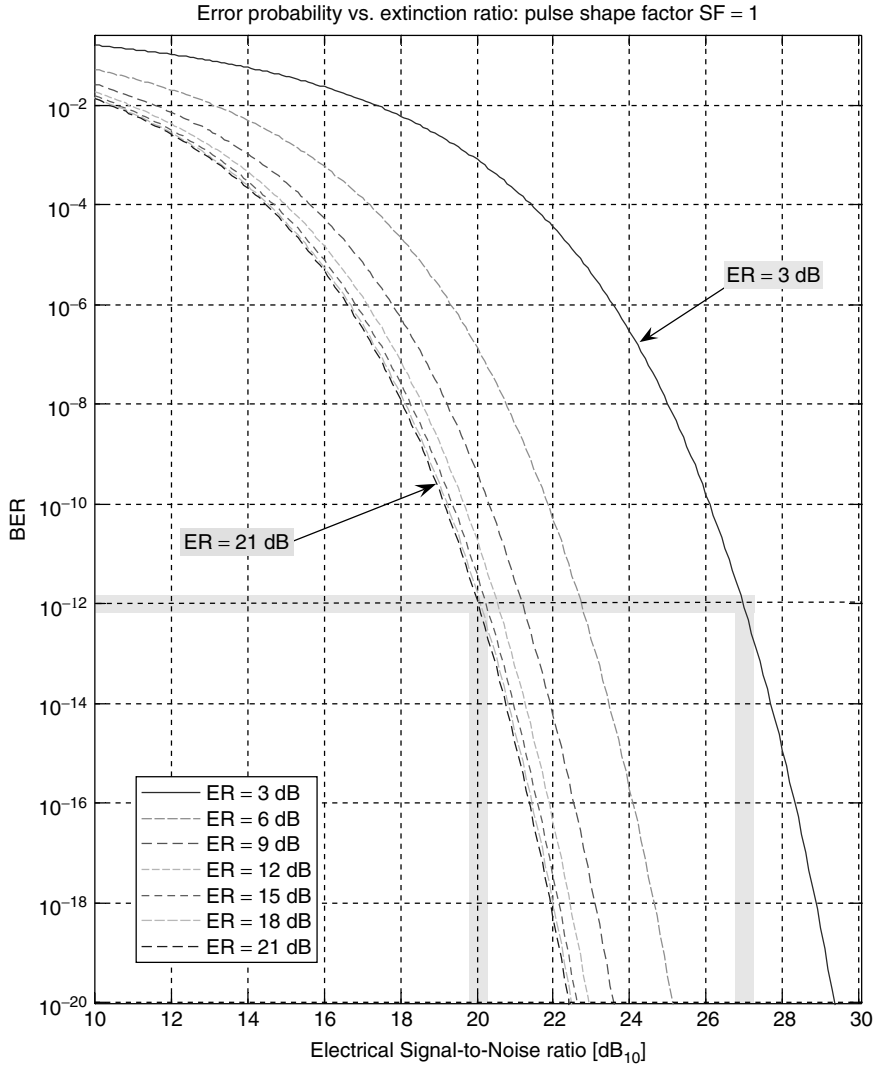

Figure 9.17 Error probability as a function of the electrical SNR, versus the extinction ratio. All plots refer to the same ideal rectangular pulse with a unit shaping factor. The required electrical SNR ratio for achieving BER $= 10^{12}$ with an infinite extinction ratio is close to $20\,\mathrm{dB}_{10}$. This value corresponds to $Q \cong 7.0344 = 16.944$ $\mathrm{dB}_{20} \Rightarrow \mathrm{SNR} \cong 98.966 = 19.955\,\mathrm{dB}_{10}$. Reducing the extinction ratio increases the required SNR for a given error probability

power, in relation to the nature of contributing terms. Three different noise term behaviors have been identified with respect to the received average optical power:

1. Constant: thermal noise and dark current shot noise
2. Linear: signal-induced shot noise
3. Quadratic: relative intensity noise of the laser source

The expression of the electrical signal-to-noise power ratio has been derived in terms of different pulse shapes assuming equiprobable NRZ binary symbols. The SNR is related to the receiving average optical power through the extinction ratio and the pulse shape factor. Most importantly, the signal-to-noise power ratio has been related to the Q-factor for the calculation of the error probability.

The last section introduced the optical power penalty and the signal-to-noise ratio penalty in terms of RIN coefficients versus the extinction ratio. The interesting conclusion is that both optical power and SNR penalties do not depend only on the RIN coefficient, but are a sensible function of the extinction ratio. This is clear since the total noise above the RIN threshold suddenly deviates from the almost flat behavior, due to the thermal noise dominant factor, toward the quadratic dependence from the average received optical power. Since the error probability is a function of the eye diagram opening (the sampled signal amplitude), for a decreasing extinction ratio a correspondingly higher optical power level is therefore required to maintain the same sampled amplitude. Because of the increased optical power level, a higher RIN contribution takes place and an increasingly strong deviation from constant thermal noise is observed. In other words, the lower the extinction ratio, the higher the average optical power must be in order to achieve the same error probability. However, the noise grows according to a combination of linear and quadratic lows, inducing an increasing power penalty. In this case optical power overcompensation is usually required.

9.3 Principles of Linear Equalization

In the first part of this book the propagation behavior and modeling principles of the multimode optical fiber have been extensively studied in order to allow multigigabit transmission. The very peculiar multimode propagation and differential group delay of multimode optical fibers severely limits the transmission range of less than one hundred meters, assuming a fiber bandwidth of 500 MHz km. As already discussed, this would set a difficult limitation on the metro area application of multimode fibers once multigigabit transmission technology is ready to be deployed for the low-cost end user. The average link length of the existing fiber infrastructure usually exceeds one hundred meters, often extending for more than two to three hundred meters. It is obvious at this point that some engineering solution must be conceived in order to raise the applicability limit of the existing fiber base up to at least the 10 GbE standard.

Among several proposals, still under discussion in recent Standardization Committees, the electronic dispersion compensation (EDC) technique will be considered. In this section, the basic principle of the linear electronic compensation will be presented, introducing the inverse linear filter equalizer and discussing both benefits and drawbacks of this solution. Due to the simplicity and ideal performance of the inverse linear filter equalizer, this solution will be referred to as the reference linear equalizer. It is important to remark, however, that the term 'reference' must not be confused with the optimum equalizer. Linear equalization in fact suffers from high noise enhancement due to a high-frequency peaking response. Accordingly, digital equalizer architectures have proved to overcome or at least reduce the noise enhancement issue.

9.3.1 The Reference Channel

In order to introduce linear equalization, the reference multimode optical fiber transmission system considered is reported in Figure 9.18. The transmitter generates the optical datastream at the operating wavelength λ_0 whose intensity envelope spectrum $X_T(f)$ measured at the optical source section S is shaped according to the square root of the raised cosine function $\Gamma_m(f)$:

$$X_T(f) = \sqrt{\Gamma_m(f)} \tag{9.60}$$

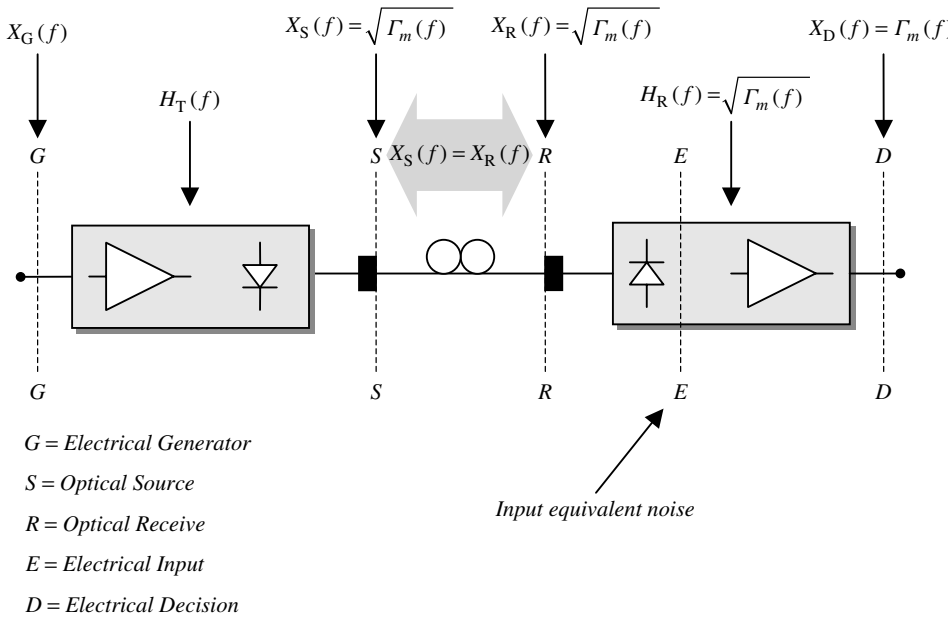

Figure 9.18 Block diagram of the reference optical transmission system. The optical link consists of a very short multimode fiber jumper (back-to-back connection) in order to provide a transmitter-to-receiver connection without adding any spectrum perturbation. The receiver transfer function, including the photodetection process, is matched to the transmit spectrum at the source section *S*. The output spectrum at the decision section *D* is shaped according to the raised cosine family of roll-off m. The receiver noise bandwidth has the minimum value achievable for the given transmission rate

The optical receive section R is connected to the point S by a very short piece of multimode fiber (jumper) which does not infer any signal degradation. Accordingly, at the receive section R the intensity envelope spectrum $X_R(f)$ coincides with the source signal $X_T(f)$. Therefore, from Equation (9.60),

$$X_R(f) = X_T(f) = \sqrt{\Gamma_m(f)} \tag{9.61}$$

The optical receiver performs first the photodetection and then the proper electrical signal amplification and filtering. It is assumed that the optical receiver frequency response $H_R(f)$, up to the decision section but including the photodetection, will be matched to the optical intensity envelope spectrum $X_T(f)$ at the source section S:

$$H_R(f) = X_T^*(f) \tag{9.62}$$

The electrical signal spectrum $X_D(f)$ at the decision section D is given by the product of the input spectrum $X_R(f)$ with the receiver transfer function $H_R(f)$. Using the matching condition (9.61), the signal spectrum at the decision section therefore coincides with the raised cosine function:

$$X_D(f) = X_R(f)H_R(f) = |X_T(f)|^2 = \Gamma_m(f) \tag{9.63}$$

The raised cosine pulse $\gamma_m(t)$ with the proper signaling rate $T = 1/B$, the shaping factor m and amplitude normalization have the following expressions:

$$\Gamma_m(f) = \begin{cases} 1, & |f|T \le \dfrac{1-m}{2},\ T = \dfrac{1}{B} \\ \cos^2\left[\dfrac{\pi}{2m}\left(fT - \dfrac{f}{|f|}\dfrac{1-m}{2}\right)\right], & \dfrac{1-m}{2} \le |f|T \le \dfrac{1+m}{2} \\ 0, & |f|T \ge \dfrac{1+m}{2} \end{cases} \tag{9.64}$$

$$\gamma_m(t) = \frac{1}{T}\,\frac{\cos(m\pi t/T)}{1-(2mt/T)^2}\,\frac{\sin(\pi t/T)}{\pi t/T}, \quad 0 \le m \le 1,\ \gamma_m(0) = \frac{1}{T} \tag{9.65}$$

The optical fiber transmission system just described represents the optimum linear transmission system. It has the minimum noise bandwidth and the output signal has no intersymbol interference pattern. In the following, this system will be referred to as the reference transmission system. The noise bandwidth of the optical receiver is obtained after integration of the square modulus of the receiver transfer function $H_R(f)$, as reported in Equation (9.4):

$$B_n \equiv \int_{-\infty}^{+\infty} \frac{|H_R(f)|^2}{|H_R(0)|^2}\,df \tag{9.66}$$

Using the definition (9.62) of the matched receiver with the required frequency response (9.64) of the raised cosine pulse (9.65) gives $H_R(f) = \sqrt{\Gamma_m(f)}$, $H_R(0) = \sqrt{\Gamma_m(0)} = 1$. Substituting in Equation (9.66) immediately gives the well-known fundamental result:

$$B_{n,ref} = \int_{-\infty}^{+\infty} \Gamma_m(f)\,df = \frac{1}{T} \tag{9.67}$$

The noise bandwidth $B_{n,ref}$ of the reference optical transmission system in Figure 9.18 is equal to the signaling rate $1/T$, for every value of the roll-off coefficient m. This is an important property of the raised cosine family. The transmission system considered so far has a better optical sensitivity for a given input equivalent noise power and detection efficiency. This is achieved according to the following two features:

1. The minimum noise bandwidth (9.67) leads to the minimum RMS noise amplitude σ_{tot} at the decision section.
2. The random sequence of binary weighted raised cosine pulses (9.65) at the decision section leads to any intersymbol interference pattern.

Inserting a multimode fiber of given length between the $S-R$ section will produce a perturbation in the signal available at the decision section, originating a corresponding amount of intersymbol interference. Figure 9.19 shows the same reference transmission system reported in Figure 9.18, with the insertion of the multimode fiber link between the optical sections S and R. In order to compensate for the frequency response perturbation introduced by the multimode fiber link, the ideal inverse filter equalizer (IFE) is added between the electrical receiver and the decision section.

The transfer function $H_{EQ}(f)$ of the ideal inverse filter equalizer is defined by the inverse transfer function introduced by the perturbing multimode fiber link:

$$H_{EQ}(f) \equiv \frac{1}{H_F(f)} \tag{9.68}$$

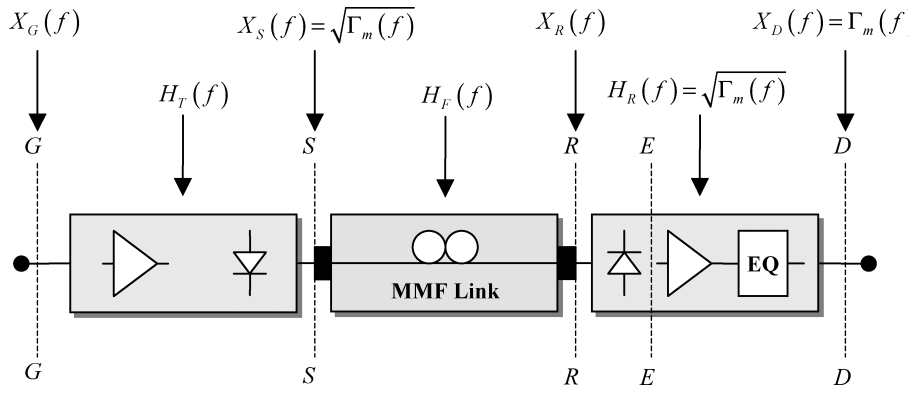

Figure 9.19 Block diagram of the linear transmission system including the multimode fiber link (mmf). The section definition is the same as that used for the reference system in Figure 9.18 and has been omitted. The optical receiver is matched to the transmitted intensity envelope spectrum. The frequency response of the fiber link introduces a perturbation to the channel response, adding intersymbol interference at the decision section

This is immediate, concluding that the overall transfer function of the equalized transmission system, including the multimode fiber link, leads to the required raised cosine signal spectrum at the decision section.

The dispersion equalization performed by the ideal inverse filter equalizer is therefore complete, restoring the original signal spectrum at the decision section that was available in the transmission reference configuration. There would be no residual ISI after the ideal inverse filter equalizer. Why has the equalizer in Equation (9.68) been defined as ideal? According to the definition (9.68), the transfer function of the linear equalizer should be exactly the inverse of the transfer function exhibited by the inserted multimode fiber link. This is not achievable in any practical situation, at least for the following reasons:

1. *High-frequency peaking.* The multimode fiber exhibits a low-pass profile response, leading to an inconsistent high-pass equalizing filter response with indefinitely high-frequency peaking to overcome fiber bandwidth restriction.
2. *Adaptation.* The multimode fiber response changes during normal field operation due to many environmental effects, such as temperature, mechanical vibrations, light polarization and any other perturbing agent. The ideal inverse equalizer should therefore have precise adaptive capabilities.
3. *Filter synthesis.* The exact electronic filter synthesis is not possible, leading to high-order polynomial approximations.
4. *Noise bandwidth enhancement.* Most importantly, the huge increment of the receiver noise bandwidth due to high-frequency enhancement of the equalizing filter will drastically degrade the optical receiver sensitivity performances, even if the intersymbol interference pattern is completely canceled by the inverse ideal equalizer.

9.3.2 Noise Bandwidth of the Equalized Receiver

Even if the filter synthesis and the adaptation problems are neglected, the noise bandwidth enhancement and the consequent optical power penalty remain. In this section, simple formulas will be derived and the optical power penalties for different equalization cases will be computed. Referring to Figure 9.19 and to the definition of the ideal inverse filter equalizer in Equation (9.68), the

transfer function of the equalized receiver using the inverse filter equalization (IFE) is given by

$$H_{\mathrm{R,EQ}}(f) = \frac{\sqrt{\Gamma_m(f)}}{H_{\mathrm{F}}(f)}$$

and the noise bandwidth of the equalized receiver is given by the following integral:

$$B_{\mathrm{n,EQ}} = \int_{-B}^{B} \frac{|H_{\mathrm{R,EQ}}(f)|^2}{|H_{\mathrm{R,EQ}}(0)|^2}\,\mathrm{d}f = \tau^2 \int_{-B}^{B} \frac{\Gamma_m(f)}{|H_{\mathrm{F}}(f)|^2}\,\mathrm{d}f > \frac{1}{T} = B_{\mathrm{n,ref}} \tag{9.69}$$

It is noted that the noise bandwidth definition is consistent with the normalization assumptions $\Gamma_m(0) = 1$ and $|H_{\mathrm{F}}(0)| = \tau$, leading to

$$|H_{\mathrm{R,EQ}}(0)|^2 = \frac{\Gamma_m(0)}{|H_{\mathrm{F}}(0)|^2} = \frac{1}{\tau^2}$$

The time constant τ specifies the amplitude of the transfer function of the multimode fiber consistently with the assumption that the corresponding impulse is dimensionless with normalized peak amplitude:

$$h_{\mathrm{F}}(0) = \int_{-\infty}^{+\infty} H_{\mathrm{F}}(f)\,\mathrm{d}f = 1$$

Assuming that the modal response of the fiber has a low-pass profile, the noise bandwidth $B_{\mathrm{n,EQ}}$ of the equalized receiver will always be larger than the noise bandwidth of the reference receiver. This is easily understood if account is taken of the fact that the normalized low-pass profile of the fiber response at the denominator of the integrand function in Equation (9.69) leads to a larger value of the integral.

9.3.2.1 Single-Pole Modal Response

In order to show quantitatively the increase of the noise bandwidth with respect to the ideal Nyquist channel when the ideal inverse filter equalizer (IFE) is used to compensate for the multimode fiber bandwidth limitations, the case is considered of the multimode fiber transfer function expressed by a dominant single-pole response. This is not intended as a real physical model. It is known that the smooth single-pole frequency response does not fit the modal bandwidth behavior of the multimode fiber very well. Nevertheless, this case is very simple to solve in a mathematical closed form, giving useful information about the general concept of the equalization noise enhancement and the related optical power penalty. Accordingly, it is considered that the multimode fiber link has the single-pole frequency response reported below, where the cut-off frequency $\alpha \equiv f_{\mathrm{c}}T$ normalized to the bit rate frequency $B = 1/T$ is expressed as

$$\left.\begin{aligned} h_{\mathrm{F}}(t) &= \begin{cases} \mathrm{e}^{-t/\tau}, & t \geq 0 \\ 0, & t < 0 \\ h_{\mathrm{F}}(0) = 1 \end{cases} \\ H_{\mathrm{F}}(f) &= \frac{\tau}{1 + j\dfrac{f}{f_{\mathrm{c}}}} \end{aligned}\right\} \Rightarrow \begin{cases} |H_{\mathrm{F}}(f)|^2 = \dfrac{T^2}{4\pi^2\alpha^2}\,\dfrac{1}{1 + (fT/\alpha)^2} \\ \text{cut-off}: \quad f_{\mathrm{c}} \equiv \dfrac{1}{2\pi\tau}, \quad \alpha \equiv f_{\mathrm{c}}T \\ \tau = \dfrac{1}{2\pi\alpha} = \dfrac{1}{2\pi f_{\mathrm{c}}} \end{cases} \tag{9.70}$$

In this particular case, the normalization time constant $H_{\mathrm{F}}(0) = \tau$ coincides with the decay time constant of the exponential impulse response. The parameter α sets the cut-off frequency of the single-pole modal response. If $\alpha > 1$, the cut-off exceeds the bit rate frequency; otherwise if $\alpha < 1$ the cut-off frequency of the multimode fiber response is below the required bit rate. Substituting

Equation (9.70) into Equation (9.69) and assuming the unit value $m = 1$ of the roll-off coefficient of the raised cosine spectrum gives the following detailed noise bandwidth calculation of the optical receiver featuring the ideal inverse linear equalizer (IFE):

$$B_{\substack{\text{n,EQ}\\(m=1)}} = 2\left(\frac{\cancel{T^2}}{\cancel{4\pi^2\alpha^2}}\right)\left(\frac{\cancel{4\pi^2\alpha^2}}{\cancel{T^2}}\right)\int_0^{1/T}\left[1+\left(\frac{fT}{\alpha}\right)^2\right]\cos^2\left(\frac{\pi}{2}fT\right)\mathrm{d}f$$

$$= 2\int_0^{1/T}\left[1+\left(\frac{f\ T}{\alpha}\right)^2\right]\cos^2\left(\frac{\pi}{2}f\ T\right)\mathrm{d}f \quad \text{(Hz)} \tag{9.71}$$

After direct integration, the following noise bandwidth for the IFE structure is obtained:

$$B_{\substack{\text{n,EQ}\\(m=1)}} = B_{\text{n,ref}}\left[1+\frac{2}{\alpha^2}\left(\frac{1}{6}-\frac{1}{\pi^2}\right)\right] \tag{9.72}$$

Equation (9.67) was used to express the noise bandwidth of the matched receiver over the reference channel, $B_{\text{n,ref}} = 1/T$. It is convenient to define the noise bandwidth enhancement factor $\Delta_{\text{n}}(\alpha)$:

$$\Delta_{\text{n}}(\alpha) \equiv \frac{B_{\text{n,EQ}} - B_{\text{n,ref}}}{B_{\text{n,ref}}} = \frac{B_{\text{n,EQ}}}{B_{\text{n,ref}}} - 1 \tag{9.73}$$

Substituting Equation (9.72) into Equation (9.73) gives

$$\Delta_{\text{n}}(\alpha) = \frac{2}{\alpha^2}\left(\frac{1}{6}-\frac{1}{\pi^2}\right) \cong \frac{0.1307}{\alpha^2} \tag{9.74}$$

From the result it can immediately be concluded that the noise bandwidth of the equalized receiver, assuming a single-pole multimode fiber frequency response, is greater than the noise bandwidth of the reference matched receiver for every value of the normalized cut-off frequency α. In particular, if the cut-off frequency coincides with the bit rate frequency, $\alpha = 1$, from Equation (9.74) it is concluded that the noise bandwidth is about 13 % larger than the available minimum noise bandwidth. This is transformed into suboptimal performance. In the case of a single-pole modal response, the quadratic dependence (9.74) of the noise bandwidth enhancement factor $\Delta_{\text{n}}(\alpha)$ from the reciprocal of the cut-off frequency leads to more than a 50 % noise bandwidth enhancement for a half-rate cutoff, $\alpha = \frac{1}{2}$. Figure 9.20 shows the computed plot of the noise bandwidth enhancement factor $\Delta_{\text{n}}(\alpha)$ for the considered case. Different modal responses of course give different curves. The single-pole response is among the smoother ones. Using the Gaussian frequency response the noise bandwidth enhancement increases relatively faster than the normalized cut-off, resulting in larger optical power penalties. Before closing this section it is important to remark that although the noise bandwidth of the matched receiver does not depend on the raised cosine roll-off coefficient m, this would not be the case when the inverse filter equalizer is used. In fact, the noise bandwidth $B_{\text{n,EQ}}$ of the equalized receiver in Equation (9.69) depends in general on the raised cosine profile. This characteristic adds one degree of freedom in choosing a better equalization.

It is known from Section 9.2.1.1, assuming uniform noise power spectral density (white noise), that the noise bandwidth ratio coincides with the noise power ratio. If the electrical SNR is considered, the obvious conclusion would be that the average signal power penalty would consequently be related to the noise bandwidth ratio. This is true for electrical transmission systems, but is not the case for the optical transmission system. The reason for this behavior is the square law process inherent to the photodetection. In fact, for every intensity modulated direct detection (IMDD) optical communication system, the bit error rate is a function of the ratio between the received optical power and the RMS noise amplitude at the input equivalent section, as reported in Equation (9.59).

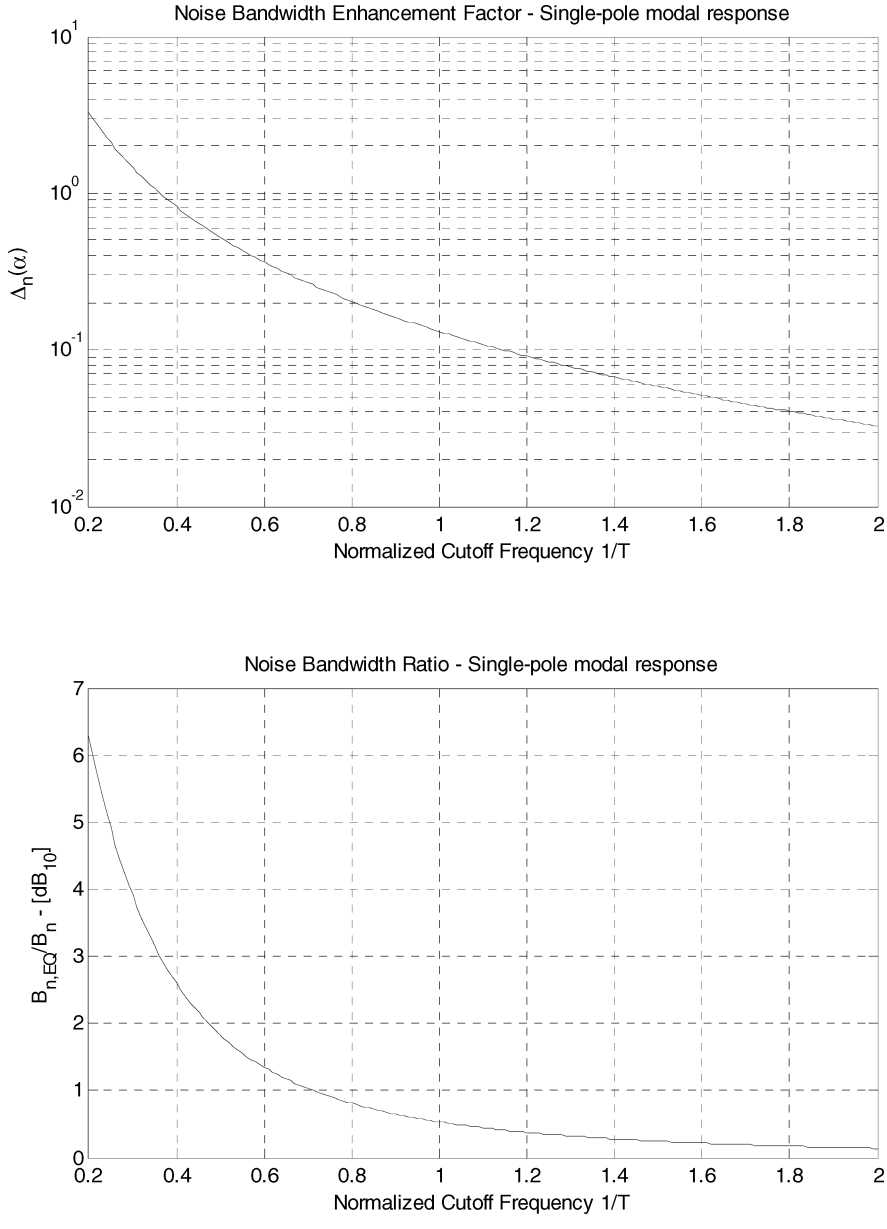

Figure 9.20 Top: computed noise bandwidth enhancement factor for the single-pole modal response. The cut-off frequency is expressed in bit rate frequency normalized units. It is clear that setting the cut-off at half the bit rate the noise bandwidth enhancement exceeds 50 % of the minimum ideal noise bandwidth. Bottom: computed plot of the noise bandwidth ratio between equalized and matched receivers. Assuming a half bit rate cut-off, the noise bandwidth ratio exceeds 1.8 dB

This makes the received optical power level required for a given error probability directly related to the RMS noise amplitude and not to the noise power. Consequently, the received optical power ratio must be related to the square root of the noise bandwidth ratio.

In the next section the optical power penalty will be derived as a consequence of the noise bandwidth enhancement factor.

9.3.3 The Optical Power Penalty

In the previous section the concept of the ideal inverse filter equalizer was introduced as the reference solution for comparing different optical channels. How could the figure-of-merit of a given multimode fiber link be quantified when ideal inverse filter equalization is applied? The answer to this question leads to the concept of the optical channel metric. The following statement defines the concept of the optical channel metric when applied to the ideal inverse filter equalizer: the optical channel metric is defined by the value ΔP_R of the average optical power penalty needed to restore a given BER value, as consequent to the application of the ideal inverse filter equalization to the reference Nyquist transmission system. The Nyquist reference transmission system is defined in the following section. For the moment the derivation of the average optical power penalty due to the noise bandwidth enhancement will be discussed.

The bit error rate (BER) of a white Gaussian noise (WGN) optical receiver affected by the input equivalent noise power σ^2 (A^2) is given by the complementary error function introduced in Equation (9.58). For simplicity the total RMS noise amplitude is indicated by the variable σ, including constant, linear and quadratic components. It should be remembered that the independent noise power components add together, while the total RMS noise amplitude is given by the square root of the quadratic term summation. Referring to Equation (9.15), the total RMS noise amplitude is written as

$$\sigma(P_R) = \sqrt{\sigma_c^2 + \sigma_d^2 + \sigma_s^2(P_R) + \sigma_{RIN}^2(P_R)} \tag{9.75}$$

Before continuing with the derivation of the optical power penalty, it is necessary to note that power-dependent noise terms are a function of time. This is due to the assumed time dependence of the intensity envelope of the detected optical signal. When the received average optical power P_R is considered, the time average of the ensemble average performed at each time instant on the random optical sequence is used. This concept is important for correctly understanding the decision process of the photodetected signal.

First a single optical pulse is considered. Both signal shot noise and RIN coincide with the intensity fluctuations of the optical intensity. What is meant by the term 'optical signal' is simply the ensemble average of the optical intensity of the pulse. Therefore, optical fluctuations are conceptually removed from what is intended as an optical signal in the detection process and are considered separately as noise contributions. The optical signal referred to in intensity modulated optical communication is obviously a function of the time, leading to the time-dependent ensemble average. This is the detected optical pulse profile $p_R(t)$ and is not a random process but is the ensemble average at every time instant of the optical random process at the photodetector input.

Now, a random sequence is launched of those optical pulses. The process now is 'twice time random': first, because it is an optical pulse and, second, because of the random sequence of those optical pulses. Implicitly, it is assumed that the ensemble average $p_R(t)$ performed at each time instant affects only the single optical pulse, only the single process realization. According to the random sequence assumption, however, the ensemble average $p_R(t)$ becomes the random process, and the proper underscore sign is added, setting $\underline{p}_R(t)$. It is in fact a random function of the time, and the stochastic nature of $\underline{p}_R(t)$ no longer depends on the optical field but instead on the random sequence itself. This is the ergodic random process representing the photodetected signal in the intensity modulated optical communication. The time average of each individual realization

of $\overline{p_R(t)}$ therefore coincides with the ensemble average $\langle \underline{p}_R(t) \rangle$, giving the received average optical power P_R:

$$\overline{p_R(t)} = \left\langle \underline{p}_R(t) \right\rangle = P_R \tag{9.76}$$

Besides the conceptual relevance of these comments, why is there a need for them? The reason is that the decision process is a punctual process. It is not an integral process. This means that the time average P_R of the detected optical pulse profile $\underline{p}_R(t)$ is not properly involved in the decision process. In particular, signal-dependent noise terms such as signal shot noise and RIN are clearly functions of the instantaneous value the optical pulse assumes at the decision instant. Accordingly, it can be concluded that both signal shot noise and RIN are functions of the process $\underline{p}_R(t)$ and not of the received average optical power P_R. The practical consequence of this behavior is the assumption of two different signal-dependent noise contributions corresponding to the high and low signal levels in the binary decision system. Due to a higher instantaneous optical power level, the shot noise term on the high signal level is considerably higher than the signal shot noise term affecting the low signal level. In order to simplify the analysis of the error probability in optical fiber communication, it is customary to adopt two different shot noise contributions, namely σ_{s0} and σ_{s1} on the low and high signal levels respectively. A very relevant practical consequence of this approach is the optimum position of the decision threshold in optically amplified links. In this case, in fact, the shot noise produced by the amplified spontaneous emission (ASE) is the dominant noise term and the optimum threshold is considerably lower (30–35 %) than the mid position. This is to compensate for the much higher shot noise power affecting the higher signal level than the lower one.

In the following derivation of the optical power penalty the different shot noise and RIN contributions on the high and low signal levels will be neglected and the symmetric noise power $\sigma^2(P_R)$ reported in Equation (9.75) affecting the binary decision process will be assumed. A second important approximation concerns the dependence of the total noise power from the received average optical power. Even if the total noise power depends on the received optical power level, it will be assumed that the variation of the received average optical power will not affect the total noise power. It is clear that this approximation will be more justified the more the signal-dependent noise terms add a negligible contribution to the total noise. The extinction ratio r and the photodetector responsivity R are given and the input equivalent noise power spectral density is represented by the constant distribution G_{in}. First the optical reference transmission system, reported in Figure 9.18, is considered, using a matched receiver over the ideal Nyquist channel. In this case, the noise bandwidth $B_{n,ref}$ coincides with the bit rate frequency B, independently from the roll-off profile chosen for the raised cosine output spectrum. The total noise power affecting the symmetric decision process is then given by Equations (9.5) and (9.67):

$$\sigma^2 = G_{in} B_{n,ref} = \frac{G_{in}}{T} \tag{9.77}$$

The bit error rate is given by Equation (9.58), where the noise term reported in Equation (9.77) has been substituted:

$$\mathrm{BER}(P_{R,ref}) = \frac{1}{2}\mathrm{erfc}\left[\frac{R P_{R,ref}}{\sqrt{2 G_{in} B_{n,ref}}}\left(\frac{r-1}{r+1}\right)\right] \tag{9.78}$$

The optical sensitivity of the reference transmission system is defined as the received average optical power P_R needed to achieve the required value of BER. In other words, it is assumed that for the given parameter set in Equation (9.78), the BER reaches the required value, i.e. $\mathrm{BER} = 10^{-12}$, at the power level $P_{R,ref}$. The average optical power level $P_{R,ref}$ is the sensitivity of the optical reference system, without any fiber link length inserted between the $S-R$ sections.

If a multimode fiber link is inserted between the transmitter and the receiver, the transmission system becomes perturbed and the performances will be altered. From the previous section it can be seen that by inserting the ideal inverse filter equalizer in front of the decision section the degraded fiber channel response due to modal bandwidth limitation can be completely recovered, leading to the required ISI-free signal at the decision section. This is achieved at the expense of a consistent increase in the noise bandwidth. Now, the simple formula expressing the optical power penalty of the optical reference system sensitivity will be derived. Since the linear equalizer is cascaded to the low-noise front end and amplifier of the optical receiver, it is reasonable to assume that insertion of the ideal inverse filter equalizer does not modify effectively the uniform spectral power density of the input equivalent noise of the optical reference system. In other words, the thermal noise added by the equalizer is negligible with respect to the total input equivalent noise level.

The input equivalent noise power spectral density of the equalized optical system using the ideal inverse filter equalizer is represented by the constant distribution G_{in}. The noise bandwidth $B_{\text{n,EQ}}$ of the equalized system is increased with respect to the noise bandwidth $B_{\text{n,ref}}$ of the ideal Nyquist channel, as reported in Equation (9.69). Substituting the equalized noise bandwidth in expression (9.78), the relationship is found between the BER and the required average optical power level $P_{\text{R,EQ}}$, including the inverse filter equalizer effect:

$$\text{BER}_{\text{EQ}}(P_{\text{R}}) = \frac{1}{2}\text{erfc}\left[\frac{R P_{\text{R,EQ}}}{\sqrt{2 G_{\text{in}} B_{\text{n,EQ}}}}\left(\frac{r-1}{r+1}\right)\right] \tag{9.79}$$

Of course, since the complementary error function is a fast decreasing function of the argument, a slight increment in the noise bandwidth corresponds to a relevant increase in the error probability. Considering the Q-factor of both the optical reference system and the equalized one, from Equation (9.53)

$$\begin{aligned} Q_{\text{ref}} &= \frac{r-1}{r+1}\frac{R P_{\text{R,ref}}}{\sqrt{G_{\text{in}} B_{\text{n,ref}}}} \\ Q_{\text{EQ}} &= \frac{r-1}{r+1}\frac{R P_{\text{R,EQ}}}{\sqrt{G_{\text{in}} B_{\text{n,EQ}}}} \end{aligned} \tag{9.80}$$

In order to restore the same BER value, both Q-factors must coincide; hence

$$\frac{P_{\text{R,ref}}}{\sqrt{B_{\text{n,ref}}}} = \frac{P_{\text{R,EQ}}}{\sqrt{B_{\text{n,EQ}}}} \Rightarrow \frac{P_{\text{R,EQ}}}{P_{\text{R,ref}}} = \sqrt{\frac{B_{\text{n,EQ}}}{B_{\text{n,ref}}}} \tag{9.81}$$

According to the definition given above, the increment $P_{\text{R,EQ}}/P_{\text{R,ref}}$ of the received average optical power needed to restore the same BER (the same *Q-factor*) coincides with the concept of the optical power penalty. Introducing the decibel notation, the optical power penalty due to the noise bandwidth enhancement for the inverse filter equalization is as follows:

$$\Delta P_{\text{R}} \equiv 10\log_{10}\left(\frac{P_{\text{R,EQ}}}{P_{\text{R,ref}}}\right) \tag{9.82}$$

From Equation (9.67) the expression for the optical power penalty due to the ideal inverse filter equalizer is

$$\Delta P_{\text{R}} = 5\log_{10}\left(\frac{B_{\text{n,EQ}}}{B_{\text{n,ref}}}\right) \tag{9.83}$$

Finally, substituting the explicit integral expression (9.69) for the equalized noise bandwidth gives the following noteworthy expression for the optical power penalty of the transmission system

represented in Figure 9.19 of the arbitrary roll-off coefficient $0 \leq m \leq 1$:

$$\Delta P_{\mathrm{R}} = 5 \log_{10} \left[2T\tau^2 \int_0^{1/T} \frac{\Gamma_m(f)}{|H_{\mathrm{F}}(f)|^2} \, \mathrm{d}f \right] \quad \text{(dB)} \tag{9.84}$$

with $\Gamma_m(0) = 1$, $|H_{\mathrm{F}}(0)| = \tau$.

The expression for the optical power penalty reported in Equation (9.84) is due to the equalization noise bandwidth enhancement and quantifies the principal limitation in using this equalizer in real multimode fiber systems. However, as already discussed, this ideal equalizer has a meaningful relevance for understanding the benefit and the limitation of digital equalization, by representing the ideal reference performance. In the following, two analytical examples will be considered.

9.3.3.1 Single-Pole Modal Response

From Equation (9.84), it is concluded that for every fixed frequency bit rate B and multimode fiber modal response $H_{\mathrm{F}}(f)$, the optical power penalty depends on the value of the roll-off coefficient m of the raised cosine output signal spectrum. The general expression of the optical power penalty of the inverse filter equalizer assuming the single-pole modal response and raised cosine output signal spectrum with a generic frequency roll-off is derived in the following section. For the moment, the case of the unit roll-off coefficient, $m = 1$, is discussed. Substituting the single-pole modal response (9.70) and the raised cosine spectrum (9.64) with $m = 1$ into Equation (9.84) gives the following expression of the optical power penalty:

$$\Delta P_{\mathrm{R}}(\alpha) = 5 \log_{10} \left[1 + \frac{2}{\alpha^2} \left(\frac{1}{6} - \frac{1}{\pi^2} \right) \right], \quad \alpha = f_{\mathrm{c}} T, \quad m = 1 \tag{9.85}$$

Assuming that the single-pole cut-off frequency is several orders of magnitude higher than the frequency bit rate leads to the negligible optical power penalty, as expected by the negligible compensation required. Figure 9.21 shows the computed optical power penalty according to Equation (9.85). The single-pole modal response considered allows a closed-form calculation of the optical power penalty through Equation (9.85). The corresponding plot in Figure 9.21 shows a relatively smooth dependence of the optical power penalty on the cut-off frequency. This behavior is characteristic of the smoothed frequency roll-off of the single-pole response. Assuming a strong single-pole bandwidth limitation close to only 20 % of the bit rate frequency, this leads, according to Figure 9.21, to $\Delta P_{\mathrm{R}} \cong 3.1$ dB. This is still an acceptable value if the limitations imposed on the optical channel frequency response is considered.

9.3.3.2 Gaussian Modal Response

The conclusions found in the previous section would be quite different if the Gaussian response had been referred to instead of the single-pole response. In this case, the analytical integration is no longer available and numerical solutions must be used. Referring to the general expression of the optical power penalty reported in Equation (9.84), the following Gaussian modal response and unit roll-off raised cosine output spectrum, $m = 1$, are assumed:

$$\Gamma_1(f) = \cos^2 \left(\frac{\pi}{2} fT \right), \quad -1 \leq |fT| \leq 1 \tag{9.86}$$

$$H_{\mathrm{F}}(f) = \tau \mathrm{e}^{-f^2/(2\sigma_f^2)} \tag{9.87}$$

Note that both frequency responses are correctly normalized assuming $\Gamma_m(0) = 1$, $|H_{\mathrm{F}}(0)| = \tau$. The Gaussian transfer function is characterized by the half-width at half-maximum or equivalently

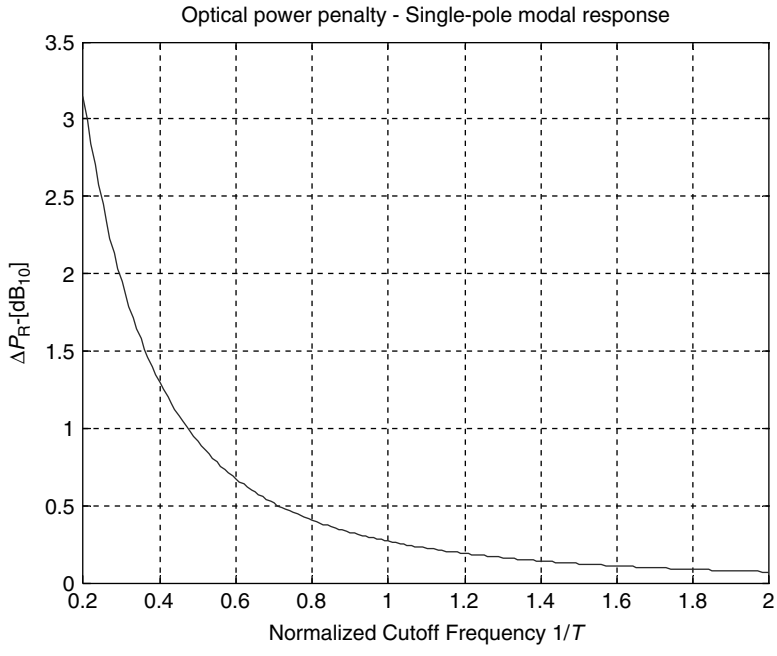

Figure 9.21 Computed average optical power penalty for the equalized transmission system assuming a single-pole modal frequency response and the unity roll-off coefficient $m = 1$. The curve is plotted versus the normalized cut-off frequency. Assuming that $\alpha = f_c T = \frac{1}{2}$ then $\Delta P_R \cong 0.9\,\text{dB}$

by the $-6\,\text{dB}$ electrical bandwidth f_c. From Equations (3.115) and (9.87), introducing the bit rate normalized cut-off frequency α gives

$$f_c \equiv \frac{\alpha}{T}, \quad \alpha > 0 \tag{9.88}$$

Substituting in Equation (9.87) gives the Gaussian modal response with the normalized cut-off frequency:

$$\left.\begin{aligned} &h_F(t) = \exp\left[-\frac{\pi^2\alpha^2}{\log 2}\left(\frac{t}{T}\right)^2\right] \Rightarrow \\ &h_F(0) = 1 \end{aligned}\right\} \Rightarrow \begin{cases} H_F(f) = \dfrac{T}{\alpha}\sqrt{\dfrac{\log 2}{\pi}}\exp\left[-\left(\dfrac{fT}{\alpha}\right)^2 \log 2\right] \\ H_F(f_c) = \dfrac{1}{2}H_F(0) \\ \tau = \dfrac{T}{\alpha}\sqrt{\dfrac{\log 2}{\pi}} \\ \sigma_f = \dfrac{\alpha}{T\sqrt{2\log 2}} \end{cases} \tag{9.89}$$

The modal transfer function $H_F(f)$ of the multimode fiber refers to the intensity of the light and not to the field amplitude. However, due to the quadratic conversion of the photodetection process, the noise response of the ideal inverse filter equalizer is given by the square modulus $|H_F(f)|^2$ of the modal fiber response. Substituting Equations (9.89) and (9.86) in Equation (9.84) requires

the following integral to be solved in order to calculate the optical power penalty for the Gaussian modal response. For the sake of clarity, the detailed dimensional constants cancellation is given:

$$\Delta P_{\mathrm{R}} = 5\log_{10}\left[2\cancel{T^2}\cancel{\alpha^2}\,\frac{\cancel{\log^2}}{\cancel{\pi}}T\frac{\cancel{\alpha^2}}{\cancel{T^2}}\,\frac{\cancel{\pi}}{\cancel{\log 2}}\int_0^{1/T}\frac{\cos^2[(\pi/2)fT]}{\mathrm{e}^{-(fT/\alpha)^2 2\log 2}}\,\mathrm{d}f\right]$$

$$= 5\log_{10}\left[2T\int_0^{1/T}\cos^2\left(\frac{\pi}{2}fT\right)\mathrm{e}^{-(fT/\alpha)^2 2\log 2}\,\mathrm{d}f\right] \tag{9.90}$$

Substituting for the normalized frequency variable $x \equiv fT$ gives

$$\Delta P_{\mathrm{R}}(\alpha) = 5\log_{10}\left[2\int_0^1\cos^2\left(\frac{\pi}{2}x\right)\mathrm{e}^{(x^2/\alpha^2)2\ln 2}\,\mathrm{d}x\right], \quad \alpha \equiv f_{\mathrm{c}}T, m = 1 \tag{9.91}$$

Figure 9.22 shows the numerical computation of the optical power penalty according to Equation (9.91), assuming that the normalized Gaussian modal bandwidth α varies from 0.2 and 2.0. Figure 9.23 presents the same calculation but using a logarithmic scale on the ordinate axis. This plot clearly shows the threshold behavior of the optical power penalty for the Gaussian modal bandwidth value lower than half a bit rate.

9.3.3.3 IV-Order Bessel–Thompson Modal Response

So far in Section 9.3 two simple analytical functions for modeling the multimode fiber response have been considered, namely the single-pole and the Gaussian transfer functions. In this section,

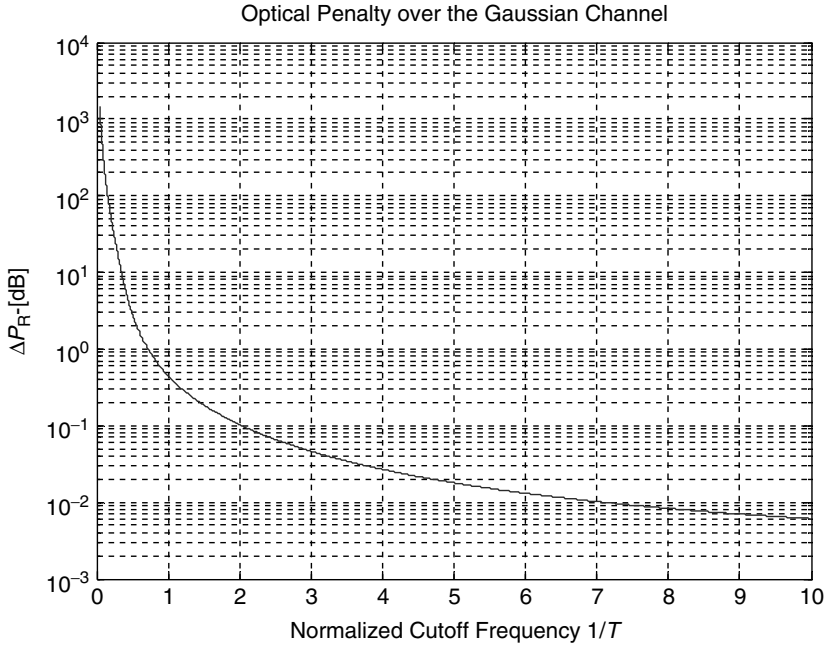

Figure 9.22 Computed optical power penalty (9.91) of the equalized system, assuming a Gaussian modal response and unit roll-off of the raised cosine spectrum. The modal cut-off interval is ranging between $0.01 \leq x \leq 10$. The optical penalty increases suddenly as the cut-off frequency decreases below the frequency bit rate

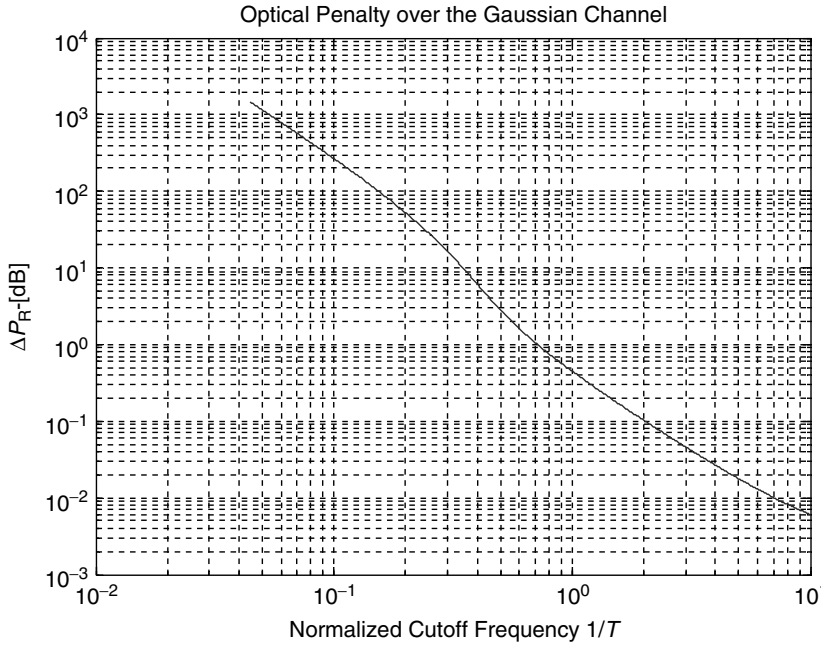

Figure 9.23 Logarithmic plot representation of the optical power penalty in Figure 9.22. At half a bit rate cut-off, $f_c = 1/2T$, the optical power penalty reaches $\Delta P_R \cong 2.8\,\text{dB}$, a higher value than the single-pole response shown in Figure 9.21

the fourth-order Bessel–Thompson frequency response will be introduced, which could be used for additional modeling of the multimode fiber behavior. At first sight, the fourth-order Bessel–Thompson function has some features that do not fit the physical requirements of the multimode fiber impulse response. First, the impulse response can assume negative values during the postcursor tail evolution. Second, the characteristic group delay is strictly determined by the cut-off frequency. These features are not physically compatible with the propagation characteristic of the light intensity in optical fibers. Nevertheless, the fourth-order Bessel–Thompson frequency response could be used for modeling some specific responses of the multimode fiber. Similar comments, on the other hand, could be raised even for the single-pole or the Gaussian pulse responses.

The normalized frequency response $S(f)$ of the fourth-order Bessel–Thompson filter is given in Chapter 8, equation (8.80). The group delay τ and the cut-off frequency f_c for a given amplitude reduction are related by specifying the scaling constant a. In order to use $S(f)$ as the multimode fiber response $H_F(f)$, some modification of the modeling introduced in Chapter 8 is needed. In order to be comparable with the other two modeling functions, the cut-off needs to be defined at half-maximum instead of the usual $1/\sqrt{2}$ and the normalization constant must satisfy the unit amplitude condition of the impulse response, $h_F(0) = 1$. Since the impulse response of the fourth-order Bessel–Thompson filter is causal, $s(0) = 0$, $t \leq 0$, and the constant τ cannot be determined as was done in the previous cases by setting $s(0) = \tau \int_{-\infty}^{+\infty} S(f)\,\mathrm{d}f = 1$.

The standard fourth-order Bessel–Thompson filter definition will be used when the frequency response has unit amplitude at the frequency origin and the cut-off frequency refers to $1/\sqrt{2}$ amplitude decay. The frequency response $S(f)$ of the standard fourth-order Bessel–Thompson

filter from Equation (8.80) is given, together with the characteristic relationships:

$$\begin{aligned} S(f) &= \frac{105}{105 + 105y + 45y^2 + 10y^3 + y^4} \\ y &= \mathrm{j}\, 2\pi\ f\ \tau_\mathrm{d} = \mathrm{j}\, a\frac{f}{f_\mathrm{c}} \Rightarrow \tau_\mathrm{d} = \frac{a}{2\pi f_\mathrm{c}} \\ S(0) &= 1, \qquad |S(f_\mathrm{c})| = \frac{1}{\sqrt{2}} \Rightarrow a = 2.1139 \end{aligned} \tag{9.92}$$

The notation τ_d for the group delay of the fourth-order Bessel–Thompson filter is used to avoid confusion with the normalization constant τ for the unit amplitude condition of the impulse response of the multimode fiber.

The first modification deals with the cut-off frequency, which must be referred to the half-maximum instead of the usual $1/\sqrt{2}$ relative level. From Equations (9.92), by setting $|S(f_\mathrm{c})| = \frac{1}{2}$ the corresponding scaling constant $a = 2.8860$ is found. The second modification operated to the standard fourth-order Bessel–Thompson filter response in Equation (9.92) regards the normalization of the impulse response. The peak of the impulse response of the fourth-order Bessel–Thompson filter (9.92) is located at τ_d and can be used for the normalization $h_\mathrm{F}(0) = 1$. In fact, multiplying $S(f)$ by the phase shift factor $\exp(+\mathrm{j}2\pi f\tau_\mathrm{d})$ gives the corresponding impulse response translated with the peak value at the origin. This allows the unit amplitude normalization of the impulse response to proceed.

Introducing the two modifications mentioned above and using the conventional bit rate frequency normalization $x \equiv fT$, $\alpha \equiv f_\mathrm{c}T$, from Equation (9.92) the following fourth-order Bessel–Thompson frequency response can be obtained, which is suitable for compliant modeling the multimode fiber impulse response:

$$\left.\begin{matrix} h_\mathrm{F}(t) \\ h_\mathrm{F}(0) = 1 \end{matrix}\right\} \overset{\Im}{\longleftrightarrow} \begin{cases} H_\mathrm{F}(y) = \dfrac{105\tau \mathrm{e}^{y}}{105 + 105y + 45y^2 + 10y^3 + y^4} \\ y = \mathrm{j}\, 2\pi\ f\ \tau_\mathrm{d} = \mathrm{j}\, a\dfrac{x}{\alpha} \Rightarrow \dfrac{\tau_\mathrm{d}}{T} = \dfrac{a}{2\pi\alpha} \\ \dfrac{|H_\mathrm{F}(f_\mathrm{c})|}{|H_\mathrm{F}(0)|} = \dfrac{1}{2} \Rightarrow a = 2.8860 \end{cases} \tag{9.93}$$

In general, the scaling constant a is obtained by solving the following equation for every fixed cut-off level ρ:

$$0 < \rho < 1 \Rightarrow \frac{|H_\mathrm{F}(\mathrm{j}a)|}{|H_\mathrm{F}(0)|} = \rho \Rightarrow a(\rho) \tag{9.94}$$

However, independently from the normalized cut-off frequency α, by setting $x = \alpha$ the variable $y = \mathrm{j}a$ leads to the same value of the scaling constant. In other words, the scaling constant a is a function of only the cut-off level ρ and not of the normalized cut-off frequency. The normalization constant τ is obtained by solution of the following condition:

$$\tau: \quad h_\mathrm{F}(0) = \frac{1}{T}\int_{-\infty}^{+\infty} H_\mathrm{F}(x)\,\mathrm{d}x = 1 \tag{9.95}$$

The area subtended by the frequency response $H_\mathrm{F}(x)$ depends on both the scaling constant a and the normalized cut-off frequency α, and hence the normalization time constant is a function of both these variables, $\tau = f(\rho, \alpha)$. However, the effect of the normalized cut-off frequency α reduces only to a proportional scaling factor, as demonstrated in the following numerical example. This can be understood by a simple reasoning: if α increases by one order of magnitude, from Equations (9.93)

Table 9.3 Computed scaling constant a and normalized time constant τ/T for the fourth-order Bessel–Thompson frequency response reported in Equations (9.93) versus the cut-off level ρ and the cut-off frequency α. The solutions corresponding to half-maximum, $\rho = \frac{1}{2}$ and the unit cut-off frequency $\alpha = 1$ are highlighted

ρ	a	τ/T			
		$\alpha = 0.01$	$\alpha = 0.1$	$\alpha = 1$ $\tau_1(\rho)/T$	$\alpha = 10$
0.1	5.3718	91.8842	9.1884	0.9188	0.0919
0.2	4.3251	73.9800	7.3980	0.7398	0.0740
0.3	3.7240	63.6997	6.3700	0.6370	0.0637
0.4	3.2736	55.9956	5.5996	0.5600	0.0560
0.5	2.8860	49.3654	4.9365	0.4937	0.0494
0.6	2.5188	43.0840	4.3084	0.4308	0.0431
0.7	2.1419	36.6364	3.6636	0.3664	0.0366
0.8	1.7227	29.4659	2.9466	0.2947	0.0295
0.9	1.2008	20.5400	2.0540	0.2054	0.0205

the variable y will assume the same values corresponding to one order of magnitude larger values of the normalized frequency x, leading to one order of magnitude larger values of the indefinite integral. Consequently, the time constants must be one order of magnitude smaller and the reciprocal scaling effect is demonstrated. Table 9.3 gives the numerical solution for the scaling constant a in Equation (9.94) and the time constant τ in Equation (9.95) for the fourth-order Bessel–Thompson frequency response (9.93) versus different cut-off levels $0.1 \leq |H_{\mathrm{F}}(f_{\mathrm{c}})|/|H_{\mathrm{F}}(0)| = \rho \leq 0.9$, assuming four different values of the normalized cut-off frequency $\alpha = (0.01, 0.1, 1, 10)$. Neglecting small differences in the scaling factor of the time constant due to numerical resolution accuracy, the inverse relationship is largely proved. From the consideration above, it can be concluded that the normalization time constant has the following expression:

$$\tau(\rho, \alpha) = \frac{1}{\alpha}\tau_1(\rho) \tag{9.96}$$

where:

$$\tau_1(\rho) \equiv \tau(\rho, 1)$$

Substituting the multimode fiber fourth-order Bessel–Thompson response (9.93) and the raised cosine spectrum (9.86) with the unit roll-off in Equation (9.84), the following normalized integral representation of the optical power penalty for the fourth-order Bessel–Thompson modal response is obtained:

$$\Delta P_{\mathrm{R}}(\alpha) = 5\log_{10}\left[2\int_0^1 \left|1 + \mathrm{j}\frac{a}{\alpha}x - \frac{3}{7}\left(\frac{ax}{\alpha}\right)^2 - \mathrm{j}\frac{10}{105}\left(\frac{ax}{\alpha}\right)^3 + \frac{1}{105}\left(\frac{ax}{\alpha}\right)^4\right|^2 \cos^2\left(\frac{\pi}{2}x\right)\mathrm{d}x\right], \quad \alpha = f_{\mathrm{c}}T, m = 1 \tag{9.97}$$

It should be remembered that the scaling constant $a = 2.8860$ with half-maximum cut-off $\rho = \frac{1}{2}$ at $\alpha = f_{\mathrm{c}}T$ and the integration variable $x = fT$ is the bit rate normalized frequency. Figure 9.24 shows the computed plot of the scaling constant a and the normalization time constant τ/T versus the cut-off level $0 < \rho < 1$ for the unit normalized cut-off frequency $\alpha = 1$. However, using the

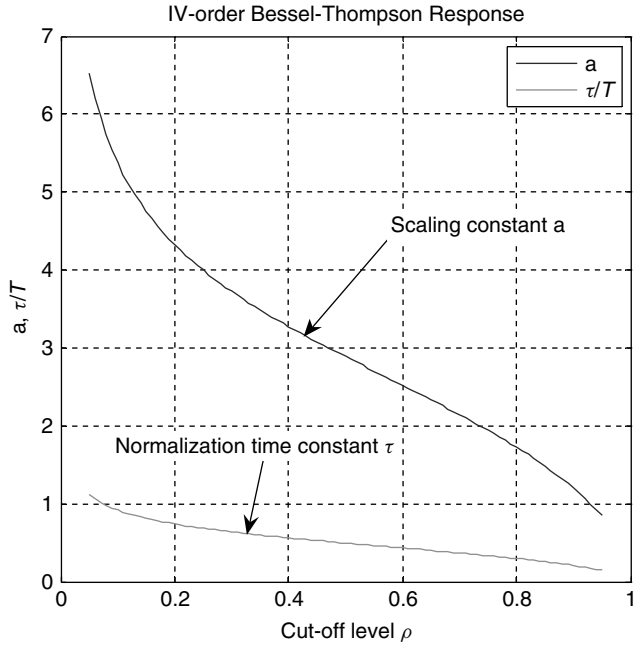

Figure 9.24 Computed scaling constant a and normalized time constant τ/T for the fourth-order Bessel–Thompson frequency response reported in Equations (9.93) versus the cut-off level ρ and the cut-off frequency α. The normalized time constant scales as the reciprocal of α

inverse relationship (9.96), the corresponding normalization time constant τ/T for every different cut-off frequency can easily be obtained. Figure 9.25 shows the computed optical power penalty versus the normalized cut-off frequency α, according to Equation (9.97).

This last example closes the section on optical power penalty calculations based on the expression (9.84). So far, a unit roll-off raised cosine spectrum has been implicitly assumed at the decision section. This reflects the higher values of optical power penalties, as will be seen in detail in the next section. In fact, the largest high-frequency content associated with the unit roll-off raised cosine spectrum determined the highest noise power due to high-frequency equalization enhancement.

9.3.4 Influence of the Raised Cosine Shaping Factor

In order to include the effects of the shaping coefficient m in the analysis of the optical power penalty, the expression (9.64) of the raised cosine spectrum is considered again and the bit rate frequency normalized variable $x = fT$ is used:

$$\Gamma_m(x) = \begin{cases} 1, & |x| \le \dfrac{1-m}{2} \\ \cos^2\left[\dfrac{\pi}{2m}\left(x - \dfrac{x}{|x|}\dfrac{1-m}{2}\right)\right], & \dfrac{1-m}{2} \le |x| \le \dfrac{1+m}{2} \\ 0, & |x| \ge \dfrac{1+m}{2} \end{cases} \tag{9.98}$$

Substituting this expression in Equation (9.84) and assuming the single-pole and the Gaussian modal responses according to Equations (9.70) and (9.89) respectively gives the following integral

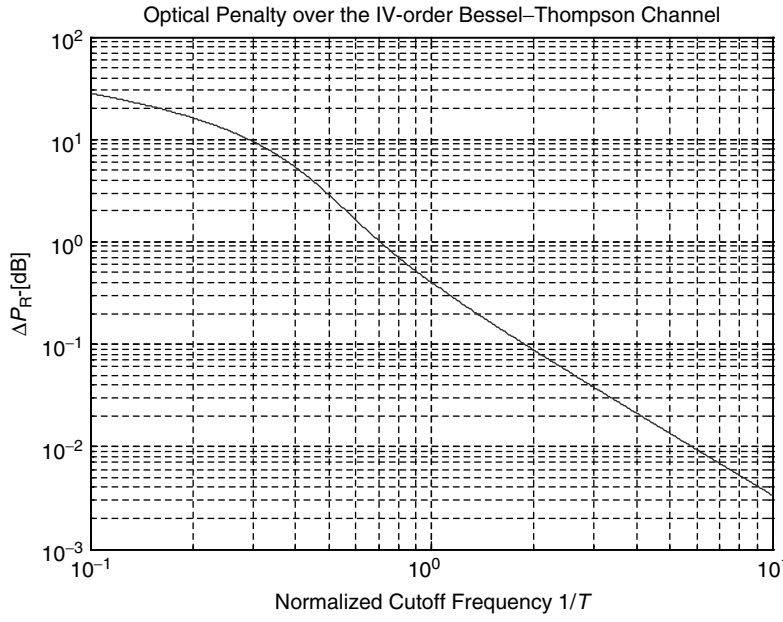

Figure 9.25 Logarithmic plot representation of the optical power penalty for the fourth-order Bessel–Thompson channel with unit roll-off of the raised cosine spectrum. At a half bit rate cut-off, the optical power penalty reaches about $\Delta P_R \cong 2.8\,\text{dB}$, as for the Gaussian channel

representations of the optical power penalties for the generic roll-off coefficient m of the raised cosine output spectrum:

$$\begin{aligned}
\underset{\text{Single-pole}}{\Delta P_R} &= 5\log_{10}\left\{2\int_0^{(1-m)/2}\left(1+\frac{x^2}{\alpha^2}\right)\mathrm{d}x\right. \\
&\qquad \left. +2\int_{(1-m)/2}^{(1+m)/2}\left(1+\frac{x^2}{\alpha^2}\right)\cos^2\left[\frac{\pi}{2m}\left(x-\frac{x}{|x|}\,\frac{(1-m)}{2}\right)\right]\mathrm{d}x\right\} \\
\underset{\text{Gaussian}}{\Delta P_R} &= 5\log_{10}\left\{2\int_0^{(1-m)/2}\mathrm{e}^{(x^2/\alpha^2)2\ln 2}\,\mathrm{d}x\right. \\
&\qquad \left. +2\int_{(1-m)/2}^{(1+m)/2}\mathrm{e}^{(x^2/\alpha^2)2\ln 2}\cos^2\left[\frac{\pi}{2m}\left(x-\frac{x}{|x|}\,\frac{1-m}{2}\right)\right]\mathrm{d}x\right\}
\end{aligned} \tag{9.99}$$

The explicit detailed expression for the fourth-order Bessel–Thompson response, which can be easily derived from Equations (9.98), (9.93) and (9.84), is omitted. In particular, setting $m = 1$ in Equation (9.99) gives the same expressions found in Equations (9.85) and (9.91) respectively. Figure 9.26 shows the computed optical power penalties for the three cases of single-pole, Gaussian and fourth-order Bessel–Thompson responses, assuming in each case the following four different values of the shaping factor, $m = 0$, $m = 0.25$, $m = 0.50$ and $m = 1$. It can be seen immediately that the case $m = 0$ leads to the lower optical power penalty for each response. This conclusion is expected because the case $m = 0$ has the narrowest signal bandwidth available for the given signaling rate and the amount of equalization noise due to high-frequency enhancement is consequently the lowest available for that configuration.

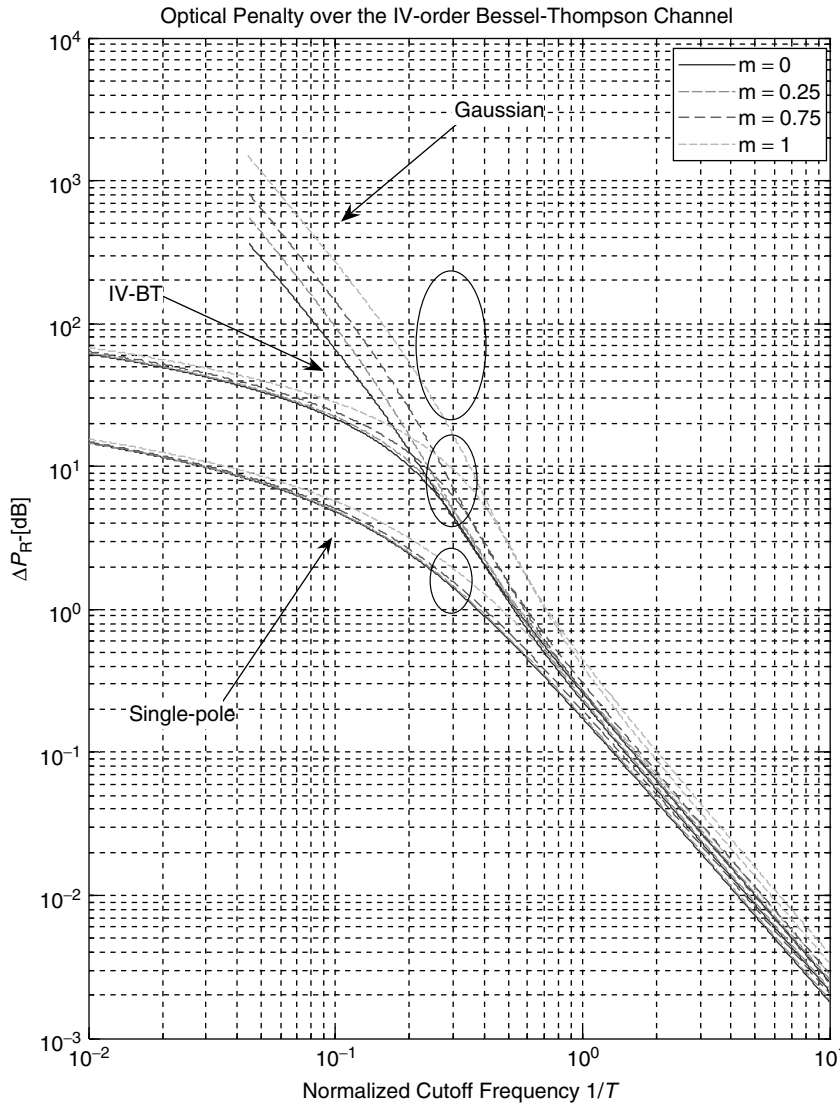

Figure 9.26 Computed optical power penalties for the single-pole, Gaussian and fourth-order Bessel–Thompson modal responses, assuming different values of the raised cosine roll-off coefficient. Increasing values of the shaping coefficient correspond to increasing high frequency content in the output signal spectrum which, requiring larger amounts of equalization, drags more noise and leads to larger optical penalties. The Nyquist shaping with $m = 0$ gives the absolute lowest optical penalty for every modal bandwidth. The encircled regions highlight the optical power penalties evaluated at cut-off frequencies about 10 % of the frequency bit rate. In this region the Gaussian channel leads to an optical power penalty approximately one order of magnitude higher than the fourth-order Bessel–Thompson channel

The computed plots in Figure 9.26 show clearly two different behaviors at relatively low and high values of the normalized cut-off frequency. At a higher cut-off frequency, under relatively broadband channel transmission, the optical power penalty achieved by the inverse linear equalization is almost the same for all three channel models selected. Some differences are still recognizable relative to the shaping coefficient of the raised cosine output spectrum. According to the peculiar square-law detection of the optical signal, in the broadband region the optical power penalty decreases with a double slope versus the increasing cut-off frequency of the fiber channel. At a narrower channel bandwidth, the equalization penalty depends more specifically on the selected channel modeling. It is clear that the single-pole modal response leads to the lowest equalization penalty, while the Gaussian modal response determines the highest relative value of the optical penalty. The fourth-order Bessel–Thompson response is between these responses. The reason for this behavior is easily understood in terms of the different amount of equalization required at higher frequencies. The sharpest Gaussian profile requires the more consistent high-frequency peaking in the inverse linear equalizer, leading to the highest noise enhancement assuming white noise distribution. The opposite happens for the single-pole channel, where the smoothest response requires the weakest equalization, leading to minimum noise dragged into the system.

Figure 9.26 shows that the lowest optical power penalty is associated with the roll-off coefficient $m = 0$. This conclusion holds for every value of the normalized cut-off frequency of each one of the represented modal responses. Setting $m = 0$ in Equations (9.97) and (9.99) gives the following simple expressions of the optical power penalties, where only the multimode fiber response is present:

$$\begin{aligned}
\Delta P_{\underset{\text{Single-pole}}{\text{R}}} &= 5\log_{10}\left[2\int_0^{1/2}\left(1+\frac{x^2}{\alpha^2}\right)\mathrm{d}x\right]_{(m=0)} \\
\Delta P_{\underset{\text{Gaussian}}{\text{R}}} &= 5\log_{10}\left[2\int_0^{1/2}\mathrm{e}^{(x^2/\alpha^2)2\ln 2}\,\mathrm{d}x\right]_{(m=0)} \\
\Delta P_{\underset{\text{IV-BT}}{\text{R}}} &= 5\log_{10}\left[2\int_0^{1/2}\left|1+\mathrm{j}\frac{a}{\alpha}x-\frac{3}{7}\left(\frac{ax}{\alpha}\right)^2-\mathrm{j}\frac{10}{105}\left(\frac{ax}{\alpha}\right)^3+\frac{1}{105}\left(\frac{ax}{\alpha}\right)^4\right|^2\mathrm{d}x\right]_{(m=0)}
\end{aligned} \tag{9.100}$$

In the next section, the relevant consequences of this choice of shaping coefficient will be seen. The case $m = 0$ has a particular relevance. It defines the Nyquist channel response characterized by having the receiver with the minimum bandwidth required for the given signal bit rate. Since the extension of the signal spectrum required at the equalizer output is the minimum available for that signaling rate, the amount of required equalization for a given multimode fiber modal response is consequently also the minimum.

This reasoning leads to the fundamental concept of the minimum available optical power penalty for every specific channel response profile and to the definition of the optical channel metric for the ideal inverse filter equalizer. Similar concepts will be introduced in the next chapter concerning digital equalizations and the related definition of the channel metrics for digital equalizers.

9.3.5 Penalty of the Inverse Filter Equalizer (IFE)

The frequency profile of the raised cosine output spectrum is determined by the roll-off coefficient, as sketched in Figure 9.27. The case $m = 0$ defines the ideal Nyquist spectrum and has the fundamental property of exhibiting the smallest frequency content available for the given signal rate.

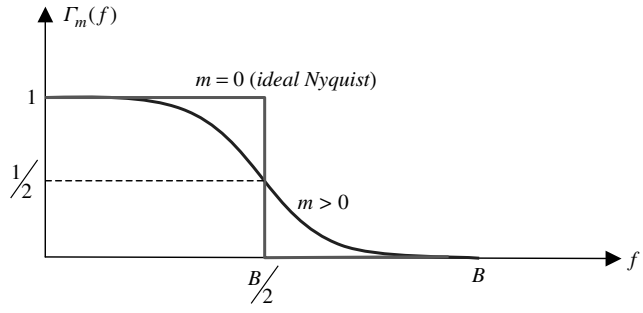

Figure 9.27 Raised cosine frequency profile versus the roll-off coefficient. The spectrum refers to the bit rate B

A very interesting feature of the ideal Nyquist spectrum is that it does not depend on the frequency: it is constant up to a half bit rate. In the following, the ideal Nyquist spectrum will be assumed to be available at the decision section of the inverse filter equalizer in the optical reference system in Figure 9.18. The corresponding optical power penalty in Equation (9.84) takes the following simple but relevant form, where the normalized frequency variable $x = fT$ is introduced:

$$\underset{(m=0)}{\Delta P_{\mathrm{R}}} = 5\log_{10}\left[2\tau^2\int_0^{1/2}\frac{1}{|H_F(x)|^2}\,\mathrm{d}x\right] \tag{9.101}$$

The normalization assumptions of the multimode fiber response are $|H_{\mathrm{F}}(0)| = \tau$. Introducing the new notation $\mathrm{PIE_I} \equiv \underset{(m=0)}{\Delta P_{\mathrm{R}}}$, the expression (9.101) is defined as the optical power penalty of the ideal inverse filter equalizer ($\mathrm{PIE_I}$, or penalty of the ideal equalizer (inverse)):

$$\mathrm{PIE_I} = 5\log_{10}\left[2\tau^2\int_0^{1/2}\frac{1}{|H_{\mathrm{F}}(x)|^2}\,\mathrm{d}x\right], \qquad |H_{\mathrm{F}}(0)| = \tau \tag{9.102}$$

The important conclusion is that the optical power penalty $\mathrm{PIE_I}$ depends only on the fiber channel response and refers to the ideal inverse filter equalizer (IFE). According to Equations (9.102), the following statements apply:

1. The function $\mathrm{PIE_I}$ is the optical channel metric for evaluating the transmission performances of the multimode fiber link assuming the ideal inverse filter equalizer (IFE).
2. The subscript I added to the notation of $\mathrm{PIE_I}$ indicates that the optical power penalty refers to the 'ideal' IFE.
3. The Nyquist reference channel is defined as the reference transmission system in Figure 9.18 where both the transmitter and the receiver frequency responses have raised cosine profiles with the ideal ($m = 0$) roll-off coefficient.

This definition is important for understanding the meaning of the Nyquist reference channel in the linear equalizer theory. These concepts will be used again later in Chapter 10 in the section dedicated to digital equalizers, with some relevant differences. Figure 9.28 gives a block diagram of the Nyquist reference channel.

The optical power penalty $\mathrm{PIE_I}$ for the ideal inverse filter equalizer working over the single-pole channel can be easily solved in closed mathematical form. Substituting the frequency response (9.70)

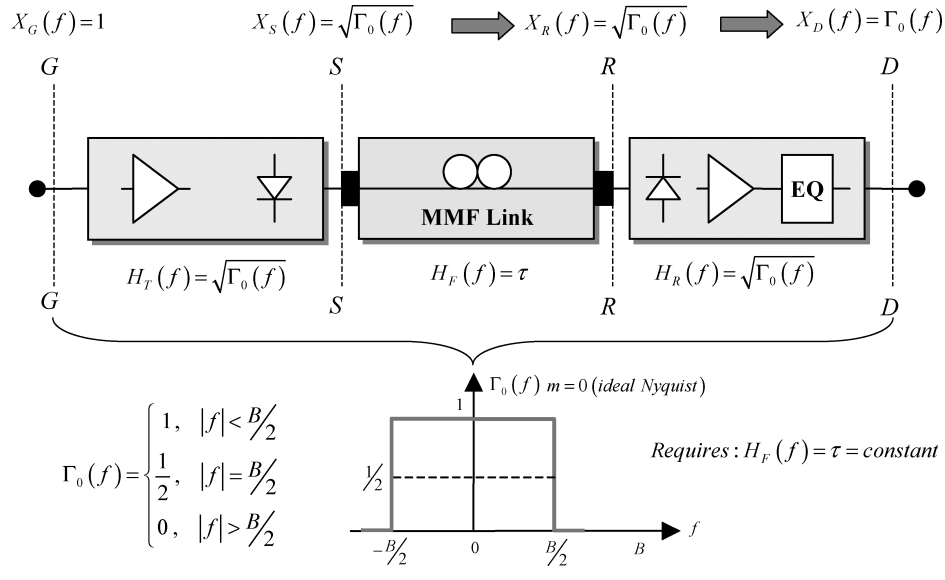

Figure 9.28 Schematic representation of the ideal Nyquist channel as the reference channel used for the definition of the optical power penalty PIE_I for the inverse filter equalizer

into Equations (9.102) gives the corresponding optical power penalty for the single-pole modal response already derived in Equation (9.100):

$$\underset{\text{Single-pole}}{PIE_I} = 5\log_{10}\left[2\int_0^{1/2}\left(1+\frac{x^2}{\alpha^2}\right)dx\right] = 5\log_{10}\left(1+\frac{1}{12\alpha^2}\right) \tag{9.103}$$

Unfortunately, the same mathematical closed form is not available for both the Gaussian and the fourth-order Bessel–Thompson modal responses and in that case, reference must be made to the numerical calculation of PIE_I using the respective responses in Equations (9.89) and (9.93).

Table 9.4 gives the PIE_I values computed using the expression (9.102) and assuming respectively the single-pole response in Equation (9.70), the Gaussian response in Equation (9.89) and the fourth-order Bessel–Thompson response in Equations (9.93).

Figure 9.29 shows the corresponding PIE_I plots versus normalized cut-off frequencies. All these results are valid for the ideal Nyquist channel, assuming that the roll-off coefficient of the raised cosine signal spectrum at the decision section is zero.

Once the reference transmission system and the ideal inverse filter equalizer have been defined, the optical power penalty PIE_I depends exclusively on the fiber modal response. In other words, PIE_I is a measure of the quality of the transmission fiber channel. It is the optical channel metric. The smaller the PIE_I, the better does the multimode link behave. Using PIE_I it is therefore possible to compare different multimode fiber links in terms of their capability to transfer information at the multigigabit rate. The fiber whose response leads to the lowest PIE_I value behaves as the best link among the available population. The large variability of PIE_I (dB_{10}) at low cut-off values shown with respect to the modal profile chosen and the dependence of the modal profile on the environmental conditions make the equalization definition a very complicated task.

In the following, the Matlab® scripts are given for the calculation of PIE_I assuming respectively the single-pole, the Gaussian and the fourth-order Bessel–Thompson responses.

Table 9.4 Optical power penalty values computation for the single-pole, the Gaussian and the fourth-order Bessel–Thompson modal responses. From the reported data, it is concluded that at every cut-off frequency the single-pole modal response guarantees the lowest value of PIE_I. The optical power penalty relative to the Gaussian and the fourth-order Bessel–Thompson modal responses suddenly increases for cut-off frequencies below 30 % of the bit rate frequency

$\alpha = f_c T$	PIE_I (dB_{10}) Single-pole	PIE_I (dB_{10}) Gaussian	PIE_I (dB_{10}) IV-BT
0.1000	4.8502	65.9360	21.5111
0.2000	2.4451	12.7389	10.0339
0.3000	1.4232	4.3360	4.4766
0.4000	0.9104	2.0568	2.0755
0.5000	0.6247	1.1985	1.1355
0.6000	0.4521	0.7887	0.7185
0.7000	0.3411	0.5605	0.4999
0.8000	0.2658	0.4199	0.3701
0.9000	0.2126	0.3268	0.2860
1.0000	0.1738	0.2619	0.2281
1.5000	0.0790	0.1135	0.0979
2.0000	0.0448	0.0633	0.0545
5.0000	0.0072	0.0100	0.0086
10.0000	0.0018	0.0025	0.0021

9.3.5.1.1 Single-Pole Response

```
% The program computes the PIE_I for the Single-pole channel
% according to (9.103).
%
clear;
xo_min=0.01; % Minimum normalized cut-off
Np=100; % Number of frequency points per decade
x1_min=xo_min;
x1=(x1_min:x1_min/Np:10*x1_min-x1_min/Np);
x2_min=10*x1_min;
x2=(x2_min:x2_min/Np:10*x2_min-x2_min/Np);
x3_min=10*x2_min;
x3=(x3_min:x3_min/Np:10*x3_min-x3_min/Np);
xo=[x1 x2 x3];
for k=1:length(xo),
    PIEI(k)=5*log10(1+1/(12*xo(k)^2));
end;
loglog(xo,PIEI,'r');
grid on;
title('Penalty of the Ideal Inverse Filter Equalizer over the Single-pole
   Channel');
xlabel('Normalized Cutoff Frequency 1/T');
ylabel('PIE_ _I - [dB_1_0]');
hold on;
```

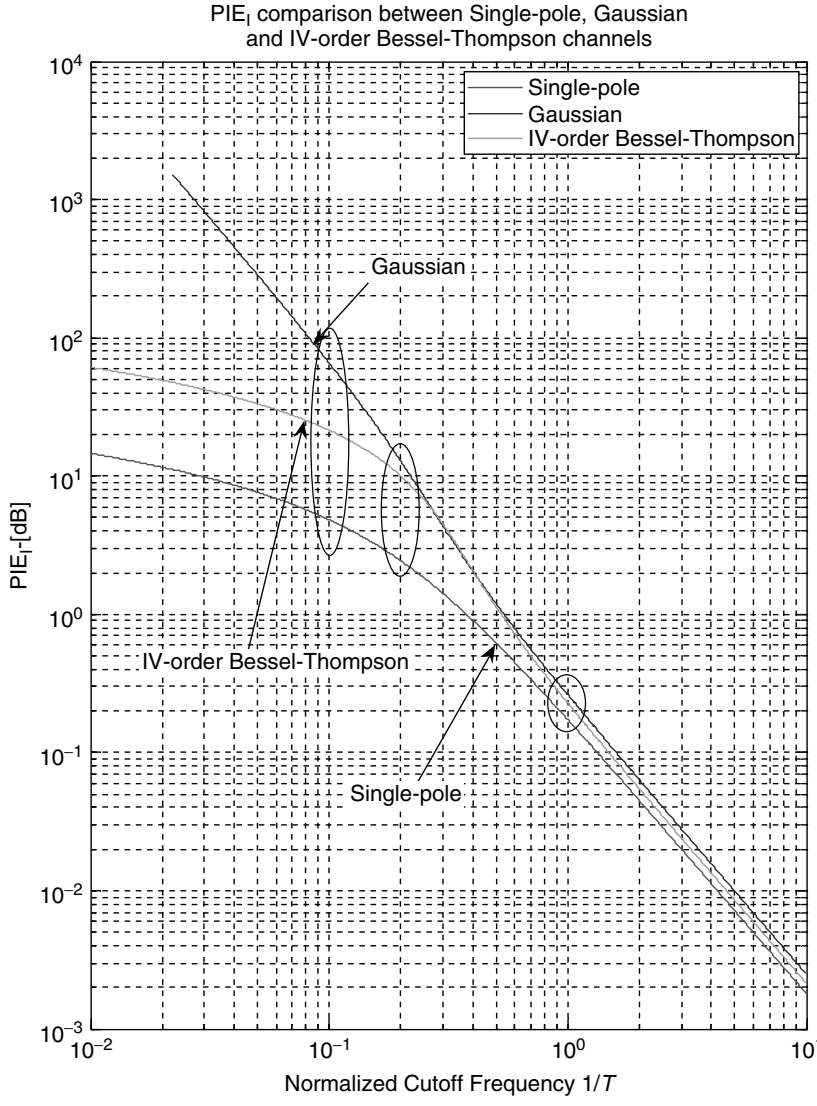

Figure 9.29 Computed PIE_I according to Equation (9.102) for three different multimode fiber responses: Gaussian, single-pole and fourth-order Bessel–Thompson. The comparison reveals the characteristic smoothed high-frequency roll-off of the single-pole response with respect to the sharpest Gaussian and Bessel–Thompson profiles. When the normalized modal response reaches about 60 % of the frequency bit rate the three responses show approximately the same penalty value, $PIE_I \sim 0.5$–0.8 dB. At lower modal cut-off, the Gaussian and the Bessel–Thompson responses increase much more rapidly, leading to almost the same value $PIE_I \sim 10$ dB at $\alpha \leq 0.2$. At decreasing cut-off values, the Gaussian response shows the worst behavior, reaching more than a 65 dB penalty at $\alpha \leq 0.1$. At the same cut-off value, the fourth-order Bessel–Thompson response exhibits about a 20 dB penalty and the smoother single-pole response remains below 5 dB

9.3.5.1.2 Gaussian Response

```
% The program computes the PIE_I for the Gaussian channel
% according to (9.102).
%
clear;
xo_min=0.01; % Minimum normalized cut-off
Np=100; % Number of frequency points per decade
x1_min=xo_min;
x1=(x1_min:x1_min/Np:10*x1_min-x1_min/Np);
x2_min=10*x1_min;
x2=(x2_min:x2_min/Np:10*x2_min-x2_min/Np);
x3_min=10*x2_min;
x3=(x3_min:x3_min/Np:10*x3_min-x3_min/Np);
xo=[x1 x2 x3];
dx=0.001;
x=(0:dx:+1/2-dx); % Integration interval
for k=1:length(xo),
    H=exp((x/xo(k)).^2*2*log(2));
    PIEI(k)=5*log10(2*sum(H)*dx);
end;
loglog(xo,PIEI);
grid on;
title('Penalty of the Ideal Inverse Filter Equalizer over the Gaussian
   Channel');
xlabel('Normalized Cutoff Frequency 1/T');
ylabel('PIE_ _I - [dB_1_0]');
hold on;
```

9.3.5.1.3 IV-Order Bessel–Thompson Response

```
% The program computes the PIE_I for the IV-order Bessel- Thompson channel
% according to (9.102).
%
clear all;
%
% Cut-off frequency range
%
xo_min=0.01; % Minimum normalized cut-off
Np=100; % Number of frequency points per decade
x1_min=xo_min;
x1=(x1_min:x1_min/Np:10*x1_min-x1_min/Np);
x2_min=10*x1_min;
x2=(x2_min:x2_min/Np:10*x2_min-x2_min/Np);
x3_min=10*x2_min;
x3=(x3_min:x3_min/Np:10*x3_min-x3_min/Np);
xo=[x1 x2 x3];
%
% IV-order Bessel- Thompson response
%
dx=0.01;
x=[dx:dx:100];
Cutoff=0.5;
eps=1e-6;
Left=0;
Right=10;
a=(Left+Right)/2;
yc=i*a;
```

```
Hc=105/(105+105*yc+45*yc^2+10*yc^3+yc^4);
Error=abs(Hc)-Cutoff;
while abs(Error)>eps,
    if Error>0,
        Left=a;
    else
        Right=a;
    end;
    a=(Left+Right)/2;
    yc=i*a;
    Hc=105/(105+105*yc+45*yc^2+10*yc^3+yc^4);
    Error=abs(Hc)-Cutoff;
end;
dx=0.001;
x=(0:dx:1/2-dx); % Integration interval for the power penalty
for k=1:length(xo),
    y=i*a*x/xo(k);
    H=105./(105+105*y+45*y.^2+10*y.^3+y.^4);
    PIEI(k)=5*log10(2*sum(1./(abs(H).^2))*dx);
end;
loglog(xo,PIEI,'g');
grid on;
title('Optical Penalty over the IV-order Bessel- Thompson Channel');
xlabel('Normalized Cutoff Frequency 1/T');
ylabel('PIE_ _I - [dB]');
hold on;
```

The numerical solution of the three cases presented shows clearly the benefits and the limitations of the ideal inverse filter equalizer. Due to the operating principle of high-frequency boosting to compensate for the channel bandwidth roll-off, the principal limitation of the IFE is the noise enhancement due to noise bandwidth amplification operated in the equalization section. Depending on the amount of equalization required, the IFE can accomplish satisfactory results or unacceptable noise corruption. This is the case of the single-pole channel response, where the smoother profile allows for correspondingly smooth equalization, leading to a few dB of optical power penalty even in the case of strong channel limitation. This is clearly quantified in Figure 9.29, where assuming a single-pole normalized cut-off of only 10 % of the signal bit rate requires less than 5 dB of optical power penalties. The same value of channel cut-off, but referred to a steeper frequency profile like the fourth-order Bessel–Thompson or the Gaussian responses, leads to unacceptable noise degradation, exceeding 20 dB and 60 dB respectively of optical power penalties.

9.4 Conclusions

In this chapter, the basic concepts and expressions have been introduced of the theory of the decision process in binary digital optical transmission with Gaussian white noise. Section 9.2 introduced noise modeling for optical fiber transmission. Different noise terms have been presented and the relative mathematical equations have been used in several examples to compare their respective contributions to system performance degradation. In particular, the distinction of noise contributions into the basic three categories of constant, linear and quadratic dependent terms from the received optical power have been detailed and their progressive contributions at increasing power levels have been analyzed. The classical bit error rate formula has been presented with some applications to fiber optic systems. The relationship with the signal-to-noise power in the electrical domain has been derived for several signal models.

Section 9.3 introduced the ideal inverse filter equalizer (IFE). This basic electrical equalizer will be used as the reference for the comparison between more suitable digital architectures. In particular, the characteristic noise enhancement factor of IFE has been quantitatively compared among three different channel models, namely the single-pole, the Gaussian and the fourth-order Bessel–Thompson responses. Closely related to the optical power penalty is the concept of the channel metric PIE_I for the ideal inverse filter equalizer. The concept of the penalty of the ideal inverse linear equalizer presented in this section will be extended using the penalty of the ideal digital equalizer according to the minimum mean square error (MMSE) optimization criteria. It will be seen that for relatively low dispersion, the linear equalization might have some benefits over the digital counterpart, but at relatively large dispersions the situation changes in favor of the digital equalizer. The digital equalizer represents today a better solution for extending the length operability of multimode fiber links compliant to IEEE 802.3 standard 10GBASE-LRM. The expression of PIE_I has been obtained with an original derivation based on the concept of noise bandwidth enhancement. The smoothed single-pole channel is suitable for compensation using the ideal inverse filter equalizer, leading to a residual penalty of less then 5 dB over only 10 % of the channel bandwidth. The conclusions are quite different when assuming steeper channel responses, such as those of the Gaussian or the fourth-order Bessel–Thompson profiles. In these cases, the inverse filter equalizer is not suitable and so different, more efficient solutions must be conceived. The expression of the channel metric for the inverse filter equalizer will be compared in the next chapter with the equivalent expressions derived for the feedforward equalizer and the decision feedback equalizer, for quantitatively classifying multimode fiber links.

10

Decision Feedback Equalization

Expanding Multimode Fiber Capabilities

10.1 Introduction

In this chapter the theory and applications will be presented of the electronic dispersion compensator (EDC) implemented using the decision Feedback Equalizer (DFE). The theory of the DFE has been developed for more than thirty years and the DFE has found many successful applications in compensating channel distortion in multipath radio link since the 1970s. The theory developed by J. Salz is presented and reference to his will be made fundamental paper 'Optimum Mean-Square Decision Feedback Equalization'.[1] This book is intended to give a self-consistent analysis of multigigabit transmission over multimode fibers, but the analysis and design of the EDC structure is outside the scope. Nevertheless, a detailed theory of operation of the DFE is presented in this chapter, assuming ideal systems assembled with digital filters of infinite length. This approach leads to relevant conclusions and underlines the interaction among the principal parameters affecting the EDC performances. The channel response and the noise-to-signal ratio play a dominant role in the ideal DFE performance and in this chapter an exhaustive treatment of three basic analytical channel models will be presented, namely the single-pole, the Gaussian and the fourth-order Bessel–Thompson frequency responses. The theory to be presented is limited to time-invariant linear systems and according to the work of J. Salz, the equalizer optimization is based on the mean square error minimization.

The last section presents a block diagram structure of a typical electronic dispersion compensator based on the decision feedback equalizer. The principal blocks are analyzed, highlighting the role of the main parameters.

10.2 Principles of Digital Equalization

In Chapter 9 the limitation of the linear equalization over noisy channels in the presence of either severe frequency attenuation or frequency nulls in the amplitude characteristic was discussed. Faster data pulse rates place signal energy well within the high-frequency part of the spectrum where the badly attenuated multimode fiber response results in a consistent intersymbol interference pattern. As demonstrated in Chapter 9, severe intersymbol interference can in principle be corrected by

[1] J. Salz, 'Optimum Mean-Square Decision Feedback Equalization', *The Bell System Technical Journal*, **52** (8), October 1973.

Multi-Gigabit Transmission over Multimode Optical Fibre: Theory and Design Methods for 10GbE Systems Stefano Bottacchi
 ISBN: 0-471-89175-4

linear methods only at the expense of a significant noise enhancement, which in turn makes most of the interference cancellation meaningless for improving receiver performances.

A great deal of research was expended more than forty years ago on the linear equalization problems and a huge amount of literature is available on those subjects. In this section, reference will be made to the mean square error (MSE) minimization procedure using the well-known decision feedback equalization (DFE) proposed by J. Salz in his paper 'Optimum Mean-Square Decision Feedback' describing his pioneering works on this subject at Bell Laboratories at the beginning of the 1970s. A meaningful picture is given of the decision feedback equalizer described in this paper by J. Salz:

> A 'bootstrap' technique, commonly referred to as 'decision feedback', when combined with linear equalization can yield significant performance improvements. In this method the samples of the pulse tails (postcursors) interfering with subsequent or future data symbols are subtracted without incurring a significant noise penalty. The effect of pulse tails (precursors) which occur prior to detection and interfere with past symbols is minimized by a conventional linear equalizer. ... We minimize mean-square error ... that allows trade-offs between added noise and intersymbol interference.

10.2.1 Problem Formulation and Modeling

The analysis starts by referring to the transmission system model shown in Figure 10.1 and including the basic block diagram of the decision feedback equalizer. In this case no particular condition will be assumed on either the transmitter or the receiver. In particular, transmitter and receiver frequency responses will not be required *a priori* as in the previous case of the reference transmission system shown in Figure 10.1 dealing with linear equalization. Unless otherwise stated, in the following derivation time domain signals will be used almost exclusively. The input signal is constituted by a random sequence of binary data symbols $\{\underline{a}\}$ picked at the rate $B = 1/T$ and, taking on values with equal probability, form the set $\{-1, +1\}$. At the sampling time $t_n = nT$ the random variable $\underline{a}$ collapses upon the symbol $a_n \in \{\underline{a}\}$, $P\{a_n = -1\} = P\{a_n = +1\} = \frac{1}{2}$. Here the bipolar binary signal is used in order to simplify the mathematical treatment. Since the analysis is developed in the electrical domain, this assumption does not influence the physical consistency of the optical signals.

The input random signal $\underline{G}(t)$ is available at the generator section $G-G'$ (see Figure 10.1) and is constituted by the sequence of equidistant delta impulses weighted by the random symbols $\underline{a}_n \in \{\underline{a}\}$:

$$\underline{G}(t) = \sum_{n=-\infty}^{+\infty} \underline{a}_n \delta(t - nT) \tag{10.1}$$

The impulsive random sequence $\underline{G}(t)$ feeds the first part of the linear channel composed of the optical transmitter and the multimode optical fiber, characterized by the impulse responses $h_T(t)$ and $h_F(t)$ respectively. The impulsive sequence $\underline{G}(t)$, after passing through the impulse responses $h_T(t)$ and $h_F(t)$, is converted into the corresponding pulse sequence, according to the same random weighting of the source (10.1).

In the following derivation, the procedure used in the paper of J. Salz will be used. In order to proceed as clearly as possible, first the dimensional gauge (ansatz) of the variables involved is defined. Conjugate linear variables in the time and frequency domains are related by the Fourier integral representation. Referring to Figure 10.1, the following ansatz will be assumed:

1. The impulse response of the optical transmitter $h_T(t)$ has the dimension of s^{-1}. This implies that the frequency response $H_T(\omega)$ is dimensionless:

$$h_T(t) \quad (s^{-1}) \Rightarrow H_T(\omega) = \frac{1}{2\pi} \int_{-\infty}^{+\infty} h_T(t) e^{+j\omega t} \, dt \tag{10.2}$$

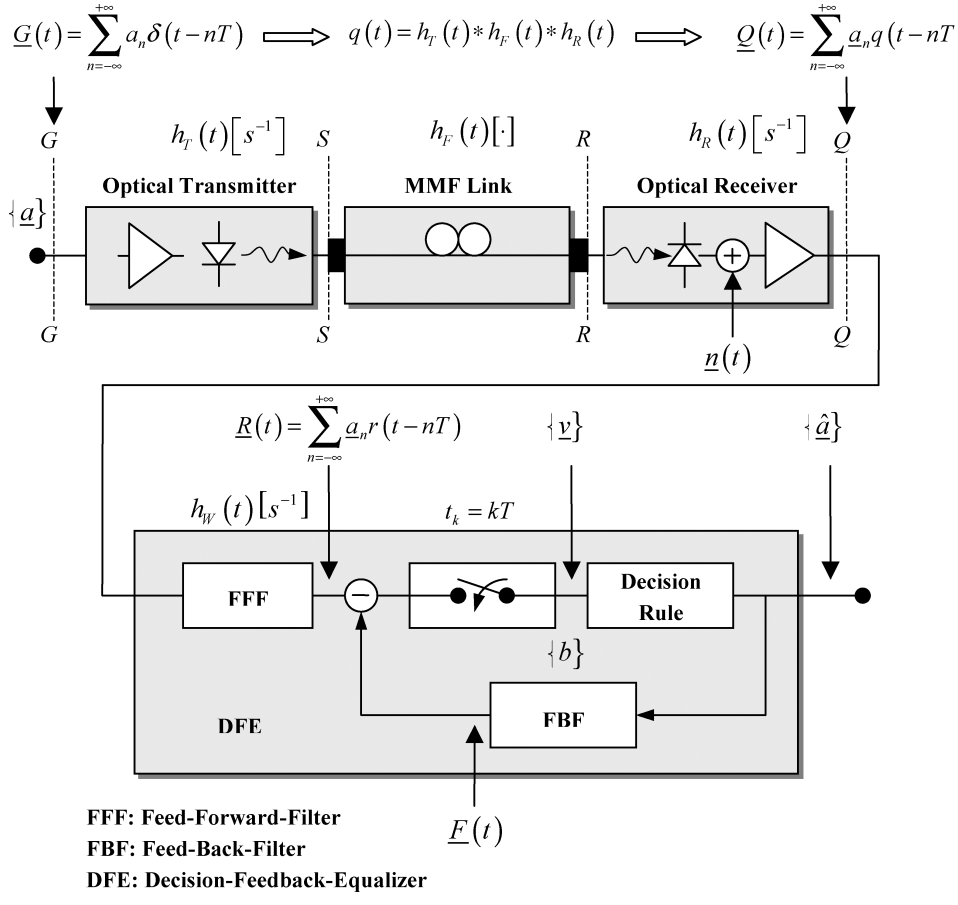

Figure 10.1 Block diagram of the transmission system using the decision feedback equalizer architecture. The transmission system is assumed to be linear up to the sampler block. The optical transmitter, the multimode fiber and the optical receiver are characterized by generic impulse responses. The input symbol random sequence is $\{\underline{a}\}$ while the output received symbol random sequence is $\{\underline{\hat{a}}\}$. The equalizer task is to provide symbol-by-symbol $\hat{a}_k = a_k$ with the minimum mean square error

2. The impulse response of the multimode fiber $h_{\mathrm{F}}(t)$ is assumed to be dimensionless and the corresponding frequency response $H_{\mathrm{F}}(\omega)$ has the dimension of time (s):

$$h_{\mathrm{F}}(t) \Rightarrow H_{\mathrm{F}}(\omega) = \frac{1}{2\pi}\int_{-\infty}^{+\infty} h_{\mathrm{F}}(t)\mathrm{e}^{+\mathrm{j}\omega t}\,\mathrm{d}t \quad \text{(s)} \tag{10.3}$$

3. The impulse response of the optical receiver $h_{\mathrm{R}}(t)$ has the dimension of s^{-1} and the corresponding frequency representation $H_{\mathrm{R}}(\omega)$ is dimensionless:

$$h_{\mathrm{R}}(t) \quad (\mathrm{s}^{-1}) \Rightarrow H_{\mathrm{R}}(\omega) = \frac{1}{2\pi}\int_{-\infty}^{+\infty} h_{\mathrm{R}}(t)\mathrm{e}^{+\mathrm{j}\omega t}\,\mathrm{d}t \tag{10.4}$$

4. The impulse response $q(t)$ of the cascaded linear subsystems, composed of the optical transmitter, the multimode fiber and the optical receiver, otherwise stated as the channel and reported in the

following expression, is dimensionless, while the frequency response $Q(\omega)$ of the channel has the dimension of time (s):

$$q(t) = h_T(t) * h_F(t) * h_R(t) \Rightarrow Q(\omega) = \frac{1}{2\pi}\int_{-\infty}^{+\infty} q(t)e^{+j\omega t}\,dt \quad \text{(s)} \tag{10.5}$$

5. The impulse response of the feedforward filter (FFF), $h_W(t)$, has the dimension of s^{-1} and the frequency response $H_W(\omega)$ is therefore dimensionless:

$$h_W(t) \quad (s^{-1}) \Rightarrow H_W(\omega) = \frac{1}{2\pi}\int_{-\infty}^{+\infty} h_W(t)e^{+j\omega t}\,dt \tag{10.6}$$

6. The impulse response $r(t)$ at the sampler input is dimensionless and the corresponding spectrum has the dimension of time (s):

$$r(t) = q(t) * h_W(t) \Rightarrow R(\omega) = \frac{1}{2\pi}\int_{-\infty}^{+\infty} r(t)e^{+j\omega t}\,dt \quad \text{(s)} \tag{10.7}$$

The optical signal available at the optical fiber output is then detected by the photodiode and converted into electrical current at the input of the optical receiver. The electrical amplifier provides the required amplification and transimpedance function. The impulse response of the complete optical receiver $h_R(t)$ includes both the photodiode and the transimpedance function.

The impulse response $q(t)$ of the linear chain including the optical transmitter, the multimode fiber and the optical receiver is then given by convolution of the corresponding individual responses:

$$q(t) = h_T(t) * h_F(t) * h_R(t) = \int_{-\infty}^{+\infty} h_R(t-\tau_2)\int_{-\infty}^{+\infty} h_T(\tau_1)h_F(\tau_2-\tau_1)\,d\tau_1\,d\tau_2 \tag{10.8}$$

Referring to Figure 10.1 and to expressions (10.1) and (10.8), the signal at the section $Q-Q'$ is given by the following expression:

$$\underline{Q}(t) = \sum_{n=-\infty}^{+\infty} \underline{a}_n q(t-nT) \tag{10.9}$$

Note that the random nature of the signal $\underline{Q}(t)$ is consequent to the random sequence $\{\underline{a}\}$ and not to the deterministic impulse response $q(t)$. The signal at the section $Q-Q'$ is affected by the input equivalent noise $\underline{n}(t)$. It is assumed that the noise is a zero-mean white random process characterized by the double-sided uniform power spectral density (white noise) G_i. The received electrical signal $\underline{Q}(t)$ plus noise is then processed by the decision feedback equalizer (DFE) reported in Figure 10.1, which is comprised of the linear digital filter (FFF) having the impulse response $h_W(t)$, the sampler, the decision rule for selecting the detected digital state and the feedback digital filter (FBF) characterized by the infinite set of real coefficients $\{b\}$. The symbol sequence at the decision output is identified by $\{\underline{\hat{a}}\}$. In other words, the sequence $\{\underline{\hat{a}}\}$ represents the received and detected symbol sequence corresponding to the input launched sequence $\{\underline{a}\}$. J. Salz gives the following problem statement:

> The general problem we would like solve is the symbol-by-symbol optimization by minimizing the mean square error (MSE) between the sampled symbol v_k and the corresponding launched symbol a_k for every sampling time instant $t_k = kT$:
>
> $$\underline{\varepsilon}_k \equiv \underline{v}_k - a_k$$
> $$\underset{(t=kT)}{\text{MSE}} = E\{\underline{\varepsilon}_k^2\} = E\{(\underline{v}_k - a_k)^2\} \tag{10.10}$$

10.2.2 Open-Loop Samples

The signal $\underline{R}(t)$ at the output of the linear feedforward filter is given by the convolution of the received signal $\underline{Q}(t)$ in Equation (10.9) with the impulse response $h_W(t)$ of the feedforward filter. Indicating the overall impulse response at the FFF output with $r(t)$, from Equation (10.8) and (10.9),

$$r(t) = q(t) * h_W(t) = h_T(t) * h_F(t) * h_R(t) * h_W(t) \tag{10.11}$$

and

$$\underline{R}(t) = \sum_{n=-\infty}^{+\infty} \underline{a}_n r(t - nT) \tag{10.12}$$

In order to make a step forward in the analysis, it is convenient to derive the open-loop signal sample available at the output of the sampler at the instant $t_k = kT$. The next section will analyze this configuration.

10.2.2.1 The Signal Sample

Referring to the transmission system model reported in Figure 10.1, we open therefore the feedback loop disconnecting the output of the feedback filter FBF from the summation node is opened and the sample $\underline{R}_k = \underline{R}(kT)$ of the signal $\underline{R}(t)$ at the feedforward filter output is evaluated. From Equation (10.12), the open-loop sample at the instant $t_k = kT$ is given by the following sum:

$$\underline{R}_k = \sum_{n=-\infty}^{+\infty} \underline{a}_n r[(k - n)T] \tag{10.13}$$

Note that the sample $\underline{R}_k$ is a random variable since it depends on the entire random symbol sequence $\{\underline{a}\}$ launched at the input section. It is important at this point to investigate a little further the structure of the sample $\underline{R}_k$.

First, the following notation is introduced for the sample amplitude of the overall impulse response:

$$r[(k - n)T] \equiv r_{k-n} \tag{10.14}$$

Setting $n = k$, the symbol $\underline{a}_k$ and the corresponding sampled pulse amplitude $r_0 = r(0)$ are identified at the selected sampling time instant $t_k = kT$. Without losing in generality, the series (10.13) can conveniently be decomposed into the following three terms, where the notation defined in Equation (10.14) is used:

$$\underline{R}_k = \sum_{n=-\infty}^{+\infty} \underline{a}_n r_{k-n} = \underline{a}_k r_0 + \sum_{n=-\infty}^{k-1} \underline{a}_n r_{k-n} + \sum_{n=k+1}^{+\infty} \underline{a}_n r_{k-n} \tag{10.15}$$

The open-loop sample $\underline{R}_k$ in Equation (10.15) has a meaningful interpretation. The three terms will be analyzed separately:

1. The first term $\underline{a}_k r_0$ is the value of the isolated sampled symbol. This is the value of the sampled pulse in the absence of any intersymbol interference from adjacent pulse contributions weighted by the symbol $\underline{a}_k$. In other words, the term $\underline{a}_k r_0$ gives the pulse amplitude at the selected sampling time $t_k = kT$, assuming either zero intersymbol interference or isolated pulse transmission.
2. The series $\sum_{n=-\infty}^{k-1} \underline{a}_n r_{k-n}$ in the second term includes all the sample contributions with the index $-\infty < n \leq k - 1$. Substituting the index n into the samples r_{k-n} leads to left-shifted pulses, or anticipated pulses with respect to the sampling instant. The pulse body occurs prior to the

selected sampling instant. This can easily be seen by considering a few cases. For $n = k - 1$ the corresponding pulse sample evaluated at $t_k = kT$ is

$$r(t - nT) = r[t - (k - 1)T] \xrightarrow{t = kT} r(T) = r_1$$

For $n = k - 2$, $r_2 = r(2T)$ is obtained. In general, for $n = k - p$ with $p \geq 1$, $r_p = r(pT)$ is obtained. In conclusion, the following interpretation of the series of the anticipated pulses is given:

(a) The series $\sum_{n=-\infty}^{k-1} \underline{a}_n r_{k-n}$ in Equation (10.15) represents the sampled contribution of the tails of pulses $r(t)$ that are located to the right of the corresponding reference pulse body.
(b) Since the tail considered is trailing the main body of the pulse, the sum $\sum_{n=-\infty}^{k-1} \underline{a}_n r_{k-n}$ represents the intersymbol contribution of all pulse postcursors.

3. The series $\sum_{n=k+1}^{+\infty} \underline{a}_n r_{k-n}$ in the third term considers all the sample contributions with the index $k + 1 < n \leq +\infty$. Substituting the index n into the samples r_{k-n} leads in this case to right-shifted pulses, or delayed pulses with respect to the sampling instant $t_k = kT$. The pulse body occurs after the sampling instant. The first contribution occurs at the index value $n = k + 1$ and the corresponding pulse sample evaluated at $t_k = kT$ gives:

$$r(t - nT) = r[t - (k + 1)T] \xrightarrow{t = kT} r(-T) = r_{-1}$$

The second contribution comes from the index value $n = k + 2$ and gives $r_{-2} = r(-2T)$. In general, for $n = k + m$, $r_{k-n} = r_{-m} = r(-mT)$ is obtained. In conclusion, the following interpretation of the delayed pulse series is given:

(a) The sum $\sum_{n=k+1}^{+\infty} \underline{a}_n r_{k-n}$ represents the sampled contribution of the tails of the pulse $r(t)$ that are located to the left of the corresponding pulse body.
(b) Since the tail considered is leading the main body of the pulse, the sum $\sum_{n=k+1}^{+\infty} \underline{a}_n r_{k-n}$ represents the intersymbol contribution of the pulse precursors.

The decomposition of the sampled amplitude in terms of precursor and postcursor contributions is fundamental. Equation (10.15) is rewritten below highlighting this result:

$$\underline{R}_k = \underbrace{\underline{a}_k r_0}_{\text{Main sample}} + \underbrace{\sum_{n=-\infty}^{k-1} \underline{a}_n r_{k-n}}_{\text{Postcursor ISI}} + \underbrace{\sum_{n=k+1}^{+\infty} \underline{a}_n r_{k-n}}_{\text{Precursor ISI}} \tag{10.16}$$

Figure 10.2 shows a graphical representation of the single-impulse response $r(t)$ assuming in general different contributions between precursors and postcursors. The impulse response in Figure 10.2 is correctly represented on the time axis, which is what can be expected at a fixed electrical section. For example, it can be imagined that the pulse is propagating along a cable or an electrical waveguide and that the time evolution of the pulse at a fixed section $z = z_0$ is measured. Imagine now that the propagation description is reversed and several pictures are taken at fixed time instants of the pulse evolution along the spatial axis. Of course, in this description, the precursors can be seen to lead the pulse body and the postcursor follows it. In other words, the pulse precursor will be at the right side of the left-to-right propagating pulse, while the postcursor will follow it to the back side. This description is qualitatively represented in Figure 10.3.

Following this reasoning, it is evident that pulse precursors will interfere with past symbols, while pulse postcursors will interfere with future symbols. It will be seen below that the DFE architecture is capable of compensating only for the pulse postcursors, leaving the mitigation of the pulse precursors to the linear feedforward filter at the input section of the DFE. This is clearly shown in Figure 10.4, where the reference pulse centered at the sampling time $t = kT$ is subjected to tail

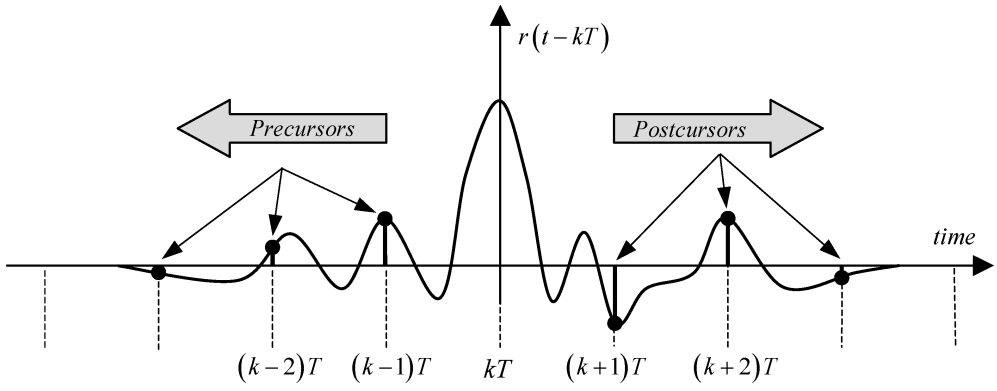

Figure 10.2 General impulse response $r(t)$ evaluated at the output of the feedforward filter. The pulse presents the main body located at the sampling time $t_k = kT$. The pulse tails that occur prior to the sampling time $t_{k-1}, t_{k-2}, \ldots, t_{k-m}, \ldots$ are defined as precursors. The pulse tails that occur after the sampling time $t_{k+1}, t_{k+2}, \ldots, t_{k+p}, \ldots$ are defined as postcursors

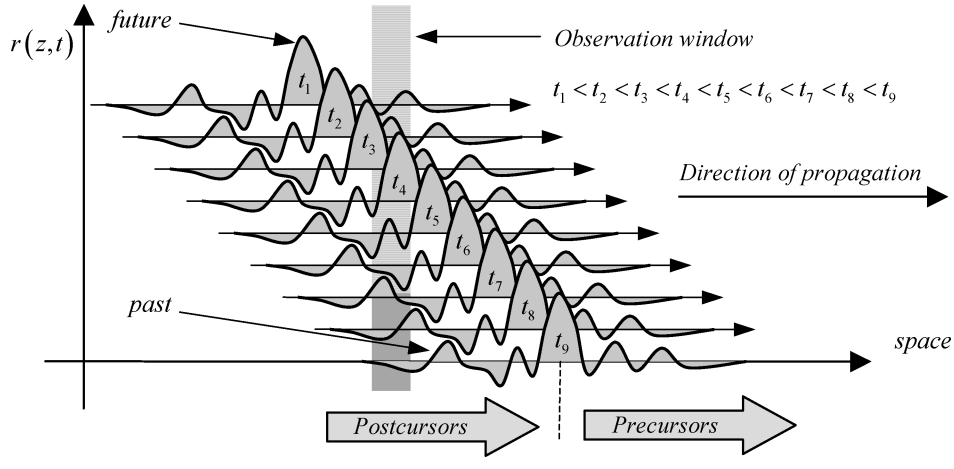

Figure 10.3 Spatial representation of the impulse response crossing the observation window. The precursors are on the pulse front, leading the pulse body, on the right side for the left-to-right propagation direction. On the contrary, postcursors are on the pulse back, following the pulse body

interference from both precursors of right-shifted (future) pulses and postcursors of left-shifted (past) pulses.

Changing the summation variable in Equation (10.16) by $j = k - n$, the two postcursor and precursor sums assume respectively the following forms:

$$\begin{aligned}
&\text{Signal postcursors} \Rightarrow \sum_{n=-\infty}^{k-1} \underline{a}_n r_{k-n} \underset{(j=k-n)}{=} \sum_{j=1}^{+\infty} \underline{a}_{k-j} r_j = a_{k-1} r_1 + a_{k-2} r_2 + \cdots \\
&\text{Signal precursors} \Rightarrow \sum_{n=k+1}^{+\infty} \underline{a}_n r_{k-n} \underset{(j=k-n)}{=} \sum_{j=-\infty}^{-1} \underline{a}_{k-j} r_j = a_{k+1} r_{-1} + a_{k+2} r_{-2} + \cdots
\end{aligned} \tag{10.17}$$

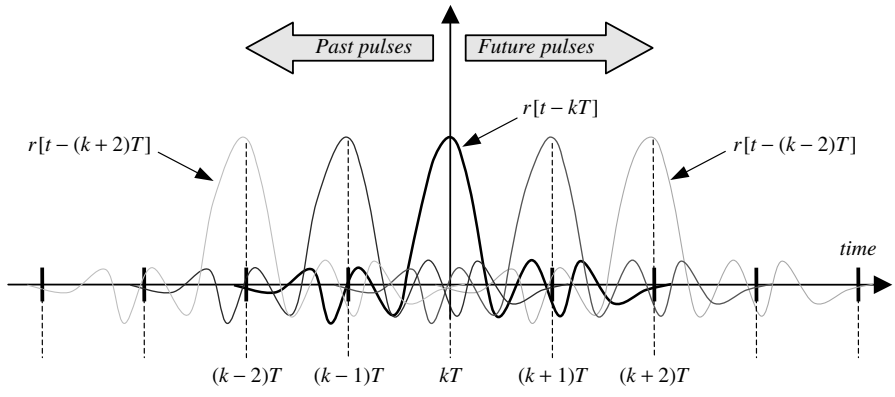

Figure 10.4 Graphical illustration of the interference between precursors and postcursors in the ISI composition at the sampling time $t_k = kT$. Future pulses interfere at the sampling time through their precursors. Past pulses interfere at the sampling time through their postcursors

After changing the summation index, the positive index sum refers to the postcursor interference term, while the negative index sum gives the precursor interference term. According to the new index $j = k - n$, at the index value $j = 1$ is associated with the first interfering term corresponding to the first postcursor sample. The dual situation occurs for $j = -1$ where the interfering term comes from the first precursor sample. Using the new notation and redefining the summation index as n, expression (10.16) can be written as follows:

$$\underline{R}_k = \sum_{n=-\infty}^{+\infty} \underline{a}_{k-n} r_n = \underbrace{\underline{a}_k r_0}_{\text{Main sample}} + \underbrace{\sum_{n=-\infty}^{-1} \underline{a}_{k-n} r_n}_{\text{Precursor ISI}} + \underbrace{\sum_{n=+1}^{+\infty} \underline{a}_{k-n} r_n}_{\text{Postcursor ISI}} \tag{10.18}$$

The above expression is the value of the sampled signal at the instant $t = kT$ evaluated at the FFF output and assuming an open-loop configuration.

10.2.2.2 The Feedback Sample

The feedback sample $\underline{F}_k$ in Figure 10.1 is constituted by the weighted sum of the output symbols $\{\underline{\hat{a}}\}$ through the deterministic sequence of coefficients $\{b\} = \{\ldots, b_k, b_{k+1}, \ldots\}$. Because of the inclusion of the random sequence $\{\underline{\hat{a}}\}$ of the output symbols, the feedback sample $\underline{F}_k$ is also a random variable. For the moment no further assumptions are made about the structure of the deterministic sequence of coefficients $\{b\} = \{\ldots, b_k, b_{k+1}, \ldots\}$. Since the ISI cancellation process by means of the feedback sample is to be investigated, the only recommendation that needs to be satisfied would be the exclusion of the reference symbol $\underline{\hat{a}}_k$ from the returned feedback sample setting the condition $n \neq k$. In that case, under the closed-loop configuration the information symbol of interest would be canceled out. Accordingly,

$$\underline{F}_k = \sum_{\substack{n=-\infty \\ n \neq k}}^{+\infty} \underline{\hat{a}}_n b_{k-n} = \sum_{n=-\infty}^{k-1} \underline{\hat{a}}_n b_{k-n} + \sum_{n=k+1}^{+\infty} \underline{\hat{a}}_n b_{k-n} \tag{10.19}$$

Using the same approach adopted for the signal sample $\underline{R}_k$, the feedback sample $\underline{F}_k$ can be decomposed into terms of both precursor and postcursor contributions. After changing the summation

variable $j = k-n$ in Equation (10.19), the same structure of the signal sample in Equation (10.18) is obtained, with the only exception being the reference symbol $\underline{\hat{a}}_k$:

$$\underline{F}_k = \sum_{\substack{n=-\infty \\ n\neq 0}}^{+\infty} \underline{\hat{a}}_{k-n} b_n = \underbrace{\sum_{n=-\infty}^{-1} \underline{\hat{a}}_{k-n} b_n}_{\text{Precursor ISI}} + \underbrace{\sum_{n=+1}^{+\infty} \underline{\hat{a}}_{k-n} b_n}_{\text{Postcursor ISI}} \tag{10.20}$$

The general structure of the feedback sample derived in Equation (10.20) shows some inconsistency: in fact, it would never be able to feed back any precursor ISI contribution prior to the precursor samples occurring. It is known that the precursor terms contributing to ISI at the sampling time $t = kT$ are generated by the tails of future pulses, for $t > kT$, not yet detected. This means that every feedback technique based on ISI cancellation is inherently not capable of compensating for pulse precursors. The consequence is that the precursor ISI summation in Equation (10.20) must be removed, reducing the general form of the feedback sample to the single postcursor ISI contribution. Accordingly, the feedback signal is given by the following sequence:

$$\underline{F}_k = \underbrace{\sum_{n=+1}^{+\infty} \underline{\hat{a}}_{k-n} b_n}_{\text{Postcursor ISI}} \tag{10.21}$$

Now, progress can now be made using the closed-loop structure, subtracting the feedback sample from the signal sample in front of the ideal sampler shown in Figure 10.1.

10.2.3 Closed-Loop Samples

Assuming the closed-loop configuration of the decision feedback equalizer in Figure 10.1, the received sample at the time instant $t = kT$ is obtained by subtracting the feedback sample in Equation (10.21) from the signal sample in Equation (10.18) and adding the filtered noise component:

$$\underline{v}_k = \underline{R}_k - \underline{F}_k + [\underline{n}(t) * h_W(t)]|_{t=kT} \tag{10.22}$$

Substituting the corresponding sequences (10.18) and (10.21) gives

$$\underline{v}_k = \sum_{n=-\infty}^{+\infty} \underline{a}_{k-n} r_n - \sum_{n=+1}^{+\infty} \underline{\hat{a}}_{k-n} b_n + [\underline{n}(t) * h_W(t)]|_{t=kT} \tag{10.23}$$

Substituting the decomposition (10.18) of the signal sample $\underline{R}_k$ in terms of the reference sample, postcursor and precursor contributions, from Equation (10.23)

$$\underline{v}_k = \underline{a}_k r_0 + \sum_{n=-\infty}^{-1} \underline{a}_{k-n} r_n + \sum_{n=+1}^{+\infty} (\underline{a}_{k-n} r_n - \underline{\hat{a}}_{k-n} b_n) + [\underline{n}(t) * h_W(t)]|_{t=kT} \tag{10.24}$$

This expression is the same as reported in the paper of J. Salz. The sampled pulse amplitude $\underline{v}_k$ is a random variable since it is the result of both the random sequence $\{\underline{a}\}$ and of the input noise $\underline{n}(t)$. Under optimum transmission conditions, without noise and interfering symbols, the sampled amplitude $\underline{v}_k$ at the time instant $t_k = kT$ would be $\underline{a}_k r_0$, which is proportional to the launched symbol $\underline{a}_k$.

10.2.4 Minimum Mean Square Error (MMSE)

Under general noisy and intersymbol interference conditions, the sample $\underline{v}_k$ will differ in general from the required symbol $\underline{a}_k r_0$. The decision error can be defined as

$$\underline{\varepsilon}_k \equiv \underline{v}_k - \underline{a}_k r_0 \tag{10.25}$$

The decision error $\underline{\varepsilon}_k$ is a random variable because it is the difference between two random variables. The optimization process of the DFE receiver proceeds with the minimization of the Mean Square Error (MSE):

$$\text{MSE} \rightarrow E\{\underline{\varepsilon}_k^2\} = E\{(\underline{v}_k - \underline{a}_k r_0)^2\} \tag{10.26}$$

The operator $E\{\cdot\}$ indicates the expected value of the ensemble average over the random quantity. In the definition of the decision error, the implicit assumption is made that the reference symbol $\underline{a}_k$ has amplitude r_0. This is consistent with the concept of the optimum transmission conditions introduced above. Substituting Equation (10.24) into Equation (10.26) gives the following explicit expression of the MSE:

$$\text{MSE} = E\{\underline{\varepsilon}_k^2\} = E\left\{\left[\sum_{n=-\infty}^{-1} \underline{a}_{k-n} r_n + \sum_{n=+1}^{+\infty} (\underline{a}_{k-n} r_n - \hat{\underline{a}}_{k-n} b_n) + [\underline{n}(t) * h_{\text{W}}(t)]|_{t=kT}\right]^2\right\} \tag{10.27}$$

A detailed calculation of the MSE is now discussed. The linearity of the expectation operator allows the calculation of the expectation value of the sum as the sum of the expectation value of each term. In particular, the square of the sum in Equation (10.27) includes six terms: three squared terms plus three mixed products. Although it seems somewhat tedious, it is instructive to consider instead all those terms and to see how most of them cancel out after the expectation operation takes place. This approach is important since the reader can clearly understand the meaning of some 'hidden' assumptions about the signal modeling. In the following, for the sake of clarity, each term will be considered separately.

The total expected value is given by the sum of the six contributions:

$$E\{\underline{\varepsilon}_k^2\} = \sum_{j=1}^{6} E_j \tag{10.28}$$

From Equation (10.27), the following expressions for each term of the above sum are obtained:

$$\begin{aligned}
E_1 &= E\left\{\left(\sum_{n=-\infty}^{-1} \underline{a}_{k-n} r_n\right)^2\right\} \\
E_2 &= E\left\{\left[\sum_{n=+1}^{+\infty} (\underline{a}_{k-n} r_n - \hat{\underline{a}}_{k-n} b_n)\right]^2\right\} \\
E_3 &= E\left\{[\underline{n}(t) * h_{\text{W}}(t)]^2|_{t=kt}\right\} \\
E_4 &= 2E\left\{\left(\sum_{n=-\infty}^{-1} \underline{a}_{k-n} r_n\right)\left[\sum_{n=+1}^{+\infty} (\underline{a}_{k-n} r_n - \hat{\underline{a}}_{k-n} b_n)\right]\right\} \\
E_5 &= 2E\left\{\left(\sum_{n=-\infty}^{-1} \underline{a}_{k-n} r_n\right)[\underline{n}(t) * h_{\text{W}}(t)]|_{t=kT}\right\} \\
E_6 &= 2E\left\{\left[\sum_{n=+1}^{+\infty} (\underline{a}_{k-n} r_n - \hat{\underline{a}}_{k-n} b_n)\right][\underline{n}(t) * h_{\text{W}}(t)]|_{t=kT}\right\}
\end{aligned} \tag{10.29}$$

Each of these terms is analyzed in detail below, commenting on the validity of the assumptions and their physical interpretation. Following the work of J. Salz, the MSE minimization will proceed in two steps:

1. Minimization with respect to the interfering symbols
2. Minimization with respect to the receiver optimization

The third optimization option reported in the work of J. Salz refers to the transmitter optimization, but this issue will not be included in the present work and the reader is referred to more specialized references. The DFE optimal design will be limited to including both minimization of the interfering terms and the linear receiver optimization, as reported in the general block diagram in Figure 10.1.

10.2.4.1 Precursor Interference

The first term in Equations (10.29) is the second-order moment of the future symbols sequence:

$$E_1 = E\left\{\left(\sum_{n=-\infty}^{-1} \underline{a}_{k-n} r_n\right)^2\right\} \tag{10.30}$$

Each term of the sequence, in fact, gives the pulse amplitude corresponding to a sampling time $t_{k+1} = (k+1)T, t_{k+2} = (k+2)T, \ldots$, following the reference sampling instant at $t_k = kT$. Those samples will be referred to as future symbols. To simplify the expression (10.30), by virtue of the statistical independence of the symbols in the sequence $\{\underline{a}\} = \{\underline{a}_{k+1}, \underline{a}_{k+2}, \ldots, \underline{a}_{k+p}, \ldots\}$, the expected value of the cross-terms coincide with the product of the respective expectations. Since the expected value of each symbol is zero, it can immediately be concluded that the expected value of all cross-terms is identically zero. Hence, from Equation (10.30),

$$E_1 = E\{\underline{a}^2\} \sum_{n=-\infty}^{-1} r_n^2 \tag{10.31}$$

This expression has a meaningful interpretation: it coincides with the sum of the square value of all precursors by the second-order moment of the symbol sequence. Of course, it must be postulated that the symbol sequence is a stationary process, so the time origin can be neglected for every statistical average evaluation. In particular, the second order moment of the precursor symbols is coincident with the same average over the entire symbol sequence $\{\underline{a}\}$. Assuming that $\{\underline{a}\}$ is the sequence of μ-ary equiprobable symbols the following expected value of the squared symbol sequence (the power of symbols assuming ergodic symbol sequence) is immediately found to be

$$\sigma_a^2 = E\{\underline{a}^2\} = \frac{\mu^2 - 1}{3} \xrightarrow{\mu = 2, \text{ binary symbols}} \sigma_a^2 = E\{\underline{a}^2\} = 1 \tag{10.32}$$

and the MSE of the precursor interference contribution is:

$$E_1 = \sum_{n=-\infty}^{-1} r_n^2 \tag{10.33}$$

10.2.4.2 Postcursor Interference

The second term in Equations (10.29) coincides with the second-order moment of the feedback error due to the past symbols sequence. It will be soon seen that this term is quite important in the DFE theory, since it is related to the strong hypothesis of correct past decisions:

$$E_2 = E\left\{\left[\sum_{n=+1}^{+\infty} (\underline{a}_{k-n} r_n - \underline{\hat{a}}_{k-n} b_n)\right]^2\right\} \tag{10.34}$$

For every detected past sample $\underline{a}_{k-n}r_n$, $n \geq 1$, the feedback loop returns the estimated past sample $\hat{\underline{a}}_{k-n}r_n$, $n \geq 1$. In general, setting

$$\underline{c}_n \equiv \underline{a}_{k-n}r_n - \hat{\underline{a}}_{k-n}b_n \tag{10.35}$$

the expression (10.34) assumes the following simplified form:

$$E_2 = E\left\{\left(\sum_{n=+1}^{+\infty}\underline{c}_n\right)^2\right\} = E\left\{\sum_{n=+1}^{+\infty}\underline{c}_n^2\right\} + 2E\left\{\sum_{\substack{n,m=+1\\ n\neq m}}^{+\infty}\underline{c}_n\underline{c}_m\right\} \tag{10.36}$$

If for every index $n \neq m$ the corresponding random variables $\underline{c}_n$ and $\underline{c}_m$ are statistically independent, from Equations (10.34) and (10.35) it can immediately be concluded that

$$E_2 = \sum_{n=+1}^{+\infty} E(\underline{a}_{k-n}r_n - \hat{\underline{a}}_{k-n}b_n)^2 + 2\sum_{\substack{n,m=+1\\ n\neq m}}^{+\infty}(E\{\underline{a}_{k-n}r_n - \hat{\underline{a}}_{k-n}b_n\}E\{\underline{a}_{k-m}r_m - \hat{\underline{a}}_{k-m}b_m\}) \tag{10.37}$$

This expression cannot be simplified further unless the strong assumption is made that all past decisions are correct. This translates immediately into the identity between sampled symbols and estimated symbols for every past decision:

$$\hat{\underline{a}}_{k-n} = \underline{a}_{k-n}, \quad n \geq 1 \tag{10.38}$$

The entire theory of the DFE is based on this hypothesis. This assumption is reported by the whole bibliography on the digital equalization using the decision feedback architecture. This condition will be adopted here and it will be assumed to be satisfied *a priori,* without any further investigation. Under the assumption of the correct past decision, the feedback loop interconnection in Figure 10.1 leads to the minimization of the RMS error due to pulse postcursors. Substituting Equation (10.38) into Equation (10.37) gives

$$E_2 = E\{\underline{a}^2\}\sum_{n=+1}^{+\infty}(r_n - b_n)^2 + 2E^2\{\underline{a}\}\sum_{\substack{n,m=+1\\ n\neq m}}^{+\infty}(r_n - b_n)(r_m - b_m) \tag{10.39}$$

Therefore the expected value E_2 is zero if and only if

$$b_n = r_n, \quad n \geq 1 \Rightarrow E_2 = 0 \tag{10.40}$$

In this expression, it is noted that the feedback digital filter has infinite length. In every practical DFE design the filter length must be decided according to the longest postcursor expected by the channel impulse response. According to the condition (10.40), it is concluded that the digital filter used for the feedback loop must have a least the same length of the not negligible postcursor samples. Figure 10.5 highlights this concept.

10.2.4.3 Equalization Noise

The third term in Equations (10.29) deals with the mean square value of the sample evaluated at $t = kT$ of the filtered white noise available at the output of the feedforward filter. In this contribution to the total MSE the interfering terms are not present. Indicating with $\underline{n}(t)$ the zero mean noise process at the input of the linear feedforward filter with the impulse response $h_W(t)$, the output response is the following process:

$$\underline{w}_n(t) = \underline{n}(t) * h_W(t) \tag{10.41}$$

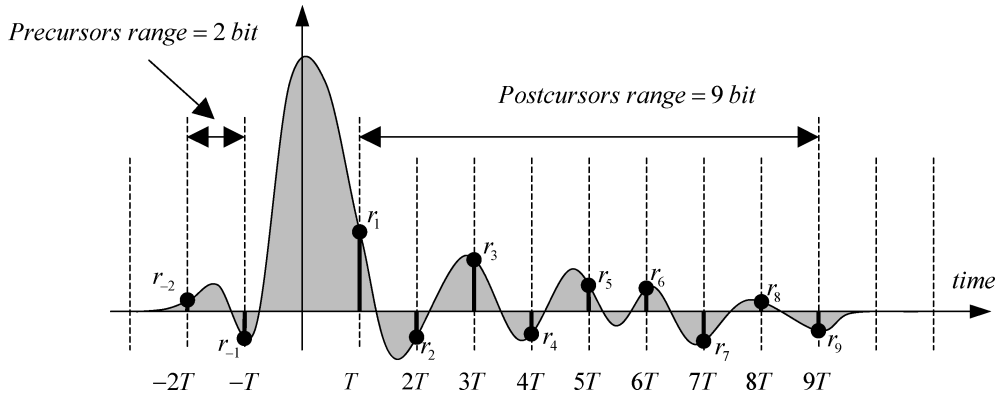

Figure 10.5 Example of the impulse response at the FFF output showing a finite postcursor extent. In the case shown the pulse energy is negligible for $t > 9T$ and $t < -2T$. This allows for assuming an FBF filter with nine taps, $\{b\} = \{b_1, b_2, \ldots, b_9\}$, in order to minimize the mean-square error of the postcursor tails

According to Equations (10.29) the expectation value of the square of the sampled output process must be solved in response to the input stationary white noise:

$$E_3 = E\{[\underline{n}(t) * h_{\mathrm{W}}(t)]^2|_{t=kT}\} = E\{|\underline{w}_n(kT)|^2\} \tag{10.42}$$

This is a well-known result of the theory of linear systems where stochastic inputs with the average power $E\{|\underline{y}(t)|^2\}$ of the output of a linear system with the impulse response $h(t)$ driven by zero mean stationary white noise $\underline{n}(t)$ the of power spectral density ζ_0 is given by the following fundamental result:

$$E\{|\underline{y}(t)|^2\} = R_y(0) = \zeta_0 \int_{-\infty}^{+\infty} |h(t)|^2 \, \mathrm{d}t \tag{10.43}$$

The average output noise power is given by the product of the noise power spectral density ζ_0 with the energy of the impulse response $h(t)$. Translating this theorem into this application, from Equation (10.43) it can immediately be concluded that the mean square value in Equation (10.42) is given by the product of the double-sided noise power spectral density G_i with the energy of the impulse response $h_{\mathrm{W}}(t)$ of the feedforward filter:

$$E_3 = G_i \int_{-\infty}^{+\infty} |h_{\mathrm{W}}(t)|^2 \, \mathrm{d}t \equiv \sigma_n^2 \tag{10.44}$$

Using Parseval's formula for finite energy signals, the same expression holds in the frequency domain, leading directly to the concept of noise bandwidth. From Equation (10.44),

$$\begin{aligned} &\sigma_n^2 = G_i \int_{-\infty}^{+\infty} |h_{\mathrm{W}}(t)|^2 \, \mathrm{d}t = G_i \int_{-\infty}^{+\infty} |H_{\mathrm{W}}(f)|^2 \, \mathrm{d}f = G_i B_{\mathrm{n}} \\ &h_{\mathrm{W}}(t) \overset{\Im}{\longleftrightarrow} H_{\mathrm{W}}(f), \qquad |H_{\mathrm{W}}(0)| = 1 \end{aligned} \tag{10.45}$$

The mean square error contribution due to the equalization noise considered here coincides conceptually with the noise enhancement penalty analyzed previously in the case of inverse filter equalization. However, there is a great difference between these two quantities. The noise penalty found in the ideal inverse filter equalizer was a consequence of the noise bandwidth increase with respect to the optimum receiver bandwidth with the input matched filter. This was clearly

stated by expressions (9.83) and (9.84), where the ideal noise bandwidth of the matched receiver is $B_n = 1/T$. The equalization noise power derived in this section, expression (10.45), is the noise power computed through the noise bandwidth of the feedforward filter and this bandwidth still needs to be compared with the ideal one, $B_n = 1/T$.

In the next section it will be shown that the receiver optimization requires an input matched filter plus a proper tapped delay line for precursor interference minimization. The difference between the equalization noise penalties in the ideal inverse filter and the DFE structure relies on the relatively low value of the MSE due to the FFF noise bandwidth with respect to the much more relevant contribution found in the case of the ideal inverse filter equalizer. A quantitative expression will be found for the calculation of the equalization noise penalty in the DFE architecture.

10.2.4.4 Cross-Terms

The last three contributions to the MSE in expression (10.29) refer to the expected values of the product of zero mean and uncorrelated random processes. The result immediately gives a null expected value for each of them. In fact, the expected value of the product of two uncorrelated processes coincides with the product of their respective expected values. Since zero mean processes are assumed for both the symbol sequence $\{\underline{a}\}$ and the input noise $\underline{n}(t)$,

$$E\{\underline{a}\} = 0, \qquad E\{\underline{n}(t)\} = 0 \tag{10.46}$$

In conclusion, each of the three terms above gives a null contribution to the total MSE. In the following the derivation of each cross-term is considered in detail.

The fourth term coincides with the expected values of the product of the precursor sequence with the compensation error of the postcursor sequence:

$$\begin{aligned} E_4 &= 2E\left\{\left[\sum_{n=-\infty}^{-1} \underline{a}_{k-n} r_n\right]\left[\sum_{n=+1}^{+\infty} (\underline{a}_{k-n} r_n - \hat{\underline{a}}_{k-n} b_n)\right]\right\} \\ &= 2E\left\{\sum_{n=-\infty}^{-1} \underline{a}_{k-n} r_n\right\} E\left\{\sum_{n=+1}^{+\infty} (\underline{a}_{k-n} r_n - \hat{\underline{a}}_{k-n} b_n)\right\} \\ &= 2E^2\{\underline{a}\} \sum_{n=-\infty}^{-1} r_n \sum_{n=+1}^{+\infty} (r_n - b_n) = 0 \end{aligned} \tag{10.47}$$

The assumption (10.28) is used to check the correctness of all past decisions.

The fifth term coincides with the expected value of the product of the precursor sequence with the noise process at the output of the feedforward filter. Proceeding as above gives

$$\begin{aligned} E_5 &= 2E\left\{\left[\sum_{n=-\infty}^{-1} \underline{a}_{k-n} r_n\right][\underline{n}(t) * h_W(t)]|_{t=kT}\right\} \\ &= 2E\left\{\sum_{n=-\infty}^{-1} \underline{a}_{k-n} r_n\right\} E\{\underline{n}(t) * h_W(t)|_{t=kT}\} \\ &= 2E\{\underline{a}\}\left[\sum_{n=-\infty}^{-1} r_n\right] E\{\underline{n}(t)\} * h_W(t)|_{t=kT} = 0 \end{aligned} \tag{10.48}$$

The sixth and last term in Equations (10.29) coincides with the expected value of the product of the compensation error of the postcursor sequence with the noise process at the output of the

feedforward filter. The calculation is the same as that above for Equation (10.48), leading to the zero contribution of E_6 to the MSE:

$$E_6 = 2E\left\{\left[\sum_{n=+1}^{+\infty}(\underline{a}_{k-n}r_n - \underline{\hat{a}}_{k-n}b_n)\right][\underline{n}(t) * h_{\mathrm{W}}(t)]|_{t=kT}\right\} = 0 \tag{10.49}$$

In conclusion, all three cross-terms in Equations (10.29) lead to a null contribution to the total MSE.

From Equations (10.33), (10.40), (10.44), (10.47), (10.48) and (10.49), the MSE expression in Equation (10.27) assumes the following form, where a perfect past decision MSE minimization due to postcursors feedback cancellation and zero mean stationary white noise are assumed for the receiver input:

$$\mathrm{MSE} = \sum_{n=-\infty}^{-1} r_n^2 + \sigma_n^2 \tag{10.50}$$

This important result can be further improved by working on the feedforward filter optimization with respect to the simultaneous minimization of both precursors and noise.

10.2.5 Receiver Optimization

The Mean square error (MSE) normalized to the average symbol power σ_a^2 given in Equation (10.32) is rewritten. Substituting in Equation (10.50) the detailed expressions (10.11) and (10.44) of the impulse response $r(t)$ and the noise power σ_n^2 respectively gives

$$\begin{aligned}\frac{\mathrm{MSE}}{\sigma_a^2} &= \sum_{n=-\infty}^{-1}\left[\int_{-\infty}^{+\infty} h_{\mathrm{W}}(\tau)q(nT-\tau)\,\mathrm{d}\tau\right]^2 + T\gamma_i\int_{-\infty}^{+\infty}|h_{\mathrm{W}}(t)|^2\,\mathrm{d}t \\ \gamma_i &\equiv \frac{G_i}{T\sigma_a^2}\end{aligned} \tag{10.51}$$

The normalized mean square error is dimensionless and can easily be verified by considering the dimension of each term at the second member. Since $q(t)$ is dimensionless and $h_{\mathrm{W}}(t)$ has dimensions of s^{-1}, it can immediately be concluded that after time convolution, the resulting integrals are still dimensionless. The second term results from the product of the integral, whose dimensions are also s^{-1}, with the dimensionless noise-to-signal power ratio γ_i and the time step T(s), which still gives a dimensionless contribution. The new dimensionless variable $\gamma_i \equiv G_i/(T\sigma_a^2)$ assumes the meaning of the noise-to-signal power ratio at the decision section, where the noise density is integrated in the ideal noise bandwidth $B = 1/T$.

The problem to solve now is optimization of the feedforward filter impulse response $h_{\mathrm{W}}(t)$ which minimizes the MSE for a given system impulse response $q(t)$ and noise-to-signal power ratio γ_i. The system impulse response $q(t)$ is given in Equation (10.8) and refers to the entire impulse response, including the transmitter, the fiber (channel) and the optical receiver up to the input section of the feedforward filter. The MSE minimization by means of the optimum impulse response $h_{\mathrm{W}}(t)$ requires the mathematical methods of the calculus of variations.

The result is an integral equation for the impulse response $h_{\mathrm{W}}(t)$ whose solution has a representation in the form

$$h_{\mathrm{W}}(t) = \sum_{n=-\infty}^{0} g_n q(nT - t) \tag{10.52}$$

where

$$g_n = -\frac{1}{\gamma_i}\int_{-\infty}^{+\infty} h_{\mathrm{W}}(\tau)q(nT-\tau)\,\mathrm{d}\tau \tag{10.53}$$

The solution $h_W(t)$ of the integral equations (10.52) and (10.53) represents the optimum impulse response that minimizes the MSE for the given system impulse response $q(t)$ and noise-to-signal power ratio γ_i between the spectral noise density G_i and the average symbol power σ_a^2.

No further progress will be made with solution of these equations, but instead the form of the expected solution given in Equation (10.52) will be assumed. Once the sequence of coefficients $g_0, g_{-1}, \ldots, g_n, \ldots = \{g\}$ is known as the solution of the integral equations (10.52) and (10.53), it is clear that the impulse response $h_W(t)$ is represented by cascading a matched filter to the system impulse response $q(t)$ with the anticausal tapped delay line with coefficients $\{g\}$. This is shown in Figure 10.6.

If the impulse response of the anticausal tapped delay line is indicated by

$$h_D(t) = \sum_{n=-\infty}^{0} g_n \delta(t - nT)$$

the impulse response of the two-cascaded systems in Figure 10.6 is given by the following convolution:

$$\begin{aligned} q(-t) * h_D(t) &= \sum_{n=-\infty}^{0} g_n \int_{-\infty}^{+\infty} q(-t+\tau)\delta(\tau - nT)\,\mathrm{d}\tau \\ &= \sum_{n=-\infty}^{0} g_n q(nT - t) = h_W(t) \end{aligned} \tag{10.54}$$

which coincides with Equation (10.52). In conclusion, the optimum impulse response $h_W(t)$ of the feedforward filter is composed of a matched filter having the impulse response $q(-t)$ followed by the anticausal tapped delay line with weights equal to the coefficients g_n given in Equation (10.53).

In the following section the expression of the minimum mean square error (MMSE) for the ideal decision feedback equalizer will be presented.

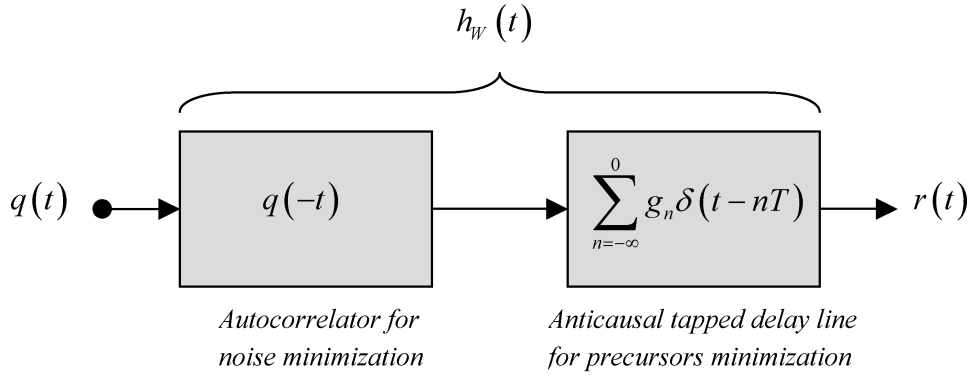

Figure 10.6 Schematic representation of the optimum impulse response of the feedforward filter in Equation (10.52) for the simultaneous minimization of the MSE due to noise and precursor interference

10.2.6 Computation of the MMSE

The expression reported in Equation (10.50) or (10.51) clearly shows that the total mean square error is given by the sum of the mean-square errors due to the power of precursors and the noise power respectively. Although this statement might be obvious, it is important to make some comments about it. The optimization of the DFE according to the theory presented so far and referenced to the work of J. Salz leads simultaneously to minimization of the intersymbol and noise power. Those two quantities are assumed to be statistically independent, which is the reason why their respective powers are summed together. The residual intersymbol due to signal precursors is then modeled mathematically as a random process, statistically independent from the noise and characterized by the variance given by the first term in Equation (10.50).

In order to quantify the equalization performances of the DFE the MMSE expression derived by J. Salz (equations 13 and 14 in the referenced paper) is given as

$$\frac{\text{MMSE}}{\sigma_a^2} = \exp\left\{-\frac{T}{2\pi}\int_{-\pi/T}^{+\pi/T} \log\left[1 + \frac{1}{T^2\gamma_i}\sum_{n=-\infty}^{+\infty} |Q(\omega - n\omega_\text{B})|^2\right] \text{d}\omega\right\},$$

$$\gamma_i \equiv \frac{G_i}{T\sigma_a^2},\ \omega_\text{B} = \frac{2\pi}{T} \tag{10.55}$$

Again, the dimensionless nature of the normalized MMSE is guaranteed by assuming that the spectrum $|Q(\omega)|$ of the impulse response $q(t)$ has the dimension of time. This is a consequence of the dimensionless assumption of the impulse response $q(t)$, as will be seen below. The function $Q(\omega)$ is the Fourier transform of the impulse response $q(t)$ defined in Equation (10.8) and corresponds to the linear channel response including the transmitter, the multimode fiber and the optical receiver, up to section $Q-Q'$ in Figure 10.1:

$$Q(\omega) = \int_{-\infty}^{+\infty} q(t)\text{e}^{-\text{j}\omega t}\,\text{d}t \quad \text{(s)} \tag{10.56}$$

The variable $\omega_\text{B} \equiv 2\pi B$ is the angular frequency corresponding to the bit rate frequency $B = 1/T$. Using the frequency variable f and normalizing to the bit rate frequency, $x \equiv fT = \omega T/(2\pi)$, from Equation (10.55)

$$\frac{\text{MMSE}}{\sigma_a^2} = \exp\left\{-\int_{-1/2}^{+1/2} \log\left[1 + \frac{1}{T^2\gamma_i}\sum_{n=-\infty}^{+\infty} |Q(x-n)|^2\right] \text{d}x\right\} \tag{10.57}$$

The MMSE is a functional of the transfer function $Q(x)$ of the linear transmission channel, defined from the input section of the transmitter up to the input section of the feedforward filter. The expression (10.57) of the MMSE, for a given noise-to-signal power ratio γ_i, depends exclusively on the channel response $Q(x)$, where $x = fT$ is the bit rate normalized frequency variable. This is one of the most relevant characteristics of expression (10.57), where the MMSE gives the quantitative measure of the expected performance of the linear transmission channel assuming ideal decision feedback equalization.

The 'ideal decision feedback equalization' refers to the model developed in Section 10.2.4, where infinite length FFF and FBF have been used. It is concluded that the maximum value of the normalized MMSE in Equation (10.57) is equal to one. This is because the second addend under the logarithmic operator is definite positive for every choice of channel response and noise-to-signal ratio. Assuming small channel contributions and a large noise-to-signal ratio leads to an almost negligible exponent value, and the MMSE is almost equal to one. In the following, some examples of MMSE calculations according to Equation (10.57) are considered.

10.2.6.1 The Ideal Nyquist Channel

The first case to be considered is the ideal transmission channel with a uniform frequency response up to a half bit rate frequency and linear phase. This is well known as the ideal Nyquist channel. Referring to Figure 10.1,

$$Q(x) = \Gamma_0(x) = \begin{cases} T, & |x| < \frac{1}{2} \\ \dfrac{T}{2}, & x = \frac{1}{2} \\ 0, & \left|x > \frac{1}{2}\right| \end{cases} \tag{10.58}$$

Figure 10.7 gives a sketch of the folded-frequency response according to the summation in Equation (10.57). The summation in (10.57) reduces to the constant

$$\sum_{n=-\infty}^{+\infty} |Q(x-n)|^2 = T^2$$

and in particular, the normalized minimum mean square error (MMSE) becomes

$$\frac{\text{MMSE}}{\sigma_a^2} = \exp\left[\log\left(\frac{\gamma_i}{1+\gamma_i}\right)\int_{-1/2}^{+1/2} \mathrm{d}x\right] \Rightarrow \frac{\text{MMSE}}{\sigma_a^2} = \frac{\gamma_i}{1+\gamma_i} \tag{10.59}$$

In particular, for the binary signal $\sigma_a^2 = 1$,

$$\text{MMSE} = \frac{\gamma_i}{1+\gamma_i} \tag{10.60}$$

This relation is quite simple and important. It states that the residual MMSE in the DFE structure operating over a white noise Nyquist channel with binary symbols depends exclusively on the noise-to-signal power ratio with the noise power computed in the ideal noise bandwidth $B_\text{n} = B = 1/T$. In particular, for a very low noise-to-signal power ratio, from Equation (10.60), we have approximately:

$$\gamma_i \ll 1 \Rightarrow \text{MMSE} \cong \gamma_i \tag{10.61}$$

On the other hand, for very large values of γ_i, the MMSE tends to one, as expected:

$$\gamma_i \gg 1 \Rightarrow \text{MMSE} \cong 1 \tag{10.62}$$

It is noted that in the case of the Nyquist channel there is no intersymbol interference and the only residual MMSE must therefore be imputed to the noise-to-signal power ratio.

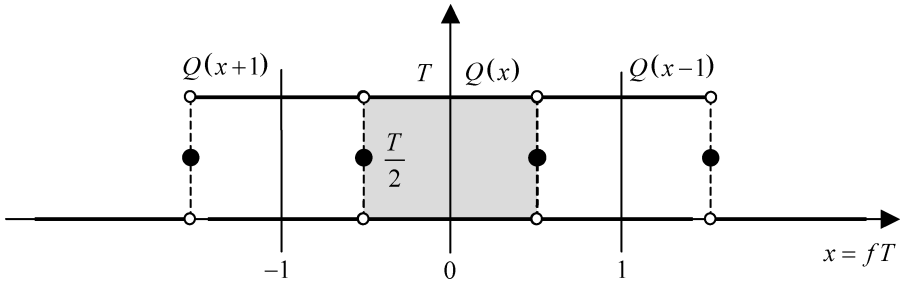

Figure 10.7 Frequency representation of the ideal Nyquist channel using the bit rate normalized frequency

10.2.6.2 Single-Pole Channel

The second example is the single-pole response of the whole transmission channel between sections $G-G'$ and $R-R'$. The causal single-pole impulse response satisfying the normalization requirement is first set:

$$q(t) = \begin{cases} e^{-t/\tau}, & t \geq 0 \\ 0, & t < 0 \end{cases}, \qquad q(0) = 1 \tag{10.63}$$

The transfer function $Q(f)$ assumes the well-known single-pole profile:

$$Q(f) = \frac{1}{1/\tau + j2\pi f} = \frac{\tau}{1 + jf/f_0}, \qquad f_0 \equiv \frac{1}{2\pi\tau} \tag{10.64}$$

Substituting for the normalized frequency $x = fT$, $x_0 = f_0 T = [1/(2\pi)](T/\tau)$, gives

$$Q(x) = \frac{T}{2\pi x_0} \frac{1}{\sqrt{1 + (x/x_0)^2}} e^{-j \arctan(x/x_0)} \tag{10.65}$$

Using the channel response (10.65), the series in (10.57) assumes the following form:

$$\frac{1}{T^2 \gamma_i} \sum_{n=-\infty}^{+\infty} |Q(x-n)|^2 = \frac{1}{4\pi^2 x_0^2 \gamma_i} \sum_{n=-\infty}^{+\infty} \frac{1}{1 + [(x-n)/x_0]^2} \tag{10.66}$$

Substituting Equation (10.66) in Equation (10.57) and assuming binary symbols ($\sigma_a^2 = 1$), the following expression of the MMSE for the single-pole channel response is obtained:

$$\text{MMSE} = \exp\left(- \int_{-1/2}^{+1/2} \log\left\{ 1 + \frac{1}{4\pi^2 x_0^2 \gamma_i} \sum_{n=-\infty}^{+\infty} \frac{1}{1 + [(x-n)/x_0]^2} \right\} dx \right) \tag{10.67}$$

Figure 10.8 gives the numerical calculation of the MMSE using the single-pole channel response in Equation (10.67) versus the normalized cut-off frequency $x_0 = f_0 T$ and assuming the noise-to-signal ratio γ_i as parameter. It can easily be concluded from the common behavior of the curves shown that the MMSE increases monotonically with the cut-off frequency x_0 and the noise-to-signal ratio γ_i. This result can reduce to a paradox at first sight, but a more in-depth reasoning clarifies this apparent contradiction. In is clear in fact that at increasing cut-off frequencies the intersymbol interference decreases accordingly, due to a much faster impulse response. This leads to a decreasing interference power in both precursors and postcursors.

The reason is different: the optimum receiver is in fact matched to the channel response, which leads to increasing noise bandwidth and corresponding noise power as the cut-off frequency increases indefinitely. Stated differently, the large bandwidth corresponding to the increasing cut-off frequency is not required by the signaling rate, it is redundant and it translates only into a waist noise power. In that condition the MMSE is almost limited by the noise power, with a negligible interference power contribution.

10.2.6.2.1 Broadband Single-Pole Channel

In the limiting case of either a very large single-pole bandwidth $x_0 \gg 1$ or a very high noise-to-signal power ratio, the previous expression tends to $\lim_{x_0 \to \infty} \text{MMSE} = 1$, leading to extremely high error powers. This can physically be explained in terms of the indefinitely large bandwidth available for the noise power calculation. At very large values of the normalized cut-off frequencies, each computed curve shows the common asymptote $\text{MMSE}_{x_0 \to +\infty} \to 1$. As already stated, this behavior is due to the large noise bandwidth consequent to the matched receiver condition.

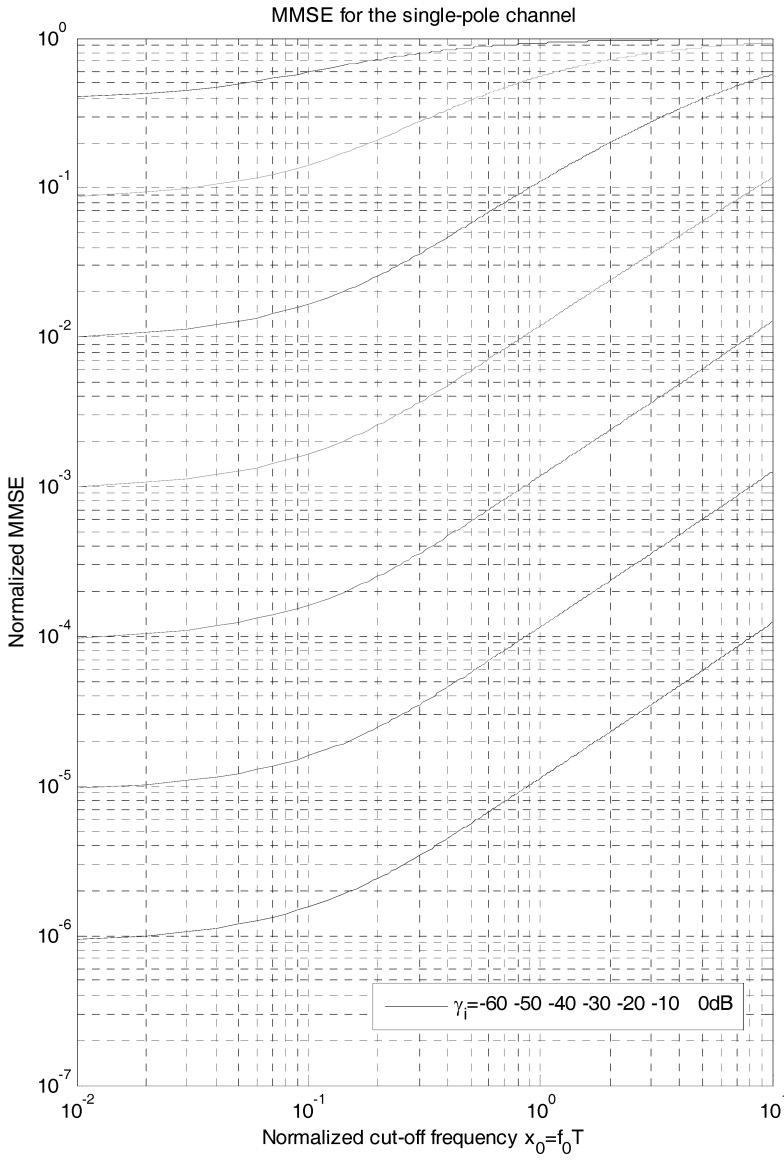

Figure 10.8 Computed MMSE for the single-pole channel reported in Equation (10.67). According to bottom-up curves, the noise-to-signal ratio γ_i assumes respectively the values between -60 dB and 0 dB with a 10 dB step each. The MMSE increases monotonically with increasing cut-off frequency, leading to a better equalization efficiency for lower cut-off frequencies

10.2.6.2.2 Narrowband Single-Pole Channel

The behavior of the MMSE for the single-pole channel is different at lower cut-off frequencies. In that region in fact the limited channel bandwidth induces a high interference power but the receiver matching condition minimizes the noise power. Figure 10.9 highlights this interesting behavior at low and high cut-off frequencies. The left graph refers to the lower cut-off frequency range, with

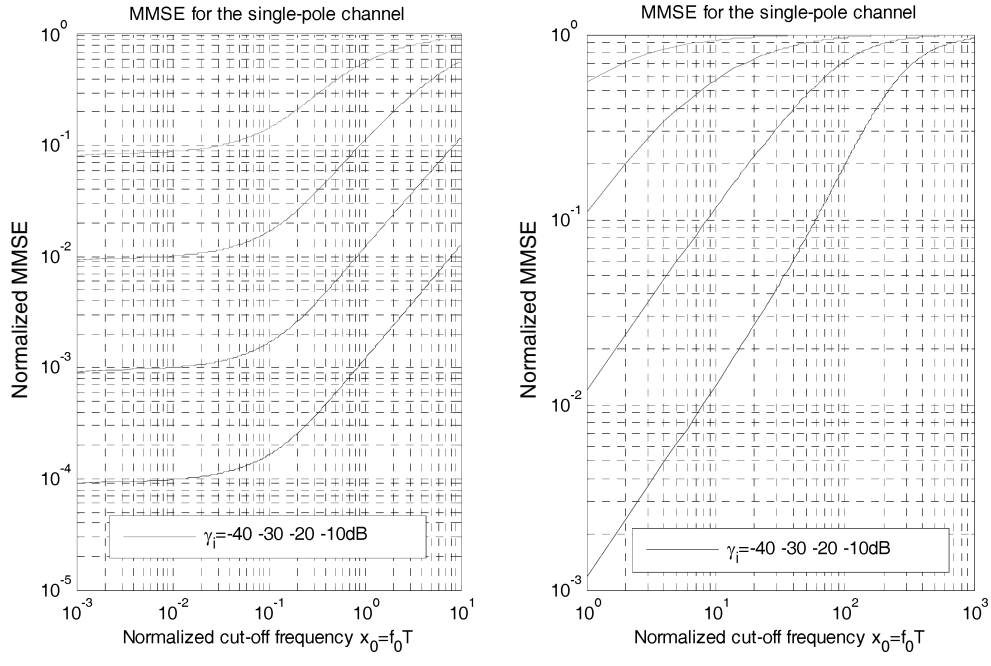

Figure 10.9 Computed MMSE for the single-pole channel response. The noise-to-signal parameters used are the same as in Figure 10.8, but the normalized cut-off frequency range has been split according to lower and higher values. It is evident, as expected, that at a lower cut-off range the MMSE has the characteristic asymptotic behavior set by the noise-to-signal floor. At higher cut-off rates, the MMSE follows the predicted asymptotic behavior towards the unit value, independently from the noise-to-signal ratio. It this case, in fact, the MMSE saturates at unity for every value of γ_i

$10^{-3} \leq x_0 \leq 10^1$ while the right graph shows the computed MMSE curves corresponding to the higher cut-off frequency range, $10^0 \leq x_0 \leq 10^3$. At a very narrow single-pole response a different asymptote corresponds instead for each noise-to-signal ratio γ_i, and the numerical computation reveals that the asymptote value is closely related to γ_i. In order to demonstrate analytically the narrowband asymptote, it is convenient to introduce the auxiliary function $W(x)$ representing the value of the series in the integrand of the MMSE expression in Equation (10.57):

$$W(x) \equiv \sum_{n=-\infty}^{+\infty} |Q(x-n)|^2 \tag{10.68}$$

In particular, for the single-pole channel, from Equation (10.66),

$$W(x) = \frac{T^2}{4\pi^2} \sum_{n=-\infty}^{+\infty} \frac{1}{x_0^2 + (x-n)^2} \tag{10.69}$$

The narrowband condition leads to a comb-like spectrum. Single terms $1/[x_0^2 + (x-n)^2]$ are centered on integer frequencies and their extent can be assumed indefinitely small for limiting values $x_0 \to 0$. This means that in the integration interval $-\frac{1}{2} \leq x \leq +\frac{1}{2}$ the only contributing term to the series is almost the central one, associated with $n = 0$. All the remaining terms lead to a negligible contribution in the limit of an indefinitely narrowband channel and the auxiliary function in

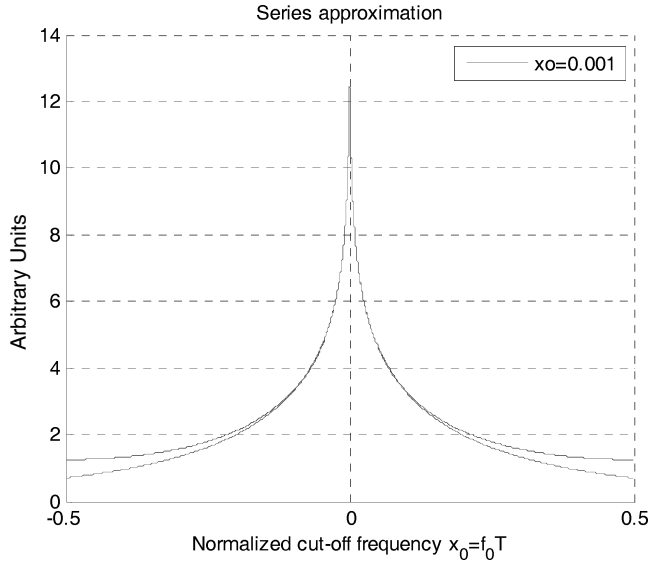

Figure 10.10 Computed integrand functions of the exact MMSE expression in Equation (10.57) and of the approximation in Equation (10.71) for the single-pole channel with $x_0 = 10^{-3}$. The logarithmic smoothing strongly raises the tails, leading to a poor function approximation in those regions

Equation (10.69) can be approximated to

$$\lim_{x_0 \to 0} W(x) \cong \frac{T^2}{4\pi^2} \frac{1}{x_0^2 + x^2} \tag{10.70}$$

Substituting into Equation (10.57) gives the approximated MMSE in the limiting case of indefinitely narrowband single-pole channel:

$$\lim_{x_0 \to 0} \text{MMSE} \cong \exp\left\{ - \int_{-1/2}^{+1/2} \left[1 + \frac{1}{4\pi^2 \gamma_i (x_0^2 + x^2)} \right] \mathrm{d}x \right\} \tag{10.71}$$

Figure 10.10 shows the comparison between computed integrand functions in Equations (10.57) and (10.71). The effect of the logarithmic smoothing on the function tails is clearly misleading, changing the approximation in those regions.

The ideal DFE is capable of compensating for the strong intersymbol interference, even for the very narrow bandwidth conditions of the single-pole channel, leading to a residual MSE limited essentially by the noise contribution. From this first example it can be concluded that the ideal DFE performs much better for very narrowband channels, achieving the lowest MMSE limited by the noise-to-signal ratio. The matching condition required at the receiving section of the feedforward filter in fact introduces a large noise power into the detection section, limiting the performance without any more chance of improvement. Of course, these considerations rely on the assumption of white noise, independently from the integration bandwidth. More realistic situations deal instead with a colored noise spectrum, usually damping the high-frequency content.

10.2.6.3 Gaussian Channel

The last example considered refers to the Gaussian channel. The Gaussian transfer function is characterized by the half-width at half-maximum or equivalently by the −6 dB electrical bandwidth

f_0. From Equation (3.115),

$$Q(f) = \frac{1}{f_0}\sqrt{\frac{\log 2}{\pi}}\ \mathrm{e}^{-(f/f_0)^2 \log 2} \tag{10.72}$$

and

$$q(t) = \mathrm{e}^{-(\pi^2 f_0^2/\log 2)t^2}, \quad q(0) = 1 \tag{10.73}$$

It is noted that the channel impulse response $q(t)$ is correctly normalized by setting $q(0) = 1$. Since the area subtended by the Fourier transform gives the value at the origin of the corresponding time domain function, from Equations (10.73) it can be concluded immediately that, independently from the cut-off frequency, every Gaussian frequency response $Q(f)$ subtends the same unity area. Using the normalized frequency variable $x = fT$ gives

$$Q(x) = \frac{T}{x_0}\sqrt{\frac{\log 2}{\pi}}\mathrm{e}^{-(x/x_0)^2 \log 2}, \quad x_0 \equiv f_0 T,\ 2f_0 = \mathrm{FWHM} \tag{10.74}$$

The normalized cut-off frequency x_0 identifies the half-width at half-maximum of the Gaussian profile:

$$Q(x_0) = \frac{1}{2}\frac{T}{x_0}\sqrt{\frac{\log 2}{\pi}} = \frac{1}{2}Q(0)$$

The Gaussian channel response (10.74) is substituted into the series term in Equation (10.57) giving

$$\frac{1}{T^2\gamma_i}\sum_{n=-\infty}^{+\infty}|Q(x-n)|^2 = \frac{\log 2}{\pi x_0^2\gamma_i}\sum_{n=-\infty}^{+\infty}\mathrm{e}^{-[(x-n)/x_0]^2 2\log 2} \tag{10.75}$$

Substituting Equation (10.75) in Equation (10.57) and assuming binary symbols ($\sigma_a^2 = 1$) gives the following expression for the MSE for the Gaussian channel response:

$$\mathrm{MMSE} = \exp\left[-\int_{-1/2}^{+1/2}\log\left(1 + \frac{\log 2}{\pi x_0^2\gamma_i}\sum_{n=-\infty}^{+\infty}\mathrm{e}^{-[(x-n)/x_0]^2 2\log 2}\right)\mathrm{d}x\right] \tag{10.76}$$

10.2.6.3.1 Narrowband Gaussian Channel

Very small values of the parameter x_0 lead to narrow Gaussian terms in the series composition. Adjacent Gaussians will not overlap significantly, leading to almost isolated contributions along the normalized frequency axis. Limiting the analysis to the integration interval, it can be concluded immediately that for $x_0 \to 0$ only the centered Gaussian results are included in the integration interval. All the translated Gaussian profiles add negligible tail contributions to the series composition. Figure 10.11 illustrates this behavior.

From Equation (10.76), the following approximation in the limit of the narrowband Gaussian channel is obtained:

$$\lim_{x_0\to 0}\mathrm{MSE} = \exp\left[-\int_{-1/2}^{+1/2}\log\left(1 + \frac{\log 2}{\pi x_0^2\gamma_i}\mathrm{e}^{-(x/x_0)^2 2\log 2}\right)\mathrm{d}x\right] \tag{10.77}$$

The integrand function in Equation (10.77) is then considered. The narrowband Gaussian profile illustrated in Figure 10.12 is concentrated around the frequency origin and extends within a very limited multiple of the cut-off frequency. This is of course a consequence of the assumption that $x_0 \ll 1$. The integrand function $\log\left\{1 + [\log 2/(\pi x_0^2\gamma_i)]\mathrm{e}^{-(x/x_0)^2 2\log 2}\right\}$ is therefore negligible everywhere on the frequency axis except within that small interval around the origin. Without losing in generality, that interval with $(-(m/2)x_0, +(m/2)x_0)$ is defined, as shown in Figure 10.12, where

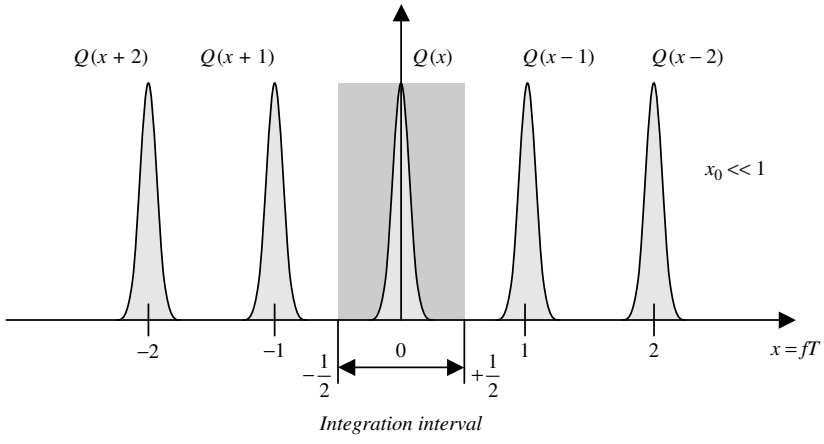

Figure 10.11 Qualitative illustration of the superposition of the translated narrowband Gaussian channel responses according to the series in Equation (10.76). Due to the assumed narrowband response with $x_0 \ll 1$, any two adjacent Gaussians will never overlap significantly. The integration interval $(-\frac{1}{2}, \frac{1}{2})$ is highlighted and includes only the contribution from the baseband channel $Q(x)$, symmetrically located around the frequency origin

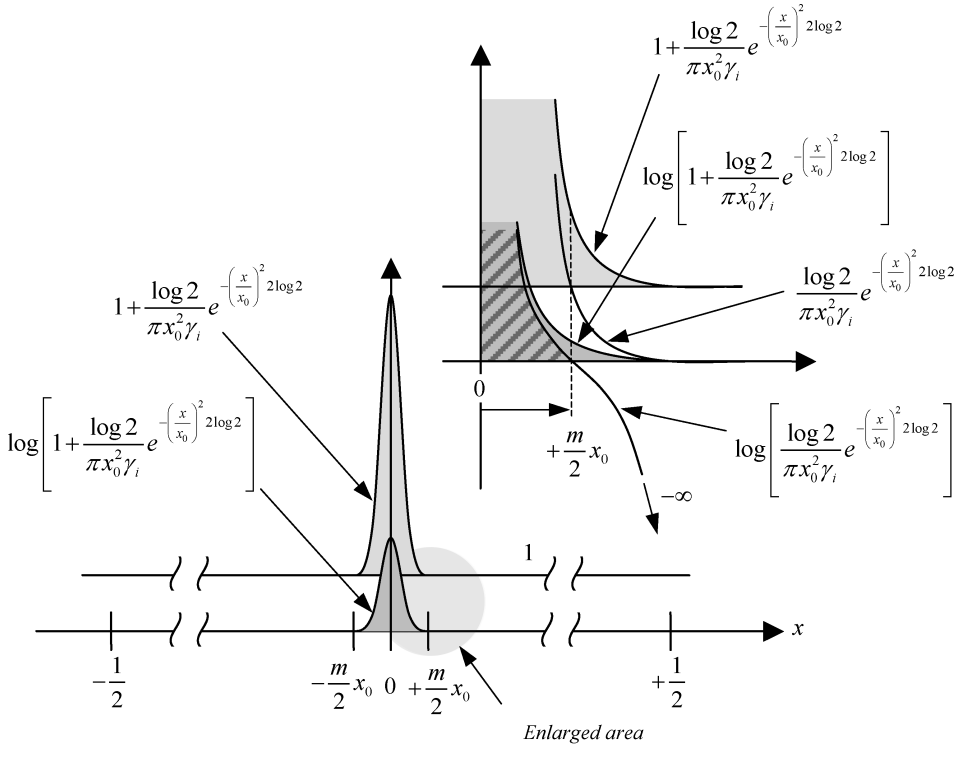

Figure 10.12 Graphical representation of the approximation (10.78) used for the calculation of the MSE for the narrow bandwidth Gaussian channel. The reduced integration interval $(-(m/2)x_0, +(m/2)x_0)$ allows for approximating the logarithmic integrand function.

$m > 1$ must be selected in order to validate the following approximation:

$$\log\left(1 + \frac{\log 2}{\pi x_0^2 \gamma_i} e^{-(x/x_0)^2 2\log 2}\right) \cong \log\left(\frac{\log 2}{\pi x_0^2 \gamma_i}\right) - \left(\frac{x}{x_0}\right)^2 2\log 2,$$
$$\left| m : x \in \left(-\frac{m}{2}x_0, +\frac{m}{2}x_0\right) \subset \left(-\frac{1}{2}, +\frac{1}{2}\right) \right. \tag{10.78}$$

From Equation (10.77) and using the approximation (10.78),

$$\lim_{x_0 \to 0} \text{MSE} \cong \exp\left\{-\int_{-(m/2)x_0}^{+(m/2)x_0} \left[\log\left(\frac{\log 2}{\pi x_0^2 \gamma_i}\right) - \left(\frac{x}{x_0}\right)^2 2\log 2\right] dx\right\}$$
$$= \exp\left[-m x_0 \log\left(\frac{\log 2}{\pi x_0^2 \gamma_i}\right) + \frac{m^3 x_0 \log 2}{6}\right] \tag{10.79}$$

After simple manipulations and using the result $\lim_{\substack{x \to 0 \\ a > 0}} x^{ax} = 1^-$ the following approximation of the MMSE for indefinitely narrowband Gaussian channel is obtained:

$$\lim_{x_0 \to 0} \text{MSE} \cong \lim_{x_0 \to 0}\left[\left(\frac{\pi \gamma_i x_0^2}{\log 2}\right)^{m x_0} e^{(m^3 x_0 \log 2)/6}\right] = 1 \tag{10.80}$$

In conclusion, for a very narrowband Gaussian channel the MMSE for the ideal DFE tends to the limiting value of one, indicating a complete lack of equalization. This feature is quite important and is completely different to the previous case where the MMSE was computed for the single-pole channel. In that case, the limiting value for the narrowband single-pole channel was asymptotically limited by the noise-to-signal ratio $\gamma_i = TG_i/\sigma_a^2$, leaving the consistent intersymbol interference completely removed by the DFE operation. This is not the case for the Gaussian channels, where the narrowband Gaussian channel leads to increasing residual errors for a decreasing narrowband response.

The different behaviors between the single-pole and Gaussian responses when operated under ideal DFE is the reason for the success of DFE in compensating for band-limited copper transmission lines, where the frequency roll-off closely resembles the single-pole of an even smoother ($\sim 1/\sqrt{f}$) profile. However, it is known that multimode fiber optic has much more exotic impulse responses, which under some circumstances can be approximated by the Gaussian profile, leading to less-efficient decision feedback equalization.

Figure 10.13 gives the computed plots of the MMSE for the Gaussian channel response assuming parametric noise-to-signal ratio variations between $\gamma_i = -60\,\text{dB}$ and $\gamma_i = 0\,\text{dB}$, with the normalized cut-off frequency ranging between a very small bandwidth up to unity roll-off $10^{-2} \le x_0 \le 10^1$. The plots report the computed dependence of the MMSE from the noise power, assuming that the lowest value corresponds to the lowest noise-to-signal ratio, for every fixed cut-off frequency. However, the computed MMSE profile versus the normalized cut-off frequency for a fixed noise-to-signal ratio clearly verifies the asymptotic behavior toward the frequency origin, as predicted in Equation (10.80).

10.2.6.3.2 Broadband Gaussian Channel

Assuming very large values of the parameter x_0 leads to broader Gaussian terms in the series composition. Translated Gaussians will overlap significantly, even for large index differences, leading to almost a uniform spectral profile in the unit integration interval in Equation (10.76). Figure 10.14 reports the computed sum of the first 21 Gaussian terms $\sum_{n=-10}^{+10} e^{-[(x-n)/x_0]^2 2\log 2}$, assuming $x_0 = 10$.

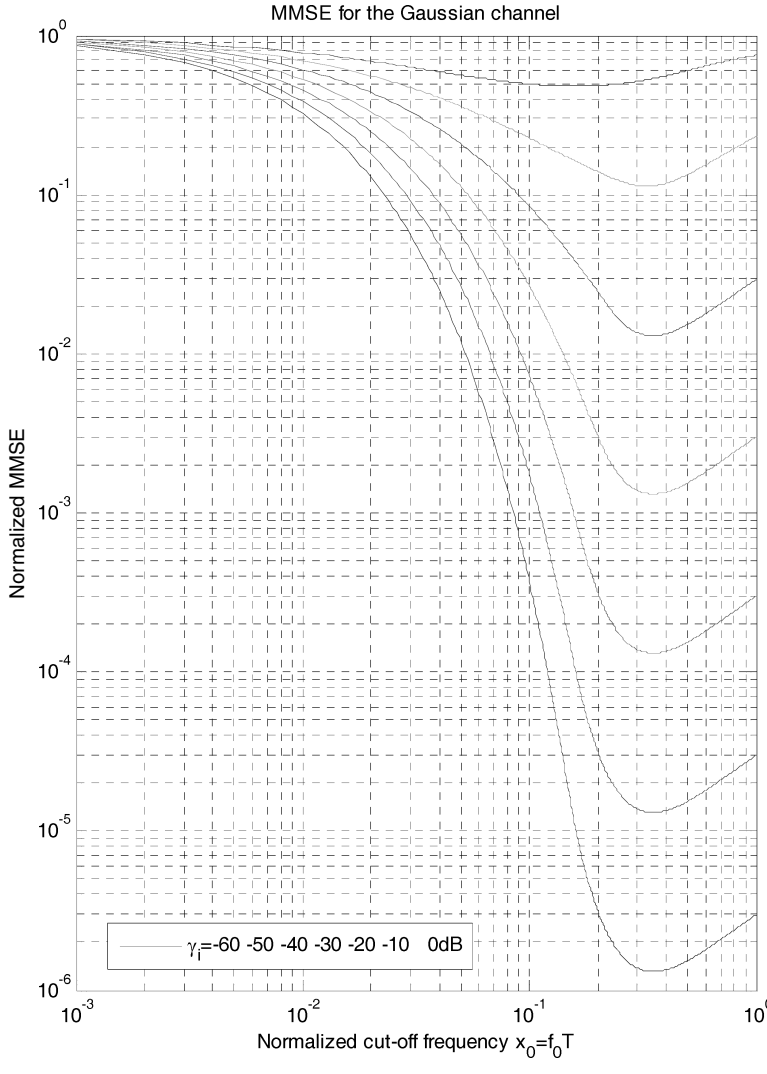

Figure 10.13 Computed MMSE profile versus the normalized cut-off frequency for the narrowband Gaussian channel response. The plots are parameterized with increasing noise-to-signal ratios, ranging from $\gamma_i = -60\,\text{dB}$ up to $\gamma_i = 0\,\text{dB}$. The relevant feature is the asymptotic behavior encountered by every MMSE plot at negligible channel bandwidth, and highlights the weakness of the DFE when solicited by the Gaussian channel response. At a relatively narrow bandwidth, in the range of one-tenth of the bit rate, the DFE performance greatly degrades for noisy channels. For typical values of the noise-to-signal ratio encountered in multimode optical fiber transmissions, $\gamma_i \sim -20\,\text{dB} - -10\,\text{dB}$, the MMSE ranges between 40 % and 60 %, leading to very weak ISI compensation

It is evident that their overlapping leads to an almost uniform profile in the integration interval $-\frac{1}{2} \leq x_0 \leq +\frac{1}{2}$.

For an increasing cut-off frequency $x_0 \to \pm\infty$, the number of Gaussian profiles contributing to the sum in Equation (10.76) increases accordingly, since each Gaussian broadens with $x_0 \to \pm\infty$. How many Gaussians will contribute to the sum for a fixed cut-off frequency? The answer is, of

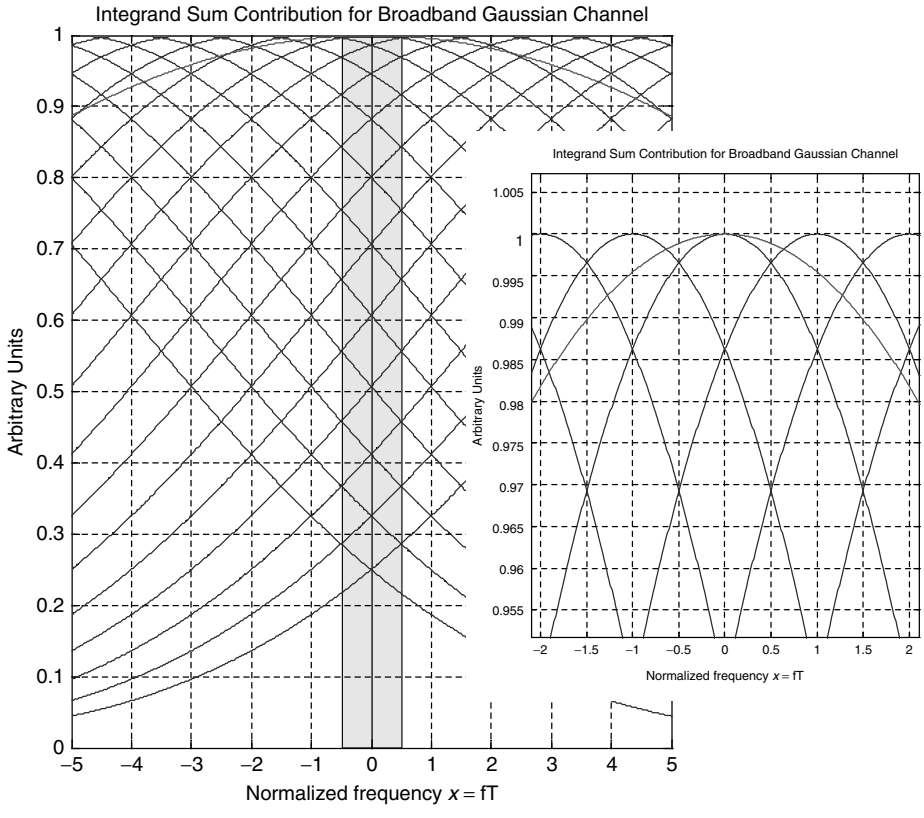

Figure 10.14 Computed sum of the first 21 Gaussian contributions in the series factor in Equation (10.76). The individual Gaussians are represented as curves while the sum is shown, and has been normalized to the maximum value in order to make a consistent comparison. The sum of the first 21 terms leads to almost a constant profile in the integration interval $-0.5 \leq x \leq +0.5$

course, that all Gaussians will contribute to the sum since each Gaussian is indefinitely extended on the frequency axis, and even indefinitely translated Gaussians will add a finite positive contribution to the integration interval.

However, only a finite number of them will add a significant contribution to the sum. This number is proportional to the Gaussian broadening factor and then to the cut-off frequency x_0. It should be clear that for a given x_0 the number of contributing Gaussians is of the same order of x_0. In fact, each term is limited at the upper end by the unit value that the Gaussian addend reaches at the origin. Assuming that the first symmetrical N Gaussians are considering, it can immediately be written that

$$\sum_{n=-N}^{+N} \mathrm{e}^{-[(x-n)/x_0]^2 2\log 2}\Bigg|_{x=0} \leq 2N+1 \tag{10.81}$$

where the equality sign holds in the limit $x_0 \to \pm\infty$-of indefinitely broadening Gaussians. Setting $N = Mx_0$, it can be conclude that

$$\lim_{x_0\to\infty} \sum_{n=-Mx_0}^{+Mx_0} \mathrm{e}^{-[(x-n)/x_0]^2 2\log 2}\Bigg|_{x=0} = 2Mx_0+1 \tag{10.82}$$

This behavior is clear by shown in Figure 10.14. The limiting value of the series term in Equation (10.76) for increasing values of the cut-off frequency is now considered. According to the consideration above, it is concluded that

$$\lim_{x_0\to\infty}\frac{1}{x_0^2}\sum_{n=-\infty}^{+\infty}\mathrm{e}^{-[(x-n)/x_0]^2 2\log 2}=\lim_{x_0\to\infty}\frac{1}{x_0^2}(2Mx_0+1)=0 \tag{10.83}$$

and the MMSE from Equations (10.76) and (10.83) becomes

$$\lim_{x_0\to\infty}\mathrm{MSE}=\lim_{x_0\to\infty}\exp\left[-\int_{-1/2}^{+1/2}\log\left(1+\frac{\log 2}{\pi x_0^2\gamma_i}\sum_{n=-\infty}^{+\infty}\mathrm{e}^{-[(x-n)/x_0]^2 2\log 2}\right)\mathrm{d}x\right]=1 \tag{10.84}$$

Figure 10.15 shows the computed MMSE for the Gaussian channel versus the normalized cut-off frequency for the parametric noise-to-signal ratio. As expected, the MMSE profile reaches

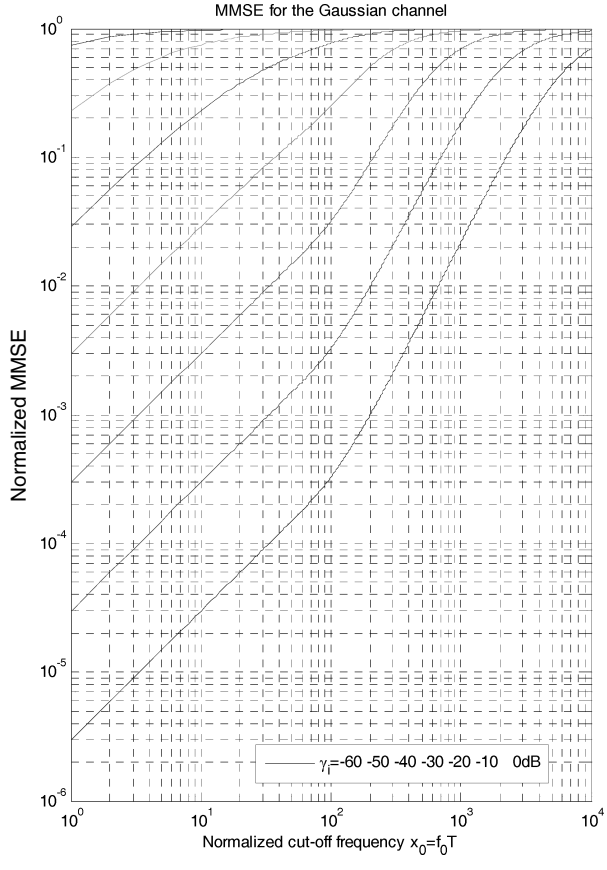

Figure 10.15 Computed MMSE profile versus the normalized cut-off frequency for the broadband Gaussian channel response. The plots are parameterized with an increasing noise-to-signal ratio, ranging from $\gamma_i = -60\,\mathrm{dB}$ up to $\gamma_i = 0\,\mathrm{dB}$. As expected, the MMSE shows the asymptotic behavior for a very large Gaussian bandwidth. According to Equation (10.76), the MMSE reaches the asymptote faster for noise-limited cases. Very low-noise situations are better for compensation by the DFE and the resulting MMSE is lower for a given Gaussian bandwidth. Large bandwidth channels are limited by the noise due to the received matching condition

asymptotically the unit value for indefinitely increasing the cut-off independently from the noise-to-signal ratio.

The effect of the noise-to-signal ratio is the dominant reason for MMSE collapse in all broadband channels. The assumption of a matched receiver in the theory of the DFE makes the amount of noise power entered proportional to the square of the channel bandwidth, leading to a noise-limited DFE characteristic. This quadratic behavior is clearly shown by the computed MMSE in the large bandwidth range and reported in Figure 10.15. Increasing the channel bandwidth above $x_0 = 100$ leads to an abrupt slope variation of the MMSE, increasing two decades for every decade increment of the channel bandwidth. This value is characteristic for the noise-limited operation.

10.2.6.3.3 Midband Gaussian Channel

The last condition to be discussed refers to the Gaussian channel whose bandwidth ranges between approximately one-tenth of the bit rate frequency and ten times that value. This will be referred to as the midband Gaussian channel. This case is most interesting since it represent the typical situation requiring the DFE operation. In fact, besides the interesting mathematical and modeling issues discussed so far, both very large and very low Gaussian channel bandwidths represent limiting cases that for some reason will not support the DFE. If the bandwidth is too large, the DFE receiver will be affected by noise limitation, while for an extremely low bandwidth, the DFE is no longer capable of canceling out the residual intersymbol interference, even assuming an ideal DFE architecture. In the midband Gaussian channel case the situation is completely different and the DFE is quite efficient at canceling the symbol interference.

Figure 10.16 presents the computed MMSE according to Equation (10.76), assuming that the normalized channel bandwidth ranges between $10^{-1} \leq x_0 \leq 10^{+1}$ and with the same parametric noise-to-signal ratio assumed in all previous examples. The benefit of MMSE is evident in the midband channel application: every MMSE curve reaches the minimum value for the corresponding noise parameter value. The minimum is closely located between 30 % and 40 % of the bit rate frequency. In conclusion, the better performances of the DFE operating over a Gaussian channel are achieved when the channel bandwidth is about one-third of the bit rate frequency.

In order to highlight this frequency range of the DFE operation for Gaussian channels, Figure 10.17 shows the computed MMSE with a higher resolution in the parametric noise variation. The noise-to-signal ratio ranges between $0\,\text{dB} \leq \gamma_i \leq 20\,\text{dB}$, with a 1 dB step. Note that the notation uses dB_{10} for the power ratio.

The result of the computed MMSE in Figure 10.16 suggests a simple example. A legacy multimode fiber link is 150 meters long and has the modal bandwidth equal to BW = 500 MHz km. Accordingly, the link bandwidth is $f_0 = \text{BW}/0.15 \cong 3.33\,\text{GHz}$, which corresponds to $x_0 = f_0 T \cong 0.323$. Assuming a Gaussian modal response approximation and $\gamma_i = -10\,\text{dB}$, from Figure 10.17 it can be concluded that $\text{MMSE} \cong 0.113$, which corresponds to $\sqrt{\text{MMSE}} \cong 0.336$ of the RMS residual interference error.

10.2.7 The Eye Diagram Opening Penalty

In this section the MSE concept developed so far will be used in order to find a quantitative relationship with the closure of the eye diagram due to residual intersymbol interference. Unless otherwise stated, reference will be made to binary bipolar signals. This simplifies the mathematical description without losing in generality for fiber optic transmission systems. Referring to the schematic representation of the signal given in Figure 10.18, it can be seen that each pulse at the decision section is affected by the interference from adjacent symbols, in terms of both pulse precursors and postcursors.

Eye opening is defined as the distance ξ between the average high level and the average low level. The eye diagram opening is very closely related to the bit error rate (BER) performance of

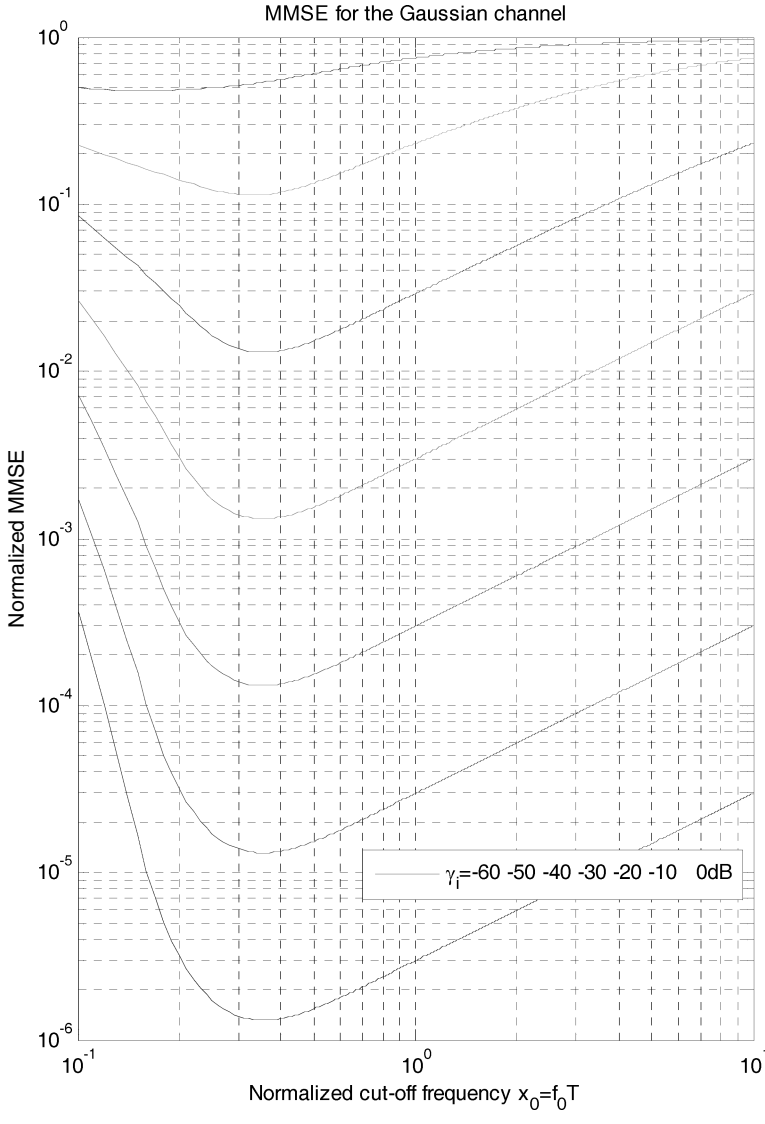

Figure 10.16 Computed MMSE for the midband Gaussian channel. The DFE case shows a consistent compensation improvement for two very extreme cases of very low and very large Gaussian channel bandwidths. The existence of the minimum value makes the MMSE less sensible to the frequency cut-off variation around the corresponding frequency minimum. As expected, the noise parameter sets the minimum height

the transmission system. First the unperturbed eye opening is considered by introducing the variable ξ_0. Referring to Figure 10.18,

$$\xi_0 = 2d \tag{10.85}$$

The MMSE derived in the previous section coincides with the power of the ISI random process $\underline{\varepsilon}_{\mathrm{ISI}}(t)$. Assuming a zero average ISI process $\langle \underline{\varepsilon}_{\mathrm{ISI}}(t) \rangle = 0$, the MMSE with the variance of the ISI distribution is identified and the RMS deviation of the ISI process is proportional to the square root

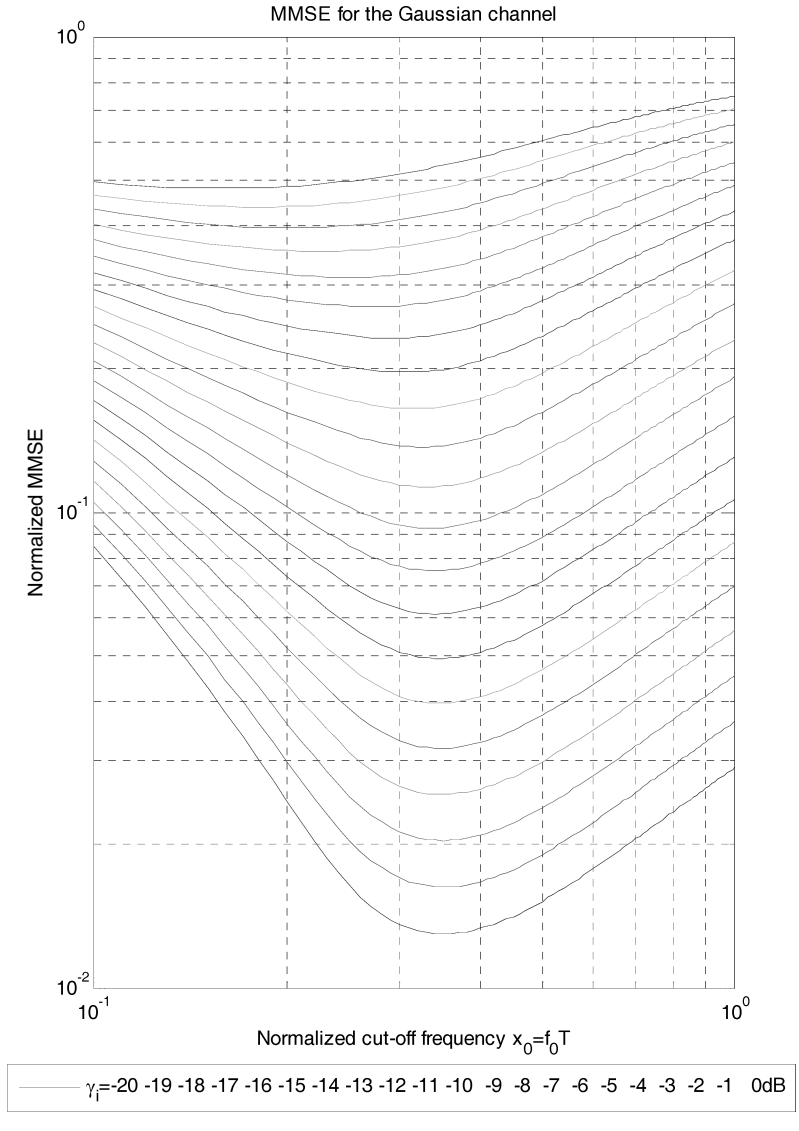

Figure 10.17 Computed MMSE for the Gaussian channel, assuming that the cut-off frequency ranges between $0.1 \leq x_0 \leq 1$. The noise parameter varies between $0 \leq \gamma_i \leq 20$ dB with a 1 dB step. The position of the frequency minimum results is almost insensible to the noise parameter and is closely located at around 35 % of the normalized bit rate.

of the MMSE:

$$\sqrt{\langle \varepsilon_{\mathrm{ISI}}^2(t) \rangle} = _{|\langle \varepsilon_{\mathrm{ISI}}(t) \rangle = 0} \ \sigma_{\mathrm{ISI}} = \xi_0 \sqrt{\mathrm{MMSE}} \tag{10.86}$$

The RMS eye opening ξ_{ISI} under perturbed conditions is due to ISI by the difference between the unperturbed eye opening ξ_0 and twice the RMS ISI amplitude:

$$\xi_{\mathrm{ISI}} \equiv \xi_0 - 2\sigma_{\mathrm{ISI}} \tag{10.87}$$

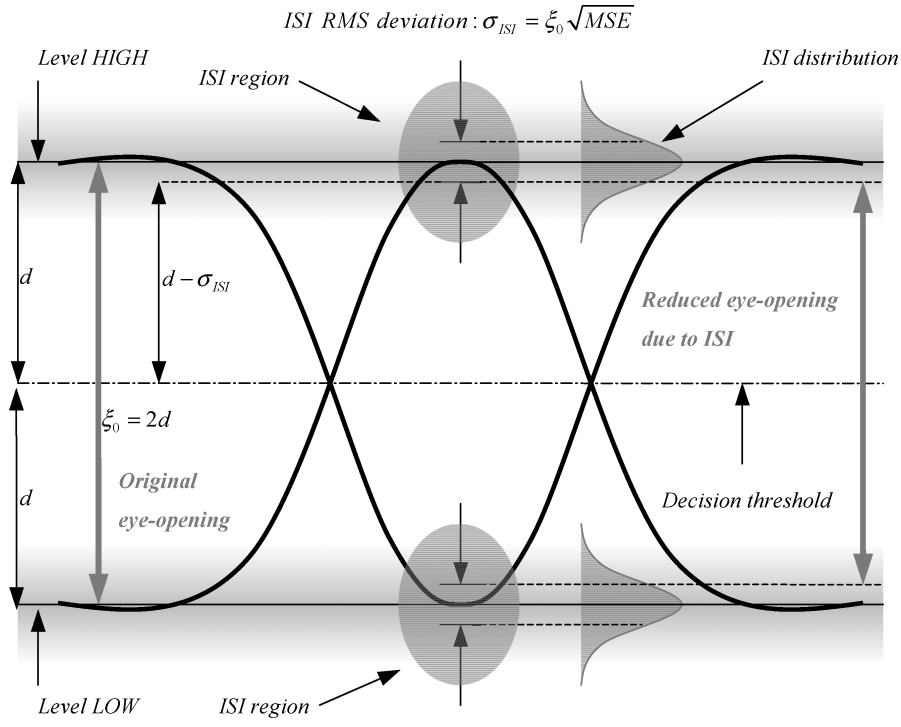

Figure 10.18 Schematic representation of the binary decision affected by intersymbol interference. The ISI affects the symbol decision at the sampling time region and is distributed across both decision levels with the reported schematic distribution. The RMS value of the ISI distribution coincides with the square root of the MMSE defined in the text. The signal decision distance d under ISI degradation is then reduced to $d - \sigma_{\mathrm{ISI}}$, where $\sigma_{\mathrm{ISI}} = \xi_0\sqrt{\mathrm{MMSE}}$

In order to obtain nonnegative eye opening, which would of course be physically inconsistent, the maximum amount of MMSE on each level must be a quarter. This condition corresponds to the RMS ISI deviation σ_{ISI}, reaching half the original eye opening amplitude. Accordingly, from Equations (10.85), (10.86) and (10.87), the following expression of the eye opening under intersymbol interference conditions is obtained:

$$\xi_{\mathrm{ISI}} = \xi_0(1 - 2\sqrt{\mathrm{MMSE}}), \quad 0 \leq \mathrm{MMSE} \leq \tfrac{1}{4} \tag{10.88}$$

Larger values of the MMSE are not consistent, leading to an over-closed eye diagram, so will not be consider here.

The bit error rate (BER) for a binary symbol affected by the same additive RMS noise σ_n on both decision levels is given by Equation (9.58) and the Q-factor is defined in Equation (9.52). Using the relationships just derived for the eye opening, the general value of the Q-factor can be expressed as follow:

$$Q = \frac{\xi}{2\sigma_n} \tag{10.89}$$

The variable σ_n is the RMS noise amplitude. In particular, using Equations (10.85) and (10.89) the expression of the Q-factor can be written for the unperturbed eye diagram and for the eye diagram

affected by intersymbol interference and noise respectively:

$$Q_0 = \frac{d}{\sigma_n} \tag{10.90}$$

$$Q_{\text{ISI}} = \frac{d(1 - 2\sqrt{\text{MMSE}})}{\sigma_n} \tag{10.91}$$

Substituting Equation (10.90) into Equation (10.91) gives the expression of the Q-factor of the perturbed eye diagram in terms of the unperturbed ones:

$$Q_{\text{ISI}} = Q_0(1 - 2\sqrt{\text{MMSE}}) \tag{10.92}$$

Referring to Equation (10.88), the factor $1 - 2\sqrt{\text{MMSE}}$ assumes the meaning of the residual eye opening due to the RMS intersymbol interference and noise under ideal DFE operation. Therefore,

$$\left.\begin{array}{l} \rho_{\text{ISI}} \equiv 1 - 2\sqrt{\text{MMSE}} \\ 0 \leq \text{MMSE} \leq \frac{1}{4} \end{array}\right\} \Rightarrow 0 \leq \rho_{\text{ISI}} \leq 1 \tag{10.93}$$

with

From Equation (10.88), the following simple and important relation can be obtained:

$$\xi_{\text{ISI}} = \rho_{\text{ISI}}\xi_0 \tag{10.94}$$

These last two expressions reveal the effect of the residual MMSE on the relative eye diagram opening penalty. It will be seen in the next section that these concepts lead directly to the calculation of the optical power penalty. However, before discussing these important concepts a step forward can be taken in the analysis of the eye diagram opening penalty due to intersymbol interference. It is known from Equation (9.58) that the BER is directly related to the Q-factor, which allows the optical power penalty to be identified as the relative variations of the Q-factor under perturbed conditions, as well as unperturbed ones. In the following statement the concept of the optical power penalty is given. In order to maintain the original BER value, the perturbed Q-factor must be restored to the original unperturbed ones, which is achieved at the expense of some extra average optical power required at the receiver input.

Although the statement is correct, it leads to erroneous calculations if applied directly to the DFE theory developed up to now. The reason is that the concept of the optical power penalty needs a reference condition to be used for comparing the perturbed situation. This seems an easy concept, almost trivial, but the DFE theory is based on the receiver matching condition and this is channel-dependent. The intention here is to provide a quantitative way to evaluate the DFE-based system performances in terms of the amount of residual intersymbol interference when the band-limited channel is applied. How could the DFE receiver performances be compared in terms of the intersymbol interference alone if they are matched to different channels and consequently would provide quite different noise bandwidths? The solution to this problem will be presented in the next section.

For the moment the eye diagram opening penalty calculations due to intersymbol interference will be continued. What is wrong? Somewhere the reader should have found an inconsistency in the last few equations. These were left because this is an example of how a modeling sometimes develops, even correcting false assumptions and eventually using themselves as new milestones. The wrong assumption was in Equations (10.90), (10.91) and (10.92). Why? It occurs because the RMS noise is different in the two cases of the unperturbed system, with the eye opening ξ_0, and the perturbed ones, with the eye diagram opening ξ_{ISI}. The original eye opening ξ_0 is based just on the symbol amplitude at the decision instant, without any added noise.

The noise contribution is embedded in the DFE theory, is not removable and is a consequence of the optimization process based on the matched receiver assumption. The noise power is then created

during the mean-square error minimization procedure, for the given channel response and noise power density. How could the eye diagram of the DFE receiver affected by noise and residual ISI be conceptually compared with the noise-free and fully opened eye diagram? Referring to Equations (10.90) and (10.91), the correct conclusion is that the RMS noise in the case of the unperturbed system must be specified in terms of some reference condition and in any case it is different from the RMS noise of the perturbed system. In conclusion, the two Q-factors are not comparable.

Limiting the analysis now to the calculation of the optical eye closure and not to the optical power penalty, the right approach is then to compare the eye opening ξ_0 of the noise-free reference eye diagram with the eye opening ξ_{ISI} of the noisy and ISI affected eye diagram after the DFE receiver. Again, the optical power penalty is not being calculated because the noise on the unperturbed eye diagram is not being taken into account. Instead, only the eye diagram openings in the two cases are compared. Assuming that the original, unperturbed eye opening is given by ξ_0, the corrupted eye diagram opening is given by ξ_{ISI} in Equation (10.94). In order to restore the original RMS of the eye opening in the presence of residual ISI and noise in the DFE receiver, the new value ξ_0' must be introduced such that

$$\xi_{\mathrm{ISI}} = \rho_{\mathrm{ISI}}\xi_0' = \xi_0 \tag{10.95}$$

Hence

$$\frac{\xi_0'}{\xi_0} = \frac{1}{\rho_{\mathrm{ISI}}} \tag{10.96}$$

The eye diagram opening penalty $\Delta\xi_{\mathrm{R}}$ due to residual ISI and noise generated by the ideal DFE receiver is defined as the ratio between the required eye opening ξ_0' and the unperturbed eye opening ξ_0:

$$\Delta\xi_{\mathrm{R}} \equiv \frac{1}{\rho_{\mathrm{ISI}}} = \frac{1}{1 - 2\sqrt{\mathrm{MMSE}}} \tag{10.97}$$

The condition $0 \leq \mathrm{MSE} \leq \frac{1}{4}$ must be fulfilled. This procedure gives the correct eye opening degradation in the DFE receiver if the perturbation, either residual intersymbol interference or noise, satisfies some requirements. In the case of the intersymbol interference, the amount of residual error is proportional to the unperturbed signal amplitude and every request to increase the received input power translates into a corresponding increase of the residual intersymbol interference in terms of the signal amplitude.

At this point it would seem meaningless to increase the optical power, but this is not the case investigated. The Q-factor expresses the ratio between signal and noise entities, and even if the relative ISI amplitude remains constant, by increasing the received optical power, the relative noise amplitude decreases accordingly once the channel remains fixed. This leads to a larger Q-factor and hence a lower BER. This reasoning is founded on the assumption that the noise is constant, independent from the signal level. If, for example, the noise amplitude increases linearly with the received optical power, the resulting Q-factor would remain constant at increasing input power and the BER performance would also improve. In this case the BER will exhibit the well-known floor behavior and required original performances would never be recovered in terms of any amount of extra power.

Another case in which the BER performance remains constant versus increasing input optical power is represented by the infinite peak ISI distribution. This is the familiar case of the Gaussian probability density function. By increasing the received optical power, the relative amount of residual ISI also increases and since it is indefinitely distributed along the amplitude axis (infinite peak ISI distribution), there would be a constant finite probability of error detection, independently from the input power level. In this case the errors are not generated by the noise level, which could be relatively depressed by increasing the signal power (if noise is additive), but are generated by unwanted (erroneous) signal transitions due to peaked ISI conditions. A clear example of an infinite

peak residual ISI distribution is the Gaussian probability density function. Of course, in practice it is quite unlikely to find the intersymbol interference distributed along the real axis with an infinite peak probability density function. Instead, under severe intersymbol conditions it is reasonable to find in practice the ISI distribution extending across the decision threshold, leading to decision errors even under noiseless conditions. In that case, even in the presence of noise, it is clear that the BER function will exhibit asymptotic (floor) behavior as opposed to the input optical power. The ISI distribution will in fact grow proportionally with the received input optical power, leading to unrecoverable error conditions.

Figure 10.19 shows a sketch of the threshold-crossing ISI distribution with the related BER floor under noisy conditions. Since the noise is statistically independent from the intersymbol process once the channels have been fixed, the probability density function of the sum of noise and ISI is distributed according to the convolution of the probability density functions of noise and ISI. The additive noise leads to a broader joint distribution than the ISI alone. Nevertheless, due to the additive assumption, the relative noise fluctuations decrease accordingly as long as the input optical power increases, leading to the joint distribution approaching the ISI alone at a higher power level. This is the case shown in the bottom graph in Figure 10.19. At relatively low input power levels, the noise contribution is still relevant to the erroneous threshold-crossing condition, but at a higher power level the depressed noise term becomes almost irrelevant to the decision process.

If the ISI distribution extends across the threshold the error rate will never be improved by increasing the input power. In fact, the ISI is proportional to the signal amplitude and then to the input optical power. This behavior leads directly to the horizontal asymptote of the BER plot, known as the BER floor. No matter how large the input power becomes the error rate will remain constant. In real systems several other factors limit the error performance to some degree. Among the most important are the timing jitter and quadratic noise terms, such as the signal-spontaneous beat noise in optically amplified systems and the RIN. Both of these noise terms depend on the square value of the optical power, making the RMS noise amplitude linearly related to the input power. This clearly determines a BER floor condition whose level depends on the quadratic noise amount.

These conclusions lead to the following important statements:

1. The RMS eye closure due to the intersymbol interference is restorable, increasing the input optical power if the following two conditions are simultaneously verified:
   (a) The ISI distribution exhibits a finite interval of definition (it is not an infinite peak distribution, i.e. the Gaussian) and it does not cross the decision threshold level.
   (b) The noise at the DFE receiver input is additive to the signal (it is not signal-dependent).
2. Once the above statement is satisfied, the RMS eye opening degradation due to both residual ISI and noise in the ideal DFE receiver is fully recoverable and the eye diagram opening penalty $\Delta\xi_R$ is given by Equation (10.97):

$$\Delta\xi_R = \frac{1}{\rho_{ISI}} = \frac{1}{1 - 2\sqrt{MMSE}}$$

with $$0 \leq MMSE \leq \tfrac{1}{4}$$

The eye diagram opening penalty $\Delta\xi_R$ is usually computed in decibels. By definition,

$$\Delta\xi_{dB} \equiv 10 \log_{10} \Delta\xi_R$$

From Equation (10.97), the following expression of the eye diagram opening penalty expressed in dB is obtained:

$$\Delta\xi_{dB} = -10 \log_{10}(1 - 2\sqrt{MMSE}) \tag{10.98}$$

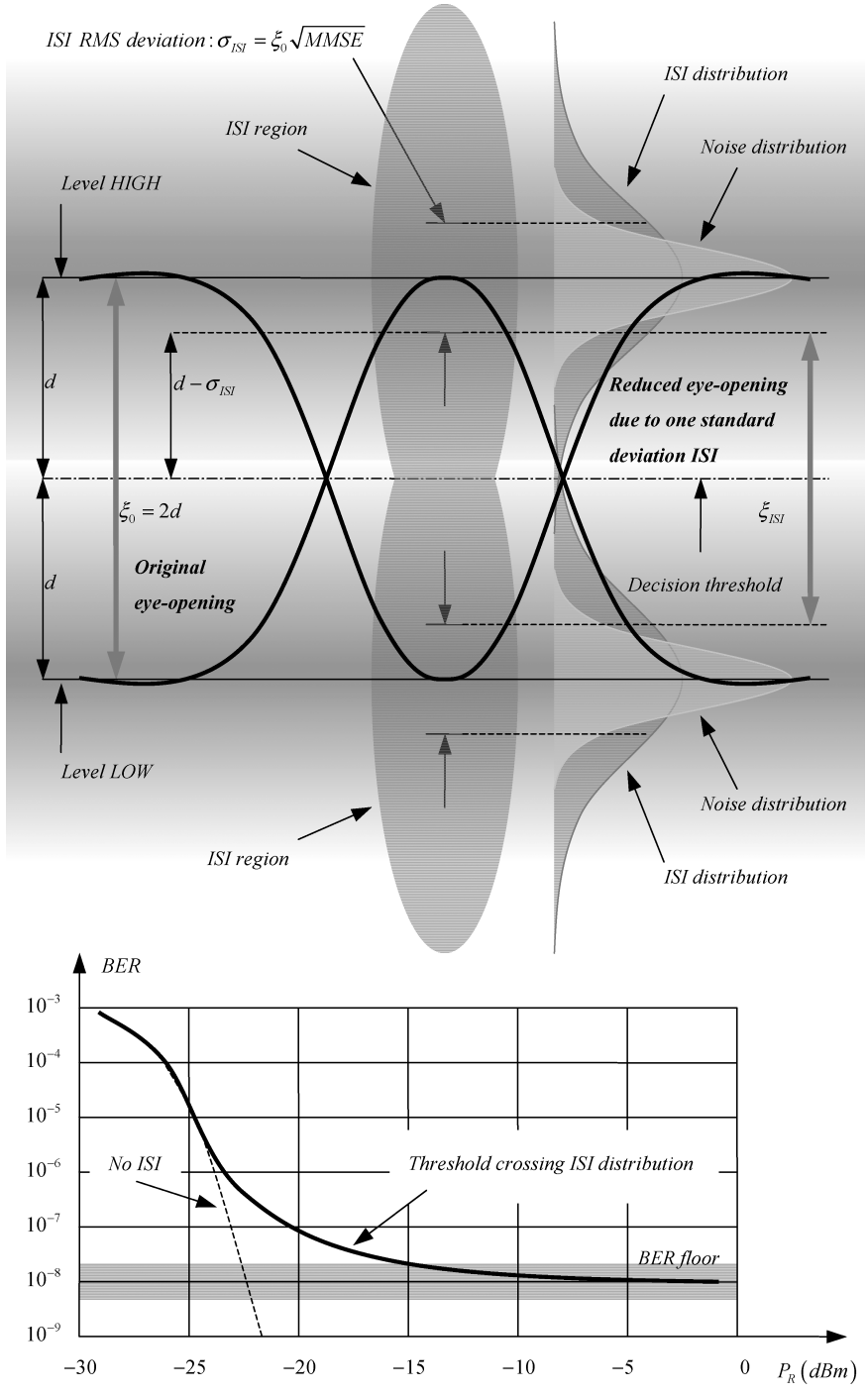

Figure 10.19 Top: severe ISI with a threshold-crossing distribution. Even noiseless conditions will generate decision errors due to an extended ISI distribution. The dashed lines indicate one standard deviation ISI amplitude. Bottom: tails of the ISI distribution cross the decision threshold position, leading to the horizontal asymptotic behavior (floor) of the bit error rate versus the input optical power

10.2.8 Calculation of the Eye Diagram Opening Penalty

In this section the optical eye diagram opening penalty is computed using Equation (10.98) for the two relevant cases of single-pole and Gaussian channel responses discussed in Section 10.2.6. Owing to the limitation to a quarter of the maximum value of the MMSE for having a consistent definition of the eye diagram opening penalty, this condition must be added to the computation of the maximum acceptable MMSE. Figure 10.20 shows the computed eye diagram opening penalty for the single-pole channel due to residual ISI using the expression (10.98) and assuming three different noise-to-signal ratios, $\gamma_i = -30\,\text{dB}$, $-20\,\text{dB}$, $-10\,\text{dB}$. As expected from the logarithmic function behavior of the negative argument in Equation (10.98), the eye diagram opening penalty in Figures 10.20 and 10.21 exhibits a sharp increase as long as the minimum mean square error approaches the value $\text{MMSE} = \frac{1}{4}$. For lower cut-off frequencies, each curve exhibits a smoothed profile, approaching the horizontal asymptote for $x_0 \to 0$. This peculiarity makes the single-pole channel very well compensated by the DFE architecture.

The eye diagram opening penalty in the case of a Gaussian channel is quite different and is characteristic of this frequency response. Figure 10.22 shows the computed MMSE and optical power penalty for the Gaussian channel, assuming the same noise conditions and cut-off frequency range as used in the single-pole case. The cut-off frequency x_0 spans three decades, ranging from 10 times the bit rate frequency down to 100 times below. As expected from the conclusions of the MMSE calculation in Section 10.2.6 for the Gaussian channel, a frequency interval exists that is characterized by the minimum residual interference. This interval is quite visible in the eye diagram opening penalty plot in Figure 10.22, which shows the characteristic bathtub profile. The interval of the minimum eye diagram opening penalty is clearly reported in Figure 10.23, where the normalized cut-off frequency spans over just one decade below the bit rate frequency. Assuming that the noise-to-signal ratio $\gamma_i = -20\,\text{dB}$, the eye diagram opening penalty is lower than approximately 4 dB in the entire frequency decade. In particular, for $x_0 = 0.1$, $\Delta\xi_{\text{dB}} \cong 3.8\,\text{dB}$.

It is interesting to compare quantitatively the eye diagram opening penalty for both the single-pole and the Gaussian channels, assuming the same noise factors and normalized frequency range. This analysis is presented in Figure 10.24, where both channel performances are shown together on the same graph. The noise-to-signal ratio assumes two values, namely $\gamma_i = -20\,\text{dB}$ and$\gamma_i = -10\,\text{dB}$. The cut-off frequency ranges between $x_0 = 0.1$ and $x_0 = 1$. For each noise factor γ_i, the eye diagram opening penalty functions intersect at the cut-off frequency $\hat{x}_0$.

In general, the following behavior is found: to the left of the cross-over frequency $\hat{x}_0$ the single-pole channel leads to a lower eye diagram opening penalty than the Gaussian channel. To the right of $\hat{x}_0$, the Gaussian channel behaves better, showing a lower eye diagram opening penalty than the single-pole channel. The reason for these opposite behaviors should be found in the different causes leading to the eye diagram opening penalty. In the case of the smoothed single-pole frequency profile, the noise is the dominant factor at higher cut-off frequencies. The steeper Gaussian profile leads instead to a higher value of the residual interference at a lower cut-off, but to a lower MMSE due to the reduced noise bandwidth at higher cut-off frequencies. It is remarkable that the net gain of the Gaussian channel with respect to the single-pole channel reduces considerably at lower noise-to-signal ratios. This can be explained in terms of a noise-limited eye diagram opening penalty at higher cut-off frequencies, located to the right of $\hat{x}_0$. Reducing the noise factor leads to a less relevant noise term and then both curves come closer together.

In conclusion, the single-pole channel leads to a lower optical eye diagram opening penalty at lower cut-off frequencies. The Gaussian channel behaves better for slightly higher cut-off frequencies, but the optical eye diagram opening penalty increases abruptly at a lower cut-off. This might explains the success of the DFE receiver in compensating for copper-based transmission lines where the channel profile closely resembles the smoothed single-pole channel. For the same reason, Gaussian-like channels are very difficult to equalize using a DFE receiver when the cut-off frequency ranges below 10 % of the bit rate frequency. In order to fix some examples, the case of

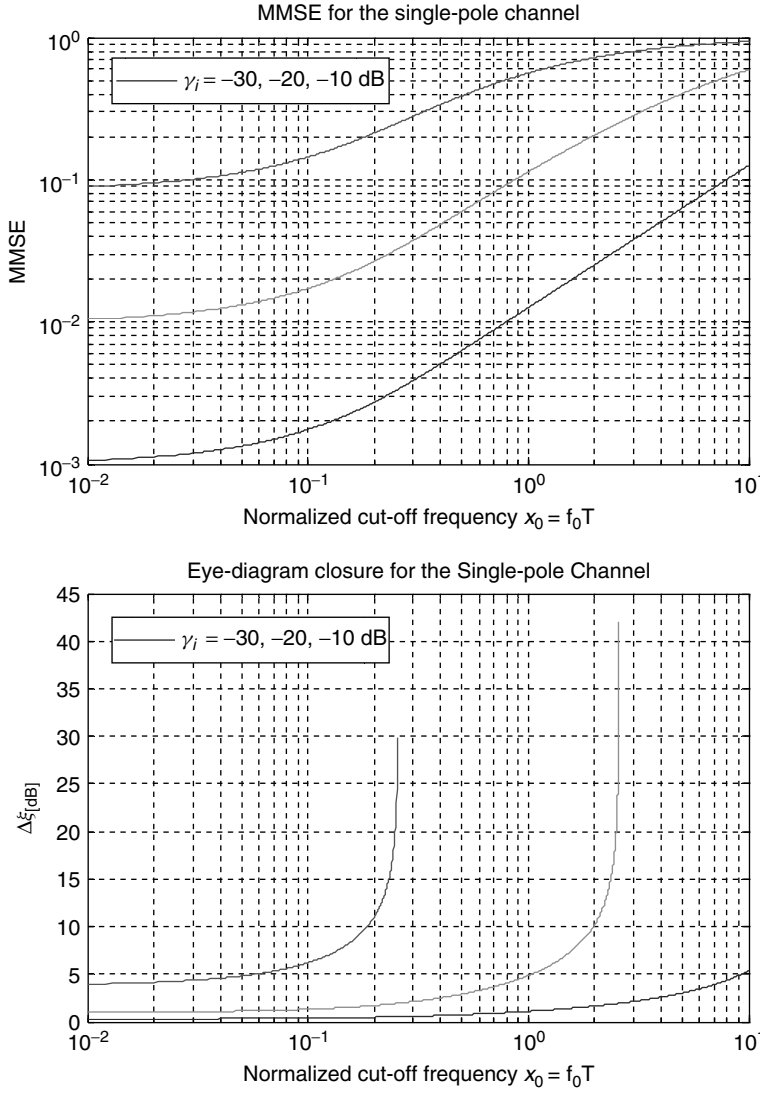

Figure 10.20 Computed MMSE (top) and optical eye diagram opening penalty $\Delta\xi_{\text{dB}}$ (bottom) of the ideal DFE versus normalized cut-off frequency for the single-pole channel according to Equations (10.67) and (10.98) respectively. The noise-to-signal ratio assumes the three values $\gamma_i = -30\,\text{dB}, -20\,\text{dB}, -10\,\text{dB}$. The definition of the optical eye diagram opening penalty implies that $0 \leq \text{MMSE} \leq \frac{1}{4}$, leading to abrupt vertical asymptotes for each curve. The corresponding cut-off frequency gives $\text{MMSE} = \frac{1}{4}$. The almost flat behavior for extremely narrowband channels reveals excellent intersymbol compensation.

a legacy multimode fiber link of 300 m is considered with a modal bandwidth of BW = 500 MHz km, operating at 10 GbE. The link bandwidth is $f_0 = 1.667\,\text{GHz}$, resulting in a normalized cut-off frequency of $x_0 = 1.667/10.3125 \cong 0.162$. Assuming a noise-to-signal ratio of $\gamma_i = -17\,\text{dB}$ gives approximately $\Delta\xi_{\text{dB}} \cong 3.1\,\text{dB}$. Figure 10.25 reports the computed optical eye diagram opening penalty.

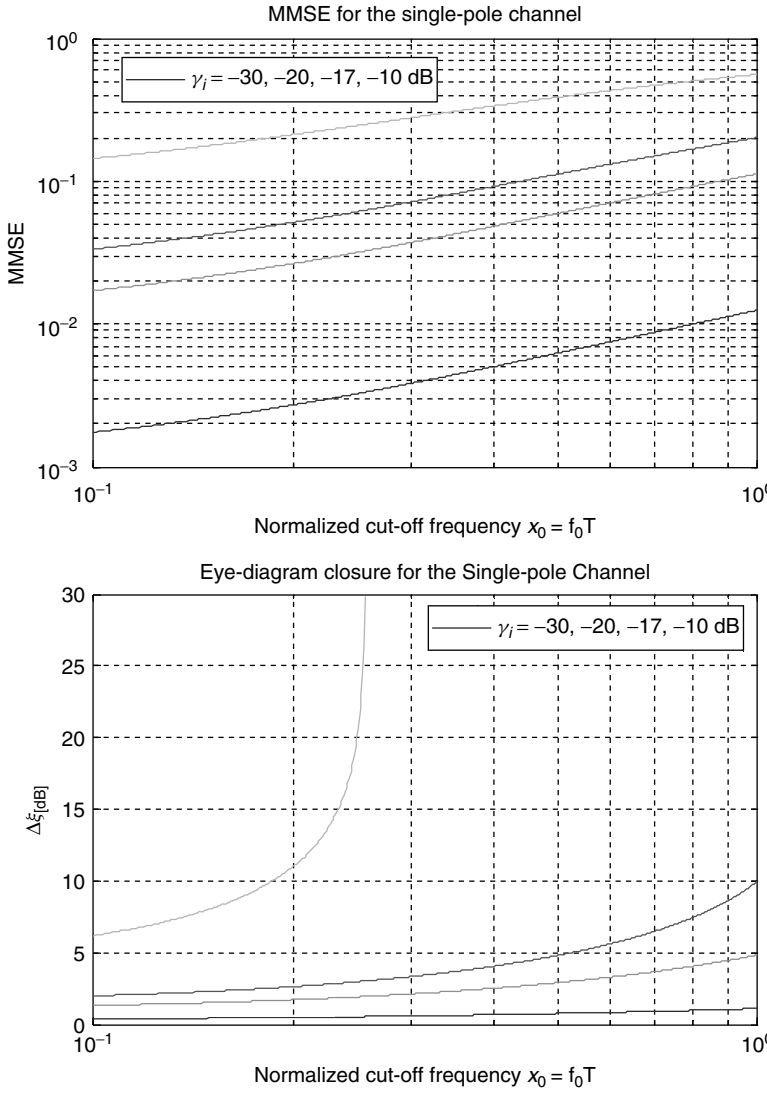

Figure 10.21 Computed MMSE (10.67) and optical eye diagram opening penalty $\Delta\xi_{\mathrm{dB}}$ (10.98) of the ideal DFE for the same case shown in Figure 10.20, but on a reduced cut-off frequency range. The most relevant behavior is the decrease in the optical eye diagram opening penalty at a reducing cut-off frequency. Assuming $\gamma_i = -17\,\mathrm{dB}$, the optical power penalty evaluated at $x_0 = 0.1$ is less than 2 dB. Of course, the optical eye diagram opening penalty decreases for less noisy signals

Before closing this section, it is important to remark that the optical eye diagram opening penalty $\Delta\xi_{\mathrm{R}}$ in Equation (10.97) gives the expected eye diagram opening penalty. This is not trivial. Depending on the probability density function of the joint process constituted by the residual ISI and the added noise, the eye diagram opening $\Delta\xi_{\mathrm{R}}$ can be more or less useful. It must be noted that statistical quantities are being dealt with and so the eye closure $\Delta\xi_{\mathrm{R}}$ represents the expected (average) eye diagram opening penalty according to the ideal DFE receiver.

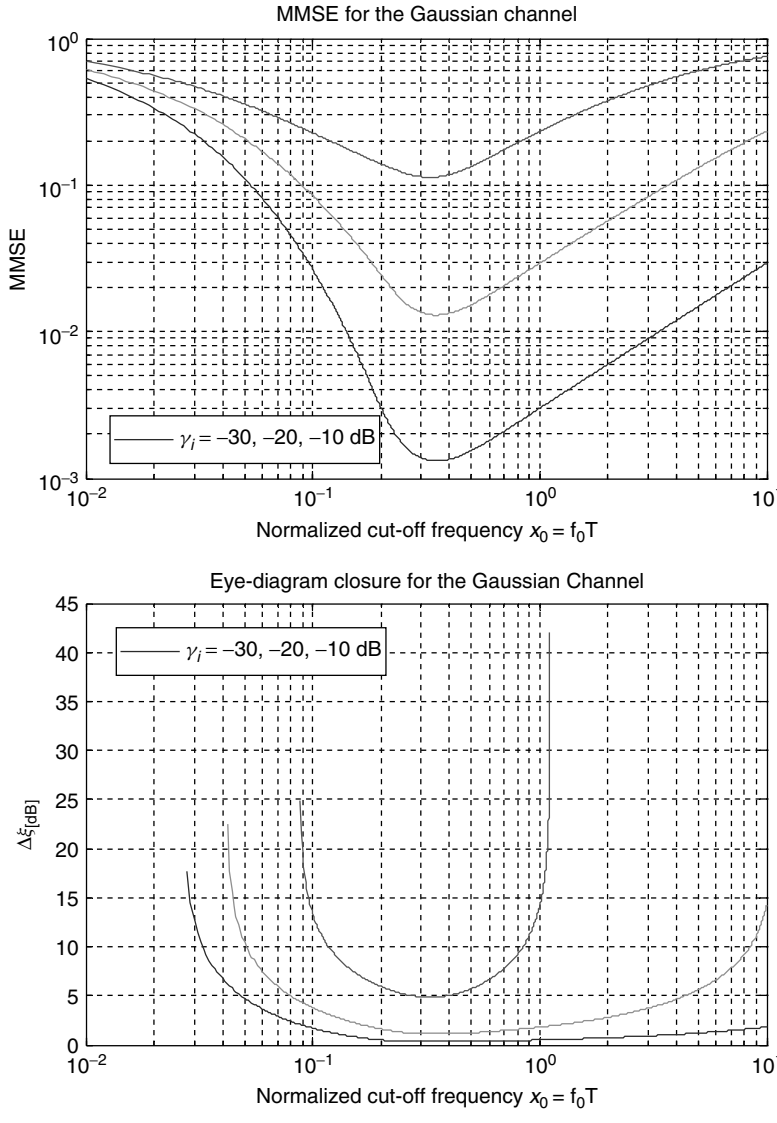

Figure 10.22 Computed MMSE (top) and optical eye diagram opening penalty $\Delta\xi_{\text{dB}}$ (bottom) of the ideal DFE versus normalized cut-off frequency for the Gaussian channel according to Equations (10.76) and (10.98). The noise-to-signal ratio assumes the three values $\gamma_i = -30\,\text{dB}, -20\,\text{dB}, -10\,\text{dB}$. The optical eye diagram opening penalty $\Delta\xi_{\text{dB}}$ for the DFE operating over the Gaussian channel reveals the characteristic bathtub profile, showing the optimum cut-off frequency for each noise-to-signal ratio γ_i

10.2.9 Comments and Conclusions

To conclude this section, a summary is given of the content derived so far. The analytic expression (10.57) of the MMSE was found for the ideal DFE operating over a channel of given frequency response $Q(x)$, where $x = fT$ is the bit rate normalized frequency. According to the work of J. Salz, the DFE theory postulates infinite length digital filters, additive white noise and correct

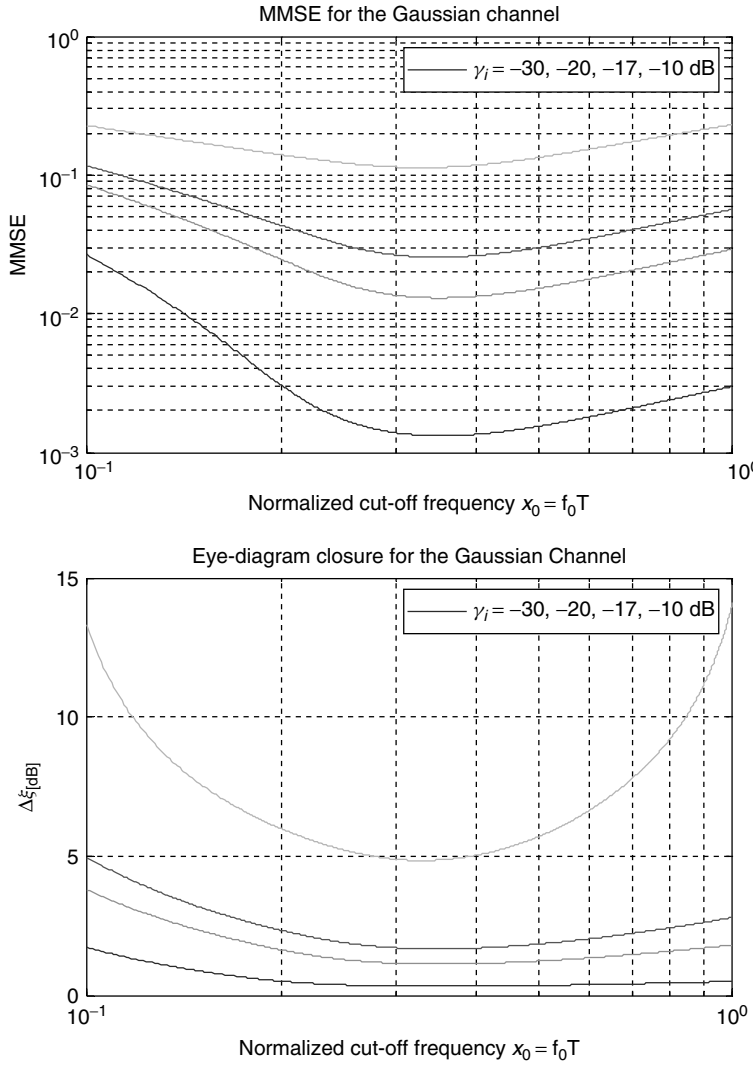

Figure 10.23 Computed MMSE (top) and optical eye diagram opening penalty $\Delta\xi_{\mathrm{dB}}$ (bottom) of the ideal DFE for the Gaussian channel with the four noise-to-signal ratios $\gamma_i = -30\,\mathrm{dB}, -20\,\mathrm{dB}, -17\,\mathrm{dB}, -10\,\mathrm{dB}$) and in the normalized cut-off frequency range $0.1 \leq x_0 \leq 1$. The optical eye diagram opening penalty $\Delta\xi_{\mathrm{dB}}$ has the position of the minimum around $x_0 \leq 0.35$, almost independently of the noise parameter. The minimum value increases accordingly to the noise power level

past decisions. All these three fundamental assumptions must be accounted for when discussing the computed results. The MMSE for three special channels have been derived analytically. The MMSE for the Nyquist channel was presented in Equation (10.60), the MMSE for the single-pole channel was derived in Equation (10.67) and the MMSE for the Gaussian channel was reported in Equation (10.76).

The optical eye diagram opening penalty $\Delta\xi_{\mathrm{dB}}$ has been defined in Equation (10.98), assuming binary symbols with additive white noise and a finite peak ISI distribution. Two important cases have

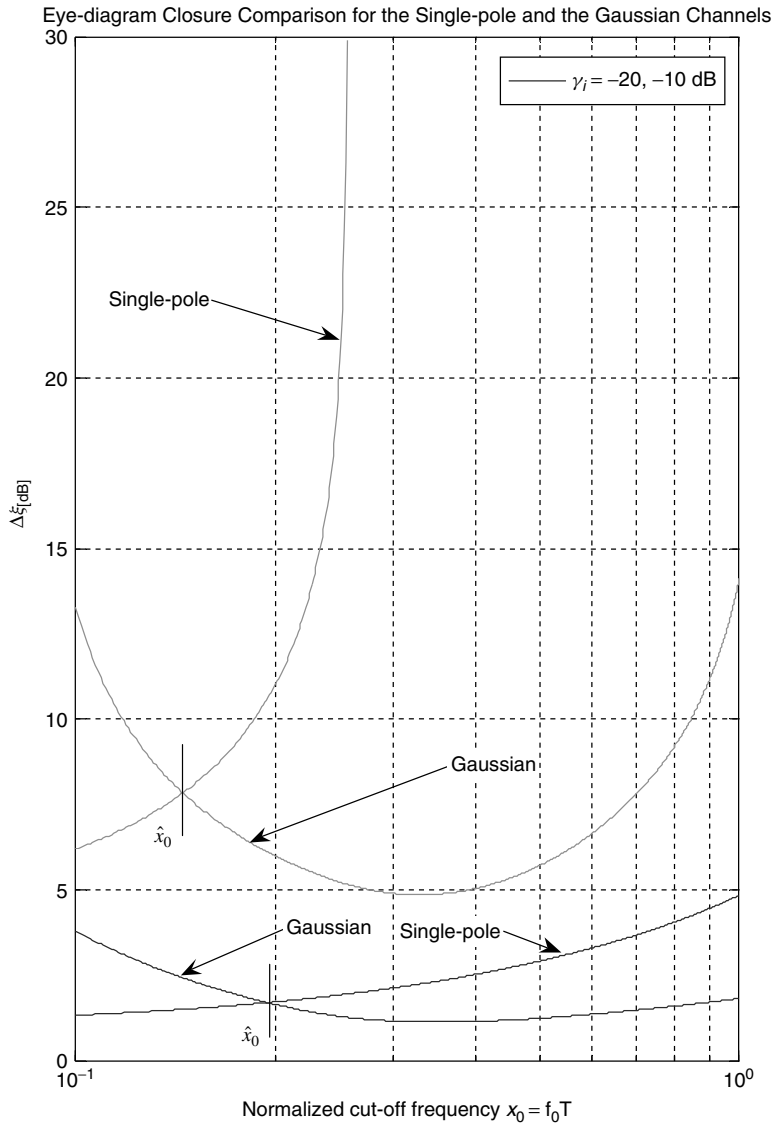

Figure 10.24 Comparison of the optical eye diagram opening penalty $\Delta\xi_{\mathrm{dB}}$ of the ideal DFE between the single-pole and the Gaussian channels versus the normalized cut-off frequency $0.1 \leq x_0 \leq 1$, with noise-to-signal ratios $\gamma_i = -20\,\mathrm{dB}, -10\,\mathrm{dB}$. For each noise-to-signal ratio, the intersection frequency between the two channels is marked by $\hat{x}_0$. The Gaussian channel behaves better at relatively higher cut-off frequencies ($x_0 \geq \hat{x}_0$) than the single-pole channel. At relatively lower cut-off frequencies ($x_0 \leq \hat{x}_0$) the single-pole channel acquires a lower optical eye diagram opening penalty than the Gaussian channels

been evaluated numerically, the single-pole and the Gaussian channel responses. These functions represent the approximate mathematical modeling of the copper-based transmission line and of the multimode optical fiber respectively. The resulting optical eye diagram opening penalties assuming ideal DFE are quite different. The single-pole response allows better compensation even assuming

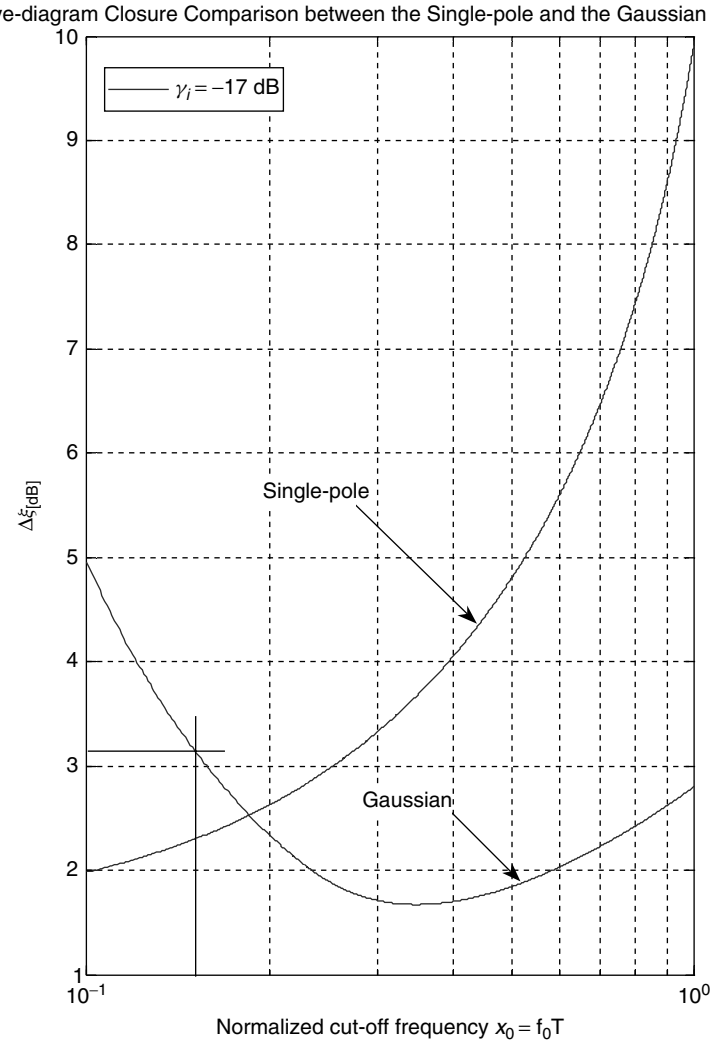

Figure 10.25 Comparison of the optical eye diagram opening penalty $\Delta\xi_{\mathrm{dB}}$ of the ideal DFE between the single-pole and the Gaussian channels versus the normalized cut-off frequency in the interval $0.1 \leq x_0 \leq 1$, with a noise-to-signal ratio $\gamma_i = -17\,\mathrm{dB}$. This value corresponds approximately to $Q \cong 7.02$, leading to BER $\cong 10^{-12}$. The optical eye diagram opening penalty for the ideal DFE over the Gaussian channel exhibits the minimum value at approximately 35 % of the bit rate frequency. The intersection between the single-pole and Gaussian performances is at $\hat{x}_0 \cong 0.18$, giving approximately $\Delta\xi_{\mathrm{dB}}(\hat{x}_0) \cong 2.55\,\mathrm{dB}$. The marked cut-off frequency at about $x_0 \cong 0.16$ corresponds to the Gaussian link bandwidth of a 300 m length of multimode fiber with a modal bandwidth of approximately BW $\cong$ 500 MHz km. The resulting optical eye diagram opening penalty $\Delta\xi_{\mathrm{dB}} \cong 3.15\,\mathrm{dB}$

extremely narrowband conditions, while the Gaussian channel exhibits the optimum bathtub profile versus the normalized cut-off range. The narrowband Gaussian channel can be equalized more easily if the cut-off frequency ranges approximately between 15 % and 100 % of the bit rate frequency, in relation to the noise power.

Table 10.1 Minimum mean square error (MMSE) and optical power penalty expressions for an ideal DFE applied to the selected channels with binary symbol transmission

Channel	MMSE	Optical eye closure	Reference
General	$\mathrm{MMSE} = \exp\left\{-\int_{-1/2}^{+1/2} \log\left[1 + \frac{1}{T^2\gamma_i}\sum_{n=-\infty}^{+\infty} \lvert Q(x-n)\rvert^2\right] \mathrm{d}x\right\}$	$\Delta\xi_{\mathrm{dB}} = -10\log_{10}(1-2\sqrt{\mathrm{MMSE}})$	(10.57) (10.98)
Nyquist	$\mathrm{MMSE} = \frac{\gamma_i}{1+\gamma_i}$	$\Delta\xi_{\mathrm{dB}} = -10\log_{10}(1-2\sqrt{\mathrm{MMSE}})$	(10.60) (10.98)
Single-pole	$\mathrm{MMSE} = \exp\left(-\int_{-1/2}^{+1/2} \log\left\{1 + \frac{1}{4\pi^2 x_0^2\gamma_i}\sum_{n=-\infty}^{+\infty} \frac{1}{1+[(x-n)/x_0]^2}\right\} \mathrm{d}x\right)$	$\Delta\xi_{\mathrm{dB}} = -10\log_{10}(1-2\sqrt{\mathrm{MMSE}})$	(10.67) (10.98)
Gaussian	$\mathrm{MMSE} = \exp\left[-\int_{-1/2}^{+1/2} \log\left(1 + \frac{\log 2}{\pi x_0^2\gamma_i}\sum_{n=-\infty}^{+\infty} \mathrm{e}^{-[(x-n)/x_0]^2 2\log 2}\right) \mathrm{d}x\right]$	$\Delta\xi_{\mathrm{dB}} = -10\log_{10}(1-2\sqrt{\mathrm{MMSE}})$	(10.76) (10.98)

Before closing the section it is important to remark that the theory of the optimum mean square decision feedback equalizer merges the input additive white noise with the residual intersymbol interference after the feedforward filter (FFF). Therefore, the residual MMSE depends on both the channel response and the noise-to-signal ratio γ_i. From the general MMSE expression reported in Equation (10.57), it can be concluded that for indefinitely low noise power, in the limit $\gamma_i \to 0$, MMSE $\to 0$ and from Equation (10.97), the optical eye diagram opening penalty is also vanishingly small, $\Delta\xi_{\mathrm{R}} \to 0$. Table 10.1 summarizes the principal formulas derived in this section.

In the next section the theory of the optical power penalty for the DFE receiver will be introduced. As already stated at the beginning of this section, the concept of the optical power penalty is related to the definition of the DFE reference receiver, still including the DFE architecture with the matched filter but operating over the reference channel. The choice of the reference channel impacts over the entire concept of the optical power penalty for the digital compensation technique using the DFE architecture.

10.3 The Optical Power Penalty

Once the eye diagram opening penalty $\Delta\xi_{\mathrm{R}}$ at the decision section of the DFE receiver due to residual intersymbol interference and noise was derived, the problem of finding the optical power penalty is directed toward the definition of the reference channel applied to the same ideal DFE receiver. One of the most peculiar characteristics of the MMSE in the DFE theory is the matching condition required at the receiving feedforward filter input. This means that every time the channel changes, the FFF of the DFE receiver automatically adapts, providing the required matching. This implies that changing the channel also changes the noise bandwidth and hence the total noise power fed at the decision section of the receiver for fixed noise power spectral density. This is one of the optimization requirements for achieving the MMSE.

10.3.1 The Reference Channel Problem

In order to proceed toward the definition of the reference channel, the initial requirement must be remembered: to find the reference transmission system, characterized by any intersymbol interference in order to compare it with the actual transmission system providing the optical power penalty consequent to the ideal DFE implementation. Of course, in order to have a consistent calculation of the DFE induced optical power penalty, the reference system must have the same transmitter and the same ideal DFE receiver architecture as the actual system, including the same noise power spectral density at the receiver input. The only difference between the reference and the actual system would therefore be confined to the transmission channel. Which reference channel could serve this purpose? At first sight, the only requirement that needs to be addressed to the reference

channel is to provide any intersymbol interference. Accordingly, the only action expected by the DFE receiver would be limited to the noise bandwidth. Any precursors or postcursors would be added to the decision sample by the reference channel and the only perturbation added to the sample would be the noise. However, since the reference channel behavior is being defined there would be an additional requirement that the noise power fed at the decision section would be the minimum available for the given noise power spectral density. It should be clear to the reader, at this point of the discussion, what configuration of the reference channel is sought. Only one channel satisfies simultaneously both the zero intersymbol interference condition and the minimum noise bandwidth under the receiving matched condition. It is the Nyquist channel. Accordingly, from Equation (9.98), the general Nyquist channel $N_m(x) \equiv \sqrt{\Gamma_m(x)}$ is the reference transmission channel for the performance comparison with the ideal DFE receiver when applied to the actual transmission channel:

$$N_m(x) = \begin{cases} T, & |x| \le \dfrac{1-m}{2} \\ T\cos\left[\dfrac{\pi}{2m}\left(x - \dfrac{x}{|x|}\dfrac{1-m}{2}\right)\right], & \dfrac{1-m}{2} \le |x| \le \dfrac{1+m}{2} \\ 0, & |x| \ge \dfrac{1+m}{2} \end{cases} \tag{10.99}$$

$$0 \le m \le 1, \quad x \equiv fT, \quad T = \frac{1}{B}$$

Figure 10.26 gives the computed plots of the Nyquist channel $N_m(x) \equiv \sqrt{\Gamma_m(x)}$ together with the squared function $N_m^2(x) = \Gamma_m(x)$. The raised cosine function $\Gamma_m(x)$ has been defined in Chapter 9, expression (9.98).

10.3.1.1 MMSE for the General Nyquist Channel

Once the reference channel in Equation (10.99) has been defined, the theory developed so far can be used to calculate the corresponding MMSE and eye diagram opening penalty. The MMSE has already been calculated for the particular Nyquist channel $N_0(x)$ with $m = 0$ in Section 10.2.6.1 and the result is given in Equation (10.60). Now, the MMSE of the general Nyquist channel $N_m(x)$ according to Equation (10.99) is derived. Substituting Equation (10.99) in Equation (10.57) gives the following MMSE expression for the general Nyquist channel:

$$\widehat{\text{MMSE}} = \exp\left\{-\int_{-1/2}^{+1/2} \log\left[1 + \frac{1}{T^2\gamma_i}\sum_{n=-\infty}^{+\infty}|N_m(x-n)|^2\right] \mathrm{d}x\right\} \tag{10.100}$$

The hat symbol has been added to the minimum mean square error evaluated for the Nyquist channel in order to differentiate from the MMSE computed for the actual channel. First the series term shown in the integrand in Equation (10.100) is considered. Substituting the Nyquist channel (10.99) gives

$$\frac{1}{T^2\gamma_i}\sum_{n=-\infty}^{+\infty}|N_m(x-n)|^2 = \begin{cases} \dfrac{1}{T^2\gamma_i}\displaystyle\sum_{n=-\infty}^{+\infty} T^2, & |x-n| < \dfrac{1-m}{2} \\ \dfrac{1}{\gamma_i}\displaystyle\sum_{n=-\infty}^{+\infty}\cos^2\left[\dfrac{\pi}{2m}\left(x-n-\dfrac{x-n}{|x-n|}\dfrac{1-m}{2}\right)\right], & \dfrac{1-m}{2} \le |x-n| \le \dfrac{1+m}{2} \\ 0, & |x-n| > \dfrac{1+m}{2} \end{cases} \tag{10.101}$$

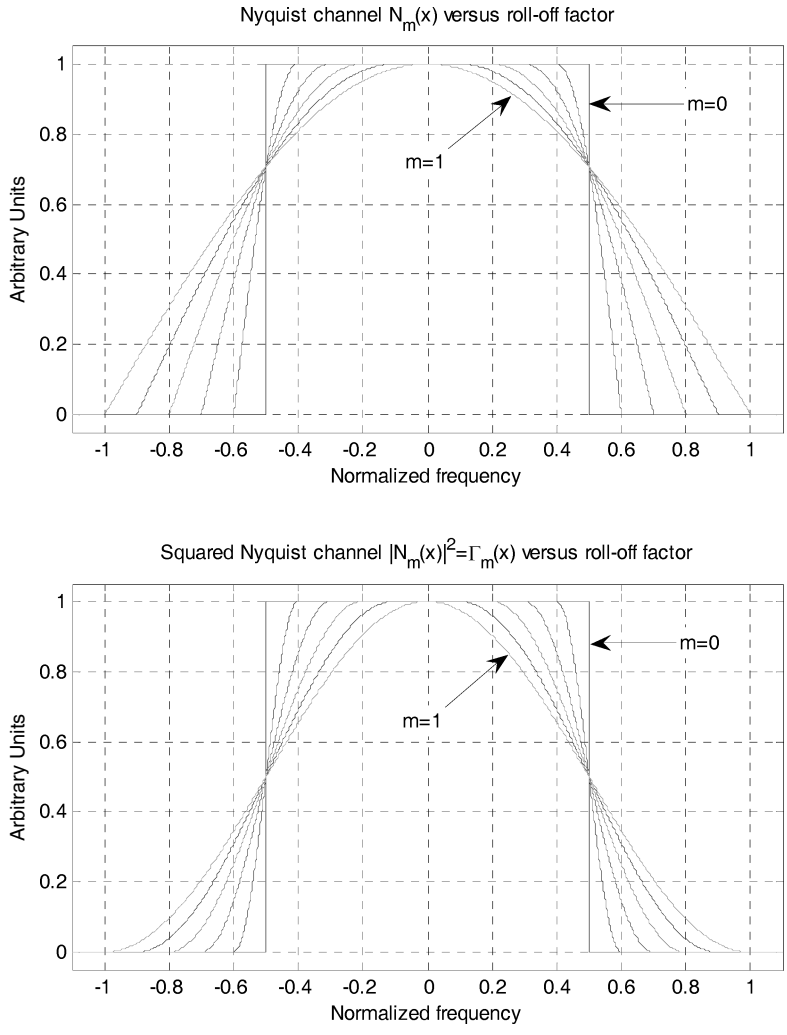

Figure 10.26 Computed spectrum of the Nyquist functions (top) and the raised cosine function (bottom) versus the normalized frequency $x = fT$ for the increasing roll-off factor $m = 0, 0.2, 0.4, 0.6, 0.8, 1$. Every profile of the raised cosine function crosses one-half of the maximum at half the bit rate frequency. This relevant property makes the double-sided noise bandwidth for the Nyquist channel independent of the roll-off and equal to the bit rate frequency

This complex series representation can be easily solved by looking inside each term. The first important remark to make regards the relationship between the integer series step $\ldots, n-1, n, n+1, \ldots$ and the interval $I_{\mathrm{N}}(0) = (|x| < 1)$, where the Nyquist function can assume nonzero values. Stated differently, the Nyquist function is identically zero for every point outside that interval:

$$\forall\, x \notin I_{\mathrm{N}}(0) = (|x| < 1) \Rightarrow N_m(x) = 0 \tag{10.102}$$

Figure 10.27 gives a graphical representation of the first few functions $|N_m(x-n)|^2$ in the above series.

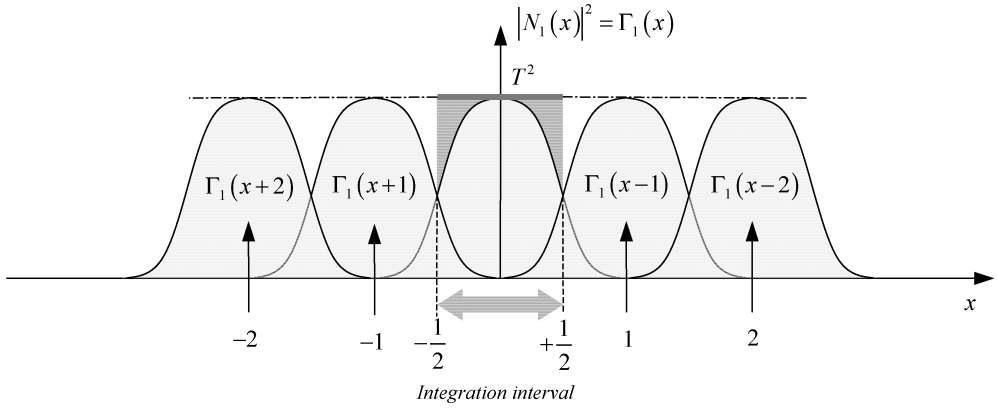

Figure 10.27 Graphical representation of the first series terms in Equation (10.101) for the case $m = 1$. Due to condition (10.103), for every integer $n \geq 2 : \left(-\frac{1}{2}, +\frac{1}{2}\right) \cap I_{\mathrm{N}}(|n| \geq 2) = \emptyset$. In the integration interval $\left(-\frac{1}{2}, +\frac{1}{2}\right)$ only the central squared Nyquist functions and the first two side functions contribute to the integration term. Their superposition in the integration interval gives the constant profile and according to Equation (10.99) equals T^2

According to the definition (10.99) and to condition (10.102), the function $N_m(x - n)$ is therefore identically zero outside the interval $I_{\mathrm{N}}(n) = (|x - n| < 1)$:

$$\forall\, x \;\notin\; I_{\mathrm{N}}(n) = (|x - n| < 1) \Rightarrow\; N_m(x - n) = 0 \tag{10.103}$$

Since each term $N_m(x - n)$ in the series is translated into the integer number n of intervals $I_{\mathrm{N}}(0)$, it can immediately be concluded that in the integration interval $-\frac{1}{2} < x < +\frac{1}{2}$ only the centered function $N_m(x)$ and at least the two side functions $N_m(x - 1)$ and $N_m(x + 1)$ contribute to the summation. For every index $|n| \geq 2$ in the series the contribution of $N_m(x \pm n)$ to the integration interval is identically null: $\left(-\frac{1}{2}, +\frac{1}{2}\right) \cap I_{\mathrm{N}}(|n| \geq 2) = \emptyset$.

From the graphical representation and the definition (10.99) it is easy to demonstrate that the value of the series in Equation (10.101) in the integration interval reduces to the constant T^2, independently of any value of the roll-off factor $0 \leq m \leq 1$. To demonstrate this theorem, it is observed that, from the even symmetry of the normalized raised cosine function in Equation (10.99) and the unit translation, the sum of the central term ($n = 0$) with the first two neighborhoods ($n = \pm 1$) has an even symmetry. Consequently, only the positive frequency half-profile can be considered. The same conclusion holds for the negative frequency axis according to the even symmetry. In the following the explicit expression of the sum of the first two terms, corresponding to $n = 0$ and $n = +1$, is considered:

$$|N_0(x)|^2 + |N_1(x-1)|^2 = \begin{cases} T^2, & 0 \leq x < \dfrac{1-m}{2} \\ T^2 \left\{ \cos^2\left[\dfrac{\pi}{2m}\left(x - \dfrac{1-m}{2}\right)\right] + \cos^2\left[\dfrac{\pi}{2m}\left(x - 1 + \dfrac{1-m}{2}\right)\right]\right\}, & \\ \qquad \dfrac{1-m}{2} \leq x \leq \dfrac{1+m}{2} & \\ T^2, & \dfrac{1+m}{2} < x \leq 1 \end{cases} \tag{10.104}$$

The value of the sum in the interval $(1-m)/2 \le x \le (1+m)/2$ can be computed immediately by observing that the contribution of $|N_1(x-1)|^2$ can be written in terms of the corresponding ones for $|N_0(x)|^2$. In fact, from Equation (10.104),

$$\cos^2\left[\frac{\pi}{2m}\left(x-\frac{1-m}{2}\right)\right]+\cos^2\left[\frac{\pi}{2m}\left(x-1+\frac{1-m}{2}\right)\right]$$
$$=1+\frac{1}{2}\left\{\cos\left[\frac{\pi}{m}\left(x-\frac{1-m}{2}\right)\right]+\cos\left[\frac{\pi}{m}\left(x-1+\frac{1-m}{2}\right)\right]\right\}$$

The second cosine term becomes

$$\cos\left[\frac{\pi}{m}\left(x-1+\frac{1-m}{2}\right)\right]=\cos\left[\frac{\pi}{m}\left(x-1+\frac{1-m}{2}-(1-m)+(1-m)\right)\right]$$
$$=\cos\left[\frac{\pi}{m}\left(x-\frac{1-m}{2}\right)-\pi\right]=-\cos\left[\frac{\pi}{m}\left(x-\frac{1-m}{2}\right)\right]$$

The following identity holds for every roll-off coefficient:

$$\cos^2\left[\frac{\pi}{2m}\left(x-\frac{1-m}{2}\right)\right]+\cos^2\left[\frac{\pi}{2m}\left(x-1+\frac{1-m}{2}\right)\right]=1,\quad \frac{1-m}{2}\le x\le\frac{1+m}{2}$$

From Equation (10.104) it can be concluded that

$$|N_0(x)|^2+|N_1(x-1)|^2=T^2,\quad 0\le x\le 1 \tag{10.105}$$

The same conclusion holds for the negative frequency interval:

$$|N_0(x)|^2+|N_{-1}(x+1)|^2=T^2,\quad -1\le x\le 0 \tag{10.106}$$

Since

$$\underbrace{\sum_{\substack{n=-\infty\\ n\neq 0,\pm 1}}^{+\infty}|N_m(x-n)|^2}_{-1\le x\le +1}=0 \tag{10.107}$$

from Equations (10.105), (10.106) and (10.107), it can be concluded that

$$\underbrace{\frac{1}{T^2\gamma_i}\sum_{n=-\infty}^{+\infty}|N_m(x-n)|^2}_{-1\le x\le +1}=\frac{1}{\gamma_i} \tag{10.108}$$

It is important to note that this result is coincident with the series calculation performed in Section 10.2.6.1. In that calculation, the special case of a Nyquist channel characterized by zero roll-off with $m=0$ was dealt with. Substituting Equation (10.108) into Equation (10.100) gives the expression of the minimum mean square error for the general Nyquist channel:

$$\widehat{\mathrm{MMSE}}=\exp\left[-\log\left(1+\frac{1}{\gamma_i}\right)\int_{-1/2}^{+1/2}\mathrm{d}x\right]$$

and

$$\widehat{\mathrm{MMSE}}=\frac{\gamma_i}{1+\gamma_i} \tag{10.109}$$

The minimum mean square error $\widehat{\text{MMSE}}$ for the DFE receiver with the noise-to-signal ratio γ_i, operating over the Nyquist channel and independently from any value of the roll-off coefficient, is expressed by Equation (10.109).

The result obtained in Equation (10.109) is as important as it is simple and of course coincides with the $\widehat{\text{MMSE}}$ value obtained in Section 10.2.6.1 for the case of the zero roll-off Nyquist channel. In fact, it is valid for every roll-off coefficient and since there is no intersymbol interference in the DFE receiver operating over the Nyquist channel, the $\widehat{\text{MMSE}}$ depends only on the noise-to-signal ratio γ_i. These results conclude the calculation of the $\widehat{\text{MMSE}}$ for the Nyquist channel. In the next section the $\widehat{\text{MMSE}}$ for the Nyquist channel will be related to the eye diagram opening penalty and finally the optical power penalty due to the DFE receiver operating over a general transmission channel will be defined.

10.3.1.2 The Eye Diagram Opening Penalty

The eye diagram opening penalty $\Delta\hat{\xi}_{\text{R}}$ for the Nyquist channel follows directly from the MMSE theory developed in the previous section and from the general eye diagram opening penalty expression derived in Equation (10.97). Substituting the $\widehat{\text{MMSE}}$ expression (10.109) for the Nyquist channel in Equation (10.97) gives

$$\Delta\hat{\xi}_{\text{R}} = \frac{1}{1 - 2\sqrt{\gamma_i/(1+\gamma_i)}}, \quad \gamma_i \equiv \frac{G_i}{T\sigma_a^2} \tag{10.110}$$

The requirement (10.88) on the maximum MMSE in order to have a consistent eye diagram opening penalty definition translates immediately to the following requirement for the maximum noise-to-signal ratio:

$$0 \le \widehat{\text{MMSE}} \le \tfrac{1}{4} \Rightarrow 0 \le \gamma_i \le \tfrac{1}{3} \tag{10.111}$$

As expected, at the limiting condition $\lim_{\gamma_i \to \frac{1}{3}} \Delta\hat{\xi}_{\text{R}} = +\infty$, an infinite eye opening is required to overcome the $\widehat{\text{MMSE}}$. Analogously to Equation (10.98), the eye diagram opening penalty for the Nyquist channel expressed in dB is defined as

$$\Delta\hat{\xi}_{\text{dB}} = -10\log_{10}\left(1 - 2\sqrt{\frac{\gamma_i}{1+\gamma_i}}\right) \tag{10.112}$$

10.3.2 Definition of the Optical Power Penalty

In the previous sections the expressions of the eye diagram opening penalty for the generic working channel have been derived, assuming ideal DFE operation over the reference Nyquist channel. The intention now is to define a consistent optical power penalty due to ideal DFE operation over a generic transmission channel. Given the noise-to-signal ratio γ_i, the optical power penalty consequent to implementation of the ideal DFE receiver derives conceptually from the comparison of the eye diagram opening between the working channel and the Nyquist channel. In Section 10.2.6.1 it was concluded that for every noise-to-signal ratio γ_i, the minimum penalty of the eye diagram opening is accomplished using the ideal DFE receiver over the Nyquist channel. This receiver coincides with the autocorrelator, without any intersymbol interference. The concept of the optical power penalty of the ideal DFE receiver therefore identifies with the comparison of the eye diagram opening penalty $\Delta\xi_{\text{R}}$ for the working channel with the eye diagram opening penalty $\Delta\hat{\xi}_{\text{R}}$ for the Nyquist channel. This is the penalty of using any channel different from the Nyquist ones but with the same noise power spectral density. Using the same approach we followed in Equation (10.97), the eye diagram opening of both the Nyquist and the working channels in terms of the respective

residual minimum mean square errors can be written as

$$\xi_{\mathrm{ISI}} = \rho_{\mathrm{ISI}}\xi_0 \tag{10.113}$$

$$\hat{\xi}_{\mathrm{ISI}} = \hat{\rho}_{\mathrm{ISI}}\xi_0 \tag{10.114}$$

The optical power penalty can be defined by means of the eye diagram opening ξ_0' required for the working channel in order to restore the residual eye diagram opening $\hat{\xi}_{\mathrm{ISI}}$ of the Nyquist channel in consequence of the given noise factor γ_i:

$$\xi_0' : \xi_0'\rho_{\mathrm{ISI}} \equiv \hat{\xi}_{\mathrm{ISI}} \tag{10.115}$$

Hence, from Equation (10.114),

$$\xi_0'\rho_{\mathrm{ISI}} = \hat{\rho}_{\mathrm{ISI}}\xi_0 \tag{10.116}$$

The optical power penalty ΔP_{R} for the DFE receiver operating over the working channel is given by the ratio between the eye diagram opening ξ_0' and ξ_0 according to Equation (10.116):

$$\Delta P_{\mathrm{R}} \equiv \frac{\xi_0'}{\xi_0} = \frac{\hat{\rho}_{\mathrm{ISI}}}{\rho_{\mathrm{ISI}}} \tag{10.117}$$

Substituting the expressions (10.93) for the cases of the Nyquist and working channels respectively gives the following explicit expression of the optical power penalty for the DFE receiver:

$$\Delta P_{\mathrm{R}} = \frac{1 - 2\sqrt{\gamma_i/(1+\gamma_i)}}{1 - 2\sqrt{\mathrm{MMSE}}} \tag{10.118}$$

As expected, once the noise-to-signal-ratio γ_i is fixed, the optical power penalty depends exclusively of the transmission channel characteristic through Equation (10.57). The optical power penalty expressed in decibels has the following expression:

$$\Delta P_{\mathrm{dB}} = 10\log_{10}\left(1 - 2\sqrt{\frac{\gamma_i}{1+\gamma_i}}\right) - 10\log_{10}(1 - 2\sqrt{\mathrm{MMSE}}) \tag{10.119}$$

Finally, using Equation (10.98) and (10.112) gives

$$\Delta P_{\mathrm{dB}} = \Delta\xi_{\mathrm{dB}} - \Delta\hat{\xi}_{\mathrm{dB}} \tag{10.120}$$

This expression summarizes the meaning of all the previous discussion regarding the effect of the reference channel for noise integration. It is important to remark, however, that since the Nyquist channel contribution $\Delta\hat{\xi}_{\mathrm{dB}}$ is strictly positive, the optical power penalty in Equation (10.120) is even lower than the corresponding eye diagram opening penalty $\Delta\xi_{\mathrm{dB}}$. The next section will present some examples about this feature.

10.3.3 Calculation of the Optical Power Penalty

In this section the numerical evaluation is presented of the optical power penalties for the same single-pole and Gaussian channels already considered in Section 10.2.8. In order to show the quantitative effect of the DFE receiver, the following graphs report the eye diagram opening penalty $\Delta\xi_{\mathrm{dB}}$ and $\Delta\hat{\xi}_{\mathrm{dB}}$ for the working channel and for the Nyquist channel respectively, together with the optical power penalty according to the definition (10.117).

10.3.3.1 Single-Pole Channel

Figure 10.28 shows the optical power penalty plots for the single-pole channel versus the normalized cut-off frequency with noise-to-signal ratios of $\gamma_i = -40\,\text{dB}, -30\,\text{dB}, -20\,\text{dB}$. At very low cut-off frequencies the noise power gathered into the system is comparably very small and the total eye diagram opening penalty $\Delta\xi_{\text{dB}}$ tends to be equal to the corresponding value $\Delta\hat{\xi}_{\text{dB}}$ for the Nyquist channel. This means that the average power of the sum of the residual intersymbol interference with the noise has been minimized by the DFE action, leading to almost the same value as that of the noise-limited Nyquist channel. In fact it should be remembered that in the case of the Nyquist channel the only cause of the eye closure comes from the input additive noise. By increasing the channel cut-off frequency, the input matching condition gathers additional noise power with respect to the Nyquist equivalent and the optical power penalty starts to increase due to the relevant noise contribution. At the cut-off frequency, corresponding to the intersection between $\Delta\hat{\xi}_{\text{dB}}$ and ΔP_{dB}, the eye diagram opening penalty is $\Delta\xi_{\text{dB}} = 2\Delta\hat{\xi}_{\text{dB}}$. This cut-off condition can be considered as a threshold for DFE noise-limited operation in the single-pole channel.

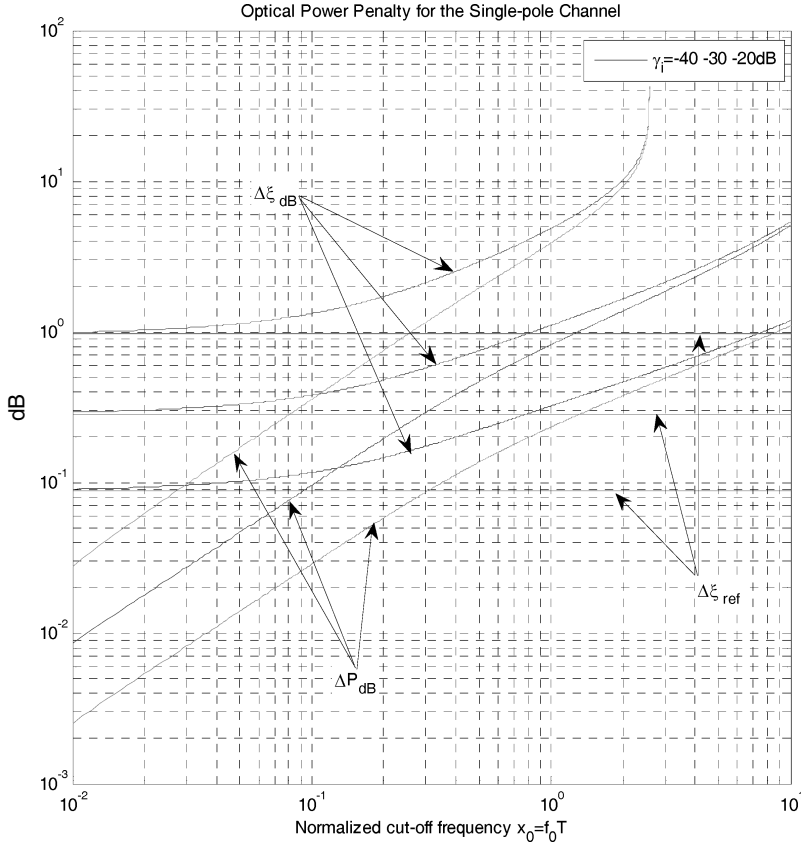

Figure 10.28 Computed optical power penalties versus the normalized cut-off frequency for the DFE receiver over the single-pole channel according to Equation (10.120). The noise-to-signal ratio has been set equal to $\gamma_i = -40\,\text{dB}, -30\,\text{dB}, -20\,\text{dB}$. The optical eye diagram opening penalties for the reference Nyquist channel are also shown as constant lines

10.3.3.2 Gaussian Channel

The optical power penalty for the Gaussian channel is presented in Figure 10.29, assuming $\gamma_i = -40\,\text{dB}, -20\,\text{dB}$. For every fixed noise value, the Nyquist channel has a constant eye diagram opening penalty $\Delta\hat{\xi}_{\text{dB}}$, given by Equation (10.112). The eye diagram opening penalty $\Delta\xi_{\text{dB}}$ for the Gaussian channel, however, exhibits the characteristic long-horn profile from the normalized frequency. The difference between these two functions defines the optical power penalty, as expressed by Equation (10.120). The optical power penalty of ΔP_{dB} follows the same long-horn profile, showing the minimum region at approximately 35 % of the normalized bit rate frequency. This suggests the optimum range of the cut-off frequency for implementing the ideal DFE over the Gaussian channel.

These examples close the section on the optical power penalty for the decision feedback equalizer. The theory has been derived starting from the work of J. Salz and has been applied to the definition of eye diagram opening impairments. The channel bandwidth has the principal role of determining the residual eye diagram opening and consequently the amount of optical power penalty. To this end, the Nyquist channel was introduced in order to provide the ultimate performing reference for every working channel.

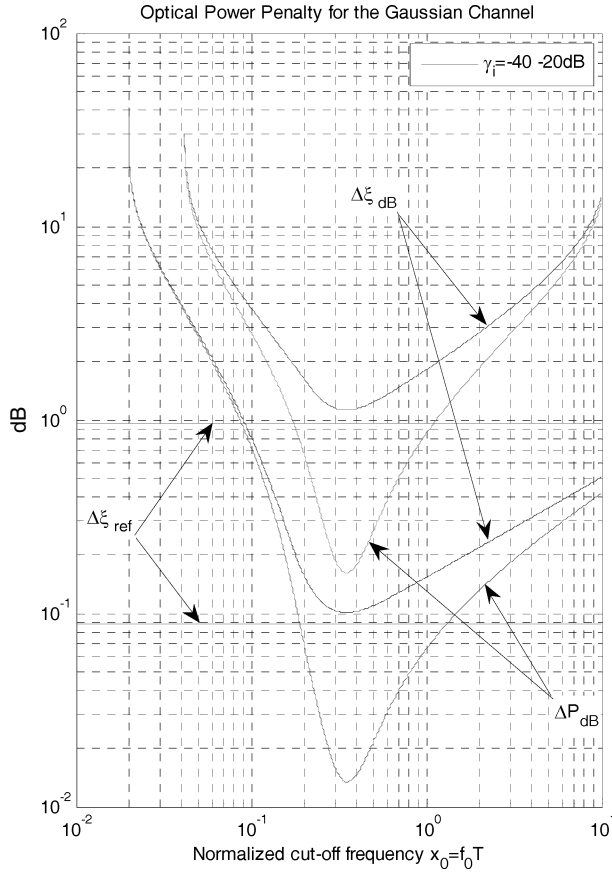

Figure 10.29 Computed optical power penalty for the Gaussian channel according to Equation (10.120). The noise-to-signal ratio assumes the value $\gamma_i = -40\,\text{dB}, -20\,\text{dB}$. The characteristic 'long-horn' profile has the minimum value at approximately 35 % of the normalized bit rate frequency

The single-pole and the Gaussian channels have been used to illustrate quantitative calculations of the optical power penalties versus the respective normalized cut-off frequencies and noise parameters. In the next section the optical power penalty will be used to generalize the concept of the channel metric, already discussed in Chapter 9, Section 9.3.3, in the case of the ideal inverse filter equalizer. One difference is noted between the ideal inverse filter equalizer and the decision feedback equalizer, namely the equalization criterion. The ideal inverse filter equalizer assumes no residual intersymbol, otherwise stated as the zero-forcing equalization. The DFE assumes instead the smoother mean square error minimization, leading to a compromise between noise and residual intersymbol interference. The corresponding channel metrics that can be defined accordingly use these criteria, and their comparison must of course account for that.

10.4 The Channel Metric

According to the Theory of digital feedback equalization (DFE) presented so far, the ideal feedback equalizer uses an infinite length feedforward filter (FFF) and feedback filter (FBF) and is based on the minimization of the mean square error, under the assumptions of correct past decisions and additive white noise. Accordingly, in the previous section the expression (10.119) of the optical power penalty ΔP_{dB} was derived for the ideal digital feedback equalizer. That expression is rewritten in order to indicate explicitly the form of the minimum mean square error according to the DFE theory reported in Equation (10.57):

$$\Delta P_{\mathrm{dB}} = 10\log_{10}\left(\frac{1-2\sqrt{\gamma_i/(1+\gamma_i)}}{1-2\exp\left\{-\frac{1}{2}\int_{-1/2}^{+1/2}\log\left[1+(1/T^2\gamma_i)\sum_{n=-\infty}^{+\infty}|Q(x-n)|^2\right]\mathrm{d}x\right\}}\right) \tag{10.121}$$

This expression is not new since it has already been used in the previous section to compute the optical power penalty for the single-pole and the Gaussian channels.

10.4.1 Penalty for the Digital Equalizer (PIE_{D})

The optical power penalty in Equation (10.121) depends exclusively on the channel impulse response $q(t)$ and on the noise-to-signal ratio γ_i. Note that the channel response $q(t)$ is given in Equation (10.8) by time convolution of the impulse responses of the optical transmitter, the multimode fiber and the optical receiver, up to the input section of the feedforward filter. The impulse response $q(t)$ characterizes the optical channel and the noise-to-signal ratio γ_i sets the normalized noise power at the receiver input. Both of these parameters uniquely define the transmission characteristic of the optical link and the corresponding optical power penalty (10.121) assumes the meaning of the optical channel metric relative to implementation of the ideal decision feedback equalization.

The DFE architecture that has been presented uses the decision feedback loop as the characteristic structure. Consequently, the expression (10.121) will be referred to as the optical power penalty of the ideal decision feedback equalizer and consequently the new notation $\mathrm{PIE_D} \equiv \Delta P_{\mathrm{dB}}$ (the suffix D stands for decision feedback) will be introduced. Equation (10.121) can be simplified by recognizing the even symmetry of the integrand function. In fact, assuming that the channel response $q(t)$ is a real function of the time, the Fourier transform $Q(x) = Q^*(-x)$ shows the conjugate even symmetry. Hence, the spectrum (modulus) $|Q(-x)| = |Q(x)|$ exhibits the even symmetry and from the mirroring property $|Q(x-n)| = |Q[-(x+n)]|$ the even symmetry of the auxiliary function introduced in Equation (10.68) can be obtained:

$$W(-x) \equiv \sum_{n=-\infty}^{+\infty}|Q[-(x+n)]|^2 = \sum_{n=-\infty}^{+\infty}|Q(x-n)|^2 = W(x) \tag{10.122}$$

Consequently, the integral at the exponent in Equation (10.121) can be computed by doubling the value relative to the positive frequency interval, and the optical power penalty of the ideal digital equalizer (DFE) becomes

$$\mathrm{PIE_D}(x_0, \gamma_i) \equiv 10\log_{10}\left(\frac{1-2\sqrt{\gamma_i/(1+\gamma_i)}}{1-2\exp\left\{-\int_0^{1/2}\log\left[1+\frac{1}{T^2\gamma_i}\sum_{n=-\infty}^{+\infty}|Q(x-n)|^2\right]\mathrm{d}x\right\}}\right), \quad \text{(dB)} \tag{10.123}$$

Although the terminology 'Penalty of the ideal digital equalizer' has been introduced, the expression (10.123) refers exclusively to the ideal decision feedback equalizer. Figure 10.30 shows the computed $\mathrm{PIE_D}$ for the single-pole and Gaussian channels. The plots are the same as already presented in the previous section, as the expression of the optical power penalty (10.120) coincides with the formula of the $\mathrm{PIE_D}$ presented in Equation (10.123). The signal-to-noise ratio is set as a parameter, ranging between $\gamma_i = -30\,\mathrm{dB}$ and $\gamma_i = -10\,\mathrm{dB}$ with 5 dB steps. For the single-pole

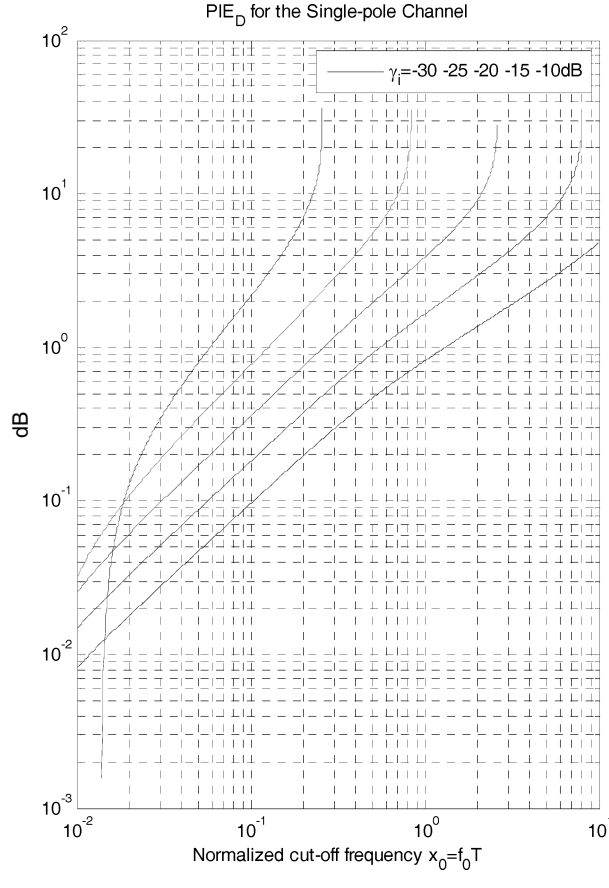

Figure 10.30 Computed $\mathrm{PIE_D}$ (x_0, γ_i) for the single-pole channel according to Equation (10.123). As reported in the text, the optical power penalty is referred to the Nyquist channel affected by the same receiver noise power

channel it is concluded that $\mathrm{PIE_D}$ (x_0, γ_i) increases monotonically versus the normalized cut-off frequency, reaching the infinite value for every fixed noise parameter γ_i. This means that the MMSE is noise-limited at increasing cut-off, reaching the value of one-quarter and leading to a completely closed (on the average) eye diagram.

Figure 10.31 gives the $\mathrm{PIE_D}$ (x_0) computation for the Gaussian channel, using Equation (10.123). The plots have the same profiles as Figure 10.29. The characteristic long-horn shaping reaches the minimum penalty at around 35 % of the normalized bit rate. This cut-off range therefore leads to better equalization results. It is interesting to compare the results of the two channels at a fixed normalized cut-off frequency by choosing, for example, $x_0 = 0.1$.

Table 10.2 reports the numerical data extracted from both Figures 10.30 and 10.31. At a consistent bandwidth reduction, assuming $x_0 = 0.10$, the optical power penalty required by the single-pole channel is considerably lower than that of the Gaussian channel. As already mentioned, this is due to the steeper slope profile of the Gaussian response with respect to the smoother single-pole one.

The optical power penalty $\mathrm{PIE_D}$ derived in this chapter is under discussion at the 10GBASE-LRM Standardization Committee (IEEE802.3) in order to be used as the reference channel metric for

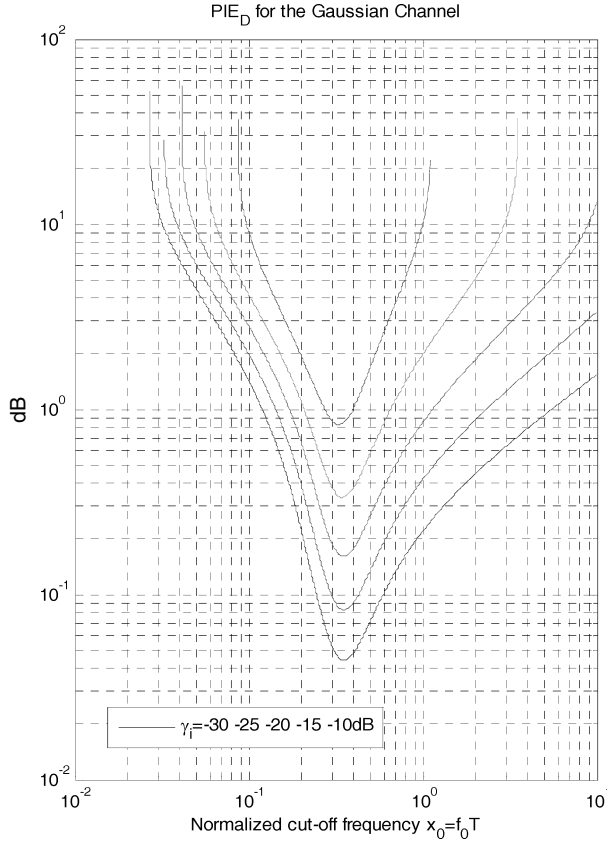

Figure 10.31 Computed $\mathrm{PIE_D}$ (x_0, γ_i) for the Gaussian channel according to Equation (10.123). The optical power penalty is referred to the Nyquist channel affected by the same receiver noise power. The increased value of the MMSE corresponds to the increased value of the penalty due to contributions of both integrated noise and residual intersymbol interference. The minimum penalty interval identifies the optimum equalization range for the Gaussian channel

Table 10.2 Comparison between the single-pole and the Gaussian channel penalties PIE_D versus the noise-to-signal ratio and assuming fixed cut-off frequencies $x_0 = 0.10$ and $x_0 = 0.35$. At $x_0 = 0.35$ the Gaussian channel gives $PIE_D < 1$ dB for every value shown of γ_i

γ_i (dB_{10})	Optical power penalty PIE_D (γ_i) (dB)			
	Single-pole $x_0 = 0.10$	Gaussian $x_0 = 0.10$	Single-pole $x_0 = 0.35$	Gaussian $x_0 = 0.35$
−10	2.1662	9.0537	∞	0.8479
−15	0.7665	4.1598	3.3969	0.3351
−20	0.3556	2.7966	1.3514	0.1605
−25	0.1806	1.9842	0.6510	0.0826
−30	0.0959	1.4208	0.3376	0.0441

quantifying the performances of suitable DFE architectures operating over multimode optical fiber link. As discussed in the first part of this book, the multimode fiber response is unfortunately not uniquely defined for a given fiber link. It depends upon several launching conditions and environmental effects, making the multimode optical channel characterization quite a cumbersome issue. The 10GBASE-LRM Standardization Committee is attempting to define the maximum allowable optical power penalty that can still be accommodated by the DFE, independently from a particular multimode fiber response. The attempt is being made to correlate the maximum value of PIE_D that can be accepted by the transmission system in order to provide the link operation under an unknown multimode fiber impulse response.

10.4.2 Penalty for the Linear Equalizer (PIE_L)

The channel metric (10.123) derived in the previous section refers to the decision feedback equalizer (DFE). However, it is possible to consider that the equalizer does not perform the MMSE postcursors interference cancellation using the nonlinear feedback loop. Instead, the MMSE signal compensation is achieved using the stand-alone feedforward equalizer (FFE). In this case, the optical power penalty refers to a different linear channel metric, and accordingly to the linear filtering provided by the feedforward filter implemented in the input stage of the FFE, this structure is referred to as the linear equalizer. The corresponding optical power penalty derived assuming the minimum mean square error criterion leads to the definition of the channel metric for the linear equalizer, otherwise stated as PIE_L.

The inverse filter equalizer developed in Chapter 9 is of course a linear equalizer but the convergence criterion for reaching the equalization is completely different. In that case, the complete interference cancellation was referred to as the zero-forcing equalization (ZFE). In the case of the FFE the convergence algorithm is based on the minimization of the mean square error, which leads to a different system optical power penalty definition.

The difference between PIE_L and PIE_D lies in the additional implementation of the feedback filter in the DFE architecture, with the implicit nonlinear characteristic. All the remaining building blocks are the same as in Figure 10.29, with the exception of the feedback filter (FBF). The minimum mean square error of the linear (FFE) equalizer has the following expression:

$$\frac{\mathrm{MMSE}_{\mathrm{FFE}}}{\sigma_a^2} = \frac{T}{2\pi}\int_{-\pi/T}^{+\pi/T} \frac{1}{1 + [1/(T^2\gamma_i)]\sum_{n=-\infty}^{+\infty} |Q(\omega - n\omega_{\mathrm{B}})|^2}\,\mathrm{d}\omega \tag{10.124}$$

The quantities:

$$\gamma_i \equiv \frac{G_i}{T\sigma_a^2}, \qquad \omega_B = \frac{2\pi}{T}$$

$$Q(\omega) \overset{\Im}{\longleftrightarrow} q(t) = h_T(t) * h_F(t) * h_R(t)$$

have the same definition as the corresponding DFE solution. Assuming binary symbols $\sigma_a^2 = 1$ and using the bit rate frequency normalized variable $x = fT$, from Equation (10.124) the following expression of the MMSE can immediately be obtained for the FFE:

$$\mathrm{MMSE}_{\mathrm{FFE}} = \int_{-1/2}^{+1/2} \frac{1}{1 + [1/(T^2\gamma_i)] \sum_{n=-\infty}^{+\infty} |Q(x-n)|^2} \, \mathrm{d}x \tag{10.125}$$

In order to have a clear comparison between the minimum mean square errors for the DFE and the FFE architectures, the dimensionless function $Y(x)$ is introduced:

$$Y(x) \equiv \frac{1}{1 + [1/(T^2\gamma_i)] \sum_{n=-\infty}^{+\infty} |Q(x-n)|^2} = \frac{1}{1 + [1/(T^2\gamma_i)] W(x)} \tag{10.126}$$

The auxiliary function has been defined in Equation (10.68). The expression (10.57) of the MMSE is considered for the DFE case, assuming binary symbols and adding the suffix DFE in order to better differentiate it from the FFE case. Substituting Equation (10.126) in both Equations (10.125) and (10.57) gives the following smart expressions for $\mathrm{MMSE}_{\mathrm{FFE}}$ and $\mathrm{MMSE}_{\mathrm{DFE}}$ respectively:

$$\mathrm{MMSE}_{\mathrm{FFE}} = \int_{-1/2}^{+1/2} Y(x) \, \mathrm{d}x \tag{10.127}$$

$$\mathrm{MMSE}_{\mathrm{DFE}} = \exp\left\{ \int_{-1/2}^{+1/2} \log[Y(x)] \, \mathrm{d}x \right\} \tag{10.128}$$

Referring to the contribution of J. Salz and using the property $0 < Y(x) < 1$, the following inequality holds:

$$\mathrm{MMSE}_{\mathrm{DFE}} = \exp\left\{ \int_{-1/2}^{+1/2} \log[Y(x)] \, \mathrm{d}x \right\} \leq \int_{-1/2}^{+1/2} \mathrm{e}^{\log[Y(x)]} \, \mathrm{d}x = \int_{-1/2}^{+1/2} Y(x) \, \mathrm{d}x = \mathrm{MMSE}_{\mathrm{FFE}} \tag{10.129}$$

This gives the following remarkable statement. Given the noise-to-signal ratio γ_i, the minimum mean square error of the ideal decision feedback equalizer is even lower than the corresponding $\mathrm{MMSE}_{\mathrm{FFE}}$ of the ideal feedforward equalizer. Only one particular function $Y(x)$ satisfies the equality sign in Equation (10.219), leading to the same value for both the $\mathrm{MMSE}_{\mathrm{FFE}}$ and $\mathrm{MMSE}_{\mathrm{DFE}}$. It is the constant function. Setting $Y(x) = Y_0$ in Equations (10.127) and (10.128) gives

$$Y(x) = Y_0 \Rightarrow \begin{cases} \mathrm{MMSE}_{\mathrm{FFE}} = Y_0 \displaystyle\int_{-1/2}^{+1/2} \mathrm{d}x = Y_0 \\ \mathrm{MMSE}_{\mathrm{DFE}} = \exp\left(\log(Y_0) \displaystyle\int_{-1/2}^{+1/2} \mathrm{d}x \right) = Y_0 \end{cases} \tag{10.130}$$

This conclusion is very important because it implies that the general Nyquist channel leads to the same minimum mean square error for both the FFE and the DFE architecture. In fact, from Equations (10.108), (10.109) and using the notation (10.126) for the function $Y(x)$,

$$\hat{Y}(x) \equiv \frac{1}{1 + \underbrace{[1/(T^2\gamma_i)] \sum_{n=-\infty}^{+\infty} |N_m(x-n)|^2}_{-1 \le x \le +1}} = \frac{\gamma_i}{1+\gamma_i} = \widehat{\mathrm{MMSE}} \tag{10.131}$$

Hence, from Equation (10.130):

$$\widehat{\mathrm{MMSE}}_{\mathrm{FFE}} = \widehat{\mathrm{MMSE}}_{\mathrm{DFE}} = \widehat{\mathrm{MMSE}} = \frac{\gamma_i}{1+\gamma_i} \tag{10.132}$$

Once the expressions (10.125) and (10.132) of the minimum mean square error of the feedforward equalizer are known, operating over the general channel and the Nyquist channel respectively, if the same procedure as the previous section is followed, the expression of the optical power penalty $\mathrm{PIE_L}$ for the ideal linear (not feedback) equalizer is derived. Following Equation (10.118),

$$\mathrm{PIE_L} \equiv 10 \log_{10} \left(\frac{1 - 2\sqrt{\widehat{\mathrm{MMSE}}}}{1 - 2\sqrt{\mathrm{MMSE_{FFE}}}} \right) \tag{10.133}$$

Substituting Equations (10.125) and (10.132) in Equation (10.133) gives the following explicit form of $\mathrm{PIE_L}$:

$$\mathrm{PIE_L}(x_0, \gamma_i) \equiv 10 \log_{10} \frac{1 - 2\sqrt{\gamma_i/(1+\gamma_i)}}{1 - 2\sqrt{2 \int_0^{+1/2} \dfrac{1}{1 + [1/(T^2\gamma_i)] \sum_{n=-\infty}^{+\infty} |Q(x-n)|^2} \, \mathrm{d}x}} \quad (\mathrm{dB}) \tag{10.134}$$

From expressions (9.102) in Chapter 9, (10.134) and (10.123), the optical power penalties $\mathrm{PIE_I}$, $\mathrm{PIE_L}$ and $\mathrm{PIE_D}$ respectively, evaluated for the Nyquist channel and expressed in decibels, are identically zero, in agreement with the definition of the Nyquist channel as the reference channel for bit error rate performances:

$$\widehat{\mathrm{PIE_I}} = \widehat{\mathrm{PIE_L}} = \widehat{\mathrm{PIE_D}} = 0 \tag{10.135}$$

Before closing this section, Table 10.3 summarizes the general expressions derived for the minimum mean square error and the optical power penalty according to the various electronic equalizer architectures. Table 10.4 reports instead the MMSE and the optical power penalties for the reference Nyquist channel.

In the following section, the three different channel metrics are compare that have been analyzed using the single-pole and the Gaussian channels versus the normalized cut-off frequencies and noise parameters. In addition to $\mathrm{PIE_D}$ and $\mathrm{PIE_L}$, a comparison will be made with the optical power penalty $\mathrm{PIE_I}$ of the ideal inverse linear filter equalizer, reported in Chapter 9, Equation (9.102).

10.4.3 Channel Metrics Comparison: PIE_I, PIE_L, PIE_D

In order to make a consistent comparison between the two different channel metrics defined in previous sections and the channel metric for the inverse filter equalizer defined in Chapter 9, the multimode fiber transmission system needs to be set up accordingly. The channel structure

Table 10.3 Summary of the general expressions of the minimum mean square error (MMSE) and of the optical power penalties $\mathrm{PIE_I}$ (9.102) in Chapter 9, $\mathrm{PIE_L}$ (10.134) and $\mathrm{PIE_D}$ (10.123) for the inverse filter equalizer (IFE), the feedforward equalizer (FFE) and the decision feedback equalizer (DFE) respectively, derived in the text for the general channel

	General working channel	
Equalizer	MMSE	Optical power penalty
IFE	–	$\mathrm{PIE_I} = 5\log_{10}\left[2\int_0^{1/2}\frac{1}{\lvert H_F(x)\rvert^2}\,\mathrm{d}x\right]$
FFE	$\mathrm{MMSE} = 2\int_0^{1/2}\frac{1}{1+[1/(T^2\gamma_i)]\sum_{n=-\infty}^{+\infty}\lvert Q(x-n)\rvert^2}\,\mathrm{d}x$	$\mathrm{PIE_L} = 10\log_{10}\frac{1-2\sqrt{\gamma_i/(1+\gamma_i)}}{1-2\sqrt{2\int_0^{1/2}\frac{1}{1+[1/(T^2\gamma_i)]\sum_{n=-\infty}^{+\infty}\lvert Q(x-n)\rvert^2}\,\mathrm{d}x}}$
DFE	$\mathrm{MMSE} = \exp\left\{-2\int_0^{1/2}\log\left[1+\frac{1}{T^2\gamma_i}\sum_{n=-\infty}^{+\infty}\lvert Q(x-n)\rvert^2\right]\mathrm{d}x\right\}$	$\mathrm{PIE_D} = 10\log_{10}\left(\frac{1-2\sqrt{\gamma_i/(1+\gamma_i)}}{1-2\exp\left\{-\int_0^{1/2}\log[1+[1/(T^2\gamma_i)]\sum_{n=-\infty}^{+\infty}\lvert Q(x-n)\rvert^2]\,\mathrm{d}x\right\}}\right)$

Table 10.4 Summary of the general expressions of the minimum mean square error (MMSE) and of the optical power penalties $\mathrm{PIE_I}$, $\mathrm{PIE_L}$ and $\mathrm{PIE_D}$ for the inverse filter equalizer (IFE), the feedforward equalizer (FFE) and the decision feedback equalizer (DFE) respectively, derived in the text for the reference Nyquist channel

Equalizer	Reference Nyquist channel	
	MMSE	Optical power penalty
IFE	–	$\mathrm{PIE_I} = 0$ dB
FFE	$\widehat{\mathrm{MMSE}} = \frac{\gamma_i}{1+\gamma_i}$	$\mathrm{PIE_L} = 0$ dB
DFE	$\widehat{\mathrm{MMSE}} = \frac{\gamma_i}{1+\gamma_i}$	$\mathrm{PIE_D} = 0$ dB

is the same for both the feedforward equalizer and the decision feedback equalizer. According to the definition given at the beginning of this chapter, it is characterized by the global impulse response $q(t)$ as reported in Equation (10.8) and corresponds to the temporal convolution of the impulse responses of the optical transmitter $h_T(t)$, the multimode fiber $h_F(t)$ and the optical receiver $h_R(t)$ respectively, up to the input section of the feedforward filter. In this model, the individual composition of these three linear subsystems are neglected and it is assumed that the global impulse response $q(t)$ follows a specified function of the time. In previous examples, the single-pole and the Gaussian functions were used extensively to model the channel response.

However, when reference is made to the inverse filter equalizer the picture involved is different. According to the theory developed in Chapter 9, the impulse response of both the optical transmitter $h_T(t)$ and the optical receiver $h_R(t)$ are uniquely specified by the inverse Fourier transform of the square root of the raised cosine transfer function with zero roll-off. This is part of the definition of the reference channel for the inverse filter equalizer. The third building block, which differentiates the working channel behavior, is the impulse response of the multimode fiber $h_F(t)$. In order to make a valid comparison among the three channel metrics $\mathrm{PIE_I}$, $\mathrm{PIE_L}$ and $\mathrm{PIE_D}$, the function $h_F(t)$

must be specified that satisfies simultaneously both the impulse response $q(t)$, common to the FFE and DFE structures, and the specific requirements for the working channel of the inverse filter equalizer. The solution to this problem is quite simple: for an arbitrary impulse response $q(t)$ assigned to the working channel, the corresponding impulse response $h_F(t)$ of the multimode fiber specified in the inverse filter equalizer channel model is given by the inverse Fourier transform $\Im^{-1}\{\cdot\}$ of the ratio between the channel response $q(t) \overset{\Im}{\longleftrightarrow} Q(\omega)$ and the raised cosine spectrum with zero roll-off, $\Gamma_0(\omega)$:

$$h_F(t) = \Im^{-1}\left\{\frac{Q(\omega)}{\Gamma_0(\omega)}\right\} \Rightarrow \begin{cases} H_F(\omega) = \dfrac{Q(\omega)}{\Gamma_0(\omega)} \\ -\dfrac{\pi}{T} < \omega < \dfrac{\pi}{T} \end{cases} \tag{10.136}$$

This statement is apparently obvious, but can lead to some misunderstandings. It is noted explicitly that if $h_R(t) = h_T(t) = \Im^{-1}\{\sqrt{\Gamma_0(\omega)}\}$ in the configuration of the working channel for the DFE and FFE structures, according to the ansatz relations (10.2) and (10.4) the raised cosine $\Gamma_0(\omega)$ must be defined with unit dimensionless amplitude in the frequency domain. This is consistent with the definition used in Equation (9.64) for the inverse filter equalizer. Substituting the corresponding impulse response $\gamma_0(t) \overset{\Im}{\longleftrightarrow} \Gamma_0(\omega)$ reported in Equation (9.65) into the channel impulse response (10.8) with $m = 0$ gives

$$q(t) = h_F(t) * \gamma_0(t) \tag{10.137}$$

The channel impulse response $q(t)$ is correctly normalized and dimensionless, while the corresponding frequency response $Q(\omega)$ assumes the dimension of time, $|Q(0)| = \tau$, in agreement with the condition (10.5). The function $\gamma_0(t)$ in Equation (10.137) coincides with the function $\mathrm{sinc}(t/T)$:

$$\gamma_0(t) = \mathrm{sinc}\left(\frac{t}{T}\right) = \frac{1}{T}\,\frac{\sin(\pi t/T)}{\pi t/T} \tag{10.138}$$

Table 10.5 reports explicit formulations of the optical transmitter, the optical receiver and the multimode fiber model equations in the cases of the ideal inverse equalizer, the feedforward equalizer and the decision feedback equalizer respectively. The only degree of freedom is represented by the choice of the channel response $Q(f)$.

From Table 10.5 it can be concluded that the frequency response $H_F(\omega)$ of the multimode fiber satisfies simultaneously both the channel response $Q(\omega)$, with the required dimension of time, and the multimode fiber response of the inverse filter equalizer. Stated differently, once the channel response $Q(\omega)$ has been defined in the FFE and DFE architectures, in order to have comparable results, the frequency response reported in Equation (10.136) is assigned to $H_F(\omega)$ in the IFE configuration. The transmitter and the receiver for these two equalizers have an impulse response equal to the square root of the dimensionless raised cosine function in Equation (10.137) with zero roll-off. Therefore the definition of the channel is the same for all three equalization schemes, the dimensional structure is respected and the corresponding results become comparable. The integration limits for the calculation of $\mathrm{PIE_I}$ in Equation (9.102) are consistent with the definition interval shown in Equation (10.136). Substituting Equation (10.136) into Equation (9.102) and using the normalized frequency variable $x = fT$ gives the following relevant result:

$$\mathrm{PIE_I} = 5\log_{10}\left[2\tau^2 \int_0^{1/2} \frac{1}{|Q(x)|^2}\,\mathrm{d}x\right] \tag{10.139}$$

$$|Q(0)| = \tau : q(0) = \int_{-\infty}^{+\infty} Q(f)\,\mathrm{d}f = 1 \tag{10.140}$$

Table 10.5 The table summarizes the equation model for the inverse filter equalizer, the feedforward equalizer and the decision feedback equalizer. The dimensional normalization has been set in order to produce comparable results of the channel metrics and compliant descriptions with the respective system model assumptions

Equalizer	$H_{\mathrm{T}}(f)$	$H_{\mathrm{F}}(f)$	$H_{\mathrm{R}}(f)$
IFE	$\begin{cases} 1, & \lvert f\rvert < \frac{1}{2T} \\ \frac{1}{\sqrt{2}}, & \lvert f\rvert = \frac{1}{2T} \\ 0, & \lvert f\rvert \geq \frac{1}{2T} \end{cases}$	$Q(f), \quad \lvert f\rvert < \frac{1}{2T}$ $\lvert Q(0)\rvert = \tau$	$\begin{cases} 1, & \lvert f\rvert < \frac{1}{2T} \\ \frac{1}{\sqrt{2}}, & \lvert f\rvert = \frac{1}{2T} \\ 0, & \lvert f\rvert \geq \frac{1}{2T} \end{cases}$
FFE	$\begin{cases} 1, & \lvert f\rvert < \frac{1}{2T} \\ \frac{1}{\sqrt{2}}, & \lvert f\rvert = \frac{1}{2T} \\ 0, & \lvert f\rvert \geq \frac{1}{2T} \end{cases}$	$Q(f)$ $\lvert Q(0)\rvert = \tau$	$\begin{cases} 1, & \lvert f\rvert < \frac{1}{2T} \\ \frac{1}{\sqrt{2}}, & \lvert f\rvert = \frac{1}{2T} \\ 0, & \lvert f\rvert \geq \frac{1}{2T} \end{cases}$
DFE	$\begin{cases} 1, & \lvert f\rvert < \frac{1}{2T} \\ \frac{1}{\sqrt{2}}, & \lvert f\rvert = \frac{1}{2T} \\ 0, & \lvert f\rvert \geq \frac{1}{2T} \end{cases}$	$Q(f)$ $\lvert Q(0)\rvert = \tau$	$\begin{cases} 1, & \lvert f\rvert < \frac{1}{2T} \\ \frac{1}{\sqrt{2}}, & \lvert f\rvert = \frac{1}{2T} \\ 0, & \lvert f\rvert \geq \frac{1}{2T} \end{cases}$

Table 10.6 Summary of the general expressions of the channel metrics $\mathrm{PIE_I}$ (10.139), $\mathrm{PIE_L}$ (10.134) and $\mathrm{PIE_D}$ (10.123) for the inverse filter equalizer (IFE), the feedforward equalizer (FFE) and the decision feedback equalizer (DFE) respectively

Equalizer	Channel metric for $Q(x)$
IFE	$\mathrm{PIE_I} = 5\log_{10}\left[2\tau^2\int_0^{1/2}\frac{1}{\lvert Q(x)\rvert^2}\,\mathrm{d}x\right]$
FFE	$\mathrm{PIE_L} = 10\log_{10}\dfrac{1-2\sqrt{\gamma_i/(1+\gamma_i)}}{1-2\sqrt{2\displaystyle\int_0^{1/2}\frac{1}{1+[1/(T^2\gamma_i)]\sum_{n=-\infty}^{+\infty}\lvert Q(x-n)\rvert^2}\,\mathrm{d}x}}$
DFE	$\mathrm{PIE_D} = 10\log_{10}\dfrac{1-2\sqrt{\gamma_i/(1+\gamma_i)}}{1-2\exp\left(-\displaystyle\int_0^{1/2}\log\left\{1+[1/(T^2\gamma_i)]\sum_{n=-\infty}^{+\infty}\lvert Q(x-n)\rvert^2\right\}\mathrm{d}x\right)}$

These expressions allow $\mathrm{PIE_I}$ to be written in terms of the channel response $Q(x)$ using the same form as the other two equalizers, providing the normalization in Equation (10.140). Table 10.6 reports the explicit form of the three expressions for the channel metric. In the following two subsections the computed plots of $\mathrm{PIE_I}$, $\mathrm{PIE_L}$ and $\mathrm{PIE_D}$ are given on the same graph versus the normalized cut-off frequency for the single-pole, the Gaussian and the fourth-order Bessel–Thompson channels. It is noted that according to the definition of the reference in the inverse filter equalizer, the noise parameter does not affect the corresponding optical power penalty $\mathrm{PIE_I}$ because the receiver is matched on the ideal Nyquist transmitter with $H_{\mathrm{T}}(\omega) = \sqrt{T_0(\omega)}$, independently of the working

channel characteristic, and the eye diagram degradation due to noise enhancement after the IFE refers to that performance.

In the FFE and DFE structure, however, the receiving filter is matched to the entire working channel $q(t)$, while the reference channel exhibits the ideal Nyquist response. In these cases, the receiver is different from the reference and the working conditions, which is the reason why the optical power penalty depends on the noise-to-signal-ratio for both the feedforward equalizer and the decision feedback equalizer. The different behaviors found at large values of the cut-off frequencies between the IFE and both FFE and DFE depend on the different roles of the time constants in front of the respective integrals, in Equations (10.139), (10.134) and (10.123). In the case of $\mathrm{PIE_I}$ the time constant coincides with τ^2, while in the cases of $\mathrm{PIE_L}$ and $\mathrm{PIE_D}$ the time constant is the time step T^2. Increasing the cut-off frequency leads to a corresponding reduction of τ, leaving the contribution to $\mathrm{PIE_I}$ unchanged. Instead, in the case of both $\mathrm{PIE_L}$ and $\mathrm{PIE_D}$, the value of the series term in the integrals reduced accordingly, determining the divergence of both channel metrics.

10.4.3.1 Single-Pole Channel

The square modulus of the single-pole channel frequency response is obtained from Equations (10.63) and (10.65), where the channel response $Q(x)$ satisfies the required normalization $|Q(0)| = \tau = T/(2\pi x_0)$ and x_0 is the normalized cut-off frequency:

$$q(t) = \begin{cases} \mathrm{e}^{-t/\tau}, & t \geq 0 \\ 0, & t < 0 \\ q(0) = 1 \end{cases} \Rightarrow \begin{cases} |Q(x)|^2\Big|_{x=fT} = \dfrac{T^2}{4\pi^2 x_0^2} \dfrac{1}{1+(x/x_0)^2} \\ \tau = \dfrac{T}{2\pi x_0} = \dfrac{1}{2\pi f_0} \end{cases} \tag{10.141}$$

Substituting Equation (10.141) in Equations (10.139), (10.134) and (10.123) gives the following expressions for the channel metrics for the inverse filter equalizer, the feedforward equalizer and the decision feedback equalizer respectively:

$$\mathrm{PIE_I}(x_0) = 5\log_{10}\left\{2\int_0^{1/2}\left[1+\left(\frac{x}{x_0}\right)^2\right]\mathrm{d}x\right\} = 5\log_{10}\left(1+\frac{1}{12x_0^2}\right) \tag{10.142}$$

$$\mathrm{PIE_L}(x_0, \gamma_i) = 10\log_{10}\frac{1-2\sqrt{\gamma_i/(1+\gamma_i)}}{1-2\sqrt{2\int_0^{+1/2}\dfrac{1}{1+[1/(4\pi^2x_0^2\gamma_i)]\displaystyle\sum_{n=-\infty}^{+\infty}\dfrac{1}{1+[(x-n)/x_0]^2}}\,\mathrm{d}x}} \tag{10.143}$$

$$\mathrm{PIE_D}(x_0, \gamma_i) = 10\log_{10}\frac{1-2\sqrt{\gamma_i/(1+\gamma_i)}}{1-2\exp\left(-\displaystyle\int_0^{1/2}\log\left\{1+\frac{1}{4\pi^2x_0^2\gamma_i}\sum_{n=-\infty}^{+\infty}\frac{1}{1+[(x-n)/x_0]^2}\right\}\mathrm{d}x\right)} \tag{10.144}$$

The channel metrics $\mathrm{PIE_L}$ and $\mathrm{PIE_D}$ have been computed numerically from Equations (10.143) and (10.144) respectively. Figure 10.32 gives the computed channel metrics for the three equalizers versus the normalized cut-off frequency x_0, assuming the same single-pole channel and the same noise-to-signal ratio $\gamma_i = -20\,\mathrm{dB}$. The most evident difference between the FFE and DFE curves from the IFE one is the opposite sloped sign versus the normalized cut-off frequency.

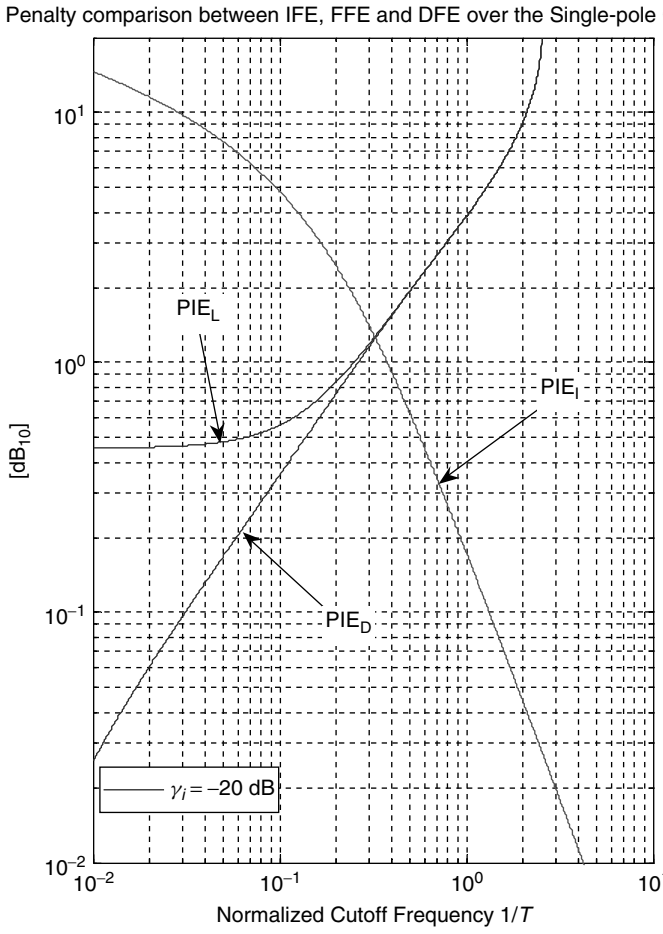

Figure 10.32 Computed optical power penalties $\mathrm{PIE_I}$, $\mathrm{PIE_L}$ and $\mathrm{PIE_D}$ versus the single-pole normalized cut-off frequency of the inverse filter equalizer (IFE), the feedforward equalizer (FFE) and the decision feedback equalizer (DFE) respectively. The noise-to-signal ratio for the FFE and DFE has been set equal to $\gamma_i = -20\,\mathrm{dB}$. The computed values report that the FFE and DFE give a better performance from the cut-off frequency approximately below $x_0 = 0.35$. In particular, at $x_0 = 0.20$ then $\mathrm{PIE_I} \cong 2.5\,\mathrm{dB}$, $\mathrm{PIE_L} \cong 0.85\,\mathrm{dB}$ and $\mathrm{PIE_D} \cong 0.75\,\mathrm{dB}$

The IFE performance is in fact monotonically improving at higher cut-off frequencies because the system tends toward the matched Nyquist reference system. Stated differently, when the channel cut-off increases by one order of magnitude or more with respect to the bit rate, the filtering effect of the channel becomes negligible and the system assumes the configuration of the matched Nyquist system. At a lower cut-off, the amount of high-frequency enhancement consequent to the bandwidth compensation in the IFE architecture drags more noise power into the receiver, leading to a decreased performance (higher power penalty).

The feedforward equalizer (FFE) behaves in a similar way to the decision feedback equalizer (DFE) at higher cut-off frequencies. This similar behavior can be easily explained in terms of the dominant noise contribution of the input feedforward filter (FFF), which is present in both configurations, with respect to the residual intersymbol interference of the feedback filter. At higher

cut-off frequencies of the single-pole channel, the amount of intersymbol feedback to the sampler is negligible and the feedback filter (FBF) almost does not work. The FFE and DFE performances at higher cut-off frequencies are determined essentially by the noise enhancement due to the input FFF matching conditions. At lower values of the cut-off frequencies of the single-pole channel, the benefit of the feedback filter in the DFE structure becomes more and more evident. For decreasing cut-off ranges of the single-pole channel, the performance of the DFE becomes superior to both the FFE and IFE, exhibiting a threshold behavior corresponding to a cut-off frequency at around 25 % of the bit rate.

To give a more complete description, Figure 10.33 shows the optical power penalty comparison for three different values of the noise-to-signal ratio, namely $\gamma_i = -25\,\text{dB}, -20\,\text{dB}, -15\,\text{dB}$. The behavior of the single-pole channel can be summarized in the following two statements:

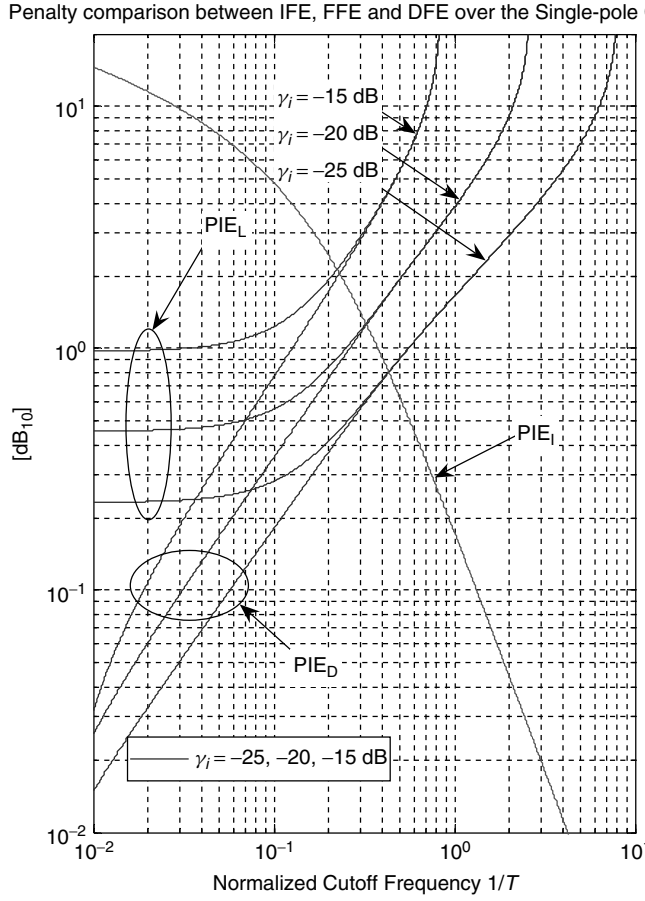

Figure 10.33 Comparison between the computed optical power penalties for the single-pole channel assuming the inverse filter equalizer (IFE), the feedforward equalizer (FFE) and the decision feedback equalizer (DFE). As explained in the text, the noise parameter does not affect the case of the IFE but it sets corresponding different curves for both the FFE and DFE. At a lower cut-off frequency the dominance of the FFE and DFE over the IFE is evident, making these equalizers very suitable for starting from the normalized bit rate cut-off frequency below 25 %. At the bit rate cut-off frequency, the high-frequency damping of the IFE has a clear benefit over the noise enhancement due to the FFE and DFE matched receivers

1. At cut-off frequencies lower than 25 % of the bit rate frequency, the FFE and DFE architectures behave much better than the IFE structure, even at a high noise level. By reducing the noise level the improvement becomes still more evident.
2. At cut-off frequencies higher than 50 % of the bit rate frequency, the equalization performance switches the behavior in favor of the inverse filter equalizer, leading to lower optical power penalties even at low noise level condition.

Table 10.7 reports the computed channel metrics PIE_I, PIE_L and PIE_D versus selected cut-off frequencies and the noise-to-signal ratio for the single-pole response. At relatively narrowband conditions, with $x_0 \cong 0.5$, the performance of the IFE is superior to those of the FFE and DFE for the assumed noise parameter values. Decreasing the cut-off frequency, the situation reverts in favor of the digital equalizers, even in noisier conditions. These considerations lead to the conclusion that the complexity of the digital filter architectures is required when the channel bandwidth limitation exceeds at last 20 % of the required bit rate frequency.

In order to complete the analysis of the single-pole channel, Figure 10.34 shows a comparison of the three channel metrics PIE_I, PIE_L and PIE_D versus the noise-to-signal ratio γ_i, assuming selected cut-off frequencies. The computed curves reveal the benefit of the digital equalization versus the IFE in the lowest range of the cut-off frequencies. However, the interesting behavior is represented by the steep increase shown by the optical power penalty of both FFE and DFE structures at relatively high noise-to-signal ratios. This behavior clearly reveals the weakness of these solutions under noisy conditions. Referring to Figure 10.34, it can be concluded that in the case of $x_0 = 0.20$, the DFE leads to unacceptable results when $\gamma_i \cong -9\,\text{dB}$. A similar behavior is observed at different cut-off frequencies. In conclusion, for a given cut-off frequency the minimum value of the noise-to-signal ratio for achieving equalization corresponds with a reasonable optical power penalty. In order to have stable behavior in the example considered in Figure 10.34, the noise-to-signal ratio should be lower than $\gamma_i \cong -11\,\text{dB}$ at $x_0 = 0.30$, about $\gamma_i \cong -9\,\text{dB}$ at $x_0 = 0.20$ and $\gamma_i \cong -6\,\text{dB}$

Table 10.7 Computed values of the optical power penalties PIE_I (10.139), PIE_L (10.134) and PIE_D (10.123) versus the selected cut-off frequencies, assuming the single-pole channel. The smooth response leads to poor benefit of the DFE structure with respect to the simpler FFE. This is clearly visible when comparing the same noise-to-signal values. The equalization gain of both the FFE and DFE is evident with respect to the IFE performances at cut-off frequencies lower than 20 %

Cut-off	PIE_I (dB_{10})	PIE_L (dB_{10})			PIE_D (dB_{10})		
x_0	–	$\gamma_i = -25\,\text{dB}$	$\gamma_i = -20\,\text{dB}$	$\gamma_i = -15\,\text{dB}$	$\gamma_i = -25\,\text{dB}$	$\gamma_i = -20\,\text{dB}$	$\gamma_i = -15\,\text{dB}$
0.1000	4.8502	0.2822	0.5604	1.2307	0.1806	0.3556	0.7665
0.2000	2.4451	0.4108	0.8300	1.9138	0.3720	0.7498	1.7200
0.3000	1.4232	0.5739	1.1810	2.8811	0.5602	1.1518	2.8034
0.4000	0.9104	0.7440	1.5592	4.0632	0.7393	1.5491	4.0324
0.5000	0.6247	0.9098	1.9417	5.4882	0.9083	1.9383	5.4756
0.6000	0.4521	1.0686	2.3221	7.3066	1.0681	2.3210	7.3011
0.7000	0.3411	1.2205	2.7007	9.9795	1.2203	2.7004	9.9766
0.8000	0.2658	1.3665	3.0801	16.1398	1.3665	3.0800	16.1364
0.9000	0.2126	1.5078	3.4631	∞	1.5077	3.4630	∞
1.0000	0.1738	1.6450	3.8528	∞	1.6450	3.8528	∞
1.5000	0.0790	2.2935	6.0194	∞	2.2935	6.0194	∞
2.0000	0.0448	2.9111	9.0753	∞	2.9111	9.0753	∞
5.0000	0.0072	7.0581	∞	∞	7.0581	∞	∞
10.0000	0.0018	∞	∞	∞	∞	∞	∞

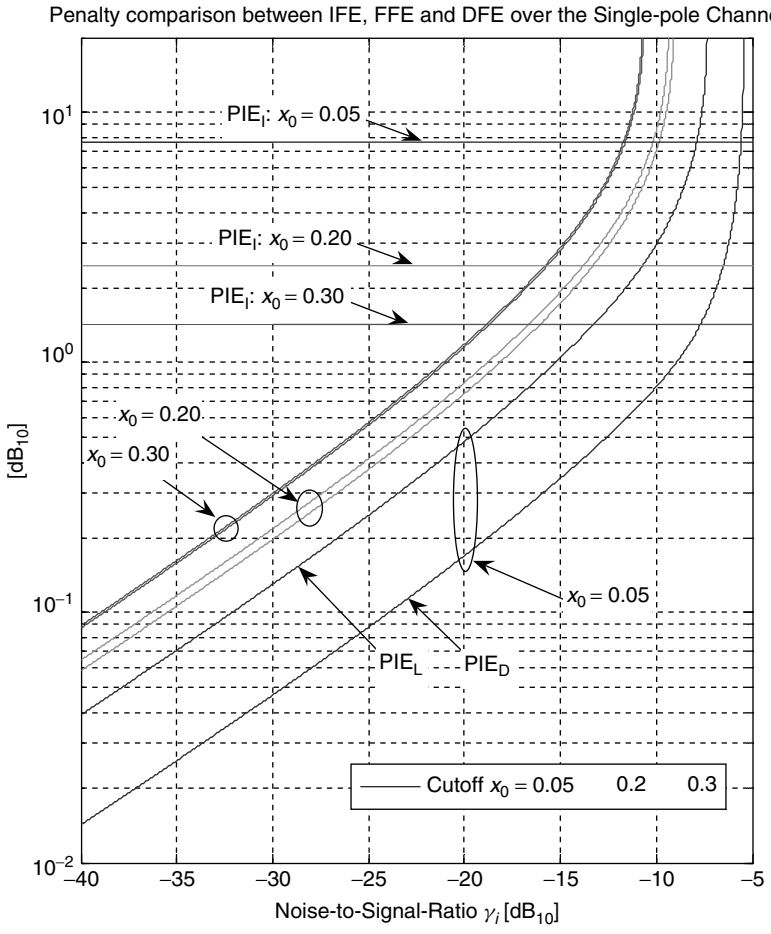

Figure 10.34 Computed channel metrics for the single-pole response versus the noise-to-signal parameter γ_i for three cut-off frequencies, $x_0 = 0.05, 0.20, 0.30$. At very low cut-off frequencies and relatively low γ_i, the benefit of the DFE is evident, leading to sensible improvements over the FFE structure. At higher values of the noise-to-signal ratio, the optical power penalty starts to increase very steeply, leading to unstable performances

at $x_0 = 0.05$ for the DFE case. These conditions should be accounted for when both FFE and DFE performances are evaluated in the range of the optical receiver sensitivity.

According to mathematical modeling and the computed profiles, the single-pole response leads to digital channel metrics PIE_L and PIE_D increasing with the constant slope, at very low noise levels, of one decade every 20 dB of the noise-to-signal ratio. At a higher noise value, both penalties increase steeply, reaching very high and unacceptable values depending on the assumed cut-off frequency. This behavior is valid for the single-pole channel, but it can approximately be assumed for real channel responses with similar smooth frequency profiles.

10.4.3.2 Gaussian Channel

The square modulus of the frequency response of the Gaussian channel is obtained from Equation (10.74), where the channel impulse response $q(t)$ has the required dimensionless

normalization:

$$q(t) = \begin{cases} \mathrm{e}^{-(\pi^2 f_0^2/\log 2)t^2} \\ q(0) = 1 \end{cases} \Rightarrow \begin{cases} |Q(x)|^2 = \dfrac{T^2 \log 2}{\pi x_0^2}\ \mathrm{e}^{-(x/x_0)^2 2\log 2} \\ \tau = \dfrac{T}{x_0}\sqrt{\dfrac{\log 2}{\pi}} \end{cases} \tag{10.145}$$

$$Q(x_0) = \tfrac{1}{2}Q(0), \quad 2x_0 = \mathrm{FWHM}, \quad x_0 \equiv f_0 T$$

The normalization constant τ is obtained by satisfying the condition (10.140). Substituting the Gaussian response (10.145) in Equations (10.139), (10.134) and (10.123), the following integral representation of the Gaussian channel metric is obtained in the cases of the inverse linear equalizer, the feedforward equalizer and the decision feedback equalizer respectively:

$$\mathrm{PIE_I}(x_0) = 5\log_{10}\left(2\int_0^{1/2} \mathrm{e}^{(x/x_0)^2 2\log 2}\,\mathrm{d}x\right) \tag{10.146}$$

$$\mathrm{PIE_L}(x_0, \gamma_i) = 10\log_{10}\frac{1 - 2\sqrt{\gamma_i/(1+\gamma_i)}}{1 - 2\sqrt{2\displaystyle\int_0^{1/2} \frac{1}{1 + [\log 2/(\pi x_0^2 \gamma_i)]\displaystyle\sum_{n=-\infty}^{+\infty} \mathrm{e}^{-[(x-n)/x_0]^2 2\log 2}}\,\mathrm{d}x}} \tag{10.147}$$

$$\mathrm{PIE_D}(x_0, \gamma_i) = 10\log_{10}\frac{1 - 2\sqrt{\gamma_i/(1+\gamma_i)}}{1 - 2\exp\left(-\displaystyle\int_0^{1/2} \log\left\{1 + \frac{[\log 2}{(\pi x_0^2 \gamma_i)]}\sum_{n=-\infty}^{+\infty} \mathrm{e}^{-[(x-n)/x_0]^2 2\log 2}\right\}\mathrm{d}x\right)} \tag{10.148}$$

Figure 10.35 shows the computed optical power penalties $\mathrm{PIE_I}$, $\mathrm{PIE_L}$ and $\mathrm{PIE_D}$ on the same graph versus the normalized cut-off frequency for the Gaussian channel assuming $\gamma_i = -20\,\mathrm{dB}$. As already discussed, the Gaussian response channel shows an optimum interval of the cut-off frequency for achieving the minimum residual error in both the FFE and DFE configurations. The minimum penalty interval is located at around 35 % of the bit rate frequency. The interesting behavior of the computed plots consists in the rapid increase of the optical power penalties as soon as the optimum interval is left. In particular, at $x_0 = 0.1$ approximately $\mathrm{PIE_D} \cong 2.8\,\mathrm{dB}$ is found while the metric for the feedforward Equalizer increases indefinitely, $\mathrm{PIE_L} \to \infty$. In Figure 10.36 the computed channel metrics are presented for the Gaussian response at three different noise-to-signal ratios. As in the previous case, the noise parameter does not have any effect on the IFE performance since it is embedded in the sensitivity of the Nyquist reference channel. It has instead a great impact on the performances of both the FFE and DFE due to the input FFF matching requirements in both equalizers. Table 10.8 reports the computed channel metrics for the IFE, FFE and DFE, according to Equations (10.146), (10.147) and (10.148) respectively.

In order to complete the analysis of the Gaussian channel providing a quantitative comparison with the single-pole response, Figure 10.37 shows the computed plots of the three channel metrics $\mathrm{PIE_I}$, $\mathrm{PIE_L}$ and $\mathrm{PIE_D}$ versus the noise-to-signal ratio γ_i, assuming selected cut-off frequencies. The computed curves have the same behavior found in the case of the single-pole response. The optical power penalty increases monotonically with the noise-to-signal ratio. Approaching the higher noise levels, the curves tend to become steely, reaching the vertical asymptote in correspondence

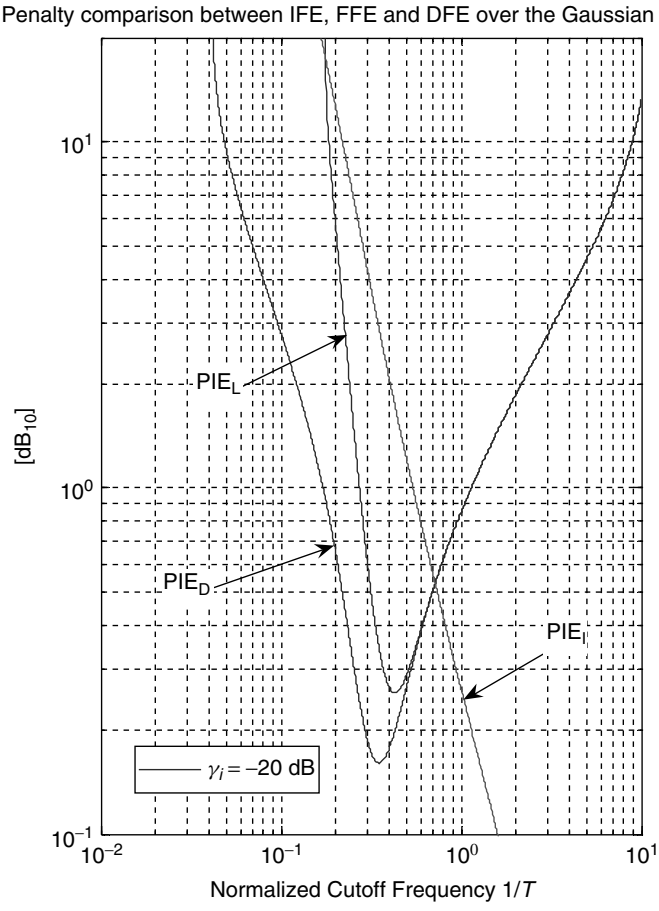

Figure 10.35 Computed optical power penalties PIE_I, PIE_L and PIE_D versus the Gaussian normalized cut-off frequency of the inverse filter equalizer (IFE), the feedforward equalizer (FFE) and the decision feedback equalizer (DFE) respectively. The noise-to-signal ratio for the FFE and DFE has been set equal to $\gamma_i = -20\,\text{dB}$. The computed values show that the FFE and DFE give a better performance at approximately $x_0 = 0.35$. In particular, at $x_0 = 0.20$ then $PIE_I \cong 12\,\text{dB}$, $PIE_L \cong 6\,\text{dB}$ and $PIE_D \cong 0.7\,\text{dB}$

with a particular value of γ_i. The profile of the optical power penalty is significant in the case of the DFE assuming a 10 % cut-off frequency. The curve increases with a constant slope of almost 1 decade over 40 dB in the log scale up to $\gamma_i \cong -15\,\text{dB}$, leading to $PIE_D \cong 4.2\,\text{dB}$. Then, by increasing the noise parameter, the slope starts to increase suddenly, almost reaching the vertical asymptote at $\gamma_i \cong -9\,\text{dB}$. As a general indication, it can be concluded that in the case of the Gaussian channel with a 10 % cut-off, the maximum value of the noise-to-signal ratio should not exceed $\gamma_i \cong -15\,\text{dB}$ in order to have a limited penalty and a repetitive equalization performance.

In the next section the block diagram will be introduced of the electronic dispersion compensator (EDC) architecture based on the DFE topology and used in commercially available integrated circuits.

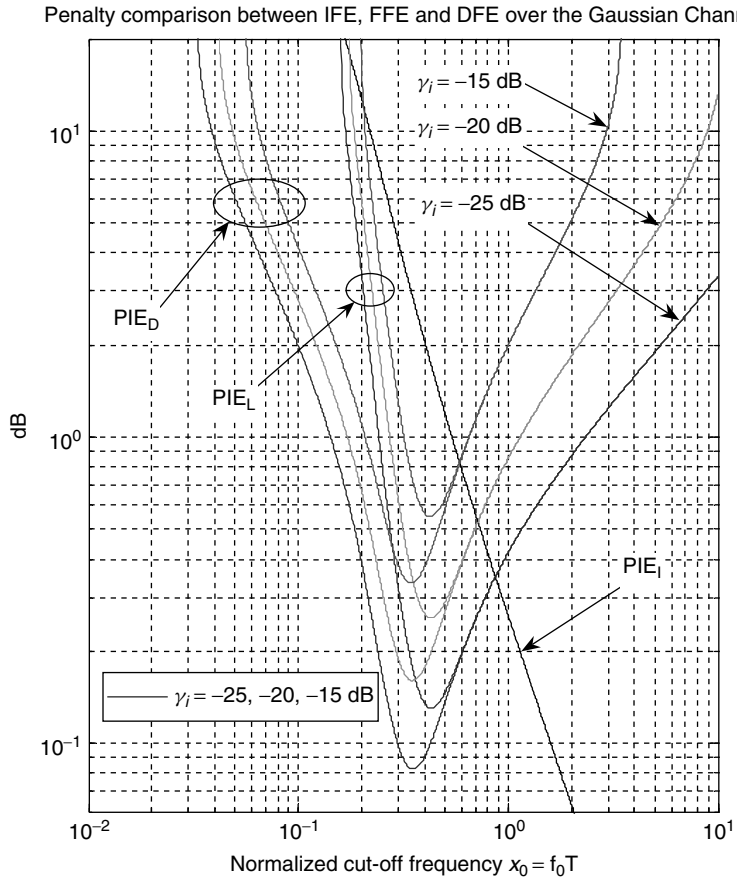

Figure 10.36 Comparison between the computed optical power penalties for the Gaussian channel assuming the inverse filter equalizer (IFE), the feedforward equalizer (FFE) and the decision feedback Equalizer (DFE). The channel metric for the IFE is not affected by the noise parameter. For cut-off frequencies above approximately the half bit rate, both the FFE and DFE behave similarly with monotonically increasing penalty versus channel bandwidth. In the lower cut-off range, the performances of the FFE and DFE split into two corresponding curve sets, according to the noise value. The DFE leads to sensible better performances at cut-off frequencies of $x_0 \leq 0.3$

10.5 DFE Architectures

In this section the general architecture of the electronic dispersion compensator (EDC) will be introduced, which is based on the decision feedback equalizer (DFE). In particular, the block diagram of the principal functions required by the DFE will be considered, as well as how this technique is used in state-of-the-art optical receivers for multigigabit applications. As a general requirement given in the previous section, the transmission channel must be linear. This means in particular that the transmission channel included between sections $S-S'$ and $Q-Q'$ in Figure 10.38, composed of the optical fiber and the optical receiver, must be linear. Assuming that the light intensity is reasonably low enough to validate the optical linear regime for the multimode fiber,

Table 10.8 Computed values of the optical power penalties PIE_I (10.146), PIE_L (10.147) and PIE_D (10.148) versus the selected cut-off frequencies assuming the Gaussian channel. The steeper response leads to consistent benefit of the DFE structure with respect to the simpler FFE at relatively low cut-off values. In the case of the Gaussian channel, the benefit of the DFE over the FFE structure is clearly visible for cut-off frequencies below $x_0 \leq 0.5$

Cut-off	PIE_I (dB_{10})	PIE_L (dB_{10})			PIE_D (dB_{10})		
x_0	–	$\gamma_i = -25\,dB$	$\gamma_i = -20\,dB$	$\gamma_i = -15\,dB$	$\gamma_i = -25\,dB$	$\gamma_i = -20\,dB$	$\gamma_i = -15\,dB$
0.1000	65.9360	∞	∞	∞	1.9842	2.7966	4.1598
0.2000	12.7389	3.3834	5.8906	15.9497	0.3899	0.6644	1.1029
0.3000	4.3360	0.3192	0.6231	1.2935	0.0983	0.1889	0.3805
0.4000	2.0568	0.1352	0.2650	0.5650	0.0907	0.1775	0.3784
0.5000	1.1985	0.1467	0.2896	0.6306	0.1360	0.2684	0.5844
0.6000	0.7887	0.1967	0.3907	0.8637	0.1944	0.3861	0.8535
0.7000	0.5605	0.2548	0.5089	1.1410	0.2544	0.5081	1.1393
0.8000	0.4199	0.3124	0.6274	1.4267	0.3123	0.6273	1.4264
0.9000	0.3268	0.3677	0.7423	1.7121	0.3677	0.7423	1.7120
1.0000	0.2619	0.4206	0.8535	1.9969	0.4206	0.8535	1.9969
1.5000	0.1135	0.6593	1.3702	3.4595	0.6593	1.3702	3.4595
2.0000	0.0633	0.8697	1.8482	5.1155	0.8697	1.8482	5.1155
5.0000	0.0100	1.8962	4.6184	∞	1.8962	4.6184	∞
10.0000	0.0025	3.3515	13.2491	∞	3.3515	13.2491	∞

there must therefore be a requirement that the optical receiver behaves linearly. Every gain section that is inserted between the optical input section $R-R'$ and the equalizer input section $Q-Q'$ in Figure 10.38 must therefore have a linear transfer characteristic over the complete optical receiver dynamic range. The impulse response of the cascaded linear systems between the $R-R'$ and $Q-Q'$ sections is the function $h_R(t)$ defined in Section 10.4. Figure 10.38 shows the general block diagram of the DFE-based optical receiver architecture.

The optical signal is converted and electrically amplified by the input stage of the optical receiver. The photodiode and the low-noise transimpedance amplifier must have a linear transfer function within the required optical dynamic range at the receiver section $R-R'$ of the transmission system. The signal amplitude at the receiver output will therefore be changing linearly with the received average optical power. For a better digital signal processing the electrical signal amplitude at the feedforward Filter (FFF) input must have a fixed amplitude. This function is achieved by the automatic gain controlled (AGC) amplifier, which provides a constant output signal amplitude at the FFF input. The feedforward filter provides optimum input noise matching and precursor power minimization by means of optimum tap weights. The output of the FFF is connected to the sum node for postcursor power minimization and the resulting signal feeds the sampler delivering quantized samples to the clock and data recovery (CDR) circuit. The digital signal at the CDR output is then fed to the digital feedback filter (FBF) whose weights have been optimized for postcursor power minimization.

A very general and demanding feature of every multigigabit optical receiver used with an multimode optical fiber link is the adaptation capability of transmission channel fluctuations. It is already known that the impulse response of the multimode fiber depends on many environmental conditions and during normal operations the optical link must be capable of adapting automatically to such response variations. To this end, every block has been designed with proper feedback loops to guaranteed adaptations. These characteristics will not be analyzed further here, nor how to implement them, but it is important to understand the operating principles of each block included in the multigigabit optical receiver designed to work on legacy multimode fibers. Referring to the general

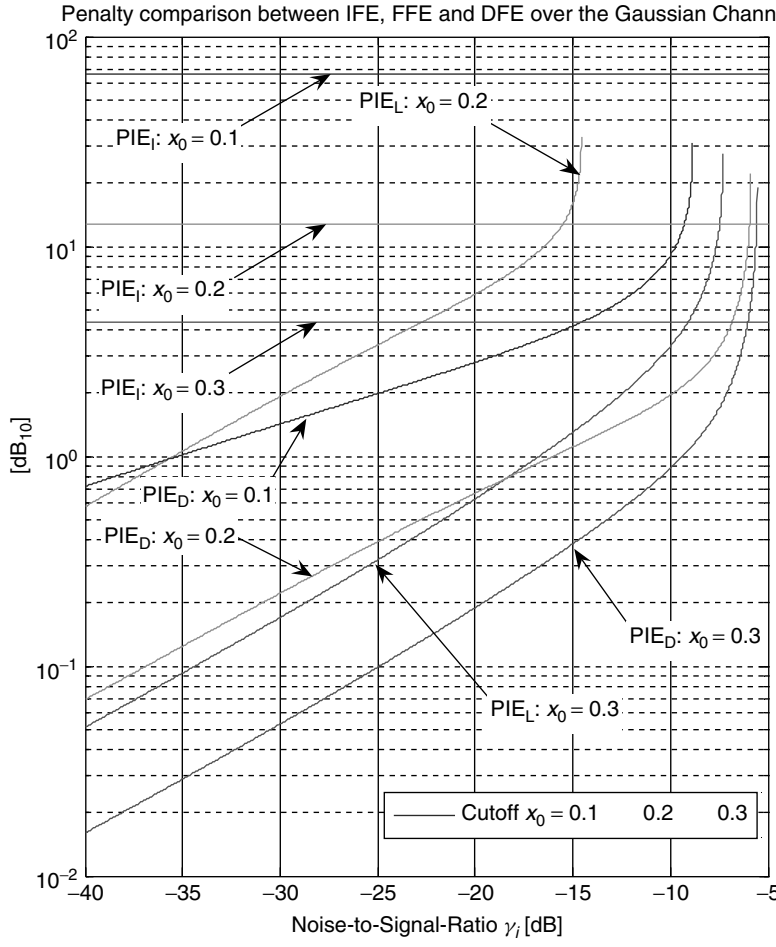

Figure 10.37 Computed channel metrics for the Gaussian response versus the noise-to-signal ratio for selected cut-off frequencies. The improvement of the DFE over the IFE and FFE structures is evident for all the noise ranges considered. The FFE does not provide suitable equalization at $x_0 = 0.1$. As expected, the best results are achieved when the cut-off frequency is close to 35 % of the bit rate frequency

block diagram in Figure 10.38, it is recognized that both digital filters should have tap weights controlled by the adaptive algorithm for a better dynamic equalization capability. The sampler is assumed to have the threshold controlled in order to minimize errors, and finally the CDR shows the optimum timing instant set adaptively. The adaptation algorithm is managed by the on-chip microcontroller. It is clear that the basic DFE architecture would not require any microcontroller of firmware to work properly according to the theory introduced in the previous section, but under a dynamic channel response minimization of the mean square error cannot be achieved without the adaptive feedback architecture. The controllability of the DFE architecture greatly increases the complexity of the receiver. This is due to the many variables involved in the optimization process and the consequent multivariable variational calculus required. The stability of the convergence of the optimization algorithm steeply reduces as the number of digital filter taps increase. Unfortunately, the more the fiber link length increases the higher does the required tap number become

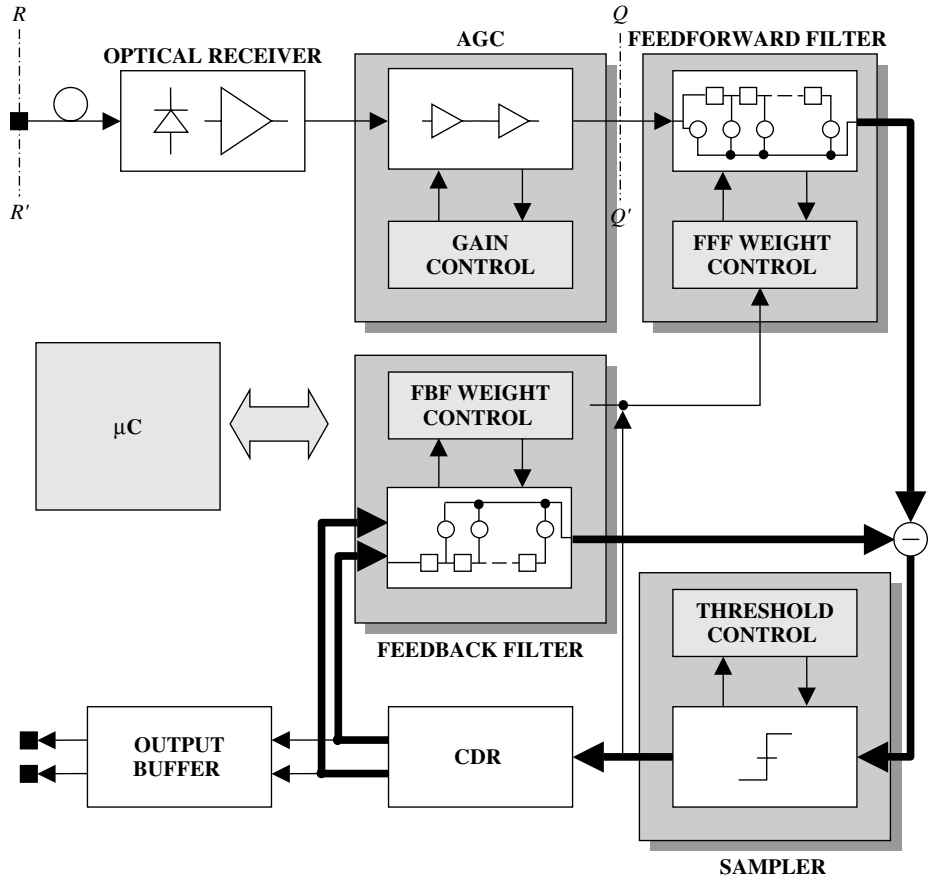

Figure 10.38 Block diagram of the optical receiver deploying the electronic dispersion compensator (EDC) implemented using the decision feedback equalization (DFE) scheme. The DFE includes four principal blocks highlighted in light brown. The automatic gain controlled (AGC) amplifier provides linear amplification with a constant output signal amplitude. The feedforward filter (FFF) provides noise input matching for minimal noise bandwidth and precursor power minimization. The sampler delivers quantized signal levels to the clock and data recovery (CDR) for proper retiming and decision. The feedback filter (FBF) returns digital samples to the sampler input for postcursor power minimization. Each function is assumed to be controlled for adaptation equalization. The on-chip microcontroller provides the required firmware and error management for digital filter weights optimization

for optimum pulse equalization. The next sections briefly describe the main building blocks of the DFE architecture.

10.5.1 Automatic Gain Controlled (AGC) Amplifier

The automatic gain controlled (AGC) amplifier provides the optimum signal amplitude to the input of the feedforward filter. It can either amplify or attenuate the electrical signal delivered by the linear optical receiver, depending on the optical input level at the receiving section. Figure 10.39 shows the block diagram of a typical AGC amplifier structure. Two basic requirements are demanded to the AGC amplifier: the dynamic range and the noise figure.

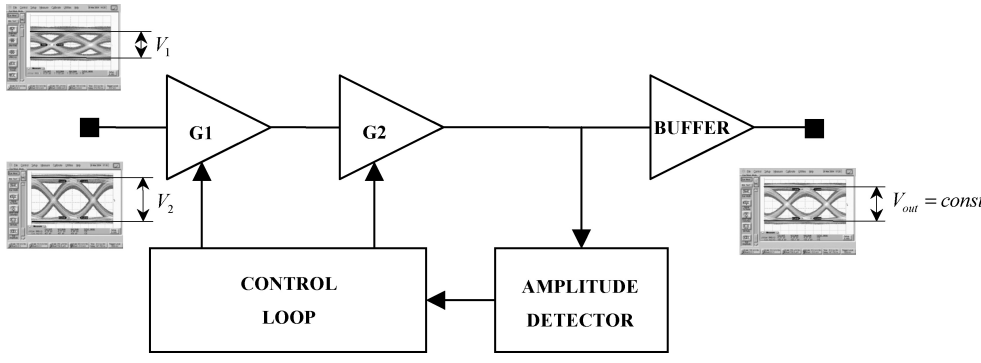

Figure 10.39 Simplified block diagram of the AGC amplifier. Variable gain stages G1 and G2 are controlled by the control loop in order to provide constant output amplitude. The amplitude detector samples the signal amplitude at the buffer input and feeds the control loop. The output buffer has unit gain and provides output line loading over the required matched impedance

The dynamic range identifies the capability of the amplifier to handle an input signal and to amplify it linearly over the complete signal excursion. It is clear that the more the required dynamic range is extended, the more complex would be the AGC design. For large dynamic range operations the amplifier bandwidth and the linearity parameters are related. According to the 10 GbE standards, typical dynamic range requirements extend to about 30 dB_e, corresponding to an input signal amplitude ranging between 30 mV_{pp} and 1000 mV_{pp}.

The noise figure of the amplifier characterizes the amount of noise power added by the amplifier to the input equivalent noise, assuming matched impedance source conditions. Due to linear amplification, the noise power generated by the AGC is easily referred to the optical input section and must be added to the total noise calculation. Typical optical sensitivity degradation accepted by the AGC noise power would be of the order of less than 0.2 dB_o.

10.5.2 Feedforward Filter (FFF)

The feedforward Filter (FFF) is located at the input of the decision feedback equalizer (DFE) and consists of a transversal filter with a finite number of taps. According to the theory presented in Section 10.4, the number of taps depends on the extent of precursors that must be minimized, so its length increases with increasing precursor tail complexity of the incoming pulse. The weight of each tap depends on the optimized solution using the variational method, as reported in the previous section. Assuming adaptive equalization, tap weights are variables according to the optimization algorithm. The value of each delay line step is equal to the time step $T = 1/B$. Figure 10.40 shows the block diagram of the feedforward filter using the classical transversal filter structure.

The impulse response $h_W(t)$ of the feedforward filter represented in Figure 10.40 is derived from the signal flow in the block diagram shown. Each delayed contribution of the input stimulus is first multiplied by the corresponding coefficient g_n and then summed at the output node. Hence:

$$h_W(t) = \sum_{n=0}^{5} g_n \delta(t - nT) \tag{10.149}$$

The signal that is easily synthesized in Equation (10.149), although correctly representing the feedforward filter impulse response in Figure 10.40, does not present the anticausal tapped delay line required in Equation (10.52) and in Figure 10.6. The analysis and the implications of this problem is outside the scope of this book and the reader is referred to more specialized references.

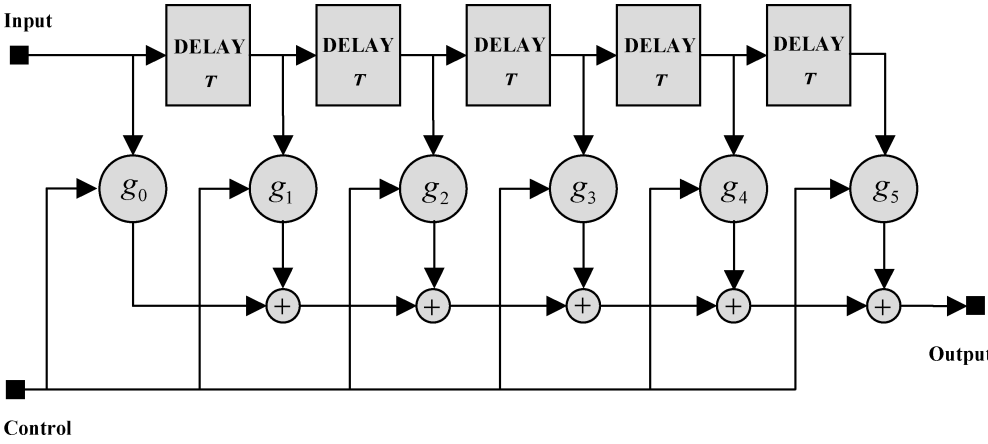

Figure 10.40 Block diagram of the six- tap feedforward filter used for precursor minimization and optimum noise filter (minimum noise bandwidth). The equalizer is realized by the transversal filter structure with a fixed delay line T and optimum tap coefficients $\{g\}$. The value of the tap coefficients is set adaptively according to the minimum error rate achievable

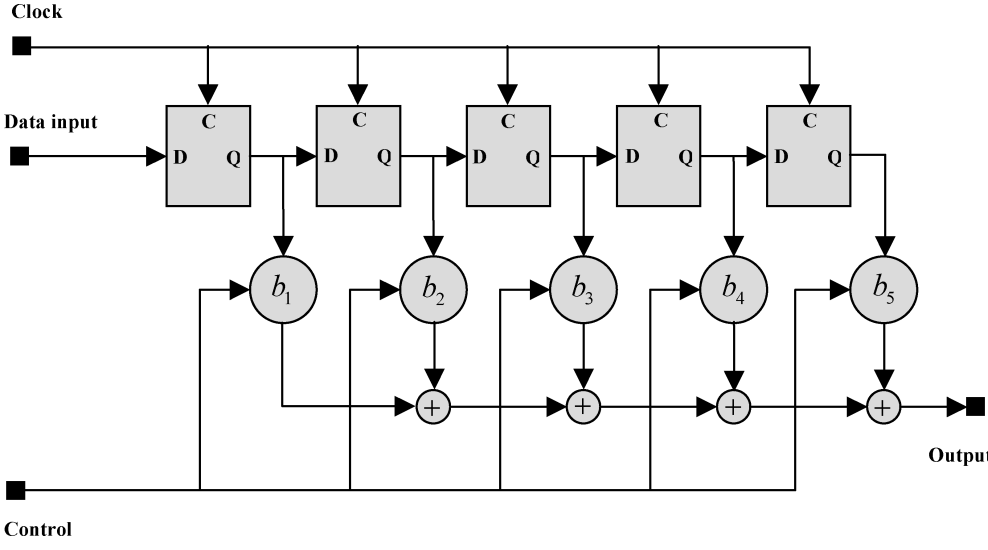

Figure 10.41 Block diagram of the five-tap feedback filter used in the DFE architecture. According to the block diagram of the DFE represented in Figure 10.1, the delay line is realized with a clocked D-Flip-Flop. This guarantees phase alignment between the current sample and the postcursors feedback samples. From Equation (10.40), the coefficients $\{b\} = b_1, b_2, \ldots$, must coincide with the postcursor samples $\{r\} = r_1, r_2, \ldots$

10.5.3 Feedback Filter (FBF)

The feedback filter is shown in Figure 10.41 and provides postcursor ISI cancellation by applying the proper weighted sum of the previous pulse tails to the current data sample. The length of the FBF depends on the extent of the postcursors to be minimized. A typical transversal filter length used in multimode fiber optic feedback equalization ranges between three and seven taps. The

filter length influences the power consumption of the DFE and must be carefully balanced between postcursor lengths and equalization efficiency.

Before closing this chapter, it should be noted that real EDC architecture is based on digital filters of finite length. The performances of the implemented EDC then approximate the performances of the ideal, infinite length structures presented in this chapter. The analysis and design of the EDC based on the finite length DFE is outside the scope of this book and is one of the 'hottest' topics of high-speed DSP applied to optical fiber multigigabit transmission.

10.6 Conclusions

These considerations close the chapter regarding the operating principles of the digital filters using the DFE architecture. This chapter should be intended as an introduction to this field. There is a very large amount of literature available on this subject which should be addressed for further knowledge. The application of digital filters to fiber optic transmission systems is quite recent since the large bandwidth of this transmission channel did not require any additional processing to achieve the required transmission performances up to the advent of multigigabit optical communication in the metropolitan area. The recent increase in transmission speed up to 10 Gb/s over multimode fiber has merged the high-speed DSP technology in the optical transmission field.

This chapter has introduced the operating principles of electronic dispersion compensation devoted to mitigate multimode fiber pulse dispersion in multigigabit transmission systems. It has already been stated that electronic dispersion compensation by means of digital signal processing is a mature technology, largely deployed in fading radio transmission, satellite communication and even speech recognition. Nevertheless, despite the last few years spent on intense technology in an attempt to achieve a single chip solution, electronic dispersion compensation still seems to be at the preliminary stage, with many interesting laboratory demonstrations but not yet any that can be deployed in the field. The reasons for these difficulties are recognized as two main issues: the high speed of the signal rate and the strong adaptation required by the multimode fiber response. The IC manufacturing capability is pushed to the limit, using 90 μm CMOS technology in a sub-watt five-by-five millimeter BGA squared package.

It is meaningful that equivalent applications of electronic dispersion compensation for single-mode fiber and copper transmission lines have been successfully tested and deployed in the field for almost five years. As extensively analyzed in the first part of this book, the impulse response of a multimode fiber link, including several connectors and standard launching conditions, is completely unpredictable, and in addition, it is very sensitive to environmental conditions and to the launching polarization. All these characteristics make multimode fiber transmission at 10 GbE a true engineering challenge.

In this chapter the first basic concepts and expressions of the theory of the decision process in binary digital transmission with Gaussian white noise are introduced. The classical bit error rate formula has been presented with some applications. The relationship with the signal-to-noise power in the electrical domain has also been considered. Sections 10.3 and 10.4 dealt with the ideal inverse filter equalizer and the digital equalization principles respectively by means of the DFE architecture. The penalty for the ideal linear equalizer, PIE_L, has been derived and used as a channel metric in optical fiber transmission. The expression of PIE_L has been obtained with an original derivation based on the concept of noise bandwidth enhancement. Using the digital equalizer, the equivalent optical power penalty for the digital equalizer, PIE_D, has been obtained. Those two expression can be conveniently adopted as the channel metric or channel figure-of-merit for quantitatively classifying multimode fiber links.

11

Transmission Experiments

Deploying Multigigabit Transmission Experiments over Multimode Fiber

11.1 Introduction

The increasing demand for multigigabit transmission over legacy multimode fiber has very recently produced a large amount of effort in characterizing the multimode fiber using laser-based optical sources. The implementation of low-cost 10GbE optical sources requires the adoption of direct modulation of the vertical cavity semiconductor laser (VCSEL), available in a receptacle plastic package and enabling flex interconnection technology. The VCSEL structure is characterized by a very low threshold current and very high modulation efficiency. Those two parameters are needed for the design of a low-cost and low-power consumption optical transmitter suitable for the large distribution of 10GbE in the metropolitan area network. The next device directly related to the success of the 10GbE network is the multimode optical fiber. There is of course no need for choosing these media, but there is the necessity to use the already installed fiber infrastructure. It is known that this infrastructure is mostly implemented using relatively old multimode fiber, not specifically designed for either multigigabit transmission or coupled to narrow beam laser sources.

After the introduction of the Gigabit Ethernet in 1997, the commercial relevance of using the existing multimode fiber infrastructure was soon adopted as a new engineering challenge for the IEEE 802.3 Committee. Extensive studies of the launching conditions and corresponding multimode fiber characterization led to a consistent amount of data summarized in the statistical distribution of the modal bandwidth of the installed fiber base. This information has been used since 2003 during the trial of the 10GbE standard using the multimode fiber. The result of these studies has not yet been released and the most crucial point, that of recognition by the Committee of including the electronic dispersion compensator into the new standard 10GBASE-LRM, has not yet taken place. Of course, more sophisticate launching conditions have been proposed and partially accepted, but since the final target of the standard would be large deployment in the metropolitan area, the engineering approach would consequently be very relaxed, minimizing sophisticated requirements and calibration procedures. In addition, the urban environment is not quite a standard office environment, leading to strong perturbation of the transmission system due to mechanical and thermal causes.

Multi-Gigabit Transmission over Multimode Optical Fibre: Theory and Design Methods for 10GbE Systems Stefano Bottacchi
 ISBN: 0-471-89175-4

This has induced the Committee to require adaptive compensation technologies, capable of restoring the minimum multimode fiber propagation capabilities in order to guarantee the multigigabit link operation.

In this chapter, a summary will be given of the large amount of measurements devoted to components and subsystems characterization for multigigabit transmission over multimode optical fiber. Collected data include multimode fibers, laser sources, optical receivers and preliminary samples of the electronic dispersion compensator available from pioneering IC companies. Those measurements have been primarily done at the Fiber Optic Department of Infineon Technologies AG, Berlin, during the last two years, in particular between 2003 and 2005, with the intention of providing the background characterization of the basic components deployed in every multigigabit transmission system using legacy multimode fiber.

11.2 Measurement Outline

In this chapter, for the first time the experimental results will be presented of transmission systems operating at the 10GbE data rate and using different samples of legacy multimode fibers. The principal actors in these measurement campaigns are the multimode fiber (MMF) and the electronic dispersion compensator (EDC), and the major focus has been concentrated during the entire characterization on those two system components. A chapter outline is now given with a summary of the performed measurements.

1. Section 11.3 describes the experimental setup, including the detailed block diagram schematics. All the major components of the measuring environment are briefly introduced and the principal parameters specified. An introductory theoretical explanation of the observed polarization-induced pulse distortion in multimode fiber is considered in the Section 11.4.
2. The reference optical transmitter and receiver used through all the subsequent measurements are presented in Section 11.5.
3. The first set of multimode fiber, otherwise known as the benchmark fiber, is characterized in Section 11.6, where both single-pulse and eye diagrams are presented according to several experimental setups.
4. Section 11.7 presents both the modeling and experimental results of the useful optical link emulator simply realized using the standard OC-48 electrical filter.
5. The first polarization measurement effects at 10GbE are presented in Section 11.8. These experiments have been conceived to raise, for the first time, the potential relevance of these effects in the performance evaluation of multigigabit transmissions over multimode fibers.
6. Section 11.9 presents the measurements of the EDC operation in highly corrupted multimode optical fiber link, including both electrical and optical characterizations. In addition to the benchmark fiber test, a complete set of new measurements performed using a second laboratory sample of multimode fiber is presented and compared with the previous one.

11.3 Measurement Setup

In this section, the general measurement setup is presented, including a brief description of the components. The measurements reported refer to the central wavelength of the second transmission window exhibited by the optical fiber, nominally at $\lambda = 1310\,\text{nm}$. This choice is compliant to the requirement for the 10GBASE-LRM standard. Figure 11.1 shows the general composition of the measurement setup. According to the specific measure, a part or all of the available components have been used.

In the following sections, a brief description is given of each block reported in Figure 11.1.

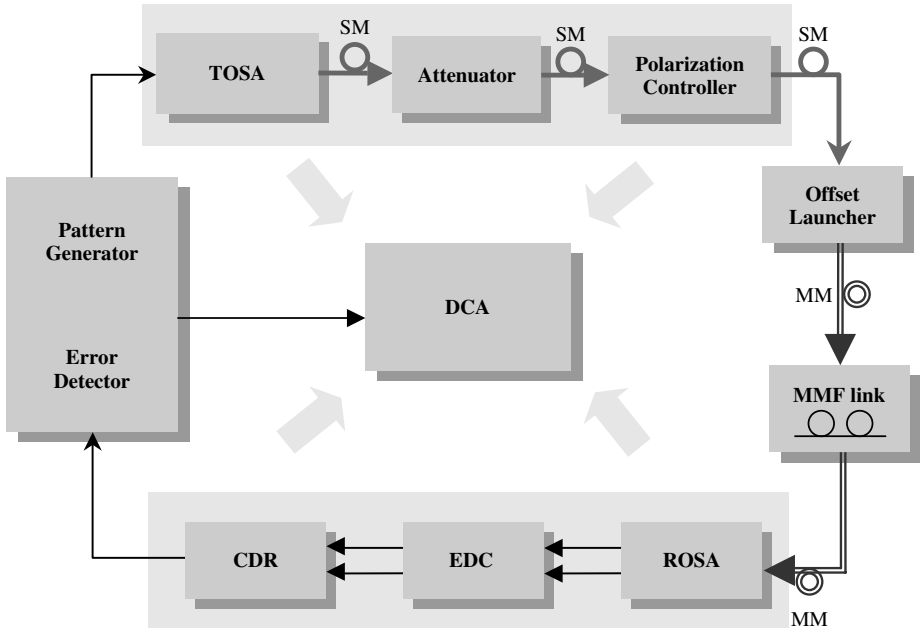

Figure 11.1 Block diagram of the general measurement setup. The two grey-shaded areas represent the transmitter (top) and the receiver (bottom). The optical channel is configured by the optical launcher, the multimode fiber link and the optical connectors inserted between any two fibers spools. Multimode fiber connections are marked with double lines

11.3.1 TOSA

The transmitting optical Subassembly (TOSA) consists of either a directly modulated distributed feedback (DM-DFB) laser diode or an electroabsorption modulator coupled with the distributed feedback (EAM-DFB) laser diode, assembled within a coaxial package with a monitor photodiode for light power monitoring. The TOSA is optically coupled to the single-mode fiber jumper by means of standard FC or SC type single-mode optical connectors. The electrical signal input is connected to the output of the pattern generator by means of standard SMA–microwave cables. The laser or modulator biasing conditions for achieving proper calibrations of the extinction ratio and average output power are accessible from standard controls available on the front panel.

Depending on the optical waveform, the extinction ratio varies between 3 dB and 10 dB with the corresponding average output optical power ranging approximately between +1 dBm and −1 dBm. Experimental evidence shows that by adjusting the laser biasing in order to increase the extinction ratio, the BER performances of the EDC receiver can be considerably improved. This is not due to a corresponding increase in the optical modulation amplitude for a given average power. Instead, moving the low level closer to the laser threshold causes the low-to-high transition affected by relevant relaxation oscillation to overshoot and allows an easier EDC recovery, even under severe pulse deformation. This effect can be depicted as a pulse pre-emphasis that increases single pulse energy and makes pulse detection recognizable after considerable pulse broadening.

11.3.2 Optical Attenuator and Polarization Controller

The output of the transmitter is directly coupled to the input of the optical attenuator using a single-mode fiber patch cord, as shown in Figure 11.1. The optical attenuator is used to adjust the

average optical power level at the input receiving section in order to allow bit error rate (BER) measurements to be taken. The output of the attenuator is then connected through a single-mode fiber patch cord to the input of the optical polarization controller using the angled single-mode connector for reducing optical reflections. The polarization controller is used to change input from any polarized or unpolarized light source into any well-defined state of polarization, feeding the subsequent multimode fiber link. The design based on a linear polarizer followed by two bulk-optic zero-order waveplates provides optimum determination and repeatability of the polarization states at the output over a wide wavelength range. The polarization controller is composed of three sections:

1. The linear polarizer
2. The λ/4 waveplate
3. The λ/2 waveplate

First, the linear polarizer (1) is aligned to the input linear polarization state from the laser source in order to maximize the transmission of the field intensity. In order to have the linear polarization at the output of the polarization controller it is necessary to set the slow axis of the λ/4 waveplate (2) orthogonal to the linear input polarization. In this case, both transversal components of the input electric field will experience the same delay when passing through the λ/4 waveplate. Both components of the output electric field will therefore be in phase and the linear polarization state results. Any other angle will result instead in the elliptic polarization state. In particular, if the λ/4 waveplate is set at 45° to the input polarization, the output field will be circularly polarized. In the third stage, the λ/2 waveplate (3) provides the rotation of the polarization vector available at the output connector.

In order to understand how the λ/2 waveplate works, Figure 11.2 shows the decomposition of the electric field in terms of the principal axes of the λ/2 waveplate. The angle between the input linear polarization state and the reference slow axis of the λ/2 waveplate is given by φ. The electric field component traveling along the slow axis of the λ/2 waveplate exhibits a 180° phase shift. If the slow

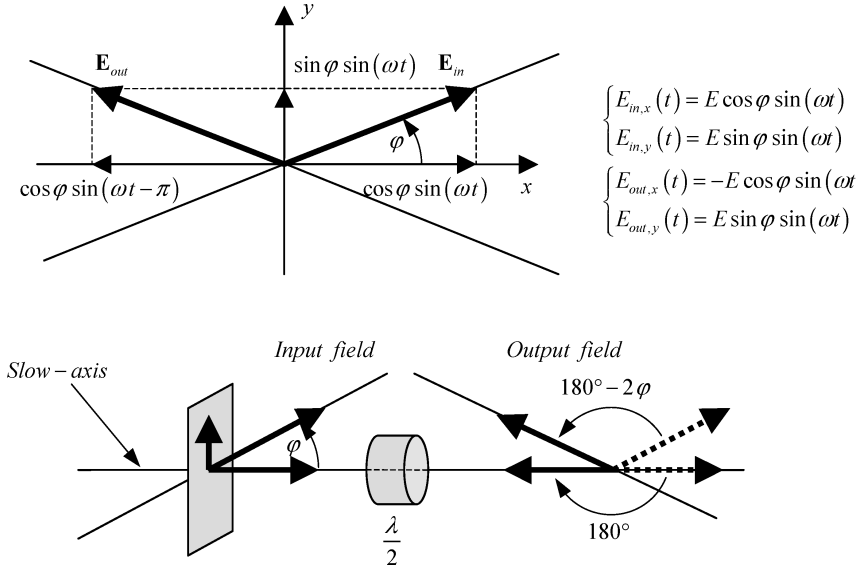

Figure 11.2 Schematic representation of the linear polarization rotation performed by the λ/2 waveplate. The electric field component oscillating along the slow axis of the λ/2 waveplate exhibits a half-period delay (180°) and the output electric field oscillates along the direction rotated by $180° - 2\varphi$

axis of the λ/2 waveplate is aligned with the input polarization, rotation of the output polarization by 180° results. If the λ/2H wave plate is set in quadrature with the input field orientation by setting $\varphi = 90°$, the output polarization state will remain unchanged since no field component will propagate along the slow axis of the λ/2 waveplate. Any angle $0 \leq \varphi \leq 90°$ will therefore provide a rotation of the output field equal to $\varphi_{out} = 180° - 2\varphi$ with respect to the input orientation.

The λ/4 waveplate operates in exactly the same way but provides a 90° phase shift (λ/4) of the electric field component aligned along the slow axis. This has a great impact on the output state of polarization. Figure 11.3 shows the schematic construction of the electric field processed through the λ/4 waveplate.

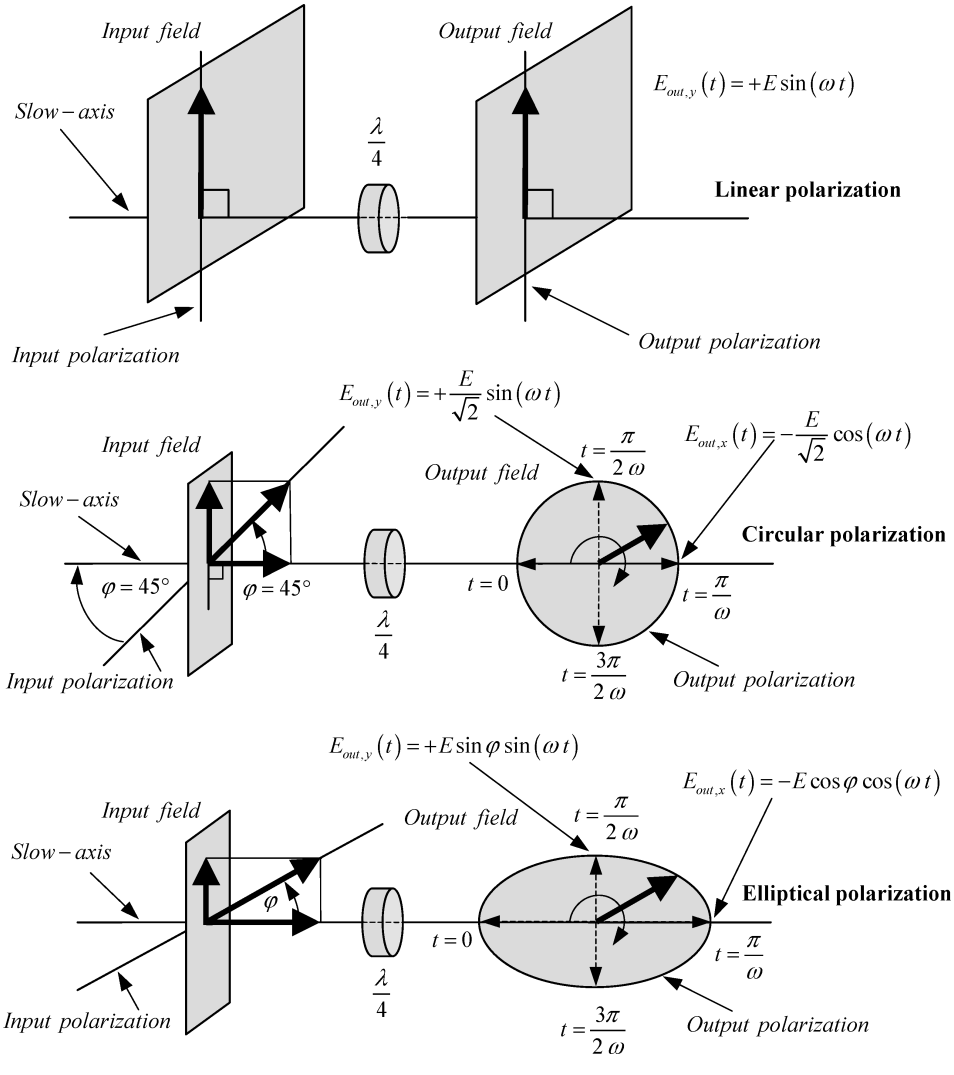

Figure 11.3 Schematic representation of the elliptical polarization (bottom) generated by the λ/4 waveplate when the slow axis is oriented with the angle φ with respect to the linear input polarization. If the slow axis is orthogonal to both electric field components (top), the input linear polarization is preserved at the output of the λ/4 waveplate. Instead, if $\varphi = 45°$ (middle), the output field is circularly polarized

It is assumed that the time-harmonic input field $\mathbf{E}_{\text{in}}(t)$ oscillates at the angular frequency ω and is linearly polarized with the angle φ with respect to the slow axis of the $\lambda/4$ waveplate:

$$\begin{aligned} E_{\text{in},x}(t) &= E\cos\varphi\sin(\omega t) \\ E_{\text{in},y}(t) &= E\sin\varphi\sin(\omega t) \end{aligned} \tag{11.1}$$

The x component passing through the slow axis of the $\lambda/4$ waveplate is delayed by a quarter of the period, and the output field assumes the following form:

$$\begin{aligned} E_{\text{out},x}(t) &= E\cos\varphi\sin\left(\omega t - \frac{\pi}{2}\right) \\ E_{\text{out},y}(t) &= E\sin\varphi\sin(\omega t) \end{aligned} \tag{11.2}$$

The x component of the output field is therefore in quadrature with the y component and, in general, their amplitudes are different, according to the value of the angle φ:

$$\begin{aligned} E_{\text{out},x}(t) &= -E\cos\varphi\cos(\omega t) \\ E_{\text{out},y}(t) &= +E\sin\varphi\sin(\omega t) \end{aligned} \tag{11.3}$$

It is clear at this point that the tip of the electric field vector describes an elliptic path every period $2\pi/\omega$, leading to the elliptic state of polarization. In particular, from Equations (11.3), if $\varphi = 45^\circ$ both components of the electric field have the same amplitude and the polarization is circular. Assuming instead $\varphi = 90^\circ$, the input electric field has no component along the slow axis and the output electric field has the same linear polarization as the input one. In conclusion, depending on the input electric field component aligned along the slow axis of the $\lambda/4$ waveplate, the resulting output field can be linear, circular or generally elliptical polarized.

11.3.3 Offset Launcher SM → MM

The single-mode output of the polarization controller is connected to the single-mode input section of the IEEE 802.3 standard offset launch (OSL) patch cord. Figure 11.4 gives a schematic drawing

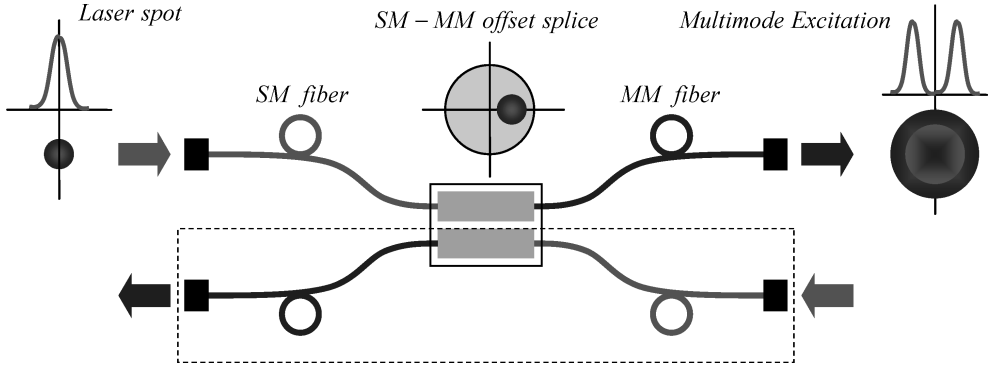

Figure 11.4 Schematic drawing of the offset launch conditioning used in the 10GBASE-LRM standard. The offset position range depends on the core diameter of the multimode fiber used. The offset launcher excites mainly the higher-order fiber modes, using mainly the middle of the core region. According to the standard, the offset ranges between $14\,\mu\text{m} \le r_0 \le 20\,\mu\text{m}$ for the $50\,\mu\text{m}$ diameter fiber and between $17\,\mu\text{m} \le r_0 \le 23\,\mu\text{m}$ in the case of the $62.5\,\mu\text{m}$ core diameter fiber

of the offset launcher. The offset launch has been proposed by the IEEE 802.3 Standard Committee during the Gigabit Ethernet definition in order to limit the variation shown by the modal bandwidth of the multimode fiber installed base. Using the offset launch, the inner radial region of the multimode fiber is excluded from laser source modal excitation, avoiding the degradation consequences of a strong refractive index profile irregularity usually affecting the axial core region. The same approach has been proposed by the IEEE 802.3 10GBASE-LRM Committee in order to reduce the modal bandwidth spreading of the legacy multimode fiber installed base. The offset launch patch cord is connected by means of either SC-PC or LC-PC standard type optical connectors. The short piece (usually less then 20 cm long) of single-mode (SM) fiber is then fusion-spliced to the multimode (MM) fiber section of the offset launcher using the specific offset coordinate required by the standards for the given multimode fiber. In the case of 62.5 μm fiber core, the offset is set in the radial range between 17 μm and 23 μm, while for the 50 μm fiber core, the offset must be within the radial range between 14 μm and 20 μm.

The intent of the offset launch is to reduce the differential group delay (DGD) providing selective launch conditions for high-order modes (skew rays) located mainly in the middle of the radial core region. This approach avoids both the axial and core regions and the core–cladding boundary, which can be affected by manufacturing defects. The problem concerning the offset launch is the conservation of the excited mode distribution along the multimode fiber link when several optical connectors are included. In fact, every connector affected by fabrication tolerances modifies the optimal launched distribution leading to increased DGD.

11.3.4 Multimode Fiber

The multimode fiber link starts at the SC-PC connector of the multimode fiber section belonging to the OSL patch cord. As reported in Figure 11.5, the multimode fiber link is assembled using one or more fiber sections according to the available spool lengths. Consequently, in the measurement setup the number of optical connectors can vary between two, in the 50 m single-section link case, up to a maximum of four, in the case of three sections of 250 m link length. The fiber type used in the measurements is the same for all the sections considered since it has been cut and connected starting from a single spool of 62.5 μm multimode fiber manufactured by Siecor in 1996. Due to the different numbers of connectors present in the different link compositions, the results are not fully comparable. Nevertheless, as reported in Figure 11.5, at least the link compositions identified as III, IV and VI, having only one link connector and the same launching fiber section (100 m–reel A), are fully comparable in terms of measured performances.

In order to preserve the same launching conditions and to allow a performance comparison, the same 100 m-A optical fiber link has been used as the launching pad for all five II... VI configurations.

11.3.5 ROSA

The receiver optical subassembly (ROSA) collects the light intensity available from the last connector of the multimode fiber link. In the experimental setup, a short fiber patch cord (1 m) is added between the multimode fiber link and the receiver receptacle, allowing easier optical power measurements to be taken. The end of the short multimode patch cord coincides with the TP3 standard section. The optical receiver includes the InGaAs PIN photodetector and the linear transimpedance amplifier suitable for 10GbE applications. The receiver background sensitivity in the back-to-back configuration has been measured in order to fix the reference performance. The receiver used in the measurement has differential output and is assembled over a ceramic evaluation board with a flexible interconnection between the coaxial packaged PIN diode and the ceramic board. The receiver package has an SC-receptacle optical input.

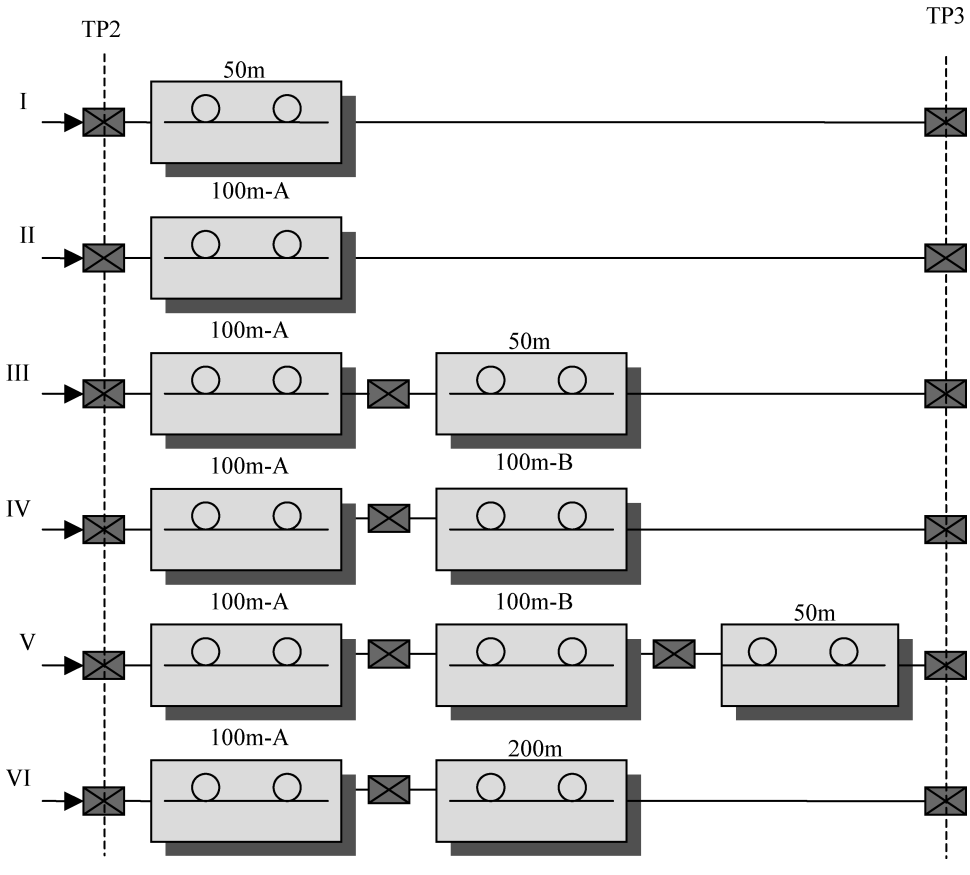

Figure 11.5 Different link compositions of the Siecor benchmark multimode fiber used in the measurements. Connector pairs are of the FC-PC type for multimode applications. TP2 is in the launch input reference section and is connected to the multimode section of the offset launcher. TP3 is in the output link section and is connected to the ROSA receptacle

11.3.6 EDC and CDR

The electronic dispersion compensator (EDC) is a single-chip device providing two-step pulse equalization using the feedforward equalizer (FFE) and the decision feedback equalizer (DFE). The equalization algorithm is based on the minimum mean square error (MMSE) principle: the residual ISI after the equalizer exhibits the minimum power achievable for the given filter structure (length, tap spacing). The EDC sample used in the experimental setup does not include a clock recovery and a digital asynchronous signal is therefore available at the device output.

The clock and data recovery (CDR) chip is driven differentially from the digital output of the EDC chip. The data have already been decided at the EDC section and the purpose of the CDR is to filter random jitter generated during the equalization procedure. In addition, in the experimental setup, the CDR provides high output swing capable of driving the error detector above the minimum signal threshold in order to provide the correct signal detection process and bit error rate measurements.

11.3.7 Data Pattern and Waveform Records

The pulse pattern generator (PPG) has been set to output either datastream according to NRZ coded PRBS (pseudo-random binary signal) of several lengths, $2^7 - 1, \ldots 2^{31} - 1$, or single words designed specifically to excite a single-pulse response. According to the specific issues of each link measurement, a minimum set of digital communication analyzer (DCA) screen shots and numeric text files have been collected at the following sections:

1. Eye diagram (.GIF file extension) at the optical transmitter output (TP2)
2. Eye diagram (.GIF file extension) at the multimode fiber link output (TP3)
3. Eye diagram (.GIF file extension) at the optical receiver output (before EDC)
4. Eye diagram (.GIF file extension) at the EDC analog output
5. Single pulse (.TXT file extension) at the multimode fiber link output (TP3)
6. Single pulse (.TXT file extension) at optical receiver output (before EDC)

Single-pulse waveforms have been collected in order to compute $\mathrm{PIE_I}$, $\mathrm{PIE_L}$ and $\mathrm{PIE_D}$ channel metrics for simulation purposes. In particular, the $\mathrm{PIE_D}$ metric is used to compare the performance of the implemented EDC with the ideal EDC equalizer.

11.3.8 Single-Pulse Excitation

The way used to excite a single-pulse response needs some comments. The whole transmission channel (transmitter, fiber, receiver, etc.) has been designed to operate with the average signal value balanced between the high and low digital states. This means that under normal operating conditions with random generated sequences the relative frequency of occurrence of the logic '0' and '1' is equal to $\frac{1}{2}$. Under these conditions, the electrical signal excursion around the average value is equal on both sides and the circuitry operates balanced. This holds in particular for the laser biasing conditions. The laser response is strongly affected by the biasing conditions and in order to have single-pulse operation closely resembling PRBS operating conditions, the single-pulse word sequence must be designed accordingly. To this purpose, it is necessary to satisfy the following two conditions:

1. The single '1' must have long enough '0' precursors and postcursors in order to behave sufficiently isolated in terms of the channel response capability.
2. The average level of the repeated word must be $\frac{1}{2}$ in order to maintain the same average biasing condition for the involved channel electronics and optics during normal PRBS operation.

According to the above criteria, the following fixed word pattern of 64 bits has been used during all fixed word experiments:

$$\underbrace{\underbrace{[1111000011110000]}_{\frac{1}{2}}\ \underbrace{[0000100000000111]}_{\frac{1}{4}}\ \underbrace{[1111100011110111]}_{\frac{3}{4}}\ \underbrace{[0000111111110000]}_{\frac{1}{2}}}_{\frac{1}{2}}$$

The 64-bit word reproduced above has the average value of $\frac{1}{2}$ and the isolated '1' have eight '0' precursors and eight '0' postcursors. Under these single word conditions, the excited optical '1' is reproduced with the same biasing conditions as for the PRBS from all the channel components involved. This means that assuming PRBS satisfies linear superposition the PRBS sequence can be reproduced exactly from the isolated pulse response by proper PRBS binary weights.

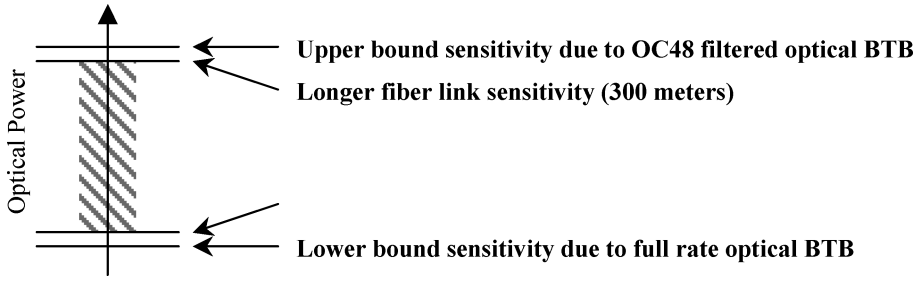

Figure 11.6 Graphical representation of the transmission system sensitivity bounds using optical back-to-back (BTB) configurations. The full-rate optical back-to-back configuration gives the best sensitivity and coincides with the lower bound. Using the OC48 filter to drive the transmitter leads to the OC48 filtered optical back-to-back configuration. This operating condition is limited by strong pulse dispersion and reasonably represents the higher sensitivity bound

11.3.9 Optical Sensitivity Bounds

In addition to the six fiber link compositions reported in Figure 11.5, the transmission experiments account for two other relevant measurements, namely the full-rate optical back-to-back and the OC48 filtered optical back-to-back links. Those two measurements are devoted to setting proper bounds to the transmission system performances. Both full-rate optical back-to-back and OC48 filtered optical back-to-back links include EDC operation. The full-rate optical back-to-back link represents the lower bound for the sensitivity performance while the OC48 filtered optical back-to-back link represents the upper bound for the sensitivity performance. It is noted that the identification as lower and upper bounds refers to the minimum (best sensitivity) and maximum (worst sensitivity) values respectively of the average optical power level needed at the receiver input (TP3) for achieving the required BER value.

The lower bound is well approximated by the 50 m fiber link length while the upper bound of the sensitivity is well approximated by the 300 m link length, assuming better polarization orientation. Figure 11.6 presents the graphical description of the concepts just described. Using the fiber link and not the link emulator through the electrical OC48 filter, the system sensitivity should be included within the lower to upper bounds range.

11.4 Polarization Effects in Multimode Fiber

This section deals with a short theoretical introduction to the polarization effect observed in multimode fiber transmission experiments. Polarization has never been accounted for in multimode fiber and no related literature has been produced up to now on these specific phenomena. Polarization-dependent distortion (PDD) in a multimode fiber pulse response was first observed by Infineon Fiber Optic, IFFO GmbH, Berlin, during the characterization of long-reach high-speed multimode fiber links according to the development of the new standard 10GBASE-LRM for the 10 Gb/s range Ethernet.

11.4.1 Introduction

It has been experimentally observed that polarization-dependent distortion (PDD) manifests itself in relatively long multimode fiber links exceeding 200 m when offset launching conditions are implemented. Optical connectors can increase the effect assuming offset launching or they can generate polarization-dependent distortion in the case of a central launch if the relevant offset is accumulated due to several deployed connectors. Either offset launch or central launch with one

or more optical connectors implemented along the optical link represents proper conditions for stimulating polarization-dependent pulse broadening. For a given data rate, the effect is enhanced for longer links and for perturbed refractive index profiles. This effect has never been accounted for up to now, probably because at the moment these conditions need to be faced due to the actual development of the 10GBASE-LRM standard, which requires simultaneously both a 10 Gb/s data rate and longer (300 m) link lengths of multimode fiber using both offset launch and several link connectors. Of course, there would be no contradiction in assuming that this effect is present, even at a lower bit rate than 10 Gb/s, but the amount of pulse distortion achieved over the same link lengths would be negligible with respect to the longer time step. Accordingly, experimental expectations would detect similar polarization-induced pulse distortions even at a lower signaling rate but for proportionally longer link lengths.

A very brief description of the polarization-dependent distortion observed in transmission experiments for multimode fibers can be tentatively stated as follows:

1. The angle determined by linear polarization of the source field with the offset launch direction changes the mode power partition among individual bound modes, leading to different DMD profiles depending on the launching polarization.
2. For a given offset launch, the amount of power coupled to slower and faster modes is therefore dependent on the input polarization, leading to a polarization-dependent output pulse. Since the effects manifest themselves through the DMD, for a given source pulse width it is necessary to take the pulse measurement after a minimum link length in order to detect consistent distortion.
3. A fundamental prerequisite for sensible polarization-induced pulse distortion is the perturbation of the refractive index with respect to the ideal graded index profile in order to have enough time resolution in the measurement. This is the reason why this effect is observed when operating within the 10GBASE-LRM standard conditions.

11.4.2 Theoretical Concepts

As already stated, a complete theory of this effect has not yet been completed. Instead, a physical justification and some theoretical concepts seem to have been accepted, giving a guide on how to proceed further in the development of the theory. An ideal clad power law refractive index profile with a single shaping coefficient α is considered, as shown in Figure 11.7.

The basic assumptions for the modal analysis of the ideal graded index multimode fiber will now be reviewed.

$$n^2(r) \equiv n_1^2\left[1 - 2\Delta\left(\frac{r}{a}\right)^{\alpha}\right], \quad 0 \le r \le a$$

$$\equiv n_1^2(1 - 2\Delta) = n_2^2, \quad r \ge a$$

$$\Delta \equiv \frac{1}{2}\left[1 - \left(\frac{n_2}{n_1}\right)^2\right], \quad \Delta = 10^{-3} \sim 10^{-2}$$

$$n_1 \cong n_2 \Rightarrow \Delta \cong 1 - \frac{n_2}{n_1}$$

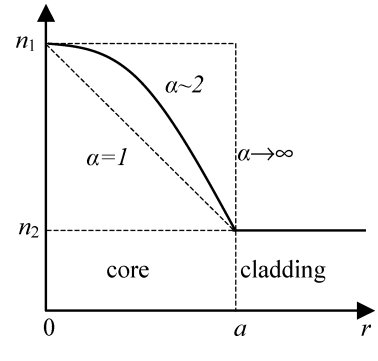

Figure 11.7 Clad power law refractive index profile showing the effect of the refractive index profile coefficient α

11.4.2.1 Cartesian Representation of the Field Components

1. The vector wave equation reduces to the scalar wave equation for each Cartesian component of the electromagnetic field.
2. Each transverse field component E_x, E_y, H_x, H_y can be expressed as a linear combination of the longitudinal component of the electric field $E_z(r, \phi)$ and the magnetic field $H_z(r, \phi)$.

11.4.2.2 Longitudinal Invariance

1. The general solution for the longitudinal component of the electric field $E_z(r, \phi)$ can be separated in the following form:

$$E_z(r, \phi, z) = \psi(r, \phi)\mathrm{e}^{\mathrm{i}(\beta z - \omega t)} \tag{11.4}$$

   The factor β is the propagation constant of the mode and ω is the angular frequency of the true monochromatic field.
2. The longitudinal components of the Cartesian representation of the electric and magnetic fields satisfy the same scalar wave equation.

11.4.2.3 Circular Symmetry

The longitudinal component of the electric field $E_z(r, \phi)$ is separable into the product of a radial dependent function $R_{\nu\mu}(r)$ and the angle dependent term $\Phi_\nu(\phi)$.

1. Bound modes supported by the longitudinally invariant and circular symmetric fiber can be represented in the following separated form:

$$\psi_{\nu\mu}(r, \phi) = R_{\nu\mu}(r) \begin{bmatrix} \cos(\nu\phi) \\ \sin(\nu\phi) \end{bmatrix} \tag{11.5}$$

2. The index ν takes the meaning of the azimuth mode number and represents the number of amplitude fluctuations of the field component versus a complete rotation around the fiber axis.
3. The index μ takes the meaning of the radial mode number and identifies the order of the eigenvalues equation solution needed for satisfying the core–cladding boundary condition. For clad power law profiles μ corresponds to the number of maxima in the radial direction.
4. According to Equation (11.5), the general solution for the angular function $\Phi_\nu(\phi)$ is a linear combination of sine and cosine terms of the argument $(\nu\phi)$.
5. The radial component $R_{\nu\mu}(r)$ in the cylindrical coordinate satisfies the following second-order differential equation:

$$\frac{\mathrm{d}^2 R_\nu(r)}{\mathrm{d}r^2} + \frac{1}{r}\frac{\mathrm{d}R_\nu(r)}{\mathrm{d}r} + \left[k^2 n(r)^2 - \beta^2 - \frac{\nu^2}{r^2}\right] R_\nu(r) = 0 \tag{11.6}$$

6. The general solution of the radial component for the clad power law refractive index profile is expressed in mathematical closed form in terms of the Laguerre–Gauss functions.

11.4.2.4 Weakly Guiding Approximation

Assuming that the relative height Δ of the refractive index between the center of the core and the uniform cladding is sufficiently small ($\Delta \sim 10^{-3}$), both electric and magnetic longitudinal components of the field are negligibly small compared with their respective transversal components. The electromagnetic field is almost linearly polarized in the transversal fiber cross-section (linearly polarized modes for a weakly guiding fiber approximation).

The solution of the boundary problem under a weakly guiding approximation leads to degenerate solutions. Degenerate individual fiber modes have the same propagation constant $\beta_{\nu\mu}$ (the eigensolution of the boundary condition problem). Those individual and degenerate modes can be collected within the same mode group. All fiber modes belonging to the same mode group propagate with the same group velocity and do not experience any relative delay differences. According to the ideal fiber model presented above, the modal solution constitutes a base set for the guided field.

11.4.3 Source Polarization and Offset Launch

Figure 11.8 shows the geometry of the offset launch with an arbitrary linear polarization. The following statements seem to find consensus and experimental support at the actual status of the theory development:

1. At the launching section, the polarization of the excited fiber modes (i.e. the direction of the electric field of each excited fiber mode) is the same as that of the exciting light source. In other words, the electric dipole oscillation in the glass composition follows the same direction of the laser source field. This assumption implies that the amorphous glass material constituting the optical fiber is linear and isotropic. More specifically, the symmetric tensor ε_{jk} of the dielectric polarization reduces to the scalar value ε and the polarization vector $\mathbf{P} = \varepsilon \mathbf{E}_s$ is simply proportional to the source electric field $\mathbf{E}_s$. In order to simplify the mathematical description, it is convenient to orient one coordinate axis, x or y, in the direction of the polarization of the input field.
2. Once one of the two coordinate axes x or y as been oriented along the input polarization direction, the offset launch condition leads to a specific amount of source power coupled into each individual bound mode. In other words, the coupled power is not equally partitioned among individual modes belonging to the same group.
3. The following is a key point: the excitation of each individual mode depends on the relative angle $\gamma = \xi - \vartheta$ between the offset direction and the input polarization (see Figure 11.8). Individual

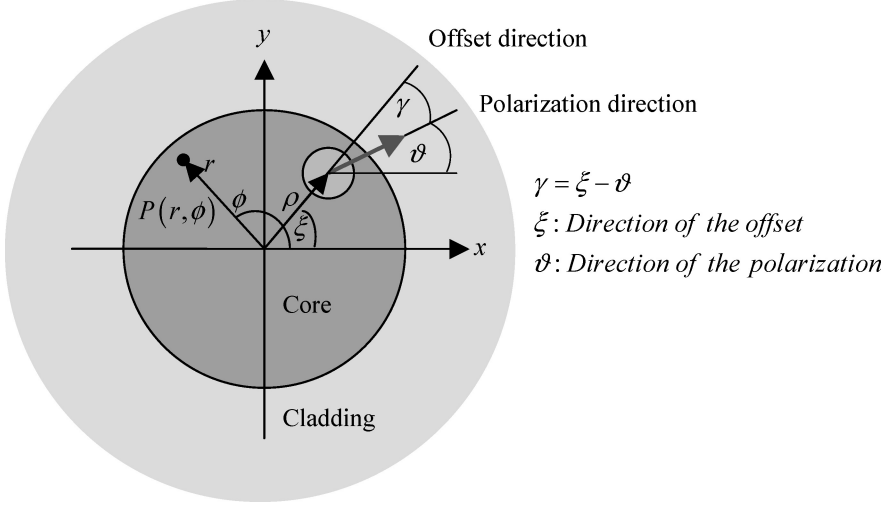

Figure 11.8 Geometrical representation of the launching section showing the laser light spot position (ρ, ξ) and the polarization orientation ϑ. The relative angle between the offset direction and the source polarization is given by the difference $\gamma = \xi - \vartheta$

modes bring a specific amount of source power, but the mode power MPD(k) supported by all the degenerate modes belonging to the same group k (same propagation constant β) is independent of the relative angle $\gamma = \xi - \vartheta$.

4. The mode power distribution MPD(k) of the excited mode groups is independent of the linear polarization of the input light source. The index k defines the mode group and it is assumed that any integer value within the mode group number N is supported by the fiber structure, $1 \leq k \leq N$.
5. Following the statements above, it is concluded that the impulse response of the unperturbed ideal multimode fiber with cylindrical symmetry is independent of the orientation of the linear input polarization.

   This is a consequence of the independence of the mode power distribution MPD(k) versus the source linear polarization. Since each mode group propagates with a characteristic group velocity, the optical impulse response at the fiber end section remains unaltered during the input polarization rotation.
6. The experienced pulse shape distortion due to polarization changes at the launching section seems to be addressed, due to the refractive index profile perturbations and to any other stress-induced birefringence that breaks the individual mode degeneracy. Each individual mode therefore contributes independently to the output pulse, without experiencing any further degeneracy. Since individual mode excitation is affected by the relative angle $\gamma = \xi - \vartheta$ between the offset direction and the input polarization, it can be concluded that under the perturbed condition, which breaks the mode degeneracy, the multimode fiber impulse response is dependent on the relative angle $\gamma = \xi - \vartheta$ between the offset direction and the input polarization.

11.4.4 Further Directions

Once the previous results concerning the ideal graded index fiber analysis is agreed, the only justification for the polarization-induced pulse distortion that results can be found in the discrepancy between the real fiber and the assumed ideal model. In the previous theory, individual modes can be grouped together into a single-mode group because they experience the degeneracy of the propagation constant. In other words, the eigenvalue equation for the boundary conditions leads to the same solution for different combinations of the mode indices.

Once the perturbed refractive index is introduced in the model due to profile perturbation and stressed induced birefringence, the degeneracy is suddenly broken and individual modes no longer belong to the same mode group. Stated differently, under perturbed conditions mode groups lose their identity and individual modes behave independently from each other, with their own propagation constant and propagation delay. Since individual mode groups have been demonstrated to be affected by the relative orientation of the input polarization for a given offset light spot, the impulse response results depend on the relative orientation of the input offset coordinate and the input polarization.

A clear picture of the effect can be seen if account is taken of the fact that in the ideal fiber individual modes belonging to the same group travel in different outer regions of the core. If the profile index is characterized by the same shaping coefficient, the delay of those individual modes will be perfectly compensated and the corresponding group behaves as the same identity. However, if the outer regions of the core are characterized by slight refractive index perturbations, the delay compensation within the same group lacks validity and individual modes split apart, each one with its own propagation constant. More important, it is assumed that the overlapping integral would not be affected at first by the perturbation of the refractive index, therefore leading to the same value of the coupled optical power as for the unperturbed mode group. However, once the perturbation breaks the propagation constant degeneracy, each individual mode will contribute to the output pulse composition at different time instants, leading to the dependence of the pulse response on the relative angle $\gamma = \xi - \vartheta$ between the offset direction and the input polarization.

11.5 Source and Receiver Characterization

In this section, some characterization measurements made on laser sources and the optical receiver used during all the multimode fiber measurement campaigns are reported. Either directly modulated or externally modulated DFB lasers have been used as reference light sources, emitting at 1310 nm. The reference optical receiver consisted of the linear transimpedance Amplifier (TIA) coupled with a high-speed PIN photodetector for multimode fiber detection. To this purpose, the diameter of the active area of the photodetector was 50 μm and the overall optical receiver bandwidth was approximately 8.5 GHz. The transmitter and the receiver responses are briefly presented according to their single-pulse response, eye diagram, PRBS data pattern and noise characteristics. All time domain measurements have been performed using the full bandwidth acquisition capabilities of the Agilent DCA (20 GHz optical and electrical bandwidths) with an external trigger connected to the pulse pattern generator synchronism signal output. Short single-mode and multimode fiber patch cords have been used during testing procedures for a total length less than 5 m in length. The optical fiber contribution to the measured transmitter and receiver performances can be fully neglected due to the very short length of the patch cords involved.

11.5.1 Optical Reference Transmitter

Figure 11.9 shows the response of the 1310 nm optical transmitter to the NRZ single pulse and to the corresponding NRZ-PRBS 2^{31}-1 eye diagram detected by the digital communication analyzer (sampling oscilloscope) equipped with a high-speed optical head. Both the detected optical single pulse and the eye diagram have been filtered internally to the DCA using the standard ITU-T STM-64 fourth-order Bessel–Thompson filter. The single-pulse response has been time-averaged (usually 128 averages per sample) in order to reduce considerably the effect of the additive noise in the measure acquisition.

Figure 11.10 shows the NRZ single-pulse response captured for the externally modulated TOSA under the same stimulus condition as above. Figure 11.11 reports a section of the PRBS 2^7-1 pattern used for generating the eye diagram. The selected pattern section corresponds to the digital sequence '... 1010101111111000000...'.

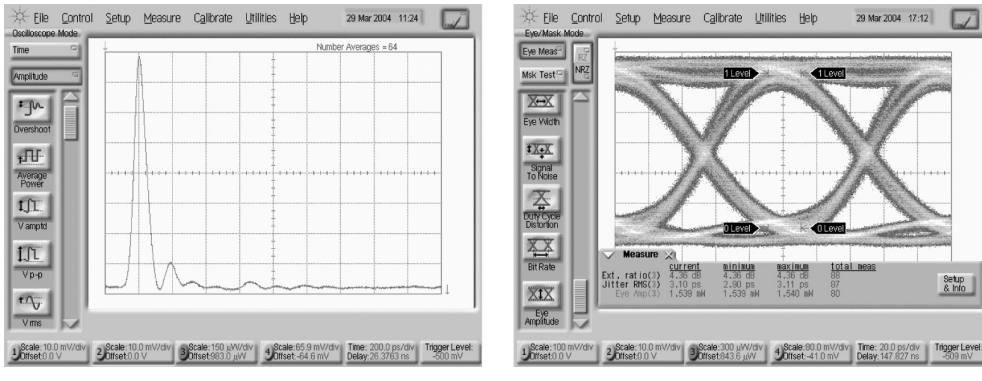

Figure 11.9 Examples of the modulated response of the TOSA used as the reference transmitter in the transmission experiments. The laser emits in the 1310 nm range and is directly modulated using an NRZ-PRBS 2^{31}-1 data pattern operating at $B = 10.3125$ Gbit/s. The eye diagram shows the extinction ratio ER $\cong$ 4.35 dB, RMS jitter $\sigma_j \cong 3.10$ ps and an optical modulation amplitude OMA $\cong$ 1.539 mW $\cong +1.87$ dBm. The small reflection detected in the time-averaged single-pulse response (postcursor) is due to electrical mismatch and is partially responsible for the intersymbol interference seen in the corresponding eye diagram

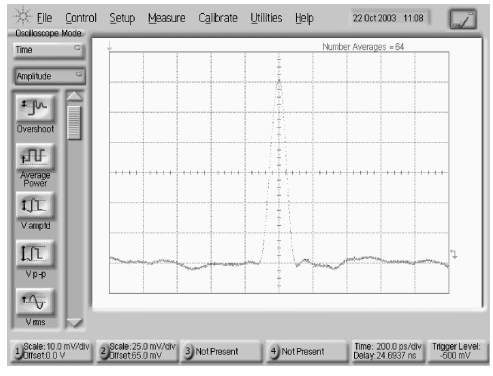

Figure 11.10 Modulated optical response of the TOSA used as the reference transmitter in the multimode fiber transmission measurements. The laser emits in the 1310 nm range and is externally modulated using the NRZ single pulse according to Section 11.3.8. The single-pulse response in this case does not exhibit any relevant reflections due to an electrical mismatch

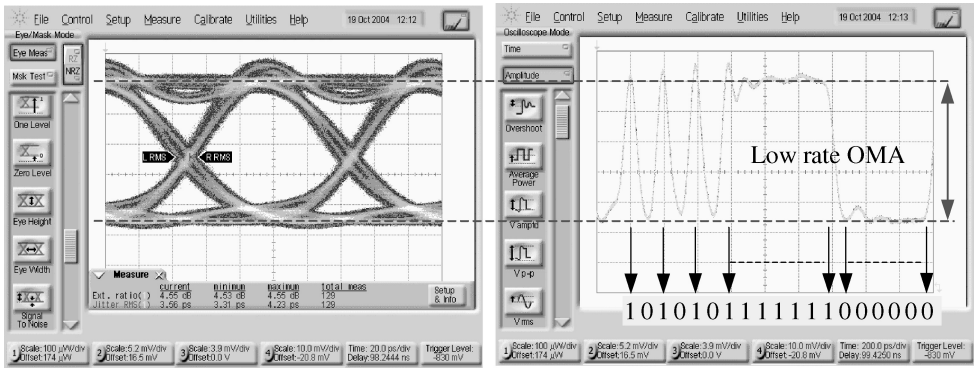

Figure 11.11 Unfiltered optical eye diagram (left) and corresponding time slot of the 2^7-1 PRBS data pattern of the DM-DFB laser after a 1 m single-mode patch cord. The laser biasing is adjusted for the extinction ratio ER ≅ 4.5 dB. Optical waveform symmetry can still be improved by decreasing the extinction ratio to about ER ≅ 3.5 dB by biasing the laser at a higher power level

11.5.1.1 Laser Pulse Pre-emphasis

According to experimental results, the best link performance using a relatively long multimode fiber and EDC does not correspond to the best-launched optical eye diagram. Due to fiber bandwidth impairments, an optical pulse pre-emphasis is quite beneficial for reducing the bit error rate after 200–300 m of legacy multimode fiber. In order to achieve laser pulse pre-emphasis it is convenient to bias the laser closer to the lasing threshold, making pulse generation more affected by relaxation oscillation and related overshoot. According to a random pattern, single bits are strongly influenced by this pre-emphasis approach due to their short duration. For the same reason, longer '1' bit sequences are qualitatively unaffected by the pre-emphasis. In that case, the overshoot influences only the pulse rising edge, which is only a short fraction of the overall pulse duration. The laser pre-emphasis is quite effective in achieving longer multimode fiber link distances. Figure 11.12 shows the eye diagram emitted from the same laser used in Figure 11.11 above, but biased closer to the lasing threshold in order to produce a relatively higher overshoot response. The effect of the

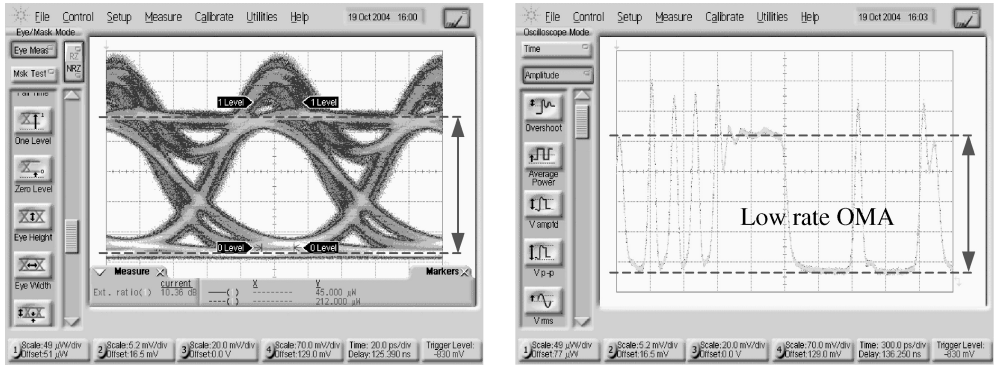

Figure 11.12 Unfiltered optical eye diagram (left) and corresponding time slot of the 2^7-1 PRBS data pattern (right) of the DM-DFB laser after a 1 m single-mode patch cord. The laser biasing is adjusted in order to exhibit relevant pulse pre-emphasis. The eye diagram has been measured with 3 dB attenuation with respect to the unbiased eye in Figure 11.11. The eye opening is therefore almost identical between the two biasing conditions. Due to the reduced laser biasing, the extinction ratio is increased up to ER $\cong$ 10.4 dB. Although low-rate OMA is almost the same as the unbiased laser condition, the strong overshoot achieved on each rising edge highly enhances single-pulse energy in order to facilitate pulse recognition, even after a severe bandwidth limitation due to the long-reach ($\sim$300 m) multimode fiber link

distorted single-pulse contributions to the overall eye diagram is evident. By lowering the value of the bias current, an increased value of the extinction ratio corresponds accordingly.

These pictures should be compared with the eye diagram and optical pattern presented above for the unbiased laser. It is evident that the overshot contribution enhances the single laser pulse. By comparing both measures, it is interesting to conclude that, although they present almost the same optical modulation amplitude evaluated at a low rate, the single-pulse overshoot is enhanced for the pre-emphasized case. This is the reason why better EDC restoration is achieved under severe bandwidth limitation.

The relevant conclusion is that although both patterns have almost the same OMA their behavior after a long multimode fiber reach is quite different, making the pre-emphasized laser much more suitable for improved link performances. In Figure 11.12 it is clear that the overshoot takes place on every rising edge of the laser transition, including the longest '1' sequence at the pattern beginning. The EDC action is mainly requested to reconstruct the smoothed and distorted single pulse by the fiber bandwidth limitation, and more specifically by the DMD characteristic. Laser pre-emphasis simplifies considerably the single-pulse recognition by adding more energy to it. Due to the nonlinear characteristic of the laser, the overshoot does not have an equivalent undershoot counterpart on the falling edge. The threshold region prevents a symmetrical rising–falling edge behavior. This is quite evident from the pattern shown in Figure 11.12.

11.5.2 Optical Reference Receiver

The optical signal generated from the modulated light source is coupled to the multimode fiber link by means of the standard offset launch patch cord, according to the measurement setup reported in Figure 11.1. In this section, the optical receiver characterization referring to the back-to-back configuration will be discussed. The input of the optical receiver is then connected to the laser source either through the offset launch patch cord or through the single-mode patch cord for comparison purposes. Before discussing signal response characteristics, the optical receiver noise measurements will be presented.

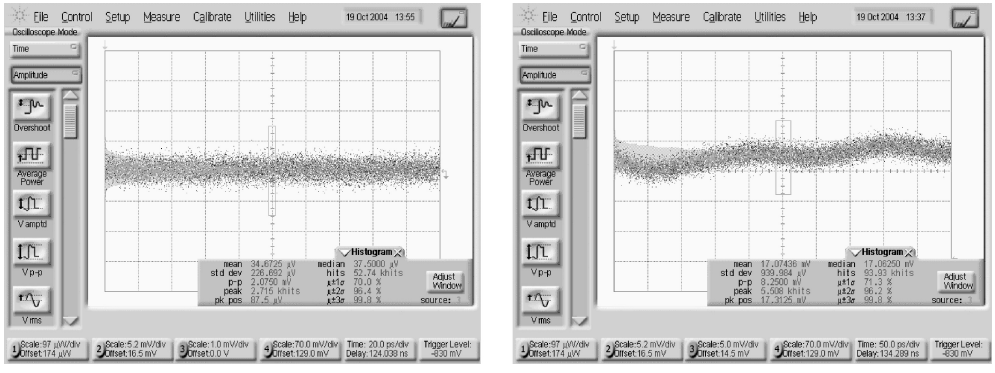

Figure 11.13 Background noise distribution of the DCA (left) and noise joint distribution of the optical receiver and DCA (right)

11.5.2.1 Noise Measurements

In order to evaluate the receiver thermal noise, Figure 11.13 shows the DCA background noise and the joint optical receiver and DCA noise statistics respectively. It can be seen that the DCA background RMS noise is given by $\sigma_{\mathrm{DCA}} \cong 227\,\mu\mathrm{V}$. The total noise is given by the sum of the contributions from the optical receiver and the DCA, $\sigma_{\mathrm{T}}^2 = \sigma_{\mathrm{DCA}}^2 + \sigma_{\mathrm{R}}^2 \cong 940\,\mu\mathrm{V}$. According to the measured noise parameters, the receiver single-ended output RMS noise is then given by $\sigma_{\mathrm{R}} = \sqrt{\sigma_{\mathrm{T}}^2 - \sigma_{\mathrm{DCA}}^2} \cong 912\,\mu\mathrm{V}$. Assuming uncorrelated noise on both outputs of the differential optical receiver, the differential output RMS noise becomes $\sigma_{\mathrm{D,out}} = \sigma_{\mathrm{R}}\sqrt{2} \cong 1.29\,\mathrm{mV}$. Once the differential RMS noise at the output of the optical receiver has been calculated, assuming Gaussian noise distribution, it is easy to estimate the differential output signal amplitude $V_{\mathrm{D,out}}$ needed to guarantee the required bit error rate. Setting $\mathrm{BER} = 10^{-12}$ with $Q \cong 7$, leads to $V_{\mathrm{D,out}} = Q\sigma_{\mathrm{D,out}} \cong 9\,\mathrm{mV}$. In conclusion, assuming only thermal noise from the receiver circuitry, the estimated receiver differential output signal swing corresponding to the sensitivity condition for having $\mathrm{BER} = 10^{-12}$ is $V_{\mathrm{D,out}} \cong 9\,\mathrm{mV}$. In order to make a negligible contribution to the optical sensitivity from the input stage of the EDC chip, it is necessary to set the EDC differential sensitivity to a value sufficiently lower than the estimated receiver differential output swing under the thermal noise sensitivity condition, namely this should require $V_{\mathrm{EDC,sens}} \ll V_{\mathrm{D,out}} \cong 9\,\mathrm{mV}$.

11.5.2.2 Signal Measurements

The signal response characterization of the optical receiver proceeds with the measurements of the optical pulse response and the corresponding eye diagram. Figure 11.14 reports the measured response at the electrical output of the reference receiver when the optical input is applied to the laser pulse, as shown in Figure 11.9. In order to compare the propagation characteristic of the standard offset launch patch cord with the single-mode patch cord, Figure 11.14 presents the optical receiver response according to both interconnections with the same laser source. It is clear that the short length of the standard offset launch patch cord does not affect the optical pulse propagation.

The weak filtering of the receiver bandwidth is evident when comparing both eye diagrams shown in Figure 11.15, which correspond to the single-mode launch patch cord (left) and the standard offset launch patch cord (right), with the transmitted eye diagram reported in Figure 11.9 shown in the right picture.

In order to document the differential output performances, Figure 11.16 shows the eye diagrams captured on both differential outputs of the optical receiver using the same optical input

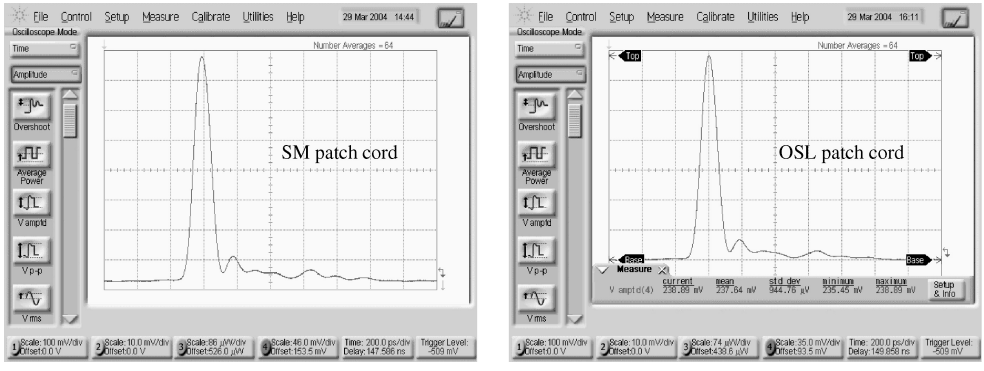

Figure 11.14 Measured pulse responses of the optical receiver assuming (left) the single-mode (SM) launch patch cord and (right) the standard offset launch patch cord. The oscilloscope time base has been set to 200 ps/div. Comparing with the laser pulse shown in Figure 11.9 it is evident that the weak filtering is performed by the receiver observing the smoothed ringing on the received pulse postcursors with respect to the sharpest ones on the launched pulse

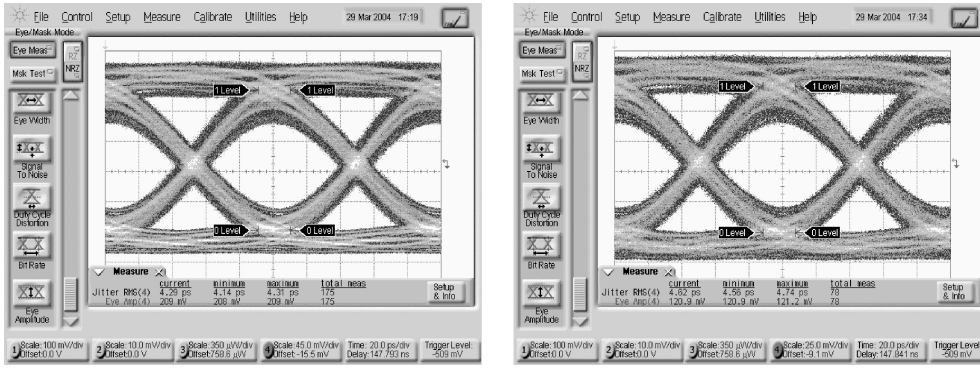

Figure 11.15 Measured eye diagram of the optical receiver assuming (left) the single-mode launch patch cord and (right) the standard offset launch patch cord. The oscilloscope time base has been set to 20 ps/div. Comparing with the eye diagram generated by the laser source shown in Figure 11.9 it is evident that the increased intersymbol is generated by the weak filtering performed by the receiver response. Both eye diagrams look very similar, confirming the negligible differences in term of propagation characteristics using either single-mode launch or standard offset launch patch cords

signal through the offset launch patch cord as given in Figure 11.15 above. The slight asymmetry observed between the two outputs might be due to either ceramic layout discrepancies or the IC amplifier itself.

Before closing this section, Figure 11.17 shows the reference eye diagram evaluated at the receiver output during the second set of measures performed in November 2003. This eye diagram will be used later for the calculation of the optical power penalty by comparison with the corresponding responses of the Siecor benchmark multimode fiber of several link lengths.

The optical transmitter and receiver characterizations briefly reported serve as a reference for comparing the following multimode fiber propagation behavior. The approach is systematic but still qualitative, with the intent of giving clear examples of the multimode fiber transmission capabilities

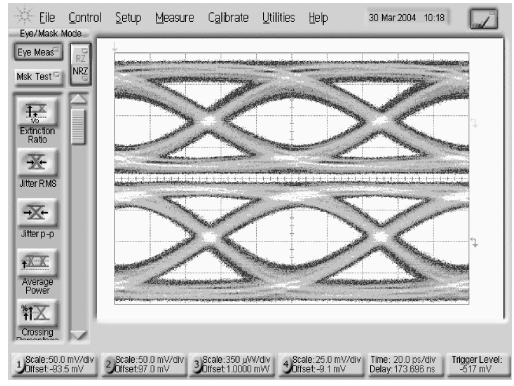

Figure 11.16 Eye diagram measured at the optical receiver differential outputs using the standard offset launch patch cord and assuming the same optical stimulus as above

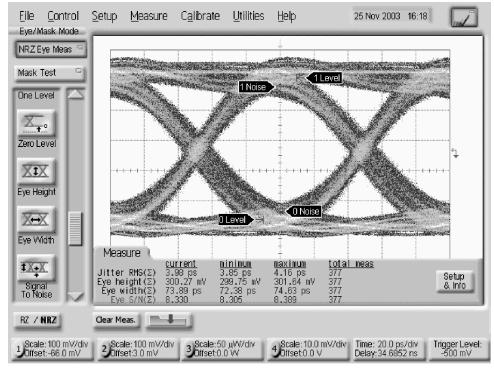

Figure 11.17 Measure of the eye diagram detected at the output of the reference optical receiver in the back-to-back configuration through a standard offset launch patch cord. This eye diagram serves as a reference for the optical power penalty computation in the second set of measures performed in November 2003. The acquisition date is displayed on the top-right corner of the screen-shot

at multigigabit data rates. A complete optical system characterization would of course be beyond the scope of this book, which relies instead on specific laboratory technical characterization reports.

11.6 The Benchmark Multimode Fiber

In this section, the principal results achieved during propagation measurements on the samples of the Siecor 62.5 µm multimode fiber are presented using selected link structures shown in Figure 11.5. The next two sections, 11.7 and 11.8, introduce the simple legacy multimode fiber link electrical emulator and the first measurements devoted to discover the polarization role in the multimode fiber impulse propagation under offset launch and semiconductor laser excitation. As already mentioned earlier, this particular multimode fiber sample offers the interesting opportunity of behaving like a legacy multimode fiber of the installed base, with almost the minimum bandwidth requirement in order to comply with the IEEE 10GbE standards. To this purpose, this fiber has been identified as the benchmark multimode fiber for 10GBASE-LRM transmission experiments. Several measurements have been performed during 2003–2005, leading to a relevant amount of recorded

data. In this section, a selection of those measurements will be presented, with particular attention to highlighting mainly the most interesting and peculiar propagation behavior observed during the laboratory measurements of the benchmark fiber. In this section, two different measurements are given of the same Siecor benchmark multimode fiber samples, but performed during two different periods. The responses look different, as expected, since the laboratory conditions, fiber layout and connector distributions were not exactly the same. The first data reported refer to the measurements performed in March 2004 while the second set was recorded in November 2003. The consistency of the pulse responses and corresponding eye diagrams can be verified by looking at the measurement date printed on each top-right corner of the screen-shots.

11.6.1 Single-Pulse Responses

During the measurements, several precautions have been kept in order to minimize every mechanical and thermal stress of the fiber layout, including the optical connectors. The launching pad has been kept fixed as much as possible in order to avoid exchanging the launching fiber link section if not strictly necessary for achieving the specific multimode fiber layout. The single-pulse pattern follows the scheme suggested in Section 11.3.8 and each measure has been conveniently averaged for background noise reduction. Of course, the same averaging process would not be allowed in eye diagram measurements, which is the reason why many more noisy eye diagrams have been detected than the acquired single pulse. Every optical and electrical parameter has been maintained among the six reported pulse responses and the corresponding eye diagrams, except for the time-averaging and selected output datastream of the pulse pattern generator.

11.6.1.1 First Set of Measures (March 2004)

The next three figures, 11.18, 11.19 and 11.20, report the pulse responses of selected link lengths of the Siecor benchmark fiber. The fiber response follows the layout reference shown in Figure 11.5, with a 50 m link length step between any two subsequent measures. The first two screen-shots in Figure 11.18 refer to 50 m and 100 m multimode link lengths respectively. The time base is 200 ps/div and is the same set for the reference pulse shown in Figure 11.15 with the offset launch patch cord. The pulse broadening, or more generally the pulse distortion, is not yet evident. It should be noted, however, that legacy multimode fibers exhibiting a perturbed refractive index profile, when excited by the semiconductor laser light spot rarely exhibit repetitive behavior, leading to controversial pulse responses that depend on launching conditions and fiber layout in the testing area. It is well known to skilled technicians that slight manipulations of the fiber layout on the testing bench leads to an unexpected pulse response. This is mainly due to the connector offsets present along the link, which by exchanging launched power distribution provide different mode excitations. For every fixed data rate, the effect of the DMD manifests itself after a minimum link length. This is easily to explain in terms of the differential delay accumulated along the pulse propagation relative to the duration of the launched pulse. The critical link length starts approximately after 150 m for legacy multimode fibers operating at 10GbE. It should be noted that the IEEE802.3 standard 10GBASE-SR, operating at 850 nm with a minimum modal bandwidth of 500 MHz km, prescribes a maximum achievable link length of only 82 m without requiring any pulse compensation technique. In conclusion, legacy multimode fibers with the minimum modal bandwidth of 500 MHz km at 1310 nm can be used to achieve link lengths below 100 m using laser sources, but every required link length extension might incur serious pulse degradation and link loss conditions.

The pulse sequence reported above is quite satisfactory, leading to a good multimode fiber link performance. However, the same fiber samples, either using a different layout, exchanging the position of the link sections or using different optical connectors to assemble the link, could lead to very different pulse responses and transmission behavior. It is known that the multimode fiber

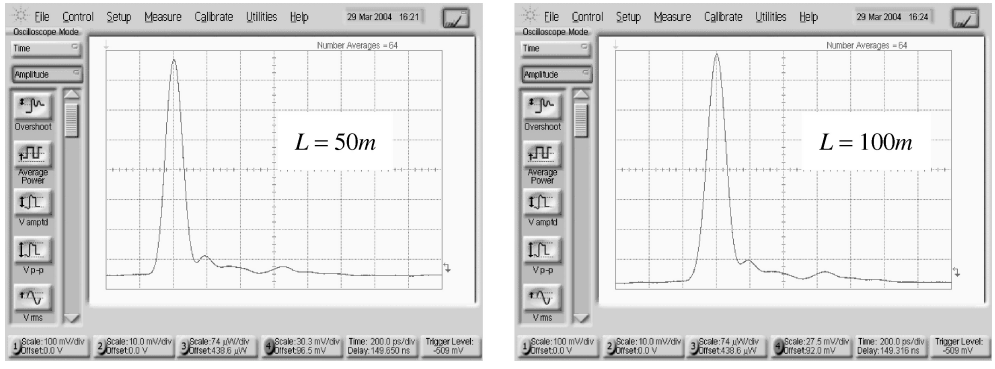

Figure 11.18 Measured pulse response of the Siecor benchmark multimode fiber with a 62.5 μm nominal core diameter operating in the 1310 nm wavelength range. The left screen-shot refers to the link length of 50 m, while the right screen-shot shows the pulse response after 100 m. It is noted that although the timescale is fixed at 200 ps/div for both measures, the vertical scale is adjusted individually for a full-range representation. Pulse distortion is almost negligible for both cases

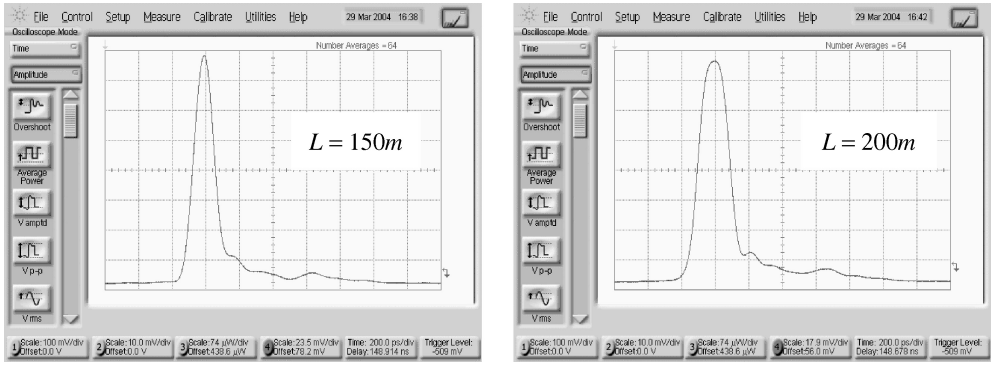

Figure 11.19 Measured pulse response of the Siecor benchmark multimode fiber with a 62.5 μm nominal core diameter operating in the 1310 nm wavelength range. The left screen-shot refers to the link length of 150 m, while the right screen-shot shows the pulse response after 200 m. It is noted that although the timescale is fixed at 200 ps/div for both measures, the vertical scale is adjusted individually for a full-range representation. Pulse distortion is evident in both measured pulses, with strong broadening in the 200 m case

response under laser light excitation is not a peculiarity of the fiber itself. It is for these reasons that the adaptability of the electronic dispersion compensator is a fundamental requirement for service deployment of multimode fiber link operating at the multigigabit data rate.

Figure 11.19 presents the two screen-shots relative to the 150 m and 200 m link lengths, still using the same time base. The distortion of the detected pulse after 200 m is evident, reaching the full-width at half-maximum at more than twice the bit rate. The large eye diagram closure is expected due to strong intersymbol interference, as discussed later. However, despite doubling the width, the pulse still has clear symmetry, without either precursors or postcursors.

Figure 11.20 shows the last two screen-shots relative to the last two fiber samples added. It is interesting to see how the 250 m link length seems to have recovered some of the initial pulse profile, showing slightly better energy confinement than the previous case of the 200 m link length.

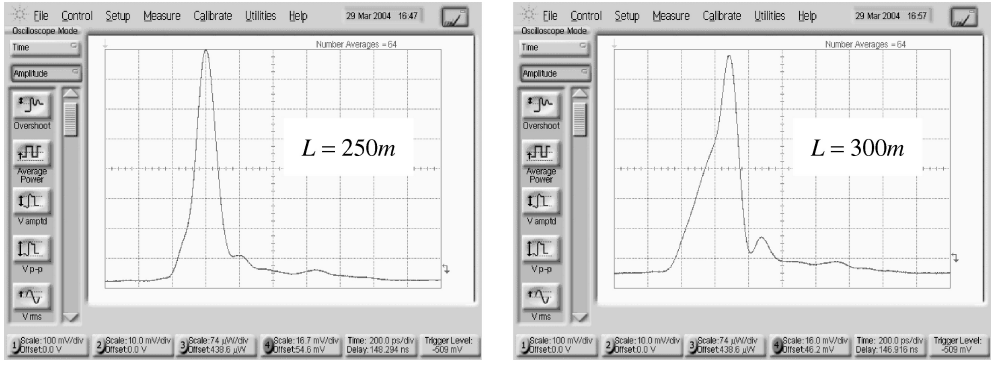

Figure 11.20 Measured pulse response of the Siecor benchmark multimode fiber with a 62.5 µm nominal core diameter operating in the 1310 nm wavelength range. The left screen-shot refers to the link length of 250 m, while the right screen-shot shows the pulse response after 300 m. The vertical scale is adjusted individually for full-range representation. Pulse distortion dramatically increases during the last 50 m of the link length. The pulse response detected after 300 m exhibits a triangular leading edge due to the relevant precursor contribution

This is part of the behavior of the multimode fiber response: the additional 50 m can accidentally lead to mode power redistribution due to the optical connector offset with a slight improvement in pulse confinement. The pulse response corresponding to the longest fiber link of 300 m, shown to the right of Figure 11.20, manifests a consistent precursor contribution, leading to a total full-width at half-maximum exceeding three times the bit duration.

11.6.1.2 Second Set of Measures (November 2003)

This second set of measures refers to the same samples of Siecor benchmark fiber, assembled according to the layout given in Figure 11.5. It is important to show these measurements together with the previous ones, in order to highlight the different responses available from the same fiber sample still operating in the same experimental setup. Figure 11.21 presents the optical receiver pulse response assuming the reference back-to-back conditions. The optical receiver input is connected directly to the optical transmitter output by means of the standard offset launch patch cord.

The pulse width measured at full-width at half-maximum Δ_t has been measured for each of the following pulse acquisitions in order to compare the pulse broadening along the multimode fiber propagation with the 50 m link length step. The reference pulse measured at the optical receiver output gives $\Delta_t = 116$ ps, revealing approximately a 20 % pulse broadening with respect to the signaling time step $T = 1/B = 1/10.3125$ GHz $\cong 96.970$ ps.

Figures 11.22 and 11.23 show the pulse responses measured after 50 m, 100 m, 150 m and 200 m of the multimode fiber link length, assuming the same configuration used in Figure 11.17. The different timescale of 100 ps/div used for the oscilloscope acquisition is noted, leading to a higher resolution of the captured sample.

The pulse response measures reveal a uniform optical pulse broadening along with the propagation length. The effect of the modal bandwidth roll-off cuts out tail ringing and other higher frequency transient responses, leading to a smoother, almost symmetric and Gaussian-like pulse response. This behavior is important and is quite common for different benchmark multimode fibers. Until the propagation distance remains below approximately 200 m, the DMD exhibited by legacy multimode fibers leads to a pulse response that measures below 200 m from the launching pad, is almost symmetric, with the characteristic bell-shaped profile, and fits the Gaussian model well. At increasing distance, the DMD leads to more consistent multipeak pulse responses, where the contributions

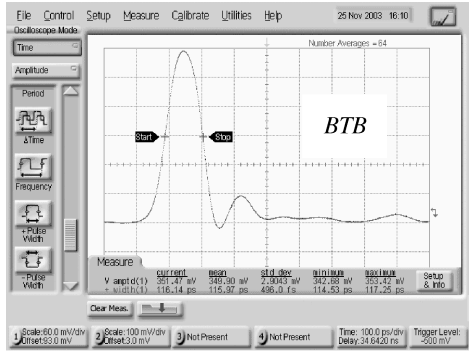

Figure 11.21 Measured pulse response of the optical receiver in the back-to-back configuration with the standard offset launch patch cord. The time base is set to 100 ps/div. The average pulse width measured at half-width at half-maximum is 116 ps, revealing the slight bandwidth limitation of the reference receiver. The small bump of the right side of the pulse (postcursor) is present even in the pulse emitted from the laser source, as reported in the left side screen-shot in Figure 11.9

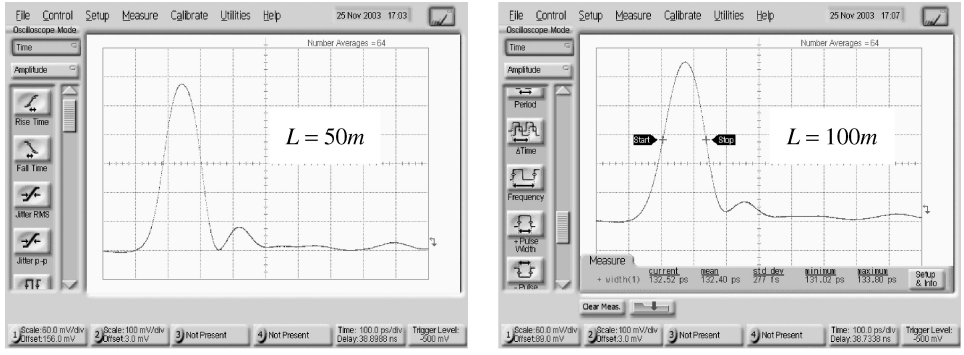

Figure 11.22 Pulse responses of the optical receiver measured after 50 m (left) and 100 m (right) of the Siecor benchmark multimode fiber. The average pulse width measured at half-width at half-maximum is 131 ps for the 100 m link length

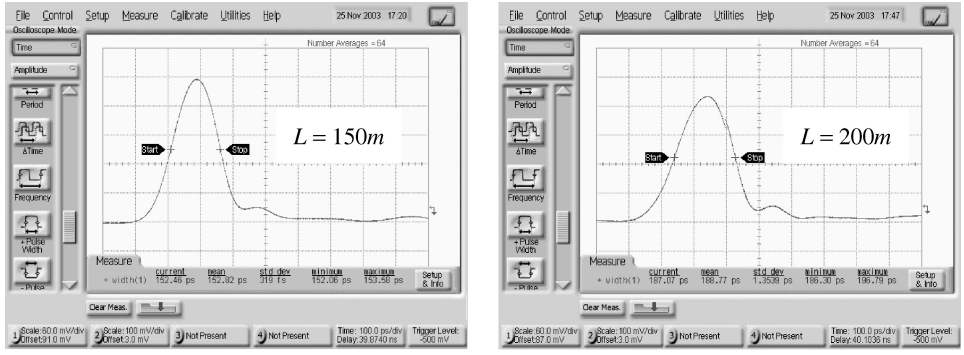

Figure 11.23 Pulse responses of the optical receiver measured after 150 m (left) and 200 m (right) of the Siecor benchmark multimode fiber. The average half-width at half-maximum pulse widths are 152 ps for the 150 m link length and 186 ps in the case of the 200 m link length. Both pulse profiles have almost symmetrical Gaussian-like profiles, with a balanced distribution of precursors and postcursors

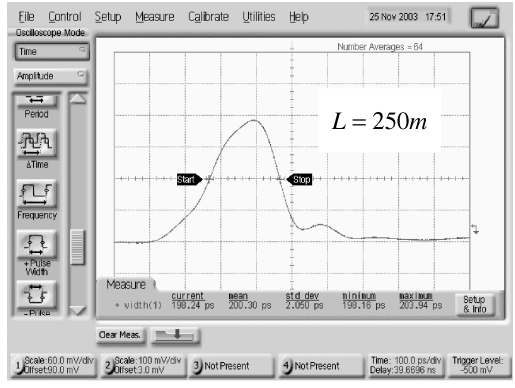

Figure 11.24 Pulse response of the optical receiver measured after 250 m of the Siecor benchmark multimode fiber. The average half-width at half-maximum pulse width is 200 ps. The pulse profile is losing the Gaussian-like shaping with more pronounced precursor terms

of both precursors and postcursors are quite evident. This is the case shown in the Figure 11.24 and refers to the 250 m link length. The pulse profile starts to lose the symmetric distribution and manifests a more consistent body structure, with a mainly precursor composition.

A further increase in the fiber length up to 300 m causes the link response to become much more unstable and sensitive to environmental conditions. A slight twist of the fiber gives a strong pulse deformation at the receiving section. An example of this peculiar response is presented in Figure 11.25, where the same multimode fiber link leads to different pulse responses as a consequence of the smooth fiber manipulation in the proximity of link connectors.

The pulse profile shown on the screen-shot to the right side in Figure 11.25 represents an interesting case of a balanced composition of postcursors and precursors, leading to the dual-bump pulse profile. In addition, this pulse represents a very difficult test for the electronic dispersion compensator running at 10 GbE because the distance between the two bumps is almost equal to the

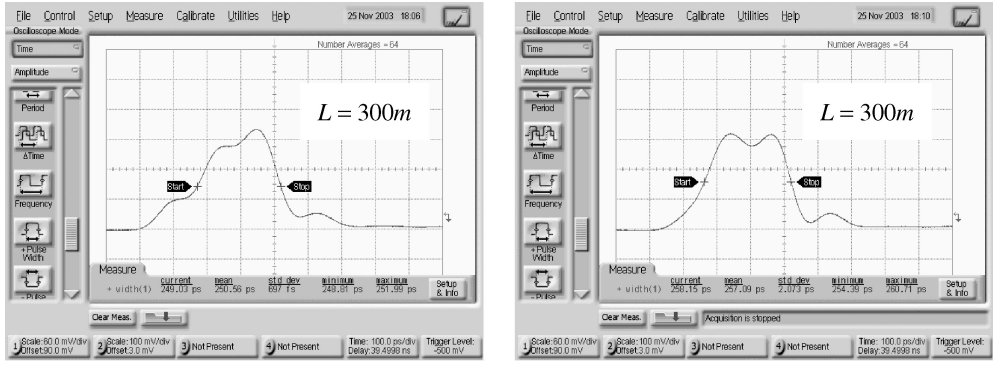

Figure 11.25 Pulse responses of the optical receiver measured after 300 m of the Siecor benchmark multimode fiber. Both pulses refer to the same experimental setup, with only a slight fiber twisting between them. The left pulse has the average full-width at half-maximum equal to 250 ps while the twisted fiber response on the right gives 257 ps. The interesting thing is not the small difference of the FWHM, but instead the different shape exhibited by the right pulse with an almost equal precursor and postcursor contribution, leading to the dual-bump pulse response

signaling time slot (approximately 100 ps). The feedback filter in the decision feedback equalizer acquires the postcursors at the clocked rate and sends them back to the sampler input for the interference cancellation, according to the principle shown in Figure 10.1 of Chapter 10. The dual-bump pulse determines the inherent ambiguity in the acquisition phase of the digital samples leading to an erroneous decision process.

These considerations close the section on the multimode fiber single-pulse response measurements. The next section presents the corresponding eye diagram measured using the same experimental setup used for the single-pulse acquisitions.

11.6.2 Eye Diagram Responses

In this section, the measured eye diagram corresponding to the single-pulse responses presented previously in Section 11.6.1.1 and 11.6.1.2 are given. While the single pulse was obtained after time averaging for the additive noise reduction, the eye diagram must be captured using a full bandwidth capability of the oscilloscope sampling head. Accordingly, in the representation of the measured eye diagram, the receiver noise has been integrated over a wide bandwidth, leading to a much noisier detected electrical signal than the single pulse acquisition using time averaging. This difference must be taken into account if the reader compares the computer-generated eye diagram using the measured single optical pulse response with the acquired eye diagram using instead the full bandwidth optical detection. A second issue concerns the implicit linearity assumption found every time the single-pulse response is used to build up the corresponding eye diagram using a computer algorithm.

In conclusion, the following two remarks are important if a correct understanding is to be gained of the relationship between the single-pulse response and the corresponding eye diagram measurement:

1. *Time averaging.* The single-pulse response has been subjected to time averaging and consequently to efficient noise reduction. The corresponding eye diagram is captured instead by using the full bandwidth sampling head acquisition, with relatively large noise bandwidth integration. This leads to a noisier eye diagram than the computer-generated one using the single-pulse response.
2. *Linearity.* The single-pulse response is used by the computer algorithm to generate the corresponding eye diagram. The algorithm simply shifts the pulse samples along the time coordinate by a finite number of integer time steps and then adds them together with the corresponding bit amplitude. Finally, the eye diagram is displayed in the required time window. During this operation, the implicit assumption of linearity is used: each time-shifted single-pulse response is multiplied by the bit amplitude and then summed together. What happens in reality is slightly different. The pattern generator supplies the long sequence of synchronized pulses weighted by the bit amplitude, which is represented as the linear superposition of impulse responses:

$$x(t) = \sum_{k=-\infty}^{+\infty} a_k s(t - kT) \tag{11.7}$$

The system composed of the laser source, the multimode fiber and the optical receiver responds to this input stimulus according to the transfer characteristic $L(\cdot)$, and the output signal $y(t)$ can be represented by the following generic transformation:

$$y(t) = L[x(t)] = L\left[\sum_{k=-\infty}^{+\infty} a_k s(t - kT)\right] \tag{11.8}$$

If the system is assumed to be linear, the transfer characteristic $L(\cdot)$ can be applied to each individual pulse stimulus $s(t)$ in order to obtain the single-pulse response $p(t) = L[s(t)]$. Then the individual pulse responses are summed:

$$y(t) = \sum_{k=-\infty}^{+\infty} a_k L[s(t - kT)] = \sum_{k=-\infty}^{+\infty} a_k p(t - kT) \tag{11.9}$$

11.6.2.1 First Set of Measures (March 2004)

Figures 11.26 and 11.27 present the corresponding eye diagrams captured from the pulse responses shown in Figures 11.18, 11.19 and 11.20. In particular, Figure 11.26 presents the eye diagrams generated by the pulse responses in Figures 11.18 and 11.19 for 50 m and 100 m link lengths respectively. Both screen-shots shown in Figure 11.27 refer instead to the same fiber link length of 150 m after a slight manipulation, but with a different redistribution of the same connected fiber link on the optical bench. The eye diagram on the left refers to the optical pulse in Figure 11.19, while the eye diagram on the right has been obtained after the same link manipulation. The corresponding pulse response was not recorded at that time. The reference eye diagram measured at the output of the optical receiver connected back-to-back to the optical transmitter using the standard offset launch patch cord has been given in Figure 11.15 on the right screen-shot. That eye diagram can be used to estimate the reference eye opening and therefore proceed to the calculation of the optical power penalty achieved at the several link lengths reported.

The optical power penalty induced by the increased link length of the multimode fiber can be estimated by measuring the eye diagram opening variation between two eye diagram measures. Referring to Figure 11.26 it can be concluded approximately that, in this case, the opening of the eye diagram measured after 100 m of link length is almost one-half of the eye diagram opening evaluated after 50 m of link length, leading to the optical power penalty of about $\Delta P \cong 3$ dB. Using the same approach for the eye diagram shown on the left screen-shot in Figure 11.27 should lead

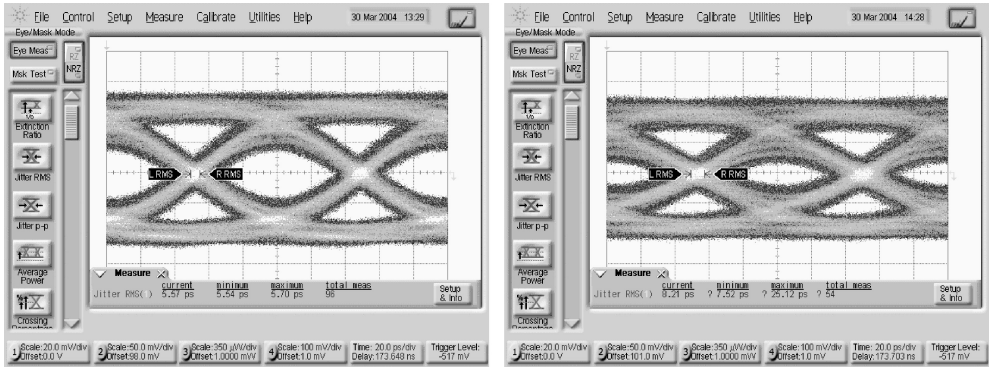

$L = 50m$ $L = 100m$

Figure 11.26 Measured eye diagrams of the Siecor benchmark multimode fiber with a 62.5 µm nominal core diameter operating in the 1310 nm wavelength range. The left screen-shot represents the eye diagram captured after 50 m of link length and corresponds to the pulse shown on the left screen-shot in Figure 11.18. The right screen-shot shows the eye diagram detected after 100 m of link length and corresponds to the pulse shown on the right screen-shot in Figure 11.18. It is evident that there is increased eye diagram closure when passing from 50 m to 100 m of link length, even if such differences are not easily appreciated when looking at the corresponding pulse responses in Figure 11.18

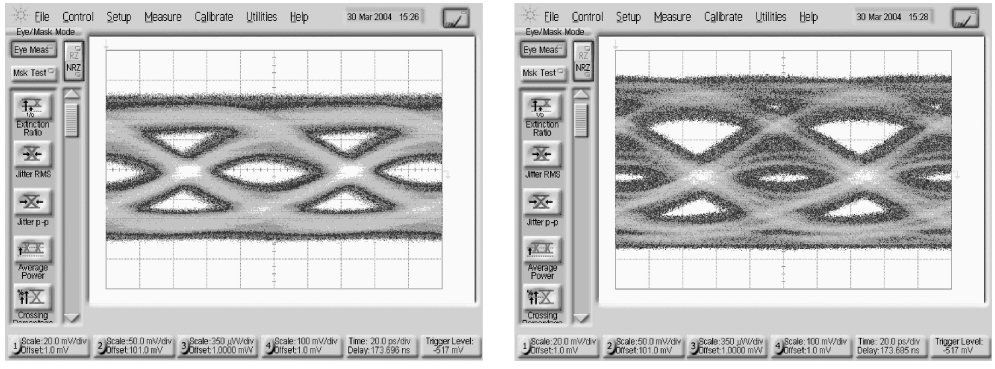

$L = 150m$ $L = 150m$

Figure 11.27 Measured eye diagrams of the Siecor benchmark multimode fiber with a 62.5 μm nominal core diameter operating in the 1310 nm wavelength range. The left screen-shot represents the eye diagram captured after 150 m of link length and corresponds to the pulse shown on the left screen-shot in Figure 11.19. The right screen-shot shows instead the eye diagram detected after the same link length of 150 m, but after slight fiber manipulation. The ordering of the fiber sections and connectors was the same as in the left case. It is evident that the increased eye-diagram closure between the two cases is due to increased pulse interferences

to the conclusion that there would be negligible degradation for the additional 50 m of link length when, moving from 100 m to 150 m. This is indeed the case when staying at the reported measures. Moreover, this conclusion is in agreement with the measured single pulse after 100 m and 150 m presented in Figures11.18 and 11.19 respectively. Both pulse responses look quite similar, if not almost identical, and it is expected that they generate almost identical eye diagrams. However, referring to Figure 11.27, using the same fiber layout, with only additional slight fiber twisting, produces the closer eye diagram shown on the right screen-shot, leading to an additional optical power penalty of $\Delta P = 4 \sim 5$ dB over the value estimated after 100 m.

11.6.2.2 Second Set of Measures (November 2003)

The following eye-diagrams presented in Figure 11.28 refer to the second set of multimode fiber characterizations performed in November 2003 at Infineon Fiber Optic Laboratory, Berlin. They have been measured using the same experimental setup that was configured for the determination of the single-pulse responses shown in Figures 11.22 to 11.25. In this case the eye diagrams have been recorded for every 50 m step, leading to one-to-one correspondence with the single-pulse response.

The eye diagram evaluated after 100 m of Siecor benchmark fiber presents about 2.1 dB of eye closure with respect to the measure detected after 50 m of link length, and the eye diagram evaluated after 150 m shows about an additional 4.3 dB closure with respect to the eye opening measured after 100 m. In total, the measured eye diagram closure between 50 m and 150 m of link length reaches about 6.4 dB. In order to compute the optical power penalty of the total link length, each eye diagram closure must be referred to the reference eye diagram evaluated at the optical receiver output connected back-to-back to the optical transmitter through the standard offset launch patch cord and shown in Figure 11.17. The eye diagram evaluated after 50 m of link length exhibits about 0.3 dB of optical power penalty with respect to the reference conditions, leading to a total optical power penalty of about 6.7 dB, reached after 150 m of link length. Increasing the link length further, the eye diagram looks completely closed and the concept of eye closure loses its meaning.

These measurements support the common conclusion that uncompensated multimode fiber link can be extended below 150 m in order to expect some residual eye diagram opening still sufficient

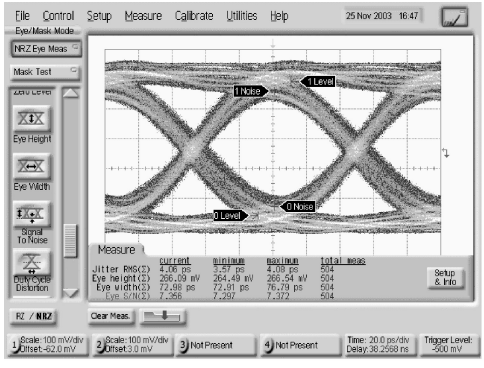

$L = 50m$

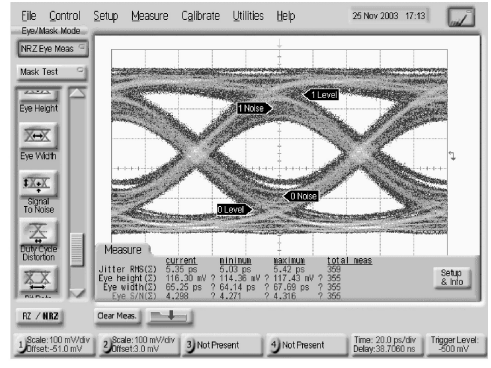

$L = 100m$

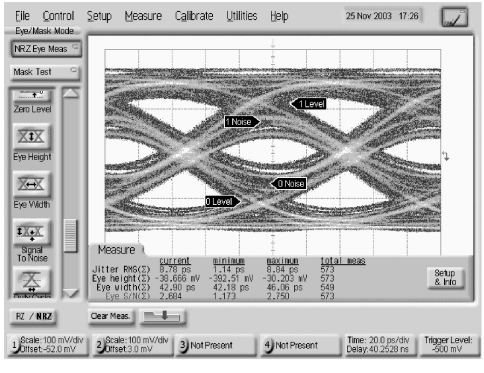

$L = 150m$

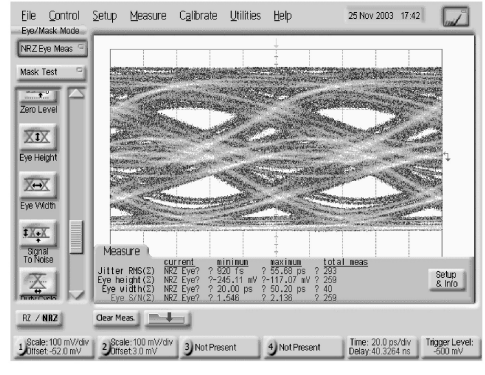

$L = 200m$

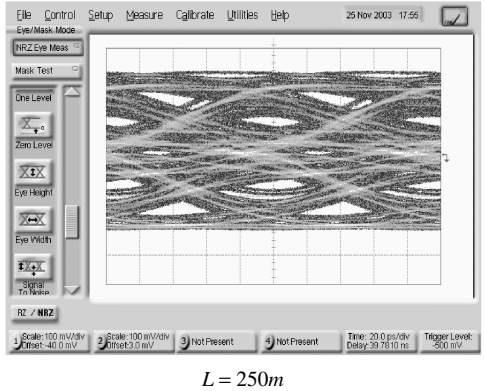

$L = 250m$

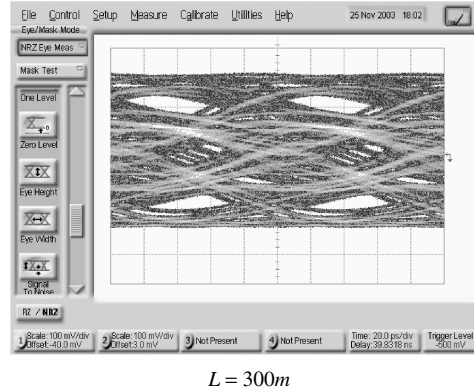

$L = 300m$

Figure 11.28 Eye diagrams measured at the output of the optical receiver after the Siecor benchmark multimode fiber with a 62.5 μm nominal core diameter operating in the 1310 nm wavelength range. The measures refer to the same transmission setup used for single-pulse acquisitions shown in Figures 11.22 to 11.25. These measures clearly report the progressive eye diagram closure as the multimode fiber link approaches 200 m. Between the link lengths of 150 m and 200 m the eye diagram closes completely, leaving an almost unrecognizable signal pattern in correspondence with the longer link length

for signal detection. However, account must be taken of the great variability of every multimode experimental setup designed to work at 10 GbE. The present two measurements, referred to as November 2003 and March 2004, are a clear example of this variability of the achievable performances. The November 2003 measurements gave better eye diagrams at the same link lengths with respect to the March 2004 ones. There might be several reasons for this, including the peculiar fiber layout, the launch polarization, the connectors and the adapter leading to different offset combinations, the electrical receiver calibration and the laser biasing conditions. For these reasons, the IEEE 802.3 10GBASE-SR recommends using uncompensated multimode fibers up to a maximum link length of 82 m, accepting a dispersion optical power penalty contribution of about 3.5 dB.

11.7 A Simple Optical Link Emulator

In this section, the application of the standard OC-48 or equivalently STM-16, fourth-order Bessel–Thompson electrical filter is introduced as the simple tool for emulating the expected response of legacy multimode fiber after approximately 200 m of link length. The measurement setup therefore includes the electrical OC-48 standard filter inserted between the pulse pattern generator and the electrical input of the optical transmitter. The transmitter bias is set according to the required condition for the fiber link testing (extinction ratio, pre-emphasis, eye symmetry, etc.). The 10 GbE NRZ-PRBS signal pattern is first filtered through the OC-48 filter with a -3 dB cut-off frequency set at $f_c = \frac{3}{4}B = 1.866$ GHz and then feeds the laser driver or the external modulator driver, according to the required modulation technique.

The result is a strongly band-limited optical signal clocked at the bit rate frequency, closely resembling the optical signal measured at an output of 200 m of link length of legacy multimode fiber excited by laser light through the standard offset launch patch cord.

11.7.1 Modeling Approach

The optical signal available at the output connector of the standard Offset Launch patch cord is used to emulate the broadened pulse shape response after approximately 200 m of link length of a legacy multimode fiber with the modal bandwidth BW = 500 MHz km. As extensively analyzed in Chapter 8, the impulse response of the fourth-order Bessel–Thompson filter is characterized by a single body, slightly asymmetric with a low-ringing postcursor tail. Assuming direct modulation, after passing through the nonlinear laser characteristic, the corresponding output optical pulse looks more symmetric, with a pronounced single body and negligible ringing tail postcursors. This pulse closely resembles the Gaussian profile. Unfortunately the multimode fiber response to a laser light stimulus is scarcely solved using only the Gaussian-like pulse response. This is mainly due to a very different DMD-induced pulse broadening, which can result from different launching conditions, refractive index profile perturbations and a stressful environment. Nevertheless, the OC-48 filtered optical link emulator provides results that are very stable and suitable for preliminary testing conditions for EDC characterization.

The following five statements summarize the advantages of this simple legacy multimode link emulator:

1. The high repeatability of the output response is due to electrical implementation of the standard OC-48 filter.
2. The frequency response of the OC-48 fourth-order Bessel–Thompson filter represents a suitable approximation to the Gaussian frequency response up to at least twice the cut-off frequency.
3. High-frequency optical interface differences are smoothed by the low frequency content of the OC-48 filter, leading to very comparable results, even using different 10 GbE ROSA and TOSA pairs. The low-frequency cut-off of the OC-48 filter in fact reduces the plausible differences that can be measured in the high-frequency behavior of different 10 GbE ROSA and TOSA pairs.

4. Symmetric, smoothed and broadened pulses are among the most difficult to be recognized and restored by FFE-DFE based electronic dispersion compensator systems.
5. The modal bandwidth under over-filled launch (OFL) conditions can be easily scaled to the fiber length equivalent of the OC-48 fourth-order Bessel–Thompson cut-off frequency evaluated at half-maximum.

The $-3\,\mathrm{dB_e}$ cutoff frequency f_c of the OC-48 filter coincides with 75 % of the OC-48 bit rate, i.e. $f_c = 1.866\,\mathrm{GHz}$. Since the modal bandwidth of the multimode fiber is defined at half-maximum of the magnitude of the intensity transfer function, in order to find the length of multimode fiber that is equivalent to the OC-48 response, first the frequency f_0 corresponding to the half-maximum of the magnitude of the OC-48 filter response must be computed. The amplitude-normalized Gaussian profile $G_F(f)$ with half-width at half-maximum f_Δ is given by the following expression, where the relationship (3.115) between f_Δ and the standard deviation σ_f is used:

$$G_F(f) = \mathrm{e}^{-(f/f_\Delta)^2 \log 2} \tag{11.10}$$

Figure 11.29 shows the optical link emulator setup. In order to obtain consistent results, the optical transmitter and the receiver used for the emulation must be the same as those used for the real transmission measurements, including the multimode fiber link.

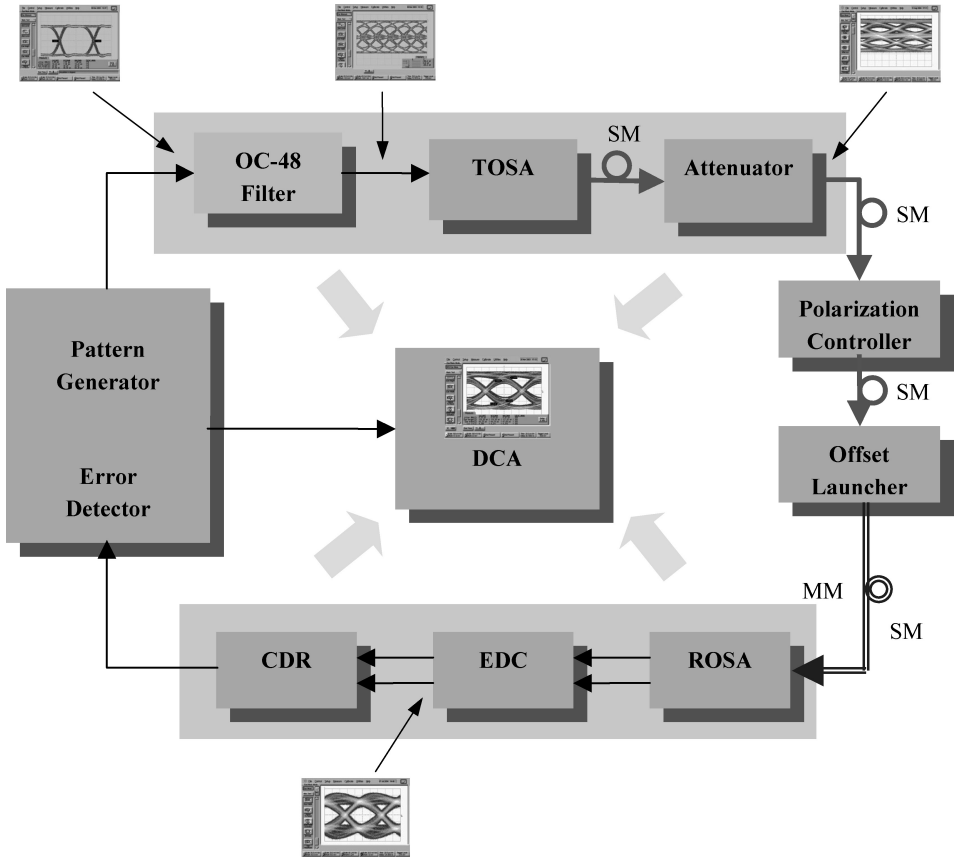

Figure 11.29 Measurement setup for the optical link emulator using the OC-48 filter to drive the optical transmitter. The insets show the expected eye diagrams according to the 10 GbE PRBS datastream

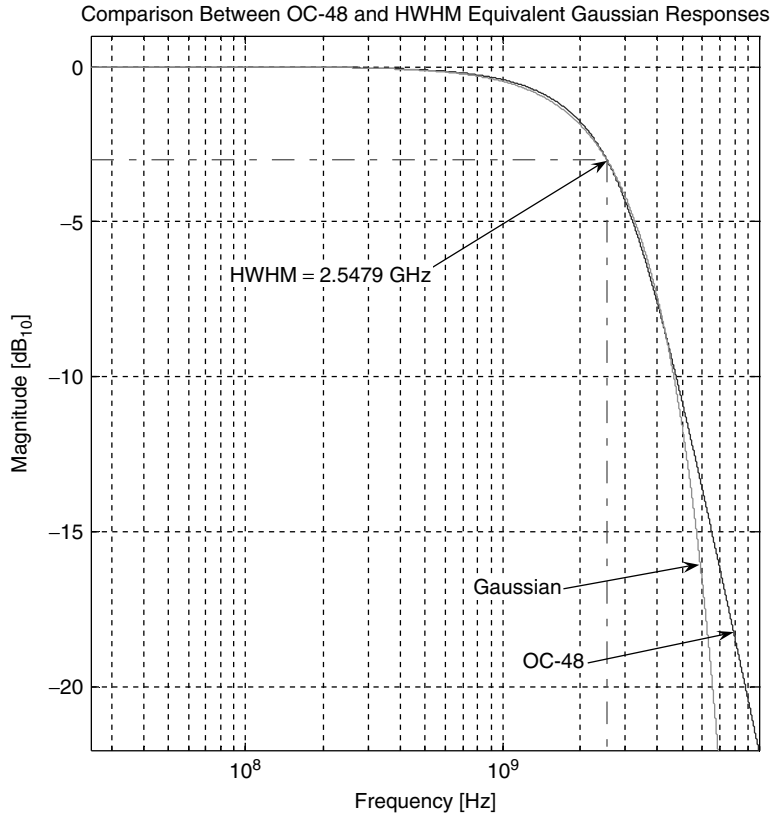

Figure 11.30 Computed magnitudes of the frequency transfer function of the OC-48 filter and of the corresponding Gaussian modal response with the same half-width at Half-maximum $f_\Delta = f_0 = 2.5479\,\text{GHz}$. The OC-48 filter fits the equivalent Gaussian response very well up to at least 13 dB, corresponding to one octave above the half-width at half-maximum frequency

The cut-off frequency of the OC-48 filter is set at $f_c = 1.866\,\text{GHz}$ and the numerical computation of the half-width at half-maximum gives $f_0 = 2.5479\,\text{GHz}$. Figure 11.30 shows the computed plots of the magnitudes of both the OC-48 filter and the corresponding Gaussian profile with the same half-width at half-maximum $f_\Delta = f_0 = 2.5479\,\text{GHz}$. If it is assumed that the multimode fiber has a Gaussian response with a modal bandwidth $\text{BW} = 500\,\text{MHz km}$, it can immediately be deduced that the link length equivalent L_{eq} of the OC-48 filter is

$$L_{\text{eq}} = \frac{\text{BW}}{f_\Delta} = \frac{500\,\text{MHz km}}{2547.9\,\text{MHz}} \cong 196\,\text{m} \tag{11.11}$$

In conclusion, the OC-48 filter is a suitable electrical emulation of a multimode fiber Gaussian response of link length $L_{\text{eq}} \cong 196\,\text{m}$.

Before closing this section, it is necessary to add one more comment about the application of the OC-48 filter as a multimode fiber link emulator. The laser diode and the electrical driver are not linear devices, as they are designed to operate with digital signals. In order to reproduce the electrical signal available at the OC-48 filter output on the optical domain, the electro-optical transducer (TOSA) should have a linear transfer characteristic. In addition, the optical signal obtained at

the transmitter output resembles closely the OC-48 datastream and, as shown in the following section, fits quite well with the real eye diagram measured at the output of multimode fiber after approximately 200 m of link length.

11.7.2 Measurement Report

Figure 11.31 presents the measured datastream of the OC-48 measurement setup, according to the block diagram shown in Figure 11.29. All signals refer to the 10 GbE clock signal with $f_{ck} = 10.3125$ GHz and an NRZ PRBS 2^{31}-1 datastream. The first picture on the top-left side refers to the signal at the output of the pattern generator. The signal then feeds the OC-48 filter whose output reports the eye diagram presented in the screen-shot to the top-right picture. The large intersymbol interference raises the characteristic pattern with the same periodicity of the clock source.

After being processed by the laser driver and the laser diode itself, the signal pattern is converted to the optical domain, passes through the offset launch patch cord, according to the block diagram

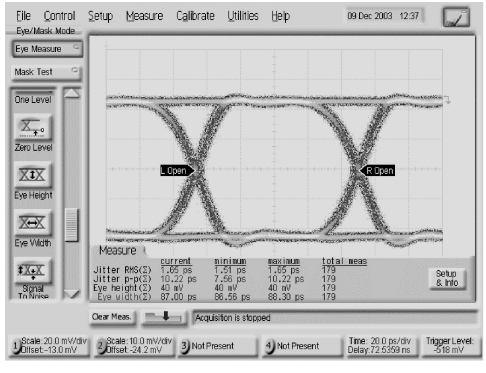

PPG output at 10GbE

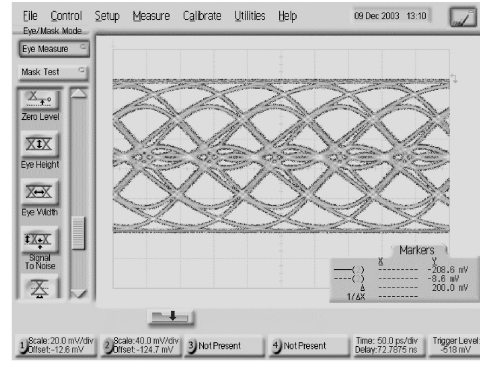

OC-48 electrical output

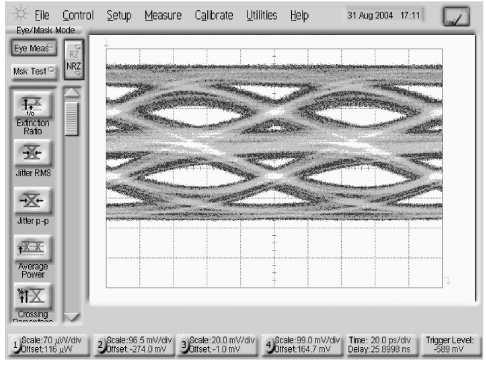

Optical Receiver output

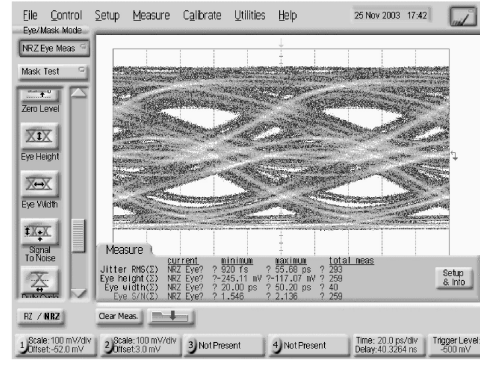

200m Siecor Benchmark Fiber

Figure 11.31 Measured eye diagrams at different sections of the OC-48 multimode fiber link emulator. The first screen-shot on the top-left side shows the 10 GbE eye diagram measured at the output of the pulse pattern generator. The screen-shot on top-right side refers to the OC-48 filtered eye diagram evaluated at the electrical filter output. The electrical cut-off frequency coincides with 75 % of the reference bit rate, i.e. $f_c = 1.866$ GHz. The bottom-left picture shows the measured eye diagram at the optical receiver output, while the bottom-right screen-shot shows the eye diagram measured after 200 m of Siecor benchmark multimode fiber. The similarity between the emulated eye diagram and the real one is noteworthy

in Figure 11.29, and after the optical receiver detection, it is down-converted back to the electrical domain. The screen-shot on the bottom-left side presents the eye diagram acquired at the optical receiver output. It is represented using the 20 ps/div timescale, leading to an eye period over about five horizontal divisions. The last picture on the bottom-right side reports instead the measurements of the Siecor multimode benchmark fiber after 200 m of link length, assuming the same measurement setup but without of course the OC-48 filter in front of the optical transmitter. The correspondence between the two eye diagrams on the bottom row is impressive, demonstrating the validity, at least in this case, of the OC-48 filter link emulation. Of course, the variability of the multimode fiber response can lead to different pulse shapes and eye diagrams, but the conclusion and the advantages of this simple multimode fiber link emulator still remains valid.

11.8 Polarization Measurements at 10 GbE

In the first part of this chapter the basic concepts behind the observed polarization effects in the optical pulse propagation along multimode fiber links operating at the multigigabit data rate have been briefly introduced. Those effects lead to the experimental evidence of the dependence of the optical pulse shape detected after relatively long multimode links on the launched polarization state for a given offset launch patch cord. It is noted that both the input polarization control and the offset launch patch cord must be simultaneously accounted for as both have a polarization-dependent pulse response in multimode fibers operating at the multigigabit data rate. Experimental evidence has shown that the input polarization orientation has no effect on the pulse propagation when the central launch is adopted. The conceptual justification of the polarization effects have already been discussed so no further details will be given. Instead, in this section the measurements performed on this phenomenon will be described and comments will be made on the interesting results obtained.

Figure 11.32 shows the experimental setup used to investigate the observed polarization-dependent pulse response in the multimode fiber link operating at multigigabit data rates. In order to highlight the polarization dependence of the propagating pulses, the procedure will follow with the measure of the eye diagram response corresponding to each orthogonal polarization state for every fixed link length. As a general procedure, for a fixed link length and offset launch patch cord, first the input linear polarization orientation leading to the best eye-diagram available at the optical receiver output will be determined. This condition identified as the input best polarization. Adjusting the polarization controller, the orthogonal polarization orientation is then set at the input optical section. The measured eye diagram was sensibly degraded with respect to the first set of the polarization state, according to the link length used; this behavior led to the definition of the input worst polarization condition. Figure 11.32 shows a sketch of the two launching polarization states. The eye diagrams have been measured at the output of the optical receiver corresponding to the best and the worst input polarization states for every 50 m increment of the link length.

In order to investigate further the relationship between the input polarization state and the radial offset launch position, a second measurement campaign has been performed using radial micro-manipulator adjustment of the launch coordinate directly on the fiber core instead of the fixed standard offset launch patch cord. In this case, of course, the launching single-mode fiber has been directly butt-coupled to the selected radial position on the launching multimode fiber core section using the micropositioning step controller. This procedure proved to be very useful in analyzing the radial uniformity of the refractive index profile. Scanning the radial coordinate from almost the center of the core toward the periphery, it would be possible to analyze the group delay compensation by measuring the transmitted pulse distortion and retrieving profile perturbations of the refractive index. The next section reports first the measurements using the standard offset launch patch cord.

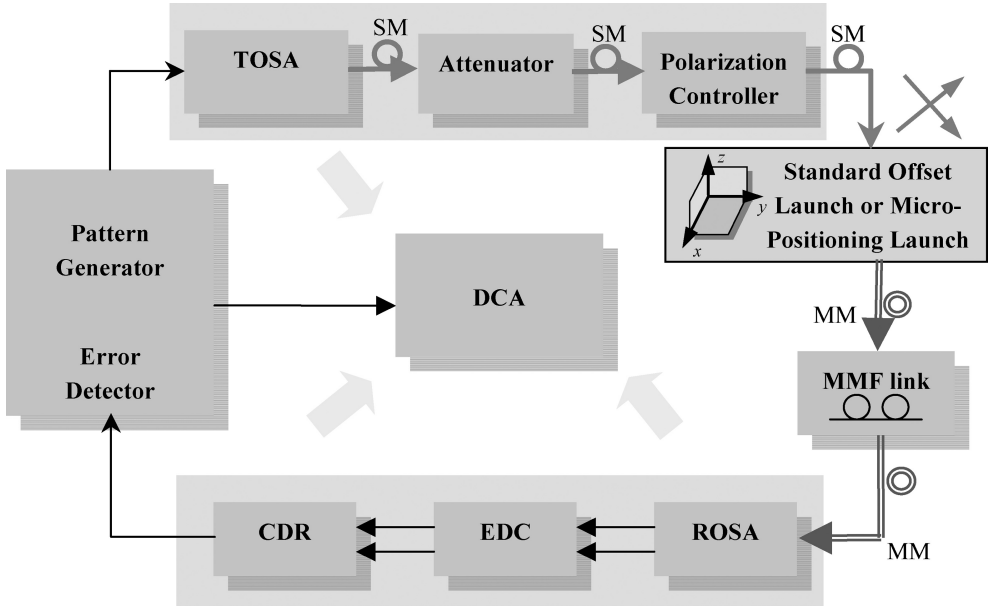

Figure 11.32 Block diagram representation of the measurement setup for the polarization-induced pulse distortion in the multimode fiber link operating at the multigigabit data rate. The polarization controller sets the two orthogonal polarizations, best and worst in the text, while the micromanipulator allows for precise radial offset launch coordinate settings

11.8.1 Standard Offset Launch

The following measurements refer to two different linear polarization states, each launched at the input section along different lengths of the same benchmark Siecor multimode fiber. It should be noted that, in order to isolate the effect of the input polarization from any other possible cause inducing pulse distortion, great attention has been paid during the experiment to modify only the linear input polarization, without changing any other parameter of the experimental setup. Of course, both the connector distribution and the fiber position on the optical bench are held to be fixed.

All of the following figures in this section report two pictures: the first one of the left side refers to the eye diagram associated with the input best polarization state, while the second one on the right side shows instead the eye diagram measured with the input orthogonal polarization state. It is evident from the measures below that by increasing the link length the polarization effect takes more and more relevance, leading to an almost closed eye diagram in correspondence with the input worst polarization when the link distance exceeds about 200 m. Figures 11.33 and 11.34 present the eye diagrams measured at the input section, after the standard offset launch patch cord and after 50 m of link length of the Siecor benchmark multimode fiber respectively. In both cases, the effect of the polarization change at the input section is not recognizable in terms of optical pulse distortion.

Figure 11.35 reports the measured eye diagrams after 100 m of link length according to the two orthogonal states of polarization. The effect on the output pulse shape is evident in this case, leading to about 2 dB of eye diagram closure in correspondence with the worst polarization state.

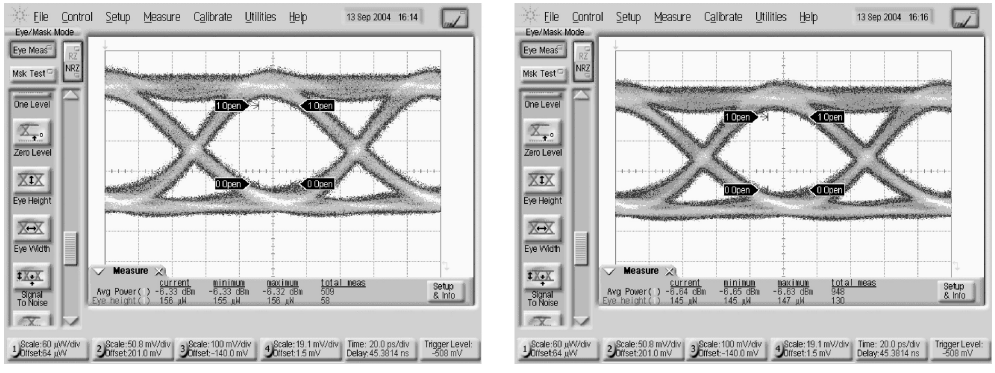

Reference: best polarization **Reference**: orthogonal polarization

Figure 11.33 Measured eye diagram at the launching pad (reference) assuming orthogonal polarization states. The left screen-shot shows the best eye diagram available versus the input polarization state and is referred to the best linear polarization. The screen-shot on the right presents the eye diagram captured using the orthogonal polarization (worst linear polarization)

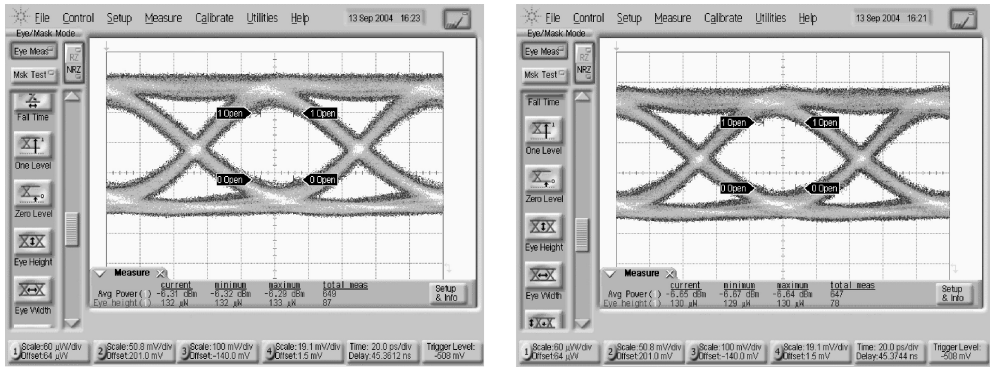

50m: best polarization **0dB** **50m**: orthogonal polarization

Figure 11.34 Measured eye diagram after 50 m of link length. The screen-shot on the left shows the best eye diagram available versus the input polarization state. The right screen-shot presents the eye diagram captured using the orthogonal polarization. The eye diagrams are almost identical, revealing any polarization effects after 50 m of link length

Figure 11.36 shows a very interesting measure of the polarization-induced pulse distortion. The link length was only 150 m and the output eye diagrams associated with the two input polarization states are quite different. The best-input polarization leads to the eye diagram on the left side, which still exhibits a satisfactory eye shaping with about a 6 dB eye closure referred to the average amplitude. The right picture shows the output of the same experimental setup where only the input polarization state has been changed to the orthogonal direction. The corresponding eye diagram is almost completely closed, leading to the estimated eye closure of about 8–9 dB. Under these conditions, the optical transmission will probably fail even using EDC correction. However, under uncontrollable input polarization states, the expected output will exhibit any eye diagram configuration between the two cases shown in Figure 11.36, leading to a large variability of pulse profile.

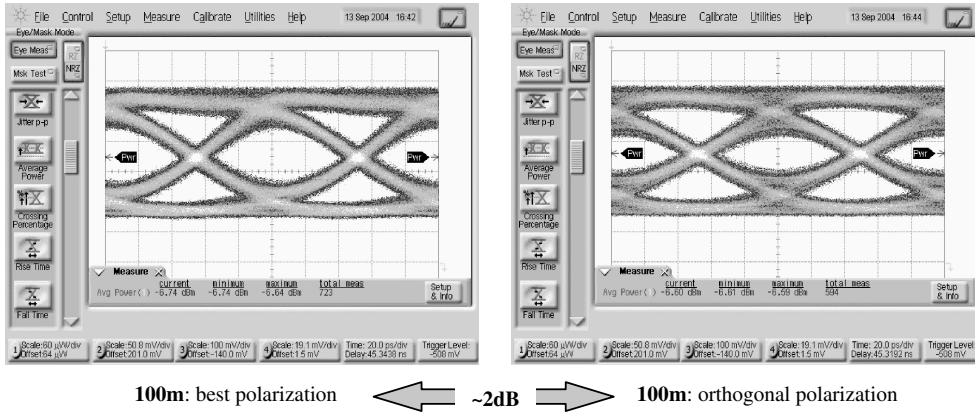

Figure 11.35 Measured eye diagram after 100 m of link length. The screen-shot on the left shows the best eye diagram available versus the input polarization state. The right screen-shot refers instead to the eye diagram captured using the orthogonal polarization. In this case, the effect of the input polarization manifests itself clearly, inducing pulse broadening. The eye diagram closure is estimated to be about 2 dB

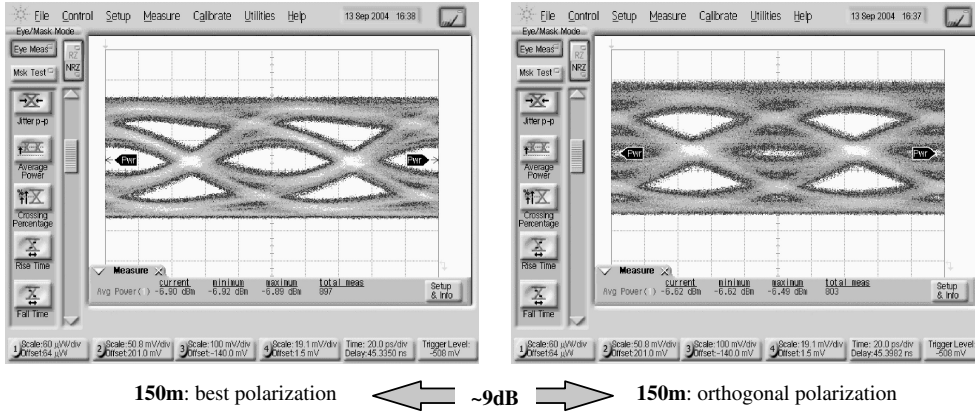

Figure 11.36 Measured eye diagram after 150 m of link length. The screen-shot on the left shows the best eye diagram available versus the input polarization state. The right screen-shot refers instead to the eye diagram captured when changing only the input polarization to the orthogonal state. In this case, the effect of the input polarization manifests itself clearly, inducing large pulse broadening and a strong eye diagram closure of about 9 dB

It is well known, for example, that in VCSEL sources the output linear polarization is not stable, leading to a time-dependent random orientation. This effect coupled with the offset launch will raise the eye diagram fluctuation after a few hundred meters.

By increasing the link length further causes the polarization effect to become more pronounced. Figure 11.37 presents the measurements of the eye diagrams and the corresponding PRBS pattern captured after 200 m of link length according to two orthogonal orientations of the input polarization. Although it is still possible to find the optimum input polarization leading to the open eye diagram after 200 m of Siecor benchmark multimode optical fiber, changing the input polarization

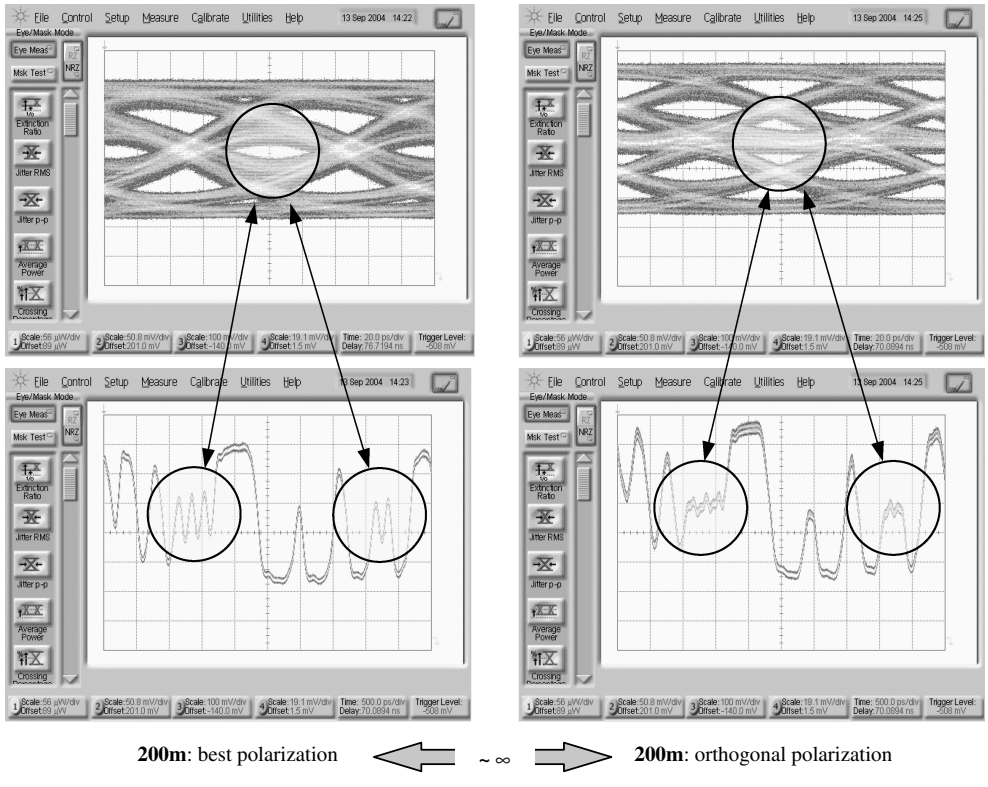

Figure 11.37 Measured eye diagram after 200 m of link length. The left side shows two screen-shots reporting the best eye diagram and a section of the corresponding PRBS patter available versus the input polarization state. The right side shows instead the eye diagram and a section of the corresponding PRBS pattern captured when changing only the input polarization to the orthogonal state. In this case, the effect of the input polarization manifests itself strongly, inducing a complete eye diagram closure. The effect of the input polarization on the pulse distortion is well represented by the corresponding highlighted sections of the PRBS pattern measured according to the input orthogonal polarizations

orientation slightly leads immediately to the link loss condition. This is well demonstrated by the right screen-shots showing the eye diagram and the PRBS pattern measured with the orthogonal input polarization state respectively. The excessive pulse broadening is then responsible for the completely closed eye diagram.

The last measure, shown in Figure 11.38, refers to the 250 m of link length. Despite the long link, properly adjusting the input polarization was still possible in order to reach the link length with the open eye diagram, as shown in the left screen-shot. It was found for the shorter 200 m case presented above that changing the polarization orientation slightly led to a completely closed eye diagram (the right side of Figure 11.37). The important conclusions of these experiments can be summarized as follows:

1. Careful adjustment of the input linear polarization orientation (best polarization state) leads to the open eye diagram, even after 250 m of Siecor benchmark multimode fiber. The same eye

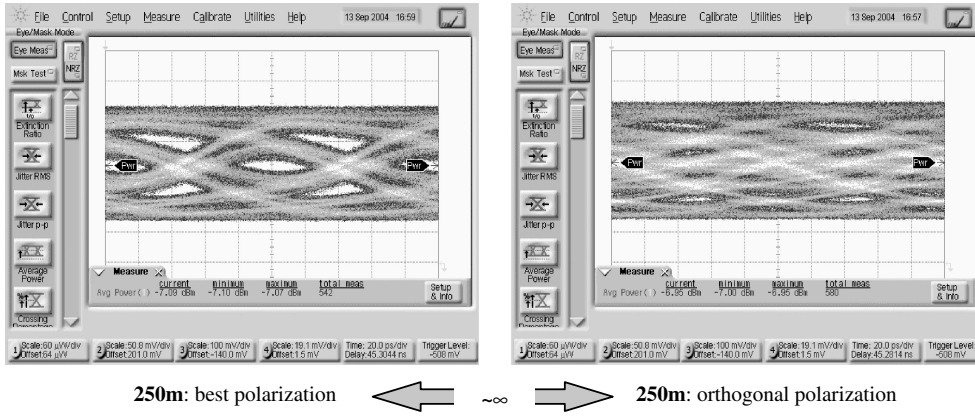

Figure 11.38 Measured eye diagram after 250 m of link length. The left side shows two screen-shots reporting the best eye diagram and a section of the corresponding PRBS patter available versus the input polarization state. The right side shows instead the eye diagram and a section of the corresponding PRBS pattern captured when changing only the input polarization to the orthogonal state. In this case, the effect of the input polarization manifests itself strongly, inducing a complete eye diagram closure. The effect of the input polarization on the pulse distortion is well represented by the corresponding highlighted sections of the PRBS pattern measured according to the input orthogonal polarizations

diagram was in general not achieved in the previous experiments where the launch polarization state was not controlled.

2. Launching the polarization orientation orthogonal to the best polarization state leads to a prematurely closed eye diagram with respect to the measurements of previous experiments where the launch polarization state was not controlled.

In conclusion, the orientation of the launching polarization affects the pulse response of multimode fiber where the standard offset launch is applied. Comparing with the same launch condition but without any polarization control, eye diagrams that are achieved under optimal launch polarization and for a given link length exhibit larger eye openings (best polarization state). Assuming an input polarization orientation orthogonal to the optimal launch polarization (worst polarization state) leads to closer eye diagrams at the same link length.

11.8.2 Controlled Offset Launch

In this section, the analysis is completed of the polarization-induced pulse distortion in the multimode fiber link operating at the multigigabit data rate, extending the measurements to controlled offset launch conditions. Since the major effects are detected at longer link lengths, as experienced with the standard offset launch, in this experiment only the 200 m length case is considered. In general, for each offset launch position two orthogonal polarizations were tested. According to the procedure described in the previous cases, first the optimum polarization associated with the best achievable optical eye diagram detected at the end section of the link length is found. Then the polarization orientation is set orthogonal to the optimum one, leading to the closest eye diagram detected at the end section of the same link. In the following measurements, the best and the worst launch polarizations will be referred to with respect to the considered multimode fiber link.

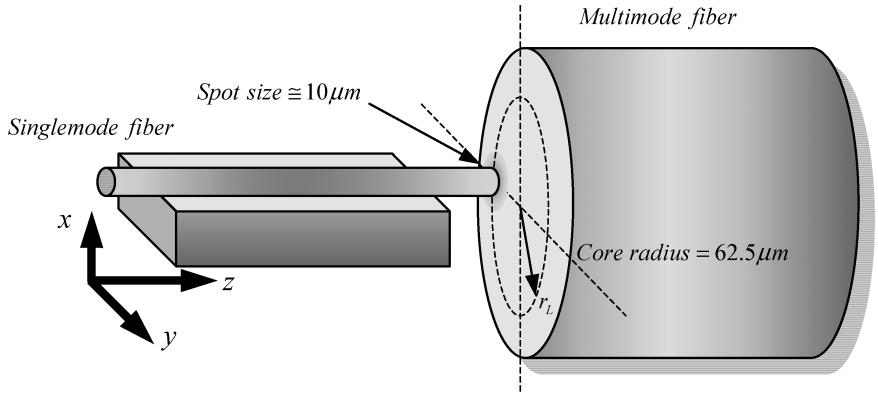

Figure 11.39 Schematic representation of the microcontrolled offset launch technique used for scanning the multimode fiber core radius with the spot size of the laser source during the polarization experiment. According to the standard offset launch specifications, the radial offset coordinate r_L for the 62.5 μm core radius must range between 17 μm and 23 μm from the fiber axis

The controlled offset launch setup is schematically represented in the Figure 11.39. The launching tool is a standard single-mode fiber jumper connected on one side only in order to provide easy laser diode coupling. The other side presents a bare cut and is manually aligned on the multimode fiber core using an accurate micromanipulator positioning laboratory tool. The laser light spot maximum emitted by the end section of the single-mode fiber is then aligned on the radial coordinate of the multimode fiber core. The mode field diameter (MFD) of the standard single-mode fiber measured at the near-field cross-section is typically 9 μm ± 1 μm, providing selective excitation of multimode fiber mode groups.

The multimode fiber under test was the Siecor benchmark sample with a 62.5 μm core radius and the standard offset launch condition must provide a light source coupling within the radial interval $17\,\mu m \leq r_L \leq 23\,\mu m$. In order to compare the standard offset launch patch cord with the microcontrolled offset launch, the following four different radial launch coordinates r_L were selected:

1. Axial launch with a nominal zero offset, $r_L = 0$
2. Radial launch with a nominal offset of $r_L = 17\,\mu m$
3. Radial launch with a nominal offset of $r_L = 20\,\mu m$
4. Radial launch with a nominal offset of $r_L = 23\,\mu m$

Figure 11.40 provides a comparison among three different launching conditions that use the same central launch coordinate, $r_L = 0$, but exhibit three different polarization angles. Apart from the best and the worst polarization orientations as usual, the 45° angle has been added. The result experienced during the central launch is quite interesting: any polarization-dependent pulse distortion can be observed. The three measured eye diagrams do not as the result of the launch polarization angle. This is explainable in terms of the axial symmetries of both the laser spot and each individual mode field.

Moving instead to a finite offset, the behavior closely resembles the measures obtained using the standard offset launch patch cord. Figure 11.41 shows the eye diagram measured assuming $r_L = 17\,\mu m$ offset and two orthogonal polarization states. The best launch polarization has been adjusted as usual to obtain the best open eye diagram. The worst launch polarization corresponds to the orthogonal direction. The relative closure of the eye diagram demonstrates the relevance of

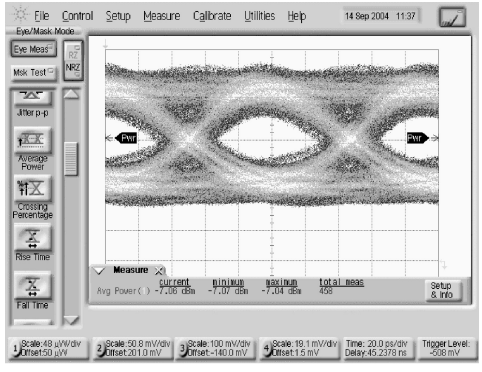

200m – Central launch: best polarization

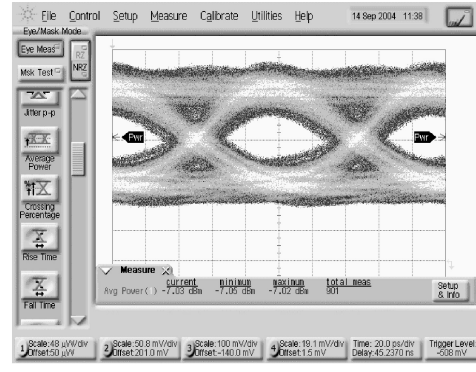

200m – Central launch: 45° polarization

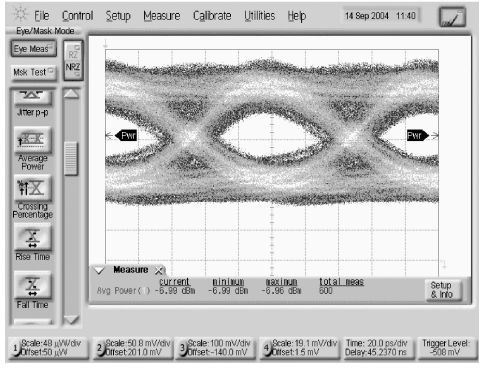

200m – Central launch: orthogonal polarization

Figure 11.40 Measurements of the eye diagram obtained after 200 m of Siecor benchmark multimode fiber using three different polarization orientations under central launch conditions. The eye diagrams look identical, showing some dependence on the launch polarization

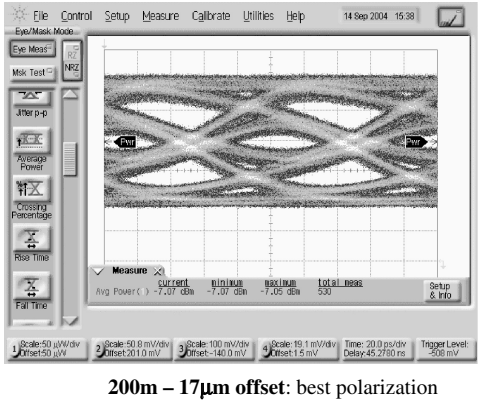

200m – 17µm offset: best polarization

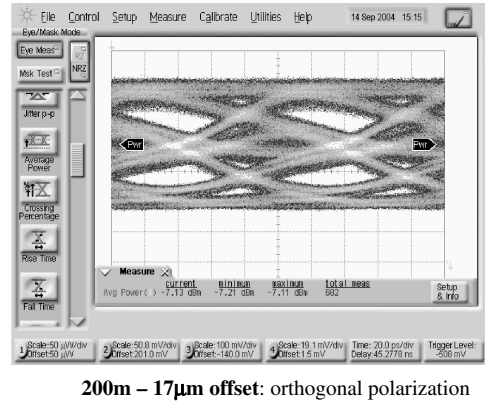

200m – 17µm offset: orthogonal polarization

Figure 11.41 The measured eye diagrams refer to the orthogonal states of the polarization assuming 17 µm offset. The eye diagram corresponding to the launch polarization orthogonal to the best orientation is completely closed. The measurement is repetitive if the launching single-mode fiber is moved to the symmetric radial offset located at −17 µm

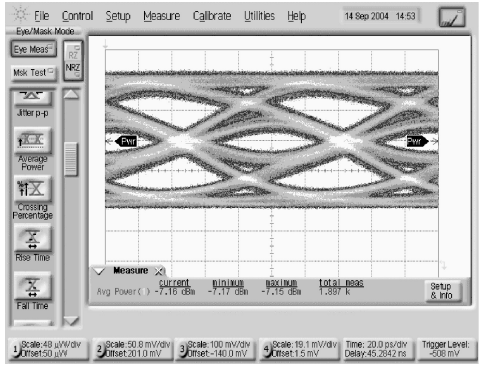

200m – 20µm offset: best polarization

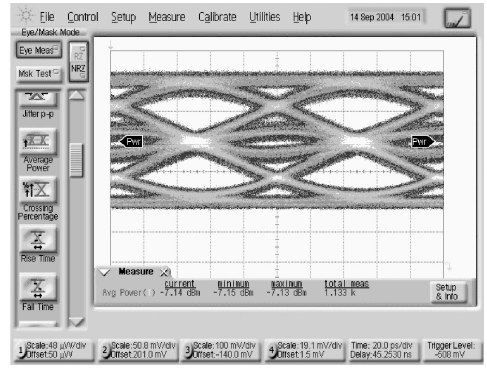

200m–20µm offset: orthogonal polarization

Figure 11.42 The eye diagrams have been measured using two orthogonal states of the launch polarization assuming 20 µm offset. The eye diagram (right) corresponding to the launch polarization orthogonal to the best orientation (left) is completely closed. As in the previous case, the measurement is repetitive if the launching single-mode fiber is moved to the symmetric radial offset located at −20 µm

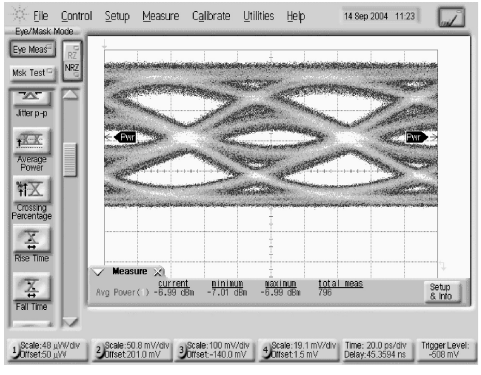

200m – 23µm offset: best polarization

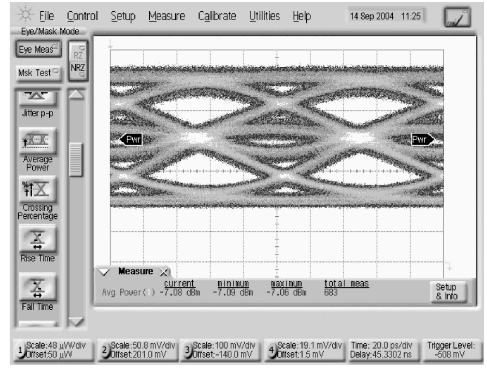

200m – 23µm offset: orthogonal polarization

Figure 11.43 The eye diagrams refer to the orthogonal states of the launch polarization assuming 23 µm offset. The eye diagram on the right screen-shot is almost closed and corresponds with the launch polarization orthogonal to the best orientation, shown on the left picture. The measurement is repetitive if the launching single-mode fiber is moved to the symmetric radial offset located at −23 µm

the input polarization in this propagation experiment. The second step moves the offset position at $r_L = 20\,\mu m$, corresponding to the middle of the launching range for the 62.5 µm multimode fiber. Figure 11.42 presents the measured eye diagram according to the two orthogonal states described above. It should be noted that the eye diagram launching the best polarization state is slightly more open than when $r_L = 17\,\mu m$ is assumed. This is of course explainable in terms of a restricted selection of different group delays coinciding with the output pulse, leading to reduced DMD contributions. The last measurement in Figure 11.43 refers to the offset position $r_L = 23\,\mu m$, corresponding to the upper value according to the launching standards. The measured eye diagram

under the best launch polarization looks quite similar to the first case where $r_L = 17\,\mu m$. The expected variation with the orthogonal input polarization is largely verified as for the other two cases.

The controlled offset measurements presented in this section were performed at Fiber Optic Laboratories, Infineon Technologies, Berlin, in September 2004. The author is grateful to Dr Joerg Kropp for conceiving the experiments, providing the related measurement setup and measuring the data. The important conclusion that emerges from these results is confirmation of the launch polarization dependencies of the pulse response in multimode fiber links excited by relatively short laser pulses (100 ps) and exhibiting offset launch conditions. The control of the launch polarization,

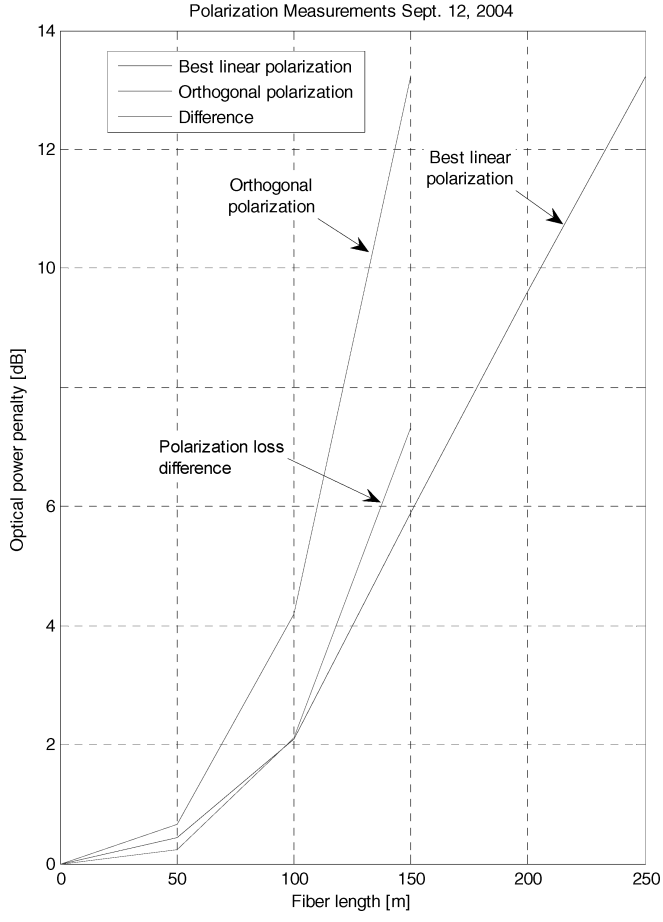

Figure 11.44 Optical power penalty expressed as the eye diagram closure measured versus increasing link length and assuming two orthogonal states of the launch polarization. The plots has been computed using the experimental data presented in the previous section regarding the polarization measurements using the standard offset launch patch cord. In addition to the eye closure data, the graph gives the relative eye diagram closure between the two orthogonal polarization states. For the link length of 150 m the relative variation of the optical power penalty reaches about 7.2 dB

the offset launch and the multigigabit pulse transmission must all be simultaneously present in order to see the effect. This is clearly demonstrated by the complete absence of any polarization-dependent effect by simply setting central launch conditions (offset null) in the above experiments.

11.8.3 Conclusions

The measurements reported in this section were performed in order to highlight the effect of the state of polarization (linear) in combination with the offset launch, connector offset and MMF link length operating at 10 GbE. The orientation of the polarization state has been changed using an Agilent polarization controller. For every fixed fiber link length, the best polarization state has been found in terms of the maximizing eye opening at the fiber end. Then the orthogonal polarization state has been launched and the corresponding eye diagram recorded.

According to the measurements, the effect of the polarization state is dramatically affecting the eye opening at longer distances. At a link length of 250 m, using the best polarization state, the eye diagram still showed some opening, but as soon as the orthogonal state was launched, the eye diagram looked completely closed. Same behavior has been noticed at shorter distances, such as 100 m, 150 m and 200 m, with a proportional increasing effect. The linear polarization state acts as a selective excitation of the higher-order modes that are not axially symmetric (azimuth dependence). The amount of power transferred to each mode depends on the overlap integral and therefore on the relative orientation between the offset direction at the launching section and the polarization orientation. Depending on the perturbation of the refractive index, the different power distributions among excited modes produce different optical pulse intensity distributions after some propagation distance. Since the linear polarization state is not fixed, but instead is a random process depending on environmental perturbations, the output eye diagram is expected to fluctuate accordingly. The amount of fluctuation in the eye diagram closure depends on the fiber length and can reach several decibels. Laser sources such as VCSEL and FP do not have a stable linear output polarization, adding more perturbation to the polarization of the launched field.

To close this section, an estimation is given of the polarization-dependent optical power penalty by measuring the relative closure of the eye diagram between the two orthogonal polarization states. Figure 11.44 shows the computed optical power penalty versus fiber length for both polarization states, assuming a standard offset launch patch cord. It is relevant that by increasing the link length the polarization effect becomes stronger, leading to an increasing optical power penalty.

In Figure 11.45 it can be seen that the important conclusion does not refer to the absolute value estimated for the eye diagram closure versus the link length; instead, the focus should be on the relative increment of the optical power penalty accumulated for each link length between the best and the worst launch polarizations. This is an indication of the expected peak-to-peak fluctuations of the eye opening, assuming random input linear polarization. The eye closure fluctuation is a monotonic increasing function of the link length and can be responsible for dramatic degradation of the link performances if the link length exceeds about 150 m.

11.9 EDC Measurements over MMF

In this section, reports are given of some of the characterization measurements of engineering samples of the electronic dispersion compensator performed at Fiber Optic Laboratories, Infineon Technologies, Berlin, during the period 2003–2004. The EDC measurements use the same experimental setup described previously in Sections 11.5 and 11.6 dealing with the reference transmission system constituted by the optical transmitter, the Siecor benchmark multimode fiber and the optical receiver. In order to present the material consistently, first the electrical performances of the sample EDC will be discussed. Then the optical compensating capabilities of the EDC using the multimode fiber link emulator discussed in Section 11.9.7 will be given. Finally, preliminary experimental

results of the EDC operation will be presented for real multimode fiber links using the reference transmission system depicted in Figure 11.1.

11.9.1 Electrical Measurements

The electrical characterization to be presented consists of the measurements of the eye diagrams generated at both the analog and digital outputs of the sample EDC when the electrical input is applied to a 10 GbE signal that is unfiltered or previously passed through the OC-48 standard filter. It is known that the EDC is realized according to the FFE-DFE equalization structure. The FFE-DFE architecture has been carefully analyzed in Chapter 10, and the general block diagram given in Figure 10.38 will be referred to here. For a given input pulse, the algorithm optimizes the weights for both the feedforward filter (FFF) and the feedback filter (FBF) in order to minimize the mean square error (MSE). The minimization of the mean square error comes through two actions: the reduction of the precursors through proper input filtering with the feedforward filter and the cancellation of the postcursors by means of the feedback filter. The equalization algorithm provides the minimum mean square error (MMSE) and not zero residual intersymbols, otherwise called zero-forcing (ZF) equalization. In addition to that, the input filtering increases the noise bandwidth and the enhanced noise power contributes to the total MMSE. The convergence algorithm is implemented into the FFE-DFE structure balance between the residual intersymbol and the enhanced noise in order to minimize the total MSE. Figure 11.45 shows the EDC output (right) after acting on the 10 GbE input electrical signal (left) provided by the pulse pattern generator. The jittered output reveals unfiltered high-frequency phase noise generated during the MMSE algorithm. The EDC output signal shown in Figure 11.45 refers to the digital samples, measured after the sampler circuit shown in Figure 10.38. In addition to the FFF equalization for input pulse precursors, it must be noted that small signals of only a few mV in amplitude, like the reported measure, demand a high gain input amplifier, which in turn increases the EDC noise figure. Once the basic functionality of the EDC working at a 10 GbE data rate has been verified using the PPG reference signal, the next step deals with the implementation of the OC-48 electrical emulation of strongly band-limited 10 GbE signals.

The 10 GbE NRZ-PRBS signal supplied from the PPG is first passed through the OC-48 filter and then input to the EDC. As seen in Section 11.7, and in particular in Figure 11.31, the output signal closely resembles the expected optical signal after about 200 m of the Siecor benchmark multimode

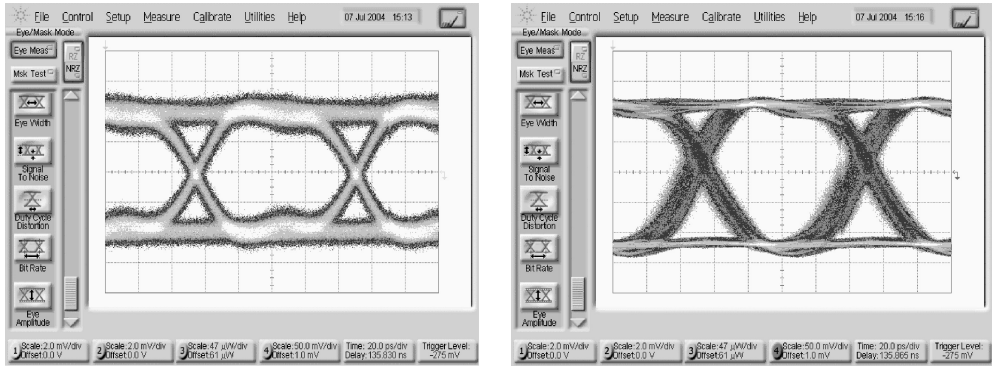

Figure 11.45 Eye diagram measurements at the EDC input (left) and output (right) when the pulse pattern generator provides the 10 GbE NRZ-PRBS signal (left). Although the EDC output signal presents a lower residual intersymbol interference, the pulse wavefront is more jittered than the input signal provided by the PPG

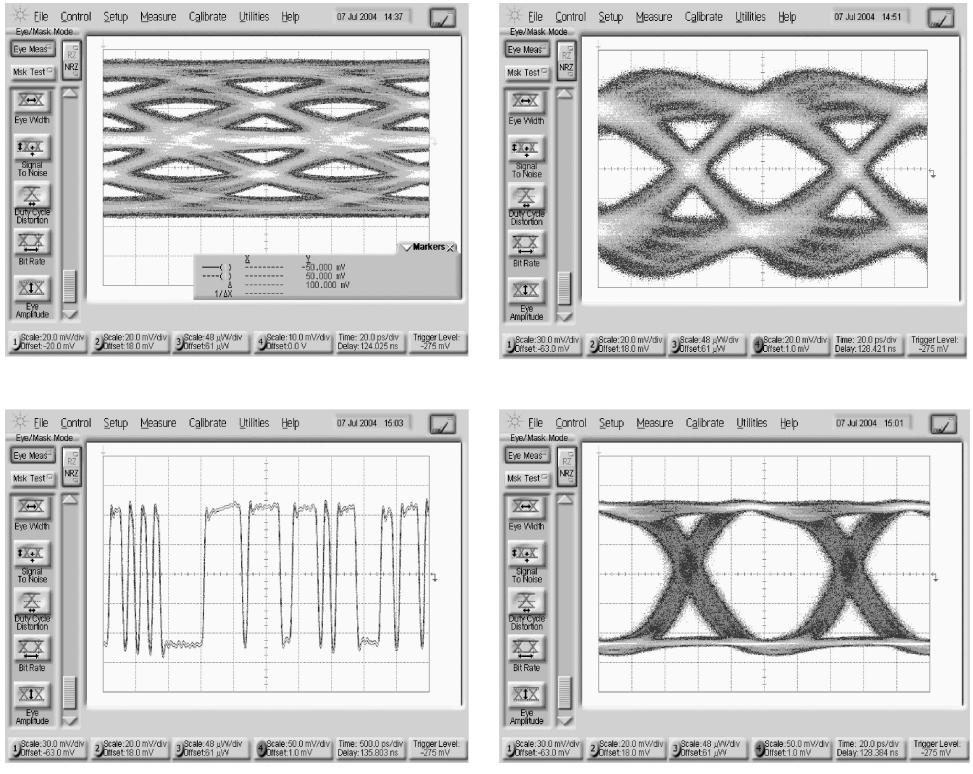

Figure 11.46 Electrical performances of the tested EDC sample using a 10 GbE input signal passed through the standard OC-48 filter. The top-left picture shows the NRZ 2^7-1 PRBS eye diagram measured at the output of the OC-48 filter. The top-right picture presents the corresponding EDC analog output. The eye diagram shows a consistent opening with small residual interference and timing jitter. The bottom-left screen-shot shows the data pattern measured at the same EDC analog output, highlighting the compensation achieved. The last picture on the bottom-right screen-shot shows the EDC digital output, after the sampler circuit

fiber. The relevant difference between the 200 m link emulation using the OC-48 electrical filter and the real multimode fiber response relies on the statistical fluctuation expected from the latter, in spite of the stationary filter response. Taking a single step forward, the electrical OC-48 test is first performed, moving into the optical modulation domain for only a second time. Figure 11.46 reports the measured performances of the EDC stimulated by the 10 GbE NRZ-PRBS electrical signal supplied from the PPG and then passed through the standard OC-48 filter. The first screen-shot on the top-left side shows the electrical eye diagram measured at the OC-48 filter. The eye diagram is completely closed, exhibiting the characteristic periodic multiple small openings. The top-right picture shows the EDC analog output, measured before the digital sampler. Referring to the EDC block diagram given in Chapter 10, Figure 10.38, the eye diagram in the top-right screen-shot has been captured after the summing node between the feedforward filter and the feedback filter, at the sampler input. Stated differently, this is still an analog signal and gives the intrinsic equalization performance, including both contributions from the two filters.

The effectiveness of the FFE-DFE architecture is self-evident from Figure 11.46, showing a good signal recovery with moderate jitter and residual intersymbol interference. In order to confirm the EDC functionality, the bottom-left picture shows the detailed NRZ-2^7-1 PRBS pattern corresponding to the EDC analog output shown in the top-right picture. The pattern is inverted, which can easily

be identified by counting seven successive zeros and six successive ones. Single time step bits are almost completely resolved, demonstrating the correctness of the FFE-DFE algorithm implemented in the tested EDC sample. The bottom-right picture shows the signal measured at the digital output of the EDC, after the sampler circuit, and corresponds to the eye diagram detected at the analog output.

The electrical test performed with the OC-48 filter gives evidence of the recovery capability of the sample EDC of strongly band-limited signals. Although the eye diagram recovered from the band-limited OC-48 electrical signal looks more than satisfactory, the bit error rate measurements raise significant performance degradation. Figure 11.47 shows the plot of the measured BER performances of both 10 GbE unfiltered signal and then the OC-48 filtered case. It is evident that the electrical sensitivity degradation is encountered by the EDC when it is solicited by the strong equalization requirement. The major reason for the degradation should be passed to the larger noise level generated by the input AGC when it is stimulated by the small band-limited single-pulse pattern sections. According to the strong frequency limitation operated by the OC-48 filter, the

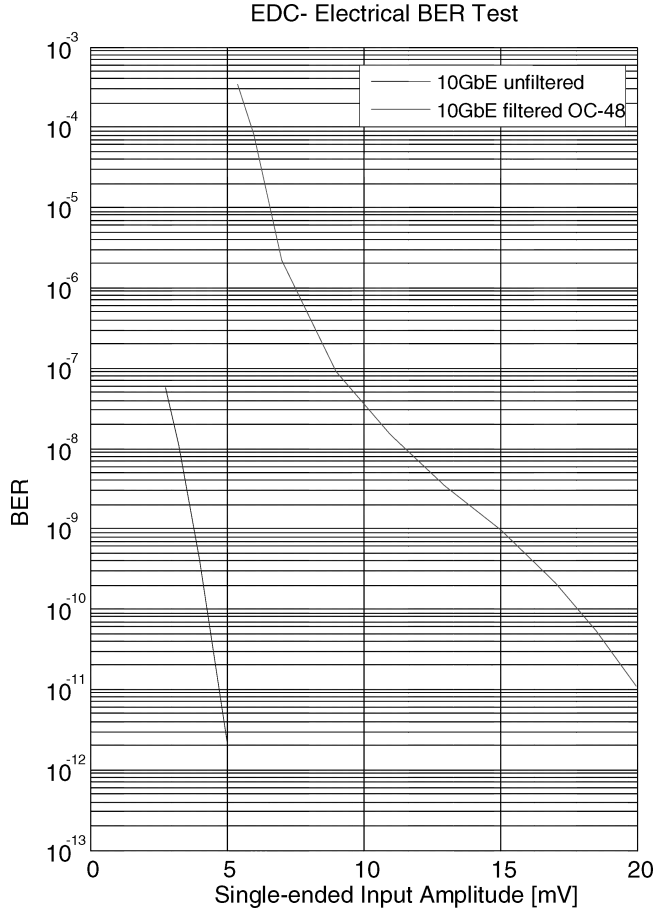

Figure 11.47 Measured bit error rate performances of the EDC with an electrical 10 GbE input datastream. The curve represents the unfiltered NRZ-PRBS measure, while the other curve refers to the OC-48 electrical filtered signal. The electrical sensitivity degradation of the EDC exceeds 12 dB evaluated at BER $= 10^{-11}$ moving from less than 5 mV to about 20 mV

input signal presents pulse sequences that are very different in amplitude, requiring a fast envelope detection capability of the AGC control circuit which in turn increases the average noise level of the EDC input stage.

The same consideration does not apply to the 10 GbE case where all the input pulse partial sequences have almost the same amplitude and the AGC is stationary. The plots in Figure 11.47 show the comparison between the measured BER versus the single-ended input sensitivity of the sample EDC. The curve represents the reference performance, assuming that the 10 GbE electrical signal from the PPG directly feeds the EDC input, as described previously. The input sensitivity reports about a 5 mV amplitude in the single-ended configuration for achieving BER $= 10^{-12}$. After passing the electrical signal through the OC-48 filter, the EDC performance degrades sensibly, requiring more than 20 mV single-ended for reaching the same BER $= 10^{-12}$, leading to about 12 dB sensitivity degradation.

The next step consists of running the same test in the optical domain, after passing the electrical OC-48 filtered signal through both the optical transmitter and receiver before inputting the same EDC sample. Further, real multimode fiber experiments will be considered. These tests are presented in the following section.

11.9.2 Optical Measurements

The block diagram of the optical link emulator achieved using the OC-48 filter to drive the optical transmitter has been presented in Figure 11.29. The EDC receives the OC-48 band-limited electrical signal detected from the optical receiver. The difference from the previous electrical test consists in the additional noise contributions generated through the electrical–optical–electrical double conversion. In conclusion, the electrical signal presented to the EDC input is noisier than the corresponding electrical case and, in some instances, even more band-limited due to the additional filtering operated by the optoelectronic conversions. Figure 11.48 presents the complete measurement acquisitions for this experiment. The pictures correspond to the same electrical test discussed in the previous section. The top-left picture shows the optical eye diagram of the 10 GbE NRZ 2^7-1 PRBS signal passed through the OC-48 filter and feeding the optical transmitter. The screen-shot shows the optical signal detected by the broadband optical head of the Agilent DCA. The similarity with the corresponding electrical response in Figure 11.46 is very good, revealing that the optical transmitter does not contribute to any significant additional filtering. Despite that, the analog output of the EDC shows sensible degradations with respect to the electrical case presented in Figure 11.46, and the equalized eye diagram shows higher jitter and residual intersymbol interference. A similar conclusion holds even for the eye diagram measure at the digital output of the EDC shown in the bottom-right picture. Compared with the corresponding electrical test response in Figure 11.46, much more jitter can be seen in this case, even if the amplitude is almost hard-limited by the digital circuit. This is one of the most important points of the EDC design and related system performances. The clock recovery circuit should be able to extract the clock frequency from the equalized analog eye diagram without incurring high phase noise using a narrowband phase lock loop filter.

The two last pictures shown in Figure 11.48 give the same section of the PRBS pattern at the input and at the analog output of the EDC. It is interesting to verify the single-bit equalization procedure worked out by the FFE-DFE architecture in the sample EDC. As expected, longer uniform bit sequences do not require significant equalization due to the lower convolution effect with the narrowband impulse response of the OC-48 filter. The shortest pulse sequences, and in particular the isolated single pulses, are instead strongly affected by the broad pulse convolution and require the maximum amount of equalization in order to remove long precursors and postcursors. The effect of the FFE-DFE structure is quite evident by comparing the upper and lower screen-shots in Figure 11.48. Almost completely absent data transitions in the input sequence are efficiently restored in the analog output pattern. This is particularly evident when examining the fast sequence 010101 at the end of the pattern period, which just precedes the longest 1111111 sequence.

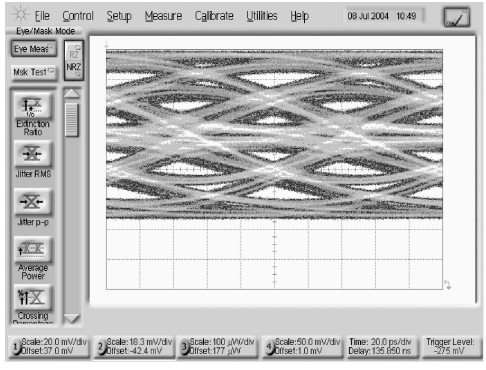

OC-48 filtered optical eye-diagram

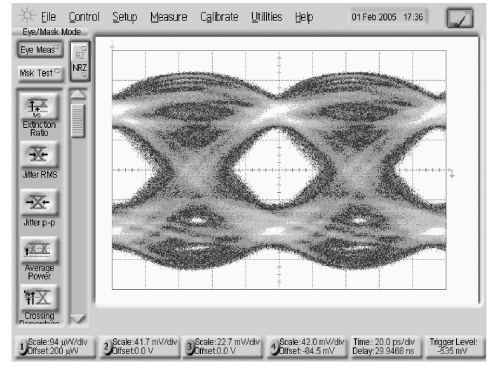

EDC analog output

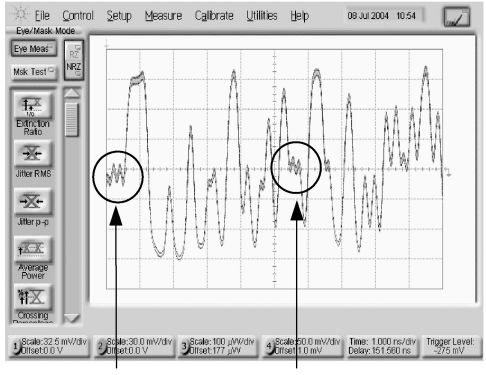

OC-48 filtered pattern – EDC input

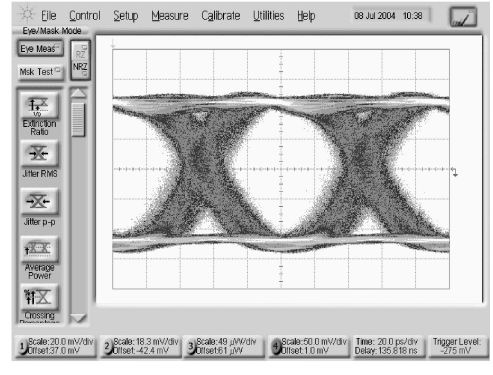

EDC digital output

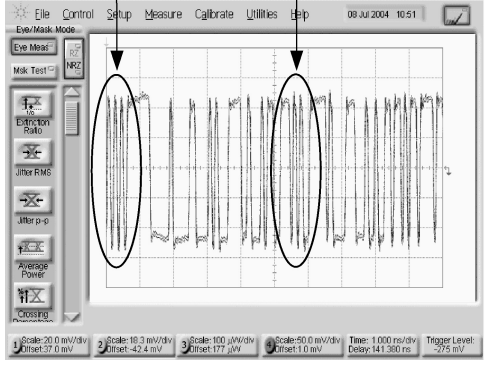

OC-48 filtered pattern – EDC output

Figure 11.48 Measurements of the OC-48 optical link emulation enabling the EDC feature. The top-left picture shows the EDC input eye diagram obtained after passing the 10 GbE PRBS through the OC-48 electrical filter and driving the optical transmitter. To the top-right is shown the EDC analog output, while the EDC digital output is shown below. The center and bottom left pictures show the PRBS pattern section captured at the input and output of the EDC respectively

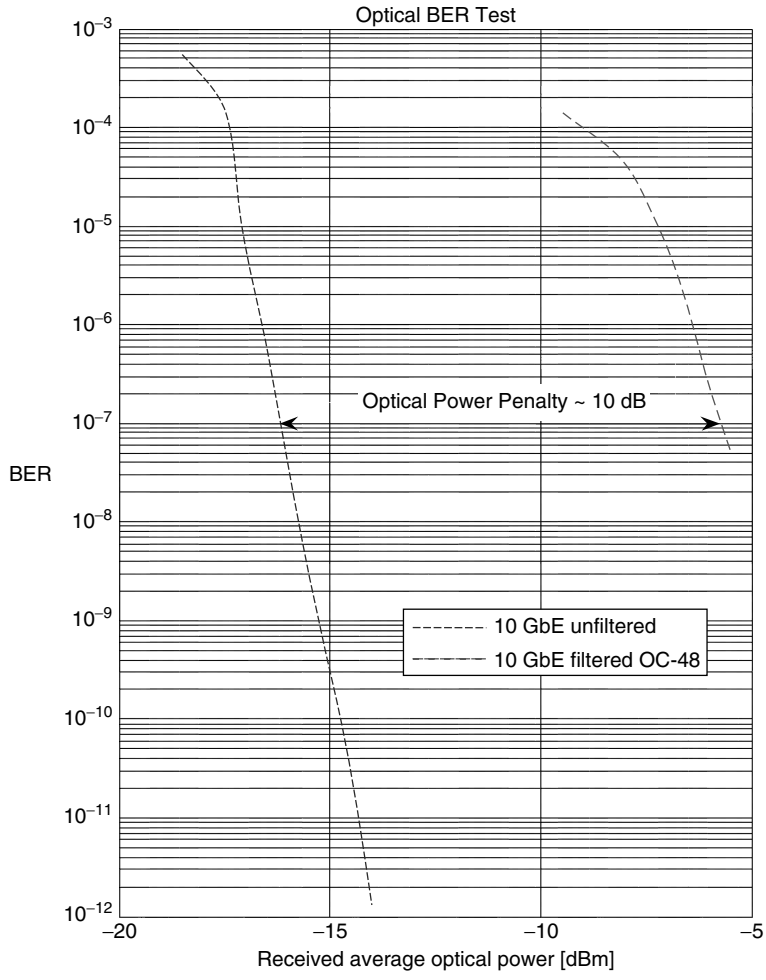

Figure 11.49 Measurement of the bit error rate performance of the sample EDC operating on the OC-48 optical link emulation. The curve shows the BER measure, assuming an optical link back-to-back configuration operating at 10 GbE. The other curve shows the same configuration when the optical transmitter is fed by means of the OC-48 electrical filter. The accumulated optical power penalty between the two transmission experiments can be estimated to be about 10 dB at BER $= 10^{-7}$

Due to strongly degraded optical signals observed in both cases of OC-48 filtering and long link lengths, EDC operation was quite stressed, including the high dynamics requirement in the first-stage amplifier (AGC). Due to an AGC dynamic demand, a relevant phase shift has been observed in all optical testing. Figure 11.49 presents the bit error rate calculation based on the current optical measurements. It is interesting to compare the reference back-to-back optical performance including the EDC but using a full-bandwidth optical link with the OC-48 emulation but inserting the standard filter in front of the optical transmitter. The result shows a consistent performance degradation of the emulated multimode fiber link with about 10 dB of optical power penalty evaluated at BER $= 10^{-7}$. It should be noted that lower BER values were not achieved in that experiment using the optical emulation link.

Once the sample EDC operation had been characterized using both electrical and optical band-limited transmission using OC-48 filter emulation, the step forward is represented by the EDC implementation into real multimode fiber links. According to the experimental setup characterized so far, the Siecor benchmark multimode fiber will continue to be used. In addition, a second sample will be tested with a 62.5 μm core diameter multimode fiber manufactured by Corning Glass Corporation in late 1998. This second fiber sample has not been used as much for laboratory measurements as the Siecor benchmark sample, but it represents a valid alternative with a better multimode fiber response and a larger modal bandwidth. In the following, the Siecor benchmark multimode fiber sample will be used first. Figure 11.50 presents the eye diagrams measured at the input and output ports of the sample EDC after 100 m and 200 m respectively of the Siecor benchmark multimode fiber. It is evident that strong eye diagram degradation is encountered between 100 m and 200 m at the optical receiver output, as shown in the upper trace of both screen-shots shown in Figure 11.50. After the first 100 m of link length, the eye diagram still presents an open profile. However, after the subsequent 100 m of link length the eye diagram looks completely closed. The corresponding EDC digital output is shown on the respective bottom traces.

Although the eye diagram measured at the EDC input after the total link length of 200 m is completely closed, the digital equalizer is still capable of recovering an open eye diagram at the digital output. The problem is represented by the very large amount of jitter shown by the EDC digital output as a testimonial of the limiting equalization capabilities. Link distances longer then 200 m have never been achieved stably using the sample EDC over the Siecor benchmark fiber.

To conclude this section on the optical compensation capabilities of the sample EDC operating over the multimode fiber, it should be noted clearly that the Siecor benchmark fiber behaves very badly, even if it is still compliant with the IEEE standard requirements for 10GBASE-LRM transmission. It may represent a limiting case but it is still a valid example of the multimode fiber channel used for testing the electronic dispersion compensator performances at 10 GbE. For the time being, the tested EDC samples were not capable of passing the target reach of 300 m over this multimode fiber. The best performance achieved refers to only 200 m, as reported in Figure 11.50. High sensitivity of the link performances exists when the multimode fiber length exceeds 200 m, requiring additional solid adaptation capabilities of the implemented EDC. Under some circumstances, during laboratory verification, longer link lengths have been achieved, but the performances were very unstable. A slight perturbation of the experimental setup led in fact to

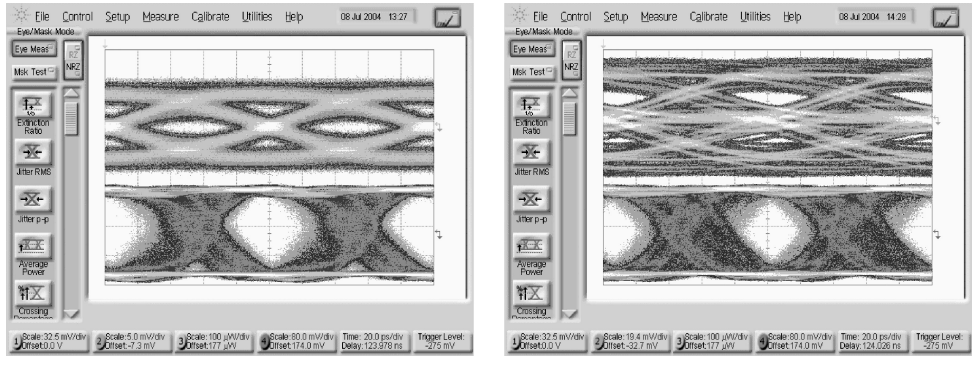

Figure 11.50 Measured eye diagram at the input (top trace) and digital output (bottom trace) of the sample EDC for the benchmark multimode fiber of link lengths 100 m and 200 m respectively. Although both equalized eye diagrams are both recognizable, the very large amount of jitter shown by the eye diagram reconstructed after 200 m of link length looks quite unpractical

immediate link loss conditions. It can be concluded instead that up to 200 m the link is satisfactorily stable, raising the confidence level for this electronic compensation solution.

In order to have a different comparison term for the EDC performances over the multimode fiber link, a second sample of the multimode fiber was used for link test experiments at 10 GbE. This is briefly presented in the following section.

11.9.3 Using a Different Multimode Fiber

The multimode fiber to consider in this section belongs to the same standards of the Siecor benchmark fiber used so far, but it exhibits a more regular refractive index profile with consequently a lower DMD and larger modal bandwidth. First a short overview is given of the single-pulse response according to the several link lengths available, using the same optical transmitter and receiver adopted for all the previous measurements. In other words, the only part that is changed in this second set of experiments is the multimode fiber link. The multimode fiber was available in three different lengths, namely 60 m, 120 m and 240 m, providing seven multiple link length configurations, as shown in Figure 11.51.

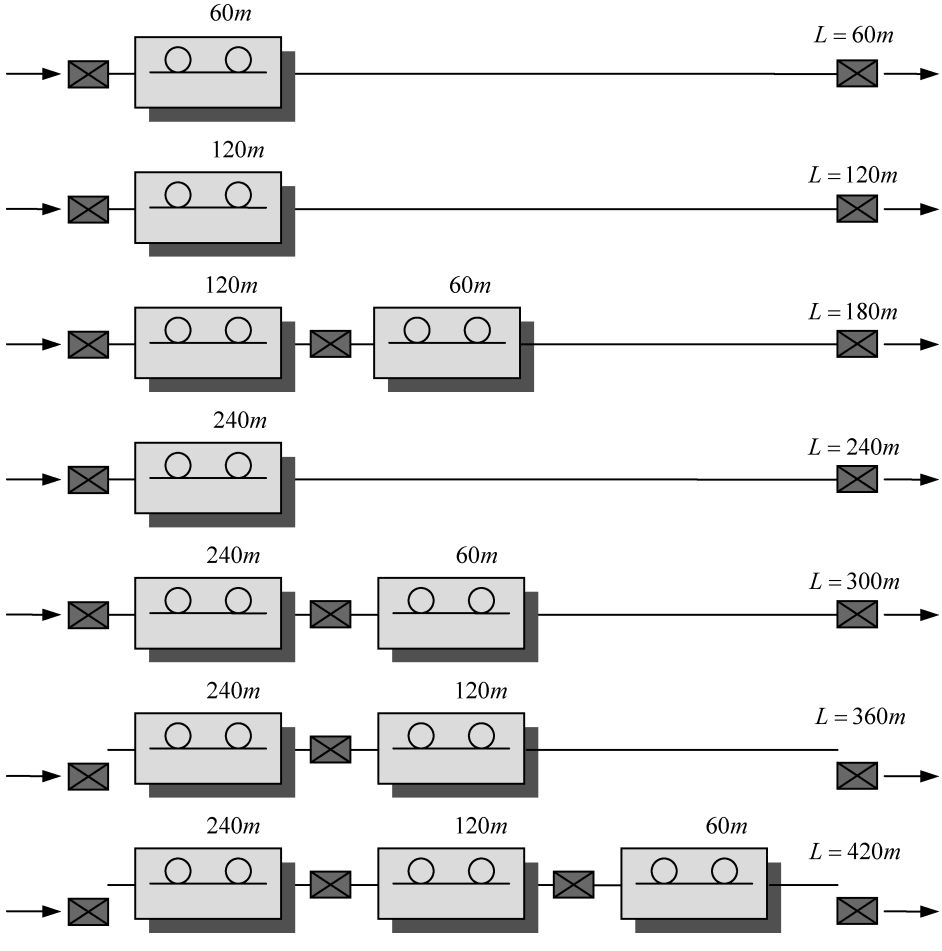

Figure 11.51 Configurations of the multimode fiber link lengths used in the transmission experiments

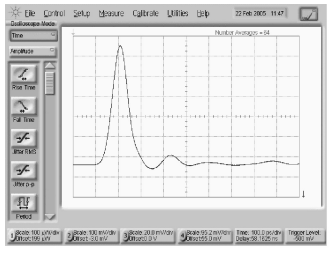

Reference

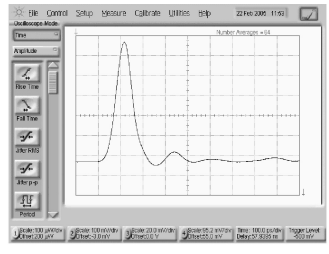

$L = 60m$

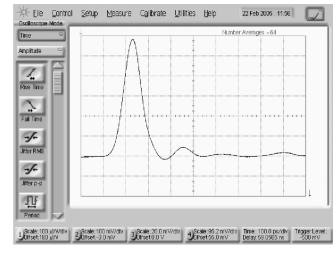

$L = 120m$

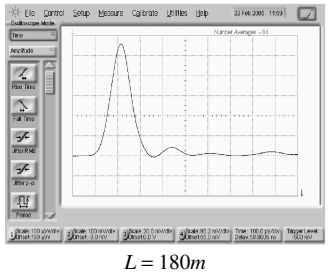

$L = 180m$

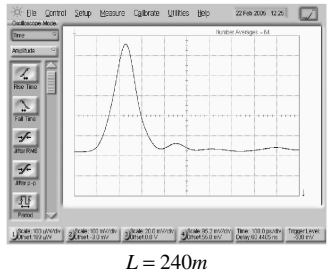

$L = 240m$

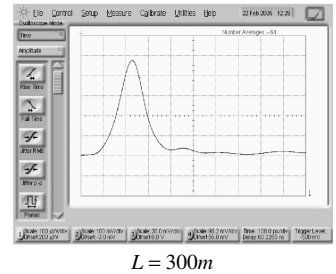

$L = 300m$

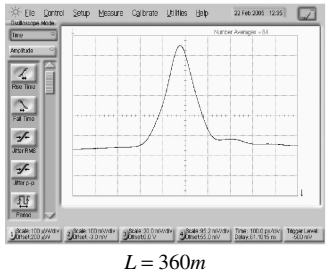

$L = 360m$

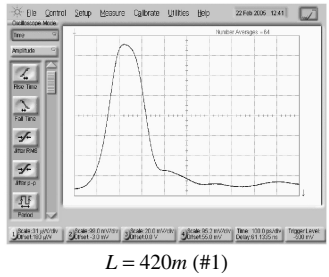

$L = 420m$ (#1)

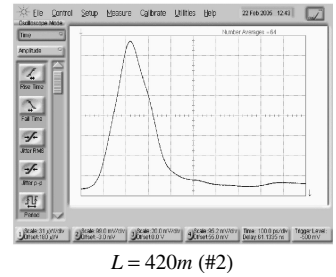

$L = 420m$ (#2)

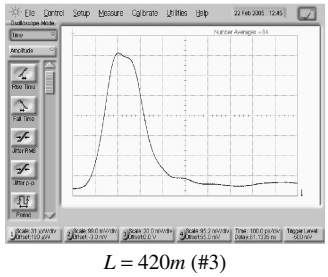

$L = 420m$ (#3)

Figure 11.52 Measure pulse response versus increasing lengths of the multimode fiber used in the second experimental setup. The pulse responses have been collected for every 60 m link length step, as reported in the layout in Figure 11.51. The propagation performances of this second fiber set are better than those of the Siecor one, which can easily be concluded by comparison with similar pulse responses given in Figures 11.18 to 11.25

Figure 11.52 shows a close-up view of the single-pulse response measured at each optical link configuration. The first picture on the top-left reports the reference transmitted pulse evaluated in the back-to-back layout. This second fiber set exhibits a larger bandwidth, which can easily be deduced by observing the single-pulse profile detected after the first two link lengths of 60 m and 120 m respectively. Up to the 300 m link length, the pulse response looks very similar to

the reference one, with smoothed profile variations but still preserving the original shape. The pulse starts to lose the original shape after almost 360 m, showing about twice the width and having a more symmetric triangular shape. At the maximum allowable link length of 420 m, three different pulse responses are evaluated according to fiber twisting and manipulations. The pulse width looks more than twice the size of the original one with either a triangular or a trapezoidal profile.

Figure 11.53 presents the two different sections of the measured 2^7-1 PRBS pattern at the optical transmitter output section and after 240 m of link length. The link bandwidth is still large enough to resolve the single-pulse transitions without losing the corresponding eye diagram opening.

To complete the experimental characterization of the 10 GbE transmission link using the second set of multimode fiber, in Figure 11.54 are shown the optical eye diagrams measured at the fiber output and at the EDC analog and digital outputs respectively for each link length step. It is evident that, although longer lengths of fibers correspond to closer eye diagrams, the detected

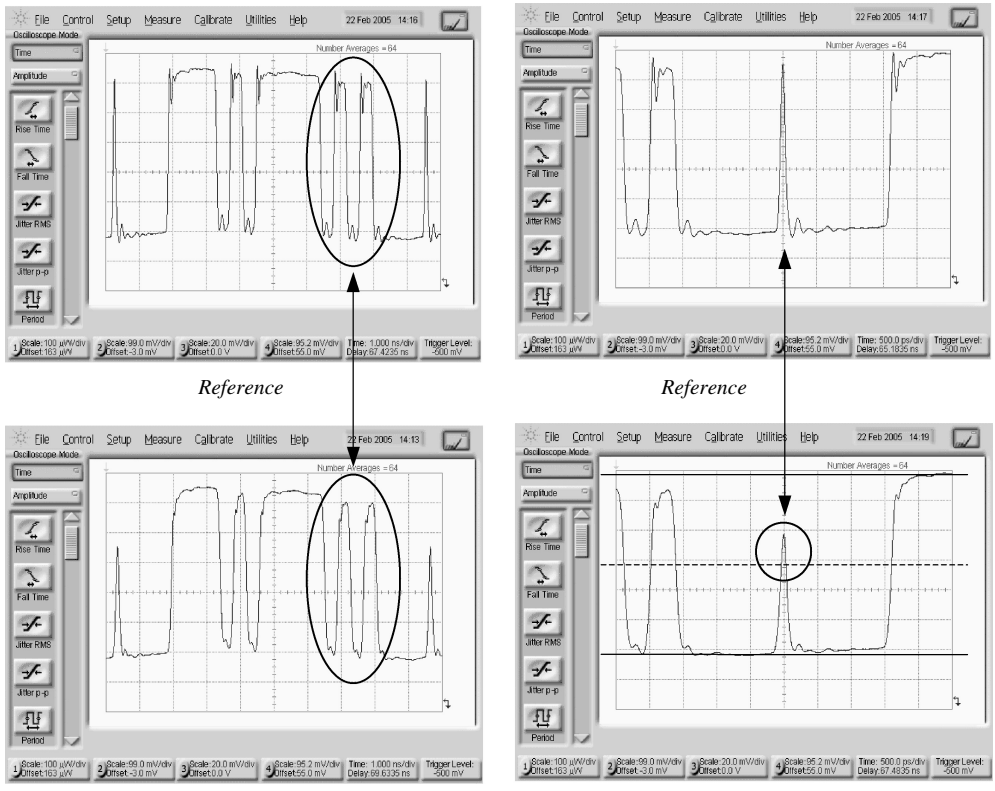

Figure 11.53 Measured 2^7-1 PRBS pattern sections at the optical transmitter output after 250 m of link length. The link bandwidth is still large enough to resolve the single pulse with sufficient amplitude to achieve open eye diagrams. This is shown qualitatively in the bottom-right screen-shot, where the single pulse crosses the mid level of the signal amplitude. The left screen-shots refer to the double bit transitions sequence 00110011

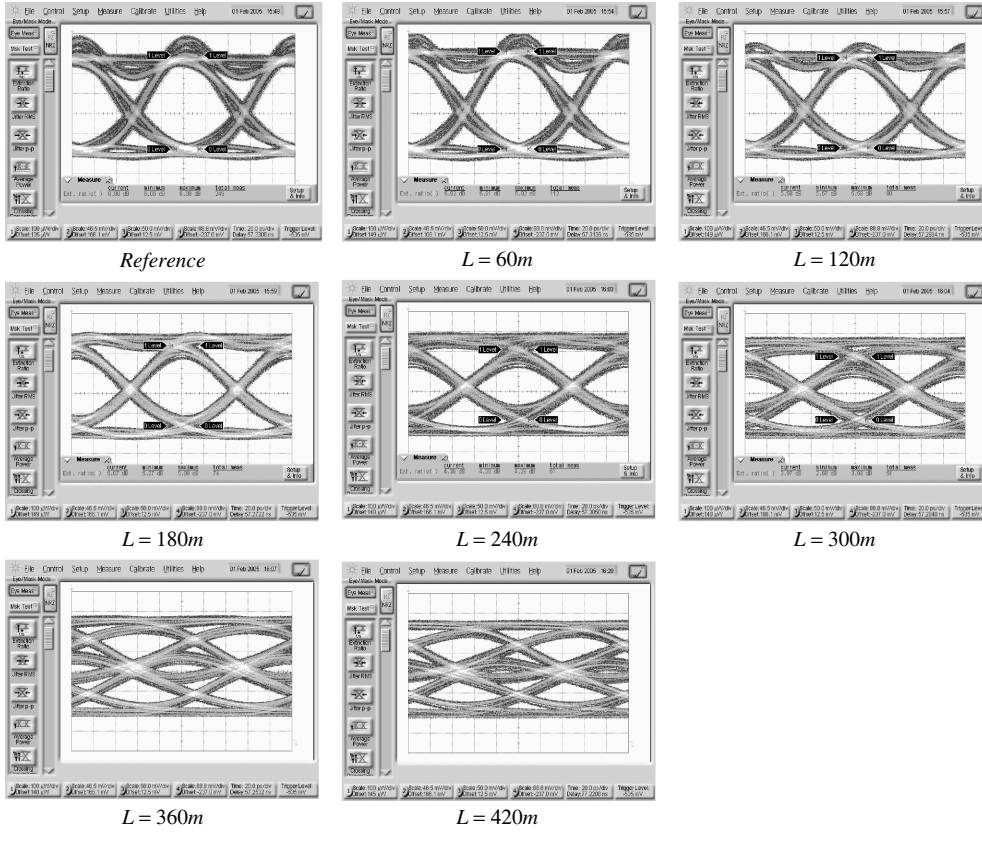

Figure 11.54 Measured eye diagrams at the multimode fiber outputs for each link length step. The measured signals correspond to the single pulse shown in Figure 11.53. After the 300 m link length, the modal bandwidth allows a still reasonable eye diagram opening

signal after 300 m is quite satisfactory in terms of eye openings, as expected from the single-pulse measurements.

The eye diagram available at the EDC analog output has been detected only for the target link length of 300 m. In order to document the equalization capability of the EDC under low signal conditions for 300 m of link length, the received average optical input power has been reduced using the optical attenuator and the corresponding analog output of the EDC has been recorded. Figure 11.55 shows these results. The additive noise contribution is evident, determining almost proportional eye diagram closure. This is an indication that the equalization algorithm should not be affected by the amount of input equivalent noise. In other words, the residual intersymbol amplitude at the equalizer output does not seem to change consistently at different noise-to-signal ratios. It should be noted that the eye diagram measurements given in Figure 11.54 have been detected directly at the fiber end, before the optical receiver, using the 20 GHz optical head of the DCA. The corresponding signal at the EDC input instead suffers an additional small bandwidth reduction operated by the optical receiver frequency response.

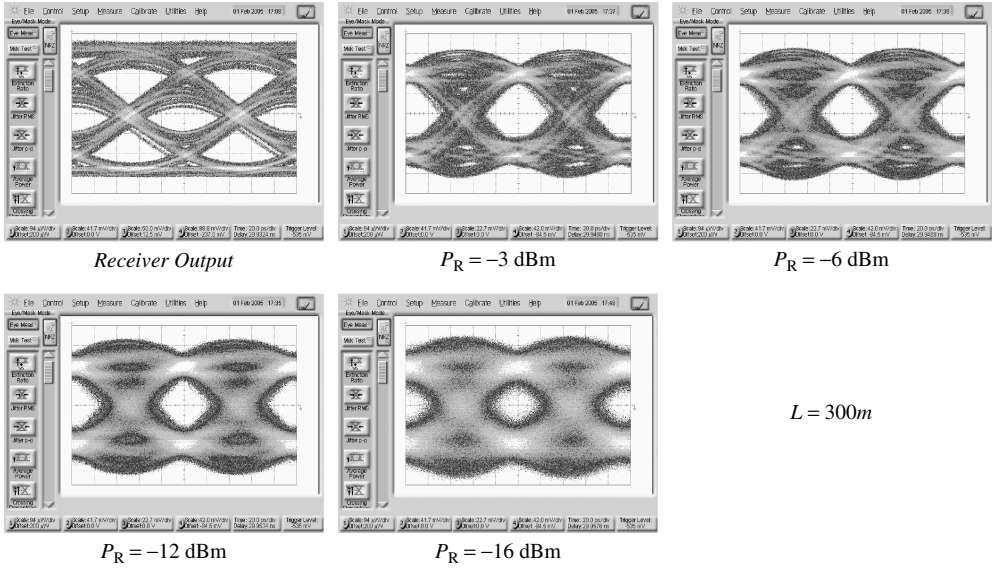

Figure 11.55 These pictures report the eye diagrams measured at the EDC analog output versus different average input optical power levels for the fixed link length of 300 m. The relative increasing noise contribution to the eye diagram closure is evident by reducing the average optical power. The input stage AGC in fact tends to maintain a constant output signal level, providing proportional noise amplification. Assuming independent statistical processes, the additive noise and the intersymbol distributions convolve together, leading to the joint statistical distribution

The last set of measurements given in Figure 11.56 refer to the eye diagram collected at the digital output of the sample EDC versus increasing multimode fiber link lengths at the fixed received average input optical power $P_R = -6$ dBm. The eye diagrams look increasingly jittered according to the compensating effort for the increasing amount of intersymbol interference. The tested transmission was properly linked to the maximum length available of 420 m, largely exceeding the target reach of 300 m. It should be remembered, however, that these promising results have been obtained with the second set of multimode fiber samples, with a better modal bandwidth response.

To conclude this section, Figure 11.57 gives the bit error rate performance evaluated for the target reach of 300 m versus the receiver input average optical power level. The transmission system experiment succeeded by showing the measured sensitivity of $P_R = -13.4$ dBm at BER $= 10^{-12}$.

These considerations close the discussion regarding the transmission system experiments devoted to understanding the compensation capabilities of the FFE-DFE electronic dispersion equalizer implemented in multigigabit transmission over multimode fibers. The results presented have been achieved using two different multimode fiber sets, with different modal responses. The first measurements reported used the Siecor multimode fiber samples that were appointed as the benchmark fiber for the critical responses achievable and the related stressed operating condition demanded for equalization techniques. The second multimode fiber sets used for transmission experiments presented instead relatively larger bandwidths, leading to simpler equalization conditions in order to reach the target link length of 300 m. It is remarked, however, that both fibers used in the testing environment were compliant with ISO/IEC 11801 specifications for the 62.5 μm core diameter multimode fibers.

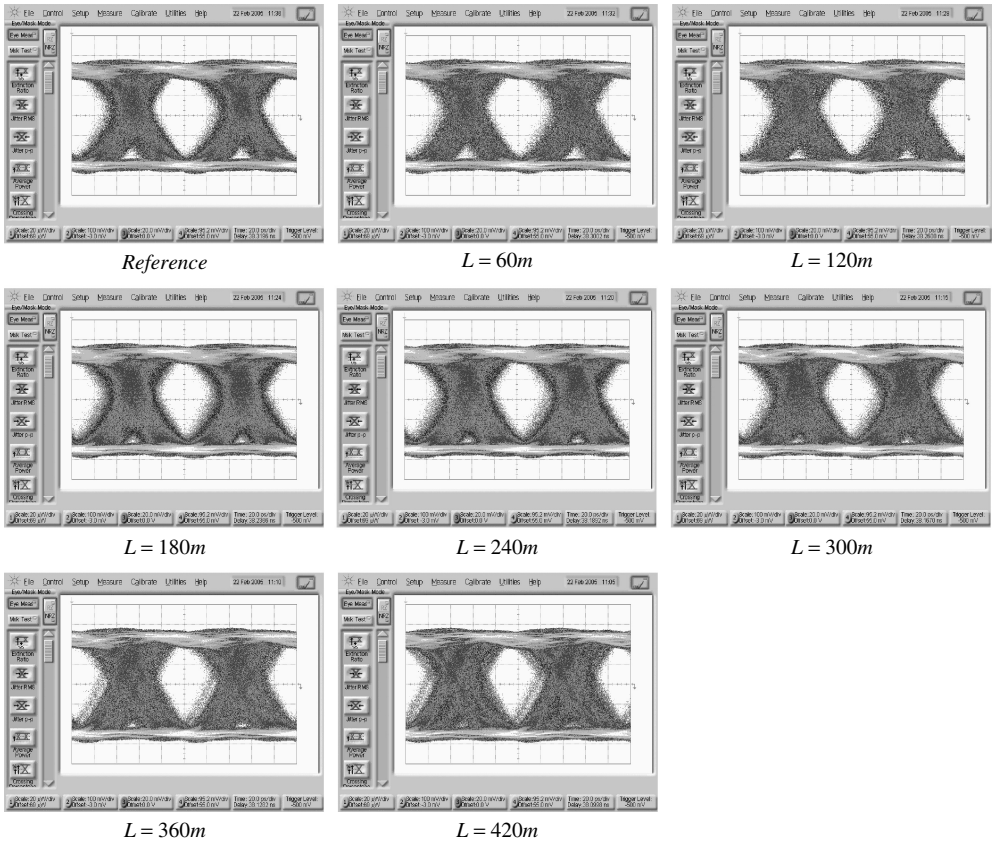

Figure 11.56 These pictures represent the eye diagram measured at the digital output of the sample EDC versus increasing link length, assuming a 60 m step and fixed received average input optical power $P_R = -6$ dBm. The corresponding eye diagrams evaluated at the analog output of the sample EDC have been shown in Figure 11.54 for the same link lengths. The increasing residual intersymbol interference translates into corresponding increasing jitter

11.10 Concluding Remarks

This chapter attempted to give an overview of the large experimental data collected during 10 GbE transmission experiments using multimode fibers. Fiber response characterization has been presented as well as direct modulated laser transmitters and PIN diode receivers. These components are intended for large distribution in the metropolitan area fast access network. Consequently, although they are required to perform at a 10 Gbs data rate, they must be cheaper than equivalent Telecom market devices. They are intended for the fiber-to-the-home (FTTH) end-user and must be easily assembled into hot-swappable small-form factor (SFF) optical modules for personal computer, gigabit Ethernet router and network server applications. It has been remarked several times that the multimode fiber is not in principle the most suitable optical transmission medium to accomplish multigigabit links, but they have largely been installed in the metropolitan area since the beginning of the 1980s and the increased bit rate demands must today relay on those media. At least alternative

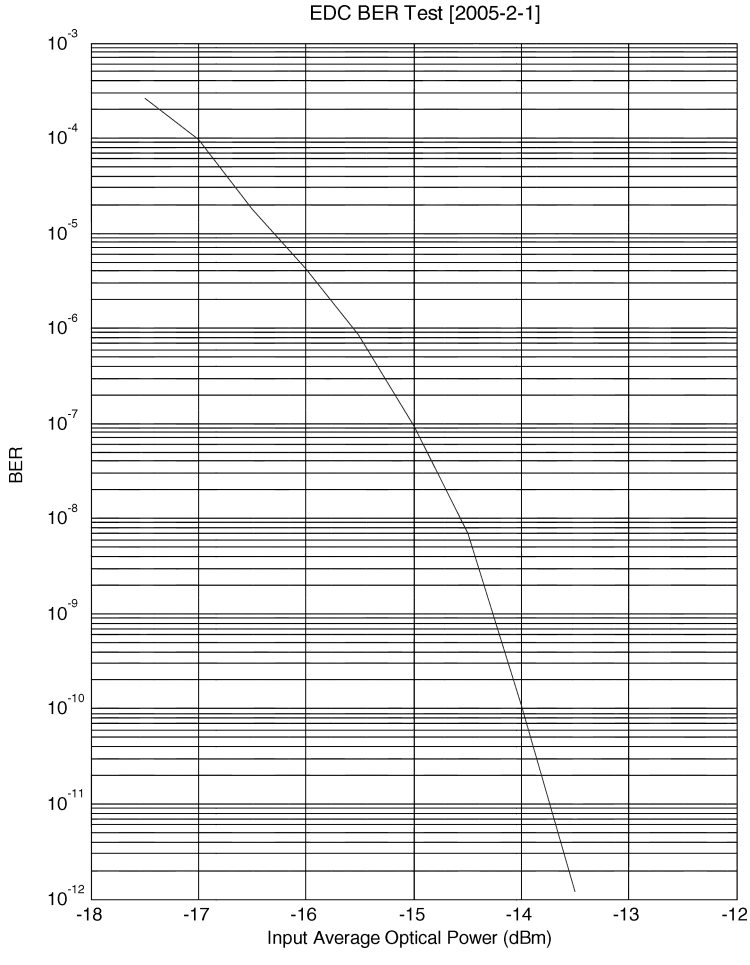

Figure 11.57 The plot reports the measured bit error rate versus the input average optical power at the receiving end section of the 300 m multimode fiber link length. The sample EDC provided the required pulse compensation, leading to the system sensitivity $P_R = -13.4\,\text{dBm}$ at $\text{BER} = 10^{-12}$

cheap solutions should be available using multimode fibers for linking several hundred meters at 10 GbE standards. This is the task of the upcoming IEEE 802.3 10GBASE-LRM standard.

The measurements reported in this chapter give a clear indication that the 10GBASE-LRM target application can be achieved using the electronic dispersion compensation (EDC) technique based on the FFE-DFE architecture. These powerful integrated circuits are beginning to be available on the market at the present time and several leading IC companies are fully engaged in this race. Due to the small-form factor standards requirements for optical modules, these ICs must be as small as possible and they must be compliant to very demanding power consumption requirements. Today, sample EDC techniques are realized using 90 nm CMOS technology and are available in small 5×5 mm or 7×7 mm square packages using ball grid array (BGA) technology, consuming less than 1 W. It is very likely that within a short time (mid-2006) the first commercially available SFF optical modules compliant with the 10GBASE-LRM standard will be on the market for field trial purposes of leading optical system manufacturers and 10GbE service providers.

Bibliography

Agrawal, Govind P., *Nonlinear Fiber Optics*, Academic Press, 1995. (**Chapters 3, 4, 5, 7**)

Belfiore, Carlos A. and Park, John H., 'Decision Feedback Equalization', *Proceedings of the IEEE*, **67**(8), 1979. (**Chapter 11**)

Bic, J. C., Duponteil, D. and Imbeaux, J. C., *Elements of Digital Communication*, John Wiley & Sons, Ltd, 1991. (**Chapters 1, 9**)

Malitson, I. H., 'Interspecimen Comparison of the Refractive Index of Fused Silica', *J. Optical Society of America*, **55**, 1965, 1205–1209. (**Chapter 3**)

Marcuse, Dietrich, *Theory of Dielectric Optical Waveguides*, Academic Press, 1991. (**Chapters 3, 4, 5, 7**)

Neumann, E. G., *Single-Mode Fibers*, Springer-Verlag, 1988. (**Chapters 3, 4, 5, 7**)

Papoulis, A., *The Fourier Integral and Its Applications*, McGraw-Hill, 1987. (**Chapters 4, 5, 8, 9**)

Papoulis, A., *Probability, Random Variables and Stochastic Processes*, McGraw-Hill, 1991. (**Chapters 8, 9**)

Ramo, S., Whinnery, John R. and Van Duzer, Theodore, *Fields and Waves in Communication Electronics*, 3rd edition, John Wiley & Sons, Ltd, 1994. (**Chapter 2**)

Römer, H., *Theoretical Optics, An Introduction*, John Wiley & Sons, Ltd, 2005. (**Chapter 8**)

Salz, J., 'Optimum Mean-Square Decision Feedback Equalization', *The Bell System Technical Journal*, **52**(8), 1973. (**Chapter 10**)

Simons, Rainee N., *Coplanar Waveguide Circuits, Components and Systems*, John Wiley & Sons, Ltd, 2001. (**Chapter 2**)

Snyder, Allan W. and Love, John, *Optical Waveguide Theory*, Chapman and Hall, London, 1983. (**Chapters 1, 3, 4, 5, 7, 11**)

Standard: Bellcore-Telcordia CR-253-CORE, March 2002. (**Chapters 1, 11**)

Standard: IEEE 802.3aq 10GBASE-LRM, Draft 2.0, March 2005. (**Chapters 6, 10, 11**)

Standard: IEEE 802.3aq, Gigabit Ethernet Standard, Draft 5.0, May 2002. (**Chapter 1**)

Standard: Fiber Channel, FC-PI, September 2001. (**Chapter 1**)

Standard: ISO-IEC 11801, 2002. (**Chapter 6**)

Standard: ITU-T G.957, October 1999. (**Chapter 1**)

Standard: ITU-T G.651, September 2000. (**Chapter 6**)

Standard: ITU-T G.691, October 2000. (**Chapters 1, 8, 11**)

Wilmsen, C., Temkin, H. and Coldren, L. A., *Vertical Cavity Surface-Emitting Lasers*, Cambridge University Press, 2001. (**Chapter 1**)

Multi-Gigabit Transmission over Multimode Optical Fibre: Theory and Design Methods for 10GbE Systems Stefano Bottacchi

ISBN: 0-471-89175-4

Index

Multi-Gigabit Transmission over Multimode Optical Fibre: Theory and Design Methods for 10GbE Systems Stefano Bottacchi

ISBN: 0-471-89175-4